www.bcri.ie

BCRI 2012

Proceedings of

Bridge and Concrete Research in Ireland Conference

6-7 SEPTEMBER 2012

Editors: Colin Caprani, Alan O'Connor
Assistant Editors: Paul Archbold, Ken Gavin, Niall Holmes, Jamie Goggins, Des Walsh

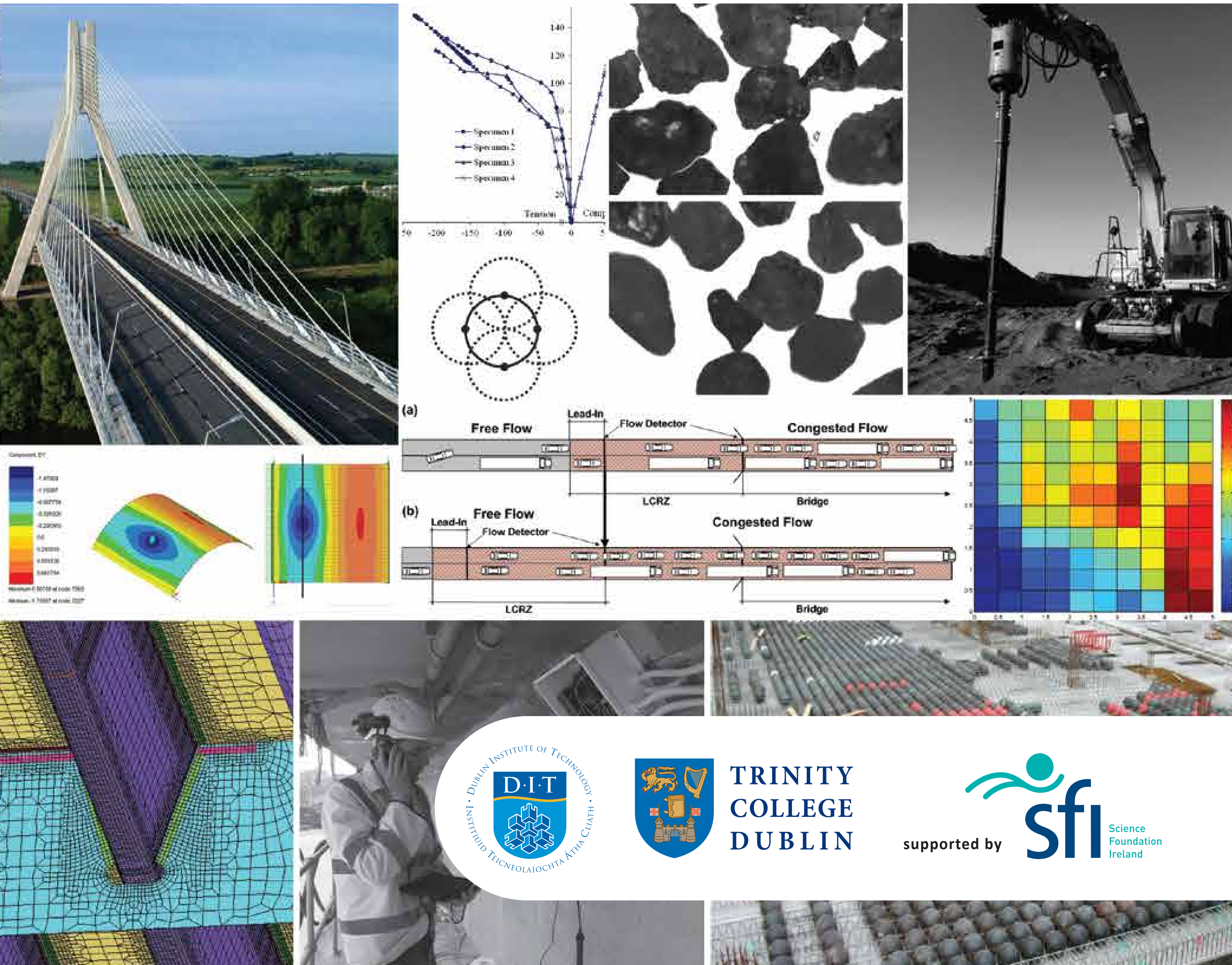

Dublin Institute of Technology
Trinity College Dublin
supported by Science Foundation Ireland

www.bcri.ie

BCRI 2012

Proceedings

6-7 SEPTEMBER 2012

supported by

A joint conference of

Bridge and Infrastructure Research in Ireland, BRI 2012
Concrete Research in Ireland, CRI 2012

Co-hosted by

Dublin Institute of Technology
Trinity College Dublin

Editors

Colin Caprani
Alan O'Connor

Assistant Editors

Paul Archbold
Ken Gavin
Jamie Goggins
Niall Holmes
Des Walsh

Published in 2012
ISBN 978-0-9573957-0-1

Published by
Bridge and Concrete Research in Ireland

This publication is part of the proceedings
of the Bridge and Concrete Research in
Ireland Conference held in Dublin Institute
of Technology and Trinity College Dublin,
Ireland, on 6-7 September 2012.

Copies of these proceedings are
available from:
Dr Colin Caprani
Dept. of Civil and Structural Engineering
Dublin Institute of Technology
Bolton St.
Dublin 1
Ireland.
colin.caprani@dit.ie;
www.colincaprani.com

Papers are also available on the
conference website, www.bcri.ie

Cover images are selected from the
aaccepted papers.

Graphic design by
Sophia Westwick
www.sophiawestwick.com

Website and conference engine by
Ex Ordo www.exordo.com

This conference is an Engineers Ireland
CPD-Approved Event

This conference forms part of the
Dublin City of Science 2012 Festival

Organizing Committee

Co-Chair	Dr Colin Caprani	Dublin Institute of Technology
Co-Chair	Dr Alan O'Connor	Trinity College Dublin
Secretary	Dr Niall Holmes	Dublin Institute of Technology
Treasurer	Dr Roger West	Trinity College Dublin
	Dr Paul Archbold	Athlone Institute of Technology
	Prof. Muhammad Basheer	Queen's University Belfast
	Dr Paul Fanning	University College Dublin
	Dr Ken Gavin	University College Dublin
	Dr Jamie Goggins	NUI, Galway
	Mr. Martin Mannion	Cork Institute of Technology
	Mr. Brian O'Rourke	Cork Institute of Technology
	Dr Vikram Pakrashi	University College Cork
	Dr Marek Rebow	Dublin Institute of Technology
	Mr. Des Walsh	Cork Institute of Technology

Scientific Committee

Dr Paul Archbold	Athlone Institute of Technology
Mr Richard Bradley	Irish Cement
Mr Brian Bryan	Arup Consulting Engineers
Mr David Cadogan	Cork Institute of Technology
Dr Colin Caprani	Dublin Institute of Technology
Mr Patrick Casey	Arup Consulting Engineers
Prof. Tom Cosgrove	University of Limerick
Dr Michael Creed	University College Cork
Mr Albert Daly	National Roads Authority
Mr Peter Deegan	Banagher Concrete
Dr Paul Doherty	GDG Geo Solutions
Dr Aidan Duffy	Dublin Institute of Technology
Dr Bernard Enright	Dublin Institute of Technology
Dr Paul Fanning	University College Dublin
Dr Ken Gavin	University College Dublin
Dr David Gill	AGL Consulting
Dr Jamie Goggins	NUI Galway
Dr Arturo González	University College Dublin
Dr Annette Harte	NUI Galway
Dr Joe Harrington	Cork Institute of Technology
Mr Paul Healy	O'Connor Sutton Cronin Consulting Engineers
Mr David Holleran	Oran Precast
Dr Niall Holmes	Dublin Institute of Technology
Dr David Hughes	Queen's University Belfast
Mr Farzin Hussein	ABM Construction
Dr David Igoe	University College Dublin
Dr Denis Kelliher	University College Cork
Dr Debra Laefer	University College Dublin
Dr Mike Long	University College Dublin
Mr Martin Mannion	Cork Institute of Technology

Mr Sean Mason	Arup Consulting Engineers
Mr John Murphy	Cork Institute of Technology
Mr John Murphy	Mott McDonald Consulting Engineers
Dr Bryan McCabe	NUI Galway
Mr Cian McGuinness	RPS Consulting Engineers
Dr Ciaran McNally	University College Dublin
Dr Danny McPolin	Queen's University Belfast
Dr Sreejith Nanukuttan	Queen's University Belfast
Dr Nora Aine NiNuallain	KTH Institute of Technology
Dr Trevor Orr	Trinity College Dublin
Dr Alan O'Connor	Trinity College Dublin
Mr Brian O'Rourke	Cork Institute of Technology
Dr Vikram Pakrashi	University College Cork
Dr Sara Pavia	Trinity College Dublin
Dr Niamh Power	Cork Institute of Technology
Dr Sarah Pritchard	Buro Happold Consulting Engineers
Mr Paul Quigley	Arup Consulting Engineers
Dr Marek Rebow	Dublin Institute of Technology
Dr Mark Richardson	University College Dublin
Mr Kieran Ruane	RPS Consulting Engineers
Mr Derek Russell	RPS Consulting Engineers
Dr Donal Ryan	University of Ulster
Mr Peter Seymour	Ecocem
Dr Mohammed Sonebi	Queen's University Belfast
Dr Su Taylor	Queen's University Belfast
Dr Gobithas Tharmarajah	Athlone Institute of Technology
Mr Des Walsh	Cork Institute of Technology
Mr Michael West	Iarnrod Eireann
Dr Roger West	Trinity College Dublin

Sponsors

This conference is kindly supported by the following organizations:

www.cement.ie

www.ecocem.ie

www.engineersireland.ie

www.istructe.ie

www.concrete.ie

www.rod.ie

www.sfi.ie

Preface

On behalf of the Organizing Committee of BCRI 2012, we are delighted to welcome you to the conference. This is the fourth such conference or joint symposia of Concrete Research in Ireland (CRI) and Bridge and Infrastructure Research in Ireland (BRI). The conference topics are broader than ever, with papers covering the usual subjects of bridges, concrete, and geotechnical engineering, as well as newer areas such as wind turbines, carbon emissions, engineering heritage, novel materials, and computational solutions to engineering problems. As such we hope that you find the conference intellectually stimulating, and that it provides you with ideas and solutions for the engineering problems of the 21st century.

As we look to the future, we are confident of the strong national and growing international support for this conference series. In the past it has proved a vital communication conduit between industry and academia on the island, and has been a formative event for many young researchers. In the future we hope to strengthen these aims. To this end, and to reflect the widening themes, the Organizing Committee of BCRI 2012 are proposing a re-branding of the series for 2014 and beyond, and the establishment of an association dedicated to running the event. All delegates are invited to attend the formative meeting (announced in the delegate pack) of the Civil Engineering Research Association of Ireland (CERAI) and to put forward their views on its governance and direction for the future.

For the present, we are extremely grateful to the joint hosts for facilitating this event. In particular the committee wishes to thank, Mr Joe Kindregan, Head of Department of Civil & Structural Engineering; Mr John Turner, Head of the School of Civil and Building Services Engineering of Dublin Institute of Technology; Prof. Biswajit Basu, Head of the Department of Civil, Structural, and Environmental Engineering; and Prof. Margaret O'Mahony, Head of the School of Engineering at Trinity College Dublin.

On your behalf, we also extend our thanks and appreciation to the members of the Scientific Committee. Throughout the organizing of the conference, they generously gave their valuable time and expertise to assure the quality and success of the conference.

Great thanks are also due to the support staff of both institutions. Administration and technical staff, and postgraduate students at both institutions played an important role in delivering the conference. Indeed the previous hosts, CIT and UCC, and in particular Dr Michael Creed, ensured a smooth transition between venues. Paul Killoran of Exordo has offered great support in the running of the website and conference engine and Sophia Westwick provided us with graphic designs in the short time available.

We are most grateful to our sponsors: Cement Manufacturers Ireland, EcoCem, Engineers Ireland, the Republic of Ireland Branch of the Institution of Structural Engineers, The Irish Concrete Society, Roughan & O'Donovan, and Science Foundation Ireland. Without their kind and generous support, it simply would not be possible to deliver the conference to the same quality and value.

Finally, we must acknowledge the dedication, hard work, and significant time commitment of the members of the Organizing Committee, many of whom incurred personal expense and spent many long hours travelling to and from meetings. The conference could not exist without this engagement of our peers and mere thanks seem insufficient recompense for their efforts. To name but one, and without fear of objection, we wish to single out Dr Niall Holmes, Conference Secretary, for special praise and thanks for his significant efforts in ensuring the success of the event.

It is our great honour and privilege to welcome you to BCRI 2012.

Dr Colin Caprani
Dr Alan O'Connor
Co-Chairs, BCRI 2012

Table of Contents

Keynote Papers

A (1) Bridges

A (2) Concrete

B (1) Bridges

B (2) Geotechnical

C (1) Bridges

C (2) Concrete

D (1) Geotechnical

D (2) Materials

E (1) Bridges

E (2) Materials

F (1) Bridges

F (2) Structures

G (1) Geotechnical

G (2) Concrete

H (1) Geotechnical

H (2) Structures

Plenary Lectures

Problems: inspiration for innovative solutions - lessons from over forty years of reinforced concrete research

Adrian E. Long[1]
[1]Emeritus Professor of Civil Engineering,, Queen's University Belfast

ABSTRACT: When reinforced concrete arrived on the scene over one hundred years ago it was acclaimed as the ideal solution to many structural problems. In particular as Roman concrete had stood the test of time its long term durability was not questioned. However it is now acknowledged that like all materials exposed to the environment reinforced concrete has its own problems in relation to long term strength and durability. Three areas of research which impinge on these important subjects will be discussed in some detail in this paper:

1. The development of innovative in-situ test equipment to monitor the long term durability of concrete and potentially estimate the remaining life of existing structures
2. Taking advantage of the benefits of the enhanced strength of restrained slabs for bridge deck slabs and for cellular concrete structures.
3. Research and development on an innovative, flexible concrete arch system which requires no centring, has no corrodible reinforcement and can be rapidly constructed.

How each of these problems arose will be discussed in order to give an insight into how problems can be a great source of inspiration to those who have accepted the challenge of finding a solution. In addition some more general guidance will be given on how the likelihood of success in solving problems can be improved.

KEY WORDS: Arch, Bridges, Compressive Membrane Action, Pull-off Test, Transport Properties, Precast Concrete, Sustainability

1 INTRODUCTION

In general members of society are anxious to avoid problems; however leading researchers and eminent engineers relish the challenge of a new problem as it often motivates them to produce a creative but practical solution. A creativity researcher at Harvard Business School, Professor Amabile, (in EPSRC Newsline, 2006) identified three essential traits that creative individuals have:

- Wide ranging and deep knowledge of their subject
- Loving their subject and a strong motivation to solve the problem
- Creative ways of thinking

Of all these, Professor Amabile considers the most important to be motivation. According to Andy Burnett of Know Innovation in an article in the EPSRC Newsline, 2006:

"It's the intrinsic motivation which actually keeps people going, nagging away at a problem long enough to develop new solutions; this probably explains where inspiration comes from".

Many attending the BCRI 2012 Conference will agree that few of us have 'Eureka' moments like Archimedes hence we can relate well to the above sentiment. Looking back on over 40 years of research I now realise how much I have depended on the motivation derived from trying to solve specific problems. Three examples are given in this paper and an attempt is made to place them in context:

1. The Development of novel in-situ test methods
2. The enhanced strength of restrained slabs and
3. The 'FlexiArch' for the rapid construction of Arch bridges.

In the article in the EPSRC Newsline it is acknowledged that even top scientists needed to use grit and determination to achieve their goals. Yes, even Albert Einstein needed great problems to inspire him-physicists around the world were striving around 1900 to understand experiments that could not be explained. Existing theories could not explain these phenomena but it really bothered Einstein and sparked his motivation so much so that in 1905 (his miracle year) he published three papers which were the foundation for his worldwide reputation.

Similarly the great biologist and bacteriologist Louis Pasteur was in no doubt as to what lay behind his great achievement- he acknowledged that the secret that led him to his goal was solely his tenacity. He also commented that "chance favours only the prepared mind," which is not dissimilar to the comment made by the great golfer Gary Player- "the more I practice the luckier I get". Thus we should not be afraid to admit that our achievements in research are often 10% inspiration and 90% perspiration. Whilst hard graft is essential we should not forget what motivates us. Our bridge research will be more effective if it is problem orientated so that we can help provide our society with a more cost effective and sustainable infrastructure in the future.

2 DEVELOPMENT OF NOVEL IN-SITU TEST METHODS

2.1 Background

In the early 1970's the problems associated with the potential collapse of hundreds of buildings in the UK, which had been built using precast concrete units manufactured using High Alumina Cement Content (HAC) concrete, were causing great concern [1]. The deterioration in strength of HAC concrete in adverse circumstances meant that there was a need for a reliable, simple and cost effective means of assessing the in-situ strength of the concrete in these units. Recognition of this problem was a major source of motivation for the development of the 'Pull-off test,' [2] a partially destructive test which caused much less damage than the extraction of cores and was more suitable for use on small precast units. The Pull-off test also had the benefit that when used with a partial core it allowed the strength of the weaker concrete in the core of the precast HAC concrete units to be assessed. Subsequently this partially destructive test has also proven to be useful for OPC concrete and for assessing the quality of patch repairs. However by the early 1980s the deterioration of more conventional RC structures had become a much greater problem for the construction industry and it became clear that there was a need for a method of assessing the permeability of concrete on site.

Traditional methods for measuring the permeation properties of concrete, such as the Initial Surface Absorption Test (ISAT) were cumbersome and very inconvenient to use on site. This was a source of motivation for the development of the CLAM test at Queen's University and over the past 3 decades much research has been carried out to develop equipment for assessing the in-situ transport properties of concrete. More specific information on these test methods will now be provided.

2.2 Measurement of Strength

2.2.1 The Pull-off test

The pull-off test is based on the concept that the "tensile strength" of a layer of surface concrete can be related to the compressive strength of the concrete (Figure 1). The "LIMPET", developed at The Queen's University of Belfast can then be used to measure the tensile force to "pull-off" the disc and a nominal tensile strength calculated on the basis of the disc diameter (usually 50mm). To convert this tensile strength into a cube compressive strength an empirical correlation curve is normally required (Figure 2). It should also be noted that the Pull-off test gives a good indication of the tensile strength or the fracture strength which is one of the most important factors in relation to the rate of deterioration. Unlike most other partially destructive tests, the variation in strength with depth can be determined by using partial coring and this technique is also invaluable for assessing the bond strength of patch repairs.

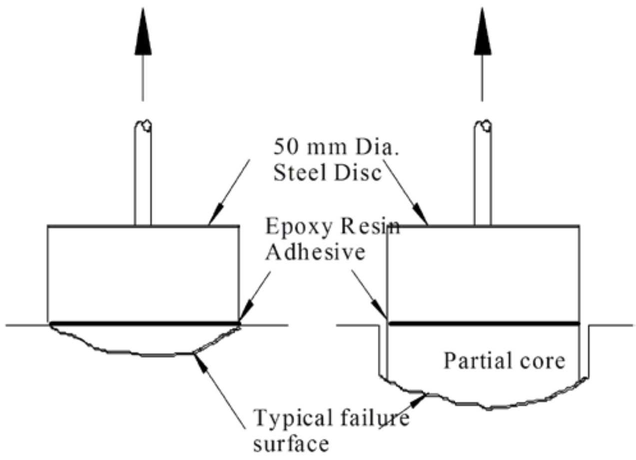

Figure 1. Schematic diagram showing the procedures used to complete a Pull-off test.

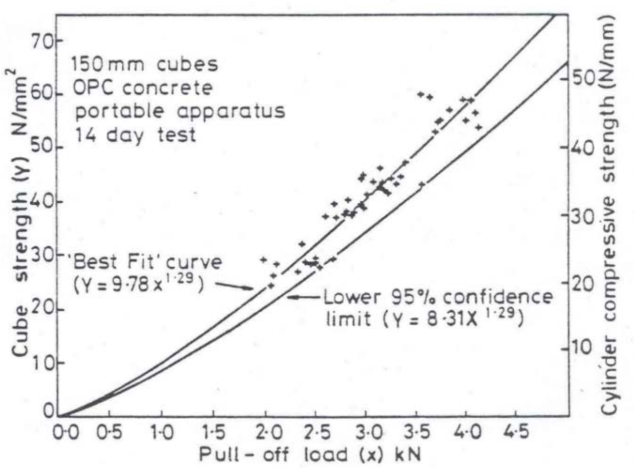

Figure 2. Pull-off test results.

Using the Pull-off test, it has been found that within-test variability is sufficiently low to allow the natural variations in strength from one location to another to be detected (eg bottom vs. top of columns). In addition, the effects of maturity are automatically included and useful information obtained on partial safety factors for in-situ variability [3].

2.3 Measurement of Permeation/Transport Properties

The main transport processes which describe the movement of aggressive substances through concrete can be categorised as absorption, permeability and diffusion [4]. Here it should be noted that the mechanisms of deterioration and their rate are controlled by the environment, the paste microstructure and the fracture strength of the concrete. Environmental factors such as seasonal temperature variations, cyclical freezing and thawing, rainfall and relative humidity changes, and concentration of deleterious chemicals in the atmosphere/water in contact with the concrete are the main causes of degradation. However, the single most important parameter that leads to premature deterioration is the ingress of moisture into the concrete [5, 6]. Permeability of concrete to the macro-environment during its service life therefore can be used as a measure of its durability.

2.3.1 Absorption and Permeability Testing

When the 'Clam' test was first reported [7], in the early eighties, it had been developed to overcome some of the problems associated with the standard Initial Surface Absorption Test (ISAT) such as achieving a watertight seal and accurately measuring the flow rate. Initially it was only a water permeability test but it was then modified and the 'Universal Clam' produced which enabled both water and air permeability to be measured. In the early nineties Basheer [8] completed further development work that not only standardised all the tests but also made the whole process fully automatic. This version of the Clam, the "AUTOCLAM", is now controlled by a microprocessor and has a complete data acquisition and transfer facility to enable analysis of the results by computer. The "AUTOCLAM" has been available commercially for over fifteen years and three types of test are now possible: water absorption, air permeability and water permeability. All three tests are quick and simple to perform both on-site and in the laboratory.

An indication of the relevance of permeability testing to durability testing can be observed from a comprehensive series of tests by Basheer [8]. The high permeability values obtained from the 'AUTOCLAM' (Figure 3) show a strong correlation with the levels of freeze-thaw damage.

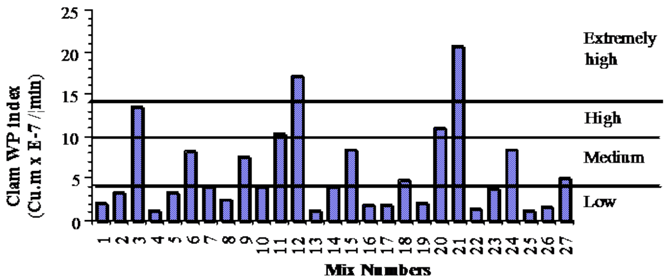

Figure 3. Risk levels based on extent of deterioration caused by freezing and thawing [8].

2.3.2 Diffusion Tests

More recently there has been an increased interest in ionic diffusion tests because the rate at which chloride ions diffuse through concrete is closely related to the corrosion of reinforcement. The chloride diffusion coefficient can be determined from several types of test, but in this paper the discussion will be limited to just one test technique which can be carried out in-situ or in the laboratory. Other tests require cores to be extracted.

'PERMIT ION MIGRATION TEST': This test, developed over ten years ago at The Queen's University of Belfast, has the advantage that the migration coefficient of concrete on site can be determined and, cores need not be taken. Full details of the equipment are given in Andrews [9] and the basic concept is shown in Figure 4.

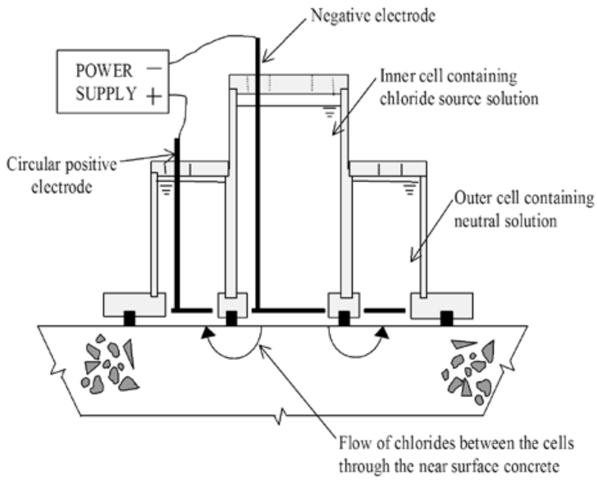

Figure 4. Section of the Permit ion migration test [9].

Basically it consists of two concentric cylinders, placed on the concrete surface, and then sealed to prevent any flow between them along the surface of the concrete. In this accelerated test a potential difference of 60v dc is applied between the anode and the cathode which forces chloride ions to travel from the anode to the cathode through the concrete in the near surface zone. After about 6 to 10 hours, depending on the quality of the concrete, a steady migration of chlorides into the outer cell is achieved, and the chloride migration coefficient can be calculated [9]. This correlates well with the effective diffusion coefficient (Figure 5). Thus the Permit ion migration test, now available commercially, can be used to determine the diffusion characteristics of concrete on site.

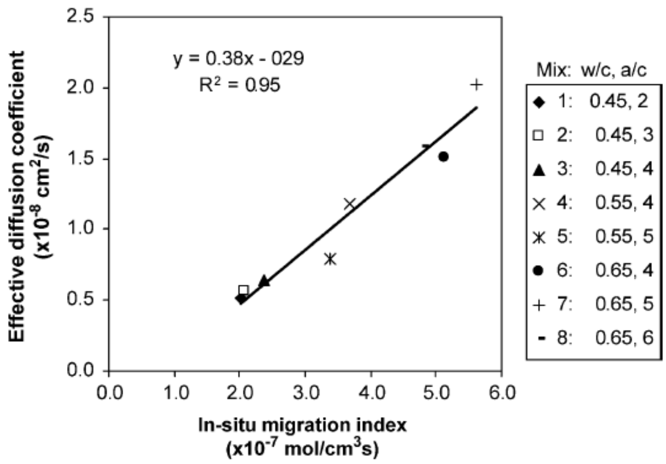

Figure 5. Correlations between Permit in-situ migration index and effective diffusion coefficient [9].

2.4 Assessment of the Durability of Concrete Bridges

Experience gained in the use of some of these tests will be presented to highlight unforeseen problems or limitations when used to assess the conditions of structures in the field.

In the late 1980s, six motorway bridges, built between 1960 and 1970, were assessed in Northern Ireland. Full details of the tests and the resulting analysis are presented in [10]. Subsequently, when one of the piers was being prepared for repair, it was found that the areas of high permeability generally coincided with locations of significant reinforcement corrosion. Thus an early evaluation of the surface permeability of the concrete in the pier would have provided useful indications of the likely future deterioration of the structure. Appropriate remedial action could then have been taken.

In 1997/98 researchers from Queen's University, Belfast, and McGill University, Montreal, along with industrial partners, were involved in the assessment of corrosion-induced damage in the deck of the Dickson bridge in Montreal [11]. An extensive half-cell potential survey was carried out, and, from the resulting contour map, thirty-five sites, measuring approximately 1m by 2m, were selected for further detailed analysis. All types of tests referred to in this part of the paper were used in this study. As expected, areas of high chloride content and low cover exhibited the highest levels of corrosion, however, variations in strength did not correlate well with evidence of deterioration. Permeability, diffusivity and resistivity measurements provided much useful information. The value of using a combination of tests was confirmed and an extremely valuable databank has been built up. More detailed information is given in reference [11].

2.5 Conclusions on In-situ Test Methods

In the assessment of durability, the following potential uses for strength, permeability and diffusion testing have been identified:

1. Estimating the life of new structures: Here the equipment has been used to develop a "mix design for durability" [12] and important trends have been identified (Figure 6) which could be extremely relevant to new construction.
2. Assessing the remaining life of existing structures: The good correlation between permeability indices and durability characteristics can allow remedial action to be taken before irreparable damage has occurred.

However to overcome the challenges in 1 and 2 it is essential for practising engineers to work closely with those involved in relevant research. In this context the 'LIMPET', the 'AUTOCLAM' and the 'PERMIT ION MIGRATION TEST' (Figure 7) could be invaluable tools for generating useful data.

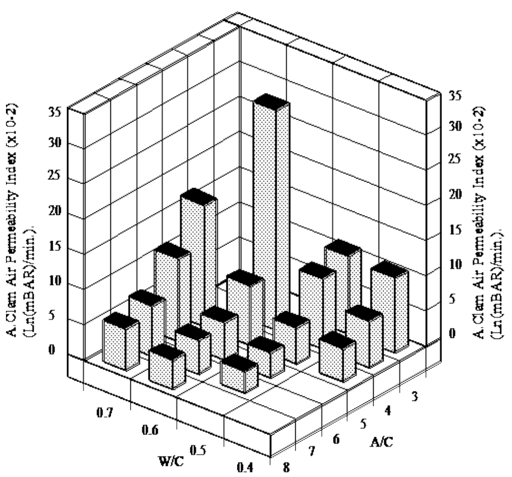

Figure 6. Influence of mixture proportion on Autoclam air permeability index (w/c – water/cement, a/c – aggregate/cement).

Figure 7. Permit, Limpet and Autoclam (from left to right).

3 ENHANCED STRENGTH OF RESTRAINED SLABS

3.1 Background

In my PhD research [13], I focused on the problem of developing a better understanding of the failures at the slab column junction of flat plates when they were subjected to shear and moment transfer. A new type of test set-up was developed where full panels were tested with their edges restrained so as to reproduce the boundary conditions which would occur (Figure 8). A number of tests were carried out in parallel with an analytically based prediction method. As very few test results were available for combined moment and shear transfer the main focus of the analysis had to be on the shear or concentrically loaded specimens, where numerous tests had been carried out between 1908 and the early 1960's. The rational approach developed gave very good correlation [14] with the test results in the literature; however when applied to the concentrically loaded full panel specimens $P_{\text{Test}}/P_{\text{Predicted}}$ was of the order of 1.4 - 1.5 i.e., the prediction model significantly underestimated the punching strength in this instance.

Very few PhD students must have encountered such a problem where their method of prediction worked well for the tests of all others but not for their own tests. However, arising from this problem, I was steered towards a very productive and rewarding area of research. By good fortune I had had an earlier introduction to the concept of Arching Action by RH Wood who subsequently wrote an outstanding book on the subject [15]. In 1964 Wood had shown me his model test specimens for the floating airport at Maplin (on the Thames Estuary) and he had rightly recognised the potential benefits Arching Action could give to Structural Engineers involved in the design of restrained slabs. Thus in my PhD thesis, I acknowledged that Arching Action was the reason for the difference and I parked the problem as a future topic for a PhD student.

3.2 The concept of Arching action in slabs

The tests carried out by Ockleston [16] on interior panels of the Old Dental Hospital in Johannesburg revealed collapse loads of 3~4 times those predicted by the yield line method. This enhanced capacity was attributed to the development of an internal arching mechanism arising from the restraining effect of the surrounding panels. The concept of arching can best be understood by referring to Figure 9. With the development of tension cracks at mid-span and at the supports the beam tries to expand longitudinally but as it is restrained, corresponding forces are induced which allow it to sustain a substantial load on the basis of the arching thrusts which develop as the deformation increases.

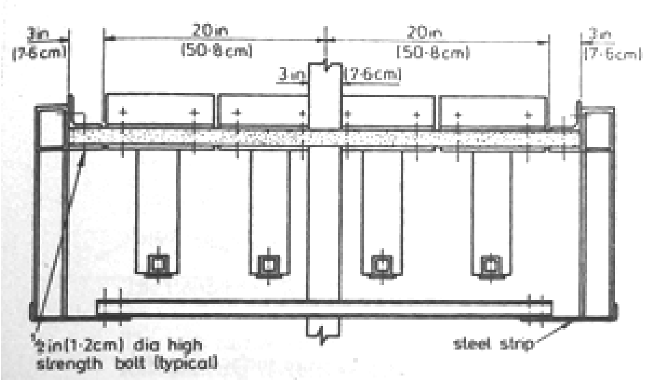

(a) Details of edge restraining system;

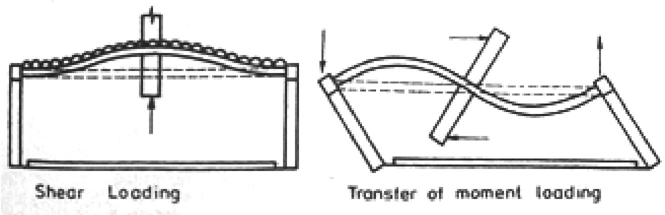

(b) Idealised function of edge restrains;

Figure 8. Boundary conditions for combined shear and moment transfer [13].

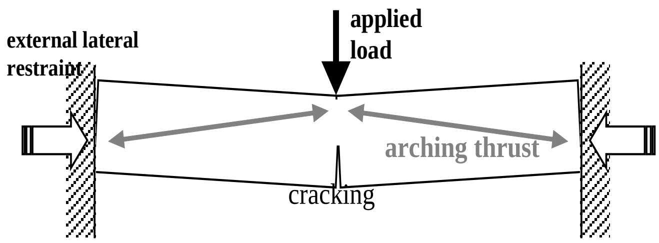

Figure 9. Arching action in a typical bridge deck slab.

Similar actions take place in two-way systems where a dome or membrane rather than an arch is generated and this phenomenon is generally referred to as "Compressive Membrane Action" (CMA) The extent of the enhancement provided by compressive membrane action, over and above the flexural strength, depends on the degree of restraint provided by the surrounding structure. A typical load deflection curve with the notional contributions of CMA and flexural action separately identified is given in Figure 10. Here it is of interest to note that my first PhD student in Canada demonstrated that, by taking into account the inherent CMA that could develop in full panel models, it was possible to accurately predict the ultimate capacity of these specimens [17].

3.2.1 Relevance to Bridge Deck Slabs

Tests on model bridge deck slabs in Canada, in the late 1960s revealed considerable reserves of strength against punching failure [18]. As a result of the author's input this enhancement was attributed to CMA and here it is important to note that bridge decks represent one of the first areas to be considered appropriate for the utilisation of these design concepts. This is largely because the major localised loading is transient in nature and hence creep, which may reduce the enhancing effects of CMA, is of little importance. Subsequently, a conservative design method was produced and the Canadian design standards [19] for beam and slab bridges, only nominal transverse reinforcement, 0.3% was required to resist concentrated wheel loadings as opposed to the 1.7% based on flexural design requirements.

Here it is important to note that bridges with spans of up to 30m constitute the vast majority of road infrastructure bridges in service across the world – whether it be for overpasses/underpasses for motorways or for minor river crossings. Within this category of bridges concrete deck slabs are widely used whether in combination with pre-cast pre-stressed concrete beams or steel girders. A similar type of deck can also be utilised for many medium span bridges hence the importance of designing a durable deck system cannot be overemphasised.

3.3 Research on Arching Action in the UK

3.3.1 Validation tests in Northern Ireland

In the knowledge of the research carried out in Canada on AASHTO girder based beam and slab bridge decks it was decided that parallel tests should be carried out on spaced M-beam (essentially a range of depths of prestressed I-beams with a narrow top flange and a broad bottom flange 1m wide) decks to determine whether similar reductions in transverse reinforcement were possible. This would allow a slightly larger M-beam to be used at a spacing of 1.5m or 2.0m with consequent savings relative to smaller M- beams at 1.0m spacing. In order to establish the strength of the slabs spanning between beams a one-third scale model bridge deck was constructed in the laboratory and tested at Queen's University Belfast, in the late 1970s. Figure 11 clearly shows that design codes do not give a satisfactory prediction of the punching shear capacity of typical bridge slabs and a more appropriate method which allows for in-plane restraint was therefore developed [20]. As can be seen from Figure 11 the proposed method of predicting the punching shear strength of reinforced concrete bridge slabs gives good correlation with the results from the one-third scale model. This method has now been endorsed by the UK Highways Agency and is included in BD81/02 [21].

The widths of the cracks induced in the slabs were monitored during the model tests however, as scale effects can affect the accuracy of these measurements full-scale tests [22] were subsequently carried out on a bridge built by the Northern Ireland Roads Service. It was found that the slabs easily satisfied the serviceability limit state requirements and this research led to the adoption of a less conservative design approach for M-beam bridge deck slabs (0.5% reinforcement) by the then Department of the Environment for Northern Ireland.

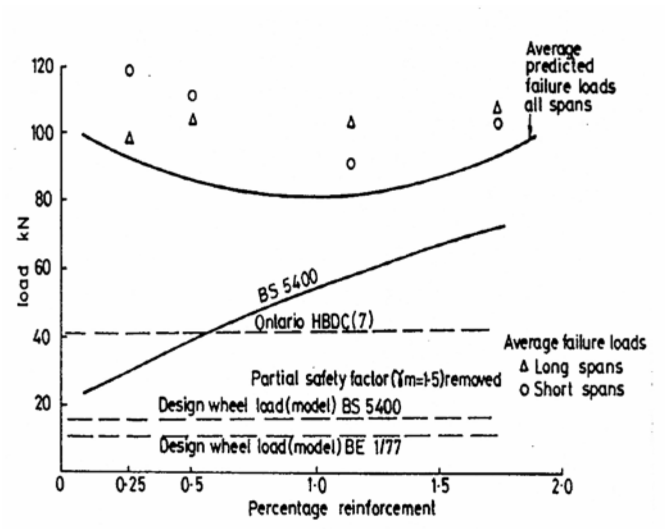

Figure 11. Test results of one-third scale model bridge deck.

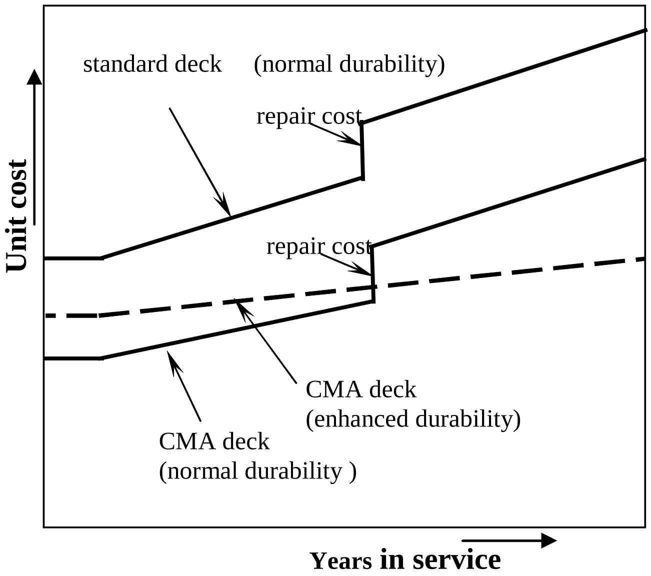

Figure 12. Comparison of the total unit cost of beam and slab superstructure over their service life.

3.3.2 Review of the Advantages Arising from CMA

From a structural viewpoint the following benefits are evident:

1. Reduction in reinforcement (from 1.7% to 0.5% or less)
2. Same slab depth for greater spacing of beams
3. Lower overall cost of bridge superstructure as one larger beam at 2m centres is less expensive than two smaller beams at 1m centres.

Thus substantial reductions in costs can be achieved whilst at the same time retaining comparable strength and durability. However, if the long-term durability of the bridge deck could be increased at a modest increase in cost then the whole life cost could be reduced as can be shown schematically in Figure 12. Thus the challenge to designers is to achieve the type of relative performance achieved by the CMA deck (enhanced durability). Significant progress of this front has been achieved in Canada and the UK in the last two decades.

A further benefit is that the enhancing effects of CMA mean that slabs can carry significantly higher loads that would have been predicted on the basis of flexural methods of analysis. This is of direct relevance to Assessment Codes [23] and this research has resulted in savings to the UK economy of well over £300M in the last decade (otherwise structures would have had to be replaced).

3.4 Improved Sustainability by Design

The system developed in Canada, focused on steel concrete composite bridges [24]. As pre-cast prestressed concrete beams tend to be significantly more popular in Europe the tests in NI [25] have focused on the following subjects:

Concrete -As well as considering the addition of fibres, advantage is being taken of the fact that for a given degree of restraint the strength of slabs developing CMA is significantly enhanced by increases in concrete strength.

Reinforcement -Apart from considering the lower percentages of top and bottom reinforcement (0.5% vs. 1.7%) site and laboratory tests have been carried out on:

4. Conventional steel reinforcement located in a single layer at the centre of the slab (greatly increased cover).
5. Glass fire reinforced plastic reinforcing bars.

Both approaches have performed well, as anticipated, and it is clear that by using high strength concrete (with or without fibres) in conjunction with corrosion free reinforcement, bridge decks could be produced which should be virtually maintenance free. However, it is not only beam and slab bridges that can benefit from the strength enhancing effect of CMA. Other forms of construction which could take advantage of CMA include box girders and cellular concrete structures such as offshore installations [26] /floating airports.

3.5 Conclusions from CMA Research

A sufficient understanding of the structural benefits of compressive membrane action for restrained slabs has now been achieved. This allows:

- The enhanced strength and serviceability of laterally restrained slabs to be taken into account in the assessment of beam and slab bridge decks, cellular concrete structures etc.
- CMA concepts to be incorporated into relevant national design codes. Already this is accepted in Ontario, Canada [19] and in the UK [21].
- The development of highly durable deck slabs for bridges or floating airports which will be virtually maintenance free.

The net effect of all the above is more cost effective slab systems that exhibit greatly enhanced sustainability relative to existing designs.

4 THE 'FLEXIARCH' FOR THE RAPID CONSTRUCTION OF ARCH BRIDGES

4.1 Background

In the 1990s the author was returning to Belfast with Gordon Millington after a meeting of the Structural Group Board of the Institution of Civil Engineers and Gordon asked this question: "Why is it that very few arch bridges have been built since the early 1900s as they are aesthetic, strong, and durable and require little maintenance?" This perceptive question identified real problems, acted as a catalyst for the work and over the next few years a number of research projects were targeted at the resolution of this issue. Early on it was realised that centring, with its high cost and intensive labour requirements, was a major stumbling block, as was the need for skilled bricklayers and stonemasons. However, it took until the late 1990s before the basic concept of the 'FlexiArch' was realised. In hindsight the previous experience of the first author had a significant influence on the Patent [27]. These included:

- Over thirty years of research on concrete including arching action in reinforced concrete slabs.
- Design of concrete hinges to allow articulation in bridges, when working on bridge design with FENCO, Toronto in the 1960s.
- Understanding of the concept of aggregate interlock as a means of resisting shear (Supervision of research in the 1980s).
- Basic understanding of geotextiles from parallel research at Queen's University Belfast in the 1980s. The flat/flexible characteristics of polymeric reinforcement are ideal for these applications and have the benefit of being non-corrodible.

Transforming these ideas into a form suitable for a patent needed someone with experience of research and bridge design and fortunately a former PhD student, Dr Jim Kirkpatrick, was able to provide this expertise with support from a Patent Agent and Queen's University. Once the Patent had been filed it was decided that close links with a Precast manufacture with relevant expertise would be essential to develop the 'FlexiArch' system. Macrete Ireland (in Toomebridge-30 miles from the University) were approached, as they had wide experience of producing precast concrete beams and arches for markets in GB and Ireland. Realising the potential of the 'FlexiArch', they became enthusiastic members of the team. Over the past 6-7 years enormous advances have been made as can be seen from the rest of this paper.

4.2 Basic concept

It is no longer economically viable to construct a masonry arch in the traditional way due to the cost of accurate centring and the preparation of the masonry blocks. In order to provide a viable alternative, the 'FlexiArch' is constructed and transported in the form of a flat pack using a polymer grid reinforcement to carry the self weight during lifting but behaves as a masonry arch once in place. Basically there are two options for the construction of the arch unit:

- The voussoirs can be pre-cast individually, laid contiguously in a horizontal line with a layer of polymer grid reinforcement placed on top. An in-situ layer of concrete, approximately 40mm thick, is placed on top and allowed to harden to interconnect the voussoirs, Figure 13(a).
- Alternatively, it can be made in a single casting operation by using a shutter with wedge formers spaced to simulate the tapered voussoirs, Figure 13(b).

The arch unit can be cast in convenient widths to suit the design requirement, site restrictions and available lifting capacity. When lifted, the wedge shaped gaps close, concrete hinges form in the top layer of concrete and the unit is supported by tension in the polymer grid. The arch shaped units are then placed on precast footings and all self-weight is then transferred from tension in the polymer to compression in the "voussoir" elements of the arch.

4.1 Fabrication and Installation

A prototype arch unit of 5m span, 2m rise and 2.5m internal radius was constructed and lifted. This arch required twenty-three precast voussoirs which were 1m wide and 200mm deep with a 40mm slab interconnecting in-situ screed incorporated 150/15 Paragrid. During lifting the arch drags at the each end and when the end cantilevers are fully effective they produce a hogging moment in the mid span region which assists in the formation of the arch. As maximum bending moment occurs at the lifting points for the cantilever ends and to simulate this condition a series of short beam elements were tested to establish the capacity and to investigate the rate of creep in the low modulus polymer reinforcement. The results of these tests have demonstrated that the arch system has an adequate factor of safety during the lifting procedure. The lifting sequence is shown in Figure 14.

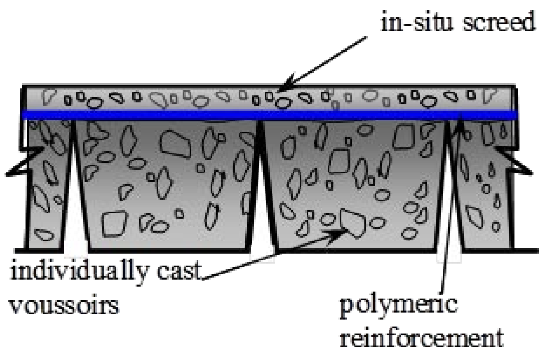

(a) Construction of arch unit using pre-cast individual voussoir concrete blocks;

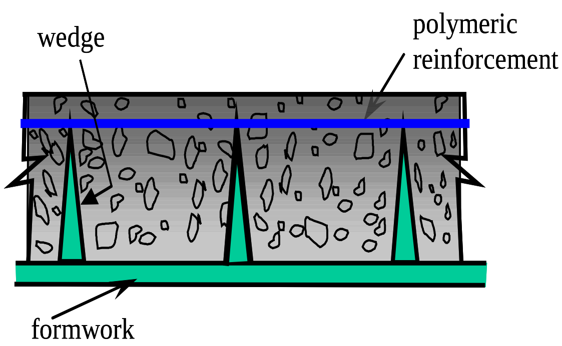

(b) Monolithic construction of the arch unit using preformed wedges.

Figure 13. Details of arch construction.

The arch unit complete with tapered seating is shown in Figure 14c. Subsequently, an anchor block detail was designed for the seating of the arch ring. The anchor block caters for the slope of the last voussoir enabling the arch to from correctly. It also provided some lateral restraint to the arch ring both during construction, prior to completion of the arch system with spandrel walls and backfill, and in the long-term under live loading.

(a) "Flat-Pack" arch system;

(b) Arch unit during lifting;

(c) Arch located on tapered seating units;

Figure 14. Arch erection sequence.

Figure 15. Full arch system.

4.2 Testing the 'FlexiArch' system

To assess the flexibility of this system whilst being back filled, a stability test was conducted and the arch unit (one meter wide) was monitored for horizontal deflections, vertical deflections and strain at the voussoirs joints. It was originally intended to use Type 6S granular backfill, however, after a preliminary cost estimate for this span, it was decided to trial the use of lean mix concrete as a backfill option. Very little movement took place and the system was very stable. This system was load tested using a simulated static wheel load applied at (1) midspan and (2) the third span of the arch ring. For both loading locations the arch system carried over 35t without showing signs of distress (that is, six times the design load for a single wheel load). Further details of the tests are given in reference [28].

A complete 5m wide arch bridge with a 5m span and 2m rise including spandrel walls and fill has been constructed at Macrete (Figure 15). Load testing up to 70t has been successfully carried out using two 50t hydraulic jacks. Subsequently, 'FlexiArch' units 10m span x 2m rise and 15m span x 3m rise have been successfully tested at Macrete and numerous model tests have been carried out at Queen's University to validate the system.

4.3 Conclusions for the Novel Arch System

Experience has shown that arch bridges are highly durable structures requiring little maintenance in comparison with other bridge forms. Thus, the objective of the new Highway Agency Standard [29] is welcomed especially if it encourages a renaissance in arch building using unreinforced masonry materials.

The novel arch system has been demonstrated, in tests reported in this and other papers, to be a viable alternative to long established methods of construction and the following advantages have been identified:

- As the Arch system is cast horizontally it can conveniently be transported to site in a "flat pack" form.
- As centring is not required during installation this greatly simplifies the process and enhances the speed of construction.
- As there is no corrodible reinforcement the long term durability should be assured.

- The system is cost competitive with alternatives such as RC box culverts which do not share the aesthetic benefits or the longevity of an arch.

Over 30 'FlexiArch' bridges have been built to date in the UK and Ireland and many advances have been made [30]. Both road and foot/cycleway bridges with spans ranging from 4m to 15m have been successfully installed and in all cases the contractors have quickly embraced the new concept. In a number of instances they have decided to utilise 'FlexiArch' units in subsequent projects.

5 CONCLUDING REMARKS

In my research over the past 40 years I have been fortunate to have worked on a number of problems which have allowed me, and the talented people I have been privileged to work with, to advance our knowledge of some factors which influence the durability and strength of Reinforced Concrete structures. In the context of the specific topics discussed in this paper the following conclusions have been reached:

1. Research and development on improved in-situ test methods for assessing the strength and in particular the transport properties of concrete have allowed progress to be made on enhanced durability by design. Commercially available equipment is now used internationally
2. Taking advantage of the benefits of compressive membrane action in restrained slabs has led to the development of highly durable bridge deck slabs and cellular reinforced concrete structures. Over the last decade savings of over £200 million have been made in the UK alone by taking advantage of this research
3. The rapid installation of arch bridges is enabled by the use of the innovative 'FlexiArch' which has been proven by research to have all the attributes of conventional masonry arch such as strength, durability and aesthetic appearance. Over thirty 'FlexiArch' bridges are now in service with spans ranging from 4m to 15m.

I would also like to take the opportunity in this keynote address of commenting more generally on the problem solving attributes that many engineers/researchers have in their DNA. Personally I have found that they love solving problems but unfortunately they are not always good at recognising the right one for them. From my own experience of research you can:

1. find a suitable problem yourself if you keep abreast of research in your field
2. stumble across a problem by accident or
3. rely on discussions with other members of our profession to help you identify problems

In order to have a better chance of achieving a successful solution you should:

- focus on those where you have inherent or natural strengths
- be selective i.e. avoid battling on too many fronts or jumping from topic to topic
- ensure it is timely i.e. not too early in the field or starting too late to make an impact, but remember that some researchers spend over 50 years working on a specific topic of research
- once you have opted for a specific problem you should embrace it and seek out all ways of arriving at a solution including working with others when the expertise in your team is lacking

It has been a great privilege to work at what you love doing but my 30 years as a Professor has made me acutely aware that all academics are not equally good at teaching, research and administration. We all have our strengths and weaknesses but by working as a team we can achieve the balance which can lead to excellence on all fronts.

ACKNOWLEDGEMENTS

The input of all my research students, colleagues and friends at Queen's University and elsewhere, is gratefully acknowledged.

REFERENCES

[1] Neville, A.M. and Wainwright, P.J., 'High Alumina Cement Concrete', Construction Press Limited, 1975, 201 pages, ISBN 0904406083.

[2] Long, A.E. and Parkinson, J., 'Pull-off testing yields promising initial results', New Civil Engineer, 27 Feb 1973, pp. 38-39.

[3] Murray, A. McC. and Long, A.E. 'A study of the in-situ variability of concrete using the Pull-Off method', *Proceedings of the Institution of Civil Engineers*, Part 2, Vol. 83, Dec. 1987, pp 731-746.

[4] Basheer, P.A.M., 'A brief review of methods for measuring the permeation properties of concrete in-situ', *Proceedings of the Institution of Civil Engineers*, Structures and Buildings, Technical Note 603, 1993, Vol. 99, pp. 74 - 83.

[5] Basheer, P.A.M., Chidiac, S. and Long, A.E., 'Predictive models for deterioration of concrete structures', *Construction and Building Materials*, Vol. 10, no. 1, 1996, 27-36.

[6] Mehta, P.K., 'Concrete technology at the crossroads - problems and opportunities', Concrete technology - past, present and future. In Proc. V. Mohan, Malhotra Symposium, ed. P. Kumar Mehta, ACI, SP 144, March 1994, 1-30.

[7] Montgomery, F.R. and Adams, A., 'Early experience with a new concrete permeability apparatus', Proceedings Structural Faults - 85, ICE London 1985, pp. 359 - 363.

[8] Basheer, P.A.M., "'Clam' permeability tests for assessing the durability of concrete", Ph.D Thesis, The Queen's University of Belfast, 1991, 438 pp.

[9] Andrews, R.J., 'Design and development of an in-situ chloride migration test', PhD thesis, The Queen's University of Belfast, Northern Ireland, September 1999, 388pp.

[10] Basheer, P.A.M., Montgomery, F.R. and Long, A.E., 'In-situ assessment of durability of concrete motorway bridges', Proc. Idorn, International Symposium, SP131, ACI, March 1990, Toronto, pp. 305-311.

[11] Fazio, R., Mirza, M.S., McCafferty, E., Andrews, R.J., Basheer, P.A.M. and Long, A.E., 'In-situ assessment of corrosion-induced damage of the Dickson Bridge Deck', Proceedings of 8dbmc, Vol. 1, Vancouver, June 1999, pp. 269-279.

[12] Henderson, G.D., 'Development of design procedures for durable, strong and workable concrete mixes', PhD Thesis, Queen's University, Belfast, 1998, pp. 396.

[13] Long, A.E., 'Punching failure of reinforced concrete slabs', PhD Thesis, Queen's University of Belfast, May 1967.

[14] Long, A.E. and Bond. D., 'Punching failure of reinforced concrete slabs', Proc. Inst. Civil Engineers, Vol. 37, pp. 109-139, May 1967.

[15] Wood, R.H., 'Plastic and Elastic design of slabs and plates', Thames and Hudson, London, 1961.

[16] Ockleston, A.J. 'Load tests on a three storey reinforced concrete building in Johannesburg'. *The Structural Engineer*, October 1955, Vol. 33, pp. 304-322.

[17] Masterson, D.M. and Long, A.E., 'The punching strength of slabs, a flexural approach using finite elements', ACI Shear Symposium, Vol. S.P. 42, 1974, pp. 747-768.

[18] Tong, P. Y. and Batchelor, B. de V. 'Compressive membrane enhancement in two way bridge slabs', Cracking, Deflection and the Ultimate Load of Concrete Slab Systems, SP-30, ACI, Detroit, 1971, pp. 271-286.

[19] Canadian Standards Association, Canadian Highway Bridge Design Code (CHBDC), CAN/CSA-S6-00 (new version available for comment 2005 CSA-Technical Committee), Canada.

[20] Kirkpatrick, J., Rankin, G.I.B. and Long, A.E. 'Strength evaluation of M-beam bridge deck slabs', *The Structural Engineer*, vol. 62B, no. 2, September 1984, pp. 60-67.
[21] Highway Agency, BD81/02, 'Use of compressive membrane action in bridge decks', Design manual for Roads and Bridges, Volume 3, Section 4, Part 20, August 2002.
[22] Kirkpatrick, J., Rankin G.I.B. and Long A.E. 'The influence of compressive membrane action on the serviceability of beam and slab bridge decks', *The Structural Engineer*, Vol. 64B, no. 1, March 1986, pp. 6-12.
[23] Highway Agency, BD44/95, 'Departmental Standard, The assessment of concrete highway bridges', Volume 1, Section 3, Department of Transport, Highway and Traffic, 1995.
[24] Mufti, A.A., Jaeger, L.G., Bahkt, B. and WEGNER L.D., 'Experimental investigation of fibre reinforced concrete deck slabs without internal steel reinforcement', *Canadian Journal of Civil Engineering*, Vol. 20, 1993.
[25] Taylor, S.E., Rankin, G.I.B. and Cleland, D.J, 'Serviceability of bridge deck slabs with arching action', *ACI Structural Journal*, Vol. 104, No. 1, Feb. 2007, pp.39-48
[26] Rankin, G.I.B., Niblock, R.A., Skates, A.S., and Long, A.E., 'Compressive membrane action strength enhancement in uniformly loaded laterally restrained slabs', *The Structural Engineer*, Vol. 69, No. 16, August 1991, pp 287-295.
[27] Long, A.E., 'International Patent No. W.O. 2004/044332A1, May 2004.
[28] Gupta, A., Taylor, S.E., Kirkpatrick, J., Long, A.E. and Hogg, I. A 'Flexible Concrete Arch System for Durable Bridges', Proceedings from IABSE Conference, Budapest, 2006.
[29] 29. Highway Agency: BD 91/04 Departmental Standard, Unreinforced Masonry Arch Bridges, Design Manual for Roads and Bridges, Vol. 1, Section 3, Part 14, Department of Transport, Highway and Traffic, 2004.
[30] Long, A.E., Kirkpatrick, J., Gupta, A., Nanukuttan, S. and McPolin, D., 'Rapid construction of arch bridges using the innovative 'FlexiArch', 15 pages, accepted for publication (May 2012), for issue on Arch Bridges, to be published in late 2012 by *ICE Bridge Engineering Journal*.

Making sense of bridge monitoring

Aleksandar Pavic[1], James M. W. Brownjohn[2]
[1]Department of Civil & Structural Engineering, University of Sheffield, Mappin Building, Mappin Street, Sheffield, S1 3JD
[2]Full Scale Dynamics Ltd, The Sheffield Bioincubator, 40 Leavygreave Road, Sheffield, S3 7RD
email: a.pavic@sheffield.ac.uk, j.brownjonh@fullscaledynamics.com

ABSTRACT: This paper presents a vision for the future monitoring systems which will become normal requirements for management of bridges as key objects of national infrastructure in the UK and elsewhere. Rather than being pushed by authorities and legislation, we expect that bridge managers will recognize the clear business cases for investing in well-designed targeted monitoring. To support this proposition, the paper presents three case studies where state-of-the-art bridge monitoring technology was used or potentially could be used to manage the following key aspects of bridge operation and maintenance:

- Assessing bridge live load and long-term ultimate strength based on realistic live strain response data.
- Deciding when to inspect and change bridge bearings
- Deciding when to close various traffic lanes to reduce probability of overstressing bridge structural components.

KEY WORDS: Monitoring, Bridge, Structural Performance Monitoring, Decision Making, Asset Management

1 INTRODUCTION

The UK Government's 2011 National Infrastructure Plan [1] signalled the need for investments of up to £250bn over 10 years to return UK infrastructure (transport, power, communications, water, and waste) to world class levels of performance. Only about a third of this can be provided from a public purse in the UK. The rest must come from private funding - most likely overseas sovereign investment funds. The key problem is clearly how to attract such funding and how to convince private finance that the investment in the UK infrastructure is sound. Having hard data about past and future physical performance of such infrastructure is a way forward to justify investment and attract private funding. In fact, it could well be the *only* way forward.

Focusing on bridges as key elements of any national infrastructure, the American Society of Civil Engineers (ASCE) reports a cost of $140bn to repair all deficient bridges in the United States [2]. Similar to the UK, whilst taxpayers in the USA can be expected to fund a small proportion of such enormous investment, as for the general infrastructure mentioned above, the remainder must come from private sources. The primary requirements for attracting both private and public investment in an infrastructure asset are managed risk and reliability of performance in continuous operation with ever increasing service and safety demands. Maximising return on investment requires minimisation of costs necessary to achieve that performance - put simply *getting more from less*. These requirements highlight the process of the whole-life performance management of civil infrastructure, a process involving decisions about design, construction, operation, maintenance, repair, decommissioning and demolition. Ensuring that such decisions are informed, correct and cost effective is the most important unsolved challenge in civil infrastructure management, attracting hundreds of researchers and multi-£M global research investment. These people and this investment are all trying to solve one of the most challenging problems in civil structural engineering nowadays: how to convert testing and monitoring data from objects of infrastructure, into knowledge and decision making when managing infrastructure as public assets? The problem is particularly acute for bridges, considering their importance, and is really about how to make sense of bridge testing and monitoring data. This research has yet to deliver significant benefits in the real world due to incoherent engagement with stakeholders, misdirected emphasis in the past focusing on hardware rather than data interpretation, tendency to view infrastructure assets in isolation and the lack of a systematic approach to link experiences between different structures. This is a recognised problem in the USA and Federal Highway Administration (FHWA) are still “working the problem” [4].

Focusing on bridges, the above stated problem is obviously not new. A paradigm shift is needed across the board and with all stakeholders in the way how bridges are managed from their conception to their decommissioning. Considerable cultural changes are needed and these will follow changes in the business models used for managing bridges including the legal and economical framework within which public assets like bridges operate. This applies not only to the USA, but also to the UK, Europe and rest of the world. The prolonged crisis which has been shaking the foundations of the world economy for several years now may well become a badly needed catalyst for the required paradigm shift.

The continued drive for better and more enduring performance from bridges is crippled by the lack of technically sound, reliable, harmonised and economic means for monitoring asset condition. Hence, informed decision making by bridge managers is severely impaired. There is potential nowadays to transform monitoring into an *enabling technology* that will revolutionise the decision making process at all stages of an infrastructure’s life-cycle: from design to demolition. This will yield extraordinary reduction of the currently very high direct and indirect cost of bridge performance management. The enabling technology will also foster growth of the infrastructure monitoring and decision support systems as a new technology sector which key role would be to resolve the £multi-trillion global challenge of managing deteriorating and failing infrastructure.

The aim of this keynote paper is therefore to present a case and vision for this paradigm shift, making use of existing examples not only in civil engineering, but also in other engineering disciplines where such paradigm shifts happened and changed forever the ways how industries operated.

2 FUNDAMENTAL CAUSES OF PROBLEM

In essence, the problem lies in the nature of civil structural engineering design and disproportionately low level and certainty of information on which it is based relative to the huge importance of such structures. Because of this, in civil engineering the acceptable level of risk of structural failure or lack of its serviceability is at least an order of magnitude lower than for more technologically advanced structures employed in mechanical and aerospace engineering [1]. There are three key reasons for this low risk approach:

1. Civil infrastructure, in particular major long-span bridges, underpin human society and supports not only traffic but the daily lives of hundreds of thousands of people and economies of linked regions.
2. Unlike aircraft, automobiles, trains and other mass produced machinery, which are extensively tested as prototypes during their design, objects of civil infrastructure including bridges are unique one-off designs with no opportunity for extensive prototype testing during design and before going into service. As such, they are designed with considerably reduced knowledge base and their structural performance is poorly understood making prediction of future behaviour difficult if not impossible.
3. The ambiguity and degree of uncertainty related to the actual operation of the structure, and potential increases in load and usage in the future, force the use of an extremely conservative design embedded in design guidelines which are used instead of prototype testing.

Notwithstanding the low-risk design methodology, critical infrastructure items such bridges deteriorate with time to such a point that, if no action is taken, they become unserviceable requiring closure and repairs, or may even collapse. To guard against this, operating authorities prescribe methods of routine, typically visual, inspection, which are slow, costly, and subjective, hence potentially quite unreliable.

The prime example of the dubious reliability of the current bridge inspection regime was generated in the UK during winter 2011/2012. A sudden and totally unexpected decision to completely close the Hammersmith flyover in London was made on 23 December 2011 after many nights of closure of the flyover for maintenance and visual inspection throughout 2011. This structure takes 90,000 vehicles per day on a strategically vital A4 route making it the prime gateway to London, not just for the West of the country, but also for one of the world's largest and busiest airports at Heathrow. This prime route remained completely closed until 13 January 2012, causing traffic chaos in West London for a period of three weeks, covering the Christmas and New Year holidays before partial reopening slightly reduced the chaos. This situation lasted for months. Apparently, an exceptional overloading event worsened the state of corroded tensioning cables of the 50-year old structure so that they started snapping at a rate fast enough for the authorities to close the flyover. This is speculation, since the structure had not been monitored over a long enough period of time. Hence, there is no information about 'normal loading' and no evidence that that the dramatic closure was actually necessary.

If anybody thought this was a chance the identification of a *new crack* on the already damaged Boston Manor viaduct forced a dramatic closure of the M4 between London and Heathrow airport – a key section along the Olympic Route Network. This lasted for five days in early July 2012. The the new crack had been identified in a "sensitive location" following the final stages of the complex repairs to 15mm long hairline cracks discovered *by chance* [5] in April in welds on the viaduct just west of junction 2 near Hounslow. A 7.5t weight restriction on the damaged stretch had been imposed immediately, diverting coaches and lorries onto busy local roads. The latest news is that Boston Manor viaduct is beyond further repairs and will be replaced.

How many similar cases and surprse total closures are are lurking within the UK fleet of key bridges on the national transportation network?

3 THE WAY FORWARD

Interestingly, if a sudden event happened to a Roll Royce aero-engine high above the Pacific, such as a lightning strike causing the engine to cough, monitoring sensors within the engine would automatically record all relevant responses. This data would be transmitted immediately from the aeroplane to the Rolls Royce 24/7 operations room in Derby, UK which continuously assesses on-line the performance of thousands of working jet engines around the world. Based on the instantaneous information from the aircraft and the expected performance, a decision would be made while the plane is still in the air if the engine requires additional inspection after landing, causing delays and financial losses. In the past and without the benefit of permanent monitoring and data streaming and analysis, this would almost certainly be the case as – similar to bridges – safety is paramount. However, it is not anymore due to this *service based* business model of manufacturing jet engines which is based on the on-line condition monitoring technology and instantaneous decision making process which Rolls Royce mastered and commercialised around the world. The data constantly collected from engines is invaluable to airlines as the information enables Rolls Royce to predict when engines are more likely to fail, letting the airlines schedule engine changes efficiently. Embracing such technology and innovation transformed Rolls Royce from a failing company in 1971 into a currently most successful manufacturer of jet engines in the world.

Why can't the same business model be employed in the management of bridges? Over many years in the UK there has seen fragmentation of construction industry and infrastructure management characterised by significant shift towards the use of subcontracting, overly complex procurement approaches and uncertainty of future work on key infrastructure due to lack of vision and leadership. This has increased transaction costs, encouraged shortermism and deterred industry from a more strategic approach to investment in skills, technology and innovation [6]. There are, however, clear signs that this approach is changing offering great opportunities to the sector, one of them being use of permanent monitoring for effective decision making in managing key objects of infrastructure, including bridges.

The 2nd Future Infrastructure Forum (FIF2), held at Cambridge University on 17-18 January 2012, established a consensus on the importance of monitoring as part of the process of managing the sustainable performance of our existing and new infrastructure. The Forum recognised that we are at the confluence of several, new, game changing, enabling technologies, such as very low cost MEMS sensors, energy harvesting, and all-pervasive high speed wireless networking and the Cloud-based computing that the latter brings. Imaginative integration of these technologies offers the potential for new, radical paradigms in infrastructure creation and performance management that could have a global transformative impact. In essence, we are at a rare convergence point in technological evolution when we can radically rethink the purpose and nature of infrastructure such that it becomes a far more effective shaper of sustainable human behaviour and societal development.

4 MOTIVATION

Wenzel [7] noted that construction sector is conservative needing strong push to motivate it to implement new technologies, such as converting monitoring data into decision making. He outlined the following motivation drivers:

1. Responsibility-driven motivation, stemming from design standards, codes and guidelines which make mandatory requirements to instrument, monitor and interpret before deciding what to do with a particular structure, such as bridge in operation. This is particularly so when covering events such as emergencies or accidents whereby monitoring data before the event can describe what is ‘normal’ and data after the event can be used to establish if the structure still behaves as ‘normal’. Conventional assessment in such situations tend to be overly conservative, usually to compensate for the lack of reliability.
2. Economy-driven motivation, stemming from, say, the need to reduce unnecessary maintenance costs, such as expensive and not particularly reliable regular inspections, or from the need to prioritise repairs within limited budgets which make use of more reliable information about the remaining life prediction of the structure. Another emerging motivation within this category is the need for an informed transfer of ownership from public to private hands, whereby hard data form the structure provides a more reliable information of the value and longevity of the structure which is an asset for the new owner, including their finance and insurance organisations.
3. Curiosity-driven motivation whereby forward-looking owners, operators and – in general – clients, understand limitations of the current civil engineering design practise and want to learn about the actual behaviour to help them plan future designs.

The following examples will demonstrate usefulness of monitoring in decision making about their operation.

5 ASSESSMENT OF BRIDGE UPGRADING

Moyo et al. [8] present the use of bridge monitoring data to assess the effects of bridge upgrading including its strengthening. This is a very powerful example of the usefulness of monitoring as it answers one of the key questions asked after a bridge refurbishment: how long will the refurbished bridge last?

To answer this fundamental question, in-service monitoring of strains of key load-carrying elements under normal live loads before and after the upgrading was carried. This yielded time series of strain data which were analysed using extreme value statistics producing the required estimates of the expected bridge life.

5.1 Structural description

The bridge in question is the Pioneer Bridge (Figure 1) built along Pioneer Road in Singapore between 1968 and 1970. The span is 18.16 m between elastomeric bearings designed as simple supports, and it’s quite wide for such span: 18.80m.

Figure 1. Pioneer Bridge before upgrading.

The bridge deck is made of 37 pre-cast pre-tensioned inverted T-beams, which cross sections are shown in Figure 2. Edge detail of the bridge deck is shown in in Figure 3.

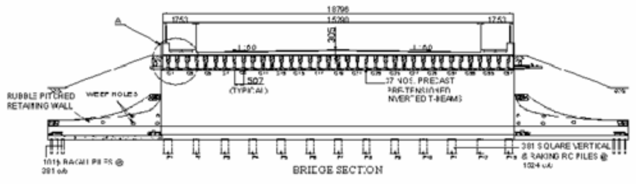

Figure 2. Pioneer Bridge before upgrading.

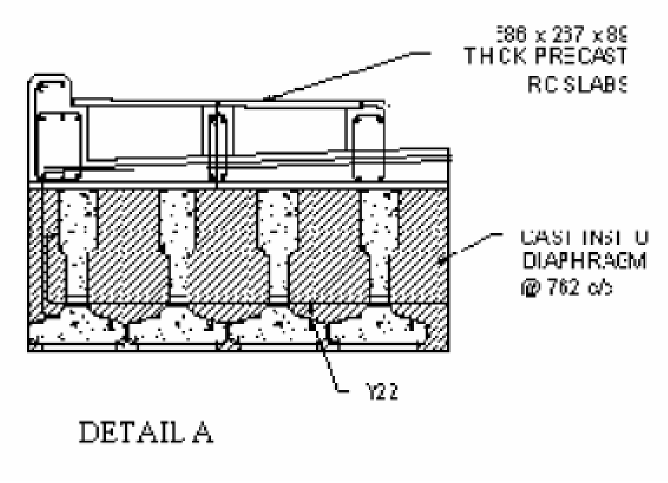

Figure 3. Pioneer Bridge before upgrading.

As with so many other bridges now approaching the end of their design life, this bridge was originally designed for the traffic loading appropriate for the 1960 era. To maintain the load carrying capacity over the extended design life stretching into the 21st century, strengthening works were proposed in which the free rotations of the simply supported system were restrained by monolithisation: making the bridge deck integral with both concrete abutments (Figure 4).

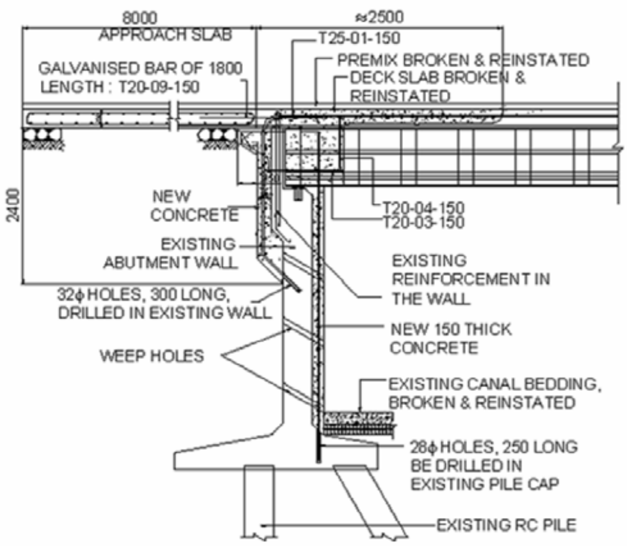

Figure 4. Monolithisation of the bridge deck with abutments.

This was achieved by additional continuation reinforcement and re-concreting of the ends of the bridge deck together with the abutment and infill behind it (Figure 4). As a consequence, reduced end rotations and lower deformations were expected under the live load, yielding lower strains and enhanced bridge life expectancy. As this is a four lane bridge, the strain gauges were mounted on the soffits of girders 7, 15, 24 and 33 under lanes 1-4, respectively.

5.2 Bridge monitoring

The upgrading program of the bridge provided an opportunity to demonstrate the application of longer-term monitoring for condition assessment of bridges. The bridge monitoring program involved continuous measurement of strain time histories at the bridge's midspan using a purpose designed bridge monitoring system. Despite the fact that the system comprised only four demountable strain gauges (DGSs) it yielded all the experimental data needed for condition assessment using measured data and extreme value statistics. Battery powered digital data acquisition at 500 samples per second for each of the four channels was triggered by normal traffic when levels of strain exceeded particular pre-determined values. Data was acquired for at least 20 days before and after the upgrade. Figure 5 shows a typical peak strain value measured at one of the four channels.

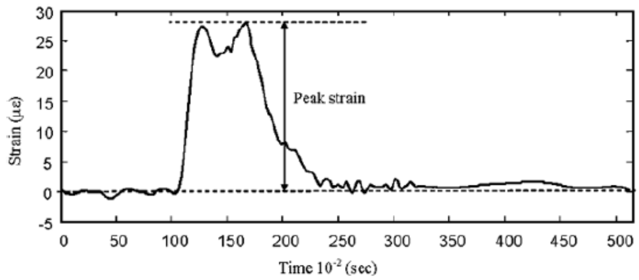

Figure 5. Typical strain record triggered by high peak strain.

Figure 6 shows the scatter plot of all peak strains recorded on the four girders on a day by day basis before the upgrade.

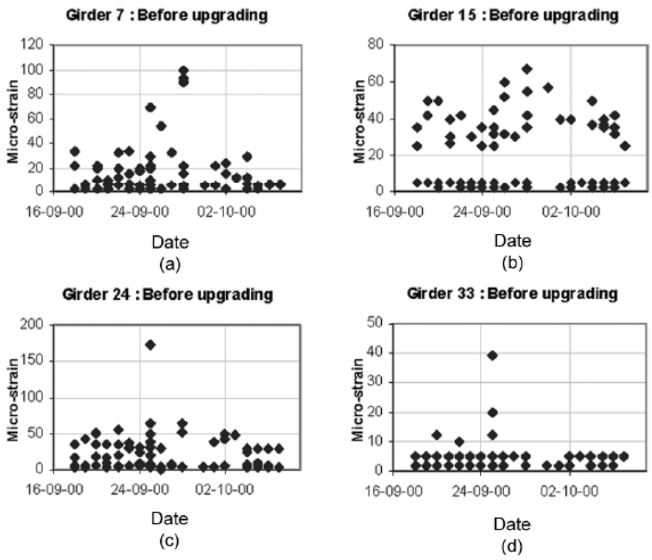

Figure 6. Peak strains before upgrading.

Figure 7 shows the scatter plot of all peak strains recorded on the four girders on a day by day basis before the upgrade.

Looking at Figure 6 and Figure 7, the maximum strain before the upgrade was recorded for girder 24 (Lane 3) at 172 micro-strain whereas its counterpart after the upgrade was recorded for Girder 15 (Lane 2) at 90 micro-strain.

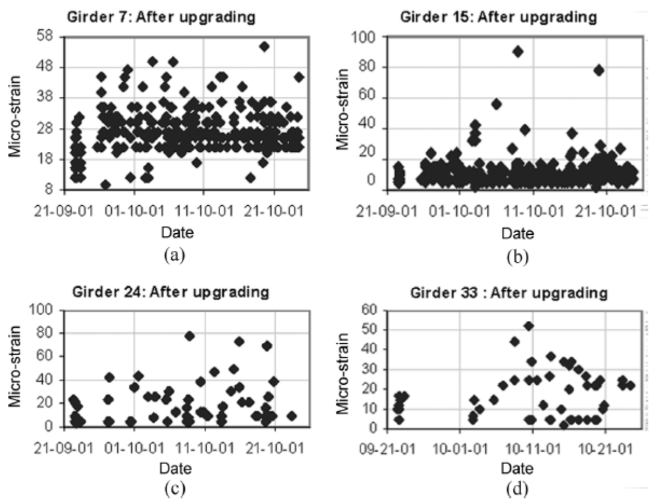

Figure 7. Peak strains after upgrading.

5.3 *Live loading assessment*

Bridges are normally evaluated using abstract live loads which are conservative but often disconnected from the reality of bridge´s day-to-day operation. On the other hand, strain measurements over a prolonged period of time integrate in the most realistic manner key aspects of bridge live loading with site specific conditions such as: traffic volume, bridge dynamic properties, road conditions, vehicle suspension, speed environment, traffic mix and many more important but difficult to quantify conditions. Therefore, a rational way forward would be to use measured peak strain values and apply theory of extreme value (or Gumbel) distribution on them, considering that such distribution was proven to be valid for the maximum traffic loading and the resulting bending moments and shear forces [9].

Figure 8 shows predicted maximum strain values in 120 years of service based on the measured data for Girder 7. The reduction of maximum values from over 215 micro-strain to 160 micro-strain is a positive consequence of the upgrading.

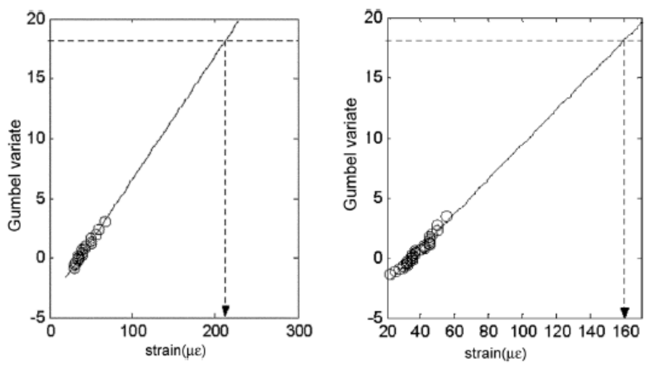

Figure 8. Girder 7 (Lane 1) 120 year live load strain before (left) and after (right) upgrading using extreme value statistics.

The calculated live load strain needs superimposing with the self-weight and dead load strain to judge the overall maximum (ultimate) strain levels which can be used to assess the improved bridge´s strength after the upgrade for the most-realistic as-measured live load conditions.

6 ASSESSMENT OF BRIDGE BEARINGS

The Humber Bridge was opened in 1981. Spanning 1410m, it held the record of the world´s longest single spans suspension bridge until 1997. The Bridge spans the Humber Estuary between Hessle (North) and Barton-on-Humber (South). The Hessle side span is 280m and the Barton side span is 530m (Figure 9).

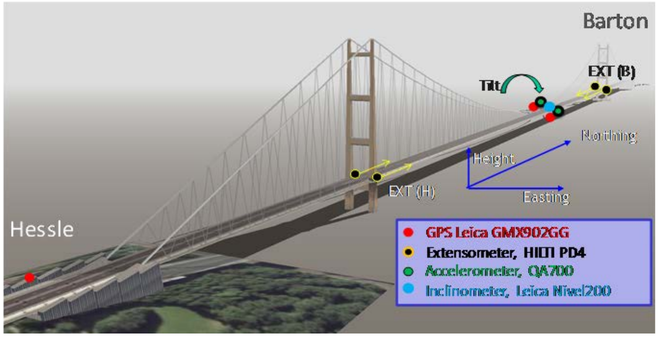

Figure 9. Humber Bridge instrumentation

The aerodynamically shaped bridge box girder is discontinuous at the towers. At each end there is a pair of ´A-frames´ which are approximately 3.8 m tall and 3.4 m wide (Figure 10). These bearings primarily accommodate axial movement of the span ends, but also permit rotation of the deck in the horizontal plane and in the vertical plane of bridge axis and towers as the bridge deforms under a combination of traffic, wind and temperature effects. In total there are 12 of these bearings, four on each span.

A pair of Hilti PD4 extensometers on each end of the main span was used to monitor the longitudinal deck movement at the positions of the two A-frames in Figure 10 (bottom). Hence, these two sets of data provided information to measure both longitudinal extension and horizontal plane rotation of the bridge at its end.

The A-frames were originally designed to accommodate around + or – 1m of longitudinal deck movement due to:

- Traffic action (+/- 0.7m)
- Dynamic wind action (+/- 0.2m)
- Thermal effects (+/- 0.3m)

The end rotation is strongly dependent on wind speeds, as shown in Figure 11.

Ambient acceleration response of the deck is continuously recorded at midspan and used to estimate (in real time) the natural frequencies and damping ratios of the lowest frequency vibration modes. For the first (lateral) mode of vibration, Figure 12 shows the estimated natural frequencies as a function of the RMS of the corresponding block(s) of acceleration data. It can be seen that at about 0.2m/s^2 RMS the frequency generally reduces and stabilises at about 0.054 Hz for higher levels of response. This indicates the likely non-linear ´stick-slip´ behaviour somewhere in the structure, as confirmed by damping estimates whereby a similar ´unsticking´ effect is observed roughly at the same RMS acceleration levels (Figure 13). The damping, however, is amplitude-dependent with lower damping corresponding to higher responses.

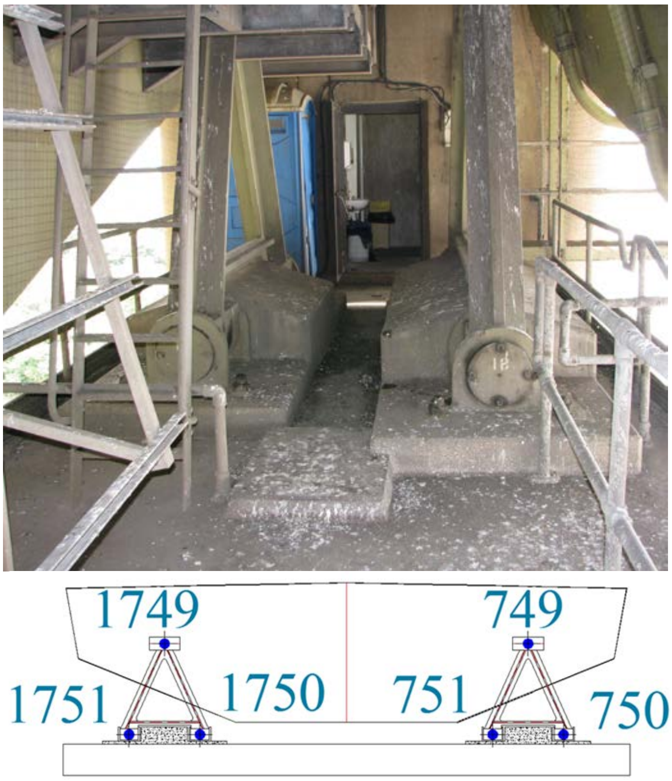

Figure 10: Top: Photo showing a pair of A-frames, one for the main and one for the side span. Bottom: The sketch shows a pair of A-frames connected to the main span box girder.

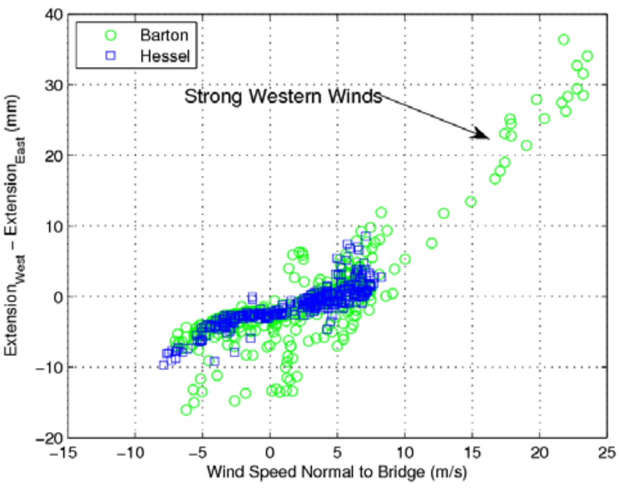

Figure 11. Hessle end rotates less than the Barton end under strong Western winds.

Figure 14 (top) shows diurnal variation of the four horizontal displacements measured bz extensiometers. Figure 14 (bottom) cumulative quasi-static horizontal displacements of the four points on the two ends of the main span which indicate that their total travel is between 2m and 3m over the 10 day analysed. This means that each bearing travelled at least 3km since the opening in 1981; this is in fact a significant underestimate since the data exclude motion with periods of up to 30 minutes arising due to vehicle transit and dynamic response. Not surprisingly, this has been linked with excessive wear at the A-frames and the likely stick-slip effect previously mentioned Closer inspection indicated that one of the bearings visibly dropped and is resting on the concrete plinth underneath due to wear of the bottom of the pin-bush arrangement. Hence, in recent years the adequacy of capacity and performance of the main span A-frames has been questioned, based on the monitoring results which highlighted potential issue in the structure.

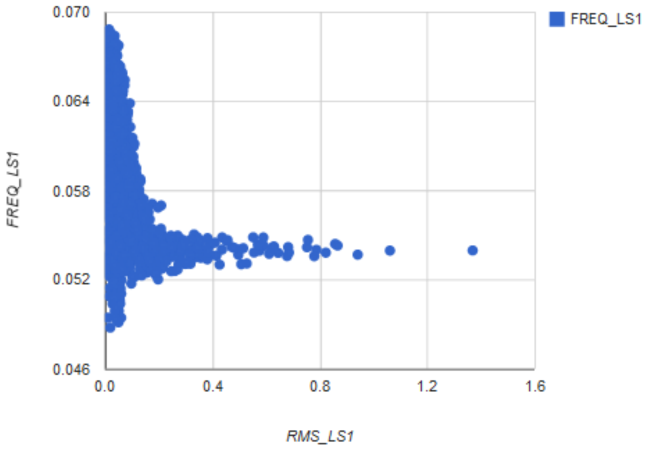

Figure 12. Amplitude-dependent natural frequency.

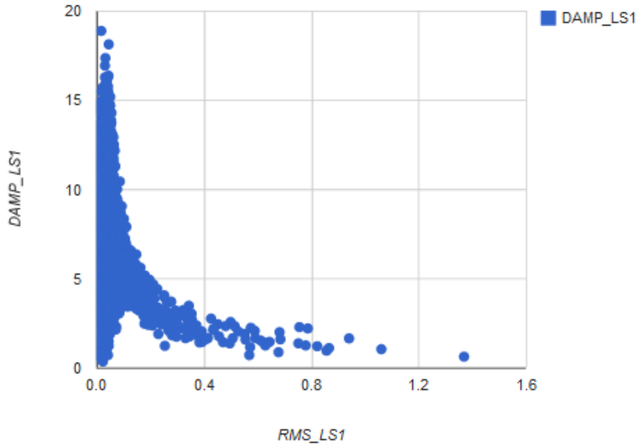

Figure 13. Amplitude-dependent damping.

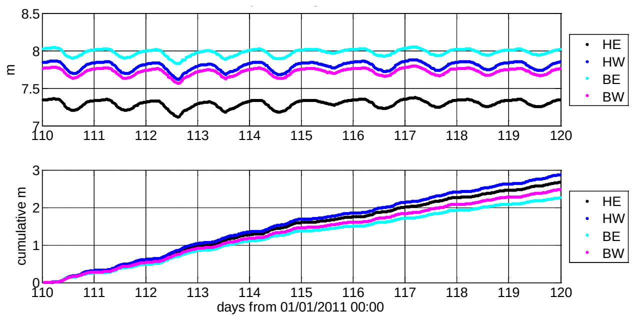

Figure 14. Diurnal variation of horizontal displacement at the bridge ends (top). Cumulative displacement of bridge decks over 10 days.

7 BRIDGE DAY-TO-DAY TRAFFIC MANAGEMENT

Modern bridge monitoring technology enables on-line access to continuous data streams, including video data, which can be used to see live performance of the bridge. Such systems may be used to control day-to-day bridge usage to avoid potential overstressing of structural elements.

Figure 15 shows a situation on a major partly suspension bridge where one half of the bridge is empty and the other is fully loaded due to a morning rush-hour accident.

Figure 15: Traffic accident scenario.

As a consequence, the on-line monitoring system immediately registered that the stay cable tensions suddenly peaked whereas the natural frequency of the system dropped suddenly (Figure 16).

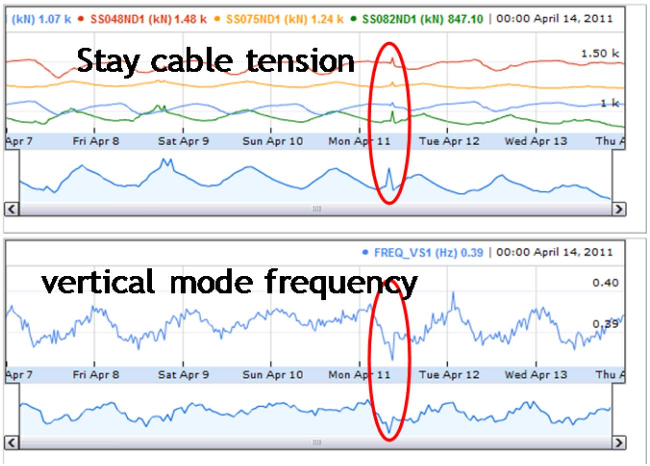

Figure 16. On line monitoring system picked up sudden tensions in stay cables and drop in the natural frequency of the bridge structure, which could be set up to trigger alert when managing traffic in cases of frequent bridge congestions.

Figure 17 shows a major 6-lane road bridge in Continental Europe. The steel structural system with inclined supports acts as a ´shallow frame with end columns rigidly connected to the structure that are ´sensitive´ to temperature effects.

Figure 18 shows bending moment diagrams due to partial traffic load and temperature effects of +35^{0}C. A potential problem for this bridge structure is that the combination of live load as shown in Figure 18 (top) with winter temperature of -35^{0}C will make sure that the two bending moments arithmetically add at the bottom of the vertical end column which is fixed.

This is potentially unsafe situation which can be managed by a permanent monitoring system which would monitor temperature and strain/stresses at the bottoms of the end columns. In case of low temperatures and if the strain readings require, the traffic over this vital bridge can be reduced, reducing the risk of a potentially unsafe situation that would otherwise require prevention by disruptive and expensive remedial work on the end columns.

Figure 17. Major road steel bridge.

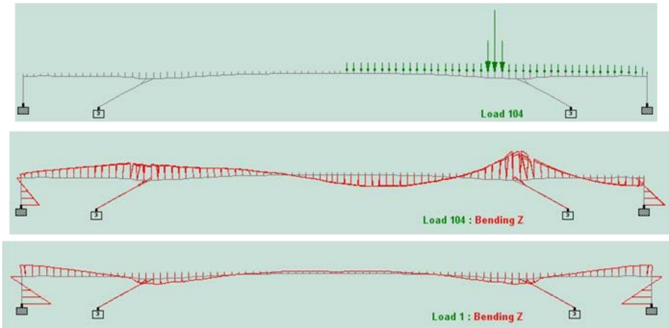

Figure 18. Bending moment diagrams due to partial traffic load and temperature effects

8 CONCLUSIONS

This paper presents a vision for the future monitoring systems which will become normal requirements for management of bridges as key objects of national infrastructure in the UK and elsewhere. Rather than being pushed by authorities and legislation, we expect that bridge managers will recognize the clear business cases for investing in well-designed targeted monitoring.

To support this proposition, the paper presents three case studies where state-of'the-art bridge monitoring technology was used or potentially could be used to manage the following key aspects of bridge operation and maintenance:

- Assessing bridge live load and long-term ultimate strength based on realistic live strain response data.
- Deciding when to inspect and change bridge bearings
- Deciding when to close various traffic lanes to reduce probability of overstressing bridge structural components.

REFERENCES

[1] National Infrastructure Plan 2011, HM Treasury. http://www.hm-treasury.gov.uk/national_infrastructure_plan2011.htm
[2] http://www.infrastructurereportcard.org
[3] Moon FL, Aktan AE 2011, International guidelines for application of technology to bridges, for FHWA Long Term Bridge Program (draft), Also Aktan et al., 2000, ASCE EMD 126(7).
[4] http://www.fhwa.dot.gov/research/tfhrc/programs/infrastructure/structures/ltbp
[5] Wynne, A. Worsening cracking problem closes M4 betwteen London and Heathrow, NCE, 7 July 2012. http://www.nce.co.uk/news/structures/worsening-cracking-problem-closes-m4-between-london-and-heathrow/8632760.article
[6] HM Treasury & Infrastructure UK, 2010.
[7] Wenzel, H. The Character of SHM in Civil Engineering, Chapter 118, Encyclopedia of Structural Health Monitoring, John Wiley & Sons Ltd. 2009.
[8] Moyo, P., Brownjohn, J. M. W. and Omenzetter, P. Highway bridge live loading assessment and load carrying capacity estimation using health monitoring ssystem. Structural Engineering and Mechanics, 18(5), 609-626, 2011.
[9] Das, P. C. Assessment loading criteria for bridge decks, piers and parapets, Structures and Buildings, ICE, 146(1), 411-421. 2001.

Keynote Lecture

Large driven piles: offshore, near-shore and land-based applications

Richard Jardine[1]
[1]Department of Civil and Environmental Engineering, Imperial College London, United Kingdom
email: r.jardine@imperial.ac.uk

ABSTRACT: Professor Richard Jardine, Head of Geotechnics and Professor of Geomechanics at Imperial College London, will present a lecture on the design and underlying research of large driven piles. With references to design guidelines, current research, suitable modelling, and recent field experimental results from across the globe, he will provide designers with a range of tools to use these piles for effective solution to significant modern geotechnical challenges.

KEY WORDS: Large driven piles; offshore; near-shore; land-based

1 BIOGRAPHICAL SKETCH

Professor Richard Jardine is Head of Geotechnics and Professor of Geomechanics at Imperial College London. He is currently involved in a major BP funded study into climate change Impact in permafrost regions, and a project into pile ageing processes. He is a member of the UK's 2008 Research Assessment Exercise Panel for Civil Engineering. He has managed several large international joint industry research projects and collaborated with many other groups worldwide. He has worked as a Visiting Professor in both Singapore and Sapporo, Japan, and is Chairman of Committee TC-29 of the ISSMGE (Advanced laboratory testing of geomaterials) and sits on API/ISO and SUT Committees on Offshore Foundations.

Professor Jardine has written over 160 academic papers and his areas of expertise include coil properties, advanced laboratory and field measurement techniques, soil characterisation; offshore geotechnics, foundation analysis, slope stability, driven pile behaviour, soft ground engineering, geotechnical instrumentation.

Figure 1. Prof. Richard Jardine.

2 CONCLUSIONS

This lecture will make the following conclusions:

- Need for improved capacity methods and SI approaches
- Background research outlined
- New API/ISO ‘sand’ methods reviewed, way forward for practical application discussed
- ICP track record reported; fit for purpose
- Many improvements possible - new research on ageing
- Preliminary discussion offered on effective stress approaches for clays and residual soils
- Ways of modernising deformation analysis also noted

ACKNOWLEDGMENTS

For many contributions:

- Research sponsors and partners: BP, BRE, IFP, EPSRC, Exxon, HSE, Shell, INPG 3S-R lab group, Total and others.
- Current and former co-workers: Andrew Bond, Fiona Chow, Pierre Foray, Tony Ho, Kostas Kanellaidis Barry Lehane, Andrew Merritt, Robert Overy, Siya Rimoy, Matias Silva, Jamie Standing, Zhongxuan Yang, Bi-tang Zhu and many others.

www.bcri.ie

BCRI 2012

Technical Contributions

Bridge-to-vehicle communication for traffic load mitigation

C.C. Caprani[1]
[1]Department of Civil & Structural Engineering, Dublin Institute of Technology, Ireland
email: colin.caprani@dit.ie

ABSTRACT: Successful mitigation of critical traffic loading events could significantly increase the useful service life of existing bridges. This work considers a communications system in which the truck receives wireless broadcast information from a bridge, before it arrives at the bridge. The broadcast informs the driver of the required gap to the vehicle in front. The driver then responds to this, increasing the gap between heavy vehicles, thus reducing the load experienced by the bridge. This work explores some of the parameters related to the bridge-to-vehicle communication system, and its effectiveness in reducing load effect. Different bridge lengths and load effects are considered, as are the required time gap adjustment, the required broadcast distance, and the required level of driver adherence to ensure success of the measure. It is found that there is a complex interaction between the problem parameters, and not all combinations are successful. However, suitable combinations can reduce extreme traffic loading by up to 30%. Therefore this work offers promise in extending the useful life of existing bridges.

KEY WORDS: Bridges; Traffic; Loads; Long-span; Congestion; Communication; Wireless.

1 INTRODUCTION

1.1 Motivation

Many long-span bridges around the world were built in the early- to mid-twentieth century. Such bridges are located on arterial transport routes, by raison d'être, and as such are critically important to the economy of the region and nation they serve. However, just as these bridges are ageing and reaching the end of their design lives, the traffic loads which they support are increasing, with road freight transport typically keeping pace with economic growth [1]. Consequently, in the coming years, the owners of such bridges will be seeking solutions that ensure public safety whilst keeping the bridge operational. This work examines a traffic control measure that may result in a reduction of traffic load effect, and meet the aforementioned goals.

1.2 Long-span bridge traffic load models

The critical traffic loading scenario for long-span bridges is congested traffic [2]. In developing codes of practice for such bridges, researchers typically assume very small gaps between the vehicles in recorded or simulated traffic. For example, in the background studies for the Eurocode, truck traffic measured from the A6 Auxerre motor-way in France, was used, with gaps of 5 m imposed between successive vehicles [3]. Bailey [4] used a beta distribution to model the distance between vehicles in congestion, the mode of the distribution gives a bumper-to-bumper gap of approximately 6.4 m, with a minimum of 1.2 m. More recently, Nowak et al. [5] removed cars from a measured vehicle stream and imposed minimum gaps of 7.6 m between trucks.

The arrival of successive vehicles has generally been taken to be independent and random. This is the case in the background studies to the Eurocode [6], and in the Markov process approach of Crespo-Minguillón & Casas [7]. Dependency between successive arrivals of vehicles has been recently studied by Enright et al. [8]. They find that platoons of trucks can be more common than independent random arrivals yield. This dependency between vehicles results from 'sorting' of vehicles by their individual desired velocities. Since trucks often have a lower speed limit than cars, car drivers will often prefer to change lane. Typically therefore, the inside lane of a highway has a higher percentage of trucks. This phenomenon is significant for bridge loading. However, if the gap between successive arrivals of trucks is controlled, then the bridge traffic load effect may be reduced.

1.3 Control of traffic loading on bridges

The control of traffic to reduce load effects on a bridge has not been the subject of much research in the past. Two methods currently used are to reduce the number of traffic lanes carried by the bridge – commonly used for longer span bridges, or to post load limits on the bridge, preventing individual heavy vehicles from using it – commonly used for shorter span bridges. For long span bridges, closing lanes reduces the load on the bridge, but by reducing the bridge traffic capacity it can lead to traffic congestion problems. Restricting heavy vehicles from using a long-span bridge is also effective, but since such bridges are critical infrastructure no alternative route may be available.

A detection and control system was installed on the Clifton suspension bridge, Bristol, UK [9]. Opitz [10] uses a Weigh-In-Motion (WIM) system to monitor the traffic loads coming on to a bridge. The proposed system sends vehicle weights back to a control station, which could then restrict access to the bridge. Atkinson et al. [11] proposed a two-lane load control system incorporating bending plate weigh beams and vehicle detector loop arrays at the approaches of the bridge. Lane closures were implemented if the combined load from the two lanes on the bridge exceeded the set limit. Kim et al.

[12] proposed a load control system where vehicles over a certain height were pre-selected for weighing. Subsequently, vehicles over 40 tonnes were not allowed access to the bridge whilst vehicles under 40 tonnes were re-injected into the traffic stream.

2 MICROSIMULATION MODEL

2.1 The Intelligent Driver Model

The Intelligent Driver Model (IDM) is a microscopic vehicle-following model developed by Treiber and others ([13][14]). Its equations describe the motion of a vehicle in response to its surroundings, given some mechanical and driver performance parameters. In particular, the IDM is based on the idea that a driver tries to minimize braking decelerations. The acceleration a vehicle undergoes is given by:

$$\frac{dv}{dt} = a\left[1 - \left(\frac{v}{v_0}\right)^{\delta} - \left(\frac{s^*}{s}\right)^2\right] \quad (1)$$

which is a combination of the vehicle's acceleration towards the desired velocity, v_0, where a is the maximum acceleration and δ is the velocity exponent (taken as 4), with the vehicle's decelerations due to interaction with the vehicle in front, based upon the ratio of the current gap, s, to the desired minimum gap, s^*, described by:

$$s^* = s_0 + s_1\sqrt{\frac{v}{v_0}} + vT + \frac{v(\Delta v)}{2\sqrt{ab}} \quad (2)$$

in which s_0 and s_1 are termed the minimum and elastic jam distances respectively, T is the desired time headway, Δv is the approach velocity to the leading vehicle, and b is the comfortable deceleration.

2.2 The MOBIL lane change model

The MOBIL lane-changing model was developed by Kesting et al. [15] and is adopted here. Figure 1 illustrates the topology of a lane change event, where the subscript *c* refers to the lane-changing vehicle; *o* refers to the (proposed) old follower; and *n* to the proposed new follower. In the following notation, the tilde (~) refers to parameter values after the potential lane change. The vehicles in front influence the event since the accelerations of the considered vehicle (*c*) are calculated according to the car-following model given in Equations (1) and (2).

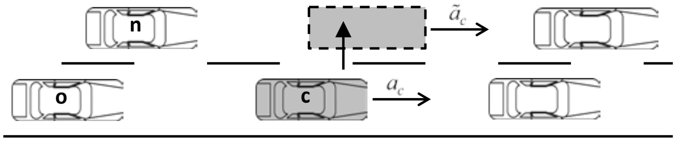

Figure 1. Vehicles involved in lane-changing manoeuvre (adapted from Kesting et al. [15])

A lane change only occurs if the incentive and safety criteria are satisfied. The incentive criterion determines the acceleration advantage that would be gained from the manoeuvre:

$$\tilde{a}_c(t) - a_c(t) \geq \Delta a_{th} + p\left[\left(a_n(t) - \tilde{a}_n(t)\right) + \left(a_o(t) - \tilde{a}_o(t)\right)\right] \quad (3)$$

The acceleration advantage to be gained by the lane-change must be greater than both a threshold acceleration, Δa_{th}, used to dampen out changes with marginal advantage, and a weighted (p) disadvantage to vehicles in both the current ($a_o(t) - \tilde{a}_o(t)$) and target ($a_n(t) - \tilde{a}_n(t)$) lanes. The politeness factor accounts for the acceleration of other vehicles, and for driver aggressiveness. It is this balancing of accelerations that gives rise to the name MOBIL, as Minimizing Overall Braking Induced by Lane changes.

The second criterion that must be satisfied for a lane change event to occur is the safety criterion, given by:

$$\tilde{a}_n(t) \geq b_{safe} \quad (4)$$

which ensures that any deceleration that would be experienced by the new follower are above a minimum safe limit, b_{safe}, typically taken as -12 m/s^2.

The formulation presented applies symmetrically between adjacent lanes, typical of some highways (the US for example). Asymmetric passing rules are implemented by including a bias acceleration Δa_{bias} towards the slow lane.

3 TRAFFIC, ROAD, & BRIDGE DESCRIPTION

3.1 Traffic data

This work uses weigh-in-motion (WIM) data obtained from the A4 (E40) at Wroclaw, Poland (Figure 2) [16]. Both lanes in one direction were measured. In total 22 weeks of traffic was recorded, including cars, from 1 January 2008 to 5 June, 2008 of which 87 days of weekday traffic are suitable for further use. Weekends exhibit quite different traffic composition, and so are excluded. Trucks with up to 9 axles were measured; no trucks with more axles were observed.

Figure 2. Weigh-In-Motion site on Autostrada A4, Euroroute E40, near Wroclaw, Poland.

Figure 3 shows the hourly flows recorded for each day, and the overall average. Some days are unusually low due to reduced economic activity, such as 1 January for example. It is clear from Figure 3 that there is a significant change in the traffic behaviour between the hours of about 22:00 and 06:00. As a result of the distinct differences in night and day traffic, this work is restricted to consideration of the daytime traffic only. The inclusion of night-time traffic into congested traffic loading scenarios on the bridge is not done due to the reduced likelihood of congestion occurring at night. Thus, only traffic between the hours of 06:00 and 22:00 is considered.

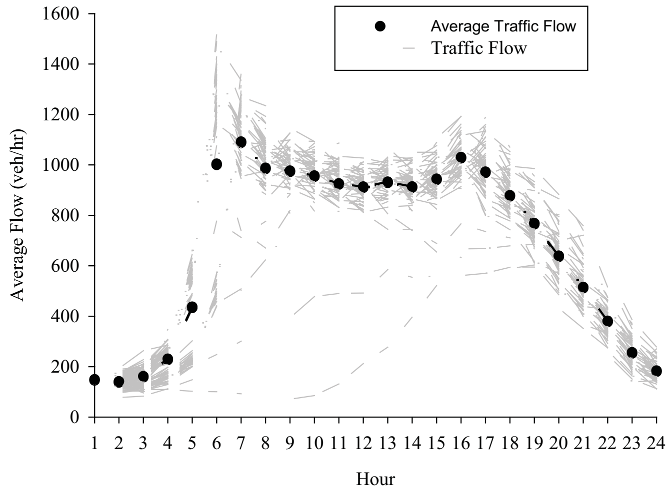

Figure 3. A4/E40 Wroclaw hourly flows.

3.2 *Microsimulation parameters*

The IDM parameters used in this study are as per Treiber et al. [13] and are given in Table 1. The desired velocity has a uniform distribution about the mean values, similar to Kesting et al. [15] in the development of the MOBIL model. The MOBIL parameters are taken from this paper also. A lane change minimum gap of 2.0 m is also enforced, and vehicles are not permitted to change lanes within 1.6 s of a previous lane change. This is to reflect the duration of a lane change in reality, which is carried out in a single time step in the simulation, which is 0.25 s as per Kesting et al. [15].

Table 1. Parameters of IDM and MOBIL models used.

	Cars	Trucks
Desired velocity, v_0	120 km/h (±20)	80 km/h (±20)
Safe time headway, T	1.2 s	1.7 s
Maximum acceleration, a	0.80 m/s^2	0.40 m/s^2
Comfortable deceleration, b	1.25 m/s^2	0.80 m/s^2
Minimum jam distance, s_0	1.0 m	1.0 m
Elastic jam distance, s_1	10.0 m	10.0 m
Politeness factor, p	0.25	0.25
Changing threshold, Δa_{th}	0.1 m/s^2	0.14 m/s^2
Maximum safe deceleration, b_{safe}	12 m/s^2	12 m/s^2
Bias for the slow lane, Δa_{bias}	0.30 m/s^2	0.3 m/s^2

A minimum limit of s_0 is applied when calculating s^* for proposed lane changes from Equation (2). This is because s^* can be negative if the front vehicle in the target lane is much faster than the vehicle considering changing lanes ([17][18]).

3.3 *Road configuration*

A 10 km long two-lane single-direction virtual road is used in this work. Vehicles are injected at the start of this road, according to their site-measured time-stamps. They are then simulated 'driving' this road using the IDM and MOBIL models. Congestion is induced throughout each day of traffic through use of a strong inhomogeneity at 9.50 km: a speed-limit of 20 km/h and an increase in the safe-time headway of 0.5 s is applied to all vehicles. The start of each of the bridges considered is located at 8.00 km. Congestion then builds, propagating backwards from 9.50 km, at a speed of about 12-15 km/h. Due to the gaps in the input traffic between 22:00 and 06:00, this induced congestion clears. As a result, each day is considered independent and identically distributed.

3.4 *Bridges and load effects considered*

The bridges considered for this work are 100 m, 200 m, and 500 m long. Load Effect 1 (LE1) which is just the total load on the bridge; and Load Effect 2 (LE2) is the hogging moment over the central support of a two-span beam. The total load effect on the bridge cross section is considered – no lateral distribution of load effect is accounted for.

4 GAP CONTROL MEASURE

4.1 *Bridge-To-Vehicle (B2V) communications*

A novel aspect of this work is the proposed bridge-to-vehicle communications (B2V) (Figure 4) to control the gaps between vehicles in such a way that bridge traffic load effect is reduced. Bluetooth or similar technology can be used to broadcast bridge-specific information to on-board speed or gap regulators to be installed on trucks. This form of Machine-to-Machine (M2M) technology is very new but shows great promise, especially in intelligent transport systems [19]. The implementation and potential effectiveness of such a system in reducing bridge traffic load effect is examined using various combinations of parameters.

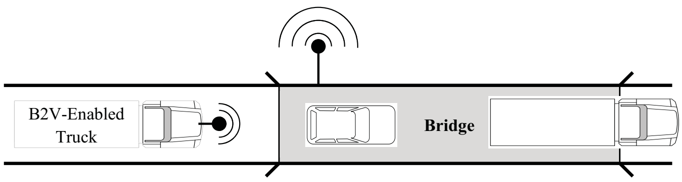

Figure 4. Bridge-To-Vehicle communications.

4.2 *Variables considered*

The main variables considered to examine the feasibility of the B2V system are given in Table 2 and described below. Low and high values for each variable are considered. Each of the three bridge lengths, and the two load effects are examined under each of the variable values shown.

The safe time headway is a parameter of the IDM that influences how close a driver travels to the vehicle in front, as may be ascertained from Equation (2). The concept of the

B2V system is that the vehicle responds to a bridge signal by gradually increasing the distance to the vehicle in front (i.e. increasing the safe time headway). The magnitude of the required vehicle response is simulated through this variable.

Table 2. Variables and values considered.

Variable	Low	High
Safe time headway (s)	2.0	3.0
Broadcast distance (m)	500	1000
Adherence Rate (%)	10	50

The broadcast distance comprises two aspects. Firstly it may represent a technological limitation of the feasible wireless communication distance. However, this can be easily overcome through the use of different technologies as may be required. Therefore, its second, more important, aspect is that it is the distance over which the vehicle has to respond to the bridge's signal to increase headway.

The adherence rate amongst the truck population reflects the number of vehicles that have both B2V capability and respond to the bridge signal accordingly. Thus, this rate accounts for B2V-enabled vehicles that may not respond to the signal. Further, this rate only applies to the trucks in the traffic stream: cars are assumed not to have B2V capability.

5 SIMULATION RESULTS

5.1 *Basis of comparison of extreme load effects*

Daily maximum load effects are determined for each B2V scenario. The Generalized Extreme Value distribution is fitted to this data and the characteristic load effect for a 1000-year return period, as used for the Eurocode [20], is predicted.

The results for each B2V scenario are compared to a benchmark scenario for each bridge length and load effect. The benchmark load case represents the current situation in which no B2V load control measures exist. The ratio of the scenario's characteristic load effect to the benchmark characteristic load effect is used as the basis for comparison. A ratio under unity therefore represents a reduction in characteristic load effect brought about by the measure.

5.2 *Preliminary results*

The ratios of the 1000-year extrapolation results are given in Table 2 and Figure 5 for each of the scenarios considered. It is immediately apparent that most results show a decrease in the characteristic load effects, demonstrating the effectiveness of the proposed intervention. Interestingly, in some cases an increase in the characteristic load effect is found.

From the presented results, it is also apparent that there is a great deal of variability in the results. It must be recalled that since the traffic is the very same for each day this variability is caused by the measures alone, and is not the result of variability between simulations. However, the individual daily maximum loading events may be different between simulations as different traffic topologies are caused by the measures. It is also clear that there is no obvious relationship between the load effects and the introduced measures immediately apparent.

Table 3. Ratios of daily maximum mean load effect.

Variable*			Load Effect 1			Load Effect 2		
T	L	A	Bridge Length (m)			Bridge Length (m)		
(s)	(m)	(%)	100	200	500	100	200	500
2	500	10	0.85	0.87	0.91	0.83	0.71	0.93
		50	0.99	0.83	0.97	1.00	0.75	0.98
	1000	10	1.17	0.90	1.00	1.14	0.76	1.01
		50	0.96	0.97	0.98	0.90	0.70	0.97
3	500	10	0.83	0.84	1.02	0.90	0.70	1.02
		50	0.86	0.95	0.89	0.82	0.83	0.96
	1000	10	0.84	0.97	0.98	1.03	0.88	1.01
		50	0.91	0.79	0.96	1.16	0.66	1.05

* T – safe time headway; L – broadcast distance; A – adherence rate

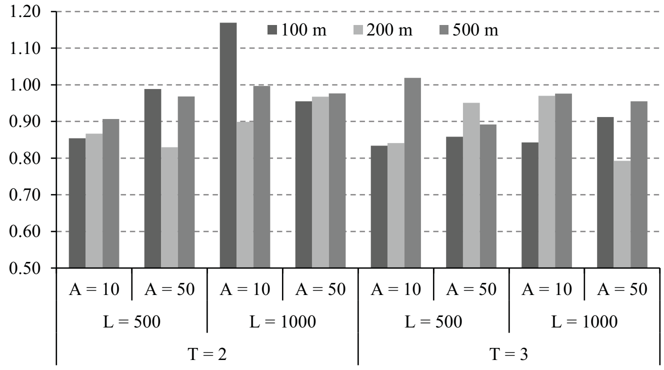

(a) Load Effect 1;

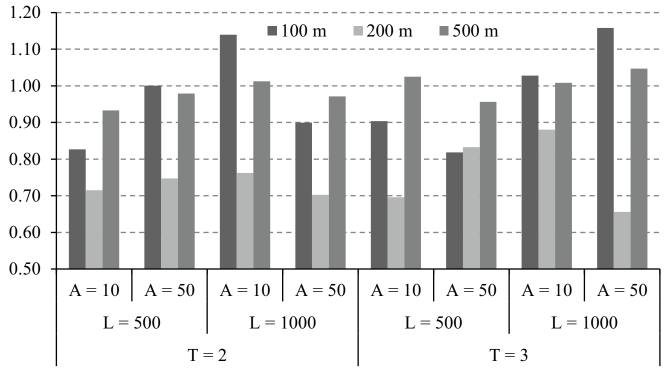

(b) Load Effect 2;

Figure 5. 1000-year extrapolation results (see footnote to Table 2 for explanation of symbols).

5.3 *Further exploration*

The variability in the results is surprising. Intuitively it may be expected that a longer broadcast distance might give trucks a better chance of adhering to the induced safe time headway. Larger safe time headway should give larger gaps, leading to lower density, and thus reduced load effect. Finally higher adherence should surely mean that more vehicles participate in developing the lower densities. Examination of the results shows that this combination of factors leads to lower load effects for the 200 m bridge length. However it is surprising that similar reduction for the other load effects is not realized. Further investigation is required to fully understand the cause of this phenomenon.

The variation in density over the simulation day is examined. Traffic densities on the road (total density across both lanes) from 8.0-8.5 km are extracted for each scenario every 15 minutes throughout the entire simulation. The mean densities at particular times of the day are found across all simulation days. A sample analysis is shown in Figure 6(a). For each scenario the mean densities thus found are given in Figure 6(b). It is clear that there is no difference in the mean densities for different scenarios. This might suggest that the increased gaps between trucks are in-filled by cars. There may also be an uneven distribution of densities between the lanes.

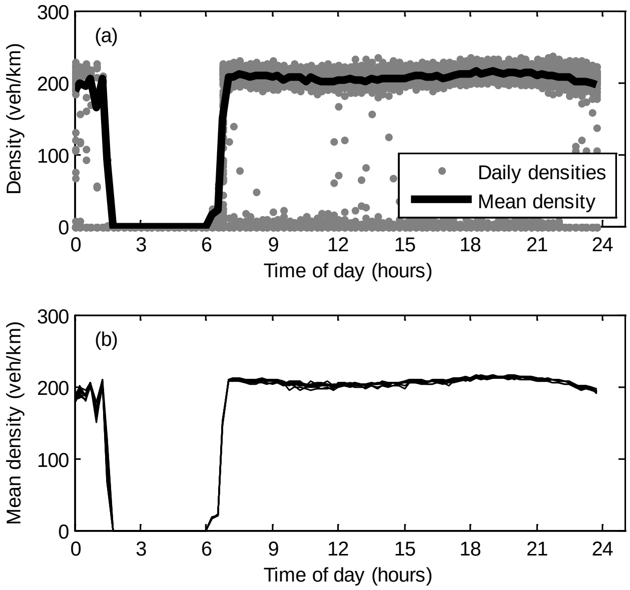

Figure 6. Mean daily densities: (a) sample analysis for the benchmark scenario; (b) mean daily densities for all scenarios.

5.4 *Analysis of Variance*

The results show that there is a complex interaction between the varied parameters to the problem. A means of extracting the influence of and the most important parameters is needed.

Analysis of Variance (ANOVA) is a statistical method of identifying trends from data (the response variable) that result from categorized (or levels of the) input variables (the factors) [21]. It is commonly used in medical trials and epidemiological studies. Specifically, ANOVA allows one to determine, using hypothesis testing, whether or not there is statistical significance in the response variable due to one or more factors. It does so by assuming the underlying populations to normally distributed, and using the *F*-test statistic to compare means, accounting for both within-group and between-group variabilities.

In this work, the response variable is the load effect ratio and it is subject to natural (within group) uncertainty regardless of the gap measures (or factors) taken (if any). Comparison of the influence of the different factors (e.g. adherence, broadcast distance) on the load effect ratio (between group) can therefore be made with statements of statistical significance.

A multi-way analysis of variance (MANOVA) is carried out on the results and is shown in Table 4. The response variable is the ratio of the 1000-year load effects to the benchmark characteristic load effect. The factors and the levels of each considered to affect the response variable are:

- Bridge length: 100 m; 200 m; 500 m;
- Load Effect: LE and LE2;
- Safe time headway: 2.0 s and 3.0 s;
- Broadcast distance: 500 m and 1000 m;
- Adherence rate: 10% and 50%.

Table 4. MANOVA calculations (see [21] for details).

Source[1]	SS[2]	DF[3]	MS[4]	F[5]	p[6]
LE	0.006	1	0.006	0.899	0.351
A	0.002	1	0.002	0.273	0.606
T	0.001	1	0.001	0.149	0.702
L	0.043	1	0.043	6.713	0.015
BL	0.225	2	0.113	17.614	0.000
LE*A	0.000	1	0.000	0.003	0.954
LE*T	0.015	1	0.015	2.384	0.134
LE *L	0.001	1	0.001	0.168	0.685
LE*BL	0.085	2	0.043	6.656	0.004
A*T	0.000	1	0.000	0.032	0.860
A*L	0.025	1	0.025	3.890	0.059
A*BL	0.001	2	0.000	0.059	0.943
T*L	0.001	1	0.001	0.183	0.672
T*BL	0.016	2	0.008	1.219	0.311
L*BL	0.028	2	0.014	2.182	0.132
Error	0.173	27	0.006		
Total	0.622	47			

[1] Sources = LE – load effect; A – adherence rate; T – safe time headway; L – broadcast distance; BL – bridge length
[2] SS = sum of squares
[3] DF = degrees of freedom of statistical model
[4] MS = mean square
[5] *F*-test statistic
[6] *p* = probability of observation less than *F* statistic

The results of the MANOVA analysis are interpreted through the calculated *p*-value. A low probability of observing the *F*-statistic (i.e. low *p*), indicates that the results are statistically significant and that there is a difference in the means of the results caused by different sources. A value such as $p = 0.05$ is usually taken as a threshold of statistical significance. In this case, the first five rows of Table 4 indicate that the order of influence of the parameters on the load effect ratio is as follows: bridge length; broadcast distance; load effect; adherence; and safe time headway. Interestingly, safe time headway and adherence have least influence on the load effect ratio ($p = 0.702$ and 0.606).

Table 4 also gives probabilities for two-factor interactions on the response variable in the lower rows. The results show that bridge length and load effect (LE*BL) are the most significantly interacting parameters (p = 0.004 < 0.05), followed by adherence and broadcast distance (A*L), with load effect-safe time headway (LE*T) and broadcast distance and bridge length (L*BL) also of influence.

6 SUMMARY & CONCLUSIONS

6.1 Summary

This work proposes a novel Bridge-to-Vehicle (B2V) communication system to influence the gaps between vehicles arriving on a bridge. Total load and central support hogging bending moments for bridge lengths of 100 m, 200 m, and 500 m are studied using real traffic data. The influence of traffic adherence rates to the control measure, as well as the system broadcast distance, and the resulting new safe time headway of the vehicle are studied. Results are related to a benchmark load effect in which no gap control measure is implemented. Ratios of characteristic 1000-year return period values are used as the basis for comparison.

It is shown that in some cases the load effect ratio increases, whilst for others it reduces. The largest reduction found is 33%, for central support hogging moment for a bridge length of 200 m, using a broadcast distance of 1000 m and a safe time headway of 3 seconds. The average reduction for scenarios showing reduction is 13%.

A multi-way analysis of variance study is carried out to identify critical parameters and their interactions on the load effect ratios. Bridge length and broadcast distance are found to be the statistically significant parameters. It is also found that the shape of the influence is important for the effectiveness of the control measure.

6.2 Conclusions

It is clear from the presented analysis that the main variables influencing the effectiveness of the gap control strategy are the bridge length and load effect. Therefore the proposed control measure will be more effective for certain combinations of length and influence line shapes. The parameters of the control measure with most influence are the adherence rate and the broadcast distance. Interestingly, the actual safe time headway induced does not appear to have great influence. For the control measure to be used in practice therefore, careful design of the parameters will be required for the particular bridge length and influence line shape deemed to be critical.

The significant reductions found for some combinations of the problem parameters are promising. Average reductions of 13% could be particularly significant in the assessment of existing long-span bridges.

Further work on this problem is required as it is clear that the interactions between the problem variables are complex and do not readily admit to intuitive understanding. For example, further analysis of the traffic composition and lane densities for each scenario could yield information on lane changes and other phenomena that might reduce the effectiveness of the proposed control measure. It may be that this control measure could be most effective in conjunction with another form of measure.

ACKNOWLEDGMENTS

The author thanks Colm Carey, PhD student at Dublin Institute of Technology, for help with this work.

REFERENCES

[1] European Commission Directorate-General for Energy, Transport and Environment Indicators (2009), European Union Energy and Transport in Figures 2009.

[2] Buckland, P.G. (1981), ‘Recommended design loads for bridges’, *Journal of the Structural Division*, ASCE, 1161–213.

[3] Prat, M. (2001), ‘Traffic load models for bridge design: recent developments and research’, *Progress in Structural Engineering and Materials*, Vol. 3, pp. 326–334.

[4] Bailey, S.F. (1996), *Basic Principles and load models for the structural safety evaluation of existing bridges*, Ph.D. Dissertation, Thesis No. 1467, École Polythechnique Fédéral de Lausanne, Switzerland.

[5] Nowak, A.S., Lutomirska, M. & Sheikh Ibrahim, F.I. (2010), ‘The development of live load for long-span bridges’, *Bridge Structures - Assessment, Design & Construction*. Volume 6, Number 1-2. 73-79.

[6] Flint, A.R. and Jacob, B.A. (1996), ‘Extreme traffic loads on road bridges and target values for their effects for code calibration’, *Proceedings of IABSE Colloquium*, Delft, The Netherlands, IABSE-AIPC-IVBH, 469-478.

[7] Crespo-Minguillón, C. and Casas, J.R. (1997), ‘A Comprehensive traffic load model for bridge safety checking’, *Structural Safety*, 19, 339-359.

[8] Enright, B., Carey, C., Caprani, C.C. and OBrien, E.J. (2012), ‘The Effect of Lane Changing on Long-Span Highway Bridge Traffic Loading, *Proc. 6th Intl. Conf. on Bridge Maintenance, Safety and Management*, IABMAS, Lake Como, Italy.

[9] Baker-Mitchell D. & Cullimore, M. (1988), ‘Operation and maintenance of the Clifton suspension bridge’, *Proceedings of the Institution of Civil Engineers*, Part 1, April, pp 291-308.

[10] Optiz R. (1993), ‘Active Bridge Control System’, *Bridge Management 2: Inspection, Maintenance, Assessment and Repair*. Thomas-Telford 989-997

[11] Atkinson T., Brown P., Darby J., Ealey, T., Smith J.W. & Zheng, Y. (2000), ‘Active Control of Bridge Loads’, In J Ryall, GAR Parke and J E Harding (eds.), *Bridge Management 4*. 475-482. London, April.

[12] Kim S, Cho K, Choi, M. (2010), ‘Reduction of design live load for bridges by controlling the heavy vehicles’. In Furuta, Frangopol & Shinozuka (eds.), *Safety, Reliability and Risk of Structures, Infrastructure and Engineering Systems, Proc. 10th Int. Conf. on Structural Safety and Reliability*, ICOSSAR, 13-17 September 2009, Osaka, Japan, London, Taylor.

[13] Treiber, M., Hennecke, A. and Helbing, D. (2000), ‘Microscopic Simulation of Congested Traffic’, *Traffic and Granular Flow ’99*, D. Helbing, H.J., Herrmann, M. Schreckenberg, D.E. Wolf (Eds.), Springer, Berlin, 365-376.

[14] Treiber, M., Hennecke, A. and Helbing, D. (2000), ‘Congested Traffic States in Empirical Observations and Microscopic Simulations’, *Physical Review E*, 62(2), 1805-1824.

[15] Kesting, A. Treiber, M. and Helbing, D. (2007), ‘General lane-changing model MOBIL for car-following models’, *Transportation Research Record: Journal of the Transportation Research Board*, Vol. 1999/2007, 86-94.

[16] Enright, B. (2010), *Simulation of traffic loading on highway bridges*, PhD Thesis, School of Architecture, Landscape, and Civil Engineering, University College Dublin, Ireland.

[17] Treiber, M. & Kesting, A. (2010), ‘An open-source microscopic traffic simulator’, *Intelligent Transportation Systems Magazine*, IEEE, 2(3): 6-13.

[18] Kesting, A, Treiber, M., & Helbing, D. (2010), ‘Enhanced Intelligent Driver Model to access the impact of driving strategies on traffic capacity’, *Philos. Trans. Royal Soc. A* 368: 4585–4605.

[19] Emmerson, R. (2010), ‘M2M: the Internet of 50 billion devices’, *Win-Win*, January, pp. 20-23.

[20] EC1.2 (2003), Eurocode 1: Actions on Structures, Part 2: Traffic loads on bridges, European Standard EN 1991-2: European Committee for Standardisation, Brussels.

[21] Maxwell, S.E. and Delaney, H.D. (2003), *Designing Experiments And Analyzing Data: A Model Comparison Perspective*, Second Edition, Routledge Academic.

Determination of minimum gap in congested traffic

Serena Blacoe[1], Colin C. Caprani[2], Eugene J. OBrien[1], Alessandro Lipari[1]
[1] School of Civil, Structural and Environmental Engineering, University College Dublin, Belfield, Dublin 4, Ireland
[2] Department of Civil and Structural Engineering, Dublin Institute of Technology, Bolton Street, Dublin 1, Ireland
email: serena.blacoe@ucdconnect.ie, colin.caprani@dit.ie, eugene.obrien@ucd.ie, alessandro.lipari@ucd.ie

ABSTRACT: Accurate evaluation of site-specific loading can lead to cost and material savings in rehabilitation and replacement of bridges. Currently, bridge traffic load assessment is carried out using long run traffic simulations based on weigh-in-motion (WIM) data obtained at the site. Congestion is the governing load condition for long-span bridges. To correctly model congestion, a minimum gap between vehicles is usually assumed. Where the gap is overestimated, the calculated characteristic load is smaller than the actual characteristic load leading to an unsafe assessment. If the gap is underestimated, the safety assessment is too conservative, which is both costly and wasteful of finite resources. This paper outlines the development of an optical method to measure parameters required to model driver behaviour in congestion. Images are obtained using a camera with a wide angle, aspherical lens. Edge detection and Hough transforms are used to location wheels and bumpers. The resulting data can increase the accuracy of traffic microsimulation and hence, the assessment of long span bridge traffic loading.

KEY WORDS: Bridge; Long-Span; Traffic; Loading; Image Processing; Hough Transform.

1 INTRODUCTION

1.1 Background

In 2007, road transport of freight was worth over €300 billion. Freight transport grows year-on-year, roughly in-line with economic growth [1]. The continued serviceability of bridges is essential to this trade growth. There are about 1 million bridges in Europe. The annual expenditure required to sustain the existing stock of bridges is estimated at €6.6 billion, with the replacement cost for bridges about €400 billion [2].

To minimize resources, more accurate assessment of the safety of bridges may yield substantial savings: over 50% of the European bridge stock is estimated to have been built pre-1970 [2]. Whilst it is important to be able to quantify the capacity of the bridge, since loading is far more variable, there is more scope for improving accuracy by determining the actual load to which it is subjected.

Site specific bridge assessment can offer accurate load prediction [3]. Data from a WIM system installed near the bridge can be used to calibrate a site-specific load model. These models are typically free-flow models for short-to-medium span bridges, or simple congestion models for long-span bridges [4]. Simulations of 1000s of years of traffic are possible with these models, giving accurate predictions.

1.2 Traffic load modelling

WIM data is usually collected for free-flowing traffic, and usually only contains trucks. This data is appropriate for bridges of short- to medium-spans [3], [5]. In the assessment of long span bridges (over about 40 m), congested traffic governs and the presence of cars must be considered. Recently traffic microsimulation has been used to model congested traffic streams for bridge loading calculation [6], [7]. A critical input parameter in such a model is the distribution of gaps between vehicles in congested traffic. As WIM data records the time between axles passing a location, from which the distance can be extrapolated if the traffic is free flowing, it is unsuitable for determining gaps in congested traffic. This is due to the fact that there may be long time gaps between axles passing a location, whilst they are physically close. Previously, minimum gaps have been simply assumed. Long-span bridge load effects are sensitive to the gap assumed and the variation can be as much as 20% to 30% [8]. This paper proposes a camera system to measure these gaps accurately, without impacting on traffic flow.

2 CAMERA SYSTEM

2.1 Previous use of cameras in similar applications

Cameras have been used previously for traffic applications such as surveillance, vehicle detection, and automatic vehicle guidance, but have not been used to calibrate a microsimulation traffic model. Frenze [8] developed a system that could identify the presence of a HGV and determine the axle configuration. Footage of traffic was captured by a camera placed roadside at an oblique angle to the direction of traffic. A region of interest (ROI) was specified, within which wheels should be found. Frames from the video footage were converted to binary colour using thresholding, after which the Sobel edge operator [10] was used to identify edges in the binary image. The circular Hough transform [11] was then used to identify likely locations of circle centres. Results were not perfect, with an over-identification of background points as wheels and only 94 out of 100 trucks detected. False positive identification of wheels was a more significant problem, which was attributed to the presence of too much information in the edge image. Fung et al [12] used a similar system. Instead of carrying out edge detection on a binary image, they carry out edge detection directly on the image obtained from the camera. In this instance, Gaussian filtering was used before applying the Sobel edge filtering to reduce noise in the image. To speed up the processing, the images were compressed using the Haar wavelet [13], [14], which reduced the size of the image without loss of detail.

Aerial cameras have also been used. Gupte et al [15] used a pole mounted camera with an aerial view of traffic for the purpose of conducting vehicle counts, classification of vehicles, and to study lane changing behaviour. Unlike the other references, vehicles were detected and classified using a template matching system. During a 20 minute sequence, their algorithm correctly detected, tracked, and classified 63% of vehicles. Errors that occurred were explained by occlusion of parts of vehicles and/or poor image segmentation. Coifman et al. [16] address partial occlusion in congested traffic. Features such as corners are tracked, rather than attempting to track the entire vehicle. As features exit the tracking region, they are grouped using a common motion constraint.

Other approaches, such as that by Achler & Trivedi [17], train an algorithm to detect wheels by manually identifying wheels in a large training set of images. From this, Gaussian mixture models of wheels and of non-wheels are developed. Images can then be compared with these models and likely candidates for wheels identified. The foreground candidate wheels are tracked.

2.2 Site arrangement

For this work, two arrangements are considered for obtaining information on gaps in congested traffic. Firstly, a single camera with a wide-angle lens placed adjacent to the slow lane is considered. The benefits are that synchronization of footage is not needed; installation is easy; and the system is portable. Drawbacks of this arrangement are the required wide-angle lens, and potential interference from fast lane traffic on the identification of vehicles in the slow lane.

The second considered arrangement involves two cameras. One camera is placed beside the slow lane to obtain the internal vehicle dimensions (such as bumper to axle, axle to axle and axle to bumper distances). The second camera is aerial-mounted to determine the gaps between vehicles. An advantage is that a wide-angle field of view is not needed at the roadside, reducing possible interference from fast lane traffic. As a result, a standard lens can be used, and the camera can be placed close to the slow lane, reducing possible interference from fast lane traffic. Disadvantages of this arrangement include the footage synchronization, increased installation apparatus, and reduced portability.

The single camera arrangement is selected for the remainder of this work. Wide-angle lenses are easily obtained and interference from the fast lane can be removed through a common motion constraint, as was done in [16].

2.3 Camera and lens description

The camera used in this work is the IDS uEye LE USB camera [18]. This camera can accept a wide-angle lens, and can take more than 10 frames per second – a minimal specification identified for this application.

Wide-angle lenses are prone to aberrations which can affect shape and/or sharpness. For this application, shape distortion is the most critical aberration to avoid, as this would create an error in the calculated distances between objects in the image. Aspherical lenses do not suffer from these shape distortions, and so a Theia SY125M lens is used this work [19].

3 IMAGE PROCESSING

3.1 Overall approach

A similar approach to Fung et al. [12] and Frenze [8] is used for this work. The image is segmented and the Hough transform used to identify the location of wheels and axles in the image. Wheels are identified in lieu of actual axle identification. The images are reduced in dimension using wavelet compression without loss of resolution. This significantly reduces processing time for the Hough transform.

3.2 Edge detection for bumper identification

Truck bumpers are often vertical (see Figure 1). The Hough transform can identify linear features in a binary (black or white) edges-only image. Conversion of colour or grey scale images to black and white is straightforward, but edge detection is not. Edge detection algorithms work by determining the location of sudden luminosity intensity changes. Both the Sobel and Canny edge detection algorithms are considered for this work [10].

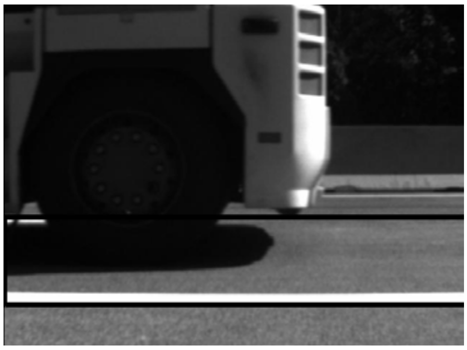

Figure 1. Sample truck bumper.

Sobel edge detection is based on a central difference approximation to the image gradient in the horizontal and vertical directions. A threshold is specified and any point with a gradient above this threshold is designated as an edge point [10]. The Canny edge detector first smooths the image using a Gaussian filter, and then determines gradients in the horizontal, vertical, and diagonal directions. The magnitude and direction of the edges are determined. Edge points are those points whose magnitudes are locally maximum in the direction of their gradients. The algorithm retains only pixels along the top of the ridges from the gradient calculation (non-maximal suppression). Two thresholds – an upper and a lower - are specified for edge points. Those points with magnitudes above the upper threshold are automatically retained as edge points. The points with magnitudes below the lower threshold are immediately discarded. Hysteresis thresholding is then carried out on the points with magnitudes that lie between the two thresholds. If a strong edge point exists in one of the eight pixels around it (8-connected to a strong edge), it is retained as an edge point; otherwise it is discarded [10]. In both the Canny and Sobel edge detector algorithms, the thresholds specify the proportion of non-zero points that are to be discarded (i.e. a threshold of 0.1 implies that 10% of non-zero points should be discarded).

The Sobel and Canny edge detection algorithms are applied to the sample truck bumper of Figure 1. The results are shown in Figure 2. As can be seen, the Sobel method fails to detect any element of the wheels (Figure 2(a)), whereas the Canny method has correctly identified the majority of the wheel outline (Figure 2(b)). It is possible to include more detail of the wheel outline by lowering the threshold in the Sobel method, but this would result in the inclusion of large amounts of noise. The Canny algorithm detects more of the wheel outline due to its inclusion of filters that detect diagonal edges. Although the algorithm does need to identify the location of the wheels, the bumper and wheel detection occur independently of each other. Consequently, the Sobel algorithm is used to create the edge image for the Hough line detection.

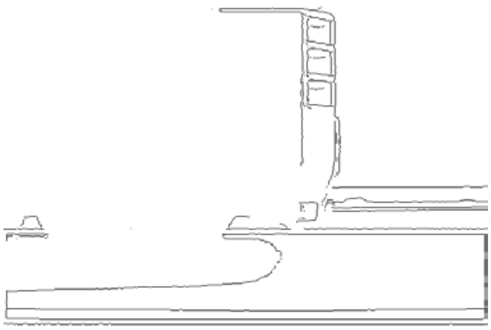

(a) Sobel method

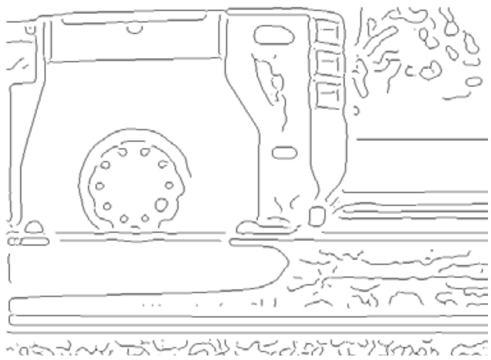

(b) Canny method

Figure 2. Edge Detection applied to Figure 1.

3.3 Hough transform for bumper identification

A Hough transform is used on the established edge image. The Hough transform is an exhaustive search method commonly used in image segmentation tasks [10]. The algorithm cycles through every edge point in the image and determines the equations of the lines that could pass through each point.

The use of Cartesian coordinates is not suitable since the slope is infinity for vertical lines. Consequently polar coordinates are used in this work instead. Considering the polar equation of a line, the set of lines that pass through a point *A* at (x_0, y_0) are:

$$R(\theta) = x_0 \cos\theta + y_0 \sin\theta \quad (1)$$

This process is illustrated in Figure 3, where example combinations of radius and angle that describe lines passing through point *A*, such as (R_1, θ_1) and (R_2, θ_2), are shown.

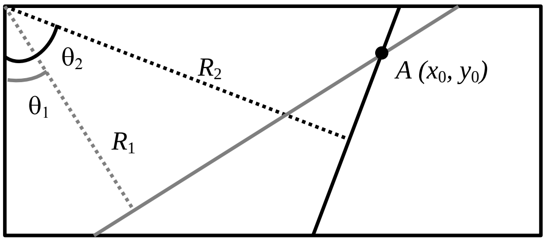

Figure 3. Polar coordinates of lines.

A two-dimensional parameter space of radius and angle can be constructed having dimensions of the discretized number of angles and radii. For each edge point, all possible radius and angle combinations are calculated. The weights of the points in parameter space corresponding to each of those combinations are incremented by +1. This is repeated for all edge points. These weights corresponding to the edge image in Figure 2(a) are shown in Figure 4. Strong linear features are evident at approximately 90 degrees at radii of about 400 and 600 pixels. These peaks in the parameter space correspond to lines in the original image as can be seen in Figure 5.

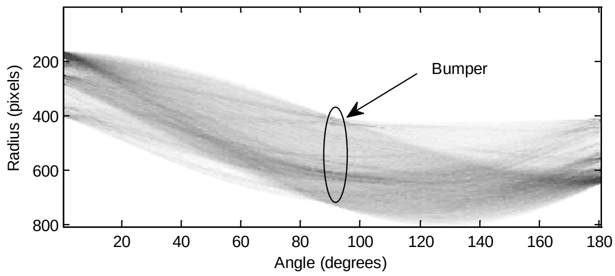

Figure 4. Hough transform parameter space.

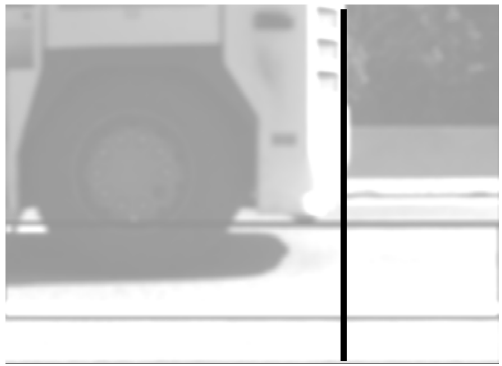

Figure 5. Detected truck bumper.

This algorithm is applied to the more difficult problem posed by a car bumper, and the result is shown in Figure 6. The failure to detect the bumper is attributed to the lack of verticality of the bumper. However, this problem can be overcome by subtracting the background from the acquired images [17], but this is not further considered for the present work.

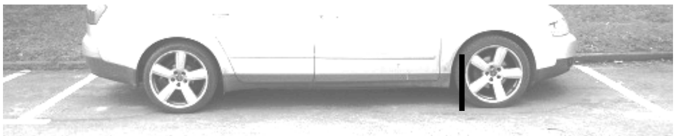

Figure 6. Incorrect detection of car bumper.

3.4 Wheel detection

The Hough transform has been successfully generalized to allow for the detection of shapes such as circles and ellipses [11]. However, the addition of the third variable – radius – to the Hough transform results in a computation of order $O(n^3)$, where n is the number of pixels. Hence the execution time increases significantly. Therefore in this work, several pre-processing steps are taken before carrying out the circular Hough transform.

A region of interest is specified around the band in the image where wheels are likely to be found. An example image is shown in Figure 7(a). As is evident from this figure, and the intensity histogram (Figure 7(b)) there can be very little contrast between the tyres, car, and road.

(a). Example image;

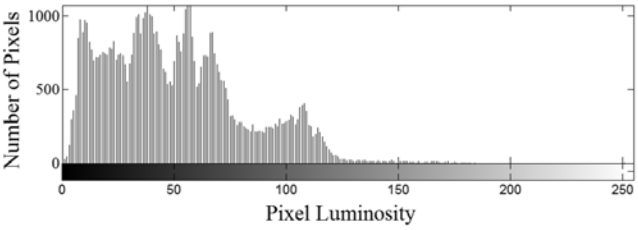

(b) Histogram of pixel luminosities;

Figure 7. Pre-processing of image with poor contrast.

The contrast in an image with poor contrast can be improved by altering the luminosity of pixels so that there are similar numbers of pixels with each value of luminosity within the image [10]. This is termed "equalizing the histogram". Figure 8 shows the same image after the histogram has been equalized and the equalized histogram.

Minimization of the number of edge points in the edges-only image is important in reducing computation. To this end, the image is morphologically opened, then closed, using a disk shaped structuring element [10]. This removes small areas of detail from the image, as shown in Figure 9.

Next, thresholding is used to convert the image to binary: pixels with luminosity values above 25 in 8-bit grayscale representation (intensities range from 0 to 255) are converted to white; pixels at or below 25 are converted to black. The threshold value is an algorithm input variable that needs to be set for a particular site and particular conditions. Any areas of small detail are removed from this image through the process of erosion [10]. This results in the image of Figure 10. Edge detection using the previously-described Sobel operator is then carried out and the result shown in Figure 11.

(a) Equalized image;

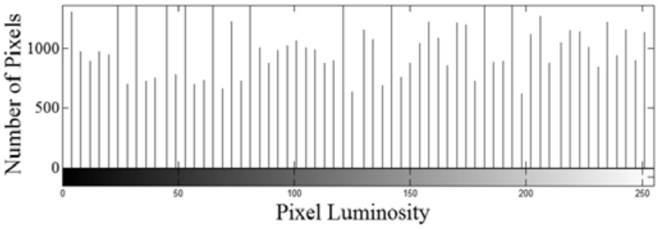

(b) Equalized histogram;

Figure 8. Image after histogram equalization.

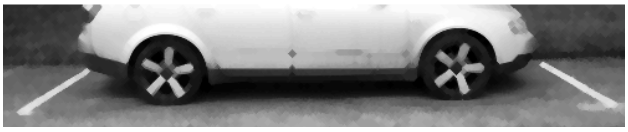

Figure 9. Example image after grayscale opening and closing morphology.

Figure 10. Binary image after erosion.

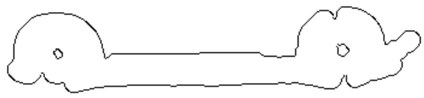

Figure 11. Wheel edge image.

The circular Hough transform is carried out on the edge image shown in Figure 11. Rearrangement of the Cartesian parametric equations of a circle allows all possible centres for a given point (x_i, y_i) to be calculated:

$$y_c = y_i - r \cdot \sin\theta \tag{2}$$

$$x_c = x_i - r \cdot \cos\theta \tag{3}$$

Each edge point (x_i, y_i) is considered to lie on a circle. Using Equations (2) and (3), every possible centre for an edge point is calculated for a given radius. The weights in the parameter space corresponding to all possible centres for the edge point are incremented by +1. This is illustrated in Figure 12. As can be seen, the true centre of the circle will be incremented more than any of the other proposed centres. This calculation is carried out for every edge point and repeated for every radius to be considered. As the equations are in Cartesian coordinates, the parameter space will have the same height and width as the image. It will consist of several layers, or pages, with each page corresponding to a discretized radius.

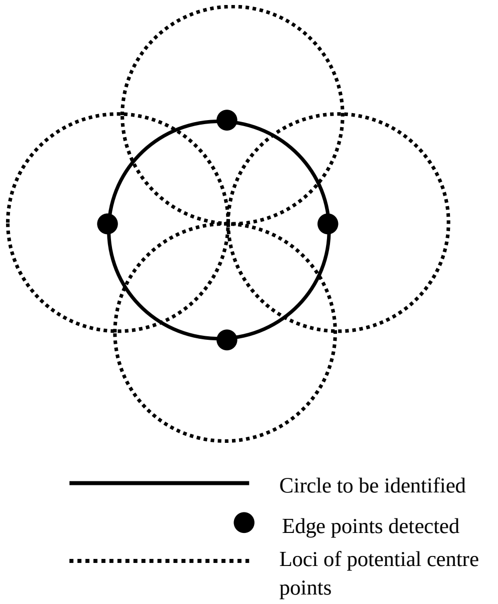

Figure 12. Circular Hough transform voting.

To reduce noise interference, all weights below a threshold are set to zero. The centre of a wheel is the centre of numerous circles, so high values should be expected at the location of a centre for a number of radii. The parameter space is ‘flattened’ by adding the weights recorded at each edge point from each layer corresponding to each radius considered. Within this space, peaks can then be identified.

Figure 13 shows the flattened parameter space corresponding to the image of Figure 7(a). It can be seen that a large number of potential circles are identified at the wheel regions. However, the most likely wheel location and radius must be identified by detecting the peak value in the parameter space.

Figure 13. Circular Hough transform parameter space.

The peak detection algorithm creates a list of weights above an appropriate threshold. This threshold is an input variable to the algorithm. It specifies an area the size of a wheel of the minimum radius considered around the first weight and identifies the maximum weight within that area. All other weights in the area are set to zero and the list of weights above the threshold updated. The algorithm cycles through the entire list until no further updates can be made. This is described in Table 1. By using a minimum radius search area, and only allowing one peak to be identified in this search area, only one wheel is identified in each wheel-sized area. Any remaining weights above the threshold are designated as wheels and their location noted. Good accuracy has been experienced with this method of peak detection. Figure 14 shows the location of the detected wheels for Figure 7(a). Figure 15 shows the results when applied to Figure 1. As can be seen in Figure 17, these techniques can be applied even to dark vehicles where contrast between the car and wheel is low. This is as a result of the morphological operations earlier described.

Table 1. Peak detection algorithm pseudo-code.

```
[peaksy, peaksx] = parameter_space ≥ peak_threshold

for i = 1 to length(peaksy)
    search_area = parameter_space(peaksy(i)±min(radius),
                                          peaksx(i)±min(radius))
    find max(search_area)
    parameter_space(search_area( ≠max(search_area))) = 0
    [peaksy, peaksx] = parameter_space ≥ peak_threshold
end
```

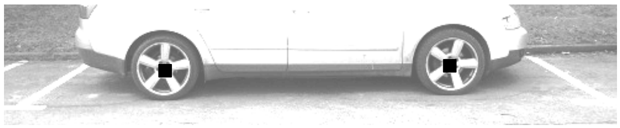

Figure 14. Detected wheels.

Figure 15. Wheel detection on HGV example.

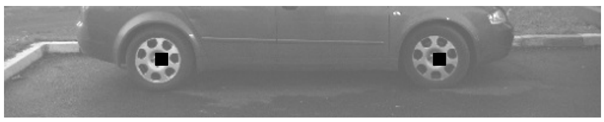

Figure 16. Low contrast example.

3.5 *Calculation of distances between objects*

Detected wheels and bumpers are converted to Cartesian coordinates and the distance in pixels between the wheel peaks and bumper peaks can be calculated. An example is shown in Figure 17 for the vehicle of Figure 1.

This pixel distance can be related to physical space using a site-calibrated transform. Depending on the lateral position of the vehicle, it may be necessary to have a reference calibration scale in each image. Trigonometry can be used to determine the physical distances from the pixel distances, once the site arrangement, lens, and camera properties are known.

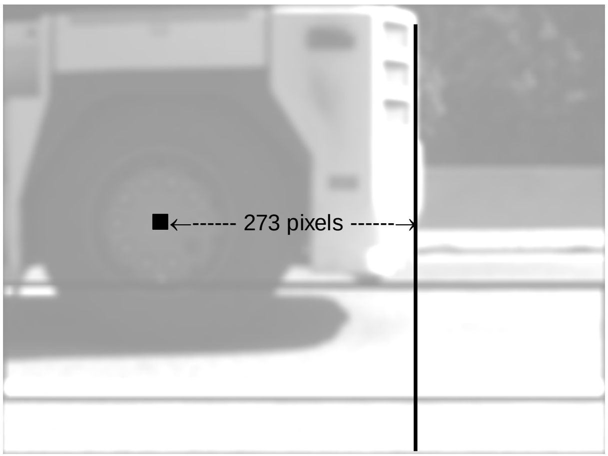

Figure 17. Distance between HGV bumper and wheel.

4 SUMMARY & CONCLUSIONS

4.1 Summary

This paper describes the development of an optical system to provide statistical information on the minimum gap in congested traffic. This information is critical to improve the accuracy of bridge safety assessment.

Images of vehicles are obtained from a camera with a wide-angle, aspherical lens. Morphological processing is used to reduce noise. Hough transforms are then used to segment the image and determine the location of the vehicle wheels and bumpers. This allows for the calculation of the distances required to calibrate a traffic microsimulation model.

As this research is a work in progress, results have yet to be obtained.

4.2 Conclusions

An important aspect of this work is edge detection. It has been shown that, although the Canny edge detection algorithm is generally better at detecting the edges of wheels, appropriate pre-processing and use of the Sobel edge detection algorithm produces adequate results for the present purpose.

The pre-processing undertaken prior to edge detection is sensitive to lighting conditions as appropriate pixel luminosity thresholds must be set. Once appropriate thresholds are set, good success has been shown in extracting circular edges and minimizing the number of edge points detected. It therefore represents an appropriate method for reducing the computation time for wheel detection. However, the prior establishment of the appropriate threshold is the cost of this efficiency.

Using the Hough transform to detect bumpers is successful where the bumper is near to vertical. However, the Hough transform is not suited to the detection of car bumpers, as they tend not to be vertical. Here, other means of bumper detection are required. Although computationally demanding, the circular Hough transform is accurate in the detection of wheel centres.

ACKNOWLEDGMENTS

The sponsorship of Science Foundation Ireland, under which this research is being conducted, is gratefully acknowledged.

REFERENCES

[1] European Commission (2010), *EU energy and transport in figures 2010*, Luxembourg, Publications Office of the European Union,2010.
[2] COST 345 (2004), 'Procedures Required for Assessing Highway Structures'. *Report of Working Group 1: Report on the Current Stock of Highway Structures in European Countries, the Cost of Their Replacement and the Annual Cost of Maintaining, Repairing and Renewing Them,* available online at http://cost345.zag.si/.
[3] COST 345 (2004), 'Procedures Required for Assessing Highway Structures'. *Report of Working Groups 4 and 5: Numerical Techniques for Safety and Serviceability Assessment for Highway Structures,* available online at http://cost345.zag.si/.
[4] Crespo-Minguillon, C. & Casas, J. R. (1997), 'A comprehensive traffic load model for bridge safety checking'. *Structural Safety,* 19(4)**,** 339-359.
[5] Sustainable and Advanced Materials for Road Infrastructure (SAMARIS) (2006), 'Guidance for the Optimal Assessment of Highway Structures'. *Competitive and Sustainable Growth Programme Deliverable D30*, available online at http://samaris.zag.si/.
[6] Caprani, C.C., Lipari, A. and OBrien, E.J. (2012), 'Load effect of multi-lane traffic simulations on long-span bridges', *International Conference on Bridge Maintenance, Safety and Management,* IABMAS, Lake Como, Italy, July.
[7] Caprani, C.C. and OBrien, E.J. (2008), 'The governing form of traffic for highway bridge loading', *Proceedings of 4th Symposium on Bridge and Infrastructure Research in Ireland*, eds. E. Cannon, R. West and P. Fanning, National University of Ireland, Galway, pp. 53-60.
[8] Caprani, C. (2005), *Probabilistic analysis of highway bridge traffic loading. Ph.D., University College Dublin*, PhD Thesis, University College Dublin, Ireland.
[9] Frenze, J.F. (2002), 'A video-based method for the detection of truck axles', *National Institute for Advanced Transportation Technology, University of Idaho,* Document Number N02-05.
[10] Gonzalez, R. C., Woods, R. E. & Eddins, S. L., *Digital Image Processing Using MATLAB,* Gatesmark Publishing, USA, second edition, 2009.
[11] Ballard, D. H. (1981), 'Generalizing the Hough transform to detect arbitrary shapes'. *Pattern Recognition,* 13(2), 111-122.
[12] Fung, Y.-F., Lee, H. & Ercan, M. F. (2006), 'Image Processing Application in Toll Collection'. *IAENG International Journal of Computer Science,* 32(4).
[13] Kaiser, G., *A friendly guide to wavelets*, Birkhaeuser, Boston, 1994.
[14] Meyer, Y., *Wavelets: algorithms and applications,* Society for Industrial and Applied Mathematics, translated by Ryan, R. D., USA, 1993.
[15] Gupte S., Masoud, O., Martin, R.F.K. and Papanikolopoulos, N.P. (2002), 'Detection and Classification of Vehicles'. *IEEE Transactions on Intelligent Transportation Systems,* 3(1), 37-47.
[16] Coifman, B., Beymer, D., McLauchlan, P. and Malik, J. (1998), 'A real-time computer vision system for vehicle tracking and traffic surveillance'. *Transportation Research Part C,* 6(4), 271-288.
[17] Achler, O. & Trivedi, M. M. (2004). 'Camera Based Vehicle Detection, Tracking, and Wheel Baseline Estimation Approach', *IEEE Intelligent Transportation Systems Conference,* Washington, D.C., USA.
[18] http://www.altavision.com.br/Datasheets/IDS_EN/UI-1245LE.html
[19] http://www.theiatech.com/products.php?lens=SY125

Effect of road quality in structural health monitoring under operational conditions

Vesna Jaksic[1], Vikram Pakrashi[1], Alan O'Connor[2]
[1]Department of Civil and Environmental Engineering, University College Cork, College Road, Cork, Ireland
[2]Department of Civil, Structural and Environmental Engineering, Trinity College Dublin, College Green, Dublin 2, Ireland
email: v.jaksic@umail.ucc.ie, V.Pakrashi@ucc.ie, alan.oconnor@tcd.ie

ABSTRACT: The effect of unevenness in a bridge deck for the purpose of Structural Health Monitoring (SHM) under operational conditions is studied in this paper. The moving vehicle is modelled as a single degree of freedom system traversing the damaged beam at a constant speed. The bridge is modelled as an Euler-Bernoulli beam with a breathing crack, simply supported at both ends. The breathing crack is treated as a nonlinear system with bilinear stiffness characteristics related to the opening and closing of crack. The unevenness in the bridge deck considered is modelled using road classification according to ISO 8606:1995(E). Numerical simulations are conducted considering the effects of changing road surface classes from class A – very good to class E – very poor. Cumulant based statistical parameters, based on a new algorithm are computed on stochastic responses of the damaged beam due to passages of the load in order to calibrate the damage. Possibilities of damage detection and calibration under benchmarked and non-benchmarked cases are considered. The findings of this paper are important for establishing the expectations from different types of road roughness on a bridge for damage detection purposes using bridge-vehicle interaction where the bridge does not need to be closed for monitoring.

KEY WORDS: Structural Health Monitoring (SHM); Euler–Bernoulli Beam; Open Crack; Road Surface.

1 INTRODUCTION

Structural Health Monitoring (SHM) is an integral part of infrastructure maintenance management. Non-destructive structural damage detection, in this regard, is becoming an important aspect of integrity assessment for aging, extreme-event affected or inaccessible structures [1-3]. A damage in a structure often tend to change only the local dynamic characteristics and markers of damage detection should attempt to capture such local dynamic changes. In this regard, employing bridge–vehicle interaction models for damage detection [4] and SHM [5-7] has gained considerable interest in recent times

Bilello and Bergman [8] have considered, theoretically and experimentally, the response of smooth surface damaged Euler–Bernoulli beam traversed by a moving mass, where the damage was modelled through rotational springs. Bu et al. [9] have proposed damage assessment approach from the dynamic response of a passing vehicle through a damage index. Poor road surface roughness was observed to be a bad detector for damage in their approach. Majumder and Manohar [10] have proposed time domain damage descriptor to reflect the changes in bridge behavior due to damage. Lee et al. [11] have experimentally investigated the possible application of bridge–vehicle interaction data for identifying the loss of bending rigidity. Law and Zhu [12] have studied the dynamic behavior of damaged reinforced concrete bridge under moving loads using as a model a simply supported beam with open and breathing cracks. Pakrashi et al. [4] have performed experimental investigation of simply supported beam with moving load subjected to different level of damage.

Local damage in beams have been modelled in a number of ways [13]. Narkis [14] has proposed a method for calculation of natural frequencies of a cracked simply supported beam using an equivalent rotational spring. Sundermeyer and Weaver [15] have exploited the non-linear character of vibrating beam with a breathing crack. The surface roughness on bridges has never been used as an aid to damage detection.

This paper proposes the use of changing road surface roughness in damage detection of beam-like structures through bridge vehicle interaction and investigates what road quality is appropriate for such detection. Harris et al [16] have proposed a method for characterisation of pavement roughness through the analysis of vehicle acceleration. Fryba [17] has shown the effect of road surface roughness (RSR) on bridge response. Abdel-Rohman and Al-Duaij [18] investigated the effects of unevenness in the bridge deck on the dynamic response of a single span bridge due to the moving loads. O'Brien et al. [19] have proposed a bridge roughness index (BRI) which gives insight into the contribution that road roughness makes to dynamics of simply supported bridges. Da Silva [20] has proposed a methodology to evaluate the dynamical effects, displacement and stress on highway bridge decks due to vehicle crossing on rough pavement surfaces. Although there are many interesting numerical and statistical markers and methods available for damage detection [21-24], surface roughness has always been treated for parameter studies, improved analysis or for establishing the bounds of efficiency of an algorithm. Jaksic et al. [25] have very recently investigated the potential of using surface roughness for detecting damage where a white noise excitation response of a single degree of freedom bilinear oscillator was investigated. The white noise represented a broadband excitation, qualitatively similar to the interaction with surface roughness and the bilinearity attempted to capture a breathing crack. First and second order cumulants of the response of this system were observed to be appropriate markers for detecting changes in system stiffness.

In this paper a beam-vehicle interaction based damage detection from multiple point observations in the time domain using the interaction with realistic surface roughness is presented. The damage has been modelled as a localized breathing crack and surface roughness has been defined by ISO 8606:1995 [26]. The responses (displacement and velocity) of the first mode of undamaged and damaged beam are observed [22, 27] since they are often easy to detect and are often a good approximation of the actual displacement. The preferable road quality for damage detection process is investigated in considerable details in this paper.

2 METHODOLOGY

2.1 Model

The bridge is represented as a simply supported Euler-Bernoulli beam with a breathing crack traversed by a single degree of freedom oscillator (Figure 1), which represents the vehicle. The vehicle is assumed to be moving on the surface without losing contact. The length of the beam is L and the crack is at a distance x_c from the left support. The beam has a constant cross-sectional area A, second moment of area I, Young's modulus E and mass density ρ. The crack can be modelled as a rotational spring [15] when the crack is open.

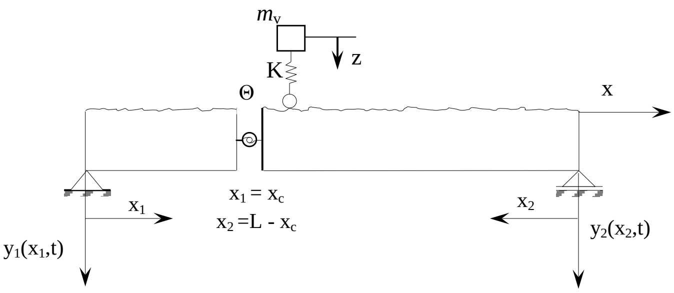

Figure 1. Simply supported beam with breathing crack modelled as two beams connected by torsional spring.

2.2 Equations of motion

The equation of motion of a beam with a breathing crack and traversed by a vehicle is given as

$$EI\frac{\partial^4 y_i(x,t)}{\partial x^4} + c\frac{\partial y_i(x,t)}{\partial t} + \rho A\frac{\partial^2 y_i(x,t)}{\partial t^2} = P\delta(x - \upsilon t);\ i = 1,2 \quad (1)$$

t is the time coordinate with the origin at the instant of the force arriving upon the beam; x is the length coordinate with the origin at the left-hand end of the beam; $y_i(x,t)$ is the transverse deflection of the beam at the point x and time t, measured from the static equilibrium position corresponding to when the beam is loaded under its own weight; c is the structural damping of the material of the beam; $m = \rho A$ is the mass per unit length; P is the external force; δ is the Dirac Delta function [17] and υt is the position of the vehicle moving with constant speed υ from left support. The external force P is defined as:

$$P = \{m_V g + K[z - y_i(\upsilon t, t) - r(\upsilon t)]\};\quad i = 1,2 \quad (2)$$

$$K[z - y_i(\upsilon t, t) - r(\upsilon t)] \geq 0 \quad (3)$$

where m_v is the mass of the vehicle; g is acceleration due to gravity; K is the equivalent stiffness of the vehicle's tires and springs; z is the vertical displacement of the vehicle with respect to its static equilibrium position; and r is the surface roughness.

2.2.1 The open crack eigenvalue problem

When the crack is open, the system consists of two beams connected by torsional spring, where each continuous segment of the beam can be described by the Bernoulli-Euler partial differential equation of motion. The eigenvalue problem can be solved through the method of separation of variables and the consideration of modal superposition:

$$y_i(x\ \ , t) = \sum_{j=0}^{n} \phi_j^i(x\ \ )\, q_j(t);\quad i = 1,2 \quad (4)$$

where Φ_i is orthogonal mode shape for the i[th] mode and q_i is the time dependent amplitude. By separating temporal and spatial variables, the following differential equation system is obtained

$$\phi_i^{i''''}(x\ \ ) - \frac{\omega_j^2\ \ \rho A}{EI}\phi_j^i(x\ \ ) = 0;\quad i = 1,2;\ j = 1\ to\ n \quad (5)$$

$$\ddot{q}_j(t) + \omega_j^2 q_j(t) = 0;\quad j = 1\ to\ n \quad (6)$$

There are no displacements or moments at the supports. Also, boundary conditions at the crack location x_c must satisfy continuity of displacement, bending moment and shear and the slope between the two beam segments can be related to the moment at this section [15]. The solution of the spatial differential equation (5) satisfying all eight boundary conditions is:

$$0 < \bar{x} < x_c \rightarrow \quad \phi = A_0(\sin a\bar{x} + \alpha \sinh a\bar{x}) \quad (7)$$

$$x_c < \bar{x} < L\ \rightarrow$$

$$\phi = A_0\left(\frac{\sin(ax_c)\sin\left(a(L-\bar{x})\right)}{\sin\left(a(L-x_c)\right)} + \alpha\frac{\sinh(ax_c)\sinh\left(a(L-\bar{x})\right)}{\sinh\left(a(L-x_c)\right)}\right) \quad (8)$$

where:

$$a^4 = \frac{\omega_j^2 \rho A}{EI};\ \ j = 1\ to\ n \quad (9)$$

$$\alpha = \frac{\cos ax_c + \frac{\sin ax_c}{\tan a(L-x_c)}}{\cosh ax_c + \frac{\sinh ax_c}{\tanh a(L-x_c)}} \quad (10)$$

and the constant A_0 is chosen so that the mode shapes are normalized as

$$\int_0^{x_c}(\phi_j(\bar{x}))^2 d\bar{x} + \int_{x_c}^{L}(\phi_j(\bar{x}))^2 d\bar{x} = 1 \quad (11)$$

The natural frequencies of the beam with the open crack can be calculated replacing boundary conditions in assumed solution of mode shape equation (5):

$$\phi(x) = A_1 \cos ax + A_2 \sin ax + A_3 \cosh ax + A_4 \sinh ax \quad (12)$$

and setting its determinant to zero, or by using equations (9-10) [15].

2.2.2 The closed crack eigenvalue problem

When crack closes, the beam is treated as one continuous Euler-Bernoulli beam and the first mode shape equation is:

$$0 < x < L \rightarrow \phi(x) = \sqrt{\frac{2}{L}} sin(ax) \quad (13)$$

Since the displacement at supports equals zero, the equation (12) is satisfied when *sin (aL)=0*, therefore the natural frequencies of the beam when crack is closed are:

$$\omega_j = j^2\pi^2 \sqrt{\frac{EI}{mL^4}}; \quad j = 1, 2, 3, ... \quad (14)$$

2.3 Equation of motion of vehicle

The equation of motion of the vehicle, represented as a single degree of freedom oscillator can be represented as

$$m_V\ddot{z} + K\left[z - r\left(vt^{-}\right) - y\left(vt^{-}, t\right)\right] = 0 \quad (15)$$

2.4 Surface roughness

From ISO 8606:1995(E) [26] specifications RSR function $r(\bar{x})$ in discrete form is:

$$r(\hat{x}) = \sum_{k=1}^{N} \sqrt{4S_d(f_0)\left(\frac{2\pi k}{L_c f_0}\right)^{-2} \frac{2\pi}{L_c}} cos\left(\frac{2\pi k f_0}{L_c} + \theta_k\right) \quad (16)$$

here $S_d(f_0)$ is roughness coefficient; $f_0 = 1/2\pi$ is the discontinuity frequency; L_c is twice the length of the bridge [6, 28]; N is number of data points of successive ordinates of surface profile; and θ_k is a set of independent random phase angles uniformly distributed between 0 and 2π. The road classification according to ISO 8606:1995(E) is based on value of $S_d(f_0)$. Five classes of road surface roughness representing different qualities of the road surface are A (very good), B (good), C (average), D (poor), E (very poor) with value of roughness coefficients 6×10^6, 16×10^6, 64×10^6, 256×10^6, and 1024×10^6 m^3/cycle, respectively. Typical irregular surface roughness profiles are shown in Figure 2.

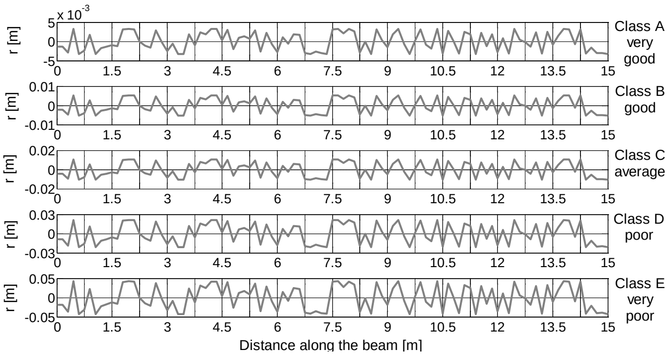

Figure 2. Typical road surface profiles.

2.5 Damaged Beam – Moving Oscillator Interaction Including Surface Roughness

The bridge-vehicle interaction can finally be expressed as a system of two second order equations. For a first mode shape consideration (subscripted 1), equations (1) and (15) can be written in matrix form as

$$\begin{bmatrix} 1 & 0 \\ 0 & 1 \end{bmatrix} \times \begin{Bmatrix} \ddot{q}_1 \\ \ddot{z} \end{Bmatrix} + \begin{bmatrix} 2\xi_1\omega_1 & 0 \\ 0 & 0 \end{bmatrix} \times \begin{Bmatrix} \dot{q}_1 \\ \dot{z} \end{Bmatrix} + \begin{bmatrix} \omega_1^2 - \frac{K}{\rho A}\phi_1(vt)\phi_1(vt) & \frac{K}{\rho A}\phi_1(vt) \\ -\omega_V^2\phi_1(vt) & \omega_V^2 \end{bmatrix} \times \begin{Bmatrix} q_1 \\ z \end{Bmatrix} = \begin{Bmatrix} \frac{m_V g}{\rho A}\phi_1(vt) + \frac{K}{\rho A} r(vt)\phi_1(vt) \\ \omega_V^2 r(vt) \end{Bmatrix} \quad (17)$$

Where the natural frequency of vehicle is $\omega_V^2 = K/m_V$; and ξ and ξ_v are damping ratio of bridge and vehicle, respectively. The displacements and velocities of the beam and the vehicle are obtained by using a 4/5th order Runge-Kutta method available in MATLAB [29].

3 DAMAGE DETECTION THROUGH SURFACE ROUGHNESS

The proposed concept of numerical analysis is shown in Figure 3.

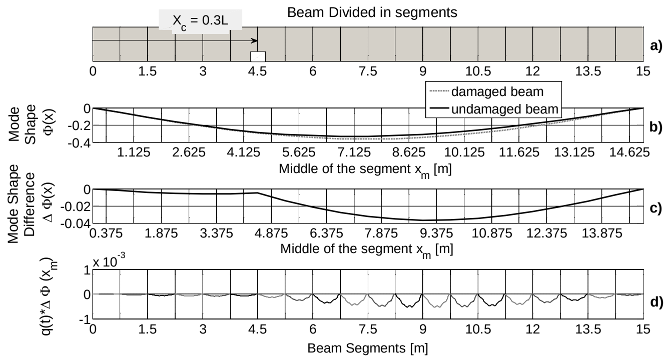

Figure 3. a) Simply supported beam with damage located at 0.3*L* divided into equal segments; b) Mode shape of damaged and undamaged beam; c) Difference in mode shape of undamaged and damaged beam; d) Difference in mode shape of damaged and undamaged beam at mid location of each segment multiplied with temporal beam displacement.

The beam is divided into a number of equal segments. In this example (Figure 3b) the crack is located at $x_c = 0.3L$. The difference between the damaged and undamaged mode shapes is found next ($\Delta\Phi_m$), which has a local maximum and discontinuous slope at the damage location [27]. In practice, the mode shape difference in the spatial domain is hard to detect. For an experimental regime, an initial estimate of the undamaged mode shape and natural frequency should be carried out and the bridge response obtained is used to create a difference function in the time domain as $\Delta\Phi_m q(t)$. This is not implicit but explicit as in reality the bridge responses may be measured at multiple locations. Random white noise is cancelled out by considering the passage of many vehicles and the consideration of normalisation. When a coloured noise is present in bridge response than the damage could not be identified due to its masking effect and therefore the proposed procedure is not applicable. Figure 3 shows that the location near the damage is affected in this differenced time domain response. The location of the damage(s) could be indicated by using wavelet analysis as shown in many papers [30-32]

The data used for the bridge model are L = 15m; modal damping ratio of the beam ζ = 2%; E = 200e9 N/m^2 and ρ =

7900 kg/m^3. The static deflection of the beam is 0.005 m based on this data. It is assumed that that the depth (h) of the beam is 1.5 times the width (b) of the beam. Other geometric descriptors like second moment of area (I), h, b, cross sectional area (A) and m are computed based on this assumption. The data used for vehicle simulation are m_v = 3000 kg and K = 3.65e6 N/m [6, 33]. The calculated natural frequencies of bridge without damage and vehicle are 4Hz and 2 Hz respectively.

Choice of Damage Detection and Calibration Markers Statistical descriptors on previously determined functions $\Delta\Phi_m q(t)$ for each segment of the beam are observed and investigated for monotonocity and consistency. The statistical parameters of function $\Delta\Phi_m q(t)$ considered included mean (μ), standard deviation (σ), skewness (λ), and kurtosis (κ). The choice of mean and standard deviation stemmed out of the recent study [25]. The parameters are computed as follows:

$$\mu = \frac{1}{m}\sum_{i=1}^{m} x_i \tag{18}$$

$$\sigma = \sqrt{\frac{1}{m}\sum_{i=1}^{m}(x_i-\mu)^2} \tag{19}$$

Figure 4 shows an example of mean and standard deviation of $\Delta\Phi_m q(t)$ function calculated for each beam segment. It is found that obtained mean and standard deviation functions are similar in shape and clearly show the discontinuous slope at the damage location, similar to mode shape difference functions. This finding is consistent with [25] where it has been proven that first and second order cumulants of bilinear and linear system response are consistent and monotonic descriptors of the system characteristics and are sensitive to system stiffness changes.

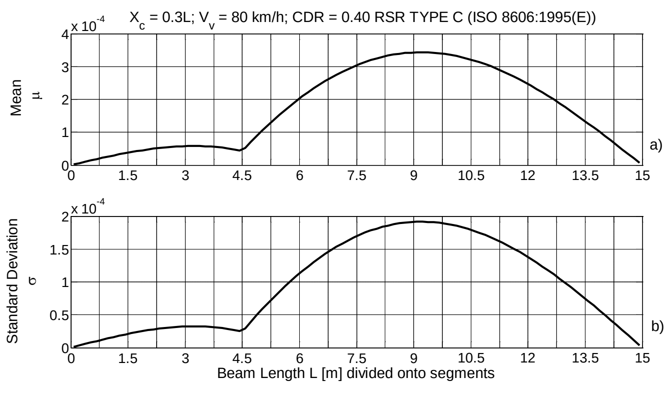

Figure 4. Example of calculated: a) Mean and b) Standard Deviation (STD) for crack located at Xc = 0.3L; Speed of the vehicle Vv = 80km/h; Crack Depth Ratio CDR = 0.40 and Type C Road Surface Roughness (RSR) defined as per ISO 8606:1995(E).

4 DISCUSSION

Figure 5 represents an example of mean and standard deviation functions for the case of different road surface roughness (A to E) where the crack is located at quarter-span, the vehicle is moving with a speed 80 km/h and crack depth ratio is 0.4. From this and the similar figures obtained by varying x_c, CDR and V_V, a number of observations are noted. It is observed that the markers μ and σ show kink at the damage location, values of statistical parameters relative to each other increase with decreasing road quality and μ and σ curves slope discontinuity at the crack location become more obvious for poor and very poor grades of road surface roughness. All of the above indicate that the location of crack can be identified by the chosen markers and that consistent calibration is possible.

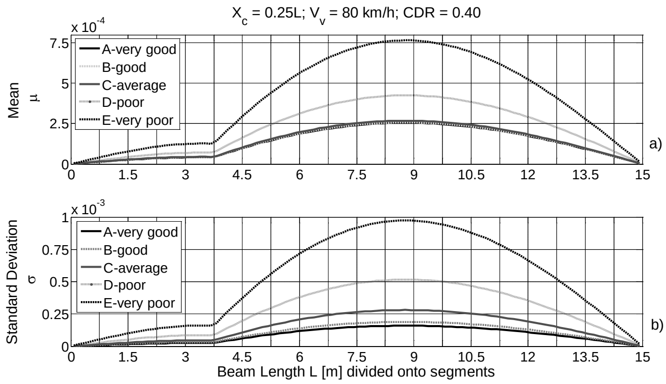

Figure 5. a) Mean and b) Standard Deviation (STD) for crack located at Xc = 0.25L; Speed of the vehicle Vv = 80 km/h; Crack Depth Ratio CDR = 0.40, and different types of Road Surface Roughness (RSR) defined as per ISO 8606:1995(E).

For illustration purposes, Figures 5, 6 and 7 representing standard deviation in relation to crack depth ratio and vehicle speed for RSR type C for case when crack is located at the edge, quarter-span and mid-span of the beam, respectively, are shown.

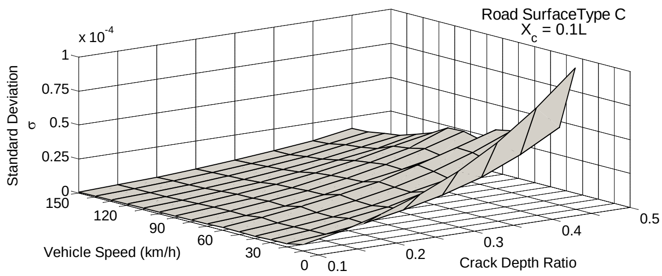

Figure 5. Standard deviation dependence on Crack Depth Ratio and Vehicle speed for Road Surface Roughness Type C for crack located near support.

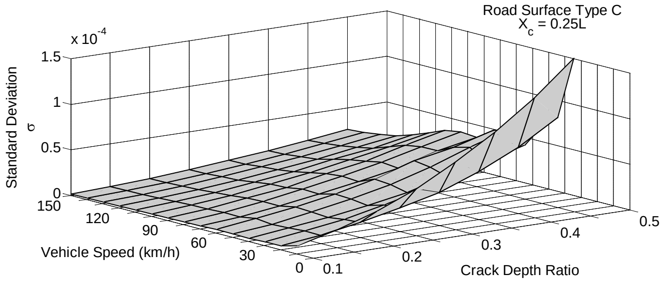

Figure 6. Standard deviation dependence on Crack Depth Ratio and Vehicle speed for Road Surface Roughness Type C for crack located at quarter-span.

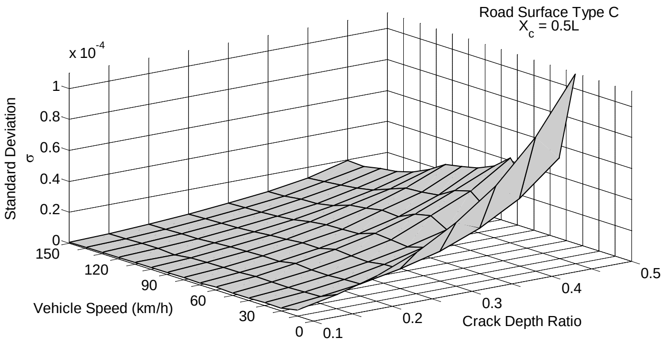

Figure 7. Standard deviation dependence on Crack Depth Ratio and Vehicle speed for Road Surface Roughness Type C for crack located at mid-span.

In general, it is observed that the relation between μ and σ and CDR for different V_V increases exponentially. It is noted that these curves are separated into 4 groups depending on V_V: very low speed 10 km/h; low speed 20 to 60 km/h; medium speed 70 to 100 km/h; and high speed 110 to 150 km/h for which variation of μ and σ is very high, high, medium, and low, respectively. This grouping becomes more obvious for higher CDR when RSR is type D and E, while for the RSR type A and B there is very little difference between statistical parameters even for a higher values of CDR. The exception is very low V_V for which statistical parameters are observed to be much higher than for other V_V for all cases of RSR. RSR type C and V_V = 80 km/h are found to be optimal for calibration purposes. In general, calibrations are monotonic (μ and σ increase with CDR) but there is no obvious relation between the curves representing different crack locations.

Figure 8 shows a generic fit, i.e the calibration of standard deviation in the function of CDR for three different vehicle speeds (low, medium, and high), analysed separately for three different positions of the crack. The best fit is represented by power equations:

$$\sigma = a \times CDR^b + c \tag{22}$$

The coeficients of fitting functions are given in Table 1.

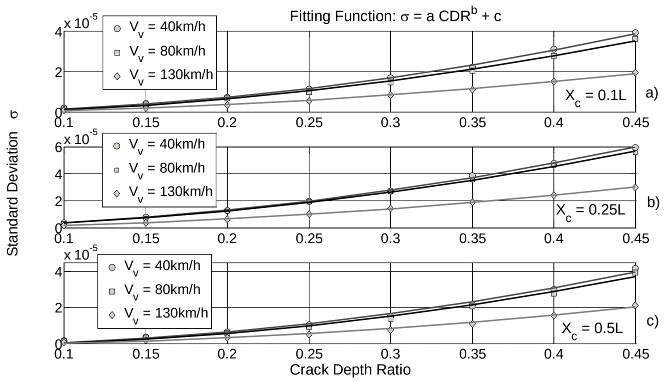

Figure 8: Calibration of Standard Deviation (STD) variation in function Crack Depth Ratio (CDR); for Low, Medium and High Vehicle Speed (Vv) and three different positions of the damage: a) Edge; b) Quarter-span and c) Mid-span.

Table 1. Calibration function for Standard deviation and CDR

Position of the crack	Vehicle speed (km/h)	*a*	*b*	*c*
0.1*L*	40	1.925e^{-4}	1.997	-4.74e^{-7}
	80	1.756e^{-4}	1.986	-7.94e^{-7}
	130	8.9e^{-5}	1.899	-6.13e^{-7}
0.25*L*	40	2.747e^{-4}	1.916	4.194e^{-7}
	80	2.629e^{-4}	1.935	6.323e^{-7}
	130	1.353e^{-4}	1.88	-7.43e^{-8}
0.5*L*	40	2.072e^{-4}	2.022	-1.59e^{-6}
	80	2.058e^{-4}	2.091	-1.48e^{-6}
	130	1.084e^{-4}	2.053	-8.13e^{-7}

5 CONCLUSIONS

The effects of road quality on bridge-vehicle interaction based surface roughness are investigated. In practice the response, displacements and / or velocities, of the bridge can be measured at multiple locations along the bridge. In order to create a difference function in time domain an initial estimate of the undamaged mode shape and natural frequency should be carried out. Mean and standard deviation of mode shape differenced temporal responses can be used as damage detection markers. Discontinuous slopes of mean and standard deviation curves give the position of damage, and the jump size is related to the damage extent.

When the road quality decreases, the slope discontinuity of mean and standard deviation curves at the crack location become more obvious. This is amplified for poor and very poor grades of road surface roughness.

The consistency of calibration depends on vehicle speed and road surface type. This is more pronounced in the case of higher damage. Damage calibration on better roads is less uncertain and gives consistent but less sensitive results. Worse roads are less consistent in calibration values but give more sensitive results. Therefore the road surface roughness type C is optimal for calibration purposes.

The study is particularly useful for continuous online bridge health monitoring since the data necessary for analysis can be obtained from the operating condition of the bridge and the structure does not therefore need be closed down.

ACKNOWLEDGMENTS

The Irish Research Council.

REFERENCES

[1] Kisa, M. (2004), ‘Free vibration analysis of a cantilever composite beam with multiple cracks’, Composites Science and Technology, 64 (9), 1391–1402.

[2] Rucka, M. and Wilde, K. (2006), ‘Crack identification using wavelets on experimental static deflection profiles’, Engineering Structures, 28 (2), 279–288.

[3] Pakrashi, V., O'Connor, A., Breysse, D. and Schoefs, F. (2008), ‘Reliability Based Assessment of Structures in Marine Environment’, MEDACHS 08 Conference on Construction Heritage in Coastal and Marine Environments, Lisbon, Portugal

[4] Pakrashi, V., O'Connor, A. and Basu, B. (2010), ‘A Bridge–Vehicle Interaction Based Experimental Investigation of Damage Evolution’, Structural Health Monitoring, 9 (4), 285 - 296.

[5] Delgado, R. M. and dos Santos, R. C. S. M. (1997), ‘Modelling of a railway bridge–vehicle interaction on high speed tracks’, Computers and Structures, 63 (3), 511-523

[6] Henchi, K., Fafard, M., Talbot, M. and Dhatt, G. (1998), 'An Efficient Algorthm for Dynamic Analysis of Bridges under Moving Vehicles Using a Coupled Modal and Physical Components Aproach', Journal of Sound and Vibration, 212 (4), 663-683
[7] Bilello, C., Bergman, A. L. and Kuchma, D. (2004), 'Experimental investigation of a small-scale bridge model under a moving mass', ASCE Journal of Structural Engineering, 130 (5), 799–804.
[8] Bilello, C. and Bergman, L. A. (2004), 'Vibration of damaged beams under a moving mass: Theory and experimental validation', Journal of Sound and Vibration, 274 (3-5), 567–582.
[9] Bu, J. Q., Law, S. S. and Zhu, X. Q. (2006), 'Innovative bridge condition assessment from dynamic response of a passing vehicle', ASCE Journal of Engineering Mechanics, 132 (12), 1372–1379.
[10] Majumder, L. and Manohar, C. S. (2003), 'A time domain approach for damage detection in beam structures using vibration data with a moving oscillator as an excitation source. ', Journal of Sound and Vibration, 268 699–716.
[11] Lee, J. W., Kim, J. D., Yun, C. B., Yi, J. H. and Shim, J. M. (2002), 'Health monitoring method for bridges under ordinary traffic loadings', Journal of Sound and Vibration, 257 (2), 247–264.
[12] Law, S. S. and Zhu, X. Q. (2005), 'Bridge dynamic responses due to road surface roughness and braking of vehicle', Journal of Sound and Vibration, 282 (3-5), 805-830
[13] Friswell, M. I. and Penny, J. E. T. (2002), 'Crack Modeling for Structural Health Monitoring', Structural Health Monitoring, 1 (2), 139 - 148.
[14] Narkis, Y. (1994), 'Identification of crack Location in vibrating simply supported beams', Journal of sound and Vibrations, 172 (4), Pages 549-558
[15] Sundermeyer, J. N. and Weaver, R. L. (1994), 'On Crack Identification and Characterization in a beam by non-linear vibration analysis', Journal of Sound and Vibration, 183 (5), 857-871.
[16] Harris, N. K., Gonzalez, A., Obrien, E. J. and McGetrick, P. (2010), 'Characterisation of pavement profile heights using accelerometer readings and a combinatorial optimisation technique', Journal of Sound and Vibration, 329 (5), 497-508.
[17] Fryba, L., Vibration of Solids and Structures under Moving Loads, Publishing house of Academy of Sciences of the Czech Republic, Thomas Telford Ltd., Prague, London, 3rd edition, 1999.
[18] Abdel-Rohman, M. and Al-Duaij, J. (1996), 'Dynamic Response of Hinged-Hinged Single Span Bridges with Uneven Deck', Compurers & Structures1996, 59 (2), 291-299.
[19] O'Brien, E., Li , Y. and Gonzalez, A. (2006), 'Bridge roughness index as an indicator of bridge dynamic amplification', Compurers & Structures, Volume 84 (12), 759–769.
[20] da Silva, J. G. S. (2004), 'Dynamical performance of highway bridge decks with irregular pavement surface', Computers & Structures, 82 (11-12), 871-881
[21] Sohn, H., Farrar, C. R., Hunter, N. F. and Worden, K. (2001), 'Structural Health Monitoring using Statistical Pattern Recognition Techniques', ASME Journal of Dynamic Systems, Measurement and Control 123 (4), 706-717.
[22] Pakrashi, V., Basu, B. and Connor, A. O. (2009), 'A Statistical Measure for Wavelet Based Singularity Detection', Journal of Vibration and Acoustics, 131 (4), 041015 (6 pages)
[23] Cacciola, P., Impollonia, N. and Muscolino, G. (2003), 'Crack detection and location in a damaged beam vibrating under white noise', Computers and Structures, 81 1773–1782.
[24] Hadjileontiadis, L. J., Douka, E. and Trochidis, A. (2005), 'Crack Detection in Beams using Kurtosis', Computers and Structures, 83 909-919.
[25] Jaksic, V., Pakrashi, V. and O'Connor, A. (2011), 'Employing Surface Roughness for Bridge-Vehicle Interaction based damage detection', ASME 2011 International Mechanical Engineering Congress and Exposition (IMECE 2011) Denver, Colorado, USA,
[26] ISO 8606:1995(E). Mechanical vibration - road surface profiles-reporting of measured data, 1995.
[27] Poudel, U. P., Fu, G. and Ye, J. (2005), 'Structural damage detection using digital video imaging technique and wavelet transformation', Journal of Sound and Vibration, 286 (4-5), 869–895.
[28] Wu, S. Q. and Law, S. S. (2011), 'Vehicle axle load identification on bridge deck with irregular road surface profile', Engineering Structures, 33 (2), 591-601
[29] MATLAB 7, 2004. The MathWorks, Inc., Natick, MA.
[30] Chang, C.-C. and Chen, L.-W. (2003), 'Vibration damage detection of a Timoshenko beam by spatial wavelet based approach ', Applied Acoustics, 64 (12), 1217-1240
[31] Okafor, A. C. and Dutta, A. (2000), 'Structural damage detection in beams by wavelet transforms', Smart Materials and Structures, 9 (6), 906–917.
[32] Loutridis, S., Doukab, E. and Trochidis, A. (2004), 'Crack identification in double-cracked beams using wavelet analysis ', Journal of Sound and Vibration, 277 (4-5), 1025-1039

The distribution of capital investment in Ireland's road network 2003-2009

Mary Moloney[1], Eamon McKeogh[2]
[1]Department of Civil, Structural and Environmental Engineering, Cork Institute of Technology
[2]Department of Civil and Environmental Engineering, University College Cork
email: mary.moloney@cit.ie, e.mckeogh@ucc.ie

ABSTRACT: There has been considerable capital investment in Ireland over the past decade, by both Government and the private sector. There are conflicting opinions as to whether Ireland has invested sufficiently in its productive networks over the past decade. Ireland may have nationally invested considerably, but how has this been distributed across the country? This paper focuses on and reviews the overall investment that has occurred in the road network, and its distribution across the country. The level of investment is correlated with possible economic and political drivers, to examine if the investment has occurred in locations that will support the future economic development and growth of the country. The paper tests the correlation of the investment relative inter alia to population density, growth projections, and distribution of overall national construction activity. A study period of 2003 to 2009 was selected as this shows the steepest growth and drop in the nation's economic history. Understandably, capital investment in Ireland over the past 3 years has been severely curtailed by the present national and international economic crisis. Ireland still performs poorly in the international measure of quality of infrastructure and quality of roads, as measured by the World Economic Forum and the International Monetary Fund. The country needs to ensure that where there is future investment in productive infrastructure, it must be targeted where it is most needed, and deliver the greatest return for the investment.

KEY WORDS: Ireland, networks, public infrastructure, roads, transport

1 IRELAND'S ECONOMIC ACTIVITY 2003 TO 2009

Ireland witnessed unprecedented growth and investment during the period 2000 to 2007. During this period Ireland's construction industry contributed in excess of 20% to the national gross domestic product (GDP). Direct employment in construction peaked at 13.5% and Ireland's economy was experiencing an extraordinary growth, in the construction sector in particular. This was one of the main factors in driving up property prices and other consumer goods. Table 1 below shows some of the key national economic statistics of the period 2003 to 2009.

Table 1. Key economic statistics 2003 – 2009.

	No of Employees in Construction (000)	Construction output as % of GDP	Gov Capital investment as % of GDP	Productive infrastructure investment as % of GDP
2003	191.4	17.01%	6.06%	3.08%
2004	206	18.39%	5.64%	2.94%
2005	242.2	19.46%	5.27%	2.64%
2006	268	21.78%	5.29%	2.57%
2007	264	20.38%	6.23%	3.20%
2008	216	18.11%	7.56%	3.67%
2009	137	11.31%	4.51%	2.84%

Source: CSO data [1] and author's own calculations

This activity peaked in 2007 and Ireland has experienced an extraordinary decline in GDP, GNP, construction activity and capital investment, since. Government capital investment peaked in 2008 with an investment of €13.6 billion, while the projected/allocated budget for capital investment in 2012 is €4 billion, a 70% reduction.

This severe cut in capital investment, despite reduced tendering costs, will certainly hamper and slow Ireland's growth in this particularly difficult phase. Certainly, Ireland invested considerably over the 'celtic tiger' period in productive infrastructure, as evidenced in Table 1 above. This paper demonstrates how Ireland still performs poorly by international comparison, and how the driver for some of the investment during this period, has not improved Ireland's growth and competitiveness.

Much has been written on the overall national investment in Ireland's infrastructure; however, little analysis has been carried out on the distribution of this investment across the country and the resulting cost benefit and strategic importance. This paper reviews how the investment has been distributed across the 26 counties of Ireland, and evaluates this against a number of possible drivers. The particular focus of this paper is the national roads investment.

2 PRODUCTIVE INFRASTRUCTURE AND IT'S IMPORTANCE

National infrastructure investment in Ireland is generally classified by the Government into social, economic, and productive infrastructure [2]. Sectoral economic infrastructure investment includes the agriculture, food, fisheries, tourism, forestry and industrial sectors. Social infrastructure includes such categories as: social housing; education and science; health; and government construction. In recent publications the Irish government has re-categorised education and science investment as productive/economic infrastructural investment. However, this paper will continue to use the term ‘productive infrastructure’ as meaning physical networks [3], i.e. water and wastewater networks; electricity infrastructure; connectivity and communications networks and roads which are the main focus of this paper.

Infrastructure, and in particular productive infrastructure, has been internationally recognised as being vital to the growth and competitiveness of an economy. Gramlich [4] clearly identified the link between productivity, economic health and infrastructure investment.

3 IRELAND ON THE INTERNATIONAL STAGE- IT’S PERFOMANCE

It is evident that Ireland has invested in productive infrastructure over the study period, with 3% to 4% of GDP, as outlined in Table 1 above. However, the question remains whether this was sufficient to improve the country’s growth and competitiveness. The World Economic Forum (WEF) publishes an annual global competitiveness report which reviews more than 130 global economies. The WEF measures an economy’s performance using 12 pillars of competitiveness [5-9]. Each country is categorised into one of 3 main headings; *basic requirements* which are key to factor driven (FD) economies; *efficiency enhancers* which are required for efficiency-driven (ED) economies and *innovation and sophistication factors* which are necessary for innovation-driven (ID) economies. Some economies are identified as being in transition between FD, ED and ID. The *basic requirement* pillars are institutions; infrastructure; macroeconomic environment; and health and primary education. The *efficiency enhancer* factors are higher education and training; goods market efficiency; labour market efficiency; financial market development; technological readiness; and market size. The *innovation and sophistication* (ID) factors are business sophistication; and readiness. Ireland’s performance in the WEF reports over the past number of reports is outlined in Table 2 below, for overall competitiveness, infrastructure generally, and roads in particular.

Ireland’s overall infrastructure score and ranking has improved from 49th position in the 2007-08 report to 29th in the 2011-12 report. However, overall quality of infrastructure has seen only a small improvement from 64th to 53rd in the same period, and with the “quality of roads” ranking improving from 60th to 40th over the same period.

The 2011 WEF report was used to prepare Figure 1 below. This identifies Ireland as being in the innovation driven stage of its development (the phase of each county’s growth is indicated). When Ireland’s performance and ranking is compared to some of the European Union (EU) and accession countries, it does not perform well.

Table 2. Ireland’s WEF performance.

	Year of report	2007-08	2008-09	2009-10	2010-11	2011-12
Overall competitiveness	Score	5.03	5	4.8	4.7	4.8
	Ranking	22	22	25	29	29
Infrastructure Pillar	Score	4.03	4	4.2	4.8	5.1
	Ranking	49	53	52	38	29
Overall quality of infrastructure	Score	n/r	n/r	n/r	n/r	4.6
	Ranking	64	64	65	69	53
Quality of Roads	Score	n/r	n/r	n/r	n/r	4.8
	Ranking	60	70	59	52	40

Source: World Economic Forum Global Competitiveness Reports [5-9]

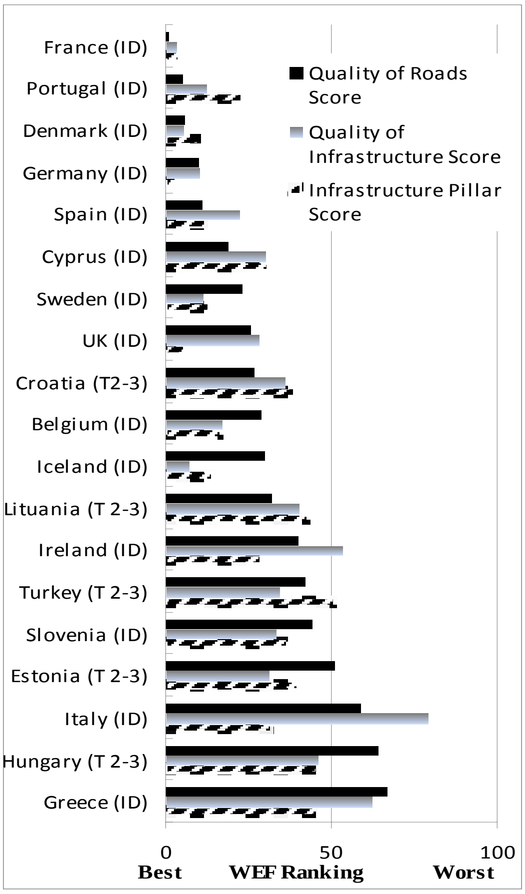

Figure 1. Plot of WEF 2011-12 best road quality and infrastructure quality for a selection of EU counties, also showing stage of development as per WEF (Source: WEF Global competitiveness report 2011-12 [9]).

Yet, when Ireland’s position is reviewed relative to some of the EU member and possible accession states, it sits alongside Lituania and Turkey, both of which are in the transition zone between efficiency driven and innovation driven economies.

Some may argue that the Global competitiveness reports are very much based on ‘perception’ and ‘opinion’. However, these reports are published annually amid much pomp and

Ireland, now more than ever needs to improve its ratings and overall international image. This is clearly presented in an International Monetary Fund (IMF) report [10] where structural reform gaps are identified, using a heatmap. Ireland has 'high' or red gaps in network regulation (a medium-term gap) and infrastructure (a long-term structural reform gap). The Irish Government in its latest book of estimates uses the 'improved' ranking of the quality of Irish roads, as published in the WEF reports, as justification for reducing its capital investment plans. This book of estimates however does not identify Ireland's poor position relative to its EU partner countries, as this paper has done, in Figure 1 above. If Ireland wants to 'show its open for business' it must increase its overall capital investment.

A World Bank (WB) [11] report notes that fast-growing countries are characterized by high levels of public investment in infrastructure, with values as high as 7% of GDP. Ireland did invest this level in 2008, but was well short of this level in the study period. If Ireland should have invested 7% of its GDP on infrastructure, then it underinvested €13.6 billion over the years 2003 to 2009. Based on figures collated, this would equate to €7 billion deficit in productive infrastructure investment. Indeed, this WB report also highlights the great shortage or unavailability of data on infrastructure investment, globally.

4 ACCESS TO RECORDS

There are poor records for national capital stock and capital investment.

4.1 Capital Stock

Keeney [12] identifies that Ireland does not have clear records of Government Capital Stock. Indeed, in the preparation of this paper and in reviewing investment patterns, it was evident that there was a lack of record-gathering over the study period and it was difficult to gain access to information. Investigating the national distribution of government capital investment across the county proved a very difficult task with a number of weaknesses identified.

4.2 Local Authorities Annual Financial Statements

In order to appraise the level of public investment in roads, the Annual Financial Statements (AFS) [13] of each county and city were reviewed for the period 2003 to 2009. These AFSs are submitted to the Department of the Environment, Heritage, and Local Government internal audit division, by the Local Authorities.

A number of observations can be made with regard to the accessibility and clarity of these records while researching for capital investment in productive infrastructure figures: there was a lack of 'standardisation' of the format, some counties recorded water and wastewater capital investment separately while others combined them under the heading 'water services'. Additionally, there is a considerable delay in the auditing of the draft accounts of the local authorities - audited accounts for 2010 have yet to be released at the time of writing this paper in early 2012. This delay in information must make it extremely difficult for counties and indeed central government departments to plan, when they cannot use historic trends.

Some of the local authorities make the information available on their websites; while for others it proved extremely difficult and in some instances impossible to get access to the records.

However, road investment has always been recorded as a separate heading, in the capital investment account and therefore these records were reasonably accessible. Also, the National Roads Authority (NRA) [14] publishes its annual reports on its website and this contains the national distribution of its grant investment to each county.

5 IRELAND'S ROAD INVESTMENT

The National Roads Authority (NRA) is responsible for the capital investment and maintenance of Ireland's motorway and national primary roads. In 2008 the NRA also became responsible for the secondary and local roads. Ireland's overall national investment is profiled in Figure 2 below.

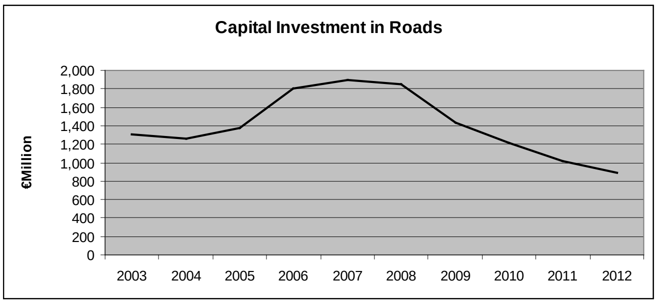

Figure 2. Capital Investment in Roads 2003 to 2011 (out-turn values) and 2012 (projected investment) [15].

Figure 2 shows that Ireland has invested considerably in roads in the study period, and this resulted in Ireland's international rating for roads improving. However, the evidence in the WB report discussed above would indicate that Ireland should continue to invest heavily in its road network. Tender prices have decreased considerably over the period 2007 to 2012 and the impact of the reduced cost of delivering capital investment relative to how much Ireland should invest, to continue its improvement in international rankings will be further researched in a later paper.

5.1 The National Distribution of this Investment

Capital investment in Ireland's road network is funded through central government grants, via the NRA and Local Government funds. Local Government is funded through a variety of sources eg. from central government, road tax and rates. There is also a category of 'development contributions'. These contributions are levied on developers, as a condition of their planning permission. They are generally calculated based on €/m^2 of the building footprint. Each Local Authority (LA) has different rates and indeed some LAs charge an additional premium for eg close proximity to rail corridors. Table 4 below illustrates the considerable positive impact, in some cases in excess of 20% [13], that these development contributions had on local authority incomes over the study period. The AFS of the LA record their capital income separately from the revenue income.

Table 4. Development Contributions as a percentage of Local Authority (local government) capital income – some examples.

	Kerry	Cork Co	Mayo
2003	2.69%	6.63%	n/a
2004	1.57%	10.06%	n/a
2005	0.97%	14.00%	n/a
2006	10.85%	20.87%	8.80%
2007	8.86%	26.61%	12.19%
2008	5.09%	8.37%	4.52%
2009	4.23%	1.54%	3.02%

(source: Local Authority AFS 2003-2009[13], where available)

Table 5 shows the profile of a number of counties road capital investments. The collective national average NRA grant was 74.2% of the national capital investment in the study period.

Table 5. Total Capital Investment (CI) in roads 2003-2009 by Local Authority, NRA grants and new Kms of motorway.

District	Total Capital Investment in Roads 03-09 €M	Total NRA Capital investment by County 03-09 €M	NRA as % of Total CI	Kms of MW* to 2009
Westmeath Co	6,055.30	572.7	94.60%	56.38
Kildare Co	9,525.90	777.1	81.60%	53.67
Galway Co	7,211.10	631	87.50%	50.69
Cork Co	5,765.40	483.5	83.90%	48.9
Tipperary, SR	4,650.70	457.1	98.30%	48.8
Cavan Co	700.3	58.1	83.00%	0
Mayo Co	1,979.60	164.8	83.20%	0
Sligo Co	1,013.80	88.4	87.20%	0
Leitrim Co	833.4	76.9	92.30%	0
Monaghan Co	1,893.00	174.6	92.30%	0

Source: Local Authority AFS [13], NRA annual reports [14], author's own calculations (MW* - Motorway)

The counties selected in table 5 are based on the top five counties per km of motorway constructed and the five counties with no motorway, but highest percentage of capital investment funded by the NRA.

If studied, the counties that have higher than average NRA grants are counties located along the motorway routes from Dublin to Cork, Limerick, Galway and Waterford, which is to be expected. A total of 662 km of motorway were constructed in Ireland during the period.

However, there are a number of counties that had a higher than average investment by the NRA, in particular Leitrim, Mayo, Cavan, Monaghan and Sligo. Roscommon, Donegal and Longford also had higher than average NRA grant assistance over the period. These counties are evaluated with a number of other variables in following section.

6 POSSIBLE DRIVERS TO INVESTMENT

Gramlich [4], in his essay on capital investment, identified a number of drivers for capital investment. These included engineering need, political decisions and econometric estimates and returns. The NRA has robust reviews of its projects, based on traffic surveys and therefore need. However, where there are projected increases in population and substantial areas zoned for housing, a 'need' for road improvements/upgrades result. There follows a discussion on some of the drivers for roads investment, all of which originated with the Government at the time and Central Government policy.

6.1 Section 23 Tax Reliefs

The Irish Government prepared a number of strategy plans during the 2000-2010 period. The National Spatial Strategy (NSS) was prepared in 2002 [16,17]. It had a great vision, that Ireland would be a better place to live with a better quality of life for all and a better spread of job opportunities. It suggested that to enable this vision, a framework of hubs, gateways and other urban and rural areas act together. In line with this, the Government set in place a number of tax relief programmes, which have come to be known as Section 23s. These gave capital tax allowances to the developer and included a vast array of developments from rural renewal, to holiday cottages, hotels, private hospitals etc. It would appear that the original function of these tax reliefs was to halt rural decline, encourage economic regeneration and develop economic and social infrastructure. A review of these was undertaken in 2005 [18] and a number of recommendations were made, including halting the reliefs immediately, to giving a five year extension. What is apparent now is that while some of these 2005 recommendations were acted on, the construction and completion of section 23 properties continued. While the original concept of the section 23 was to deliver specific types of development in highlighted geographical locations, the overall quantity and spatial distribution went somewhat unmanaged.

The Irish Department of Finance issued an impact assessment consultation paper in June of 2011 to review the impact of amending existing property tax reliefs [19]. This paper presents the Section 23 reliefs linked to the residing county of the tax payer. This means that if the tax payer resides in Cork, they make their tax return to the appropriate Cork tax district of the Office of the Revenue Commissioners, the tax payer lists/documents their Section 23 property or properties for which they are claiming relief against their income tax. However, this tax return information does not register the address of the section 23 property.

Clearly, therefore, the Revenue Commissioners information does not identify the location of the Section 23 properties. From discussions with the Departments of Finance, there is no 'list' of where these properties are located. This Department of Finance consultation paper [19] identified that there were 74,003 claims of tax relief for Section 23 properties (living accommodation only), over the period 2004 to 2009.

During the preparation of this paper, previously unpublished records were received from the Department of the Environment, which identified the number of certificates granted for the purpose of claiming the tax relief. These certificates were issued by the Department of the Environment to each owner of a property. These certificates allow the pattern of Section 23 properties to be mapped across the country, as per Table 6 below. In total, from the records received, it would appear that there were 37,117 certificates of compliance issued. Some certificates are for a number of properties. Section 23 properties included in table 6 are for third level student accommodation, living over the shop scheme, sea-side resorts, town renewal and urban renewal.

Table 6. The percentage of Section 23 certificates issued per county as a proportional of the national total, 2000-2009.

County	As % of total Section 23 certificates issued in period 2000 to 2009	County	As % of total Section 23 certificates issued in period 2000 to 2009
Dublin	16.03%	Louth	1.03%
Longford	13.63%	Wexford	1.03%
Leitrim	13.44%	Carlow	0.99%
Roscommon	11.12%	Donegal	0.97%
Sligo	10.51%	Kildare	0.87%
Limerick	6.17%	Kilkenny	0.69%
Cork	4.39%	Clare	0.57%
Waterford	4.31%	Tipperary	0.53%
Cavan	3.94%	Meath	0.51%
Galway	3.60%	Laois	0.47%
Westmeath	1.98%	Offaly	0.38%
Kerry	1.32%	Wicklow	0.17%
Mayo	1.19%	Monaghan	0.16%

Source: Department of the Environment, Heritage and Local Government (previously unpublished numbers)

Table 6 shows the very large proportion of section 23 properties that have been constructed in the Border- Midlands –West (BMW) region, Longford at 13.6%, Leitrim 13.4%, Roscommon 11% and Sligo at 10.5%. There was also considerable section 23 development/activity in Cavan and Westmeath.

6.2 Methodology and Analysis of investment data

Considerable data has been collated in the preparation of this paper. This included roads investment by local authority, NRA grants to each local authority. A number of data sets were collated and prepared to test if there was a correlation between roads capital investment and other variables. These correlations are a test of the linear relationship between a set of values, with a correlation coefficient of 1, demonstrating a perfect match in the 2 data sets. It was decided to test using area of the local authority, population, population density, Section 23 properties, housing stock, with a focus on some BMW counties.

6.3 Housing Vacancy Rates

With such construction activity, it was decided to focus on a number of BMW counties, to understand if there was a correlation between the level of road capital investment and the recent housing boom. The counties analysed were Cavan, Donegal, Galway, Leitrim, Longford, Mayo, Monaghan, Roscommon, Sligo. Bearing in mind that both Roscommon and Galway had considerable motorway investment as identified in table 4 above, a second scenario of excluding Galway County and Roscommon is analysed. Records of housing stock i.e. the number of units existing and available to be lived in, the number of units occupied and the overall vacancy rates in these counties were analysed. The results are presented in Table 7 below.

Table 7. Correlation coefficients of Roads, investment and housing development, population distribution.

Area in hectares **AND** kms of road, for all cities and counties	0.942
Population density **AND** kms road, for all cities and counties	-0.42
Hectares of County **AND** % of NRA as Capital Investment, for all cities and counties	0.45
Hectares **AND** NRA as % of all BMW counties	0.56
Pop density **AND** NRA as % of BMW counties	-0.538
Pop density **AND** %NRA of CI*, for all cities and counties	-0.562
No of Households and NRA roads CI	0.441
Total CI* in roads **AND** housing stock	0.794
Total CI* in roads **AND** housing stock, incl Roscommon and Galway Co (BMW region)	0.695
Roads CI per capita **AND** housing stock, excl Galway Co and Roscommon (BMW region)	-0.907
Roads CI per capita **AND** housing stock, incl Galway and Roscommon (BMW region)	-0.629

*CI** - capital investment

This table shows a number of correlations. The kilometre of roads is in line with the hectares of the county as would be expected. There is reasonably close correlation of -0.42 between the population density of a county and the kilometres of road, as the population per hectare increases, the kms of road decreases. There is a reasonable correlation of -0.538 inversely between the grant aid of the NRA to the BMW counties and the population density of the BMW counties. This indicates that the lower the population density, the higher the grant aid to the county.

There are very close correlations between the national capital investment in roads and the housing stock by county. Considering the high vacancy rates across the country, it would indicate that housing development influenced the investment in the roads network. The length of Ireland's road network is dependent on the hectares of the county (0.942 correlation) and the higher the population density the fewer kilometres of roads, as would be expected.

The National Roads Authority provides varying grant assistance to local authorities. These grants have generally been in line with motorway investment. However there is evidence that considerable grants have followed the house building trend, with a correlation co-efficient of 0.441. This trend would suggest that Ireland, with an average house vacancy rate in excess of 15% (with some counties as high as 25% to 30% vacancy rate) may have invested in regional areas, where there is not the expected return inter alia of population and therefore traffic volumes.

Indeed the national trend of a 0.794 correlation between capital investment in roads and households by county, would clearly indicate that road investment followed the national housing bubble

6.4 Political Influence

The Government developed the National Spatial Strategy (NSS) in 2002 and subsequent National Development Plans (NDP). These documents gave considerable focus to increasing the population in the BMW counties, consequently leading to considerable productive infrastructure investment. While it was necessary to a certain extent, the tracking of the developments to ascertain when there was sufficient was not done. There are now counties where there was sufficient housing stock in the 2006 census to accommodate the population recorded in the 2011 census, with surplus.

7 CONCLUSIONS

The review of Ireland's investment in its road network has identified a number of interesting observations:

- The roads investment was generally in line with motorway construction and road improvement. Road investment was in line with the hectares of the counties with a correlation of 0.942
- There is evidence of a correlation between the roads investment and the housing bubble, a 0.794 correlation
- Ireland's international rating of quality of roads has improved over the study period; however we are at the same ranking as EU countries with less innovative and far lower GDP economies, eg Turkey, Lituania, Slovenia and Iceland.
- The IMF in a recent paper clearly identified Ireland's infrastructure as being a 'high level' structural reform gap.
- This situation has to be improved with more targeted road investment, outside of political influence and government polices.
- There has been a lack of record keeping over the period, eg of tax relief data, housing stock figures in the 2002 census and distribution of investment in local authorities
- Development contributions had a large positive impact on local authority budgets over the study period (as high as 20%). This aided the development of productive infrastructure. This finance is not available at present to the local authorities.
- It is strongly recommended that a complete review of national development and planning strategies be undertaken, and a more balanced and sustainable policy be developed. Ireland, at this very difficult economic time needs to ensure that where there is investment, it will lead to economic growth and improve Ireland's international rating.

REFERENCES

[1] CSO, Central Statistics Office: Cork, Ireland.
[2] Dept of Finance, Infrastructure Investment Priorities 2010-2016. 2010, Irish Government: Dublin.
[3] Moloney, M, Menzel, M & McKeogh, E; Quantifying Ireland's Infrastructural Deficit in BCRI conference 2010: Cork.
[4] Gramlich, E.M., Infrastructure Investment: A Review Essay 1994, Journal of Economic Literature.
[5] Schwab, K., The Global Competitiveness Report 2007-2008. 2007, World Economic Forum: Geneva.
[6] Schwab, K., The Global Competitiveness Report 2008-2009. 2008, World Economic Forum: Geneva.
[7] Schwab, K., ed. The Global Competitiveness Report 2009-2010. 2009, World Economic Forum: Geneva.
[8] Schwab, K., ed. The Global Competitiveness Report 2010-2011. 2010, World Economic Forum: Geneva.
[9] Schwab, K., ed. The Global Competitiveness Report 2011-12. 2011, World Economic Forum: Geneva.
[10] Allard, C and Everaert, L et al: Lifting Euro Area Growth: Priorities for Structural Reforms and Governance: Lifting Euro Area Growth: Priorities for Structural Reforms and Governance. 2010, IMF International Monetary Fund.
[11] Development, C.o.G.a., The Growth Report Strategies for Sustained growth and Inclusive Development. 2008, The World Bank Washington.
[12] Keeney, M.J., Measuring Irish Capital. The Economic and Social Review, 2007. 38(Spring 2007): p. 25-62.
[13] Section, L.G.F., H.a.L.G. Department of Enviroment, Editor, Irish Government: Wexford.
[14] National Roads Authority, Annual Reports 2003-2009, Irish Government Stationary Office: Dublin.
[15] Local Government Agency, Revised Estimates for Public Services. 2012, Government Publications Office, Ireland.
[16] Dept of Environment, Heritage and Local Government, National Spatial Strategy for Ireland 2002-2020. 2002, Irish Government Stationary Office: Dublin.
[17] Dept of Environment, Heritage and Local Government, National Development Plan 2007-2013 Transforming Ireland A better quality of life for All, Annual Report 2007, Irish Government Stationary Office: Dublin
[18] Dept of Finance, Review of Tax Incentives Schemes: Consideration of Consultancy Studies. 2005, Irish Government.
[19] Dept of Finance, Impact Assessment of Legacy Property Reliefs. 2011, Irish Government.

Freeze-thaw resistance of fibre reinforced concrete

David Dunne[1], Moray Newlands[2], Andy Waite[1]
[1]Halcrow Group Limited, A CH2M Hill Company, Redhill House, 277 London Road, Worcester, England, WR5 2JG
[2]Department of Civil Engineering, University of Dundee, Dundee, Scotland, DD1 4HN
email: dunnedj@halcrow.com, m.d.newlands@dundee.ac.uk, waiteaj@halcrow.com

ABSTRACT: A key issue in attaining durability of concrete is the prevention of freeze-thaw and, its associated affects. This durability issue pertains primarily to flat, horizontal and water saturated concrete structures, which include: footway pavements; carriageways; seawalls; dams and; bridges. Whilst aesthetical resulting in a concrete with a poor appearance, more importantly, the affects of freeze-thaw gives rise to a hazard, that if untreated can endanger the structural integrity of a concrete element. As a result, air-entraining agents have in the past, been applied to counteract this intrinsic durability issue. Fibres, used to reinforce concrete, are commonly acknowledged as improving specific properties of concrete. These include compressive strength, engineering properties and abrasion resistance. Therefore, it was thought possible that they may also improve a concretes freeze-thaw resistance. Where, concrete mixes were developed, using different types and dosages of synthetic fibres. Mechanical properties of compressive, tensile splitting and flexural strength were recorded, and freeze-thaw resistance was measured under accelerated conditions, after 45, 90 and 135, 24-hour cycles of exposure. This study indicates that synthetic fibres improved compressive strength by up to 14% at 28 days testing, and tensile splitting strength by up to 22%, whilst, flexural strength in general, is maintained or slightly improved in comparison to the reference concrete. The results demonstrated at best similar, and in the main slightly reduced resistance to the affects of freeze-thaw exposure. Finally, linear regression analysis was applied, to statistically establishing the degree of association between concrete freeze-thaw resistance and its mechanical properties. The strongest correlation was obtained with comparison of compressive strength.

KEY WORDS: Freeze-thaw; Synthetic fibres; Concrete; Engineering properties.

1 INTRODUCTION

The resulting affects on concrete, due to freeze-thaw affects, not only poses a problem aesthetically, where surface damage results in poor appearance, but also in respect to more severe hazards that can jeopardize the integrity of a whole structure. The most common forms of freeze-thaw damage in concrete are: surface scaling; concrete pop-out; d-cracking and; internal damage. The distinctions between these are arbitrary. While the first two are surface or near-surface phenomena, the latter two may occur throughout a concrete element. This durability issue pertains principally, to flat horizontal surfaces such as roads, and saturated concrete structures such as sea walls, dams, and bridges.

Unlike ordinary reinforced concrete which, contains an appropriate minimum percentage of reinforcement bars, fibre reinforced concrete contains discrete dispersed fibres. The concept of utilising fibres to enhance construction material properties can be traced back over 4000 years, to the use of straw in bricks and horse hair in plaster [1]. Patents have been granted since the turn of the century for various methods of incorporating wire or metal chips into concrete. The first significant development is often credited to Joseph Lambot [2]. He inferred in his 1847 patent that the addition of continuous fibres to concrete in the form of wires or wire meshes created a new building material. Thirty years later, A. Bernard from California managed to create an artificial stone by the addition of granular waste iron to a concrete mix [3]. Indeed, many credit him with inventing modern day steel fibre reinforced concrete where, in 1874 he patented the concept of strengthening concrete with the addition of steel splinters [3].

Fibres of various shapes and sizes produced from steel, synthetics, glass and natural materials find application in concrete. General consensus suggests that fibres do improve specific properties of concrete, and that fibres can be particularly beneficial under extreme environments. However, where air-entraining agents are commonly applied to improve concretes resistance to freeze-thaw resistance, it is not unreasonable to infer that fibres may also improve its freeze-thaw resistance properties. The principal aim of this research was to investigate this affect. Different types and dosages of synthetic fibres where used. The scope of this research assessed the performance of a selective range of strength characteristics, in addition to freeze-thaw resistance of fibre reinforced composites. This facilitated comparisons to be made with plain un-reinforced concrete, and a determination of the suitability of applying strength characteristics of fibre reinforced concrete to estimate freeze-thaw resistance.

2 PROGRAMME OF WORK

This paper reports on the characteristics of three fibres, applied in different dosages and combinations to concrete, namely: (i) Fibremesh 150 (Propex); (ii) Enduro HPP 45 (Propex) and; (iii) Strux 90/40 (Grace), at a single w/c ratio of 0.50. The strength characteristics that are investigated included: (i) compressive strength; (ii) flexural strength and; (iii) tensile splitting strength. Freeze-thaw resistance of concrete when placed in an accelerated exposure environment was investigated thereafter.

3 MATERIAL AND MIX PROPORTIONS

The performance of three fibres were examined in this work: (i) a micro-synthetic fibre (Fibremesh 150); (ii) and two macro-synthetic fibres (Enduro HPP 45 and Strux 90/40). Key characteristics of the three fibres are given in Table 1.

Table 1. Chemical and physical properties of fibre.

Chemical and Physical Properties	Fibremesh 150	Enduro HPP 45	Strux 90/40
Specific Gravity	0.91	0.91	0.91
Fibre Length	12mm	45mm	40mm
Material	Polypropylene	Polyolefin	Polypropylene
Type/Shape	Fine/Micro	Macro	Macro
Melt Point	162°C	164°C	160°C
Ignition Point	593°C	>550°C	590°C
Acid and Salt Resistance	High	High	High
Alkali Resistance	Alkali proof	Alkali proof	Alkali proof

Natural sand and natural gravel conforming to BS EN 12620:2008 was used as fine aggregate in all mixes. A single sourced CEM I 42.5N cement, conforming to BS EN 197-1:2000 was utilised, with the key characteristics of the cement given in Table 2. Seven concrete mixes were proportioned for a single w/c ratio of 0.50, total cement content of 330 kg/m^3 and single water content of 165 kg/m^3. These are in accordance with the BRE method for designing normal concrete mixes [4]. The mix design was to achieve a consistence conforming to the S3 slump class in BS 8500-1:2006. Table 3 gives the standard CEM I mix design. Figure 1 and Table 4 outlines the fibres and concrete mix fibre proportions, expressed as a percentage of the total cement content.

The specimens were cast in moulds and, cured under damp hessian and polythene sheeting to maintain a high humidity (> 95%) for 24 hours. The specimens were then de-moulded, marked for identification and cured in water at 20°C ± 2°C, in accordance with BS EN 12390-2:2000, until time of testing.

4 EXPERIMENTAL FINDINGS

4.1 Compressive strength

The compressive strength of all concretes was determined by testing 100mm cube specimens in accordance with BS EN 12390-3:2002. The relationship between time and 3, 7, and 28 day compressive strength for all concretes are shown in Figure 2. In all cases, these exhibited the typical shape that would be expected. For any given concrete, the addition of fibres in the cementitious matrix gives rise to a concrete which exhibits higher strength than that of plain concrete lowest.

Table 2. Cement properties.

Material	Property Measured: Fineness*, m^2/kg	Loss on Ignition, %	Particle Density, g/cm^3
CEM I	414	1.74	3.14

*Tested by Blaine fineness method

Table 3. Concrete mix constituent proportions.

Mix Constituent Proportions, kg/m^{3*}					
w/c ratio	Cement	Water	Aggregates (mm): Natural Sand 0/4	Natural Gravel 4/10	Natural Gravel 10/20
0.50	330	165	750	395	770

*Glenium 51 a high range water reducing superplasticising admixture was added to all concrete at a dosage of between 0.2 and 0.8l/m^3 per 100kg of cement

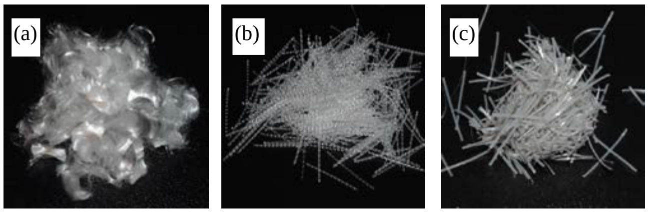

Figure 1. Fibre types (a) Fibremesh 150; (b) Enduro HPP 45 and; (c) Strux 90/40.

Table 4. Concrete mix fibre type, combination and percentage details.

Concrete Mix Number	Concrete Mix Details, % of total cement content
Mix 1	CEM I (*reference concrete*)
Mix 2	CEM I + 0.3% Fibremesh 150
Mix 3	CEM I + 1.7% Enduro HPP 45
Mix 4	CEM I + 1.5% Strux 90/40
Mix 5	CEM I + 0.3% Fibremesh + 1.7% Enduro HPP 45
Mix 6	CEM I + 3.0% Enduro HPP 45
Mix 7	CEM I + 3.0% Strux 90/40

Test results demonstrate that the addition of steel fibres increase compressive strength almost linearly. This rate of increase is higher at early 3 day testing to that of later 28 day testing. As outlined in Table 5, on analysing the data further, the strength of fibre reinforced concretes at a given day, were up to 19% higher than that of plain unreinforced concrete. These results indicate that Mix 2 was the best performing concrete in compression to the plain un-reinforced CEM I reference concrete. Thereafter, Mix 4 and Mix 5 indicated increases in strength development in the ranges of 19% and 17% after 3 days and 7% and 5% respectively after 28 days water curing. The results of Mix 3 and Mix 6, indicate that the addition at the two levels of Enduro HPP 45 fibres in the cementitious matrix provided the slowest rate in strength gain over the three test ages. These are in comparison to the remaining fibre reinforced concretes.

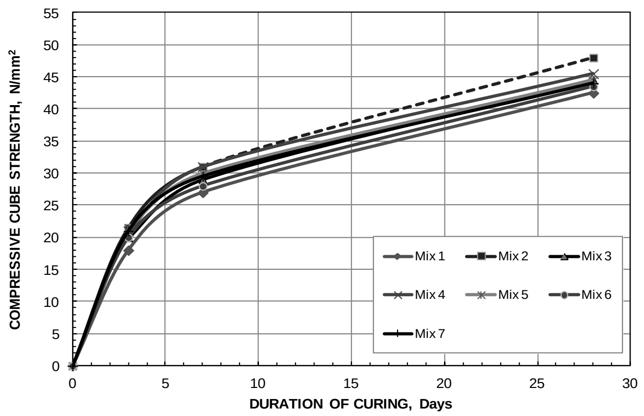

Figure 2. Compressive strength development of concretes.

With respect to the addition of Strux 90/40 fibres, it was noted that the strength development of Mix 7 was less than that of Mix 4. This would indicate an optimum fibre addition level, to that of the 3% addition to Mix 7. The workability of concrete was found to reduce significantly during concrete production, when fibre content increased to the higher dosage level (3% by total cement content). Fibres introduced at the mixer should be added gradually as bunching of the fibres was initially observed during concrete production. This would be seen as a contributing factor to the trends in these results, and this will be discussed in further detail in Section 6.

Table 5. Compressive cube strength development of concretes.

Concrete Mix Number	Compressive Cube Strength, % of CEM I Reference Concrete		
	3 day	7 day	28 day
1	100	100	100
2	119	115	113
3	111	107	105
4	119	115	107
5	117	111	105
6	111	104	102
7	117	109	104

Finally, on examination of the concrete cube specimens after compressive strength testing, the actions of the fibres are more apparent. The photographs presented in Figure 3, demonstrate how the unreinforced plain concrete breaks in a brittle manner after initiation of the first cracks. However, in respect to the reinforced concrete the presence of fibres inhibits this extensive crack propagation process.

4.2 Tensile splitting strength

Tests for tensile splitting were carried out in accordance with BS EN 12390-6:2000 at 28 days. The tensile splitting strength results indicate that the addition of fibres improves tensile strength of concrete. Plain unreinforced concrete would be expected to be weaker under this type of loading, in comparison to fibre reinforced concrete. This is an important parameter for beams, as tensile splitting strength provides an indication of concretes shear strength in diagonal tension, where increases can be utilized in structures subjected to shear loading.

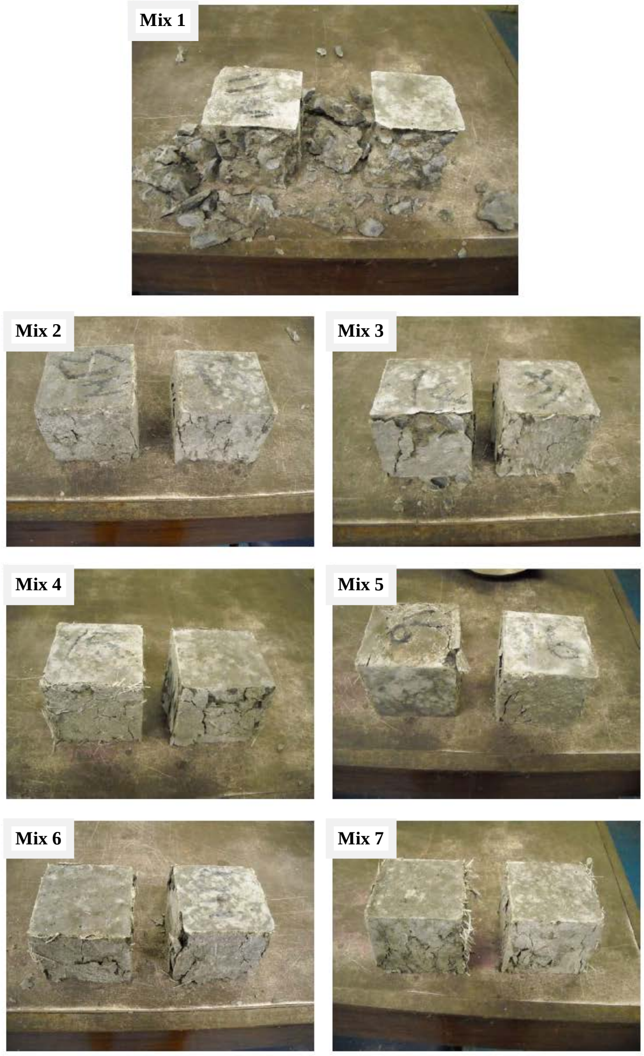

Figure 3. Compressive strength tested specimens after 28 day compressive strength testing.

Typically these increases ranged from 11% - 22%, to that of the reference CEM I concrete, as presented in Figure 4. Concrete Mixes 2 and 7 demonstrated the greatest improvements at 22% and 21%, when compared to the reference concrete. The results indicate similar performance with the 0.3% Fibremesh 150 and 3.0% Strux 90/40 fibres, and reduced improvement in performance with the inclusion Enduro HPP 45 fibres. Thereafter, binary blending of fibres resulted in reduced performance in comparison to the urinary blended fibre reinforced concretes.

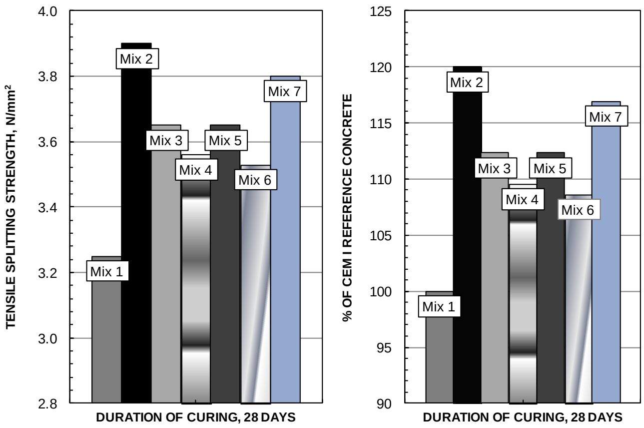

Figure 4. Tensile splitting strength results after 28 days moist curing.

Finally, on analysing the mode of failures in Figure 5, the affect of fibres on the tensile fracture behaviour of concrete can be further understood. Notably, unlike the spalling and subsequent cracking behaviour of the reference CEM I concrete, the fibre reinforced concrete demonstrated greater ductility. Significantly, only Mix 3 demonstrated a brittle failure which may be attributed to the scanty of 45mm long fibres at the 1.7% addition level.

4.3 Flexural strength

Flexural strength was carried out to BS EN 12390-5:2000, at 28 days. The analysis of data obtained from Table 2 appears to indicate that there was no significant increase in concrete performance with the inclusion of fibres. Mix 6, proved an exception, demonstrating a 7% decrease in flexural strength which, corresponds with the trends observed from compressive strength. Thereafter, the remaining fibre reinforced concretes demonstrated similar or slightly higher measured values to that of the unreinforced concrete.

However, in understanding this behaviour, one should note that fibres operate by improving the post-cracking ductility of a cementitious matrix. Plain and reinforced concretes have approximately the same behaviour in the pre-crack phase. Fibres are added to concrete, primarily to improve its toughness or energy absorption capacity (i.e. the area under the complete load-deflection curve in flexure). This is achieved in fibre reinforced concrete, through the bond of fibres to the cement matrix. Therefore, analysing the load-deflection behaviour and not only the load-crack behaviour of the concrete, during testing, would provide more advantageous data.

The flexural test results also revealed that specimens without fibre had little ductility, and once the maximum flexural strength was reached, the specimens failed suddenly. However, the failure characteristics were completely changed with the introduction of fibres. Fibre reinforced concrete specimens did not fail suddenly after the occurrence of initial cracks. This can be attributed to the randomly oriented nature of the fibres crossing the cracked section, which facilitates greater resistance to the propagation of cracks and subsequent separation of the section. This facilitates an increase in the load carrying capacity.

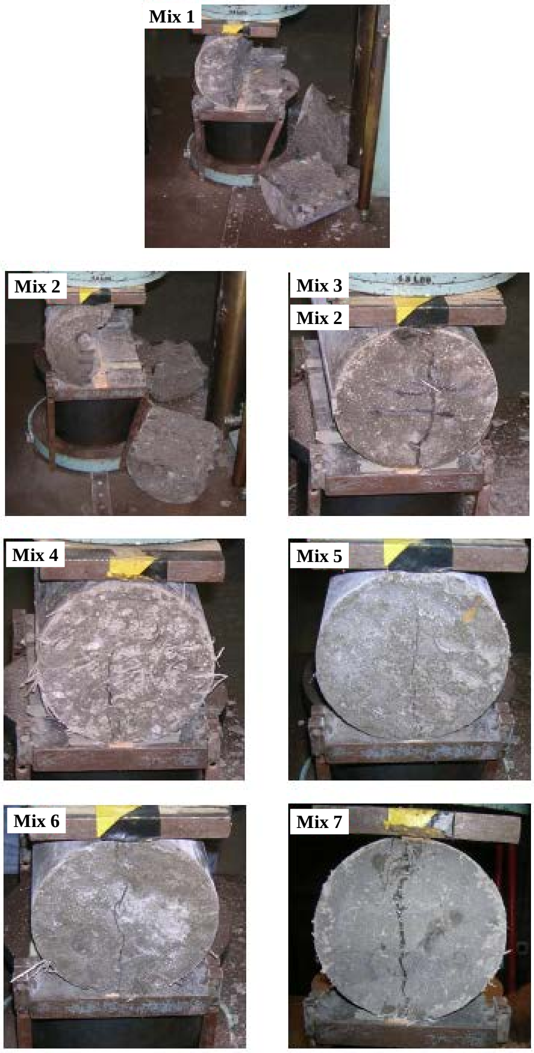

Figure 5. Tensile splitting specimen after 28 days testing.

4.4 Freeze-thaw resistance

The freeze-thaw resistance test was determined on 28 day water cured 50mm × 150mm × 150mm concrete samples which, were cut from 150mm × 150mm cube specimens after 45, 90 and 135, 24-hour cycles of laboratory simulated freeze-thaw exposure. The specific detail of the test procedure which, was adopted is not detailed herein. The reader should refer to [4] to obtain this information.

The results demonstrate the no overall benefits were obtained in respect to enhancing freeze-thaw properties of concrete, when fibres are added to the cement matrix. Scaling of all the concretes was similar, increasing linearly in volume with time. This can be seen in Figure 6 and Figure 7. The average quantity of scaled material recorded was 0.196 kg/m^2 for the plain un-reinforced CEM I concrete, whilst scaled material values for the fibre reinforced concretes ranged from 0.197 kg/m^2 to 0.209 kg/m^2 respectively.

Table 6. Flexural strength at 28 days testing.

Concrete Mix Number	28 Day Flexural Strength	
	f_{cf}^*, N/mm^2	% of CEM I Reference Concrete
Mix 1	5.43	100
Mix 2	5.47	101
Mix 3	5.38	99
Mix 4	5.38	99
Mix 5	5.65	104
Mix 6	5.07	93
Mix 7	5.78	106

f_{cf}^* the calculated flexural strength

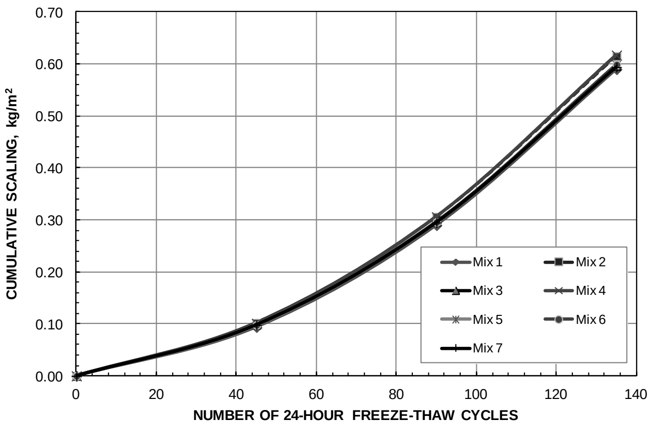

Figure 6. Cumulative freeze-thaw scaling affects after 45, 90 and 135, 24-hour cycles of laboratory simulated freeze-thaw exposure.

In addition, on assessing cumulative scaling affect with time, it was established, that that the percentage of scaled material removed, in comparison to the CEM I reference concrete reduced with each extended length of exposure. In all instances, the quantity of scaled material was higher than that of the reference concrete. These findings are presented in Figure 7, were across the range of concrete the value of total scaled material increased from plus 1%-11% respectively.

A reduction in total scaled material quantities with increased duration of testing, may reflect an expected increase in formation of the hydrated cement matrix which, would occur over this period. Whilst the hydration process would be altered due to the exposure environment, these statements cannot be substantiated without further microscopic examination. Furthermore, it is likely, that the addition of fibres to the cement matrix may result in a less dense concrete microstructure. This in turn, would result in the fibre blended concretes possessing a coarser internal pore structure, which would allow space for water pressure to release after the thaw process takes place and during the freezing process.

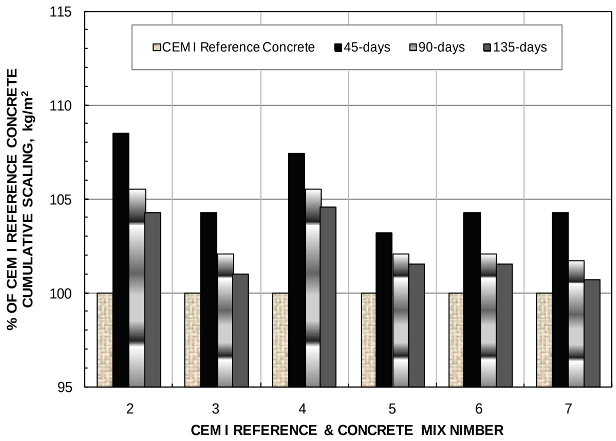

Figure 7. Cumulative freeze-thaw scaling affects as a percentage of the CEM I reference concrete.

5 SUITABILITY OF APPLYING STRENGTH CHARACTERISTICS OF FIBRE REINFORCED CONCERTE TO ESTIMATE FREEZE-THAW RESISTANCE

Concrete compressive strength is related to the hydrated cement paste structure, and is influenced by the number, type, size and distribution of pores present. Researchers have reported on the possibility of applying this parameter in attaining information into overall concrete quality [5, 6]. In statistically establishing the degree of association between concrete freeze-thaw resistance and, the three strength characteristic, linear regression analysis was applied. This allowed correlation coefficients (r) and coefficients of determination (r^2) to be attained. Whilst representing a simplified technique, this approach will indicate whether the pairs of variables in different units are related.

Table 7 outlines the relationships which developed between the cumulative freeze thaw measurements of the concrete, and the strength characteristic measurements. Due to the limited amount of data generated during this study, the seven concrete types were combined in generating the statistical output. Although linear regression of the data tended to generate weak correlation coefficients (r ± 0.80) [7], it was observed that these regressions did represent the underlying data trend. The current data set suggests that the strength characteristics of tensile splitting and flexural strength are not suitable to be applied when estimating freeze-thaw resistance of concrete.

The strongest correlation was obtained when comparisons were made with compressive strength. These findings are best illustrated in Figure 8 where, the key characteristics of the compressive strength regression analysis with that of cumulative scaling, after 45, 90 and 135 days of 24-hour exposure are represented. Significantly, this demonstrates the potential of applying compressive strength characteristics when estimating the freeze-thaw resistance of fiber reinforced concrete. In addition, noting that their correlations were developed across the seven different concrete types, if a greater set of data were available to allow comparison within fiber reinforced concrete types, it is expected that these correlations would improve even further.

Table 7. Correlation comparisons between freeze-thaw properties and strength characteristics.

	Number of Free-Thaw Cycles	Compressive Strength	Tensile Splitting Strength	Flexural Strength
Pearsons Correlation Coefficient (r)	45	0.862	0.879	0.829
	90	0.723	0.568	0.089
	135	0.071	0.089	0.152
Coefficient of Determination (r^2), %	45	0.743	0.772	0.687
	90	0.528	0.323	0.193
	135	0.005	0.008	0.023

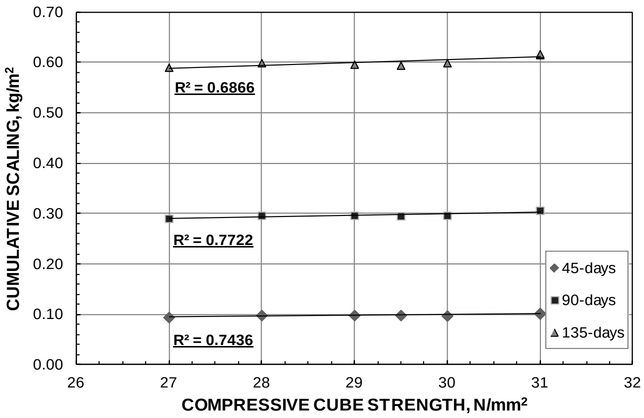

Figure 8. Regression analysis of compressive cube strength at 28-days, and cumulative scaling after 45, 90 and 135, 24-hour cycles of laboratory simulated freeze-thaw exposure.

6 CONCLUSION AND RECOMMENDATIONS

The aim of this research was to analyse the freeze-thaw resistance of concrete when reinforced with synthetic fibres. Both strength characteristic and freeze-thaw testing were completed to achieve this.

Based on the work presented in this paper, it can be concluded that; (i) fibre inclusion does result in higher rates of compressive strength gain; (ii) in the attainment of higher tensile strength and; (ii) have no positive effect on flexural strength development. However, they do increase post-crack ductility of concrete, in comparison to plain unreinforced concrete. In particular, it was observed that the inclusion of fibres into the cement matrix imparts little benefit to the freeze-thaw resistance properties of concrete. Where benefits are observed, these are limited to less than 10% of the reference concrete in the research.

In addition, some recommendations for further investigations can be suggested. The suggestion from the data presented in this paper, is that the addition of fibres to the cement matrix, may result in a less dense concrete microstructure and consequently further research is recommended on this aspect. Further research should be undertaken on concrete with varying w/c ratios, and total water and cement contents. This would allow for greater conclusions to be drawn on the practicalities of fibre inclusion in resisting freeze-thaw, and in applying the compressive cube strength of fibre reinforced concrete, as a measure of potential freeze-thaw resistance.

There are limits in relation to how fibres can be used in concrete. In particular, fibres can import significant constraints on concrete workability, even with the inclusion of a superplastercising admixture. A method of concrete production is required to counteract fibre bunching in the mixer. One proposal is to utilise a 25mm - 30mm sieve when adding fibres to the cement matrix, as this will reduce the occurrence of fibres forming balls. However, whilst acceptable for controlled laboratories environments, this may not be practical in site conditions. A method of working needs to be developed to ensure that adequate mixing procedures are followed.

ACKNOWLEDGMENTS

This research was undertaken by the first author with undergraduate Erasmus student Paola Turchi whilst, reading for his PhD in Civil Engineering, at Concrete Technology Unit, University of Dundee, Scotland. She, along with the technical staff at the University of Dundee, Civil Engineering Department, are acknowledged for their help in undertaking the experimental work. The assistance and financial support provided by Halcrow Group Ltd, A CH2M Hill Company in entering this paper is greatly acknowledged.

REFERENCES

[1] D. Wimpenny, *The use of Steel and Synthetic Fibres in Concrete under Extreme Conditions*, Concrete 09, Sydney, 2009.

[2] Antoine, E.N. (1985), 'Fibre reinforced for concrete', *Concrete International*, March 1985, pp 21-25.

[3] D. R. Maidl, Eds., *Steel Fibre Reinforced Concrete*, Ernest and Sohn, 1995.] D. C. Teychenne, R. E. Franklin, and H. C. Ernroy, *Design of normal concrete mixes*, Second Edition, amended by B K Marsh. Building Research Establishment, 1997.

[4] Dhir, R. K., Tittle, P. A. J. and McCarthy, M. J. (2001), 'Role of cement content in the specification for durability of concrete', University of Dundee, 2001.

[5] Basheer, L., Kroop, J., and Cleland, D.J. (2001) 'Assessment of the durability of concrete from permeation properties: a review', *Construction and Building Materials,* Vol. 15, 2001, pp. 93 - 103, 2001.

[6] Dunne, D. (2010), *Chloride Durability and Working Life Investigations of Cement Combination Concretes*, PhD Thesis, University of Dundee, Scotland.

[7] N.J. Salkind eds., *Statistics for people who (think they) hate statistics,* Sage Publications, Inc., 2000.

Cracking in concrete walls due to an external temperature load

John J. O'Donnell[1], Andrew Speares[2]
[1]Department of Civil/Structural Engineering, Dublin Institute of Technology, Bolton Street, Dublin 2, Ireland
[2]S.Wilkin and Sons Ltd, Rockcorry, County Monaghan, Ireland
email: john.odonnell@dit.ie, ajspeares@hotmail.com

ABSTRACT: Considerable research has been carried out on thermal cracking of concrete due to heat of hydration but less work has been done on cracking due to external heating. External heating can occur due to normal environmental conditions such as heating of concrete pavements or bridge beams by the sun but this paper is concerned with situations where the maximum concrete temperature reached is greater than that produced by solar heating, though less than 100 ^{o}C. Examples include storage of heat-producing substances in industrial and agricultural facilities and accidents involving the release of high temperature liquids or gases. A theoretical model is proposed that allows the effects of various external heating events to be calculated. In particular, the model can be used to predict the time-varying temperatures and stresses induced across the concrete element. This information can be used to predict whether thermal cracking will take place and whether the moment capacity of the section will be reduced due to unfavourable combinations of thermal and other loads. Both transient and steady-state temperature profiles are predicted by the model. The model also allows for different restraint conditions. The theoretical model was applied to a laboratory test which was designed to simulate a real reinforced concrete wall in a concrete silo used to store mushroom compost. A temperature load of about 80 ^{o}C arose in this structure from the internal heat generated by the compost. The predicted temperatures were found to match the measured ones quite well and the predicted stresses provided a good indication of when cracking first occurred.

KEY WORDS: concrete walls; thermal cracking, temperature load, thermal stresses

1 INTRODUCTION

Thermal cracking of concrete usually refers to cracking caused by the temperature rises due to heat of hydration. Considerable work has been done on modelling temperature and thermal stress in this context [1]. However, cracking can also be caused by external heating and this is the subject of this paper. Temperatures of less than 100^{o}C only are considered so that issues such as spalling due to steam pressure do not arise.

Thermal cracks are obviously undesirable so it is useful to be able to predict whether a given concrete member will crack in any external heating scenarios that may arise during its design life. The likelihood of cracks occurring will depend on many different factors including the size and shape of the member, the restraint conditions, the size of the temperature rise and how rapidly the heating occurs. Thermal restraint can also induce another form of load that acts in combination with the other loads that the member must resist.

A theoretical model is described in this paper that predicts temperature and stress profiles in concrete members subjected to external heating. The model is then applied to one particular member type, namely a long, high wall. As the length and height of the wall are much greater than its thickness, the heat flow can be approximated as being one-dimensional. A particular restraint condition is modelled which allows linear expansion but prevents curving of the wall due to the temperature difference between the sides.

2 BACKGROUND THEORY

2.1 Transient and Steady-state temperature distributions

The situation being modelled involves a concrete wall at room temperature being exposed to a sudden increase in temperature on one side only. If the initial heating takes place rapidly and the elevated temperature is then maintained for a considerable period of time, there will two distinct stages: transient heat flow and steady-state heat flow.

In the transient stage, as the wall heats up, the concrete has a temperature distribution which is non-linear across the wall thickness. Ignoring any heat losses perpendicular to the main heat flow direction, the temperature distribution across a wall of width L can be described by equation (1) together with boundary equations (2) and (3):

$$\frac{\partial T}{\partial t} = \propto \frac{\partial^2 T}{\partial x^2} \tag{1}$$

$$\left(\frac{\partial T}{\partial x}\right)_{x=0} = \frac{h_h}{k}(T_{ah}-T_h) \tag{2}$$

$$\left(\frac{\partial T}{\partial x}\right)_{x=L} = \frac{h_c}{k}(T_{ac}-T_c) \tag{3}$$

where,

$T = T(x,t)$ is the temperature in ^{o}C at a distance x from the heated face at time t

α is the thermal diffusivity of the hardened concrete in m^2/s

h_h , h_c are combined convection and radiation coefficients from the hot and cool face of the concrete in W/m^2^{o}C.
k is the conductivity of the concrete in W/m^{o}C
T_{ah} is the ambient temperature adjacent to the hot face
T_{ac} is the ambient temperature adjacent to the cool face
T_h is the surface temperature of the hot face
T_c is the surface temperature of the cool face

h_h and h_c may differ significantly as the hot face is gaining heat from outside while the cool face is losing heat. The convection and radiation conditions may also be different on the two faces if, for example, the hot face is inside a building and the cool face is outside. From equations (1) to (3), it can be seen that the temperature history can be calculated from the initial temperature if three parameters are known, namely α, $\frac{h_h}{k}$ and $\frac{h_c}{k}$. These are assumed to be constants under the conditions considered for this project. If the ambient temperatures remain relatively constant (after the initial rapid temperature elevation on one side) eventually $\frac{\partial^2 T}{\partial x^2}$ and $\frac{\partial T}{\partial t}$ both reach a value of zero resulting in a linear temperature distribution that does not vary with time. This is the steady-state condition.

2.2 Restraint Conditions

If the source of restraint is external to the member it is called *external restraint*. If the restraint arises internally from one part of the member restraining another part then we call it *internal restraint*. Some thermal stresses arise due to internal restraint, other stresses are caused by external restraint.

To illustrate this, three different types of restraint are illustrated in Figure 1. In each case a beam is subjected to an elevated temperature on one side only. The beams are insulated on all sides except the side opposite the heat source (the heat source itself also being surrounded by insulation) so the heat flow is approximately 1-dimensional from the heated face to the opposite cool face. The deformed shape due to thermal expansion is shown dotted for Beams 2 and 3 (there is no deformation in Beam 1). These deformations are exaggerated in the diagrams.

Beam 1 is fixed at both ends preventing both axial and curvature deformation. This effectively restrains all of the thermal strain as the wall is unable to expand. The whole beam goes into compression in both the transient and steady-state conditions. There will be no thermal cracking.

Beam 2 is simply-supported and there is effectively no external restraint. The beam is completely free to expand and change shape (this situation will not arise in a wall as there will always be restraint at the foundation level). During the transient stage, the increase in temperature will cause linear expansion as shown. Also, since the side being heated will try to expand more than the cool side, the beam will also bend into a curve as illustrated in the diagram. This type of situation has been analysed in detail in the context of simply-supported bridge beams subjected to solar heating [2, 3]. It has been found that stresses can arise, due to internal restraint, during the transient heating stage which can, in some cases, cause thermal cracking.

Beam 3 beam is free to expand axially but there are moment restraints at the ends which prevent the beam from curving. This is equivalent to Beam 2 with a uniform sagging moment added to prevent the curvature of the beam. This situation can cause significant tensile stress at the bottom surface of the beam and so could result in thermal cracking. This is the situation that is examined in this paper.

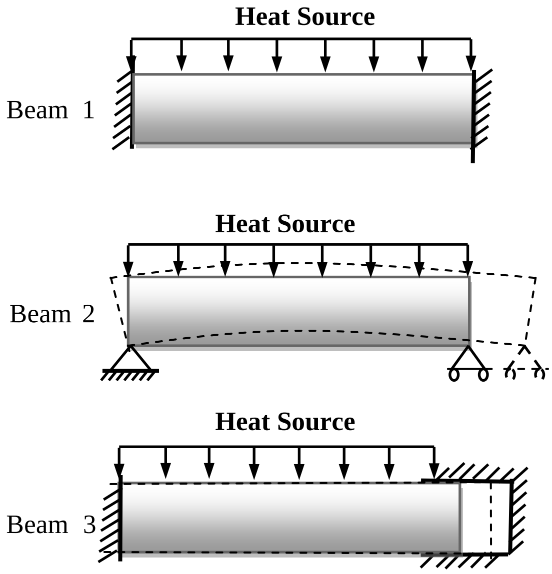

Figure 1. Three Restraint Conditions.

2.3 Thermal stresses

When a concrete member is prevented from expanding or contracting freely as it heats up or cools down, there is restraint present. The type of restraint has a big influence on the thermal stresses induced in concrete members by external heating. Different restraint conditions will cause different thermal stresses. For the 1-dimensional case the 'free strain', which is the strain that would occur if there was no restraint, can be calculated from:

$$\varepsilon_F = \alpha(\Delta T) \tag{4}$$

where;

ε_F = Free Strain
ΔT =temperature increase at the point
α = co-efficient of thermal expansion of the concrete

The restrained strain can be calculated from:

$$\varepsilon_R = (\varepsilon_A - \varepsilon_F) \tag{5}$$

where;

ε_A = Actual Strain (e.g. from a strain gauge reading)
ε_R = Restrained Strain

Finally, the thermal stress induced in the concrete is given by:

$$\sigma_T = E\,(\varepsilon_R) \tag{6}$$

where;

σ_T = thermally induced stress in the concrete
E = Modulus of Elasticity of the concrete

It can be seen that the stress induced depends on the restrained strain rather than on the actual strain. For example, in the fully restrained case, the actual (measured) strain is zero but a large compressive stress arises in the concrete.

3 THEORETICAL MODEL

There are many "off-the shelf" finite difference and finite element programs available for modelling 1-dimensional heat flow through walls. However, in this study, a model was needed that allowed for various temperature loading situations (i.e. various ambient temperature/time profiles on the hot and cool side), various restraint conditions and various thermal properties to be tried out and quickly analysed. It was concluded that an EXCEL based model developed specifically for this purpose would be much more flexible and convenient. Accordingly, a theoretical model was developed to predict the temperature and thermal stress profiles induced in concrete elements. The model consists of two main components – a transient temperature prediction model and a stress calculation module.
The procedure is summarised below:

(i) A set of n equally spaced nodes along a line, perpendicular to the wall surface is defined by the set $\{x_i, i=1,n\}$ with x_1 denoting the heated surface and x_n denoting the cool surface. The size of n may be varied as required

(ii) If the set $\{T_i, i=1,n\}$ denotes the temperatures at nodes $\{x_i, i=1,n\}$ at a particular time t then the second derivative of the temperature profile is approximated using the following finite difference approximation:

$$\frac{\partial^2 T}{\partial x^2} \approx \frac{T_{i+1}-2T_i+T_{i-1}}{\delta x^2} \quad (7)$$

where δx is the nodal spacing.

(iii) The temperature/time gradient at an internal node can approximated by:

$$\frac{\partial T}{\partial t} \approx \frac{\Delta T_i}{\delta t} \quad (8)$$

where ΔT_i is the temperature increase at node *i* over a short increment of time δt

Substituting these approximations into the equations in Section 2.1 results in the following equation for the temperature increase at an internal node *i* over time interval δt:

$$\Delta T_i \approx \delta t \propto \left[\frac{T_{i+1}-2T_i+T_{i-1}}{\delta x^2}\right] \quad (9)$$

(iv) Finite difference approximations are also used to find the temperature increase at the surface nodes that satisfy the boundary equations at the hot and cool faces. This was achieved by introducing "dummy nodes" x_0 and x_{n+1} and calculating temperatures for these nodes that ensured that the boundary conditions were satisfied at each stage

(v) The "locked in" increment of compressive stress for each node $\Delta\sigma'_i$ is then calculated from:

$$\Delta\sigma'_i = E\varepsilon_f = E\alpha(\Delta T_i) \quad (10)$$

(vi) for the Beam 3 restraint condition, the average compressive stress is calculated and subtracted from the $\Delta\sigma'_i$ values to give the final thermal stress increment $\Delta\sigma_i$ for each node. This adjustment allows for the free axial expansion assumed for Beam 3 as described in Section 2.2

(vii) When all of the temperature and stress increases have been calculated for each node the temperature and stress at each node at the end of the time step is calculated by adding the calculated changes to the values at the beginning of the time step:

(viii) The above procedure is repeated for each time step

4 CASE STUDY

The case study considered in this paper was a mushroom compost plant comprising ten large reinforced concrete bunkers [4]. Each bunker was 8.5m wide by 40 metres long on plan and was 9m high. All bunkers shared a 300mm thick back wall (approximately 85 metres long) and were separated from each other by nine 40m long, 0.3m thick internal walls. Each of these walls ended in a 0.5m x 0.5m open pier. Figure 2 illustrates a plan view of one of these walls.

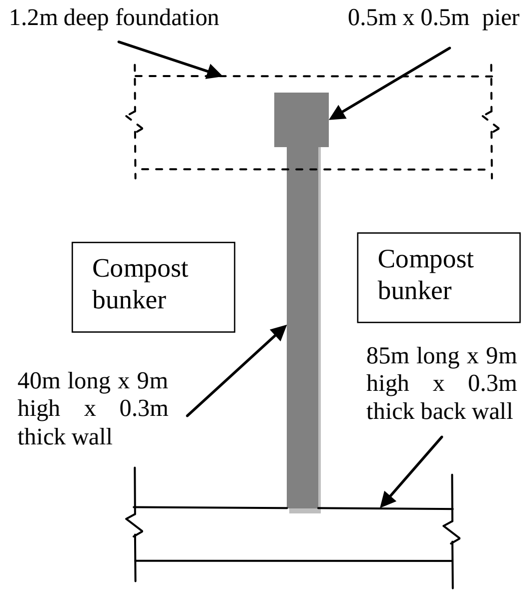

Figure 2. Plan view of internal wall of silo (not to scale).

Mushroom compost generates heat internally reaching temperatures of up to 80°C. In normal use, a situation would often arise where there was compost in one bunker but not in the adjacent one. This would cause a temperature load to be experienced by one side only of the relevant internal wall. This was the situation examined in this paper.

The effects of thermal expansion were taken into consideration in the design of the bunkers by pouring a 1.2m deep foundation at the front of the building over its full length (shown dotted in Figure 2). This acted as an anchor into which the walls were tied. The rest of the building and foundations were poured as a raft with friction between the raft and the ground being reduced to a minimum by methods such as pouring them onto polythene sheets. Despite these precautions, extensive cracking of the internal walls was observed. One aim of this project was to investigate whether the cracks in these walls were thermally induced and whether the measures taken to prevent cracking were appropriate.

It was first noted that the construction method used could have created restraint conditions in the internal walls similar to Beam 3 described in section 2.2 as firstly it was designed to allow free axial expansion and secondly it seems likely that the internal wall was restrained from curving along its 40m length due to the restraint provided by the pier, the end wall, the foundation of the wall itself and possibly the roof. As noted in section 2.2, this restraint condition results in the most severe tensile thermal stresses of the three restraint conditions and may not have been appropriate in this case.

An experimental test was carried out to mimic the temperature and restraint conditions experienced in the internal walls of the compost bunker. Measured results from this test were then compared with theoretical predictions.

5 EXPERIMENTAL STUDY

An experimental test was undertaken as a final year student project [4] . A 2.4m x 0.5m x 0.3 concrete test piece was made up (see Figure 3) that was designed to mimic a portion of one of the 0.3m thick internal walls of the bunker having a similar concrete strength (30 N/mm^2) and reinforcement arrangement (H12 @ 150mm cc in both directions) to the real wall. The temperature and restraint conditions of the test specimen were designed to mimic the real bunker wall. Figure 3 also shows a timber wand attached to the end of the test piece. This was used to monitor end rotations by placing a displacement dial gauge at each end of the wand.

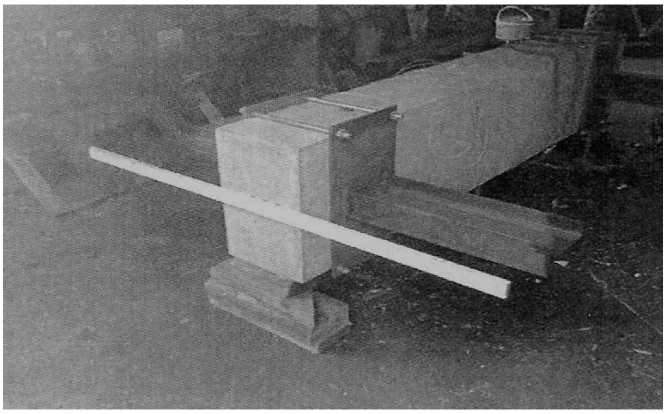

Figure 3. Concrete test piece.

To achieve the required restraint conditions the test piece was encased in a metal frame which was designed to provide a time-varying bending moment just large enough to counteract any curvature caused by temperature. The method was similar to that used by Elbadry and Elzaroug in a previous study [5]. A metal clamp with two cantilever beams was attached to each end of the specimen. One of these can be seen in Figure 3. A compression boom was then formed between the ends of the two cantilevers on one side while a tension boom was formed between the ends of the two cantilevers on the other side. Both booms can be seen on plan in Figure 4 which shows half of the test piece only.

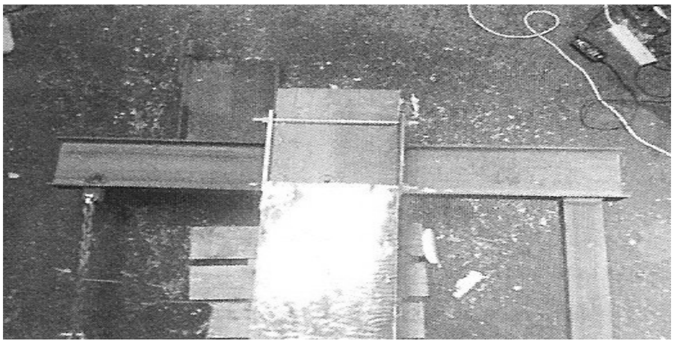

Figure 4. Plan view showing half of specimen and frame.

The compression boom consisted of two beam sections with end plates. A load cell was then fitted between the endplates Figure 5 illustrates this (load cell is not in place in this photo).

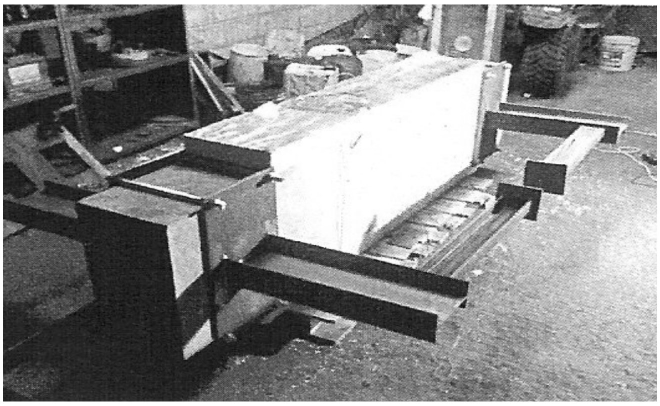

Figure 5. Test piece and compression boom.

The tension boom consisted of a chain with a turnbuckle which could be twisted to produce the required tension. The chain can be seen in Figure 4. To achieve the required temperature load one 2.4m x 0.5m side of the specimen was heated by enclosing it in an insulated, silvered light-box containing three sodium lamps which is illustrated in Fig. 6. The lightbox was built from 18mm plywood with 50mm polystyrene insulation. This was used to create an ambient temperature of up to 142oC on the heated side. The opposite side was left exposed to ambient air temperature. All other sides of the test piece were insulated so that heat flow was approximately one-dimensional through the 300mm thickness of the wall.

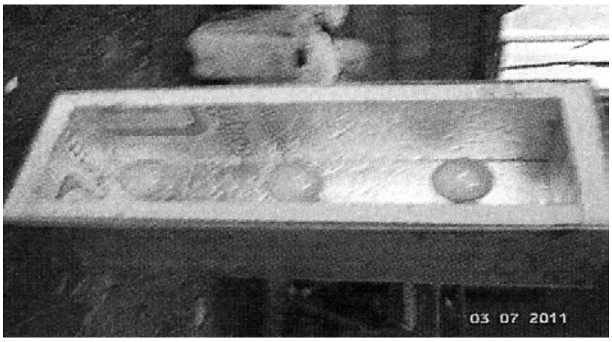

Figure 6. Lightbox with three sodium lamps.

A line of temperature gauges was embedded in the concrete test piece from the centre of one 2.4m x 0.5m face to the centre of the opposite face. The gauges were placed at 75mm intervals with the first being placed just below the surface on the hot face and the last being just below the surface on the cool face giving five gauges in all. Two additional temperature gauges were used to measure the ambient temperatures inside the light-box and adjacent to the cool face. Temperatures were measured at five minute intervals. The test piece was made from rapid-hardening concrete and was left to set for 30 days so that hydration would have reduced to very low levels.

The temperature gauges were connected to a data logger and temperatures automatically measured at 5 minute intervals throughout the test.

At the start of the test, the sodium lamps were switched on leading to a rapid increase of temperature on the heated face. As the concrete heated up, any curvature detected by the displacement gauges was removed by increasing the loads in the compression and tension booms. These loads and the times at which they were changed were recorded. The appearance of any visible cracks was also noted.

6 MEASURED RESULTS AND THEORETICAL PREDICTIONS

Figure 7 shows recorded temperature/time plots for the light-box and for ambient temperature adjacent to the cool face. As the graph shows, the temperature in the lightbox increased rapidly to over 90^{o}C after one hour and then increased more gradually peaking at 142^{o}C after fifteen hours. The ambient temperature was relatively constant, fluctuating between 17.5 and 19.5^{o}C.

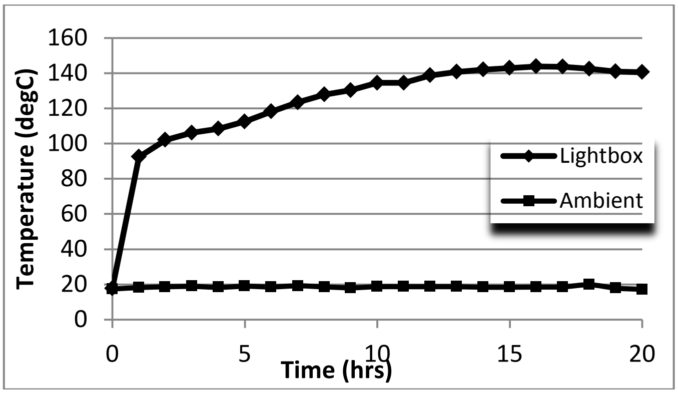

Figure 7. Lightbox and Ambient temperature plots.

The theoretical model described earlier was applied to the test sample and calculated temperatures were compared to measures values. Figure 8 shows measured and predicted temperature/time profiles for the hot face, the centre of the wall and the cool face respectively.

The results showed that the theoretical predictions were in good agreement with measured values for the temperatures at each node up to about 18 hours. Between 18 and 20 hours the experimental temperatures showed an unexpected drop while the predicted theoretical temperatures continued to increase. These predictions were made using an assumed thermal diffusivity (α) value for the concrete (which was made with limestone aggregate) of 8 x 10^{-6} m^2/s and experimentally determined values for $\frac{h_h}{k}$ and $\frac{h_c}{k}$ which were estimated from the steady state temperature profile in the specimen. It should be noted however that the accuracy of the predicted temperatures is quite sensitive to the values of the three thermal properties so these need to be measured experimentally, as accurately as possible, to ensure a good predictive model.

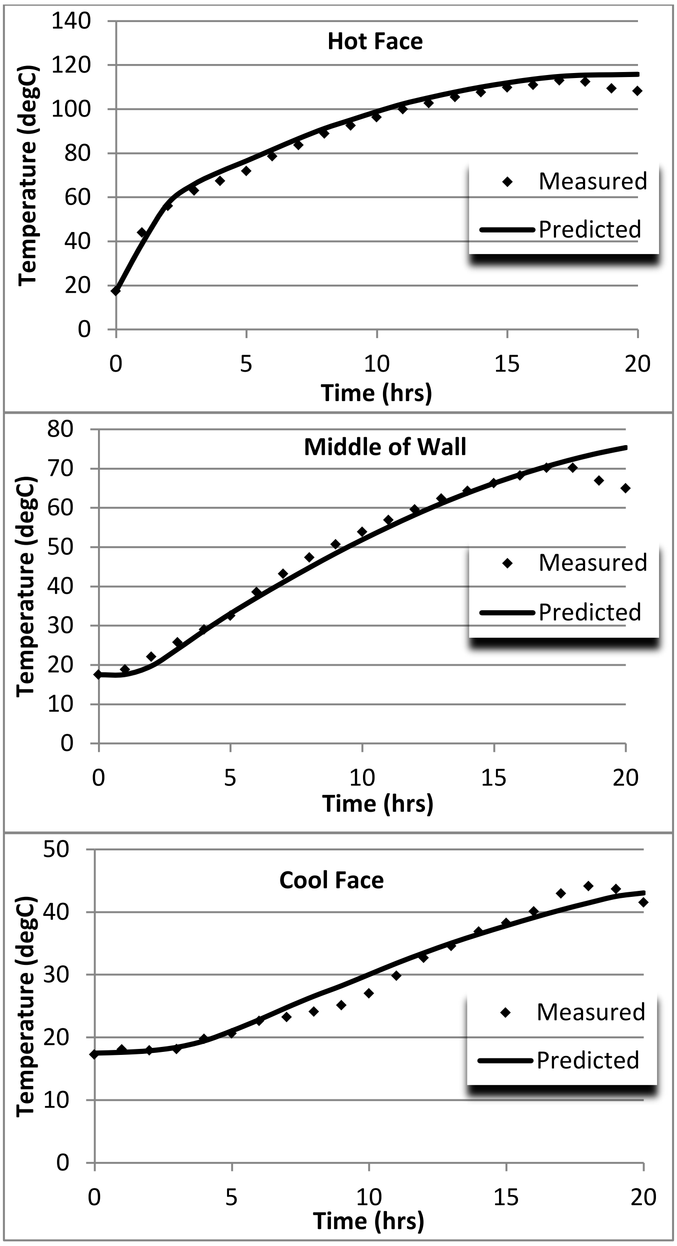

Figure 8. Measured and predicted temperature/time plots.

The temperature profiles across the wall, from hot face to cool face, after two hours and eighteen hours, are illustrated in Figure 9. It is clear that the profile is highly non-linear at the earlier time but is close to linear (steady-state) at the later time. Again, there is a reasonably good match between predicted and measured temperatures.

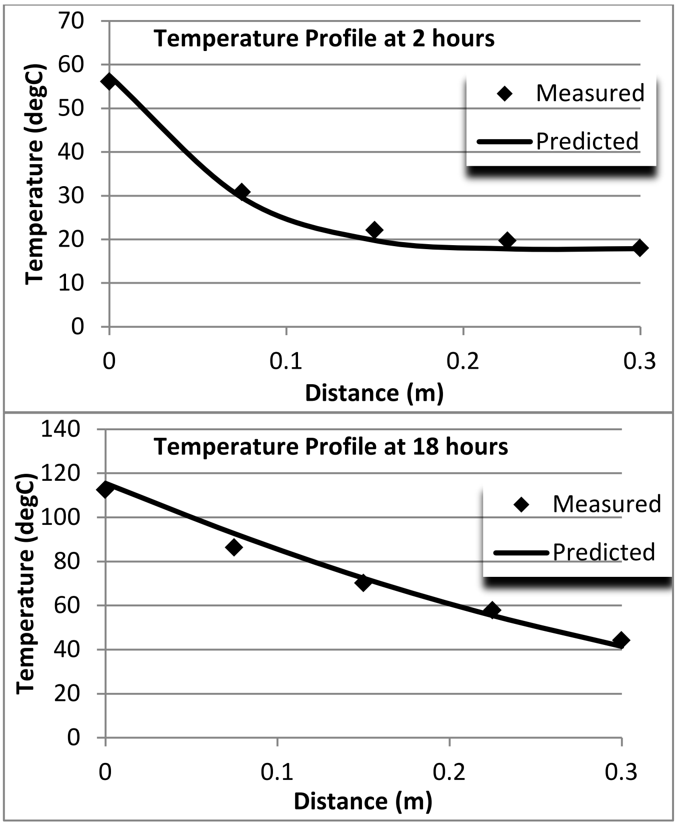

Figure 9. Measured and predicted temperatures across wall.

The thermal stresses were then calculated, (for an uncracked section) using the method described in section 2.4. Figure 10 illustrates the predicted stress profile after 2 hours (tensile stresses are negative). At this stage the temperature profile was highly non-linear.

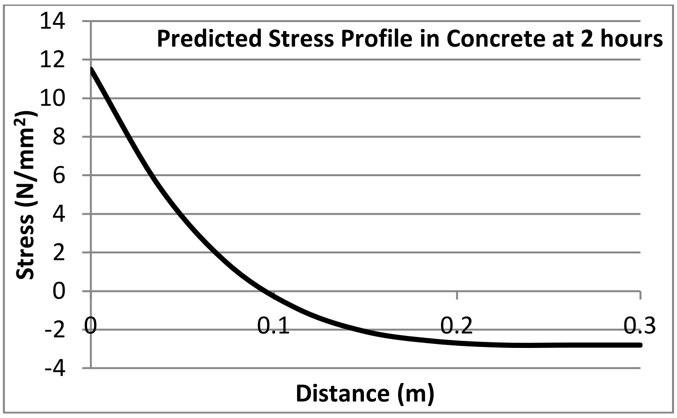

Figure 10. Predicted stress profile after 2 hours.

The predicted stresses vary from 11.5 N/mm2 compression on the heated side to 2.8 N/mm2 tension on the cool side. The theoretical model predicted that the thermal tensile stress on the cool face would exceed the tensile strength of the concrete (assumed to be one tenth of the compressive strength or 3N/mm2 in this case) after just over 2 hours. Thus, it was predicted that the transition from un-cracked to cracked section began at this time.

The experimental results were consistent with the predicted behaviour as the moment that had to be applied (using the tension and compression booms) to prevent curvature of the specimen increased steeply in the first 2 to 3 hours and then levelled off, indicating the transition from un-cracked to cracked behaviour. In the experiment, the first visible, substantial crack was not detected until much later, after approximately eight hours with further visible cracks after approximately nine and ten hours. The theoretical model cannot currently be used to predict if or when cracks wider than the allowable crack width first appear but it is planned to develop it further to make this possible.

7 CONCLUSIONS

A theoretical model is described for predicting temperature and thermal stress profiles in concrete walls subjected to external heating on one side under various restraint conditions. The model was tested against experimental data and was found to make reasonably accurate predictions of temperature profiles.

In an experimental test, it was found that the highly non-linear temperature profiles that resulted from rapid heating caused the tensile strength of the concrete to be exceeded after approximately two hours. However, substantial, visible cracks did not appear until about eight hours into the test.

The theoretical model was used to predict the time at which the concrete first begins to crack and this prediction was consistent with the experimental measurements. The theoretical model is not sufficiently developed at present to predict if or when cracks wider than the allowable crack width will appear.

REFERENCES

[1] O'Donnell, J.J, O'Brien, E.J. (2003), 'A new methodology for determining thermal properties and modelling temperature development in hydrating concrete', *Construction and Building Materials*, Elsevier, 17(3): 189-202.

[2] Church, J,G, Clark, L.A. (1987), The effect of combined thermal and force loads on the behaviour of reinforced concrete beams', *The Structural Engineer*, *volume 66, No. 16, August*, 262-267

[3] Richardson, M, Selby, A.R. (1988), Measured diurnal thermal strains in reinforced concrete beams', *The Structural Engineer, volume 65B, No. 1, March* 11-15

[4] Speares, A (2011), The effects of a Temperature Load on a Reinforced Concrete Wall, *Final Year Thesis*, Department of Civil/Structural Engineering, DIT Bolton Street, Ireland.

[5] Elbadry, M, Elzaroug O (2004), Control of Cracking due to Temperature in Structural concrete reinforced with CFRP bars, *Composite Structures*, Elsevier, Volume 64, Issue 1, p. 37-45.

Incorporation of life cycle models in determining optimal wind energy infrastructural provision

B.Cleary [1], A.Duffy[1], A.O'Connor[2]
[1] School of Civil and Building Services Engineering, Dublin Institute of Technology, Dublin, Ireland
[2] Department of Civil, Structural and Environmental Engineering, Trinity College, Dublin, Ireland
email: brendan.cleary1@mydit.ie, aidan.duffy@dit.ie, alan.oconnor@tcd.ie

ABSTRACT: The deployment of wind energy has grown rapidly over the last two decades with an average annual growth rate of more than 26% since 1990. During this period the development and innovation of wind turbines has resulted in continual growth in wind turbine size with output ranges of 10-15MW likely to be deployed by 2020. This increased output has a knock-on effect on the growth of rotor diameters and tower heights. Wind turbine towers are required to become taller, stronger and stiffer in order to carry the increased weight and associated structural loading. Consequently, the dimensions of the tower cross-sections must be increased which results in manufacturing and transportation difficulties as well as increased material costs. Thus, this paper focuses on the development of wind energy technology over the last two decades and the optimisation techniques cited in current literature. From this, a multi-objective optimisation problem is defined as maximising the structural performance of wind turbine towers while simultaneously reducing the life cycle costs and emissions associated with electricity generation from wind. A multi-objective optimisation model based on a harmony search algorithm is presented. This model is proposed to be developed further in order to determine a set of optimal combinations known as Pareto optimal solutions, which will allow a trade-off between the life cycle costs and emissions. Findings from the continuing research are envisaged to support the deployment of large scale wind turbines both onshore and offshore from structurally more promising, economically more competitive and environmentally greener towers.

KEY WORDS: Optimisation; Life cycle cost; Life cycle assessment; Wind turbine towers; Steel; Concrete; Wind turbines.

1 INTRODUCTION

Wind energy has gained popularity worldwide as countries strive to increase the production of renewable energy technologies in order to mitigate global warming and meet future energy demand. Over the last decade the utilisation of wind energy worldwide has grown rapidly with an average annual growth rate of about 30% [1].

This is driven by the implementation of legislation such as the European Commission's Renewables Directive 2009/28/EC and Strategic Energy Technology Plan (SET-Plan) which support the development of cost effective low carbon energy technologies such as wind energy [2–4]. This framework is required to help meet the 2020 targets to reduce greenhouse gas (GHG) emissions by 20% and ensure that 20% of Europe's energy comes from renewable energy sources [3].

To achieve these targets the European Wind Initiative's main objective is to maintain technology leadership in both onshore and offshore wind energy by making onshore and offshore wind the most competitive energy sources by 2020 and 2030 respectively [4]. This has led to research activities into the development of the technology used in wind turbines and their manufacture both for onshore and offshore applications with the aim of reducing the cost of wind energy. As a result, a large prototype offshore wind turbine with 10-20MW output range will be developed and demonstrated [4].

Furthermore, the development and innovation of wind turbines over the last two decades has resulted in continual growth in size with output ranges of 10-15MW likely to be deployed by 2020. This increased output has a knock-on effect on the growth of tower heights and rotor diameters requiring wind turbine towers to become taller, stronger and stiffer to carry the increased weight and associated structural loading.

The predominant designs for worldwide wind turbine towers are tubular steel tower solutions primarily due to the mastering of their design and ease of installation [5]. However, with increasing steel prices, manufacturing, transportation and vibrational issues, concrete towers are becoming a viable, if not optimal solution for taller towers [5–8].

Furthermore, research into reducing the cost and improving the design of these towers has been limited and with the ever increasing size of the next generation wind turbines the need to optimise the wind turbine tower structure is vital to reduce the cost of wind energy [9].

This paper focuses on the development of wind energy technology over the last two decades and the optimisation techniques cited in past publications. From this, the proposed optimisation methodology for the continuing research into the optimisation of wind energy infrastructures is defined and discussed.

2 BACKGROUND AND SIGNIFICANCE

2.1 *Industrial background*

There is a large amount of research papers and reports highlighting wind energy as the world's fastest growing energy source [1], [2], [4], [9–12]. The annual European installed wind energy capacity has increased steadily over the last 17 years from 814MW in 1995 to 9,616MW in 2011 with an average annual growth rate of 15.6% [13]. During this period the trend was to have large scale and more powerful wind turbines in order to capture more energy and to bring down the cost of wind energy generation. This resulted in the sizes of the turbines, including blade length, tower height and generation capacity becoming larger and larger [1].

Moreover, rotor diameters have increased eight fold and the average capacity of wind turbines installed around the world during 2007 was 1.5MW whereas now Enercon operates the world's largest onshore wind turbine rated at 7.5MW at a hub height of 135m [6]. Currently, Clipper is planning to manufacture a 7.5MW turbine with both Clipper and Sway developing 10MW prototypes for offshore deployment [1].

Due to the tendency towards larger wind turbines on taller towers a number of difficulties has arisen in relation to the predominately used tubular steel tower designs. As a result, manufacturing and transportation difficulties arise as the dimensions of the tower cross sections must be increased to accommodate the increased weight [5], [6], [8].

For example the lower sections of steel towers 90m or greater can no longer be transported by road due to the European road width and bridge clearance limits [6]. Additionally, shaping of the steel sheets for the steel towers require special machines for diameters greater than 4.5m which are not always available in steel fabrication workshops [5]. In Ireland, for example, no indigenous steel industry exists; therefore steel towers are designed, fabricated and imported from abroad; which adds to transport costs and transport related GHG emissions.

Moreover, it has been established that as towers go beyond 85m problems arise with the current tubular steel tower designs due to the vibrations induced by the wind turbine [14]. This has led to alternative proposals such as the use of precast or in-situ prestressed and reinforced concrete and/or hybrid materials [8], [14], [15]. Also extensive research is being carried into the development of glass fiber reinforced polymers for tower solutions [16].

According to Tricklebank et al. [8] the use of concrete in the wind energy sector has been 'predominantly in foundation applications either to form gravity foundations or pile caps'. Nevertheless concrete tower solutions are being used onshore by at least three wind turbine manufacturers Enercon, GE Wind and Nordex. Yet no manufacturers have exploited their use offshore.

Recently Enercon completed the Castledockrell windfarm in the southeast of Ireland which consists of eighteen 2.3MW turbines on 84m precast concrete towers; this was the first time this type of tower had been used in Ireland [17]. More recently Enercon installed Europe's highest elevation wind turbine on a 83m precast concrete tower in the Swiss canton of Valais 2,465m above sea level [18]. This tower solution was chosen due to the extreme conditions and the technological and logistical challenges at this location.

Nordex have solved the logistical and resonance frequency problem of towers with a hub height of over 100m by developing a special concrete/steel hybrid tower [8], [19]. Up until 2006, they only used steel towers but have recognised that concrete offers a relatively inexpensive alternative. The tower solution involves the use of locally supplied materials and ensures an optimal tower height to make the most of the prevailing conditions [19].

This underlines concrete's adaptability in terms of manufacture and transport compared to steel as well as the ability to alter the tower design for particular scenarios. This influences the challenge to optimise tower designs which are subject to aggressive environments and vibrational behaviour. Additionally, these structures must be cost effective and possess minimal construction and maintenance GHG emissions over their design life.

Although some research has been conducted into the optimisation of wind turbine towers limited research has focused on their structural performance, cost and environmental impact [15], [20–22]. Consequently, this gives rise to the need to identify an optimal tower solution based upon the trend of increasing wind turbine sizes and hub heights in order to reduce the cost of wind energy.

2.2 Research significance and objective

The wind turbine tower structure is the most material consuming part of the wind turbine system (rotor, nacelle and tower) accounting for 26% of the material cost of the system [9]. However, the drive to improve its design or reduce its material consumption and cost has been limited. Thus, this presents an opportunity to investigate the application of new materials for the tower structure.

This requires a thorough investigation into the material selection process for the tower where the material will need to withstand the wind turbines structural demands while minimising cost and environmental impact.

Hence, the purpose of this research is to identify an optimal solution for the tower design with the objective of maximising the structural performance while simultaneously reducing the cost of wind energy and its associated environmental impact.

3 AN OVERVIEW OF OPTIMISATION

In mathematics, optimisation refers to the process of choosing the best alternative from some set of available alternatives [23]. This means solving problems in which one seeks one or more feasible solutions to minimise or maximise one or more objective functions by systematically choosing the solutions from within an allowed set [23].

Typically, optimisation is used to minimise cost and/or maximise performance levels subject to engineering or regulatory constraints. Over the past few decades, designers have spent considerable effort to integrate design techniques from different disciplines. This integration is motivated by the idea that better designs can be achieved through concurrent engineering and the commercial imperatives of reducing both design time and cost [7], [23].

According to Baños et al. [24] 'computational optimisation can be defined as the process of designing, implementing and testing algorithms for solving a large variety of optimisation problems'. This method of optimisation includes the disciplines of mathematics to formulate the model, computer science for algorithmic design and analysis, and software engineering to implement the model [24].

Although computational optimisation methods have focused on solving single objective problems there exists multi-objective algorithms for the simultaneous optimisation of several objectives [24]. As a result, large numbers of optimisation techniques for handling multi-objective optimisation problems are cited in over 5,600 publications up to January 2011 [25].

The purpose of a multi-objective optimisation problem (MOP) is to find a vector of the design space that optimises a set of objectives and meets a set of constraints. The objective functions are the quantities that the designer wishes to maximise, minimise or match a certain value. The mathematical problem in standard form for minimisation is formulated as follows [26]:

$$\text{Minimise:}\quad \mathbf{f(x)} = \{f_1(\mathbf{x}), f_2(\mathbf{x}), ..., f_M(\mathbf{x})\} \tag{1}$$

$$\text{subject to:}\quad g_i(\mathbf{x}) \le 0, \qquad i = 1,..., L \tag{2}$$

$$h_j(\mathbf{x}) = 0, \qquad j = 1,..., K \tag{3}$$

$$x_l^l \le x_l \le x_l^u \qquad l = 1,..., N \tag{4}$$

where:

$\mathbf{x} = (x_1,\ldots,x_N)$ is the design vector with N variables;

f (x) is the objective vector with M objective functions; and

g and h are the inequality and equality constraints respectively on the design vector and the constraints (4) are called boundary constraints.

When M = 1, there is only one objective function to be minimised and the problem is referred to as single objective optimisation. In this case, classic optimisation methods or evolutionary methods such as genetic algorithm (GA) or simulated annealing (SA) can be used to solve the problem [26]. When M > 1, the problem is known as multi-objective optimisation. In this case, minimising several objectives at the same time may not be possible and the concept of a Pareto solution must be used [26].

According to Maginot [26] the general consensus of engineers and mathematicians working in the area of optimisation is that the Pareto optimal set may contain information that can help the designer to make a decision and thus arrive at better trade off solutions. When solving a MOP with conflicting objectives a unique solution generally does not exist; but a set of non-dominated solutions known as the Pareto solution exists. A feasible design point is said to be Pareto optimal if no other feasible design can improve some of the objectives without simultaneously being detrimental to others [26].

In order for the decision maker to quickly assess the trade-off between the two objectives a Pareto front needs to be plotted. [27]. The plot of the objective functions whose non-dominated vectors are in the Pareto optimal set is called the Pareto front. Figure 1 shows an example of a Pareto front for a MOP whose objectives are $CO_{2\text{-eq}}$ emissions and life cycle cost. These objectives are naturally conflicting where the cost of environmental friendly materials is usually higher than conventional materials. As a result, the need for a multi objective optimisation approach is required.

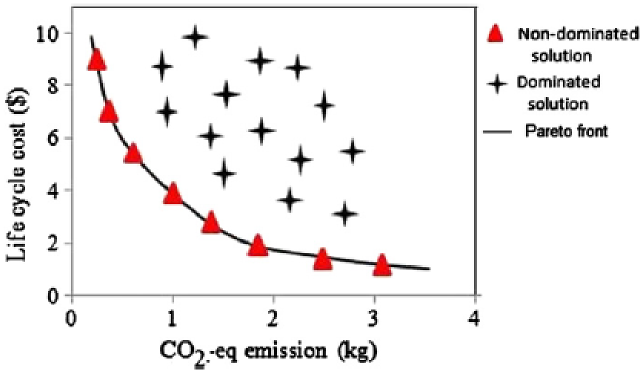

Figure 1. A sample Pareto front [27]

In literature, several algorithms have been suggested for the approximation of Pareto fronts [7], [24–26]. Among them are evolutionary multi-objective optimisation algorithms (EMOA) which have become increasingly popular and have attracted a considerable amount of research effort over the last 20 years [25]. They are considered to be robust with design flexibility as they can be applied for different representations and adapted to different computing environments [26].

A survey cited by Zhou et al. [25] indicates the research work on EMOA from different aspects. Some are based mainly on generic methodologies, theoretical developments and special methods for MOPs, for example SA, particle swarm optimization (HPSO) and harmony search (HS).

Traditional mathematical techniques such as linear programming (LP), non-linear programming (NLP) and dynamic programming (DP) have frequently been used for solving optimisation problems [28]. These techniques can guarantee global optima in simple and ideal models but for real world problems there are some weaknesses. In LP, considerable losses occur when a linear ideal model from a non-linear real world problem is developed, in NLP, if the functions used in computation are not differentiable, the solving algorithm may not find the optimum and in DP, an increase in the number of variables would exponentially increase the number of evaluations of the recursive functions and tax the core-memory [28].

In order to eliminate the above weakness of mathematical techniques, heuristic optimisation techniques based on simulation have been introduced. These allow a good solution to be found within reasonable computation time and with reasonable use of memory. These techniques include GA which uses reproduction, crossover and mutation operators to define fitness and to create new solutions. The main characteristic of GA which differs from SA is the simultaneous evaluation of many solutions. This feature can be advantageous enabling a wide search and potentially avoiding convergence to a non-global optimum [28].

Harmony search (HS) is a new meta-heuristic technique and is inspired by the natural musical performance process that occurs when a musician searches for a better state of harmony [28]. In a HS algorithm, the solution vector is analogous to the harmony in music and the local and global search schemes are analogous to the musician's improvisations. According to Pan et al. [29] the HS algorithm imposes fewer mathematical requirements and can be easily adapted for solving various kinds of engineering optimisation problems.

Numerical comparisons demonstrated that the evolution in the HS algorithm was faster than GA. The main difference between GA and HS is that HS makes a new vector from all the existing vectors (all harmonies in the harmony memory) while GA makes the new vector only from two of the existing vectors (the parents) [28]. Moreover, HS can independently consider each component variable in a vector while it generates a new vector whereas GA cannot because it has to keep the structure of a gene. As the GA is a global search algorithm which is based on the concepts from natural genetics [30].

Hence, the HS algorithm has captured much attention and has been applied to solve a wide range of practical optimisation problems, such as structural optimisation, cost reduction in power generation systems integrating large scale wind energy conversion systems, vehicle routing, combined heat and power economic dispatch, design of steel frames and transport energy modeling [29], [30].

From the optimisation methods considered and proposed in literature, a multi-objective optimisation approach with a HS algorithm currently presents itself as the most appropriate to the objective of the present work.

4 METHODOLOGY

4.1 *Problem definition*

The present problem involves maximising the structural performance of the wind turbine tower while simultaneously minimising the levelised cost of electricity production (LCOE) and the emissions intensity of electricity production (EIOE). Hence, the optimisation approach aims to minimise two objective functions, f_1 and f_2 represented by expressions (5) and (6) while satisfying the constraints of expression (7):

$$LCOE = f_1(x_1, x_2, ...x_n) \tag{4}$$

$$EIOE = f_2(x_1, x_2, ...x_n) \tag{5}$$

$$g_i(x_1, x_2, ...x_n) \leq 0 \tag{6}$$

The design variables $x_1, x_2, ...x_n$ and the parameters of the problem are all the data required to define a given wind farm whether onshore or offshore. The design variables are the magnitudes subject to optimisation, while the parameters are all the remaining data relating to the wind farm. The parameters of the tower are all the magnitudes taken as fixed data, including durability conditions, material density and design loads considered. The main design variables that will affect the LCOE and EIOE are the rotor diameter, wind turbine rating and hub height.

The constraints g_i are the tower limit states as well as the wind regime and wind turbine size. The tower limit state for each tower height will be defined as the minimum extreme displacement of the tower tip at the maximum mean hub height wind velocity [6].

4.2 *Objective functions*

The first objective LCOE is the ratio of the cost to produce the energy to the amount of energy that is produced and is given by:

$$\text{LCOE} = \text{NPC} \Big/ \sum_{i=1}^{n} \left(E_i (1+r)^{-i} \right) \tag{7}$$

where:
E_i is the electricity produced in year i (kWh);
r is the discount rate (%) ; and
n is the lifespan (years).
NPC is the life cycle net present cost of electricity generated given by:

$$\text{NPC} = \text{CC} + \sum_{\text{i}=1}^{\text{n}} \left[(\text{MC} + \text{OC})(1+r)^{-i} \right] + DC(1+r)^{-n} \tag{8}$$

where:
CC is the capital cost in year 0 (€);
MC is the maintenance cost in year i (€);
OC is the operating cost in year i (€);
DC is the decommissioning cost in year n (€); and
r is the discount rate (%).

The NPC covers the wind turbine costs including items such as transportation from factory to site, engineering services, grid connection, operation and maintenance (O&M) and decommissioning. Cost data for the various items associated with the wind energy facility are proposed to be obtained from industry sources and a meta-analysis of reported costs in publications.

The second objective seeks to minimise the EIOE due to the CO2-eq emissions that arise during the production and operation of the wind energy facility. The EIOE is given by:

$$\text{EIOE} = \text{LCE} \Big/ \sum_{i=1}^{n} (E_i) \tag{9}$$

where:
E_i is the electricity produced in year i (kWh); and
n is the lifespan (years).
LCE are the life cycle emissions of electricity generating given by:

$$\text{LCE} = \text{CE} + \sum_{\text{i}=1}^{\text{n}} \left[(\text{ME} + \text{OE}) \right] + DE \tag{10}$$

where:
CE are the capital related emissions in year 0 ($tCO_{2\text{-eq}}$);
ME are the maintenance emissions in year i ($tCO_{2\text{-eq}}$);
OE are the operational emissions in year i ($tCO_{2\text{-eq}}$); and
DE are the decommissioning emissions in year n ($tCO_{2\text{-eq}}$).

An emissions life cycle assessment (LCA) will be developed using a process based hybrid analysis which incorporates both process and input-output (I-O) analyses. By adopting the hybrid methodology the embodied $CO_{2\text{-eq}}$ for the wind farm can be obtained for each life cycle stage and in turn for the LCE.

4.3 *Proposed optimisation methodology*

A HS based optimisation process is proposed for searching for the wind turbine tower that has minimum LCOE and EIOE for a specific wind energy facility. This algorithm offers several advantages over traditional optimisation methods such as [31]; (a) it imposes fewer mathematical requirements and it does not require initial value setting of the decision variables, (b) it uses stochastic random searches, derivative information is unnecessary, (c) it generates a new vector after considering all of the existing vectors. The flow diagram of the optimisation model is illustrated in Figure 2.

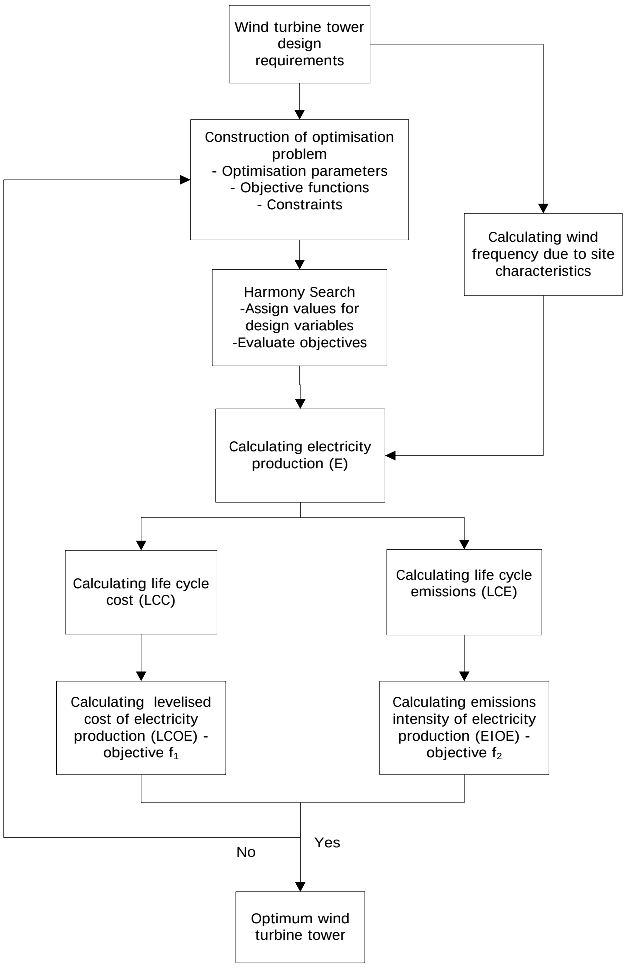

Figure 2. Flow diagram of the proposed optimisation model

The first step of the optimisation process is the determination of the fundamental design requirements and constraints such as the selection of the wind farm site, wind velocity, wind turbine rating and hub height. After the selection of the wind farm site, the wind frequency will be calculated using Weibull analysis.

After the design requirements are determined, the optimisation problem is constructed by selecting an appropriate objective function, optimisation parameters and constraints. The objective functions for this study are selected as LCOE and EIOE. The optimisation parameters are the wind turbine tower dimensions, namely height, wall thickness and diameter.

The optimisation process starts by assigning initial values of the design variables within the defined range of variables of the HS algorithm. Using the assigned design parameters, initially, the electricity produced (E) by each new design is calculated. Following the E calculation, the LCC and LCE are calculated for the wind turbine tower. Using E, LCC and LCE, the LCOE and EIOE are calculated using equations (8) and (10) respectively.

Next, based on the initial results, the HS algorithm sets new values for the design variables and another simulation is performed to evaluate the objectives of the new design. The new values of the design variables can be chosen either randomly or using the best obtained values which are already stored in the harmony memory (HM) of the algorithm. In case the new solution is better than the worst solution available in the HM, the worst solution is replaced by the new solution [27].

As the optimisation routine proceeds, step by step, the solutions stored in the HM become better and approach the optimum solution. The process is continued until a pre-specified maximum number of iterations are reached.

5 CONCLUSIONS

This paper set out to highlight the development of wind energy technology over the last two decades and its knock-on effect to wind turbine towers. An overview of the different optimisation techniques from past publications was conducted and from this a multi objective optimisation harmony search algorithm approach was deemed to be the most appropriate.

A description of the problem definition and objective functions was outlined where the optimisation process aims to find an optimal tower design that minimises life cycle costs and emissions. It remains for continuing research to study the effects of several wind turbine tower designs and to develop the optimisation model further using different optimisation techniques.

ACKNOWLEDGMENTS

The author would like to express his appreciation to Dublin Institute of Technology for funding this research through the Fiosraigh Dean of Graduate Research School Award 2011.

REFERENCES

[1] D. Y. C. Leung and Y. Yang, “Wind energy development and its environmental impact: A review,” *Renewable and Sustainable Energy Reviews*, vol. 16, no. 1, pp. 1031-1039, Nov. 2011.
[2] E. Martinez, F. Sanz, S. Pellegrini, E. Jimenez, and J. Blanco, “Life cycle assessment of a multi-megawatt wind turbine,” *Renewable Energy*, vol. 34, no. 3, pp. 667-673, Mar. 2009.
[3] European Parliament, *Directive 2009/28/EC of the European Parliament and of the council of the European Union on the promotion of the use of energy from renewable sources*. European Parliament, 2009, pp. 16-62.
[4] The European Wind Energy Association, “Wind power research and development for the next ten years,” EWEA, 2010.
[5] E. Hau, *Wind Turbines: Fundamentals, Technologies, Application, Economics*, 2nd ed. Berlin: Springer, 2006.
[6] A. Quilligan, A. O’Connor, and V. Pakrashi, “Fragility analysis of steel and concrete wind turbine towers,” *Engineering Structures*, vol. 36, pp. 270-282, Mar. 2012.
[7] P. Pardalos and D. Du, *Handbook of combinatorial optimisation: supplement volume B*. Springer, 2005.
[8] A. H. Tricklebank, B. J. Magee, and P. H. Halberstadt, “Concrete Towers for Onshore and Offshore Wind Farms,” The Concrete Centre, 2007.
[9] M. I. Blanco, “The economics of wind energy,” *Renewable and Sustainable Energy Reviews*, vol. 13, no. 6–7, pp. 1372-1382, Aug. 2009.
[10] R. Saidur, N. A. Rahim, M. R. Islam, and K. H. Solangi, “Environmental impact of wind energy,” *Renewable and Sustainable Energy Reviews*, vol. 15, no. 5, pp. 2423-2430, Jun. 2011.
[11] A. Mostafaeipour, “Productivity and development issues of global wind turbine industry,” *Renewable and Sustainable Energy Reviews*, vol. 14, no. 3, pp. 1048-1058, Apr. 2010.

[12] S. Krohan, P.-E. Morthorst, and S. Awerbuch, “The Economics of Wind Energy,” EWEA, 2009.
[13] The European Wind Energy Association, “Wind in power,” EWEA, 2012.
[14] J. A. Paredes, A. H. Barbat, and S. Oller, “A compression–tension concrete damage model, applied to a wind turbine reinforced concrete tower,” *Engineering Structures*, vol. 33, no. 12, pp. 3559-3569, Aug. 2011.
[15] R. Harte and G. Vanzijl, “Structural stability of concrete wind turbines and solar chimney towers exposed to dynamic wind action,” *Journal of Wind Engineering and Industrial Aerodynamics*, vol. 95, no. 9–11, pp. 1079-1096, Oct. 2007.
[16] D. J. Polyzois, I. G. Raftoyiannis, and N. Ungkurapinan, “Static and dynamic characteristics of multi-cell jointed GFRP wind turbine towers,” *Composite Structures*, vol. 90, no. 1, pp. 34-42, Sep. 2009.
[17] A. K. Gilberg and R. Brand, “First wind farm delivered by E-Ship 1,” *Windblatt*, p. 10, 2010.
[18] F. Rehwald, “E-70 at the Gries is Europe’s highest WEC,” *Windblatt*, pp. 14-15, 2011.
[19] N. SE, “Added yields in non-coastal regions Turbines installed on 120 meter high hybrid towers.” [Online]. Available: http://www.nordex-online.com/en/products-services/hybrid-towers.html. [Accessed: 09-Feb-2012].
[20] M. J. Clifton-Smith and D. H. Wood, “Optimisation of Self-Supporting Towers for Small Wind Turbines,” *Wind Engineering*, vol. 34, no. 5, pp. 561-578, Oct. 2010.
[21] H. M. Negm and K. Y. Maalawi, “Structural design optimization of wind turbine towers,” *Mechanical Engineering*, vol. 74, no. 6, pp. 649-666, 2000.
[22] P. Uys, J. Farkas, K. Jarmai, and F. Vantonder, “Optimisation of a steel tower for a wind turbine structure,” *Engineering Structures*, vol. 29, no. 7, pp. 1337-1342, Jul. 2007.
[23] P. Pardalos and M. Resende, *Handbook of applied optimisation*. Oxford University Press, 2002.
[24] R. Baños, F. Manzano-Agugliaro, F. G. Montoya, C. Gil, a. Alcayde, and J. Gómez, “Optimization methods applied to renewable and sustainable energy: A review,” *Renewable and Sustainable Energy Reviews*, vol. 15, no. 4, pp. 1753-1766, May 2011.
[25] A. Zhou, B.-Y. Qu, H. Li, S.-Z. Zhao, P. N. Suganthan, and Q. Zhang, “Multiobjective evolutionary algorithms: A survey of the state of the art,” *Swarm and Evolutionary Computation*, vol. 1, no. 1, pp. 32-49, Mar. 2011.
[26] J. Maginot, “Sensitivity Analysis for Multidisciplinary Design Optimisation,” Cranfield University, 2007.
[27] M. Fesanghary, S. Asadi, and Z. W. Geem, “Design of low-emission and energy-efficient residential buildings using a multi-objective optimization algorithm,” *Building and Environment*, vol. 49, pp. 245-250, Mar. 2012.
[28] Z. W. Geem, J. H. Kim, and G. V. Loganathan, “A New Heuristic Optimization Algorithm: Harmony Search,” *Simulation*, vol. 76, no. 2, pp. 60-68, Feb. 2001.
[29] Q.-K. Pan, P. N. Suganthan, M. F. Tasgetiren, and J. J. Liang, “A self-adaptive global best harmony search algorithm for continuous optimization problems,” *Applied Mathematics and Computation*, vol. 216, no. 3, pp. 830-848, Apr. 2010.
[30] K. Lee and Z. Geem, “A new meta-heuristic algorithm for continuous engineering optimization: harmony search theory and practice,” *Computer Methods in Applied Mechanics and Engineering*, vol. 194, no. 36–38, pp. 3902-3933, Sep. 2005.
[31] M. Mahdavi, M. Fesanghary, and E. Damangir, “An improved harmony search algorithm for solving optimization problems,” *Applied Mathematics and Computation*, vol. 188, no. 2, pp. 1567-1579, May 2007.

Influence of corrosion propagation of ggbs concretes on whole life cost of bridge structures in chloride environments

Sean Downey[1], Alan O'Connor[1]
[1]Department of Civil, Structural & Environmental Engineering, Trinity College Dublin, Ireland
email: downeysw@tcd.ie, alan.oconnor@tcd.ie

ABSTRACT: The current concrete design code (EN206-1:2000) provides for durable design in chloride-rich environments by specifying measures to inhibit chloride ingress and delay corrosion initiation. As such measures include the provision for using ground-granulated blastfurnace slag (GGBS) as a substitute for CEM II type cements, it is worthwhile to examine the behaviour of GGBS concretes in the corrosion propagation phase. This has been achieved by the authors in previous studies using accelerated corrosion testing in the laboratory and finite element modelling of the cracking process. The results obtained from this study have provided us with a set of constants which govern the linear cracking behaviour of GGBS concretes and allowed us to expand the scope of the work to predicting crack propagation behaviour and service GGBS concretes and to compare it to that of a standard CEM II concrete. The results of the study show that, while there is a small difference in the expected service life, the model is more sensitive to other input parameters.

KEY WORDS: Corrosion; Chlorides; GGBS.

1 INTRODUCTION

One of the primary functions of the cover concrete in a reinforced concrete (RC) section is the protection of the steel contained therein, particularly from aggressive agencies including chlorides. The most common sources of chlorides in structures are (i) de-icing salts, which are placed on road surfaces generally during winter and affect highway structures, and (ii) those present in marine environments [1-2]. Chlorides may enter the concrete through either a diffusion or permeation process [3]. These chlorides break down the alkaline environment and passive layer surrounding the reinforcing bars and can lead to corrosion of the steel in the presence of moisture and air [1]. This is known as the corrosion initiation phase, the first of a two-stage process described first by Tuutti [4]. During the corrosion process, a rust product, that has a larger volume than the steel it replaces, forms on the surface of the steel bar. This induces tensile stresses in the surrounding concrete, subsequently causing cracking and spalling of the cover concrete during the corrosion propagation phase. The concrete design standard EN 206-1:2000 [5] provides measures which can be taken to reduce or eliminate the risk of chloride-induced corrosion according to four exposure classes of increasing severity. These measures include, for example, increased depth of cover and increased cement content. One measure also allowed by the standard and shown in the literature [1] as inhibiting the initiation of corrosion, is the inclusion of ground-granulated blastfurnace slag (ggbs). However, experimental work by the authors [6] has shown that, when considering the corrosion propagation phase, the substitution of 50% of the cement with ggbs increases the rate of corrosion propagation over the life of the specimen, despite ggbs being shown to inhibit corrosion by a factor of 3 in an Irish study by Evans and Richardson [7]. The difference in crack propagation behaviour is illustrated in Figure 1, below.

Hence, it is proposed to study the effect on the deterioration of the structure of the inclusion of ggbs with a numerical model, to determine the effect on the initiation time and the time at which the corrosion crack width reaches a severity which requires a maintenance action; that is the service life of the structure before a repair is required.

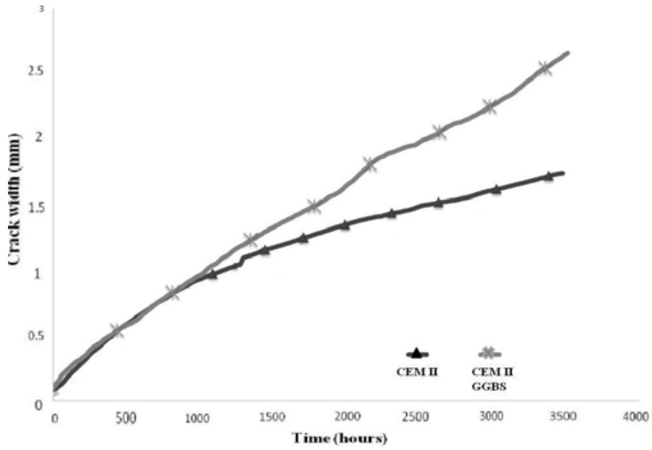

Figure 1 Crack propagation rates (from [6]).

2 BACKGROUND

As the service life prediction of a structure is of such importance, there are many studies which attempt to predict the rate and severity of corrosion damage. These studies can fall into one or more of the areas including accelerated corrosion experimental tests [8-10], finite element modelling [11], modelling of the corrosion rate [12], numerical modelling [8-9,13], modelling of the electrochemical process [14-15] and spatial variability modelling [16], with many approaches possible in each of these areas. However, the reality is that any such attempts at replicating corrosion conditions and parameters are constrained by the lack of real-time data from corroded structures and rely heavily on extrapolating data and parameters from short scale tests and models over the design life of a structure, which could be 120 years. Hence, validation of the models can be difficult. Otieno et al. [17] describes the problems associated with modelling cracking using any process other than empirical data, due the vast number of parameters which may influence the corrosion process: environment, availability of chlorides, moisture and oxygen, interference between adjacent reinforcement bars and confinement provided by the concrete, concrete type, microstructure and quality etc; simply that there are far too many factors to be considered for the model to be reliable and an accurate predictor of crack propagation behaviour.

For this reason, the most common and practical approach to model the corrosion process is to evaluate experimental data and relate it to real-world conditions – it may be possible to model accurately only isolated parts or particular scenarios in the corrosion process, but the applicability of such models to general corrosion theory or scenarios extrapolated far away from those studied is dubious and likely to lead to under or over estimation of the service life of the structure. Where such models may be useful, is undertaking comparative studies and determining the likely effect of altering one or more parameters - geometry, materials etc of the structure and it is in this realm that this paper will concentrate.

2.1 Review of the Vu et al. 2005 Model

The model proposed by Vu et al. [9] itself following the work of Andrade et al. [12] and Liu & Weyers [13] and verified by Mullard and Stewart [8] will form the basis of the comparison in this paper.

In Vu et al. 2005 [9], the critical Influence of *w/b* ratio and cover depth, *C* – described as "concrete quality" is quantified in terms of the possible corrosion rate up to and including the time of to corrosion-induced cracking. The model attempts to allow for the time-variant nature of the corrosion process. This model does not take account of concrete type (i.e. binder properties). This model also attempts to provide for objective crack propagation analysis irrespective of the accelerated corrosion rate on which the data is based – previous studies [12,18] have shown the crack propagation behaviour to be highly sensitive to the simulated corrosion rate, $i_{corr,exp}$, and thus call into question the applicability of accelerated corrosion data to real-world timescales. This is because, at extremely high corrosion rates, (for example, >>200mA/cm2 as discussed by El Maaddawy and Soudki [18]) the ability of the corrosion product to dissipate into the pore structure of the concrete is limited by the short time available for this process to take place and the resultant stress experienced by the concrete is excessively large, leading to abnormal deformation rates. Hence, the Vu model proposes a "rate of loading" correction factor to minimize the error in extrapolating accelerated corrosion data to real world structures. As the extrapolation is large (from a scale of days to many years) it is clear that small errors, inherent to the test procedure, in the accelerated corrosion data may be significant when extrapolated into real-world timescales.

2.2 Mullard & Stewart Model 2011

The Vu et al. model of 2005 was further verified in the experimental work of Mullard [8], in particular the effect of applying the loading rate correction factor, k_r, to the experimental results in order to extrapolate into real-time corrosion processes. Mullard's model also proposes a correction to take into account the confinement of the reinforcement and interaction between adjacent bars – as this data is not relevant to the experimental results obtained by the authors, it will not be considered in this paper.

2.3 Selection of a deterioration threshold

In order to provide a level of deterioration at which the materials can be objectively compared at, it is necessary to define a crack width threshold. This threshold is the point at which a repair or remedial action on the structure is deemed necessary by the asset manager, and with it, the time at which the cost of repair is incurred. The threshold may be either serviceability or ultimate limit state criteria. Most often, the structure will suffer unsightly cracks and severe staining before the safety of the structure is compromised, with a loss of only 10 – 20% of the steel section being noted in studies by Downey et al. [6], Stewart and Val [19] and Mullard and Stewart [20] when the structure had far exceeded the serviceability criteria, hence the serviceability limit state is considered to be most critical. As such, the maximum crack width threshold used in this study is 1.0mm, as proposed by Vu et al. [9]. Other studies by Stewart [19] have suggested that crack widths in the order of just 0.3 - 0.5mm can be seriously detrimental to the service life of a structure and so, crack width limits of 0.3mm and 0.5mm will also be considered in the model for the purpose of comparison. Few, if any, existing models consider corrosion damage beyond the 1.0mm limit, as by this stage, the nature of the cracking is so severe that random spalling and flaking occur and the structure is in imminent danger; the spalling effect has been observed in experimental work by the authors [6].

2.4 Input data and parameters

Once the appropriate modelling process has been selected, it is necessary to obtain the relevant input parameters for the model. As discussed in section 2.1, the outputs of the corrosion damage modelling process are highly sensitive to the inputs, due to the large extrapolation of the accelerated corrosion data that occurs. To this end, the input parameters must be selected carefully and are drawn from a number of sources, including previous accelerated corrosion test data from the authors, and other relevant parameters proposed by other modelling attempts in the literature. The most pertinent source of data and parameters is the model of Vu et al [9] this model is especially relevant to the authors own work as many of the geometrical and electrochemical properties of the previous accelerated corrosion tests [6] are similar to the accelerated corrosion tests performed by Vu et al; and hence a level of compatibility was achieved. In particular, this allows the use of real constants derived by Vu et al. [9] and verified by Mullard and Stewart [8] which describe the non-linearity of corrosion process and allow the translation of accelerated corrosion data into real-time data. These constants hold only for the exact geometry and concrete type studied – an alternative set of constants would need to be derived for alternative setups, this would require extensive accelerated corrosion data and is beyond the scope of this paper.

3 MODELLING PROCESS

As discussed previously in Section 2.1, the model of Vu et al. can be used to predict the corrosion behaviour of an RC structure, focussing on an RC slab with a reinforcing bar of 16mm diameter, 25mm cover and 0.5 water/binder ratio. Knowing the accelerated corrosion rate, $i_{corr,exp}$ and the corrosion propagation rate, Vu et al. determined the likely service life of the slab, predicting when the concrete cracks would cross the crack width threshold after which a repair must be performed. However, the model of Vu et al. does not take into account the binder type and any influence which this might have on the service life, despite the fact that substitutions for CEM II cements are often performed for the purpose of extending the service life of a structure in chloride-rich environments, as permitted by the design code EN 206-1:2000 [5].

3.1 Finite element modelling

As the Vu et al. model does not currently have a parameter which describes the role of the binder type in the crack propagation process, it is required to alter the equations to allow for this. For this reason, the finite element model of Thoft-Christensen [11,21] was considered – this model, which is based on the linear relationship between crack width, bar diameter and cover depth, does not itself take account of binder type, but the finite element modelling process is one which can be used as the basis for evaluating the influence of binder type when considered in conjunction with the experimental results. In effect, the "concrete quality" parameter, common to the Thoft-Christensen model and the Vu et al. model will be adjusted to also take into account the binder type, by a factor which brings the model into agreement with the experimental results – the experimental results for concrete with solely CEM II binder already shows good agreement with the Thoft-Christensen model.

The relationship between the crack width and the change in reinforcing bar diameter is well established, as demonstrated by Thoft-Christensen [11] and Andrade et al. [12], who proposed that the crack width, wcrack, is a linear function of the change in bar diameter, ΔDbar:

$$\Delta w_{crack} = \gamma \Delta d_{bar} \tag{1}$$

where the γ factor is a function of the diameter of the reinforcing bar and the depth of cover (i.e. the concrete quality defined by Vu et al.) and can be quantified by experimental or numerical means for any given system geometry. It is proposed that an alternate relationship,

$$\Delta w_{crack} = \tau \gamma \Delta d_{bar} \tag{2}$$

be considered where τ is a function of the binder type. This τ will account for a change in the linear relationship caused by the blending of cements and will be quantified by experimental practice and finite element modelling.

Thoft-Christensen has derived, by finite element analysis, a complete set of gamma factors for common cover depths and reinforcement bar sizes (with four-point interpolation possible across the range if necessary). The relevant gamma factor for the system considered in the experimental work (25mm cover, 16mm bar diameter) is 4.12.

In order for the model data to be compared over a progessive time period, the loss of steel area must correspond to the corrosion rate of the experimental work, 100 μA/cm^2, which in makes it possible to relate the loss of steel to a discrete time period, according to the ASTM G1-90 [22] formula:

$$i_{corr} = \frac{(K \times W)}{(0.0166)(A \times T \times \rho_s)} (\mu A / cm^2) \tag{3}$$

where K is a constant = 78,900 as defined by ASTM G1-90, W is mass loss in grams, A is area in cm^2, T is the time of exposure in hours, and ρ_s is the density of steel. Thus, each discrete change in D_{bar} can be related to both a time since corrosion initiation and, through the Thoft-Christensen model, a crack width. By rearranging the equation, it is possible to find the time required to cause a given reduction in the cross section of the bar.

Using this data, an ANSYS finite element model was prepared, which tracked the width of the surface crack for discrete displacements of the surface of the reinforcing bar and comparing the finite element model results with the experimental results, good agreement is found between the crack width – change in bar diameter plot for τ=1; γ=4.12, as shown in Figure 2:

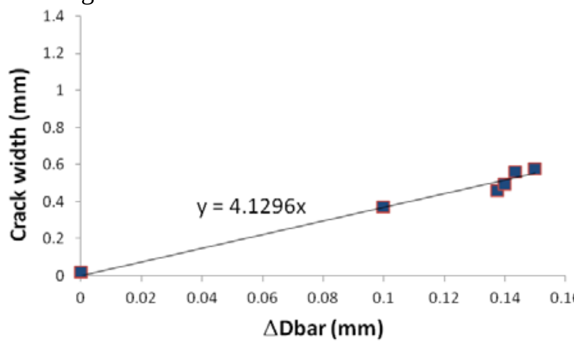

Figure 2 ANSYS model output for CEM II concrete.

The next step is to find a value for τ which correctly reflects the change in crack propagation slope to the 50% GGBS/50% cement. Using the ANSYS model in an iterative procedure, it is possible to quantify τ, the value which describes the difference in crack propagation due to binder type.

3.2 Application of Vu model

Using the data (τ parameter) obtained in the finite element analysis to account for the difference the addition of ggbs makes to the propagation behaviour of the concrete allows us to refine the Vu model to be thus:

$$t_{ser} = A((1/\tau) \times (C/wc))^B \tag{4}$$

where t_{ser} is the time since corrosion initiation in hours, C is cover depth, wc is the water/binder ratio and τ is the slag correction factor. A and B are constants of the system, related to the required crack width limit as described in Table 1:

Table 1. A and B constants (from [9]).

Limit crack width	A	B	Coefficient of correlation
W_{lim} = 0.3mm	65	0.45	0.89
W_{lim} = 0.5mm	225	0.29	0.60
W_{lim} = 1.0mm	700	0.23	0.45

3.3 Correction factor for rate of loading

As discussed in Section 2.1, if accelerated corrosion test data is being used to predict the corrosion performance of a real-world structure, the model must allow for a rate of loading correction to override discrepancies which may arise due to the rapid nature of the testing.

$$t_{cr(real)} = k_r \times \frac{i_{corr,exp}}{i_{corr,real}} t_{cr,exp} \qquad (5)$$

where $t_{cr,real}$ is the time to cracking in real RC structures, $t_{cr,exp}$ is the time to cracking in the experimental program, k_r is the rate of loading correction factor, $i_{corr,exp}$ is the corrosion rate in the experiment and $i_{corr,real}$ is the expected corrosion rate in real world conditions (nominally ~ 1µA/cm2)

As $i_{corr,exp}$ is less than 200mA/cm^2, the empirical Vu and Alonso equations for k_r can be followed, giving:

$$k_r = 0.95\left[exp\left(-\frac{0.3 i_{corr,exp}}{i_{corr,real}}\right) - \frac{i_{corr,exp}}{2500 i_{corr,real}} + 0.3\right] \qquad (6)$$

3.4 Expected service life

Finally, the expected service life of the structure with the given set of parameters can be obtained, with both time-variant and invariant corrosion rates.

The time-invariant corrosion process assumes that the i_{corr} value remains constant throughout the life of the structure – this is an over-simplification and unrealistic, given that the corrosion rate is dependent on environmental factors and the availability of chlorides, moisture and oxygen – all of which can vary as the crack propagates. The time to excessive cracking, *tsp*, can be evaluated as:

$$t_{sp} = t_{1st} + k_r \times 0.0114 i_{corr,real} \times A((1/\tau)(C/wc))^B \qquad (7)$$

with t_{1st}, the time of first cracking in the range of 30-50 years [9].

The variant corrosion rate, i_{corr}, can be modelled over a time *t* as:

$$i_{corr}(t_p) = i_{corr}(1) \times \alpha t^{\beta}{}_p \qquad (8)$$

where t_p is the time since corrosion initiation and is greater than 1 year. For a time-invariant rate, α = 1 and β = 0, but regression modelling by Vu and Stewart [9] has found, for time variant corrosion, for the system being studied that α = 0.85 and β = –0.3.

Rearranging and applying to the time-invariant service life gives the time-variant service life prediction:

$$Tsp = \left[\frac{\beta+1}{\alpha} \times \left(t_{sp} - 1 + \frac{\alpha}{\beta+1}\right)\right]^{\frac{1}{\beta+1}} \qquad (9)$$

4 RESULTS & DISCUSSION

For the purpose of illustrating the difference in service life, *Tsp*, between two different concretes, data from the experimental study will be applied to the modified Thoft-Christensen finite element model and subsequently, the modified Vu service life prediction model. The two concretes to be studied were prepared with (i) 100% CEM II cement and (ii) a blended cement of 50% CEM II & 50% ggbs. The experimental work to observe the crack propagation, described in Downey et al. [6] showed that for similar concrete specimens: f_{cu} = 42 MPa, *w/b* = 0.5, rebar diameter = 16mm, cover, *C* = 25 mm, $i_{corr,exp}$ = 100 µA/cm^2, the 100% CEM II concrete specimen exhibits a slower crack propagation rate than the 50 % ggbs concrete, as shown previously in Figure 1.When an ANSYS finite element model is prepared with these parameters, and the results matched to those of the experimental work, it is possible to evaluate γ in the equation:

$$\Delta w_{crack} = \tau\gamma\Delta d_{bar} \qquad (10)$$

The output of the ANSYS model is shown in Figure 3 and gives Δw_{crack} = 4.5223 ΔD_{bar}. Hence, as γ = 4.12, τ = 1.10.

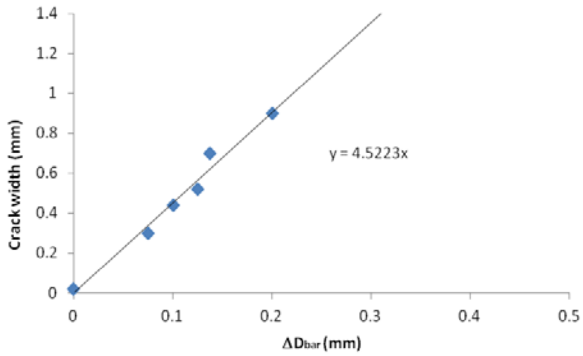

Figure 3 ANSYS model output for 50% CEM II /50% GGBS concrete.

The τ value and accelerated corrosion data is then applied to the Vu et al. model and extrapolated to give an expected service life comparison in years, for structures undergoing time variant corrosion, between the two concretes, which will be evaluated at 0.3, 0.5 and 1.0mm crack widths, as in Table 2.

Table 2 Tsp results, in years.

Concrete type	T_{sp} W_{lim} = 0.3mm	T_{sp} W_{lim} = 0.5mm	T_{sp} W_{lim} = 1.0mm
CEM II	28.58	32.81	46.22
50% CEM II, 50% GGBS	28.36	32.54	45.70

The difference in crack propagation rates of the accelerated tests is reflected in the small additional service life predicted by the model, and as expected given the slower crack propagation of the CEM II concrete, a longer service life may be expected in a structure containing only the CEM II concrete. It must be noted, however, that the difference is so small in the context of the whole lifespan of the structure as illustrated by Figure 44, as to be insignificant in reality, especially considering the uncertainty which may be involved in evaluating the parameters of the model.

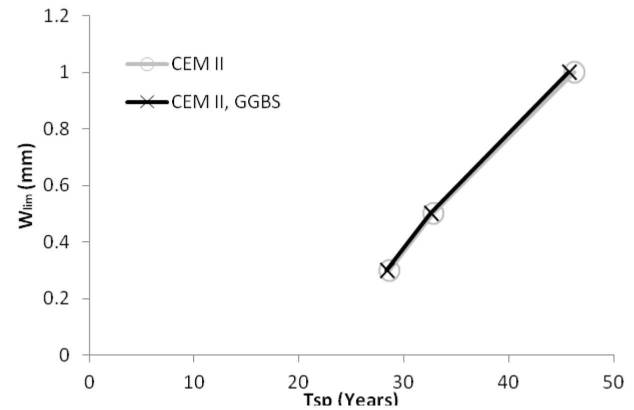

Figure 4 Crack width and Service life (T_{sp}).

When extrapolated over the life of the structure to determine the time to reach the crack width limit in real-time, the difference between the 100% CEM II concrete and the 50% ggbs concrete is very small and highlights the sensitivity of the model to correction factors when extrapolating short-timescale data out over many years. An estimation by Vu et al.[9] shows that the service life prediction may change by 20% depending on the concrete quality parameter, but 80% depending on the rate of loading correction, which highlights the need for improved accuracy in models which extrapolate the accelerated corrosion data. A small sensitivity study illustrates this point. Choosing one variable in the model, the corrosion rate i_{corr}. which may to be difficult to ascertain accurately and whose value may vary widely depending on the technique used to determine it [13,17], especially in the early stages of corrosion and applying a range of likely values for i_{corr},, from 0.1 μA/cm^2 to 5 μA/cm^2, yields a far greater difference (between 23 to 46 years) in service life prediction at the 1.0mm crack width limit than the effect of significantly changing the binder type parameter, τ as shown in Figure 5:

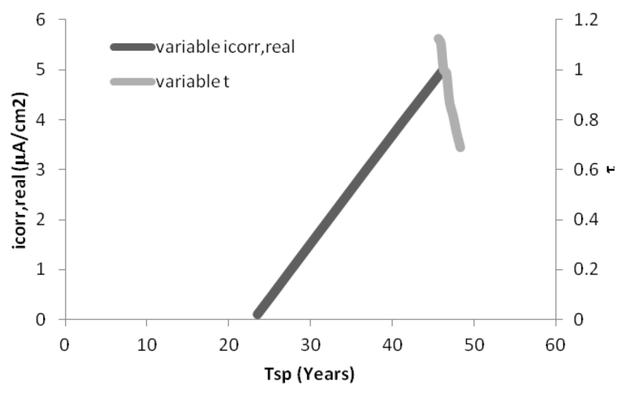

Figure 5 Sensitivity of T_{sp} to i_{corr} and τ.

5 CONCLUSION

The previous experimental work of the authors showed a pronounced difference in crack propagation behaviour between concrete prepared with CEM II and concrete prepared with a 50/50 blend of CEM II and ggbs. This paper presents an attempt to use this data by deploying the separate approaches of the models of Thoft-Christensen and Vu et al, both eminent publications on the subject, to evaluate the difference in service life which the change in binder materials effects. The difference in crack propagation behaviour gave rise to a small but discernible difference in the expected service life of structures containing the concretes, however the difference is so small as to be negligible given the sensitivity of the model to factors other than the concrete type and the assumptions inherent in the model. That the model is many times more sensitive to the measured corrosion rate than the demonstrated crack propagation behaviour of materials used illustrates the need for extensive real-world data collection from the individual structure or network of structures being considered, such data may be collected on a local scale as it may be dependent on the local environment, climate and level and nature of chlorides present, and may be time-variant. The results of the model presented herein show that whilst a general framework for a degradation model exists, meaningful service life predictions can only be made when the input parameters for the model are accurate for the structure. The difficulty in applying accelerated data to the problem may be overcome with the advent of real-world chloride ingress and corrosion data collection from structures over longer time-frames, however until this data becomes available questions about the accuracy and usefulness of models will remain. Future study by the authors will focus on identifying which parameters the service life of the structure is most sensitive to, identifying those which slow the crack propagation process and seeking to optimise these parameters to extend the service life, in doing so reducing the cost of maintaining an infrastructure network.

REFERENCES

[1] Neville, A.M., Properties of Concrete, 4th Edition. 1995: Pearson Prentice Hall.

[2] Beasley, K.J., Failure of Exposed Concrete Caused by Corrosion of Embedded Steel. Journal of Performance of Constructed Facilities, American Society of Civil Engineers, 2003. 107.

[3] Conciatori, D; Sadouki, H; Bruhwiler, E., Capillary Suction and Diffusion Model for Chloride Ingress into Concrete. Cement and Concrete Research, Elsevier, 2008. 38: p. 1401-1408.

[4] Tuutti, K., Corrosion of Steel in Concrete. 1982, Swedish Foundation for Concrete Research: Stockholm.

[5] BSI, BS EN 206-1:2000, in Concrete: Specification, performance, production and conformity 2000, British Standards Institute: Milton Keynes.

[6] Downey, S;O'Connor, A; Sheils, E., Experimental Investigation of Chloride-Induced Crack Propagation in Reinforced Concrete, in Bridge & Concrete Research in Ireland. 2010: Cork.

[7] Evans, C; Richardson, Mark G., Service Life of Chloride-Contaminated Concrete Structures, in Concrete Research in Ireland Colloquium. 2005: Belfast.

[8] Mullard, J.A; Stewart, M.G., Corrosion-Induced Cover Cracking: New Test Data and Predictive Models. ACI Structural Journal, 2011. 108(1).

[9] Vu, K; Stewart, M.G; Mullard, J. , Corrosion-Induced Cracking: Experimental Data and Predictive Models. American Concrete Institute Structural Journal, 2005. 102(5): p. 719-726.

[10] Sheils, E. , Optimisation of inspection planning for structures, in Dept of Civil, Structural & Environmental Engineering. 2008, Trinity College Dublin.
[11] Thoft-Christensen, P., Frandsen, H.L., Svensson, S., Numerical study of corrosion crack opening. Structure and Infrastructure Engineering, 2008. 4(5): p. 381-391.
[12] Andrade, C., Alonso, C. & Molina, F.J., Cover Cracking as a Function of Bar Corrosion: Part 1-Experimental Test. Materials and Structures, Springer, 1993. 26: p. 453-464.
[13] Liu, Y., and Weyers, R. E., Modeling the Time-to-Corrosion Cracking in Chloride Contaminated Reinforced Concrete Structures. ACI Materials Journal, 1998. 95(6, Nov.-Dec. 1998): p. 675-680.
[14] Isgor, O., B. & Razaqpur, A. G. , Modelling steel corrosion in concrete structures. Materials and Structures, Springer, 2006. 39: p. 291-302.
[15] Kim, C. Y. & Kim, J. K., (2008) Numerical analysis of localized steel corrosion in concrete. . Construction and Building Materials, 2008. 22((6): p. 1129-1136.
[16] Stewart, M.G. & Suo, Q., Extent of spatially varaiable corrosion damage as an indicator of strength and time-depenadant reliability of RC beams. Engineering Structures, 2008.
[17] Otieno, M; Beushausen, H. and Alexander, M, Prediction of Corrosion Rate in RC Structures - A Critical Review. Modelling of Corroding Concrete Structures, 2011. RILEM Bookseries 5,.
[18] El Maaddawy, T, A; Soudki, K, A, Effectiveness of Impressed Current Technique to Simulate Corrosion of Steel Reinforcement in Concrete. Journal of Materials in Civil Engineering, American Society of Civil Engineers, 2003. 15(1): p. 41-47.
[19] Stewart, M.G. & Val, D.V., Multiple limit states and expected failure costs for deteriorating RC bridges. Journal of Bridge Engineering, ASCE, 2003. 8(6): p. 405-415.
[20] Mullard, J.A; Stewart, M.G., Repair efficiency and timing of maintenance for RC structures subjected to spatially variable corrosion damage, in Applications of Statistics and Probability in Civil Engineering. 2007, Taylor & Francis Group, London: Kanda, Takada & Furuta.
[21] Thoft-Christensen, P. , Corrosion and Cracking of Reinforced Concrete, in Life Cycle Performance of Deteriorating Structures: assessment, design and management. Proc of 3rd IABMAS Workshop on Life-Cycle Cost Analysis and Design of Civil Infrastructure Systems and JCSS Workshop on Probabilistic Modeling of Deterioration Processes in Concrete Structures, . 2003: Lausanne. p. 26-36.
[22] ASTM, G1-90 Standard Practice for Preparing, Cleaning, and Evaluating Corrosion Test Specimens. 1999: ASTM International, West Conshohocken, PA.

Finite element modelling of transverse load distribution in masonry arch bridges

Helen Dunne[1], John J. Murphy[1], Kieran Ruane[1, 2]
[1]Department of Civil, Structural and Environmental Engineering, Cork Institute of Technology, Bishopstown, Cork, Ireland
[2]RPS Group, Inishmore, Ballincollig, Co. Cork, Ireland
email: helen.dunne@mycit.ie, john.justinmurphy@cit.ie, kieran.ruane@rpsgroup.com

ABSTRACT: Various methods are used to assess masonry arch bridges including the popular Modified MEXE Method and mechanism analysis. An issue of particular interest is how the loads are distributed transversely in the arch. The current load model for masonry arch bridges calls for the utilisation of an effective strip when dealing with the transverse distribution of an applied load [1]. In this paper transverse load patterns on masonry arch bridges are assessed using LUSAS finite element analysis (FEA) software. An arch is modelled using thick shell elements to represent voussoirs, with consideration given to the reduced stiffness of the mortar joints between each voussoir. The overall aim is to develop an enhanced load distribution model to improve current mechanism methods for the design and assessment of masonry arch bridges.

KEY WORDS: Masonry arch; Transverse load distribution; LUSAS; Finite element analysis.

1 INTRODUCTION

Masonry arch bridges account for a large proportion of the bridge stock in Ireland. On national roads, 36% of the bridge stock comprises masonry arches. By international standards for strategic transport routes, this is high [2].

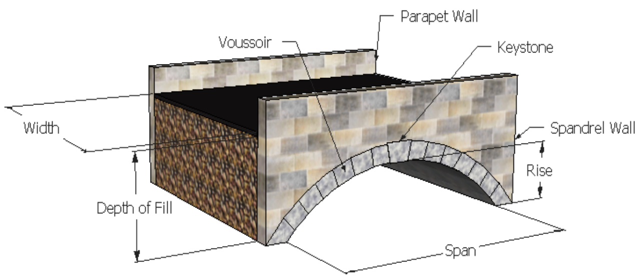

Figure 1. Typical Masonry Arch.

Currently, the most popular method of analysis used by practising engineers is the modified MEXE method [3], which has proven to be inaccurate in many instances [4]. Analysis through computer modelling programs such as LimitState Ring and Archie M is becoming increasingly popular. These packages offer essentially two dimensional analyses, with simplified load distribution in the transverse direction.

Although numerous studies have been undertaken to analyse arch behaviour along the span, few explore how an arch behaves transversely. In reality, loads are not applied uniformly across the arch width and the distribution of loads thus needs consideration. By simplifying the transverse distribution of loads, it is difficult to determine the true capacity of an arch bridge.

The aim of this paper is to study the structural behaviour of a typical arch, in order to determine the extent of transverse load distribution. Results obtained from an arch modelled in LUSAS finite element analysis (FEA) software were analysed in order to determine transverse load distributions under a set of varying point loads.

2 CURRENT ANALYSIS METHODS

The British Design Manual for Roads and Bridges (BA16) describes the assessment of masonry arch bridges using the modified MEXE method [3]. It also recognises alternatives to the MEXE method such as computer packages based on Castigliano's elastic method and the mechanism method. The effective strip used in masonry arch analysis is set out in BD21 of the British Design Manual for Roads and Bridges [1].

2.1 *Modified MEXE Method*

The MEXE method was developed from research carried out by Pippard in the 1930's. The method was first set out by the British military as a means to carry out rapid field assessments of arch bridges subject to military loads. This method has evolved into the modified MEXE method, which is a semi-empirical analysis method that calculates the load capacity of the bridge using empirical formulas, and then applies a series of subjectively estimated modifying factors to the capacity [5].

The arch is surveyed, and parameters such as span, rise at centre, rise at quarter points, ring thickness and fill depth are recorded. Parameters relating to the bridge profile, materials, and condition are also required.

A provisional axle loading is determined from a nomogram of span and crown thickness. This axle loading is then modified by a series of modification factors. These include the span/rise factor, profile factor, material factor, condition factor, barrel factor, fill factor, width factor, mortar factor and depth factor.

The Modified MEXE method has a number of shortcomings. Pippard's theoretical assumptions lead to an overestimation of capacity in short span arch bridges [4]. Also, the modifying factors are determined based on a visual inspection of the bridge, leading to an increased risk of human error when determining the appropriate modifying factors [5].

2.2 Transverse Load Distribution in BD21

BD 21 calls for the distribution width of a masonry arch bridge to be calculated as shown in Figure 2 [3]. The width is calculated based on the depth of the fill at the point where the load is applied. This generates a uniform effective width strip for the full span.

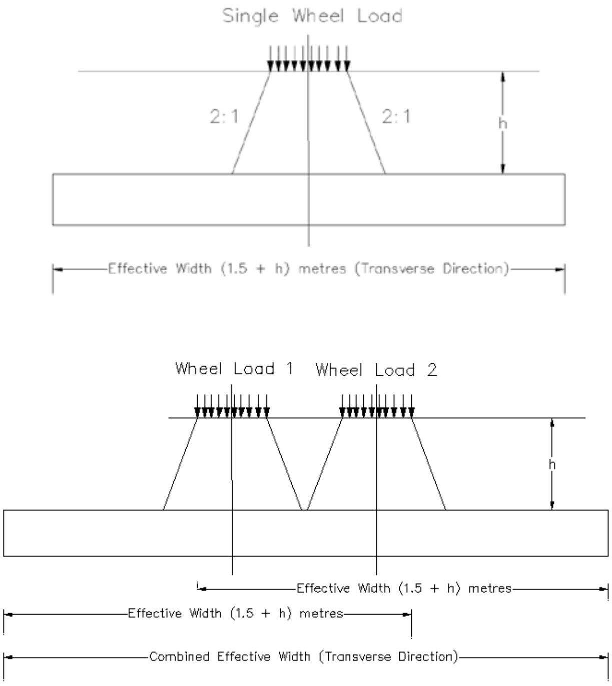

Figure 2. Transverse distribution through fill.

The diagrams in Figure 3 show how this distribution rule applies to a typical arch bridge.

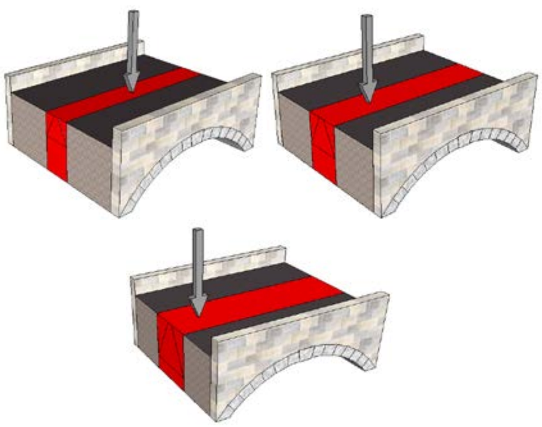

Figure 3. Effective strip visualisations.

2.3 Limitstate Ring

Limitstate Ring (see Figure 4) is a rigid block analysis computer package developed in conjunction with the International Union of Railways [6]. The main program input parameters are bridge geometry, unit weight of masonry and fill, friction at joints, backfill angle of friction and cohesion and loading details.

The Limitstate Ring software idealises a masonry bridge as a series of rigid blocks in order to carry out a limit analysis, determining the amount of live load that can be applied before structural collapse due to mechanism failure. It also permits investigation of the mode of response when supports undergo small movements [6].

Limitstate Ring software requires a user specified fixed bridge width and does not account for the effects of spandrel walls. There is an option for the user to input simple user defined transverse distribution rules.

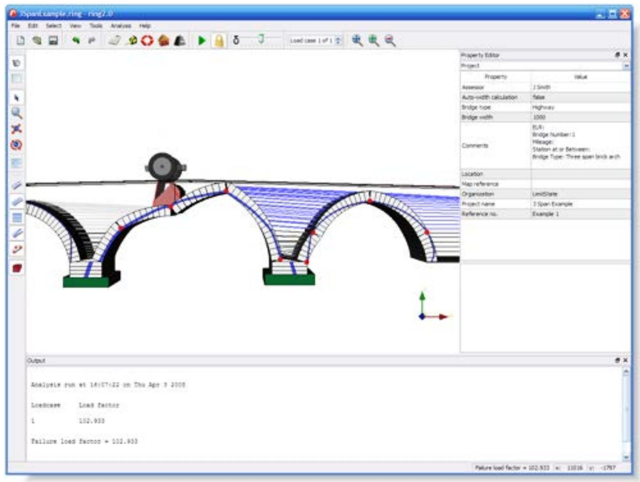

Figure 4. Screenshot from Limitstate Ring [6].

2.4 Archie-M

Archie-M is a computer package developed by Obvis Ltd that uses a thrust zone analysis (see Figure 5). Its interface encourages users to explore possibilities when analysing arches rather than obtaining results from set load cases [7]. The inputs to the programme are similar to those in the Limitstate Ring software.

Similar to Limitstate Ring, Archie-M allows the application of prescribed rules set out in BD21 [3] when considering the effect of transverse load distribution. The Archie-M user manual goes so far as to state “the effective width model specified by various authorities has been shown to be wrong. It causes over estimation of the capacity of bridges under 5m span with shallow fill” [8].

Figure 5. Archie-M Screenshot [7].

2.5 Finite Element Modelling

Finite element models of varying complexity have been used to determine arch behaviour. One, two and three dimensional FE analyses were carried out by Choo and Gong in conjunction with British Rail in 1990-1992 [9]. Tapered beam elements were used in the models. Backfill was modelled using a Mohr-Coulomb failure criterion, and the load was applied using a Boussinesq distribution at a fixed dispersal angle. The bridges analysed were then tested to collapse. The results varied in accuracy, with the one and two dimensional models yielding results 50% lower than the three dimensional model. However, the 1-D and 2-D results compared favourably with experimental results [10]. This suggests a possible error in the distribution assumptions made in the 3-D model.

Finite element analysis was carried out by Fanning et al. [11] to investigate transverse loading effects. Three dimensional non-linear models were created. The model split the masonry arch bridge into three main components; the masonry, the fill and the pavement. The masonry was modelled using a homogeneous isotropic material with a failure criterion similar to that of concrete. The fill was modelled using a Drucker-Prager yield criterion, and between the fill and the masonry one dimensional friction elements were used. The use of a non-linear model allowed for the failure mode to be more accurately determined.

3 LUSAS FINITE ELEMENT MODELLING

In this study, LUSAS FEA software was used to model three masonry arches. The arch geometries are outlined in Table 1. Arch 1 is representative of a typical arch bridge and Arch 3 is akin to a culvert or tunnel. Arch 2 is not a typical arch geometry and was modelled solely for analytical purposes. Arch 1 can be seen in Figure 6.

Table 1. Arch Geometries.

	Arch 1	Arch 2	Arch3
Span	10m	10m	10m
Width	10m	1m	50m
Shape	Segmental	Segmental	Segmental
Height Midpoint	2.5m	2.5m	2.5m
Height Quarterpoint	1.84m	1.84m	1.84m
Ring Thickness	0.5m	0.5m	0.5m
End Conditions	Pinned	Pinned	Pinned

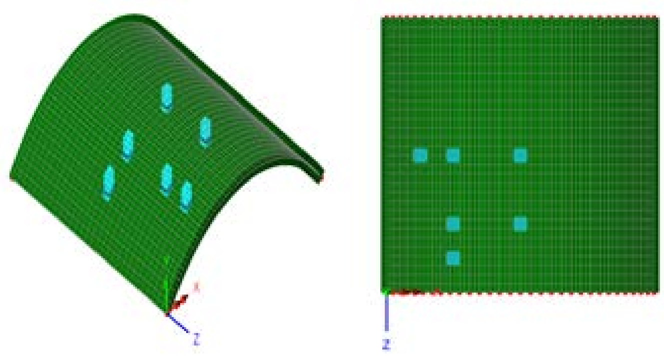

Figure 6. Arch with point loads.

3.1 *Arch 1*

The arch was divided into 31 voussoirs. Each voussoir was modelled as a thick plate element. A quadrilateral shaped mesh approximately 200mm x 200mm of quadratic interpolation order was used (see Figure 7). The mortar joint between each voussoir was modelled using a material of relatively reduced Young's Modulus compared with that of the voussoir; this was to account for the reduced stiffness at the mortar joint. The Young's Modulus values of stone used for a typical arch barrel and the lime mortar typically used can vary greatly [12]. For this paper, a Young's Modulus ratio between stone and mortar of 3 was used.

The arch was loaded at six separate locations with a 300mm x 300mm square point load of magnitude 100kN (see Table 2 and Figure 6). This generated results for six loadcases. Results were obtained for vertical and horizontal displacements, axial stress and axial force.

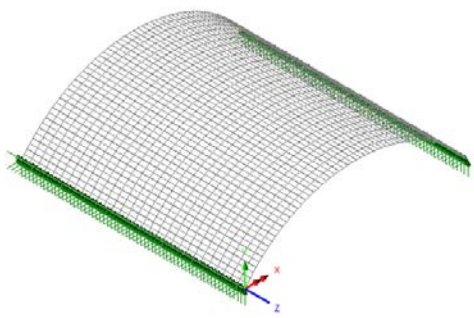

Figure 7. Arch mesh.

Table 2. Point Load Locations.

Loadcase	X (m)	Z (m)
1	1.25	-5.0
2	2.5	-5.0
3	5.0	-5.0
4	2.5	-2.5
5	5.0	-2.5
6	2.5	-1.25

3.2 *Arch 2*

Arch 2, which is 1m wide, is not a geometrically typical masonry arch. It was modelled in order to determine transversely undistributed load patterns for comparison with Arch 1. Arch 2 also contains 31 voussoirs modelled with thick plate elements with a quadrilateral mesh. This arch was loaded at three separate locations (X = 1.25m, X = 2.5m and X = 5.0m) with a line load across its full width of magnitude 100kN and thickness 300mm (See Figure 8).

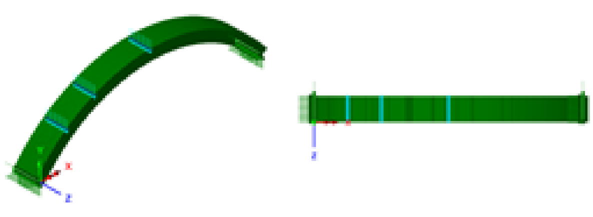

Figure 8. Arch 2 with line loads.

3.3 *Arch 3*

Arch 3 is a wide arch. It was modelled in order to approximate the affected width of an arch bridge subject to a point load. Again, it comprises 31 voussoirs modelled with thick plate elements with a quadrilateral mesh. This arch was loaded with a central point load of 100kN. Results for vertical displacement obtained from this model demonstrate the extent of the transverse effect of a point load.

4 LUSAS RESULTS

4.1 Effective Width

The width of bridge affected by a point load at centre span was determined for Arch 3. It can be seen in Figure 9 that the effective width by consideration of deflection is approximately 15m.

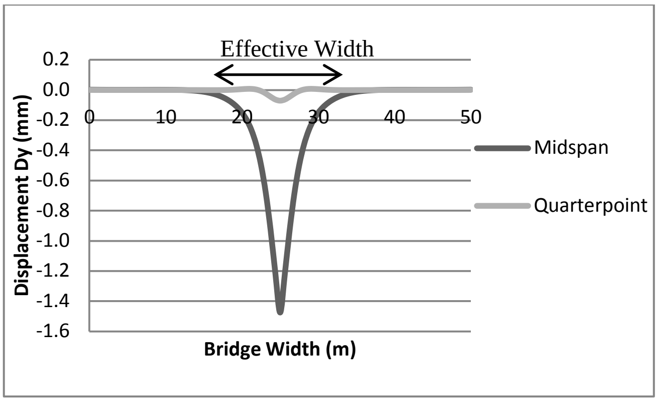

Figure 9. Vertical Displacement in 50m wide bridge.

4.2 Results for Arch 1

Results are presented in this paper for three of the six loadcases analysed. For each loadcase, LUSAS contour diagrams were used to visualise the results for displacements and axial stress (see Figure 10 and Figure 11).

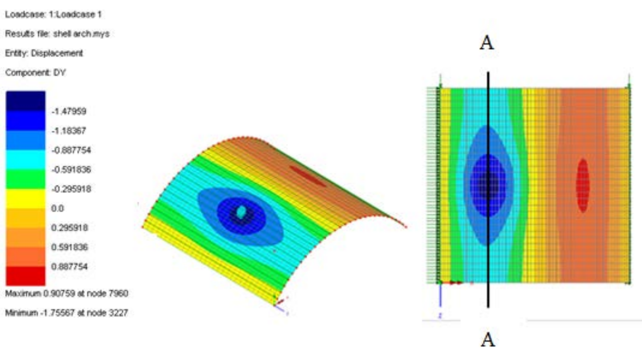

Figure 10: Displacement (d_y) contour diagram, loadcase 2.

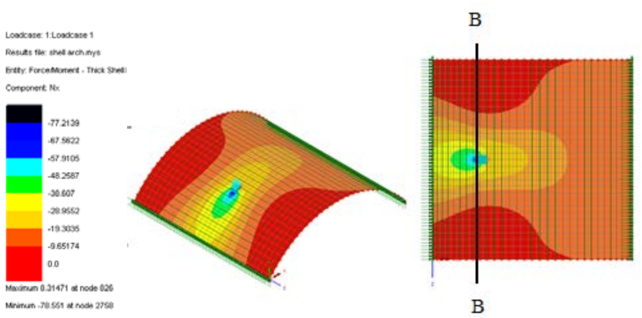

Figure 11. Axial Stress contour diagram, loadcase 2.

Displacement results were obtained at 18 strips across the bridge width (see Figure 12). The displacements were expressed as a percentage of the displacement under the point load for each loadcase. The results form contour diagrams (see Figure 14, Figure 17 and Figure 20).

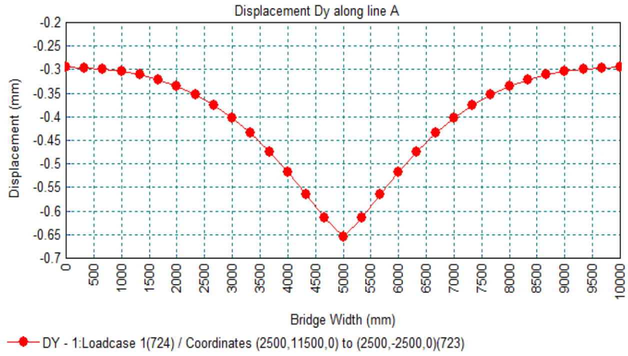

Figure 12. Displacement across bridge width through load location (Loadcase 2, Line A, Figure 10).

Axial stress results were also obtained at 18 strips across the bridge width. The stresses along each strip form a curve (see Figure 13). These stresses are expressed as a percentage of the stresses along the same strip in the 1m wide arch. The results are presented in the form of contour diagrams (see Figure , 18 and Figure).

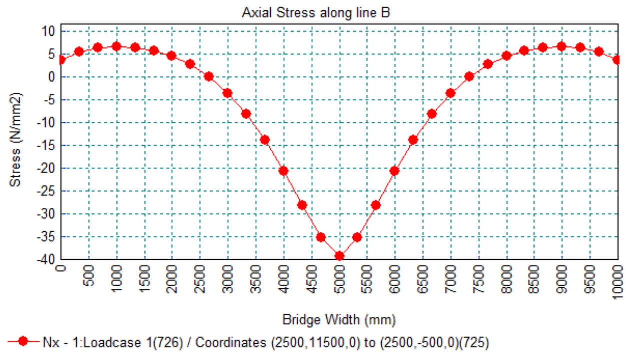

Figure 13. Axial stress across bridge width through load location (Loadcase 2, Line B, Figure 11).

The axial stresses can be summed along any strip to determine the axial force within any segment of the arch along the strip. From this, axial force envelopes showing the percentage of force distributed across the arch are obtained (see Figure , Figure 19 and Figure). For example, in Figure 22, at mid span, 70% of the load is contained within a strip of 1.75m width, 80% is contained within a strip of 2.5m width and over 90% is distributed across the full arch width. This demonstrates the extent to which the load is distributed transversely in the arch.

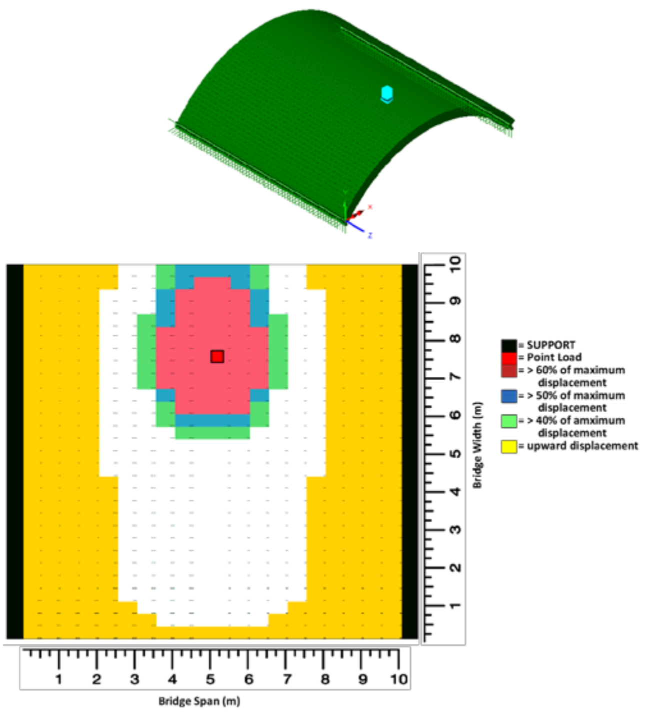

Figure14. Vertical displacement displayed as % of displacement under point load (Loadcase 5).

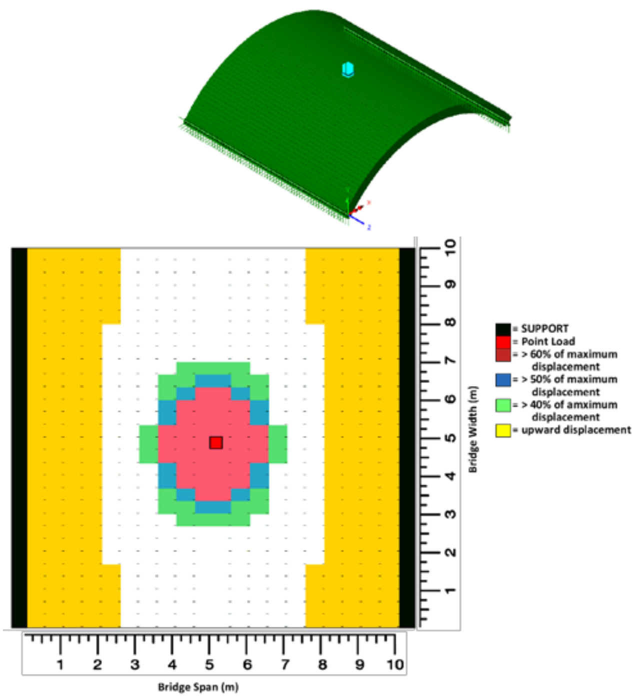

Figure 17. Vertical displacement displayed as % of displacement under point load (Loadcase 3).

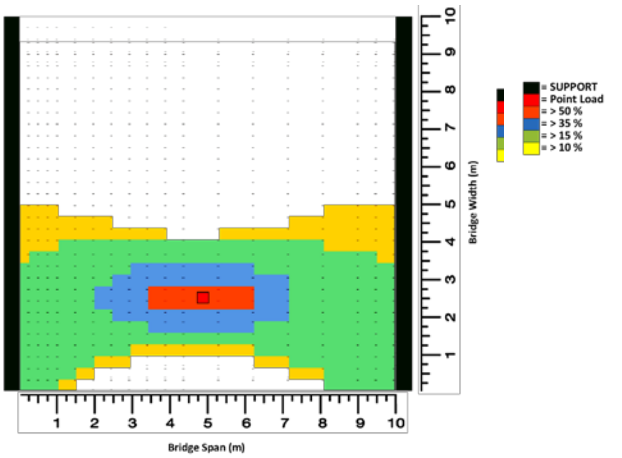

Figure 15. Axial stress displayed as % of stress in undistributed strip (Loadcase 5).

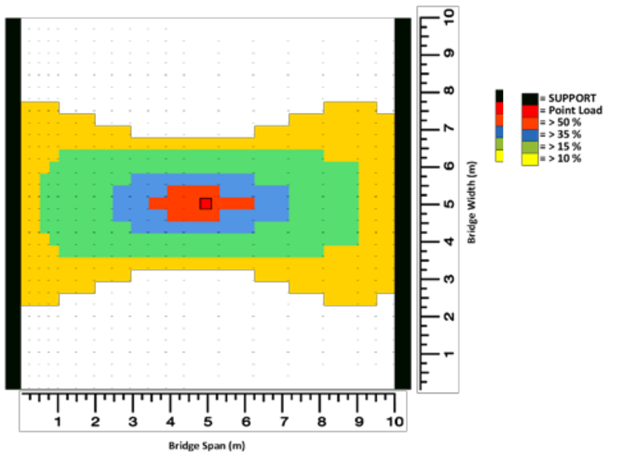

Figure 18. Axial stress displayed as % of stress in an undistributed strip (Loadcase 3).

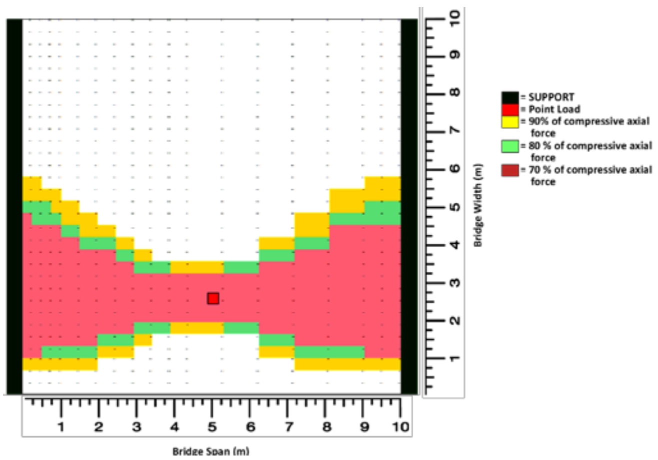

Figure 16. Axial force envelope (Loadcase 5).

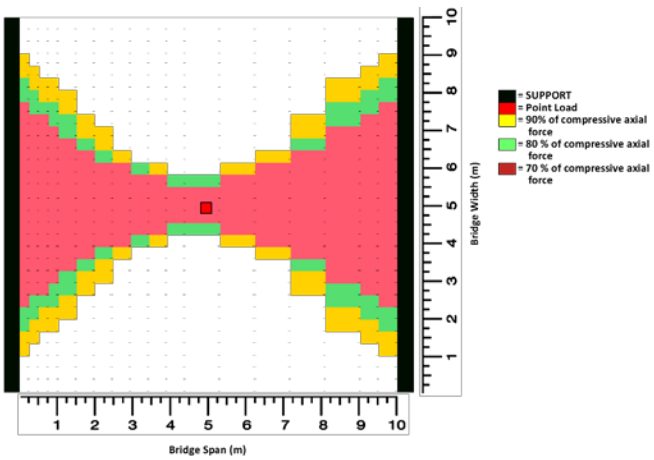

Figure 19. Axial force envelope (Loadcase 3).

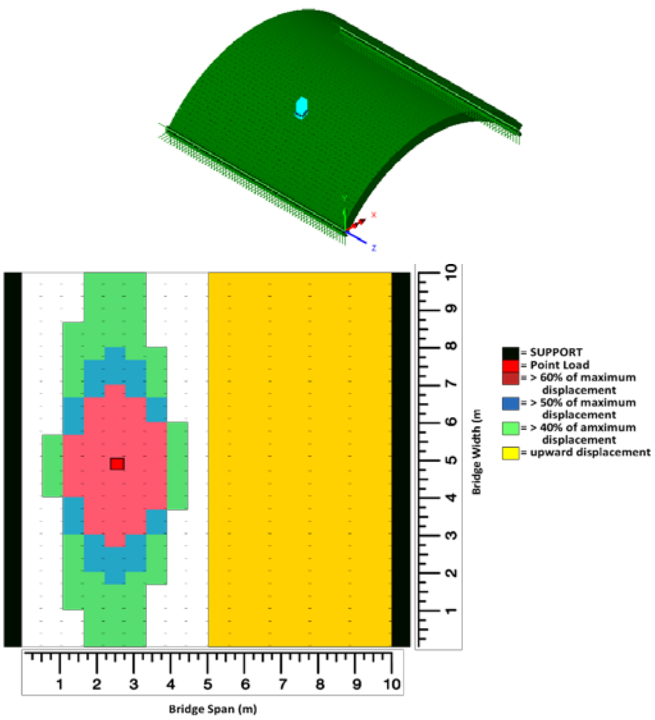

Figure 20. Vertical displacement displayed as % of displacement under point load (Loadcase 2).

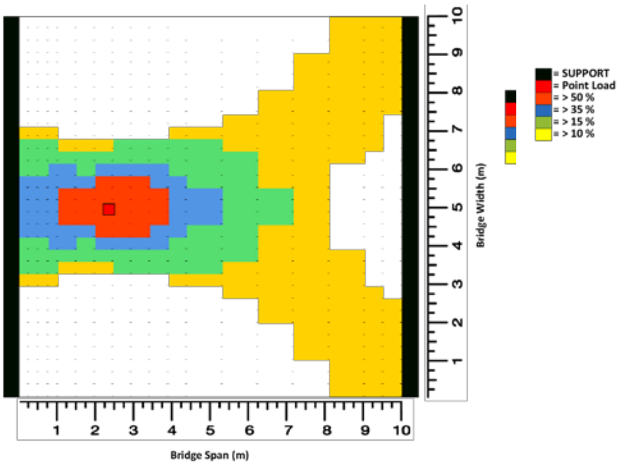

Figure 21. Axial stress displayed as % of force in an undistributed strip (Loadcase 2).

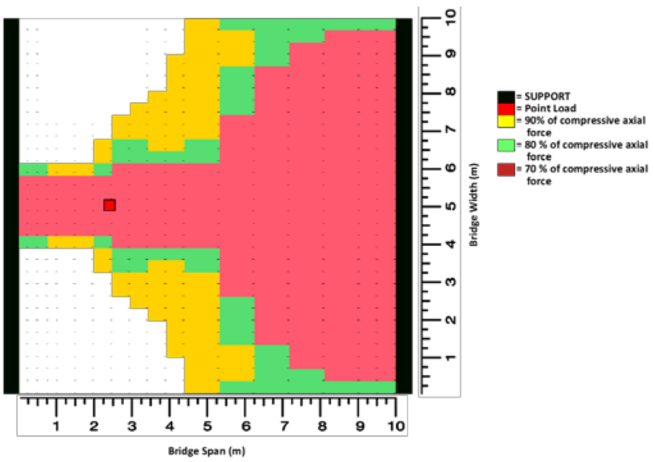

Figure 22. Axial force envelope (Loadcase 2).

5 CONCLUSIONS

Research thus far has determined that using a uniform effective bridge width along the length of the span is an overly simplistic load model. The results obtained show that the load effect fans outwards with increasing distance from the point load. Results gathered for axial stress and displacement both show similar results.

The results also show that where the load is located away from the arch centreline, there is an unsymmetrical spread of the load.

6 FUTURE WORK

The aim is to further develop the LUSAS models to incorporate fill and spandrel walls. The model will also be expanded to include a soil block at the arch abutments. The effect of skew on transverse load distribution will also be investigated by creating a series of LUSAS FEA models with varying skews.

ACKNOWLEDGMENTS

The authors would like to thank David Hodge (Cork Institute of Technology) for his assistance with LUSAS FEA software.

REFERENCES

[1] The Highways Agency, Design Manual for Roads and Bridges, V. 3. Section 4, Part 3. *The Assessment of highway bridges and structures (BD21)*, London, 2001.

[2] Duffy, L., 'Development of Eirspan: Ireland's bridge management system', *Proceedings of the Institution of Civil Engineers (Bridge Engineering)*, 2004, pp 139-146.

[3] The Highways Agency, Design Manual for Roads and Bridges, V. 3. Section 4, Part 4. *The Assessment of highway bridges and structures (BA16)*, London, 2001.

[4] Melbourn, C., Wang, J. and Gilbert M. S. C. 'Review of Assessment Methods for Masonry Arch Bridges', *CSS Masonry Arch Research Project*, Final Draft Report, 2009.

[5] Orban, Z. 'UIC Project on assessment, inspection and maintenance of masonry arch railway bridges', *ARCH'07: 5th International Conference on Arch Bridges*, Multicomp, Lda Publishers, Madeira, 2007.

[6] Limitstate, Limitstate Ring Theory and Modelling Guide Version 2.0oj, Sheffield. [Online]. Available: www.limitstate.com. [Accessed 23 November 2011].

[7] Obvis, 'Obvis Masonry Arch Analysis Software,' 2011. [Online]. Available: www.obvis.com. [Accessed 22 November 2011].

[8] Obvis Ltd, Archie-M Masonry Arch Bridge and Viaduct Assessment Software User Guide, 2010. [Online]. Available: www.obvis.com. [Accessed 22 November 2011].

[9] Choo, B., Gong, N. and Coutue, N. 'Finite Element Analysis of Masonry Arches Using Tapered Elements', *Proceedings of the Institution of Civil Engineers*, 1991, pp 775-770.

[10] Keooi-Hock, NG., *Analysis of Masonry Arch Bridges*, PhD Thesis, Napier University, Edinburgh, United Kingdom, 1999

[11] Fanning, P., Boothby, T. and Roberts, B. 'Longitudinal and transverse effects in masonry arch assessment', *Construction and Building Materials*, 2000, vol. 15, no. 1, pp 51-60.

[12] Bosiljkov, V., Totoev, Y. and Nichols, J. 'Shear Modulus and Stiffness of Brickwork Masonry: An Experimental Perspective', *Structural Engineering and Mechanics*, vol. 20, no. 1, 2003, pp 21-44.

Nonlinear three dimensional finite element modelling of a masonry arch bridge

Niamh Gibbons[1], Paul J. Fanning[1]
[1]School of Civil, Structural & Environmental Engineering, University College Dublin, Ireland
email: niamh.gibbons@ucd.ie, paul.fanning@ucd.ie

ABSTRACT: Masonry arch bridges are estimated to account for more than 40% of the European bridge stock. Often more than 100 years old these bridges have performed well in service and are arguably the most durable and sustainable bridge type. However the gradual deterioration of materials with time, coupled with the increase in loading from modern road and rail vehicles, make re-assessment, maintenance and repair inevitable. Masonry arch bridges are complex three dimensional structures, the strength of which are determined not only by the longitudinal and transverse capacities of the arch barrel itself, but also the soil structure interaction, the presence of spandrel walls, the relieving effects of dead load, the stiffness of the abutments and the distribution of the applied loads through the fill material. The assessment methods that are available make various simplifying assumptions in order to provide useful tools for assessing the capacity of masonry arch bridges and as such do not account for all of these factors, but the extent to which these simplifying assumptions effect the assessed capacity is unquantified. To address this issue, a nonlinear three dimensional finite element model which considers constitutive material models enabling progressive cracking and failure of the complete structural system were used to predict the ultimate load capacity for a single span masonry arch. The model was validated against measured responses at service load levels under a passing truck load. In order to quantify the degree of conservatism associated with more simplified assessment approaches the predicted ultimate load capacity and the corresponding failure mechanisms from the three dimensional nonlinear model were compared to the assessed capacities determined from five other assessment methods.

KEY WORDS: Masonry arch bridges; Finite element modelling; Ultimate capacity assessment.

1 INTRODUCTION

Masonry arch bridges constitute approximately 80% of bridges in Ireland [1] and are a predominant structural form on the road, rail and canal networks. There are a wide range of assessment methods available to predict the ultimate capacity of masonry arch bridges, although experimental data for the validation and quantification of conservatism of these methods is limited. A comparison of results from a selection of simplified two dimensional assessment methods with load tests to collapse of real bridges is provided in BA 16 [2]. However these experiments were set up to replicate two dimensional conditions resulting in uncertainty as to the relationship with the actual capacity of the structure.

Griffith Bridge shown in Figure 1 is an over bridge for the Grand Canal in Dublin currently carrying road traffic. The bridge was tested under service load levels and the measured deflections were used to validate a three dimensional nonlinear finite element model. This model was then used to predict the ultimate capacity of the bridge under assessment loading conditions for highway structures and to examine the behaviour of the arch leading up to failure. The predicted ultimate capacity was then compared with assessment ratings determined using a range of more simplified methods.

Figure 1. Griffith Bridge.

2 EXPERIMENTAL SERVICE LOAD TESTING

Griffith Bridge is a 7.84m wide, 9.46m single span bridge with a span-to-rise ratio of 3.5 and an elliptical or three-centred profile. The depth of fill at the crown is 0.126m. The arch ring is 0.446m thick and is of ashlar limestone construction with granite fascia stones. The mortar joints are approximately 5mm wide. These dimensions are summarized in Table 1.

Table 1. Griffith Bridge dimensions.

Dimension	[m]
Span	9.460
Rise at centre	2.700
Rise at quarter span	2.284
Ring thickness	0.446
Depth of fill	0.126
Width	7.840

Full scale testing of the bridge was carried out under a slow moving truck load. The gross vehicle weight when fully loaded was 31.6 tonnes. The truck consisted of a 1.7m spaced double axle at the front and a 1.42m spaced double axle at the rear, carrying 10.5 tonnes and 21.1 tonnes respectively, with the front and rear bogies at a 5.56m spacing. Multiple passes were made across the bridge at a slow speed. The bridge was instrumented with linear variable differential transformers and measurements were taken at the crown, abutments and haunches both along the centreline of the bridge and at the edges. Further details of the testing programme can be found in [3].

3 FINITE ELEMENT MODEL

3.1 Material models and material properties

The bridge was modelled using ANSYS v13, a general purpose finite element software package. The masonry units and mortar were treated as a single continuous material with reduced values assigned for stiffness and strength compared with that of the stone itself. The fill and road surfacing were also treated as a single material.

Solid65 eight noded isoparametric elements which allow for nonlinear material behaviour in the form of cracking, crushing and plastic deformation were used to model both the masonry and the fill material.

For the masonry a concrete material model based on the Willam and Warnke failure criteria to predict the failure of brittle materials was used [4,5]. If the principal stresses exceed the specified tensile capacity of the material at one of the integration points in the element a plane of weakness, or a smeared band of cracks, is introduced orthogonal to the principal stresses; reducing the stresses in this region and redistributing them locally. Following the formation of the first crack, the material model is capable of forming a second and third crack in orthogonal directions for each integration point.

For the fill the material is treated as elastic-perfectly plastic and a Drucker-Prager yield criterion is used [5,6]. This uses an outer cone approximation to fit a smooth yield surface around the Mohr-Coulomb surface as shown in Figure 2. The parameters used for the Drucker-Prager material model are cohesion, the angle of internal friction and the dilantancy angle. Either an associative flow rule, with the dilantancy angle equal to the angle of internal friction, or a nonassociative flow rule, with the dilantancy angle less than the angle of internal friction, can be used to control the increase in volume due to yielding. For the model of Griffith Bridge the associative flow rule was used.

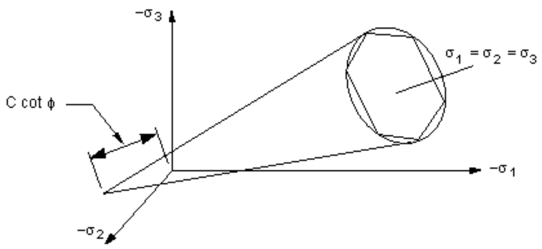

Figure 2. Drucker-Prager and Mohr-Coulomb yield surfaces, reproduced from [5].

A frictional interface was applied at the contact area between the masonry and fill, allowing the fill to slide along the surface of the masonry. A frictional coefficient of 0.2 was applied.

The masonry was assumed to have a Young's modulus of 10GPa, Poisson's ratio of 0.3 and a compressive strength of 10MPa. A limited tensile strength equal to 5% of the compressive strength was also assigned to the masonry. The fill was assumed to have a Young's modulus of 500MPa, Poisson's ratio of 0.23, a cohesion value of 1000MPa and both the angle of internal friction and the dilantancy angle equal to 44 degrees. The material properties for both the masonry and the fill are summarized in Tables 2 and 3.

Table 2. Masonry material properties.

Masonry	
Young's modulus [GPa]	10
Poisson's ratio	0.3
Density [kg/m³]	2200
Compressive strength [MPa]	10
Tensile strength [MPa]	0.5

Table 3. Fill material properties.

Fill	
Young's modulus [MPa]	500
Poisson's ratio	0.23
Density [kg/m³]	1700
Cohesion [MPa]	1000
Angle of internal friction [deg]	44
Angle of dilantancy [deg]	44

3.2 Finite element mesh and boundary conditions

The finite element mesh consisting of approximately 12000 elements is shown in Figure 3. As both the bridge geometry and the loading were symmetrical about the centreline only half of the bridge was modelled. Similar to the modelling techniques described in [7] the fill was modelled 6m beyond the extent of the spandrel walls in order to ensure that the boundary conditions applied at the extremities of the fill did not interfere with the response at the abutments. The fill and the masonry were also extended 1m below the springing point of the arch. A coarser mesh was used for the extended sections of fill and a more refined mesh was used along the line of the load path.

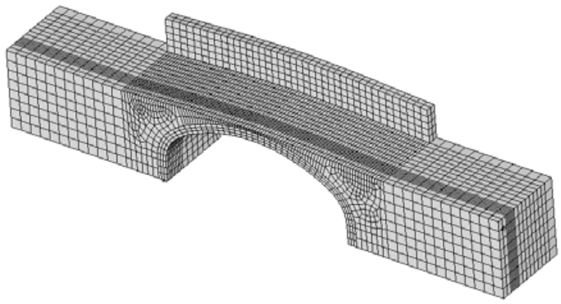

Figure 3. Finite element mesh.

Compression only support was applied to the bottom faces of the fill and the masonry. The base of the 1m section of masonry below the arch barrel was restrained against horizontal movement in the x-direction. Compression only support was also applied to the vertical faces of the fill at either end of the model. The front face of the fill in line with spandrel wall and the section of masonry extended 1m below the springing point were restrained in the z-direction against outward movement. Rather than modelling the wing walls as shown in Figure 1 as solid elements the edge of the spandrel walls were restrained in the z-direction against outward movement. A selection of the constrained faces of the model are shown in Figure 4.

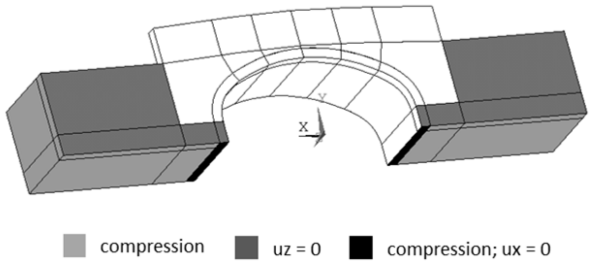

Figure 4. Boundary conditions.

4 EXPERIMENTAL LOAD SIMULATIONS

4.1 Loading

A multi-step analysis was used to simulate the slow moving 31.6 tonne truck used in the on-site experimental testing programme. In the first load step acceleration due to gravity was applied to model. In the subsequent load steps static point loads were applied to the surface nodes of the fill material, moving across the bridge in 1m increments in a series of 23 load steps.

4.2 Results and validation of the model

The deflections for the three dimensional nonlinear finite element model (line with marker points) are plotted against the measured deflections from the experimental testing at the crown and abutments in Figure 5(a-e). The results of the FE model show very good correlation with the experimental data and the peaks in deflection due to the passing of the front and rear axles are clearly identifiable. The maximum deflection at the crown centre, Figure 5(a), is within 0.01mm of the experimental results. Figures 5(c-e) show the model to be slightly less stiff at the abutments while Figure 5(b) shows that there is less deflection in the model at the crown edge indicating that there may be some existing damage at the spandrel arch interface which is not captured by the finite element model under these load conditions.

5 PREDICTION OF ULTIMATE LOAD CAPACITY

5.1 Assessment loading

To allow for comparison with other methods of assessment as is discussed in Section 6 the ultimate capacity predication was carried out using the loading specified in the current guidance for Ireland and the UK for the assessment of masonry arch bridges [2,8]. These specify the use of axle loads rather than

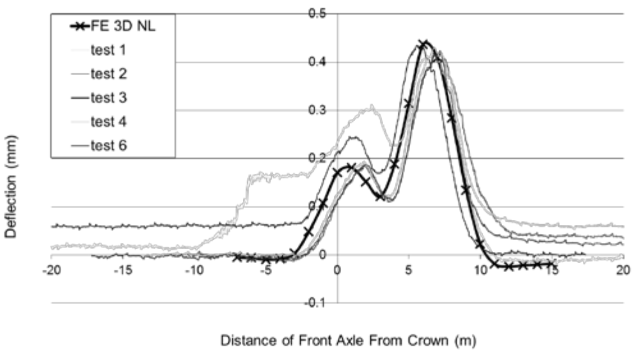

(a) deflection at crown centre.

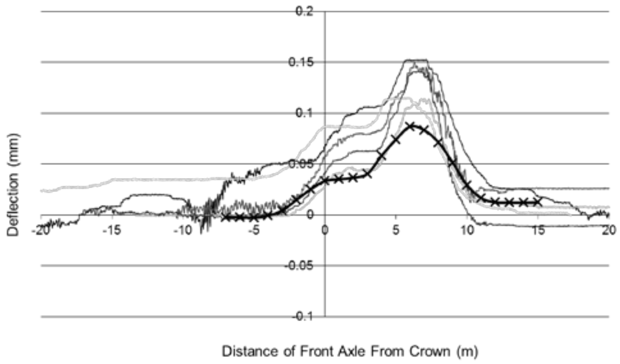

(b) deflection at crown edge.

(c) deflection at south abutment centre.

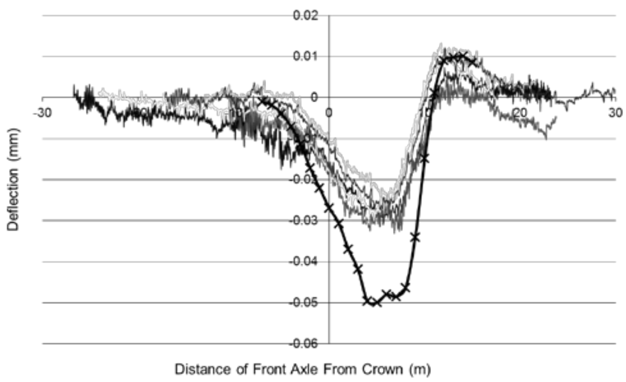

(d) deflection at north abutment centre.

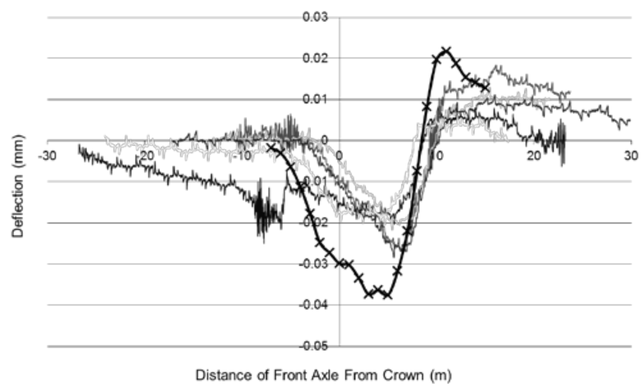

(e) deflection at north abutment edge.

Figure 5 (a-e). Deflections for moving truck load.

vehicle configurations or a uniformly distributed load with a knife edge load as is used for the assessment of other highway structures. For a double axle bogie a load factor of 1.9 is applied to each of the axles and a further impact factor of 1.8 is applied to one of the axles. No factor is applied to the dead load as this has a relieving effect for arches.

A 1.8m spaced double bogie with the load factors specified above was applied to the model for the ultimate load capacity prediction. The load was applied at the most onerous location with the centre of the bogie located 1.9m from the crown.

5.2 Solution

Although the solution controls for both the experimental service load simulation and the ultimate capacity prediction were similar, they are discussed in this section as they were more critical to the solution at ultimate capacity failure.

An iterative Newton-Raphson solution using a sparse direct equation solver was used [5]. The sparse direct solver was chosen as it is more robust for nonlinear solutions. However it uses significantly more memory. The augmented Lagrange algorithm [5] was used for the frictional contact surfaces. As large loads were being transferred across small contact areas the contact stiffness was updated at each iteration to minimise convergence difficulties associated with contact penetration.

As before, an initial gravity step was applied. The double axle load was then applied in 1 tonne increments for each substep with a force convergence tolerance for the out of balance loads equal to 1% of the applied live load increment. This equated to a convergence criteria of 98.1 N for each substep. Up to 50 equilibrium iterations were allowed for each substep.

5.3 Load deflection response and cracking patterns

The load deflection response at the crown centre for the total factored load for the full bridge width is plotted in Figure 6. Graphical representations of the cracking at each of the labelled loads on the load deflection plot are also shown.

At the end of the gravity step some very minor cracking has occurred at the base of the spandrel arch interface. At 26 tonnes longitudinal cracking has developed underneath the heavier axle load. The bridge still exhibits a linear response up to 32 tonnes at which point it plateaus prior to the formation of a transverse crack underneath the heavier axle load and cracking at the spandrel arch interface at 36 tonnes. Vertical cracking up through the parapet wall has also occurred. At 42 tonnes a second transverse crack or hinge has formed along the haunch on the loaded side of the arch. At 100 tonnes longitudinal cracks have formed in the haunch on the unloaded side of the arch with some diagonal cracking moving out from the bottom of the longitudinal cracks towards the spandrel walls. Beyond 114 tonnes the model is no longer in equilibrium and the solution diverges.

5.4 Ultimate capacity and failure mechanism

The last load step in equilibrium is at 114 tonnes. Therefore

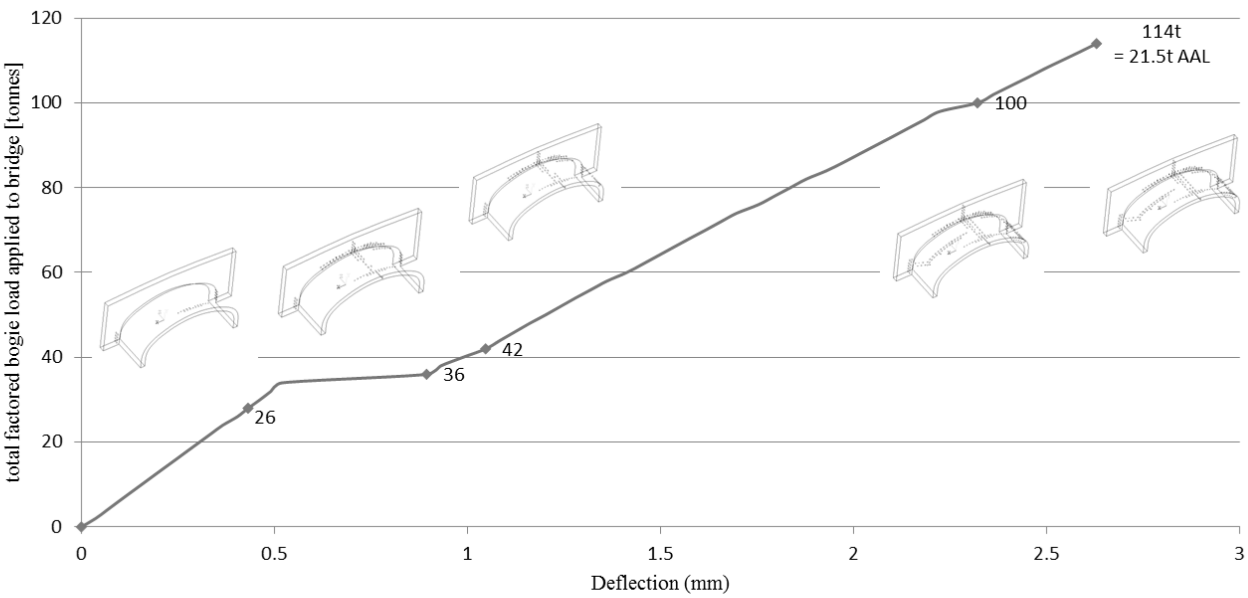

Figure 6. Load deflection response for 1.8m spacing double axle bogie.

this is taken as the lower bound solution for the ultimate capacity of the bridge. This equates to an allowable axle load of 21.5 tonnes per axle for a 1.8m double axle bogie. The crack pattern and deflected shape at 114 tonnes are shown in Figure 7 and Figure 8 respectively. The cracking pattern shows the formation of transverse cracking underneath the load and close to the abutments on the loaded side of the arch. Some diagonal cracking has also occurred close to the abutment on the unloaded side of the arch, i.e. the start of formation of a third hinge. The deflected shape is in line with that associated with the formation of a four hinge mechanism. However, the arch has also exhibited extensive longitudinal cracking due to transverse bending of the arch barrel with longitudinal cracking being exhibited prior to the formation of any transverse cracks.

With the presence of extensive longitudinal cracking and large deflections concentrated underneath the heavier axle load and in the absence of the full formation of a three hinge mechanism or significant movement of the spandrel walls at the lower bound solution, the predicted failure mechanism for the bridge is by punch through underneath the heavier axle load.

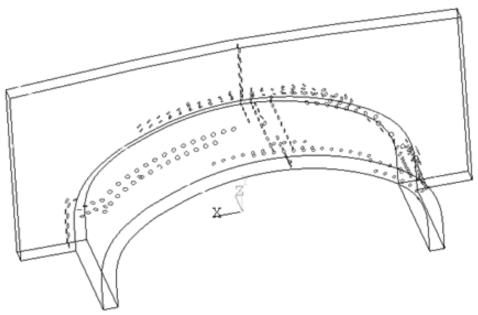

Figure 7. Crack pattern at 114 tonnes.

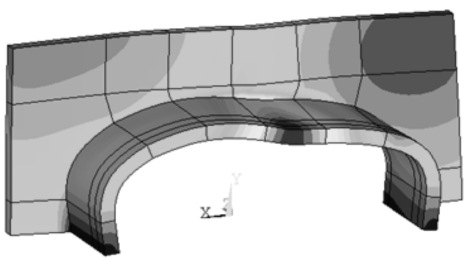

Figure 8. Deflected shape at 114 tonnes, scaled x 150.

6 ULTIMATE CAPACITIES PREDICTED FROM OTHER ASSESSMENT METHODS

6.1 Assessment methods and results

Griffith Bridge was also assessed for a double axle bogie using five different assessment methods. The other assessment methods used were the modified MEXE method [2], a three hinge limit analysis method [9] and the four hinge rigid block limit analysis method [10], a 2D elastic analysis using beam elements [11,12] and a 3D elastic analysis using shell elements. These methods and the assessment results achieved for Griffith Bridge are discussed in greater detail in [13]. A summary of the results are presented in Figure 9 for comparison with the ultimate capacity predicted by the three dimension nonlinear finite element model.

6.2 Discussion

The initial indication is that all of the other assessment methods give conservative results in relation to the three dimension nonlinear finite element model. However, a number of important points should be made.

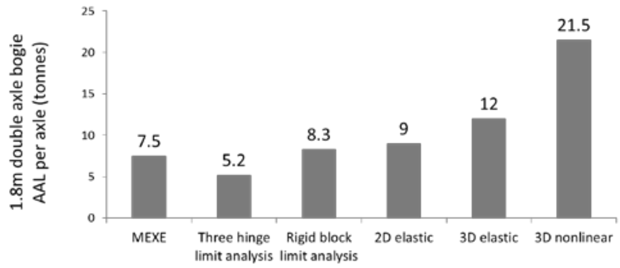

Figure 9. Allowable axle loads for a 1.8m double axle.

For the three hinge limit analysis and the four hinge rigid block limit analysis methods the load distribution model set out in [8] was applied. This model distributes the load in the transverse direction at a ratio of 1:2, horizontal to vertical, and then increases the effective width beyond the distributed width in an attempt to take account of the transverse structural action of the bridge, as shown in Figure 10, based on work carried out by Davy [14] and Chettoe and Henderson [15]. A unit width load is then determined and applied to the two dimensional model. For the 2D elastic method the transverse load distribution is simply assumed to act over a 3m width.

Due to the shallow depth of fill for this particular bridge the two dimensional methods only accounted for load dispersion over widths in the range of 3.0m – 3.5m, i.e. that each 3.0m – 3.5m wide section of arch barrel can accommodate the assessment loads given in Figure 9. Griffith Bridge is 7.840m in width and therefore the two dimensional methods indicate that the entire arch barrel could carry double the capacities listed for the two dimensional methods and whilst still conservative for this structure it is markedly less so. The two dimensional methods do not account for the transverse structural behaviour of the arch and the conservativeness of the assessment results may be dictated by the carriageway arrangements rather than actual structural response. Many arch bridges have shallow depths of fill and the presence of single or multiple lanes will make limited or no difference to effective width, Figure 11, or the assessment ratings achieved with the two dimensional methods. This will have implications for the conservativeness of two dimensional assessment methods applied to wider masonry arches with multiple lane loading.

For all of the two dimensional assessments and for the 3D elastic assessment the abutments were assumed to be fixed against horizontal displacement. Horizontal movement can be accounted for in the 2D and 3D elastic methods if required by the inclusion of spring supports. For Griffith Bridge the experimental results demonstrated a stiff abutment response with the maximum deflections under the 31.6 tonne truck less than 0.05mm. In addition to the assessment carried out using a fill stiffness of 500MPa, assessments were carried out for fill stiffness values of 15MPa and 100MPa to investigate the effect on the ultimate capacity. The resulting allowable axle loads are presented alongside the assessment capacities from the other methods in Figure 12. The fill stiffness dictates the amount of spread at the abutments and the ultimate capacity predicted by the three dimensional nonlinear model is highly sensitive to this parameter.

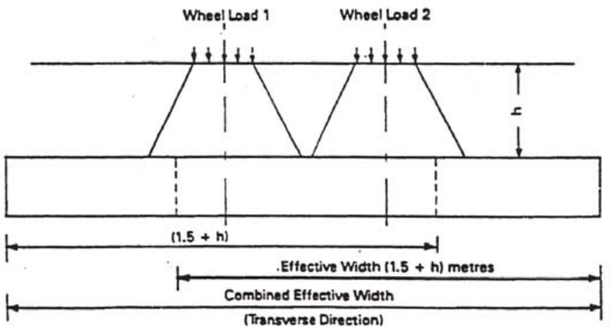

Figure 10. Model for effective width, reproduced from [8].

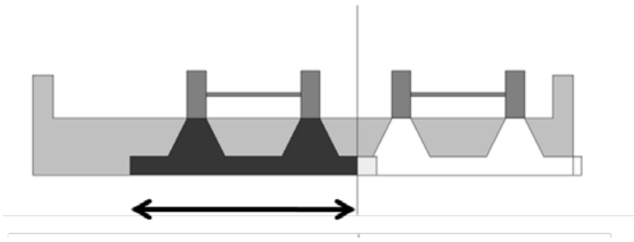

Figure 11. Effect of multiple lanes on effective width.

This variation in assessed capacity with fill stiffness demonstrates the importance of selecting an assessment method which can adequately account for the abutment response where the supports cannot be assumed to be stiff. The MEXE method, the three hinge limit analysis method and the four hinge rigid block limit analysis method cannot account for movement at the abutments and therefore should not be used where the abutments cannot be assumed to be stiff.

The three dimensional nonlinear finite element analysis indicates that the bridge experiences significant transverse bending giving rise to extensive longitudinal cracking and that the predicted failure mechanism is by punch through underneath the heavier axle load. The MEXE method and the limit analysis methods are based on the assumption of the formation of hinges leading to a four hinge mechanism failure and these methods cannot account for any other type of failure mechanism.

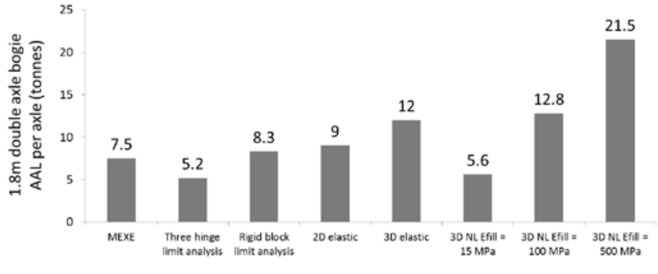

Figure 12. Allowable axle loads for a 1.8m double axle.

7 CONCLUSIONS

While simpler approaches are desirable for the assessment of the majority of arch bridges, they do not capture important structural behaviour affecting the capacity of the bridge. The experimental testing carried out on Griffith Bridge demonstrated a linear response at the service load level and a high level of stiffness at the abutments. These results were used to validate the three dimensional nonlinear finite element model which captures the interaction between the fill, arch barrel and spandrel walls as well as the surrounding soil medium; accounting for the transverse capacity of the arch barrel, providing an accurate representation of axle load distribution and capturing the abutment response. Beyond this level of loading, the finite element model was used to predict the behaviour of the arch bridge under high load levels, the ultimate load capacity of the structure and the associated failure mechanism. The model indicated the formation of longitudinal cracking, transverse cracking, separation at the spandrel arch interface and vertical cracking in the parapet prior to failure by punch through of the arch barrel under the heavier axle load. The assessment capacities for the other assessment methods were shown to be conservative within the limits set out for this particular structure, i.e. stiff abutments and single lane loading. However, they are not able to account for many of the important factors influencing the actual behaviour of the arch and provide very little diagnostic information for bridges exhibiting signs of damage.

ACKNOWLEDGMENTS

The authors gratefully acknowledge the National Roads Authority of Ireland for funding this research under the National Roads Authority Research Fellowship Programme.

REFERENCES

[1] Molloy E. (1988) *Report on inspection, assessment and rehabilitation of masonry arch bridges*, Dublin, Department of the Environment.

[2] Department of Transport (1997), BA 16/97 The Assessment of Highway Bridges and Structures, *Design Manual for Roads and Bridges*, Volume 3, Section 4, Part 4, London, HMSO.

[3] Fanning P.J. and Boothby T.E. (2001), Three-dimensional modelling and full-scale testing of stone arch bridges, *Computers and Structures*, 79(29-30), 2645-2662.

[4] Willam K.J. and Warnke E.D. (1975), Constitutive Model for the Triaxial Behavior of Concrete, *Proceedings International Association for Bridge and Structural Engineering, ISMES*, Bergamo, Italy, Vol. 19, 174-179.

[5] ANSYS Inc. (2010), *ANSYS Help Manual*, Canonsburg, PA.

[6] Drucker, D. C. and Prager, W. (1952), Soil mechanics and plastic analysis for limit design, *Quarterly of Applied Mathematics*, Vol. 10, No. 2, 157–165.

[7] Fanning P.J., Sobczak L., Boothby T.E. and Salamoni V. (2005), Load testing and model simulations for a stone arch bridge, *Bridge Structures*, 1(4), 367-378.

[8] Department of Transport (2001), BD 21/01 The Assessment of Highway Bridges and Structures, *Design Manual for Roads and Bridges*, Volume 3, Section 4, Part 3, London, HMSO.

[9] Harvey W.J. (1988), Application of the mechanism analysis to masonry arches, *The Structural Engineer*, 66(5), 77-84.

[10] LimitState (2007), *Theory and modelling guide, Version 2.0*, Sheffield, Limit State.

[11] Boothby T.E. (2001), Load rating of masonry arch bridges, *Journal of Bridge Engineering*, 6(2), 79-86.

[12] Boothby T.E. and Fanning P.J. (2004), Load rating of masonry arch bridges: Refinements, *Journal of Bridge Engineering*, 9(3), 304-307.

[13] Gibbons, N. and Fanning, P.J. (In Press), Rationalising assessment approaches for masonry arch bridges, *Proceedings of the ICE - Bridge Engineering*.

[14] Davy, N. (1953), *Tests on Road Bridges, National Building Studies Research Paper No. 16*, HMSO.

[15] Chettoe, C.S. and Henderson, W. (1957), Masonry arch bridges: a Study, *Proc. Inst. Civ. Eng. London*, 7(4), 723-762.

Future state prediction of reinforced-concrete bridges allowing for chloride-induced deterioration

Tara Reale[1], Alan O'Connor[1]
[1]Department of Civil, Structural and Environmental Engineering, Trinity College Dublin, Dublin, Ireland
email: realet@tcd.ie, alan.oconnor@tcd.ie

ABSTRACT: This paper proposes a method of predicting the future condition rating of RC bridges subjected to Chloride-induced corrosion. This future state is predicted using a Markovian, integer-based approach, suitable for use with a bridge management system. In the absence of sufficient quantities of inspection information, analytical deterioration models are employed for the different phases. Since chloride-induced corrosion is itself non-linear and non-homogenous in time, the derived state transition probabilities are age-dependant and so non-stationary Markov chains are used to represent structural degradation and predict future bridge condition state distributions with greater accuracy. The analysis is carried out with reported diffusion coefficients and surface chloride content values suitable for calibrating matrices from an Irish perspective. Furthermore, the concrete cover and corrosion rate can also be varied to account for the variability in both environmental and exposure conditions throughout the country. To represent network level condition prediction, the Irish structural stock of RC bridges has been broken down into appropriate age-groups, and an example of the overall model network implementation given. These derived distributions can then be used to help implement maintenance planning and allow for the estimation of future budgets and the development of comprehensive bridge management policies.

KEYWORDS: Bridge Management Systems; Chloride-induced Corrosion; Markov Processes.

1 INTRODUCTION

As bridges age, and environmental concerns and sustainability issues come more and more to the fore, bridge maintenance and management has become a significant challenge. To deal with this problem, Bridge Management Systems (BMS) have been implemented effectively in many countries worldwide (Ireland, US, Switzerland, Denmark etc). In 2008, the IABMAS Bridge Management Committee decided to conduct an investigation on the bridge management systems of the world to be issued in conjunction with the 2010 IABMAS conference. This report was based on the completed questionnaires from 18 bridge management systems in 15 countries. The report found that the majority of these systems have only come into place in the last 10 to 20 years [1], and that of the 18 systems, deterioration is taken into account in 12 of them, although the level of complexity varies widely. The German 'Bauwerk Management System' and the Finnish Bridge Management System appear to be among the most technically advanced, with sophisticated deterioration models which allow for age-behaviour models in the Finnish case and particular deterioration models for specific deterioration mechanisms in the German case. Ireland, as yet does not utilize such deterioration models and so consequently this paper outlines the development of a Markovian-based model suitable for predicting structural degradation due to chloride-ion ingress on RC structures on the Irish road network.

Ideally, given sufficient quantities of inspection data, the deterioration modules of Bridge Management Systems would be calibrated directly from the raw data obtained from inspections. In the meantime however future bridge condition needs to be estimated using predictive models. Naturally, the predictive powers of the system are only as good as the underlying models describing the physical deterioration processes themselves. RC structures deteriorate due to a number of different mechanisms acting in tandem but for application purposes, the deterioration model developed here is based on that of chloride-induced corrosion.

The model is Markovian in nature, due to the fact that the predefined states of condition assigned to structures upon visual inspection lend themselves very well to the discrete states needed for a Markov process. Furthermore, discrete parameter Markov chains, which define distinct states of condition and discrete transition time intervals, are commonly used for modelling bridge deterioration because they eliminate the computational complexity of continuous condition states and simplify the decision-making process [2]. This choice of a Markovian basis also ensures that the developed procedure could be incorporated into a discrete-state Bridge Management System.

2 CHLORIDE –INDUCED CORROSION

Chloride-induced corrosion of reinforcement is one of the major worldwide deterioration mechanisms for steel reinforced concrete structures. Hence, much research has been undertaken in an attempt to develop appropriate deterioration models to help management authorities make informed, cost-effective decisions concerning the time to repair, rehabilitate or replace debilitated structures. The mechanism itself is generally accepted to be electrochemical in nature [3, 4]. The alkaline environment of concrete results in the formation of a passive film of iron oxides at the steel-concrete interface which protects the steel from corrosion. Chloride ions can destroy this passive film and once the layer breaks down, corrosion is initiated. Due to the presence of both moisture and oxygen, a range of expansive, corrosive products (rust) are then formed. These expansive products give rise to tensile stresses on the concrete surrounding the reinforcing bar, which leads to cracking and spalling of the cover layer [3-5].

A conceptual model for service life prediction of corroded RC structures was first developed by Tuutti [6]. Consisting of two phases, the first phase, T_i, represents the time required for the chloride ions to diffuse to the steel-concrete interface, and the surface chloride concentration to exceed a limiting value, thereby initiating corrosion. The second phase, the propagation period, T_{cr}, represents the time after corrosion initiation, as crack generation occurs.

However, further research carried out by Weyers [7] suggested that in fact, not all of the corrosion products contribute immediately to the expansive pressure on the concrete. Instead, some were considered to fill the voids and pores around the reinforcing bar. This porous zone results in dividing the propagation period into two distinct and separate phases. The first, commonly referred to as T_{1st} is the time to the appearance of first crack - generally taken to be a hairline crack of approximately 0.05mm [8-10], and represents the period of free expansion until the rust products reach the concrete and thus initiate cracking. This is depicted diagrammatically in Figure 1. The second propagation phase, T_{sp} is then referred to as the time to severe cracking.

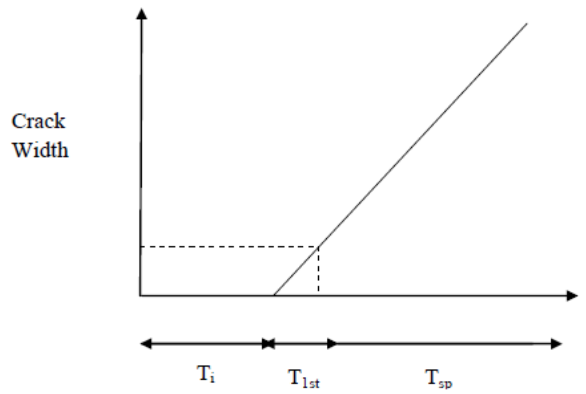

Figure 1. Three-stage chloride-induced corrosion process.

2.1 Modelling of Corrosion Process

A rigorous literature review revealed the existence of many models and methods available to estimate the duration of each deterioration phase [10, 11]. However, the three analytical models outlined below were deemed most appropriate for use, given the end purpose of integrating the model into a bridge condition prediction module. Monte Carlo simulation about a defined mean and variance of the parameters involved was used to construct a database of 2000 bridges over a 100-year return period, suitable for simulating an overall network life-cycle effect. Table 1 lists the statistical parameters of these variables. The analysis was also carried out under the Eurocode specifications for the tensile strength and the effective Young's Modulus of C50 concrete [12].

Table 1. Statistical parameters of random variables used.

Parameter	Units	Mean	COV	Dist.	Literature Reference
Surface Chloride Content, C_0	Kg/m^3	4.57	0.2	*LN*	Lounis et al. [13]
Diffusion Coefficient, D_{app}	m^2/s	9.34 x 10^{-13}	0.2	*LN*	Leung and Lai [14]
Critical Chloride content	Wt% of concrete	0.139	0.375	*N*	Val and Stewart [15]

* *LN*, lognormal distribution; *N*, normal distribution

2.1.1 Time to Initiation

The corrosion initiation phase T_i is generally the longest of the three phases. The duration of this phase is estimated, as is common practice, using Fick's 2nd Law [16]. This is represented as follows:

$$C(x,t) = C_i + (C_s - C_i)\left[1 - erf\left(\frac{x}{\sqrt{D_{app}t}}\right)\right] \tag{1}$$

Where $C(x,t)$ = chloride content at depth of reinforcement x, at time t, C_s = surface chloride concentration, C_i = initial chloride concentration - taken as being 0 for new structures, D_{app} = apparent diffusion coefficient and t = time.

2.1.2 Time to First Crack

This is the time it takes from corrosion initiation to the time of first crack. A model based on that proposed by El Maaddawy and Soudki [5] is used to represent this phase. The original El Maaddawy model however has been modified to take account of an earlier trigonometrical error upon which the El Maaddawy model was derived. This model is as outlined in Reale & O'Connor [17] and is represented in Equation 2.

$$T_{1st} = \left[\frac{7117.5(D+2\delta_0)(1+\nu+\psi)}{i_{corr}E_{ef}}\right]\left[\frac{2(C+D)f_{ct}}{D} + \frac{2\delta_0 E_{ef}}{(D+2\delta_o)(1+\nu+\psi)}\right] \tag{2}$$

The corrosion rate i_{corr} was taken as 1μA as in Al Harthy and Stewart [18]. The thickness of the porous zone, δ_0, is generally taken to be between 10 and 20 μm [19]. However Chernin and Val [20] claim that under the El Maaddawy model, the time to crack initiation is underestimated with porous zones in such a range. In their study they allowed for two thicknesses of porous zone δ_0 to be compared (10 and 20 μm respectively) and found that the latter, larger porous zone gave better results. Ultimately they suggest that the thickness of the porous zone (or more correctly, the amount of corrosion products penetrating into concrete pores and microcracks) may be larger than has been previously estimated. To this end, a larger porous zone of 25 μm was investigated in Reale & O'Connor [17] and was found to bring computed values in line with observed values of previous tests, where they had formerly been out of bounds. Note that this increase in the porous zone is not justified by experimental analysis of the mechanism in question, it merely serves to make the model more suitable for prediction purposes. Further information on this 'modified' method is outlined in Reale & O'Connor [17].

2.1.3 Time to Severe Cracking

The third and final deterioration phase, corresponding to T_{sp} in Figure 1 is referred to as the time to severe cracking. The model used was based on work by Mullard and Stewart [21] and works on the principle that it estimates the time to a specific crack width, up to a limiting value of 1.0 mm. This is quite conducive for the purposes of developing a state-based deterioration system for use in a BMS, since the state limits or bounds can be defined in terms of crack width which can be visually assessed. The equation is represented as:

$$T_{sp} = T_{1st} + k_R \frac{w_{\lim} 0.05}{k_c r_{crack}} \frac{0.0114}{i_{corr}} \quad (3)$$

where T_{sp} = the time to severe cracking, T_{1st} = time to first crack from Equation 2, k_R = the rate of loading correction factor, k_c is a confinement factor which represents an increase in crack propagation due to the lack of concrete confinement around external reinforcing bars – taken to be 1.0 if the reinforcing bar is in an internal location and w_{lim} is the limiting crack width, specific to each condition states. For the purposes of defining state bounds for the system under development, these limiting values are taken to be as represented in Table 2.

Table 2. Markov condition states as applied to chloride-induced corrosion in model.

Condition State	Degradation State
0	$t <= T_i$, Initiation has yet to begin
1	$T_i < t < T_{1st}$, Initiation has begun, before time to first crack
2	$w \leq 0.2$ mm
3	0.2mm < $w \leq$ 0.5mm
4	0.5mm< $w \leq$ 1mm
5	w > 1mm

3 MARKOV THEORY AS APPLIED TO BRIDGE CONDITION DETERIORATION PREDICTION

The physical deterioration models outlined above are then integrated into a discrete state-based Markovian deterioration system in order to develop the model further into one which can be implemented as part of a BMS.

A Markov process itself may be defined by the following equation:

$$P(t) = P_0 * P^t \quad (4)$$

Where:
$P(t)$ = Probability distribution of condition at time t
P_0 = Initial probability distribution of condition
P = A transition probability matrix, the general form of which is given as:

$$\begin{matrix} P_{11} & P_{12} & \dots & P_{1n} \\ P_{21} & P_{22} & \dots & P_{2n} \\ \vdots & \vdots & \dots & \vdots \\ P_{n1} & P_{n2} & .. & P_{nn} \end{matrix} \quad (5)$$

Where (i) For each i, $i=1{:}n, \sum_{j=1}^{n} p_{ij} = 1$. (ii) All matrix entries must be positive.

The expected condition rating $E[X(t)]$ at time t can then be calculated by multiplying the probability distribution vector $P(t)$ by a condition rating vector Q (see Table 2) as shown in Equation 6.

$$E[X(t)] = P(t) * Q^t \quad (6)$$

A discrete time model with fixed time units of one year has been adopted, hence the probability of deteriorating by more than one state (i.e. multiple damage states transitions) may be assumed negligible. This again is common practice [22-24]. Since deterioration only is considered here, it is not necessary to account for the effects of repair and rehabilitation and so P_{ij} = 0 for j < i.

The transition matrix to be populated then with experimental results is as depicted below:

$$\begin{bmatrix} P_{00} & 1-P_{00} & 0 & 0 & 0 & 0 \\ 0 & P_{11} & 1-P_{11} & 0 & 0 & 0 \\ 0 & 0 & P_{22} & 1-P_{22} & 0 & 0 \\ 0 & 0 & 0 & P_{33} & 1-P_{33} & 0 \\ 0 & 0 & 0 & 0 & P_{44} & 1-P_{44} \\ 0 & 0 & 0 & 0 & 0 & 1 \end{bmatrix} \quad (7)$$

Where P_{ij}, represents the probability of starting in state i and transitioning to state j.

Markov chains can be defined as both stationary and non-stationary. Stationary means the process is stable or homogeneous in time, i.e. the probability of going from one state to another is independent of the time at which the step is performed. In mathematical terms, the initial state vector P_0 as shown in Equation 4 will remain the same for all t.
Non stationary chains change with respect to time which implies the use of a different transition matrix before and after t. In this case the vector of probability distribution of condition at time t will become the starting vector of condition for the next chain, which will then proceed with a different transition matrix. For n groups, there are n transition probability matrices, P, and n initial probability distributions, P_0.

$$P(n, t_n) = P_0(n) * P(n)^{t_n} \quad (8)$$

As shown in Reale and O'Connor [25], a non-homogeneous process is deemed best for estimating Markovian transition probabilities over a significant time period, as is the case here, and so they shall be used to enable accurate prediction of future structure condition state.

4 METHOD OF OBTAINING TRANSITION PROBABILITIES

As illustrated in Equation 7, the only variables available to characterise the future or expected state of the structure in question given the stated assumptions, are those on the diagonal of the transition probability matrix. Consequently they need to be as accurate as possible, and so numerous methods abound as to how best to estimate them. Kallen [26] and Madanat and Wan Ibrahim [2] provide a literature review of some of the most common of these approaches, including Maximum-Likelihood estimation, Poisson regression, non-linear minimization, ordered probit models, survival models and so forth. A Non-Linear programming approach however, based on the expected value of condition, is by far the most common technique found in the literature for estimating matrices for bridge and pavement management systems [22, 24, 27]. This is represented in Equation 9.

$$\text{Minimize:} \quad \sum_{t=1}^{N} \left| S(t) - E[X(t)] \right| \tag{9}$$

where *S(t)* = facility condition at transition period *t* based on a regression curve; *E[X(t)]* = expected value of facility condition at transition period *t* based on Markov chains.

Having investigated this objective function however, it has been found that this minimization technique yields insufficiently accurate results, as the condition scale of expected value inherently skews the results. That is, an expected value of 5 has much more weight than an expected value of 1 or 0 for a particular bridge, hence the average network expected rating becomes unrealistically influenced. Instead, it is the expected distribution of condition states which should be minimized. This is shown in Equation 10.

$$\sum_{t=1}^{N} \sum_{n=0}^{n} \left| A(t) - A'(t) \right| \tag{10}$$

where $A(t)$ = the probability distribution of condition rating as defined in the database, $A'(t)$ = the probability distribution of condition rating as computed by the Markov process.

Many algorithms to solve these objective functions have also been investigated - Carnahan et al. [28] used a descent method [29], Jiang et al. [22] utilised the gradient projection method and Costello et al. [30] and Ortiz-Garcia et al. [31] employed the use of another non-linear algorithm; the GRG2 code incorporated into the solver program in EXCEL in their study. However the latter two both concluded that more robust methods ought to be investigated in an effort to improve existing systems. To this end, and since it requires fewer input variables than either Genetic Algorithms or Neural Networks, Reale and O'Connor [25] investigated the use of Cross-Entropy, a robust, iterative algorithm as a means of obtaining more appropriate transition probabilities.

It was found that Cross-Entropy tended to avoid deviating towards solutions on the bound constraints of the problem, hence making it especially suitable for probability estimation. This robustness in obtaining suitable probabilities is most notable in the context of obtaining better solvers for transition probability estimation in bridge management systems. Pontis for instance, the US system, frequently obtains negative and larger than unity transition probabilities [32], thereby indicating that the 'engine' of transition probability determination, i.e. either the solver or optimization objective function in use is inappropriate.

5 MODEL IMPLEMENTATION

Since an age-dependant process was employed, i.e. chloride-induced corrosion is dependant on time, the different matrices in the non-homogeneous chain represented in Equation 8 are dependent on time, or age when applied to a structure. Figure 2 depicts the expected life-cycle curves for four different values of concrete cover over a 100-year period.

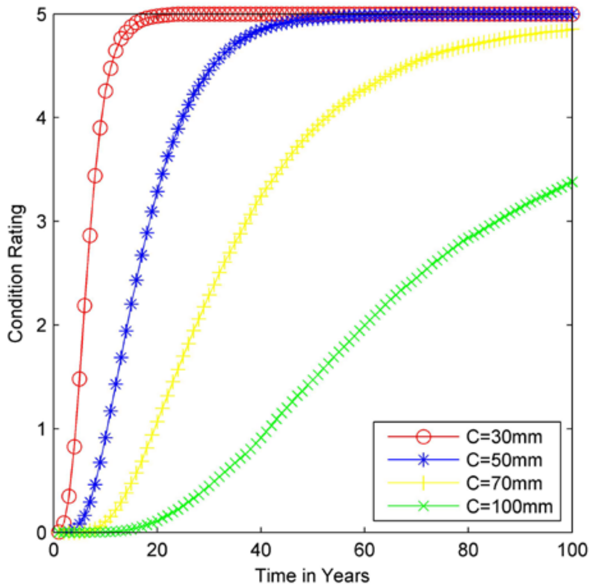

Figure 2. Variation in Assigned Condition Rating with time for different cover depths.

For the simulated 100 year lifecycle, 10 transition matrices each representing structural deterioration in 10 year bands were utilized. Therefore, each curve in Figure 2 is described by 10 Transition Matrices, denoted T1 to T10. Since this means that Transition Matrix 1 represents the expected structural deterioration in the first 10 years of a structures lifecycle, it should only be applied to structures within the limit of these bounds, i.e. structures less than 10 years old. Transition Matrix 2 then represents the expected deterioration of structures aged between 10 and 20 years old. Tables 3 and 4 depict the first two of these matrices, T1 and T2 respectively. Note that 10 year bands were chosen to calibrate the transition matrices as it was felt to be an acceptable timeframe in which to expect the general pattern of network level deterioration to change.

Table 3. Transition Probability Matrix *T*1 for Structural State Deterioration, ages 0-10.

P_{00}	P_{11}	P_{22}	P_{33}	P_{44}	P_{55}
0.98	0.02	0	0	0	0
0	0.84	0.16	0	0	0
0	0	0.84	0.16	0	0
0	0	0	0.89	0.11	0
0	0	0	0	0.95	0.05
0	0	0	0	0	1

Table 4. Transition Probability Matrix *T*2 for Structural State Deterioration, ages 11-20.

P_{00}	P_{11}	P_{22}	P_{33}	P_{44}	P_{55}
0.88	0.12	0	0	0	0
0	0.28	0.72	0	0	0
0	0	0.34	0.66	0	0
0	0	0	0.69	0.31	0
0	0	0	0	0.80	0.20
0	0	0	0	0	1

As expected, P_{00} of *T*1 is extremely high at 0.98, which is as expected, given that the mean-time to corrosion initiation using the given data was 12.5 years, thereby suggesting an extremely high probability of remaining in state 0 throughout that initial 10 year period. Likewise, Table 4 gives the probabilities of transitioning between the defined condition states for structures aged from 11 to 20 years. It can be seen that while P_{11}, the probability of staying in State 1 if it started in State 1 was 0.84 in Table 3 for the first 10 years of the structures life, it has now decreased to 0.28. Again, this is in keeping with the expected results as the mean time to first crack in the developed model was found to be in the region of 2 years. Hence after 14.5 years the structure could be reasonably expected to be in condition state 2 and so P_{12} of 0.72 in Table 4 corresponds to this probable deterioration.

5.1 *Application of Developed Process*

As outlined in Equation 4, the prediction of future bridge condition state is a product of two vectors – an initial state vector P_0 and a Transition Probability Matrix *P*. Since, as stated above, these Transition Matrices have been calibrated on an age-dependant process, and so are inherently age-dependent, they need to be combined with initial state-vectors which are also dependant on age. Upon investigation of the EIRSPAN database, the P_0, initial-state vectors were derived directly to represent the proportion of RC bridges in each 10-year bin. It was found that of the 1576 RC bridges in the system, the age is known for 856 of these and that consequently there are 13 such initial state vectors – one each for every decade until 1900 and then two 50-year bins were utilized to represent structures dating from 1850 to 1900 and 1800 to 1850 respectively. These vectors are listed in Table 5.

Table 5. Initial State vectors of Condition State Distribution for various age-groups of Irish RC bridges.

		State					
#	Bridge Age	0	1	2	3	4	5
1	1800-1849	1	0	0	0	0	0
2	1850-1899	0	0	0	0	0	0
3	1900-1909	0	0	0	0	0	0
4	1910-1919	0	0	0	1	0	0
5	1920-1929	0	0.33	0.33	0.33	0	0
6	1930-1939	0	1	0	0	0	0
7	1940-1949	0	0.67	0.33	0	0	0
8	1959-1958	0	0	0.67	0.33	0	0
9	1960-1969	0	0	0.67	0.33	0	0
10	1970-1979	0.28	0.53	0.29	0	0	0
11	1980-1989	0.07	0.57	0.31	0.05	0	0
12	1990-1999	0.28	0.53	0.17	0.014	0	0
13	2000-2009	0.7	0.23	0.06	0.009	0.002	0

The initial state vectors in Table 5 have been segregated and grouped purely on age. They have not been sub-divided into different environmental categories concerning exposure to chlorides and concrete cover but this can easily be incorporated into the described deterioration model to allow for further accuracy and assessment.

These initial state vectors are then combined with the respective age-dependant transition matrix in order to predict future structural condition ratings as a consequence of chloride-ion ingress. For instance, initial state vector 13 deteriorates initially according to T1 as depicted in Table 3. Initial state vector 12 deteriorates initially according to T2 as seen in Table 4. After the initial ten years then, the first transition matrix *T*1 is no longer utilised in the process, unless of course new structures have been added to the database. Initial state vector 13 now deteriorates according to *T*2, the age-dependant matrix which considers the probability of chloride-induced corrosion in structures 11 to 20 years old. Initial state vector 12 is now combined with T3, corresponding to structures between 21 and 30 years old. P_0 11 is combined with T4 and so forth. Note that since there are only 100 years of transition matrices simulated, i.e. ten matrices, the last transition matrix, corresponding to structures aged 90 years to 100 years is considered to be an absorbing matrix in that all structures more than 90 years old are assumed to follow the deterioration pattern as defined in this matrix.

Utilising the method outlined above, future state distributions for each of the 13 initial age-groups will be obtained. In order to obtain an estimate of predicted network level performance then, the effect of each group is aggregated and weighted according to the number of structures in that particular age-group.

6 CONCLUSION

This paper proposed a method of predicting bridge deterioration in time using non-homogeneous, age-dependant Markovian transition probability matrices. The method was designed with the idea of incorporating it into existing bridge management systems in an effort to improve them. Consequently a robust, previously unused solver in this field – Cross-Entropy, was employed in order to obtain appropriate transition probabilities. Furthermore, the matrices were calibrated based on well-known physical models of chloride-induced corrosion as opposed to purely statistical distributions. As a result, the obtained transition probabilities are as accurate as is inherently possibly, given the limitations in observed field data at the present time. It is envisaged that through the reliable prediction of future structural condition, the model could be used for maintenance planning by allowing for the conjecture of future budgets and the development of comprehensive rehabilitation policies.

ACKNOWLEDGMENTS

This research is funded by the National Roads Authority of Ireland (NRA) and the authors wish to express sincere thanks for the financial support and assistance they have provided.

REFERENCES

[1] Adey B.T., Klatter L. and Kong J.S. (2010), ‘The IABMAS Bridge Management Committee overview of existing Bridge Management Systems’.

[2] Madanat, S. And Wan Ibrahim, W.H. (1995), ‘Poisson Regression Models of Infrastructure Transition Probabilities’, *Journal of Transportation Engineering*, 121(3).

[3] Liu Y, and Weyers R.E. (1998), ‘Modeling the time-to-corrosion cracking in chloride contaminated reinforced concrete structures’, *ACI Materials Journal*, 95(6):675-81.

[4] Bazant, Z.P. (1979), ‘Physical model for steel corrosion in concrete sea structures-theory’. *Journal of the Structural Division*, 105(6):1137-53.

[5] El Maaddawy, T and Soudki, K. (2007), ‘A model for prediction of time from corrosion initiation to corrosion cracking’, *Cement and Concrete Composites*, 29:168-75.

[6] Tuutti, K. (1979), ‘Service life of structures with regard to corrosion of embedded steel’, *Metal Construction*, 1:293-301.

[7] Weyers, R.E. (1998), ‘Service life model for concrete structures in chloride laden environments’, *ACI Materials Journal*, 95(4):445-53.

[8] Vu, K.A.T, Stewart, M.G. and Mullard, J.A. (2005), ‘Corrosion-Induced Cracking: Experimental Data and Predictive Models’, *ACI Structural Journal*, 102(5):719-26.

[9] Mullard, J.A. and Stewart, M.G. (2009), ‘Stochastic Assessment of Timing and Efficiency of Maintenance for Corroding RC Structures’, *Journal of Structural Engineering*, 135(8):887-95.

[10] So, K.K.L., Cheung, M.M.S. and Zhan, E.X.Q. (2009), ‘Life-cycle cost management of concrete bridges’, *Proceedings of the ICE - Bridge Engineering*, Volume 162 (Issue 3):103 –17.

[11] Markeset, G. and Murdal, R. (2008), COIN report 7-2008, Modelling of reinforcement corrosion in concrete - state of the art. SINTEF Building and Infrastructure.

[12] BS EN 1992 (2004), Eurocode 2: Design of concrete structures. Part 1-1 – General rules and rules for buildings.

[13] Morcous, G., Lounis, Z. and Cho, Y. (2010), ‘An Integrated System for Bridge Management using Probabilistic and Mechanistic Deterioration Models: Application to Bridge Decks’, *KSCE Journal of Civil Engineering:* 14(4):527-537.

[14] Leung, W.C. and Lai, T.K. (2002), Maintenance strategy of reinforced concrete structures in marine environment in Hong Kong. In *International Congress on the challenge of concrete construction.* Dundee.

[15] Val, D.V. and Stewart, M.G. (2003), Life-cycle cost analysis of reinforced concrete structures in marine environments. *Structural Safety* 25(4): 343-362.

[16] Suo, Q. and Stewart, M.G. (2009), ‘Corrosion cracking prediction updating of deteriorating RC structures using inspection information’, *Reliability Engineering & System Safety*, 94(8):1340-8.

[17] Reale, T. and O' Connor, A. (*in press*), ‘A review and comparative analysis of corrosion-induced time to first crack models’, *Construction and Building Materials*.

[18] Al-Harthy AS, Stewart MG. ‘A review of predictive models for cracking in concrete due to reinforcement corrrosion’, University of Newcastle, Australia: Centre for Infrastructure Performance and Reliability; 2006.

[19] Thoft-Christensen, P. (2000), ‘Stochastic modelling of the crack initiation time for reinforced concrete structures’, *ASCE Structures Congress*, Philadelphia.

[20] Chernin, L. and Val, D. (2011), ‘ Prediction of corrosion-induced cover cracking in reinforced concrete structures’, *Construction and Building Materials*, 25:1854-69.

[21] Mullard, J.A. and Stewart, M.G. (2010), ‘Corrosion -Induced Cracking: New Experimental Data and Predictive Model’, *The 5th Civil Engineering Conference in the Asian Region and Australasian Structural Engineering Conference*, Sydney.

[22] Jiang, Y., Saito, M. and Sinha, K.C. (1988), ‘Bridge Performance Prediction using the Markov Chain’, *Transportation Research Record 1180*.

[23] Morcous, G., Lounis, Z, Mirza, M.S. (2003), ‘Identification of Environmental Categories for Markovian Deterioration Models of Bridge Decks’, *Journal of Bridge Engineering*, 8(6):353-61.

[24] Baik, H.S., Jeong, H.S. and Abraham, D.M. (2006), ‘ Estimating Transition Probabilities in Markov Chain-Based Deterioration Models for Management of Wastewater Systems’, *Journal of Water Resources Planning and Management*, January/February:15-24.

[25] Reale, T. and O'Connor, A.J. (2012), ‘Cross-Entropy as an Optimization Method for Bridge Condition Transition Probability Determination’, *Journal of Transportation Engineering*, 138(6):741-750.

[26] Kallen, M.J. (2007), *Markov Processes for Maintenance Optimization of Civil Infrastructure in The Netherlands*, PhD Thesis, Delft University of Technology, The Netherlands.

[27] Morcous, G. (2006), ‘Performance Prediction of Bridge Deck Systems Using Markov Chains’, *Journal of Performance of Constructed Facilities*, 20(2):146-55.

[28] Carnahan, J.V., Davis, W.J., Shahin, M.Y., Keane, P.L. and Wu, M.I. (1987), ‘Optimal Maintenance Decisions for Pavement Management’, *Journal of Transportation Engineering*, 113(5):554-72.

[29] Fletcher, R. and Powell, M. (1963), ‘A rapidly convergent descent method for minimization’, *Computer Journal*, 6:163-8.

[30] Costello, S.B., Ortiz-García, J.J. and Snaith, M.S. (2011), ‘Analytical Tool for Calculating Transition Probabilities for Pavement Performance Prediction’, *TRB 2011 Annual Meeting*, Washington D.C.

[31] Ortiz-Garcia, J.J, Costello, S.B., Snaith, M.S. and Godfrey, M.S. (2006), ‘ Derivation of Transition Probability Matrices for Pavement Deterioration Modeling’, *Journal of Transportation Engineering*, 132(2):141-61.

[32] Fu, G. and Devaraj, D. (2011), ‘Structure lifecycle as a non-stationary random process’, *ICASP '11 - Applications of Statistics and Probability in Civil Engineering*. Zurich: Taylor & Francis Group, London; p. 626-33.

The design and construction of Glanmire bowstring arch bridge

Conor McGuinness[1], Aonghus O'Keeffe[2], Mark Kilcullen[2]
[1]Iarnród Éireann, Track & Signal HQ, New Works, Inchicore, Dublin 8, Ireland
[2]Roughan & O'Donovan Consulting Engineers, Arena House, Arena Road, Sandyford Dublin 18, Ireland
email:, conor.mcguinness@irishrail.ie, aok@rod.ie, mk@rod.ie

ABSTRACT: As part of the Iarnród Éireann Glounthaune to Midleton Railway Scheme, Roughan & O'Donovan was commissioned to provide design services to facilitate the closure of a level crossing at Woodhill, Co. Cork. A feasibility study showed that the optimum solution was the construction of a road bridge to replace the level crossing. Various design options were investigated for the bridge, the outcome being a 28m span bowstring arch structure spanning the railway and the N8 Glanmire Road. The site was bounded by steep escarpments and residences to the north and the River Lee to the south, while the live road and railway provided further constraints to the design and construction of this scheme. The southern approach embankment was constructed in the tidal river following an initial archaeological survey and with careful environmental monitoring throughout. To minimise the amount of work to be carried out over the live road and railway, the structural steelwork and in situ concrete deck were assembled on the partially completed river embankment and lifted into place during a railway possession. The curved form of the steel arch and the approach embankments coupled with the high quality finish contributed to providing a distinct though appropriate feature on the eastern gateway to Cork City.

KEY WORDS: Bowstring arch; Composite deck; Heavy lift; Level crossing closure; Marine environment; Railway overbridge.

1 INTRODUCTION

As part of the Iarnród Éireann Glounthaune to Midleton Railway Scheme, Roughan & O'Donovan was commissioned to provide design services to facilitate the closure of railway level crossing XC241at Woodhill, Co. Cork. This paper describes the stages of the design process, including feasibility, options selection and detailed design. The construction of the scheme is outlined and conclusions regarding the success of the scheme are provided.

2 NEED FOR THE SCHEME

2.1 Level Crossing Closure

The Cork to Cobh railway line is parallel to the Lower Glanmire Road and the River Lee on the immediate approach to Cork train station. This section of line contained a group of level crossings which have been historically troublesome for Iarnród Éireann, users and the local authority. A number of them were removed over time leaving three level crossings XC238, XC241 and XC243 remaining. XC243 was user operated and was closed in 2008 as part of the Level Crossings Programme. The others were railway operated serving 27 properties and the listed Carraig House. The crossing gates were located immediately adjacent to the N8 footpath and caused road traffic to back up when in use. There were significant operational problems caused by the presence of the crossings and a temporary speed restriction was imposed to reduce the risk at one. Concerns were expressed by the Railway Safety Commission about the operation of the crossings in the light of the proposed reopening of the railway line between Glounthane and Midleton, which would double the number of passenger trains through these crossings in both directions. Although efforts had progressed over many years to remove the level crossings, the planned reopening of the railway provided sufficient impetus for expenditure on a significant component of infrastructure at this very sensitive location.

Figure 1. Level crossing XC241.

2.2 Site Description

XC241 facilitated access from the N8 Glanmire Road to houses on the north side of the railway. The houses are situated at the base of steep escarpments. The hillside has significant tree cover and is designated a Special Area of Conservation.

South of the crossing, the Lower Glanmire Road runs alongside the River Lee. This part of the river is tidal and is approximately 140m wide.

2.3 Feasibility Study

Due to the requirement to retain access to the houses on the north side of the railway, straight closure of the level crossing was not an acceptable solution. The feasibility study investigated a number of alternative solutions:

- Road access down the escarpment from the north in three different configurations;
- The provision of remote control of the crossing via CCTV;
- The construction of a vehicle and pedestrian bridge over the railway.

Gradients and space restrictions prevented the advancement of the road access options from the north. The CCTV scheme would have required extensive realignment of the N8 over a length of approximately 400 m to facilitate two cars queuing to access the N8 after using the level crossing. This would have involved reclamation of up to 15m width from the river Lee over the 400m length. As well as the initial capital cost of installation, CCTV control requires ongoing operational expenditure.

For the bridge solution, the limited space available between the road and railway necessitated the construction of the southern approach in the River Lee. Therefore, the bridge spans the N8 and railway. The feasibility stage scheme included a retained roadway running east and west to facilitate access to all properties.

Having reviewed the solutions, it was determined that the bridge over the road and railway was necessary.

2.4 Design Options

The scheme layout is shown in Figure 2. The design of the bridge and its approaches required careful consideration due to the setting, as follows:

- The site is located in a Special Area of Conservation with cultural, heritage, landscape and environmental interests to be protected;
- The location of the bridge is on a principal access route to Cork city;
- The bridge would be highly visible to marine vessels arriving in Cork;
- The topography, setting, and physical constraints on the scheme provided a natural opportunity to offer a landmark and gateway structure for Cork.

Three structural options of high architectural merit were proposed as shown in Figure 3. The first option entailed the construction of a single span steel bowstring arch. The bridge would be accessed to the south by a solid approach embankment outside the existing quay walls.

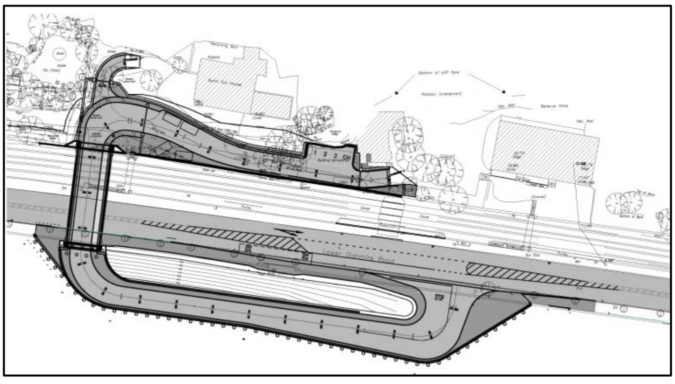

Figure 2. Scheme layout.

The second option involved the construction of a two span curved prestressed concrete beam structure with single inclined pier in the river. This option was considered to be over intrusive given the depth of construction required for the deck. The costs associated with temporary works during construction worked against this option also.

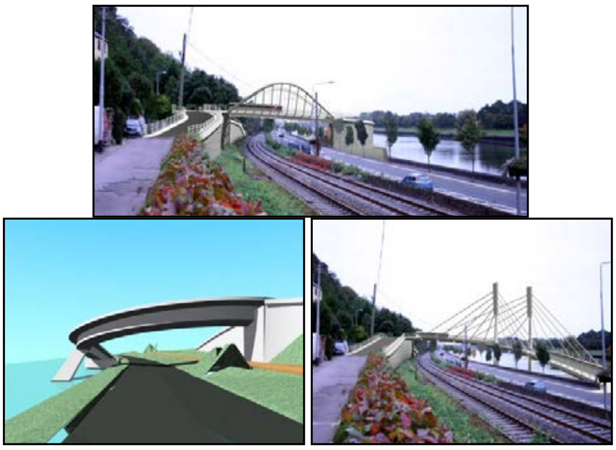

Figure 3. Alternative bridge options.

The third option involved the construction of a cable-stayed bridge with twin pylons carrying both the main span and the approach ramp. While a visual impact assessment showed this option to be less intrusive than the arch, the arch emerged as the preferred choice on evaluation of all assessment criteria.

3 PLANNING

Planning for this scheme was secured as part of the Glounthaune to Midleton Railway Order process. An Environmental Impact Statement was prepared with supporting studies. Critical issues included the visual impact of the scheme, heritage, the construction impacts on residents, the public and the railway, pollution control and the presence of contaminated materials, the impact of the structure on avian flight paths and the impact of the works on the hydraulic regime of the river. The decision in favour of the scheme excluded permission for a roadway west from the bridge to facilitate the closure of XC238 where CCTV control was ultimately installed.

4 PRELIMINARY AND DETAILED DESIGN

4.1 Design Standards

The scheme was designed in accordance with the National Roads Authority Design Manual for Roads and Bridges (NRA DMRB) [1]. As the bridge is carrying a limited amount of local traffic and the approaches include tight bends, the bridge was designed to carry HA and 37.5 units of HB loading, as well as the other permanent and transient loads, in accordance with BD 37/01 [2].

The structural steelwork and reinforced concrete were designed to the relevant parts of BS 5400 [3]. However, the design of steel members subject to the combined effects of torsion and bending is not specifically covered in BS 5400 Part 3. Therefore, the steelwork was designed for these combined effects using the recommendations of SCI Publication 057 [4].

4.2 Aesthetics

The profile of the steel arch, Figure 4, was designed to make a contemporary statement while referring to historical structural forms, materials and finishes in keeping with the setting.

The southern approach embankment was kept as short as possible to minimise the intrusion on the landscape. Also, it was located to the east of the bridge crossing to limit the impact on the views from the nearby Myrtle Hill Terrace.

To match and respect the existing infrastructure, the bridge abutments and walls on the approaches were designed to be clad in coursed random rubble masonry. This also limited the apparent scale of the southern approach. Figure 14 illustrates the extensive masonry on the scheme.

The aesthetic configuration of the arch was heavily influenced by technical elements of the design. The decision to bench the arch supports into the abutments was driven by the presence of visually solid containment to the railway and the need to manage movement joints at bridge ends discretely and effectively. The arch geometry combining straights and a radius assisted with steelwork detailing while providing an elegant form. This was supplemented by the tapered trapezoidal configuration of the arch cross section detailed to interface seamlessly with the deck edge beam. The configuration facilitated the use of steel plate without bending or distortion in fabrication. Another significant driver of the aesthetic configuration was the constraint on visual impact. This dictated the lowest practicable deck level. While the arched configuration itself facilitated this, the transverse design of the deck was configured to enhance the effect. The transverse steel members were made composite with the deck slab and the sequence of construction was configured so as to take best advantage in design. In addition, the transverse deck components were depressed relative to the edge beams to the degree that they manifest a pronounced saddle configuration visually evident in passing under the bridge.

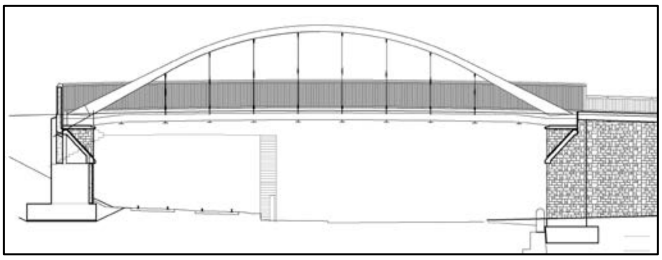

Figure 4. Bridge elevation.

4.3 Southern Approach Embankment

Ground investigations showed the overburden layers in the river bed to be soft silts of thickness 1 – 4 m above dense alluvial gravels of up to 8 m thickness. It was decided to excavate the silt and replace it with Class 6 granular fill up to high water level. This would provide the foundation for the southern approach embankment. The extent of the excavate and replace was to be defined by a line of concrete piles bored to bedrock. The piles were included provide enhanced stability to the embankment and to reduce embankment settlement due to lateral movement at the toe. The Contractor proposed an alternative design for the embankment during construction which was accepted and is described in Section 5.4 below. Granular fill below water level is protected by rock armour. An embankment section is shown in Figure 5.

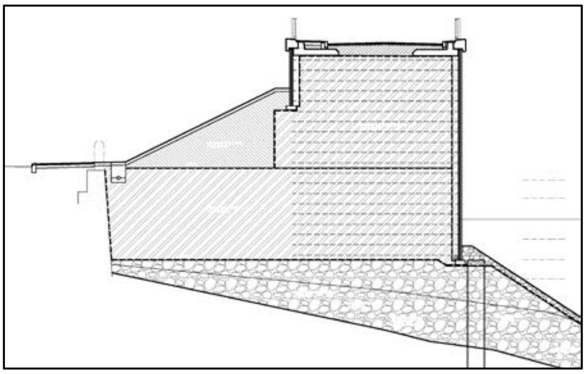

Figure 5. Cross section through south embankment.

Above water level, the embankment comprises the Terratrel reinforced earth system clad in masonry. The approach parapets are supported on precast edge beams which are stitched onto in situ reinforced concrete restraining slabs.

A hydraulic study was carried out by the Hydraulics and Maritime Research Centre, University College, Cork. It modelled the impact of the proposed river embankment works on the flow conditions. A pre-existing model of the river was calibrated using flow and level measurements made by Irish Hydrographics Ltd. for this scheme. River flows were modelled to represent the river condition before and after the works. The effect of varying the embankment profiles was examined so as to determine the configuration which impacts least on the river hydraulics while remaining cost effective and buildable.

The scheme required works either side of the existing quay walls. The geotechnical investigation was configured so as to confirm the construction and formation of the existing quay wall. Initial visual inspections of the walls showed a mix of quality and type of masonry construction. Portions of the wall comprise cut stone in sandstone and limestone. Other portions comprise very poor quality open jointed masonry construction in limestone and sandstone.

Slit trenches and boreholes were carried out at locations along the wall, and these indicated gravels and silts in the vicinity of the wall.

Remedial treatments had been carried out to the wall at intervals over its lifetime. Visual inspection confirmed the presence of sheet pile rock filled protection and a concrete plinth at bed level at various locations along the wall.

4.4 Foundations and Substructure

The proximity of the bridge abutments to the road and railway required that they be designed to resist impact loads. The loads were determined in accordance with the NRA DMRB for road vehicles and UIC 777-2 [5] for rail traffic. The geometry of the large abutments ensured that they have a large mass and high section capacities to resist the impact loads.

The location of the bridge on the side of a river valley led to considerable differences in rock head level at each abutment. The north abutment base is founded directly on siltstone and sandstone bedrock and mass concrete.

However, the silts and gravels in the river bed were not appropriate for supporting the south abutment. As such, nine bored cast-in-place piles were required, each with a 5m rock socket. The slightly weathered mudstone rockhead in this area was found at 6 to 8 m below datum.

The bridge abutments were predominantly in situ concrete while small sections with complex geometry were precast, see Figure 6. The space limitations and difficulty of access precluded the inclusion of abutment galleries. Inspection of the bearings and joints is possible from the front of the abutments and a removable mesh screen was provided to protect the bearing shelf from nesting birds.

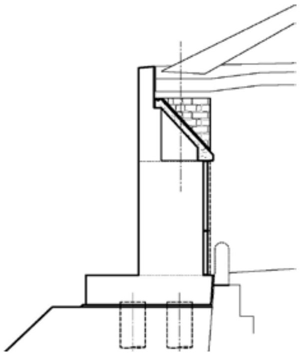

Figure 6. Cross section through south abutment.

4.5 Bridge Superstructure

The bridge deck is supported by twin 28m span arches, 5.5m high with vertical Macalloy tension bars at approximately 2.5m centres. The deck comprises UB transverse beams made composite with an in situ deck slab, as shown in Figure 7.

The profile of the trapezoidal top chord was carefully designed and modelled in 3D to facilitate fabrication. The slopes of the side faces of the chords were optimised to provide structurally efficient sections while minimising the potential of glare for train drivers below.

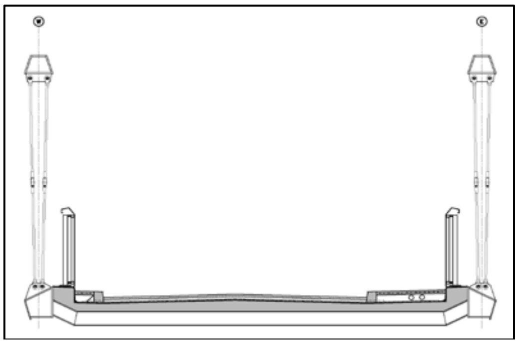

Figure 7. Deck cross section.

The superstructure is supported on six bearings, two mechanical bearings below the middle of the end diaphragms and four elastomeric bearings below the ends of the arches.

A series of analysis models was developed for the superstructure. A linear-elastic global 3D frame model, with the composite deck represented by a grillage, provided the design load effects for the structural members. A similar model was developed for the Category 2 check, using beam and shell elements to represent the deck. An eigenvalue analysis was performed on the 3D frame model to establish the effective length of the arch. A geometric non-linear analysis model, based on the 3D frame model but with geometric imperfections included, was used to check the outcome of the buckling analysis. Finally, finite element analysis models were developed of the steelwork above the corner bearings, and the connections between the tie rods and the top and bottom chords (Figure 8). Where necessary, material non-linear analysis was performed to confirm the capacity of the steelwork at ULS. Figure 9 shows a selection of images which illustrate the complexity of steelwork.

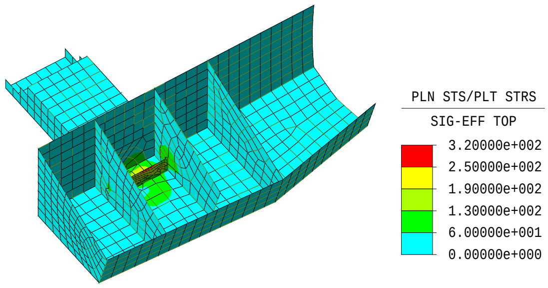

Figure 8. Elastic SLS stresses, support steelwork (N/mm^2).

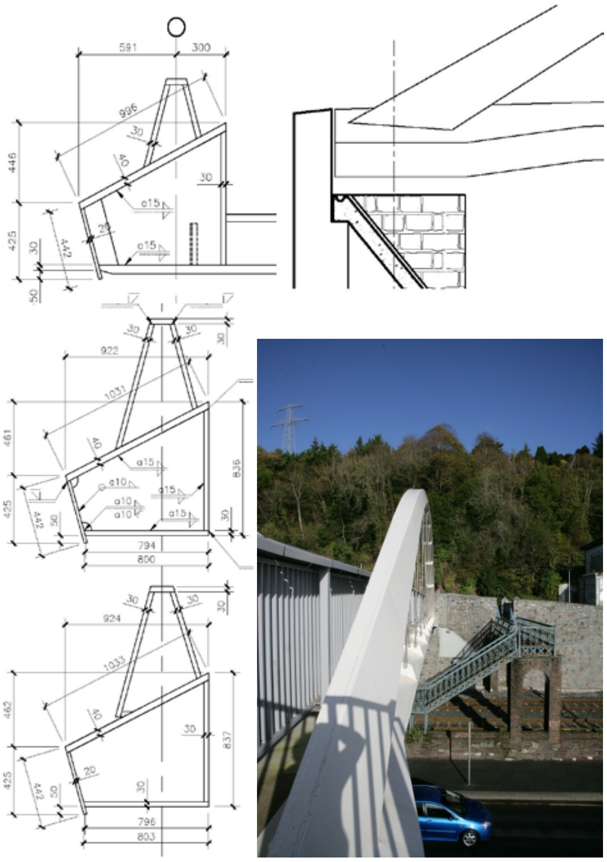

Figure 9. Arch steelwork details, .

5 CONSTRUCTION

5.1 Construction Contract

The construction contract was tendered under the framework for the Iarnród Éireann Level Crossings Project. The contract was awarded to BAM Civil Ltd. and works commenced on site in August 2008.

The FIDIC Conditions of Contract for Construction [6] were utilised for the scheme and the contract documents were based on the National Roads Authority Manual of Contract Documents for Road Works [7].

5.2 Preliminary Works

An important aspect to the construction phase was minimising the impact of the works on local residents, road rail and river users. A temporary traffic management plan was implemented to manage the N8 and facilitate the use of the level crossing by local residents until such a time as the bridge could be opened to public traffic.

Following an initial desktop study, an underwater archaeological survey recorded that nothing of particular note existed in the area of the river bed affected by the works. Environmental monitoring of the river water quality was carried out prior to any river works and regularly until after the completion of works in the river.

5.3 Southern Approach Embankment

BAM proposed an alternative design for the foundations of the southern embankment. The extent of the excavate and replace was increased, thus facilitating the removal of the line of bored piles from the design. Two layers of Stabilenka soil reinforcement were placed below the reinforced earth embankment to improve the foundation stability. Figure 10 shows the construction of the south approach embankment in progress.

Figure 10. Construction of the south approach embankment.

Contamination testing recorded the existence of chlorides, sulphates, selenium and hydrocarbons in the river bed silt. Although it was envisaged in the Contract that the contractor would dispose of the contaminated material at licensed facilities, the contractor secured a permit to dump the material at sea.

Excavations were carried out from a floating barge tied off to the quay wall. Mackintosh probing was employed to ensure that excavations had reached the alluvial gravels prior to installation of the granular fill material. The probe results were cross-referenced to telemetry in the excavator, which experienced greater resistance once the gravels were reached.

Figure 11. Construction of the southern rock armour, masonry and abutment.

During the final stages of the silt replacement activity, a section of the quay wall fell into the river. A temporary road closure was enacted while remedial works were put in place and this section of the works was temporarily suspended while the stability of the works was confirmed. The design of the works was subsequently adapted to incorporate the remedial measures.

5.4 Piling

Piling operations were carried out by a specialist subcontractor. The satisfactory completion of static load test confirmed the design assumptions and enabled permanent piling works to commence. The partially completed southern embankment was used as the piling platform and permanent casings were used on the piles.

Telemetry from the rock boring rig confirmed the level of competent limestone and determined the start of each rock socket. These levels were compared to the results of the rotary cores from the ground investigation. Following the cleaning of the pile bore, concrete was installed using a tremmie pipe and the reinforcing cage was plunged into the wet concrete.

Figure 12. Preparations for the bridge deck lift.

5.5 Steelwork

BAM appointed Thompson of Carlow to carry out the fabrication of the bridge steelwork. The design, construction and fabrication teams worked closely to agree on the optimum fabrication methodology. A rigorous quality assurance procedure was employed during fabrication, with frequent monitoring carried out by independent inspectors on behalf of Iarnród Éireann.

The completed steelwork was transported to Keep Ltd. in Antrim for application of the corrosion protection. The paint specification required the application of aluminium metal spray prior to the epoxy base and intermediate coats. Aluminium metal spray provides a long-term corrosion protection to the steel structure due to the formation of insoluble salts produced on the surface of the metal.

The application of the thermal metal spray requires a high level of steel cleanliness and surface profile, achieved through dry shot blast cleaning. Atmospheric conditions were carefully controlled to maintain the steel finish between the time of blasting cleaning and spraying, and to ensure that the temperature of the steel was within the defined limits.

While it was envisaged that final assembly of the steelwork could be carried out elsewhere along the river before floating the structure to the site, BAM constructed a working platform on the south embankment above the tidal zone. This enabled delivery of the steel components directly to site. Enclosures were set up to achieve the atmospheric conditions necessary for site welding and painting. As per the shop works, the site works were independently monitored to ensure that the high quality of finish was maintained.

The MacAlloy rods were installed and tensioned by a specialist. The anticipated tensile forces at various construction stages were defined on the design drawings and were used by the specialist to inform the tensioning process.

5.6 Composite Deck

To facilitate the composite action in the deck from first application of load, it was necessary that the temporary formwork for the deck slab be supported independently of the steelwork. Once the concrete had gained sufficient strength, the formwork was lowered in a controlled staged fashion to limit the shear stresses induced on the slab.

Figure 13. Superstructure installation.

5.7 Superstructure Installation

The contract required the installation of the structure in a single lift with the deck slab and parapets in place. While this necessitated a large crane to lift the 324 tonnes, it minimised the subsequent works required over the live road and railway. The inclusion of the parapets provided a safer working area on the bridge deck once it was lifted into place.

Bespoke lifting straps, as well as their connections to the end diaphragm beams, were included in the design. A 600 tonne mobile crane lifted the superstructure into place in April 2009. The crane requires 14 hours to mobilise with the assistance of a slave crane and it was necessary to take possession of the Lower Glanmire Road and the railway for a long weekend.

Figure 14. Completed bridge, masonry cladding and existing footbridge.

Temporary supports were installed on each abutment to restrain lateral movement of the bridge until the grout below the mechanical bearings had gained strength. Figure 13 shows the bridge lift in progress.

5.8 Finishes

The bespoke parapets along the south approach and over the bridge provide N2 vehicular containment. This was considered acceptable over and alongside the railway due to the low speed environment of the access road. The bridge parapets were faced with perforated plate and extend to 1.8 m above footpath level. All steel parapets were galvanised and painted.

Figure 15. Aerial photograph of the completed scheme.

Architectural lighting was installed below the bridge. Lights were positioned to provide illumination to the underside of the steel arches. Accommodation works included the provision of new boundary walls to residences on the north side as well as automated gates and improved car parking. Navigation lights were installed at both ends of the southern embankment.

The masonry cladding throughout the scheme was specified to include red and grey limestone indigenous to Cork. The pattern was carefully stipulated and a number of trial panels were constructed to ensure that the final product was as envisaged in the design.

6 CONCLUSION

The successful completion of the Iarnród Éireann Glanmire Road Railway Bridge marks the start of a new relationship between residents who have traditionally used the level crossings on Lower Glanmire Road and the railway. It provides a new landmark for those living and arriving in Cork and marks the completion of the Glounthaune to Midleton Railway Scheme. The scheme was fraught with significant challenges from the outset and the project team is grateful for contributions of all parties to the scheme.

REFERENCES

[1] National Roads Authority, *NRA Design Manual for Roads and Bridges*, NRA, Dublin, updates to 2008;

[2] National Roads Authority, *NRA Addendum to BD 37/01 – Loads for highway bridges*, NRA, Dublin, 2002;

[3] British Standards Institution, *BS 5400 – Steel, concrete and composite bridges*, BSI, London, 1978 to 2005;

[4] Nethercot, D. A., Salter, P. R., Malik, A. S., *Design of Members Subject to Combined Bending and Torsion*, Steel Construction Institute, Publication 057, Ascot, 1989;

[5] Union Internationale de Chemins de Fer, *UIC 777-2 – Structures built over railway lines – Construction requirements in the track zone*, UIC, Paris, second edition, 2002;

[6] Fédération Internationale des Ingénieurs-Conseils, *Conditions of Contract for Construction for Building and Civil Engineering Works Designed by the Employer*, FIDIC, Geneva, first edition, 1999;

[7] National Roads Authority, Manual of Contract Documents for Road Works, NRA, Dublin, updates to 2008.

Development of a 15^o skew FlexiArch^{TM} bridge

Paul Mc Nulty[1], Susan Taylor[1], Desmond Robinson[1], Adrian Long[1]
[1]School of Planning, Architecture and Civil Engineering, Queen's University Belfast, David Keir Building, Stranmillis Road, Belfast, Northern Ireland, BT9 5AG
email: pmcnulty06@qub.ac.uk, s.e.taylor@qub.ac.uk, des.robinson@qub.ac.uk, a.long@qub.ac.uk

ABSTRACT: A novel system for constructing an arch from a flat bed of voussoirs connected together by a polymeric membrane has been developed by Queen's University Belfast. This FlexiArch patented system avoids modern durability issues of rebar corrosion as it requires no internal reinforcement. This research involved the design, construction and testing of a third-scale 15^o skew FlexiArch system which forms an S-shape in the flat form and has torsional forces which do not occur in the equivalent square arch. A square spanning bridge spans a crossing at right angles. However, it is common for a bridge to span at an oblique angle. Square span arches may still be used but the more structurally efficient, sustainable and lower carbon choice is a skew arch. The skew FlexiArch was loaded to failure at the third span point, and the results were compared to the equivalent maximum European special vehicle (SV) axle load. The results obtained from the testing were compared with an analytical model and a non-linear finite element analysis model to validate the analysis and to enable a parametric study on a wider variety of variables without the need for further physical testing.

KEY WORDS: Arch; Concrete; FlexiArch; Non-linear finite element analysis; Polymer reinforcement; Pre-cast; Skew.

1 INTRODUCTION

Masonry arch bridges are structurally efficient, aesthetically pleasing and highly durable structures which have been in use for over 2000 years. Arch bridges were originally built of stone or brick but are now generally built of reinforced concrete or steel. The introduction of these materials allowed longer span and lower height arch bridges to be installed faster as they are manufactured as pre-cast concrete or assembled on site in steel. However, a common problem with such bridges is corrosion of steel and particularly reinforcement. The UK Highway Agency [1] states that consideration shall be given to all means of reducing or eliminating the use of corrodible reinforcement and includes the use of plain concrete structural elements. It also recommends the use of the arch form of construction where ground conditions permit. However, a major constraint in the construction of masonry arch bridges at present is the time and labour costs associated with the temporary formwork, or centering, and the masonry arch formation.

Hence, an arch bridge system with low or zero amounts of corrodible reinforcement which does not require centering has been developed under a Knowledge Transfer Partnership (KTP) through Queen's University Belfast. This flexible arch system can be fabricated off site and transported to site flat and lifted into position [2]. This form of construction makes the flexible arch cost competitive with other forms of bridges while offering superior durability and lower long term maintenance. The procedure for the construction of the flexible arch is simple. The individual voussoirs are cast in concrete, cured and placed adjacently on a construction bed. A polymeric reinforcement is placed on top of the voussoirs and is connected via a top screed (Figure 1). The polymeric reinforcement consists of a polyester filament core with a polyethylene sheath. There are both longitudinal and transverse polymer elements. When the flat arch is lifted at three lifting points, the tapered cross-section of the voussoirs enables the arch to form with the desired dimensions. A spandrel wall is positioned at the elevation of the bridge, which acts as permanent formwork for the granular backfill.

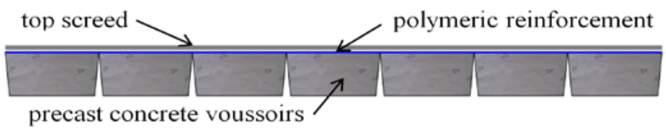

Figure 1. Fabrication of the Flexible Arch.

A square spanning bridge spans a crossing at right angles. However, it is common for a bridge to span at an oblique angle. Square span arches may still be used but the more efficient and sustainable choice is a skew arch, as shown in Figure 2. The square arch requires a width x, with the equivalent skew arch bridge having a lesser width y, and is therefore more efficient and uses less space.

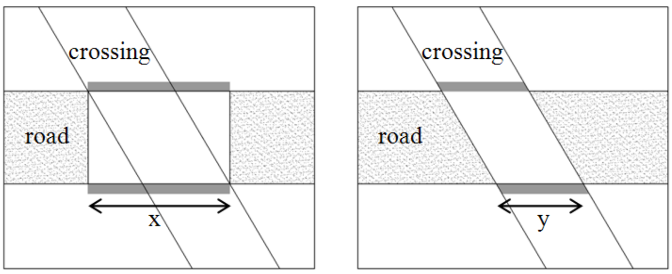

(a) Square arch (b) Equivalent skew arch

Figure 2. Advantage of a skew arch.

Theories of skew arch behaviour have been presented in the past [3 to 6]. However, there is little experimental research to validate these theories. Therefore, a major objective of this research was to analyse the behaviour of the skew FlexiArch system. A third scale 5m x 2m (span x rise) FlexiArch system with a 15^{o} skew angle was tested with the materials scaled accordingly. The arch details are presented in Table 1. The arch was loaded at the third span as this was shown in the numerical modelling to have the most adverse affect on the arch system, and corroborated the findings of Heyman [7].

Table 1. Arch details.

	Full Scale	Third Scale
Voussoir dimensions (mm)	324, 200, 300	108, 67, 100
Clear span (m)	5.00	1.67
Intrados rise (m)	2.00	0.67
Depth of arch ring (m)	0.24	0.08
Width of arch ring (m)	1.00	0.33
Number of longitudinal polymer elements	12	4
Longitudinal polymer element strength (kN)	6.0	6.0
Transverse polymer element strength (kN)	3.4	3.4
Arch ring compressive (N/mm^2)	40	40
Backfill type	Type 3 GSB	Third scale of Type 3 GSB

The results obtained from the experimental programme are compared against an analytical model used to predict the forces in the polymeric membrane, and a finite element analysis model of the FlexiArch system being loaded at the third span. Providing that the models can be proven to accurately represent the behaviour of the skew arch, they can then be used to conduct a parametric study on a wider variety of variables, eliminating the need for further physical testing.

The corresponding and considered values for the serviceability limit state (SLS) in this paper are a SV axle load of 150kN [8], which would typically be applied over a 3m notional lane. A 1m wide arch ring would therefore take a load of 50kN (150kN / 3). As this experiment is a third scale model of a three dimensional arch ring, a load of 5.6kN (50kN / 9) is used to relate the results from this experiment to practical full scale structures.

2 EXPERIMENTAL PROGRAMME

The desired angle of skew is created by varying the step distance between the voussoirs when they are in the flat form. The step distance has to vary to enable a consistent angle of skew across the span of the arch as the voussoirs at the crown of the arch have a larger horizontal projection than those at the abutments, due to the decreasing vertical angle of the voussoirs from the springing to the crown. This results in a higher step distance between the voussoirs at the crown, forming an S-shape when flat (Figure 3).

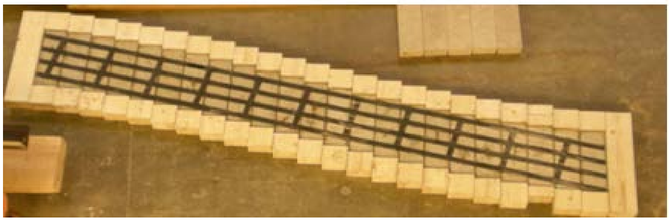
Figure 3. Voussoir alignment and polymer for casting screed.

The skew FlexiArch was lifted at three lifting positions as shown in Figure 4. Electrical resistance strain gauges were used to measure the strains in both the longitudinal and transverse polymer elements at the two outer lifting points. Previous testing of the FlexiArch [9] focused on the strains in the longitudinal polymer elements but these tests were on systems with no skew. The introduction of the skew could cause strains in the transverse polymer elements due to torsional effects caused by the line of action of the forces due to self weight. The arch was lifted and lowered three times, with the strains in the polymeric reinforcement recorded at every 60mm increase in the lifting height at the crown.

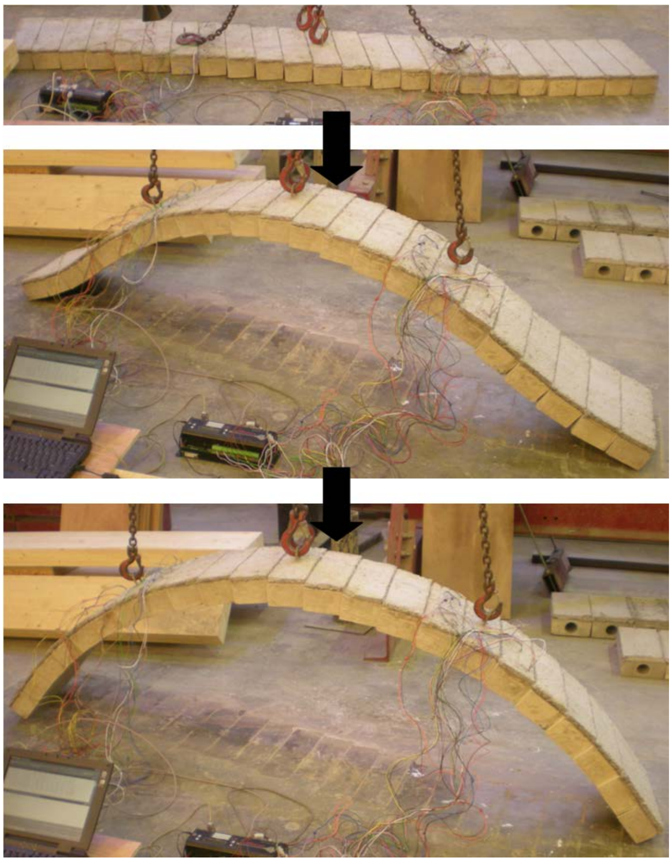
Figure 4. Lifting the skew FlexiArch.

The arch was lifted into position under an accurately calibrated 600kN capacity hydraulic actuator. Backfill was applied with formwork providing horizontal support and simulating spandrel walls in the full scale system. The use of a transparent thermoplastic sheet enabled visual observation of the behaviour of the arch during backfilling and loading. Polystyrene wedges were used to fill the stepped gaps between the voussoirs and the spandrel (Figure 5). The polystyrene contained the backfill but did not contribute to the strength of the system. The well graded and appropriately scaled granular backfill was based on the 'Type 3 GSB' fill and was compacted in 200mm layers using a vibro compactor.

Figure 5. Backfilling the skew arch.

A rigid steel loading plate 150mmx330mm was placed at the loading point in order to distribute the load over the full width of the arch ring and to simulate a 150kN SV axle load. Two test loads were applied prior to the arch being loaded to failure. Displacement transducers and vibrating wire strain gauges measured the displacement and the strains on the arch ring intrados at critical locations and at each increment of load.

3 EXPERIMENTAL RESULTS

Figure 6 shows the average change in forces in the longitudinal polymer elements during three consecutive lifts (based on the measured strains). As expected, the greatest force occurred when the arch ring was fully suspended from the ground during the first lift; when the screed first cracked and induced additional strains in the polymer. The tensile strength of a longitudinal polymer element is 6kN [10]. With an average force of 0.65kN in the longitudinal polymer element when the arch is freely suspended from the ground, this gives an experimental factor of safety (FOS_e) of ~9 (6kN / 0.65kN = ~9).

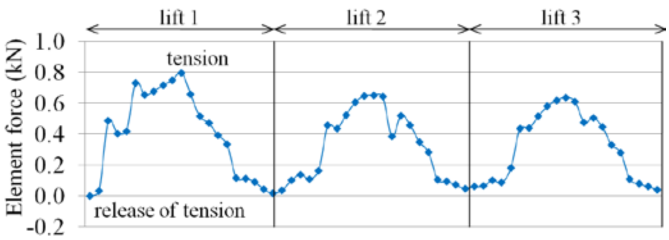

Figure 6. Average change in forces in longitudinal polymer elements during three consecutive lift.

The strains recorded in the transverse polymer elements were averaged for the gauges at similar positions and gave a maximum force of 0.12kN (Figure 7), which is small in comparison to the longitudinal elements. When the arch was lifting off the ground, the transverse polymer element at the outer lifting point has strain as the skew cantilever starts to develop. At a crown rise of ~100mm an additional transverse polymer element also takes some strain. The maximum strain value was reached at a crown lifting height of ~400mm as the transverse polymer elements at the root of the cantilever have strain. In summary, the transverse polymer elements distribute the loads due to self-weight during the lifting procedure.

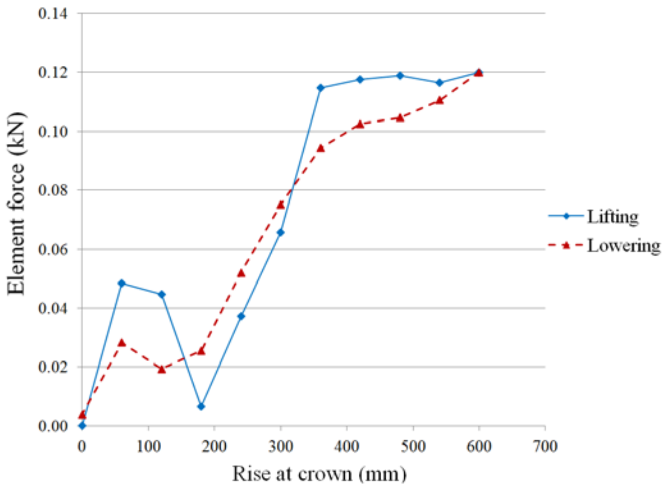

Figure 7. Average change in forces in transverse polymer element.

The arch system sustained a peak load of 22.9kN prior to failure occurring by the formation of a mechanism. The failure load was in excess of the equivalent service axle load of 5.6kN. The four hinges that formed the mechanism are shown in Figure 8.

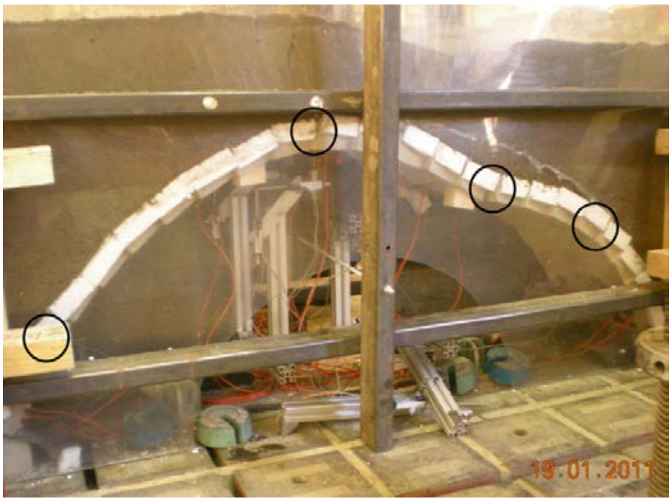

Figure 8. Hinge points on failed skew arch.

As well as distributing the load across the arch ring, the backfill generated compression within the ring and as a result of this build up in compression, a greater applied load was required to produce tension in the ring to form plastic hinges.

Figure 9 shows the stresses in the voussoirs based on recorded strain results and as expected, the largest value of compression, 2.0N/mm^2, occurred at the two thirds point along the arch span, at the opposite side to the loading position. At the service load of 5.6kN, the maximum change in stress is a low compressive value of 0.2N/mm^2. The largest recorded joint opening occurred under the loading point.

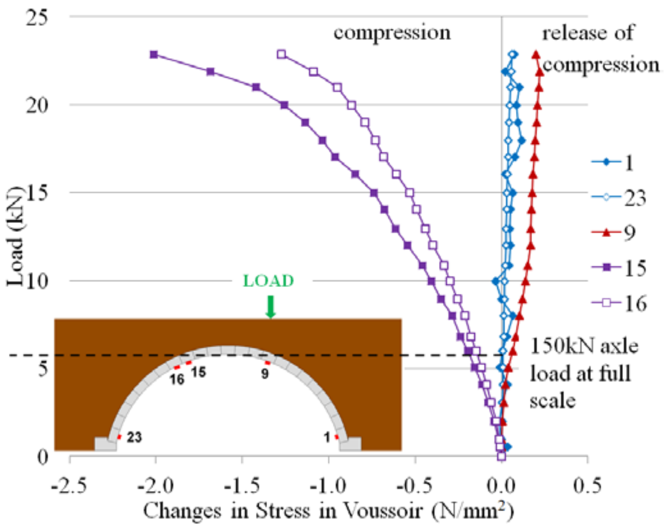

Figure 9. Change in stresses in voussoirs – full load test.

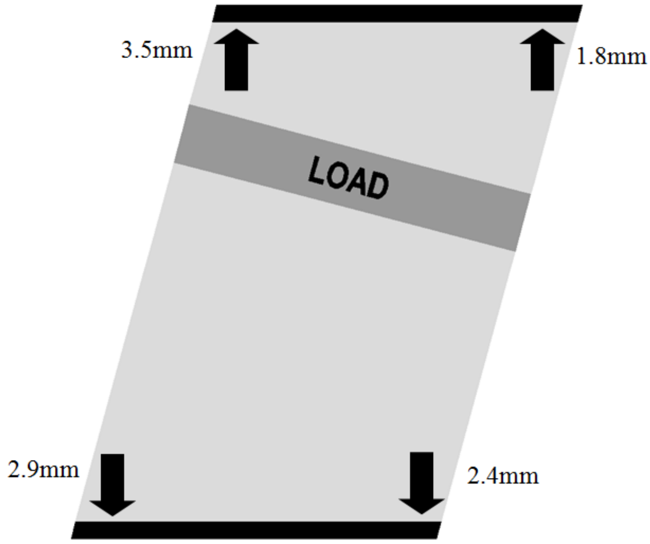

Figure 11. Intrados displacements.

Figure 10 presents the average displacements at selected locations. The highest displacement occurred under the loading point with a maximum inwards displacement of 20.6mm. The highest outwards displacement of 17.3mm occurred at the opposite two third span position. The displacement was slightly less at the opposite two thirds point as the backfill and the polymeric reinforcement provided additional resistance to outwards movement. At the equivalent service axle load of 5.6kN, the maximum change in displacement was ~2mm, well within acceptable limits for displacement of effective span/250 or 7.7mm.

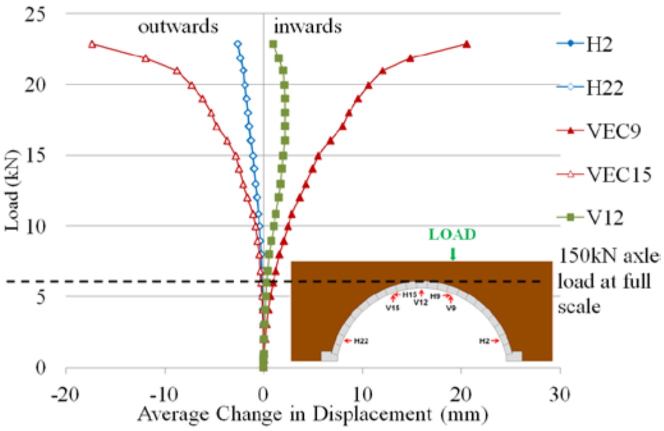

Figure 10. Average change in displacements – full load test.

Figure 11 summaries the acute and obtuse angle displacements on a plan view. At voussoir 2 (closest to the loading point) the obtuse angle corner moved outwards by 3.5mm, compared to 1.8mm at the acute angle corner. This was expected, as in a skewed arch the obtuse angle corner was expected to attract a larger proportion of the thrust in comparison to the acute angle corner; that is the arching thrust spans the shortest distance.

4 ANALYTICAL MODEL – POLYMER FORCES

A spreadsheet was developed to predict the forces in the polymer for circular shaped arches with no skew and the calculation steps are detailed below, with Figure 12 illustrating the dimensions.

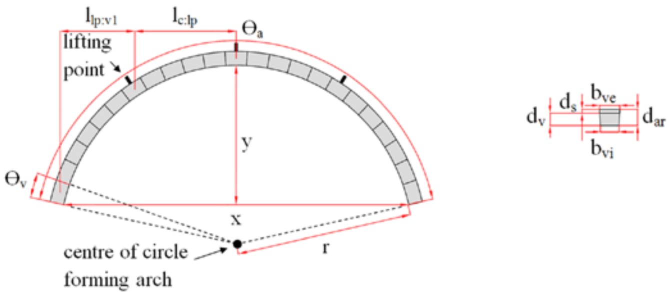

(a) Section through arch (b) Voussoir

Figure 12. Dimensions used to calculate the polymer forces.

Initially the intrados radius of the arch (r) is given by:

$$r = [\,(x/2)^2 + y^2\,] / (2y) \qquad (1)$$

The arch segment angle from the centre of the circle (Θ_a) is given by:

$$\Theta_a = 2\,[\,\sin^{-1}(x/2) / r\,] \qquad (2)$$

The angle per voussoir from the centre of the arch circle (Θ_v) is given by:

$$\Theta_v = \Theta_a / n_v \qquad (3)$$

The weight per voussoir (W_v) is given by:

$$W_v = \{\,[\,(b_{ve} - b_{vi}).d_v\,] + (b_{vi}.d_v)\,\}\,.\,w_v\rho_c \qquad (4)$$

Where w_v = Width of voussoir

The weight of screed per voussoir (W_s) is given by:

$$W_s = (c_s.d_s.w_v.\rho_c) / n_v \tag{5}$$

The total weight per voussoir (W_{v+s}) is given by:

$$W_{v+s} = W_v + W_s \tag{6}$$

For each of the voussoirs forming the cantilever from the outer lifting points, the horizontal distance from the lifting point to the centre of the selected voussoir ($l_{lp:v}$) is given by:

$$l_{lp:v} = \sin \{ \Theta_v . [(v_n/2) - v_{n-1}] - (\Theta_v/2) \} . [r + (d_{ar}/2)] - l_{c:lp} \tag{7}$$

Where v_n = Voussoir number from cantilever tip

The total bending moment caused by the voussoirs (M_a) is:

$$M_a = \sum (W_{v+s}.l_{lp:v}) \tag{8}$$

By assuming tension is taken fully by the polymer, and by assuming a linear variation in the compressive stress with a neutral axis at the voussoir mid depth, the moment of resistance (M_r) of the longitudinal polymer elements is given by:

$$M_r = [d_{ar}.(5/6) - d_s] . \sigma_{tp} \tag{9}$$

Where σ_{tp} = Tensile strength of the polymer

The theoretical Factor of Safety (FOS_t) is given by:

$$FOS_t = M_r/M_a \tag{10}$$

For this test the theoretical factor of safety (FOSt) was 8, which is comparable to the experimental value of 9 based on the measured strain values in the polymer. The theoretical predictions do not take into account the bond between the polymer and the concrete nor does it consider the forces taken by the transverse polymer elements. However, the theoretical factor is slightly conservative and the predictions gave a good correlation to the experimental values.

5 NON-LINEAR FINITE ELEMENT ANALYSIS (NLFEA)

NLFEA models are able to capture the behaviour of arches due to the non-linear plasticity modelling capabilities of the method. An explicit analysis was used to alleviate the convergence problems which are associated with highly non-linear contact plasticity models when the traditional implicit approach is adopted [11]. The explicit approach is commonly used for transient dynamic problems. However, if the loading is applied slowly, the inertia effects become insignificant and a pseudo static analysis can be achieved.

The skewed nature of the arch means that from a modelling perspective the arch much be considered as a full three dimensional structure. The 23 voussoirs of the arch ring are modelled as individual parts with the fill being modelled as a further part, giving a finite element model with 24 different parts. The parts are related through the definition of interfaces with one part being prevented from penetrating into another but there can be a gap between parts. If two parts are in contact with each other then a relationship can be specified between the normal and the transverse shear stresses. For the work presented here the simple coulomb's law of friction is adopted where the transverse stress is directly proportional to the normal stress with the constant of proportionality being given by the coefficient of friction μ, taken as 0.6 [12].

The concrete voussoirs that form the arch ring were taken to behave elastically as the stress levels do not exceed the yield compressive stress value and the tensile strength was zero as the joints can open. For the granular backfill a Drucker/Prager plasticity model with a friction angle of 46^o [12] was adopted to capture the spread of the load through the backfill, as this is essential for the accurate prediction of the failure load for the arch.

Creating a finite element model of the stepped arch ring was achievable. However, applying the backfill proved to be difficult, as it also had to be stepped. A finite element analysis of the stepped arch ring on its own, with loading applied at the crown, demonstrated that the stepped profile of the ring had little influence on the alignment of the thrust line (Figure 13).

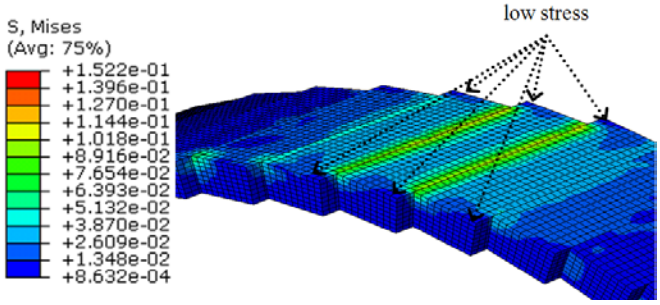

Figure 13. Stress distribution with loading at crown.

The geometry of the skew arch was therefore simplified by basing it on the profile of a straight arch but with a skew of 15^o (Figure 14) and applying the backfill to this model proved to be simpler. The width of this skew arch model was reduced to account for the step in the voussoirs.

(a) Reduced width straight edge skew arch ring model

(b) Skew arch ring model with straight edge

Figure 14. Straight edged skew arch model.

The three dimensional geometry was created by lofting between two planar profiles that were offset from each other. The model was meshed using wedge elements rather that hexahedral elements. The hexahedral quadratic elements are not available for the explicit method, however there is no restriction on the quadratic wedge element and it was thought that the quadratic wedge would perform better than a linear hexahedral.

The model was loaded in two steps, first the self weight of the system was applied, namely the arch ring and backfill, and in the second step a patch load was applied at the arch span third point, similar to that in the experimental test. The arch failed at a peak load of 23.2kN, which is comparable to the 22.9kN from the experiment. Figure 15 shows that the four hinges formed in the exact same locations that they did during the experiment. It also illustrates that, as expected, the arching thrust spans the shortest distance, creating a concentration of stresses at the obtuse corners where the hinge points form.

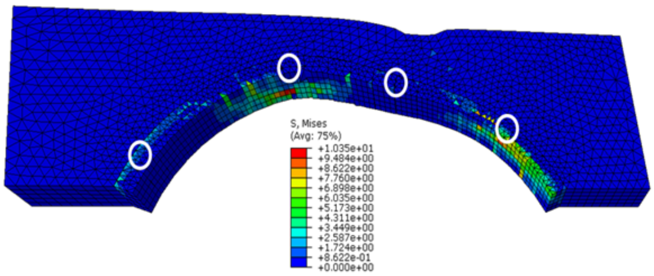

Figure 15. Hinge points on failed skew arch.

6 CONCLUSIONS

The 15^{o} skew FlexiArch bridge had strengths far in excess of the equivalent SV axle load under testing and sustained a peak load of 22.9kN prior to failure occurring by the formation of a mechanism. The failure load was ~4 times the equivalent scaled SV axle load of 5.6kN. The results show that the skew FlexiArch is a viable structural solution for medium span bridges.

It was found that the highest forces in the polymeric reinforcement occurred during lifting, and the transverse polymer elements had negligible forces in comparison to the longitudinal elements but did assist in the distribution of torsional forces. The analytical model used to predict the forces in the polymer for circular shaped arches with no skew gave a good correlation to the experimental results. The finite element model gave a predicted failure load that was close to the experimental value, with the compressive stress pattern similar to that of the experimental test. It can therefore be concluded that both the analytical model for predicting the polymer forces and the finite element model of the FlexiArch system during loading can both accurately represent the behaviour of the skew arch. Future research relating to the skew FlexiArch will investigate the effect of varying the angle of skew, increasing the span to rise ratio and double radius arches.

ACKNOWLEDGMENTS

The Authors would like to thanks the staff at QUB who assisted with this research project namely, S Gildea, G Davis, K McDonald, H Laing, D Ferguson and W Mc Roberts.

REFERENCES

[1] UK Highway Agency. (1995). BD 57/95 & BA 57/95, design for durability design manual for roads and bridges, volume 1, section 3.Department of Transport, Highway and Traffic.

[2] Taylor, S., Long, A. E., Robinson, D., Rankin, B., Gupta, A., Kirkpatrick, J., & Hogg, I. (2007). Development of a flexible concrete arch. Proceedings of the 11th International Conference on Structural Faults and Repairs.

[3] Chandler, H. W., & Chandler, C. M. (1995). The analysis of skew arches using shell theory. The 1st International Conference on Arch Bridges, 195.

[4] Harvey, W. J. (2004). Skew arch behaviour. The Structural Engineer, 82(5), 13-15.

[5] James, J., & Augarde, C. (2001). Modelling skewed masonry arches. The Structural Engineer, 79(7), 14-15.

[6] Melbourne, C., & Hodgson, J. A. (1995). The behaviour of skewed brickwork arch bridges. Paper presented at the The 1st International Conference on Arch Bridges, 309.

[7] Heyman, J. (1982). The masonry arch (First ed.). West Sussex, England: Ekkis Horwood Limited.

[8] BSI. (2008). EC1 - actions on structures - part 2: Traffic loads on bridges. London: BSI.

[9] Taylor, S., Robinson, D., Long, A. E., Gupta, A., & Kirkpatrick, J. (2011). Testing of a novel flexible concrete arch system. Antrim: Macrete.

[10] Linear Composites. (2005). PARAGRID for soil reinforcement: Product data table. Retrieved 12/23, 2010, from http://www.maccaferri.co.uk//images/library/00371.pdf?id=okadTFbD

[11] Molins, C., & Roca, P. (1998). Capacity of masonry arches and spatial frames. Structural Engineering, 123(1), 653-663.

[12] Robinson, D., Johnston, R., & Taylor, S. (2010). Finite element analysis of a skewed flexi-arch. Belfast: Queen's University Belfast.

Behaviour of unbonded post-tensioned segmental box girders with dry joints

Michael Matson[1,3], Kieran Ruane[2,3]
[1] Hurst Pierce + Malcolm LLP, Celtic House, 33 John's Mews, London, WC1N 2QL
[2] RPS Group, Inishmore, Ballincollig, Co. Cork, Ireland
[3] Department of Civil, Structural & Environmental Engineering, Cork Institute of Technology, Rossa Avenue, Bishopstown, Cork, Ireland
email: mmatson@hurstpm.co.uk, kieran.ruane@rpsgroup.com

ABSTRACT: The use of dry joints has become a more popular form of precast post-tensioned segmental box girder bridge construction, in climatically suitable countries, over recent years. Time and cost savings achieved using dry joints, in lieu of glued joints, are significant due to the economies of scale involved and the repetitive nature of the construction. A number of formulae, presented in guidance documents and published papers, are typically used to determine the shear capacity of dry jointed keys. When these formulae were examined, significant differences were noted in the shear capacities obtained, deeming further research necessary. A program of laboratory testing and LUSAS finite element modelling was developed to decipher which formula is most appropriate for use. Destructive and non-destructive tests were carried out on test segments representing the interface between adjacent box girder webs with full sized shear keys. Failure loads and failure modes were determined during the laboratory testing. A series of LUSAS finite element models, based on the laboratory test setup, was also developed. Results obtained from the laboratory testing and finite element modelling were found to lie between results calculated using formulae by AASHTO and Hewson, with the Hewson formula deemed to be most representative. A suitable modification factor, to be used in conjunction with this formula, was developed to reflect the test results more accurately.

KEY WORDS: Dry joints, shear capacity, precast segmental box girder, post-tensioned, epoxy.

1 INTRODUCTION

The speed at which construction projects are built has a significant impact on their overall cost. Designers and contractors are continually striving to develop and hone methods of construction, in an attempt to reduce a project's construction phase and cost. This principle is particularly applicable to precast segmental bridges.

Figure 1. Precast segmental box girder with shear keys.

A precast box girder bridge segment with typical shear key layout is shown in Figure 1. Traditionally, when segments are joined, a thin layer of epoxy is applied to the shear keys, prior to the tensioning of the external tendons. This joint is referred to as a "glued joint". In recent years, a method known as "dry jointing" has been used, where segmental bridges have been constructed without epoxy in the joints.

Research undertaken examined a number of available formulae taken from guidance codes and published papers commonly used to calculate the shear capacity of dry jointed precast segments. Results obtained from each formula were compared with those from LUSAS [1] finite element models, which were calibrated against a series of laboratory test models.

2 GUIDANCE CODES AND DOCUMENTATION

The following codes of practice and published documents provide formulae for determining the capacity of shear keys:

- AASHTO Guide specification for design and construction of segmental concrete bridges, 2nd Edition, 1999 [2];
- I.S. EN 1992-1-1: 2005 – Design of concrete structures: General rules and rules for buildings [3];
- Dry Joint Behaviour of Hollow Box Girder Segmental Bridges – Dr. Guenter Rombach [4];
- Prestressed Concrete Bridges: Design and Construction – Mr. Nigel R. Hewson [5].

The shear capacity of a section of typical box girder web was calculated, using each of the above formula. A spreadsheet enabled the easy comparison of results for a range of varying inputs, including:

- Width of segment web;
- Number of shear keys considered;
- Shear key dimensions;
- Characteristic compressive strength of concrete;
- Compressive stress in concrete, due to prestressing force.

A graphical comparison of the examined formulae, generated using results obtained from this spreadsheet, is provided later in this paper.

3 LABORATORY TESTING

A program of laboratory testing was developed to determine the capacity of a number of shear keys and to calibrate a series of LUSAS finite element models. This calibration was based on the comparison of the failure modes, failure loads and crack / crush patterns obtained for each of the laboratory test specimens and LUSAS models. Following this calibration, a number of models were further developed. These were tested with loads in excess of the maximum loads available for the laboratory test.

Four test specimens were constructed to represent the interface between adjacent box girder webs. Each specimen was made up of 2 no. segments placed on top of each other and each contained full sized shear keys of typical dimension. This was to ensure that tests undertaken would not be distorted by scaling effects. Various documents, in which dry joints were illustrated, and projects, in which they were utilised, were examined to determine suitable key dimensions. A segment width of 350 mm was chosen, as it represented the typical web width of a full sized box girder section.

In a casting yard, each box girder segment is match cast against its adjacent segment, in order to achieve as best a fit as possible. To reflect this process, the second segment of each pair was match cast against the first. A test segment with 4 no. male shear keys was deemed to be most suitable, as it was of a size appropriate for testing, whilst also being easily constructed and handled. Figure 2 shows the construction of a laboratory test specimen.

Figure 2. Construction of a laboratory test specimen.

Six 100x100 mm cubes were made with each segment pour. Cubes were crushed at 7 days, 28 days and again on the day the individual specimens were tested.

Figure 3 shows the laboratory setup for a typical test. The test specimen was vertically loaded with 2 no. 55 tonne jacks, attached to the top of an existing test rig, to represent the box girder web in its prestressed state. These jacks were individually pumped using 2 no. single action hand pumps. Lateral loads were then applied by 2 no. 150 tonne jacks, contained within a fabricated lateral load test rig, to reflect the shearing forces, typically induced on the segments by the bridge self weight, by traffic and by pedestrian loads. Both of these jacks were pumped using the same double action hand pump.

Four prefabricated load cells were used to measure the loads applied to the test segments by each of the jacks. These load cells were connected to a data logger, which was set to record 10 no. readings per second, enabling comprehensive load data to be gathered.

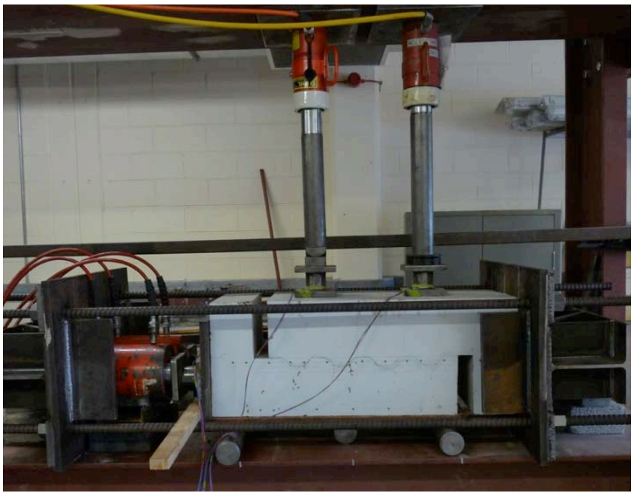

Figure 3. Laboratory test setup.

A Demec mechanical strain gauge was used during the testing process to measure the relative displacement between the two segments. This instrument was capable of measuring movements of 0.001 mm. The gauge was used in conjunction with Demec studs, which were attached to either side of the test segment.

A full set of Demec readings was taken during each of the tests, at the following stages:

- After the Demec studs were attached to the test specimen;
- Before the prestressing load was applied;
- After the prestressing load was applied;
- After each shearing load increment was applied.

When analysing the horizontal movement of the shear keys, the relative movement between the top and bottom segments was measured at 4 no. locations, as shown in Figure 4.

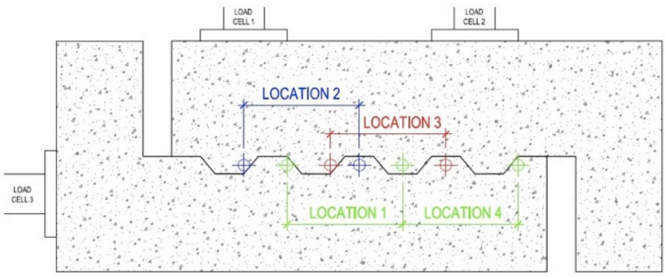

Figure 4. Measurement locations.

Eight tests were carried out on the 4 no. test specimens. The laboratory test schedule, shown in Table 1, provides load details for each of these tests.

Test 1, carried out on Specimen 1, was seen as a trial test to establish the test methodology. The Specimen 1 failure mode indicated the lateral load application point needed to be altered for subsequent tests. Its location during Test 1 caused excessive load to be transmitted through the narrow upstand of Segment 1, causing it to bend and fail. Lowering the application point ensured that an increased load could be transmitted to the shear keys.

Tests 2, 3, 5 and 6 were non-destructive tests, used to demonstrate the effect a varying prestressing force had on the relative movements of the test segments.

Table 1. Laboratory test schedule.

Laboratory test schedule									
		Initial prestressing force applied			Shear force applied				
Test No.	Test specimen	Load cell 1	Load cell 2	Total	Load cell 3	Load cell 4	Total	Max. prestressing force	Max. shearing force
		kN	kN	kN	kN	kN	kN	kN	kN
1	1	250	250	500	100	100	200	504	795
					200	200	400		
					400	400	800		
2	2	100	100	200	50	50	100	220	414
					100	100	200		
					150	150	300		
					200	200	400		
3	2	200	200	400	50	50	100	418	409
					100	100	200		
					150	150	300		
					200	200	400		
4	2	250	250	500	50	50	100	538	809
					100	100	200		
					150	150	300		
					200	200	400		
					300	300	600		
					350	350	700		
					400	400	800		
5	3	100	100	200	50	50	100	247	414
					100	100	200		
					150	150	300		
					200	200	400		
6	3	200	200	400	50	50	100	405	411
					100	100	200		
					150	150	300		
					200	200	400		
7	3	250	250	500	50	50	100	551	752
					100	100	200		
					150	150	300		
					200	200	400		
					300	300	600		
					350	350	700		
					400	400	800		
8	4	200	200	400	50	50	100	480	713
					100	100	200		
					150	150	300		
					200	200	400		
					250	250	500		
					300	300	600		
					350	350	700		

During Test 2, a 200 kN prestressing force was applied. A 400 kN prestressing force applied during Test 3. In both instances the specimen was loaded with a total shearing force of 400 kN, applied in 100 kN increments. Tests 5 and 6 replicated Tests 2 and 3 respectively and were performed to ensure that the results obtained were reliable.

Figure 5 superimposes the deflections measured, at each of the four locations, during Test 2, on those recorded during Test 5. Both sets of deflections are seen to be of similar magnitude. In each instance, the most significant movement is seen to occur at location 1, followed by those at locations 4, 3 and 2, respectively. Negative values indicate a shortening of the measured distance.

As results from both tests correlated well, they can be presented with a greater amount of certainty. These results also show that the individual tests were undertaken and measured consistently.

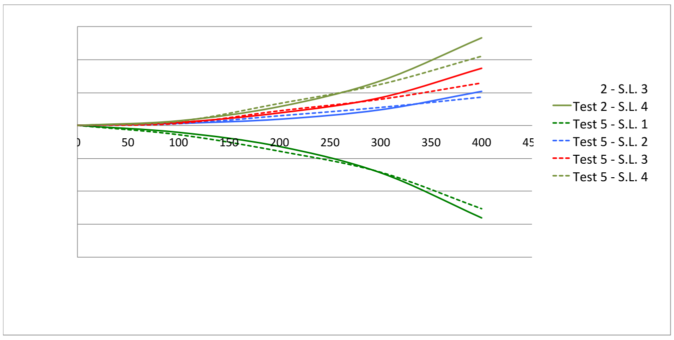

Figure 5. Comparison between results of Test 2 and Test 5.

Figure 6 superimposes the deflections measured, at each of the four locations, during Test 3, on those recorded during Test 6. As before, the most significant movement is seen to occur at location 1, followed by those at locations 4, 3 and 2, respectively.

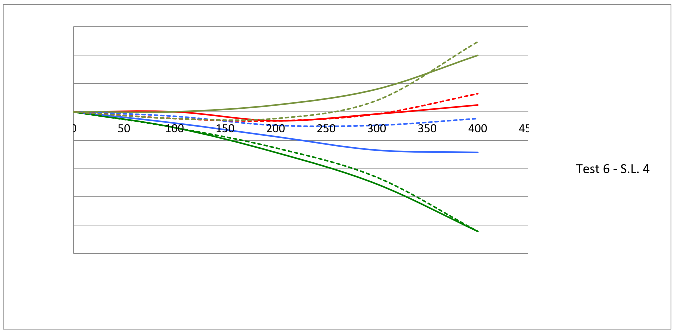

Figure 6. Comparison between results of Test 3 and Test 6.

Significant correlation can be seen between deflections measured at three of the four locations, with slight variations inevitable due to the magnitude of the displacements being measured.

Having completed Tests 2, 3, 5 and 6, it was evident that increasing the prestressing force applied to the test specimen, led to a reduction in the relative movement between the segments, caused by the applied shear force. A 100% increase in the applied prestressing force, from 200 kN to 400 kN, led to an average reduction of 75% in recorded deflections. Favourable correlation of test results also showed that a consistent testing and measurement procedure was being achieved.

Tests 4, 7 and 8 were destructive tests carried out on Specimens 2, 3 and 4 respectively. The prestressing forces applied and resulting specimen failure loads are detailed in Table 2.

Failure of Specimen 2 was caused by the development of significant cracks due to the crushing of concrete at shear keys 1 and 2. Figure 7 shows the failure at these locations.

Failure of Specimen 3 was caused by cracking at the top right hand side of the test specimen. This cracking, caused by bending of the top segment upstand, became evident with an applied lateral load of 250 kN and got progressively worse with increasing load. Significant cracking was also noted at the first and second shear keys, as shown in Figure 8, but these were not the cause of the specimen failure.

Table 2. Laboratory test failure loads.

	Test specimen	Prestressing force applied		Test failure load
		kN	N/mm^2	kN
Test 4	2	500	1.667	809
Test 7	3	500	1.667	752
Test 8	4	400	1.333	713

Figure 7. Failure of Specimen 2.

Figure 8. Failure of Specimen 3.

Failure of Specimen 4 was caused by cracking at the first and second shear keys. Cracking, due to concrete crushing, became evident at the first shear key with an applied shearing force of 300 kN. Two separate cracks appeared, as shown in Figure 9. These cracks increased in severity, with additional lateral load, until the eventual failure of the shear key. The failed key is also shown in Figure 9.

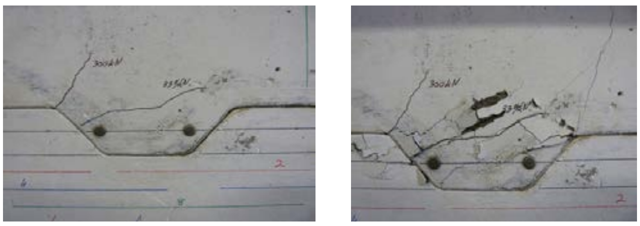

Figure 9. Failure of Specimen 4.

4 FINITE ELEMENT MODELLING

A program of LUSAS finite element modelling was devised to determine the capacity of a specific number of shear keys, under varying levels of prestress. Initial models were calibrated using the test data obtained from the laboratory testing. Once the finite element model was deemed to adequately reflect the behaviour of the test segments, additional, increased loads, that could not be reached during the laboratory testing, due to the limited jack and rig capacities, were applied. Results obtained from these tests were then compared with those obtained using the available shear key capacity formulae.

As the segments were of constant cross section, 2D modelling was utilised. It was meshed with 4-node plane stress continuum elements. To reflect the laboratory testing conditions, the bottom segment, was placed on a flat surface, fixed in the X, Y and Z directions. This represented the bed of the test rig. The left hand end face of the top segment was fully restrained in both the X and Z directions. This again represented the testing condition, with the segment being restrained by the fabricated test rig.

The inclusion of slidelines allows the movement of two adjacent surfaces over each other. The friction created between the two surfaces, dependent on their material, is specified as part of their application. Two slidelines were used in this model. The first was between the underside of the bottom segment and the top of the support surface. A slideline, with a Coulomb friction coefficient of 0.1 was utilised, to allow near frictionless movement between the two elements. The second was at the interface between the two segments. In this instance, a Coulomb friction coefficient of 0.6 was used, as it is representative of concrete on concrete surfaces [6]. The use of slidelines required a non-linear analysis to be carried out.

As the prestressing and shearing loads were not applied simultaneously during the laboratory testing, load curves were utilised to stagger their application in the finite element model. Typical crack / crush and stress diagrams, taken at failure, are shown in Figure 10.

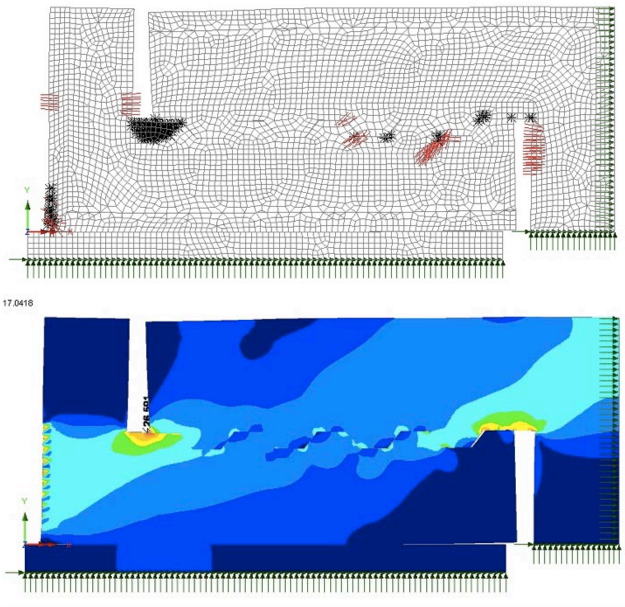

Figure 10. Crack / crush and stress (x-x direction) diagrams of specimen at failure.

When the failure loads and crack / crush patterns adequately matched those of the three laboratory specimens tested to failure, the finite element models were deemed to be sufficiently calibrated for further use.

5 COMPARISON OF DRY JOINT FORMULAE WITH LABORATORY TESTS AND FINITE ELEMENT RESULTS

The Excel spreadsheet developed was used to calculate the shear capacity of a section of segment web, in accordance with each formula considered. The web section properties were as follows:

- Width of segment web = 350 mm;
- No. of shear keys being considered = 4;
- Width of shear key = 30 mm;
- Compressive strength of concrete = 40N/mm2;
- Compressive stress in concrete, due to prestressing force, applied normal to and evenly across the joint: 1N/mm2 – 15N/mm2.

Results obtained were graphed, enabling easy comparison of the formulae. Unfactored results are shown in Figure 11. Significant differences were found between the shear capacities provided by each formula, with results differing by in excess of 100%.

Results obtained from the finite element modelling of an identical web section are graphed in Figure 12.

As each laboratory test specimen also consisted of 4 no. shear keys, each of the three test failure loads have also been included in Figure 13, for easy comparison with the shear capacities obtained from both the formulae and the finite element modelling.

Figure 14 focuses on the test results for applied compressive forces of between 1 N/mm^2 and 4 N/mm^2, clearly showing their correlation with the laboratory test results.

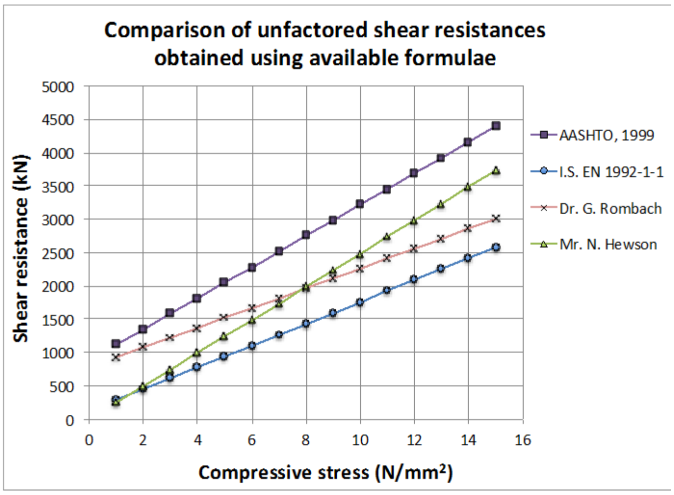

Figure 11. Comparison of formulae results.

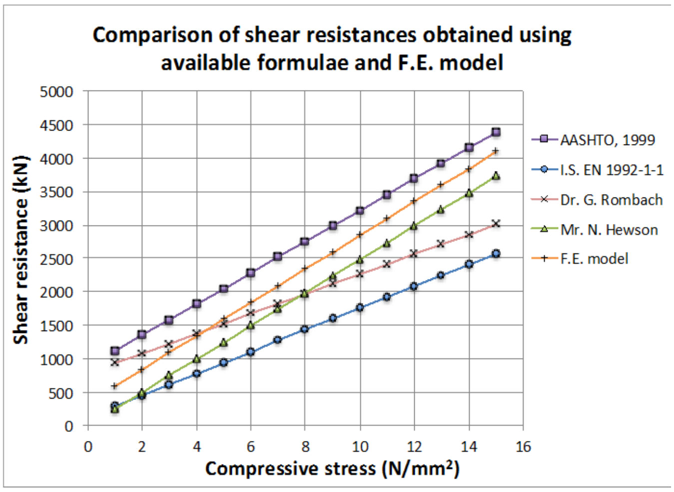

Figure 12. Comparison of F.E. results with formulae.

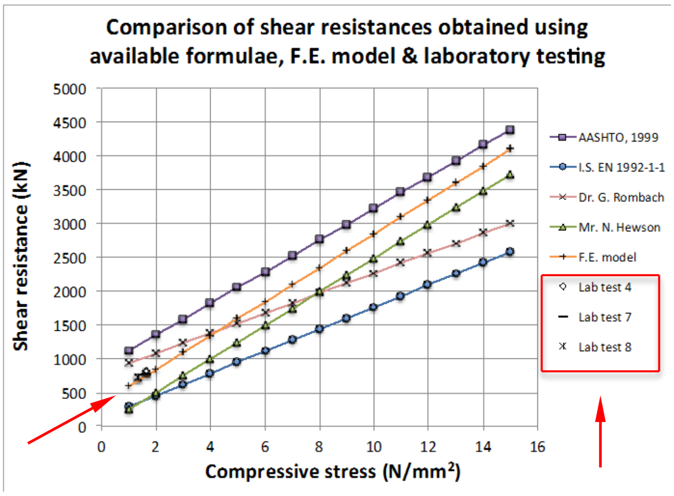

Figure 13. Shear resistances with laboratory tests included.

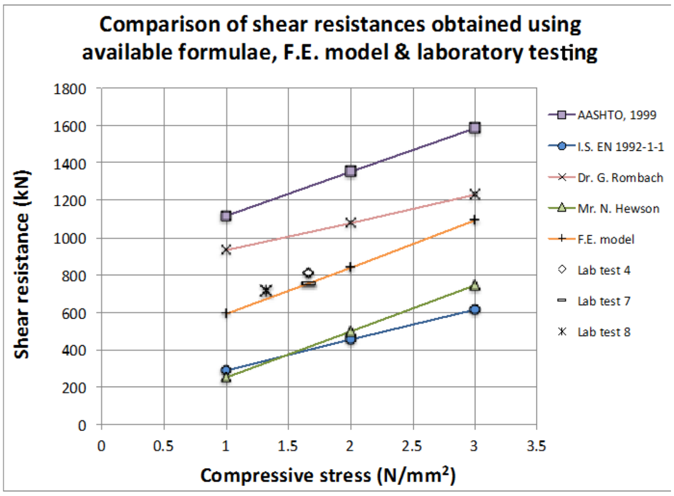

Figure 14. Shear resistances with laboratory tests included.

6 CONCLUSIONS

It was found that the shear resistance of the section calculated using the finite element model fell between the resistances obtained from the formula provided in the AASHTO, 1999 document [2] and that proposed by Nigel Hewson. As the laboratory test specimens contained four shear keys, the results got from the three destructive tests were also compared. Figure 13 and Figure 14 show good correlation between the laboratory test and finite element modelling results.

Hence, it is concluded that the formula detailed in I.S. EN 1992-1-1:2005 [3] provides the most conservative shear key capacity. The formula proposed by Nigel Hewson is also deemed to marginally underestimate the shear capacity. Conversely, and perhaps more significantly, the AASHTO 1999 document [2] appears to overestimate the capacity of the studied section. The formula developed by Dr. Rombach was found to overestimate the shear capacity for applied stresses of between 1 and 4 N/mm^2 but was found to be conservative for applied stress in excess of this.

Figure 12 shows that the Hewson formula is most representative. From the results obtained, it was found that this formula could be multiplied by a further factor based on the applied compressive stress, f_c, to more closely represent the finite element modelling and laboratory test results. The proposed modified Hewson formula is shown below:

$$V_{j\ unfact} = 2\left[1.4\, f_c A_{sk} \;+\; 0.6\, f_c \left(A_w - A_{sk}\right)\right]\sqrt{\frac{1}{\sqrt{f_c}}} \qquad (1)$$

Figure 15 shows the modified Hewson formula superimposed on the comparison of shear capacities obtained from the formulae examined and the finite element modelling.

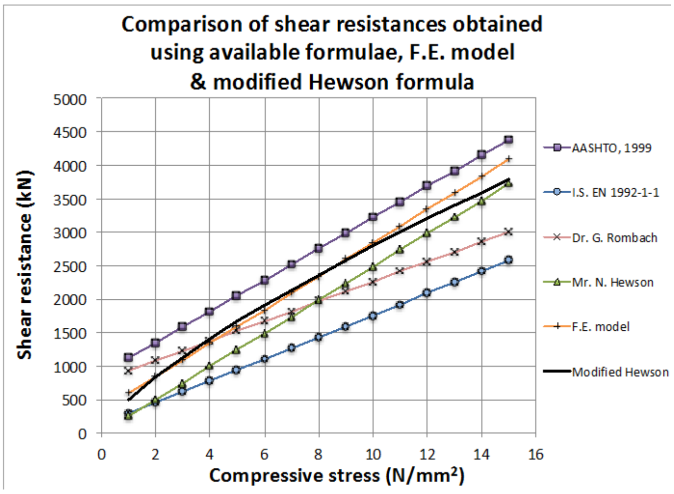

Figure 15. Comparison of shear resistances with modified Hewson formula included.

It can be seen that the line denoting the modified Hewson formula is non linear. However, between the commonly used compressive stresses of 4 N/mm^2 and 10 N/mm^2, it is seen to closely represent the results obtained from the finite element modelling and, hence, is deemed appropriate.

ACKNOWLEDGEMENT

I would like to thank Mr. John J. Murphy, Department of Building and Civil Engineering, Cork Institute of Technology, for his advice during the laboratory testing phase of the project.

The research reported in this paper was conducted as part of the taught MEng (Structural Engineering) programme at Cork Institute of Technology.

REFERENCES

[1] Finite Element Analysis LTD, *LUSAS*, Kingston upon Thames, 1982-2011.

[2] American Association of State Highway and Transportation Officials, *Guide specification for design and construction of segmental concrete bridges*, AASHTO, Washington, D.C., 1999.

[3] NSAI Standards, I.S. EN 1992-1-1:2005, *Design of concrete structures: General rules and rules for buildings*, NSAI, 2005.

[4] Rombach, G. (2004), 'Dry joint behaviour of hollow box girder segmental bridges', *Proceedings of FIB Symposium on Segmental Construction in Concrete*, New Delhi.

[5] N.R. Hewson, *Prestressed concrete bridges: Design and construction*, Thomas Telford Publishing, London, 2003.

[6] Tanner, J.A. (2008), 'Calculating shear friction using an effective coefficient of friction', *PCI Journal*, 114-120.

A seismic risk assessment of reinforced concrete integral bridges subject to corrosion

M. Ní Choine[1], A. O Connor[2], J.E. Padgett[3]
[1]Department of Civil, Structural and Environmental Engineering, Trinity College, Dublin 2, Ireland
[2]Department of Civil, Structural and Environmental Engineering, Trinity College, Dublin 2, Ireland
[3]Department of Civil and Environmental Engineering, Rice University, Houston, Texas, USA.
email: nichoinm@tcd.ie, alan.oconnor@tcd.ie, jamie.padgett@rice.edu

ABSTRACT: This paper seeks to determine the effect deterioration has on the seismic vulnerability of a 3 span integral reinforced concrete bridge. Traditionally it has been common to neglect the effects of deterioration when assessing the seismic vulnerability of bridges. However, since a lot of the bridges currently being assessed for retrofit are approaching the end of their design life, deterioration is often significant. Furthermore, since deterioration affects the main force resisting components of a bridge it is reasonable to assume that it might affect its performance during an earthquake. For this paper, chloride induced corrosion of the reinforcing steel in the columns and in the deck has been considered. Corrosion is represented by a loss of steel cross section. A 3 dimensional non-linear finite element model is created using the finite element platform Opensees. A full probabilistic analysis is conducted to develop time-dependent fragility curves. These fragility curves give the probability of reaching or exceeding a defined damage limit state, for a given ground motion intensity measure taken as Peak Ground Acceleration (PGA). This analysis accounts for variation in the ground motion, the material and geometric properties of the bridge, and the levels of deterioration when assessing its overall seismic performance as well as the performance of its most critical components. The results show that neglecting to include deterioration results in an underestimation of the seismic demands placed on the bridge and therefore the bridge may be more vulnerable than acknowledged. Further work is recommended including the development of fragility curves to include different retrofit options and deterioration levels. As the deteriorated bridge performs differently to the pristine structure, the inclusion of deterioration may alter the optimal retrofit strategy selected and is therefore an important area of research.

KEY WORDS: Deterioration; Bridge; Seismic; Fragility; Corrosion.

1 INTRODUCTION

Throughout the United States and the rest of the world there are hundreds of thousands of bridges located in seismic zones. In the aftermath of an earthquake, it is very important for bridges to be functioning as they make up key components of the transport network and are vital to facilitate a rescue and recovery effort. As a result of this importance, a large amount of research has gone into predicting the likelihood of bridges reaching defined damage states for a given earthquake intensity. However, it is also important to note that a lot of these bridges were built 40-50 years ago and may have suffered high levels of deterioration resulting in a reduced load carrying capacity. Over half the bridges in the United States are approaching the end of their design life [1], which would suggest that including deterioration in the seismic fragility estimation of bridges is very important. Despite this, a relatively small amount of research has gone into assessing the impact deterioration has on the response of RC structures subjected to earthquake events. Recent work by Choe et al. [2,3] used a probabilistic approach to estimate the reduction in column capacity and the increase in demand of a typical single bent bridge in California due to corrosion. Choe et al. [4] developed fragility increment functions to determine the fragility of corroding RC bridge columns. This work provides estimates of the fragility at a time of interest based on the fragility of the pristine bridge column without having to carry out additional reliability analyses. This work may provide an effective time saving measure. The deterioration of both the RC columns and steel bearings has been accounted for by Ghosh and Padgett [5] for multispan continuous highway bridges. Akiyama et al [6] evaluated the reduction in capacity of corroded RC columns due to airborne chlorides. This work also proposed a novel computational approach to integrate the probabilistic hazard associated with airborne chlorides into the life-cycle reliability of the proposed columns. Most recently, Alipour et al. [7] studied the life-cycle performance and cost of reinforced concrete bridges exposed to earthquake ground motions as well chloride induced corrosion. This study attempts to provide a more accurate prediction of the corrosion initiation time by taking into account some of the parameters that can affect the corrosion process when developing time-dependent fragility curves. As well as the probabilistic structural evaluation, the results of the fragility analysis are used to estimate the total life-cycle cost of the bridges.

2 BRIDGE MODELLING

A reinforced concrete, 3 span, fully integral bridge was used for the fragility analysis carried out in this study. A 3D finite element model of the bridge in its pristine condition was developed using the finite element software Opensees [8]. The total length of the bridge is 52.518m. This is made up of a centre span measuring 29.078m and two side spans each measuring 11.72m. The piers consist of 2 1m diameter circular columns. Each column has a clear height of 6.831m. A schematic of the bridge can be seen in figure 1.

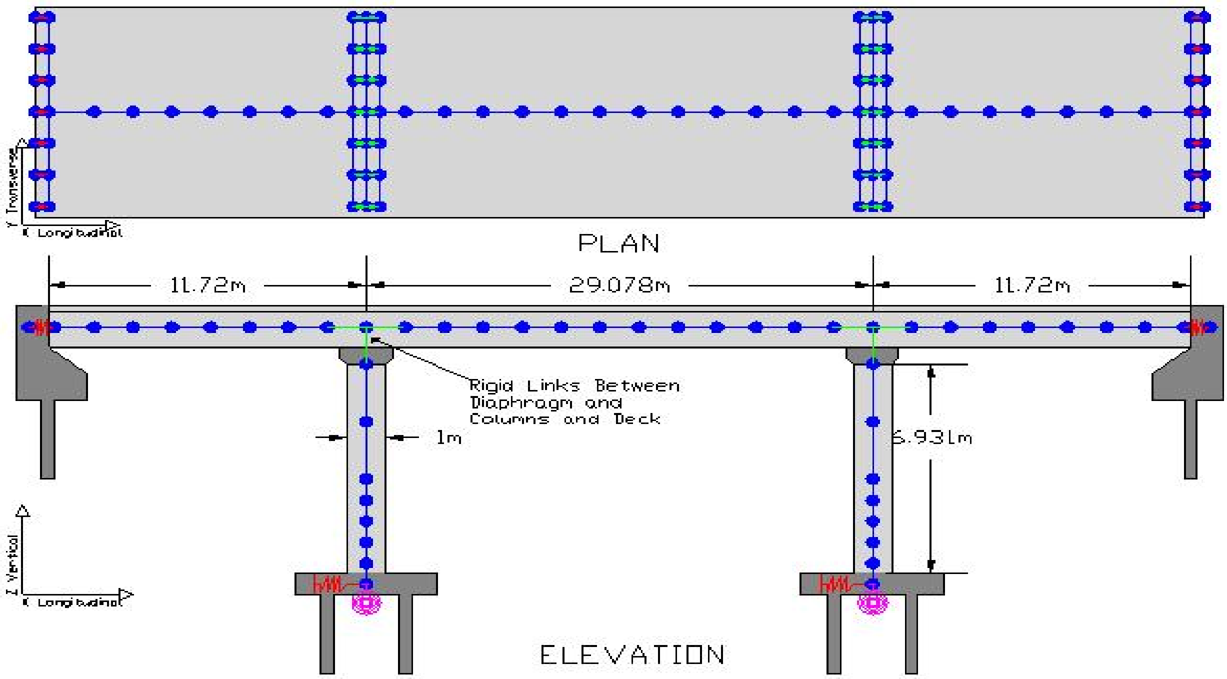

Figure 1. Elevation and Plan View of the 3-Dimensionsal Nonlinear Analytical model of the 3 Span Reinforced Concrete Integral Bridge.

The superstructure consists of a 10m wide reinforced concrete deck slab supported on 5 prestressed U11 beams. Composite action of the slab and the girders is taken into account and superstructure is modelled using an elastic beam-column element located at the centroid of the section. It is assumed for this research that the superstructure elements will remain in the elastic range following recommendations by Aviram et al. [9].

The columns at each bent are modelled using nonlinear beam column elements with a fiber cross section. To define the fiber cross section, the concrete column section is discretized into a number of fibers, made up of 8 rings and 12 wedges. The 18 reinforcing steel bars are included as an extra layer. The confined and unconfined concrete strength parameters for the columns are calculated using the approach described by Mander et al. [10].

The abutments are modelled using simplified non-linear translational springs. Only the contribution of the piles is considered in the active direction. In the passive direction the contribution of the soil and the piles is considered. The abutment-backfill soil interaction is modelled following the recent work by Shamsabadi et al. [11] which gives numerical simulation models which have been validated using data from recent experiments on the lateral response of typical abutment systems. This applies for abutment heights of up to 2.5m and a silty sand or clayey silt backfill. The following equation describes the lateral force-displacement relationship for the two backfill types [10]

$$F(y) = \begin{cases} \dfrac{410.6y}{\left(\frac{H}{1m}\right)+1.867y}\left(\dfrac{H}{1m}\right)^{1.56}, y \leq 0.05H(Silty\ sand\ ) \\ \dfrac{249.1y}{\left(\frac{H}{1m}\right)+.8405y}\left(\dfrac{H}{1m}\right)^{1.05}, y \leq 0.10(Clayey\ silt) \end{cases} \quad (1)$$

where $y =$ the maximum value of lateral displacement in cm, $F(y) =$ the lateral force in KN/m and $H =$ the abutment height in m.

The foundations are modelled using simplified nonlinear translational and rotational springs using a method outlined by Nielson [12]. For the translation springs the contribution of the piles and the pile cap which is embedded in the ground is considered.

Variation in certain modelling parameters is accounted for including concrete compressive strength, steel strength, soil stiffness, horizontal pile stiffness, vertical pile stiffness, mass, damping and concrete cover depth.

3 DETERIORATION MODELLING

For this study, chloride induced corrosion of the reinforcing steel in the concrete columns is considered. According to Tilly [13], this form of deterioration is responsible for more than 55% of concrete repairs carried out. Therefore, there has been a significant amount of research into developing probabilistic chloride-induced corrosion models. Thoft-Christensen et al. [14] and Duracrete [15], developed probabilistic models for the corrosion process. Stewart and Rosowsky [16], Vu and Stewart [17] and Enright and Frangapol [18,19] developed probabilistic models for the corrosion of bridge slabs, beams and girders.

For this study deterioration is divided into two phases, the diffusion phase and the deterioration phase. The time to concrete cracking has been modelled by previous researchers [2,6,7] but is beyond the scope of this paper.

3.1 Time to Initiation

The duration of this phase is generally estimated using the solution of Fick's second law [17] which can be represented as

$$C(x,t) = C_s\left[1 - erf\left(\frac{x}{2\sqrt{D_c t}}\right)\right] \quad (2)$$

where D_c = diffusion coefficient; C_s = surface chloride concentration; $C(x,t)$ = chloride ion concentration at a time t and a distance x from the concrete surface and erf = Gaussian error function. It is assumed that corrosion of the reinforcing steel begins at a time T_{corr}, when the chloride ion concentration at the cover depth reaches a critical chloride concentration, C_{cr}. The time to corrosion initiation can be found by using $C(x,t) = C_{cr}$ and solving for T_{corr}. For this study the values for C_s, C_{cr} and D_c were taken from Vu and Stewart [17] and can be seen in Table 1.

Table 1. Statistical Parameters for Corrosion Initiation Time.

Parameter	Mean	COV[a]	Distribution
Cover (cm)	3.5	.2	Lognormal
D_c (cm^2/year)	0.63072	.2	Lognormal
C_s (kg/m^3)	2.95	.5	Lognormal
C_{cr} (kg/m^3)	0.9	.19	Uniform(0.6-1.2)

[a]COV = Coefficient of Variation

The distribution for the corrosion initiation time is found using Monte Carlo simulation with a sample size of 50,000. A lognormal distribution for T_{corr} with a mean of 11.16 and a standard deviation of 6.94 years is found to be a good fit to the simulated data for corrosion initiation time.

3.2 Deterioration Phase

Once corrosion has initiated, the loss of steel cross section begins and the load carrying capacity of the column reduces with time. To estimate the loss of steel cross section with time, a time dependent corrosion rate is used developed by Vu and Stewart [17]. Although a lot of time dependent fragility analyses have used a constant corrosion rate, Vu and Stewart [17] suggest that the formation of rust on the steel surface will reduce the diffusion of the iron ions away from the steel surface and will also reduce the area ratio between the anode and the cathode. This would cause the corrosion rate to reduce with time. The time dependent corrosion rate can be written as

$$i_{corr}(t_p) = i_{corr}(1) \cdot 0.85 t_p^{-0.29} \quad (3)$$

where t_p= time since corrosion initiation and $i_{corr}(1)$ = the corrosion current density and the start of the deterioration phase and can be written as

$$i_{corr}(1) = \frac{37.8(1 - {}^{w}/_{c})^{-1.64}}{cover} \; ({}^{\mu A}/_{cm^2}) \quad (4)$$

where ${}^{w}/_{c}$ = water cement ratio and $cover$ = the concrete cover in mm. Faraday's law states that a corrosion current density of $i_{corr} = 1\mu A/cm^2$ corresponds to a uniform corrosion penetration of 11.6μm year^{-1} [20]. Therefore, the reduction in reinforcing bar diameter can be calculated directly from the corrosion current density using the following equation. [20]

$$\Delta D(T) = 0.0232 \int_{Ti}^{tp} i_{corr}(t_p) \; ({}^{mm}/_{year}) \quad (5)$$

From equation 4 it can be seen that the corrosion rate depends on the concrete quality and the cover depth. This paper investigates the effect both these parameters have on the loss of cross section with time. In figure 2 the influence of the concrete compressive strength and cover on $i_{corr}(1)$ can be seen. It is clear from figure 2 that an increase in cover and compressive strength results in a decrease in the corrosion rate.

For this paper, a cover of 35mm and a concrete compressive strength of 30MPa are assumed. The resulting loss of cross sectional area with time can be seen in figure 3. After 100 years of exposure there is a 13.6% loss of steel cross section. This reduction of steel can easily be included in the Opensees finite element model by reducing the area of each reinforcing bar in the fiber section.

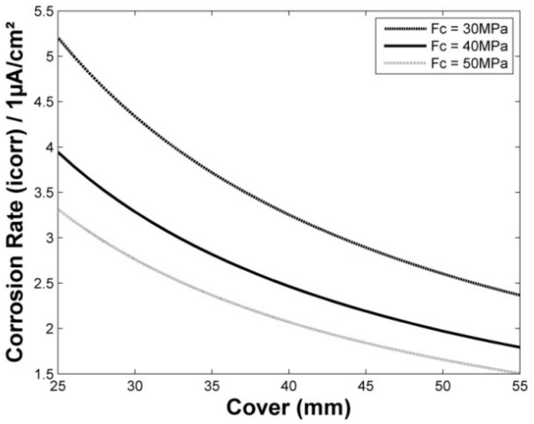

Figure 2. Influence of concrete strength and cover on corrosion rate.

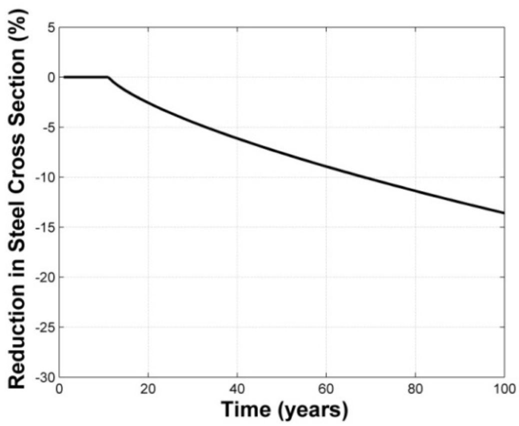

Figure 3. Reduction in reinforcing steel cross section with time for 35mm cover.

3.3 Loss of Steel Strength

It has also been suggested by Du et al [21] that the onset of corrosion results in a reduction of the strength of the steel. They carried out both accelerated and simulated corrosion tests on reinforcing steel bars embedded in concrete and concluded that the strength of steel bars decreases significantly with chloride penetration. They proposed the following empirical equation to estimate the time-dependent loss of yield strength due to corrosion:

$$f_y(t) = [(1 - .005A(t))f_{yo}] \quad (6)$$

where $f_y(t) =$ the yield strength of corroded reinforcement at each time step; $f_{y0} =$ the yield strength of noncorroded reinforcement; $t =$ time elapsed since corrosion initiation (years) and $A(t) =$ percentage of steel mass loss over time calculated from the consumed mass of steel per unit length divided by the original steel mass. For this study the loss of strength after 100 years is calculated and input into the Opensees finite element model.

4 IMPACT OF DETERIORATION ON SEISMIC RESPONSE OF RC COLUMNS

This study considers the seismic response of the columns and abutments of this integral bridge. However, for brevity only the response of the columns will be shown here as a preliminary study showed these as the most vulnerable components.

For this study the column demand is taken as the curvature ductility ratio and can be written as

$$\mu_\phi = \frac{k_{max}}{k_{yield}} \quad (7)$$

where $k_{max} =$ the maximum curvature demand and $k_{yield} =$ the curvature in the column which causes first yield of the outermost reinforcing bar. The curvature ductility demand ratio is calculated in the longitudinal and transverse directions and the column demand is taken as

$$\mu_\varphi = \sqrt{\mu^2{}_{\varphi-longitudinal} + \mu^2{}_{\varphi-transverse}} \quad (8)$$

In order to find k_{yield} a moment curvature analysis of the reinforced concrete circular section was carried out. With the onset of deterioration the loss of steel cross section and strength will result in a reduction in k_{yield}. After 100 years k_{yield} is reduced by 9.6% from .0041/m to .0037/m.

As a first step for this study, the pristine and deteriorated bridges are subjected to a sample ground motion with a peak ground acceleration of .9864g in the longitudinal direction. Figure 4 shows the increase in seismic demand placed on the structure after 100 years. For this sample ground motion the maximum curvature increased from .0381/m to .0519/m representing an increase of 36.2%.

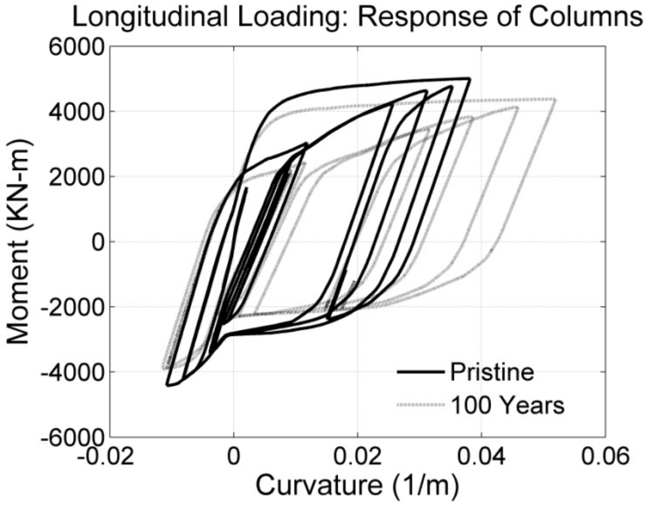

Figure 4. Increase in curvature demand for the 100 year old bridge.

5 DEVELOPMENT OF COMPONENT FRAGILITY CURVES

Seismic fragility curves offer conditional statements of probability of a bridge reaching a defined damage state for a given ground motion intensity level. The first step involved in developing a fragility curve is to develop a probabilistic seismic demand model. Once the 3D finite element model has been generated it is subjected to a suite of ground motions to account for uncertainty in ground motion level. For this paper a suite of 80 ground motions are used which have been identified by Gupta and Krawinkler [22] from the PEER strong motion database along with another 20 identified by Krawinkler et al. [23] from the SAC project database. All 100 ground motions are representative of seismicity in the California region. The 80 ground motions gathered from the PEER data base have an even selection of time histories from four bins including low and high magnitudes and long and short epicentral distances. The magnitudes vary between 5.8 and 6.9 and the epicentral distances range from 10-60km. The 20 ground motions are made up of 10 pairs with intensities of 2% and 10% probability of exceedence in 50 years respectively. As well as uncertainty in ground motion, material uncertainty is also accounted for. The peak component demand for each ground motion is then recorded. For this paper, only the column and abutment demands are considered. Future work could extend the components considered to the deck and the foundations. Cornell et al. [24] suggests that the relationship between seismic demand, S_D and intensity measure, IM follows a power law model and can be written as:

$$P[D > C|IM] = \Phi\left(\frac{\ln({}^{S_D}/_{S_C})}{\sqrt{\beta^2{}_{S_D|IM} + \beta^2{}_C}}\right) \quad (9)$$

The fragility can be evaluated directly knowing the capacity and the PSDM parameters (a, b, $\beta_{SD|IM}$) by rearranging equation 9 into the following form

$$P[D > C|IM] = \Phi\left(\frac{\ln(IM) - \frac{\ln(S_C) - \ln(a)}{b}}{\frac{\sqrt{\beta^2{}_{S_D|IM} + \beta^2{}_C}}{b}}\right) \quad (10)$$

6 COLUMN FRAGILITIES

The components of this bridge which could experience possible damage during a seismic event include the foundations, deck, abutments and columns. However, a fragility analysis has not been carried out for each of these. The foundation fragilities are not calculated for this study because without fully considering soil structure interaction in the Opensees model, it is thought that the response of the foundations is not sufficiently accurate to justify carrying out a full component fragility analysis. A preliminary investigation into the deterministic response of the deck when the bridge is subjected to a .9864g earthquake shows that it will remain elastic and is therefore not considered a vulnerable component and also omitted from the fragility analysis. Previous research carried out by the authors show that beyond the moderate damage state the abutment fragilities are insignificant and therefore the fragility curves are not shown here [25]. Therefore, for this paper, only the column fragilities are calculated and shown in figures 5-8.

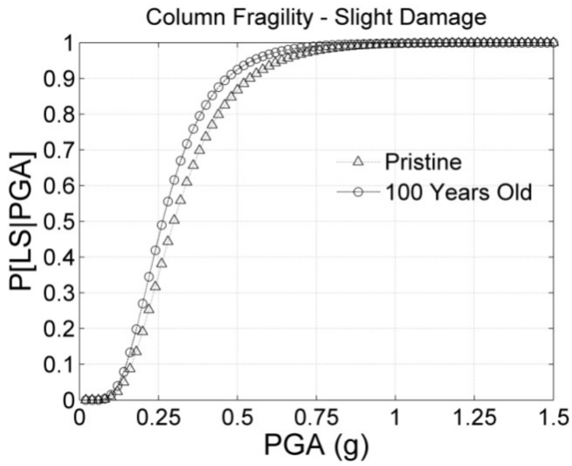

Figure 5. Column fragility curves: Slight Damage State.

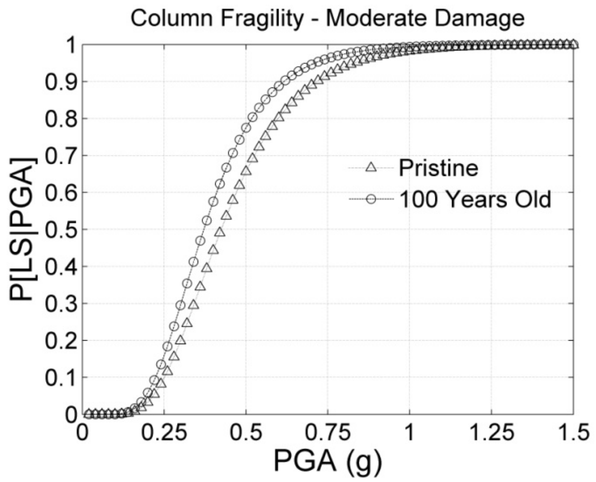

Figure 6. Column fragility curves: Moderate Damage State.

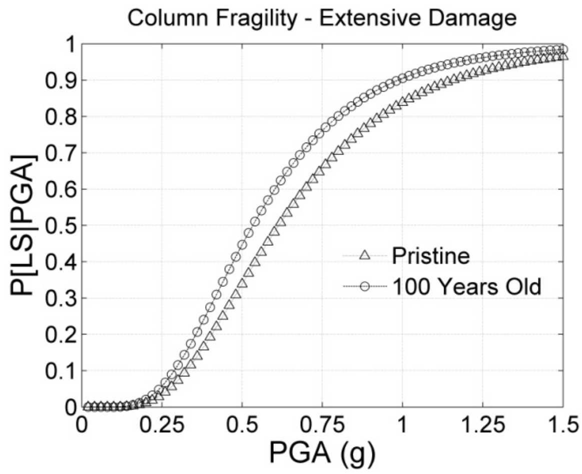

Figure 7. Column fragility curves: Extensive Damage State.

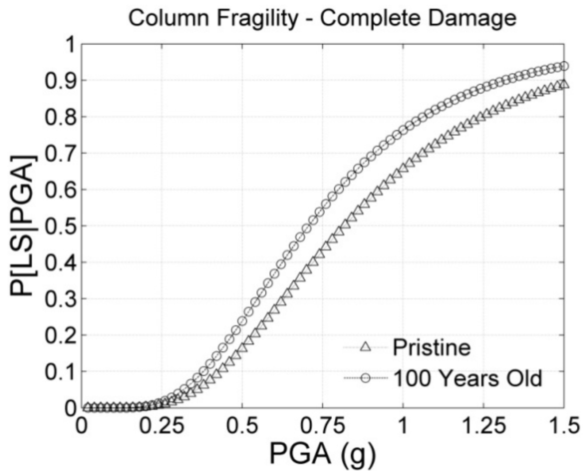

Figure 8. Column fragility curves: Complete Damage State.

7 SCOPE FOR FUTURE WORK

For this research chloride induced corrosion of the steel reinforcement is considered assuming a marine environment less than 1km from the coast. A review of the literature, as well as previous work carried out by the authors [25] shows that the deterioration model chosen has a huge influence on the levels of deterioration of the bridge. It is therefore recommended that different deterioration models representing various environments are considered when carrying out a seismic fragility analysis. This would provide a better insight into which environments cause the greatest increase in seismic vulnerability with age and therefore could be used to prioritise maintenance and retrofit scheduling.

Although chloride induced corrosion has been cited as the most severe form of deterioration [26], other deterioration mechanisms such as carbonation may be significant in certain environments and should be investigated. It has been suggested that carbonation rates may vary from one part of the structure to another [27]. For example, if a component is permanently sheltered the carbonation rate may be significantly higher than those parts exposed to the rain. This suggests that carbonation of the columns should be investigated to establish if it is causes significant levels of deterioration.

More research into how to include deterioration in the calculation of component limits states for columns is needed. For this study, curvature ductility was chosen as the column limit state. Deterioration was accounted for by reducing the yield curvature. However, a more accurate estimate of deteriorated capacities is needed accounting for loss of steel, loss of bond between the steel and the concrete and concrete cracking and spalling.

Although material uncertainty is accounted for in this paper, a single deterministic model is used for the geometry of the bridge. Previous studies which have carried out fragility assessments of deteriorating RC bridges have accounted for geometric uncertainty therefore would be a necessary future step for this study [5,7].

8 CONCLUSION

This paper provided a time dependent fragility analysis of a 3 span integral reinforced concrete bridge. Only deterioration of the RC columns is considered. The deterioration mechanism chosen for this paper is chloride induced corrosion and is represented by a loss of steel cross section and a reduction in steel strength. Corrosion models from previous research carried out by Vu and Stewart [17] are used assuming the bridge is located in a marine environment less than 1km from the coast. A full probabilistic analysis is carried out to account for variability in ground motion and material parameters. Variation in geometric parameters of the bridge is beyond the scope of this paper. Only fragilities of the RC columns are calculated. Foundation, abutment and deck fragilities are neglected for reasons given in section 6 of this paper. The column fragilities calculated show an increase in column vulnerability with age. For example, a 13.6% decrease in the median value PGA for the complete damage state was seen after 100 years. It is worth noting that this increase in fragility is significantly less than increases seen when different deterioration models are considered [5]. This emphasises the effect the deterioration model chosen has on the time-dependent fragility curves and the importance of looking at multiple deterioration models.

A general conclusion from the findings in this paper and others [2,3,4,5,6,7], is that the inclusion of bridge age and exposure condition in seismic risk assessments is necessary to offer a more realistic estimate of the seismic vulnerability of the bridge. Although very recently researchers have begun to study the effects of aging on the seismic performance of bridges, work to date has been limited to certain bridge types and exposure conditions. More work is necessary if aging is to be included in future seismic risk assessments, which could lead to more accurate estimates of life cycle costs and more efficient rehabilitation strategies.

ACKNOWLEDGMENTS

The authors would like to sincerely thank the Irish Research Council for Science Engineering and Technology for financially supporting the research. They would also like to express sincere gratitude to the Fulbright Commission in Ireland and CRH Ireland for financially supporting research carried out by the authors at Rice University, Texas.

REFERENCES

[1] ASCE. 2009. ASCE: Infrastructure fact sheet. (http://www/infrastructurereportcard.org/sites/default/files/RC2009_bridges.pdf) (May 22, 2009)

[2] Choe, D., Gardoni, P., Rowowsky, D., and Haukaas, T. 2008. Probabilistic capacity models and seismic fragility estimates for RC columns subject to corrosion. Reliab Eng. Syst. Saf, 93(3), 383-393.

[3] Choe, D., Gardoni, P., Rowowsky, D., and Haukaas, T. 2009. Seismic fragility estimates for reinforced concrete bridges subject to corrosion. Struct Safety, 21(4), 275-283.

[4] Choe, D., Gardoni, P., and Rosowsky, D. 2010. Fragility increment functions for deterioration reinforced concrete bridge columns. J. Eng. Mech. 136(Compendex): 969-978.

[5] Ghosh, J., Padgett, J. E. 2010. Aging considerations in the development of time-dependent seismic fragility curves. Struct. Eng. 136(12) 1497-1511.

[6] Akiyama, M., Fragopol, D. M., Matsuzaki, H. 2011. Life-cycle reliability of RC bridge piers under seismic and airborne chloride hazards. Earth. Eng. Struct. Dyn. 40(15): 1671-1687.

[7] Alipour, A., Shafei, B., and Shinozuka M. 2010. J. Bridge. Eng. 16(5) 597-611.

[8] Opensees [Computer software]. OpenSees Development Team, Pacific Engineering Research Center, University of California, Berkeley, CA.

[9] Aviram, A., Mackie, K. R., Stojadinovic, B. 2008. Guidelines for the nonlinear analysis of bridge structures in California. Pacific Earthquake Engineering Research centre.

[10] Mander, J. B., Priestly, M. J. N., and Park, R. 1988. Theoretical stress-strain model for confined concrete. J. Struct. Eng., 112(8), 1804-1826.

[11] Shamsabadi, A., Khalili-Tehrani, P., Stewart, J. P., and Taciroglu, E. 2009. J. Bridge. Eng. 15(3) 302-311.

[12] Nielson, B. 2005. Analytical fragility curves for highway bridges in moderate seismic zones. Ph.D. thesis, Georgia Institute of Technology, Atlanta, Ga.

[13] Tilly, G. 2007. The durability of repaired concrete structures. Proceedings of the International Association for Bridgee and Structural Engineering Symposium (IABSE), Weimar, Germany.

[14] Thoft-Christensen, P., Jensen, F. M., Middleton, C.R., and Blackmore, A. 1996. Assessment of the reliability of concrete slab bridges. Conf. or Workshop Item, Univ. of Cambridge, Cambridge, U.K.., (http://publicationis.eng.cam.ac.uk/6361/) (Mar. 5, 2010)

[15] Duracrete. 2000 Statistical quantification of the variables in the limit state functions. The European Union Brite EU Ram 3 contract BRPR-CT95-0132 Project BE95-1347 Report no BE95-1347/R7

[16] Stewart, M.G., Rosowsky, D.V. 1998. Structural safety and serviceability of concrete bridges subject to corrosion. J. Infra. Syst ASCE. 4(4) 146-55.

[17] Vu, K.A.T., Stewart, M.G. 2000 Structural reliability of concrete bridges including improved chloride-induced corrosion models. Struct. Saf. 22(4) 313-33.

[18] Enright, M.P., Frangapol, D.M. 1998a. Probabilistic analysis of resistance degradation of reinforced concrete bridge beams under corrosion. Eng Struct. 20(11) 960-71.

[19] Enright, M.P., Frangapol, D.M. 1998b. Service life prediction of deteriorating concrete bridges. J. Struct. Eng ASCE. 124(3) 309-17.

[20] Val, D. V., Stewart, M.G., Melchers, M.E. 1998.Effect of reinforcement corrosion on reliability of highway bridges. Eng Struct. (20)11 1010-19.

[21] Du, Y.G., Clark, L. A., and Chan, A. H. C. 2005a. Residual capacity of corroded reinforcing bars. Mag. Concr. Res. 57(3) 135-147.

[22] Gupta, A., and Krawinkler, H. 2000. Behavior of ductile SMRFs at various seismic hazard levels. J. Struct. Eng. 126(1) 98-107.

[23] Krawinkler, H., Medina, R., and Alavi, B. 2003. Seismic drift and ductility demands and their dependence on ground motions. Eng. Struct. 25(5) 637–653.

[24] Cornell, C.A., Jalayer, F,. Hamburger R.O., and Foutch, D. A. 2002. Probabilistic basis for 2000 SAC Federal Emergency Manafement Agency steel moment frame guidelines. J. Struct. Eng. 128(4) 526-533.

[25] Ní Choine, M. O Connor, A. Padgett, J.E. 2012. Impact of Corrosion on the Seismic Vulnerability of Multispan Integral Concrete Bridges. Proceedings of the 6th International Conference on Bridge Maintenance, Safety and Management. Lake Como, Italy

[26] Silano, L. G., and Brinckerhoff,P. 1993. Bridge inspection and rehabilitation. Wiley-IEEE, New York.

[27] Bertolini, L., Elsener, B., Pedeferri, P. Polder R.P. 2004. Corrosion of Steel in Concrete Prevention, Diagnosis Repair. Germany. Wiley -vch

2D finite element stability analysis of a reinforced piled embankment

K. Jennings[1], P. J. Naughton[1]
[1]Geotechnical Research Group, School of Engineering, Institute of Technology Sligo, Ireland
email: jennings.keith@itsligo.ie, naughton.patrick@itsligo.ie

ABSTRACT: Piled embankments are widely used for the construction of roads and rails over soft and/or compressible soils. Traditional design methods, such as BS 8006 assume that the lateral trust is carried by geosynthetic reinforcement placed at the base of the embankment directly over the pile caps. At the extremities of the embankment both horizontal equilibrium and strain compatibility between the different components; the embankment fill, the geosynthetic reinforcement, the pile group and the soft soil, must be achieved. This study using finite element analysis found that the stability of these structures was dependent on the ratio of embankment height to clear spacing between pile caps and the steepness of the embankment side slopes. Increasing the pile caps size, geosynthetic reinforcement stiffness, pile stiffness modulus and soft soil stiffness modulus increased stability. Decreasing the side slope steepness, embankment height and centre to centre spacing of the piles also increased stability.

KEY WORDS: Embankment; stability; geosynthetic reinforcement; pile; FEM.

1 INTRODUCTION

The design of piled embankments is a complex soil-structure interaction problem involving embankment fill, geosynthetic reinforcement, a pile group, and the soft underlying soil (Love & Milligan, 2003). In designing a piled embankment both vertical and horizontal equilibrium must be achieved. The internal horizontal (lateral) forces from the embankment fill acting outwards need to be balanced by a combination of tension in the horizontal geosynthetic reinforcement, lateral loads on the pile group and resistance from the soft soil. In addition to equilibrium considerations, strain compatibility between the displacement of the geosynthetic reinforcement, the pile group and the soft soil must be achieved (Love and Milligan, 2003). Structural stability must be achieved through equilibrium and strain compatibility considerations without having a detrimental effect on the serviceability of the structure. The stability of a structure is expressed in terms of its factor of safety. The stability of the structure may be calculated by utilizing limit equilibrium (LE) or finite element analysis (FE).

The conventional limit equilibrium methods of slope stability analysis used in geotechnical practice investigate the equilibrium of a soil mass tending to move downslope under the influence of gravity (Anon, 2003). A comparison is made between forces, moments, or stresses tending to cause instability of the mass, and those that resist instability (BS 8006, 1995 & Aryal, 2006).

Slope stability analysis by the finite element method use similar failure definitions as the limit equilibrium method for the soil mass but offer many advantages over limit equilibrium methods (Griffiths & Lane, 1999), such as the ability to develop the critical failure surface automatically with fewer assumptions (Kiousis et al., 2010). The FE method is particularly useful for soil-structure interaction problems (Aryal, 2008) in which structural members interact with a soil mass. The simplifying assumptions of the limit equilibrium approach hinder its ability to adequately model the complete geosynthetic-pile-soil interaction (Rowe & Soderman, 1985) in comparison to finite element analysis.

A reinforced embankment founded on a pile group (GRPE) is less prone to shear strength failure. The pile group is subjected to two destabilizing loads (vertical and lateral). The finite element method is most widely used to perform the analysis of piles under different types of loading (Chik et al, 2009). The first attempt to study the lateral behaviour of piles included two dimensional finite element models in the horizontal plane (Poulos & Davis, 1980). The influence of vertical load, such as that from embankments, on the lateral response of the pile through an experimental model supported by two-dimensional (2D) finite-element analysis was minimal (Anagnostopoulos & Georgiadis, 1993). The pile soil interaction is a complex three dimensional phenomenon and a 2D analysis may not properly simulate the behaviour when piles are under induced lateral soil movements (Karthigeyan et al., 2003, Kok and Huat, 2008). 2D analysis of the GRPE has a tendency to underestimate both the bending moments and pile group deflections (Kok and Huat, 2008). However, van Duijnen and Kwast (2003) found that plain strain 2D calculations when calibrated with correction factors matched the accuracy of 3D calculations very well for a reinforced piled embankment. Plane strain analysis models the cross section of the GRPE as a homogenous continuum longitudinally. Consideration of pile spacing in the longitudinal direction and its resultant effect on load, stress distribution and global stability are outside the scope of computation. Expressions may be developed with respect to the trend of deformations, loads and stresses with the discrepancies of the computed absolute values of the field variables acknowledged.

This study examines the suitability of the BS 8006 (1995) design methodology, through a finite element stability analysis approach. The effects of certain pertinent factors; the pile spacing, pile cap size, stiffness of the geosynthetic reinforcement, height of the embankment and the effect of the soft soil layer under the embankment were investigated.

Embankments require the use of the soil mechanics definition of a safety factor, which is the ratio of the available shear strength to the minimum shear strength needed for equilibrium (Plaxis 2010). Plaxis 2D finite element analysis computes this factor of safety using a phi-c reduction procedure. Expressions are developed giving the degree of structural stability offered by the pile geometric characteristics, embankment characteristics, geosynthetic reinforcement and the underlying soft soil.

2 NUMERICAL ANALYSIS

The numerical analysis was performed using the Finite Element code-Plaxis 2D Version 9.0. The generic model consisted of an embankment 4.0m in height with a 1V:2H side slope. The concrete piles, 10 m in length, were at 3.0m centres with a 1.0m wide pile cap, Figure 1. The geosynthetic reinforcement had a stiffness of 500kN/m and was placed 100mm above the pile cap. The underlying soft soil depth was 8.0m. The surcharge loading at the top of the embankment was 10kN/m as commonly used in practice (Han and Gabr, 2002). The embankment height, H, was varied from 2.0m to 6.0m, the steepness of the side slope from 1V:2H to 1V:3H, the pile spacing, s, from 1.5m to 4.5m, the pile cap size, a, from 0.3m (i.e. no pile cap) to 2.0m, the soft soil depth from 8.0m to 15.0m and the stiffness of the geosynthetic reinforcement from 0kN/m (unreinforced case) to 4000kN/m.

The pile was assumed fixed against rotation by penetrating into a firm bearing stratum, Figure 1. Plaxis 2D modelled the pile element with interfaces as a plate model with a linear elastic material set applied, Table 1. The Young`s modulus of the pile ranged from a stiff (E_p = 2.8×10^7 kPa) to a flexible modulus (E_p = 3.5×10^6 kPa) (Karthigeyan et al, 2003). The soil model used in the analysis was the Soft Soil Model selected from the Plaxis code due to its Cam Clay like properties especially under primary loading particularly for normally consolidated clay type soils. The soil parameters, Table 1, range from a very soft peat (SSM 1) to a normally consolidated clay (SSM 2). The embankment fill was modelled using typical values for a granular base material, Table 1. A Mohr Coulomb model was selected for the embankment fill, Table 1.

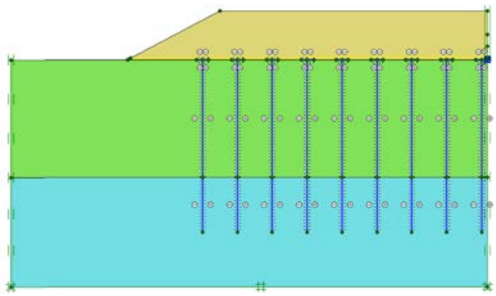

Figure 1. Plaxis 2D reinforced piled embankment model.

The Plaxis 2D analysis used a plastic updated mesh analysis with a staged construction and drained conditions to simulate the long term behaviour of the structure. The global coarseness of the mesh was selected as very fine with a local refinement at the pile group/reinforcement location. 15 node element mesh density was selected to accurately predict global stabilty, 6 node element mesh was found to compute a lower structural deformational repsonse. Axioms such as a horizontal ground level, parallel horizontal soil layers/pheatric levels enable a K_0 procedure to be adopted in calculating initial stresses within the soil, unconformity of field based Irish conditions to these stipulations would require gravity loading to be used instead.

3 RESULTS OF FINITE ELEMENT STABILITY ANALYSIS

3.1 *Stiffness of the Geosynthetic Reinforcement*

Stability of the geosynthetic reinforced piled embankment (GRPE) structure increased for an increase in the geosynthetic reinforcement stiffness for both side slope steepness, Figure 2. The most significant improvement in structural stability was for the initial inclusion of reinforcement to the structure. The inclusion of geosynthetic reinforcement (0→500 kN/m) increased the factor of safety by 0.137 (1V:2H side slope) and 0.266 (1V:3H side slope), Figure 2. Further increases of the geosynthetic reinforcement stiffness, from 500 kN/m to 4000 kN/m, yielded only a marginal increase (0.017) in the factor of safety for a 1V:2H side slope and a 0.189 increase for a 1V:3H side slope, Figure 2. The relationship between the factor of safety and the stiffness of the geosynthetic reinforcement was inversely correlated with the deformational response of the structure, this relationship was also observed by Han and Gabr (2002).

Table 1 Material characteristics.

	***E* (kN/m²)**	***v***	***c* (kN/m²)**	***Φ* Deg (°)**	***ψ* Deg (°)**	**γ_{unsat} (kN/m³)**	**γ_{sat} (kN/m³)**	***Rinter* -**
Embankment Fill[1]	20000	0.2	0	35	0	19	20	0.85
Pile[2]	3.00E+07							
	λ* -	**κ* -**	***Φ* Deg (°)**	***c* (kN/m²)**	***ψ* (°)**	**γ_{unsat} (kN/m³)**	**γ_{sat} (kN/m³)**	***Rinter* -**
Soft Soil (SSM 1)[3]	0.12	0.04	15	5	0	12	12	0.65
Soft Soil (SSM 2)[3]	0.03	0.01	25	1	0	19.5	19.5	0.7
	***EA* (kN/m)**							
Geosynthetic Reinf[2]	500							

Note: ¹ Gangakhedkar 2004, ² Han and Gabr 2002, ³ Farag 2008,

3.2 *Embankment Height*

Stability of the GRPE decreased for an increase in embankment height, Figure 3, where the pile group geometric layout (pile spacing and pile cap size) remained constant. For all embankment heights, global stability is predominantly influenced by the degree of arching present and the destabilizing lateral thrust acting outwards from the embankment centre.

The degree of arching present within the GRPE increased as the embankment height approached the critical height required for full arching (defined as 1.4 times the clear spacing between pile caps in BS 8006, 1995). Figure 3 suggests that whilst an increase in embankment height resulted in an improvement in the degree of arching, the improvement in load transfer efficiency was insignificant in comparison to the destabilizing lateral forces which resulted in an overall reduction in global stability.

An increase in embankment height corresponded to a linear increase in the lateral thrust of the embankment fill acting outwards. The increase in lateral thrust mobilized an increase in the lateral deformational response of the pile group, and resulted in a lower overall global stability for both cases of side slope steepness, Figure 3.

Vertical deformation of the side slope between the toe of the embankment and the outer row pile increased linearly with embankment height. The deformational response of the side slope was correlated with the overall global stability of the GRPE structure.

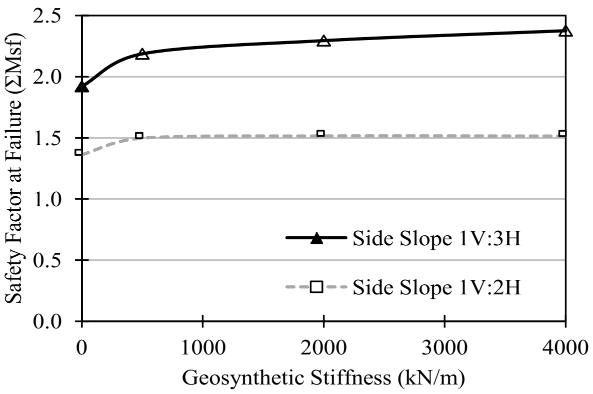

Figure 2. Safety Factor at failure for a range of geosynthetic stiffness.

3.3 *Embankment Side Slope*

GRPE stability increased for a decrease in the steepeness of the embankment side slope, Figure 4. Under the side slope, the embankment fill was subjected to lateral stresses due to the horizontal spreading effect of the slope (Rowe & Li, 2002). Resistance to the lateral thrust must be met by a combination of tension in the reinforcement, deflection of the pile head and deformation of the embankment fill (Love and Milligan, 2003). BS 8006 (1995) assumes that the geosynthetic platform is almost perfectly rigid. The location of the outer most pile in relation to the embankment crest is based on an empirical estimation of Rankine`s active earth pressure. The vertical deformations of the geosynthetic reinforcement/ embankment fill near the toe of the embankment exacerbated the imbalance of passive-active earth pressure within the side slope, thus mobilizing an increase in magnitude of the failure mechanism. An increase in the side slope steepness corresponded to an increase of vertical deformation of the reinforcement/fill near the toe (Jennings and Naughton, 2011), mobilization of horizontal deformation in the fill and a reduction in stability.

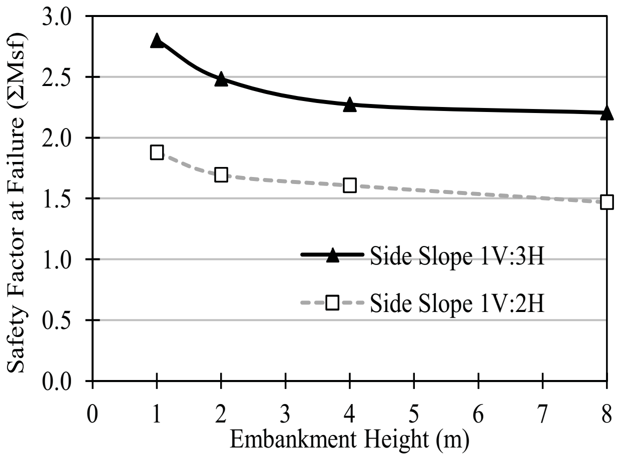

Figure 3. Safety factor at failure for a range of embankment heights.

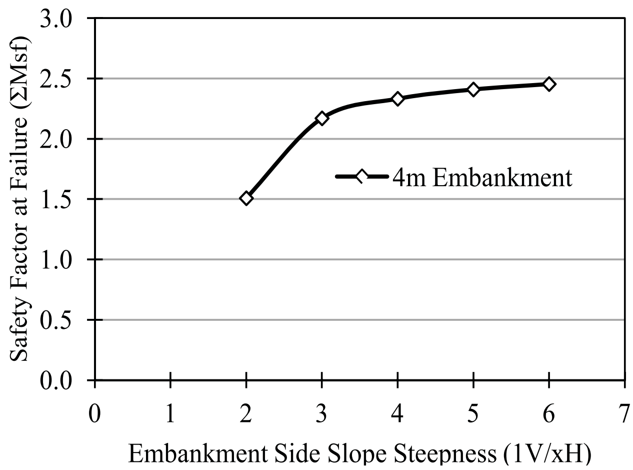

Figure 4. Safety factor at failure and embankment side slope steepness (1V:xH).

As the side slope steepness increased, the differential between the passive and active earth pressure mobilized a lateral deformational response in the embankment fill outwards from the embankment centre until equilibrium was achieved. The resultant deformational response of the fill yielded deflection of the pile head and a subsequent decrease in structural stability.

An increase in the steepness of side slope (1V:6H→1V:3H) resulted in a linear decrease in structural stability, Figure 3. A further increase in the steepness of the side slope (1V:3H→1V:2H) signifcantly reduced the structural stability of the embankment. An increasingly dominant active earth pressure in the side slope resulted in an increase in the destabilization rate for an increase in embankment side slope steepness.

3.4 *Pile Group*

Increasing pile centre to centre spacing within the pile group had only a marginal affect on structural stabilty, Figure 5(a). The resistance of pile group to lateral loading is the sum of the individual piles lateral load capacities. An increase in pile spacing reduced the number of piles contained within the pile group extent, thus reducing the total lateral load resistance capacity of the group, which corresponded to an increase in pile head deflections and bending moments (Jennings & Naughton, 2011).

For the 1V:3H side slope, increasing the pile spacing from 1.5m to 3.0m yielded a 0.103 reduction in the safety factor. Increasing the pile spacing from 3.0m to 4.5m yielded a 0.151 reduction in stabilty, Figure 5a. The stability of the 1V:2H side slope was immune to a variation of pile spacing as the destabilizing active earth pressure present within the side slope far outweights the stabilizing influence of a decrease in the pile centre to centre spacing.

An increase in the pile cap size yielded an increase in the stability of the structure, Figure 5(b). Increasing the pile cap size from 0.3 m to 2.0 m increased stabilty by 0.591 for the 1V:3H and 0.021 for the 1V:2H. An increase of the pile cap size had a more prominant effect on the stability of the 1V:3H side slope. Similar to the pile spacing, the stabilty of the 1V:2H side slope was unresponsive to a variation of pile cap size, Figure 5(b).

Increasing the pile cap size reduced horizontal deformation of the embankment fill outwards from the embankment centre, and increased the load transfered to the pile heads, thus increasing the efficiency of the pile group (Jennings and Naughton, 2011). This resulted in an overall increase in stability of the GRPE.

The stability of the GRPE increased for an increase in the outer row pile rake angle, Figure 6(a). The outer row pile rake angle was varied from 0° to 30° in 5° increments. An increase of pile rake imcreased the piles resistance to lateral loads (a portion of lateral load converted into vertical vector and transferred axially to pile head). Jennings and Naughton (2011) suggested that a outer row pile rake angle increase from 0° to 15° yielded the greatest reduction in the horizontal deformations of the embankment. A futher increase in pile rake (greater than 15°) corresponded to a reduction in stability due to the outer row pile head deforming laterally towards the embankment centre as a result of vertical load resulting in an increase in embankment fill horizontal deformation outwards for both side slope steepness, Figure 6(a).

The depth of the soft soil layer, and consequently the length of the piles, had an insignificant effect on the overall stability of the GRPE , Figure 6(b). The stability of the structure remained constant for both a range of soft soil depths and steepness of side slopes, Figure 6(b). Jennings and Naughton (2011) suggested that an increase in the soft soil depth would, by virtue of a corresponding increase in the lever arm length to the point of full fixity, result in an increase in pile head deflection and bending moments due to the lateral forces exerted on the pile head. However, the increase in pile head deflection as a result of an increased depth of soft soil was not sufficient to reduce the stability of the GRPE.

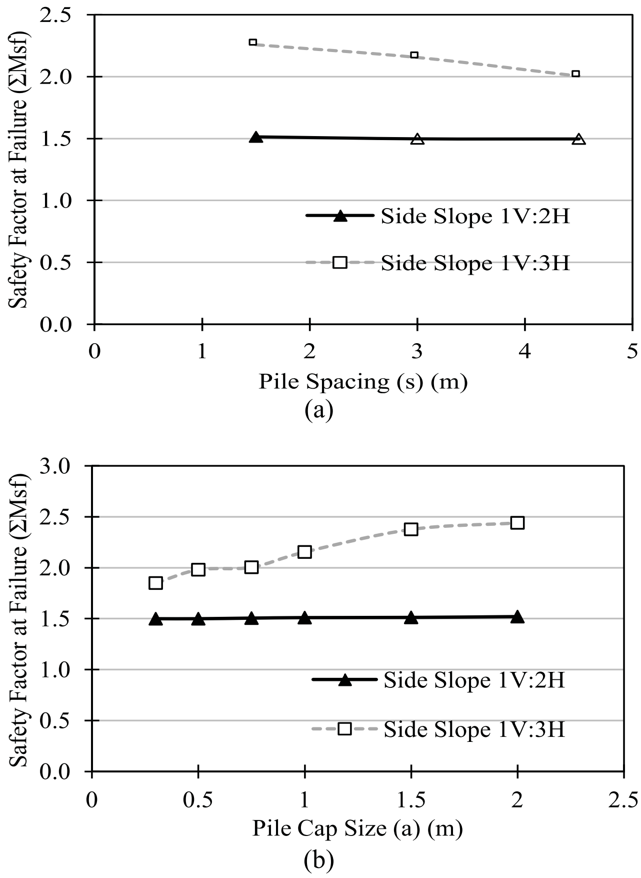

Figure 5. Safety factor at failure for a range of (a) pile spacing, (b) pile cap size.

The geometric ratio (H/(s-a)) was found to influence the stability of the structure , Figures 7(a) and (b). An increase in the pile spacing (reduction of geometric ratio) yielded a minor reduction in the stabilty for 1V:3H side slope and an insignificant reduction for the 1V:2H side slope, Figure 7(a) and (b). Similar to a variation in the pile spacing, an increase in the pile cap size improved the stability for the 1V:3H side slope, Figure 7(a) but not for the 1V:2H, Figure 7(b).

3.5 *Pile-Soil Interaction*

The pile group underlying the reinforced embankment is required to support the vertical loading from the embankment and resist the lateral loads due to the horizontal spreading effect of the embankment fill. The resistance of the piles to lateral loads is a complex soil structure interaction problem. A variation of the Young`s Modulus of both the pile and soil enabled the influence of the complex interaction to be quantified. The pile relative stiffness factor K_R was defined by Karthigeyan et al. (2003) as:

$$K_R = E_P I_P / E_S L^4 \quad (1)$$

where, E_P is the Young`s modulus of the pile, $I_P$ is the moment of inertia of the pile section, $E_S$ is the Young`s modulus of soil and L is the embedded length of pile (Karthigeyan et al., 2003).

The stability of the geosynthetic reinforced piled embankment increased for an increase in pile stiffness (increase of relative stiffness factor, K_R) for both side slope cases, Figure 8(a). An increase in the piles relative stiffness factor K_R (increase of piles Young`s modulus of flexible pile (3.5×10^6 kPa, to that of a stiff pile, $E_p = 2.8\times10^7$ kPa) yielded a 0.027 increase in stability for the 1V:2H side slope and a 0.13 stability increase for the 1V:3H side slope. Whilst the stability of the embankment increased for an increase in pile stiffness, the improvement in stability was only marginal, Figure 8(a).

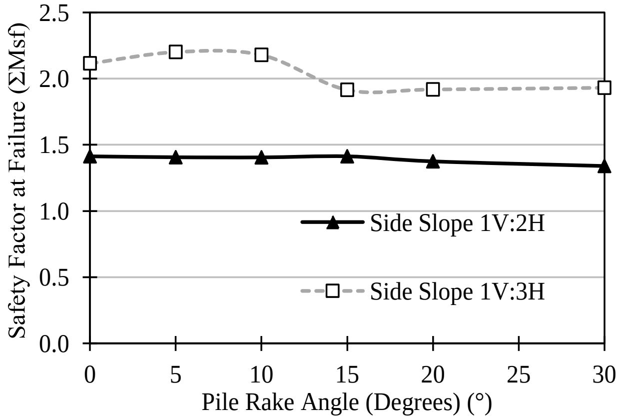

(a)

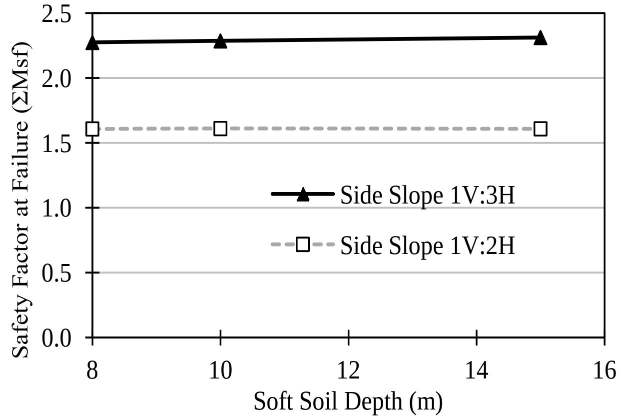

(b)

Figure 6. Safety factor at failure for a range of (a) pile rake angle, (b) soft soil depth.

Increasing the stiffness of the soft soil layer (decrease of relative stiffness factor, K_R) underlying the GRPE structure resulted in an increase in structural stability, Figure 8(b). An increase in soft soil stiffness from 800kN/m^2 to 3333kN/m^2 increased the factor of safety of the GRPE by 0.2 for a 1V:3H side slope and only marginally for the 1V:2H side slope, Figure 8(b).

Similar to other parametric variations of the GRPE structure, the 1V:2H side slope yielded an insignificant improvement in structural stability for a pile/soil increase in stiffness, Figure 8(a) & (b). An increase in the side slope steepness from 1V:3H to 1V:2H mobilized an increase in magnitude of the failure mechanism that dominated any improvement in stability by a variation of the geometric layout of the GRPE structural members. The stability of the GRPE was most responsive to an increase in the soil stiffness, Figure 8(b), in comparison to the pile stiffness particularly for the 1V:3H side slope.

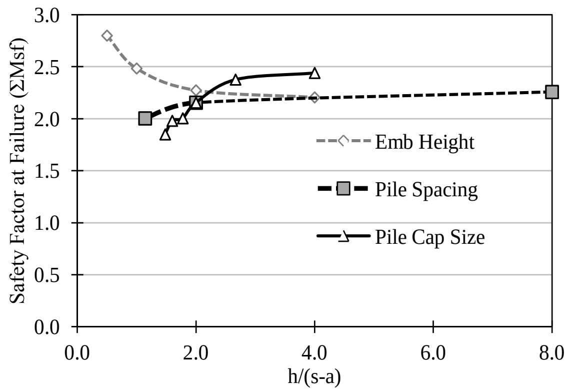

(a)

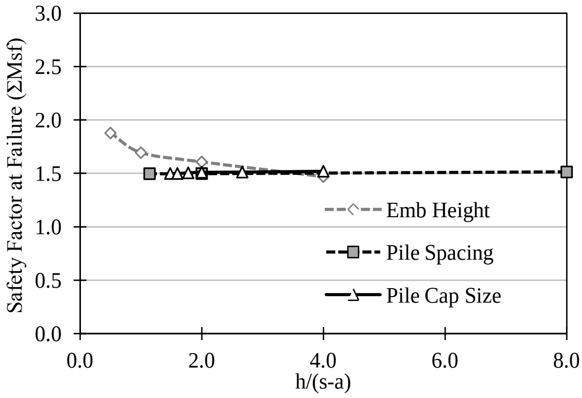

(b)

Figure 7. Safety factor at failure for a range of geometric ratios for (a) a 1V:3H side slope, (b) a 1V:2H side slope.

4 CONCLUSION

A finite element stability analysis using Plaxis 2D V9.0 of a GRPE, which investigated the influence of the pertinent geometric and characteristic embankment, pile, soil and reinforcement properties on the overall structural stability, was presented.

The analysis indicates that structural stability was most sensitive to embankment side slope steepness and the embankment height. An increase in side slope steepness mobilized both vertical and horizontal deformation of the embankment fill and reinforcement near the embankment toe, thus decreasing the overall stability of the structure. The analysis suggests that the side slope has an influence on the overall performance of the structure and not just at the extremities.

An increase in the pile cap size, geosynthetic reinforcement stiffness, pile stiffness modulus, soft soil stiffness modulus and a reduction of side slope steepness, embankment height and pile centre to centre spacing increased the stability of the geosynthetic reinforced piled embankment.

The pile-soil interaction of the pile group and its influence on the stability of the geosynthetic reinforced piled embankment was deemed most sensitive to the stiffness of the soft soil. However, the complex pile soil interaction cannot be accurately modelled as a 2D problem. Further analysis to calibrate the 2D pile-soil interaction and its influence on the stability of the geosynthetic with a 3D problem would be required. A 2D analysis of the geosynthetic reinforced piled embankment has a tendency to under estimate the bending moments and deflections of the piles.

The degree of improvement for a variation of geometric layout is a function of the side slope steepness. The greater the steepness of the side slope, the lower the improvement in stability.

Slope stability considerations dictate the necessity of an extension of the pile group extents further toward the embankment toe than presented suggested in BS 8006 (1995). Future studies on the influence of the outer row pile location are required. The subsequent development of an empirical expression of the most advantageous location of the outer row pile that is cognisant of the previous studies of the conditions near the extremities of GRPE`s is necessary.

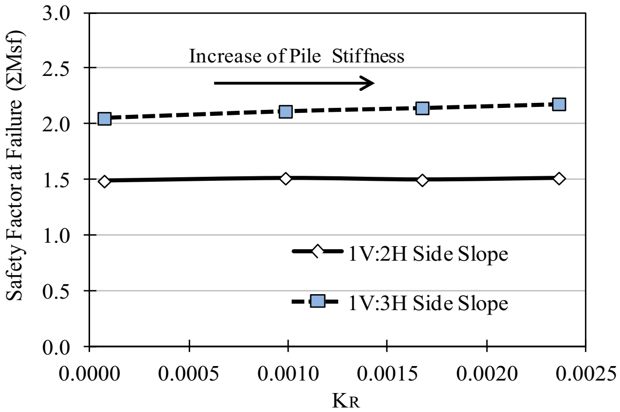

(a)

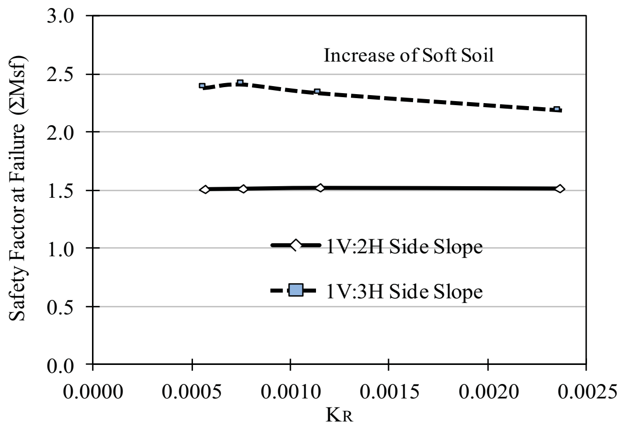

(b)

Figure 8. Safety factor at failure for a range of relative stiffness factors K_R for (a) a range of pile stiffness, (b) a range of soil stiffness.

REFERENCES

[1] Anagnostopoulos, C, and Georgiadis, M, (1993). "Interaction of axial and lateral pile responses." *J. Geotech. Eng. Division,* 119(4), pp 793–798.

[2] Aryal, K.P., (2006). "Slope stability evaluation by LE and FE methods." Ph D thesis, Norwegian University of Science and Technology, NTNU: Electronic version: http://www.diva-portal.org/ntnu/abstract.xsql?dbid=1868

[3] Aryal, K.P., (2008). "Differences between LE and FE method used in slope stability evaluation." *Proc. 12th Intl. Conference of International Association for Computer Methods and Advances in Geomechanics*, India, pp 4509 - 4516.

[4] British Standard BS 8006. (1995). "Code of practice for strengthened/reinforced soils and other fills." *British Standard Institution*, London, 162.

[5] Chik, Z.H, Abbas, J.H, Taha, M.R. and Shafiqu, Q.S.M, (2009). "Lateral behaviour of single pile in cohesionless soil subjected to both vertical and horizontal loads." *European Journal of Scientific Research*, 29(2), pp 194-205.

[6] Anon, (2003). "*Slope Stability manual*." EM 1110-2-1902, Washington, DC: Department of the Army, Office of the Chief Engineers.

[7] Griffiths, D.V, Lane, P.A. (1999). Slope Stability Analysis by Finite Elements. Geotechnique, 49(3):387-403.

[8] Han, J., and Gabr, M.A, (2002). "Numerical analysis of geosynthetic reinforced and pile supported earth platforms over soft soil." *Journal of geotechnical and geoenvironmental engineering*, ASCE, 128(1): 44-53.

[9] Jennings, K., Naughton, P.J., (2011). "Lateral deformation under the side slopes of piled embankments." *Proc. Geo-Frontiers*, Dallas.

[10] Karthigeyan, S., Ramakrishna, VVGST, Rajagopal, K., (2003). "Numerical modeling of piles under induced lateral movement in soft clay." *Proc. Intl. Workshop on Geotechnics of Soft Soils*, the Netherlands; pp 311-316.

[11] Kiousis, P.D, Griffiths, D.V. and Stewart, J.A, (2010). "Optimization of Stabilization of Highway Embankment Slopes Using Driven Piles (Phase 1)." Colorado Department of Transportation – Research, Report No. CDOT-2010-8.

[12] Kok, S.T. and Bujang B.K. Huat, (2008). "Numerical Modelling of Laterally Loaded Pile." *American Journal of Applied Sciences*, 5 (10) pp 1403-1408.

[13] Love, G, and Milligan, G, (2003). "Design methods for basally reinforced pile supported embankments over soft ground." *Ground Engineering*, March: 39-43.

[14] Plaxis, (2010). Finite Element Code for Soil and Rock Analyses. Plaxis 2D Version 9, Reference Manual, Edited by Brinkgreve, et al., DUT, the Netherlands. www.plaxis.nl.

[15] Poulos, H.G. and E.H. Davis, 1980. "*Pile Foundation Analysis and Design*". First addition. John Wiley and Sons, Inc., United States.

[16] Rowe, R.K. and Soderman, K.L., (1985). "An approximate method for estimating the stability of geotextile-reinforced embankments." *Canadian Geotechnical Journal.* (22), pp 392-398.

[17] Rowe, R.K., Li, A.L., (2002). "Geosynthetic reinforced embankments over soft foundations." *Proc. 8th Intl. Conference on Geosynthetics*, Delmas; pp 5-34.

[18] van Duijnen, P.G. and, Kwast, E.A. (2003). "3D modeling of a piled embankment on soft soil." *Proc. Intl. Workshop on Geotechnics of Soft Soils*, The Netherlands; pp 589-594.

Analysis of interface friction effects on microtunnel jacking forces in coarse-grained soils

Ciaran C. Reilly[1] and Trevor L.L. Orr[1]
[1]Department of Civil, Structural and Environmental Engineering, University of Dublin, Trinity College, Dublin 2, Ireland
email: creilly1@tcd.ie, torr@tcd.ie

ABSTRACT: Microtunnelling is an important trenchless construction technique that is used to successfully install essential utility pipelines in increasingly congested urban centres around the world. An important consideration for a microtunnelling project is the magnitude of the jacking force that will be required to advance the microtunnelling shield and the string of product pipes from the starting shaft to the receiving shaft. Frictional resistances along the surface of the pipeline have a major contribution to the total jacking force. This paper considers the frictional resistance mechanism involved in advancing concrete pipes through a coarse-grained soil and describes laboratory testing carried out with the aim of physically modelling the process. Comparisons are made with case histories from microtunnelling projects recently completed in coarse-grained soils. Recommendations are made on predicting likely jacking forces in advance of future projects.

KEY WORDS: Microtunnelling; Pipe-jacking; Interface friction; Coarse-grained soils.

1 INTRODUCTION

The use of microtunnelling as a cost effective, safe and environmentally sound means of providing utility pipelines is slowly being accepted in Ireland [1], while the technologies have been in extensive use elsewhere in the world for a great many years [2]. The prediction of jacking forces during a microtunnelling project is important for reasons of economy and to establish confidence in the proposed method of works, but these predictions are quite difficult due to the complex soil-structure interactions present [3]. The ground resistances, which the jacking force must overcome, are a combination of face resistance at the front of the shield and frictional resistance along the surface of moving pipeline, which increases as more pipes are added. The frictional resistance tends to be much greater in magnitude than the shield face resistance. It is more readily related to quantifiable pipe-soil interactions than the face resistance, which can be heavily operator-dependent [4]. As lengths demanded of microtunnels get longer [5, 6], and curved drives become more common [7], the mechanism of frictional resistance is an obvious area for further study with the objective of proposing suitable methods to predict and reduce it.

Several factors effect the generation of skin frictional resistances during a pipe jacking operation [8, 9]:

- Type of soil and variation along the pipeline
- Normal stresses acting on pipeline
- Roughness of pipeline surface
- Contact conditions between pipe and soil
- Overcut during excavation
- Position of water table
- Type and consistency of lubricant (if any)
- Duration of stoppages during driving
- Pipeline misalignment and/or curvature.

All of these factors are in some way related to the properties of a thin zone of intensely shearing material in the contact zone between a jacked pipe and the soil. The soil in this zone will be extensively reworked and remoulded as the pipeline advances at rates upwards of 30mm/minute. Much research has been undertaken on the shearing mechanism between soil and construction materials [10-15]. The main factors shown to affect interface friction behaviour under direct loading are interface roughness, soil density, mean particle size, particle angularity and normal stress across the interface. Uesegi et al. [12] performed simple shear tests between air-dry sand and concrete which showed that the peak coefficient of friction depends on the maximum peak-to-valley surface roughness (R_{max}) of the concrete and the mean particle size (D_{50}) of the sand. It was found that as the normalised roughness increases, a critical roughness is reached after which the coefficient of friction ssumes a peak value, as shown in Figure 1.

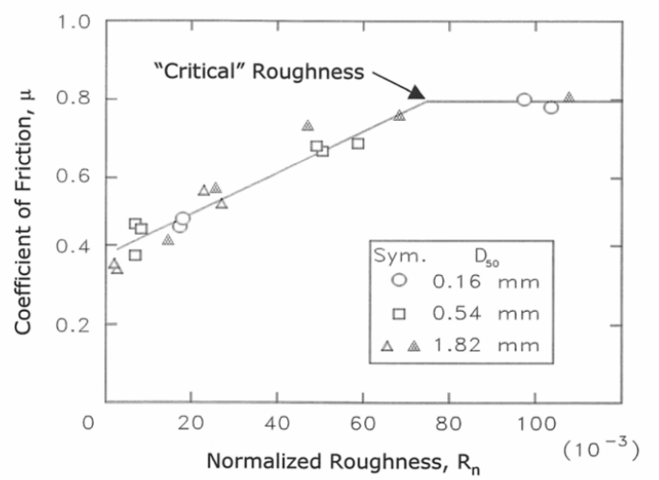

Figure 1. Coefficient of friction reaches a peak value at critical normailsed roughness of steel, $R_n = R_{max}/D_{50}$ [11].

Many studies have attempted to model the behaviour of the soil being sheared between a jacked pipe and the soil. Zhou [16] carried out numerical modelling using interface elements and found that in coarse soils the pipe separates or almost separates from the surrounding soil over a large proportion of the upper pipe surface area, and that normal stresses between the pipe and the soil over this part are low. Phelipot et al. [17] used a device similar to an annular shear apparatus to meaure the effects of overcut and lubrication on the advance of a model micro tunnel boring machine and pipe string. Iscimen [18] and Staheli [4] describe tests carried out using a novel shear testing apparatus capable of accepting curved sections of pipe. Shou et al. [19] use a simple apparatus to quantify the impact of different lubricant mixes on the jacking forces in sandy laterite gravel. In all the studies referred to above, large variations were reported between the experimental modelling results and field measurements. A common uncertainty is the contact area between the pipeline and the soil.

This paper gives preliminary results from physical modelling carried out using coarse-grained soils in order to better understand the pipe-soil interface present in pipe jacking. These results are compared to the frictional stresses observed during a number of pipe jacking operations, and an attempt is made to relate measured field values to the results of physical modelling.

2 JACKING FORCE PREDICTION

In microtunnelling, a force P_{total} needs to be provided to advance the microtunnelling shield and the string of product pipes behind it through the ground. P_{total} needs to overcome the combination of the face resistance at the front of the shield, P_F and the skin friction resistance along the pipeline, P_S:

$$P_{total} = P_F + P_S \tag{1}$$

2.1 Face resistance

Face resistance has been found to be dependent on operator influence, and as such is hard to predict. The face resistance must be maintained higher than the active earth pressure and lower than the passive pressure in order to prevent settlement or heave on the surface, and must be adjusted on site to suit the conditions encountered [20].

2.2 Frictional resistance

Depending on the stability of the soil during pipe jacking, the pipeline may slide along in an open bore, or the soil may collapse onto the pipe barrel. These two cases will produce markedly different frictional resistances, although even when the soil has collapsed onto the pipe, arching in the ground above the collapsed soil will reduce the normal stress acting on the pipe barrel below the initial in-situ value [21].

As the effective angle of friction, ϕ', defines the shearing resistance of a soil, the angle of interface resistance, δ, defines the shearing resistance of an interface. The interface friction angle is usually less than the effectice angle of friction. For convenience, an interface friction coefficient, μ, is defined:

$$\mu = \tan\delta \tag{2}$$

Eventual collapse of an excavated face is inevitable in a coarse-grained soil due to lack of undrained shear strength, although there is some evidence that suction effects in partially saturated coarse-grained soils may allow for some stand-up time, and short term stability. Stability can also occur if correct lubricant pressure is maintained during pipe jacking. The case histories in Section 4 will elaborate on this.

2.2.1 Stable ground

For coarse-grained soils, the frictional resistance acting on a pipe string sliding in a stable bore is a function of the weight of the pipes and the frictional properties of the pipe-soil interface:

$$P_S = \mu \cdot W \tag{3}$$

where W is the weight of the pipe string per linear metre and L is the length of drive. If the bore is located in ground water, the bouyant weight of the pipeline should be used:

$$P_S = \mu \cdot \left(W - \pi\gamma_w \frac{D_P^2}{4}\right) \tag{4}$$

where γ_w is the unit weight of water and D_P is the outside diameter of the pipeline, shown in Figure 2.

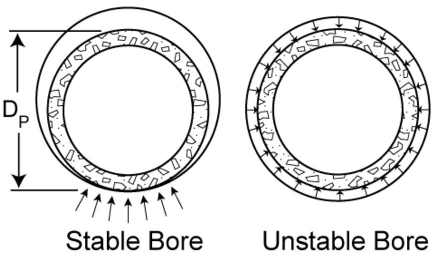

Figure 2. Stable and unstable bore situations.

2.2.2 Unstable ground

The frictional resistance acting on a jacked pipeline in unstable ground is a function of the normal force acting on the pipeline, N, and the coefficient of friction, μ:

$$P_S = \mu \cdot N \tag{5}$$

The normal force is the integral of normal stress, σ_N, over the pipeline surface. The normal stress, σ_N, is the stress due to soil and groundwater loading acting perpendicular to the pipeline surface. It has been shown that there is good agreement between the vertical stress acting at the pipe crown level, σ_{EV}, and σ_N [4], due to the effects of arching. This allows for estimation of the normal force directly from arching theory, as follows [22], with reference to Figure 3:

$$\sigma_{EV} = \frac{\gamma B}{2K \cdot \tan\phi}\left(1 - e^{-K \cdot \tan\phi \cdot H/B}\right) \tag{6}$$

where K is the coefficient of lateral earth pressure above the microtunnel (taken as 1 following recommendations in the literature, [3]), H is the height of cover over the roof of the pipe and B is the width of affected ground, defined as follows:

$$B = D_P\left(1 + 2\tan\left(\frac{\pi}{4} - \frac{\phi}{2}\right)\right) \tag{7}$$

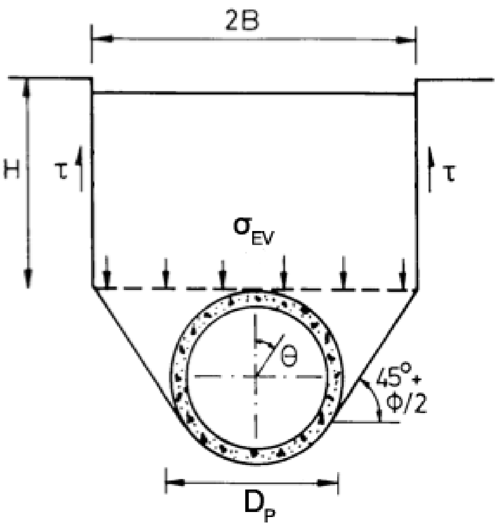

Figure 3. Silo pipe loading model after Terzaghi [25].

3 TESTING

Tests using a standard small shear box were carried out at TCD's Geotechnical Laboratory to establish the interface friction characteristics of two types of sand against a rough concrete surface, approximating the surface of a jacking pipe.

3.1.1 Soil properties

Two different fine to medium silica sands were tested – Glenview sand and Irish Glass Bottling (IGB) sand. Glenview sand is manufactured by crushing sandstone while IGB sand is a Belgian silica sand that was obtained from the Irish Glass Bottle plant in Ringsend, Dublin. The properties of each sand are listed in Table 1. Both sands are uniformly graded. The biggest difference observed between the sands is the shape of particles; this difference is shown clearly in Figure 4. Soils were tested dry. A loose density was achieved by air pluviating the sands into the shear box. A loose density was considered appropriate to model the effects of the overcut, where the TBM excavates a space with diameter D_S which is larger than the diameter of the pipes, D_P.

Table 1 - Soil properties

Sand	Glenview	IGB
D_{10}	0.08mm	0.164mm
D_{50}	0.2mm	0.23mm
C_U	2.85	1.60
C_Z	1.23	0.885
$\gamma_{d,max}$	16.0 kN/m^3	15.7 kN/m^3
$\gamma_{d,min}$	13.8 kN/m^3	14.2 kN/m^3
Shape	Angular to very angular	Subrounded to subangular

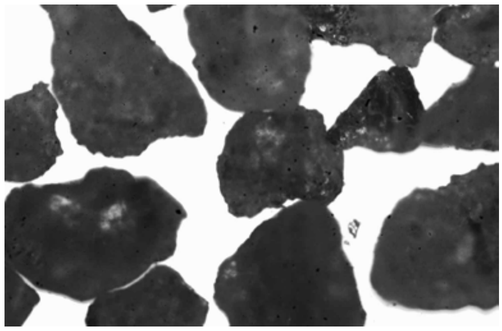

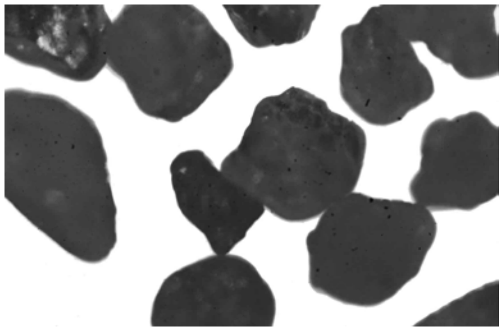

Figure 4. IGB sand (top) & Glenview sand (bottom).

3.1.2 Concrete

Concrete jacking pipes used in Ireland are typically manufactured using the dry cast concrete process, where the pipes are formed by mechanically placing low-slump concrete between a vibrating core former and a stationary outer form. The resulting pipes are strong and impermeable. The outer finish is generally quite rough, as illustrated in Figure 5 (a) & (b) below, but can vary to quite smooth in some cases due to variations in the manufacturing process (Figure 5 (c)).

To attempt to model the shearing behaviour of coarse-grained soils against concrete jacing pipes, a concrete sample was manufactured. Its dimensions were 60mm x 60mm x 20mm and a strong concrete mix was used. The main considerations in making the slab were durability during repeated shearing and achieving a surface finish close to what would be expected for jacking pipes.

3.2 Testing

Tests were conducted on a small shear box apparatus on dry samples of each type of sand. Sand was pluviated to unit weights as specified in Table 2. A shearing rate of 1.2mm/min was chosen for convenience. Other work on sand/concrete interface testing [23] showed that while both δ and ϕ increase with shearing rate, the ratio δ/ϕ remains the same. Sufficient travel was allowed for the sand to reach critical state values of ϕ and δ, ϕ_c and δ_c. Results of interface friction testing are set out in Table 3. Figure 7 shows plots of shear stress against horizontal displacement for some of the tests on IGB sand. It is notable that the shear stress plot isn't smooth, as would be expected, but quite rough. This may be because of the roughness of the interface. While δ_c/ϕ_c decreases with normal stress for Glenview sand, it remains constant for IGB sand.

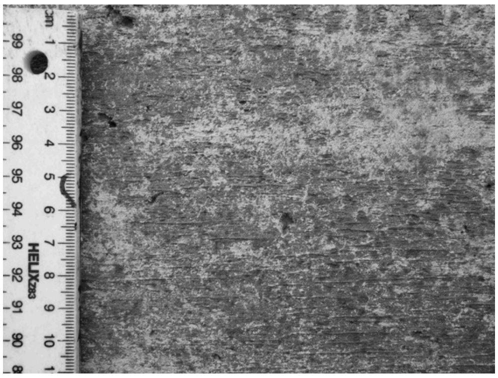

(a) Rough finish

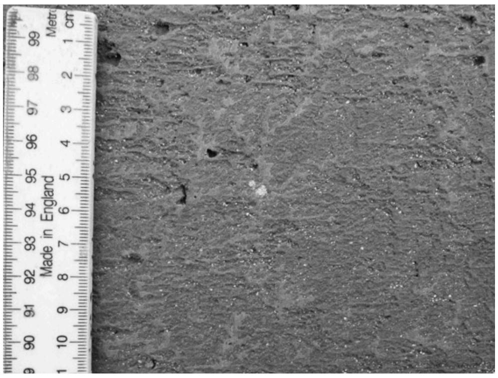

(b) Medium finish

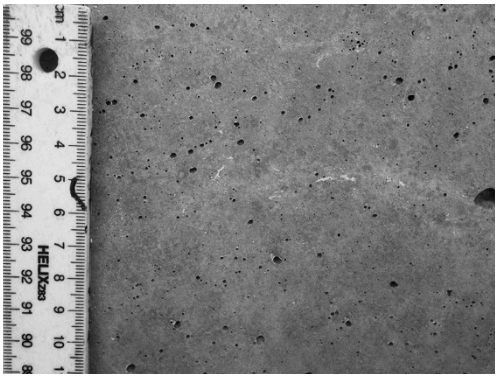

(c) Smooth finish

Figure 5. Typical dry cast concrete jacking pipe.

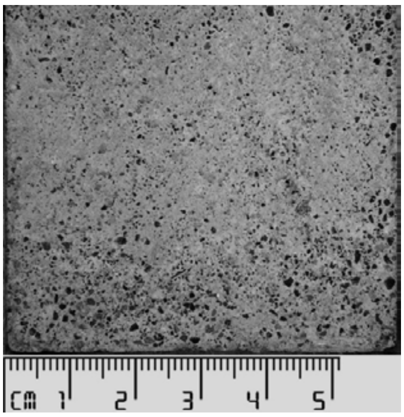

Figure 6. Concrete test surface.

Table 2. Testing conditions for each sand.

Sand	Glenview	IGB
$\gamma_{d,\text{test}}$	13.8 kN/m^3	14.6 kN/m^3
ϕ_c	36.5º	33º

Table 3. Results of interface friction tests between rough concrete and two types of sand.

	Glenview sand				IGB sand		
σ_N (kPa)	18.6	25	50	100	18.6	25	50
τ (kPa)	18.7	20.2	38.8	68.8	12.4	16.5	33
δ_c	45º	39º	38º	35º	34º	33º	33º
μ_c	1	0.81	0.78	0.69	0.67	0.66	0.66
δ_c/ϕ_c	1.23	1.07	1.04	0.96	1.03	1.0	1.0

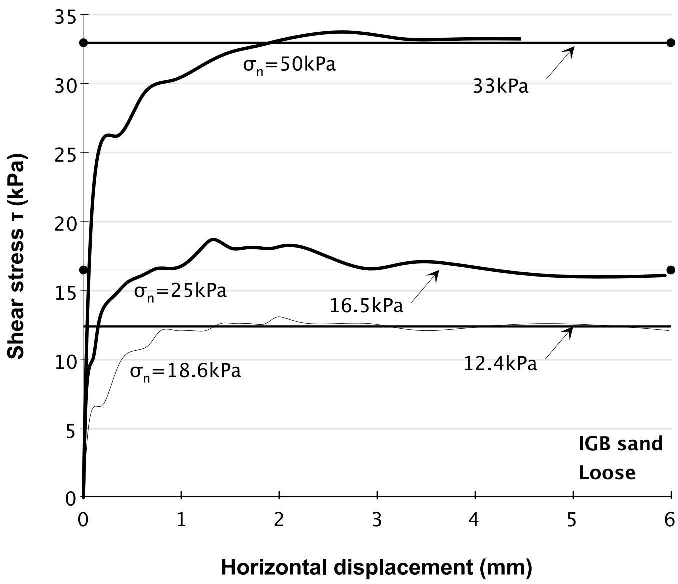

Figure 7. Testing results for IGB sand sheared against the concrete test surface in direct shear.

4 CASE HISTORIES

The findings from the authors' laboratory tests were compared to measurements made during two microtunnelling schemes in sandy soil; one in Ireland and one in France reported as part of the French national project “Microtunnels” [3].

4.1 Case History 1

In Howth, Co. Dublin, three 1000mm internal diameter microtunnel drives of 60m to 110m in length were carried out in slightly silty estuarine sand and sandy gravel as part of a wastewater network improvement scheme [24]. The effective angle of friction from shear box testing was in the range 37º to 42.5º. Average saturated unit weight was 21.2kN/m^3. The tunnelling shield used was a Herrennecht AVN 1000 with diameter, D_S, of 1295mm. The pipes had an outer diameter, D_P, of 1200mm and a cover depth of 2.5m to 3.9m at the start of each drive. A 10m section at the start of each drive was unlubricated for operational reasons, while the remainder of each drive was lubricated with an average of 60 litres/linear metre of bentonite lubricant. Table 4 shows the relevant parameters for both the initial unlubricated section and the remainder of the drive which was lubricated, along with the reduction in resistances observed due to the effects of lubrication.

Table 4. Frictional stress measured & predicted for Howth.

	Unlubricated	Lubricated	Reduction
Normal stress σ_N (kPa)	16.5 – 19.1	16.5 – 19.1	No change
Measured friction (kPa)	2.3 – 6.0	1.4 – 2.1	65 – 185%
Calculated friction ($P_S = \mu N$)	8.1 – 24	5.6 – 8.7	31 – 64%
Calculated friction ($P_S = \mu W$)	0.11 – 0.35	0.08 – 0.12	33%
Calculated δ	6.8º – 19.8º	4.6º – 7.4º	32 – 62%
Calculated μ	0.12 – 0.36	0.08 – 0.13	33 – 62%
Calculated δ/ϕ	0.16 – 0.46	0.11 – 0.17	31 – 63%

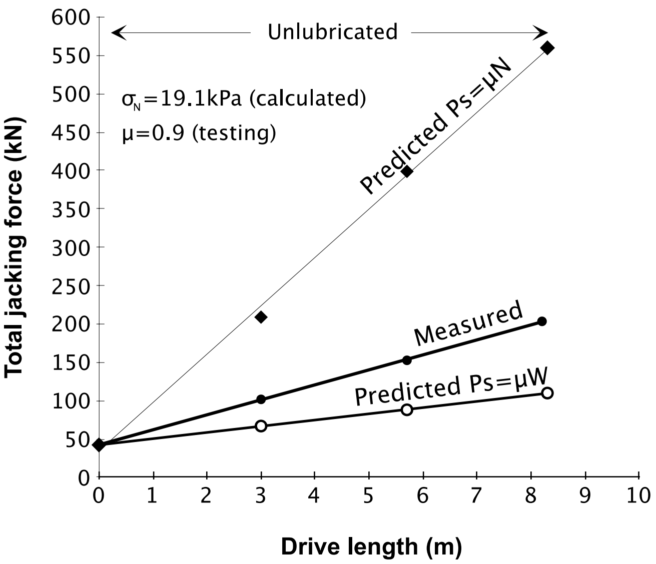

Figure 8. Unlubricated section of Howth drive 1 in sand, showing predicted and measured total jacking forces.

"Calculated" indicates values back calculated from site records and based on the assumption of uniform all-round contact between the soil and the pipe. This approach is useful and common in practice [20]. Figure 8 outlines how the measured jacking forces compare to both the stable bore (F=μW) and unstable bore (F=μW) models discussed earlier, using a value for μ obtained for a fairly similar soil through laboratory testing at the appropriate density and normal stress. It is noted that measured total jacking force lies between both sets of predictions, indicating that neither entirely stable nor unstable bore conditions prevailed. A possible explanation for this is that a combination of the large overcut created (42.5mm on the radius) and the slight siltiness of the soil allowed the overcut to remain partly open during pipe jacking.

4.2 Case History 2

Three drives were constructed in clean sand in Bordeaux, France, using a Markham 500 microtunnel boring machine [3]. The sand had a unit weight of 18 to 20 kN/m^3 and an effective angle of friction was in the range 30 to 35°. The outside diameter of the pipeline was 650mm, and a 10mm overcut was created. The cover depth was 7m and the average length of drive was 90m. Bentonite lubricant was used after 16m, and applied at a rate of 168 litres/linear metre. Table 5 shows the relevant data for this project, together with the reduction in resistances caused by lubrication.

Table 5. Frictional stress measured & predicted for Bordeaux.

	Unlubricated	Lubricated	Reduction
Normal stress σ_N (kPa)	18	18	No change
Measured friction (kPa) *	4.7	0.5* – 2.5	89%
Calculated friction ($P_S = \mu N$)	5 – 5.4	2.7 – 2.9	86%
Calculated friction ($P_S = \mu W$)	0.4 – 0.5	0.4 – 0.5*	No change
Calculated δ	15.1 – 18.8	5.7 – 8.0	57 – 62%
Calculated μ	0.27 – 0.34	0.1 – 0.14	50 – 70%
Calculated δ/ϕ	0.43 – 0.63	0.16 – 0.27	57 – 63%

* At some locations, average measured frictional stress was of the same magnitude as calculated self-weight friction stress.

There are similarities with the results obtained from Case History 1, in that values for the coefficient of friction μ for sliding contact between the soil and the pipe would not accurately predict the observed jacking forces. A back calculated coefficient of friction, μi, gives a reasonable prediction of observed values. It is notable that at times, a stable bore situation was achieved, indicated by * in Table 5 above. This, along with the consistent and large percentage reductions in frictional resistance force PS between unlubricated and lubricated driving, indicates that the lubrication regime was effective here.

5 DISCUSSION

The interface shear tests performed produced results largely in line with literature. Potyondy [10] observed values of μ up to 0.97 in tests with dry sand and rough concrete. μ was observed to decrease as the normal force increased, in common with other works [10, 18]. It is notable that the grain shape of the sands leads to differences in the density achieved through pluviation into the shear box apparatus and differences in shearing behaviour observed, with the rounder sand achieving a lower shear strength but higher density, most likely as the particles can more easily and smoothly translate with respect to each other.

Neither the fully stable, nor the fully unstable models for pipe-soil contact in pipe jacking are found to be appropriate for the case histories presented, at least not using interface friction coefficients established from laboratory tests. If laboratory interface friction coefficients, ranging from 0.7 to 1.0, are utilised, the stable bore model underestimates the jacking forces, while the unstable bore model overestimates them. If an interpreted interface friction coefficient μ_i is utilized, ranging from 0.12 to 0.36, good agreement can be found. Clearly, there is a difference in the mechanism causing the interface frictional behaviour between small scale tests in the laboratory and full scale pipe jacking in the field. Field results analysed by Norris [25] showed highly localised and irregular contact between the pipe and the soil. In silty sand, soil was found to collapse onto the top of the pipe, while horizontal stresses varied from low to high. This is an area which requires further research.

6 CONCLUSION

Physical modelling of soil-pipe interaction during pipe jacking and comparison to field results has raised some interesting questions.

1. It is clear that the interface friction during pipe jacking is influenced by parameters common to other soil-structure interface friction situations, including particle shape and size, soil density and the state of stress normal to the interface surface.
2. Due to differences in the magnitude of forces observed between physical modelling and the case histories, it is concluded that uniform contact conditions do not occur around a jacking pipe.
3. Possible reasons for this include short-term stability provided by suction in partially saturated soils, pipe misalignment and stoppages during jacking. These are areas that require further research.
4. Two methods have been examined which facilitate the prediction of jacking forces during pipe jacking. Neither method has been found reliable when combined with interface friction parameters derived from physical modelling.
5. Empirically derived interface friction parameters may be used to predict likely jacking forces with reasonable reliability, once good judgement is exercised.

ACKNOWLEDGMENTS

The support of the Irish Research Council is gratefully acknowledged. Terra Solutions Ltd. are acknowledged for providing access to jacking force records for Case History 1.

REFERENCES

[1] Curran, B. G., McCabe, B. A. & Ward, M. J. (2010), Microtunnelling - the future for pipeline construction? *The Engineers Journal,* 64(1), pp. 16-20.

[2] Nicholas, P. (1998), 'Microtunneling in urban areas - Past, present and future trends', *ITA World Tunnel Congress 1998 - Tunnels and Metropolises,* Sao Paulo.

[3] Pellet-Beaucour, A.-L. & Kastner, R. (2002), 'Experimental & analytical study of friction forces during microtunneling operations', *Tunneling and Underground Space Technology,* 17(1), 83-97.

[4] Staheli, K. (2006), *Jacking Force Prediction: An Interface Friction Approach Based On Pipe Surface Roughness,* PhD thesis, Georgia Institute of Technology.

[5] Overby, C., Roberts, M. & Kolell, C. (2009), 'The Longest Drive—Portland's CSO microtunnels', *Rapid Excavation and Tunneling Conference (RETC)*, Las Vegas, NV.

[6] Schuermans, M. (2011), 'Record trenchless installation of seawater intakes and outfalls for a fish farm project in Portugal', *ISTT International No-Dig 2011*, Berlin. 1A-1-1 - 10.

[7] Lang, G. (2010), 'Clean Water Project / East Side CSO', *NASTT Northwest Trenchless Conference,* Edmonton, AB.

[8] Marshall, M. A. (1998), *Pipe-Jacked Tunnelling: Jacking Loads and Ground Movements.* PhD thesis, University of Oxford.

[9] Chapman, D. N. & Ichioka, Y. (1999), 'Prediction of jacking forces for microtunnelling operations', *Tunnelling and Underground Space Technology,* 14(1), 31-41.

[10] Potyondy, J. G. (1961), 'Skin friction between various soils and construction materials', *Géotechnique,* 11(4), 339-353.

[11] Uesugi, M. & Kishida, H. (1986), 'Infuential factors of friction between steel and dry sands', *Soils and Foundations,* 26(2), 33-46.

[12] Uesugi, M., Kishida, H. & Uchikawa, Y. (1990), 'Friction between dry sand and concrete under monotonic and repeated loading', *Soils and Foundations,* 30(1), 115-128.

[13] Zong-Ze, Y., Hong, Z. & Guo-Hua, X. (1995), 'A study of deformation in the interface between soil and concrete, *Computers and Geotechnics,* 17(1), 75-92.

[14] Gómez, J. E., Filz, G. M. & Ebeling, R. M. (1999), *Development of an improved numerical model for concrete-to-soil interfaces in soil-structure interaction analyses*, Report for US Army Corps of Engineers Waterways Experiment Station.

[15] Lemos, L. J. L. & Vaughan, P. R. (2000), Clay-interface shear resistance', *Géotechnique,* 50(1), 55-64.

[16] Zhou, J. Q. (1998), *Numerical analysis and laboratory tests of concrete jacking pipes.* PhD Thesis, University of Oxford.

[17] Phelipot, A., Dias, D. & Kastner, R. (2003), 'Influence of overcut and lubrication during microtunneling', *ISTT International No-Dig 2003,* Los Angeles, CA.

[18] Iscimen, M. (2004), *Shearing Behavior of Curved Interfaces.* MS thesis, Georgia Institute of Technology.

[19] Shou, K., Yen, J. & Liu, M. (2010), 'On the frictional property of lubricants and its impact on jacking force and soil-pipe interaction of pipe-jacking', *Tunnelling and Underground Space Technology,* 25(4), 469-477.

[20] Stein, D., Möllers, K. & Bielecki, R. (1989), *Microtunneling: Installation and Renewal of Non-Man Size Supply and Sewage Lines by the Trenchless Construction Methods,* Berlin, Ernst and Sohn.

[21] Tien, H.-J. (1996), *A Literature Study of the Arching Effect.* MSc thesis, Massachusetts Institute of Technology.

[22] French Society for Trenchless Technology (2006), *Microtunneling and Horizontal Drilling Recommendations,* ISTE Ltd.

[23] Al-Mhaidib, A. I. (2006), 'Influence of shearing rate on interfacial friction between sand and steel', *Engineering Journal of the University of Qatar,* 19.

[24] Reilly, C. C. & Orr, T. L. L. (2011), 'Microtunnelling - recent experience in Ireland', *ISTT International No-Dig 2011*, Berlin. 2A-4-1 - 2A-4-10.

[25] Norris, P. 1992. *The Behaviour of Jacked Concrete Pipes during Site Installation.* PhD Thesis, University of Oxford.

An investigation of the arching mechanism in a geotechnical centrifuge

David Lally[1], Patrick J. Naughton[1]
[1]School of Engineering, Institute of Technology, Sligo, Ireland
email: david.lally@mail.itsligo.ie, naughton.patrick@itsligo.ie

ABSTRACT: Plane strain physical models of a piled embankment were investigated in a geotechnical centrifuge at up to 110 times earth's gravity (g). The test series had constant pile geometry, but different embankment heights to understand better the deformational response of these systems. A linear increase in both surface settlement mid span between piles and differential settlement between the pile cap and the embankment midspan between the piles was observed. Embankments constructed from dense sand displayed lower settlements than those constructed from loose sand. As the height of the embankment increased relative to the clear spacing between adjacent piles (H/(s-a)), the midspan surface settlement together with the differential settlement reduced. The deformed shape of the reinforcement was found to be that of a parabola.

KEY WORDS: Arching, critical height, differential settlement, geosynthetic reinforcement, piled embankment, soft soil.

1 INTRODUCTION

A piled embankment consists of piles, usually on a square grid, driven through an unsuitable foundation soil to a firm-bearing stratum. The piles directly reinforce the soft soil and transfer the embankment load directly to the firm stratum. A geosynthetic layer may be installed over the pile caps at the base of the embankment to further assist in the transfer of load, Figure 1.

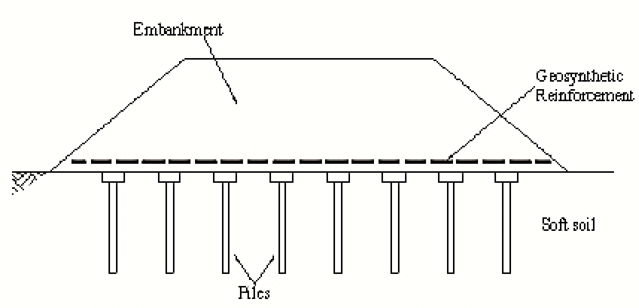

Figure 1. Typical piled embankment [1].

Terzaghi [2] described arching as "one of the most universal phenomena encountered in soils both in the field and in the laboratory". Soil arching involves a redistribution of stress in a soil mass and occurs as a result of differential settlement in the soil due to the partial yielding of a support. In the case of piled embankments arching occurs because the soft sub-soil consolidates and settles relative to the stiff piles. This differential settlement mobilises shear stresses in the embankment fill resulting in the formation of a three-dimensional soil arch that spans between adjacent pile caps. Arching increases the vertical embankment load bearing on the piles and reduces the vertical load acting on the weak subsoil. The load on the subsoil is further reduced by the installation of geosynthetic reinforcement which transfers the load of the unarched fill onto the pile caps [3].

A number of authors, Naughton & Kempton [4] and Stewart & Filz [5], have concluded that various analytical methods proposed for arching in piled embankments give different results in specific situations. Naughton et al. [6] considered the historical development of piled embankments and concluded that the design of these systems was complex and not yet fully understood, particularly with respect to tension in the geosynthetic reinforcement and support from the soft subsoil.

This study investigates the plane strain deformational response of the embankment fill and geosynthetic reinforcement in a piled embankment using a geotechnical centrifuge.

2 CENTRIFUGE MODELLING OF PILED EMBANKMENTS

Geotechnical centrifuge modelling is a well-established means of providing insight into geotechnical engineering problems. Typically a 1/Nth scale model of the problem is constructed and subjected to an inertial acceleration field of N times earth's gravity (g). This produces a stress similarity between the model and the full-scale prototype, for example the stresses produced beneath a 5 m embankment in earth's gravity are identical to those beneath a 50 mm model embankment spun at a centrifugal acceleration of 100g [7].

Previous studies on the phenomenon of soil arching in piled embankments conducted using a geotechnical centrifuge include those of Bujang & Faisal [8] and Ellis & Aslam [9, 10]. Bujang & Faisal [8] reported a series of tests on a 1/100 scale model and examined the influence of parameters such as fill height, pile area ratio and fill properties on arch formation. Large differential settlements and low efficacy (proportion of embankment weight carried by piles) values were observed at lower embankment height (H) / spacing (s) ratios indicating a poor arch formation, whereas higher H/s ratios yielded higher efficacy values with the fill surface remaining relatively even. It was also concluded that high quality fill with high strength and stiffness and high pile area ratios result in a more efficient arching mechanism.

Ellis and Aslam [9, 10] compared the results of centrifuge tests investigating the performance of unreinforced piled embankments constructed over soft soil with current piled embankment design approaches [2, 3, 11, 12]. The foundation soil was modelled using expanded polystyrene styrofoam and the model piles were constructed from 25 mm diameter aluminium tubes. It was concluded that the Hewlett and Randolph [11] method appeared to be the most rational design approach as it considers all geotechnical parameters, soil strength and punching shear failure at the pile caps. The possibility of using a ground reaction curve (GRC) in the design process was also examined by Ellis and Aslam. A GRC is a plot of the stress reduction ratio (σ_s / γH_e) vs. the ratio of uniform surface settlement to the pile cap clear spacing (δ/(s-a)) for a series of g-levels (1g to 60g). It was concluded, that with further research, GRCs could potentially be used in design to form interaction diagrams to examine whether the response of the subsoil and any geosynthetic reinforcement would be sufficient for a particular embankment.

3 CENTRIFUGE TESTING FACILITY

The geotechnical centrifuge at the Institute of Technology, Sligo (ITS), illustrated in Figures 2 and 3, is a 9 g-tonne machine with a maximum acceleration level of 300g and a maximum rotational speed of 638 rpm. The centrifuge has a 0.75 m long beam rotor with two strongboxes at either end. In the interests of safety, a 12 mm thick steel casing with an outer diameter of 1.7 m surrounds the centrifuge.

Figure 2. IT Sligo geotechnical centrifuge [13].

The strongboxes currently in use are designed to carry a maximum sample size of 300 x 180 x 100 mm and are safety certified for a 6 g-tonne payload. The strongbox contains two removable Perspex panels on each side which allow for image capturing on either side of the soil sample in-flight. Also for this purpose a camera and light are fixed on a custom built bracket on the side of the strongbox. A Canon S series compact digital camera with an image resolution of 5 to 8 Mega Pixels at 0.5–1.0 Hz is used as it is known to perform well at centrifugal accelerations of up to 160 g.

A more specific discussion on the main features of the ITS centrifuge, including control and data acquisition systems can be found in O'Loughlin et al. [13].

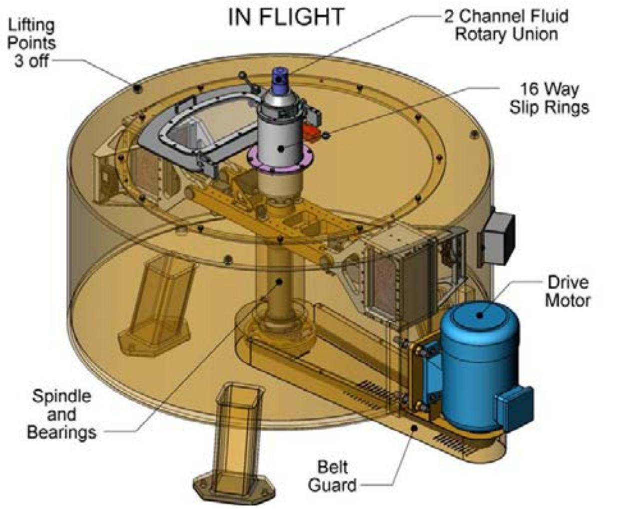

Figure 3. IT Sligo beam centrifuge general arrangement [13].

4 CENTRIFUGE EXPERIMENTAL MODELLING

4.1 Model dimensions

The plane strain piled embankment model, illustrated in Figure 4, was designed for the centrifuge strongbox which has internal plan dimensions of 300 x 100 mm and a height of 180 mm. The model incorporates seven piles (P1 to P7) with a clear spacing between piles (s-a) of 27 mm, equivalent to 2.7 m at 100g. The piles are held firmly in place at the base by a fixing mechanism consisting of a series of Perspex spacers and threaded steel bars, which passed through the piles and the spacer blocks fixing them rigidly together at the base of the model.

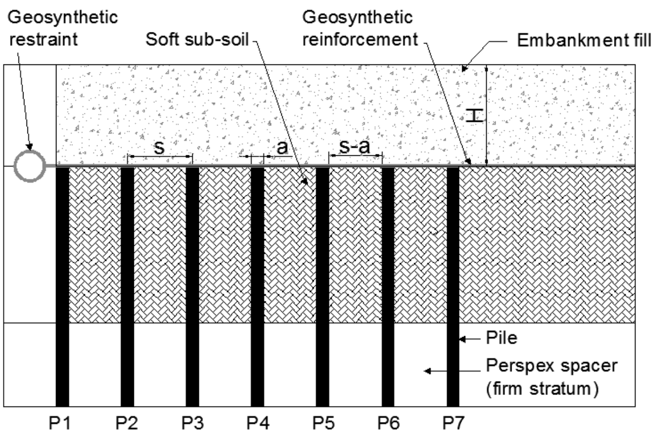

Figure 4. Piled embankment model.

4.2 Model piles

The piles used in the test were manufactured from Perspex sheets and had plan dimensions of 100 x 5 mm and a height of 65 mm. The Young's modulus, determined from beam-deflection testing, was 1.6 GPa, giving an average axial stiffness of 0.8 MN which is equivalent to 8 GN at 100g. This is comparable to 270 x 270 mm concrete piles arranged in a square grid at 2.7 m centre to centre spacing in earth's gravity. Pile caps were not used in this study as the piles themselves were considered to be of sufficient width (5 mm or 0.5 m at 100 g) to be representative of the lower end of pile cap sizes used in practice.

4.3 Soft subsoil

The subsoil was modelled using synthetic sponge cut into blocks of 100 x 65 x 22 mm, which fitted snugly between the model piles. Synthetic sponge was used to model the soft-soil because it offered considerable convenience and repeatability of the compression stiffness. Ellis and Aslam [9, 10] previously made use of synthetic materials for the modelling of soft-soil. The depth of the soft subsoil, 65 mm, corresponded to 6.5 m at 100g. The stiffness of the sponge was determined in a modified oedometer apparatus and found to be approximately 110 kPa, Figure 5.

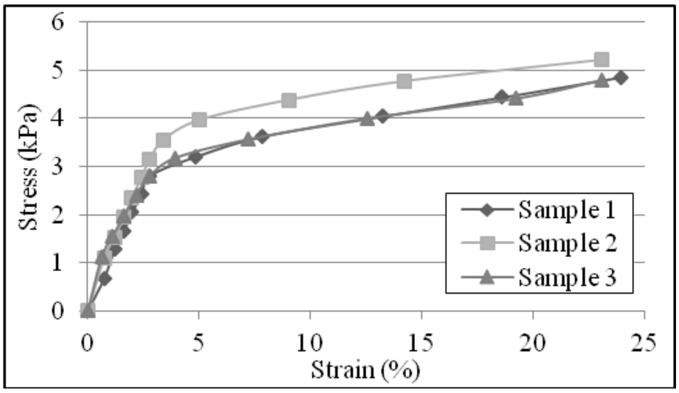

Figure 5. Load – deformational response of sponge used in this test programme.

4.4 Geosynthetic reinforcement

The geosynthetic reinforcement was modelled using custom cut polyethylene sheets. The sheets were fully restrained along one side of the model (parallel to the piles) and free at the other. Tensile testing of the polyethylene sheet, Figure 6, indicated a linear response followed by significant plastic straining. The linear portion of the curves gave an elastic stiffness of 4.7 kN/m width, corresponding to a stiffness of 470 kN/m, at 100g.

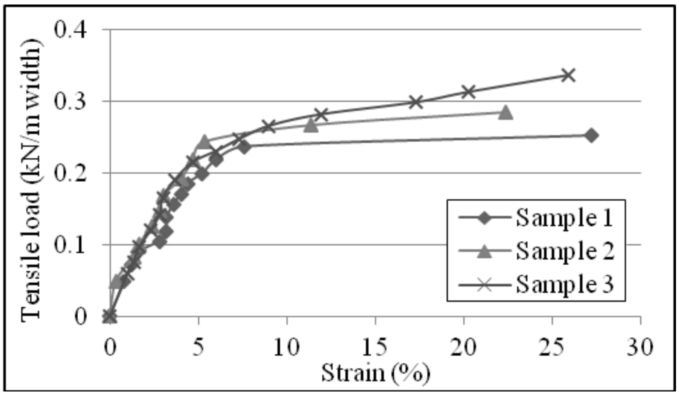

Figure 6. Tensile test data.

4.5 Embankment fill

The fill used in this study was a uniform, slightly silty, medium sand, retrieved from a beach at Ballyshannon, Co. Donegal. A summary of the mechanical properties of the test sand, determined in accordance with BS 1377 [14], is provided in Table 1.

Table 1. Properties of sand used in this study.

Property	Value
Coefficient of curvature, C_c	1.1
Coefficient of uniformity, C_u	1.53
Particle density, ρ_s (Mg/m^3)	2.62
Maximum dry density, $\rho_{d,max}$. (Mg/m^3)	1.75
Minimum dry density, $\rho_{d,min}$. (Mg/m^3)	1.35
Peak angle of internal friction, φ_{peak}	37°
Constant volume angle of internal friction, $\varphi_{c.v.}$	28 - 32°
Maximum angle of dilatancy, Ψ_{max} [1]	9°
Maximum angle of dilatancy, Ψ_{max} [2]	3 - 10°

4.6 Experimental procedure

A series of centrifuge tests were performed on the piled embankment model. The in-flight movement of the model was monitored using the digital camera mounted on the side of the strongbox. No further instrumentation was used in this test series.

To ensure homogeneity of the sand in the embankment models, sand was poured at a constant rate from a constant height of approximately 50 mm to obtain loose samples. Homogenous dense samples were formed using a sand raining technique which involved allowing the sand to pass through a perforated plate, with 10 mm diameter holes arranged on a 50 x 35 mm rectangular grid, followed by a 2 mm diffuser sieve located 150 mm below the perforated plate. The density index (I_D) achieved for the samples ranged from 45 – 65 %, termed loose sand samples, and 76 – 90 %, termed dense sand samples, respectively. A layer of kaolin clay was placed against the Perspex side of the strongbox every 5 mm vertically to enhance the visual inspection of the samples in-flight.

The model was accelerated in 10 g increments to 110 g, thus producing data for a range of geometries with embankment height, subsoil thickness, pile width (a) and pile spacing increasing directly proportional to the g-level. However for any one test, the ratio of H/(s-a) remained constant, therefore a number of tests were conducted incorporating different embankment heights to illustrate the effect of H/(s-a) on

[1] Estimated from the relationship between peak and constant volume shear stress ($\psi_{max} = 1.25[\varphi_p - \varphi_{c.v.}]$) [15].

[2] Calculated from the relationship between vertical and horizontal displacements, obtained from shearbox testing on dense sand samples.

arching in the embankment fill. H/(s-a) was varied from 0.7, corresponding to a very low embankment to 2.5, corresponding to a high embankment for both the loose and dense sand embankments. The tests reported in this paper are summarised in Table 2. Subsoil thickness, pile width and pile spacing were kept constant, at 65 mm, 5 mm and 27 mm respectively, for all tests and all embankments contained geosynthetic reinforcement.

Table 2. Centrifuge test summary.

	Test no.	H (mm)	H/(s-a)	Dry density of fill (Mg/m^3)	Density index (I_D) of fill (%)
Loose sand	1	15.4	0.70	1.576	62.7
	2	22.0	1.00	1.575	62.5
	3	28.6	1.30	1.506	45.3
	4	35.2	1.60	1.558	58.4
	5	44.0	2.00	1.587	65.3
	6	49.5	2.25	1.529	51.2
	7	55.0	2.50	1.521	49.2
Dense sand	8	15.4	0.70	1.636	76.5
	9	22.0	1.00	1.655	80.6
	10	28.6	1.30	1.666	83.0
	11	35.2	1.60	1.690	88.0
	12	44.0	2.00	1.691	88.2
	13	49.5	2.25	1.701	90.3
	14	55.0	2.50	1.684	86.8

5 CENTRIFUGE EXPERIMENTAL RESULTS

5.1 Embankment mean surface settlements

The embankment surface settlements were determined directly above the midpoint of the piles and at the midspan between the piles. The deformations were measured by importing the photographs obtained during testing directly into Autocad. The range of settlements observed in Test No. 8 and 14 are illustrated in Figures 7 and 8 respectively. The results indicate a linear increase of surface settlement with g-level. The data also shows a larger range of settlements in Test No. 8 which indicated higher differential settlements at low H/(s-a) ratios.

Figures 9 and 10 illustrate the range of settlements observed in all tests for dense and loose sand respectively. Generally the results indicate an increase in settlement with increased H/(s-a), with the main contrast being that the loose sand settled slightly more than the dense sand. The results also indicate a decrease in the range of settlements as H/(s-a) increased. There is also more evidence of increased differential settlements at low embankment heights.

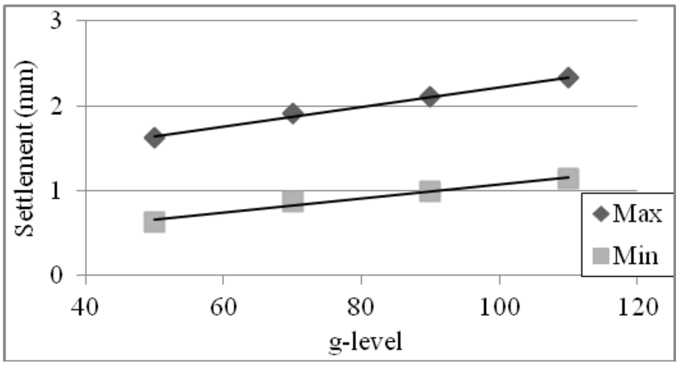

Figure 7. Range of surface settlements in Test no. 8 (model scale).

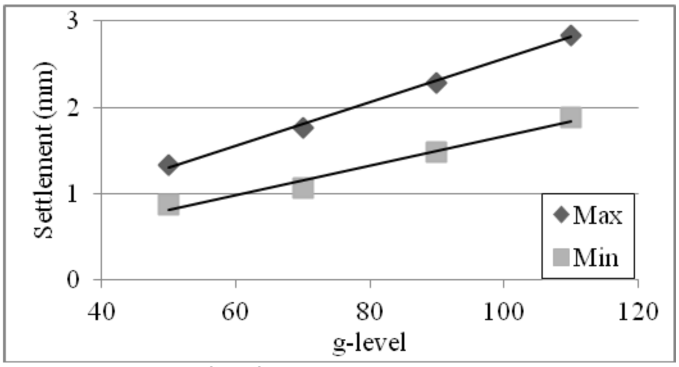

Figure 8. Range of surface settlements in Test no. 14 (model scale).

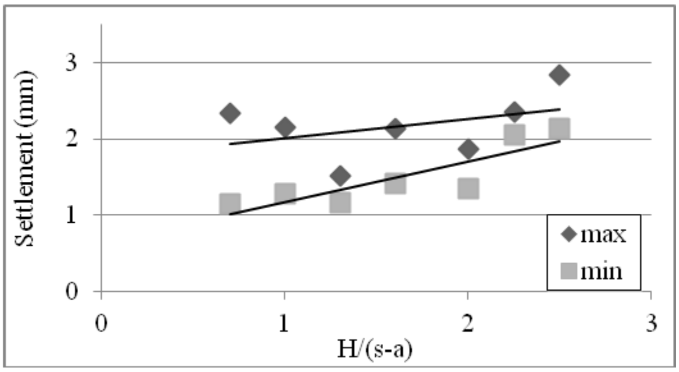

Figure 9. Range of surface settlements for dense sand at 110 g (model scale).

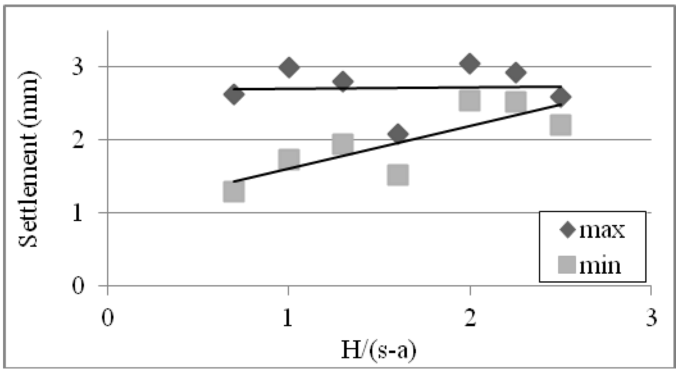

Figure 10. Range of surface settlements for loose sand at 110 g (model scale).

The ratio of surface midspan (d_m) to surface pile cap displacement (d_{pc}) rapidly decreased as H/(s-a) increased, for low height embankments, with the rate of decrease reduced as

d_m/d_{pc} approaches unity, for higher embankments, Figures 11 and 12. The ratio of d_m/d_{pc} appears to be independent of g-level, corresponding to constant H/(s-a) ratios.

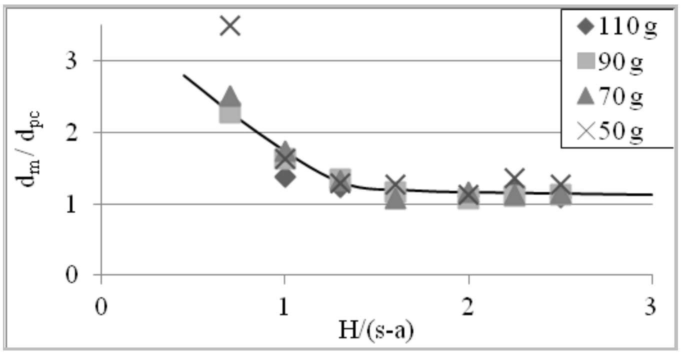

Figure 11. Surface midspan / surface pile cap displacement v. H/(s-a) for Tests 1-7 (loose sand, model scale).

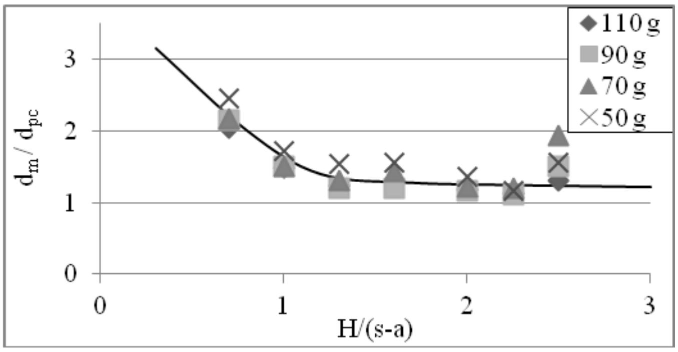

Figure 12. Surface midspan / surface pile cap displacement v. H/(s-a) for Tests 8-14 (dense sand, model scale).

5.2 Embankment differential settlements

In this study differential settlement (δ_s) was defined as the difference in settlement between the midpoint of the pile cap and the midspan between the piles at the embankment surface. The differential settlement at the embankment surface steadily decreased as H/(s-a) increased, Figures 13 and 14. The loose sand displayed more differential settlement than the dense sand, particularly at low embankment heights. Some variation in the differential settlement was evident at different g-levels, corresponding to constant H/(s-a) ratios.

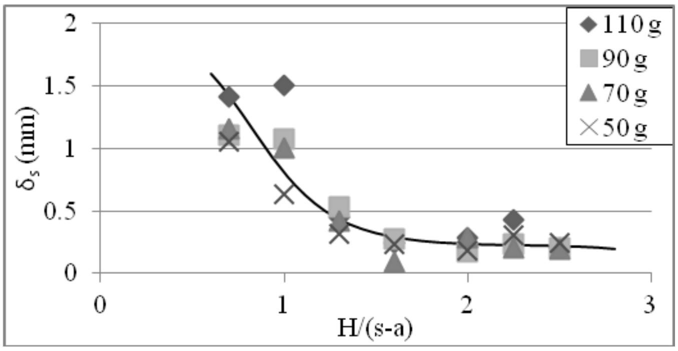

Figure 13. Differential settlement at embankment surface for Tests 1-7 (loose sand, model scale).

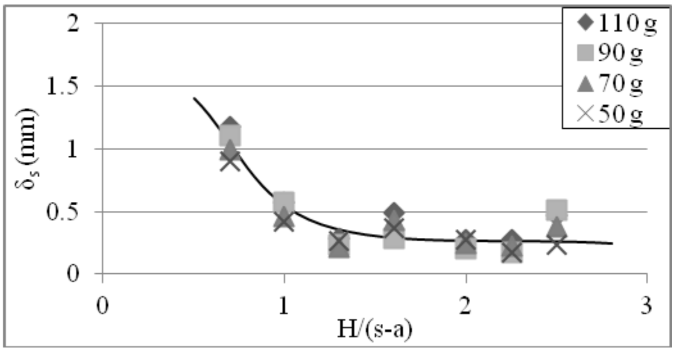

Figure 14. Differential settlement at embankment surface for Tests 8-14 (dense sand, model scale).

5.3 Deformation of the geosynthetic reinforcement

Figures 15 and 16 illustrate the typical measured deformed shape of the geosynthetic reinforcement, between P3 and P5 in Test Nos. 1 and 7 respectively. Reasonable agreement was found between the deformed shape of the reinforcement in adjacent spans and the deformed shape of a parabola.

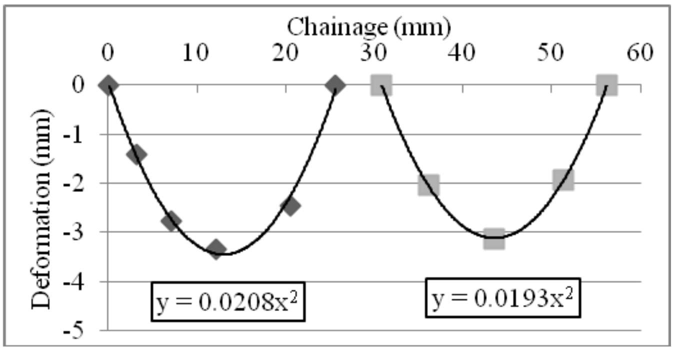

Figure 15. Deformed shape of geosynthetic reinforcement during Test 1 at 110 g (model scale).

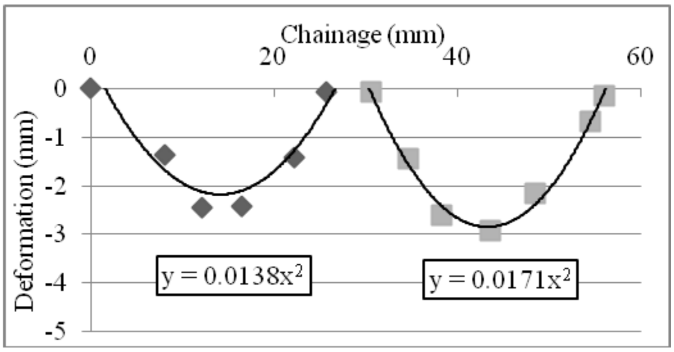

Figure 16. Deformed shape of geosynthetic reinforcement during Test 7 at 110 g (model scale).

The maximum vertical deformation of the geosynthetic reinforcement was measured at the midspan between the piles. The ratio of surface differential settlement (δ_s) to maximum geosynthetic displacement (d_g) decreased as H/(s-a) increased and stabilised at a value of approximately 0.1, Figures 17 and 18. The rate of decrease of δ_s / d_g was greater for the dense sand indicating a more efficient arch formation.

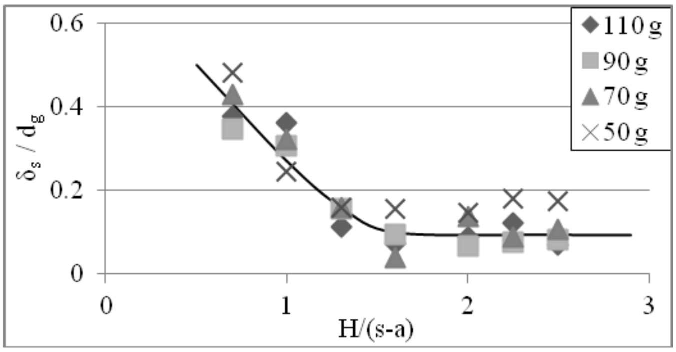

Figure 17. Surface/base differential settlement v. H/(s-a) for Tests 1-7 (loose sand, model scale).

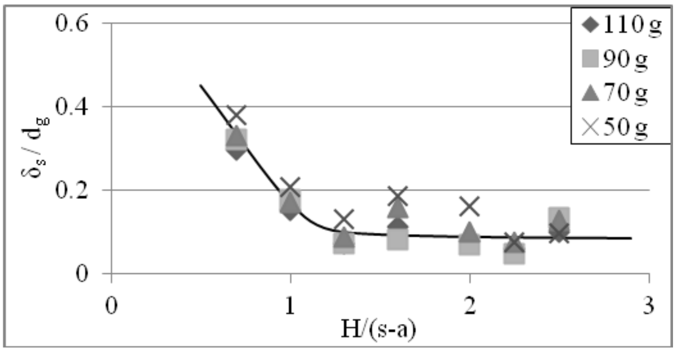

Figure 18. Surface/base differential settlement v. H/(s-a) for Tests 8-14 (dense sand, model scale).

6 CONCLUSION

Geotechnical centrifuge testing was carried out to investigate arching and surface deformations in piled embankments for a range of geometries and loadings typically used in design. Photographic images were used to determine the deformations in the plane strain model. The test models were subjected to a range of g-levels and the results indicated a consistent linear increase of surface and geosynthetic deformations with g-level.

The ratio H/(s-a) was varied by investigating different embankment heights in the models. The results highlighted the importance of this parameter in the differential response of the embankment. As H/(s-a) increased the differential settlement at the embankment surface decreased. The density of the fill also appeared to influence arch formation. The dense sand displayed considerably lower differential settlements than the loose sand for a given H/(s-a). This suggests a more efficient arch formation. The typical measured deformed shape of the geosynthetic reinforcement was that of a parabola.

The experimental work discussed in this paper is currently ongoing and samples will be tested to investigate the effects of other parameters, such as fill angle of internal friction and strength of geosynthetic reinforcement, on the arching mechanism.

REFERENCES

[1] Britton, E.J. & Naughton, P.J. (2008), ‘An experimental investigation of arching in piled embankments’, *19th European Young Geotechnical Engineers’ Conference*, Györ, Hungary.

[2] Terzaghi, K. (1943), *Theoretical Soil Mechanics*, John Wiley & Sons, New York, USA, pp. 66-76.

[3] Kempfert, H.G., Göbel, C., Alexiew, D. and Heitz, C. (2004), ‘German recommendations for reinforced embankments on pile-similar elements’, *Proceedings of the 3rd European Geosynthetics Conference, EuroGeo3*, Munich, Germany, pp. 279-284.

[4] Naughton P.J. & Kempton, G.T., 2005. *Comparison of Analytical and Numerical Analysis Design Methods for Piled Embankments*. GSP 131, ASCE, GeoFrontiers, Austin Texas, CD ROM.

[5] Stewart, M.E. & Filz, G.M., 2004. Influence of Clay Compressibility on Geosynthetic Loads in Bridging Layers for Column-Supported Embankments. Contemporary Issues in Foundation Engineering, GSP 131, ASCE, GeoFrontiers, Austin Texas, CD ROM.

[6] Naughton, P.J., Scotto, M., & Kempton, G.T., 2008. *Piled embankments: Past experience and future perspectives.* Proceeding of the 4th Euro. Conf. Geosynthetics, Edinburgh, UK 7-10 Sept, CD ROM

[7] Taylor, R.N. (1995), *Geotechnical Centrifuge Technology*, Blackie Academic and Professional, London, UK.

[8] Bujang, B.K.H. and Faisal, H.A. (1993), ‘A contribution to the design of a piled embankment’, *Pertanika Journal of Science & Technology*, Universiti Pertanian Malaysia Press, 1(1), pp. 79-92.

[9] Ellis, E. and Aslam, R. (2009), ‘Arching in piled embankments: comparison of centrifuge tests and predictive methods – part 1 of 2’, *Ground Engineering*, 42(6), pp. 34-38.

[10] Ellis, E. and Aslam, R. (2009), ‘Arching in piled embankments: comparison of centrifuge tests and predictive methods – part 2 of 2’, *Ground Engineering*, 42(7), pp. 28-31.

[11] Hewlett, W.J. and Randolph, M.F. (1988), ‘Analysis of piled embankments’, *Ground Engineering*, 21(3), pp. 12-18.

[12] BS 8006 (2010), *Code of Practice for strengthened / reinforced soils and other fills*, British Standards Institution.

[13] O'Loughlin, C.D., Naughton, P.J., Baker, N. and Ainsworth, A. (2010), ‘Establishing a beam centrifuge facility at the Institute of Technology, Sligo, Ireland’, *Proceedings of the 7th International Conference on Physical Modelling in Geotechnics*, Zurich, Switzerland, pp. 255-260.

[14] BS 1377-2 (1990), *Methods of test for soils for civil engineering purposes - classification tests*, British Standards Institution.

[15] Bolton, M.D. (1986), ‘The strength and dilatancy of sands’, *Géotechnique*, 36(1), pp. 65-78.

Characterisation of soft Irish soils using a piezoball penetrometer

C. Colreavy[1], C.D. O'Loughlin[1]
[1]Centre for Offshore Foundation Systems, The University of Western Australia, Perth, WA6009, Australia
email: 21164076@student.uwa.edu.au

ABSTRACT: Much of Ireland's road network passes through soft ground. This presents significant geotechnical design challenges. A precise measurement of the undrained shear strength (s_u) is critical for the design and performance of geotechnical structures on these soft sediments. In-situ penetration tests, in which a probe at the end of a series of rods is pushed vertically into the ground, are often used to characterise soft soils. s_u is derived from the penetration resistance (q) of the probe through a constant factor (N); s_u = q/N. Although the cone is the most common probe, full-flow probes such as the ball have become popular in recent years. Pore pressure measuring elements have recently been added to the ball which allows pore pressure to be measured during penetration and also allows dissipation tests to be conducted; these tests have particular merit in assessing consolidation characteristics. This paper discusses the use of full-flow penetrometers in characterisation of soft soils. Piezoball (a ball penetrometer with a pore pressure measuring element) penetration and dissipation tests for a number of sites are presented. The merits of the piezoball penetrometer are assessed by comparing test results with other field and laboratory test results.

KEY WORDS: Piezoball, CPT, soft soil, in-situ, characterisation

1 INTRODUCTION

Accurate and precise determination of the undrained shear strength (s_u) is essential for the design and performance of all structures founded on soft sediments. In most instances s_u is determined from a combination of laboratory and in-situ tests. Laboratory determinations of s_u require high quality undisturbed soil samples [1]. The difficulty in obtaining undisturbed and representative soil samples has led to an increased reliance on in-situ testing. The vane shear test and in-situ penetration tests are commonly used for the characterisation of soft soil, both onshore and offshore. While the former provides a direct measurement of undrained shear strength, the measurements can be affected by factors such as the waiting time after insertion, the rate of vane rotation, etc. [2]. Furthermore, the vane test can only be carried out at discrete depths. Penetration tests are carried out by vertically pushing a probe at the end of a series of rods into the ground at a constant rate. The undrained shear strength is then derived from the tip resistance (q). The cone penetration test (CPT) is the most commonly used in-situ penetration test. The cone gives a full resistance profile with depth, unlike the vane (i.e. continuous rather than at discrete depth intervals). However, unlike the vane, the cone does not give a direct measurement of s_u.

In the last 20 years, a new type of full-flow penetrometer has emerged in which the cone tip is replaced with a probe that is either a cylindrical T-bar or a sphere (Figure 1). There are a number of advantages of these new full-flow penetrometers over the cone [3]:

1. There is little, or no, correction necessary to provide net resistance compared to potentially significant adjustments to the cone resistance.
2. Improved accuracy is obtained in soft soils due to the larger projected area.
3. Accurate plasticity solutions exist relating the penetration resistance to the shear strength of the soil.

This paper presents the results of full-flow penetration tests at three soft soil sites in Ireland. By comparing the results of piezocone and piezoball tests, the relative merits of the piezoball are assessed. The usefulness of using a constant factor of N_{Ball} = 10.5 is assessed by comparing s_u profiles from ball tests with cone and shear vane results. The trends of excess pore water pressure during cyclic remoulding and dissipation tests are also examined.

2 BACKGROUND TO PENETRATION TESTING

2.1 *Cone penetration testing*

The standard cone penetrometer used today has an apex angle of 60° and a projected area of 1,000 mm^2 (diameter of 35.7 mm) as specified in the ISSMFE International Reference Test Procedure for CPT [4]. The standard rate of penetration is 20 mm/s.

The main limitation in the use of the CPT is in relating the measured cone resistance to the undrained shear strength profile of the soil. Measured cone resistance must be corrected for the unequal pore pressure and overburden pressure acting above and below the cone. The cone tip resistance is related to the undrained shear strength of the soil through:

$$s_u = \frac{q_{net}}{N_{kt}} \tag{1}$$

where q_{net} is the net cone resistance and N_{kt} is an empirically derived CPT resistance factor.

Although extensive theoretical solutions and empirical correlations exist to guide the selection of an appropriate value of N_{kt}, it is customary to calibrate N_{kt} for each new site with laboratory data, due to the variability of N_{kt} depending on soil properties such as soil stiffness and the in situ stress ratio [5]. The need for high quality laboratory determinations of s_u to interpret CPT data negates the advantage of penetration tests over laboratory testing.

The unequal pore pressure in the cone penetration test is caused by the pore pressure acting on the shoulder of the cone. The measured cone resistance must be corrected for this effect:

$$q_t = q_c + u_2(1-\alpha) \tag{2}$$

where q_t is the total measured cone tip resistance, q_c is the measured cone resistance, u_2 is the measured pore pressure behind the cone shoulder and α is the unequal area ratio. The net tip resistance is calculated by subtracting the overburden pressure, σ_v:

$$q_{net} = q_t - \sigma_v \tag{3}$$

In some cases the correction to the measured tip resistance can be significant. In tests on Burswood clay, the difference between the measured tip resistance and net resistance was found to be 19 % [6].

The use of a piezocone (a cone penetrometer with pore pressure measurement) improves soil stratigraphy and behaviour determinations. Measurement of pore pressure also allows in-situ determination of the consolidation characteristics of a soil through dissipations tests, where penetration is stopped and the decrease in pore pressure is measured over time.

2.2 *Full-flow penetrometers*

The rationale behind the introduction of full-flow penetrometers is that accurate plasticity solutions exist that relate the penetration resistance to the undrained shear strength. This means that (in theory) shear strength measurements from full-flow penetrometer tests do not need to be calibrated against laboratory derived measurements. Furthermore, since soil is able to flow around the probe, the overburden pressure is equal above and below the probe (bar the small shaft area). The larger projected area of the full-flow probes also leads to improved accuracy in soft soil – generally full-flow probes have a projected area of 10,000 mm^2, i.e. 10 times that of the standard cone.

The cylindrical T-bar was first devised as an instrument for determining s_u in geotechnical centrifuges [7]. The device was originally developed to combine the direct undrained shear strength correlations of the vane with the continuous profile given by the cone. The success of the T-bar in the centrifuge led to its use in the field [8].

The ball penetrometer was introduced to overcome the possibility of bending moments on the T-bar load cell. Centrifuge and in-situ tests have shown that ball and T-bar s_u profiles are similar [6] and give good agreement with laboratory s_u measurements determined from high quality samples [3].

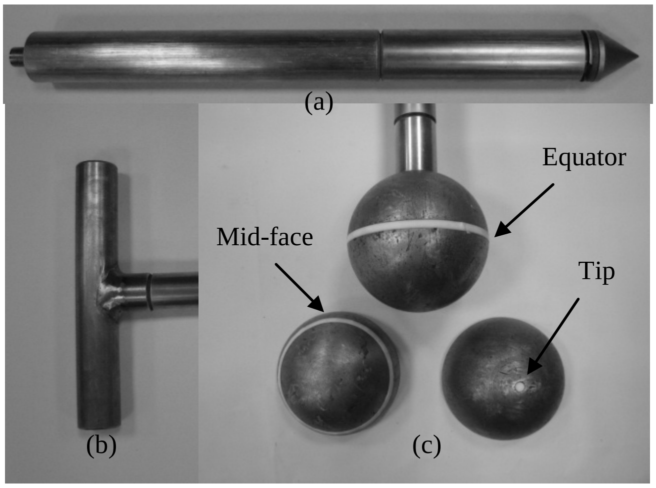

Figure 1. (a) Piezocone, (b) T-bar, and (c) Piezoball probes with pore pressure measurement at equator, mid-face and tip.

The measured ball resistance can be corrected in a similar manner as the CPT using equation 4 below [6]. Since the ratio of the shaft area to the area of the probe (A_s/A_p) is generally 0.1 for the ball, the correction to the measured resistance is usually small.

$$q_{ball} = q_c - [\sigma_v - u_0(1-\alpha)]A_s / A_p \tag{4}$$

where q_{ball} is the net ball resistance and u_0 is the hydrostatic pressure.

In addition to the intact undrained shear strength, full-flow penetrometers can be used to assess the remoulded shear strength (s_{ur}) and sensitivity by carrying out cyclic remoulding tests. These tests are performed by cycling the penetrometer about the desired depth. The cycling interval should be at least two to three probe diameters [9]. The minimum number of cycles required to reach the remoulded strength (where each penetration plus extraction is considered one full cycle) is soil dependent although 10 cycles is often recommended [9]. In many cases however, the soil will fully degrade in less than 10 cycles. The degradation factor is calculated by dividing the mean resistance in each stoke by the initial penetration resistance.

Recently, pore pressure sensors have been incorporated into full-flow probes. The first T-bar tests to be carried out offshore used a T-bar which measured pore pressure at two points on the neutral axis [10]. Since the introduction of the ball penetrometer, pore pressure measurement has been used more extensively with measurements at a number of different locations. Kelleher & Randolph [11] and Low et al. [12] used piezoballs which measured pore pressure at the equator position while Boylan & Long [13] used a piezoball which measures pore pressure through two holes one third up the ball face. Colreavy et al. [14] used a modular piezoball which allowed pore pressure measurement at one of three locations (tip, mid-face or equator) at any one time.

Peuchan et al. [15] showed that the pore pressure parameter from piezoball tests (B_{ball}) has potential for defining soil stratigraphy in a similar way to the piezocone pore pressure parameter (B_q). Boylan & Long [13] showed the potential for B_{ball} to identify peat humification.

$$B_{ball} = \frac{\Delta u}{q_{ball}} = \frac{u_{ball} - u_0}{q_{ball}} \tag{5}$$

$$B_q = \frac{\Delta u}{q_{net}} = \frac{u_2 - u_0}{q_{net}} \tag{6}$$

where u_{ball} is the pore pressure measured during ball penetration.

Like the piezocone, the piezoball can be used to carry out dissipation tests. Low et al. [12] and Colreavy et al. [14] carried out extensive piezoball dissipation testing using a piezoball with pore pressure measurement at the equator position. Their results showed that if the piezocone and piezoball penetrometers were to have the same diameter, the excess pore pressure around the ball would dissipate faster around the ball than around the cone. This may indicate an advantage of the piezoball over the piezocone for estimating the coefficient of consolidation. However, at present, a theoretical solution does not exist for the interpretation of piezoball dissipation tests.

3 SITES

3.1 Athlone

The Athlone site is located within the River Shannon flood plain. The stratigraphy of the site consists of a thin layer of peat on top of a layer of calcareous soil (known locally as 'calc marl'), overlying a layer of grey organic clay and then brown laminated clay. Moisture contents in the grey clay layer fall from approximately 100 % at the top of the layer to 80 % at the bottom while it remains close to 30 % in the brown clay. Plasticity indices decrease with depth with values of 25 – 50 % in the grey clay and 5 – 20 % in the brown clay. The moisture content is close to the liquid limit throughout. The unit weight of the clays increase relatively linearly with depth from approximately 15 kN/m^3 at the top of the grey clay to 20 kN/m^3 at the bottom of the brown clay. Full details of the Athlone clays are given in Long & O'Riordan [16].

3.2 Belfast

The Belfast site is located on the south side of Belfast Lough, 10 km north east of Belfast city. The main sediment of interest at the site is a layer of soft estuarine clayey silt, known locally as 'sleech', which is overlain by a layer of sandy 'sleech' and a layer of recently placed fill. Moisture contents in the 'sleech' are in the range 50 – 65 %. Liquid and plastic limits are in the range 60 – 75 % and 25 – 35 % respectively. Like the Athlone clays, the moisture contents are close to the liquid limits throughout. The 'sleech' has an average unit weight of 17.7 kN/m^3. Lehane et al. [17] give more details of the Belfast 'sleech'.

3.3 Lough Erne

Lough Erne, which is comprised of two lakes, is located in Co. Fermanagh, in the north west of Ireland. The test site is located in the north west of the lower lake. Water depths in the area where the tests took place are in the region 3.5 – 4 m. Moisture contents are high throughout in the range 270 – 520 %. The Atterberg limits are also high with plastic limits of 130 – 180 % and liquid limits of 250 – 315 %. The moisture content is approximately 1.5 times the liquid limit throughout. The unit weight of the soil is only marginally higher than water at 10.5 kN/m^3. Further details are given in Colreavy et al. [18].

4 TEST RESULTS

CPT and ball results for the three sites are shown in Figure 2. All tip resistance values have been corrected for overburden and pore pressure. In the case of the ball, the correction is generally small (<10 %).

In Athlone, the cone tip resistance is higher than the piezoball profiles. The resistance profile in the grey clay layer is seen to remain tolerably constant over the initial 2 m and then decreases slightly between 2 and 4 m. In the brown clay the penetration resistance is seen to increase slightly or stay tolerably constant with depth.

Piezoball and piezocone excess pore pressure profiles at the Athlone site are also shown in Figure 2a. The pore pressure at the ball equator profile is consistently lower than the corresponding CPT profile (at the u_2 position) which is in line with previous studies [12, 19]. The pore pressure profile measured at the piezoball mid-face was found to be broadly similar to that measured at the piezoball equator.

Profiles for Belfast are shown in Figure 2b. The profiles originate at the bottom of the sandy 'sleech' layer at 2.5 – 3 m. The piezoball profile is compared with a previously established CPT profile from Lehane et al. [17]. The CPT and piezoball resistance profiles are broadly similar although the piezoball resistances are slightly higher. The excess pore pressure measured at the piezoball equator is also similar to the piezocone pore pressure measured at the u_2 position.

The Lough Erne tip resistance and pore pressure profiles are shown in Figure 2c. The piezocone recorded zero or negative resistance throughout and when corrected, the net tip resistances are negative. This highlights a drawback of the CPT in very soft sediments. Excess pore water pressure profiles for a piezocone and piezoball test (with pore pressure measured at the equator) are also shown. Similarly to Belfast, there is very good agreement between the piezocone and piezoball profiles, with the piezocone showing slightly more scatter.

The ratio of ball tip resistance to net cone resistance (q_{ball}/q_{net}) for Athlone and Belfast is also shown in Figure 2. In the Athlone grey clay the ratio is approximately 0.84 while in the brown clay the ratio reduces to 0.52. Boylan et al. [19] noted a similar change in ratio with a change in facies at Bothkennar, with the ratio decreasing from 0.8 to 0.75. q_{ball}/q_{net} for Belfast averages at just over 1. As there is no net cone resistance profiles for Lough Erne, the resistance ratio can not be derived.

Pore pressure parameters for all three sites are presented in Figure 2. In the grey clay at Athlone, both B_{ball} and B_q vary. However in the lower half of the layer the profiles are similar and converge at the bottom. In the brown clay B_q remains constant at about 0.75. There is more scatter in the B_{ball} profile but it does remain close to the B_q value. Kelleher & Randolph [11] and Boylan & Long [13] both found that B_{ball} was in line with B_q. Low et al. [12] found B_q to be greater than B_{ball} while Boylan et al. [20] showed B_{ball} (with pore pressure measured at the tip) to be greater than B_q whilst B_{ball} (with pore pressure measured at the equator) was lower. In Belfast, both B_q and B_{ball} remain fairly constant with depth at 0.46 and 0.34 respectively. In Lough Erne, B_{ball} remains constant at 0.4. DeJong et al. [21] similarly found B_{ball} to remain constant at 0.4 with depth at Burswood. However this in contrast with Low et al. [12] who found B_{ball} to be 0.2 at the same site.

4.1 Undrained Shear strength

The undrained shear strength is determined from the resistance profiles using Equation 1. The choice of appropriate cone N factor (N_{kt}) is difficult and is often calibrated against laboratory s_u determinations. In this case the choice of N_{kt} is

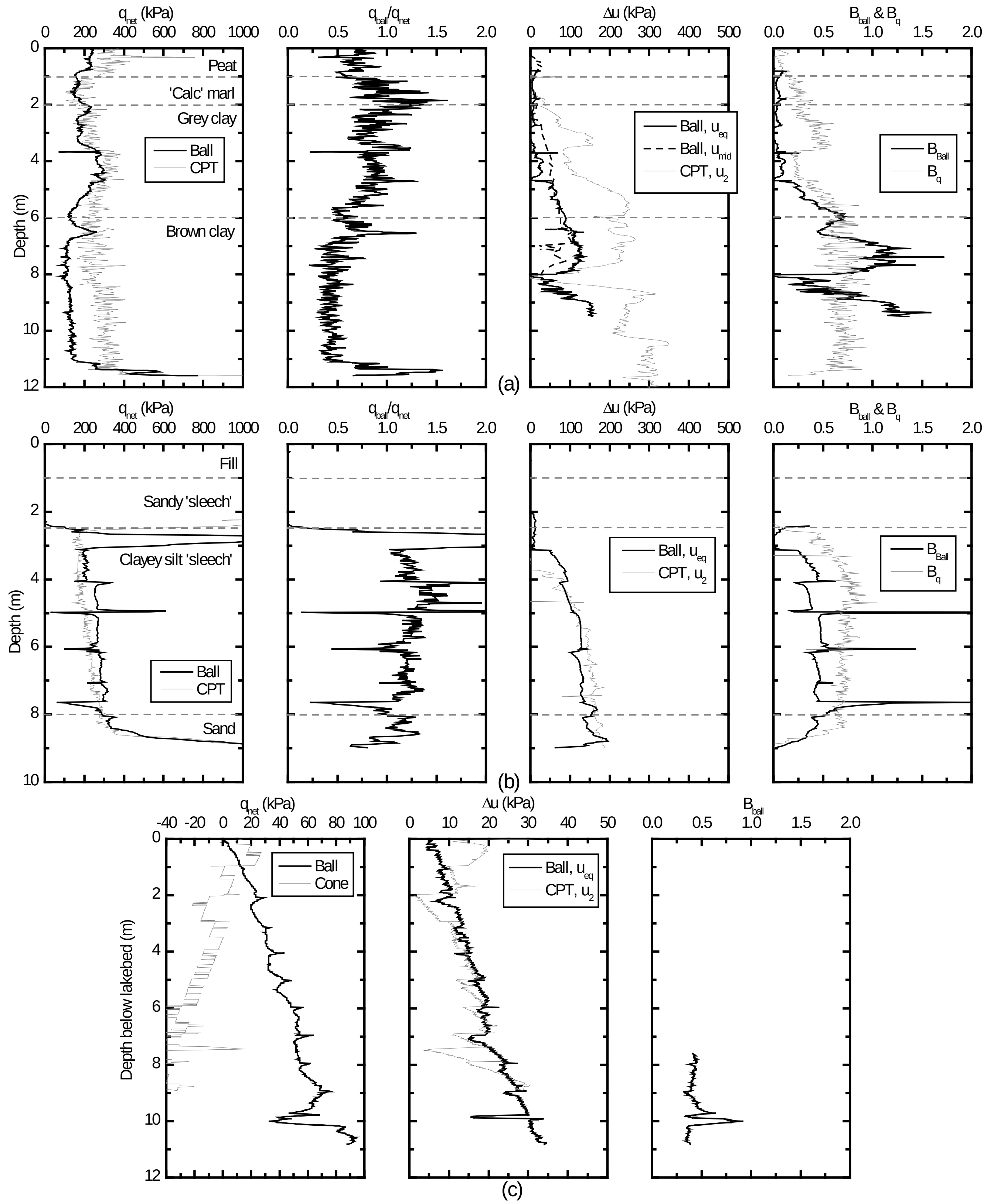

Figure 2. CPT and piezoball profiles for (a) Athlone, (b) Belfast, and (c) Lough Erne.

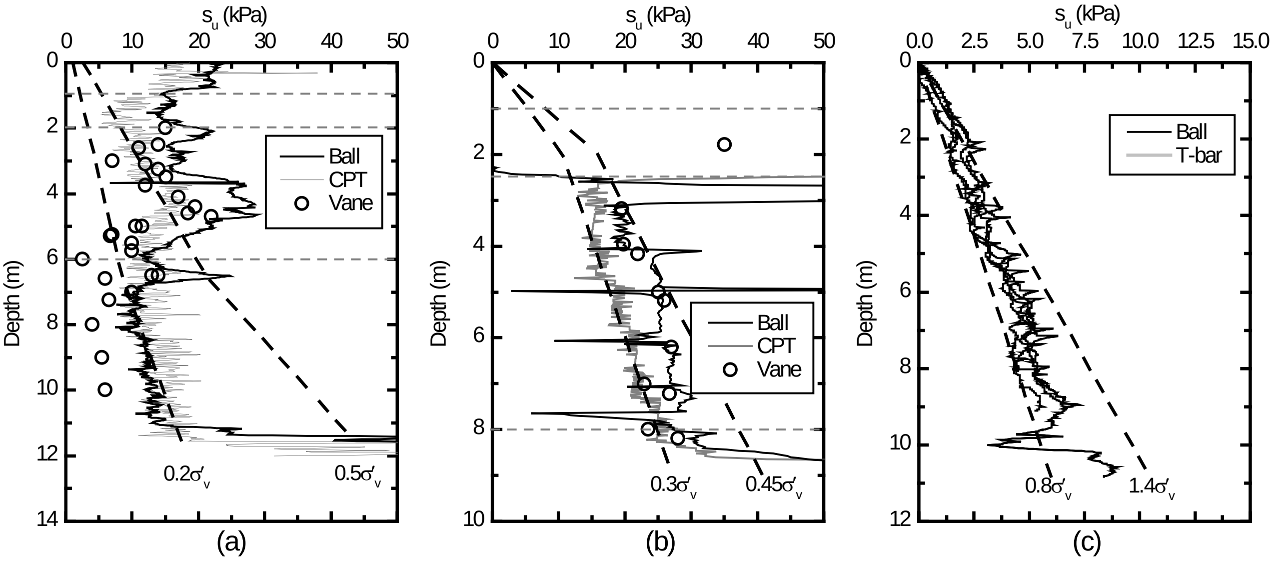

Figure 3. Undrained shear strength profiles for (a) Athlone with FVT from Long & O'Riordan [16], (b) Belfast with FVT from Lehane et al. [17], and (c) Lough Erne.

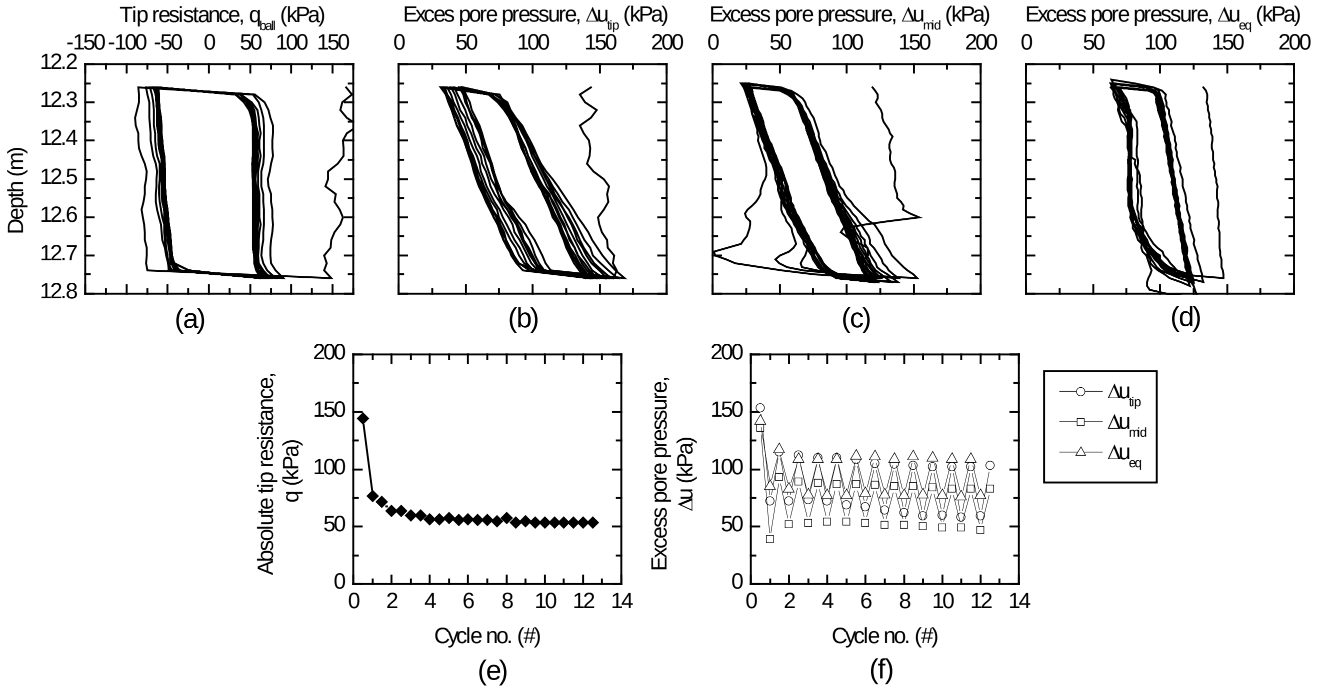

Figure 4. Piezoball cyclic remoulding test at Athlone. (a) tip resistance, (b) excess pore pressure measured at the tip, (c) excess pore pressure measured at the mid-face, (d) excess pore pressure measured at the equator, (e) tip resistance degradation, and (f) excess pore pressure degradation.

based on previous experience for the sites and by comparison with field vane results. The selection of an appropriate N factor for the ball penetrometer is often more straightforward and many field and centrifuge studies have shown that using a factor of N_{ball} = 10.5 produce s_u profiles that are consistent with expected values [6, 22].

Figure 3a compares the piezoball and piezocone s_u profiles for Athlone with a previously established field vane profile. Long & O'Riordan [16] found that a factor of N_{kt} = 20 gave good overall agreement. In this case the piezocone profile is in good agreement with the ball profile in the brown clay. In the grey clay however s_u from the ball is higher than that from the cone. The vane results are quite scattered. However there is reasonably good agreement with the penetrometer profiles in the grey clay. In the brown clay, the vane results are lower than the ball and cone profiles. In the grey clay, s_u from the ball is in the region of 0.8 times σ'_v whereas for the cone it is close to 0.5 times σ'_v. In the brown clay, s_u is closer to 0.2 times σ'_v for both probes. Interestingly this is close to the back analysis of trial embankments loaded to shear failure (Long & O'Riordan [16]) which indicated s_u/σ'_v = 0.2 to 0.25 for the brown clay. Both the piezocone and piezoball were found to give better agreement with the vane results at Belfast. In this instance a cone factor of 11 (based on the findings of McCabe & Phillips [23]) was used. This gave good agreement with the piezoball profile using a factor of 10.5. The vane results are in in particularly good agreement with the piezoball profile. The cone s_u profile is in line with 0.3 times σ'_v throughout, while the ball profile is closer to 0.45 times σ'_v. This is higher than would be expected for a normally consolidated soil, although 0.3 to 0.45 times σ'_v agrees well with laboratory s_u/σ'_v values reported by Lehane [24] of 0.41 for triaxial compression and 0.29 for triaxial extension.

The undrained shear strength profile for Lough Erne is also shown in Figure 3. However in this case there is no other strength data available for comparison. All the profiles are bound by the lines representing 0.8 times and 1.4 times the effective stress. Above 2 m the profiles are in close agreement with 1.4 times the vertical effective stress. Below 2 m, the s_u/σ'_v ratio falls to closer to 0.8. Like Belfast, this is much higher than the s_u/σ'_v = 0.2 to 0.3 typically encountered for normally consolidated soils. This is attributed to the extremely low effective unit weight of 10.5 kN/m^3.

4.2 Cyclic Remoulding

The results of piezoball cyclic remoulding tests carried out in the brown clay layer at Athlone, with pore pressure measured at all three locations is shown in Figure 4. The results are shown in terms of measured tip resistance and excess pore pressure. The degradation in absolute tip resistance and excess pore pressure with the cycle number are also shown.

The tip resistance response during cycling can be used to estimate the sensitivity of the soil. This assumes that the intact strength factor and the remoulded strength factor are the same. Although this has been shown not to be the case [25], using the ratio of intact resistance to remoulded resistance does give an initial estimate of sensitivity. The results suggest a sensitivity of about 3 for the Athlone brown clay.

The tip resistance value reaches stability in 5 – 6 cycles. In contrast the pore pressure in all three cases reaches stability in only three cycles. Boylan et al. [20] and DeJong et al. [21] both found similar results. DeJong et al. [21] hypothesised that the quicker degradation in pore pressure is due to the fact the bulk soil structure is fully degraded in the first few cycles. In later cycles the degradation is due to the remoulding of soil clusters which takes place without further contractive or dilative volumetric tendencies which generate excess pore pressure.

Interestingly there is a difference between the pore pressure at the equator during the penetration and extraction strokes. In fact the average difference between penetration and extraction pore pressure is quite similar for all three positions; 40 kPa, 35 kPa and 32 kPa for the tip, mid-face and equator respectively. This is contrary to the findings of Boylan et al. [20] and DeJong et al. [21] who both showed the excess pore pressure at the equator to be similar during penetration and extraction. It is suggested that the differences in penetration and extraction pore pressure is due to the presence of the shaft which alters the flow mechanism [20].

4.3 Dissipation test results

A number of dissipation tests have been carried out at both the Athlone and Belfast sites. All piezoball dissipation tests relate to the equator position. Typical dissipation profiles are shown in Figure 5. Although the shape of the dissipation curves are similar, a noticeable increase in the piezoball pore pressure over the initial 50 seconds is observed. Although this

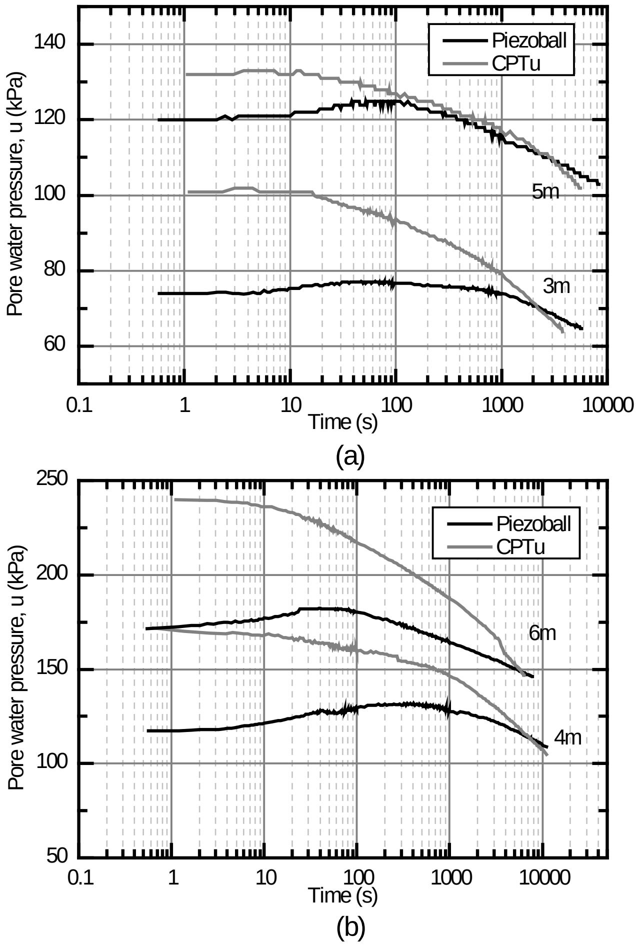

Figure 5. Dissipation curves for (a) Athlone and (b) Belfast from Colreavy et al. [14].

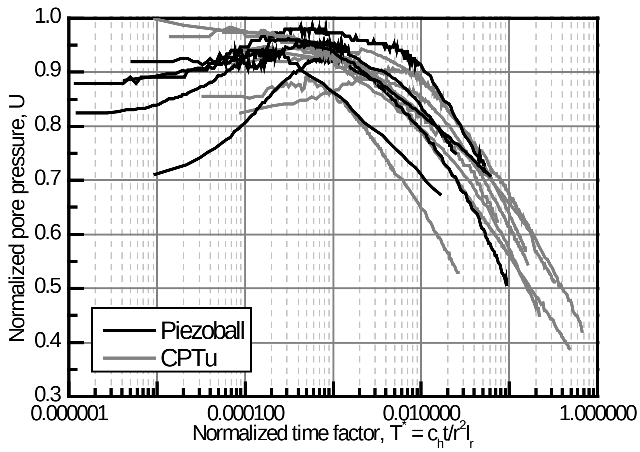

Figure 6. Normalised dissipation curves for Athlone and Belfast from Colreavy et al. [14].

could indicate inadequate saturation, a similar trend has been observed in previous piezoball tests [12, 21] where efforts were made to ensure proper saturation. In those cases the pore pressure lag was attributed to short-term equalisation of the pore pressure around the probe, rather than inadequate saturation.

A comparison between the piezocone and piezoball profiles is facilitated by using the normalised time factor, T*:

$$T^* = c_h t / r^2 \sqrt{I_r} \qquad (7)$$

where t is the dissipation time, c_h is the horizontal coefficient of consolidation, r is the penetrometer radius and I_r is the rigidity index. The coefficient of consolidation is calculated from the piezocone data in accordance with the method suggested by Teh & Houlsby [5]. This value is then used to interpret the piezoball dissipation data since there is currently no theoretical solution available to interpret piezoball dissipation data.

The normalised dissipation curves for Athlone and Belfast are compared in Figure 6. The normalised time factors are similar for both penetrometers. This implies that the rate of dissipation around the ball is faster than around the cone when the diameters are accounted for which is in line with previous studies [12].

5 CONCLUSIONS

A series of penetration tests carried out at a number of soft soil sites in Ireland have been presented. The test results have been compared with other in situ data to assess the usefulness of the piezoball in quantifying the undrained shear strength of soft soil.

The piezoball pore pressure parameter has been shown to have potential in assessing soil classification or stratigraphy. Interestingly the ratio of ball tip resistance to net cone resistance (q_{ball}/q_{net}) is shown to change in different soil layers.

The quicker decay in pore pressure compared with tip resistance was highlighted in cyclic remoulding tests. Further analysis of the tip resistance and pore pressure during cycling may lead to better understanding of the soil degradation process.

Piezoball dissipation curves were shown to have a similar shape to piezocone dissipation curves. The piezoball dissipation may prove to be useful in assessing the consolidation characteristics once a suitable theoretical framework has been established.

ACKNOWLEDGEMENTS

The first author would like to acknowledge the financial support of the Irish Research Council for Science Engineering and Technology (IRCSET) in conducting this research. The authors are grateful for the support of In Situ Site Investigation Ltd. who conducted the field testing.

REFERENCES

[1] Ladd, C.C. and DeGroot, D.J. (2003). "Recommended practice for soft ground site characterization." The Arthur Casagrande Lecture, *Proceedings of the 12th Panamerican Conference on Soil Mechanics and Geotechnical Engineering*, Boston, MA, 3-57.

[2] Chandler, R.J. (1988). The in-situ measurement of the undrained shear strength of clays using the field vane. *Vane Shear Testing of Soils: Field and Laboratory Studies, ASTM STP 1014*, A.F. Richards, Ed., 13 – 44.

[3] Randolph, M.F. (2004). Characterisation of soft sediments for offshore applications. *Proc. of 2nd Int. Conf. on Geotechnical and Geophysical Site Characterization - ISC'2*, Porto, 1, 209-232. Millpress.

[4] ISSMFE IRTP (1999). International reference test procedure for the cone penetration test (CPT) and the cone penetration test with pore pressure (CPTU). *Report of the ISSMFE, Technical Committee 16 on Ground Property Characterisation from In-Situ Testing, 1999 (corrected 2001)*, International Society for Soil Mechanics and Geotechnical Engineering.

[5] Teh, C.I. & Houlsby, G.T. (1991). An analytical study of the cone penetration test in clay. *Geotechnique* 41(1), 17 – 34.

[6] Chung, S.F. & Randolph, M.F. (2004). Penetration resistance in soft clay for different shaped penetrometers. *Proc. 2nd Int. Conf. on Site Characterisation – ISC 2*, Vol. 1, Porto. Rotterdam: Millpress, 671 – 678.

[7] Stewart, D.P. & Randolph, M.F. (1991). A new site investigation tool for the centrifuge. *Proc. Int. Conf. on Centrifuge Modelling – Centrifuge 91*, Boulder, Colorado, 531 – 538.

[8] Stewart, D.P. & Randolph, M.F. (1994). T-bar penetration testing in soft clay. *Jour. Geot. Eng. Div., ASCE*, 120(2), 2230 – 2235.

[9] DeJong, J.T., Yafrate, N.J., Degroot, D.J., Low, H.E. & Randolph, M.F. (2011) Recommended practice for full-flow penetrometer testing and analysis. Geotech. Test. Jour., Vol. 30, No. 2, pp. 1 – 13.

[10] Randolph, M.F., Hefer, P.A., Geise, J.M. & Watson, P.G. (1998). Improved seabed strength profiling using the T-bar penetrometer. *Offshore Site Investigation and Foundation Behaviour '98, Science and Underwater Technology*, London, 221 – 236.

[11] Kelleher, P.J. & Randolph, M.F. (2005). Seabed geotechnical characterisation with the portable remotely controlled drill. In Gourvenec S and Cassidy M (eds), *Proc. Int. Symp. on Frontiers in Offshore Geotechnics: ISFOG 2005.* London: Taylor and Francis, 365 – 371.

[12] Low, H.E., Randolph, M.F., Kelleher, P. & Williamson, P. (2007). Comparison of pore pressure generation and dissipation rates from cone and ball penetrometers, *Proc. of 6th Int. Conf., Soc. for Underwater Technology, Offshore Site Investigation and Geotechnics (SUT-OSIG)*, London, 547 – 556.

[13] Boylan, N. & Long, M. (2006). Characterisation of peat using full flow penetrometers. *Proc. of the 4th Int. Conf. on Soft Soil Engineering*, Vancouver, Canada, 403-414.

[14] Colreavy, C., O'Loughlin, C.D., Long, M., Boylan, N. & Ward, D. (2010) Field experience of the piezoball in soft clay. *Proc. 2nd Int. Sym. On Cone Penetration Testing, CPT10*, Huntington Beach, May.

[15] Peuchan, J., Adrichem, J. and Hefer, P.A. (2005). Practice notes on push-in penetrometers for offshore geotechnical investigation. In Gourvenec S and Cassidy M (eds), *Proc. Int. Symp. on Frontiers in Offshore Geotechnics: ISFOG 2005*. London: Taylor and Francis, 973 – 979.

[16] Long, M. & O'Riordan, N.J. (2001). Field behaviour of very soft clays at the Athlone embankments. *Géotechnique* 51, 293 – 309.

[17] Lehane, B.M., Jardane, R.J. & McCabe, B.A. (2003). Pile group tension cyclic loading: Field test programme at Kinnegar Northern Ireland, Health and Safety Executive Research Report RR101, HSE Books, Sudbury, UK.

[18] Colreavy, C., O'Loughlin, C.D. & Ward, D. (2012) Piezoball testing in soft lake sediments. *Proc. of 4th Int. Conf. on Geotechnical and Geophysical Site Characterisation – ISC '4*. **Submitted.**

[19] Boylan, N., Long, M., Ward, D., Barwise, A. & Georgious, B. (2007). Full flow penetrometer testing in Bothkennar clay. *Proc. of 6th Int. Conf., Soc. for Underwater Technology, Offshore Site Investigation and Geotechnics (SUT-OSIG)*, London, 177 – 186.

[20] Boylan, N., Randolph, M.F. & Low, H.E. (2010). Enhancement of the ball penetrometer test with pore pressure measurements. *Proc. 2nd Int. Symp. On Frontiers in Offshore Geotechnics (ISFOG 2010)*. Perth, Australia.

[21] DeJong, J.T., Yafrate, N.J. & Randolph, M.F. (2008). Use of pore pressure measurements in a ball full-flow penetrometer. *Proc. of 2nd Int. Conf. on Geotechnical and Geophysical Site Characterisation – ISC'3*, Taiwan. London: Millpress, 1269 – 1275.

[22] DeJong, J.T., Yafrate, N.J., DeGroot, D.J. & Jakubowski, J. (2004) Evaluation of undrained shear strength profile in soft layered clay using full-flow probes. *Proc. of 2nd Int. Conf. on Geotechnical and Geophysical Site Characterization - ISC'2*, Porto. 1. pp. 679 – 686. Millpress.

[23] McCabe, B.A. & Phillips, D.T. (2008). Design lessons from full-scale foundation load tests. *Proc. Of 2nd Int. Conf. on Geotechnical and Geophysical Site Characterisation – ISC'3*, Taiwan. London: Millpress, 615 – 620.

[24] Lehane, B.M. (2003). Vertically loaded shallow foundations on soft clayey silt. Proc. of the Institution of Civil Engineers, Geotechnical Engineering 156, 17 – 26.

[25] Yafrate, N.J, DeJong, J.T. (2006) Interpretation of Sensitivity and Remolded Undrained Shear Strength with Full Flow Penetrometers. *ISOPE-06: International Society for Offshore and Polar Engineering*, San Franciso, CA.

Appraisal of current settlement prediction methods applicable to vibro replacement design

B.G. Sexton[1], M.M. Killeen[1], B.A. McCabe[1]
[1]College of Engineering and Informatics, National University of Ireland, Galway, Ireland
email: b.sexton1@nuigalway.ie, michealkilleen@gmail.com, bryan.mccabe@nuigalway.ie

ABSTRACT: Numerous analytical approaches exist for the prediction of the settlement improvement offered by the installation of granular columns in weak or marginal soil deposits. In this paper, an appraisal of some of the more popular settlement prediction methods applicable to vibro-replacement design is carried out. The settlement improvement factors calculated using the different design methods are compared with both the 'bottom feed' and 'top feed' data from a previously published database of settlement improvement factors for stone columns in soft clays and silts. The calculated improvement factors are plotted as a function of the main variables in vibro-replacement design, namely the area-replacement ratio (a measure of the amount of in-situ soil replaced with stone), and the modular ratio, which relates the stiffness of the column to that of the in-situ soil. In addition, finite element analyses have been carried out using PLAXIS 2D for comparison with both the field data and the design method predictions. Load settlement behaviour (primary settlement) has been analysed using the Hardening Soil Model to model the behaviour of both the column material and the treated soil. The majority of the design methods appear to predict similar settlement improvement factors. Purely elastic methods overestimate the settlement improvement factor for large modular ratios while it appears that better matches between finite element and analytical predictions are found at higher modular ratios, as the analytical methods assume a significant bulging mechanism which is more prevalent in soft soils.

KEY WORDS: Stone Columns; Settlement Improvement Factor; Analytical Design Methods; Finite Element Analyses.

1 INTRODUCTION

The use of Vibro Stone Columns (VSCs) as a ground improvement technique has gained popularity in recent years. It is now widely accepted that stone columns reduce settlement [1, 2], improve bearing capacity [3], and accelerate consolidation [4, 5, 6]. In addition, VSCs provide a suitable economic alternative to piled foundations, while the construction time associated with VSCs is also significantly shorter than that associated with piling and other alternative foundation solutions. The vibro-replacement process and equipment have been described in detail by [7] and [8].

Vibro stone columns can be constructed using either a top feed method or a bottom feed method using either wet or dry jetting processes. In the case of the top feed method (e.g. Figure 1), stone is tipped into a hole formed by a vibrating poker, whereas for the bottom feed method, stone is added through a delivery tube along the side of the poker and exits at the poker tip. In both cases, compaction is carried out in stages from the base of the hole upwards. Air is used to aid construction and maintain stability of the hole for the dry method whereas water is used for the same purpose where the wet method is concerned.

Aggregate of size 40-75mm is used for the top feed method whereas for the bottom feed method, the size of the aggregate used ranges from 15-45mm [9]. The wet top feed method is suited to soft cohesive soil deposits where the ground water level is high while the dry top feed method is mainly used for firmer soil deposits with lower ground water levels. The dry bottom feed method is now the preferred construction technique in softer cohesive soil deposits (its use has largely replaced the wet top feed method [10] since its development in the 1970s) and enables columns to be constructed in soils with low undrained shear strengths, c_u << 15-20kPa [10]. Use of the wet method has weaned in recent years with the disposal of 'flush' becoming an ever-increasing problem.

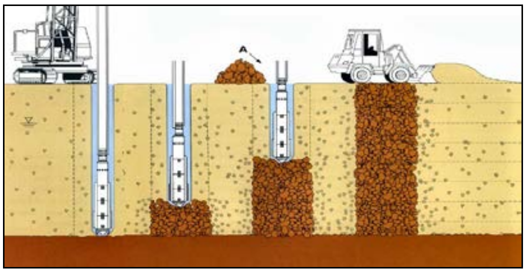

Figure 1. Schematic of wet top feed method - Raju *et al.* [11].

McCabe *et al.* [10] compared predicted settlement improvement factors using Priebe's [12, basic settlement improvement factor, n_0] method for a column friction angle, φ'_c, of 40^o with measured settlement improvement factors for the different methods of column construction. In that research, bottom feed columns tended to behave better than predicted, whereas for top feed columns, the opposite was generally the case. Their comparisons indicated that a design friction angle, φ'_c, of 40^o is a conservative assumption for the bottom feed system; however, for the top feed system, φ'_c = 40^o may lead to over-predicted settlement improvement factors.

The purpose of this study is to review and evaluate a selection of the more popular analytical settlement prediction methods. The predictions are compared with the field data from [10]. A numerical study is also conducted for comparison purposes. The predictions are plotted as a function of the main variables of vibro-replacement design; the area-replacement ratio, A_c/A (where A is the cross-sectional area of a unit cell treated with a single stone column of cross-sectional area, A_c, see Figure 2), and the modular ratio, E_c/E_s, where E_c is the stiffness of the column and E_s is the stiffness of the in-situ soil.

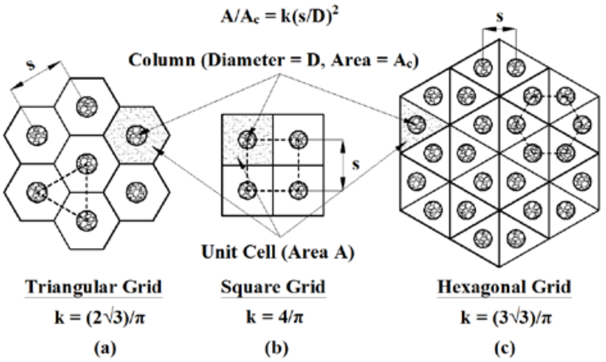

Figure 2. Typical Column Grids encountered in practice.

2 SETTLEMENT PREDICTION METHODS APPLICABLE TO VIBRO-REPACEMENT DESIGN

A significant amount of analytical solutions have been proposed to assess and predict the settlement improvement offered by granular columns [12-20]. As noted by Hughes and Withers [21], stone column design has always been somewhat empirical. The aforementioned design methods are either elastic (yielding of the column material not considered) or elastic-plastic. Elastic-plastic methods are preferable to purely elastic methods because elastic methods tend to over-predict the settlement improvement offered by column installation [14, 18, 19], especially for high modular ratios. Elastic methods tend to assume the stress concentration factor (SCF) to be equal to the modular ratio, whereas in reality, the SCF tends to be much lower. It has been suggested by Barksdale and Bachus [3] that commonly encountered SCFs in practice range from 3-10 for reciprocal area-replacement ratios, A/A_c, between 5 and 10, where the SCF is the ratio of the stress in the column to that in the surrounding soil (SCF = σ_c/σ_s).

The majority of the design methods are derived for a unit cell representing an infinite column grid. The unit cell approach, based on the assumption that all columns and tributary soil within a loaded area exhibit similar behaviour is valid except for columns near the edges of the loaded area [17, 22]. The design methods generally capture the improvement contributed by stone columns in the form of a dimensionless ‘settlement improvement factor’, n, relating the settlement of the untreated ground to the settlement of the ground treated with stone columns ($n = s_{untreated}/s_{treated}$).

Aboshi *et al.* [15] developed their simple equilibrium method based on elastic theory assuming the soil and column to behave as elastic materials. The method necessitates the selection of a SCF whereas Priebe [12, 14] and others worked out the SCF using cylindrical cavity expansion (CCE) theory. The method is based on simple equilibrium theory assuming equal vertical strain of both the soil and the column. Aboshi *et al.* [15] have placed limits on allowable SCFs based on the friction angles of the soil and column materials as well as the undrained shear strength of the soil. The method by Aboshi *et al.* [15] method is the simplest method of column design; the improvement factor can be evaluated knowing A_c/A with an assumption of the SCF (n is calculated as in Equation 1).

$$n = 1 + \frac{SCF - 1}{A / A_c} \quad (1)$$

Like Aboshi *et al.* [15], Balaam and Booker [17] adopted an elastic approach, based on a unit cell, assuming the columns to fully penetrate the soil layer. The soil and column are assumed to undergo equal vertical displacements. Depending on whether the columns are arranged in square, triangular, or hexagonal grids, the domain of influence of the column is approximated by a unit cell of effective diameter, d_e (Figure 3). Balaam and Booker [18] extended the 1981 solution using an interaction analysis to take account of yield of the granular material. The clay is assumed to behave elastically while the stone is assumed to behave as a perfectly elastic-plastic material (non-associative flow rule) satisfying the Mohr Coulomb failure criterion. Elasto-plastic finite element analyses were performed to validate the assumptions inherent in the interaction analysis.

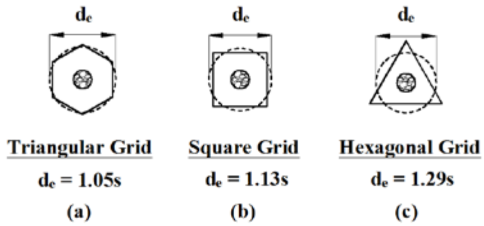

Figure 3. Domain of influence for different column grids.

Baumann and Bauer [13] also developed an analytical elastic approach assuming equal settlements of the soil and column. The total settlement of the loaded soil layer is assumed to consist of the immediate settlement (no volume change) and the consolidation settlement. Secondary settlement has been ignored.

Goughnour and Bayuk [16] formulated an elastic-plastic method based on a unit cell of effective diameter, $d_e = 1.05s$, representing an infinite arrangement of columns on a triangular grid, where s is the column spacing. The soil and column are assumed to undergo equal displacements under the applied load. As consolidation proceeds, stresses are gradually transferred from the soil to the column. Two sets of analyses are performed, considering both elastic and plastic behaviour of the column material. Firstly, an analysis is performed assuming that the stone undergoes plastic deformation while the surrounding soil undergoes consolidation. A second analysis is performed assuming the stone to behave elastically up until the end of consolidation. The vertical strains (ε_v) evaluated using the two methods are compared. The long-term vertical strain is then taken to be the larger of the two values, and the resulting settlement, ΔH, can be calculated as $\Delta H = \varepsilon_v.H$, where H is the layer thickness.

Despite its heavily empirical basis, Priebe’s [12] method is one of the most popular design methods (European practice) for evaluating the settlement improvement factor associated with vibro-improved ground. Like most other analytical and numerical design methods in existence, Priebe’s method [12, 14] is formulated based on a unit cell representing an infinite column grid. The method is based on elastic-plastic theory accounting for yield of the granular column material (the soil behaviour is assumed to remain elastic). Priebe's method [12] is an extension (described in the following paragraph) of Priebe's method [14] in which CCE theory has been used to evaluate the stresses in the column and surrounding soil (and hence the SCF). Priebe [14] accounts for the densification of the surrounding soil as a result of column installation by using an increased coefficient of lateral earth pressure (K = 1) in the design procedure. Priebe [14] makes a number of simplifying assumptions to calculate a 'basic' improvement factor, n_0, as defined in Equation 2, assuming a Poisson's ratio, ν, of 0.33 (the method does allow for different Poisson's ratios) for the soil, where A_c/A is the area-replacement ratio, and φ'_c is the friction angle of the granular material. In the calculation of n_0, it is assumed that bulging is constant over the length of the column, the column material is incompressible, and the bulk densities of the soil and column are neglected.

$$n_0 = 1 + \frac{A_c}{A}\left[\frac{5 - \frac{A_c}{A}}{4.\left(1 - \frac{A_c}{A}\right).\tan^2\left(45 - \frac{\phi'_c}{2}\right)} - 1\right] \quad (2)$$

Priebe's method [12] accounts for the column compressibility (n_1) and the bulk densities of the soil and column materials (n_2). Consideration of the compressibility of the column material means that load application can result in settlement that is not connected to column bulging. The calculation of n_1 involves 'shifting' the n_0 curve (based on the modular ratio) to work out $\Delta(A/A_c)$. $\Delta(A/A_c)$ is then added to A/A_c and a new improvement factor is evaluated.

Consideration of the soil and column unit weights (n_2) means that the columns are provided with more lateral support (hence increasing the bearing capacity of the composite system). Neglecting the bulk densities implies that bulging would be constant over the length of the column (because the initial pressure difference between the columns and the soil which leads to bulging will be constant over the length of the column). However, consideration of the soil and column weights means that the initial pressure difference between the columns and soil will decrease asymptotically with depth thus leading to a reduction of bulging with depth. Priebe's improvement factor n_2 [12] also allows for the input of different K values by modifying the depth factor, f_d, used in the calculation of n_2.

Similar to Priebe's method [12], Pulko and Majes [19] formulated their method based on elastic-plastic theory. Their method [19] is as an elastic-plastic extension to the earlier elastic solution proposed by Balaam and Booker [17]. Pulko and Majes [19] derived their method for a unit cell treated with end-bearing columns. Soil behaviour is assumed to remain elastic, while the column behaves as an elastic-plastic material (Mohr Coulomb failure criterion) with non-associative flow rule. The stresses at the interface of the soil and the column are assumed equal. Priebe's [12] method assumes the granular material to deform at constant volume when loaded (no dilation, i.e. dilatancy angle, $\psi = 0^o$) whereas Pulko and Majes [19] account for dilation of the granular material (constant dilatancy angle, ψ) at yield based on Rowe's stress-dilatancy theory.

Borges *et al.* [20] proposed a design method (based on a numerical rather than an analytical approach) relating the settlement improvement factor (n) to the area-replacement ratio, A_c/A, and to the ratio of the deformability of the soft soil to the deformability of the column material (alternatively the modular ratio, E_c/E_s). The method is based on a series of axisymmetric finite element analyses of a unit cell with a program incorporating Biot consolidation theory with the p-q-θ model (extension of the Modified Cam-Clay (MCC) Model, based on the Drucker-Prager failure criterion).

The authors adopted a value of K = 0.7 for the coefficient of lateral earth pressure at rest following column installation; in between the conservative approach assuming $K_0 = 1 - \sin\varphi'$ for normally consolidated soils, and the approach adopted by Priebe [14] and Goughnour and Bayuk [23], both of which use K = 1 for design purposes. The settlement improvement factor (Equation 3) has been derived based on statistical analysis techniques; and has been related to the two factors that the authors found most significant: A/A_c and E_c/E_s. A design chart has been developed based on this equation, which is applicable for $10 \le E_c/E_s \le 100$ and $3 \le A/A_c \le 10$, with calculated improvement factors greater than 1.5.

$$n = \left(0.125\frac{E_c}{E_s} + 0.7742\right)(A/A_c)^{\left(-0.0038\frac{E_c}{E_s} - 0.3423\right)} \quad (3)$$

Unfortunately, most (if not all) of the existing analytical design methods tend to ignore secondary settlement. Secondary settlement can be significant, if not dominant, in normally consolidated cohesive and especially organic soils [24, 25]. Since stone columns are now extensively used to improve such deposits, some effort should be made to quantify the impact that columns have on the in-situ soil. In another study [26], settlement improvement factors predicted using the Soft Soil Creep Model (PLAXIS 2D) have been compared to predictions using a selection of the design methods to assess how these secondary settlement improvement factors compare with corresponding improvement factors for primary settlement.

3 AXISYMMETRIC FINITE ELEMENT MODEL

A series of axisymmetric finite element analyses have been carried out to compare the results with the field data and design method predictions. A unit cell approach (column radius, R_c = 0.3m, column length = 5m, Figure 4) has been adopted to represent the behaviour of a single column within an infinite grid, e.g. [27]. Horizontal deformation has been restricted at the sides and both vertical and horizontal deformations have been restricted at the base. The water table is located at the surface. The columns are fully penetrating and have been wished in place (no installation effects). Densification as a result of column installation has been accounted for by using an increased coefficient of lateral earth pressure, $K_0 = 1$ [e.g. 12, 14, 23].

The behaviour of the composite model was studied under a 100kPa load applied through a plate element (normal stiffness, EA = $5x10^6$ kN/m, flexural rigidity, EI = $8.5x10^3$ kNm^2/m, Poisson's ratio, ν = 0). Different series of analyses were carried out for different modular ratios, E_c/E_s, of 5, 10, 20 and 40 (good comparison with elastic methods necessitates the use of low E_c/E_s ratios). In all cases, the properties of the column material were fixed, while the soil properties were varied to produce the necessary E_c/E_s ratios. The diameter of the unit cell was altered to study the effect of different area-replacement ratios (the column diameter was fixed at 0.6m).

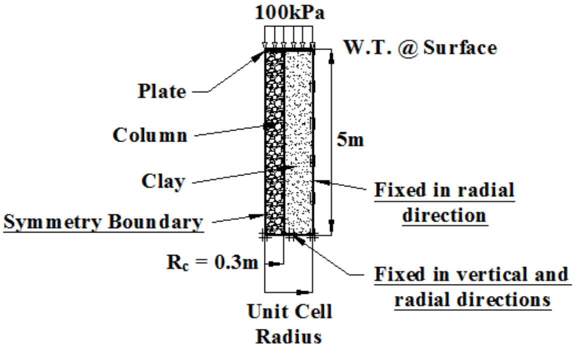

Figure 4. Unit Cell Model (100kPa Load).

Load settlement behaviour (primary settlement) was analysed using the Hardening Soil (HS) Model to model both the clay and the stone. Both were modelled as fully drained materials. Similar results would be achieved modelling the clay as an undrained material with a follow-up consolidation period (analyses have been carried out to verify this). The HS Model is a hyperbolic elastoplastic model that accounts for increasing soil layer stiffness with depth (no viscous effects). Its formulation has been described in detail by [28]. A detailed explanation of the HS Model and its parameters is given by [29]. A friction angle (φ') of 45° was selected for the stone, representative of bottom feed columns, while the dilatancy angle (ψ) was calculated as ψ = φ' - 30° [10]. E_{oed}^{ref} (oedometric modulus) was assumed approximately equal to E_{50}^{ref} (secant modulus) and E_{ur}^{ref} (unload-reload modulus) was taken as $3E_{50}^{ref}$.

Table 1. Parameters used in the Finite Element Model.

	Clay (Drained)	Stone Backfill (Drained)
γ_{unsat} (kN/m^3)	16.5	19
γ_{sat} (kN/m^3)	16.5	19
k_x (m/day)	1×10^{-4}	1.7
k_y (m/day)	6.9×10^{-5}	1.7
e_{init}	2.0	0.5
ϕ' (°)	34	45
ψ (°)	0	15
c_{ref} (kPa)	1.0	1.0
K_0^{nc}	0.4408	0.296
E_{oed}^{ref} (kPa)	3472	69440
E_{50}^{ref} (kPa)	4340	70000
E_{ur}^{ref} (kPa)	21874	210000
m (power)	1.0	0.3
p_{ref} (kPa)	100	100
ν'_{ur}	0.2	0.2
K_0	1.0	0.296
OCR	1.5	-

A complete list of the parameters used in the finite element model for the case when E_c/E_s = 20 (ratio of the constrained/oedometric moduli) is given in Table 1, which is a simplified single layer profile loosely based on parameters for the Bothkennar test site (the stiff crust has not been included in the soil profile) documented elsewhere [29]. The values of E_{oed}^{ref}, E_{50}^{ref}, and E_{ur}^{ref} have been doubled and quadrupled for modular ratios of E_c/E_s = 10 and 5 respectively, while they have been halved for E_c/E_s = 40 (with all remaining soil properties remaining fixed).

4 COMPARISON OF DESIGN METHOD PREDICTIONS WITH NUMERICAL RESULTS AND FIELD DATA

The field data presented by [10] pertain to long-term settlements from full-scale load tests and construction projects (both published and unpublished data) and is compared with the numerical predictions for the different modular ratios in Figure 5. Note that comparison with the field data could be influenced by factors such as the differences between 'as-constructed' column spacings and diameters, as well as the stage after loading at which treated and untreated settlements were measured in the field (since columns accelerate primary consolidation, fair comparison with untreated soils will only be achieved if the settlements are compared at the same stage of settlement, e.g. after primary consolidation, rather than at specific times). Additionally, the field data can only be plotted as a function of the area-replacement ratio, because the corresponding modular ratio is unknown.

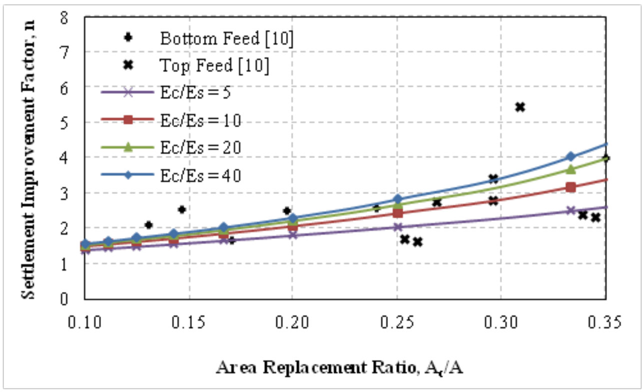

Figure 5. n versus A_c/A for numerical simulations.

The results in Figure 5 indicate that improvement factors predicted using the finite element method increase as the modular ratio increases, which is to be expected. The finite element data appears to be converging as the modular ratio is increasing, i.e. the influence of the modular ratio becomes negligible. Parameters with a more dominant influence on the settlement behaviour include the friction angle of the column material, ϕ'_c, and the coefficient of earth pressure, K_0.

The numerical results and the bottom feed field data appear to be in good agreement for modular ratios of 10, 20, and 40, while the top feed field data appears to be in best agreement with the numerical results for a modular ratio of 5, i.e. for stiffer soils. This finding reflects prior research [10]; thus, conservative design parameters could be used for the bottom feed method but unsafe settlement predictions may result if adopting conservative parameters for the top feed method.

The settlement improvement factors calculated using a selection of the closed form analytical design methods are compared to the bottom feed and top feed field data [10] and to the numerical results in Figures 6a-d. Due to the simplified nature of the method proposed by Aboshi *et al.* [15], it has not been included in the figures.

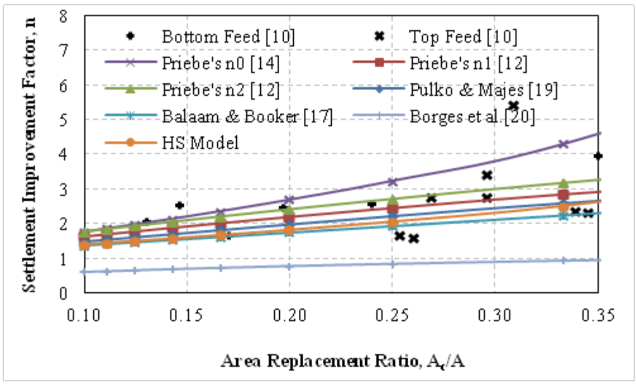

Figure 6a. n versus A_c/A for E_c/E_s = 5.

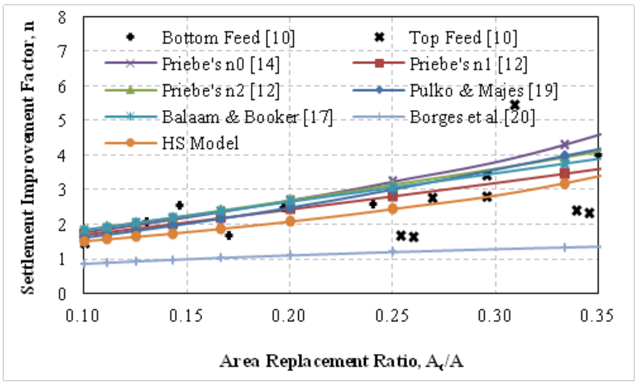

Figure 6b. n versus A_c/A for E_c/E_s = 10.

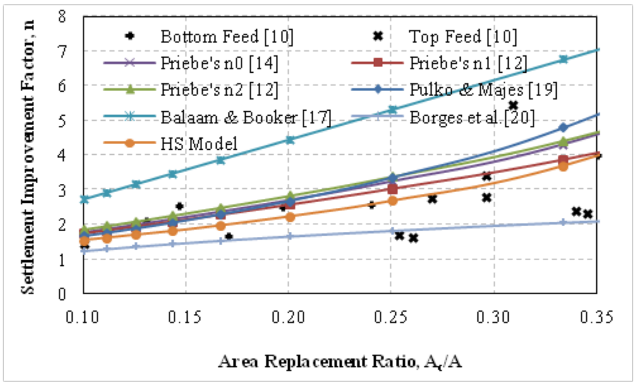

Figure 6c. n versus A_c/A for E_c/E_s = 20.

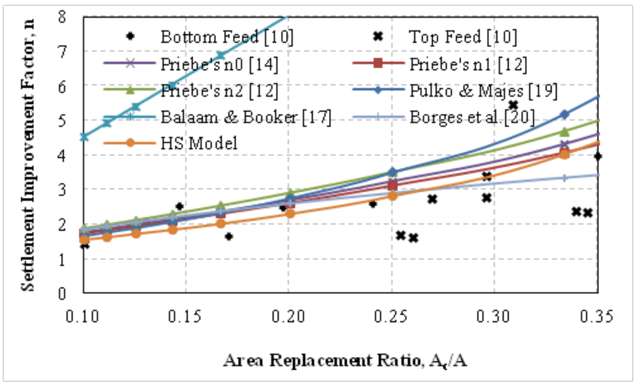

Figure 6d. n versus A_c/A for E_c/E_s = 40.

Examination of Figures 6a-d indicates:

- Elastic methods, e.g. Balaam and Booker [17], overpredict the settlement improvement for large modular ratios. For elastic methods, the SCF will be too high because yielding of the column is ignored (yielding/plastic strains reduces the SCF and hence the predicted settlement improvement).
- Priebe's n_0 [14] doesn't consider the influence of the modular ratio, E_c/E_s. Therefore, the n_0 line remains in the same position on all four graphs. Priebe's n_1 and n_2 [12] predict larger settlement reductions for larger modular ratios.
- Priebe's n_1 [12] predicts less of an improvement than n_0 in all cases, i.e. accounting for the compressibility of the column material removes any overestimation of the settlement improvement predicted by n_0. For larger area-replacement ratios (i.e. more stone), there is more compressible column material to be accounted for, and hence n_1 gets further and further away from n_0 as the area-replacement ratio increases.
- n_2 (considering soil and column unit weights gives more lateral support) is above n_1 in all four graphs. n_2 is only above n_0 at low area-replacement ratios (for E_c/E_s = 5 and 10) because at high area-replacement ratios, the starting point for n_2 (i.e. n_1) is much less than n_0 to begin with.
- The design chart developed by Borges *et al.* [20] indicates that the design equation should only be applied in a certain range (although not explicitly stated). It appears that the design equation predicts lower n values than the other design methods for modular ratios of 5, 10 and 20, i.e. n values < 1.5 (which do not appear on the design chart). For E_c/E_s = 40, Borges *et al.* [20] shows better agreement with the other design methods for area-replacement ratios up to approximately 0.3 (range of applicability), with divergence thereafter. For ever-increasing modular ratios, the method proposed by Borges *et al.* [20] predicts ever-increasing improvement factors (greater than those predicted by the analytical methods), so it appears the method is considerably more sensitive to the modular ratio than the analytical design methods (owing to the numerical basis of the method).
- Priebe's n_2 [14] and Pulko and Majes [19] appear to be in relatively good agreement for E_c/E_s = 20 and 40, with improvement factors predicted by [19] slightly larger for larger area-replacement ratios.
- In general, elastic-plastic design methods predict larger improvement factors when columns are subjected to lower applied loads (as does PLAXIS). However, for E_c/E_s = 5, Pulko and Majes [19] predicts lower n values at lower applied loads (in contrast with other methods), and perhaps indicates that the method may not be applicable for $E_c/E_s \leq 5$. It also predicts larger improvement factors for shorter columns (when $E_c/E_s \leq 5$) whereas Priebe [12] predicts larger improvement factors for longer columns. A similar inverse effect occurs where the coefficient of lateral earth pressure, K_0 is concerned.
- As expected, both Priebe [12, 14] and Pulko and Majes [19] predict more of an improvement for higher column friction angles, φ'_c. The method by Borges *et al.* [20] is

independent of the column friction angle, while the elastic methods are over-simplified in this respect.

- Examining the field data, it appears that bottom feed columns have performed similar to what the design methods have predicted, while the top feed columns generally performed worse than predicted by the design methods (similar to what [10] have concluded). The analytical methods are in good agreement with the bottom feed data and are perhaps only suitable for the design of bottom feed columns in practice (it may be necessary to apply a safety factor to the analytical design methods where top feed columns are concerned).
- Finite element predictions (HS Model) are in better agreement with analytical predictions at higher modular ratios, as the analytical methods assume a significant bulging mechanism which is more prevalent in soft soils.

5 CONCLUSIONS

- Predicted settlement improvement factors using a selection of different analytical design methods appear to be in relatively good agreement.
- Elastic methods overpredict the settlement improvement and should really only be used in relatively stiff soils in which the modular ratio, E_c/E_s, will be relatively small.
- The numerical predictions for this study appear to be in good agreement with the field data and analytical predictions (especially at higher modular ratios).
- Both the analytical and finite element predictions are in good agreement with the bottom feed field data for E_c/E_s = 10, 20, and 40. The top feed field data are in best agreement with the predicted settlement improvement factors for $E_c/E_s = 5$.
- When using analytical design methods in practice, care needs to be taken to ensure the selection of a suitable modular ratio (in the absence of suitable site investigation data) for top feed columns to prevent under-design.

ACKNOWLEDGMENTS

The authors would like to acknowledge the support provided by the Irish Research Council for Science Engineering, and Technology (IRCSET).

REFERENCES

[1] Mitchell, J.K. and Huber, T.R. (1985), 'Performance of a Stone Column Foundation', *Journal of Geotechnical Engineering*, 111, 2, 205-223.

[2] Watts, K.S., Johnson, D., Wood, L.A. and Saadi, A. (2000), 'An instrumented trial of vibro ground treatment supporting strip foundations in a variable fill', *Géotechnique*, 50, 6, 699-708.

[3] Barksdale, R.D. and Bachus, R.C. (1983), 'Design and Construction of Stone Columns - Volume I', *Federal Highway Administration Report FHWA/RD-83/026*, National Technical Information Service, Springfield, Virginia.

[4] Munfakh, G.A., Sarkar, S.K. and Castelli, R.J. (1983), 'Performance of a test embankment founded on stone columns', *Proceedings of the International Conference on Advances in Piling and Ground Treatment for Foundations*, London, 193-199.

[5] Han, J. and Ye, S.L. (2001), 'Simplified Method for Consolidation Rate of Stone Column Reinforced Foundations', *Journal of Geotechnical and Geoenvironmental Engineering*, 127, 7, 597-603.

[6] Castro, J. and Sagaseta, C. (2009), 'Consolidation around stone columns. Influence of column deformation', *International Journal for Numerical and Analytical Methods in Geomechanics*, 33, 7, 851-877.

[7] Slocombe, B.C., Bell, A.L. and Baez, J.I. (2000), 'The densification of granular soils using vibro methods', *Géotechnique*, 50, 6, 715-725.

[8] Sondermann, W. and Wehr, W. 'Deep vibro techniques', *Ground Improvement*, second edition (Moseley, M.P. and Kirsch, K. Eds.), Spon Press, Abingdon, England, 2004, 57-92.

[9] McCabe, B.A., McNeill, J.A. and Black, J.A. (2007), 'Ground improvement using the vibro-stone column technique', *Transactions of the Institution of Engineers of Ireland*, Galway.

[10] McCabe, B.A., Nimmons, G.J. and Egan, D. (2009), 'A review of field performance of stone columns in soft soils', *Proceedings of the ICE - Geotechnical Engineering,* 162, 6, 323-334.

[11] Raju, V.R., Hari Krishna, R. and Wegner, R. (2004), 'Ground Improvement using Vibro Replacement in Asia 1994 to 2004 - A 10 Year Review', *Proceedings of the 5th International Conference on Ground Improvement Techniques*, Kuala Lumpur.

[12] Priebe, H.J. (1995), 'The design of vibro replacement', *Ground Engineering*, 28, 10, 31-37.

[13] Baumann, V. and Bauer, G.E.A. (1974), 'The performance of foundations on various soils stabilized by the vibro-compaction method', *Canadian Geotechnical Journal*, 11, 4, 509-530.

[14] Priebe, H.J. (1976), 'Evaluation of the settlement reduction of a foundation improved by Vibro-Replacement', *Bautechnik*, 2, 160-162.

[15] Aboshi, H., Ichimoto, E., Enoki, M. and Harada, K. (1979), 'The "Compozer" - a method to improve characteristics of soft clays by inclusion of large diameter sand columns', *Proceedings of the International Conference on Soil Reinforcement: Reinforced Earth and Other Techniques*, Paris, 211-216.

[16] Goughnour, R.R. and Bayuk, A.A. (1979), 'Analysis of stone column-soil matrix interaction under vertical load', *Proceedings of the International Conference on Soil Reinforcement: Reinforced Earth and Other Techniques,* 1, Paris, 271-277.

[17] Balaam, N.P. and Booker, J.R. (1981), 'Analysis of rigid rafts supported by granular piles', *International Journal for Numerical and Analytical Methods in Geomechanics*, 5, 4, 379-403.

[18] Balaam, N.P. and Booker, J.R. (1985), 'Effect of stone column yield on settlement of rigid foundations in stabilized clay', *International Journal for Numerical and Analytical Methods in Geomechanics*, 9, 4, 331-351.

[19] Pulko, B. and Majes, B. (2005), 'Simple and accurate prediction of settlements of stone column reinforced soil', *16th International Conference on Soil Mechanics and Geotechnical Engineering,* Osaka, 1401-1404.

[20] Borges, J.L., Domingues, T.S. and Cardoso, A.S. (2009), 'Embankments on Soft Soil Reinforced with Stone Columns: Numerical Analysis and Proposal of a New Design Method', *Geotechnical & Geological Engineering,* 27, 6, 667-679.

[21] Hughes, J.M.O. & Withers, N.J. (1974), 'Reinforcing of soft cohesive soils with stone columns', *Ground Engineering*, 7, 3, 42-49.

[22] McKelvey, D.V., Sivakumar, V., Bell, A. and Graham, J. (2004), 'Modelling vibrated stone columns in soft clay', *Proceedings of the ICE - Geotechnical Engineering,* 157, 3, 137-149.

[23] Goughnour, R.R. and Bayuk, A.A. (1979), 'A Field Study of Long Term Settlements of Loads Supported by Stone Columns in Soft Ground', *Proceedings of the International Conference on Soil Reinforcement: Reinforced Earth and Other Techniques*, 1, Paris, 279-285.

[24] Simons, N.E. and Som, N.N. (1970), 'Settlement of Structures on Clay: With Particular Emphasis on London Clay', *CIRIA (Construction Industry Research and Information Association) Report 22.*

[25] Simons, N.E. (1974), 'Normally consolidated and lightly overconsolidated cohesive materials - Review Paper Section II', *Proceedings of the Conference on Settlement of Structures*, Massachusetts, 500-530.

[26] Sexton, B.G. and McCabe, B.A. (2012), 'A Preliminary Numerical Study of the Improvement to Secondary Settlement offered by Granular Columns', *International Conference on Ground Improvement and Ground Control (ICGI 2012)*, Woolongong.

[27] Ambily, A.P. and Gandhi, S.R. (2007), 'Behavior of Stone Columns Based on Experimental and FEM Analysis', *Journal of Geotechnical and Geoenvironmental Engineering,* 133, 4, 405-415.

[28] Schanz, T., Vermeer, P.A. and Bonnier, P.G. (1999), 'The hardening soil model: Formulation and verification' *Beyond 2000 in Computational Geotechnics - Ten Years of PLAXIS International*, Amsterdam, 281-290.

[29] Killeen, M.M. and McCabe, B.A. (2010), 'A Numerical Study of Factors Affecting the Performance of Stone Columns Supporting Rigid Footings on Soft Clay', *Proceedings of the 7th European Conference on Numerical Methods in Geotechnical Engineering,* Trondheim, 833-838.

Factors affecting embodied carbon and embodied energy associated with ground improvements techniques for construction on peat

A. Duggan[1], B.A. McCabe[1], J. Goggins[1], E. Clifford[1]
[1]College of Engineering and Informatics, National University of Ireland, Galway, Ireland
email: alan.duggan@nuigalway.ie, bryan.mccabe@nuigalway.ie, jamie.goggins@nuigalway.ie, eoghan.clifford@nuigalway.ie

ABSTRACT: In addition to the traditional drivers of cost and timely programme delivery, embodied energy (EE) and embodied carbon (EC) have emerged as major considerations in all aspects (including geotechnical) of large construction projects. Foundation engineers are beginning to undertake comparisons of the EE/EC associated with various piling and ground improvement options as part of an overall appraisal of scheme feasibility. Where construction involves the modification or removal of peat, these calculations become more challenging as allowances should be made for the impact on the carbon stored within the peat and the gases potentially released from peat. Using a calculator developed at NUI Galway, research is underway to consider the EE/EC associated with piling, soil-mixing and excavate-and-replace—options that can facilitate road/motorway construction on peat. Several high-profile motorway projects in Ireland will provide data for the analysis. Also, with the help of scientists presently measuring Greenhouse Gas (GHG) emissions from peat, the research will investigate GHG emissions from peat under various management practices, restoration techniques, and mitigation against drainage methods, assessing their strength in terms of hydrology and carbon storage potential. This paper summarises a literature review carried out to identify specifically the ‘peat-related’ factors that will impact upon EE/EC calculations on construction of a road/motorway on peat.

KEY WORDS: Embodied carbon; Embodied energy; Ground improvement techniques; Road; Peat drainage.

1 INTRODUCTION

Peatlands account for approximately 20% of Ireland’s land area [1]. The advent of significant motorway projects in Ireland in the first decade of the 21st century (such as the M6 Athlone to Galway section) has required geotechnical engineers to consider carefully how to deal with the large volumes of peat encountered along these routes. Challenges posed by peat for highway construction over peatlands include its high moisture content, compressibility and creep, and low shear strength, which necessitate the use of ground improvement options such as soil-mixing, piling and excavate-and-replace methods.

As stricter environmental regulations are introduced in Ireland, it is imperative that energy and emissions associated with road construction are calculated accurately. Examples of moves towards quantifying the emissions and energy associated with geotechnical processes in the UK include Egan and Slocombe [2] and Inui et al [3]. In this type of study, it is usual to look at the embodied energy (EE) and embodied carbon (EC) of a product. EE can be taken as the total primary energy consumed over a product’s life cycle while EC is associated with GHG emissions released over the lifetime of a product. EC is measured in carbon dioxide equivalents (CO_2e) which includes carbon dioxide (CO_2), methane (CH_4), nitrous oxide (N_2O) and perfluorocarbons (PFCs) [4].

Using current EE techniques, it is expected that the EE related to excavate-and-replace will be less energy intensive than soil-mixing and piling, as replacement of peat with fill (such as aggregates of low EE) is relatively cheap and environmentally friendly. These materials come straight from quarries, while the EE associated with binder in soil-mixing and pile production in piling is environmentally and energy intensive because of the additional production stage [2].

In calculating EE and EC inputs for materials and transport, few have included indirect inputs such as indirect energy and emission inputs relating to the extraction and transport of primary fuels and materials, together with the refining, distribution, storage and retail of finished fuels and materials [5]. Using the EE/EC calculator produced by McCaffrey [6], which totals inputs, these indirect inputs can be quantified as EE intensities (MJ/kg) and EC intensities (kgCO_2e/kg) for materials and transport energy costs. With the aid of the aforementioned calculator and life cycle inventories such as the ICE V2.0 [4], direct and indirect inputs can be accounted for. Nevertheless, even when indirect inputs are included, similar results of EE and EC can be expected in the cited ground improvement techniques.

Generally, high EE produces high EC: the more energy used in a construction project, the more gas emissions created. Construction in peatlands poses an additional complication. While its excavation and replacement with more competent fill seems greener than the other methods, the excavation process and the extent of drainage due to construction have a detrimental effect on the carbon stored within the peat. This carbon is now released from the peat as CO_2 and other GHGs, and the peat is no longer able to absorb carbon.

Where information giving comprehensive representations of the dynamics of gas emission and removal are limited, the Intergovernmental Panel on Climate Change (IPCC) and other organisations have provided basic figures to estimate emissions from damaged peatlands [7]. Both Nayak et al. [8] and Hall [9] used these basic assumptions to estimate the carbon cost of building a windfarm on peat and examined the issues of drained peatlands and forest removal associated with construction. Up to now, only simple calculations have been applied to some peat–related factors in EE/EC summations. This paper highlights the need for a robust software tool to perform a life cycle assessment (LCA) to quantify EE and EC, a model to calculate more accurately the cost of drained peatlands and forest removal. As well as explaining these and other potential factors that influence EC, the paper suggests some means of reducing the total EC in a road construction project.

The estimation of EC as a consequence of a particular method of road construction depends on a wide range of factors and construction activities that are the subject of this paper. These include the following: construction operations, peat drainage, peat stability, restoration of peatlands, vegetation/forest, and the effect of climate change. When the preceding factors are taken into account in EC summations, the choice of method to use for ground improvement must be reconsidered.

2 ROAD CONSTRUCTION OPERATIONS ON PEAT

Road construction on peat comes at a high energy and environmental cost. Surcharging, a ground improvement technique often used on soft soils is not used, as settlement in peat is difficult to predict and the duration required for it to impact significantly on secondary consolidation is excessive. Other ground improvement techniques must be used.

Since the 20th century, excavate-and-replace has been considered the most reliable method available of building major roads on peat, a method that involves peat removal and replacement with low EE fills such as aggregates, thereby providing a more stable and stronger platform to build the road [10]. Complete removal of peat is undertaken by machine if its thickness does not exceed 3–4m [11]. Dredging of this material is not usually energy intensive because of the semi-liquid state of the peat.

In peat deposits of between 4–10m deep, excavation and replacement may be considered too expensive. ‘Peat-left-in-place’ techniques are used instead [10]; i.e., soil-mixing and piling. Soil-mixing is becoming increasingly common as a method of ground improvement and works by injecting suitable binders into the ground, such as cement or combinations of cement and ground granulated blastfurnace slag (GGBS) for peat [12].The binder creates a homogenous mass in the peat structure, which in turn solidifies to strengthen the peat and reduce settlement. Although expensive, piling tends to be used in situations where settlement control is critical.

The above techniques all require the removal of some peat. If removed, it can be dried and burned as a fuel, and it can be assumed that it will emit all its carbon, thus dramatically impacting on EC summations. Excavated peat can be utilised, also, in the landscaping of roadsides, in filling in borrow pits, and it can be dried for agriculture purposes or laid on both sides of a road in peat disposal areas to restore the disturbed peat. Under anaerobic conditions, it could potentially retain a large percentage of its carbon content, but peat laid on the surface to dry will lose a high proportion of its carbon as GHGs, increasing substantially the EC total.

3 DRAINAGE AND ITS IMPACT ON EC

3.1 Introduction to drainage

The excavate-and-replace technique requires peat to be excavated, allowing the usual sources of water to enter the excavation; namely, ground, surface and rain water. Ground water flow enters the excavation, necessitating drainage of some of the surrounding peatland and resulting in a water table drawdown [13]. Even when the excavation is filled with materials, drainage is still occurring in the surrounding ground. This is due to the installation of drains along either side of the road, resulting in a permanent lowering of the water table. The extent of drainage can vary from less than a 1.5m radius to greater than a 50m radius [8]. Drainage of a peatland drastically alters the hydrological regime, leading to significant water loss, loss of habitat structure and subsidence of the peatland [14].The extent of the water table reduction around the road and its likely impact on gas emissions need to be estimated so that it can be included in EC summations.

In the absence of detailed measurements of peat hydrogeology on a level site with uniform soil distribution, the extent of drainage on each side of the road can be estimated using the regression equation below [8]:

$$E = 11.958 \times \log(k) - 9.361 \qquad (1)$$

where E is the extent of drainage around the road (m) and k is the hydraulic conductivity (mm/d).

In the case of soil-mixing and piling, little or no peat is removed during the operations, but drainage is still prominent because of the drains placed at either side of the road. In soil-mixing, the natural water content of the peat to be stabilised prior to mixing could be over 500%; but because of the reaction of water with the binder, the water content reduces significantly. This hydration process affects drainage, but the extent has not yet been ascertained. Irrespective of the extent, however, CO_2 is released from the stabilised and surrounding peat. Piling, on the other hand, has very little effect on the peat itself, apart from initially applying lateral pressures on the upper layers and, consequently, expelling pore water and causing possible heave. Some peat may dry because of this, but the extent is not known either.

To lower CO_2 emissions and thus EC, there are methods available to mitigate the extent of drainage on the surrounding peatland; such as, the installation of low permeability peat plugs along a road, described by Gill [15].

3.2 Carbon dioxide

The addition of organic matter to the peat surface on pristine peatlands exceeds decomposition losses as a result of anaerobic conditions created by the high water table [16]. Consequently, peat gathers carbon and restricts aerobic decay. Over centuries, intact peatlands slowly remove and store more carbon from the atmosphere than they produce, exerting a net cooling effect on the global climate [1]. Near-intact peatlands in Ireland may sequester on average only $0.21MtCO_2$/yr as 80-95% of organic matter is still decomposed by aerobic bacteria [17, 18]. Construction of a road will drain the nearby peatland and reverse the peat storing process into emitting carbon as CO_2.

Drained peat allows stored carbon to readily decompose due to the aerobic conditions created, releasing a substantial amount of CO_2, the level of which will need to be accounted for. CO_2 emissions vary mostly according to depth to water level, peat depth, and temperature [19]. Due to peat oxidation in the aerobic layer, intensified by the lowering of the water table, an area of raised bog damaged by extraction or cutting may emit as much as six to seven times more CO_2 than in a near-intact peatland [1]. Currently, damaged Irish peatlands may emit an estimated 9.68MtCO_2/yr [17]. The reason for such a large figure is that up to 100% of organic matter may decompose in the deep aerobic layer, in addition to organic matter that has been stored for many years. It is imperative that this accounted for in EC calculations.

3.3 Methane

Undrained healthy peatlands have negative effects, too, as CH_4 emissions are released in an intact peatland. CH_4 has a global warming potential (GWP) of 25 meaning that a large amount of heat is trapped in the atmosphere relative to CO_2, which has a GWP of 1 [19]. CH_4 can be released by three processes: diffusion across the air-water interface, bubble emissions, and transport via vascular plants (Figure 1) [7, 21].

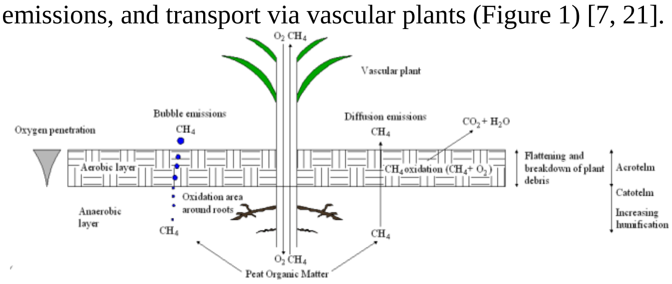

Figure 1. Methane release from a peatland site [22, 23].

The IPCC [7] suggests that when conducting a basic calculation of CH_4 emissions it is satisfactory to count diffusive emissions. During cold periods when peat is frozen, CH_4 emissions are negligible [7, 23]; therefore, it is important to factor this into EC calculations. The IPCC have not released guidelines for calculating CH_4 emissions because pristine peatlands are not anthropogenic and, as such, are not relevant under the United Nations Framework Convention on Climate Change (UNFCCC) [22]. Restoration of a peatland, which may take place after road construction is, however, anthropogenic and must be reported. The emission factors shown below, produced by Couwenberg [22], are based on climate, water table, and vegetation.

Table 1 illustrates the importance of incorporating into calculations CH_4 transport via vascular plants, as emissions average 170kgCH_4ha^{-1}yr^{-1} in a wet peatland. Transport through the aerenchymous shunts (air channels in the roots) bypasses the aerobic zone and travels straight into the atmosphere [22, 24]. Frequently, the majority of CH_4 transported through diffusion is lost in the upper aerobic zone due to oxidisation by methanotrophic bacteria, producing CO_2 in the process [21, 25]. This aerobic zone decreases in thickness at higher water levels, leading to reduced CH_4 oxidation and increased CH_4 production, and vice versa [26]. It must be remembered, however, that CH_4 production is offset by the amount of carbon sequestered by peat. In any case, Table 1 shows the necessity of calculating CH_4 released from restoring peatlands as part of road construction.

Table 1. Emission factors (Dry = mean annual water level -20cm, Wet = above -20cm) [22]

kg CH_4ha^{-1}yr^{-1} mean (range)			
Climate	Dry	Wet	
		Without shunts	With shunts
Temperate	0.2(-4.0-9.0)	50(-0.2-250)	170(0-763)

3.4 Nitrous oxide

N_2O is even more damaging to the atmosphere than CH_4 and has a GWP of 298. N_2O emissions depend on many factors, not just on the water table position. Glatzel et al. [27] found N_2O release was higher at the edge of site than the centre despite the lack of a difference in water table. Factors influencing N_2O emissions include the presence of organic nitrogen, the degree of humification, the presence of vascular vegetation and pH [28]. Drainage permits bacteria to convert the organic nitrogen in peat to nitrates, which are then carried by leaching to the surface where they are finally reduced to N_2O [7]. According to Glatzel et al. [27], only cultivated or drained peatlands release >100µgN_2O m^{-2}h^{-1}. Although it may seem that N_2O release should be highest in summer because of drier weather, N_2O release is negligible due to competition among plants for uptake of excess nitrogen and NO_3 [29,30].

N_2O emissions from Irish oligotrophic (nutrient-poor) peatlands are small or negligible because of their low nitrogen concentration [31]. Consequently, this is not a significant factor in emissions from road construction in Ireland, unless the site is a nutrient-rich fen. Klemedtsson et al. [32] reports that significant N_2O emissions can occur if the C/N ratio drops below 25; otherwise, they should be considered negligible in calculations.

In addition to the level of the water table, other factors such as peat properties, vegetation, weather and temperature will influence emissions. Table 2 lists research from several authors showing how each factor influenced emissions.

Table 2. Summary of factors affecting emissions

Ombrotrophic Raised/Blanket Bog with a Temperate Climate								
		Carbon dioxide		Methane		Nitrous Oxide (low emissions)		
		Uptake	Release	Release	Negligble	Uptake	Release	Negligble
Water table	Undrained	[1, 18, 22, 44]		[18, 22, 26, 27]		[31]	[18]	[22]
	Drained		[1, 18, 22, 44]		[21, 24, 27]		[20, 27, 28, 31]	[28]
Temperature	High			[23]			[31]	
	Low (<0)				[21, 23]			[31]
pH	Low (1-7)			[23]			[28]	[31]
Von Post scale	High							
	Low		[27]	[27]			[27]	
Weather	Wet	[16]			[27]			[30]
Season	Winter				[24]			[31]
	Summer			[24, 27]			[31]	[27, 29]
Vegetation	Not vascular		[48]	[22]	[24]		[27]	
	None							[27]
	Vascular			[22, 24, 26]				
Note:	Negligible: zero to low release except for nitrous oxide where negligible is close to zero Release: medium to high release except for nitrous oxide where release is small							

3.5 Peat stability

Soil disturbance should be minimised to prevent establishing aerobic conditions, which are ideal for decomposition and, therefore, the release of CO_2. There are many factors that may reduce the stability of the peat and impact on EC summations.

Water is the main cause of slope instability and acts in reducing the shear resistance of the underlying layer. Loading of the underlying material by saturation of the overlying layer may exceed the frictional resistance of the soil, causing it to fail. In peat excavate-and-replace, the water content of the peat on the excavation slope may exceed its liquid limit and collapse. Peat translational slides tend to occur where the slide's base meets the peat-substrate interface because natural lines of drainage exist along this interface [33].

Artificial drainage lines may induce shear stresses and cause potential failures; so, too, can the presence of water in cracks, which are indicative of compression and tension [34, 35]. Peat stability may be critical in all drained peatlands, a potential factor to be considered after applying any of the three ground improvement methods mentioned. As a result of drying, cracks will start appearing, decreasing the peat's strength to potential failure in heavy rainfall, as shown in Figure 2.

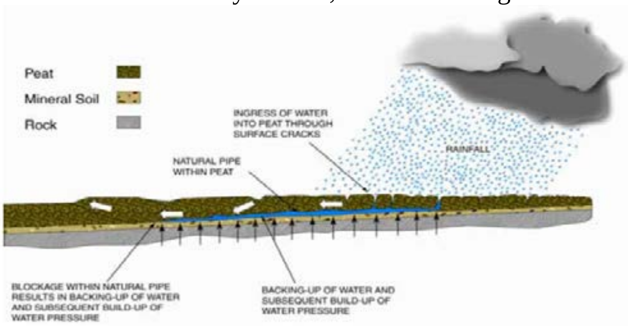

Figure 2. Typical water ingress through peat matrix [13].

The loss of surface vegetation due to construction leaves the peat surface fragile and without sufficient tensile strength [35]. Furthermore, loading of the peat mass by heavy machinery, structures, or overburden causes an increase in shear stress. Until pore pressures dissipate, peat stability is at its most vulnerable [13].

Peat stability and peat failures must be taken into account in the summation of emissions. Peat failures in blanket bogs and peat disposal areas due to construction have raised questions about the ability of the Environmental Impact Assessment (EIA) to fully assess the likely environmental impacts [1]. Blanket bogs are more prone to peat collapses than raised bogs because of their formation on slopes. Most slides occur in slope angles of 2-20°, where 20° appears to be the limiting gradient for deep peat [13]. Peat erosion has in the past decade been cited as a significant factor in losses of carbon due to drying out of the dislodged material, which can be from a few hundred m^3 to >100,000m^3 of peat [36]. In calculating emissions, it may be necessary to include a factor for peat erosion collapses because of peat debris drying out and hence releasing CO_2. Protecting this peat carbon store must become a priority in construction management [37].

3.6 *Restoration*

Any improvement plan for restoring a peatland that has suffered because of road construction should demonstrate a high probability that peat hydrology will be restored, disturbance of peat minimised, and subsidence stopped [14]. Peatlands often have complex modes of water transport, and identifying these pathways is crucial if saturated conditions in the peat and its dependent ecology are to be restored to their original status of sequestering carbon.

To restore peatlands, simple techniques are used. Drains can be blocked to promote rewetting after construction [15]. Soft rushes and sphagnum can be planted to bind the peat together, which leads to a complete cover and stabilisation of the introduced peat [38]. Shade can be provided to lower the temperature and increase relative humidity near the surface, impacting on CO_2 and CH_4 emissions and thus EC. These techniques can be also used for peat disposal sites.

3.7 *Vegetation/Forest*

Another common practice after road construction is to continue drainage on disposal sites and drained lands and to plant trees on these sites. During the first few years, a net CO_2 release occurs due to the exposure of soil carbon to aerobic conditions, but the uptake of carbon in vegetation and trees will somewhat offset oxidation losses. In 4–12 years after restoration, the site will become a net sink, the changeover varying according to vegetation dynamics, climate, peat depth and type, and site productivity [39]. This timeframe for emissions is shown in Figure 3. CH_4 emissions will cease due to increasing aerobic conditions in the peat profile. In addition to this positive EC impact, the average loss of carbon due to decomposition decreases from 1 to 14.6$tCO_2ha^{-1}yr^{-1}$ in the first rotation to a smaller figure after two or three rotations, which means that more carbon will be stored in the peatland forest annually [40]. During the first few rotations, though, some subsidence takes place depending on the bulk density of the peatland. Lindsay [23] found that this occurrence may extend up to 50–60m around the forest with time, somewhat draining the adjacent land and, inevitably, increasing GHG emissions.

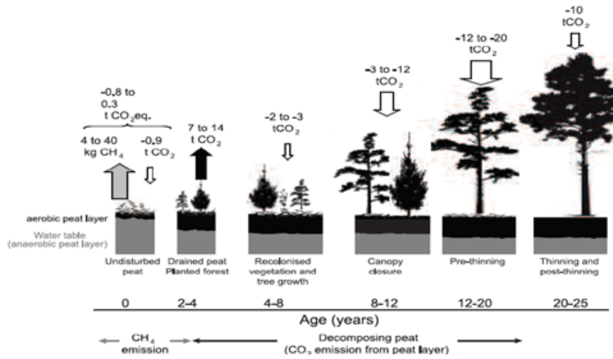

Figure 3. GHG balance of peatlands following afforestation. Values represent an annual flux of CO_2/ha [39].

For construction itself, it may be necessary to clear a forest, resulting in a CO_2 loss, although the amount of carbon loss depends on the type of tree, the age of crop on felling and the end use of the timber. A drained peatland cleared of forest continues to release CO_2. However, the trees are no longer present; therefore, there is no carbon uptake, which means a net loss of CO_2 is taking place and must be accounted for [39].

It is essential, also, to evaluate the carbon and nitrogen content of the biomass layer as well as the peat [23]. The clearance of vegetation such as sphagnum and vascular plants due to road construction can lead to GHG emissions. Vegetation is a source of carbon and nitrogen and, if destroyed, harmful gases are released [41, 42]. Lindsay [23], suggested that a 15cm sphagnum layer has a carbon content of 183.3tCO_2/ha, while a damaged peatland dominated by vascular plants is thought to have a lower carbon content of 36.7tCO_2/ha. The reason for the difference is that the greater resistance to decay of sphagnum compared to that of vascular plants allows undecayed material to pass to the anaerobic zone, where the decomposition is so slow that peat accumulates carbon [23]. It would be advisable, therefore, to plant sphagnum rather than vascular plants to reduce EC.

4 VARIABILITY IN PEAT AND UNCERTAINTY OF EMISSIONS

As stated earlier, each peat site is different in climate, landscape, properties and characteristics. Aggregated emission factors from the IPCC only estimate emissions from an undrained or drained peatland and nothing in between; consequently, in calculating emissions from a near-intact peatland, there is little guidance. Site-specific equations developed by Nayak et al. [8] can be used to estimate GHG emissions from peat more accurately. Even with these, there are substantial inaccuracies in relation to emissions. For example, CH_4 takes at least a month to revert to producing emissions after restoration because of suppression of CH_4 due to methangoens requiring a long regeneration period following exposition to aerobic conditions [27, 44].

It is significant that peatland restoration over a short period of time may lead to higher GHG emissions than if it were in a drained state. The peatland may still be releasing CO_2 through the aerobic layer and, simultaneously, releasing CH_4 from rewetting areas, though CH_4 emissions will not generally exceed the emission levels of the original natural state [23]. A rising water table then stimulates growth of sphagnum and other vegetation, increasing carbon accumulation, raising the surface of the peatland and, in effect, lowering the water table, which leads to a slight decrease in CH_4 release. A near-intact peatland may be mildly contributing to climate change or global cooling on a 100 year timeframe [23]. It would appear crucial, therefore, that new published EC summation models take the above factors into account.

A sphagnum-rich peatland is likely to be beneficial to climate change, even if CH_4 is more damaging than CO_2. When CO_2, CH_4, and N_2O are discussed, it is vital to bear in mind that CO_2 is the biggest emitter even when GWPs are taken into account as shown in Table 3. Drained peatlands, therefore, should be avoided in road construction.

Table 3. Rank of importance of GHG emitters.

Gas	Emission release generally dealt in (g, mg, µg) per m^2 per day		Rank	100 Year GWP	Effect on Environment (g,mg, µg)
CO_2	g	1	1	1	1
CH_4	mg	0.001	2	25	0.025
N_2O	µg	0.000001	3	298	0.000298

5 PEATLAND'S RESPONSE TO CLIMATE CHANGE

Climate change will have an impact on GHG release on peatlands affected by road construction. Holden et al. [45] predicts that temperatures will rise by about 1.68°C in Ireland by 2075. High rainfall sites will become more seasonally extreme through a decrease in rainfall in spring and summer and a slightly wetter autumn and winter.

Researchers have produced climate models showing that evapotranspiration will lead to a 100% increase in CO_2 emissions from peatlands because of increased temperatures and lower water tables [21]. Additionally, the carbon cycling of degraded peatlands may be more affected by global warming and future climate changes than healthy peatlands, signalling the importance of peat restoration.

The annual range of CH_4 emissions seems to be strongly related to temperature. Higher CH_4 fluxes occur in years with the warmest and coldest seasons [16]. With climate change, this aspect warrants consideration.

Nitrogen deposition is anticipated to increase [46]. N_2O fluxes were found to be high by Glatzel et al. [27] because the site in question had a history of drainage, experienced high atmospheric input and a rapid fluctuation in water table, which could be part of climate change and more extreme weather [46]. Dowrick et al. [47] furthered this notion by showing that an extreme drought caused an exponential increase in N_2O release compared to a moderate drought (water table at –8cm below the surface).

If warm and dry weather occur prior to prolonged rainfall, peat that shrank and dried will not return to its original condition on rewetting. Alternating dry and wet weather periods puts great stress on the peat and may result in failure due to loss of shear strength [37], leading to further CO_2 emissions. Table 4 shows that the top metre of soil generally holds the most carbon, highlighting why erosion of the top surface must be stopped immediately and the peatland restored to ensure that this high level of carbon is not released as CO_2. Climate change is likely to have a negative impact on the environment and will increase EC.

Table 4. Estimated carbon stocks (MtCO_2) for peat soils of Scotland [43].

Major Soil Subgroup	Stock (>1 metre depth)	Stock (<1 metre depth)	Total Stock
Blanket peat	1048	2930	3978
Basin peat	240	213	453
Semi-confined peat	492	1595	2087
Deep peat total	1780	4738	6518

6 CONCLUSIONS

- A more accurate model for estimating EC and EE from construction on peat must be developed, taking all peat–related factors into account and using the most accurate databases and calculators available. The model could guide engineers in deciding which ground improvement techniques to use on a proposed road on peat, and how to mitigate environmental effects with future legislation
- Large reductions of CO_2 and N_2O emissions can be achieved through restoration and rewetting of peatlands.
- Methods of mitigating lateral drainage need to be more thoroughly investigated in order to cut emissions.
- Afforestation could play a key role in the aftermath of peat disposal and drainage. As the need for timber increases, trees could be planted on drained peatlands and sustainably managed. Over the course of a tree's lifespan, the area would lower CH_4 release and take in carbon, offsetting the carbon released from peat.
- Site-specific data could be used to enhance estimations of emissions.

ACKNOWLEDGMENTS

The first author would like to thank the College of Engineering and Informatics at NUI Galway for its support under the Postgraduate Research Scholarship Scheme.

REFERENCES

[1] Renou-Wilson, F., Bolger, T., Bullock, C., Convery, F., Curry, J., Ward, S., Wilson, D. and Müller, C. *A Protocol for Sustainable Peatland Management in Ireland*, Environmental Protection Agency (EPA), University College Dublin, Ireland, 2011.

[2] Egan, D. and Slocombe, B. (2010), 'Demonstrating environmental benefits of ground improvements', *Proceedings of the Institute of Civil Engineers-Ground Improvement,* February, 163, 63-69.

[3] Inui, T., Chau, C., Soga, K., Nicolson, D. and O'Riordan, N. (2011), 'Embodied energy and gas emissions of retaining wall structures', *Journal of Geotechnical and Geoenvironmental Engineering*, October, 137, 958-967.

[4] Hammond, G. and Jones, C., *Inventory of Carbon & Energy Version 2.0 (ICE V2.0),* University of Bath, UK, 2011.

[5] DECC, Department of Energy and Climate Change and Defra, Department for Environment, Food and Rural Affairs, '*Guidelines to Defra/ DECC's GHG Conversion Factors for Company Reporting*', UK, 2011.

[6] McCaffrey, M. (2011*), An I-O hybrid methodology for environmental LCA of embodied energy and carbon in Irish products and services - A study of reinforced concrete,* M.Eng.Sc Thesis, National University of Ireland, Galway.

[7] Intergovernmental Panel on Climate Change (IPCC), *Guidelines for National Greenhouse Gas Inventories, Vol. 4,* 2006.

[8] Nayak, R., Miller, D., Nolan, A., Smith, P. and Smith, J., *Calculating carbon savings from wind farms on scottish peat lands - A new approach*, School of Biological Science, University of Aberdeen, and Macaulay Land Use Research Institute, Aberdeen, Scotland, 2008.

[9] Hall, M., *A guide to calculating the carbon dioxide debt and payback time for wind farms,* Renewable Energy Foundation, London, UK, 2006.

[10] Munro, R., *Dealing with bearing capacity problems on low volume roads constructed on peat,* Roadex II Project, The Highland Council, Transport, Environmental and Community Service, HQ, Glenurquhart Road, Inverness, Scotland, 2004.

[11] Woijtasik, A., Lecki, P., Troc, M. and Dojcz, P. (2006), 'Geotechnical conditions and soil improvement techniques applied in construction of the A2 motorway in Poland', *2nd International Conference on Problematic Soils*, Selangor, Malaysia.

[12] Timoney, M., McCabe, B. and Bell, A. (2011), 'Experiences of dry soil mixing in highly organic soils', *Proceedings of the of the Institute of Civil Engineers-Ground Improvement*, February, 164, 1-12.

[13] MacCulloch, F., *Guidelines for the risk management of peat slips on the construction of low volume/low cost roads over peat,* Forestry Civil Engineering, Forestry Commission, 2006.

[14] Regan, S. and Johnston, P. (2010), 'Consequences of marginal drainage from a raised bog and understanding the hydrogeological dynamics as a basis for restoration', *Geophysical Research Abstracts*, EGU, May, 12.

[15] Gill, M., *Peatland Hydrology Impact Assessment, Corrib Onshore Pipeline*, Hydro-Environmental Services (HES), 2010.

[16] Koehler, A., Sottocornola, M. and Kiely, G. (2011) 'How strong is the current carbon sequestration of an Atlantic blanket bog?', *Global Change Biology*, 17, 309–319.

[17] Wilson, D., Müller, C. and Renou-Wilson, F. (2011), 'Carbon gas fluxes from Irish peatlands: current and future trends'

[18] Crill, P., Hargreaves, K. and Korhola, A. *The Role of Peat in Finnish Greenhouse Gas Balances,* Ministry of Trade and Industry-Energy Department, Helsinki, Finland, 2000.

[19] IPCC, *Summary for Policymakers, Climate Change,* 2007.

[20] Martikainen, P., Nykanen, H., Alm, J. and Silvola, J. (1995), 'Change in fluxes of carbon dioxide, methane and nitrous oxide due to forest drainage of mire sites of different trophy', *Plant and Soil*, 168-169, 571-577.

[21] Strack, M., Waddington, J. and Tuittila, E. (2004), 'Effect of water table drawdown on northern peatland methane dynamics: Implications for climate change' *Global Biochemical Cycles*, 18, GB4003.

[22] Couwenberg, J., *Methane emissions from peat soils (organic soils, histosols),* Greifswald University, Wetlands International, 2009.

[23] Lindsay, R., *Peatbogs and Carbon, a critical synthesis*, University of East London: Environmental Research Group (ERG), UK, 2010.

[24] Laine, A., Wilson, D., Kiely, G. and Bryne, K. (2007), 'Methane flux dynamics in an Irish lowland blanket bog', *Plant Soil,* 299, 181-193.

[25] Segers, R. (1998), 'Methane production and methane consumption: A review of processes underlying wetland methane fluxes', *Biogeochemistry*, 41, 23-51.

[26] Whalen, S. (2005), 'Biogeochemistry of methane exchange between natural wetlands and the atmosphere' *Environmental Engineering Science*, 22, 73-94.

[27] Glatzel, S., Forbrich, I., Krüger, C., Lemke, S. and Gerold, G. (2008), 'Environmental controls of greenhouse gas release in a restoring peat bog in NW Germany', *Biogeosciences*, 5, 213-242.

[28] Regina, K., Nykänen, H., Silvola, J. and Martikainen, P. (1996), 'Fluxes of nitrous oxide from boreal peatlands as affected by peatland type, water table level and nitrification capacity', *Biogeochemistry*, 35, 401–418.

[29] Silvan, N., Tuittila, E., Kitunen, V., Vasander, H. and Laine, J. (2005), 'Nitrate uptake by Eriophorum vaginatum controls N_2O production in a restored peatland', *Soil Biology and Biochemistry,* 37, August, 1519-1526.

[30] Rückauf, U., Augustin, J., Russow, R. and Merbach, W. (2004), 'Nitrate removal from drained and reflooded fen soils affected by soil N transformation processes and plant uptake', *Soil Biology and Biochemistry*, 36, January, 77-90.

[31] Martikainen, P., Nykänen, H., Crill, P. and Silvola, J. (1993), 'Effect of a lowered water table on nitrous oxide fluxes from northern peatlands', *Nature*, 366, November, 51-53.

[32] Klemedtsson, L., Von Arnold, K., Weslien, P. and Gundersen, P. (2005), 'Soil CN ratio as a scalar parameter to predict nitrous oxide emissions', *Global Change Biology*, 11, July, 1142-1147.

[33] Boylan, N., Jennings, P. and Long, M. (2008), 'Peat slope failure in Ireland', *Quarterly Journal of Engineering Geology and Hydrogeology*, 41, February, 93-108.

[34] Wilson, P. and Hegarty, C. (1993), 'Morphology and causes of recent peat slides on Skerry Hill, County Antrim, Northern Ireland', *Earth Surface Processes and Landforms*, 18, November, 593-601.

[35] Scottish Executive, Natural Scotland, *Best Practice Guide for Proposed Electricity Generation Developments." Peat landslide hazard and risk assessment,* Scottish Executive, Edinburgh, Scotland, 2006.

[36] Dykes, A. and Warburton, J. (2007), 'Mass movements in peat: A formal classification scheme', *Geomorphology*, 86, 73–93.

[37] Warburton, J., Holden J. and Mills, A. (2004), 'Hydrological controls of surficial mass movements in peat', *Earth-Science Reviews*, 67, 139-156.

[38] Bord na Móna (BnM), *Srahmore Waste Licence W199-1. Appendix 9.1 Annual Environmental Report,* Tullamore, Co. Offaly, Ireland, 2005.

[39] Black, K. and Gallagher, G. *The greenhouse gas balance of peatland forest*, Environment No. 11, Coford, Ireland, 2010.

[40] Hargreaves, K., Milne, R. and Cannell, M. (2003), 'Carbon balance of afforested peatland in Scotland', *Forestry,* 76, 299-317.

[41] Institute of monitoring of climatic and ecological systems (IMCES) SB RAS, '*Mass loss and nutrient release during litter decay in oligotrophic peatland'* July, 2011, IMCES, Russia

[42] Schiller, C., Hastie, D. (1996), 'Nitrous oxide and methane fluxes from perturbed and unperturbed boreal forest sites in northern Ontario', *Journal of Geophysical Research*, vol., October, 101, 22767-22774.

[43] Scottish Executive Environment and Rural Affairs Department, SEERAD, *Estimating carbon in organic soils sequestration and emissions (ECOSSE)*, Scottish Executive, Edinburgh, Scotland, 2007.

[44] Tuitilla, E., Komulainen, V., Vasander, H., Nykänen H., Martikainen, P. and Laine, J. (2000), 'Methane dynamics of a restored cut-away peatland', *Global Change Biology*, 6, January, 569-581.

[45] Holden, N., Brereton, A., Fealy, R. and Sweeney, J. (2003), 'Possible change in Irish climate and its impact on barley and potato yield' *Agriculture and Forest Meteorology,* 116, 181-196.

[46] Jones, M., Donnelly, A. and Albanito, F. (2006), 'Response of Irish vegetation to future climate change', *Biology and Environment: Proceedings of the royal Irish academy*, 106, August, 323-334.

[47] Dowrick, D., Hughes, S., Freeman, C., Lock, M., Reynolds, B. and Hudson, J. (1999), 'Nitrous oxide emissions from a gully mire in mid-Wales, UK, under simulated summer drought', *Biogeochemistry*, 44, April, 151-162.

[48] Glatzel, S., Basiliko, N., Moore, T. (2004), 'Carbon Dioxide and Methane Production, Potentials of Peats from natural, harvested and restored sites, Eastern Quebec, Canada' *Ecoscience*, 24, June, 261-267.

The value of ground investigations in Ireland

Paul Quigley[1]
[1]Arup, 50 Ringsend Road, Dublin 4, Ireland
email: paul.quigley@arup.com

ABSTRACT: Ground investigations are an essential aspect of risk management for building and infrastructure projects. The current economic environment is increasing pressures on promoters to cut costs across the board. However, the judicious use of ground investigation can provide greater cost certainty and reduce overall costs. Unforeseen ground conditions are one of the most common causes of project delays, most of which could have been avoided with better ground investigation. Similarly, accurate ground investigation can result in major savings if more favourable conditions are exposed. This paper examines a large dataset of ground investigations in Ireland over an eight year period. The study compares tender and construction costs to investigate the degree of overspend on ground investigation contracts. The data suggests the presence of a "pessimistic bias" when geotechnical engineers plan ground investigations. Consequently, the recently introduced contracts for public works in Ireland may be both commercially and technically disadvantageous for promoters. The paper also compares the intensity of ground investigation points against recommendations presented in Eurocode 7. A comparison between the ground investigation costs and the overall project capital costs are also presented for both building and road projects and compared to published international correlations. Finally, ways of increasing the value and quality from ground investigations are suggested.

KEY WORDS: Ground investigation, cost comparison, risk.

1 INTRODUCTION

All civil engineering projects transfer loads to the ground and consequently the nature of the ground is important when assessing how the structure will behave. There are numerous modes of failures in geotechnical engineering such as shear failure of the foundations, unacceptable differential settlements, excessive seepage issues or environmental issues from contamination. According to Brandl [1] and based on European statistics, about 80 to 85% of all building failures and damages relate to problems in the ground. Chapman [2] highlighted some typical delays for UK projects and suggested that about 40% of projects are delayed significantly and approximately 30% to 50% of those delays are ground related (Figure 1).

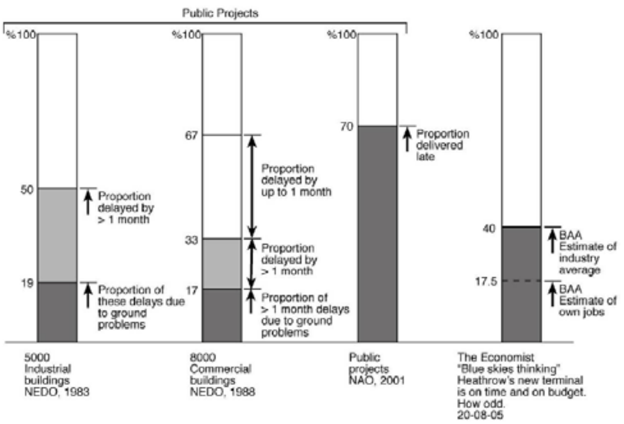

Figure 1. Typical UK delays for projects against time (Chapman, [2]).

Clayton [3] reviewed data collated by Mott MacDonald and Soil Mechanics [4] during a study of the efficiency of ground investigations on road projects in the UK (Figure 2). The current level of spend on ground investigations for road projects would suggest that the risk exposure for the highest increases in construction costs occur at the lowest investment on ground investigation works (Figure 2). The data suggests that significant investment in ground investigation, while probably inefficient, probably significantly reduces overall risk and could make financing of the project easier.

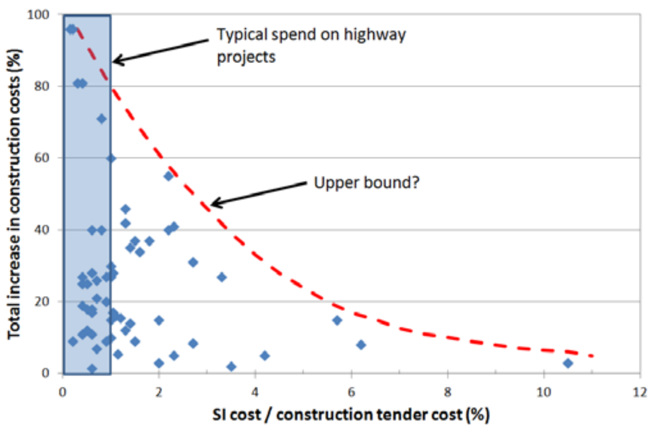

Figure 2. Comparision of GI expenditure and cost overruns for highways (from Clayton [3]).

Comparable studies are not readily available for Irish projects. However, as the construction process in Ireland is similar to that used in the UK it is probable that similar levels of project delays are encountered here. IEI [5] noted that cost overruns were averaging close to 40% between the acceptance of tenders for civil engineering projects and project completion. The impact of these delays can be very significant. The cost of remedial measures including maintaining and committing extra resources to complete the project, loss in revenue especially when missing critical periods such as Christmas for retail units or commencement of the academic year for education facilities, and professional fees for legal and engineering experts required to resolve disputes typically dwarf the ground investigation costs. Chapman [2] provides a useful economical comparison on the impact of poor geotechnical risk management. Chapman notes that developers crave certainty even above cheapness, in order to ensure that project costs are within budget and forecasted profits or benefits are realised. He notes that the UK Government has studied the tendency of project costs and works durations to increase and has come up with advice in its Green Book [6,7] to redress the systematic optimism (which it terms "optimism bias") that has historically afflicted the appraisal process for major projects. It suggests the two main causes for this bias in capital cost estimates are:

- poor definition of the scope and objectives of projects in the business case, due to poor identification of stakeholder requirements, and
- poor management of projects during implementation, so that schedules are not adhered to and risks are not mitigated.

As ground related risk is so significant it would seem reasonable that better ground investigation and design should reduce this risk.

2 RISK MANAGEMENT

Ground investigation works are an essential part of civil engineering projects, yet contribute only a small portion of the overall construction cost, typically 0.05% to 0.22% for buildings and 0.20% to 1.55% for road projects (Rowe [8]). The ability to mitigate risk is greatest at the start of a project and decreases rapidly as the project progresses (Figure 3). The appointment of experienced and qualified geotechnical specialists early in the planning process can help manage issues that can be expensive and costly to remediate later in the project cycle.

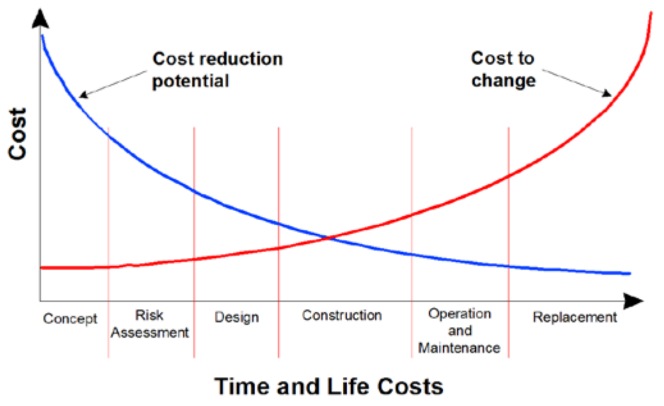

Figure 3. Typical value management cycle for most projects.

2.1 Causes of delays

A number of studies have examined the link between geological related problems and project delays. Bea [9] reviewed about 600 well documented cases of failures in civil engineering projects during the previous 20 years. The main finding was that about 80% of failures were due to people failure such as poor communication or organisation. Sowers [10] presented similar findings from a review of 500 well documented foundation failures with some 88% of failures being linked to people failures and the remaining 12% due to a failure in the technology used.

Abdulahad et al. [11] carried out a review of 41 legal cases involving geotechnical practice in Canada over a 25 year period. The most frequent cause of disputes was found to be different soil conditions and recommendations than expected from those given in the geotechnical report, inaccuracies in the design plans and specifications, and the owner's failure to disclose important information. The paper also suggested precautionary measures to reduce the number of disputes or to arrive at an equitable resolution. These measures require more proactive planning and may require additional funds before tender stage to perform a more detailed ground investigation, keeping communication clear between all parties and making a greater effort to provide accurate designs and specifications.

2.2 Managing geotechnical risk

Geotechnical risks can be managed and mitigated. Sound geotechnical practices can reduce risks substantially (Figure 4).

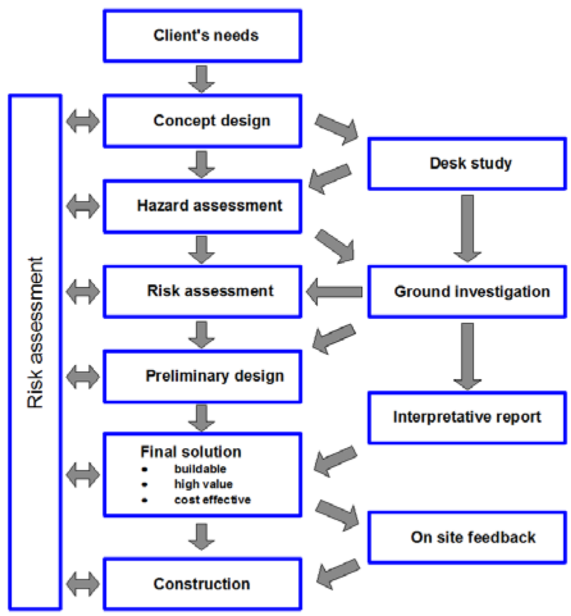

Figure 4. Risk management process for geotechnical design.

To design the ground investigation properly, an outline of the proposed foundation or geotechnical structure is required. The preliminary conceptual model derived from the desk study and site reconnaissance is used to give a starting point for the geotechnical design. The outline design will then determine the basic requirements of the ground investigation. The level of sophistication required will be proportional to the risks. Five key questions should be answered before a ground investigation commences in order to provide direction to the process (BRE, [12]):

1. What is the purpose of the investigation?
2. What information is required and when?
3. What areas and depth of the ground are to be investigated?
4. What is the time required for the investigation?
5. What is the estimated cost?

Frequently, the best design solution is to carry out the ground investigation in stages, allowing for targeting specific areas or changing techniques if necessary. While this approach is often slower and more expensive, the improved quality of the design often outweighs the disadvantages.

3 REVIEW OF GROUND INVESTIGATION PROJECTS

The recent implementation of the Public Works Contract prompted the author to review ground investigation costs valued in excess of €10,000 from 2003 to 2010. It was suspected that the new contract is commercially and technically disadvantageous for the client and designer. The €10,000 threshold was chosen as it represents a moderate ground investigation with scope for variation. These ground investigation would typically include a minimum of three cable percussive boreholes, some trial pits and associated geotechnical and environmental testing of samples.

The study compared the tender price against the final payment and the data is presented in Figure 5. The data is normalised by dividing the payment by the tender price and plotted against the tender price. When the payment/tender ratio is less than 1.0 the projects comes under budget; it is apparent that the majority of projects came in under budget.

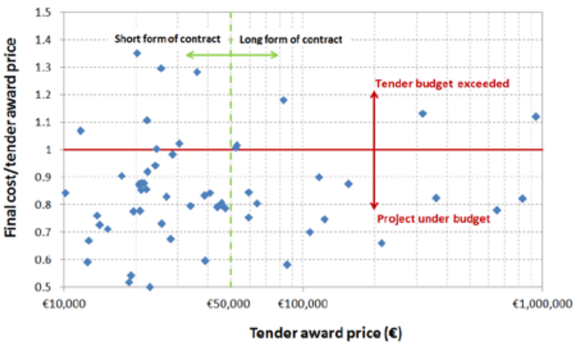

Figure 5. Comparison of tender price against the final payment

Figure 6 shows a histogram of the data and 85% of the projects came in or under budget. It is evident that the designers in this study typically adopted a “pessimistic bias” when estimating quantities and potential geohazards.

Discussions with ground investigation contractors and other consultants suggest that this “pessimistic bias” concerning quantities is not unique to Arup. The exact quantities for a ground investigation are not easily defined at the outset and are frequently modified during the works as information becomes available. The glacial environment that dominates the Irish landscape creates a difficult environment for sampling and carrying out ground investigation. Consequently ground investigations are rarely straight forward projects. All of the contracts in this study were procured using a remeasurable form of contract. Therefore, where projects exceeded the original tender budget additional work was carried out rather than paying extra for the same end product.

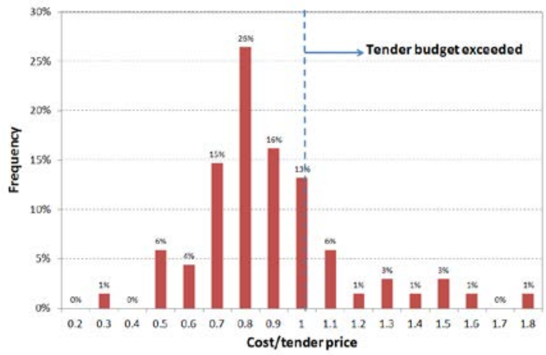

Figure 6. Histogram distribution of cost/tender ratios.

4 CONTRACTS FOR GROUND INVESTIGATIONS

The Public Works Contracts has caused disquiet among geotechnical designers and it is becoming apparent that the contract structure may not be best suited to medium to large ground investigations. The contracts are fixed price and the data from this study suggests that promoters typically pay more than necessary. Under remeasurable contracts designers were able to adopt a “give and take” within the budget as the investigation results were reviewed. For example a road project running through a karstic area requires careful examination as the consequence of a sinkhole opening up following the opening of the road to traffic could be very serious. Geophysics and trial pitting are effective and relatively inexpensive methods of assessing large areas. If the initial results are favourable more expensive boreholes and drilling may be reduced or relocated elsewhere. If the results are less favourable than expected then a potential major hazard can be mitigated at the design stage and at a much lower overall cost than later in the construction programme.

Fixed price contracts do not incentivise carrying out additional work such as chiselling through hard strata or waiting for groundwater to rise, etc. With the reduction of site supervision on many schemes the ground investigation results may not be as useful as it could or should be.

Many cost overruns are blamed on an “optimistic bias” described earlier. The introduction of the Public Works Contracts is an attempt to provide greater cost certainty. A Department of Finance review of the Construction Procurement Reform [13] suggested that the introduction of the fixed price contract may discourage consultants from increasing the scope and cost of projects as the consultant’s fee is often linked to a percentage of the construction cost. However this is not applicable for ground investigations as the contract value is usually too small to generate a sufficient fee income and the design services are generally part of a larger design commission.

In the UK the Institution of Civil Engineers withdrew the ICE Conditions of Contract in August 2011 in order to consolidate all contracts under the New Engineering Contract. However the value of the original contract was recognised and the contract has now been replaced by the Infrastructure

Conditions of Contract, with the ownership transferred to the Association for Consultancy and Engineering and Civil Engineering Contractors Association. The contract was based on the traditional pattern of an investigation designed by an Engineer and carried out by a Specialist Contractor. The contract is viewed as ideally suited for ground investigations as the promoter and designer have greater control of the works and costs. The equivalent contract in Ireland is administered by Engineers Ireland and is well established.

4.1 Quality and adequacy of ground investigation

A change in contract type will not solve all issues. Quality and thoroughness are key and poor ground investigation does not allow promoters to properly assess the risks, engineers to design appropriate foundations or contractors to price the required work. Promoters must recognise that driving down budgets and costs invariably compromises quality and ultimately increases overall project risks. Oftentimes gaps in ground investigations lead to increased project costs and significant delays. Under the Public Works Contract the State is transferring the risk of unforeseen ground conditions to the contractor. However, in order to assess the risk the State has to provide a comprehensive ground investigation to allow a fair assessment of the risk. If the ground conditions encountered during construction are significantly adverse to that indicated in the tender documentation then lengthy and expensive challenges between contractors and the promoter are likely.

5 EXPENDITURE ON GROUND INVESTIGATIONS IN IRELAND

There is limited information available on ground investigation expenditure on various projects. Rowe [8] included some data on various project types (Table 1).

Table 1. Comparison of expenditure on various civil engineering areas (from Rowe, [8])

Type of Work	% of capital costs of works	% of earthworks and foundation cost
Earth dams	0.89 - 3.30	1.14 - 5.20
Embankments	0.12 - 0.19	0.16 - 0.20
Docks	0.23 - 0.50	0.42 - 1.67
Bridges	0.12 - 0.50	0.26 - 1.30
Buildings	0.05 - 0.22	0.50 - 2.00
Roads	0.20 - 1.55	(1.60)? - 5.67
Railways	0.60 - 2.00	3.5
Overall mean	0.7	1.5

This study examined a limited number of projects where both the construction cost and the ground investigation costs are available (Figures 7 and 8). The data suggests that the proportion spent on ground investigation decays with the increasing value of the project. The study was limited to commercial buildings and road projects which were constructed since 2003.

The data was more difficult to compile for road projects as projects go through multiple phases of ground investigation and usually are undertaken by different ground investigation contractors for various parties. The author has reviewed a limited number of road projects where the ground investigation contracts are known or can be estimated based on similar contracts undertaken at the same time (Figure 8). The projects range in value and geological complexity, from glacial tills and limited soft ground areas to deep deposits of peat and soft soil. Additional data is required before a typical trend on GI expenditure to construction cost can be identified. It is probable that the additional expenditure on investigating challenging ground conditions is offset with the higher cost involved in building the road. Further investigation is required and can only be effectively carried out in cooperation with the National Road Authority.

For both building and road projects it is interesting that proportional expenditure on ground investigation hasn't changed significantly in the 40 years since Rowe presented his Rankine lecture.

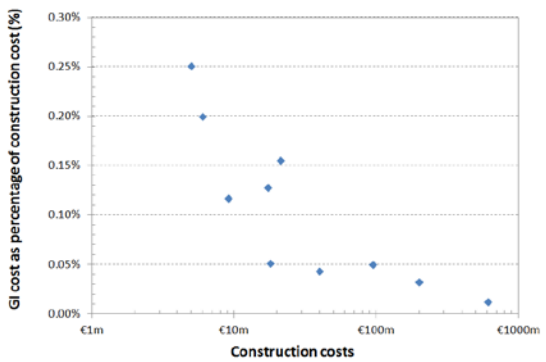

Figure 7. Comparison of construction costs to ground investigation expenditure for buildings.

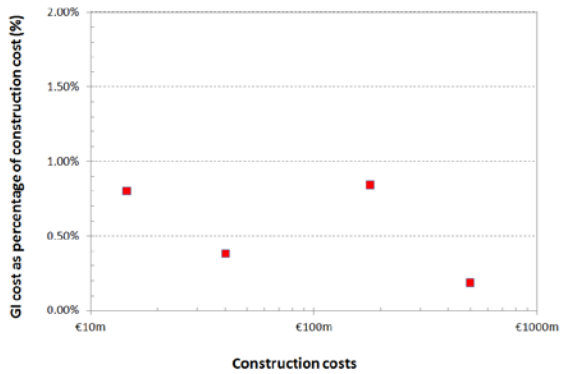

Figure 8. Comparison of construction costs to ground investigation expenditure for road projects.

6 EUROCODE AND GROUND INVESTIGATION IN IRELAND

The recent adaption of Eurocode 7 [14,15] in Ireland for geotechnical design has introduced new requirements for the industry. The purpose of Eurocode 7 is to harmonise geotechnical engineering across Europe and improve the field testing and design processes. The design process is described in IS EN 1997 Part 1 and ground investigations are covered by IS EN 1997 Part 2. Some of the changes to the design process include the mandatory production of a Geotechnical

Interpretation Report (GIR) and Geotechnical Design Report (GDR). Ground investigation processes involve ensuring that equipment such as the Standard Penetration Test is calibrated. However, Quigley [16] commented on the cost of carrying out such calibrations and has noted that designers are not requesting the certification as part of recent project requirements.

IS EN 1997 Part 2 [15] has also introduced requirements for the quality of sampling. Certain tests such as triaxial and consolidation tests require high quality sampling. The Engineers Ireland Specification for Ground Investigations in Ireland is currently being revised and more guidance on techniques such as geophysics, Geobore S and sonic drilling will be provided.

6.1 Depth and frequency of explorations

Eurocode 7 provides an outline to the suggested frequency of explorations and is outlined in Table 2.

Table 2. Suggested intensity of ground investigation points according to EuroCode 7.

Structure	Spacing	Arrangement
High-rise and industrial	15 – 40m	Grid
Large area	≤60m	Grid
Linear – Roads, railways, channels, pipelines, dikes, tunnels, retaining walls	20 – 200m	-
Dams and weirs	25m– 75m	Vertical sections
Special – *Bridges, stacks, machinery foundations*	2 – 6 per foundation	

Annex B.3 of IS EN 1997-2 [15] provides examples of recommendations for the spacing and depth of investigations. For high-rise structures and civil engineering projects, the minimum recommended depth should be the larger value of the following conditions:

$$z_a \geq 6 \text{ m; or } z_a \geq 3.0 b_F. \quad (1)$$

where b_F is the smaller side length of the foundation (Figure 9).

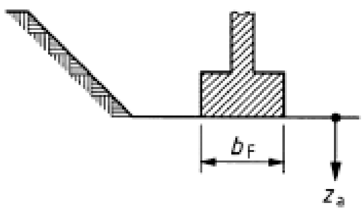

Figure 9. Comparison between building area and the number of boreholes.

The author's review of ground investigation suggests that on quantity alone that most road projects satisfy the requirements of Eurocode 7. However the quality, nature and frequency of soil tests can be insufficient for certain foundation solutions.

The frequency of boreholes for building projects was reviewed by comparing the number of both cable percussive boreholes and rotary core boreholes to the building footprint area and the construction cost (Figure 10 and 11 respectively). The extent of ground investigation was reviewed from available ground investigation reports and also by reviewing the Geological Survey of Ireland (GSI) online database of borehole records. All projects have been constructed since 2002. A screen grab showing a typical layout is shown in Figure 12. The borehole records were exported to a GIS program and overlaid on an Ordnance Survey map.

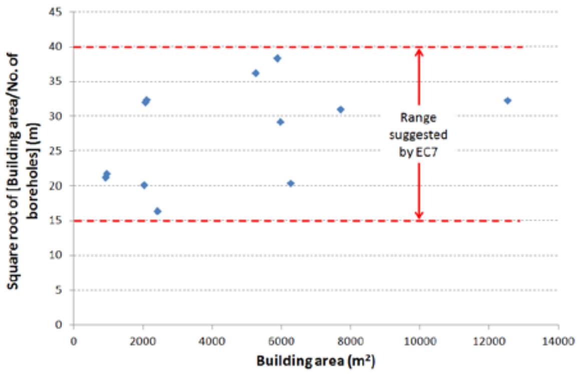

Figure 10. Comparison between building area and the number of boreholes.

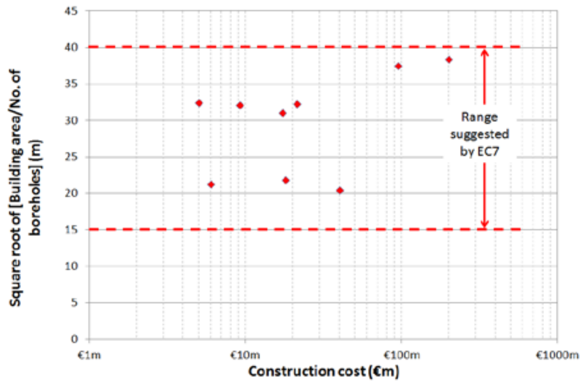

Figure 11. Comparison between construction cost and the number of boreholes.

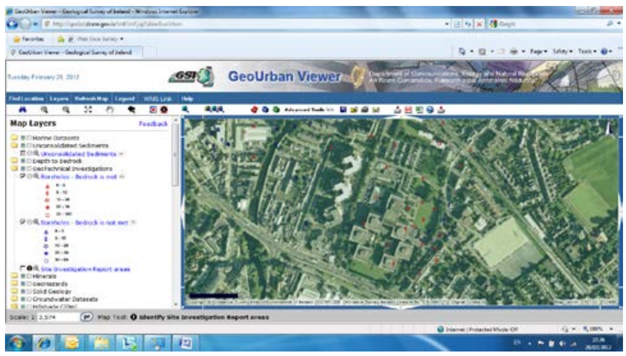

Figure 12. Typical screen grab from GSI GeoUrban viewer.

7 POSSIBLE DESIGN ISSUES

7.1 Cable percussive rigs and worker safety

Probably the most common investigation method, along with trial pitting, is the cable percussive tool. The drilling rigs are light, easy to maintain and the equipment has changed little over 50 years. However, the rigs require two operators working in close proximity to heavy, moving equipment. The introduction of methods such as sonic coring has the attraction of ensuring a safer working environment and the ability to provide greater penetration and reliability for testing in glacial soils. The cost of the new equipment is significantly greater than for cable percussive rigs and cable percussive boreholes remain the dominant form of borehole. It would be interesting to know how the frequency of injuries associated with cable percussive rigs compare to newer drilling methods. If the frequency of injuries is higher for a particular method then designers may have to tailor their ground investigation designs to avoid methods that expose workers to higher risks of injury.

7.2 Quality of ground investigation

Ultimately all ground investigations, from a relatively simple investigation on a rural greenfield site to more complex urban tunnel projects, result in a written report. Many project managers may not be able to discern the technical quality of the drilling and laboratory testing from the report alone. It would be useful if promoters requested a technical evaluation of the ground investigation from designers at the end of the contract and that these assessments formed part of future tender assessments. In addition, a report stating the compliance with Eurocode 7 may help with the adoption of the current code of practice. Hopefully this will encourage ground investigation contractors to maintain or improve quality in a very competitive environment. Similarly it would be useful for promoters to request a basis of design document from designers before tendering ground investigations. This document should describe why the techniques in the contract document are being proposed and how the various techniques are to be combined. A discussion on techniques considered but discounted would also provide a clearer understanding of the risk management techniques employed by the designer and improve communication between the designer, promoter and the contractor.

8 CONCLUSIONS

Deficiencies in ground investigation can result in conservative or inappropriate design assumptions, additional costs arising from problems encountered on site, additional costs incurred through delays in completion, and possibly highly expensive remedial action at a later date. If appropriate risk management techniques are adopted then the geological hazards can be greatly reduced.

This study suggests the presence of a “pessimistic bias” when designers are assessing potential geohazards. Consequently most ground investigation contracts are completed for less than the tender price. The recently introduced Public Works Contract does not appear to be suited to medium to large ground investigations and probably represents poor overall value to the promoter as a result. A remeasureable form of contract would be a better choice for most medium to large ground investigations.

A review of the frequency of boreholes suggests that current practices in this study are in line with the recommendations in Eurocode 7. A study of the expenditure on ground investigations compared to the project construction cost suggests that ground investigation expenditures decreases as the project value increases for both building and road projects. Improvements in risk management and communication could be achieved by Clients requesting a basis of design document for ground investigations and a technical evaluation of the quality of the ground investigation following completion.

There have been considerable improvements and innovations in ground investigation practice in Ireland during the past ten years. The number of ground engineering specialists has increased significantly and there is considerable capability in the market place for high quality service. The industry has also innovated considerably to suit Irish ground conditions such as developing improved use of geophysics, a greater understanding of sampling disturbance in soft soils and high quality drilling methods such as Geobore S and sonic coring in stiff glacial till. The more sophisticated techniques and the appointment of geotechnical specialists carry a price premium but better ground investigation results in better design which in turn leads to greater cost certainty. Isn’t this what every promoter would want?

ACKNOWLEDGMENTS

The author wishes to thank Con Hogan, Deborah Gaffney and Juli Crowley who collated much of the data and Patrick Casey, Brian Byrne, Joanna O’Brien (Arup) and Bronwen Coyle (MBSL) who provided some useful suggestions. The views expressed in this paper are the author’s own.

REFERENCES

[1] Brandl, H. (2004), *The Civil and Geotechnical Engineer in Society: Ethical and Philosophical Thoughts, Challenges and Recommendations*, The Deep Foundations Institute, Hawthorne.

[2] Chapman, T.J.P. (2008), ‘The relevance of developer costs in geotechnical risk management’, *Foundations: Proceedings of the Second BGA International Conference on Foundations*, ICOF2008.

[3] Clayton, C.I. (2011), ‘Managing Geotechnical Risk – 10 years on’, *Proceedings of Geotechnical Risk Management: adding value to construction projects*, Southern Wales Regional Group of the Geological Society.

[4] Mott MacDonald and Soil Mechanics Limited (1993), *Project report 60: Study of the efficiency of site investigations practices*, Transport Research Laboratory, UK.

[5] IEI (2003), ‘Project cost and estimation and control’, an IEI submission to the Minister for the Environment and Local Government.

[6] HM Treasury (2003) *The Green Book – appraisal and evaluation in Central Government*, TSO, http://greenbook.treasury.gov.uk/

[7] HM Treasury (2003), *Supplementary Green Book Guidance – Optimism Bias*, www.hm-treasury.gov.uk

[8] Rowe, P. W. (1972), ‘The relevance of soil fabric to site investigation practice’, *Géotechnique*, Vol. 22, Issue 2, p195 –300.

[9] Bea, R. (2006), ‘Reliability and human factors in geotechnical engineering’, *Journal of Geotechnical and Geoenvironmental Engineering*, ASCE, May 2006, pp. 631-643.

[10] Sowers, G.F. (1993), ‘Human factors in civil and geotechnical engineering failures’, *Journal of Geotechnical and Geoenvironmental Engineering*, ASCE, February 1993, p238 – 256.

[11] Abdulahad, S., Jergeas, G., and Ruwanpura, J. (2010), ‘A review of 41 legal cases involving geotechnical practice in Canada’, *Canadian Geotechnical Journal*, Vol 47, p1047 – 1059.

[12] BRE (2002), *Optimising ground investigation*, Digest 472.

[13] Department of Finance (2011) *Value for Money and Policy Review of the Construction Procurement Reform Initiative*, downloaded from http://constructionprocurement.gov.ie/ on 29 February 2012.

[14] IS EN 1997-1 (2005), *Eurocode 7 - Geotechnical design – Part 1 General rules*, NASI

[15] IS EN 1997-2 (2007), *Eurocode 7 - Geotechnical Design – Part 2: Ground Investigation and Testing*, NASI

[16] Quigley, P. (2011), ‘Talking point’, Ground Engineering, September 2011, p7.

Assessment of over-bridges on the Sallins – Tullow railway line

Dermot O'Dwyer[1], Niall Kelleher[1]
[1]Department of Civil, Structural and Environmental Engineering, Museum Building, Trinity College Dublin, Ireland
email: dwodwyer@tcd.ie, kellehn@tcd.ie

ABSTRACT: This paper describes a series of over-bridges that were constructed as part of the railway that ran from Sallins to Tullow via Baltinglass. The bridges were constructed in the early 1880's and have a number of interesting features. The most interesting of these bridges are a series of single-span bridges each comprising a series of parallel cast iron girders. The parapets comprise cast iron panels that are bolted together and connected to the edge girders. The bridge decks comprise a series of tied brick jack arches that span between the lower flanges of the parallel girders. This deck arrangement was widely used in the UK but Irish examples are less common. Although the Sallins to Tullow line was closed in 1959 these bridges still carry road traffic over the original railway alignment. The paper describes the difficulties associated with analysing these structures and identifying appropriate means of assessing their load capacity. Assessing these bridges is complicated by the brittle failure mode of cast iron and the difficulty of inspecting the wrought iron transverse ties. The paper presents the results of a literature review of material dealing with iron structures from the second half of the nineteenth century. The information gleaned from this study suggests an appropriate range of material property values. The structural analysis of these bridges must consider the main girders, parapet walls and tied-arch decking, and take into account how these structures will continue to perform into the future. The paper describes some recent work that Wicklow County Council has undertaken to strengthen one of these bridges by bonding glass fibre reinforced plastic (GFRP) strips to the underside of the cast iron girders.

KEY WORDS: bridge, assessment, jack arch, over-bridge, cast iron, wrought iron

1 INTRODUCTION SALLINS TO TULLOW RAILWAY

Robert Workington won the contract to construct the GS&WR branch railway line from Sallins to Baltinglass and began construction in March 1883. He was subsequently awarded the contract for the Baltinglass to Tullow section. The line was open to Baltinglass by 1885 and to Tullow by 1886 [1].

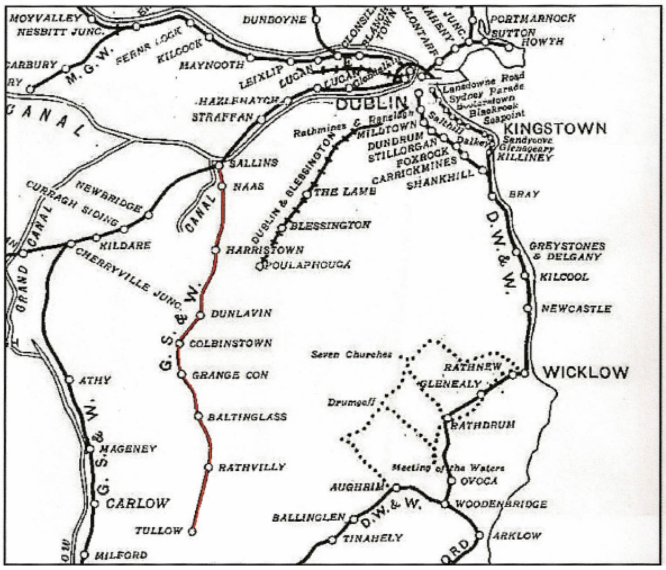

Figure 1. 1906 Viceregal Commission Rail Map.

In total the branch line was 34½ miles long and had a total of 55 bridges. The line carried traffic until 1959 when it was closed.

By the 1880's the initial railway mania had subsided and most of the Irish railway lines that remain in service today had been constructed. Railways had revolutionised transport within Ireland and they were still relatively new. The subsequent contraction of the extended railway network, due to the development of motorised road vehicles, was not on the horizon. The railway companies were privately owned and they made a profit, at least once the infrastructure had been put in place. Of course infrastructural development, then as now, was seen as a method of developing industry. Thus railway lines to the western seaboard were planned and constructed with a view to encouraging the Irish fisheries. In a similar manner, rural lines were seen as providing the means to export agricultural produce [2]. In the end, just like the canals, many of these rural lines imported as much produce as they exported.

From a structural engineering perspective the 1880's are interesting. The science of structural engineering had been developed by this time and a large number of engineers had received a technical education at university. At a professional level, the Institution of Civil Engineers of Ireland, and the Institution of Civil Engineers in London were firmly established although not all practicing engineers were members.

The materials available at that time included structural masonry, wrought iron, cast iron, timber and steel. Steel had been available since the 1850's but initially it had not been as reliable as wrought iron. The construction of the Forth Rail Bridge in 1890 is often taken as the date when steel effectively replaced wrought iron as the material of choice for metal bridges.

Figure 2. Railway viaduct crossing the Liffey.

2 BRIDGES ON THE SALLINS – TULLOW RAILWAY

A bridge on a railway line is described as an under-bridge if it supports the railway track and an over-bridge if it spans the railway. This paper is concerned with the over-bridges because these bridges are still carrying road traffic. However, one under-bridge on the line does deserve a brief mention. This is the fine five span skew masonry viaduct that carried the railway line over the river Liffey. This bridge is shown in Figure 2.

The over-bridges can be organized into three categories that reflect their construction materials, namely; masonry, wrought iron and cast iron. The masonry bridges are arches and, as one would expect of masonry arches constructed in the late nineteenth century, they are in very good condition. Figure 3 shows one such bridge at Knockbarn. Not all the masonry bridges had stone arch barrels, some had brick barrels with ashlar facing.

Figure 3. Masonry arch over-bridge.

A small number of the over-bridges were constructed using wrought iron. Two notable surviving examples are the bridge on the Friary road in Naas, shown in Figure 4, and the bridge

Figure 4. Wrought iron bridge with transverse trough deck at Friary Street Naas.

in Baltinglass, which is shown in Figure 5. These are traditional wrought iron girders with wrought iron trough decks. One interesting difference in these bridges is the direction in which the decks span. The bridge in Naas, shown in Figure 4, comprises two main girders with the trough deck running at right angles to the main girders and transferring load to them.

Figure 5. Wrought iron over-bridge in Baltinglass with side girders that act as parapets.

In contrast, in Baltinglass the decking, shown in Figure 6, runs parallel with the side girders and transfers the loads directly to the supports. This is sensible given that the bridge's span is less than its width.

Wrought iron has many desirable structural properties. Its strength is close to that of mild steel and it is less prone to corrosion. However, many early wrought iron bridges were of riveted construction with intricate structural details that were difficult to inspect and paint and as a result many suffered from corrosion.

By 1879 rolled wrought iron I beams of up to 14” depth were widely available.

Figure 6. Trough deck in Baltinglass.

2.1 Cast iron jack arch bridges

The third type of bridge, and the main subject of this paper, are cast iron girder bridges with brick jack arch decks. Cast iron jack arch bridges are common in the UK but few such bridges are in use in Ireland. These bridges are constructed of parallel cast iron girders. The deck comprises shallow brick vaulting with the horizontal force from the vaulting being taken by wrought iron tie rods [3].

Figure 7 shows the underside of the over-bridge in Sallins, which was the first bridge on the Sallins–Tullow line. The bridge is accessible from the appropriately named Oldbridge housing estate in Sallins.

Cast iron is rarely used nowadays as a structural engineering material despite the fact that cast iron can be cast into intricate shapes and despite its resistance to corrosion. Cast iron is strong in compression and has significant tensile strength too. However, cast iron loaded in tension fails in a brittle manner and its ultimate tensile strength is governed by the presence of inclusions. These are very undesirable properties in a structural engineering material.

Figure 7. Underside of the over-bridge in Sallins showing the cast iron girders, brick deck arches and wrought iron tie-rods.

Figure 8 shows a side elevation of another cast iron bridge at Kennycourt in County Kildare. Each parapet comprises seven cast iron panels that are bolted together. A top cast balustrade rail further ties the panels together. The parapet does not carry the longitudinal loads caused by the traffic but does resist lateral loading.

Figure 8. Cast iron parapet.

All the cast iron bridges span the original railway track thus they all have broadly similar spans and have similar details. However, Figure 9 shows a skewed variant of the general arrangement and Figure 10 shows a photograph of the cast iron bridge in Grange Con taken from the road it carries. The situation of the bridge is such that it is difficult to view the structure and it could easily escape notice as a cast iron bridge.

These cast iron bridges were manufactured by Courtney, Stephens and Bailey in Dublin. Some of the parapet panels are dated 1883, which agrees with the dates of the original construction.

Figure 9. Skewed bridge at Ballynure.

The details that indicate that the girders used in these bridges were cast include the vertical “stiffeners” and the fillets between the web and flanges of the girders. Close inspection shows sharply defined details that indicate that they were cast rather than rolled or welded. The foundry name and the fine details on the parapet panels also point to the members having been cast.

Figure 10. Cast iron bridge with stone parapets in Grange Con.

3 ASSESSMENT OF CAST IRON BRIDGES

Cast iron is resistant to corrosion. The bridges on the Sallins – Tullow line bear this out and the main girders are apparently free from corrosion. These bridges have been in service for almost one hundred and forty years and they appear, in most cases, to be functioning adequately. Therefore, given their performance to date and the lack of obvious deterioration they would appear to promise many more years of useful life.

Although deterioration of the main girders due to corrosion, which would be a primary concern with a steel or wrought iron bridge, is not a significant concern there are other potential failure mechanisms that deserve consideration. Cast iron is a brittle material. When loaded in tension it fails suddenly without warning and the failure load is governed by the presence of internal irregularities present since the time of casting. For this reason the use of cast iron girders had largely died out by the end of the nineteenth century. When assessing existing cast iron girders the procedure is to adopt an allowable stress approach using allowable stresses that incorporate a large material factor of safety [3].

Table 1 gives the compressive and tensile strengths of good quality cast iron from various foundries [3]. This table was first published in 1879, a few years before the cast iron girders on the Sallins to Tullow line were cast. The table shows that strengths varied from foundry to foundry. Bates [3] suggests 6 tons/ sq. in. (92.7 N/mm^2) as a conservative estimate of the true tensile capacity. However, he recommends that cast iron girders from before 1900 should be assessed using an allowable stress approach with a factor of safety of 5, so that the allowable bending stress in tension is limited to 1.2 tons/ sq. in. (18.5 N/mm^2).

The cast iron used on the Sallins – Tullow line was cast in the Courtney Stephens Foundry in Dublin. In the absence of other information the allowable tensile stresses suggested by Bates are probably appropriate for these bridges but there is no certainty that this is the most appropriate value. Unfortunately it is almost impossible to calculate the true collapse load for a cast iron girder with certainty. Previous studies on the performance of similar structures were undertaken by Chetto et al. in the 1940's [4] and by Daly and Ragget [5], and Swailes [6], in the 1990's.

Table 1. Cast Iron Strengths, (Bates 1984)

Ultimate Strengths of Cast Iron 1879

Description of Iron		Compressive Strength	Tensile Strength
		tons/sq inch	
Lowmoor Iron	No 1	25.2	5.7
Lowmoor Iron	No 2	41.2	6.9
Clyde Iron	No 1	39.6	7.2
Clyde Iron	No 2	45.5	7.9
Clyde Iron	No 3	46.8	10.5
Blenavon Iron	No 1	35.9	6.2
Blenavon Iron	No 2	30.6	6.3
Calder Iron	No 1	33.9	6.1
Coltness Iron	No 3	45.4	6.8
Brymbo Iron	No 1	33.8	6.4
Brymbo Iron	No 3	34.3	6.9
Bowling Iron	No 2	33.0	6.0
Ystalyfera Iron	No 2 (anthracite)	42.7	6.5
Ynis-cedwyn Iron	No 1	35.1	6.2
Ynis-cedwyn Iron	No 2	33.6	5.9
Average		34.24	6.77

Cast iron jack arch girders are vulnerable to corrosion in one regard. The decking on these bridges is supported by brick vaulting that spans between the lower flanges of the cast iron girders. These brick vaults apply horizontal lateral forces to the girders but, in the case of the internal girders, the horizontal forces from the adjacent vaults balance. However, the edge girders experience an unbalanced lateral force which is resisted by tie bars that link the girders in the transverse direction. These tie bars are formed from wrought iron and hence are vulnerable to corrosion. In addition, the connection details between the tie rods and the girders are inaccessible and cannot be inspected. Figure 11 shows the end of a tie rod with clear evidence of corrosion.

Figure 11. Corrosion of the tie rods.

4 REHABILITATION OF CAST IRON GIRDER BRIDGES

There are many potential methods of repairing or strengthening bridges. Cast iron bridges jack iron bridges may need strengthening to carry increased loading, or to provide an additional margin of safety. In addition, the problems associated with corrosion of the tie rods may need to be addressed. Figure 12 shows the underside of one of the cast iron over-bridges in Dulavin Co. Wicklow. GFRP strips have been bonded to the underside of the cast iron girders to increase their capacity to carry imposed loading. The figure also shows that some additional lateral ties have been added to the structure to counteract corrosion of the original wrought iron tie rods.

Figure 12. Strengthening using GFRP plates.

These additional ties restrict the lateral movement of the outside girders. However, they do not tie all the girders in the transverse direction.

In addition to strengthening of the main girders, it is important to maintain the road surface to prevent water flowing through the bridge deck. It is also important to establish the integrity of the cast iron parapets and repair them as necessary.

5 PROPOSED MATERIAL TESTING

Table 1 listed the strength of good quality cast iron from different UK foundries. It is reasonable to make an initial assumption that cast iron from the Courtney Stephen's foundry has similar properties. However, given the variation in cast iron strengths highlighted in Table 1 and the underlying risk of brittle fracture it would be useful to try to establish the strength of the cast iron used in the Sallins – Tullow bridges.

The difficulty in assessing the strength of cast iron is that there is no suitable non-destructive test to establish its tensile strength. Indeed, given the brittle nature of failure even the results of destructive tests need to be treated with care, because size effects can be very important. All but one of the cast iron bridges on this line carry road traffic and obtaining material from these bridges is not a viable option. However, the cast iron parapet of one of these bridges, which is located on a sharp corner, was hit by a vehicle and a section from the damaged parapet has been located.

The intention is to cut samples from this piece and perform a series of tensile tests, the results from these tests should be available for the conference. These tests will not give a definitive strength for the cast iron nor will they facilitate a reduction in the factor of safety: at best they will confirm that the cast iron used in these bridges is broadly similar to that used in other cast iron bridges of the time.

In addition to undertaking a series of material tests a finite element model of the strengthened cast iron bridge in Dunlavin will be developed. The object of developing the model is to explore how the strengthened bridge is resisting the lateral loads applied to the girders by the jack arches. This model will be capable of modeling the variation in structural behavior in the event of the loss of the tie rods due to corrosion.

6 CONCLUSIONS

The primary purpose of the paper is to highlight the fact that there are a number of cast iron girder jack arch bridges from the 1880's still carrying road traffic in Ireland. Although this form of bridge is common in the UK, Irish examples are rare.

The paper comprises a brief summary of the cast iron bridges on this line and contains photographs of many of them. These bridges carry local roads over the original rail alignment. Their condition is good but in some of the bridges the tie bars, which resist the lateral forces applied by the jack arches, are showing signs of corrosion.

Assessing the load capacity of these bridges is made more difficult by the brittle failure mode of cast iron girders. A sample piece of cast iron from one of these bridges has been located and will be tested. The results of these tests will add additional information on the strength of these bridges.

The bridge in Dunlavin, which has been strengthened with GFRP plates, will be modelled with a view to understanding the behaviour of the altered structure.

ACKNOWLEDGMENTS

The authors would like to acknowledge the cooperation of both Wicklow and Kildare County Councils.

REFERENCES

[1] T. Pigot (1893), 'Presidential Address', Transactions of the Institution of Civil Engineers of Ireland, Vol. , 1893

[2] J. O'Meara (2002), 'Tullow Branch', *Journal of the Irish Railway Records Society*, Vol. 148, June, 257-281.

[3] W. Bates (1984), *Historical Structural Steelwork Handbook: Properties of UK and European Cast Iron, Wrought Iron and Steel Sections including Design, Load and Stress Data since the Mid 19th Century*, British Constructional Steelwork Association.

[4] S.C. Chettoe, N. Davey and G.R. Mitchell (1944), The Strength of Cast Iron Grider Bridges, *Journal of the Institution of Civil Engineers*, Vol. 22, Issue 8, 1st October 1944, 243-307.

[5] A.F. Daly and S.J. Raggett (1991), *Load Test on a Jack Arch Bridge with Cast Iron Girders*, Transport and Road Research Laboratory. Bridges Division, Volume 310.

[6] T. Swailes (1996), 19th century cast-iron beams: their design, manufacture and reliability, *Proceedings of the Institution of Civil Engineers, Civil Engineering*, February, 1996, 25-35

Fatigue assessment of railway bridges using WIM data

Andreas Ottosson[1], Alan O'Connor[2]
[1]Department of Bridges, Rambøll Danmark A/S, Hannemanns Allé 53, DK-2300 Copenhagen, Denmark
[2]Department of Civil Structures and Environmental Engineering, Trinity College Dublin, Dublin 2, Ireland
email: aao@ramboll.dk, oconnoaj@tcd.ie

ABSTRACT: Bridge owners/managers face the common problem to reduce spending while attempting to operate and manage an increasingly ageing bridge stock. Increased understanding of the influence on fatigue assessment using realistic load models can reduce maintenance cost through avoidance of unnecessary repair/rehabilitation. This paper demonstrates the variation in calculated fatigue damage caused by railway traffic mixes defined by the Eurocode in comparison to those derived from weigh in motion (WIM) data. The fatigue assessment is carried out on continuous bridges with two spans and according to the cumulative damage method defined in Eurocode. As expected the calculations demonstrate that the Eurocode traffic mixes generate the greatest fatigue damage per tonne in an overwhelming majority of the bridge configurations considered. However, configurations were identified where the Eurocode gave non-conservative results compared to the WIM data.

KEY WORDS: Weigh in motion; train load; steel bridges.

1 INTRODUCTION

Taking fatigue into account for in the design of new bridges or assessment of existing bridges goes without saying these days. Even though fatigue became known as a technical problem in the middle of the 19th century it was not until about 100 years later that significant improvement of our knowledge about fatigue was made [1]. As a consequence there are many bridges today reaching the end of their design life which have not been designed with fatigue taken into account.

This paper demonstrates the variation in calculated cumulative fatigue damage caused by railway traffic mixes defined by the Eurocode [2] in comparison to those derived from weigh in motion (WIM) data. The assessment of cumulative fatigue damage is carried out according to the cumulative damage method defined in the Eurocode [3].

The bridges used to investigate the fatigue damage are continuous bridges over two spans of equal lengths, with overall lengths ranging from 20 m to 120 m. Section properties have been optimized in sections throughout the bridges at the ultimate limit state without any consideration to fatigue limit state. The calculations in ultimate limit state were done using the Eurocode Load Model 71 [2] with corresponding dynamic enhancement factors.

2 TRAFFIC LOAD

2.1 *Weigh in motion*

The weigh in motion (WIM) data was collected during 2010 by Danish railway operators and contains information on ~6500 freight trains corresponding to an annual traffic volume of 8.9 million tonnes.

The data provides information on the individual wagons of each train, in terms of their length, weight, number of axles, axle distance and axle load. This information was supplemented by certain assumptions such as axle distance within bogies (set to 1.8 m), the number of bogies and their position (determined based on the information given on respective wagons). With determined axle position for all wagons, a load model was assembled for each train. Table 1 shows the statistics from the assembled train models. For the bridge where the trains were registered, the maximum allowed load was set to 225 kN/axle and 64 kN/m.

2.2 *Eurocode*

The Eurocode include two different methods for calculating fatigue assessment, the λ-coefficient method and the cumulative damage method. The λ-coefficient method is a simplified method where a reference train model is used and combined with various correction factors to compensate for different conditions.

The cumulative damage method accounts for each stress range that the structure is subjected to with a given load history. As the load history, the Eurocode [2] defines twelve train configurations consisting of passenger trains, freight trains and underground trains. The trains and their annual quantities are combined in three traffic mixes to choose from depending on whether the structure carries mixed trains, predominantly heavy freight traffic (25 t axles) or lightweight passenger traffic [2]. Since the WIM data used consist solely of freight trains, the lighter traffic mix was not included in this analysis.

The standard traffic mix comprises eight of the twelve train configurations with a maximum axle load of 225 kN and an annual traffic of 24,455 trains corresponding to a traffic volume of 24.95 million tonnes. The heavy traffic mix comprises only four train configurations but with a maximum axle load of 250 kN. It has an annual traffic of 18,615 trains corresponding to a traffic volume of 24.78 million tonnes.

The annual traffic volumes differ with approximately a factor of three between the Eurocode traffic mixes and the WIM data. In order to satisfactory compare them between themselves and their results from the calculations, it was decided to evaluate effects per million tonnes of traffic volume.

Statistics for standard traffic mix and heavy traffic mix are shown in Table 2 and Table 3 respectively. Compared to the WIM data, the train configurations in the Eurocode have shorter and fewer wagons per train resulting in an average train length of half the average WIM train. With heavier average axle load, the Eurocode trains consist of heavier wagons and with greater line loads for both the wagons and the entire trains. The distribution of axle load corresponding to per million tonnes of respective traffic mix is illustrated in Figure 1 to Figure 3. The figures illustrates that the WIM data contains a large mix of heavy and light axles while the Eurocode trains are composed of only a few axle loads.

3 CONSIDERED BRIDGES

The cumulative fatigue damage has been calculated for eight fictitious bridge configurations assumed to carry one line of track. These representative structures are all modeled as continuous bridges with two spans of equal length, with span length ranging from 10 m to 60 m.

Table 1. WIM data statistics.

	Average	Standard deviation
Wagons per train	24.5	23.8 %
Wagon length [m]	23.1	28.7 %
Train length [m]	565.2	17.9 %
Axle load [kN]	132.5	43.9 %
Wagon load [kN]	562.4	49.1 %
Train load [kN]	13782.1	27.3 %
Wagon line load [kN/m]	25.3	53.4 %
Train line load [kN/m]	24.7	25.8 %

Table 2. Eurocode standard traffic mix statistics.

	Average	Standard deviation
Wagons per train	15.3	29.9 %
Wagon length [m]	17.9	30.4 %
Train length [m]	274.2	19.1 %
Axle load [kN]	177.3	31.9 %
Wagon load [kN]	666.8	55.0 %
Train load [kN]	10201.2	49.2 %
Wagon line load [kN/m]	39.2	57.1 %
Train line load [kN/m]	38.0	49.4 %

Table 3. Eurocode heavy traffic mix statistics.

	Average	Standard deviation
Wagons per train	17.8	28.1 %
Wagon length [m]	13.8	28.9 %
Train length [m]	245.6	22.5 %
Axle load [kN]	223.6	20.6 %
Wagon load [kN]	748.4	50.2 %
Train load [kN]	13310.4	24.6 %
Wagon line load [kN/m]	51.9	34.2 %
Train line load [kN/m]	55.0	19.2 %

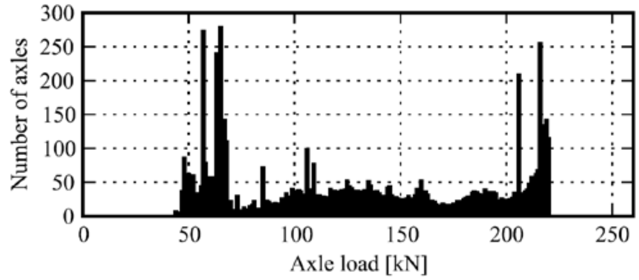

Figure 1. Axle load distribution, WIM data.

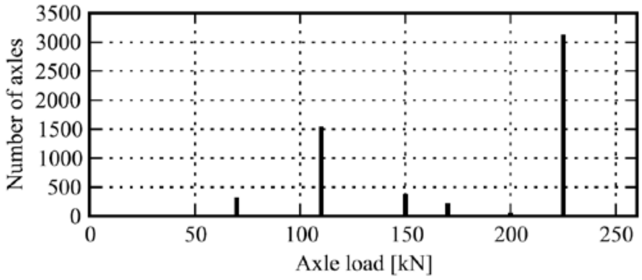

Figure 2. Axle load distribution, Eurocode standard traffic mix.

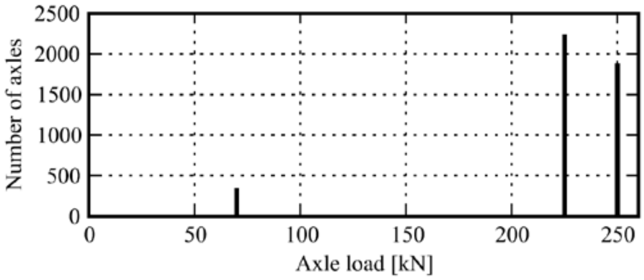

Figure 3. Axle load distribution, Eurocode heavy traffic mix.

The bridges are analyzed in six sections located at midspan ($0.5L_{span}$), midsupport ($1.0L_{span}$) and evenly distributed between the two ($0.6L_{span}$, $0.7\ L_{span}$, $0.8\ L_{span}$, and $0.9\ L_{span}$).

Influence lines for bending moment are defined by ordinates specified at 0.5 m intervals for each considered sections. Common characteristics for the influence lines for sections $0.5L_{span}$ to $0.8L_{span}$ are one span consisting of entirely negative values while the other consist of only positive values. The influence lines are illustrated in Figure 4 for a selection of the sections.

The determinant length is used to calculate dynamic enhancement factors and is therefore defined for each section. The span length was use as determinant length for section 0.5L to 0.8L and for section 0.9L and 1.0L the overall length of the bridge was used.

The largest bending moment was calculated using the influence lines with the Eurocode Load Model 71 [2] at the most unfavorable position. A dynamic enhancement factor, see Equation 1, was added to the bending moment based on standard maintenance in the Eurocode [2]:

$$\Phi_3 = \frac{2.16}{\sqrt{L_\Phi} - 0.2} + 0.73 \tag{1}$$

$$\textit{with} \qquad 1.0 \le \Phi_3 \le 2.0$$

where L_Φ is the determinant length.

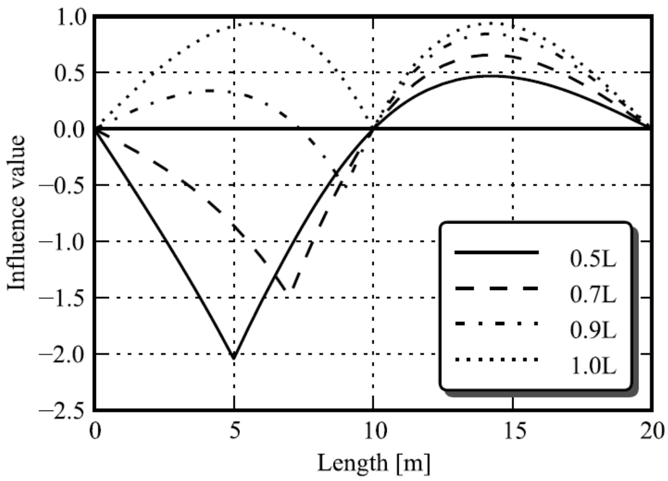

Figure 4. Influence lines example.

3.1 Section properties

The bridges are only subjected to bending moment in one direction and because just the largest stress in the sections are of interest when calculating fatigue, the section modulus is the only section property needed for the stress calculations. Therefore no geometric information regarding the cross sections was necessary for this study.

Based on the largest absolute value of bending moment, the section modulus for each cross section was calculated to correspond to a maximum design stress of 50 MPa. The bridges are then optimized in each section for the ultimate limit state and still with no account taken to the fatigue limit state.

To determine the fatigue damage, a reference value of the fatigue strength must be selected and based on the Eurocode Load Model 71 generated stress ranges, detail class 90 [3] was chosen for all section in all bridge lengths.

4 CALCULATIONS OF CUMULATIVE FATIGUE DAMAGE

The fatigue assessment is based on damage accumulation and is carried out according to the cumulative damage method defined in the Eurocode [3]. The train load models were moved over the bridges with a step length of 0.5 m. A shorter step length would provide more precise results but previous calculations by the author have shown sufficient accurate result using step lengths of 0.5 m.

Each axle load positioned on the bridges, combined with the influence line for respective section, generated a bending moment and the principle of superposition was employed to determine the total bending moment for each step. When an axle was positioned between two influence ordinates, linear interpolation was employed.

Corresponding stresses for each step were calculated using the section modulus for the considered section and then multiplied with a dynamic enhancement factor for real train [2], shown in Equation 2:

$$1+\frac{1}{2}\left(\varphi'+\frac{1}{2}\varphi''\right) \tag{2}$$

where φ' depend on maximum permitted vehicle speed and φ'' depend on determinant length. A stress history was defined when then entire train load model had been stepped over the bridge. The stress histories were then subjected to cycle counting using a rainflow cycle counting algorithm. The counted stress ranges are composed in a stress range spectrum.

The fatigue strength curves are represented by S-N curves, also known as Wöhler curves [3]. They represent the relationship between the stress range and the number of stress cycles to fatigue failure. Before the fatigue damage was calculated, safety factors were employed for both the calculated stress range $\Delta\sigma_{load}$ and the fatigue strength $\Delta\sigma_{strength}$ (detail class 90), see Equation 3 and Equation 4:

$$\Delta\sigma_{load}\cdot\gamma_{Ff} \tag{3}$$

$$\frac{\Delta\sigma_{strength}}{\gamma_{Mf}} \tag{4}$$

where the partial safety factor for fatigue strength, γ_{Mf}, was set to 1.35 and the partial safety factor for fatigue loading, γ_{Ff}, to 1.00.

Empoying Miner's summation, a linear cumulative damage calculation based on the Palmgren-Miner rule [1], the total fatigue damage can be determined for all the stress ranges in the stress range spectrum. The damage calculation is shown in Equation 5 and the structure is considered to have reached failure when the damage sum reaches and/or exceeds 1.0. N_i is the number of cycles to fatigue failure according to the S-N curves for each stress range.

$$D=\sum_{i}^{n}\frac{1}{N_i} \tag{5}$$

5 RESULTS

The cumulative fatigue damage was calculated in six sections, evenly distributed between midspan and midsupport, for each bridge with various span length and the results are presented as the average fatigue damage per million tonne.

Figure 5 and Figure 6 illustrate the variation of cumulative fatigue damage along two of the bridges with span lengths of 15 m and 50 m respectively. The results have been mirrored to the second span for visualization purposes.

The results exhibit particularly good resemblance between the calculated fatigue damages for spans lengths greater than 20 m. Both traffic mixes from the Eurocode generate a larger damage than the WIM data, as illustrated in Figure 6.

The most critical section for cumulative fatigue damage for the shorter bridge is clearly located at section $0.8L_{span}$ while the longer bridge show about the same level of damage in both section $0.7\ L_{span}$ and section $0.8\ L_{span}$. The position of the most critical section is expected as due to the influence line shape, the section is subjected to a smaller bending moment at the ultimate limit state and as a consequence its section modulus is 30 % to 45 % smaller, depending on span length, compared to the section at midspan ($0.5L_{span}$).

The largest generated fatigue damage per tonne for sections $0.5L_{span}$ to $0.8L_{span}$, visualized in Figure 7 to Figure 10, was found in the bridge with the shortest span (10 m). This was expected given that for shorter spans, each bogie will have a bigger influence on the generated stress cycles.

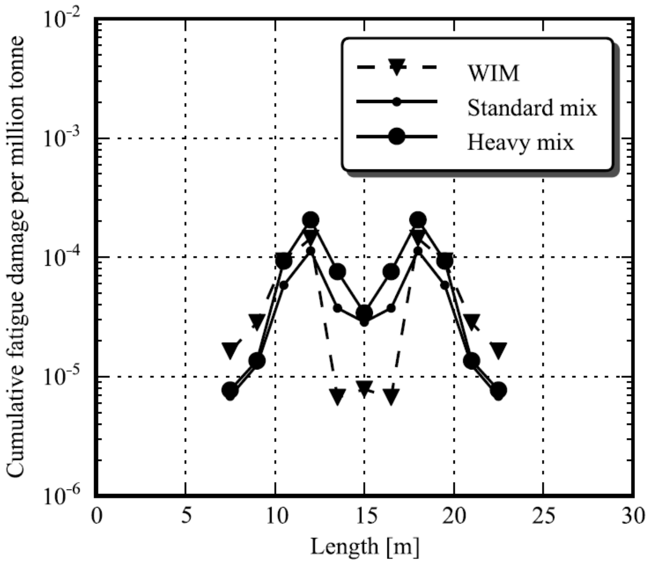

Figure 5. Damage in sections on bridge with 15 m spans.

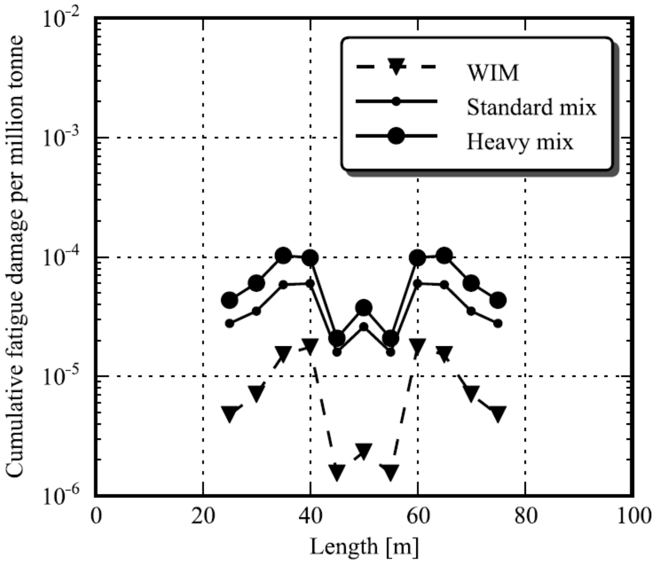

Figure 6. Damage in section on bridge with 50 m spans.

When analyzing the variation in fatigue damage per section, with increased span length, a clear change of direction can be seen for the curves. For the Eurocode traffic mixes this change most often appear at span lengths of 15 m while for the WIM data it is always located at span lengths of 20 m. Considering section $0.5L_{span}$ and $0.6L_{span}$, illustrated in Figure 7 and Figure 8, it is demonstrated that where these changes in direction take place is also where the least fatigue damage of all the span lengths are generated. This could be explained by the average length of the wagons corresponding to the span lengths, resulting in the wagons bogies cancelling each other's contribution to the bending moment out.

The bridge with span length of 15 m is especially interesting since the fatigue damage generated by the WIM data is larger than the damage generated by the Eurocode traffic mixes. The difference which is the largest at midspan attenuates as the midsupport is approached, as visualize in Figure 5.

For the section at midsupport, the Eurocode traffic mixes generate about the same fatigue damage for all span lengths with the exception of a small peak for span length of 15 m. The shape of the influence lines combined with a wagon length close to span length will lead to larger amplitude of the generated stress cycles due to possible loading and unloading. Longer spans will have less unloading since there will always be contributing loads on the bridge.

The WIM data generates less damage compared to the two traffic mixes from the Eurocode, with increased span length. This could be explained by a decreased average axle load on the bridge due to the large variation in axle load within the WIM data.

6 SUMMARY AND CONCLUSIONS

The cumulative fatigue damage has been calculated in several sections between midspan and midsupport on continuous bridges with two spans. The properties for each section was determined and optimized at the ultimate limit state. The calculated cumulative fatigue damage was divided with the total weight from the train passed to get the damage per million tonne. This was done due to the large difference in annual load between the WIM data and the Eurocode traffic mixes.

The calculations showed that section $0.8L_{span}$ and/or $0.7L_{span}$, depending on span length, are the most susceptible to fatigue damage. These sections are subjected to a smaller section force in ultimate limit state and consequently they have reduced capacities compared to other sections.

The calculations demonstrate that the traffic mixes provided by the Eurocode result in fatigue damages per tonne which exceed the damage generated by the WIM data in a majority of the bridge configurations considered. A span length was however found where the fatigue damage generated by the WIM data exceeded the damage caused by both the Eurocode traffic mixes in several sections.

This critical span length is shown to correspond to the average wagon length for the Eurocode traffic mixes, making a wagon's two bogies cancel each other's contribution to the sectional force out. This is seen for the WIM data as well but for longer span length due to its longer average wagon length.

The use of train models based on WIM data illustrates a much larger spread in axle loads compared to the train models supplied by the Eurocode, making various combinations of heavy and light wagons possible. The combination of heavy and light wagons and their position relative each other will have an important impact on fatigue damage for the shorter span lengths. Contrary to the WIM data, a large portion of the train models used in the Eurocode traffic mixes, are comprised of an engine followed by a various number of identical wagons. The lack of variation in wagon lengths within the train models is believed to be the cause of the non conservative results, shown in this paper, compared to the WIM data.

Even though the results are interesting one must remember that the damage used in the comparison was per tonne, meaning the total cumulative fatigue damage was larger for the Eurocode traffic mixes.

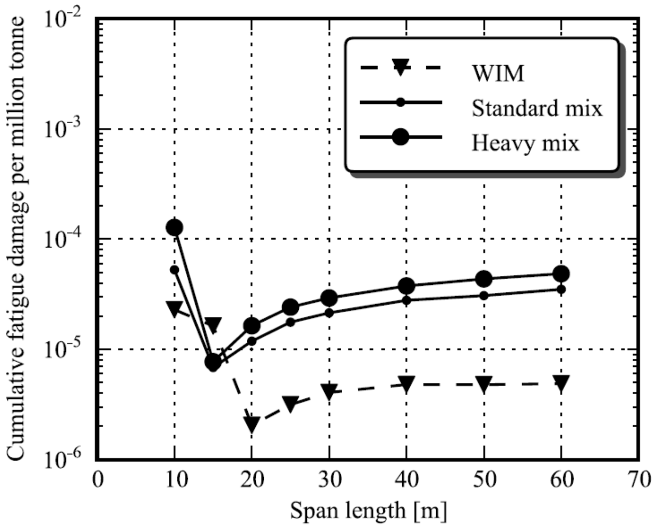

Figure 7. Damage in section $0.5L_{span}$ (midspan).

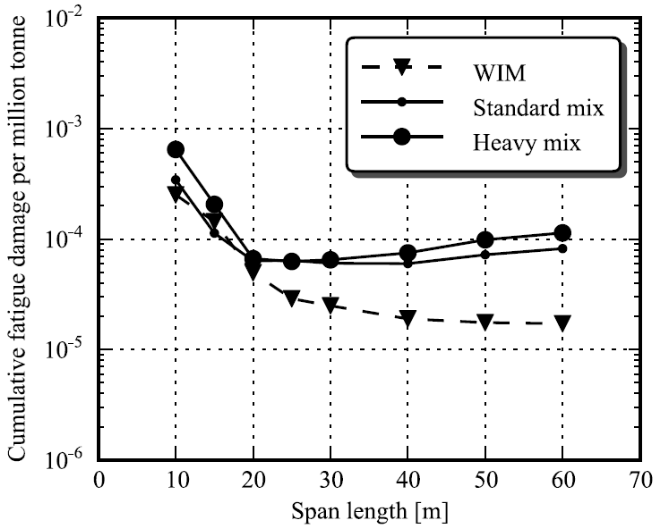

Figure 8. Damage in section $0.8L_{span}$.

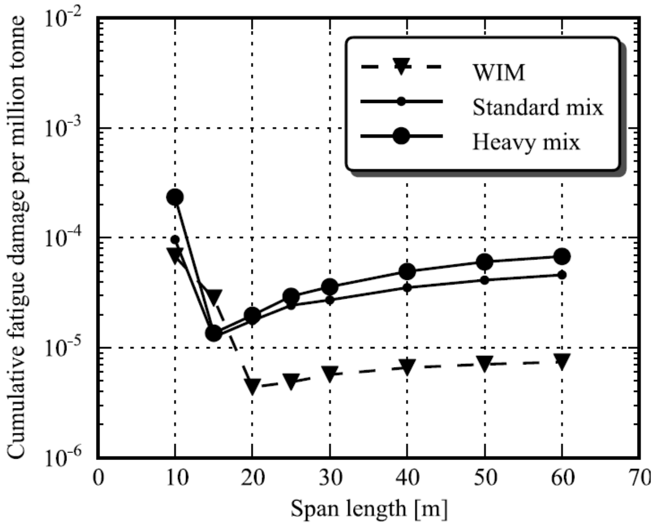

Figure 9. Damage in section $0.6L_{span}$.

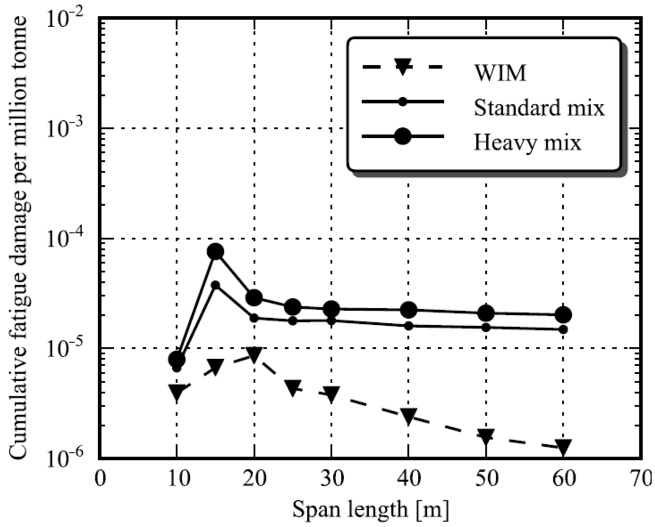

Figure 10. Damage in section $0.9L_{span}$.

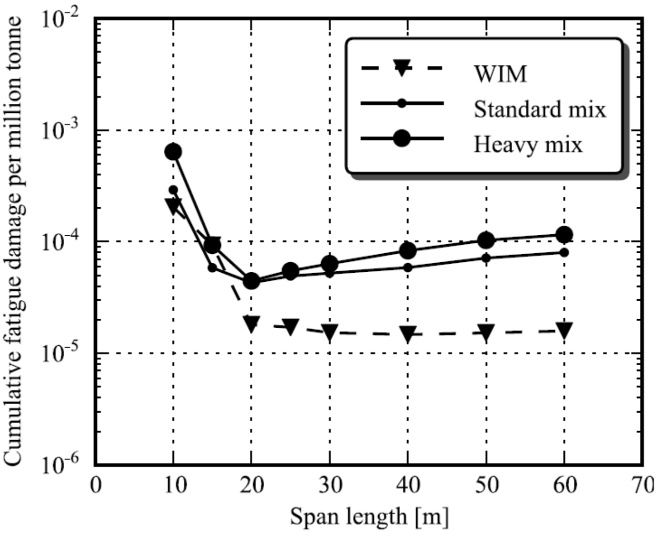

Figure 11. Damage in section $0.7L_{span}$.

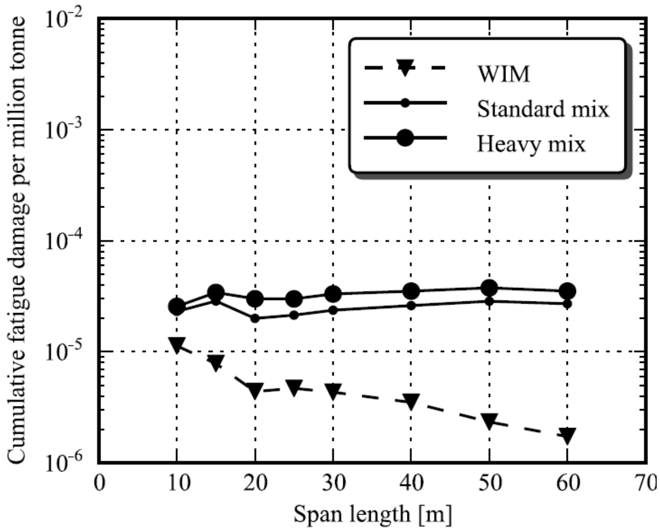

Figure 12. Damage in section $1.0L_{span}$ (midsupport).

ACKNOWLEDGMENTS

The TEAM project is a Marie Curie Initial Training Network and is funded by the European Commission 7th Framework Program (PITN-GA-2009-23648).

REFERENCES

[1] Schijve, J. (2003), 'Fatigue of structures and materials in the 20th century and the state of the art', *International Journal of Fatigue*, Elsevier Science Ltd, 25, 679-702.

[2] European Committee for Standardization (CEN), *Eurocode 1: Actions on structures – Part 2: Traffic loads on bridges*, CEN, Brussels, Belgium, EN 1991-2:2003 E, 2003.

[3] European Committee for Standardization (CEN), *Eurocode 3: Design of steel structures – Part 1-9: Fatigue*, CEN, Brussels, Belgium, EN 1993-1-9:2005: E, 2005.

[4] European Committee for Standardization (CEN), *Eurocode 3 – Design of steel structures – Part 2: Steel bridges*, CEN, Brussels, Belgium, EN 1993-2:2006: E, 2006.

[5] Hunter, J.D. (2007), 'Matplotlib: A 2D Graphics Environment', *Computing in Science & Engineering*, Vol. 9, No. 3, 90-95.

Enhancing railway safety, Level Crossings Programme 1999-2010

Conor McGuinness[1], Mark Kilcullen[2]
[1]Iarnród Éireann, Track and Signals HQ, Inchicore Works, Inchicore, Dublin, Ireland
[2]Roughan & O'Donovan Consulting Engineers, Arena House, Arena Road, Sandyford, Co. Dublin, Ireland
email: conor.mcguinness@irishrail.ie, mk@rod.ie

ABSTRACT: In 1999, an Iarnród Éireann Project team was set up to implement the Level Crossings Programme with a mandate to enhance safety through the upgrading or removal of level crossings across the Republic of Ireland. As part of the programme 742 level crossings were removed from the railway network. The programme remains active at the time of going to print. The programme was subject to somewhat unique constraints which affected designs including limited power to compulsorily purchase land, cost benchmarking against CCTV control at level crossings for road and bridge schemes and road design standards which were developed for one purpose but applied across the board. This paper sets out the principal constraints which have driven the development of Works proposals at level crossings over the past eleven years with particular emphasis on bridge schemes and describes the evolution of bridge engineering solutions at level crossings.

KEY WORDS: railway, level crossing, railway safety programme, closed circuit television (CCTV), precast portal, overbridge, underbridge, possession, ground granulated blastfurnace slag (GGBS), road design.

1 INTRODUCTION

In November 1997 a passenger train derailed at Knockroghery, Co. Roscommon. Following this accident, in 1998, the Dept of Public Enterprise, as it was then known, commissioned a strategic review of all aspects of the safety of Iarnród Éireann's railway network to be carried out by consultants International Risk Management Services Ltd. As a result of the recommendations contained in this report[1], the Government requested Iarnrod Eireann (IE) to prepare a Railway Safety Programme.

As part of the safety review it was determined that level crossings pose one of the largest single risks to the operational railway. It was later confirmed that the greatest tangible gain could be achieved by direct investment in the removal of level crossings[2]. Separately, consultants A. D. Little had been commissioned to carry out a safety review of level crossings and their recommendations were incorporated into the Railway Safety programme.

In 1999, an IE project team was set up to implement the recommendations of the A. D. Little report. The Level Crossings Programme was established with a mandate to enhance safety through the upgrading or removal of level crossings across the Country. The programme remains active at the time of going to print.

The purpose of this paper is to set out the principal constraints which have driven the development of Works proposals at level crossings over the past eleven years with particular emphasis on bridge schemes and to describe the evolution of bridge engineering solutions at level crossings to date.

2 LEVEL CROSSINGS PROGRAMME

The Iarnród Éireann railway network is largely rural in nature and consequently is characterised by large numbers of level crossings. This is typical of rural networks and it is evident that the costs associated with level crossings on such networks are a significant and ongoing burden to be carried by the railway operators [3]. Figure 1 shows a map of the IE railway network. At the outset of the Railway Safety Programme there were in excess of 2500 level crossings across all lines, over 2000 on used lines and 1600 on passenger lines. There are in total approximately 2033km of passenger line on the network. This corresponds to an average of one level crossing per km of passenger line.

Railway Level Crossings are typically either 'user worked' or 'railway worked'. In Ireland 80% of all level crossings are user worked, operated by landowners or the public. Most were put in place when the railway was constructed. Many of those on public roads have been specifically identified in the railway act instituting the line. Others are the subject of agreements between the railway and specific users.

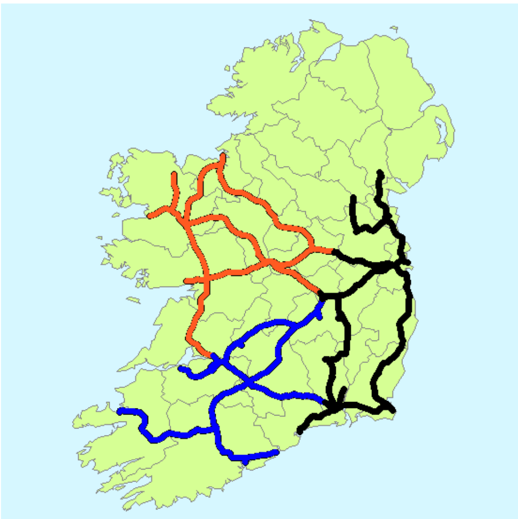

Figure 1. IE railway network.

At the outset of the Level Crossings Programme, the investment on individual railway level crossings was prioritised on the basis of the individual risk to a regular user, and each crossing was given a priority score or risk ranking generated from a Risk model. In recent years a new risk model has been used to prioritise the investment and this model includes risks to the travelling public and others as well as the individual user. This has enabled an absolute ranking of crossings in relation to both Collective Risk and Individual Risk.

It was decided that the expenditure of funds on physical Works to close many level crossings was warranted. Such Works included roads and bridges with associated earthworks, drainage and ancillary works. Consulting Engineers were engaged to design and manage the works. Initially, 3No. Consultants were commissioned, each to work on a regional basis. This was subsequently reduced to one.

In terms of construction works, panels of contractors were prequalified to tender for all works on this project. Initially 3No. panels were prequalified , one for each region. This was subsequently reduced to a single panel of 8No. contractors working on a national basis.

As part of the programme 742 level crossings have been closed to date. This has been accomplished through 526 land purchases or swaps, the construction of 49 railway overbridges, 28 railway underbridges and the construction of 82 access roads. In addition CCTV control was applied to in excess of 100 level crossings. Approximately €150m has been spent to date on level crossings closure.

3 LEVEL CROSSING SCHEME CONSTRAINTS

A number of constraints exist to the advancement of level crossing schemes which are very particular in nature and have a strong bearing on the approach to each scheme. They are set out below.

3.1 Compulsory Purchase Powers

In relation to level crossings the power to purchase land compulsorily has not been available to Iarnród Éireann until the enactment of the Railway Safety Act [4] in 2005. Prior to this land acquisition was typically carried out by agreement. Given that there may be multiple users and multiple affected landowners at a level crossing, the attainment of agreement becomes critical to the success of a proposed scheme. The location of dividing property lines can consequently have a significant effect on the geometry and configuration of a proposed scheme.

Given that local authorities have responsibility for road safety in the vicinity and on the approaches to level crossings and given the significant effect the presence of a level crossing can have on a locale, it is not difficult for local authorities to justify sufficient interest in individual level crossings to warrant the Local Authority pursuing planning permission for schemes through Part VIII of the Planning Regulations 2001 [5] and where necessary compulsory purchase under the Forestry Act [6]. The programme has benefited on a number of occasions with the adoption of this partnering approach with local authorities.

In recent years Iarnród Éireann has been exploring its compulsory purchase powers. The project remains however, heavily constrained by land acquisition issues. This has dictated that a significant bank of schemes be in development on an ongoing basis so as to ensure targeted expenditure was achieved.

3.2 Interface with the Live Railway

This is an obvious constraint which again has a significant effect on scheme development. The issues around this relate to the impact on railway traffic, the risk of construction activities to the live railway, the risk of bridgeworks to the railway embankment, the demand on railway resources in support of construction activities and the long term impact of the Works on the railway. Over the past ten years the constraints have become increasingly difficult with the introduction of more onerous safety legislation and more rigorous safety procedures. In addition, the ongoing drive for enhancement of service to costumers has made the interface with the operational railway more constrained.

3.3 Cost Benchmarking

In the management of expenditure on the programme the cost of public road bridge schemes was inevitably benchmarked against the cost of implementation of CCTV control on level crossings. Although CCTV control reduces the risk rating of the crossing, CCTV infrastructure is expensive to install, needs ongoing maintenance and the level crossing furniture requires replacement on a 25 year cycle. Whole life cost modelling was used to demonstrate that capital expenditure of between €1.5m and €2.0m on bridge schemes (year 2002) was justifiable at level crossings where CCTV control is an acceptable alternative.

This whole life comparison provided an upper threshold of scheme value which incentivised the application of appropriate design standards to road schemes. Although specific level crossings warranted greater expenditure, the relatively limited upper cost threshold has been dictated by the availability of CCTV technology.

3.4 Road Design Standards

Since the initiation of the Level Crossings Programme road design standards have gone through significant change. Important developments which have affected scheme configurations are as follows:

- The implementation of the NRA DMRB [7];
- The increased use of the road safety audit process;
- The application of the formal risk assessment process in design;
- Ongoing revisions to NRA TD 9 [8] including the extension of the standard to address regional and local road design;
- The implementation of HA TD 40 [9] and the increased use of compact junction configurations on national roads;
- The aggressive application of the above standards in design and build road schemes across the country.

A unique aspect of level crossing schemes is that although they often involve the insertion of a new length of road within the existing road infrastructure the schemes are driven by and funded by the railway operator. Consequently the scheme objectives typically differ from those motivating road authorities to build roads.

From the first introduction of the DMRB local authorities required that it be applied to the design of regional and local road realignments and were cautious in accepting proposed relaxations and departures from standard. This approach from local authorities is not surprising due to the lack of familiarity with the new standards. In addition local authorities have typically sought the provision of enhancements within the schemes to cater for potential future development or the upgrade of roads.

Following the initial introduction of the NRA DMRB schemes were developed on small local roads which were often incongruous in their rural context and inherently uneconomical. With time it has become easier to convince local authorities that schemes with relatively constrained road alignments can be designed to be safe.

Critical to the successful application of more constrained alignments in grade separation at level crossings was the incorporation within the NRA DMRB of the requirements of HA TD 40 [9]. The compact junction configurations which have since been applied on single and dual carriage roads across the country incorporate horizontal radii at tight as 40m. With the provision of adequate visibility and appropriate traffic calming measures it has been possible to design safe schemes which fit well within the local road infrastructure and which have better fitted within the budget constraints on the scheme. Figure 2 shows the layout of a scheme which recently received planning permission in County Mayo.

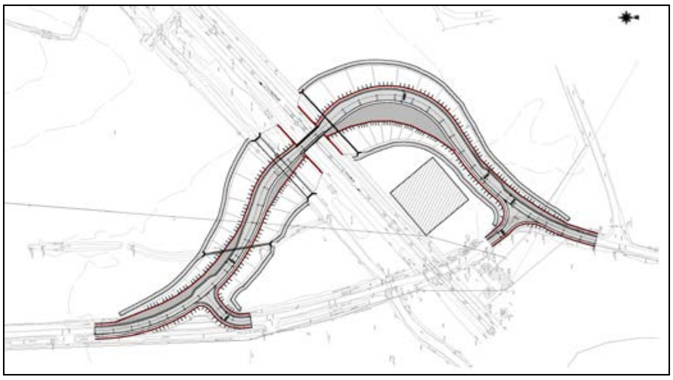

Figure 2. Sample public road scheme layout.

It is worth noting a number of items in relation to this scheme as follows:

- The pre-existing low standard narrow approaches to the level crossing;
- The presence of tight horizontal radii in the proposed design, with graduated reduction in radius on the approach to the railway overbridge;
- The presence of significant verge widening for forward sight visibility, again graduated downward along the approach to the bridge;
- The use of a nominal 4.0m carriageway width with laybys to force traffic speeds down;
- The positioning of safety barriers to enhance the 'corridor effect' without compromising visibility, consequently reducing traffic speeds;
- The single lane square bridge crossing configuration;
- The small footprint of the scheme;
- The square bridge crossing.

The growing acceptance of scheme designs driven by safety focused engineering, rather than the traditional broadstroke application of development and upgrade criteria, will be important to the advancement of future schemes on the programme, given that many of the easier crossings have now been dealt with and more challenging lie ahead.

4 BRIDGE ENGINEERING

At the outset of the programme, each of the three Consulting Engineers developed their own concepts for bridge configurations at level crossings. They worked largely independently with the IE project team steering developments in the direction of preferred design solutions.

The initial concepts were developed in an era before the implementation of integral bridge concepts in Ireland and consequently incorporated details which would not be contemplated today. Standardisation was envisaged with a view to reducing cost and facilitating rapid scheme development. The principal constraints on development of bridge designs related to the presence of the live railway. This manifest itself in a number of ways as follows:

- Works adjacent to or over the railway were required to be carried out under possession. Short possessions were typically available at night, circa 5hrs, longer possessions at weekends, 16 to 22hrs. Long weekends occasionally facilitated possessions of 30 hours. Possession activities included railway fencing, excavations, piling, use of cranes, heavy lifts, installation of temporary support, concrete pours and level crossing works. During the initial phases of the projects speed restrictions were available and facilitated some work between trains under lookout possession. In recent years the availability of speed restrictions and possession has been significantly restricted;
- Maximum use has been made of pre-casting from the outset of the scheme;
- Minimising the impact on the railway embankment was a significant constraint on option development;
- Due to the desire to keep road alignments low, the depth of deck construction was a key feature of design development;
- Work in concrete was preferred for deck and parapet construction due to relatively low maintenance characteristics of concrete.

4.1 Standard Overbridges

The concept developments were driven by plans for generic designs to be easily adapted to different skew and width configurations. The Roughan & O'Donovan generic design was as follows: Precast infill concrete deck comprising TY and TYE beams with reinforced concrete parapet, supported on strip bearings, buried joint, span 17m and skew range 0 to 15 , supported on reinforced concrete full height abutment. A typical cross section is shown in Figure 3 below.

It quickly became apparent that only a few schemes would be built in this form. This was due to the wide variety of span and skew configurations which emerged consequent on the constraints identified above. Longer span configurations became more typical dictating a move to beam and slab configurations. Through the following years the design of small to medium size overbridges followed typical practice in the industry with integral bridge principals being implemented across the board. A distinction was drawn between public road and private farm accommodation bridges where a sacrificial layer of concrete replaced the deck surfacing. Two sample deck cross sections are shown in Figure 4. Figure 5 shows a near completed bridge crossing a single track line and adjacent access road.

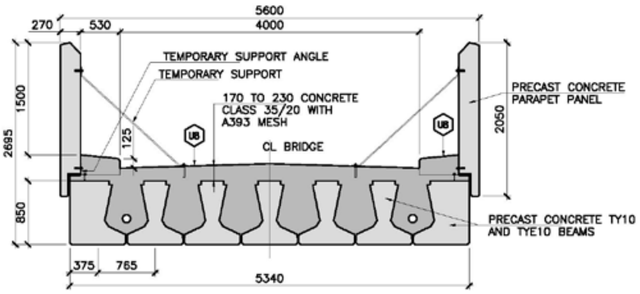

Figure 3. Typical deck cross section.

In recent years due principally to movements in accepted road design practice, the optimisation of bridge configuration has been revisited with renewed vigour. The project team examined the proprietary ABM precast portal format with a view to using a variant on this configuration in combination with reinforced earth over the railway. A couple of sample details of what became a relatively standard configuration are shown in Figures 6 and 7.

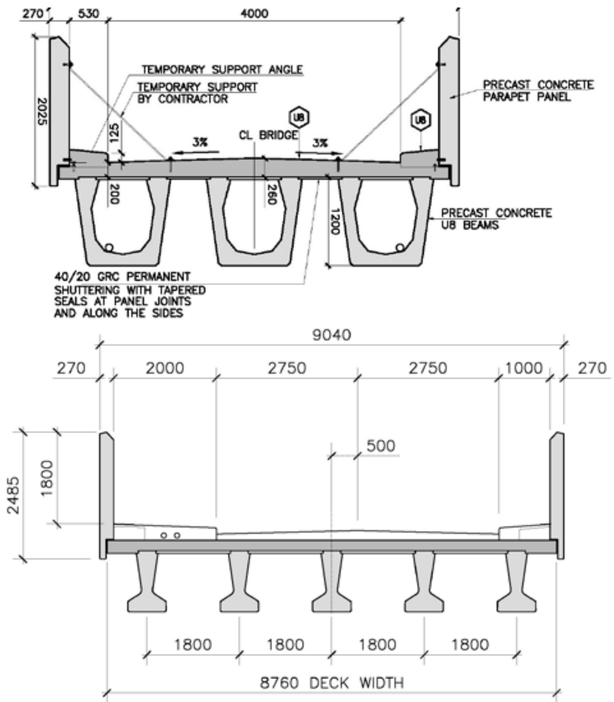

Figure 4. Sample deck cross sections, larger spans .

This concept was initially examined for use in a three unit configuration for private accommodation bridges. It proved appropriate for use on wider bridges and with skewed crossings with the incorporation of a redundant corner in the configuration. A skewed portal version of this system was

Figure 5. Public road overbridge .

also examined but the skew was limited to 10 degrees or the width of a single unit. This has been limited to date due to the difficulty in modelling and accommodating the cyclical effects associated with earth pressure effects as skews increase.

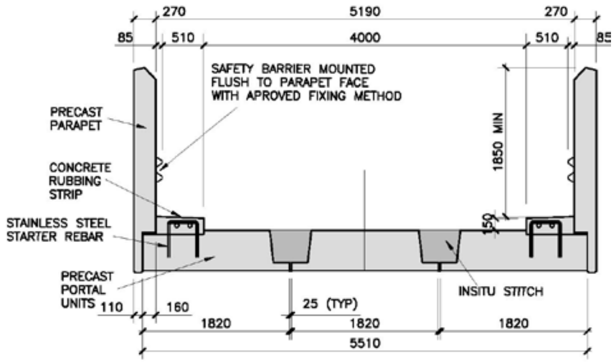

Figure 6. Generic portal cross section .

The design specification for the unit is set out below:

- The unit comprises a reinforced concrete modular buried system incorporating upper and lower elements connected with a ball and socket type knuckle joint. The system is self-stabilising in the temporary construction phase under its own weight;
- The ball socket joint detail is configured to promote rotation, to encourage soil-structure interaction and to optimise the efficiency in the section design;
- The Structure is designed in accordance with the National Roads Authority Design Manual for Roads and Bridges.
- Load Design Standard: National Annex to IS EN 1991 Pt2 2003: Live Loading: LM1, LM2, LM3(SV100) [10];
- Reinforcement crossing the interfaces between precast concrete and in-situ concrete is of stainless steel;
- The concrete specification requires cement replacement with ground granulated blastfurnace slag by 50% or more;
- The bridge system incorporates an insitu concrete section of slab which provides connection between individual portal units;
- The individual portal units incorporate an insitu roof stitch detail which provides full transverse connectivity;
- The underside of the portal base is typically set 1.0m below track level and a track clearance envelope of 5.3m

is typically accommodated. The knuckle joint provides flexibility in the structure height;
- Where piles are required an insitu pilecap is cast prior to placement of the portal units and the insitu connecting slab is configures to tie the portal units and the pilecap together.
-

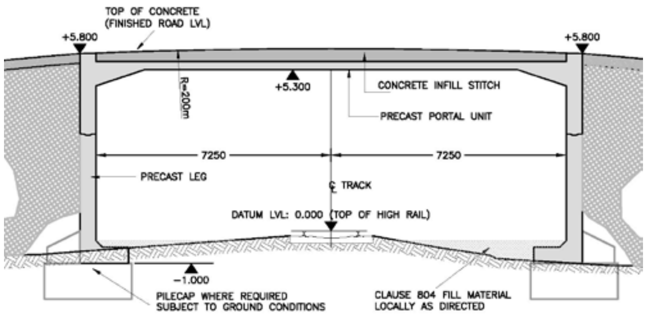

Figure 7. Generic bridge long section .

The system has proved to be very effective for the following reasons:

- It is specified as a contractor designed element allowing multiple precast manufacturers configure their investment in the system to suit their own design and workshop setup. To date the system has been supplied by three different manufacturers and others have shown an interest in getting involved. Significant financial savings have emerged from this development;
- The principal components of the bridge can be erected in one or two night time possessions with parapets being erected separately. The reinforced earth can be installed without impact on the railway;
- The standardisation of activities has provided significant safety benefits;
- Through the use of GGBS cement replacement in reinforced concrete, stainless steel reinforcement in vulnerable locations such as insitu stitches, and the current eurocode crack width limitation of 0.1mm the system is inherently durable. The most vulnerable element of the structure is the knuckle joint. This is a concession to the constraints associated with construction in the live railway environment.
- With the progress made in the acceptance of more constrained road alignment configurations, this system has proved versatile where skews can be kept reasonably low.

Figure 8 shows photographs of this system under construction and following completion.

Figure 8. Portal erection under possession and completed .

4.2 Underbridges

The clearance envelopes inside railway accommodation underpasses are typically small. These envelopes have normally been accommodated using precast concrete box sections or opticadre units placed in open excavation. Box units have been used on the programme for envelopes up to 3.3m square. The opticadre system has been used for spans of up to 9.0m and to clear openings of 4.5m high, see Figure 9.

The design of underbridges have typically incorporated a ballasted track configuration. Embedded rail is generally avoided due to the consequent incorporation of hard spots on an otherwise flexible formation. A minimum 300mm ballast provision was accommodated.

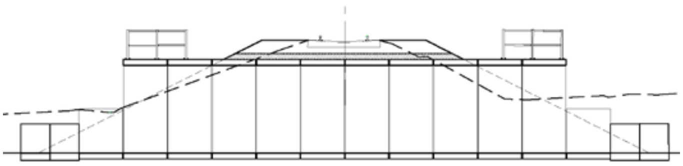

Figure 9. Sample longitudinal section through underpass.

Design loading was in generally accordance with the NRA DMRB [8] with heavy rail traffic accommodated.

Figure 10 shows an example of a typical box accommodation underpass under construction. The box units have typically been installed under the railway in possessions of 16 to 22 hours duration depending on the size of unit being installed.

Figure 10. Box Culvert Underpass under Construction.

Figures 11 and 12 show the installation of a larger 9.0m span unit. It was installed over a 32 hour possession on a long weekend. The logistical exercise in preparing and carrying out the erection of a bridge of this scale is significant.

Figure 10. Preparation of Formation for Opticadre Portal .

A number of larger more complex underbridge schemes have been examined as part of the programme. Open excavation was not practicable in these instances and consequently more intensive proprietary sliding bridge systems or continuous piled arrangements have been examined. These schemes have yet progressed to construction.

Figure 11 Opticadre underbridge assembly .

4.3 Unique Schemes

As part of the programme a selection of more elaborate schemes have been designed and constructed. A 30m Steel composite arched bridge was constructed over the N8 Lower Glanmire Road in Cork. A photograph of this scheme is shown Figure 12. Detailed information on this scheme is provided as part of a separate paper presented to this conference[11].

Figure 12 Glanmire Road Railway Bridge .

The detailed design of a public road bridge over the Dublin to Galway railway and the Royal canal has recently been completed to facilitate the closure of level crossing XG002 in Cabra. This is an arched truss, approximately 70m long and on a skew of 39 . A photomontage of this bridge is shown in Figure 13 below.

5 CONCLUSION

Iarnród Éireann has been engaged in a dedicated process of safety enhancement at road rail interfaces over the past 11 years. Significant advancement has been made in reducing risk on the railway network. Many of the straight forward

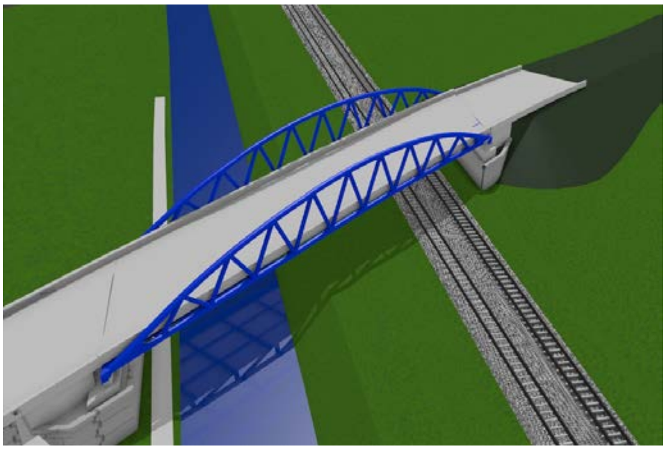

Figure 13 Reillys Bridge, Cabra .

level crossings have been closed. Most of the level crossings on the Dublin Cork line have now been removed. More challenging crossings remain to be dealt with in the upcoming stages of the programme. The programme has had unique constraints and challenges. The bridge solutions implemented have, over time, become increasingly efficient, durable, economical and safe and will continue to evolve with the programme. With the ongoing advances in road and bridge engineering this programme offers a valuable cost effective tool for the enhancement of safety on the railway.

ACKNOWLEDGMENTS

The authors wish to acknowledge the contributions of Aidan Bermingham, James Kenny and Pat Egan, members of the level crossing team who assisted with the assembly of data for this paper.

REFERENCES

[1] A Review of Railway Safety in Ireland, International Risk Management Services (UK) Ltd, October 1998;

[2] Value for Money Review of Irish Rail's Second Railway Safety Programme, Issue 1, Department of Transport, December 2008;

[3] John Tilly, Level Crossings on Rural Railways: Can the Railway Continue to Subsidise Rural Settlements, The Institution of Railway Signal Engineers, UK, 08 Dec 2000;

[4] Railway Safety Act, 2005, Pt 14: Provisions Relating to Corás Iompair Éireann, Paragraph 127, Compulsory acquisition of land.

[5] SI 600: Local Government (Planning and Development) Regulations 2001, Part VIII: Requirements in respect of Specified Development by, on Behalf of, or in Partnership with Local Authorities.

[6] The Forestry Act (1946), Part III. Compulsory Purchase of Land,

[7] The National Roads Authority, Design Manual for Roads and Bridges.

[8] National Roads Authority, Design Manual for Roads and Bridges: NRA TD 9: Road Link Design, 2012.

[9] HA TD 40: Layout of Compact Grade separated Junctions, Highways Agency, Design Manual for Roads and Bridges . (1994).

[10] IS EN 1991 Pt2, National Standards Authority of Ireland, 2003

[11] Conor Mc'Guinness, Aonghus O'Keeffe, Mark Kilcullen, The Design and Construction of Glanmire Bowstring Arch Bridge, BCRI, 2012.

Semi-active damping systems for railway bridges

Andreas Andersson[1,2], Raid Karoumi[2], Alan O'Connor[1]
[1]Roughan & O'Donovan Innovative Solutions (RODIS), Arena House, Arena Road, Sandyford, Dublin 18, Ireland
[2]Royal Institute of Technology (KTH), Brinellvägen 23, 100 44 Stockholm, Sweden
email: Andreas.Andersson@rod.ie, Raid.Karoumi@byv.kth.se, Alan.OConnor@rod.ie

ABSTRACT: In this paper, a semi-active control system for vibration mitigation of railway bridges is presented. The real time frequency response is estimated using a short-time Fourier transform, employing curve fitting to relevant peaks for increased accuracy. A control algorithm developed in MATLAB® is linked to a commercial FE-software, facilitating application on arbitrary structures. A numerical study of an existing tied arch railway bridge is presented. From earlier field measurements and numerical analysis, resonance of several hangers during train passage was observed. This was shown to significantly reduce the fatigue service life of the hangers and for the most critical section about 50% of the cumulative damage was related to free vibrations. A system of passive dampers was later installed and the increase in resulting damping was measured. Within the present study, the previous results are reanalysed and compared with a semi-active approach. The natural frequencies of the hangers vary as a result of the variation in axial force. A semi-active control system has the potential to improve the vibration response of the structure when compared to the installed passive system.

KEY WORDS: Bridge dynamics; railway bridge; semi-active damping; finite element method.

1 INTRODUCTION

There is a constant demand on the railway authorities to increase both the allowable axle loads and the allowable speed on existing railway lines. An increased utilization of bridges can sometimes be justified based on refined capacity assessments and field measurements.

In design of railway bridges, dynamic effects are most often accounted for by dynamic amplification factors (DAF) of the static response. This does not account for resonant behaviour and for bridges on high-speed lines separate dynamic calculations are required.

A refined dynamic assessment of a tied arch railway bridge is presented. The project was initiated since excessive vibrations of several hangers were detected. Based on field measurements and numerical simulations, the remaining fatigue service life of the hangers was estimated, as presented in [1],[7]. An existing stabilizing system was later replaced with passive dampers, mounted on the longer hangers, [5],[6].

In this paper, some of the previous field measurement have been reanalysed and employed in updating a simplified 2D finite element model of the bridge. The model is used for estimating the effect of increased damping measured by [5] after installation of the passive dampers. Further, a semi-active damping system is proposed and its potential performance is compared with the passive system, based on numerical simulations.

1.1 The Bridge

The bridge was built in 1959 and is designed as a single span tied arch railway bridge. A photo of the bridge is presented in Figure 1. The mid-support is a remnant from the previous bridge and is not utilized.

Figure 1. View of the Ljungan railway bridge.

The deck is designed as an unballasted steel grillage consisting of main beams, cross beams and stringers. Wooden sleepers are supported directly by the stringers. A cross-section of the deck is illustrated in Figure 2. The distance between the cross beams is 3.75 m, which is the same for the hangers. The hangers consists of solid steel rods with a diameter of 80 mm at the threaded section. The arch has a circular shape with a radius of 31.9 m and a height of 8.9 m, measured from the top of the main beam to the arch centre line.

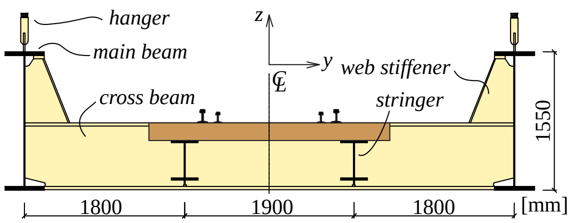

Figure 2. Cross-section of the grillage deck.

Due to excessive vibration of the hangers, a system of diagonal RHS-beams was installed in the 1980's as an attempt to stabilize the hangers. These beams can be seen in Figure 1.

2 FIELD MEASUREMENTS

2.1 Instrumentation

Field measurements were carried out in June 2003, comprising 16 strain gauges and 12 accelerometers, mounted on hangers 2 to 5. During the measurements, the stabilizing system of RHS-beams was removed. The position of the gauges and details of the hangers are presented in Figure 3. The total length L_h and distance L_a to the accelerometers are given by Table 1. At each position, three accelerometers are mounted together, measuring in *xyz*-directions. Also, four strain gauges are instrumented at the distance z_1 = 100 mm above the threaded section, spaced 90° apart along the perimeter of the hanger.

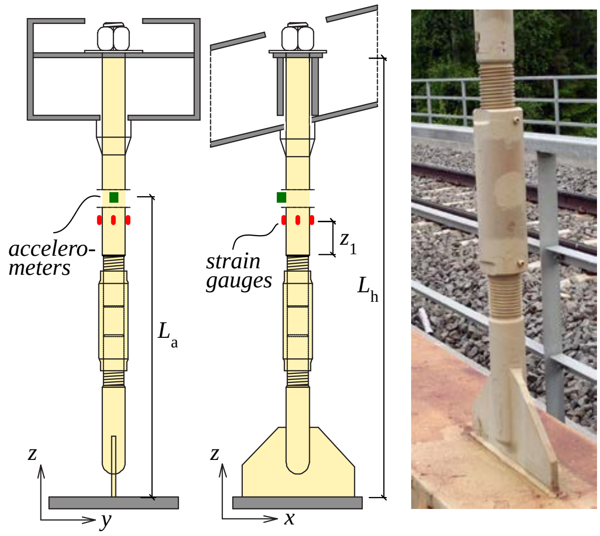

Figure 3. Detail of the hangers, a) section across the bridge, b) section along the bridge, c) photo of the turn buckle.

Table 1. Length of the hangers L_h (according to original drawings) and position of accelerometers L_a, rounded to 5 cm.

Hanger:	1	2	3	4	5	6
L_h (m):	1.30	3.54	5.20	6.30	6.95	7.15
L_a (m):	-	1.55	1.90	2.15	2.30	-

2.2 Natural frequencies and damping

The natural frequencies and damping ratios of the hangers were estimated based on free vibration tests. Each hanger was exited by a swift knock in each direction. Based on a Maximum Likelihood estimate of the free decay of motion, the results in Table 2 and Table 3 were obtained. The results show good agreement with similar measurements in [5].

Table 2. Estimated natural frequencies, based on free vibration measurements.

Hanger:	$f_{1,x}$ (Hz)	$f_{2,x}$ (Hz)	$f_{1,y}$ (Hz)	$f_{2,y}$ (Hz)
2	16.0	44.9	10.9	34.0
3	7.9	23.1	6.1	18.9
4	7.2	19.2	6.0	16.5
5	4.3	13.5	3.6	11.4

The average difference on estimated frequency was about 0.1%. The difference of individual damping ratio scatters significantly, but the average for all hangers is 0.2%, both from [5] and Table 3.

Table 3. Estimated damping ratios, based on free vibration measurements.

Hanger:	$\zeta_{1,x}$ (%)	$\zeta_{2,x}$ (%)	$\zeta_{1,y}$ (%)	$\zeta_{2,y}$ (%)
2	0.33	0.18	0.14	0.46
3	0.16	0.22	0.42	0.16
4	0.09	0.08	0.14	0.19
5	0.15	0.05	0.30	0.24

3 FINITE ELEMENT ANALYSIS

3.1 2D model

A 2D FE-model of the bridge is created using the commercial FE-software SOLVIA03. Half of the bridge is included, comprising one arch, one main beam, one stringer and all hangers on one side. All components are modelled using Euler-Bernoulli beam elements, except the cross beams that are modelled as vertical springs. The spring stiffness is calculated to produce the same vertical displacement as a simply supported beam subjected to two point loads. The model is illustrated in Figure 4. The detailed connections of the model are shown in Figure 5. All elements are modelled along their centre line. To obtain the correct length of the hangers, the connection with the main beam is extended using a rigid link, and is considered as fully clamped. The connection with the arch is however considered hinged. This is accomplished by releasing the rotational degree of freedom belonging to the end node of each hanger.

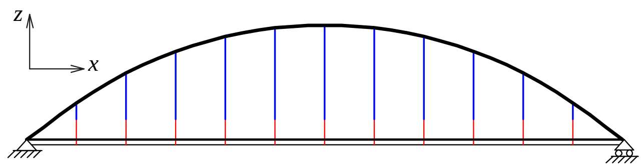

Figure 4. Elevation of the FE-model.

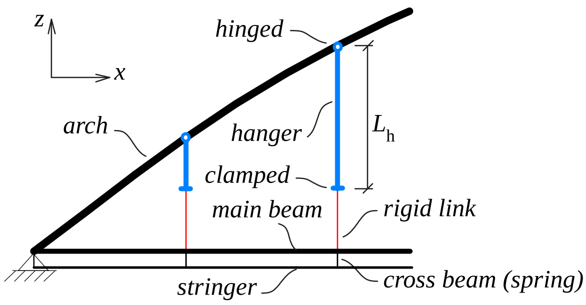

Figure 5. Details of the FE-model.

3.2 Natural frequencies

An Eigen-value analysis is performed to calculate the frequencies of the structure. The permanent load is applied prior to the Eigen-value analysis, to account for the axial stress in of the hangers. The results are presented in Table 4.

Table 4. Natural frequencies of the hangers, predicted by the 2D FE-model and a comparison with measured results.

	FEM		FEM / measured	
Hanger:	$f_{1,x}$ (Hz)	$f_{2,x}$ (Hz)	$f_{1,x}$ (-)	$f_{2,x}$ (-)
2	16.1	50.5	0.99	0.89
3	7.8	23.8	1.00	0.97
4	7.4	19.8	0.97	0.97
5	4.5	13.4	0.95	1.01
6	4.3	12.7	-	-

Initially, the frequencies for hanger 4 was f_{1x} = 5.4 Hz and f_{2x} = 16.3 Hz, in poor agreement with the measured data. The model was modified at this location, assuming the arch-to-hanger connection as fully clamped, with the result in Table 4.

For the sake of comparison, this assumption is used in further analysis. Since the hangers are relatively independent on each other, the corresponding hanger 8 is still assumed hinged. The two lowest global modes of the bridge are illustrated in Figure 6. The global modes generally excite all hangers, especially if the arch and the main beam are out of phase.

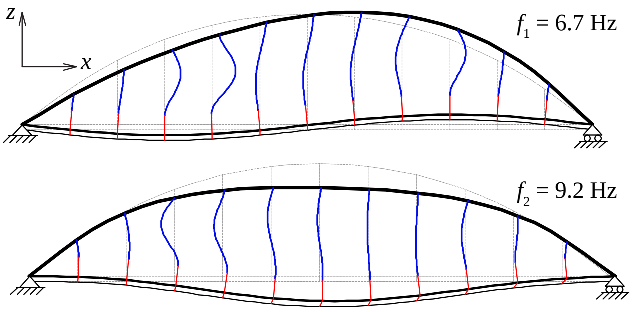

Figure 6. The two lowest global modes of vibration.

3.3 Dynamic analysis of passing trains

The 2D FE-model has been used for dynamic analysis of passing trains. The train is modelled as vertical point loads only, travelling along the stringer beam. Since the model only comprises half of the bridge, half of the axle load is applied. The pre-stress of the hangers due to permanent load is accounted for, as well as increased load during train passage. Hence the analysis is considered nonlinear. For this reason, a direct time integration scheme is employed instead of modal superposition. One drawback of the direct time integration is that constant modal damping can not be used. Instead, a frequency dependent material damping according to Equation (1) is used, often denoted as Rayleigh damping. It consists of two components, α for mass proportional damping and β for stiffness proportional damping, Equation (2). For the present case, a critical damping ratio ζ = 0.2% is used, fitted by the frequencies f_m = 4 Hz and f_n = 20 Hz.

$$\begin{Bmatrix}\alpha\\ \beta\end{Bmatrix} = \frac{2\zeta}{\omega_m + \omega_n}\begin{Bmatrix}\omega_m\omega_n\\ 1\end{Bmatrix} \tag{1}$$

$$\mathbf{c} = \alpha\mathbf{m} + \beta\mathbf{k} \tag{2}$$

The train set is composed of one locomotive and 19 wagons. Both the locomotive and the wagons consists of two bogies with two axels in each bogie. For the locomotive (Swedish Rc4), the axle distance is 2.7 m, the bogie distance 7.7 m, the total length 15.5 m and the load 195 kN/axle. Standardized freight train wagons are assumed according to load class D2. This corresponds to an axle distance 1.8 m, bogie distance 9.2 m, length 14.0 m and the load 225 kN/axle. The train speed is varied between 60 to 140 km/h in increments of 10 km/h. Time history data is extracted in positions corresponding to the field measurements.

3.4 Increased hanger damping

To attenuate the resonant behaviour and resulting bending stresses of the hangers, passive dampers were installed on hanger 3 to 9 on each side of the bridge. The installation of the dampers and additional measurements is reported in [6]. The dampers consists of cylindrical shells, each containing four pendulums partly surrounded by a silicone oil. The diameter of the dampers is 310 mm and the height 350 mm. Based on free vibration tests, the damping ratio was estimated for each hanger. In average, the damping in the longitudinal direction ranged between 1.8 – 6.4%, with an average of 3.6%. The 2D FE-model has been updated to account for the increased hanger damping. Since the resulting damping is available, an increased Rayleigh damping using ζ = 3.5% for all hangers is assumed. The additional mass of the dampers is neglected.

3.5 Influence of axial force

It may be noted that all the estimates presented above of natural frequencies and damping is based on free vibrations of the unloaded bridge. During train passage, increased tensile force in the hangers will result in increased frequency. For an Euler-Bernoulli beam, the relation between natural frequency f_n, flexural rigidity EI and axial force N follows Equation (3). For the bi-pinned case, $\mu_n = n\pi$. For the pinned-clamped case, $\mu_1 \approx 1.25\pi$ is an approximation for the first mode of vibration. Based on the 2D FE-model, the axial force in hanger 5 is estimated as 20 kN due to permanent load and additional 120 kN due to vertical train load type D2. This results in an increase in natural frequency from 4.5 Hz to about 7 Hz using Equation (3) [4].

$$f_n = \frac{\mu_n^2}{2\pi}\sqrt{\frac{EI}{mL^4} + \frac{N}{mL^2\mu_n^2}} \tag{3}$$

The existing passive damping system is tuned based on free vibrations and its properties during train passage are not readily known. Approximating this behaviour with an increased material damping may overestimate its damping characteristics outside of the tuned frequency range.

4 PASSIVE AND SEMI-ACTIVE CONTROL

In the field of external damping for dynamic mitigation, the tuned mass damper (TMD) is one of the most common systems. In its simplest form, it consists of a sprung mass tuned to the frequency of the structure it is mounted on. Regarding the structure as a single degree of freedom (SDOF) system, the combined response with the TMD can be regarded as a 2DOF system, as illustrated in Figure 7.

A passive TMD has fixed properties that can not be altered. It often has a narrow efficient bandwidth and may be highly inefficient outside that range, e.g. due to changed frequency of either the structure, the forced vibrations or the TMD itself. This may partially be overcome using a semi-active system, that has the ability to change in either stiffness or viscous damping due to a control input, usually voltage. Analyses of a semi-active tuned mass damper (SATMD) is performed based on a variable stiffness $k_d(\theta)$. The control input θ is assumed proportional to the stiffness k_d. Damping is introduced to the systems by dashpots c and c_d with constant values.

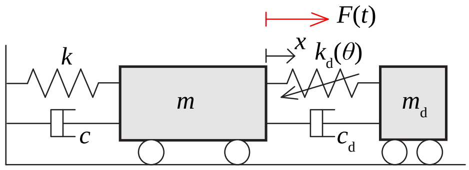

Figure 7. 2DOF model of a TMD/SATMD.

The success in minimizing the dynamic response of the main structure depends on the choice of objective function. In the present study, the stiffness is tuned to the frequency of highest energy.

4.1 Simple TMD model

The potential of dynamic mitigation of hanger 5 is studied for both a passive TMD and semi-active SATMD. Based on the natural frequencies and displacement according to Equation (4), the modal mass and stiffness is found according to Equation (5). A harmonic load according to Equation (6) is used. The steady state response can then be expressed according to Equation (7) [3].

$$\omega_{\mathrm{SDOF}} = \sqrt{\frac{k}{m}},\ \omega_{\mathrm{beam}} = \sqrt{\frac{EI}{m_{\mathrm{beam}} L^4}},\ \delta_{\mathrm{beam}} = \frac{FL^3}{48EI} \tag{4}$$

$$m = \frac{48 m_{\mathrm{beam}} L}{\pi^4},\ k = m\left(2\pi f_1\right)^2,\ c = 2\zeta\sqrt{k\cdot m} \tag{5}$$

$$F(t) = F_0 \sin\left(\omega t\right),\ F_0 = kx_{\mathrm{static}} \tag{6}$$

$$R_d = \frac{1}{\sqrt{\left[1-\left(\frac{\omega}{\omega_n}\right)^2\right]^2 + \left[2\zeta\left(\frac{\omega}{\omega_n}\right)\right]^2}} \approx \frac{1}{2\zeta},\ \zeta < 0.1 \tag{7}$$

For hanger 5 the modal mass is m = 135 kg. Further, using f_1 = 4.3 Hz and ζ = 0.15% results in k = 100 kN/m and c = 11 Ns/m. Due to the low damping, the dynamic amplification factor at resonance is about 300 times the static response. From field measurements, the magnitude of dynamic displacement was estimated as 5 mm, based on integrating the acceleration. The duration of the train passage was only 10 s, thus the time required to reach resonance is more than one minute. To obtain a dynamic displacement of 5 mm after 10 s, a harmonic load with F_0 = 4.5 N is required. At steady state, this corresponds to a displacement of about 15 mm.

The optimal damped mass m_d is estimated based on a uni-variable analysis of the steady state response. Results for different damping ratios are presented in Figure 8. In further analysis, m_d = 1 kg is used, resulting in k_d = 0.6 kN/m.

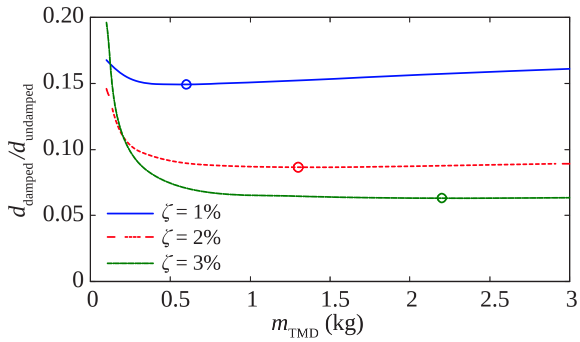

Figure 8. Influence of the TMD mass and damping ratio on the dynamic amplification of the displacement, circles denotes maximum vibration mitigation.

The steady state response is shown in Figure 9. Introducing the TMD attenuates the natural frequency of the structure but introduces two new frequencies, governed by the 2DOF system. For no additional damping, the new peaks are of similar magnitude to the case without the TMD. Due to the low existing damping of the present structure, even very low additional damping of the TMD attenuates the peaks significantly. However, the system is sensitive to mismatch in frequency and a TMD with 5% detuned frequency shows a significant disimprovement.

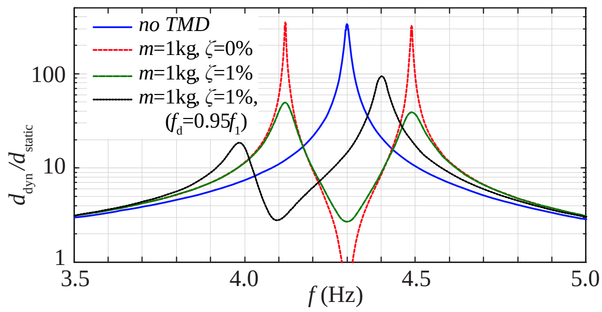

Figure 9. Steady state response for the passive TMD model.

4.2 Simple SATMD model

A simple semi-active control algorithm is developed where the frequency of the TMD is controlled by means of a variable stiffness $k_d(\theta)$. The algorithm is programmed in MATLAB® and uses the solver of the same FE-software as the bridge has been modelled in. The variable stiffness is modelled as a truss element with temperature dependent stiffness properties. Applying a stationary variable temperature load facilitates direct control of the stiffness in incremental dynamic analyses.

The value of the stiffness is determined based on estimates of the governing frequency of the system at the present time. This is accomplished by studying a short part of the signal with duration Δt prior to present time. The frequency content of the short time signal may be estimated using either a Short Time Fourier Transform (STFT) or Wavelet Transform (WT). In the current study, the STFT method is used. The time signal is multiplied with a window function before performing the Fast Fourier Transform available in MATLAB®. Since the frequency resolution is proportional to the time duration, poor estimates are obtained for small values of Δt. This may partially be improved either by zero-padding the signal or applying a curve-fit of the dominant frequency peak.

Recalling Equation (7), the shape of the steady state response is recognized as a 4th order polynomial. This has shown to be successful in estimating frequencies of known signals. Increasing Δt results in less rapid estimates of changing frequencies but is more successful in identifying close modes. The rate of finding changes in frequency can partially be improved by overlapping the time signal. This is accomplished by forwarding the analysis by an increment $t_{incr} < \Delta t$ and analysing the previous Δt of time.

The developed SATMD is tested on the same model as the passive TMD. The influence of changing the initial TMD frequency f_d and forced vibration frequency f_F in comparison with the natural frequency f_1 is studied according to Table 5.

Table 5. Studied configurations of frequencies.

Model:	f_1 (Hz)	f_d (Hz)	f_F (Hz)
a)	4.3	f_1	f_1
b)	4.3	f_1	$0.95f_1$
c)	4.3	$0.95f_1$	f_1
d)	4.3	$0.95f_1$	$0.95f_1$

Tuning the SATMD to the frequency of highest energy may cause it to be detuned if either of the resulting frequencies of the 2DOF system is higher than f_1. This may partially be overcome by choosing a suitable time increment. For the current study, using $\Delta t = t_{incr} = 4$ s was found to give reliable results. Further, all analyses are based on $m_d = 1$ kg and $\zeta_d = 1\%$. The forced vibration has a duration of 10 s.

A summary of peak responses from the different models are presented in Table 6. For the SDOF-model without TMD, a peak displacement of ~5 mm and acceleration of ~3.6 m/s^2 is obtained. Using a passive TMD reduces the responses by a factor ~10. This extreme attenuation is a result of the low existing damping of the structure. Similar results are obtained with the SATMD. Shifting the load frequency by 5% according to model b), the response of the passive TMD increases by a factor 3 while the SATMD remains relatively unchanged. It is noted that the passive TMD shows even higher response than the SDOF-model for the same load. Shifting the TMD frequency by 5% according to model c) results in an increase by a factor ~2 using the passive TMD and about 40% using the SATMD. A potential improvement of the SATMD may be possible by changing either the incremental time or the objective function. In model d), both the load and the TMD are detuned 5% compared to the structure, hence the TMD is perfectly tuned to the load instead of the structure. For this case, the SATMD is not working optimally, likely due to same reasons as for model c).

Table 6. Summary of peak responses of the primary mass from the 2DOF-model.

	Displacement (mm)			Acceleration (m/s^2)		
Model:	SDOF	TMD	SATMD	SDOF	TMD	SATMD
a)	4.98	0.53	0.53	3.64	0.39	0.39
b)	0.88	1.50	0.48	0.61	1.00	0.34
c)	4.98	1.13	0.75	3.64	0.84	0.55
d)	0.88	0.48	0.97	0.61	0.33	0.68

4.3 *TMD and SATMD on the 2D bridge model*

The SATMD algorithm is implemented on the 2D-model of the bridge previously presented in Figure 4. From the model without external damping, resonance of hanger 5 was found at 90 km/h for train load model D2. A comparison of the measured response and the simple 2D-model is presented in Figure 10, for the case of no external damping system. The displacement is obtained from time integration of the measured acceleration, introducing some uncertainties. During integration, a high-pass filter is applied and only the relative motion of the hanger is obtained. For comparison, the same filtering is performed on the displacements predicted by the FE-model. The FE-model generally shows larger response, likely caused by being closer to resonance and subjected to a passing train of equal load and axle distance. Further, no motion in the transverse direction is possible.

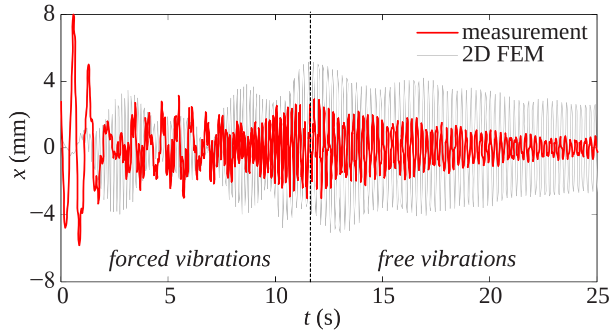

Figure 10. Displacement of hanger 5, comparison of measured response (time integrated from acceleration) and 2D FE-model without external damping.

The SATMD on the bridge model is detailed in Figure 11, positioned at the midpoint of hanger 5. The variable spring stiffness is modelled similar to the previously presented 2DOF model. The damped mass is lumped at two nodes, connected with a rigid link. Both masses are constrained in the vertical direction to follow the motion of the connecting node of the hanger. In further analysis, $m_d = 1$ kg and $\zeta = 3.5\%$ is used. The time increment $\Delta t = t_{incr} = 1$ s was found to give reliable results. The same model is also used for analysis of a passive TMD, by setting a constant damper stiffness. Both the TMD and the SATMD are initially tuned to the first mode of vibrations, $f_1 = 4.5$ Hz.

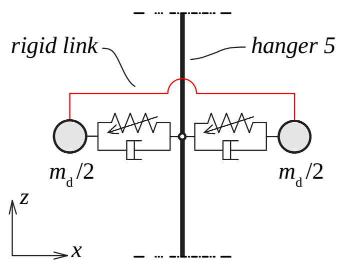

Figure 11. Detail of the SATMD on hanger 5.

Figure 12 presents the time history for displacement of hanger 5. The TMD is found efficient in attenuating the free vibrations, but show little reduction during forced vibrations. The SATMD on the other hand successfully attenuates both the forced and free vibrations.

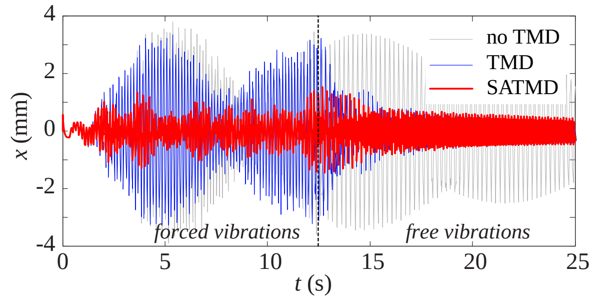

Figure 12. Displacements of hanger 5 predicted by the FE-model during train passage.

The difference of the TMD and the SATMD is further illustrated by studying the frequency content in Figure 13. The unloaded and loaded natural frequency is found at 4.5 Hz and 6.9 Hz respectively (4.3 Hz and 6.3 Hz from the measurements). Without external damping, both peaks show high energy content, as a result of the high magnitude in Figure 12. The passive TMD successfully attenuates the unloaded peak, but is out of range to affect the loaded peak. The SATMD on the other hand attenuates both peaks as result of the control algorithm.

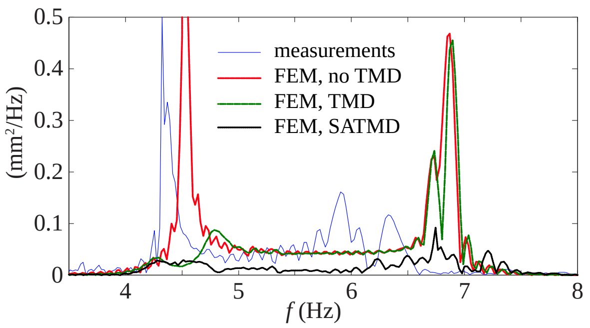

Figure 13. Frequency content from displacement of hanger 5 during train passage.

5 CONCLUSIONS

In this paper, the dynamic behaviour of a tied arch railway bridge has been analyzed. Based on field measurements, very low damping of the hangers was found, on average 0.2%. As comparison, a damping ratio of 0.5% is often used for design of steel bridges [2]. Resonant behaviour of several hangers was observed from field measurements of passing trains. Similar behaviour was obtained by means of a simple 2D FE-model.

The resonant behaviour has earlier been found to decrease the fatigue service life [1],[7] and a system of passive dampers was later installed [5],[6]. The natural frequencies of the hangers change as a result of increased axial force during train passage. Theoretical studies of a semi-active damping system to account for the frequency variation is presented and compared with a corresponding passive system. The results show that a passive damper is sensitive to small changes in frequency, causing inefficient vibration mitigation. Using a simple semi-active control incrementally tuned to the dominant frequency is generally shown to improve the vibration mitigation significantly.

6 FURTHER RESEARCH

Although the current semi-active algorithm was shown to attenuate the dynamic response significantly, several areas for improvement has been identified.

Separating closely spaced modes using the Short Time Fourier Transform method is often a trade off between frequency resolution and incremental response time. If instead wavelet transforms are employed, variable frequency resolutions can be obtained by scaling, potentially improving the accuracy in estimated frequency and facilitate a shorter response time.

In the current algorithm, the damper is tuned to the frequency of highest energy. The choice of another objective function may be called for, especially if the dynamic response is governed by several simultaneous frequencies.

In the present study, only the stiffness of the damper is modified. In many applications, the viscous properties are instead altered, e.g. by using magnetorheological dampers.

The results for the studied bridge are based on a simple 2D-model. From the field measurements, significant transverse vibration of the hangers was found [1],[7]. Due to different boundary conditions, different natural frequencies in each direction was estimated, Table 2. This may be accounted for using a 3D-model. Introducing semi-active dampers in two directions may call for a modification of the current algorithm.

The present study mainly focus on attenuating the dynamic displacement of the hangers. A factor of greater importance is however the mitigation of stresses, to improve the fatigue service life. Cumulative fatigue damage is highly non-proportional to the stress range and the choice of optimizing the damper for either forced or free vibration is not obvious.

Finally, verification of the developed routines by physical testing may be of interest, both experimentally and in-situ.

ACKNOWLEDGMENTS

The field measurements in 2003 were commissioned by the Swedish Transport Administration (former Banverket) and performed by KTH. Development of the semi-active routines and models were performed within the Long Life Bridges project, funded by the European Union 7th framework programme and coordinated by ROD. All funding and support mentioned above is greatly acknowledged.

REFERENCES

[1] Andersson, A., Malm, R. (2004). Measurement Evaluation and FEM Simulation of Bridge Dynamics. *MSc Thesis, KTH Royal Institute of Technology, Sweden*.

[2] CEN (2003). Eurocode 1: Actions on structures – Part 2: Traffic loads on bridges. *EN 1991-2:2003*.

[3] Chopra, A.K. (2001). Dynamics of Structures, Theory and Application of Earthquake Engineering. *Prentice-Hall Inc, 2nd Edition*.

[4] Géradin, M., Rixen, D. (1997). Mechanical Vibrations, Theory and Application to Structural Dynamics. *John Wiley & Sons, 2nd Edition*.

[5] Hortmanns, M., Schäfer, N. (2005). Ljungan Bridge, Ånge Sweden – Full Scale Measurements. *Technical report, Prof. Sedlacek & Partner (unpublished)*.

[6] Hortmanns, M. (2005). Ljungan Bridge, Ånge Sweden – Design of dampers for the hangers 3 to 6. *Technical report, Prof. Sedlacek & Partner (unpublished)*.

[7] Malm, R., Andersson, A. (2006). Field testing and simulation of dynamic properties of a tied arch railway bridge. *Engineering Structures 28, pp. 854-863*.

Effect of single-lane congestions on long-span bridge traffic loading

Eugene J. OBrien[1], Alessandro Lipari[1], Colin C. Caprani[2]
[1]School of Civil, Structural and Environmental Engineering, University College Dublin, Newstead Building, Dublin 4, Ireland
[2]School of Civil and Structural Engineering, Dublin Institute of Technology, Bolton Street, Dublin 1, Ireland
email: eugene.obrien@ucd.ie, alessandro.lipari@ucd.ie, colin.caprani@dit.ie

ABSTRACT: It is well known that traffic loading of long-span bridges is governed by congestion. In spite of the fact that field observations in the past decades have shown that congestion can take up different forms, most previous studies on bridge traffic loading consider only a queue of standstill vehicles. In this paper, a micro-simulation tool is used for generating congested traffic on a single-lane roadway. The underlying micro-simulation model has been found capable of successfully replicating observed congestion patterns on motorways by simulating single-lane traffic with identical vehicles. Here trucks are introduced into the model, in an investigation of the total load for a 200 m span bridge. Different congestion patterns are found and studied in relation to their effect on loading. It is found that the bumper-to-bumper queue is not necessarily the most critical situation for the sample long-span bridge, since it does not allow the flowing of vehicles and therefore decreases the probability of observing critical loading events. Slow-moving traffic, corresponding to heavy congestion, can be more critical, depending on the truck proportion.

KEY WORDS: Long-span; bridge; traffic; loading; micro-simulation; congestion.

1 INTRODUCTION

1.1 Motivation

It is generally acknowledged that short span bridges are governed by small numbers of vehicles in free flowing traffic, with an allowance for dynamic amplification. On the other hand, bridges with span longer than about 50 m are governed by congested conditions, when a great number of vehicles are present at much closer spacing. In the latter case, no allowance for dynamics is appropriate.

Traffic loading for long-span bridges is not taken into account in most codes, due to their relatively low number. Common design practice for traffic loading on long-span bridges relies on conservative assumptions about the traffic and does not consider the variability of congestion patterns and driver behaviour. This has important implications for the assessment of existing bridges as it could make the difference between performing rehabilitation or not. Maintenance operations for long-span bridges are expensive and conservative assumptions may play a decisive role, resulting in unnecessary expenditure and traffic disruption.

1.2 Available models

The available models for traffic loading on long-span bridges take into account the variability of truck weights, but they often assume a mix of cars and heavy vehicles at a minimum bumper-to-bumper distance [1-6].

Truck weight data for these models comes either from traffic surveys or, more recently, from weigh-in-motion stations. Other traffic data (such as average speeds or car counts) generally comes from embedded loop detectors, which may be combined with weigh-in-motion stations. Data is very often collected during free-flowing traffic, due to the fact that it occurs more frequently than congested traffic and the sensor accuracy is generally less of a problem.

An important feature of traffic in the context of bridge loading is that drivers do not usually like staying between larger vehicles and therefore cars typically move out from between trucks, as traffic becomes congested. This results in the formation of truck platoons in the slow lane, changing the car-truck mix during congestion events. This makes the direct use of the widely available (and used) free-flowing traffic measurements problematic. Videos have been used for collecting suitable congested data for bridge loading [5, 7] but not frequently.

1.3 The use of traffic micro-simulation

Traffic micro-simulation (i.e., simulating the motion of individual vehicles) describes the interactions between vehicles, effectively generating different congestion patterns. Notably, free traffic measurement can be used as initial traffic conditions for a micro-simulation model. OBrien et al. [8] studied a heavily-congested Dutch long-span bridge and used a commercial micro-simulation tool with WIM data, videos and strain gauge measurements. Chen & Wu [9] used the cellular automata model, [10], dividing the bridge into 7.5 m cells. However, the cellular structure does not allow for the variability of vehicle lengths and gaps between vehicles.

In this paper, the car-following Intelligent Driver Model is used [11]. The flow of two classes of vehicles (cars and trucks) running on a single-lane road is studied. Two different truck percentages are considered. The different congested states are identified and the total load on a 200 m long bridge is computed. The simulations are carried out using an in-house program called *Simba* (*Sim*ulation for *B*ridge *A*ssessment). A similar study for identical vehicles has been presented in Lipari et al. [12].

2 TRAFFIC MICRO-SIMULATION

2.1 Overview

Micro-simulation is widely used today in traffic studies. Models vary in their levels of complexity and accuracy. The so-called *car-following* models consider driver behaviour within a single lane, simulating the interaction between a vehicle and its leader [13, 14]. More complex lane-changing models are also available.

While macro-simulation considers only the aggregate properties of a traffic stream, micro-simulation considers the motion of individual vehicles. Aggregate properties can be extracted from micro-simulation models as well, but this may be insufficient to validate all results. Unfortunately, microscopic (individual vehicle) data is difficult to collect, with the result that microscopic models are often only calibrated at an aggregate level [15]. Suitable data for calibrating lane-changing models is even more difficult to collect, since it requires, for instance, video tracking over a long stretch of road to capture the interaction between all the vehicles involved in lane-changing manoeuvres.

2.2 The IDM car-following model

Treiber et al. [11] present the 'Intelligent Driver Model' (IDM), a car-following model that gives a good match, at macroscopic level, with real congested traffic from several motorways [11, 16]. It has a modest number of physically-meaningful parameters and has been also calibrated with real trajectory data [17-19]. Results from the calibrated IDM are comparable with more complex models [20, 21].

The IDM is implemented for this study in the *Simba* program. The motion is simulated through an acceleration function:

$$\frac{dv}{dt} = a\left[1 - \left(\frac{v(t)}{v_0}\right)^4 - \left(\frac{s^*(t)}{s(t)}\right)^2\right] \tag{1}$$

where a is the maximum acceleration, v_0 is the desired speed, $v(t)$ is the current speed, $s(t)$ is the current gap to the vehicle in front, and $s^*(t)$ is the minimum desired gap, given by:

$$s^*(t) = s_0 + Tv(t) + \frac{v(t)\Delta v(t)}{2\sqrt{ab}} \tag{2}$$

In Equation (2), the term s_0 is the minimum bumper-to-bumper distance, T is the safe time headway, $\Delta v(t)$ is the speed difference between the current vehicle and the vehicle in front, and b is the comfortable deceleration. An advantage of this approach is that just five measureable parameters are sufficient to capture driver behaviour.

The length of vehicles must be known as well. A simulation step of 250 ms is used for discretising the system with Equations (1) and (2). The IDM can be extended to multi-lane simulation with the lane-changing model MOBIL [22].

3 CONGESTED TRAFFIC STATES

3.1 Inducing congestion

Congestion can be easily generated by applying flow-conserving inhomogeneities [11]. This is achieved through a local variation of the parameters. For example, the desired speed, v_0, is decreased or the safe time headway, T, is increased downstream. These changes have a similar effect as an on-ramp bottleneck or a lane closure. This approach has been successfully applied to *single*-lane and identical vehicle simulations for simulating congested traffic observed on some *multi-lane* German and Dutch motorways [11].

In this paper, inhomogeneity is generated by increasing the safe time headway, T, to a new level, T', downstream from where the congestion is sought. Treiber et al. [11] suggest that this is more effective than decreasing v_0.

The bottleneck strength, ΔQ, is a measure of the strength of the congestion-inducing phenomenon. It is defined as the difference between the outflow, Q_{out}, with the original parameter set and the outflow, Q'_{out}, with the modified set, in this case with the modified safe time headway T':

$$\Delta Q(T') = Q_{out}(T) - Q'_{out}(T') \tag{3}$$

Treiber et al. [11] refer to the outflow Q_{out} as the *dynamic capacity*, i.e., the outflow from a congested state. It is less than the static capacity Q_{max}, which is only achieved in free equilibrium traffic.

Table 1 lists six alternative forms of congestion [11, 23]. The traffic can take up any of these states, depending on the combination of inflow Q_{in} and bottleneck strength ΔQ. Combinations of these congested states are also possible and previous traffic history can influence the state of congestion.

Table 1. Definition of traffic states.

Acronym	Explanation of traffic state
FT	Free traffic
MLC	Moving localized cluster
PLC	Pinned localized cluster
SGW	Stop and go waves
OCT	Oscillatory congested traffic
HCT	Homogeneous congested traffic

3.2 Dynamic capacity of multi-class traffic

The work of Treiber et al. [11] is based on identical vehicles. In order to make meaningful comparisons between traffic congestions with different truck percentages, it is necessary to appropriately scale the variables that govern the congestion.

It is well known that the capacity of a road reduces as truck proportion increases. The Highway Capacity Manual (HCM) [24] uses passenger car equivalents f_{hv} in order to scale mixed traffic to an equivalent reference flow made up of only passenger cars. For the purposes of this paper, it seems appropriate to set out an equivalence in terms of the dynamic capacity Q_{out}, since this is a key parameter in predicting the congested states [11, 23, 25] and it is the one that characterises the bottleneck properties through Equation (3). Unfortunately, the dynamic capacity $Q_{out}(T)$ is not straightforward to calculate. In fact, it is necessary to induce congestion without modifying the original parameter set (Table 3), and therefore inhomogeneities cannot be introduced.

Here the outflow is worked out by creating an overflow, i.e., by injecting a number of vehicles higher than the road capacity $Q_{max}(T)$. Doing so leads to the formation of localized vehicle clusters. The outflow from those clusters is deemed to be dynamic outflow $Q_{out}(T)$.

Table 2 gives the outflow from mixed traffic conditions. The reference condition 0% and the 100% trucks are included for comparison.

Table 2. Dynamic capacity for multi-class traffic.

Truck percentage	Q_{out} (veh/h)	f_{hv}
0%	1686	1.00
20%	1590	0.94
50%	1462	0.87
100%	1291	0.77

4 MODEL AND SIMULATION PARAMETERS

4.1 *Traffic stream*

For this study, the vehicle stream is made up of two vehicle classes: cars and trucks. The parameters for each class are shown in Table 3. The car-following parameters are based on those used in [11]. Trucks have a smaller desired speed and are longer. All the parameters are constant, except for the truck gross vehicle weight (GVW), which is normally distributed with a coefficient of variation (CoV) of 0.1.

Table 3 - Model parameters of IDM

	Cars	Trucks
Desired speed, v_0	120 km/h	80 km/h
Safe time headway, T	1.6 s	1.6 s
Maximum acceleration, a	0.73 m/s^2	0.73 m/s^2
Comfortable deceleration, b	1.67 m/s^2	1.67 m/s^2
Minimum jam distance, s_0	2 m	2 m
Vehicle length, l	4 m	12 m
Gross Vehicle Weight	20 kN	432 kN*

* Normally distributed with CoV = 0.1

20% and 50% of trucks are randomly injected between cars in the slow lane. 20% is a typical truck proportion on a busy highway, while the 50% trucks accounts for the phenomenon of truck platoons in multi-lane roadways, which leads to a greater truck percentage in the slow lane. Significantly, the lane change rate is low during congestion [26], thus making the present single-lane approach suitable for multi-lane roadways as well. Indeed truck platoon formation is most likely to occur while approaching the congestion front when there are still available gaps for lane-changes.

A standard truck configuration with GVW taken as the common European highway maximum of 44 t was assumed as the mean (Figure 1). The distribution of weights between axles is based on WIM data from a French motorway [27]. Front and back overhangs of 0.9 m are also assumed.

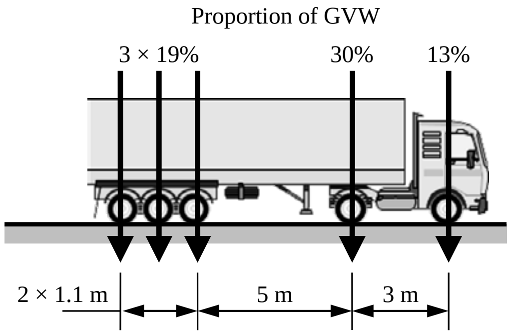

Figure 1. Assumed truck configuration.

4.2 *Road geometry and bottleneck strengths*

A single-lane 5000 m long road is considered. Inflows Q_{in} equal to the dynamic capacities Q_{out}, are considered for the two truck percentages selected (see Table 2). Such inflows are deemed equivalent in terms of expected congested states, so that $Q_{in,eq}$ = $Q_{out,eq}$ = 1686 pceq/h (passenger car equivalents per hour).

From 0 to 2700 m the safe time headway is T (see Table 3), then it increases linearly to 3300 m until it reaches the value T'. Five different values of T' (1.9, 2.2, 2.8, 4.0, and 6.4 s) are considered for the simulations, each of which is 1 hour long. These values are chosen in order to generate a wide range of congestion types.

For each pair of T' and truck percentage, twenty-five one-hour simulations are carried out, in order to account for the randomness involved in the truck injection and weight. Figure 2 shows the relation between the applied inhomogeneity $\Delta T = T' - T$ and the resulting equivalent bottleneck strength ΔQ_{eq}.

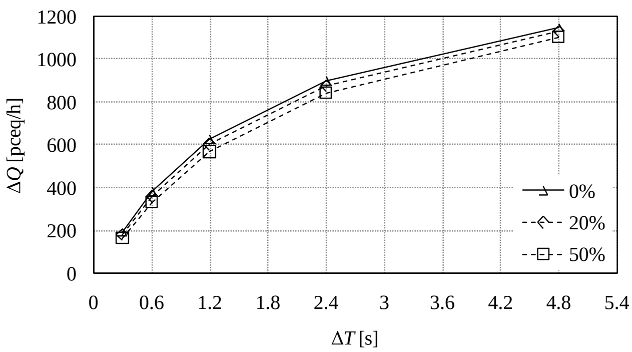

Figure 2. Equivalent bottleneck strength.

It can be seen from Figure 2 that the same inhomogeneity, ΔT returns similar equivalent bottleneck strengths ΔQ_{eq}, regardless of the percentage of trucks. For further comparison with the available traffic loading models, the full stop condition is also simulated (FS). It corresponds to infinite ΔT or $Q'_{out,eq}$ = 0 pceq/h. Then ΔQ_{eq} = 1686 pceq/h, according to Equation (3). Again, twenty-five simulations are carried out for each truck percentage. On the whole, 300 hours of simulations are run and analysed.

5 TRAFFIC RESULTS

5.1 *Typical spatio-temporal congestion patterns*

Spatio-temporal plots are useful for a global of view of the congestion over time and space. The speed axis is plotted upside down, so that peaks represents congestion. Figure 3 shows a typical spatio-temporal plot for the SGW state, resulting from a light bottleneck strength.

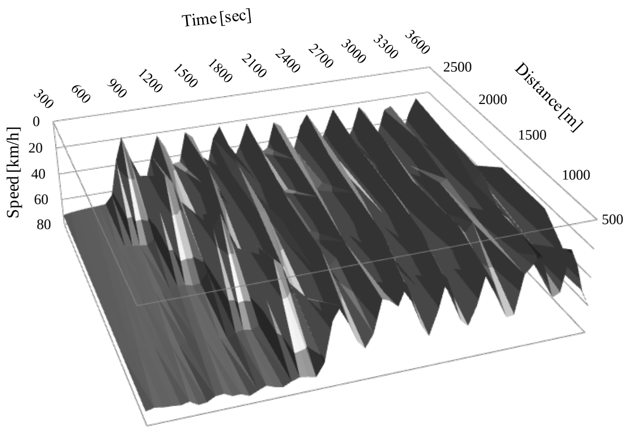

Figure 3. Typical SGW state (ΔQ_{eq} = 181 pceq/h, 20% trucks).

As bottleneck strength increases, the oscillations reduce. Figure 4 shows a combined HCT/OCT state, where traffic is homogeneously slow near the inhomogeneity, while it is more oscillating upstream.

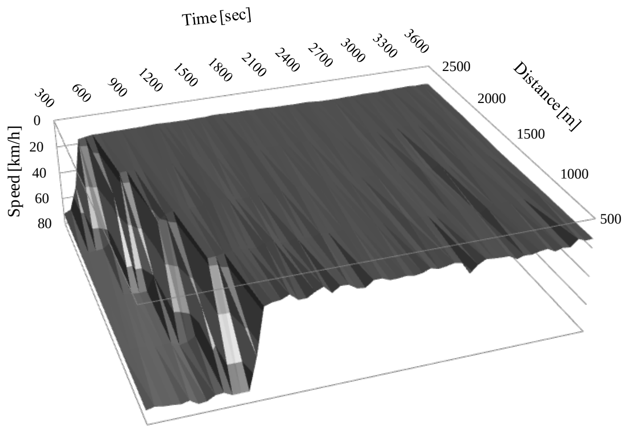

Figure 4. Typical HCT/OCT state (ΔQ_{eq} = 603 pceq/h, 20% trucks).

As bottleneck strength increases further, the congestion gets more homogeneous, finally reaching the HCT state throughout.

5.2 *Effect of truck proportion*

After having set a passenger car equivalent for the different traffic compositions analysed, it is interesting to see how different the congested states are in relation to the different truck percentages. It is convenient to draw a comparison in terms of average speed over the congested space-time domain, since both flow and density would vary depending on the truck percentage.

The generated congested states are actually similar, showing small differences in the average speed in the congested area (Figure 5). The case of traffic with no trucks is illustrated as a reference. The mean speed drops down to 5 km/h for the highest bottleneck strength, which represents very heavy congestion.

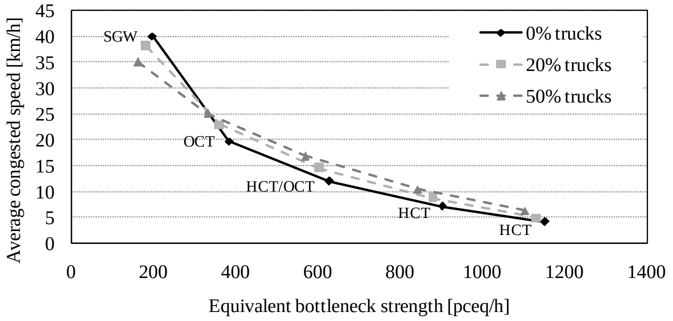

Figure 5. Average congested speed.

It is also interesting to analyse the traffic oscillation properties. A greater coefficient of variation of the speed indicates prominent stop-and-go waves behaviour. Indeed the lightest bottleneck strengths show a high coefficient of variation, which reduces as the bottleneck strength increases (Figure 6).

It is interesting to note how the truck presence actually dampens the speed oscillations during stop-and-go waves, probably due to their slower desired speed. On the other hand, their different properties introduce a small disturbance in the homogenous congested states which, in the absence of trucks, show no oscillations at all.

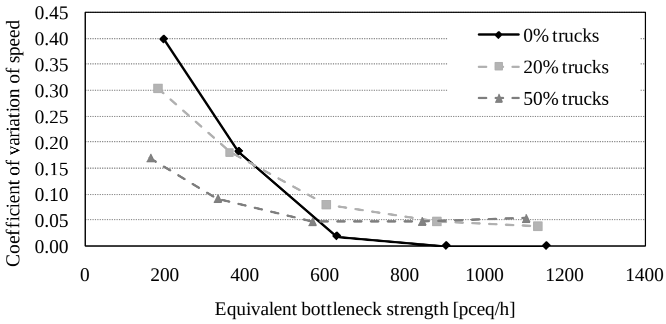

Figure 6. Coefficient of variation of congested speed.

6 LOAD EFFECT RESULTS

6.1 *Introduction*

In this section the load effects induced by the different congested traffic states on a sample bridge are studied to identify the most critical congestion states for bridge loading. A 200 m long single-lane bridge is placed from location 1900 to 2100 m. For each one-hour simulation, the maximum total load on the bridge is computed.

For the purpose of comparison, by assuming no cars, minimum bumper-to-bumper distance and truck average GVW, the total load on the bridge is 6048 kN (14 trucks).

6.2 20% trucks

Figure 7 shows the total load on the bridge against the bottleneck strength for the case of 20% trucks. It can be seen that the load effect increases approximately linearly until the HCT point corresponding to ΔQ = 1132 pceq/h. Then, the maximum hourly load decreases as it approaches the full stop point (ΔQ_{eq} = 1686 pceq/h). Notably, the average maximum hourly load corresponding to full stop is of the same order of magnitude as the lightest congestion. However, the hourly load at full stop shows a significant scatter.

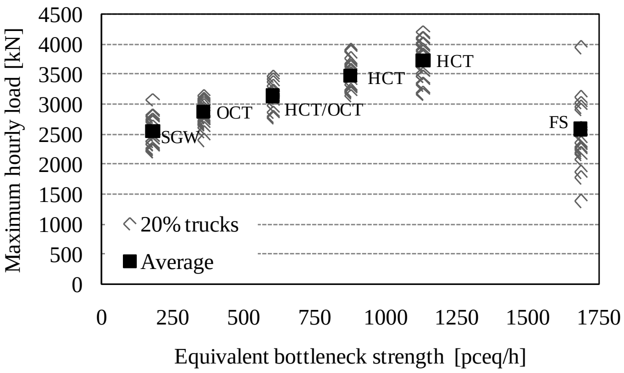

Figure 7. Maximum hourly total load (20% trucks).

The finding that full stop is not the critical loading case is significant, since most previous load models assumed this condition. Such a finding can be explained by considering that, the heavier the congestion, the slower the speed and the closer the vehicles. On the one hand, heavy congestion results in greater load effects (since vehicles are more closely spaced), but on the other, fewer vehicles have the chance to cross the bridge and the probability of having a high number of heavily overloaded trucks decreases. This explains also the wide scattering in the hourly maxima at full stop.

6.3 50% trucks

For the higher truck percentage, the results are shown in Figure 8. The full stop load has, on average, the same order of the slow moving traffic HCT. Again, it shows a higher variation about the average value, relative to the other congested states.

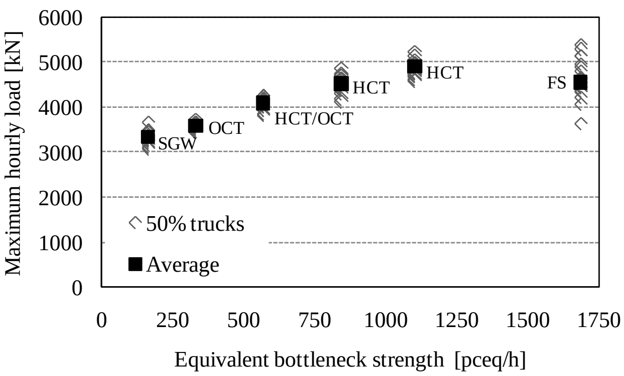

Figure 8. Maximum hourly total load (50% trucks).

6.4 Summary

From the results presented it is clear that it may be non-conservative to assume the full stop condition as the most critical for bridge loading. For the 20% truck percentage, the heavy-congested and slow-moving HCT state is clearly the most critical one for the bridge considered, while differences are less when the truck percentage is higher. Figure 9 gives the average values for the two different traffic compositions.

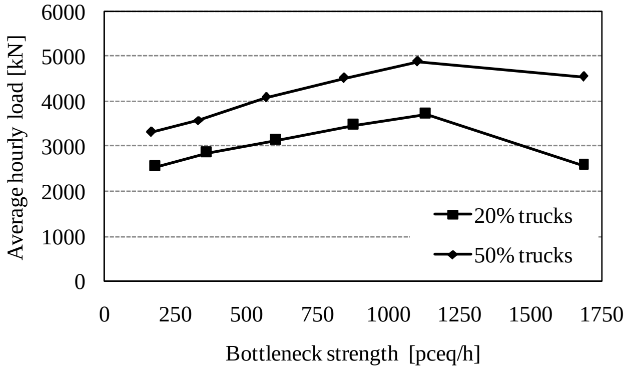

Figure 9. Average maximum hourly load.

Furthermore, it is noted that a greater truck percentage reduces the variation between hourly maxima (Figure 10). Finally, the full stop condition has a significantly greater coefficient of variation, since for every one-hour simulation, there is only one possible configuration of vehicles.

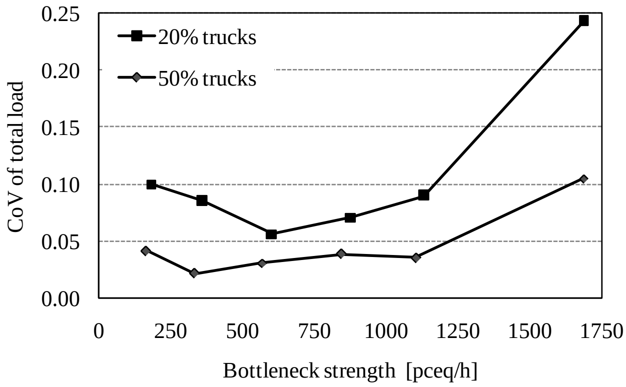

Figure 10. Coefficient of variation of the maximum hourly total load.

7 CONCLUSIONS

This paper investigates the effect of different congestion patterns on the total load of a sample single-lane long-span bridge, using a micro-simulation tool. Previous load models neglect congestion patterns, assuming a queue of vehicles at minimum bumper-to-bumper distances. The car-following model used here has been shown to reproduce observed congestion patterns, using identical vehicles. Here we extend the use of this model to multi-vehicle-class simulations, necessary to investigate the load effects on a sample bridge.

We show that the bumper-to-bumper queue is not necessarily the most critical situation for the sample long-span bridge, since it does not allow the flowing of vehicles and therefore decreases the probability of observing critical loading events. Indeed slow-moving traffic, corresponding to heavy congestion, are more critical states for the bridge. In this case, speeds are low enough (order of 5 km/h) to have the vehicles closely spaced, but it still allows the turnover of vehicles and the sampling of a greater number of truck combinations. This is especially valid for typical proportions of trucks, while the difference is less sharp for very high truck percentages, which may occur in the slow lane of a multi-lane highway.

ACKNOWLEDGMENTS

This work is part of the TEAM project (Training in European Asset Management). The TEAM project is a Marie Curie Initial Training Network and is funded by the European Commission 7th Framework Programme (PITN-GA-2009-238648).

REFERENCES

[1] Ivy, R.J., Lin, T.Y., Mitchell, S., Raab, N.C., Richey, V.J. and Scheffey, C.F. (1954), 'Live loading for long-span highway bridges', *American Society of Civil Engineers Transactions*, 119, 981-1004.

[2] Committee on Loads and Forces on Bridges of the Committee on Bridges of the Structural Division (1981), 'Recommended design loads for bridges', *Journal of the Structural Division*, 107(7), 1161-1213.

[3] Flint and Neill Parternship, *Interim design standard: long span bridge loading*, Transport and Road Reseach Laboratory, 1986.

[4] Ditlevsen, O. and Madsen, H.O. (1994), 'Stochastic Vehicle-Queue-Load Model for Large Bridges', *Journal of Engineering Mechanics*, 120(9), 1829-1847.

[5] Nowak, A.S. and Lutomirska, M. (2010), 'Live load for long span', *Proceeding of the Tenth International Conference on Structural Safety and Reliability*, Osaka, Japan.

[6] Prat, M. (2001), 'Traffic load models for bridge design: recent developments and research', *Progress in Structural Engineering and Materials*, 3, 326-334.

[7] Ricketts, N.J. and Page, J., *Traffic data for highway bridge loading*, Transport Research Laboratory, 1997.

[8] OBrien, E.J., Hayrapetova, A. and Walsh, C. (2012), 'The use of micro-simulation for congested traffic load modelling of medium- and long-span bridges', *Structure and Infrastructure Engineering*, 8(3), 269-276.

[9] Chen, S.R. and Wu, J. (2011), 'Modeling stochastic live load for long-span bridge based on microscopic traffic flow simulation', *Computers and Structures*, 89(9-10), 813-824.

[10] Nagel, K. and Schreckenberg, M. (1992), 'A cellular automaton model for freeway traffic', *Journal de Physique I France*, 2(12), 2221-2229.

[11] Treiber, M., Hennecke, A. and Helbing, D. (2000), 'Congested Traffic States in Empirical Observations and Microscopic Simulations', *Physical Review E*, 62(2), 1805-1824.

[12] Lipari, A., Caprani, C.C. and OBrien, E.J. (2010), 'Load effect of single-lane traffic simulations on long-span bridges', *Proceedings of the Joint Symposium on Bridge and Infrastructure Research in Ireland*, Cork, Ireland.

[13] Brackstone, M. and McDonald, M. (1999), 'Car following: a historical review', *Transportation Research Part F*, 2, 181-196.

[14] Orosz, G., Wilson, R.E. and Stépán, G. (2010), 'Traffic jams: dynamics and control', *Philosophical Transactions of the Royal Society A*, 368, 4455-4479.

[15] Hidas, P. and Wagner, P. (2004), 'Review of Data Collection Methods for Microscopic Traffic Simulation', *Proceedings of the World Conference on Transport Research*, Istanbul, Turkey.

[16] Helbing, D., Treiber, M., Kesting, A. and Schönhof, M. (2009), 'Theoretical vs. Empirical Classification and Prediction of Congested Traffic States', *The European Physical Journal B*, 69, 583-598.

[17] Kesting, A. and Treiber, M. (2008), 'Calibrating Car-Following Models by Using Trajectory Data', *Transportation Research Record*, 2088, 148-156.

[18] Chen, C., Li, L., Hu, J. and Geng, C. (2010), 'Calibration of MITSIM and IDM Car-Following Model Based on NGSIM Trajectory Datasets', *Proceedings of the International Conference on Vehicular Electronics and Safety*, QingDao, China.

[19] Hoogendoorn, S. and Hoogendoorn, R. (2010), 'Calibration of microscopic traffic-flow models using multiple data sources', *Philosophical Transactions of the Royal Society A*, 368, 4497-4517.

[20] Brockfeld, E., Kühne, R.D. and Wagner, P. (2004), 'Calibration and validation of microscopic traffic flow models', *Transportation Research Record*, 1876, 62-70.

[21] Punzo, V. and Simonelli, F. (2005), 'Analysis and Comparison of Microscopic Traffic Flow Models with Real Traffic Microscopic Data', *Transportation Research Record*, 1934, 53-63.

[22] Kesting, A., Treiber, M. and Helbing, D. (2007), 'General Lane-Changing Model MOBIL for Car-Following Models', *Transportation Research Record*, 1999, 86-94.

[23] Schönhof, M. and Helbing, D. (2007), 'Empirical Features of Congested Traffic States and Their Implications for Traffic Modelling', *Transportation Science*, 41(2), 135-166.

[24] Transportation Research Board, *Highway Capacity Manual - Fourth Edition*, TRB, 2000.

[25] Kerner, B.S. and Rehborn, H. (1996), 'Experimental features and characteristic of traffic jams', *Physical Review E*, 53(2), R1297-R1300.

[26] Sparmann, U. (1979), 'The importance of lane-changing on motorways', *Traffic Engineering & Control*, 20(6), 320-323.

[27] Grave, S.A.J., OBrien, E.J. and OConnor, A.J., 'The determination of site-specific imposed traffic loadings on existing bridges', in *Bridge Management 4*, 2000.

Estimating characteristic bridge loads on a non-primary road network

Eugene J. OBrien[1], Bernard Enright[2], Brendan Williams[3], Cathal Leahy[1]
[1] UCD School of Civil, Structural and Environmental Engineering, Dublin 4, Ireland
[2] Dublin Institute of Technology, Bolton Street, Dublin 1, Ireland
[3] UCD School of Geography Planning and Environmental policy, Dublin 4, Ireland
email: eugene.obrien@ucd.ie, bernard.enright@dit.ie, brendan.williams@ucd.ie, cathal.leahy@ucdconnect.ie

ABSTRACT: When collecting truck loading data on a primary road network a common, approach is to install a large network of permanent pavement based Weigh-In-Motion systems. An alternative to this approach would be to use one or more portable Bridge Weigh-In-Motion systems which could be moved between bridges at regular intervals to determine the traffic loading throughout the network. A data collection strategy is needed to put such a system to best use. This paper details the data collection strategies which were examined for the National Roads Authority in Ireland. The use of urban economic concepts including Central Place Theory are discussed as methods for analysing which roads are expected to experience the greatest truck loading.

KEY WORDS: Bridge; Weigh-In-Motion; WIM; B-WIM; Data Collection Strategy; Secondary Roads; Traffic; Loading; Economics; Central Place Theory.

1 INTRODUCTION

A common method for collecting load data on a road network is to install permanent pavement based Weigh-In-Motion (WIM) sensors at a large number of sites on the network. Such a system is expensive and installation and maintenance causes disruption to traffic. An alternative which is less expensive is to use a portable Bridge WIM (B-WIM) system which is moved periodically between bridges on the network. With the recent advances in nothing-on-road axle detection [1] this allows truck loading across the network to be investigated with little or no disruption to traffic. This paper considers the implementation of such a system on a non-primary road network where traffic flows are relatively low.

All roads do not experience the same volumes of truck traffic. Extremely heavy special permit trucks have the greatest influence on a bridge's characteristic load effects. As the number of permit trucks is very small in comparison with regular trucks, in short term weighing operations they may not be captured in sufficient volumes to provide accurate statistical data. A method of finding roads which experience large volumes of permit trucks is needed to focus random weighing operations across a non-primary road network.

The volumes of regular trucks are also important as the critical bridge loading event may involve a permit truck meeting a regular truck on the bridge. To try and predict the volumes of both truck types, Central Place Theory and other urban economic concepts relating to sector location are examined to identify economic activities which "generate" these trucks. A basic methodology for estimating the volumes of permit truck on a given road is also formulated.

A strategy for locating sites for the portable B-WIM system is also needed in order to put the system to best use. This strategy allows an accurate estimation of the general truck loading throughout the network as well as the loading on roads which are found to have high probabilities of very heavy permit trucks. The system must also be capable of targeting "problem" areas such as ports, steel manufacturers, etc.

This is not the first time data collection strategies have been considered for determining the location of weighing operations. Data gathered from an extensive WIM network is used in Montana, USA [2] to choose sites for weight enforcement the following year. Methods are developed for processing the WIM data on a month by month basis and determining the areas to be targeted. It is estimated that this targeted enforcement strategy was saving $500,000 a year (2001-2002) in pavement damage. This strategy is not directly comparable however as it is used for locating weight enforcement activities rather than WIM data collection sites.

This paper examines work which was completed for the National Roads Authority (NRA) [3]. The NRA is currently (2012) installing a system of permanent pavement based WIM sensors on Ireland's major inter-urban roads. These permanent systems will not provide any data on Ireland's non-primary road network. This work investigates the use of a portable B-WIM system to gather data on the 15,000 km of national secondary, regional and legacy national primary roads (i.e., former national primary roads which, although still in use, have been superseded, typically by motorways). These roads will be referred to in this paper collectively as the non-primary road network. As this portable B-WIM system would be moved around the network at regular intervals, a data collection strategy is needed for selecting suitable sites.

2 SOURCES AND DESTINATIONS OF TRUCK TRAFFIC

2.1 *Central Place Theory*

Central Place Theory was developed by Christaller [4] to explain the location of cities and towns within a region relating to their function. The basis of the theory is that different types of business serve differently sized populations and that these businesses aim to locate at the centre of the population they serve. The size of these market areas vary across different industries. For example, all towns require a grocery store and a butcher shop whereas only larger towns have more specialised functions such as computer stores. The theory generates a hierarchy of central places with the range of goods available increasing with the size of the city/town.

Assuming that there is a boundless homogeneous plain that can be settled uniformly, and that each city/town within the central places hierarchy is equidistant from other cities/towns of similar size, Christaller finds that the only settlement pattern that satisfies these criteria is a hexagonal one - see Figure 1.

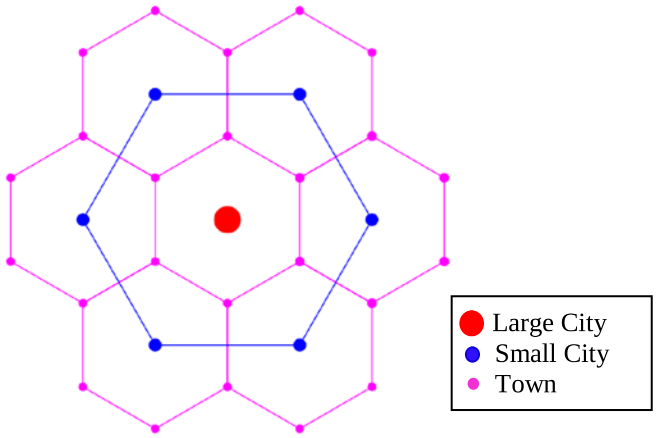

Figure 1. Hexagonal pattern for locating central places.

If this theory is to be used to determine the routes most used by truck traffic, the key is that there are different types of cities with definite patterns of trade between them. Each city/town imports from a larger city/town and exports to a smaller city/town [5]. Cities of similar size are assumed not to trade (clearly a simplification in the theory). While there are clear limitations to Central Place Theory, in particular noting the existence of industrial and other transport intensive uses in out-of-urban locations, it can be adapted to forms a basis for a discussion on the sources and destinations of truck traffic.

2.2 Regular Trucks

When examining bridge loading there are two distinct types of truck, regular and permit. Regular trucks carry mostly consumer goods such as food, furniture, clothes and electrical products between central places. These generally have 2 or 3 axles on a rigid base or a 5 or 6 axle articulated configuration. Although they can be involved in critical bridge loading events they tend not to be the dominant truck in such events. Variations in the weight/frequency of these trucks has only a small influence on the total load effect in critical bridge loading events.

Using Central Place Theory it can be assumed that these trucks are found mainly on the roads connecting larger cities/towns with smaller cities/towns.

2.3 Permit Trucks

Permit trucks are those which exceed the normal legal limits for vehicle weight and/or dimensions. They generally weigh over 40 tonnes and consist of crane-type vehicles or low loaders. Crane-type vehicles - mobile cranes and trucks carrying crane ballast - have heavily loaded closely spaced axles. Low loaders comprise of a tractor unit pulling a trailer and have a single large axle spacing of about 11 m. These trucks are important for hogging moment over an internal support in multi-span continuous bridges.

Permit trucks make up a very small proportion of the overall truck population but they are the dominant vehicle in critical bridge loading events on short to medium span bridges. WIM data from 5 European sites containing 2.4 million trucks are examined and it is found that permit trucks make up an average of 1.63% of the truck population.

Permit trucks are almost entirely related to the construction industry. Over 900 hundred photographs of trucks from a WIM site in the Netherlands are examined. 390 of these are clearly identified as loaded permit trucks. Of these 328, were construction related, the nature of 56 could not be conclusively identified and 6 were found to be non-construction related. The non-construction related trucks were carrying boats and buses.

Construction is associated with areas which are experiencing economic growth. As the wealth of an urban or city region grows, new domestic and commercial buildings need to be constructed [5] as well as new infrastructure such as bridges, roads and tunnels. It is these construction projects that are the main destinations for permit trucks. It is assumed that, unlike regular freight movement, construction traffic is then not directly proportional to the size of nearby cities but rather proportional to both size of the city/town and its economic growth. Regular trucks, on the other hand, are associated with trade and their number can be reasonably assumed to be proportional to city size. The ratio of regular trucks to permit trucks is then not constant and varies depending on economic growth. At the five European WIM sites, the percentage of permit trucks is not constant and varies between 0.74% and 2.71%. However, it is unclear whether or not this is due to economic growth in nearby cities.

The destinations of permit trucks are generally cities experiencing economic growth but they could also be travelling to other locations dispersed throughout a country or region. For example roads, tunnels and railways are constructed between cities and other once off developments such as wind turbines, power plants and cement factories are usually located away from large towns and cities.

The sources of permit trucks are also more dispersed than the sources of regular trucks. Large scale manufacturing facilities - which can require large areas of land - are often located away from large cities where land is expensive. Permit trucks can also originate from a port. The various origins and destinations of these permit trucks suggest that many of them use the non-primary road network for at least part of their journey.

The conclusion then is that most permit trucks are travelling from anywhere to a city/town experiencing economic growth and a lesser percentage travel from anywhere in the country to anywhere else. The relative probability of a permit truck occurring at any location on the non-primary road network can then be calculated and decreases from a maximum near cities experiencing high levels of economic growth to a minimum background level at the furthest distances from these cities. This needs to be taken into account when designing a data collection strategy for a portable B-WIM system on the non-primary road network.

3 REVIEW OF IRISH ROAD NETWORK

The methods outlined in Section 3 and 4 are similar to those described in a previous paper by some of the same authors [6].

The non-primary road network in County Kildare is examined to get an idea of the number of bridges throughout Ireland which are suitable for B-WIM. An NRA database is used to examine the bridges on legacy national primary and national secondary roads. As no such database is available for regional roads, a site visit was made to a number of these roads and their bridges surveyed - see Figure 2.

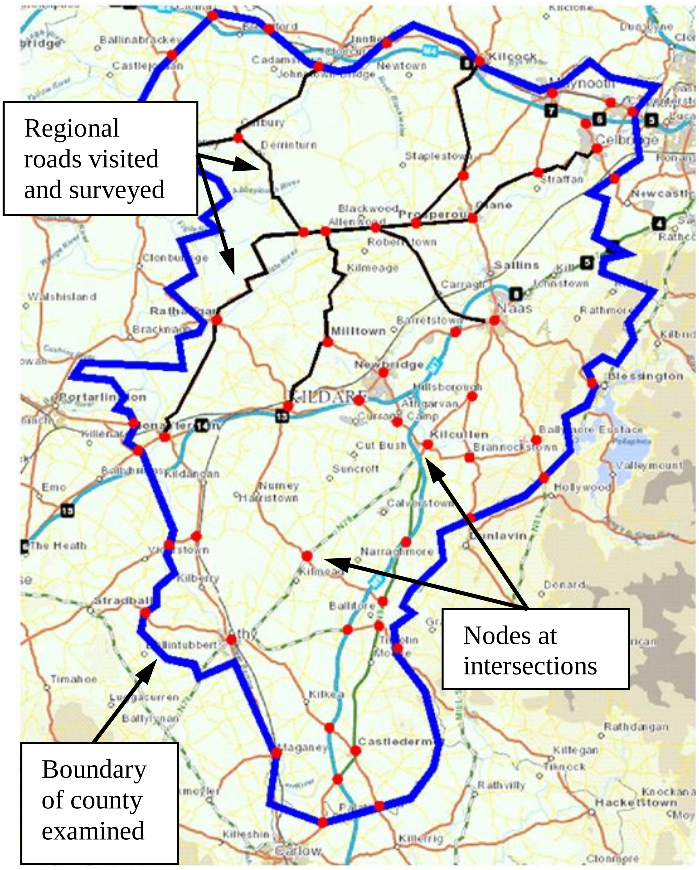

Figure 2. County Kildare showing regional roads surveyed and nodes at intersections of relevant roads.

3.1 *Suitability for B-WIM*

The suitability of a bridge for B-WIM [7] is assessed using four criteria:

1. **Construction material:** Steel or iron is best, as larger strains are induced, but reinforced concrete bridges can also be used. Masonry and other arched bridges are deemed unsuitable.
2. **Access:** Soffit of the bridge must be accessible in order to install the BWIM system. Ideally this is done while standing beneath the bridge but waders, boats and scaffolding are often used to aid installation. Bridges located over fast flowing rivers or busy roads/railways are deemed unsuitable.
3. **Span:** Short, simply supported, spans are preferred (ideally 10 - 20 m). The strain at midspan is generally measured in such bridges. Continuous bridges can also be used.
4. **Skew:** Skewed bridges develop bending moments differently to bridges without skew and so complicate the relationship between measurements and vehicle weight. Ideally the bridges should not be skewed although some skew can be allowed for in the B-WIM software.

Using the four criteria listed above, the suitability of bridges for a B-WIM system, was assessed and bridges divided into the following categories:

Category 0: Not Feasible – Bridge not suitable for B-WIM installation
Category 1: Feasible – Possible to install system, but with some complications
Category 2: Ideal – System could easily be installed on this bridge

3.2 *Suitability of Irish Bridges*

Tables 1 and 2 provide summary information on the bridges examined and their suitability for B-WIM. Most of the bridges examined were in category 0 and this was largely due to their masonry arch construction. Ireland has a relatively high proportion of these bridges [9], which are unsuitable due to the manner in which they carry loads. The proportion of B-WIM suitable bridges in countries with fewer masonry arch bridges may to be higher than in Ireland. Restricted access was the main reason for classifying bridges as category 1. Photographs of bridges in each of the three categories are provided in Figure 3.

Table 1. Summary of bridges on each road type examined and suitability for B-WIM.

Road Type	Length (km) Examined	No. of Bridges	Cat. 0	Cat. 1	Cat. 2
Legacy	116	41	34	5	2
Secondary	62	47	39	6	2
Regional	122	44	36	7	1

Table 2. Suitability of bridges examined for B-WIM system.

Road Type	% Suitable for B-WIM (Cat. 1 or 2)	Average Distance Between Suitable Bridges (km)
Legacy	17	17
Secondary	17	8
Regional	18	15

(a) Category 0 (not feasible)

(b) Category 1 (feasible)

(c) Category 2 (ideal)

Figure 3. Samples of the bridges examined.

4 DATA COLLECTION METHODS

Data collection methods for selecting the roads on which the portable B-WIM system is installed are examined. The aim is to cover the entire non-primary road network with a focus on roads which are expected to experience high volumes of permit trucks.

4.1 Length Method

Every road in the network has a road number. The length method uses these numbers to identify the roads in the network and then each of these roads is divided into sections of about 15 km in length. A section of road is picked randomly – with equal probability of all such sections being selected – and the B-WIM system installed on a suitable bridge on this section of road. If a suitable bridge is not available on that section, then the nearest suitable bridge on the same road is used. The B-WIM system is left at each site for a week before being moved to another randomly chosen section of road. Sections with a higher probability of permit trucks could be weighted to increase their probability of being selected. An installation period of a week was chosen so the system could measure vehicle weights on many different roads and a general picture of the loading on the entire road network could be obtained.

The average distance between suitable bridges - shown in Table 2 - suggests that a majority of the sections selected should either contain a suitable bridge or be reasonably close to one.

Once a section of road has been chosen it is either excluded from future selections or included. If it is excluded:

- Every section of road in the country is covered in a fixed time.
- Existing sources of heavy loads that repeatedly use the same roads are found in that fixed time.
- If a new source of heavy loading emerges on a route that has already been picked, it cannot be detected until the cycle of all roads is complete.

If selected road sections are included as candidates for future selection:

- It is not possible to guarantee that every section of road in the country is selected in a fixed time period.
- New and emerging sources of heavy loads are just as likely to be selected as existing sources.

Given the extremely long cycle to cover all sections - 20 years based on an estimated 15,000 km of roads - the latter approach is recommended. It is also recommended that the selection of road sections should take account of their relative probability of the truck traffic containing permit trucks.

4.2 Node Method

This method uses nodes to divide up all the roads being examined into segments. A node is located at each intersection of these roads. The network is then divided up into sections, with each section beginning at one node and finishing at the next node encountered. Sections are then randomly chosen and the B-WIM system installed on a suitable bridge on this section of road. If no suitable bridge is found then another section is randomly chosen. As with the length method, sections with a higher probability of permit trucks could be weighted to increase their probability of being selected. This method was applied to County Kildare and 56 nodes were found – see Figure 2 – which resulted in 75 sections of road. Assuming that each of the 26 counties of Ireland contains the same number of road sections, we get an approximation of 1,950 road sections for the whole country.

Large loads travel the full length of sections of road between pairs of nodes, with the exception of the sections at the beginning and end of their journey. The aim of this method then is to divide the network into stretches of road which experience near uniform loading. The disadvantage of this method is that it results in more road sections than the length method and it would take nearly twice as long to examine every section in the country. These sections of road also tend to be short, with lengths varying between about 2.5 km and 15 km, based on the data collected for the county examined. Therefore when a short section is chosen it is unlikely to contain a suitable bridge, which leads to some inconsistencies.

4.3 Targeted Data Collection

This method uses the portable B-WIM system to solely target known or perceived sources of heavy loads. The system is moved around the country on a weekly basis or as required, between areas that were identified as likely to experience illegally overloaded vehicles. If overloaded vehicles are detected on a road, the police could then be asked to target this route and set up checkpoints or to visit repeat offenders. There is some anecdotal evidence that this kind of approach is working well elsewhere in Europe. Sources of overloading may include:

- Precast concrete manufacturers
- Steel suppliers/manufacturers
- Logging areas and sawmills
- Ports
- Crane suppliers/manufacturers

A targeted data collection approach could also be used to examine sections of road:

- Where abnormal road surface deterioration is experienced. Such roads may be identified using local knowledge or by comparing yearly road roughness data.
- With high ADTT.
- Which are alternatives to tolled motorways.
- Where there is concern about the condition of a particular bridge.
- Which are close to a known source of, or destination for, heavy vehicles.

The advantage of this method is that it is much more likely to capture extreme events than the length and node methods. The disadvantage is that the data collected is biased and does not give an indication the underlying general trend on the road network.

4.4 Case Study

A hypothetical scenario is created, and each of these methods is applied to it, in order to assess their ability to capture extreme loading events. The scenario considers that a destination of heavy vehicles emerges in Cavan Town and that, once a week, a very heavy permit truck travels from Athlone to Cavan (see Figure 4). It is assumed that this journey occurs once a week for one year. The route is chosen as it does not contain any inter-urban roads and uses only roads on the non-primary road network. It covers 81 km of regional and national secondary roads. It is assumed that a single portable B-WIM system is used to cover all 26 counties in the Irish non-primary road network.

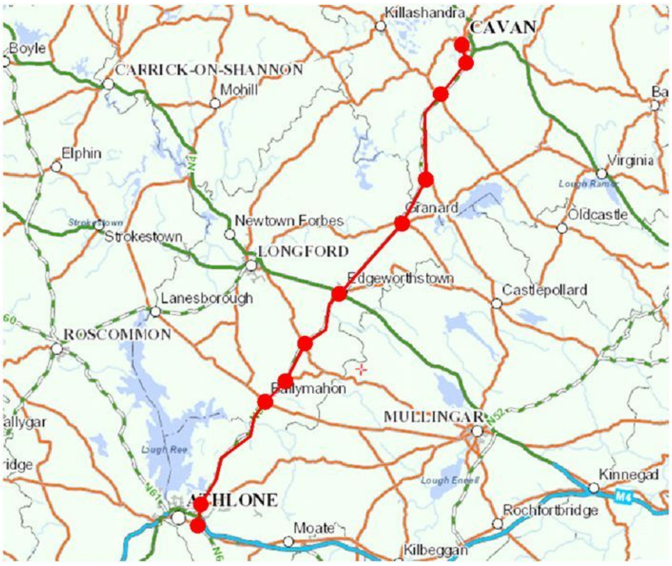

Figure 4. Hypothetical route examined - route highlighted and nodes shown.

4.4.1 Length Method

As the route covers 81 km of road, it contains 5.4 (81/15) road sections according to the length method. Based on an estimated total length of 15,000 km, there are 1,000 segments of road in the country. The probability of successfully capturing the event at least once in one year (50 working weeks) is calculated from basic probability concepts [10] using Equation (1):

$$\text{P(Capturing Event)} = p + qp + q^2p + q^3p + \ldots\ldots + q^{49}p \quad (1)$$

where: p = the probability of any of the 5.4 sections being measured in a given week
q = the probability of one of the sections not being measured in a given week

Using Equation (1), the probability of this Athlone/Cavan event being captured by the length method is 23.7%.

4.4.2 Node Method

The route in question was found to contain 10 road segments – see Figure 4. For the purposes of this study, the crude assumption is made that each of these road segments contains a suitable bridge. In reality it is unlikely that this would be the case. It is also estimated, by extrapolating from the county examined, that there are 1950 road sections in the country. The probability of this event being captured by the node method is then calculated as 22.7%.

4.4.3 Mixed Targeted and Random Approach

The random (length and node) methods give better statistical information on the complete distribution of loading in the target network. Targeting likely locations of overload on the other hand is statistically biased – the data collected tends to represent the upper end of the true loading distribution and its use could result in excessive conservatism in pavement design or bridge assessment. However, targeting has the advantage that it may result in a reduction in the extent of overloading which saves costs in the pavement maintenance budget in particular. A compromise between these two approaches is to divide the B-WIM system equally between random and targeted approaches. Assuming that the hypothetical event is not among the routes targeted, the probability of it being detected is reduced to 12.7% for the length method or 12.1% for the node method. Doubling the number of B-WIM systems would result in nearly double the probability of success while also allowing one sensor to be permanently used for the targeted approach.

5 CONCLUSIONS AND RECOMMENDATIONS

Central Place Theory and related concepts to economic growth are presented here as a framework for determining the origins and destinations of regular and special permit trucks. Construction is identified as a key source of permit trucks, which are the dominant vehicle in extreme bridge loading events. Economic growth is presented as a generator of permit truck movements. Regular trucks - whose movements can be predicted using Central Place Theory - play a minor role in these extreme events.

Two different data collection strategies for determining sites for portable B-WIM operations on a non-primary road network are examined. Both methods perform similarly in the case study, i.e., each gives a similar probability of detecting the repeated overloading scenario. The length method is recommended as it is more straightforward to implement than the node method. It is also recommended that repeat selections be allowed in order to avoid problems associated with the long cycle required.

In order to overcome some of the shortfalls of the methods, which are discussed in Section 4, it is recommended that the B-WIM system operate the length method for half the time and be used for targeted data collection for the other half. This allows the loading conditions on the non-primary road network to be examined while also targeting problem areas.

A permanent WIM installation and a portable B-WIM system have similar capital costs. As the data collection strategy proposed here requires weekly reinstallations and recalibrations it will have significantly higher operational costs than a single permanent system. However, if the aim is to cover an entire non-primary road network then the portable B-WIM proposal offers a significant cost advantage over a network of permanent systems.

ACKNOWLEDGMENTS

The authors gratefully acknowledge the financial support and assistance of the Irish National Roads Authority.

REFERENCES

[1] OBrien, E.J., Žnidarič, A., Ojio, T. (2008). 'Bridge Weigh-In-Motion – Latest Developments And Applications World Wide'. *Proceedings of International Conference on Heavy Vehicles*, Eds. B. Jacob, E.J. OBrien, P. Nordengen, A.J. O'Connor, & M. Bouteldja. May 19-22, Paris, 25-38, ISTE/Hermes (London).

[2] Stephens, J., Carson, J., Hult, D.A., Bisom, D. (2003), 'Preservation of Infrastructure by Using Weigh-in-Motion Coordinated Weight Enforcement'. *Journal of the Transportation Research Board*, 1855, 143-150.

[3] Leahy, C. & OBrien, E.J. (2011). *Bridge Weigh in Motion Systems.* Report to the National Roads Authority. Report No. 2011-1, UCD School of Civil, Structural & Environmental Engineering, Dublin.

[4] King, L., *Central place theory*, Sage, London, 1984.

[5] O'Sullivan, A., *Urban economics*, McGraw-Hill/Irwin, Boston, 2009.

[6] Enright, B., Leahy, C., OBrien, E.J., Keenahan, J. (2012), 'Portable Bridge WIM Data Collection Strategy For Secondary Roads'. *6th International Conference on Weigh-In-Motion*, June 4-7, Dallas, ISTE/J. Wiley (London).

[7] Hitchcock, W.A., Toutanji, H., Richardson, J., Salama, T., Callahan, D., Jackson, J., Zhao, H. (2011), 'Expanding Portable B-WIM Technology', *UTCA Project No. 08204*.

[8] Žnidarič, A., Lavrič, I., Kalin, J. (1999), 'Bridge WIM Measurements on Short Slab Bridges', *Weigh-In-Motion of Road Vehicles*, ed. B. Jacob, Hermes Science Publications, Paris, 217-226

[9] Gibbons, N. and Fanning, P.J. (In Press) 'Rationalising assessment approaches for masonry arch bridges'. *Proceedings of the ICE - Bridge Engineering.*

[10] Ang, A. H.-S. and Tang, W.H., *Probability concepts in engineering : emphasis on applications in civil & environmental engineering*, Second Edition, Wiley, New York, 2007.

Using instrumented vehicles to detect damage in bridges

Eugene J. OBrien[1], Jennifer Keenahan[1], Patrick McGetrick[2], Arturo González[1]
[1] UCD School of Civil, Structural and Environmental Engineering, Dublin 4, Ireland
[2] Kyoto University, Japan
email: eugene.obrien@ucd.ie, jennifer.nichoinneachain@ucdconnect.ie, mcgetrick@gmail.com, arturo.gonzalez@ucd.ie

ABSTRACT: This paper describes a 'drive-by' method of bridge inspection using an instrumented vehicle. Accelerometers on the vehicle are proposed as a means of detecting damage on the bridge in the time it takes for the vehicle to cross the bridge at full highway speed. For a perfectly smooth road profile, the method is shown to be feasible. Changes in bridge damping, which is an indicator of damage, are clearly visible in the acceleration signal of a quarter-car vehicle on a smooth road surface modelled using MatLab. When road profile is considered, the influence of changes in bridge damping on the vehicle acceleration signal is much less clear. However, when a half-car model is used on a road with a rough profile, it is again possible to detect changes in bridge damping, provided the vehicle has two identical axles.

KEYWORDS: Bridge; Damage; Damping; Dynamics; Vehicle Bridge Interaction; Damage detection; Drive-by.

1 INTRODUCTION

Loading, environmental factors and ageing result in the continuous degradation of highway structures such as bridges. Bridge management systems have been introduced in most developed countries, which are designed to provide a high level of protection and early warning if the bridge becomes unsafe as well as to facilitate a cost-effective distribution of the resources available for maintenance of the road infrastructure network. In most cases, bridges are inspected visually with an inspector looking for cracking and other indicators of damage. This is not only time consuming and expensive, but is unreliable as some forms of damage are not immediately visible.

In recent years, there has been a significant increase worldwide in the number of bridges being instrumented and monitored electronically [1], [2]. This process requires the installation of sensing equipment and data acquisition electronics in the bridge, which can be expensive. While it will undoubtedly become much more common in the future, it is unlikely in the medium term for the thousands of minor structures that make up the majority of the bridge stock in most countries.

This paper investigates the use of a vehicle fitted with accelerometers on its axles as an alternative method of 'inspecting' bridges. The vehicle drives over the bridge at full highway speed. The hypothesis is that damage in the bridge will manifest itself as small changes in the acceleration signals of the vehicle axles. This is based on the premise that bridge damage will result in significant changes in its structural damping, as has been reported by a number of authors [3], [4]. The bridge damping changes, in turn, cause changes in the vehicle acceleration signals.

So called 'drive-by' inspection of bridges is a relatively new field. [5] show that bridge frequencies can be extracted from the acceleration signal of a passing sprung mass. First natural frequency is a function of stiffness so damage that reduces stiffness will result in a reduction of bridge natural frequency. [6] verified this approach experimentally using a heavy tractor towing an instrumented trailer. They got good results for speeds of up to 40 km/h but had difficulty at higher speeds.

[7] built a 3-dimensional vehicle-bridge dynamic interaction model to test the drive-by concept for a range of speeds, road roughnesses and damping levels. They also carried out field trials but concluded that the bridge frequency can only be determined with a drive-by system for lower speeds and when the excitation of the bridge is high.

A number of authors [8–10] report on the results of scale laboratory models to test the drive-by concept. These show promising results but the speeds are much slower than would be expected on a real bridge.

2 QUARTER-CAR MODEL SIMULATIONS

A theoretical quarter-car model is first used here to test the drive-by concept. The quarter-car (Figure 1) has two degrees-of-freedom, corresponding to the body bounce and axle hop motions.

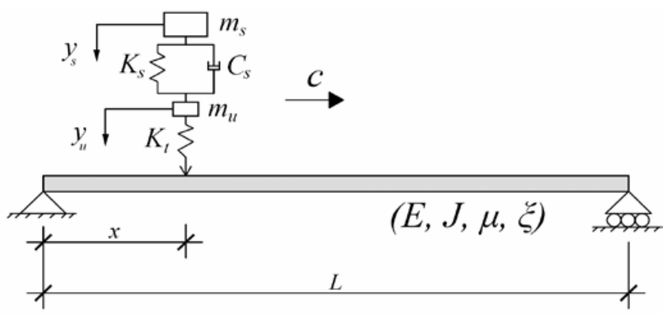

Figure 1. Theoretical quarter-car model.

The properties of this vehicle model are based on values obtained from work by [11] and [12]. Details are given by [13].

2.1 Vehicle-bridge dynamic interaction model

The equations of motion of the vehicle derive from the equilibrium of all forces and moments acting on the vehicle expressed in terms of the degree of freedom displacements, velocities and accelerations as shown in equation 1,

$$M_v\ddot{y}_v + C_v\dot{y}_v + K_v y_v = f_v \tag{1}$$

where M_v, C_v, and K_v are the mass, damping and stiffness matrices of the vehicle respectively. For this quarter car, the displacement vector, $y_v = \{y_s, y_u\}^T$, contains the sprung and unsprung displacements (see Figure 1). The excitation force vector, $f_v = \{0, -F_t\}^T$ contains the time varying interaction forces applied to the vehicle. The component, F_t, represents the dynamic interaction force at the base of the wheel as shown in equation 2,

$$F_t = K_t\,(y_u - w_v) \tag{2}$$

where w_v is the displacement of the base of the wheel. In general, this parameter represents the sum of the bridge displacement and road profile displacement under the wheel, r and w_b respectively.

Each vehicle model travels over a 15 m long simply supported Euler-Bernoulli beam. It consists of 20 discretised beam elements, each with two degrees of freedom and with a constant modulus of elasticity $E = 3.5 \times 10^{10}$ N/m^2. Therefore, the beam model has a total of $n = 42$ degrees of freedom. The bridge has a constant mass per unit length, $\mu = 28{,}125$ kg/m, and the second moment of area $J = 0.5273$ m^4. The speed of the vehicle is maintained in simulations at 20 m/s. Prior knowledge of the first natural frequency of the bridge is assumed here at 5.6 Hz. The response of a discretised beam model to a series of moving time-varying forces is given by the system of equations that can be seen in equation 3,

$$M_b\ddot{w}_b + C_b\dot{w}_b + K_b w_b = N_b f_{int} \tag{3}$$

where M_b, C_b, and K_b are $(n \times n)$ global mass, damping and stiffness matrices respectively, w_b, $\dot{w}_b$, and $\ddot{w}_b$ are the $(n \times 1)$ global vectors of nodal bridge displacements and rotations, their velocities and accelerations respectively, and $N_b f_{int}$ is the $(n \times 1)$ global vector of forces applied to the bridge nodes. The term, f_{int} represents the interaction force between the vehicle and the bridge and is described using the $(n_f \times 1)$ vector, as shown in equation 4,

$$f_{int} = \{P_1 + F_t\} \tag{4}$$

The matrix, N_b distributes the n_f applied interaction forces on beam elements to equivalent forces acting on the nodes. This location matrix can be used to calculate the bridge displacement under each wheel w_b using equation 5,

$$\{w_b\} = \mathrm{N}_\mathrm{b}^\mathrm{T}\, w_b \tag{5}$$

Rayleigh damping is adopted here to model viscous damping. Hence, equation 6 shows,

$$C_b = \propto M_b + \beta K_b \tag{6}$$

where α and β are constants.

The crossing of the vehicle model over each bridge is described by a system of coupled differential equations as proposed by [14]. The dynamic interaction between the vehicle and the bridge is implemented in MatLab. The vehicle and the bridge are coupled at the tyre contact force, f_{int}. The coupled equation of motion is formulated as in equation 7,

$$M_g\ddot{u} + C_g\dot{u} + K_g u = F \tag{7}$$

where M_g and C_g are the combined system mass and damping matrices respectively, K_g is the coupled time-varying system stiffness matrix and F is the system force vector. For the coupled system, $u = \{y_v, w_b\}^T$ is the displacement vector. The system of equations is solved using the Wilson-Theta integration scheme [15]. The value of θ used is 1.420815 [16].

2.2 Results of quarter-car simulations

The quarter-car model is first tested for a bridge with an idealised perfectly smooth profile, i.e., the displacement at the base of the wheel, w_v is exactly equal to the bridge displacement, w_b. The vehicle is simulated crossing six bridges that are identical except for differences in their damping coefficients, which range from 0% through to 5%. The bridges are excited by the passing of the vehicle along the span. The acceleration signals at the centre of the bridge are analysed and the Power Spectral Density is plotted in Figure 2(a). In each case, there is a peak in the acceleration spectrum at a frequency of 5.85 Hz. This is near the bridge first natural frequency of 5.6 Hz. The inaccuracy is due to the resolution of the spectra (± 0.96 Hz) which can be improved by driving the vehicle at a slower speed.

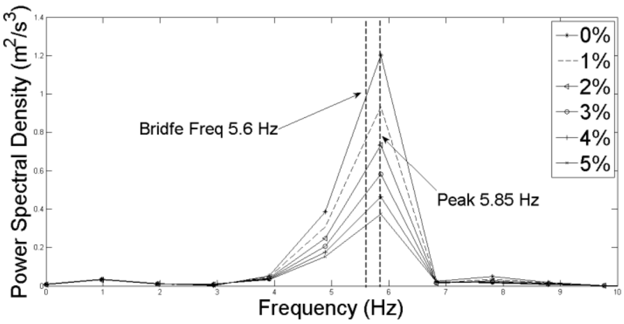

(a) Accelerations on bridge

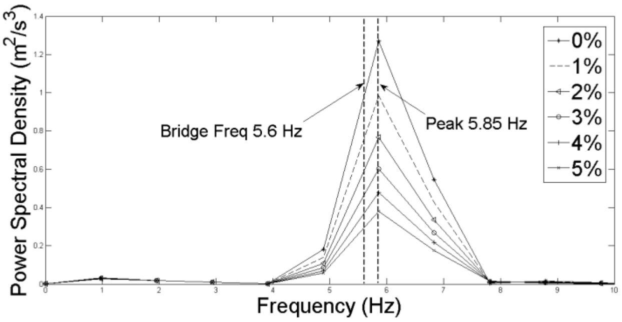

(b) Accelerations on vehicle

Figure 2. Power spectral density of acceleration signals (perfectly smooth road profile).

There are clear differences in the signals when the damping coefficient of the bridge is changed. This confirms that, if an accelerometer were installed at the centre of the bridge, it could be used to detect changes in damping and hence changes in its damage state. However, the drive-by concept seeks to detect damage in the bridge from the acceleration signals in the vehicle. Figure 2(b) shows these spectra and confirms that, in this case, an accelerometer on the passing vehicle is just as effective at detecting damage as an accelerometer attached to the bridge.

In the example of Figure 2, the road surface is perfectly smooth, clearly an unrealistic scenario. The simulations are repeated for the same quarter-car vehicle and bridge, but this time with a non-zero road surface profile. The road irregularities are randomly generated according to ISO [17] The simulated road profile is of Class 'A' according to the ISO standard, as would be expected on a well maintained motorway surface. In such a case, the random road surface variations are far greater (± 4 mm) than the deformations due to bridge deflection. As a result, while the spectra for accelerations on the bridge are similar to Figure 2(b), the spectral densities are much greater for the quarter-car accelerations as seen in Figure 3.

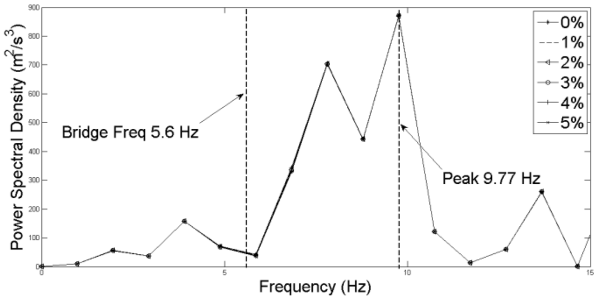

Figure 3. Power spectral density of acceleration signals (Class A road profile).

The excitation caused by the road surface profile variations is so great that there is no longer any visible difference in the six graphs plotted in Figure 3. All six spectra, regardless of damping level, are almost exactly the same. In this case, there is no longer a peak in spectral density at the bridge first natural frequency. The peaks that are shown relate to the road surface profile rather than to any property of the bridge.

3 HALF-CAR SIMULATIONS

A similar series of simulations is carried out with a more realistic half-car vehicle model. The half-car (Figure 4) has two degrees of freedom per axle with springs corresponding to suspension system and tyres. Unsprung masses correspond to the weights of the suspension system while the single sprung mass is shared between the axles, thereby allowing rocking as well as bouncing motions.

3.1 *Vehicle-bridge model for half-car*

The equations of motion of the half-car vehicle are similar in form to those of the quarter-car. Equation (1) still applies except that, this time, the vector, $y_v = \{y_s, \theta_s, y_{u1}, y_{u2}\}^T$ has four components corresponding to the four degrees of freedom of the vehicle. Similarly, the interaction force vector, $f_v = \{0, 0, -F_{t,1}, -F_{t,2}\}^T$ contains four components for the half-car system. The term $F_{t,i}$ represents the dynamic interaction force at wheel i as displayed in equation 7,

$$F_{t,i} = K_{t,i}\,(y_{ui} - w_{v,i}) \quad i = 1, 2 \tag{7}$$

$w_{v,i}$ is the total displacement under wheel i, made up of the road profile displacement and bridge displacement r_i and $w_{b,i}$ respectively.

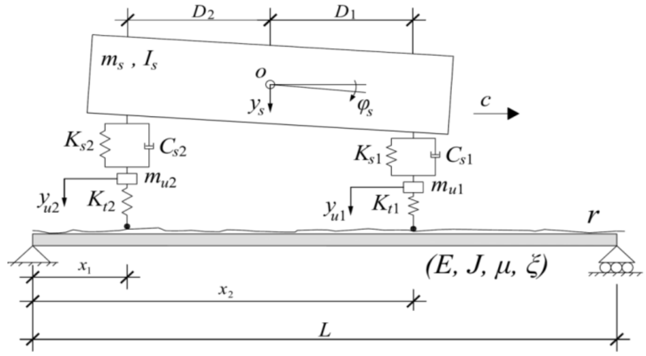

Figure 4. Half car model on bridge beam model.

Equation (3) describes the beam model and applies for both quarter-car and half-car vehicles. However, for the half-car system, there are two interaction forces between the vehicle and the bridge with the result that f_{int} is a (2 × 1) vector as shown in equation 8,

$$f_{int} = \begin{Bmatrix} P_1 + F_{t,1} \\ P_2 + F_{t,2} \end{Bmatrix} \tag{8}$$

Similarly, N_b is an (n × 2) location matrix for the half-car vehicle that distributes the two applied interaction forces on beam elements to equivalent forces acting on the nodes.

3.2 *Results of half-car simulations*

As for the quarter-car simulations, in the half-car simulations bridge accelerations are found to change significantly as the damping of the bridge changes, as would be expected in response to certain kinds of damage. When the road surface is perfectly smooth, the spectra of vehicle accelerations also change in response to bridge damping changes. However, when there is a non-zero road profile, the vehicle acceleration spectra are similar in form to those of Figure 3. For all six cases of damping, the spectra are almost identical.

For a half-car with two identical axles, the excitation applied by a road surface profile is identical for each axle. Hence, the acceleration signals should be very similar, except for a phase difference due to the time difference between the two axles passing a given point. When the half car is crossing a bridge with a rough road profile, each axle is being excited by the same (time shifted) road profile but by a different part of the bridge. Hence, the time shifted *difference* between the accelerations in identical axles should be largely unaffected by road profile but strongly influenced by the bridge vibration.

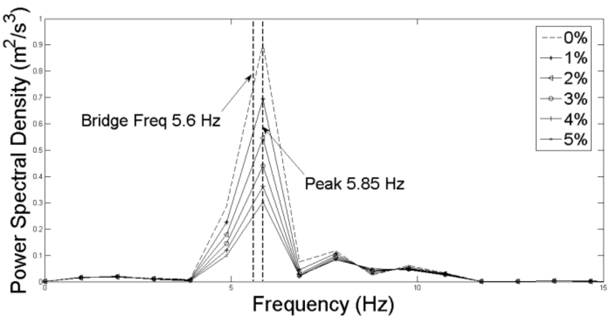

Figure 5. Power spectral density of difference between axle vibration signals.

The feasibility of this approach is confirmed in Figure 5, which illustrates the power spectral densities of the time shifted differences between the axle vibration signals in the half car. There are clear differences between the six graphs, showing, once more, a strong dependence on bridge damping. The dominance of road profile influences on the quarter-car (Figure 3) is absent. It would appear that using a vehicle with identical axles and analysing the differences in the axle accelerations does have potential to be used as a drive-by damage detection system.

4 CONCLUSIONS

A 'drive-by' concept for bridge damage detection is tested in numerical simulations, i.e., the concept that acceleration signals in a vehicle passing over a bridge can be used to detect damage in the bridge itself. It is assumed that damage is correlated with bridge damping so that the goal is to use the passing vehicle to detect a change in bridge damping.

A quarter-car model shows that the passing vehicle can detect changes in damping when the road surface is perfectly smooth. However, even a good quality road surface is sufficient to completely change the vehicle excitation and to mask the influence of small changes in bridge properties.

A half-car model gives similar results to the quarter-car. However, the concept of using a half-car with two identical axles shows some promise. By subtracting the acceleration signals from subsequent axles, it is shown that the influence of the road surface profile can be removed and bridge damage can once more be detected.

ACKNOWLEDGMENTS

The authors gratefully acknowledge the financial support of Science Foundation Ireland.

REFERENCES

[1] P. C. Chang, A. Flatau, and S. C. Liu, "Review paper: health monitoring of civil infrastructure," Structural Health Moitoring, vol. 2, no. 3, pp. 257-267, 2003.

[2] J. M. W. Brownjohn, "Structural health monitoring of civil infrastructure," Philosophical Transactions of the Royal Society A: Mathematical, Physical and Engineering Sciences, vol. 365, no. 1851, pp. 589-622, 2007.

[3] R. O. Curadelli, J. D. Riera, D. Ambrosini, and M. G. Amani, "Damage detection by means of structural damping identification," Engineering Structures, vol. 30, no. 12, pp. 3497-3504, 2008.

[4] C. Modena, D. Sonda, and D. Zonta, "Damage localization in reinforced concrete structures by using damping measurements," Key engineering materials, vol. 167, pp. 132-141, 1999.

[5] Y. B. Yang, C. W. Lin, and J. D. Yau, "Extracting bridge frequencies from the dynamic response of a passing vehicle," Journal of Sound and Vibration, vol. 272, no. 3-5, pp. 471-493, 2004.

[6] Lin, C.W. and Yang, Y.B., "Use of a passing vehicle to scan the fundamental bridge frequencies: An experimental verification," Engineering Structures, vol. 27, no. 13, pp. 1865-1878, 2005.

[7] A. González, P. Rattigan, E. J. OBrien, and C. Caprani, "Determination of bridge lifetime dynamic amplification factor using finite element analysis of critical loading scenarios," Engineering Structures, vol. 30, no. 9, pp. 2330-2337, 2008.

[8] C. W. Kim and M. Kawatani, "Challenge for a drive-by bridge inspection," Proceedings of the 10th International Conference on Structural Safety and Reliability, ICOSSAR2009. Osaka, Japan, pp. 758-765, 2009.

[9] Y. Oshima, T. Yamaguchi, Y. Kobayashi, and K. Sugiura, "Eigenfrequency estimation for bridges using the response of a passing vehicle with excitation system," Proceedings of the Fourth International Conference on Bridge Maintenance, Safety and Management, IABMAS2008. Seoul, Korea, pp. 3030-3037, 2008.

[10] T. Toshinami, M. Kawatani, and C. W. Kim, "Feasibility investigation for identifying bridge's fundamental frequencies from vehicle vibrations," Proceedings of the Fifth International Conference on Bridge Maintenance, Safety and Management, IABMAS2010. USA, pp. 317-322, 2010.

[11] D. Cebon, Handbook of Vehicle-Road Interaction. The Netherlands: Swets & Zeitlinger, 1999.

[12] N. K. Harris, E. J. Obrien, and A. González, "Reduction of bridge dynamic amplification through adjustment of vehicle suspension damping," Journal of Sound and Vibration, vol. 302, no. 3, pp. 471-485, 2007.

[13] J. Keenahan, E. J. OBrien, P. J. McGetrick, and A. González, "Using instrumented vehicles to detect damage in bridges," in 15th International Conference on Experimental Mechanics (ICEM15), 2012.

[14] L. Frýba, Vibration of solids and structures under moving loads. London: Thomas Telford, 1999.

[15] J. W. Tedesco, W. G. McDougal, and C. A. Ross, Structural dynamics: theory and applications. Addison Wesley Longman, 1999.

[16] W. Weaver and P. R. Johnston, Structural dynamics by finite elements. Prentice-Hall, 1987.

[17] ISO 8608:, "Mechanical vibration-road surface profiles - reporting of measured data," 1995.

Non-intrusive bridge scour analysis technique using laboratory test apparatus

Luke J. Prendergast[1], Kenneth Gavin[1], John O'Sullivan[1]
[1]School of Civil, Structural and Environmental Engineering, University College Dublin, Ireland
E-mail: luke.prendergast@ucdconnect.ie, kenneth.gavin@ucd.ie, jj.osullivan@ucd.ie

ABSTRACT: Larger and more frequent flood flows expose foundation soils to stronger erosive forces, increasing the likelihood that scour of piers (and abutments) will compromise the structural integrity of some bridges. The development of low-cost, low maintenance, non-destructive methods of bridge scour analysis is therefore becoming ever more important in light of the current economic climate. The use of embedded sensors that measure vibration responses of a structure, due to train loading, may offer potential to track changes in the foundation soil stiffness matrix caused by scour and may inform engineers in implementing appropriate protection schemes. This paper presents a laboratory investigation in which the dynamic response of a scaled pier, installed in a bed of sand and instrumented with an accelerometer, is recorded for a constant and repeatable excitation. Sand stiffness properties were manually altered by increasing the scour depth in progressive experiments. For each experiment, a vibration response was recorded and this was converted to a frequency response using a fast Fourier transform (FFT). Differences between the dynamic signatures of the pier for the different scour conditions investigated were analysed to explore whether this type of non-destructive testing could provide a viable method of detecting scour before the structural integrity of the bridge reaches a critical stage. Results indicate that significantly different frequency responses are recorded for decreasing elevations of bed material around the model pier, indicating that the method may provide the basis for a simple and effective means of monitoring scour around bridge piers.

KEY WORDS: Bridge Scour, Vibration, Monitoring, Infrastructure

1 INTRODUCTION

Scour can be defined as the excavation and removal of material from the bed and banks of streams as a result of the erosive action of flowing water [1]. There are three main forms: general scour, contraction scour and local scour. General scour includes the aggradation and degradation scour that may result from changes in the fundamental parameters that control channel form such as flow rate and changes in the sediment supply to the river system [2]. Contraction scour occurs due to an increase in flow velocity and resulting shear stresses caused by a decrease in the river cross-sectional area due to the presence of a bridge. Local scour arises due to increased velocities and associated vortices as water accelerates around the corner of abutments and piers, inducing downward flow and subsequent scour of the riverbed [1]. The scour hole generated can reduce the carrying capacity of the foundation and can lead to catastrophic structural collapse. Adverse hydraulic action, including scour, are deemed to have accounted for over 53% of bridge failures in the United States between 1989 and 2000 [3]. This paper assesses whether dynamic vibration signals can be used to detect changes in the fundamental frequency of a pier arising from changes in the stiffness of the foundation system from increased local scour. The assessment utilises a laboratory arrangement in which a vertical pier installed in a sand matrix and instrumented with an accelerometer is subjected to a constant and repeatable excitation for varying scour conditions.

2 BACKGROUND

Scour poses significant risks to bridges and it's extent can be difficult to detect, particularly for situations where the scour hole partially refills after a flood has subsided (termed the live-bed condition). The concept of instrumenting bridges and their foundations to detect changes in scour levels has gained considerable interest in recent years. Many different methods have developed over time and these are employed to monitor scour around piers and abutments. The use of Ground Penetrating Radar (GPR) as outlined in [2] can be particularly effective in a freshwater environment as it can detect geophysical subterranean changes that occur when a scour hole develops and subsequently refills. It can prove difficult, however, to undertake these surveys during flood conditions, as water flow rates can often be dangerously high. Other methods such as the use of sonar detection systems mounted on bridge piers, together with the installation of buried "Sedimetri" systems close to piers, can be quite promising. These, however, require care to accurately interpret the results [4]. The use of accelerometers on bridge piers to detect changes in dynamic frequency has gained a high level of interest in recent times as a method of long-term, non-intrusive monitoring of bridge stability. In one example, a field test is described where a pair of bridge piers, instrumented with wireless accelerometers, were subjected to free vibration before and after a simulated scour event with the aim of detecting changes in their natural frequency [5]. Another case outlines a study of a road bridge in Turin, Italy, that was instrumented with accelerometers to detect changes in dynamic signatures of different piers relative to one another during the progression of scour as well as before and after the planned retrofitting of one of the piers [6]. Briaud [7] describes a major study aimed at developing correlations between different scour assessment techniques with the change in acceleration profile and natural frequency of bridge piers as scour holes develop both under laboratory conditions and on real bridges subject to traffic loading.

3 EXPERIMENTAL APPARATUS

An experimental investigation into the analysis of acceleration profiles and frequency plots obtained during simulated scouring of a model bridge pier was undertaken.

3.1 Sand Characteristics

Blessington sand (Co. Wicklow, Ireland), with a bulk density in the region of $2.03 Mg/m^3$ and specific gravity value of 2.3, was used in the experiments. A sieve analysis was undertaken on the sand in order to establish the grading (Figure 1). Figure 1 indicates that the sand was closely graded with 50% by weight being less than 0.26mm.

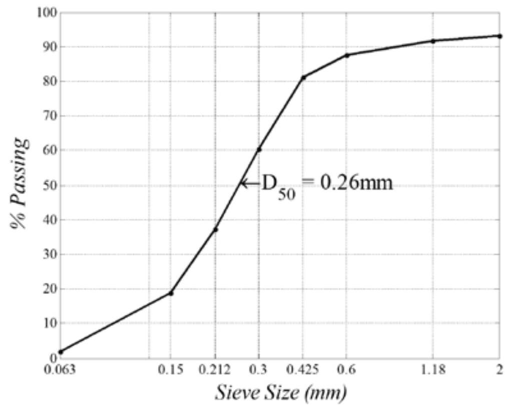

Figure 1. Sieve Analysis.

The measured moisture content of the sand was 13%. No attempt to model hydrodynamic loads was undertaken and the experiment was performed using partially saturated (air-dried) sand.

3.2 Steel Container Set-up

The experiment was assembled in a bolted together steel box with dimensions of 1m x 1m x 1m (Figure 2). The box housed the vertical pier installed in the bed of Blessington sand.

Figure 2. Steel Box.

The significant mass of the box provided a rigid structural framework in which to conduct the dynamic tests on the pier. It was also sufficiently strong to support the weight of soil to be placed in the box.

3.3 Model Bridge Pier

The upright pier structure was a hollow steel box-section with properties as defined in Table 1.

Table 1 Hollow Section Properties

Property:	**Value:**
Mass (kg):	31.182
Length (m):	1.260
X-Sectional Width (m):	0.1
X-Sectional Length (m):	0.1
Thickness (m):	0.008
X-Sectional Area (m^2):	2.944×10^{-3}
Moment of Inertia (m^4):	4.181×10^{-6}
Assumed Density (kg/m^3):	7850

Figure 3. Pier Structure.

The pier (Figure 3) is placed on a bed of sand 300mm in height from the bottom of the steel box. This distance from the base should be enough to neglect the edge effects of the support condition here, i.e. the zone of influence should be within this depth. The pier was instrumented with an accelerometer mounted on its top (the unrestrained end of the structure). The mass of the accelerometer is negligible compared to the mass of the pier and its influence on the overall vibration is therefore considered to be insignificant.

3.4 Accelerometer

The type of accelerometer used was a BDK3 model from Sensors UK[1]. It is a capacitive spring-mass accelerometer with integrated sensor electronics. The accelerometer has a bolt-like appearance allowing for ease of installation onto the hollow section and has properties as outlined in Table 2.

[1] Accelerometer information available at: http://www.sensoruk.com/

Table 2. Accelerometer Specifications.

Property:	Specification:
Measuring Range:	±3g (ca.±30ms^{-2})
Resolution:	< 10^{-3}g
Frequency Range:	1 - 300Hz
Sensitivity at U_B=5V:	Appr. 150mV/g
Temperature Drift of Sensitivity:	< + 6 x 10^{-2}%/K
Temperature Drift of zero point:	< 0.1mV/K
Zero Offset:	(2.5 ± 0.1) Volt
Output Impedance:	Approx. 100 Ohm
Linearity Deviation:	< 1%
Nominal Supply Voltage:	U_{bN} = 5V
Permissible Supply Voltage:	U_{bZ} = 2V – 16V

3.5 Datalogger

The datalogger used was the CR9000x model from Campbell Scientific[2]. It is capable of sampling at a frequency of 1000 Hz, a value that is ideal for observing the acceleration signal from a vibrating structure. This high sampling rate allows for the reception of a relatively full waveform, which can be analysed via a fast Fourier transform (FFT) to obtain the frequency of the signal and hence, the natural frequency of the structure. The data was acquired using accompanying "loggernet" software, which stores the data in real-time.

3.6 Excitation Device

In order to excite the hollow section in an appropriate manner, it was required to establish the most likely mode shape that would result prior to deciding at which location along the height of the pier to apply the force. Forcing the pier at different locations along its height may incite different mode shapes. Since it is the first natural frequency that we would most likely obtain (other frequencies are also possible), it is the first mode shape corresponding to this that we should aim to achieve. For an upright cantilever, ignoring the self-weight (gravitational) effects on natural frequency, the mode shape in Figure 4 corresponds to the first natural frequency [8]. The equation shown in Figure 4 is true for a mass distributed over the entire length of the pier.

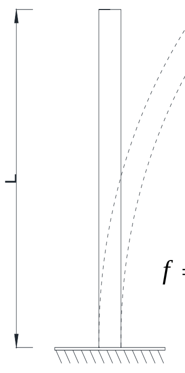

$$f = \frac{1}{2\pi}(1.875)^2\sqrt{\frac{EI}{mL^4}}$$

Figure 4. Mode Shape at First Natural Frequency.

[2] Campbell Scientific, UK. Specification available at www.campbellsci.com/cr90000x

In order to excite the hollow section appropriately, a load on a swinging arc was applied to the top of the section as an impulse force. The swinging arc mechanism allowed for repeatability of the same force to maintain consistency in the experiment. The subsequent excitation was at the first natural frequency of vibration [9]. Figure 5 shows the experimental configuration that consisted of a pendulum device clamped into a supporting retort stand and allowed to swing through a fixed arc. By pulling back to a set point, repeatability of the impulse force can be achieved. A small amount of cushioning material was placed around the top of the section to prevent a high frequency ping from distorting the data. This ensured that the majority of the kinetic energy is transferred into the pier.

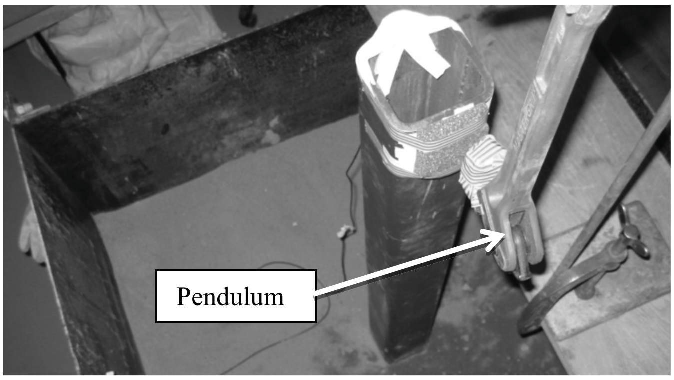

Figure 5. Swinging Pendulum Device.

4 EXPERIMENTAL METHODOLOGY

The first step was to assemble the steel box by bolting together the sides and fixing to the base. Using the roof crane in the Civil Engineering laboratory, a bag of Blessington sand was lifted into the air above the box and the box was filled to a level of approximately 100mm.Using a compaction hammer, the sand was compacted in order to create a stiffer base upon which to found the model pier. It is important to compact in 100mm increments to ensure that adequate compaction and uniformity of density is achieved. The sand was filled to an initial height of 300mm above the base. The model pier was placed vertically in the centre of the box, equidistant from all four edges. Sand was continually added in increments of 100mm, surrounding the pier, until a final fill level of 700mm had been achieved and a free space of approximately 300mm from the top of the steel box remained.

Figure 6. CR9000x Datalogger.

The accelerometer was placed on the top of the pier (Figure 7), ensuring that it was orientated correctly and fixed in place. The datalogger (Figure 6) was connected and programmed accordingly using the loggernet software to take readings at a frequency of 1000 Hz. The free acceleration of the pier was measured after subjecting it to an impulse force at the free end in order to infer initial displacement [9]. This step was repeated a number of times to ensure consistency of data. To simulate the effects of scour, it was decided to add sand to the box in 100mm increments. This is in essence the reverse of a scour process but it allows for re-testing by removing the sand layers thereafter. The sand was re-compacted after each fill event. A new acceleration signal was obtained at each new level to display a static scheme of signals as a scour process develops over time. The acceleration signal for these steps should be different from those found previously.

For continuity of data, a normal scour process was also simulated upon reaching the fill capacity, whereby sand was removed from around the pier in increments of 50mm and new acceleration signals were obtained at each level. The purpose of re-testing was to offset the effects of placing new sand on top of existing layers and the associated loss of homogeneity in soil conditions associated with this. For instance, the new sand that was added may have had a different moisture content to that of the existing sand in the box and the effects of this may have gone un-noticed. For this reason, it was imperative to leave the latter testing phase until some time had passed and where the sand could gain a more uniform constitution. Moisture contents were assessed over a number of days prior to re-testing.

Once all the data had been obtained, an FFT analysis was undertaken in MATLAB to ascertain the natural frequency peaks at each bed level.

Figure 7. Attaching accelerometer.

5 RESULTS

The levels at which scour simulation takes place are divided up as base level 0, level 1, level 2 and level 3. These correspond to the fill levels for initial scour testing and represent sand depths along the pier separated by 100mm intervals (Figure 8).

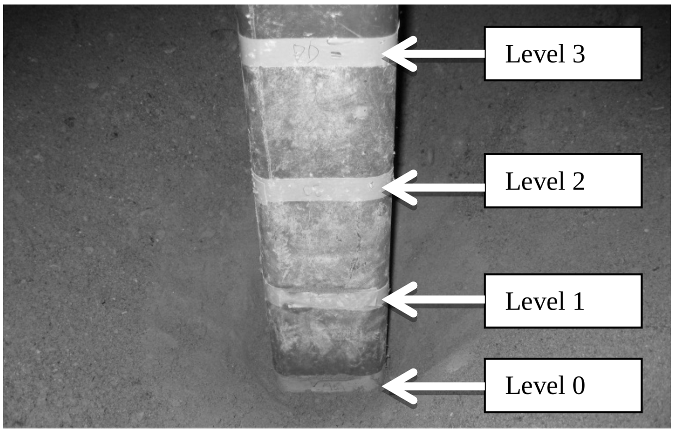

Figure 8. Bed Levels.

At each bed level, an acceleration signal was obtained in the form of a voltage readout vs. time from the datalogger. This was then converted to acceleration in terms of gravity (g) using the conversion factors specified by the manufacturer. The signal obtained varies as the pier vibrates. A typical example is displayed in Figure 9. The time period is normalised for the purpose of graphical representation.

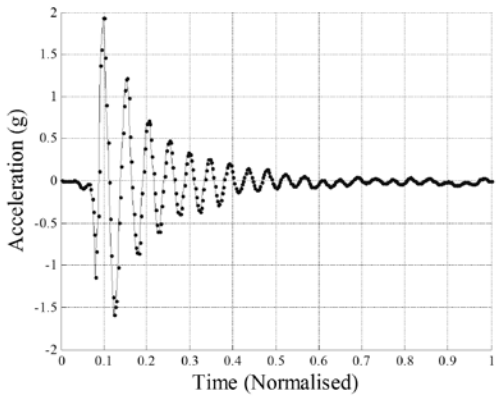

Figure 9. Typical Acceleration Signal.

This signal was then fed through an FFT in MATLAB, where it was converted into a frequency plot, the magnitude of which is displayed on the vertical axis. The plot corresponding to the signal in Figure 9 is shown in Figure 10. The peak value of the graph corresponds to the natural frequency value.

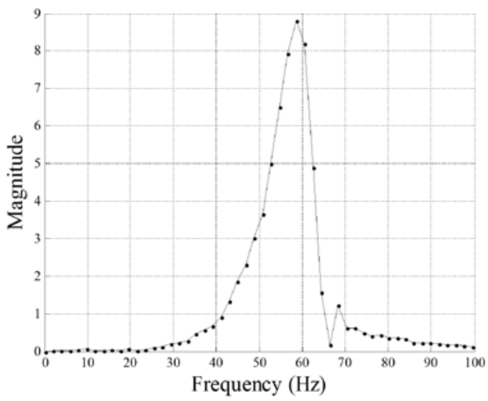

Figure 10. Typical Frequency Plot.

The actual signal obtained can be compared to the theoretical signal for an upright cantilever with simplified lumped mass at the top founded on an infinitely stiff base as calculated with Eqn. 1.

$$f = \frac{1}{2\pi}\sqrt{\frac{3EI}{\rho A L^4}} \qquad (1)$$

where f is the frequency (Hz), E is the Young's modulus (GPa), I is the moment of inertia (m^4), ρ is the density (kg/m^3), A is the area (m^2) and L = length (m)

Values from Eqn. 1 show the upper bound obtainable solution. Table 3 shows the pier responses during the fill testing phase, which are graphed in Figure 11.

Table 3. Frequency Responses.

Level:	Pier Length (m)	Theoretical Frequency (Hz)	Measured Response (Hz)
Level 0	0.968	56.0	29.58
Level 1	0.868	69.6	42.82
Level 2	0.768	88.9	60.22
Level 3	0.668	117.5	73.89

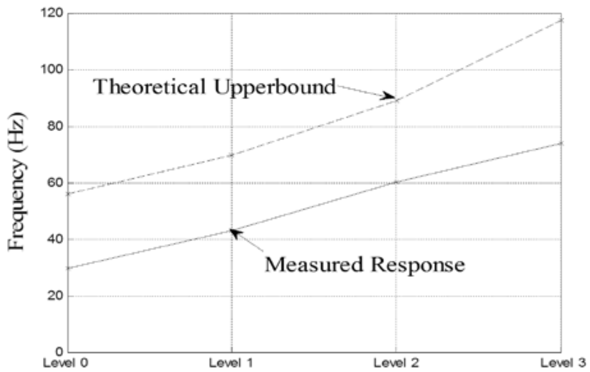

Figure 11. Frequency Change with Increasing Bed Level.

Once the fill testing phase has been completed, actual scour simulation may take place by manually removing sand from around the base of the model pier in the reverse sequence of the original testing regime. The benefit of this is that sand properties (such as moisture content) will remain constant throughout the experiment duration (which is short). Thus the only factor affecting stiffness changes is the level of sand on the pier itself. Sand is removed to level 2 and removed in 50mm increments thereafter. These recorded responses are set out in Table 4 and graphed in Figure 12.

Table 4. Frequency Responses.

Level:	Pier Length (m)	Theoretical Frequency (Hz)	Measured Response (Hz)
Level 2	0.768	88.9	68.36
Level 2-1	0.818	78.4	59.9
Level 1	0.868	69.6	49.16
Level 1-0	0.918	62.2	41.83
Level 0	0.968	56	34.18

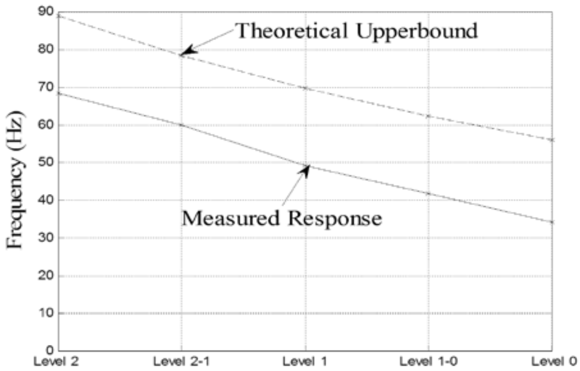

Figure 12. Frequency Change with Decreasing Bed Level.

The purpose of removing the top layer of sand from level 3 to level 2 is to offset the fact that surface sand may exhibit different properties to other sand at greater depths. For reasons of homogeneity, the results from level 3 to level 2 are omitted. In-situ sand properties should be more homogeneous at levels below these.

6 DISCUSSION

As is evident, changes in the natural frequency can be detected by changing the level of the sand around the pier in the laboratory experiment. It must be noted, however, that the conditions in which this experiment was undertaken are highly idealised. An actual bridge pier does not have a free end, thus placement of accelerometers on real bridges would require a more detailed primary analysis of where the maximum oscillations are likely to occur. The presence of a bridge deck may increase the stiffness significantly. Further research into this is underway. In reality, it is assumed that train loading will provide the impulse force required for the bridge to oscillate and that changes in frequency will relate to compromised support due to scour, amongst other causes.

The results displayed here are in line with physical expectations. A decrease in frequency is noted as the effective length of the pier increases. The fact that this change is measurable at this laboratory scale is encouraging and further research at larger scales is planned. It must be noted, however, that larger structures will undergo much smaller frequency variations upon changes to effective lengths. Therefore, accurate measuring equipment is vital at these scales. The results obtained here also lie below the theoretical upper bound that an infinitely stiff foundation would provide. Although this is based on some simplifying assumptions, it shows that the results are realistic in this light.

From the data in Tables 3 & 4, we can see that different frequency values were obtained at equivalent bed levels. The reason for this is as outlined previously in Section 4. The scour simulation phase of removing sand from around the pier was undertaken several days after the initial fill phase. Over these few days, the moisture content of the sand lowered due to surface evaporation and downward draining. This had the result of stiffening the sand, which explains the higher frequencies obtained in Table 4 relative to Table 3. In a saturated hydraulic environment, where scour would occur, this would not be an issue.

An issue that arises with this test is that the steel box in which the pier is placed is subject to vibration as the pier is excited. It was initially intended that the mass of the box would be such that the effects of vibrating the pier would not transfer into the box itself. This may lead to skewed results being obtained and therefore research in the free field, without the constraints of a rigid boundary, is required to offset the effects of this.

Another point of note is that the sampling rate of 1000Hz may not be adequate in determining the exact frequency of this structure since the period of vibration is in the region of fractions of a second. Upon close analysis, only a small sample length is obtained during the actual vibration, since it dampens quite rapidly. Further research at higher sample rates would be of help in determining more exact values of fundamental frequencies at this scale.

Attempts were made to make correlations between the damping ratios of the signals at different bed levels. No consistent trend was observed when using the logarithmic decrement method [9], [10]. This is most probably due to the small scale of the experiment. Therefore the results of this have been omitted and research on larger structures is recommended.

7 CONCLUSIONS AND RECOMMENDATIONS

Frequency changes are shown to have potential in detecting scour around the base of an upright cantilever pier structure. The measured responses are shown to follow reasoned logic. This experiment has yielded interesting results and expansion of this data is required. The authors feel that some of the issues encountered at this scale may not occur at larger scales, such as the issue of low sampling in the vicinity of the vibration and poor correlation of damping ratios. These issues may simply be due to the scale of the experiment. Larger structures will have lower fundamental frequencies and damping estimation may be more accurate as higher relative sampling rates will yield more accurate acceleration curves. Conversely, frequency changes at larger scales will be more difficult to detect as only minor variations will exist as bed levels vary. For both of these reasons, it is recommended that this analysis be expanded to larger structures and undertaken in the free field. This work is currently in progress.

ACKNOWLEDGEMENTS

The authors would like to acknowledge Dr David Igoe, Dr Paul Doherty and Mr Derek Holmes for their help with the set-up of the experiment. Special thanks to Mr Mike Collins, Campbell Scientific, UK for his advice on wiring the accelerometer.

The authors would like to acknowledge the support of the Earth and Natural Sciences (ENS) Doctoral Studies Programme, funded by the Higher Education Authority (HEA) through the Programme for Research at Third Level Institutions, Cycle 5 (PRTLI-5), co-funded by the European Regional Development Fund (ERDF).

REFERENCES

[1] L. Hamill, Bridge Hydraulics. 1999.

[2] M. C. Forde, D. M. Mccann, M. R. Clark, K. J. Broughton, P. J. Fenning, and A. Brown, “Radar measurement of bridge scour,” NDT&E International, vol. 32, pp. 481-492, 1999.

[3] K. Wardhana and F. C. Hadipriono, “Analysis of Recent Bridge Failures in the United States,” Journal of Performance of Constructed Facilities, pp. 144-151, 2003.

[4] F. De Falco and R. Mele, “The monitoring of bridges for scour by sonar and sedimetri,” NDT&E International, vol. 35, pp. 117-123, 2002.

[5] T.-hsuan Lin, Y.-chi Lu, and S.-lin Hung, “Field Study of Bridge Scour Using Imote2 . NET-Based Wireless Monitoring System,” 2011.

[6] S. Foti and D. Sabia, “Influence of Foundation Scour on the Dynamic Response of an Existing Bridge,” Journal Of Bridge Engineering, no. April, pp. 295-304, 2011.

[7] J.-louis Briaud et al., “Realtime monitoring of bridge scour using remote monitoring technology,” 2011.

[8] L. N. Virgin, S. T. Santillan, and D. B. Holland, “Effect of gravity on the vibration of vertical cantilevers,” Mechanics Research Communications, vol. 34, no. 3, pp. 312-317, Apr. 2007.

[9] A. K. Chopra, Dynamics of Structures. A Primer. Earthquake Engineering Research Institute, 1981.

[10] G. Gutenbrunner, “Sensitivity Studies on Damping Estimation,” vce.at, 2007.

Effect of the type of viscosity-modifying admixtures and metakaolin on the rheology of cement-based grouts

M. Sonebi[1], MK. Adzri[1], and S. Taylor[1]
[1]School of Planning, Architecture and Civil Engineering, Queen's University Belfast, Belfast, BT7 1NN, Northern Ireland, UK
email: m.sonebi@qub.ac.uk; mhajali02@qub.ac.uk; s.e.taylor@qub.ac.uk

ABSTRACT: The Viscosity-modifying admixtures (VMAs) contribute to the control of the rheology of grouts and are used to enhance plastic viscosity, cohesion, stability, and resistance to bleeding of cement-based systems. This paper reports the results of an investigation on the effect of metakaolin (MTK), VMAs, namely two types of diutan gums and a welan gum, plus a superplasticiser, on the rheology behaviour of cement grouts. All mixes were made with polycarboxylic superplasticiser at 0.6% and 0.9%. The dosages of VMAs were 0.05%, and 0.10%, with a fixed water-to-binder ratio of 0.40. The investigated fresh properties of the grouts included the mini-slump flow, plate cohesion, and rheology parameters: namely yield value and plastic viscosity. The rheological parameters were obtained using a vane viscometer. Control grouts (with and without superplasticiser and VMA) were also tested and compared to mixes containing VMAs. The results indicated that the incorporation of MTK reduced the fluidity and increased the plate cohesion and yield stress, and plastic viscosity due to the higher surface area of MTK. The diutan gum grouts improved the grout fresh properties and rheology compared to the welan gum grouts.

KEY WORDS: Metakaolin, Plastic viscosity, Superplasticiser, Viscosity-modifying admixture, Yield stress

1 INTRODUCTION

Grouts are widely used in injection grouting of cracks in massive structures since their physical and mechanical properties can be easily controlled. Viscosity-modifying admixtures (VMAs) are commonly used in conjunction with superplasticiser (SP) where highly flowable, yet stable and homogeneous, cement-based grouts are needed for applications, such as injection grouting, post-tensioning grouting and anchorage sealing, etc. [1, 2]. Grouts containing VMA are also used for filling ducts, where it is important to ensure high resistance to sedimentation and bleeding, hence ensuring corrosion protection of stressed tendons. Moreover, VMAs are widely used in concrete applications, such as self-compacting concrete, underwater concrete, and shotcrete [1-7]. VMAs are highly effective in controlling bleeding as the long-chain molecules of VMA adhere to the periphery of water molecules, thus it adsorb and fix part of mix water which in tem increase the yield value and plastic viscosity of the cement-based grouts. Several researchers have related the improvement in rheological properties and the performance of cement-based grout to the addition of VMA and SP [1-7]. Most VMA solutions are pseudo plastic (shear thinning) which means that an increased shear rate causes a progressive decrease in apparent viscosity [6, 7].

This investigation aimed to characterise the fluidity and the cohesiveness measured by mini-slump, Lombardi plate cohesion and the rheological parameters of diutan gums and welan gum and to evaluate the influence of the dosages of VMAs and SP on the fresh properties and the rheological parameters of grouts made with 0.40 water-to-binder (W/B). The effect of the replacement of cement by 7% metakaolin (by mass) is also investigated with the variation of the dosages of VMAs and SPs. A similar OPC control grout and another one made with MTK and without VMA and SP were investigated in order to compare the fluidity and the rheological parameters to VMA-grouts.

2 EXPERIMENTAL PROGRAM, MATERIALS AND TEST METHODS

2.1 *Experimental program*

In this investigation, fifteen grouts were made with W/B of 0.40 (Table 1). Fresh properties of cement-based grouts made with 7% of metakaolin, incorporating three types of VMAs welan gum (WG), and two diutan gums (DGs), namely DG-1 and DG-2, were investigated. Two dosages of the VMAs were used (0.05% and 0.10% by the mass of mixing water) along with two dosages of SP (0.6% and 0.9% by the mass of cement, Table 1). Additionally, two systems: one without any SP and VMA and another with MTK were tested. The following properties of the grouts were examined: the mini-slump flow, Lombardi plate cohesion, and rheological properties (yield value and plastic viscosity).

2.2 *Materials used*

Portland cement CEM I in accordance with BS EN 197-1: 2000 was used in all mixes. The chemical and physical characteristics of the cement and metakaolin (MTK) are given in Table 2. A synthetic polycarboxylate polymer-based superplasticiser (SP) with solid content of 42% and specific gravity of 1.08 was used. The water content in the mixes was adjusted to take into account the water contained in the SP. Two types of DGs: DG-1 and DG-2 and one WG were employed as VMAs (their quantities are expressed per mass of the mixing water).

Both welan and diutan gums are high molecular weight, long chain microbial polysaccharides. Welan gum has monosaccharide side-chain (L-rhamnose, partially replaced by L-mannose), while diutan gum incorporates disaccharide L-rhamnose side-chain. In both cases, the side-chain is linked to one of the two glucose units [8, 9, 10]. The molecular length of diutan gum is up to three times longer than that the welan gum. The molecular weights of diutan and welan gum are about 2.88 to 5.18 million Daltons and 0.66 to 0.97 million Daltons, respectively [10]. Diutan and welan gums are compatible with cement hydration products. According to the supplier of the VMAs, the viscosity obtained with tap water of DG-2 was higher (3000-6000 mPa•s) than those of DG-1 and WG (>2800 mPa•s and 1000-2000 mPa•s, respectively). This indicates that DG-2 has higher polymerisation degree (longer chains) than the two other VMAs [10].

Table 1. Mix composition of the grouts.

Description	Dosage [%]			
	Cement	MTK	SP#	VMA*
Ref1-No VMA/SP/MTK	100	0	0.0	0.00
Ref2-No VMA/SP-7%MTK	93	7	0.0	0.00
MTK-6% SP	93	7	0.6	0.00
DG-1 =0.05%	93	7	0.6 & 0.9	0.05
DG-1 =0.10%	93	7	0.6 & 0.9	0.10
DG-2 =0.05%	93	7	0.6 & 0.9	0.05
DG-2 =0.10%	93	7	0.6 & 0.9	0.10
WG =0.05%	93	7	0.6 & 0.9	0.05
WG =0.10%	93	7	0.6 & 0.9	0.10

- by weight of cement, * - by weight of water

Table 2. Chemical and physical properties of cement and metakaolin.

	Cement	MTK
SiO_2	20.8	51.7
Al_2O_3	5.0	43.2
Fe_2O_3	3.2	0.4
MgO	2.6	--
CaO	63.7	--
Na_2O eq	0.39	--
SO_3	2.83	--
LOI	0.65	0.16
Specific gravity	3.08	2.2
% passing 45 µm sieve	85	--
Mean particle size [µm]	22	1.4
Specific surface area [m^2/kg]	360	13200

2.3 Mixing and testing procedures

The grouts were prepared in a 5-L planar-action high-shear mixer, in 2-L batches. Tap water (16 ± 0.5 °C) and SP were added together to the mixer and mixed one minute at a low speed (140 rpm). Next, premixed solid components, such as cement, MTK and VMA, were introduced within 2 min, at the end of which the mixer was stopped and any possible lumps of solids formed were crushed (1 min). Then, the grout was mixed again for 2 min at a higher speed (285 rpm) and for 1 min at the low speed (140 rpm). The temperature of the grouts after mixing was 20 ± 1 °C.

For all tests, the timing is given from zero time – that is, the time when the cement particles come into contact with the mixing water. The mini-slump flow test was started at 6 min (immediately after the end of mixing). The transparent cone-shaped mould described elsewhere [11] was placed in the centre of a smooth Plexiglas plate. After filling with grout, the cone was gently lifted (approximately 30 s after finishing of placing of the grout). When the flow stopped, the spread of the grout was measured with a ruler in two perpendicular directions.

The cohesion of the grout was determined at 8 ± 1 min with a Lombardi plate cohesion meter [12]. A thin galvanized steel plate (100×100×1 mm) was immersed in the grout and hung on a stand placed on an electronic balance. The mass of the grouts that remains on the plate were recorded when the dripping of the grout had stopped. This test was followed by the fresh density measurement of the grout with a mud balancer, as specified in Reference [13]. Knowing the fresh density of the grout, it is possible to calculate the mean thickness on the grout of the plate.

The rheological measurement was carried out with a computer-controlled vane viscometer (Haake VT550). At 13 ± 1 min, approximately 800 ml of the sample was introduced into a plastic container where the vane was plunged. After 30 seconds rest, the test was started, and the same testing parameters as above (velocities and their durations) were followed. The shear rate steps used in this investigation are presented in Figure 1. For each step, when the equilibrium was reached, the strain rate was increased from an initial value of 0.188 s^{-1} to a top value of 41.6s^{-1} (ascending curve), and afterward, it is decreased to ending the descending curve.

The two rheological parameters, yield stress (τ_0) and plastic viscosity (μ_p), were obtained with Herschel-Bulkely model by fitting the shear stress-shear rate data. This model is given by equation (1):

$$\tau = \tau_0 + k\gamma^n \qquad (1)$$

where τ_0 is the yield stress, k is the consistency, and n is the characteristics of the mix's pseudoplastic behaviour. The mix is shear-thinning when n < 1 and shear-thickening when n > 1.

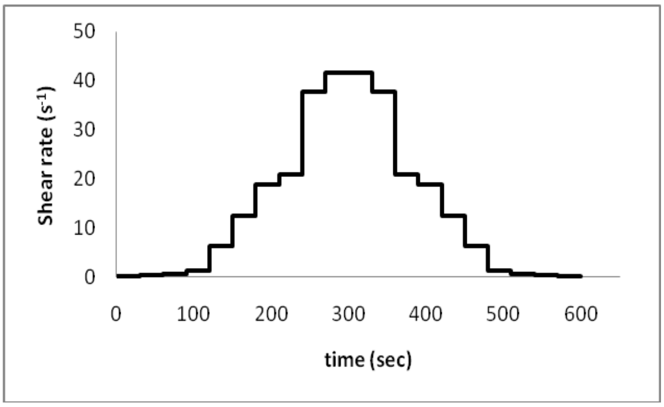

Figure 1. Shear rate steps applied to paste using step-by-step procedure.

3 RESULTS AND DISCUSSION

3.1 Effect of dosages of VMAs, SP, and MTK on mini-slump

Results of the mini-slump flow are shown in Figure 2. The reference mix Ref1 (No SP/VMA/MTK) had a low spread, whereas the incorporation of the 0.6% (Figure 2(a) or 0.9% (Figure 2(b) of SP dramatically increased the spread. The increase of dosage of SP is shown to exhibit the greatest effect on the mini-slump. This is attributed to better steric and electrostatic repulsions among cement particles that react with the SP which leads a better deflocculation of the particles in the paste.

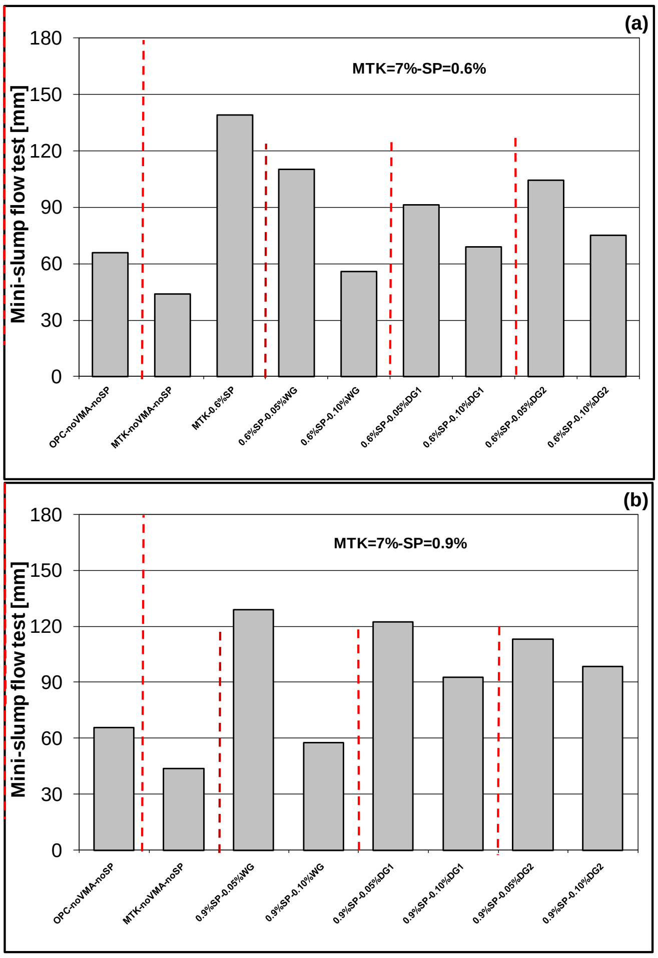

Figure 2. Variation of mini-slump with type of VMAs, SP and MTK.

The replacement of cement by 7% MTK led to a significant reduction of fluidity from 66 mm (Ref1) to 44 mm due to the high surface area of MTK. It can be noted that high amount of surface of area of MTK is likely to reduce the amount of SP per unit surface area so that Van der Waals based particle-particle attractions may eventually become increasingly important.

The addition of any VMA decreased the spread. An increase of VMA (0.05% and 0.10%) at a fixed SP dosage caused a gradual reduction of the spread for both systems of MTK grouts (SP=0.6% and 0.9%, Figure 2). VMAs appear to have adsorbed and fixed part of free water, so this water is no longer available for lubrication of particles.

The trends obtained for both diutan gums (DG-1 and DG-2) in similar fashion. Even low dosage of DG-1 and DG-2 (0.05%) in grouts containing 7% MTK and 0.6% SP significantly decreased the spread flow (93 mm and 105 mm, respectively), compared to the systems without VMA (139 mm). It was not so significant in the case of WG (126 mm).

In comparison with the DGs, consecutive dosages of the WG resulted in a sharper decrease in the mini-slump flow for any given dosage of SP. Therefore, the rheological behaviour of the systems incorporating DGs were easier to control than those with WG. Worth mentioning, no significant difference was observed between the two DGs.

3.2 Effect of dosages of VMAs, SP, and MTK on plate cohesion

As expected, the addition of any VMAs affects significantly the cohesion plate values. An increase of VMA (0.05% and 0.10%) caused a gradual increase in the thickness of plate cohesion (Figure 3). The increase in cohesion was very sharp for grouts containing the welan gum. This can be attributed to the entanglement and intertwining of adjacent polymer chains. For any given dosage of SP and VMA, it can be noted that DG2 exhibited lower values of plate cohesion compared to grouts with DG2.

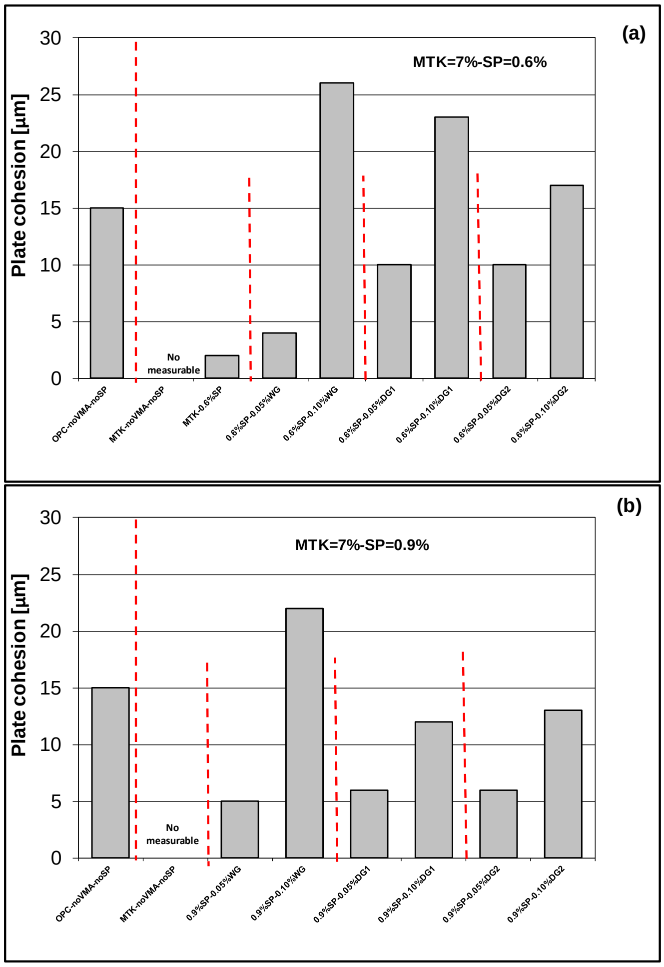

Figure 3. Variation of plate cohesion vs. VMAs, SP, and MTK.

Conversely, for any given VMAs, an increase in SP from 0.6% to 0.9% (Figure 3(a) vs. Figure 3(b)) led to a reduction in cohesion plate values. The addition of MTK is shown to increase the cohesion plate value. This can be attributed to high surface area of MTK which resulted in an increase of cohesion.

The effects of SP and VMAs confirm other findings on the effect of these chemical admixtures on cement grouts containing fly ash and limestone powder [6, 13].

3.3 *Effect of dosages of VMAs, SP, and MTK on yield value*

Figures 4(a) and (b) present the yield stress results of grouts made with OPC, and 7% MTK and two dosages of VMAs at 0.05% and 0.10% for dosages of SP of 0.6% (a) and 0.9% ((b), respectively. The Ref1 mix (No-VMA/SP) had a value of yield stress of 29.3 Pa. In none superplasticised mix, the addition of 7% MTK increased dramatically the yield value so the mix was very cohesive and it was impossible to measure the yield stress with the viscometer. This was due to the high surface area of MTK. Similar findings for MTK were also observed in previous work [14] using metakaolin blended cements. The incorporation of MTK resulted in increased yield stress in the case of MTK, whereas yield stress values decreased with the addition of SP. The addition of 0.6% SP decreased significantly the yield value due to the dispersion effect of SP on cement particles. Addition of SP produces a thicker adsorbed polymer layer and consequently weaker van der Waals attractions between the particles, therefore lower energy is needed to disperse the particles and secure lower yield stress [15].

In general, for any given dosage of diutan gums or welan gum, the increase in the dosage of SP resulted in a reduction of yield stress. For any given dosage of SP, the introduction of VMAs (DG1, DG2 or welan gum) resulted in significant increase in yield stress results. For example, for grout containing 0.6% of SP, the increase in concentration WG from 0.05% to 0.10% resulted in an increase in yield stress from 8.5 Pa to 78.2 Pa (9 times increase). In the case of DG1 and DG2, the increase in yield stress compared to the reference mix were approximately twice and half, respectively.

At low shear rate, where mini-slump flow and yield value are believed to characterise cement-based system rheology [13, 16], the polymer chains entangle and intertwine, thus increasing the apparent viscosity of the grout [7].

The comparison between the results of yield stress of diutan gums and welan gum indicates in general that for similar dosage of VMA the grouts containing diutan gums led to greater values of yield stress than those of welan gum particularly for a low dosage (VMA=0.05%). It can be attributed to the diutan's molecular weight and high pseudo-plasticity [10] and water retention. The increase of molecular weight led to improvement of water retention [17]. Thus, to achieve a similar viscosity, diutan gum required lower dosage than welan gum.

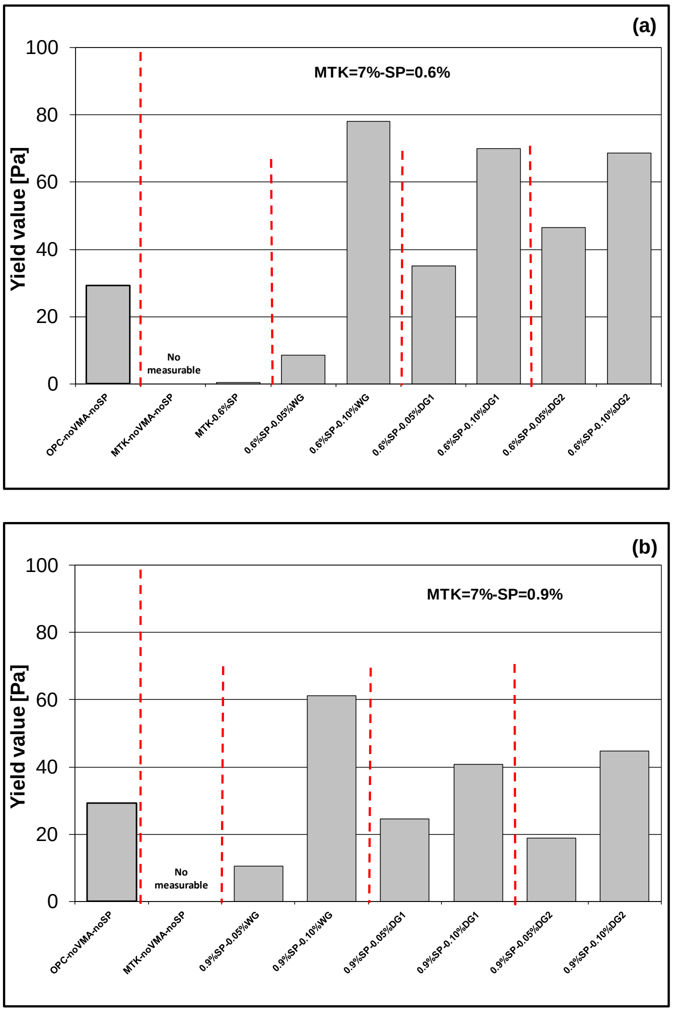

Figure 4. Variation of yield value vs. VMAs, SP, and MTK.

3.4 *Effect of dosages of VMAs, SP, and MTK on plastic viscosity*

Figure 5 describes the effect of MTK, VMAs and SP dosages and type of the corresponding VMAs on the plastic viscosity of grouts. The VMAs dosage had the greatest influence on plastic viscosities. The dosage of SP and MTK replacement level also influenced the plastic viscosity values.

An increase in VMAs dosage led to an increase in the plastic viscosity values for all of the grouts considered in this study. Adding 0.05% of WG, DG1, and DG2 to the mix made with 0.6% SP resulted in an increase in plastic viscosity of 380%, 815%, and 735%, respectively.

An increase in SP dosage induced a decrease in plastic viscosity values for any given dosage of VMAs. At 0.05% of VMAs, it appears that the plastic viscosity reduced significantly when the dosage of SP increased from 0.6% to 0.9% particularly for both diutan gums (DG1 and DG2).

It can also be observed that the addition of MTK resulted in a substantial increase in plastic viscosity due to the high surface area of MTK. Adding 7% MTK to the control mix without any SP and VMA led to very stiff mix and it was impossible to measure the plastic viscosity with Vane viscometer.

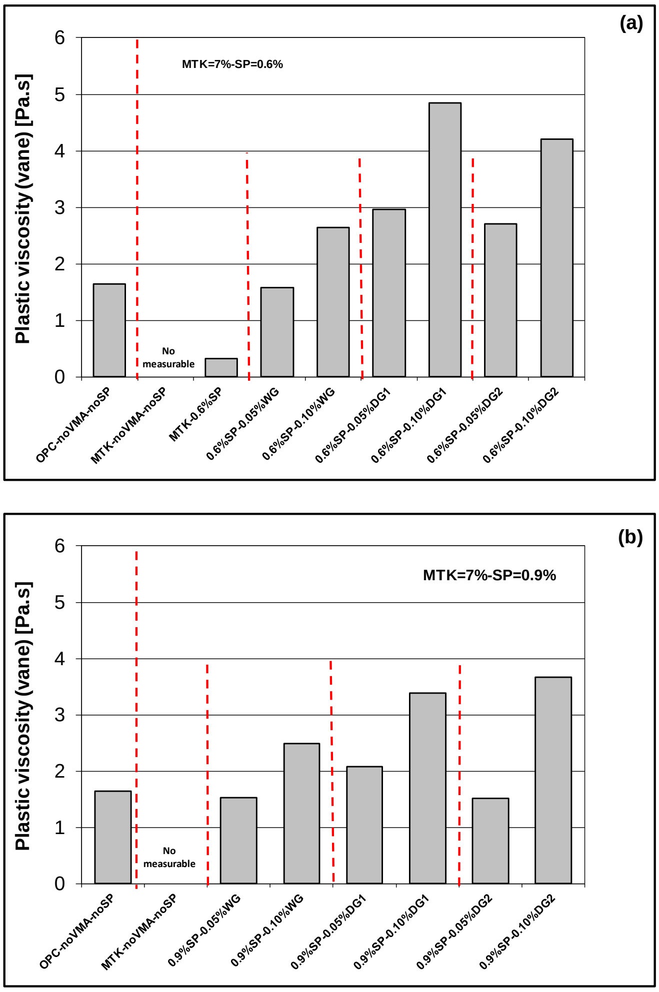

Figure 5. Variation of plastic viscosity vs. VMAs, SP, and MTK.

In general, the plastic viscosities of diutan gums indicate that for similar dosage of VMA, the grouts containing diutan gums had greater values of the plastic viscosities compared to those of welan gum. It can be attributed to the diutan's molecular weight and high pseudo-plasticity [10] and water retention ability [16].

4 CONCLUSIONS

Based on the results presented in this paper, the following conclusions have been drawn:

- The addition of all three VMAs caused an increase in the yield values and a reduction in the corresponding fluidity compared to the reference mix.
- Both plastic viscosity and cohesion plate values increased with the addition of all three VMAs.
- The increase of SP led to an improvement of fluidity and a reduction of the plate cohesion, yield stress, and plastic viscosity values. This has attributed to better steric and electrostatic repulsions among the cement particles that react with SP which leads a better deflocculation of the particles in the paste.
- The addition of MTK resulted in a reduction of fluidity and an increase in plate cohesion, yield stress, and plastic viscosity due to the high surface area.
- DGs were better in controlling grouts fluidity and flowability. No significant difference was observed between DG-1 and DG-2.

ACKNOWLEDGMENTS

The authors would like to acknowledge Optipozz Company and CP-Kelco for generously supplying free samples of MTK and VMAs, respectively.

REFERENCES

[1] Skaggs CB., Rakitsky WG., Whitaker SF., 'Applications of Rheological Modifiers and Superplasticizers in Cementitious Systems', Proceedings of Fourth CANMET/ACI International Conference on Superplasticizers and Other Chemical Admixtures in Concrete, Montreal, Canada, October 1994, (1994), 189-207.

[2] Khayat K.H., 'Viscosity-Enhancing Admixtures for Cement-Based Materials - An Overview', Cem. Concr. Compos., 20 (2-3) (1998) 171-188.

[3] Sonebi M., Tamimi A.K. and Bartos P.J.M., 'Application of Factorial Models to Predict the Effect of Anti-Washout Admixture, Superplasticizer and Cement on Slump, Flow Time and Washout Resistance of Underwater Concrete', Materials and Structures, 33(5)(2000) 317-323

[4] Lachemi M., Hossain KMA., Lambros V., Nkinamubanzi P.-C., Bouzoubaa N., 'Performance of New Viscosity Modifying Admixtures in Enhancing The Rheological Properties of Cement Paste', Cement and Concrete Research, 34(2) (2004) 185-193.

[5] Saric-Coric M., Khayat K.H., Tagnit-Hamou A., 'Performance Characteristics of Cement Grouts Made with Various Combinations of High-Range Water Reducer and Cellulose-Based Viscosity Modifier', Cem. Concr. Res., 33(12) (2003) 1999-2008.

[6] Sonebi M., 'Rheological Properties of Grouts with Viscosity Modifying Agents as Diutan Gum And Welan Gum Incorporating Pulverised Fly Ash', Cem. Concr. Res., 36 (9) (2006) 1609-1618.

[7] Sonebi M., 'Rheological Characterization of Cement-Based Materials Pastes Containing Diutan Gum and Limestone Powder', Proceedings of 12th International Congress on Chemistry of Cement, Montreal, Canada, 8-13 July 2007, (2007), CD, 10p.

[8] Stankowski J.D., Zeller S.G., 'Location of the O-acetyl group in welan by the reductive-cleavage method', Carbohydr. Res., 224 (1992) 337-341.

[9] Diltz S., Zeller S.G., 'Location of O-acetyl groups in S-657 using the reductive-cleavage method', Carbohydr. Res., 331 (3) (2001) 265-270.

[10] Phyfferoen A., Monty H., Skaggs B., Sakata N., Yanai S., Yoshizaki M., 'Evaluation of the biopolymer, diutan gum, for use in self-compacting concrete', Proceedings of the First North American Conference on the Design and Use of Self-Consolidating Concrete, Chicago, USA, (2002) 141-146

[11] Kantro D.L., 'Influence of Water Reducing Admixtures on Properties of Cement Paste - A Miniature Slump Test', Cem. Conc. Aggr. J., 2(2), (1980), 95-10.

[12] Lombardi, G., 'The Role of Cohesion in the Cement Grouting of Rock." Proceedings of Fifteenth Congress on Large Dams. International Commission on Large Dams, Q.53, R.B., 3, (1985) 235-261

[13] Svermova L., Sonebi M., Bartos PJM., 'Influence of Mix Proportions on Rheology of Cement Grouts Containing Limestone Powder', Cement Concrete and Composite, 25 (7) (2003) 737-749.

[14] Moulin E., Blanc P., Sorrentino D. 'Influence of key cement chemical parameter on the properties of MK blended cement', Cement Concrete and Composite, 23(6) (2001) 463-469.

[15] Lowke D. 'Interparticle forces and rheology of cement based suspensions'. Proceedings of the NICOM3 - Nanotechnology in Construction, Prague, 2009, 295-301

[16] Roussel N., Coussot P. 'Fifty-Cent Rheometer for Yield Stress Measurements: From Slump to Spreading Flow', J. Rheol., 49 (3) (2005) 705-718.

[17] Pouchez J., Peschard A., Crosseau P., Guyonnet R., Guilhot B., Vallée F, 'HPMC and HEMC influence on cement hydration', Cement and Concrete Research 36(2) 2006 288-294.

Evaluation of chloride ingress parameters in concrete using Backscattered Electron (BSE) imaging to assess degree of hydration – A proposal

A. Attari[1], C. McNally[1], M. Richardson[1]
[1]School of Civil, Structural and Environmental Engineering, University College Dublin, Ireland
email: azadeh.attari@ucd.ie, ciaran.mcnally@ucd.ie, mark.richardson@ucd.ie

ABSTRACT: The aim of current study is to propose a novel methodology for more precise modelling of diffusivity parameters in concrete. One of the main causes of deterioration of reinforced concrete structures is the corrosion of rebar due to penetration of chloride through the concrete cover. Since the most prominent mechanism of chloride transport in concrete is by diffusion, modifying the models currently used in estimating diffusion coefficient is of great importance for more realistic prediction of the extent of deterioration. This will enhance optimizing the extent and timing of required maintenance measures, resulting in considerable savings in infrastructure management. In the proposed methodology, degree of hydration and porosity of concrete are considered as indices of maturity and attempts are made to predict diffusion coefficient, based on the above mentioned parameters. While indirect methods based on chemically bound water or the released heat of hydration are the common approaches for determining degree of hydration, this study proposes the use of backscattered electron images for measuring degree of hydration. In BSE images, different phases of concrete display various levels of grey colour intensity based on their mean atomic number. Different phases of concrete can therefore be distinguished based on their displayed colour. A pixel by pixel count, using image analysis software, reveals the amount of pores, hydrated cement particles and anhydrous cement grains in each image. This data can be used to estimate degree of hydration of concrete samples, in a direct method, based on the amount of cement gel formed during hydration. The results to date are encouraging; however, the effectiveness of the proposed method can be further enhanced by increasing the quality of images compared to what has currently been produced.

KEY WORDS: Scanning Electron Microscopy, Hydration, Image analysis, Diffusion Coefficient, GGBS

1 BACKGROUND TO PROPOSAL

1.1 Context – bridge infrastructure management

Corrosion of reinforcement is one of the main sources of durability failure in reinforced concrete infrastructures. Corrosion occurs due to the depassivation of reinforcement by carbonation or the build-up of chlorides in the concrete cover. The corrosion products have a greater volume than the original source material, exerting internal pressure on the concrete surrounding the rebar, resulting in cracks and eventual spalling of the concrete cover.

The cost of repair and maintenance of deteriorated infrastructure takes up a huge portion of the annual budget available to road authorities for highway infrastructure design, construction and maintenance. Therefore, any improvement in the reliability of predicting timing and the extent of required maintenance will result in considerable cost savings. Reliable modelling of chloride transport through the concrete cover, an essential part of any life-time prediction model, is of ongoing concern to concrete technology researchers.

The current work proposes a novel methodology for evaluating the true chloride diffusion characteristics of concrete. The proposed method is non-destructive, enhancing its applicability to bridge management.

1.2 Chloride diffusion coefficient

There are three mechanisms of chloride ion transport in concrete: capillary absorption, hydrostatic pressure and diffusion [1]. Among these, the most important is diffusion, which is the movement of chloride ions through continuous liquid phases of concrete pore solution, under a persisting concentration gradient [2]. Crank's error function solution to Fick's second law of diffusion is widely used for modelling diffusion of chloride ions into concrete [3]. The diffusion coefficient of concrete is a key parameter in this equation used to characterise the performance of concrete in resisting chloride ingress.

More reliable estimation of this parameter is therefore of a great importance. Although it is well-documented in the literature that diffusion coefficient of cementitious systems decrease over time due to chloride binding, the refinement of pore structure and continued hydration of cement [4], some of the more popular models for chloride transport do not consider this effect and rely on a constant diffusion coefficient value over the lifetime of the structure at time of evaluation.

Utilising a constant value for diffusion coefficient over the life-time of structure leads to overestimation of chloride ingress and subsequent conservative durability design. This is even more noticeable when Supplementary Cementitious Materials (SCMs) are present in the concrete mix. For example ground granulated blast-furnace slag (GGBS) increases the amount of Calcium Silicate Hydrates formed in the cement paste over a longer hydration period [5].

1.3 Modelling chloride diffusion coefficient

Several models have been proposed so far to consider the decrease in diffusivity of concrete. Some of them use the mix proportions as their input parameters, while others describe this reduction solely as a function of time [6]. However, the refinement of pore structure is not only a function of time or ageing of the specimens; some of the other influential parameters to be mentioned are curing condition and temperature, compaction, porosity and pore size distribution [2]. Considering all these various factor, it is postulated that maturity of concrete is the most appropriate factor to cover these different aspects.

Degree of hydration (α) is defined as the ratio between the quantity of hydrated cement grains and the original quantity of cement grains available in the mix, and increases with concrete age and maturity improvement and can be considered as an indication of maturity [7]. The proposed methodology utilises the ability to determine degree of hydration by backscattered electron imaging.

2 PROPOSED METHODOLOGY FOR MODELLING CHLORIDE DIFFUSIVITY

2.1 Novel numerical modelling of D_{eff}

While indirect methods, based on the amount of heat generated during hydration are the most commonly used approaches for determining degree of hydration [7], a more direct method is proposed, based on analysing Backscattered Scanning Electron Microscopic images. In this technique, the quantity of each phase in cement paste is determined based on the various grey colour levels they display. In this study, the target is to quantify porosity and the amount of anhydrous cement grains in the mix, and to then use these values in order to estimate the degree of hydration.

Then, a novel numerical model is sought to predict the changes in diffusion coefficient, based on maturity of concrete and degree of hydration development. This is being developed through an experimental programme studying diffusion coefficient and degree of hydration at specific time intervals. Special consideration is being given to concrete mixes with supplementary cementitious materials.

2.2 Determining the degree of hydration by BSE

The rate of hydration development depends on too many factor to be easily determined using a pure mechanistic model. Therefore, experimental approaches based on the amount of chemically-bound water, or the amount of heat generated during hydration has commonly been employed for indirect characterisation of hydration process in cementitious system. However, it is widely accepted that this way, making a precise estimate of the amount of cement gel formed in the concrete mix is unlikely [7]. Therefore the method adopted here for characterising the formation of hydration products and determining the degree of hydration of the mix is to use backscattered scanning electron microscopy.

Image analysis is undoubtedly a valuable technique to quantify the hydration degree, whatever the material maturity may be [8]. Images are taken from flat, polished surface of concrete specimens at maturity levels corresponding to those of specimens when diffusion coefficients were measured. Image processing is employed then, to determine the quantity of different phases in cement paste, based on the various grey colour levels they display in the images. This procedure allows for the determination of porosity and also the ratio of anhydrous remnant cement grains to the original quantity of cement grains by pixel count of the relevant phases. This ratio is then used as an indication of the hydration improvement.

Hydration degree is then obtained using Equation 1 [8]:

$$\alpha = 1 - \left(A/\Gamma \right) \tag{1}$$

where α is the hydration degree, A represents the amount of anhydrous phase in terms of total cement paste, and Γ is the initial volume fraction of cement grains present in the fresh paste (excluding the aggregates).

2.3 Relevant aspects of scanning electron microscopy

Image analysis of backscattered electron images has often been used to quantify the microstructure of cement pastes, including the determination of porosity, pore structure, anhydrous cement content and characterization of the structure of fresh cement paste [9].

Scanning Electron Microscopy (SEM) is capable of reflecting the differences in atomic numbers by scanning a high energy electron beam across the surface of concrete. In the case of a low atomic number material, most of these electrons are absorbed, and little scattering takes place [10, 11]. The signal resulting from the interaction of electron beam and the specimen, which is called the backscattered electron, will be measured by the equipment and the corresponding colour will be displayed on the image. Although SEM images are monochrome, since they only display the difference in the electron flux, each pixel in the image will have one of the 256 different levels of intensity of the grey colour. Different particles in the matrix can then be distinguished based on the displayed colours [10]. The anhydrous cement particles have higher atomic numbers compared to the components of hydration products, and therefore they appear brightest in the BSE images. This property can be expressed through the backscattered electron coefficient (Z), which is a function of atomic number of the material [12].

SEM also produces X-ray signals, which are able to identify elements on a continuous spectrum by the position of their peaks [10, 13]. This option can also be used in the cases where contrast between the colours displayed on BSE images is so weak that different materials cannot be discriminated [10].

3 EXPERIMENTAL PROGRAM

3.1 Materials

The investigation is being conducted through samples derived from 4 different concrete mixes based on limestone cement (CEM II/A-LL), with various replacement levels of GGBS. Mix proportions are presented in Table 1. The recent widespread application of SCMs in concrete mixes, underscores the need for more close investigation of their properties.

Table 1. Material proportions for the four different mixes (in kg per cubic metre of concrete).

GGBS (%)	Cement	GGBS	Sand	Coarse 5-10 mm	Coarse 10-20 mm	Water
	323	0	1003	330	660	163
30	222	95	987	325	649	177
50	160	160	995	328	655	169
70	96	224	994	327	654	170

3.2 Rapid Chloride Migration test

Cores of 100 mm diameter were drilled from 300 x 300 mm slabs of concrete, 150 mm deep, cast from each mix. These were tested to determine diffusion coefficient at different intervals during the first 6 months after casting. Diffusion Coefficients are measured using Rapid Chloride Migration test, in accordance with NT Build 492, NORDTEST standard [14]. Samples are tested at regular intervals to allow for characterisation of the influence of pore structure refinement with respect to time on the improvement of impermeability.

3.3 Preparing samples for BSE

Specimens used in this experiment require measures to arrest hydration through control of access to water in order to preserve them in the target level of maturity without their degree of hydration being changed.

Also, the intensity of each pixel's colour in the BSE images not only depends on the atomic number of the materials, but also on the topographical variations on the surface of the specimen. Therefore, in order to have a crisp image, with sharp distinction of the phases, it is essential to minimize these variations, and to produce a finely ground and polished surface [15].

It is the objective of specimen preparation to provide for the above mentioned measures. In the case of poor preparation, contract and clarity of the image will decrease, and the inter-mixed phases will not be discerned accurately [16].

3.3.1 Drying

The specimens are immersed in acetone at specific ages, once they have reached the desired degree of hydration. This is in order to stop further hydration of concrete [17], and the specimens can be left in acetone for several hours; they are then placed in a dessicator with anhydrous calcium chloride and held at a vacuum pressure of approximately 0.5 torr overnight, as recommended in [17], so that no water remains in the pore structure of concrete.

3.3.2 Resin Impregnation

After drying, the specimens are resin-impregnated under vacuum. By keeping the specimens under the vacuum, we can assure that the air voids and pores are filled with resin. Resin will preserve the original microstructure, enabling it to withstand the stresses caused by polishing and grinding, and prevents void walls from collapsing during polishing and grinding of the sample. Since epoxy impregnation is performed ahead of grinding and polishing, it becomes evident that pores filled with epoxy resin are real features of the microstructure, and not a result of particles being plucked out during preparation. Filling the voids with resin is also essential in order to obtain the desired flatness in the surface of specimen. Also, since electrons tend to accumulate in empty pores, the epoxy resin is used to bridges the pore and prevents charging. Resin impregnation produces a solid mass of the original sample for grinding and polishing, and improves the overall integrity and ease of handling [12, 16, and 18].

3.3.3 Grinding and Polishing

Grinding is performed using Silicon Carbide sheets with grits sizing from 220 to 1000. Specimens are polished afterwards with Silicon Carbide paper of size 2400 and a fine cloth like polishing paper as the final stage. Special care should be taken at this stage, since excessive polishing wears away the relatively soft hydration products, which can lead to the introduction of further topographical variations to the surface of specimen [17].

3.4 Image processing

Key parameters in the procedure of image acquisition are the choice of appropriate accelerating voltage and magnification.

Lower voltages will result in low contrast of the image, which makes it difficult to discern the features of the image. However, increasing the voltage will also reduce the resolution of images, leading to the possible loss of information about the features of the specimen being investigated. The choice of proper magnification will also involve a compromise between resolution and the size of sampling area. Increased magnification will increase the resolution of images, but at the same time, it corresponds to a small sampling area. With smaller sampling areas, the minimum number of required images to produce a reliable estimate of the features on the surface of specimen increases noticeably [17, 12].

In this study, an accelerating voltage of 15.0 kV is used. Images are taken from 5 arbitrary selected points of view, at the magnification of 500X. This magnification produces a resolution of 0.5 μm per pixel. It has been shown that the estimated area fraction of different phases of cement remains almost the same after four images are averaged at this magnification [10]. The current study however, utilizes at least 5 images from each specimen.

Consequently, these images should undergo the procedure of image analysis in order for the different phases to be distinguished. This is in fact composed of two distinct steps. Image processing which is used to enhance the details and feature clarity of the image, and image analysis in order to measure those parameters such as area fraction, size and distribution of the features of interest [10]. One of the stages of image processing is segmentation, through which different features of the image are separated based on the intensity of grey colour of pixels [11]. When segmentation is applied to an image, a brightness threshold is defined, and the pixels which satisfy the given criteria are assigned a true value (are set to one), while others are labelled false (or are given the value of zero). Thresholding methods can be applied either manually or automatically [19].

4 RESULTS AND DISCUSSION

Results of the experiment to determine diffusion coefficients are provided in Figure 1 and Table 2. It can be seen that the values obtained for diffusion coefficient decrease, as expected, with the ageing of concrete and increasing GGBS replacement levels.

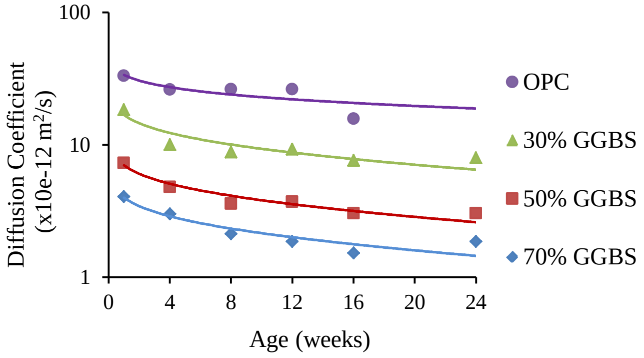

Figure 1. Trends of diffusion coefficient change.

Table 2. Diffusion coefficients of the 4 mixes during the first 6 months of concrete age.

Age (weeks)	70% GGBS	50% GGBS	30% GGBS	Plain OPC
1	4.06	7.32	18.42	33.35
4	3.01	4.80	10.03	26.17
8	2.12	3.60	8.83	26.30
12	1.86	3.72	9.31	26.33
16	1.52	3.04	7.64	15.76
24	1.86	3.05	7.99	-

The part of experiments concerned with BSE imaging is still on-going. Sample data obtained from BSE imaging and X-ray analysis of the specimens are provided in Figures 2, 3 and Table 3. From these examples, it can be perceived that the corresponding intensity of grey colour level, spotted on the image of Figure 2, contains the elements shown in Table 3, with the corresponding weight percents.

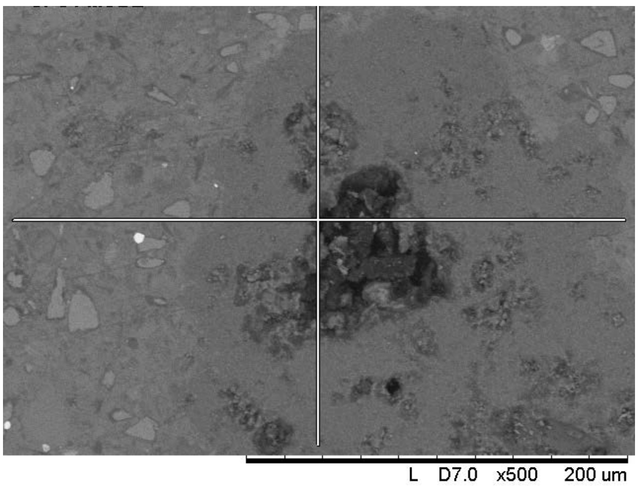

Figure 2. BSE image of the sample with 50% GGBS at the age of 12 weeks.

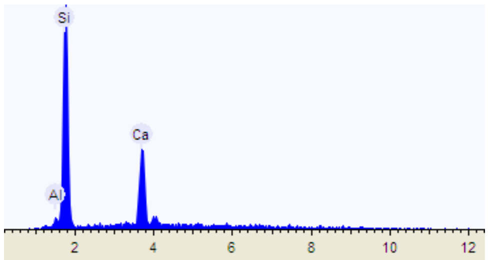

Figure 3. X-ray analysis results for the image of Figure 2.

Table 3. X-ray analysis results and element identification.

Element	Weight %
Aluminium	1.8
Silicon	61.6
Calcium	36.6

The histograms of grey level distributions obtained by analysing each image, reveals several peaks, each representing various phases in the cement paste; namely, anhydrous material, calcium hydroxide and calcium silicate hydrate [12]. An example of BSE image along with its corresponding histogram of grey colour levels are also presented in Figures 4 and 5, to demonstrate the technique in the proposal advanced in this paper.

Results to date are encouraging; however, it is felt that the effectiveness of the proposed method could be further enhanced by trying microscopy with different image acquisition systems and various accelerating voltages, to produce more informative images.

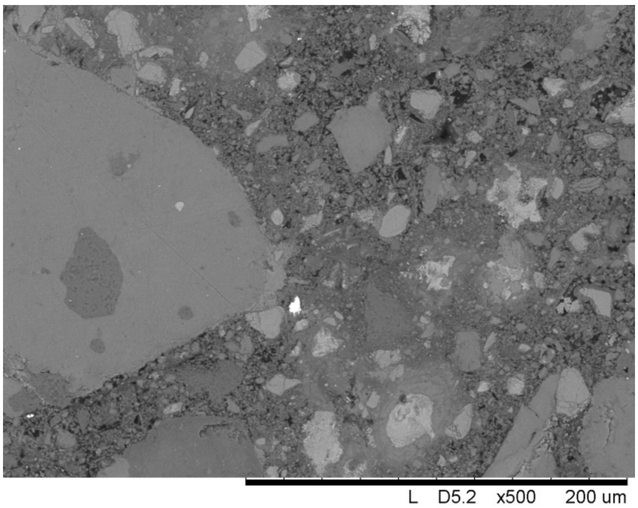

Figure 4. BSE image of a sample with 30% GGBS replacement at the age of 1 week.

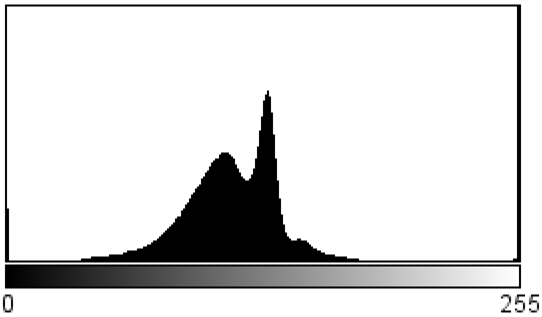

Figure 5. Histogram of grey colour levels corresponding to the image of Figure 4.

5 CONCLUSION

This paper puts forward a novel methodology for improving accurate modelling of the chloride diffusivity parameters of concrete, especially during the early service life of structures, with the aim of enhancing infrastructure management. The results to date are encouraging in respect of validating the applicability of the proposed method.

ACKNOWLEDGMENTS

The TEAM project is a Marie Curie Initial Training Network and is funded by the European Commission 7th Framework Programme (PITN-GA-2009-238648).

REFERENCES

[1] Neville, A. M., (1996), *Properties of concrete*, Wiley, New York.

[2] Stanish, K. D., Hooton, R. D., Thomas, M. D. A., (1997), ‘Testing the chloride penetration resistance of concrete: a literature review’, *FHWA contract DTFH61-97-R-00022, "Prediction of chloride penetration in concrete"*, University of Toronto, Toronto, Ontario, Canada.

[3] Collepardi, M., Marcialis, A., Turriziani, R., (1970), 'The kinetics of chloride ions penetration in concrete (In Italian)', *Il Cemento*, 67, 157-164.

[4] Luping, T. & Gulikers, J., (2007), ‘On the mathematics of time-dependent apparent chloride diffusion coefficient in concrete’, *Cement and Concrete Research*, 37(4), 589-595.

[5] Smolezyk, H. G., (1986), ‘Durability and pore structure on very old concretes (dauerhaftigkeit und porenstruktur von sehr alten betonen)’, *Beton-Informationen 26 Heft 1.*

[6] Callanan, T. M., (2003), ‘Diffusivity of chloride ions in the context of Irish concrete practice and environments’, PhD Thesis, University College Dublin, Ireland.

[7] Schindler, A., Folliard, K., (2005), 'Heat of Hydration Models for Cementitious Materials', *ACI Materials Journal*, Title no. 102-M04.

[8] Mouret, M., Ringot, E., Bascoul, A., (2001), 'Image analysis: a tool for the characterisation of hydration of cement in concrete - metrological aspects of magnification on measurement', *Cement and Concrete Composites*, April, 23(2), 201-206.

[9] Yang, R., Buenfeld, N. R., (2001), 'Binary segmentation of aggregate in SEM image analysis of concrete', *Cement and Concrete Research,* 31, 437-441.

[10] Stutzman, P., (2004), 'Scanning electron microscopy imaging of hydraulic cement microstructure', *Cement and Concrete Composites*, 26, 957-966.

[11] Sahu, S., Badger, S., Thaulow, N., Lee, R. J., (2004), 'Determination of water–cement ratio of hardened concrete by scanning electron microscopy', *Cement & Concrete Composites*, 26, 987–992.

[12] Zhao, H., Darwin, D., (1992), 'Quantitative backscattered electron analysis of cement paste', *Cement and Concrete Research*, 22(4), 695-706.

[13] Marusin, S. L., (1995), 'Sample Preparation – the key to SEM studies of failed concrete', *Cement and Concrete Composites*, 17, 311-318.

[14] NT BUILD 492, (1999), 'Concrete, mortar and cement-based repair materials: Chloride migration coefficient from non-steady-state migration experiments.'

[15] Soroushiana, P., Elzafraneya, M., Nossonib, A., (2003), 'Specimen preparation and image processing and analysis techniques for automated quantification of concrete microcracks and voids', *Cement and Concrete Research*, 33, 1949–1962.

[16] Kjellsena, K.,O., Monsøyb, A., Isachsenb, K., Detwiler, R. J., (2003), 'Preparation of flat-polished specimens for SEM-backscattered electron imaging and X-ray microanalysis—importance of epoxy impregnation', *Cement and Concrete Research*, 33, 611 –616.

[17] Kjellsen, K. O., Detwiler, R. J., Gjorv, O. E., (1991), 'Development of microstructures in plain cement pastes hydrated at different temperatures', *Cement and Concrete Research*, 21(1), 179-189.

[18] Jana, D., (2006), 'Sample preparation techniques in petrographic examinations of construction materials: a state-of-the-art review', *Proceedings of the twenty-eighth conference on cement microscopy*, Denver, Colorado, USA.

[19] Coster, M., Chermant, J., (2001), 'Image analysis and mathematical morphology for civil engineering materials', *Cement and Concrete Composites*, 23, 133– 151.

Reinforced concrete deterioration of a 100 year old structure in a marine environment

R.O'Donovan[1,2], B.D. O'Rourke[1], K.D.Ruane[1,2], J. J. Murphy[1]
[1]Department of Civil, Structural & Environmental Engineering, Cork Institute of Technology, Bishopstown, Cork, Ireland
[2]RPS Group Ltd, Innishmore, Ballincollig, Cork, Ireland
email: ross.odonovan@rpsgroup.com, brian.orourke@cit.ie, kieran.ruane@rpsgroup.com, john.justinmurphy@cit.ie

ABSTRACT: The current study investigates the deterioration of a 100 year old bridge located in a harsh marine environment. Constructed in 1908 - 1909, the Mizen Head bridge was one of the oldest reinforced concrete bridges in Ireland. The demolition of the bridge in 2009 provided a unique opportunity to examine its service life and to extract concrete samples for analysis and investigation. This research provides a review of reinforced concrete practice at the time of construction and its influence on the service life of the bridge. The maintenance regime that the bridge was subjected to was investigated with a view to analysing its influence on the behaviour of the concrete. Reinforcement corrosion due to chloride ingress was identified, modelled by Fick's Second Law, and compared with samples tested from the bridge. This research may provide valuable advice and guidance for the asset management of similar structures.

KEY WORDS: Historic structure; Chloride attack ; Fick's Second Law; Anaerobic corrosion.

1 INTRODUCTION

The first Mizen Head bridge, a heritage structure on the south-west coast of Ireland, was replaced in 2009 with a replica structure after some years of investigation to determine its structural adequacy.

This research provides a study of the behaviour of a reinforced concrete structure in a harsh marine environment with approximately 100 years of exposure.

2 EVALUATED STRUCTURE

Mizen Head and Cloghan Island are located on the south west coast of Ireland (Figure 1). Following a series of shipwrecks in the area at the turn of the 20^{th} century, the United Kingdom Board of Trade gave sanction in 1905 for a lighthouse and fog signal station to be erected at Cloghan Island, Mizen Head, County Cork [1] [2]. In order to gain access to Cloghan Island from the mainland, it was necessary to construct a bridge across a sea gorge [1] [2] [3].

Figure 1. Mizen Head [2].

Following a design and construct competition in 1907 a reinforced concrete through-arch bridge design was selected in lieu of several structural steel options [1]. This was the era of reinforced concrete systems and the selected design incorporated the bridge designer's (Noel Ridley) patented Ridley-Cammell corrugated dovetail sheeting [3].

Access to the bridge site was in difficult terrain. It necessitated a staged construction for each bridge member (Figure 2) using various construction methods (Table 1).

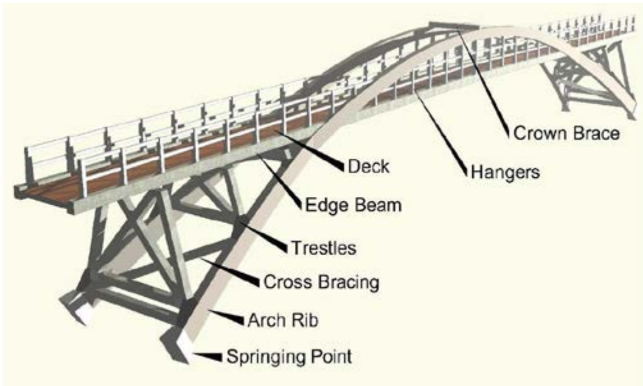

Figure 2. Bridge members.

Table 1. Various types of construction used on the bridge.

Type of Construction	Bridge Member
Precast Concrete	Handrail, Trestles, Edge beam.
In-situ Concrete	Bridge deck, Post, Hangers, Cross head, Concrete stitches.
Composite In-situ (using Ridley-Cammell system with U-trough and concrete rendering)	Arch ribs.

For this research the constuction of each bridge member was derived using photographic records (Figure 3a-d), contract drawings, contract specifications and available literature.

Figure 3a. Launching of steel corrugated arch trough [3].

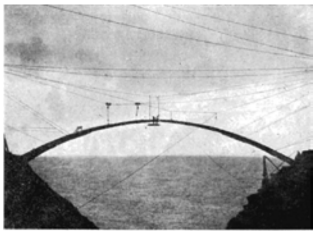

Figure 3b. Completion of the arches [3].

Figure 3c. Completion of back span trestles [6].

Figure 3d. Bridge near completion [3].

Composite in-situ arch ribs and precast trestles consisted of Ridley-Cammell corrugated dovetail sheeting shaped into an open trough encased in concrete [3] [10]. The trough was open at the top and had two "flat bars" attached at each corner (Figure 4a-c).

Fig 4a Ridley-Cammel sheeting (Photograph by R. O'Donovan, Dec 2011).

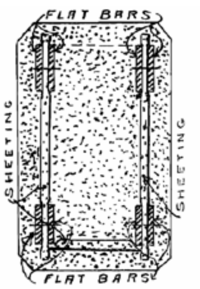

Figure 4b. Ridley-Cammell system used in the arch rib [3].

Figure 4c. Cut section of arch rib taken during the demolition (Photograph by R. O'Donovan, March 2010).

2.1 Materials

The original hand written specification for the bridge was produced and dated 16th July 1908. A concrete mix for the bridge members was specified in the construction drawings. The prescribed concrete mixes are presented in Table 2. The practice at the time would most likely have been to use different gauge boxes for aggregate, sand and cement to measure the prescribed mix proportions. In calculating the volume and dimensions of the aggregate gauge box, the percentage voids present in the selected aggregate would have been allowed for. The dimensions of the cement gauge box were correlated to the weight of a bag of cement [4].

Table 2. Specified concrete mix for the bridge.

	Concrete mix proportions (from bridge specification and construction drawings)	Estimated 28 day cube strength (N/mm²) [8]
Reinforced Concrete Work	1:1.5:3 (Best Portland Cement : Clean Sand : Broken Stone to pass a ¾" mesh)	Between 17.6 and 22.7
Rendering to the Corrugated Sheeting	1:2.5 (Portland Cement : Clean Sand)	Below 11.0
Foundations	1:2:6 (Cement : Sand : Broken Stone obtained from excavations, sufficient sand being used to fill the interstices)	Below 11.0
Foundation Wall	1:2:6 (Cement : Sand : Stone)	Below 11.0
Foundation Base	1:2:4 (Cement : Sand : Stone)	11.0

2.2 Service Life

On May 3rd 1909, the fog signal station was established. The bridge originally provided access to the Mizen Head Fog Signal Station on Cloghan Island for the Commissioners of Irish Lights and in later years was used as a cable route for services and subsequently as a tourist attraction [5]. During its service life of almost 100 years the bridge underwent various maintenance, inspections and repairs as follows:

1. Prior to 1939, evidence of deterioration was present and repairs were carried out. The repairs consisted of cutting away defective areas of concrete and replacing with new concrete [1] [9].
2. In 1972 extensive remediation work was carried out on the bridge, which consisted of cutting away defective concrete and treatment of exposed surfaces with a fungicide to remove organic growth, the covering of all structural elements with a bituminous material coated with a mica and a fine hard granite aggregate. The purpose of this seems to have been an attempt to repair visible defects and to seal exposed concrete surfaces from further chloride ingress [1] [9].
3. Throughout the 1980's and 1990's the bridge again showed signs of deterioration due to reinforcement corrosion. Previously attached membranes were removed and concrete around corroded reinforcement was cut out. Concrete surfaces were cleaned, and steel and concrete surfaces primed with polymer cement slurry. Finally, the concrete profile was restored with a modified cement mortar and finished with masonry paint to match. Again the strategy of repair seemed to have been an attempt to carry out localised repairs and to re-seal exposed concrete surfaces from chloride ingress [9] [11].

In 2004, it was concluded that many of the concrete elements in the structure were effectively unreinforced due to the corrosion of the reinforcement and that the structure may be subject to brittle failure [2] [11] [13]. The bridge was subsequently demolished in 2009 and a replica structure was constructed [12].

2.3 Field Observations During Demolition

Prior to the demolition of the bridge, rust staining was visible through the bituminous material and several layers of finish coat (Figure 5). The bituminous material showed localised signs of failure due to material loss.

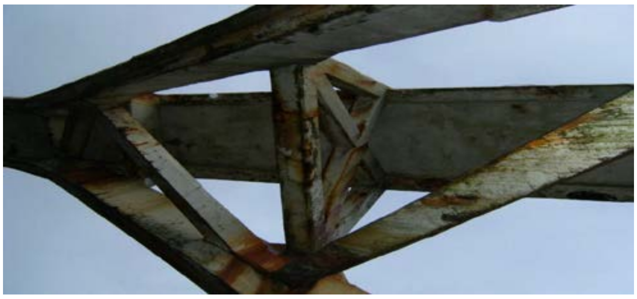

Figure 5. Extensive rust staining through the external coating system (Photograph by R. O'Donovan taken at underside of trestles, December 2009).

Concrete spalling was noted at the underside of the edge beams and cracks were present under the external coating on the hangers, posts, trestles and handrails members. When cutting out members during demolition it was observed that the bridge deck slab had delaminated between the granolithic surfacing and the reinforced concrete deck slab. Extensive deck slab delamination was observed in the deck at midspan of the bridge (Figure 6).

Figure 6. Delamination crack through cut section of bridge deck slab (Photograph by R. O'Donovan, March 2010).

It was noted from field observations during demolition that the deterioration of the bridge may be attributed to the following factors:

1. Poorly compacted concrete with large voids present was observed at the underside of the edge beams. These edge beams were flexural members. In 1909 standard practice relied on hand held tamping tools (Figure 7a) to tamp wet concrete into place. This method had limited effect in compacting concrete in difficult to reach areas. The importance of mechanically compacted concrete was not recognised in the industry until several years post-construction [8]. It was observed at the time of demolition that extensive reinforcement corrosion and concrete spalling had occurred on the underside of the edge beams (Figure 7b).

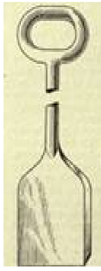

Figure 7a. Typical hand concrete tamper [4].

Figure 7b. Spalling of concrete on the underside of the edge beam (Photograph by R. O'Donovan June, 2010).

2. The Ridley-Cammell reinforcement system, which consisted of corrugated dovetail sheeting showed signs of poor bond between concrete and steel. This is attributed to the small gauge profile of the corrugated sheet, which did not permit the ¾" (≈ 20mm) aggregate and cement paste to bond between the corrugations. This is illustrated in Figure 8a-b.

Figure 8a Poor bond between corrugated sheeting and concrete in the edge beam member (Photograph by R. O'Donovan, June 2010).

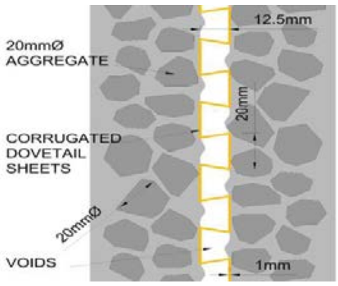

Figure 8b. Section though corrugated sheeting and concrete interface.

3 SAMPLING AND TESTING

During the demolition of the bridge, reinforced concrete samples were selected and extracted from all bridge members. The samples were labelled according to bridge member, position and orientation. Bulk samples were taken for smaller members such as posts, rails, hangers and the deck. Cores were extracted from larger members such as the arch ribs and trestles. Tests carried out on the samples determined concrete compressive strength to IS EN 12504-1:2000 [14], chloride content to BS 1881-124:1988:10.2, concrete density to IS EN 12390-7:2009, concrete pH to BS 1377-3:1990 and reinforcement tensile strength to BS EN ISO 6892-1:2009.

Previous studies had identified that little or no carbonation of the cover layer had occurred [11].

The concrete pH was found to be in the range of 12.4 to 12.6 and concrete density ranged from 2,150 kg/m³ to 2,330 kg/m³. Ultimate tensile strength of the reinforcement ranged from 385 N/mm² to 515 N/mm².

It was found that the concrete compressive strengths were generally lower in flexural and tension members than in compressive members (Table 3). This may be related to the predominant structural action in the member. It is also observed that the concrete compressive strength results were higher than the estimated 28 day strengths noted in Table 2.

Table 3. Compressive strengths of extracted cores.

Bridge member	Structural action	Lowest result for crushed test core (N/mm²)	Equivalent cube strength (by interpolation of Table 3.1 BS EN 1992-1-1:2004) (N/mm²)
Hanger	Tension	26.7	32.3
Edge Beam	Flexural	28.2	34.4
Deck Slab	Flexural	31.0	38.5
Trestle	Predominantly Compression	32.4	40.8
Arch	Compression	35.4	45.4

4 CHLORIDE ATTACK

It is well established that corrosion of steel is due to an electrochemical process [15]. The relationship between corrosion and chlorides is complex. In concrete, the passive layer around the reinforcement is continually breaking down and reforming. Chlorides interrupt this process. At low chloride levels the passive layer reinstatement process slows down and eventually a chloride threshold content is reached at which the rate of reinstatement fails to match the rate of breakdown of the passivating layer. At this stage complete depassivation occurs.

There are two stages to this process:

1. Initiation
2. Propagation.

During the initiation stage, the steel surface becomes susceptible to corrosion but it is during the propagation stage that active corrosion occurs.

4.1 Initiation

Chlorides in sufficient quantities break down the passive oxide layer on the embedded steel, thereby leading to corrosion propagation.

4.2 Propagation

Once the passive oxide layer has been broken down, corrosion of the reinforcing steel begins in the presence of moisture and oxygen.

Under these conditions, the surface of the reinforcing steel acts as a mixed electrode, upon which coupled anodic and cathodic reactions take place. At the anodic sites, metal ions pass into solution as positively charged ferrous ions and the excess free electrons flow through the reinforcing steel to cathodic sites where they react with dissolved oxygen to produce hydroxyl ions.

Oxygen availability at cathodic sites is essential for corrosion to occur and, therefore, the rate of oxygen diffusion through the concrete cover influences the rate of corrosion.

To prevent electrical charge accumulating on the electrode surfaces, hydroxyl ions diffuse through the electrolyte towards the anode, while the ferrous ions diffuse towards the cathode. Where the hydroxyl ions meet the ferrous ions, they electrically neutralize, forming ferrous hydroxide. The ferrous hydroxide in turn reacts with oxygen and water to form haematite, which is familiar as red-brown rust.

Rust occupies considerably more volume than the original steel. Consequently, tensile stresses develop in the concrete. Cracks may appear in the concrete cover, thus accelerating the whole corrosion process, eventually causing the concrete to spall.

Prior to demolition of the bridge the presence of anaerobic corrosion was noted [12]. Anaerobic corrosion is a rare form of corrosion that occurs when the oxygen supply is limited at active anodes. The resulting corrosion may be observed as green, white or black in colour (Figure 9) [16] [17].

Figure 9. Black corrosion product and pitting observed on edge beam reinforcement. (Photograph taken by R. O'Donovan, June 2010).

The green product is believed to be a chloride complex while the black product is magnetite. Corrosion under oxygen deficient conditions is considered to be more serious than normal aerobic corrosion, as it may be active for some time before there is any visible evidence at the surface of the concrete [16] [18].

A proposed model (Figure 10) for reinforcement corrosion in concrete has been developed [19]. This suggests that during the corrosion process, the rate of oxygen diffusion to the corroding bars through the rust layer is so low that anaerobic corrosion activity occurs.

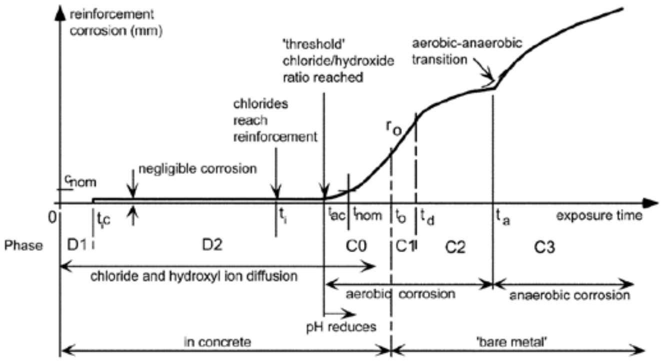

Figure 10. Proposed model for reinforcement corrosion in concrete [19].

4.3 *Chloride Ingress*

There are several mechanisms by which chloride transport can take place in concrete. The two main transport mechanisms for chloride ingress are diffusion, which is the movement of chloride ions under a concentration gradient and advection, which is the flow of water containing chlorides under a pressure gradient due to capillary suction or an external head of water.

For concrete under saturated conditions, diffusion is the dominant transport mechanism. For reinforced concrete structures that are unsaturated and are subjected to wet and dry cycles, advection may be the dominant transport mechanism [15] [20].

The movement of chlorides in concrete is complicated by the physical and chemical interactions that take place between the chloride ions and the cement matrix. Chloride binding removes chlorides from the pore solution and retards the rate of chloride ingress into the concrete. The level of chloride binding varies with the quantity of free chlorides at higher chloride levels and is influenced by the total chloride content, the pore solution pH, the reactivity of cement and temperature. Chloride levels are most commonly expressed as the percentage of chloride by weight of the cement [21].

4.4 *Fick's Laws of Diffusion*

Fick's Laws of Diffusion are used to evaluate chloride transport in concrete. For isotropic conditions under steady state conditions, chloride diffusion is given by Fick's First Law of Diffusion as follows [21]:

$$J = -D\frac{\partial C}{\partial x} \tag{1}$$

where

J	rate of chloride transfer per unit length of section
D	diffusion coefficient
C	concentration of diffusing substance
x	space coordinate measured normal to the section.

Chloride ion diffusion is not a steady state process and the differential equation, known as Fick's Second Law of Diffusion, is applicable [20] [22]:

$$\frac{\partial C}{\partial t} = D\frac{\partial^2 C}{\partial x^2} \tag{2}$$

A solution of Fick's Second Law of Diffusion (also known as Crank's Solution) yields the following [24]:

$$C_x - C_b = (C_s - C_b)\left(1 - erf\,\frac{x}{2\sqrt{Dt}}\right) \tag{3}$$

where the coefficients are described in Table 4.

In this study, chloride profiles using Fick's Second Law were calculated using values from Table 4. The profiles calculated using Equation 3 are compared with the test results recorded from the samples and are illustrated in Figure 11.

Table 4. Values used in Fick's Second Law.

Function	Description	Values used to determine a solution to Fick's Second Law
C_x	Chloride content at depth x (% chloride by weight of cement)	This value was calculated at depths of 25, 50 and 75mm and compared with test results
C_s	Chloride content at surface (% chloride by weight of cement)	Assumed value taken as 3.3% [23]
C_b	Background chloride content (from the mix constituents) (% chloride content by weight of cement)	Values taken between 0.2% to 2.0% [20] [22]
D	Effective chloride diffusion coefficient (m²/sec)	Coefficient in the order of 10^{-12} m²/s for a 60 year old structure [22]
t	Exposure period (seconds)	Period taken as 63 years, the period between 1909 to 1972 when the external surface of the bridge was exposed. After 1972 it is assumed that external surfaces were effectively sealed against chloride ingress
erf	Error function	Value taken as 1.0

Figure 11 shows that the measured chloride profiles are not the same as those calculated by the application of Fick's Second Law. Normally, higher concentrations of chlorides would be expected at the external surface and chloride concentration would reduce with increasing depth. In this instance the measured chloride concentrations are uniform throughout the concrete section. Investigation and modelling of chloride transport due to advection may further explain the behaviour.

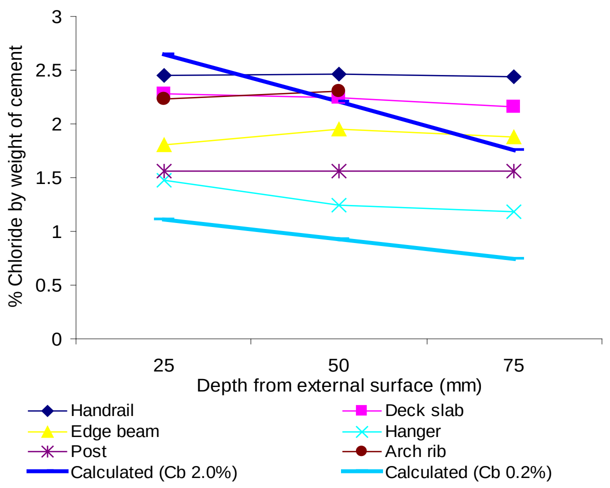

Figure 11. Calculated predicted chloride levels compared with measured values.

5 CONCLUSIONS AND FURTHER RESEARCH

The Ridley-Cammell corrugated reinforcement system had an inherent design flaw that did not allow sufficient bond between the small corrugations and concrete, which caused a weak point in the edge beam. Modern design codes address this problem by specifying a minimum cover and reinforcement spacing (maximum aggregate size plus 5 mm). At the time of construction a lack of awareness about the importance of mechanically vibrated concrete led to areas of poorly compacted concrete in the structure. It is likely that these areas were more susceptible to chloride attack.

During demolition it was noted that structural defects such as cracking and spalling were more extensive in flexural and tension members such as the deck slab and edge beams. These members also exhibited weaker concrete compressive strengths than the compression members.

The maintenance and repair strategy of the bridge consisted of patch repairs to spalled or damaged concrete and sealing of exposed concrete surfaces from chloride ingress. Modern techniques such as chloride extraction or cathodic protection may have prevented further deterioration of the bridge if available at the time.

The chloride profiles measured show a uniform dispersion of chloride content, which is not in accordance with Fick's Second Law. This may be attributed to the fact that the bridge surface was effectively sealed from the external environment from 1972 onwards. Chlorides that had been present prior to 1972 may have dispersed uniformly throughout the concrete sections. Investigation and modelling of chloride transportation may further explain this behaviour.

Although the structure was effectively sealed from the external environment and further chloride ingress for a period of 37 years, the condition of the bridge continued to deteriorate. Under these conditions it is suspected that prior to 1972, chloride attack was at an advanced stage of propagation. This may have facilitated anaerobic corrosion of the reinforcement in later years.

REFERENCES

[1] Stephens, L.F., *The Bridge at Mizen Head*, Irish Engineers, Volume 27, No. 7, July/August 1974.

[2] Doyle S., *Mizen Head Footbridge*, Beam - The Journal of the Irish Lighthouse Service, Volume 34, 2006.

[3] Ridley N., *Dovetail Corrugated Sheeting*, paper read at the 84th meeting of the Concrete Institute January 23rd 1919.

[4] Jones B.E., *Cassell's Reinforced Concrete*, Cassell & Company Ltd., 1913.

[5] Unknown, *Mizen Head Ireland*, Engineering Contracting Volume XXXIV, The Nyron Clarke Publishing Co., 1910.

[6] Hall C., *Conquest of the Sea, Conquest of Engineering*, Blackie & Son Ltd, c1910s.

[7] Graham A., *Forms for Concrete Work*, 46th Meeting of the Concrete Institute, c1920s.

[8] Sutherland J., Humm D., Chrimes M., *Historic Concrete Background to Appraisal*, Thomas Telford, 2001.

[9] MacCraith S., *Performance of an 80 year old reinforced concrete bridge in an extreme environment*. Corrosion of Reinforcement in Concrete. Elsevier Applied Science, London, 1990.

[10] Cox R.C., Gould M., *Ireland's Bridges*, Wolfhound Press, 2003.

[11] Ruane K.D., Healy A, *'Assessment testing Mizen Head Footbridge Ireland'*, Proceedings of the Institution of Civil Engineers, Bridge Engineering 157, September 2004 Issue BE3, 2004.

[12] Ruane K.D., O'Donovan R., O'Keeffe N., Lehane E., Coleman M., Power K., Minihane B., Collery E., *The Design and Construction of the New Mizen Head Footbridge*, Paper accepted for publication in the Proceedings of the Institution of Civil Engineers, publication date September 2012.

[13] Ruane K.D., *Mizen Head Structural Evaluation*, RPS MCOS Consulting Engineers, 2005.

[14] National Standards Authority Ireland, *Testing concrete in structures – Part 1: Cores specimens – Taking, examining and testing in compression, Irish Standard I.S. EN 12504-1:2000*, National Standards Authority Ireland, 2000.

[15] Neville A.M., *Properties of Concrete*, Pearson, 4th edition, 2006.

[16] Arya C., Wood L.A., *The Relevance of Cracking in Concrete to Corrosion of Reinforcement*, Concrete Society, Technical Report No. 44, 1995.

[17] Concrete Society Working Party, *Diagnosis of deterioration in concrete structures Identification of defects, evaluation and development of remedial action*, Concrete Society, Technical Report No. 54, 2000.

[18] Karimi A., Buenfeld N.R., *Service life prediction of concrete structure based on automated monitoring*, Imperial College London, 2007.

[19] Melchers R.E., Li C.Q., *Phenomenological modelling of reinforcement corrosion in a marine environment*, ACI materials Journal, January-February 2006.

[20] Cuding T., Nilsson L., Basheer M., *Resistance of Concrete to Chloride Ingress*, Spon Press, 2012.

[21] Building Research Establishment, *Corrosion of steel in concrete investigation and assessment*, Building Research Establishment, Digest 444, Part 2, February 2000.

[22] Richardson M.G., *Fundamentals of Durable Reinforced Concrete*, Spon Press, 2002.

[23] Ormellese M., Berra M., Bolzoni F., Pastore T., *Corrosion inhibitors for chlorides induced corrosion in reinforced concrete structure*, Cement and Concrete Research, 2005.

Texture analysis based detection and classification of surface features on ageing infrastructure elements

Michael O'Byrne[1], Bidisha Ghosh[1], Vikram Pakrashi[2], Franck Schoefs[3]
[1] Trinity College Dublin, Department of Civil, Structural and Environmental Engineering, Dublin 1, Ireland
[2] University College Cork, Department of Civil and Environmental Engineering, College Road, Cork, Ireland
[3] LUNAM Université, Université de Nantes-Ecole Centrale de Nantes, CNRS, GeM UMR 6183, IUML FR 3473, Institute for Research in Civil and Mechanical Engineering, 2, rue de la Houssinière BP 92208 44322 Nantes Cedex 3, France.
email: obyrnemj@tcd.ie, bghosh@tcd.ie, v.pakrashi@ucc.ie, franck.schoefs@univ-nantes.fr

ABSTRACT: This paper presents a texture analysis based approach for the detection of damaged regions on the surface of infrastructural elements. A *k*-means clustering algorithm was used to partition regions with similar textural properties. Four texture measures were derived from a Grey Level Co-occurrence Matrix (GLCM) namely; contrast, homogeneity, entropy and Angular Second Moment (ASM). The approach is validated successfully on an image of a damaged concrete bridge beam. The performance of this Non-Destructive Testing (NDT) technique is evaluated for various values of *k* through the use of performance points in the Receiver Operating Characteristic (ROC) space. The technique may be deployed as a Structural Health Monitoring (SHM) tool to track the extent of surface damage, and can used in a Bridge Management System (BMS) to aid structured decision making and scheduling of repair work.

KEY WORDS: Damage Detection, Image Processing, Texture Analysis, Grey Level Co-occurrence Matrix (GLCM), k-means Clustering, Bridge Management Systems (BMS).

1 INTRODUCTION

Bridges may be subjected to numerous forms of damage during their service life. The damage may include cracking, corrosion of reinforcement bars, leaching, rust spotting, spalling, honeycombing, collision damage, efflorescence, wear etc. [1].With this in mind, regular inspections of the integrity of structures are vital to ensure they remain safe and fit for purpose. Currently, many structures are assessed under a regime of visual inspections of varying scope; from a cursory check for gross defects, to a close examination of all surfaces, including the use of special equipment if necessary. The quality of data collected often depends on the ability of the inspectors to observe and objectively record details of damage. The damage is usually described and archived qualitatively by the inspector, with appropriate photographs attached as evidence behind the qualitative comments. An attempt to quantify the severity of the damage is generally made at this stage through the use of a numerical scale. The scales typically range over a limited number of categories (e.g. 5 levels), leading to some degree of uncertainty and vagueness. The use of numerical scales, though helpful for relative ranking and prioritising, does not lend itself to be integrated with future quantitative analyses or experiments and repair options as this level are usually based on qualitative comments based on personal expertise. The output from visual inspections can markedly vary and can have a lower level of accuracy and repeatability of detection compared to other inspection methods [2]. An image processing based detection approach acts as a relatively inexpensive tool to facilitate maintenance management and can offer a greater reproducible and measurable performance over visual inspection techniques [3]. Image processing based techniques have received significant attention in many other fields. However, they are yet to be explored to their full potential in the area of Structural Health Monitoring (SHM).

Image based analysis is a form of Non-destructive testing (NDT), which can provide useful information on the state of the structure [4]. This in turn may be fed into a Bridge Management System (BMS). The output from the BMS can help in the planning of long-term repair strategies and enable informed decisions to be made when prioritising resources towards the correction of deficiencies. Furthermore, information acquired from NDT techniques increase understanding of damage mechanisms which enables engineers to better predict the behaviour of a particular structure and thus achieve a more reliable and suitable management strategy. This aspect has attracted a growing interest in recent years as the importance of life cycle optimisation and the related financial benefits continue to be recognised [5, 6]. An important aspect of managing a bridge is having a means to determine the current health of bridge elements based on past inspection data. An image processing approach caters for this as captured images can be archived for assessment of degradation over time, thereby enabling the rate of propagation of damage to be estimated. Image processing techniques are particularly relevant to bridge monitoring as there are typically large sections that are largely inaccessible to close-up visual inspections and other NDT techniques. From an image processing perspective, the images can be acquired from a relatively far distance from the surface under consideration thereby minimising road user delay costs, minimising inspection time and cost related to access equipment, improving safety aspects of the inspection process, and keeping the structure in operation. There exists a broad range of NDT techniques used to asses structural integrity such as ultrasonic scanning [7], acoustic emission techniques and eddy current testing [8]. The most suitable choice of NDT for a given application will largely depend on the damage to be detected and will require an in-depth knowledge of the advantages and limitations associated with each option. The measure of the on-site performance of a NDT tool is still a pertinent question in many cases [9]. Image processing based techniques, in conjunction with powerful detection algorithms, can be considered as an accessible, inexpensive, and easily deployable technique for visual inspection. The primary limitations of this approach are the lack of penetration below the surface of the material and the requirement of good visibility and lighting conditions. Previous image processing based methods have relied on colour information [10, 11], textural information [12], or a combination of the two (Wu and Tsai, 2006) to segment and extract regions of interest in images.

Texture and colour based segmentation approaches are the primary modes of segmentation employed for image analysis. While both approaches have important applications in image processing methods, the colour based methods have been researched to a much greater extent. Texture may be considered as an innate property of surfaces. It may be qualified by terms such as fine, coarse, smooth, rippled, molled, irregular, or lineated [13]. Texture segmentation finds particular relevance in cases where the regions of interest are more separable from the background based on their texture than colour. There are numerous texture based image segmentation techniques. Such techniques include wavelet analysis [14], Laws' texture energy [15] and Grey Level Co-occurrence Matrix (GLCM) [16]. This paper presents an enhanced texture based detection technique involving GLCM. GLCM is a well established texture analysis method and offers a highly accurate approach for quantifying the perceived texture in an image. *k*-means clustering is subsequently used to partition regions of similar texture features together. GLCM had been used previously in conjunction with *k*-means classification on magnetic resonance images [17], however their algorithm used a different set of statistics. It is felt that the four statistics used in the proposed technique provide a well-rounded description of the texture in the image whilst offsetting unnecessary computational time that would result from the inclusion of additional statistics that would only contribute to a minimal increase in accuracy of detection.

The methodology of the proposed technique is detailed in the following section. The technique is applied to an image of a concrete bridge beam featuring cracking to concrete and exposed reinforcement. The successful application of the method is presented and the performance of the technique is evaluated.

2 METHODOLOGY

A semi-automatic image based damage detection algorithm is proposed in this paper. A schematic of the methodology is presented in Figure 1. The algorithm involves two steps; the first step is using a GLCM to develop to a texture characteristics map of an image of a damaged surface. The image is in a greyscale form which is represented by a single numerical array, or plane, that is populated by pixel intensity values. Typical ranges for intensity values are 0 to 255, or 0 to 1. Black is represented by 0 in both cases while white is denoted by 255 and 1 respectively. Values within this range represent intermediate shades of grey. The second step in the algorithm is to partition the damaged regions in the image using *k*-means clustering. These two steps are discussed in detail in the following subsections.

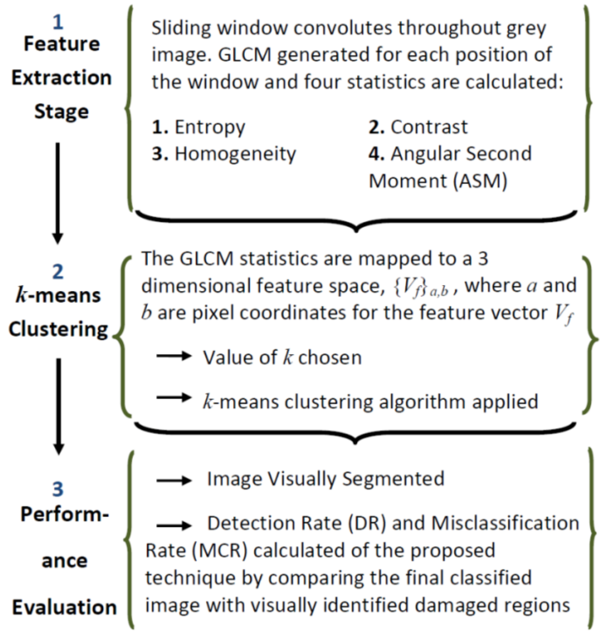

Figure 1. Flow chart of the proposed methodology.

2.1 *Texture Characteristics Map*

A texture characteristics feature vector $\{V_f\}_{a,b}$ has to be generated for each pixel within the original image, *I*, where *f* indicates the index of the vector element, while *a* and *b* indicate the spatial coordinates of a pixel. The GLCM is a matrix of frequency values that combinations of pixel intensities appear in some specific spatial arrangement within an image or sub-image. In this paper, the GLCM is generated for a sub-image that is attained through a sliding window, *SW*, of size *N*-pixel x *N*-pixel with centre positioned at (*a*,*b*) at any stage of the convolution throughout the overall image. There are four texture features calculated from the GLCM, namely: homogeneity, contrast, entropy and Angular Second Moment (ASM). Some of these features relate to certain texture characteristics in the image such as homogeneity or contrast. Other features describe aspects such as image complexity or the transition of pixel intensity values. However, in spite of each of the aforementioned features containing some degree of information about the texture characteristics of the image, it is difficult to establish which textural trait is represented by each feature.

Each entry in the GLCM corresponds to the number of occurrences of a pair of grey levels (i,j,d,θ) in the sliding window, where *i* denotes the grey level in the reference pixel, *j* denotes the grey level in the destination pixel, *d* is the interpixel distance and θ is the angle of offset between neighbouring pixels. Both *i* and *j* can take integer values between 1 and *G*, where *G* is the total number of grey levels. The grey levels are defined on a scale of 1 - 12 instead of a typical scale of 1 - 255. Quantisizing in this manner promotes computational parsimony and avoids sparse matrices. Pixel combinations that are close together tend to be more relevant than pixel combinations that are far away from each other in terms of interpixel distances. With this in mind, a value of 1 was chosen as the interpixel distance (i.e. only combinations of pixels which shared a corner or had a shared edge were counted). This allowed for an algorithm that considered a significant amount of useful information whilst minimising computational time. Four angles for the offset were chosen: $\theta = 0°$, $\theta = 45°$, $\theta = 90°$, $\theta = 135°$. The GLCM is calculated for each of the four offsets for each position of the sliding window. The GLCM is populated as per equation 1.

$$P(i, j, d, \theta) = \frac{1}{N^2} \sum_{u=1}^{N} \sum_{v=1}^{N} A \tag{1}$$

$$\text{where } A = \begin{cases} 1 & \text{if } SW(u,v) = i \\ & \text{and } SW(u+d_x, v+d_y) = j \\ 0 & \text{otherwise} \end{cases} \tag{2}$$

where d_x and d_y are the horizontal and vertical offsets between neighbouring pixels in the sliding window which are dependent on d and θ, and $SW(u,v)$ gives the quantized pixel intensity value at the spatial coordinates u and v in the window.

An important prerequisite to the process of generating statistics from the GLCM is to normalise the matrix which is achieved through:

$$p(i, j, d, \theta) = \frac{P(i, j, d, \theta)}{R} \tag{3}$$

where R represents the total number of grey level pairs (i,j) for a given (d, θ) pair within the window. This normalised GLCM was used to calculate four values for each of the four texture measures corresponding to the four offset angles. As it is not known which angle of offset provides the most meaningful value for each texture measure, the average of the four texture measures was calculated and assigned to the texture measure in question, as per equation 4.

$$v_f = \sum_{\theta} \frac{v_{f,\theta}}{length(\Theta)} \tag{4}$$

$$\text{where } \Theta = \{0°, 45°, 90°, 135°\}$$

The following features were determined from the GLCM:

1. ***Homogeneity*** gives a measure of the similarity in the image.

$$Hom = \sum_{i=1}^{G} \sum_{j=1}^{G} n \cdot p(i, j) \quad \text{where } n = |i - j| \tag{5}$$

Hom ranges from 0 to G-1. A value of 0 indicates a strong similarity in the image.

2. ***Contrast*** is a measure of the local variations present in an image. If there is a high amount of variation the contrast will be high.

$$Con = \sum_{n=0}^{G-1} n^2 \left\{ \sum_{i=1}^{G} \sum_{j=1}^{G} p(i, j) \right\} \tag{6}$$

Con ranges from 0 to $(G\text{-}1)^2$. A value of 0 indicates a constant image.

3. ***Entropy*** is a statistical measure of randomness.

$$e = -\sum_{i=1}^{G} \sum_{j=1}^{G} p(i, j) \times \log_2(p(i, j)) \tag{7}$$

e ranges from 0 to infinity.

4. ***Angular Second Moment (ASM)*** represents the uniformity of distribution of grey level in the image.

$$ASM = \sum_{i=1}^{G} \sum_{j=1}^{G} \{p(i, j)\}^2 \tag{8}$$

ASM ranges from $1/G^2$ to 1. A value of 1 indicates a constant image.

2.2 *k*- means Clustering

The *k*-means clustering algorithm partitions *N* observations into *k* clusters in which each observation belongs to the cluster with the nearest cluster centre by iteratively minimizing the squared sum of a computed norm from each observation to its cluster centre, over all clusters. The result is a set of clusters that are as compact and well-separated as possible.

For a Euclidean norm, the overall objective function, $\bar{J}$, is minimised as:

$$\bar{J} = \sum_{j=1}^{k} \sum_{l=1}^{N_{\hat{c}}} \left\| A_l - A_{\hat{c}} \right\|^2 \tag{9}$$

where $\left\| A_l - A_{\hat{c}} \right\|^2$ is the distance measure between a data point A_l and the cluster centre $A_{\hat{c}}$, is an indicator of the distance of the $N_{\hat{c}}$ data points from their respective cluster centres. An optimum value of *k* can generally be attained by considering the level of detail or precision required. For a higher *k* value, there will be a stronger correlation between pixels within each cluster. This is advantageous if one wishes to reduce the rate of misclassification. An ROC based optimization framework is explored in Section 3, where different *k* values are tested in an attempt to determine which produces the best outcome.

3 EVALUATION OF TECHNIQUE

The proposed technique was performed on an image of exposed reinforcement on an outer bridge beam (Figure 2).

Various *k* values were used in the *k*-means clustering stage; ranging from 2 to 5. The detected regions using the proposed technique for each value of *k* are presented in Figure 3.

The performance of the texture analysis based detection in conjunction with the *k*-means clustering for various values of *k* is evaluated by plotting performance points in the Receiver Operating Characteristic (ROC) space. The ROC space provides a common and convenient tool for graphically characterising the performance of NDT techniques and its usage has recently been extended to image detection [18]]. A box counting approach similar to the procedure described in [19] was employed to calculate the Detection Rate (DR) and Misclassification Rate (MCR) for each image. This involved visually segmenting the images and comparing them with the *k*-means clustered images.

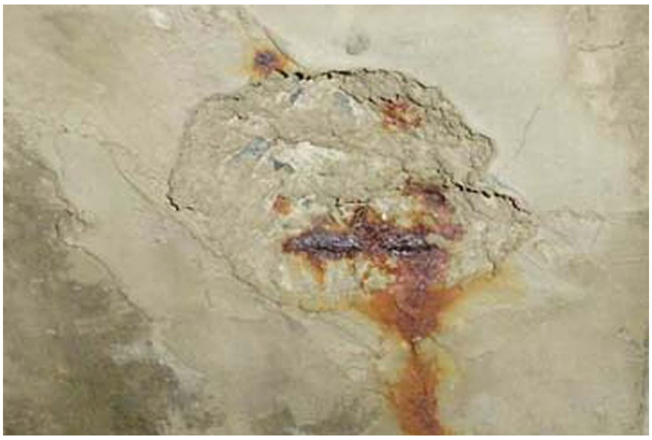

Figure 2. Sample Image of a Damaged Bridge Beam.

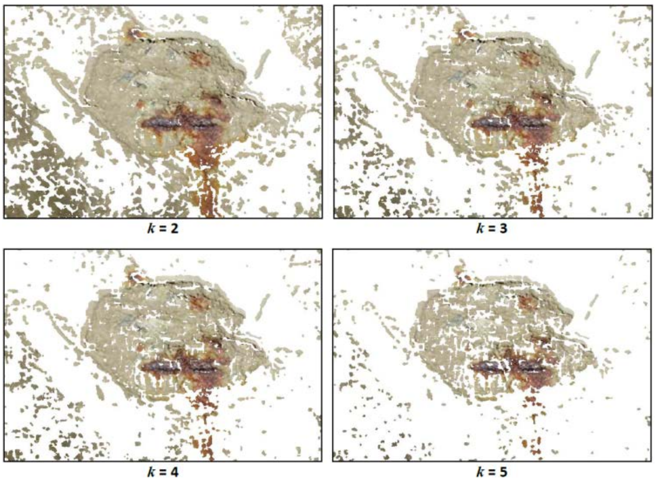

Figure 3. Detected Regions for Various Values of *k*.

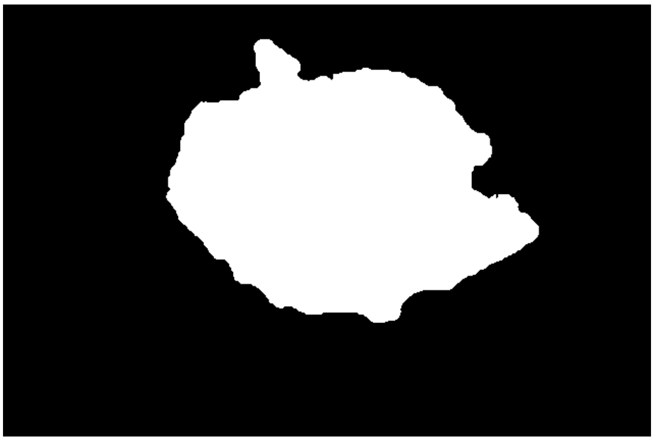

Figure 4. Visually Identified Damaged Region.

The DR and the MCR provide the coordinates for a point in the ROC space, which allows for a graphical illustration of the performance of the technique. A convenient way of ranking and analysing the performance of points in the ROC space is by means of the alpha-delta method [20, 21]. Essentially, this method relies on calculating the angle, α, and the Euclidean distance, δ, between the best performance point (coordinates (0,100%)) and the considered point to give a measure of the performance of the considered point. For this situation only the delta, δ, parameter is required. A low value for δ is indicative of a strong performing technique. The detection and misclassification rates, along with the δ value, are summarized in Table 1 and the corresponding coordinate points are shown in the ROC space in Figure 5. A fitted curve is also shown for illustration purposes.

Table 1 - Performance of the Proposed Technique.

k- clusters	DR	MCR	δ
$k = 2$	96.55%	28.12%	0.283
$k = 3$	88.61%	15.80%	0.195
$k = 4$	85.43%	14.11%	0.203
$k = 5$	72.00%	12.12%	0.305

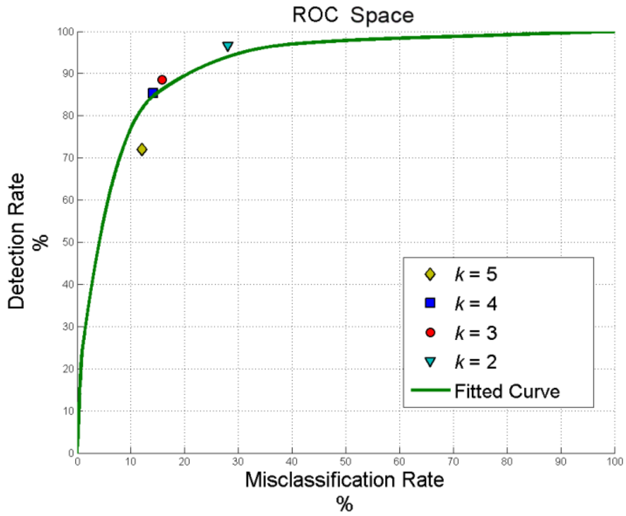

Figure 5. Performance Points in the ROC Space for the Proposed Technique.

The proposed technique performed well at defining the outer shape and size of the damaged region. However, as the value of k is increased, the detected regions become less homogenous with a greater prominence of undetected regions contained within the greater damaged area. It may be noted from the Figure 5 that when *k* is equal to either 3 or 4, a high performance level is achieved. The value of 3 for *k* is slightly better as evident from the lower value of δ. There is a relatively low detection rate in the case when *k* is equal to 5, while the converse is true for when k is equal to 2, i.e. there is a relatively high misclassification rate. As a result, relatively large values of δ accompany both of these cases.

A significant proportion of the misclassification rate may be attributed to the small spurious regions that are frequently included in the cluster corresponding to the damaged region. A simple way of reducing the misclassification rate without any significant reduction in the detection rate would be to apply an additional algorithm that removes these isolated regions that are below a certain area.

The result from performing *k*-means clustering directly on the colour image to group regions with similar pixel intensity values is graphically illustrated in Figure 6.

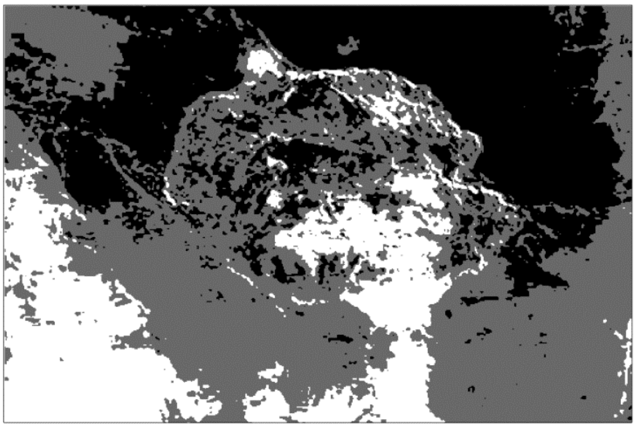

Figure 6. Image Clustered Based on the Pixel Intensity Values.

It may be observed that this approach produced extremely poor results, so much so that it is not even apparent which cluster predominantly corresponds to the damaged region. This comparison highlights the usefulness of texture analysis on images featuring damaged regions that are more separable based on their textural characteristics rather than colour information. In this case the image was partitioned into 3 clusters; however other values of *k* performed to a similar level.

4 CONCLUSION

A texture based image processing technique to detect damage on the surface of bridge elements has been proposed. Although popular in other fields, image processing techniques have received little attention in the field of Structural Health Monitoring (SHM). Their potential as a tool that could be employed in a Building Management System (BMS) has been outlined. As a case study, the proposed technique was successfully applied to an image of a damaged concrete bridge beam. The statistics derived from the Grey Level Co-occurrence Matrix (GLCM) were found to be effective at describing the perceived texture in the image, while the *k*-means clustering demonstrated a strong ability at grouping texture features corresponding to damaged regions for a range of *k* values. The ROC space was employed as a tool to evaluate the performance of the technique and as a means to obtain an optimum value of the *k* parameter to maximise the detection accuracy of the algorithm.

ACKNOWLEDGMENTS

The authors wish to thank the Irish Research Council for Science, Engineering and Technology (IRCSET) for providing a grant to support this research and CAPACITES/IXEAD society for the practical and financial assistance.

REFERENCES

[1] Tarighat, A. and Miyamoto, A. (2009), 'Fuzzy concrete bridge deck condition rating method for practical bridge management system', *Expert Systems with Applications*, 36(10), 12077-12085.

[2] Agin, G.J. (1980), 'Computer Vision Systems for Industrial Inspection and Assembly', *Computer*, 13(5), 11-20.

[3] Gallwey, T.J. and Drury, C.G. (1986), 'Task Complexity in Visual Inspection', *Human Factors: The Journal of the Human Factors and Ergonomics Society*, 28(5), 595-606.

[4] Sinha, S.K., Fieguth, P.W., and Polak, M.A. (2003), 'Computer vision techniques for automatic structural assessment of underground pipes', *Computer-Aided Civil and Infrastructure Engineering*, 18(2), 95-112.

[5] Sarma, K.C. and Adeli, H. (1998), 'Cost optimization of concrete structures', *Journal of structural engineering*, 124(5), 570-578.

[6] Sirca Jr, G.F. and Adeli, H. (2005), 'Cost optimization of prestressed concrete bridges', *Journal of Structural Engineering*, 131(3), 380-388.

[7] Iyer, S.R., Sinha, S.K., and Schokker, A.J., (2005), 'Ultrasonic C-Scan Imaging of Post-Tensioned Concrete Bridge Structures for Detection of Corrosion and Voids', *Computer-Aided Civil and Infrastructure Engineering*, 20(2), 79-94.

[8] Yusa, N., Janousek, L., Rebican, M., Chen, Z., Miya, K., Chigusa, N., and Ito, H. (2006), 'Detection of embedded fatigue cracks in Inconel weld overlay and the evaluation of the minimum thickness of the weld overlay using eddy current testing', *Nuclear Engineering and Design*, 236(18), 1852-1859.

[9] Schoefs, F., Abraham, O., and Popovics, J. (2012), 'Quantitative evaluation of NDT method performance: application example based on contactless impact echo measurements for void detection in tendon duct', *Construction and Building Materials (CBM), in press*.

[10] Iyer, S. and Sinha, S.K. (2006), 'Segmentation of Pipe Images for Crack Detection in Buried Sewers', *Computer-Aided Civil and Infrastructure Engineering*, 21(6), 395-410.

[11] Tsai, Y. and Huang, Y. (2010), 'Automatic Detection of Deficient Video Log Images Using a Histogram Equity Index and an Adaptive Gaussian Mixture Model', *Computer-Aided Civil and Infrastructure Engineering*, 25(7), 479-493.

[12] Cord, A. and Chambon, S., (2011), 'Automatic Road Defect Detection by Textural Pattern Recognition Based on AdaBoost', *Computer-Aided Civil and Infrastructure Engineering*, 27(4), 244-259.

[13] Haralick, R.M., Shanmugam, K., and Dinstein, I.H. (1973), 'Textural Features for Image Classification', *IEEE Transactions on Systems, Man and Cybernetics*, 3(6), 610-621.

[14] Lu, C.S., Chung, P.C., and Chen, C.F. (1997), 'Unsupervised texture segmentation via wavelet transform', *Pattern Recognition*, 30(5), 729-742.

[15] Choi, B., Han, S., Chung, B., and Ryou, J. (2011), 'Human body parts candidate segmentation using laws texture energy measures with skin color', *13th International Conference on Advanced Communication Technology: Smart Service Innovation through Mobile Interactivity, ICACT 2011*, Institute of Electrical and Electronics Engineers, Gangwon-Do, Korea.

[16] Gadelmawla, E.S. (2004), 'A vision system for surface roughness characterization using the gray level co-occurrence matrix', *NDT and E International*, 37(7), 577-588.

[17] Bastos, L.D.O., Liatsis, P., and Conci., A. (2008), 'Automatic texture segmentation based on k-means clustering and efficient calculation of co-occurrence features', *Proceedings of 15th International Conference on Systems, Signals and Image Processing, IWSSIP*, Inst. of Elec. and Elec. Eng. Computer Society, Bratislava, Slovakia.

[18] Pakrashi, V., Schoefs, F., Memet, J.B., and O'Connor, A. (2010), 'ROC dependent event isolation method for image processing based assessment of corroded harbour structures', *Structure and Infrastructure Engineering*, 6(3), 365-378.

[19] O'Byrne, M., Ghosh, B., Pakrashi, V., and Schoefs, F. (2011), 'Receiver Operating Characteristics of a Modified Edge Detection for Corrosion Classification', *Proceedings of Forum Bauinformatik 23rd European Conference*, University College Cork, Cork, Ireland.

[20] Schoefs, F., Boéro, J., Clément, A., and Capra, B. (2012), 'The αδ method for modelling expert judgment and combination of NDT tools in RBI context: application to Marine Structures, Structure and Infrastructure Engineering: Maintenance, Management, Life-Cycle Design and performance (NSIE), *Monitoring, Modeling and Assessment of Structural Deterioration in Marine Environments,* 8(6), 531-543.

[21] Baroth, J., Breysse, D., and Schoefs, F., 'Construction Reliability', 1st Edition, Wiley, (2011).

The interaction of multiple mode deterioration by chloride and carbon dioxide in mortars exposed to cyclic wetting and drying

J. Backus[1], D. McPolin[1], P.A.M. Basheer[1], A. Long[1]
Queen's University Belfast, David Keir Building, Belfast
email: jbackus01@qub.ac.uk, d.mcpolin@qub.ac.uk

ABSTRACT: Carbonation and chloride ingress are the two main causes of corrosion in reinforced concrete structures. An investigation to monitor the ingress of chlorides and carbonation during a 24-week wetting and drying exposure regime to simulate conditions in which multiple mode transport mechanisms are active was conducted on a variety of binders. Penetration was evaluated using water and acid soluble chloride profiles, and phenolphthalein indicator. X-ray diffraction was also used to determine the presence of bound chlorides and carbonation. The effect of carbonation on binding capability was observed and the relative quantity of chlorides also showed a correlation with the amount of chlorides bound in the form of Friedel's salt. As carbonation was mainly observed to be a surface effect in this study it did not alter the overall ability of the materials to resist chloride penetration.

KEY WORDS: X-ray Diffraction; Chloride; Blended cement; Pore solution; Chloride binding; Carbonation; Fly ash; Blast-furnace slag.

1 INTRODUCTION

Chloride ingress and carbonation together account for over 50% percent of deterioration of concrete structures. For corrosion to occur, the passivating film that protects steel in concrete needs to be destroyed and both oxygen and sufficient humidity should be present at the steel. Chloride ingress is one of the primary reasons for the destruction of the passivating film. When chloride ions reach the protective passive film on the surface of the reinforcing steel, they destroy the film, making the steel at that region act as an anode, while the remainder of the steel surface acts as a cathode [1].

Similarly, carbonation reduces the pH of the concrete surrounding the steel, making the protective passive film unstable and exposing. When the concrete surrounding the steel is wet, an electrolytic cell is completed and steel starts to corrode.

As modern concretes are free from internal chlorides, in general, the corrosion due to chlorides is caused by those penetrating through the concrete cover from an exposure environment. This movement of chlorides can be represented by an increasing chloride concentration with time. Furthermore, sufficient quantities of chloride ions are required to depassivate the reinforcement. This quantity is known as the threshold chloride content. Therefore, the distribution of chloride ions within reinforced concrete is of great importance.

Carbonation will occur when carbon dioxide penetrates from the external environment and interacts with the hydrated cement. The progression of carbonation can be monitored by measuring pH levels and identified as a carbonation front. Carbon dioxide penetrates primarily through diffusion and for carbonation to occur an optimum range of moisture conditions within the concrete are required.

Chloride ingress, on the other hand, is a complex process as there are different mechanisms by which chlorides can penetrate concrete depending on the local physical conditions.

1.1 Chloride transportation and quantification

The ingress of chlorides is caused generally by three mechanisms, viz. absorption, permeation and diffusion. It is often the measurement of the coefficients of these transport mechanisms which are used to define durability of concretes, though it should be noted that it is often a combination of the mechanisms which lead to the chloride ion movement. Hence, it may be argued, that a more realistic approach is to define an apparent diffusion coefficient that will include all of the transport phenomena based on obtained chloride profiles within the concrete, rather than pure diffusion. The movement of liquid, which may contain aggressive agents such as carbon dioxide or chloride ions, can be described as convection and can be caused by permeability or absorption.

These mechanisms transport solids, liquids and gases through the cementitious material, via the pore network. As the binder type influences the micro-structure of the hydrated cement paste (hcp), it therefore will have an influence on its permeation properties. In the case of permeability a review by Kropp [2] suggested that only pores greater than 0.1μm can transport water under pressure. For transport to occur these pores must also be continuous. The shape of the pores will also affect the transport of liquids as a pore with a large surface area can trap a large amount of water, thus slowing the transportation.

The effect of ground granulated blast-furnace slag (GGBS) and pulverised fuel ash (PFA) considered in this study, is to reduce permeability. The reason for this reduction is due mainly to the Pozzolanic reaction of calcium hydroxide [3]. However, other effects include increased workability with the inclusion of PFA [3], increased packing effect through the smaller size of all particles [3], lower density and slower strength gain but higher maximum strength due to hydraulic latency.

Relevant to all the transport mechanisms, for transport to occur the pores must be continuous and the effectiveness of the transport through continuous pores will also be affected by the size of the pores.

1.2 Chloride binding

As stated earlier there is a critical concentration of chloride ions which is required to initiate corrosion within reinforced concrete, but this concentration is complex to define due to the phenomenon of chloride binding. Due to the structure of hcp chlorides can exist in two forms, free chlorides and bound chlorides. Free chloride ions are dissolved in the concrete pore solution and bound chlorides are either physically bound by being adsorbed on the surface of the gel pores or chemically bound by being incorporated in the products of hydration, [1] [2].

The two types of chlorides normally exist together to maintain a chemical equilibrium, [1] [2] [4]. However, it is generally accepted that the free chlorides contained within the pore fluid are the chlorides which can cause corrosion. It is known that the amount of chlorides which are bound physically and chemically is affected by mineral admixtures [5]. More specifically, the increased aluminate content of both SCMs [4,5] allow more chemical binding of chlorides while the increased surface areas provided by the smaller particles create more physical binding sites.

1.3 Carbonation

Similar to chloride ingress, there is a critical threshold for carbonation, after which corrosion can occur. This threshold is the pH at which the passive oxide layer becomes unstable and is simpler than the chloride threshold. As carbon dioxide dissolves in the pore fluid to form carbonic acid, it reacts with the calcium hydroxide dissolved in the pore fluid from the hydration process and creates the less soluble calcium carbonate. The removal of calcium hydroxide from the pore fluid causes as decrease in pH, while the calcium carbonate can contribute to a denser matrix. The inclusion of PFA and GGBS are known to decrease the pH of the mortar.

2 EXPERIMENTAL PROCEDURE

2.1 Specimen Preparation

Three mixes were used in this study, incorporated Portland cement (PC), pulverised fuel ash (PFA) and ground granulated blast-furnace slag (GGBS). The details of all the mixes are shown in table 1. The chemical and physical compositions are shown in table 2. A water-binder ratio of 0.42 was chosen for all mixes so as to produce reasonable workability in the range of 350-450 mm according to BS EN 12350-5: 2000 [6]. The aggregate binder ratio was 1.67 for all mixes. The specimens were prepared from slabs of size 250 x 250 x 100 mm. Three specimens were cast per mix, totalling nine for use in this experiment.

The specimens were manufactured according to BS 1881: 125 [7] using a pan mixer. Specimens were cast within one week and removed from the moulds 24 hours after casting.

2.2 Curing, preparation, and chloride exposure

After demoulding, the specimens were stored in a water bath (20±1°C) for three days. They were then removed from the water bath and transferred to a constant temperature room at 20±1°C, 55±1% relative humidity for continued hydration until they were 28 days old. After 28 days, a total of twenty-seven 60 mm cores were cut from the three slabs manufactured for each mix. The cores were cut from the slabs before exposure to the chloride and carbonation environments. Water was used as the coolant during coring and would have affected the chloride distribution if the coring had been done after exposure to the chloride environment. Three 100 mm cubes were tested for compressive strength at the age of 28 days.

After conditioning to 20±1°C, 55±1% relative humidity the cores were coated on the circumference with two coats of epoxy emulsion (Sikaguard 680), forming a barrier which prevented any lateral ingress of chloride ions or carbon dioxide. To facilitate ponding, a 60 mm diameter pipe of length 50 mm was placed over the top of each core forming a reservoir in which a salt solution could be contained. The joint between the pipe and the core was tight and was packed with silicone sealant to ensure no leaking occurred during ponding. The cores were ponded with a 0.55 M (3.2%) *NaCl* solution for 1 day and the following day the saline solution was removed and the surface exposed to air for 6 days at 20±1°C, 55±1% RH. This regime was chosen to simulate real exposure conditions in the splash zone which Bamforth [8] identified as the most extreme zone with regard to the accumulation of surface chlorides whilst potentially allowing carbonation to occur. This wetting and drying exposure has been used by previous researchers [9]. This cycle was repeated every week for twenty four weeks.

Table 1. Mix design used in experiments to yield 1m^3 of mortar (mass in kg).

Mix	Binder	PC	PFA	GGBS	FA	W
PC	100% PC	734	-	-	1226	308
PFA	30% PFA	496	213	-	1184	298
GGBS	50% GGBS	363	-	363	1213	305

Note: FA : fine aggregate (2 mm max size), W : water (does not include additional water added to alter aggregate from oven dry to saturated surface dry state)

2.3 Measurement of acid soluble chloride

The acid soluble chloride content of the various mixes was determined after twenty four weeks of ponding. The sample was profile ground at discrete depths of 0-1 mm, 1-2 mm, 2-3 mm, 3-4 mm, 4-5 mm, 5-10 mm, 10-15 mm and 15-20mm. This dust was then used to extract chlorides using nitric acid according to the method described in BS EN 14629: 2007 [10].

2.4 Measurement of free chloride concentration

The free chloride content was determined for each of the mortars after twenty four weeks of cyclic exposure to the chloride environment. To obtain the chloride concentration of the pore fluid at different depths, twenty-one cores (to obtain sufficient pore fluid for analysis) were sliced into 3 mm thick discs with a precision saw, as described above. The resultant discs were representative of a discrete depth range within the mortar e.g. 0-3 mm, 5-8 mm, 10-13 mm, and 15-18 mm. The pore fluid was expressed from these discs using a pore fluid expression device [11].

Table 2. Chemical composition and physical properties of binders.

Chemical composition (%)	PC	PFA	GGBS
SiO_2	19.88	59.01	35.2
Al_2O_3	6.03	22.8	13.96
Fe_2O_3	2.73	8.8	0.25
CaO	64.45	2.38	41.21
MgO	1.69	1.39	8.18
SO_3	3.14	0.27	-
K_2O	0.78	2.8	0.42
Na_2O	0.13	0.74	0.19
Cl	0.007	-	-
TiO_2	-	1.15	0.57
Mn_2O_4	-	0.08	0.55
MnO	-	-	0.49
P_2O_3	-	0.39	
Specific surface area (m^2/kg)	322	340	600

2.5 Measurement of water soluble chloride concentration

The water soluble chloride content was determined for each of the mortars after twenty four weeks of cyclic exposure to the chloride environment. To obtain the chloride concentration at different depths, each of the specimens were ground at discrete depths as with the acid soluble chloride concentration. The water soluble chloride concentration was then determined with a technique similar to that described by Haque, et al. [12] using potentiometry.

2.6 Phenolphthalein indicator measurements

A cylinder from each mix was split prior to testing and at the conclusion of the twenty four week ponding regime and sprayed with phenolphthalein indicator. Five readings were taken to give an average, with the maximum and minimum depths also noted as described in BS EN 14630 (2006) [13].

2.7 Measurement of pH

Using the dust samples prepared for water soluble chloride analysis, the pH was measured using a Gelplas reference combination pH electrode. This was used as a more accurate indicator of carbonation.

2.8 X-ray diffraction analysis of dust

Once again dust was extracted from discrete layers for analysis. The use of XRD determined the presence of Friedel’s salt and identified chlorides that had become bound in this form. This test does not accurately quantify the amount of chemically bound chloride ions but allowed the various mixes to be ranked in terms of the amount of chloro-aluminate quantities. The XRD scan was also used to determine the presence or absence of peaks associated with calcium carbonate formed due to carbonation.

3 RESULTS

3.1 Acid soluble chloride distribution

The acid soluble chloride content was plotted against depth and hence an acid soluble chloride concentration profile was developed for each mix. These acid soluble chloride profiles are shown in Figures 1-3.

As would be expected with an external chloride source the profiles generally show a high concentration of chlorides near the surface which decreases with depth as the mortars resist the penetration of the chloride ions. The profiles for all mortars have a lower chloride concentration in the surface layer and a peak is observed at about 3 mm.

Possible reasons for this could be that carbonation at the surface modified the pore structure and limited further penetration of chlorides, the lower pH due to carbonation released previously bound chlorides, driving the diffusion gradient [14], or an outward movement of chlorides occurred when the ponding solution wasn’t present.

The apparent diffusion coefficient was calculated for each of the mixes using a non linear curve fitting method, developed by NT Build 443 [15]. The calculated diffusion coefficients are shown in table 3. The inclusion of GGBS and PFA all had the effect of reducing the apparent diffusion coefficient relative to the PC mix.

The reason for the reduction in the apparent diffusion coefficient can be attributed to either increased chloride binding [8] or decreased permeability [16] or a combination of both.

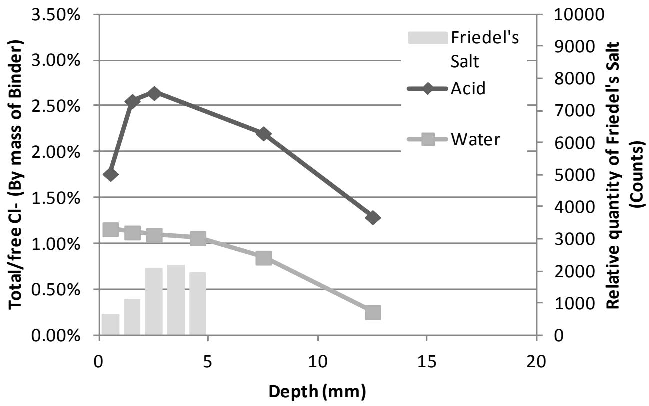

Figure 1. PC profiles.

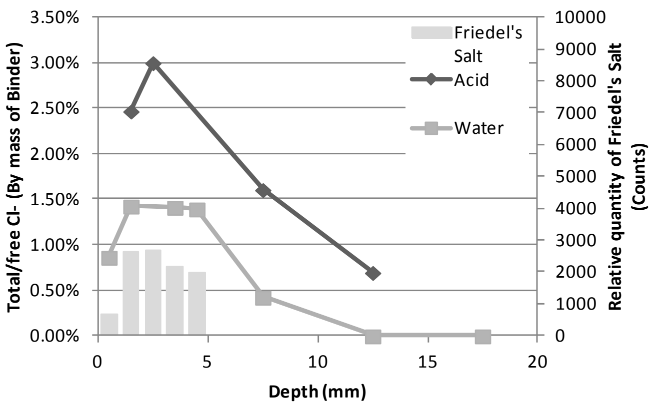

Figure 2. PFA profiles.

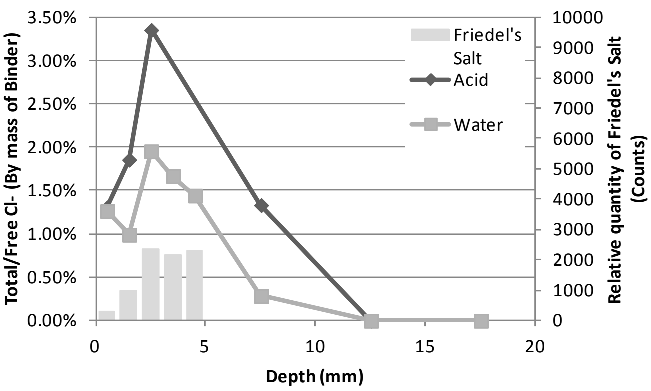

Figure 3. GGBS profiles.

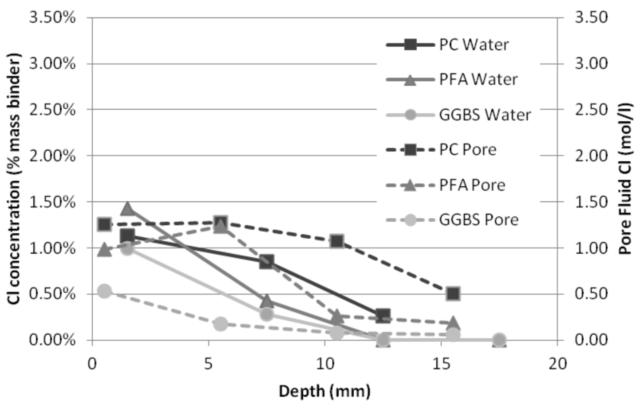

Figure 4. Correlation of pore fluid and water soluble chloride contents.

Table 3. Apparent diffusion coefficients.

	C	FA	GBS
Apparent diffusion coefficient ($x10^{-12}$ m^2/s)	1.63	.09	.77

3.2 Water soluble and free chloride concentration distribution

The water soluble and pore fluid chloride contents shown in Figure 4display a good correlation; however as the water soluble values can be directly compared to the acid soluble values they were plotted against depth on the same graph as the acid soluble profiles. The water soluble chloride profiles are therefore also shown in Figures 1-3.

Similar to those for acid soluble chloride, the profiles show a high chloride concentration nearer the surface and a decreasing concentration with depth. All three profiles follow the same trend as the total chlorides after the peak with the PFA and GGBS exhibiting the same rapid decrease which would suggest that the addition of these materials have caused a decrease in permeability.

However, unlike the acid soluble chloride profile, there is a lack of peak in the PC mix while both the PFA and GGBS have a less distinct peak. This difference can be partly explained by chloride binding as both the PFA and GGBS would be expected to increase chloride binding. The presence of peaks in the water soluble chloride in GGBS and PFA might be caused by the lower pH in the surface layers of both the GGBS and PFA mixes relative to that of the PC mix; releasing bound chlorides and driving the diffusion gradient. At the surface layer of the GGBS mix, the water and acid soluble values are the same, suggesting that carbonation had released all the bound chlorides.

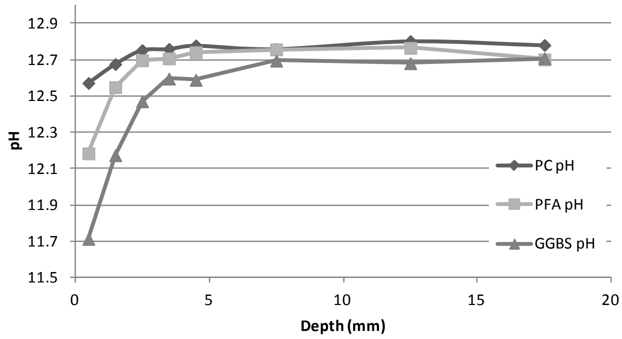

Figure 5. PH profiles.

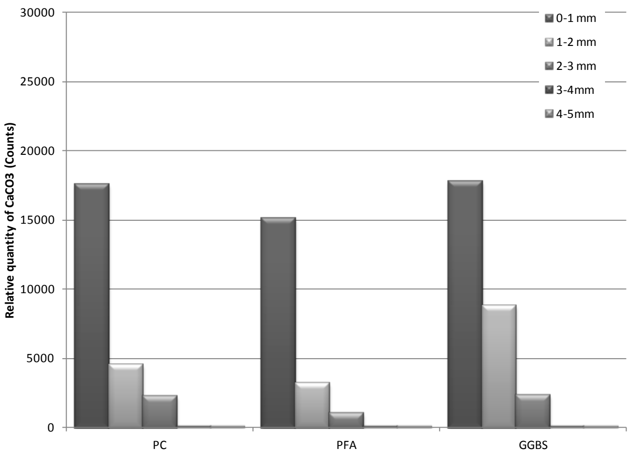

Figure 6. Relative XRD counts of calcium carbonate.

3.3 Phenolphthalein indicator measurements and pH profiles

The results from the phenolphthalein indicator are shown in Table 4. The results would suggest that very little carbonation had occurred in the samples, with only GGBS showing any indication of carbonation occurring.

Although the phenolphthalein indicator didn't identify carbonation as having occurred in the PFA or PC mixes, when the pH values were plotted against depth (fig. 5) it can be seen that the pH for all mixes dropped in the initial layers of the concrete. GGBS had the most carbonation as indicated by the phenolphthalein, followed by PFA and then PC.

Table 4. Depth of carbonation as measured by phenolphthalein indicator.

Mix	Depth before exposure (mm)	Depth after exposure (mm)
PC	0	0
PFA	0	0
GGBS	0	1

3.4 X-ray diffraction analysis of dust

The XRD micrographs were analysed qualitatively to determine the presence of Friedel's salt and calcium carbonate. The presence of calcium carbonate was used to indicate that carbonation was occurring even although not at sufficient quantity to show up on the phenolphthalein test.

The relative count of calcium carbonated peaks is presented in Figure 6. XRD analyses were only carried out in the first 5mm of the sample, where it can clearly be seen it is present, declining rapidly over the first 3mm and not present in the last 2 mm. GGBS has the most calcium carbonate present, followed closely by PC mix with PFA having the least as would be expected given the smaller quantity of calcium oxide in its composition.

The quantity of Friedel's salt for each sample, as determined from the peak count in the micrographs, is presented in Figures 1-3. The results revealed that the specimens with the greatest to least quantities of Friedel's salt were PFA, GGBS and PC. These results were not unexpected as from literature it is known that Friedel's salt is formed by chloride ions combining with calcium aluminate hydrate present in the mortar. PFA contains a high quantity of alumina (Al_2O_3) and therefore would be expected to increase the binding. The GGBS mix showed a decrease in binding. This would be expected as Friedel's salts decompose in lower pH environments.

4 DISCUSSION

4.1 Comparison of water and acid soluble chloride

The nature of the relationships is dependent on the chloride binding properties of the binders used in each mix. As the alumina content in each of the binders was different, it is reasonable to expect varying amounts of chemical binding in the form of chloroaluminates to have occurred. This is reflected in the relative quantity of Friedel's salt detected in the XRD analysis of the different binders. The relationship between water and acid soluble chlorides is also affected by physical chloride binding of the chloride ions, which is influenced by the specific surface area of the binder particles.

4.2 Chloride profiles and X-ray diffraction results

The purpose of the X-ray diffraction was to account for chemically bound chlorides and to help explain the differences between the water and acid soluble chloride profiles. It may be argued that the presence of Friedel's salt in the matrix, can partly explain the difference between the chloride concentration profiles for the water and acid soluble chlorides. As chlorides contained in the Friedel's salt will not be present in the pore water, the chloride concentration will differ from the acid soluble chloride content, which contains most of the chlorides present in the matrix.

The general trend between the difference in acid and water soluble profiles and Friedel's salt would suggest that low values of Friedel's salt coincide with a convergence of the graphs while higher quantities of Friedel's salts result in a divergence.

The variation in Friedel's salt quantity also appears to be dependant on the pH value at that depth, with a lower pH value, less Friedel's salt is present. This was as expected as carbonation is known to release bound chlorides [2] [4].

4.3 Effect of different cement blends on chloride ingress and carbonation

From the profiles it can be stated that despite resisting carbonation the least, the GGBS matrix was the best at resisting chloride ingress as determined by all of the tests. Although the surface quantities of chlorides in the GGBS was high, a lot of these were bound and as the depth increased, it had less chlorides than PFA and significantly less than PC at 15 mm. The GGBS and PFA mixes had the greatest quantities of Friedel's salt in the initial layers and a sharp drop in both chloride concentrations after this. It can be seen therefore from all the tests that the inclusion of cement replacement materials, increases the chloride penetration resistance of cements.

The phenolphthalein indicator, pH profiles and XRD results all confirm that the GGBS mix was most susceptible to carbonation, while the PFA despite having a lower pH had less calcium carbonate present than the PC.

5 SUMMARY AND CONCLUSIONS

The acid soluble chloride profiles which were obtained had a similar trend to the water soluble and free chloride profiles. Although quantification of the water soluble/free chlorides may be a more accurate way of assessing corrosion risk than acid soluble chlorides, it is a higher risk method as additional bound chlorides are also present, which are not accounted for. Should conditions arise which causes liberation of these additional bound chlorides, such as carbonation, there is potential for a sudden increase in free chloride concentration within the material.

One of the most important factors affecting corrosion of reinforcing steel is the concentration of free chlorides as they are the chlorides which are available to cause active corrosion.

In this study both carbonation and chloride ingress occurred and although carbonation occurred, its effect was near surface – resulting in a high surface chloride concentration – but it did not significantly alter the overall performance of the materials.

A strong relationship was observed between Friedel's salt and the difference between free/water soluble and acid soluble chloride concentration. The effect of carbonation on binding was significant and it is recommended that it should be measured in conjunction with chloride concentration when using materials with chloride binding capability.

REFERENCES

[1] Neville A.M., (1995), *Properties of concrete*, fourth edition, Harlow: Longman

[2] Kropp J., (1995), 'Performance criteria for concrete durability', *RILEM report 12*, London: E and FN Spon, Chapman and Hall

[3] Mehta P.K., Monteiro P.J.M., (2006), *Concrete: Microstructures, properties and materials*, Third edition, London: McGraw-Hill

[4] Nilsson L. O., HETEK, (1995), 'Chloride penetration into concrete, State-of-the-Art', *HETEK project by Danish Road Directorate*, Report No. 53

[5] Arya C., Xu Y. , (1995), ' Effect of cement type on chloride binding and corrosion of steel in concrete', *Cement and concrete research*, 25(4): 893-902

[6] BSI, (2000), *Testing fresh concrete. Flow table test.* BS EN 12350-5

[7] BSI, (1986), *Testing concrete: Methods for mixing and sampling fresh concrete in the laboratory*. BS EN 1881 Part 125

[8] Bamforth P. B., (1997), *An international review of chloride ingress into structural concrete,* Contractor Report 359, Edinburgh: Transport Research Laboratory

[9] Polder R., Peelen W., (2002), 'Characterisation of chloride transport and reinforcement corrosion in concrete under cyclic wetting and drying by electrical resistivity', *Cement and Concrete Composites*, 24(5):427-435

[10] BSI, (2007), *Products and systems for the protection and repair of concrete structures-Test methods-Determination of chlorides content in hardened concrete*. BS EN 14629

[11] Bjork F., (2002), 'Measurement of alkalinity in concrete by a simple procedure, to investigate transport of alkaline material from the concrete slab to a self-levelling screed', *Construction and building materials*, 16(8):535-542

[12] Haque, M.N., Kayyali, O.A., (1995), 'Free and water soluble chloride in concrete', *Cement and Concrete Research*, 25(3):531-524

[13] BSI, (2006), *Products and systems for the protection and repair of concrete structures-Test methods-Determination of carbonation depth in hardened concrete by the phenolphthalein method*. BS EN 14630

[14] Suryavanshi A.K., Swamy R.N., (1996), 'Stability of Friedel's salt in carbonated concrete structural elements', *Cement and Concrete Research*, 26(5):729-741.

[15] Nordtest Method, NT Build 443, (1995), *Concrete, Hardened: Accelerated chloride penetration*, NORDTEST, Norway,

[16] Lea F.,(1998), *Lea's Chemistry of cement and concrete*, fourth edition, London: Arnold

Thermal and chemical activation of pulverised fuel ash in Portland cement based systems

M.I. Russell[1], P.A.M. Basheer[1], R.Kant[2]
[1]School of Planning, Architecture and Civil Engineering, The Queen's University of Belfast, Stranmillis Road, Belfast BT7 1NN, UK
[2]Visiting student, BHU India
email: m.i.russell@qub.ac.uk, M.Basheer@qub.ac.uk

ABSTRACT: Pulverised fuel ash (PFA), a by-product of the coal-fired electric power stations and the most common pozzolanic material in Europe, has been used for many years as a Portland cement (PC) replacement material in concrete. Its incorporation has resulted in improved concrete properties, particularly durability in chloride environments. However, despite such benefits, the use of PFA in concrete is limited due to its slow pozzolanic reactivity, and resulting poor strength development at early ages. To overcome this problem a recent research at Queen's University Belfast has focused on methods of activating the pozzolanic potential of PFA thereby permitting more PFA to be used in concrete without adversely affecting the early strength development. This paper reports results of an investigation to assess two such methods: thermal and chemical activations. PC/PFA based systems (PFA amounts to 50% of the binder) were activated chemically by anhydrite (5% replacement of PC) and thermally by curing at 60^0C in a moist environment for 24 hours. The effects of the thermal and chemical activations at early (3 and 28 day) and later (90 and 200 day) ages were ascertained by compressive strength testing and X-ray diffraction (XRD) and thermogravimetric techniques (TGA). Results from these tests have indicated that the pozzolanic potential of PFA can be activated using both these methods and improved early strength development can be obtained. Moreover, the 3 day compressive strength of some activated PC/PFA blends (with a PC content of 45%) exceeded the 3 day strength of 100% PC pastes.

KEY WORDS: Pulverised fuel ash (PFA); pozzolan; activation.

1 INTRODUCTION

For many years the construction industry has used pulverised fuel ash (PFA), a by-product of coal combustion, as a partial replacement for cement in the manufacture of concrete. PFA is a pozzolanic material. A pozzolan refers to "siliceous/aluminous materials which, in the presence of water, will react chemically with calcium hydroxide (CH) to form compounds that possess cementitious properties" [1]. Compounds formed by this reaction include calcium silicate hydrate (C-S-H) gel [2]. There are many benefits associated with the utilisation of PFA including lower heat of hydration, enhanced long term concrete strength development and improved concrete durability [3-5]. The utilisation of PFA also leads to cost reduction and is considered to be environmentally friendly [4].

The benefits of using PFA as a cement replacement in concrete are numerous; however, it can only replace up to 30% PC without affecting the long-term strength and durability of the concrete [6-8]. When PFA is added in larger quantities early concrete strength development will decrease compared to concrete without PFA [9]. The disadvantages of using PFA as a pozzolanic material are the long setting time and slow strength development of the concrete. During early age cement hydration PFA behaves as an inert material with the main pozzolanic reaction only occuring in "an advanced age" [10]. Consequently, the use of PFA is limited and is not being utilised widely. To overcome the reduction in early-age strength research has focused on several ways to accelerate the pozzolanic reactivity of PFA. These include different forms of mechanical, thermal and physical activation processes or a combination of all three [11].

In this study two methods of activation were investigated: chemical activation and elevated curing (thermal activation). There are numerous types of chemical activation including the use of alkalis and chlorides; however, in this study calcium sulphate (anhydrite) activation was investigated. The use of calcium sulphate to activate PFA chemically has previously been studied [12-17]. This technique is based on the reaction of sulphates with the amorphous aluminate present in PFA, to form the mineral ettringite (AFt). AFt contributes to early strength because it infills the pore space and gives strength to the matrix. The second type of activation utilised in this study was thermal activation. It is recognised that elevated curing temperature enhances the pozzolanic reactivity of PFA [3, 18, 19].

This paper investigates how anhydrite and elevated temperature curing conditions activate PFA blended cements. The rationale for conducting this research was to determine the impact of the two methods of activation (anhydrite and thermal activation), individually and in combination, on PFA blended cements and to understand more clearly how activation mechanisms modify the various cement hydration and pozzolanic reactions.

2 EXPERIMENTAL PROGRAMME

2.1 Materials

PFA conforming to BS EN 3892: Part 1: 1997 [20] was supplied by Conexpo (NI) Ltd and the PC used was class 42.5N Portland cement [2], purchased from Lafarge. The anhydrite was supplied by a local chemical supplier. The chemical compositions of the materials used in this study are reported in Table 1.

Table 1. Chemical composition of materials - results by XRF, except anhydrite which was obtained from a local supplier

Oxides (%)	PC	PFA	Anhydrite
SiO_2	21.41	56.32	-
TiO_2	0.36	1.04	-
Al_2O_3	5.11	23.54	-
Fe_2O_3	2.61	4.72	-
CaO	61.50	4.39	41.19
MgO	1.78	1.80	-
SO_3	3.03	0.56	58.81
Na_2O	0.33	1.01	-
K_2O	0.61	1.81	-
P_2O_5	0.16	0.73	-
LOI*	2.58	3.58	-

*loss on ignition

2.2 Sample Preparation

The type of mixes and their notations are given in Table 2. PC and PC/PFA blends (with 0.4 water to cementitious materials ratio) were manufactured using a mechanical mixer and placed in 50 mm size cube moulds. The samples were then tamped with a metal rod until the air bubbles stopped appearing at the surface. The samples were used to assess compressive strength of the various blends as well as their hydration and mineralogical changes.

Table 2. Mix proportions of cement blends investigated.

Notation	PC	PFA	Anhydrite
PC-W	100	0	0
PFA-W	50	50	0
PFA-T	50	50	0
AN-W	45	50	5
AN-T	45	50	5

2.3 Curing Regime

Immediately after casting, the various blends were cured in one of two ways. Firstly, blends with notation –W (i.e. PC-W, PFA-W, AN-W) were covered with a damp hessian cloth and placed in a constant temperature condition (20^0C±1^0C) for 24 hours. After this period the samples were demoulded and placed in a constant temperature (20^0C±1^0C) water bath for a further two days. Following this, the samples were wrapped in a damp hessian cloth, covered in a black polythene sheet and then placed in the constant temperature room (20^0C±1^0C) until age of testing. Secondly, steel moulds containing blends with notation -T (i.e. PFA-T, AN-T) were covered in a damp hessian cloth, wrapped in black polythene sheet and placed in an environmental chamber set to 60^0C and 95% RH. These blends were cured in such conditions for 24 hours. After this period the blends were demoulded and then cured similarly to the other specimens until the age of testing.

Samples were stored in constant temperature conditions (20^0C±1^0C) until testing at 3, 28, 90 and 200 days.

2.4 Test Methods

The activation of PFA in the various blends was determined from compressive strength and mineralogical data from the pastes. The mineralogical information was ascertained by X-ray diffraction (XRD) and thermogravimetric (TGA) techniques. At the specified ages three samples of each mix were tested for their compressive strength. Powder samples were obtained from each of the crushed cubes for testing by XRD and TGA.

For TGA the paste samples (~20 mg) were placed in an alumina crucible and heated in Netzsch's STA 449C at 10^0C/min up to 1000^0C. An inert nitrogen atmosphere was used and results were plotted on the TG curve, with weight against temperature. The amount of calcium silicate hydrates (C-S-H) and portlandite (CH), which gives an indication of the degree of hydration, was calculated as mass loss on the TG curve in the respective temperature range of 200-400^0C and 450-520^0C respectively.

XRD analysis was also carried out on the powder samples. Samples produced a series of diffraction peaks over the 2θ range 5–65^0, with the pattern of diffraction peaks indicating the mineral phases present within the sample. The XRD was carried out using PANalytical's X'Pert Pro Diffractometer. This machine, equipped with the X'celerator detection unit, permits excellent scans over a short time interval, with mineral phases identified using PANalytical's X'Pert Highscore Plus software in conjunction with the Powder Diffraction File database from the International Centre for Diffraction Data (ICDD).

3 RESULTS AND DISCUSSION

3.1 Effect of activation techniques on paste strength

The compressive strength of each paste sample is illustrated in Fig. 1. With the exception of AN-T at 3 days, the replacement of Portland cement by PFA and anhydrite, both with and without thermal activation at 60^0C, has had a detrimental effect on strength development.

Comparing the compressive strength of PC-W and PFA-W it is clear that the pozzolanic reaction is very slow when 50% PFA replacement is used. After 3 days the strength of PFA-W is only 40% of PC-W and by 28 days this has slightly increased to 54%. After 28 days the pozzolanic reaction begins to take effect and the differences in compressive strength values start to narrow, with PFA-W obtaining 80 and 90% strength of PC-W at 90 and 200 days respectively.

3.1.1 Effect of Thermal Activation on Strength Development

When PC/PFA blend (PFA-T) was cured at elevated temperatures, the initial 3 day strength was improved compared to PFA-W which was cured at 20^0C in a water bath. However, by 28 days the compressive strength development of both blends was similar. By 90 and 200 days PFA-T strength development is much less than PFA-W and at these ages the thermally activated PFA blend only achieved 60% strength of the blend (PFA-W) that was cured at 20^0C. Although steam curing is beneficial for early age strength development it is shown to be detrimental to the later strength development of PC/PFA blends. Indeed, the compressive strength of PFA-T after 28 days is consistently less than all other blended samples. The lack of later age strength development in PFA-T strongly indicates that the pozzolanic reaction is not occurring in this sample after 28 days.

3.1.2 Effect of Sulphate Activation on Strength Development

In samples AN-W 5% Portland cement was replaced by anhydrite. This caused the strength of the paste to decrease in comparison to PFA-W at 3 days (~50% reduction). Subsequently, the strength development accelerated in this blend between 3 and 28 days, to become slightly better than PFA-W at 28 days. However, at 90 and 200 days the strength of the PFA-W was greater. Therefore, the use of a sulphate activator during normal curing conditions only slightly improves strength at 28 days. The strength development at 28 days is noteworthy given the fact AN-W contains 5% less PC than PFA-W and therefore less strength producing cement hydrates should form. AN-W has a greater strength development than PFA-T at 28, 90 and 200 days.

3.1.3 Effect of Combined Thermal and Sulphate Activation on Strength Development

When PC/PFA blends are activated by sulphates and cured at elevated temperatures (AN-T) the early age strength is not only enhanced compared to PFA-T and PFA-W but is also enhanced compared to 100% Portland cement paste (10% stronger). This is all the more remarkable when it is considered that AN-T only consists of 45% PC. AN-T also exhibits greater strength development than all other blends at 28 days, although the strength of PC-W now exceeds it. However, such gains are short lived and by 90 days PFA-W (no activation) exhibits greater strength than the activated samples. Indeed, AN-T displays only marginal development in strength beyond 28 days. Although this is so, it is still important to recognise that when sulphate (anhydrite) is added to the PC/PFA blend and thermally cured, the compressive strength was consistently greater than PFA-T, which exhibits the lowest compressive strength values at 28, 90 and 200 days. Accordingly, the inclusion of anhydrite has provided some benefit during thermal curing of PC/PFA blends.

The following conclusions can be made regarding the strength development:

- Elevated curing promotes early age strength development but thereafter there is little or no strength development.
- Sulphate activation improves strength at 28 days (although lower at 3 days).
- A combination of thermal and chemical activation techniques can allow 3 day strength development to be greater than 100% PC and 3 and 28 day strength to be greater than all other blends.
- At 90 and 200 days the two lowest strength materials are the blends which have been cured at the elevated temperature. Whereas, the two samples exhibiting greatest strength development are the samples which have not been activated by either elevated temperature or sulphates.

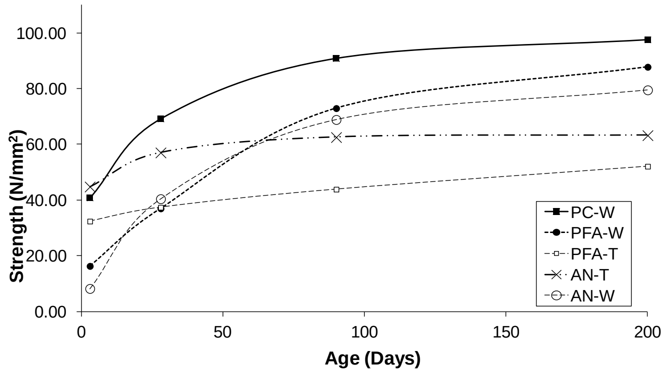

Figure 1. Compressive strength of pastes from 3 to 200 days.

3.2 Mineralogical Composition of Pastes

Identification of cement hydrates permitted an assessment of the degree of hydration as well as an understanding of the reasons for the variations in compressive strength results between the different pastes. Various hydration products obtained from XRD and TGA are discussed below:

3.2.1 Ettringite (AFt) – $Ca_6[Al(OH)_6]_2(SO_4)_3.26H2O$

In this study the XRD technique was used to determine the presence of AFt in each cement blend. An example of how AFt can be identified using XRD is shown in Fig. 2. This figure, which includes XRD traces of each sample after 28 days of hydration, highlights the 2 theta position of the main AFt peaks at ~9.1^0 and 15.8^0 2 theta. Results indicate that AFt is present in all pastes except PFA-T. To illustrate the change in AFt through time and the difference between each cement blend, the counts associated with these two main (highest intensity) peaks were taken, added together and presented in Fig. 3. It is worth noting at this point that the greater the peak height the greater the amount of AFt in the sample.

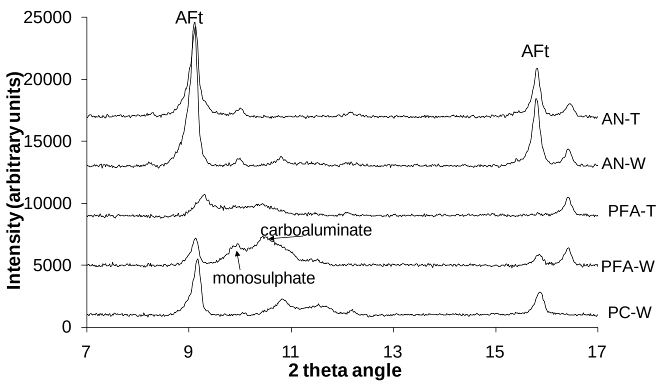

Figure 2. XRD traces of pastes after 28 days highlighting the AFt peaks.

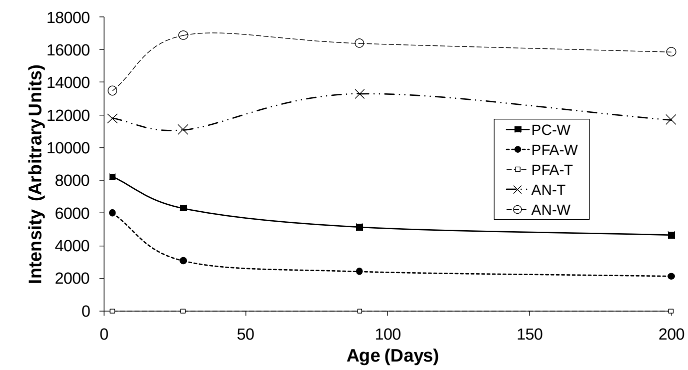

Figure 3. Development of AFt through time as determined by the intensity of main AFt XRD peaks.

In Portland cement AFt forms in the presence of moisture by reaction of C_3A and calcium sulphate minerals. However, in this study AFt formation was also the result of added anhydrite reacting with the amorphous aluminate phases within PFA, as well as any residual C_3A. It is clear that, as expected, samples containing anhydrite (AN-W, AN-T) exhibit the greatest amount of AFt. This indicates that PFA is not totally inert at early ages (3 days) and that some aluminates are readily reactive.

Although AN-W and AN-T contain the same amount of sulphate it is uncertain why AFt development is greatest in AN-W. Previous research [21] suggests that AFt may not form at high curing temperatures, with some sulphates rather going into the pore solution or becoming loosely bound in the C-S-H structure. The effect of this is to risk the occurrence of delayed ettringite formation (DEF). This is potentially what has partially occurred in AN-T and more fully in PFA-T, which exhibits no AFt formation (see Figs. 2 and 3).

The impact of AFt development on strength is unclear at this point. However, as AFt infills pore space, giving strength to the cement matrix, it is likely that the increase in early strength (between 3 and 28 days) in sulphate activated samples is partly a result of increased AFt content. This will be discussed more fully later in the paper.

PC-W and PFA-W show a decrease in AFt content through time (see Fig. 3). This is due to AFt reacting with aluminate phases in cement or PFA to form AFm phases such as monosulphate and carboaluminate (see Fig. 2).

3.2.2 Calcium Silicate Hydrate (C-S-H)

C-S-H makes up approximately 50-60% of a fully hydrated cement paste [22] and is principally responsible for the strength forming properties of that material. The presence of C-S-H in cementitious materials can be explained by two separate processes: hydration of calcium silicates in Portland cement and reaction of pozzolanic materials with calcium hydroxide in Portland cement. In this section TGA was used to give an indication of the relative amount C-S-H in each paste by determining the amount of water released during TGA experiment in the temperature range 200 to 400^0C.

Results in Fig. 4 indicate that PC-W (100% PC) exhibits the greatest degree of C-S-H formation at most ages. This was to be expected given that all other pastes contain either 45 or 50% PC. Blends that have been thermally activated initially exhibit (at 3 days) higher C-S-H values than the other blends but thereafter (28 to 200 days) display less C-S-H development. Accordingly PFA-T and AN-T also demonstrate the least amount of strength development after 28 days.

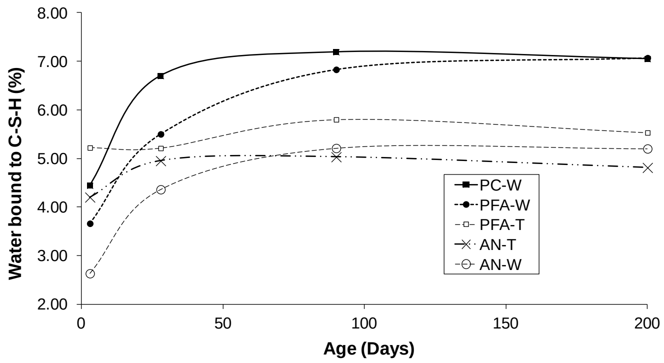

Figure 4. Amount of water bound to C-S-H (3-90 days) as determined by mass loss in TGA trace between 200-400^0C

Although thermally activated samples without added anhydrite exhibit greater 3 day compressive strength compared to their normally cured analogue, later strength development is less. The can be adequately explained by the C-S-H results. After the initial burst of pozzolanic reaction to form C-S-H, the development of further C-S-H 'stalled' and consequently so did strength development.

Compressive strength development of PFA-T is less than that of AN-T. This result however cannot be explained alone by the amount of C-S-H in each paste due to the fact that AN-T contains less C-S-H than in PFA-T. Rather the presence of AFt, which is greater in AN-T, has had a positive impact on strength development.

Figs. 3 and 4 highlight that AN-W contains the greatest amount of AFt but the least C-S-H. It is clear therefore that AFt formation, exceeding that formed during 'normal' Portland cement hydration, has had a detrimental impact on C-S-H formation in PFA blended systems.

Concluding this section it is important to state that although thermal activation can enhance early pozzolanic activity the long term pozzolanic reaction is detrimentally effected; hence lower rates of long term strength development in such samples are observed. On the other hand, strength development progresses in AN-W even though the production of C-S-H has been hindered. Here strength development is due in part to the benefit of excess AFt in the cementitious structure. However, the positive impact of AFt in the cement structure, which aids strength development, must be balanced with the adverse impact this has on the production of the strength forming hydrate C-S-H.

3.2.3 Calcium Hydroxide (CH) – $Ca(OH)_2$

The determination of the amount of CH is important when discussing both the degree of cement hydration, as well as the development of the pozzolanic reaction. During cement hydration the CH values increase; whereas during pozzolanic activity the CH will be consumed in a reaction that forms C-S-H gel. Thermogravimetry (TGA), coupled with its derivative (DTG), was used to quantify CH content of the hydrated pastes at 3, 28, 90 and 200 days. During heating CH will dehydroxylise at approximately 450^0C. This reaction, which results in a mass loss within the sample, can be accurately determined from TGA curves over the temperature range identified by the DTG trace. The mass loss determined by TGA, which relates to H_2O, can then be used to calculate the quantity of CH in each sample (e.g. see Fig. 5). Fig. 6 presents CH values calculated from TGA traces from each sample at all ages.

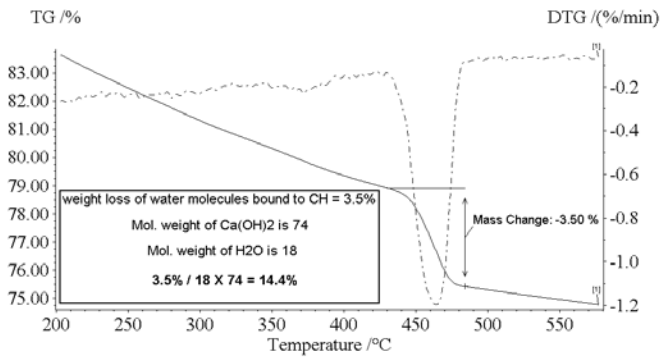

Figure 5. Determination of calcium hydroxide content by thermogravimetry – PC-W at 28 days.

Results indicate that CH values of pastes with no PFA (PC-W) continuously increased during hydration; whereas the opposite was so in PFA-W. In this sample the decrease of CH with time can be explained by the pozzolanic reaction consuming CH and forming additional C-S-H (see Fig.4). Compared to the non-activated PFA-W, other blends (PFA-T, AN-W and AN-T) exhibit lower CH values at all ages. There are three possible reasons for this. Firstly, thermal activation has resulted in greater pozzolanic reactivity, especially at 3 days. This was confirmed by the fact that PFA-T and AN-T exhibit the greatest amount of C-S-H formation of all blends at 3 days. Secondly, thermal activation of PFA/PC blends impedes hydration [23] and therefore less CH will form. Thirdly, CH in sulphate activated samples (AN-W, AN-T) was consumed by the production of AFt. Indeed twice as much Ca^{2+} ions are required to form AFt than can be supplied by anhydrite. Accordingly, this has implications for continued pozzolanic activity. If CH is depleted then the pozzolanic reaction, which aids long term strength development, may be hindered.

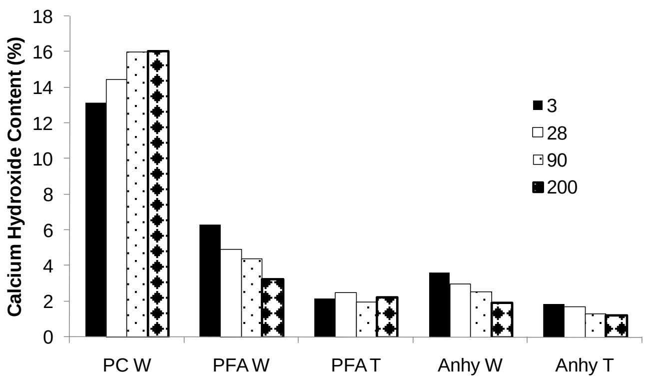

Figure 6. CH values (%) of Pastes from 3 to 200 days.

4 CONCLUSIONS

Based on the results in the paper the following conclusions have been reached:

- C-S-H development, and consequently compressive strength development, is initially accelerated in thermally activated samples. However, long term C-S-H and strength development are hindered.
- Long term C-S-H formation is hindered in all activated PFA blends.
- Combined sulphate and thermal activation of PFA can produce greater 3 day compressive strength results for blends containing 45% PC (AN-T) compared to 100% PC samples (PC-W). In these samples strength development is aided by enhanced pozzolanic reactivity, as well as the formation of AFt in the cement structure.
- AFt, which forms to a greater degree in samples that contain additional anhydrite, is produced by the reaction of sulphates with amorphous aluminate in the PFA. This reaction has both positive and negative influences associated with it: Positive - AFt infills pore space, giving strength to the cement matrix. Negative – AFt formation hinders the development of C-S-H. The mechanisms for this need to be investigated further, although the reduction in CH during the formation of AFt may be a factor.

Finally, it has been demonstrated that both activation methods alter the hydration and pozzolanic processes. Although these changes have been determined it will be necessary for further research to look more closely at why these changes occur. Accordingly, a greater understanding of these activation methods may make it may possible to select optimum conditions for activation (i.e. sulphate content and curing temperature) to enable use of high volume PFA in blended cements that exhibit both early activation and long term strength development.

REFERENCES

[1] ASTM C593-95, Standard specifications for fly ash and other pozzolans for use with lime, Annual Book of ASTM Standards, (1995)

[2] British Standard EN 197-1, Cement- Part 1: Composition, specifications and conformity criteria for common cements, British Standard Institution (BSI), London, (2000)

[3] Fraay, A.L.A., Bejen, J.M. and de Haan, Y.M., The reaction of fly ash in concrete: a critical examination, *Cement and Concrete Research*, Vol. 19, pp 235-246 (1989)

[4] Bijen, J., Benefits of slag and fly ash, *Construction and Building Materials*, Vol. 10, No. 5, pp. 309-314 (1996)

[5] Bye, 'Portland Cement', 2nd edition, Thomas Telford Ltd, London, (1999)

[6] Berry, E.E. and Malhotra, V.M., Fly ash for use in concret – a critical review, *ACI Mater Journal*, 77(8), pp. 59-73, (1980)

[7] Lam, L., Wong, Y.L. and Poon, C.S., Effect of fly ash and silica fume on compressive and fracture behaviours of concrete, *Cement and Concrete Research*, Vol. 28, pp 271-283, (1998)

[8] Han, S-H., Kim, J-K. and Park Y-D., Prediction of compressive strength of fly ash concret by new apparent activation energy function, *Cement and Concrete Research*, Vol. 33, pp 965-971, (2003)

[9] Malhotra, V.M. and Mehta, P.K., Pozzolanic and Cementitious Materials, Gordon and Breach Publishers, SA, 199pp, (1996)

[10] Hardtl, R., The pozzolanic reaction of fly ash in connection with different types of cement, valuation of hydration of Portland cement, *Proceedings of the 10th International Congress on the Chemistry of Cement (ICCC)*, pp. 3v082, (1997)

[11] Arjunan, P., Silsbee, M.R. and Roy, D.M., Combined effect of chemical, mechanical and thermal activity of low calcium fly ash,

Proceedings of the 11th International Congress on the Chemistry of Cement (ICCC), Vol. 4, pp. 951-957, (2003)
[12] Aimin, X., Microstructural study of gypsum activated fly ash hydration in cement paste, *Cement and Concrete Research*, Vol.21, pp. 1137-1147, (1991)
[13] Xu. A and Sarkar. S.L., Microstructural study of gypsum activated fly ash hydration in cement paste, *Cement and Concrete Research*, Vol. 21, pp 1137-1147, (1991)
[14] Yan, P. Yang, W. Qin, X. and You, Y., Microstructure and properties of the binder of fly ash-fluorogypsum-Portland cement. Cement and Concrete Research, Vol. 29, pp. 349-354, (1999)
[15] Bhanumathidas, N. and Kalidas, N., Influence of sulfate on cement admixtures containing fly ash or blast-furnace slag, *Seventh CANMET/ACI International Conference on fly ash, silica fume and natural pozzolans in concrete*, SP 199-35, pp 622-633 (2001)
[16] Poon, C.S., Kou, S.C., Lam, L. and Lin, Z.S., Activation of fly ash/cement systems using calcium sulphate anhydrite (CaSO4), *Cement and Concrete Research*, Vol. 31, pp. 873-881, (2001)
[17] Min, Y., Jueshi, Q. and Ying, P., Activation of fly ash-lime systems using calcined phosphogypsum, *Construction and Building Materials*, Vol. 22, pp 1004-1008, (2008)
[18] Hanehara, S., Tomosawa, F., Kobayakawa, M. and Hwang, K.R., Effects of water/powder ratio of fly ash, and curing temperature on pozzolanic reaction of fly ash in cement paste, *Cement and Concrete Research*, Vol. 31, pp 31-39, (2001)
[19] Kobayakawa, M., Hanehara, S., Hwang, K. and Tomosawa, F., Pozzolanic reaction of fly ash cement system, *Proceedings of the 11th International Congress on the Chemistry of Cement (ICCC)*, Vol. 2, pp 736-746, (2003)
[20] British Standard EN 3892-1, Pulverised fuel ash- Part 1: Specification for pulverised-fuel ash for use with Portland cement, British Standard Institution (BSI), London, (1997)
[21] Taylor, H.F.W., Famy, C. and Scrivener, K.L., Delayed ettringite formation, *Cement and Concrete Research*, Vol, 31, pp 683-693, (2001)
[22] Glasser, F.P., Fundamental aspects of cement solidification and stabilisation, *Journal of Hazardous Materials*, 52, pp 151-170 (1997)
[23] Narmluk, M. and Nava, T., Effect of fly ash on the kinetics of Portland cement hydration at different curing temperatures, *Cement and Concrete Research*, Vol. 41, pp 570-589, (2011)

Factors affecting the measurement of solar reflectance using an albedometer

Angharad Sweeney[1], Roger West[1], Peter Seymour[2]
[1]TrinityHaus, Centre for Construction Innovation and Sustainability, Trinity College, University of Dublin, Dublin 2, Ireland
[2] Ecocem Ireland Ltd., Thorncastle Street, Ringsend, Dublin 4, Ireland
email: sweenean@tcd.ie, rwest@tcd.ie, pete.seymour@ecocem.ie

ABSTRACT: This paper presents an aspect of ongoing research at Trinity College into the influence of a number of parameters on the measurement of surface reflectance using an albedometer. Research carried out indicates that the Portland cement replacement GGBS (ground-granulated blast-furnace slag), which is naturally lighter in colour than CEM I or CEM II cements, increases the solar reflectance or albedo of concrete. This, however, is dependent on the nature of the surface finish of the concrete. There are a number of advantages to improving surface albedo including the mitigation of the urban heat island effect and subsequent reduction in air conditioning use. Furthermore, the amount of light reflected back out into space can be converted into, and quantified as, an equivalent reduction in CO_2 emissions. A number of different instruments are being used to directly or indirectly monitor the surface albedo of the slabs in this research, however, for the purpose of this paper the main focus is on the calibration of an albedometer which has proven to be problematic. This method will subsequently be compared with the use of a lux meter which measures only visible light, while the albedometer measures across three wavelengths, namely visible, near infrared and ultraviolet light. The objective of this paper is to assess the feasibility of calibrating an albedometer in order for the instrument to measure the albedo of a small surface area. A number of parameters are being investigated, namely the height of the instrument, restriction of the field view of the device, the time of day the reading is taken and the incoming solar radiation. The results indicate that the use of a cone to restrict the field view results in a significant reduction in the reading and sensitivity of the lower dome and consequently the albedo value. There is also an indication that the albedo value increases throughout the day although it is assumed to be constant. The change in height of the instrument resulted in a change in measured albedo also. Results of the calibration testing indicate that the device, while highly sensitive, is difficult to calibrate for small specimens due to the number of variables while testing.

Key words: Surface finish, surface albedo, solar reflectance, instruments, moisture

1 INTRODUCTION

Solar reflectance, or albedo, is defined as the ratio of reflected to incident radiation at a particular surface or combination of surfaces, over all wavelengths of solar irradiation [1]. It is measured on a scale of zero to one, where an albedo value of 0 indicates a “black” body that does not reflect any light whereas an albedo value of 1 indicates a “white” perfectly reflective surface [2]. Some typical values are given in Table 1.

Dark pavement materials with a low albedo, such as asphalt, absorb the incoming solar radiation which is converted into heat. This causes the surface temperature to become higher than the ambient air temperature which can create a ‘heat island’ as the near surface air and surface temperatures are warmer than their surrounding areas [3]. The heat island effect has a number of disadvantages including the increased energy demand to cool buildings, which results in larger air conditioning costs and it also increases the formation of smog as a higher air temperature induces higher rates of photochemical reactions. Benefits of increasing the albedo of a surface include increased visibility, especially at night time, leading to reduced lighting by approximately 30% [4] and improved safety [5].

In developed urban areas, paved surfaces account for a high percentage of the total surface area, typically between 30% and 40% [6]. In order to reduce the heat island effect, one such method is to increase the albedo, which can be achieved by using high solar reflectance concrete. The albedo of a surface is measured using an albedometer for both the incoming and reflected solar radiation. However, a less expensive instrument is a lux meter which measures the visible light only, but can be indicative of the reflectivity of a surface. In this paper the calibration of the albedometer will be discussed and this will be compared with the method of using a lux meter. There are factors which affect the albedo, principally moisture content and age, but they are outside the scope of this paper, although they are being considered in the research project. At no stage was there any presence of algae growth on the concrete.

The objective of this paper is to evaluate parameters affecting the accuracy of an albedometer to measure the albedo of a surface, with the intention of using the instrument on small scale surfaces. These parameters include the height of the instrument, restricting the field view of the instrument and the intensity of incoming light. This will be compared with an alternative means of measuring light reflectance using a lux meter.

Table 1 Typical albedo values [6]

Surface	Albedo
Snow	0.90
Ice Caps	0.80-.90
White Paint	0.80
GGBS Concrete (50%)	0.50
New Concrete(Traditional)	0.30-0.40
Aged Concrete(Traditional)	0.20-0.30
Aged Asphalt	0.10-0.15
Ocean	0.06-0.10
New Asphalt/Black paint	0.05

2 MATERIALS AND INSTRUMENTATION

2.1 Ground-Granulated Blast Furnace Slag (GGBS)

The cement replacement GGBS is a waste product from the blast furnace production of iron from ore (Figure 1). Its use as an ordinary Portland cement alternative in concrete at sufficiently high replacement rates results in a concrete that is lighter in colour, thus increasing its albedo. Limited research carried out by Boriboonsomsin and Reza [2] using 30, 60 and 70% GGBS replacement had indications that concrete has increasingly higher albedo values than a conventional mix and that the albedo of concrete consistently increases as the percentage of slag increases. The samples containing 70% slag achieved an albedo of 0.58 at 14 days which is approximately 70% higher than conventional concrete. Similarly, Levinson and Akbari [7] examined the correlation between the albedo of smooth concrete and cement albedo. The albedo was measured using a solar spectrum reflectometer. They manufactured 32 concrete mixes using two types of cement (white cement and normal Portland cement), four types of sand and four types of rock. The four most reflective unexposed smooth samples from the 32 samples were constructed using white cement with albedo values ranging between 0.68 and 0.77. The four least reflective unexposed smooth samples had results ranging between 0.44 and 0.52 and were made with normal grey cement.

Figure 1. GGBS and Ordinary Portland cement [8].

2.2 Albedometer

An albedometer measures the albedo of a surface and consists of two components, an upper dome to measure the incoming solar radiation and a lower dome to measure the reflected solar radiation (Figure 2). It has a spectral range from 285-2800nm and measures solar radiation across three wavelengths, visible, infrared and ultraviolet light, up to a maximum of 4000W/m^2. This instrument was purchased for measuring the albedo value of small concrete specimens which were manufactured and is a highly sensitive and expensive instrument. It measures albedo from a recommended height of 1.5m and the lower dome has a field view of 170°. It is also a requirement that the upper dome has an unobstructed horizon. As the concrete specimens are 300 mm square, it is necessary to scale down and calibrate the instrument by restricting the field view of the lower dome. A stand was designed and manufactured specifically for the albedometer in the laboratory in Trinity College in order to support and keep the instrument level for taking albedo measurements.

Figure 2. Albedometer.

2.3 Lux meter

A lux meter is used to measure visible light reflectance only. It is used in conjunction with a black box specifically designed by the authors to eliminate background light, as seen in Figure 3 [9]. The box is placed on top of the slab and they are rotated in a horizontal plane so that the tunnel points towards the incoming sunlight. Both the slab and the box are then tilted in the vertical plane until there is no shadow cast on the surface of the slab, at which point the incoming rays are parallel to the sides of the tunnel. The incoming light is measured orthogonal to the ray at the slab surface and the reflected light is measured through a hole at the back of the box (see Figure 3)

Figure 3. Lux meter and black box.

3 METHODOLOGY

The main focus of this paper is to measure albedo using two different test methods, namely an albedometer and lux meter. A total of 96 concrete slabs were manufactured which comprises four different percentages of GGBS (0, 30, 50 and 70%), four different surface finishes and three aggregate types. Two specimens of each type were manufactured for repeatability purposes. The surface finishes which represent typical application types, comprise two smooth finishes, cast and screeded, and two rough finishes, brushed and tamped. They were exposed to a strict and consistent curing regime for the first 24 hours and cured in air subsequently before being placed on a rooftop within Trinity College in September 2010. The specimens are shown in situ in Figure 4.

It was necessary to calibrate the instrument before taking albedo readings of the concrete specimens. The albedometer has a field view of 170° so in order to eliminate the background light from the reading, a black cone was used on the lower dome to restrict the view so that only reflected light from the specimen was being measured.

Figure 4. Set up of specimens in Trinity College.

3.1 *Using the Albedometer*

The albedometer is used in conjunction with a stand and is set up as in Figure 5. The apparatus is leveled over the chosen surface at a height of 1.5m. A voltmeter is used to measure the solar radiation of both the upper and lower dome. An albedo value is calculated as a ratio of the reflected to the incoming light from the readings of the upper and lower dome.

To calibrate the albedometer, a number of parameters were tested to observe their effect on the albedo. The height of the instrument was altered and a black cone was introduced to restrict the field view of the lower dome. The location at which the readings were taken on a given surface was changed by repositioning the instrument. This was to ensure that there was no inconsistency within results obtained on the same surface. These readings were recorded over a number of hours during the day to observe the change in albedo, if any, over different sun intensities and altitudes.

Figure 5. Albedometer setup.

4 RESULTS

4.1 *The effect of using a cone to restrict reflected light*

To calibrate the albedometer in order to measure the albedo of the specimens manufactured, it was necessary to restrict the field view of the lower dome. This was achieved by using a black cone on the lower done which was 300mm in length and diameter. Figure 6 displays the results of albedo taken at a height of 1.5m on 21st April 2010 on a weathered concrete surface in Trinity College. The albedo recorded without the cone increases linearly with a rising sun from 0.12 to 0.17, however, the addition of the cone results in reduced albedo values ranging from 0.05 to 0.075 and increasing at a lower rate. The presence of the cone greatly reduces the amount of reflected light reaching the lower dome, thus reducing the albedo value by less than half. The general increase in albedo is due to the increase in the incoming solar radiation, and yet one would expect the albedo to be a constant for a given surface at a given age.

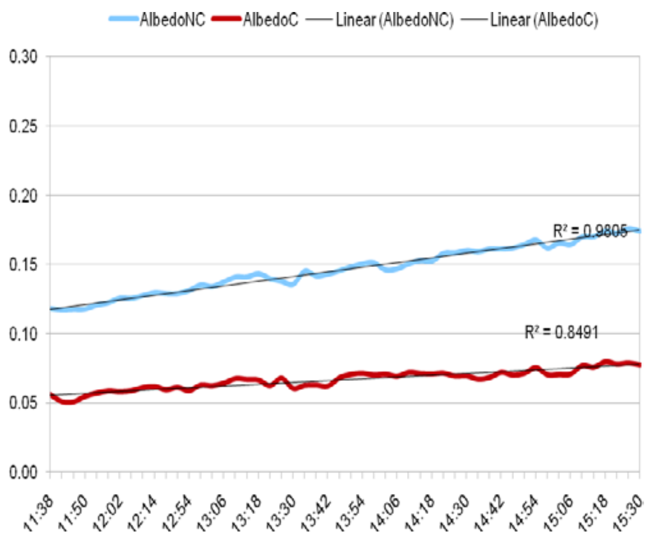

Figure 6. Albedo results recorded (h=1.5m) with the cone (C) and without the cone (NC) on a weathered concrete surface.

4.2 *The change in albedo over time*

The albedo was recorded every 4 minutes over the duration of four hours on 3rd June 2011 at a height of 0.5m on a new polished concrete surface at Dun Laoghaire pier. Figure 7 demonstrates that the pyranometer, which measures incoming light on the upper dome, increases slowly until it reaches a peak, before decreasing again. This is due to the change in the height of the sun at any given point in the day. The change in the upper dome ranges from 5.70 to 7.30μV. There is a corresponding change in the reflected light as seen in the albedometer result which changes from 1.64 to 2.0μV at the peak. Results were also taken using the cone and they range from 0.51 to 0.61μV. These results indicate that the solar reflectance is not a constant as the reading of the pyranometer depends on the nature of incoming light and the reflection off a surface which is effectively undulating and thus is, apparently, dependent on the angle of incidence.

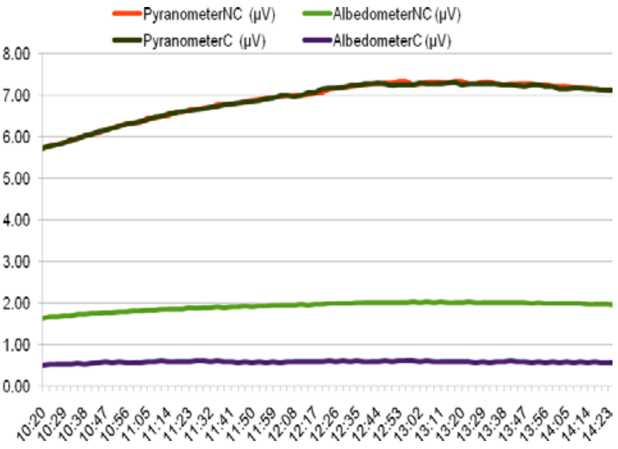

Figure 7. Results recorded from the albedometer at Dun Laoghaire pier (*h*=0.5 m) with and without the cone.

This increase in incoming solar radiation is observed in the corresponding albedo results of the concrete surface (Figure 8). The albedo value recorded with no cone ranges from 0.265 to 0.275. This is close to the published value of new concrete which is approximately 0.30. The albedo is significantly reduced when the cone is used and is less than one third the original value, where the albedo decreases from 0.077 to 0.085. There is, however, potential for the two to be correlated.

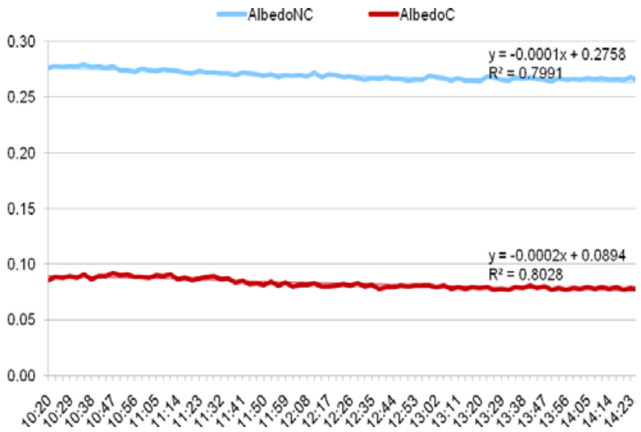

Figure 8. Albedo results recorded in Dun Laoghaire (h = 0.5m) with and without the cone.

4.3 *The effect of changing height at which albedo is measured*

Figure 9 displays results of albedo taken on 27th May 2011 at a height of 0.5m on weathered concrete in Trinity College, the same location as in Figure 6. The results of albedo without the presence of the cone range from 0.265-0.280 whereas this decreases significantly when the field view is restricted. The albedo results when the cone is used, remains constant at 0.080. This would imply that when using the cone to restrict the field view, there is not enough sensitivity in the amount of light reflected to measure any change in albedo.

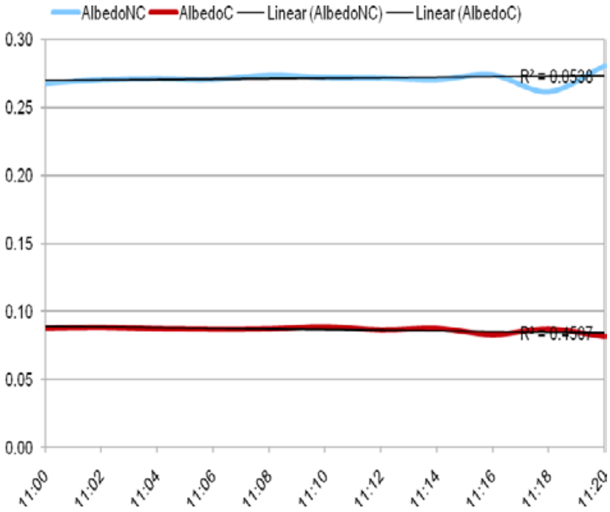

Figure 9. Albedo Results recorded in Trinity College Dublin (h=0.5m) with and without the cone (May 2011).

The incoming solar radiation was higher on this particular day (6-7μV) whereas it was lower on the day recording at 1.5m (4-5μV).

In conclusion, the results would imply that either a reliable alternative to an albedometer is needed, or the albedometer needs to be calibrated noting that it is likely to be less sensitive as there is less incoming light reaching the lower dome.

4.4 *Measuring albedo on different days*

The results in Figure 10 were recorded on 27th April 2011in the same location in Trinity College as those illustrated in Figure 9, also at a height of 0.5m. The albedo result corresponding to this data ranges between 0.18 and 0.20 without the cone over the duration of the four hours. This differs to the results obtained in Figure 9 as the incoming light is not the same.

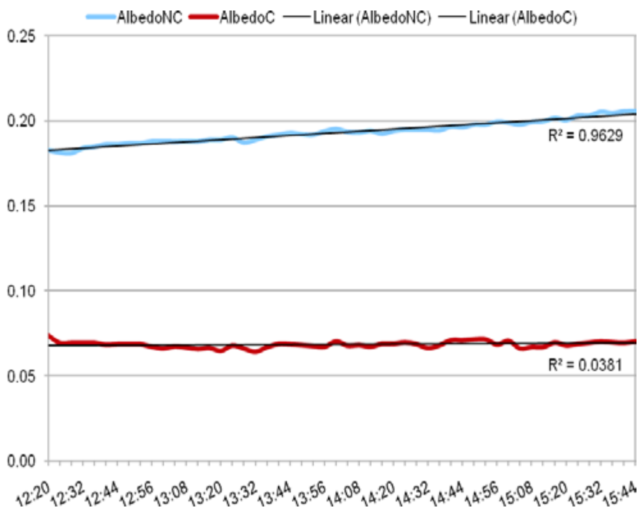

Figure 10. Albedo Results recorded in Trinity College Dublin (*h*=0.5 m) with and without the cone (April 2011).

This is a significant cause for concern as the solar reflectance should be an inherent property of the surface and should be time invariant over a short period.

4.5 The use of a lux meter as an alternative

As a consequence of the foregoing, a viable alternative was sought. Although a lux meter only measures light over the visible spectrum, it is proposed to investigate its suitability as a viable alternative to the albedometer. A measure of visible light reflectance was taken for the slabs using a lux meter as illustrated in Figure 3. Results are presented in Table 2 for 0% and 70% GGBS concrete for two surface finishes, screed and tamped. The results indicate that the presence of GGBS does increase the amount of light reflectance off the surface of the slab. It signifies that a lux meter is a good indicator of albedo despite only measuring in the visible range. It also has the advantage over the albedometer of being cheaper and robust.

Table 2. Average light reflectance for 0% and 70% GGBS slabs.

% GGBS	Surface Finish	Average Light Reflectance Ratio (%)
0	Screed	7.52
	Tamp	5.46
70	Screed	8.09
	Tamp	6.73

5 CONCLUSIONS

The main objective of this paper was to assess the feasibility of calibrating an albedometer in order to measure albedo of a smaller surface area, in addition to studying parameters which affect albedo, namely the height of the instrument, the time of day the reading is taken and the incoming solar radiation. In order to test these parameters the albedometer was tested at two different heights, both with and without a black cone to restrict the field view, and over a number of hours and days. The measurements were taken in sunshine only as the presence of clouds would hugely affect the readings and meter readings are not taken when cloudy.

Based on the results obtained, the use of a cone to restrict the field view results in a significant reduction in the reading of the lower dome. In Figure 6, it is also evident that the albedometer is not as sensitive when the cone is used as the rate of change in albedo is not the same as when there is no cone present. This unfortunately makes it significantly more difficult to calibrate. The results also indicate that the incoming solar radiation increases throughout the day until it reaches a peak, before reducing again. This is due to the change in position of the sun and thus would also depend on latitude and the time of the year.

There is also a corresponding increase in the amount of reflected light. This increase in sunshine results in a decrease in albedo (Figure 6), indicating that measured albedo changes with time, throughout the course of one day despite assumptions to the contrary.

The change in height of the instrument resulted in a change in measured albedo also. Although the testing surface remained the same, the tests were carried out on different days. The height of 1.5m resulted in an albedo ranging between 0.12-0.17, with a maximum value of incoming solar radiation of between 4-5μV. This increased significantly to 0.27 at a height of 0.5m with a maximum value of incoming solar radiation of 7μV. There are two important parameters here, the intensity of sunshine and the height of the instrument.

In conclusion, based on the results to date, the albedometer is a very sensitive instrument and difficult to calibrate for small specimens. The results indicate that there are a number of parameters which affect the albedo value, including the height of the instrument and also the reduction in field view of the lower dome. The lux meter (Figure 3) only measures visible light however it is a less expensive alternative which it also gives an indication of the albedo of a surface.

ACKNOWLEDGMENTS

The authors wish to gratefully acknowledge the support provided by Mr. John Newell of Ecocem Ireland in the execution of this work.

REFERENCES

[1] TAHA, H., AKBARI, H., ROSENFELD, A. and HUANG, J., ‘Residential cooling loads and the urban heat island – the effects of albedo’, *Building and Environment*, Vol. 23, No. 4, 1988, pp 271-283

[2] BORIBOONSOMSIN, K. and REZA F., ‘Mix Design and Benefit Evaluation of High Solar Reflectance Concrete for Pavements’, *Journal of the Transportation Research Board,* No. 2011, Transportation Research Board of the National Academics, Washington D.C., 2007, pp. 11-20

[3] GARTLAND, L. , *Heat Islands*, Earthscan, 2008

[4] Riley, R.C., ‘The Cool Solution to Sustainable Pavements’, Illinois Chapter 27.2, Illinois *Ready Mixed Concrete Association*, 2008

[5] SCA, *‘Slag Cement and the Environment’* , Slag Cement in Concrete*, Slag Cement Association*, 2003

[6] ACPA, ‘Albedo: A Measure of Pavement Surface Reflectance’, *American Concrete Pavement Association*, 2002

[7] LEVINSON, R. and AKBARI, H., ‘Effects of Composition and Exposure on the Solar Reflectance of Portland Cement Concrete’, *Cement and Concrete Research*, 32, 1679-1698, 2002

[8] Ecocem, ‘GGBS and Reducing Global Warming – The Albedo Effect’, *www.worldcement.com* , 2009

[9] SWEENEY, A., WEST, R. and O’ CONNOR, C. , ‘ Parameters affecting the albedo effect in concrete’, Proceedings of BCRI 2010, Cork, 2010, pp. 513-520.

Measurement of time-dependent colour variation in concrete

Peter Deegan[1], Alan O'Connor[2] & Paul Archbold[3]
[1]Banagher Concrete Ltd.
[2]Department of Civil, Structural & Environmental Engineering, Trinity College Dublin
[3]STRAIT, Structures & Materials Research Group, Athlone Institute of Technology
email: peterd@bancrete.com, alan.oconnor@tcd.ie, parchbold@ait.ie

ABSTRACT: The phenomenon of colour variation in finished concrete has become a contentious issue in recent years as engineers and designers strive, not only for blemish free finishes, but crisp "white" concretes with uniformity throughout. Three factors determine what colour an observer perceives: (i) the light source, (ii) the object surface and (iii) the observer himself. Several methods have been identified for the evaluation of colour yet in most cases in the absence of suitable measuring equipment; it is the observer who will decide. Given that colour variation may present differently depending on aspects such as the viewing distance, the ambient light and the viewing angle, this typically results in a subjective assessment devoid of any quantitative metrics. This paper presents the results from an experimental programme aimed at developing a robust and repeatable quantitative methodology for concrete colour measurement. Controlled concrete specimens have been studied over a 3 year period, for 3 different exposure conditions. Initially the exposure conditions are evaluated against each other but, more importantly, changes, monitored over time have also been recorded.

KEY WORDS: Chroma Meter; Colorimetry; Curing.

1 INTRODUCTION

The most consistent thing about concrete is its inconsistency. Today with advances in computer batching technology and state of the art plant, anecdotal evidence suggests that variation still exists. The aim of this paper is to investigate colour variation in concrete exposed to 3 different curing regimes, but more importantly to investigate if changes occur over time. In tandem, the hypothesis that colour and durability

1.1 Concrete Colour Measurement

The real concern with colour measurement is the subjectivity of the assessment of colour variation. Objects modify light, colorants such as pigments or dyes, in the object, selectively absorb some wave lengths of incident light while reflecting or transmitting others (Tominaga, 1985).

Colorimetry is the science of measuring and evaluating colour. The colour specification of a self-luminous colour (sources, CRTs, VDUs, LCDs) or a surface colour (opaque or transparent materials) consists of a set of three numbers – X, Y and Z, termed the tristimulus values, which give the relative amount of three reference primary colours required for a colour match (Zwinkels 1991). It should be noted that Luminosity is the relative sensitivity of the human eye to various wave lengths of light (Tominaga, 1985).

A variety of instruments are available for colour measurement.

Tristimulus colorimeters use a filtered light source and three or four filtered detectors whose modified spectral response approximates that of a particular CIE standard illuminant/observer combination. They give a direct measure of colorimetric quantities (tristimulus values) but provide no information on the underlying spectral data. They are used for Colour measurement of both surface colours and self-luminous colours. Their advantages are their speed, ease of operation, and good measurement repeatability, which makes them well suited for field use and for production quality control, particularly for colour-difference evaluation.

In their paper, Yuzer et al. (2004) employed the Munsell Colour System in identifying colour changes in mortars subjected to high temperatures. In this system, the attributes hue, value and chroma of colour are divided into equal perceptual intervals and denoted through the use of decimals. Hue is the dimension which distinguishes one colour family from another, as red from yellow, or green from blue.

In their work, Lemaire (2005) and Shang (2005) employed a method proposed by CIE (International Commission of Lighting) referred to as CIE-Lab, due to its use of L (luminance) and a & b (chromatic values) respectively. The methodology effectively defines colour in a three-dimensional light space. Three factors determine what colour an observer perceives: the light source, the object surface and the observer himself (Lemaire, 2005).

These factors are crucial when working outdoors as time of day and time of year affect data collection. Monks (1973) found that viewing distance, ambient light and viewing angle must be considered.

Figure 1 shows the AFNOR standard's seven levels of grey and their corresponding luminance values. Determination of these properties of colour requires the use of specific Colorimetry equipment.

Adopted by CIE in 1976 as models that better showed uniform colour spacing in their values. CIE-Lab is an opponent colour system based on the earlier system of Richard Hunter developed in 1942, called L, a, b. Colour opposition correlates with discoveries in the mid-1960s that somewhere between the optical nerve and the brain, retinal colour stimuli are translated into distinctions between light and dark, red and green, and blue and yellow. CIE-Lab indicates these values with three axes: L*, a*, and b* (the full nomenclature is 1976 CIE L*a*b* space).

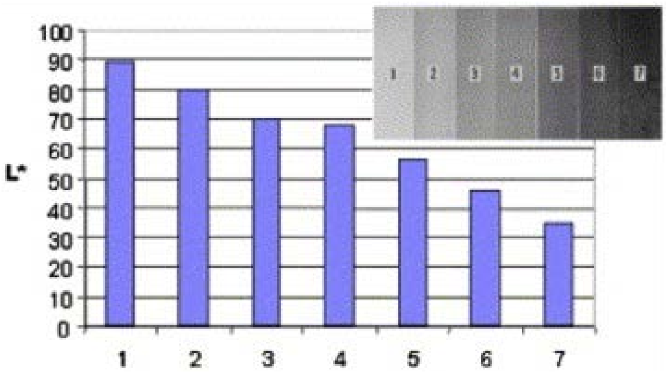

Figure 1. Grey classes of the standard NFP 18-503 and corresponding luminance’s (Lemaire, 2001).

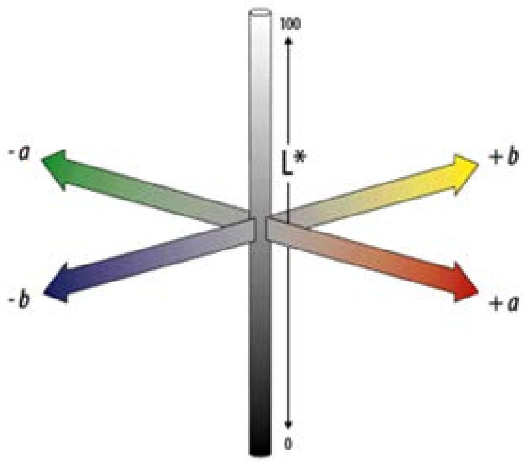

Figure 2. CIELAB.

The central vertical axis represents lightness (signified as L*) whose values run from 0 (black) to 100 (white). This scale is closely related to Munsell’s value axis except that the value of each step is much greater. This is the same lightness valuation used in CIELUV.

The colour axes are based on the fact that a colour can’t be both red and green, or both blue and yellow, because these colours oppose each other. On each axis the values run from positive to negative. On the a-a’ axis, positive values indicate amounts of red while negative values indicate amounts of green. On the b-b’ axis, yellow is positive and blue is negative. For both axes, zero is neutral grey. Therefore, values are only needed for two colour axes and for the lightness or grayscale axis (L*), which is separate (unlike in RGB, CMY or XYZ where lightness depends on relative amount of the three colour channels).

The instrument chosen for this experiment is a Konica Minolta Chroma meter data processor DP-400 as shown in Fig. 3.The instrument is first calibrated with a true white Calibration plate before sampling begins and then readings may be taken at 3 second intervals. Results may be recorded manually or stored on the unit (max 2000 results) and printed on completion.

Figure 3. Chroma Meter.

2 EXPERIMENTAL PROGRAMME

The experimental programme consisted of producing concrete samples from two discrete concrete mixes – a self-compacting concrete with a design strength of 60N/mm2 (SCC) and a second mix, again a semi self-compacting concrete with a design strength of 60N/mm2, but with 30% GGBS cement replacement (GGBS). This forms part of a PhD study over three years and year 1 (2010) results will be presented in this paper.

2.1 Sample Preparation

The aggregates for both mixes are locally sourced limestone gravel of a carboniferous age and are both of pale and dark variety in almost equal measure. The concrete has been batched in a 1.5 m3 pan mixer with microwave moisture control and a computer controlled weigh system accurate to 0.2%. The trial moulds (300mm x 300mm x 100mm) were made from steel to reflect the type of mould most used in an Irish precast operation.

The moulds were cleaned and an application of release agent - Gemleaze, GP Bio - was applied. The concrete mixes were taken to the lab and poured into the moulds. The SCC mix received no vibration but the GGBS samples were placed on a vibrating table for 10 seconds. The samples were then left uncovered to cure overnight in the laboratory and stripped the following morning approximately 18 hours later. Once stripped, the samples were left for 2 hours before being initially photographed. A total of 72 samples were prepared. A sample of initial photographs are shown in Figure 4.

Figure 4. Colour change over time.

2.2 Curing Conditions

Normal industrial practice offers a variety of curing conditions for precast concrete specimens. Moreover, practical experience has shown that colour variation tends to present more frequently in specimens which are developed and cured in winter months, inferring that ambient curing conditions may be influential in terms of achieving uniformity of colour. In an attempt to replicate these conditions and to examine the effects of curing on the finished colour of the specimens, three different curing scenarios were employed for each of the concrete mix samples as follows:

2.2.1 Curing Tank (Tank)

Samples were placed in a curing tank, with the temperature maintained at 20oC for the entire period. Samples cured in the curing tank will be denoted as Tank herein. A photograph of a curing tank used can be seen in Figure 5(a).

2.2.2 Stacking (Stack)

Samples were stacked on top of one another with the mould face, facing down and placed outside for the test period. These samples will be referred to as Stack in this paper. A photograph of a stack used can be seen in Figure 5(b).

2.2.3 Storage Rack (Rack)

Samples were placed on a storage rack, facing due south to maximize exposure to sunlight. A photograph of the rack used can be seen in Figure 5(c).

(a) Tank (b) Stack

(c) Rack

Figure 5. Samples in Curing Regimes Employed.

3 TESTING PROGRAMME

Experiments began in spring 2010 with follow on sampling in summer and winter of the same year. Once stripped, samples are given a specific identity mark and photographed using a digital camera in a designated photobooth. They are then placed in their respective curing conditions for the duration of the test. Chroma readings are taken at 28 days, 6 months and 1 year intervals. For the purpose of this paper only 28 day and 1 year intervals will be presented.

3.1 *Chroma Testing*

Each sample is measured and divided into 9 equal squares. The data processors photo lens is placed in the center of each square and an image taken, this result is recorded and the average of all 9 results will be used as the individual result. As stated and shown in Figure 3 Chroma readings were taken using a Konica Minolta Chroma meter at our Lab in Banagher Precast Concrete Ltd. Each sample is first cleaned using a soft cloth, measured and divided into 9 equal squares.

4 RESULTS

Tables 1, 2 and 3 present the chroma readings from year 1 samples. For the purpose of this paper SCC and GGBS concretes are presented together to assess changes over seasons and time rather than between individual mixes. Table 1 illustrates results from spring 2010/2011 while Tables 2 and 3 continue with summer and winter.

In each table, results are presented in their respective curing conditions. In Spring 2010 Mix A (SCC) produced the brightest colour and similarly an adjacent panel recorded the highest result in 2011, both were cured on the south facing rack system .On completion of sampling in 2010 early indicators suggested that seasonal changes impacted on colour. An average increase in the L* value was recorded from Spring to Summer of 4.79% but equally a drop was recorded in the subsequent winter sampling from Summer to Winter of 5.38%.

Interestingly, SCC presented a higher % L* value than GGBS in the spring sampling despite the fact that anecdotal evidence suggests that GGBS concrete is brighter. This would also back work done by Bennett 2008 which stated that the finest particle sizes would determine colour.

This may be due in some respect to a high crushed limestone content. It must be noted that this was only the case for the spring sampling with the subsequent summer and winter sampling supporting the anecdotal evidence that GGBS concrete is brighter. This variation supports the belief that seasonal change impacts on colour of concrete.

Variation between both mixes was also found; however, it too is seasonally affected. Average changes in L* values vary from season to season. The most consistent variable found in all results was a gradual average increase in lightness over time. An average increase is L* values from Spring 2010 to 2011 of 9.73%, Summer 2010 to 2011 of 3.88% and Winter 2010 to 2011 of 5.38%, as illustrated in Figures 5, 6 and 7.

Table 1. Results of Spring Samples 2010.

Spring Samples 2010	Mix	L* 2010	L* 2011
Rack 01/04/10	GGBS	69.05	70.19
Rack 31/03/10	GGBS	68.12	69.98
Rack 30/03/10	GGBS	67.33	70.43
Rack 29/03/10	GGBS	64.57	55.74
Stack 01/04/10	GGBS	69.52	70.85
Stack 29/03/10	GGBS	66.31	69.41
Stack 31/03/10	GGBS	66.18	68.52
Stack 30/03/10	GGBS	66.10	68.99
Tank 01/04/10	GGBS	58.67	64.51
Tank 30/03/10	GGBS	57.18	66.35
Tank 31/03/10	GGBS	47.83	64.51
Tank 29/03/10	GGBS	47.27	66.35
Rack 23/03/10	SCC	70.99	72.58
Rack 25/03/10	SCC	70.14	72.68
Rack 24/03/10	SCC	70.39	73.35
Rack 26/03/10	SCC	66.46	68.57
Stack 25/03/10	SCC	69.39	71.43
Stack 24/03/10	SCC	68.57	70.49
Stack 26/03/10	SCC	68.13	70.91
Stack 23/03/10	SCC	66.33	68.43
Tank 23/03/10	SCC	53.11	66.54
Tank 25/03/10	SCC	50.90	59.89
Tank 26/03/10	SCC	50.76	68.44
Tank 24/03/10	SCC	48.18	57.13

Table 2. Results of Summer Samples 2010.

Summer Samples 2010	Mix	L* 2010	L* 2011
Rack 03/06/10	GGBS	69.60	71.25
Rack 01/06/10	GGBS	69.37	70.86
Rack 31/05/10	GGBS	68.94	72.08
Rack 02/06/10	GGBS	68.21	66.33
Stack 03/06/10	GGBS	69.45	69.06
Stack 01/06/10	GGBS	68.78	66.38
Stack 02/06/10	GGBS	65.69	65.47
Stack 31/05/10	GGBS	65.30	67.32
Tank 03/06/10	GGBS	70.37	65.87
Tank 31/05/10	GGBS	66.33	64.23
Tank 02/06/10	GGBS	54.84	56.76
Tank 01/06/10	GGBS	49.65	67.49
Rack 25/05/10	SCC	71.17	73.09
Rack 28/05/10	SCC	70.89	71.08
Rack 27/05/10	SCC	69.84	70.99
Rack 26/05/10	SCC	68.62	69.23
Stack 28/05/10	SCC	70.83	65.91
Stack 25/05/10	SCC	69.44	64.84
Stack 26/05/10	SCC	69.20	61.54
Stack 27/05/10	SCC	69.13	50.60
Tank 25/05/10	SCC	64.22	71.63
Tank 27/05/10	SCC	55.81	67.61
Tank 28/05/10	SCC	51.60	67.53
Tank 26/05/10	SCC	49.02	68.91

Table 3. Results of Winter Samples 2010.

Winter Samples 2010	Mix	L* 2010	L* 2011
Rack 04/11/10	GGBS	57.68	68.74
Rack 05/11/10	GGBS	55.69	63.82
Rack 08/11/10	GGBS	52.39	57.97
Rack 09/11/10	GGBS	61.21	66.16
Stack 04/11/10	GGBS	65.69	66.71
Stack 05/11/10	GGBS	64.49	66.53
Stack 08/11/10	GGBS	68.91	65.82
Stack 09/11/10	GGBS	66.84	62.09
Tank 04/11/10	GGBS	64.91	65.52
Tank 05/11/10	GGBS	64.60	66.29
Tank 08/11/10	GGBS	66.23	68.46
Tank 09/11/10	GGBS	62.59	65.92
Rack 11/11/10	SCC	44.21	48.79
Rack 12/11/10	SCC	42.68	47.07
Rack 15/11/10	SCC	60.56	70.94
Rack 17/11/10	SCC	47.14	51.88
Stack 11/11/10	SCC	69.86	68.38
Stack 12/11/10	SCC	62.57	60.45
Stack 15/11/10	SCC	70.11	67.16
Stack 17/11/10	SCC	62.04	62.20
Tank 11/11/10	SCC	64.20	69.96
Tank 12/11/10	SCC	58.57	63.74
Tank 15/11/10	SCC	64.71	70.07
Tank 17/11/10	SCC	59.80	63.85

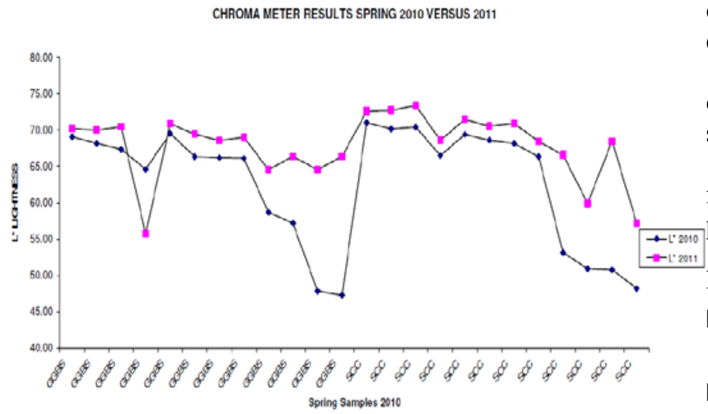

Figure 6. Spring 2010 vs Spring 2011.

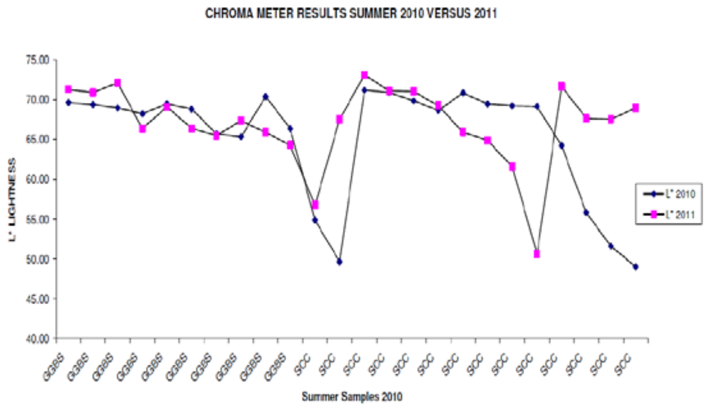

Figure 7. Summer 2010 vs Summer 2011.

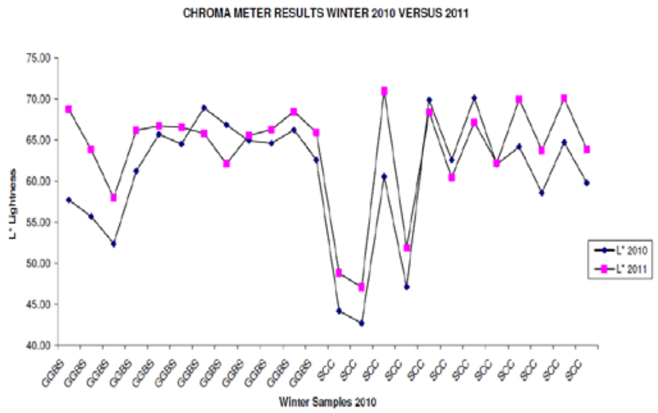

Figure 8. Winter 2010 vs Winter 2011.

5 CONCLUSION

The aim of this study is to monitor colour variation in various curing conditions over time, and the results presented so far suggest that colour does change with time. Similarly the season when casting and type of curing also play a role. The results clearly show that samples cured on a rack, south facing formation presented brighter than those consistently submerged in water (tank). This may also suggest that early curing conditions are critical as concrete continually kept damp presented darker.

In addition average improvements were found in all curing conditions irrespective of mix constituents or sampling season.

Further work has also been done in assessing each sample for durability matrices and this forms part of a PhD Thesis in progress.

REFERENCES

[1] Bertolini, L. & lollini, F. 2010. Effects of weathering on colour of concrete paving blocks. *European Journal of Environmental and Civil Engineering*, 15, 939-957.

[2] Coster, M. & chermant, J. L. 2001. Image analysis and mathematical morphology for civil engineering materials. *Cement and Concrete Composites*, 23, 133-151.

[3] Lemaire, G., escadeillas, G. & Ringot, E. 2005. Evaluating concrete surfaces using an image analysis process. *Construction and Building Materials*, 19, 604-611.

[4] Monks, W. L. 1973. *Colour Variation In Smooth Concrete Surfaces*. Concrete (London), 7, 22-23.

[5] Tominaga, S. 1985. A mapping method for computer color vision based on the theory of colorimetry. *Transactions of the Information Processing Society of Japan*, 26, 318-28.

Laboratory experiment to measure soil matrix suction and examine the effect of infiltration

Cormac Reale[1], Kenneth Gavin[1], Alan O'Connor[2]
[1]Department of Civil, Structural and Environmental Engineering, Newstead Building, University College Dublin, Dublin 4, Ireland
[2]Department of Civil Engineering, Trinity College Dublin, Dublin 2, Ireland
email: cormac.reale@ucdconnect.ie, kenneth.gavin@ucd.ie, alan.oconnor@tcd.ie

ABSTRACT: Climate change is affecting rainfall patterns which in turn are having a demonstrable effect on slope stability. This is a serious safety concern for EU rail networks. Accurately assessing slope stability is critical in maintaining a safe and efficient railway infrastructure. Soil matric suction is naturally present in all soils which lie above the water table. Therefore, it is a critical component in maintaining embankment stability. Rainfall infiltration causes a decrease in matric suction which subsequently reduces the shear strength of the soil. This can be a triggering effect for many slope failures. This paper describes a tensiometer based apparatus for measuring soil matric suction in a laboratory environment. It also outlines a method for determining the minimum matric suction left during a heavy rainfall or flood event.

KEY WORDS: matric suction; pore pressure; partial saturation; laboratory equipment; slope stability.

1 INTRODUCTION

Soil suction plays a vital role in maintaining the stability of unsaturated slopes [1], [2]. Soil suction is present in all grounds that lie above the water table[3], [4]. In saturated conditions, the voids within the soil are full of water with a small percentage of occluded air. Therefore, under these conditions, the pore water pressure is considered hydrostatic and has a positive value. Above the water table, physio-chemical and molecular forces between the soil and water particles combine to create a slight vacuum within the soil[4]. This attraction that the soil exerts on the water is known as soil suction and acts as a tensile hydraulic stress in the soil. This tensile stress has a capillary effect within the soil drawing water up from the water table to fill empty void spaces. It also acts as an impediment to water infiltrating through the soil as it draws the infiltrating water into empty pore spaces near the soil surface and holds it there thus preventing further infiltration.

The magnitude of the soil suction is a function of the moisture content of the soil as well as its pore size. The pore size is of vital importance as smaller pores will result in greater capillarity. The lower the moisture content, the higher the soil suction necessary to remove the remaining moisture. This is because it is more difficult to remove water from smaller pores. Because the exit points are smaller and as there is also a greater percentage of water in direct contact with the soil due to the decreased pore space, more bonds are formed and hence greater energy is needed to remove the water from the pore space.

Rainfall infiltration causes a decrease in matric suction which in turn causes a short term reduction in the shear strength of the soil[5], [6]. As a result, rainfall infiltration is one of the leading causes of slope failure. This paper proposes a method of monitoring soil suction under an applied rainfall in a laboratory environment.

1.1 Background

In soils compacted dry of optimum moisture content large interconnected pores form between clods of clay which causes the soil to have a coarse look to it. These relatively large pore spaces allow for fast drainage under matric suction. Therefore, this macrostructure controls the rate of desaturation in clay dry of optimum. When soils have large interconnected pores they are said to have an *open* structure[7].

In soils compacted wet of optimum interconnected pores are rarer and therefore the desaturation process is more reliant on the microstructure of the specimen in question. For clays, this results in a much slower rate of desaturation as the microscopic pores within clay clods offer much greater resistance to flow than the interconnected pores between clods. When pore spaces are like this they are said to be in an *occluded* state. Therefore, the rate of desaturation of the soil is dependent on both the compaction and initial water content of the soil which in turn controls the aggregation of the soil.

This paper examines a new method of monitoring soil suction in a laboratory environment using a combination of modified common laboratory equipment and available equipment. Further using this equipment this study observes the effect ponding has on soil suction.

2 EXPERIMENTAL MATERIALS

2.1 Soil Properties

All samples used were glacial till samples taken from a depth of 1m at a railway embankment in Nobber, Co. Meath. The samples had an approximate dry density of 1.8Mg/m^3. A particle size distribution analysis was carried out in accordance with BS1377:Part2:1990 (Figure 1). The soil was found to consist of 50.35% gravel, 29.45% sand, 12.9% silt and 7.3% clay. Several moisture content samples were taken over a period of three months with insitu moisture contents ranging from of 17.4% to 23.5%.

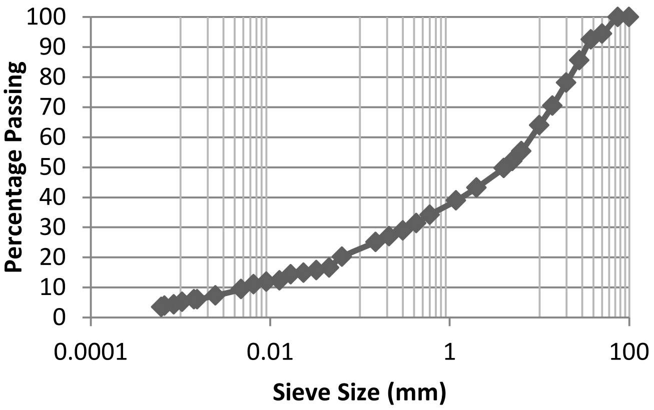

Figure 1. Combination of sieving and sedimentation curves for glacial till sample from Nobber Co. Meath.

2.2 Experimental Apparatus

Minor modifications were made to the baseplate of a California Bearing Ratio mould to allow for the insertion of a porous disk and a small reservoir. This was in turn connected to a pressure transducer to measure the stress. (Figure 2,3). This enabled direct suction measurements to be made through the use of a high air entry ceramic disk. This disk allows both air and water to flow through it under normal conditions. However, when fully saturated, the contractile skin that forms on its surface prevents air from entering the disk until the matric suction exceeds the disks air entry value[8], [9]. The tensiometer works on the premise that if the porous disk is above the prevailing water table, water will be drawn from the tensiometer into the soil. This will then create a tensile hydraulic stress within the tensiometer which can be measured by means of a pressure transducer or a bourdon gauge[9]. The air entry value for the pressed kaolin disk used was 152kPa.

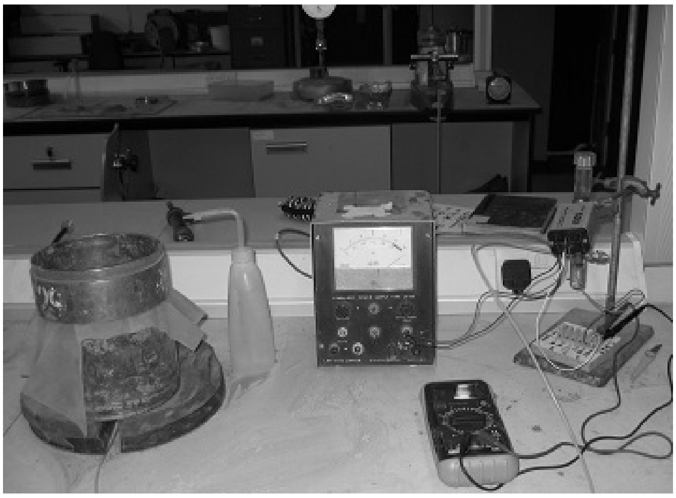

Figure 2. The modified CBR mould can be seen on the left of the picture. The tensiometer with attached pressure transducer can be seen in the far right of picture. The ammeter is in the foreground.

Table 1. Tensiometer Specifications

Model No. 2100F soil moisture probe	
Power Requirement	12-40 VDC at 50mA
Operating Range	0-100kPa
Temperature Range	0-60^{o}C
Linearity	.25% full scale max
Output	4 to 20mA
Hysteresis	Less than 1%
Maximum Pressure Diff	200kPa

In order to measure the suctions accurately, a small tip tensiometer with flexible coaxial tubing (Soil moisture Equipment Corporation) was modified by removing the porous ceramic cup supplied and attaching the free end to a quick release fitting. This quick release fitting was then threaded into the baseplate underneath the reservoir. The tensiometer had a pressure transducer attached to it which was in turn connected to an ammeter. This allowed suction readings to be taken in terms of milli-Amps. This was easily converted to a suction calibration using a suction pump and a bourdon gauge. From this calibration a linear relationship was established which allowed conversion between soil suction (kPa) and mA.

The response time of the instrument was difficult to gauge, as all samples were reconstituted. This meant that the pore pressures were equalising during the first 24-48 hours before eventually stabilising.

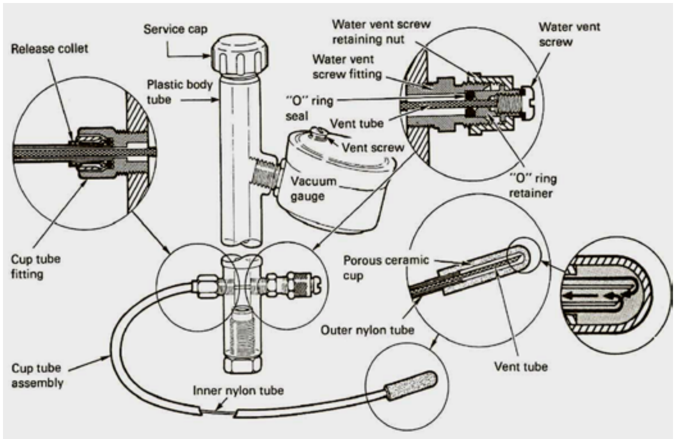

Figure 3. Small tip tensiometer with coaxial cabling from Soil moisture Equipment Corporation. For this experiment the porous ceramic cup was removed from the end of the cabling and a quick release fitting was attached which allowed it to be connected to the modified CBR mould.

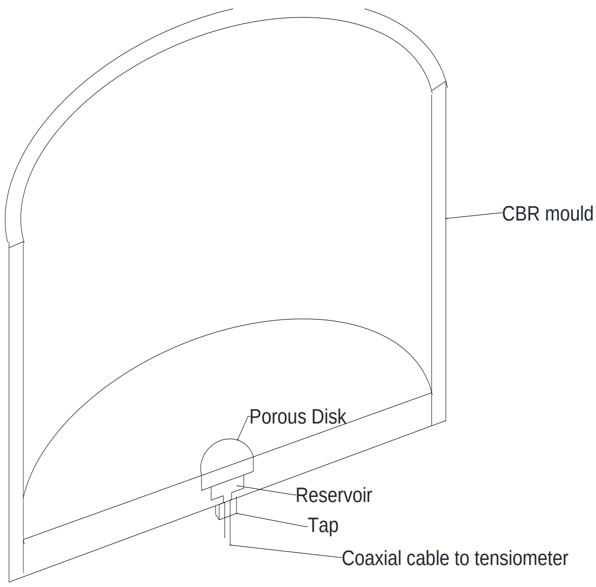

Figure 4.Crosssectional schematic showing modifications made to CBR mould.

3 EXPERIMENTAL METHOD

3.1 Apparatus Preparation

The tensiometer was connected to the base of the CBR mould by means of the coaxial cable and a tap. The tensiometer was then filled with de-aired water and any remaining air was removed using a vacuum pump. This is very important as tension in the water will remove air from imperfections in the equipment which will affect readings. The base of the CBR mould was flooded with water, and left to stand overnight, to ensure full saturation of the porous disk. The water was then removed from the mould and a base reading of 4mA was recorded which corresponds to a pore pressure of 0kPa. Full saturation can be checked by applying a water pressure through the coaxial cabling until the porous disk appears to perspire.

3.2 Sample Preparation

The soil sample was dried overnight in the oven at 105^{o} and weighed. The sample was then dry sieved and all particles greater than 20mm were removed and weighed. Water was then added to generate the predefined gravimetric water content for each sample. When the soil was adequately mixed the sample was compacted into the CBR mould in three layers each layer received 62 blows of a 2.5kg rammer. After the sample was compacted, a plastic sheet was placed on top of the mould preventing moisture loss to the atmosphere and the sample was left to stand until pore pressures equalised, approximately 24 hours.

3.3 Experimental procedure

When pore pressures equalised the collar of the CBR mould was screwed on and sealed. A layer of water was then applied to the top of the sample and allowed to pond. Readings were then taken at regular time intervals. The suction was deemed to be at a minimum when no variation in readings was witnessed for more than ten hours. Samples were then cored and moisture content tests were performed on these cores to develop a moisture content profile of the sample. The procedure was then repeated for differing initial moisture content values.

4 RESULTS

An initial moisture content of 15% was chosen for sample no. 1. A maximum suction value of 56kPa was reached before the initial suction in sample 1 stabilised at 40kPa (see Figure 5). The sample was then flooded with water so that ponding would occur. No change in pore pressure was witnessed over the first two hours of ponding. This was due to the relatively high initial suction holding the infiltrating water in place near the soil surface thus preventing further infiltration. However, shortly after three hours, a significant drop-off in suction was recorded. This decline eventually leveled out approximately 24hours into the experiment. A relatively constant suction measurement of 2kPa was achieved after 40 hours (Figure 6). This value, which will henceforth be called its residual value, underwent no appreciable change over the next ten hours and was taken as being constant.

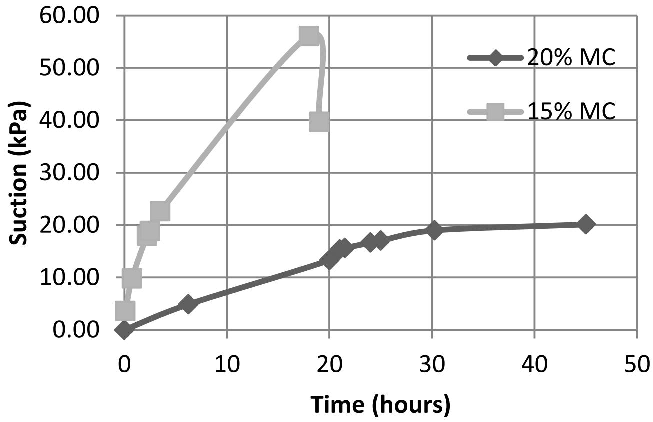

Figure 5. Illustrates the trend in pore pressure build up from compaction to equalisation.

The second sample had an initial moisture content of 20%. It reached a maximum suction value of 20kPa and stabilized at that value (Figure 5). After the sample was ponded there was a small but immediate decrease in suction. This downward trend continued before eventually reaching a minimum value of 3.8kPa (Figure 6).

4.1 Moisture content results

The moisture content profiles were taken from the centre of each mould after the experiment had ended. The core was then divided into smaller samples to develop a profile. The moisture content results for Sample no. 1 varied from 29.9% to 17.3%. The moisture contents were arranged in order of the depth the sample was taken from. A linear regression analysis was performed on the data and a R^2 value of *0*.66 was achieved (Figure 7).

The moisture contents from Sample no. 2 varied from a maximum of 24.5% to a minimum of 18.8%. When linear regression analysis was performed on Sample no. 2 no relationship of note was observed.

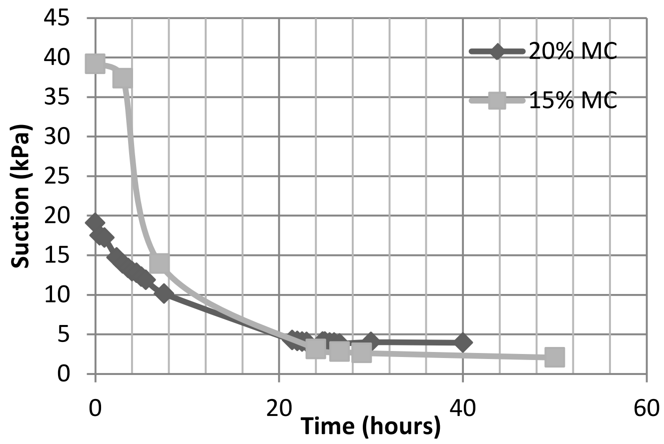

Figure 6. Suction drawdown over time due to infiltration. Sample 1 which had a much larger initial suction is represented by the 15% moisture content line. Sample 2 is represented by the 20% moisture content line.

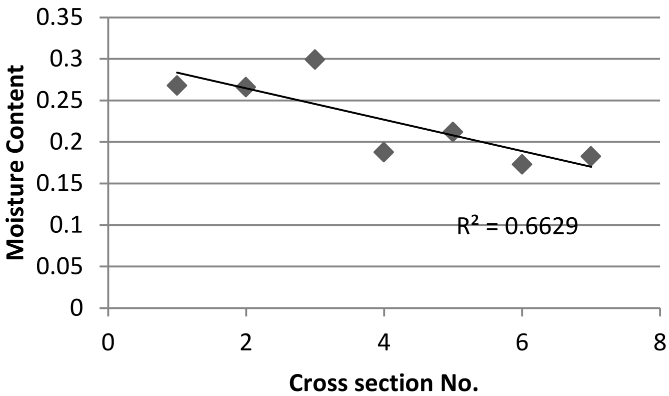

Figure 7. Moisture content profile of sample 1. Initial moisture content of the sample was 15%. Cross section 1 represents the top surface of the sample while cross section 7 represents the base.

Table 2. Summary

Sample no:	1	2
Initial Moisture Content	15%	20%
Dry Density	1.8Mg/m³	1.80Mg/m³
Bulk Density	2.07Mg/m³	2.13Mg/m³
Residual Suction value	2kPa	3.8kPa
Max Suction	56kPa	19.8kPa

5 DISCUSSION

Both Samples no.1 and 2 demonstrated significant decreases in soil suction when water was applied to the soil surface. However, the rate of decrease differed greatly between samples. The downward trend in sample no.2 due to infiltration was immediate and relatively constant. This is in sharp contrast to the trend in sample no.1 where no change in suction was witnessed over the first three hours until a sudden and sharp decline was seen during hour four (Figure 2). This can be attributed for by the high initial suctions displayed in sample no. 1. These suctions would have acted as an impediment to infiltration as they would have held the infiltrating water in place essentially clogging the pore space.

Both samples approached their minimum suction values after approximately 24 hours with sample no. 1 showing some minor fluctuations until approximately 40 hours. This minimum suction value is important as it provides additional stability to partially saturated slopes even during heavy rainfall events. Both samples appeared to follow an exponential decay in the form of:

$$\psi = Ae^{-Bt} \tag{1}$$

Where ψ is soil matric suction, A and B are constants and t represents time in hours. Both samples followed this function with varying degrees of accuracy. A regression coefficient of R^2 =.83 was obtained for sample 1 whereas a R^2 value of .99 was achieved for Sample no. 2.

Sample no. 1 achieved a much higher initial suction figure of 40kPa as opposed to 20kPa in Sample no. 2. This correlated well with expected results given that Sample no. 1 had a lower initial moisture content and numerous studies have shown that suction increases with decreasing moisture content[10–13].

The moisture content profile obtained from sample 1 was as expected showing a marked decrease in moisture content with depth. This correlates well with the development of a wetting front near the soil surface. There were small fluctuations in the moisture contents with depth (Figure 7). However, due to the high gravel content in the soil this is to be expected. The moisture content profile from Sample no.2 did not give satisfactory results as when the sample was cored the core underwent significant deformation. This resulted in substantial moisture loss from the sample. As a result, the data is deemed to be inaccurate.

Interestingly, significant swelling was noted for sample no. 1 but no volume change was detected for sample no. 2.

6 CONCLUSION

The apparatus works well for measuring suctions in a laboratory environment. Suctions measured were in line with expectations. Both samples tested showed a marked decrease in soil suction with infiltration. Furthermore, a correlation between increased moisture content and decreased soil suction was observed. A faster initial decrease in negative pore water pressure was observed in sample 2. However, after 3-4 hours, the rate of decrease of sample 1 increased significantly. Moisture contents of both samples increased but neither sample achieved full saturation before negative pore water pressures stabilized. The initial moisture content has an enormous effect on both the soil suction and the rate of change of soil suction. This experiment is ongoing and further results will be published for a wider range of initial soil moisture contents.

ACKNOWLEDGMENTS

The authors would like to acknowledge the help given to them by Dr. David Igoe and Dr. Paul Doherty. They would also like to thank Frank Dillon for his help in modifying the CBR mould. A special thanks to George Cosgrave for his continuous support in all laboratory experiments.

The authors would like to acknowledge the support of the Earth and Natural Sciences (ENS) Doctoral Studies Programme, funded by the Higher Education Authority (HEA) through the Programme for Research at Third Level Institutions, Cycle 5 (PRTLI-5), co-funded by the European Regional development Fund (ERDF).Lastly the authors would like to thank Irish Rail for their support in all aspects of this project.

REFERENCES

[1] [1] K. Gavin and J. Xue, "Design Charts for the Stability Analysis of Unsaturated Soil Slopes," *Geotechnical and Geological Engineering*, vol. 28, no. 1, pp. 79-90, Nov. 2009.

[2] [2] A. Jotisankasa and W. Mairaing, "Suction-monitored direct shear testing of residual soils from landslide-prone areas," *Journal of geotechnical and geoenvironmental engineering*, vol. 136, no. 3, p. 533, 2010.

[3] [3] A. Ridley, K. Dineen, J. Burland, and P. Vaughan, "Soil matrix suction: some examples of its measurement and application in geotechnical engineering," *Geotechnique*, vol. 53, no. 2, pp. 241–253, 2003.

[4] [4] A. Ridley, B. McGinnity, and P. Vaughan, "Role of pore water pressures in embankment stability," *Proceedings of the Institution of Civil Engineers-Geotechnical engineering*, vol. 157, no. 4, pp. 193–198, 2004.

[5] [5] J. Xue and K. Gavin, "Effect of Rainfall Intensity on Infiltration into Partly Saturated Slopes," *Geotechnical and Geological Engineering*, vol. 26, no. 2, pp. 199-209, Oct. 2007.

[6] [6] H. Rahardjo, E. Leong, and R. Rezaur, "Instrumented slopes for the study of rainfall-induced slope failures," *Geotechnical Engineering, Swets & Zeitlinger, Lisse*, vol. 3, no. December, pp. 307–312, 2003.

[7] [7] S. K. VANAPALLI, D. G. FREDLUND, and D. E. PUFAHL, "The relationship between the soil-water characteristic curve and the unsaturated shear strength of a compacted glacial till," *ASTM geotechnical testing journal*, vol. 19, no. 3, pp. 259-268.

[8] [8] D. G. Fredlund and H. Rahardjo, *Soil Mechanics for Unsaturated Soils*. John Wiley and Sons, INC., 1993.

[9] [9] A. Tarantino, A. M. Ridley, and D. G. Toll, "Field Measurement of Suction, Water Content, and Water Permeability," *Geotechnical and Geological Engineering*, vol. 26, no. 6, pp. 751-782, May 2008.

[10] [10] K. Gavin and J. Xue, "A simple method to analyze infiltration into unsaturated soil slopes," *Computers and Geotechnics*, vol. 35, no. 2, pp. 223-230, Mar. 2008.

[11] [11] S. K. Vanapalli, W. S. Sillers, and M. D. Fredlund, "THE MEANING AND RELEVANCE OF RESIDUAL STATE TO UNSATURATED SOILS," in *Construction*, 1998, pp. 1-8.

[12] [12] D. Fredlund, A. Xing, and S. Huang, "Predicting the permeability function for unsaturated soils using the soil-water characteristic curve," *Canadian Geotechnical Journal*, vol. 31, no. 4, pp. 533–546, 1994.

[13] [13] D. Fredlund and A. Xing, "Equations for the soil-water characteristic curve," *Canadian Geotechnical Journal*, vol. 31, no. 3, pp. 521-532, 1994.

Use of helical piles as anchors to increase the resistance of steep slopes

Kenneth Gavin[1,2], Paul Doherty[2], Donal Murphy[3]
[1]Department of Civil Engineering, University College Dublin,
[2]GDG Ltd.
[3] Screwpile Ireland Ltd.
email: kenneth.gavin@ucd.ie, paul.doherty@ucd.ie, info@screwpile.ie

ABSTRACT: Helical piles (or screw piles) consist of a steel shaft, either square or circular, with a helix of constant radius welded at one or more points along the pile shaft. The helical pile is installed by applying a rotational force to the pile shaft, using a hydraulic drive unit. Advantages of this method of piling include (i) no spoil is created, making the method particularly environmentally friendly; (ii) installation is very quick and (iii) the piles can be loaded immediately after installation. In this paper the efficacy of the use of screw piles to increase the factor of safety of steep glacial till slopes is evaluated using finite element analyses.

KEY WORDS: driven piles, sand, pile dynamics

1 INTRODUCTION

In recent years, there have been a number of slope failures throughout Ireland, and in particular along Irish infrastructure routes. In order to prevent such failures from occurring, remediation solutions are often undertaken to improve the stability of critical slopes. This paper explores the possibility of using a helical anchor system as a novel solution to stabilise these critical embankments.. Finite element analysis (FEA) was used to study the behaviour of the helical piles and to assess their role in improving the embankment safety. Helical piles (or screw piles) consist of a steel shaft, either square or circular, with a helix of constant radius welded at one or more points along the pile shaft (See Figure 1). The helix consists of a circular steel plate, which is split radially and pulled out of shape to give a leading and trailing edge, separated by a fixed distance known as the helix pitch. The helical pile is installed by applying a rotational force to the pile shaft, using a hydraulic drive unit (See Figure 1). The applied torque is transferred to the ground when the leading edge of the helix engages the soil, advancing the pile into the ground as the shaft rotates. Under ideal conditions, the pile should advance at the rate of one pitch per revolution.

As the pile is installed, it displaces the soil required to accommodate the pile shaft and helix geometry. A major advantage of this method of piling is that no spoil is created, making the method particularly environmentally friendly. The lead section can contain one or more helixes depending on the load carrying requirements of the pile. Similarly, extension pieces can be bolted on to the lead section using coupler connections to install the screwpiles to a depth that can provide the necessary load resistance. Once installed to the final depth, the pile can resist both tension and compression loads by transferring the force into the bearing stratum. In addition, the piles can resist some lateral loads through the friction mobilised against the shaft, combined with the force required to rotate the embedded helix. The pile installation angle can vary from vertical to almost horizontal.

Figure 1. Installation of helical pile.

Helical piles are installed using a torque motor that applies a force to the pile head, which allows the pile to rotate into the ground. The applied torque should be monitored throughout installation for construction control and quality assurance, as well as to estimate the pile capacity from empirical correlations. The capacity of the torque motor used to install the piles and the machine that it is mounted on, will govern the ease of installation and factors such as the maximum pile lengths and diameters achieved.

2 STABILITY ANALYSES OF EMBANKMENTS

2.1 *Background*

Rainfall induced landslides are a major cause of disturbance to transport networks in many parts of the world. In slopes where the water table is some depth below the ground surface, negative pore water pressure (suctions) develop in the near surface soils which contribute significantly to their overall stability. However, these suctions are transient and reduce as water percolates into the slope (and a wetting front develops) during periods of heavy or prolonged rainfall.

2.2 Modelling slopes using apparent cohesion

Fourie et al. [1] note that in most slope failures caused by infiltration, the failure plane forms parallel to the existing slope. The failure surface is formed by the downward migration of a wetting front (caused by infiltration into the partially saturated soil). The authors suggest using an infinite slope model in which the soil strength is described using an appropriate model. Fredlund et al. [2] expanded the Mohr-Coulomb model to incorporate negative porewater pressure (matric suction) effects:

$$\tau = c' + (\sigma_n - u_a)\tan\phi' + (u_a - u_w)\tan\phi^b$$
$$= C + (\sigma_n - u_a)\tan\phi' \qquad (1)$$

where τ =shear strength of unsaturated soils, c´ is the effective cohesion, σ_n is the total normal strength on the failure plane , u_a is the pore-air pressure on the failure plane, ϕ' is the angle of internal friction associated with the net normal stress state variable σ_n-u_a, u_w is the pore-water pressure on the failure plane, u_a-u_w is the matric suction on the failure plane, and ϕ^b is the angle indicating the rate of increase in shear strength relative to the matric suction. The effects of c´ and the contribution of matric suction (u_a-u_w) tanϕ^b can for the sake of convenience be combined into a single parameter (C), known as the apparent cohesion.

The Factor of Safety (FOS) for the planar slip surface is given by:

$$FOS = \frac{C + \gamma h \cos^2\alpha \tan\phi}{\gamma h \cos\alpha \sin\alpha} \qquad (2)$$

where γ is the unit weight of soil, h is the wetting front depth and α is the slope angle. C can be measured either in the laboratory or by the use of in-situ direct shear tests (see Springman et al.)[3].

There are many uncertainties associated with the choice of which variables to use in the analysis of the stability of a soil slope. All soils are heterogeneous, and therefore soil properties vary with depth and location. Additional uncertainties associated with the analysis of unsaturated slope stability problems include; the variation of total cohesion when suctions reduce as a result of changes in water content during infiltration and difficulties in assessing the rate at which wetting front development occurs. The depth to which infiltrating water will penetrate into a slope, which represents the depth from ground surface to the slip surface, depends on many parameters, a number of which are highly variable. These include the initial suction profile, the geometry of the slope, soil permeability, rainfall intensity and duration amongst other factors. Traditional deterministic design methods, in which the soil properties are assigned fixed (conservative) values, cannot adequately model the dynamic process of wetting front development and its effect on the disturbing forces causing slope failure, and the resistance (soil strength) preventing failure. For this reason, Zhang et al. [4], Babu and Murthy [5], Xue and Gavin [6] and others propose the use of probabilistic design approaches.

In probabilistic approaches, natural variability can be explicitly included in estimates of the probable capacity and disturbing forces. This makes them ideal for slope stability analysis. However, due to their simplicity and perceived transparency, deterministic methods remain the industry standard. In deterministic design, the target Factor of Safety (FOS) is normally set as a minimum of value, e.g. 1.3. The soil properties are usually chosen based on characteristic values as defined in EC7 [7], often referred to as moderately conservative parameters. In practice, this means adopting design values which are below the actual mean value of the available measurements of soil properties such as shear strength. The design values are often chosen without regard for the actual variation of soil properties, which means that although the FOS value is fixed, the reliability index will vary, reducing as the variability of the soil properties increase. In these situations, the adoption of conservative input parameters does not in fact guarantee a safe design. An alternative approach would be to set a fixed minimum target reliability index (β_T), which would represent an acceptable probability of failure for a slope. For a given slope, a rational design approach which does not involve a full probabilistic analysis would be to determine the factor of safety required to obtain the set target reliability index. The FOS required to meet this β_T value will naturally increase as uncertainties regarding the input parameters for the slope stability analysis increase.

Considering Equation 2, routine laboratory tests are used to obtain values of friction angle, ϕ and unit weight, γ. In common soils these values are relatively well defined and therefore mean design values can be assigned with some confidence. Because of significant recent interest in the behaviour of partly saturated soils, major developments in laboratory and field measurement complemented by modelling have been achieved. It is relatively straightforward to measure the total cohesion C, in the laboratory or field (Springman et al [3], Xue [8]). An estimate of the wetting front depth h, can be obtained using simple empirical methods Gavin and Xue [9] or more accurate complex numerical analyses Ng et al. [10]. By making a number of such determinations the variability of the critical input parameters can be determined.

The use of reliability theory to select a factor of safety consistent with a target reliability index has been discussed by Benjamin and Cornell [11], and Whitman [12]. The choice of β_T is normally based on; (i) historical data, (ii) mathematical modelling based on probability theory or (iii) quantification of expert systems (Paikowsky [13]). Although for most geotechnical problems the choice of β_T is not straightforward, Chowdhury and Flentje [14] suggest that for most slopes (outside of those in urban areas) β_T can be set at 2.0, which corresponds to a probability of failure of 2.23%. Although this reliability index would classify the performance as poor in accordance with USACE [15], it is consistent with β_T which is implied by conventional practice in geotechnical engineering Whitman [12] and will be adopted in this report.

Gavin and Xue [16] performed a suite of probabilistic analyses, with a fixed β_T of 2.0, and have derived design charts to allow designers to choose a target FOS value, given uncertainty in the choice of wetting front depth h, and apparent cohesion, C. The results of these analyses for slopes where the soil has a peak friction angle, ϕ_p of 40° (equivalent to the friction angle adopted for glacial till in this report) are illustrated in Figure 2. In Figure 2a, the estimate of the wetting front depth was assumed to have a coefficient of variation (COV) of 0.05, i.e. assumed to be very reliable. It is clear that for the base case slope angle of 45°, the FOS required to ensure β_T can be set at 2.0, increased from FOS = 1.26 when COV value for the estimate of apparent cohesion, C was 0.1 (i.e. the estimate was very accurate), to FOS = 1.84, when the estimate of C was more uncertain (COV C = 0.4).

In Figure 2b, the estimate of the wetting front depth was assumed to have a coefficient of variation (COV) of 0.15, i.e. be relatively unreliable. For the base case slope angle of 45°, the FOS required to ensure β_T can be set at 2.0, increased from FOS = 1.46 when COV value for the estimate of apparent cohesion, C was 0.1 (i.e. the estimate was very accurate), to FOS = 2.16, when the estimate of C was more uncertain (COV C = 0.4).

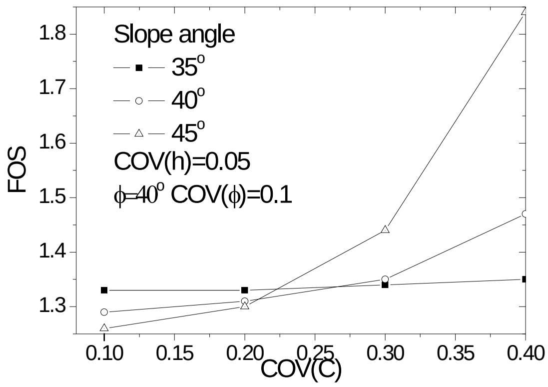

Figure 2a. Target FOS values for slopes where the wetting front depth can be accurately predicted

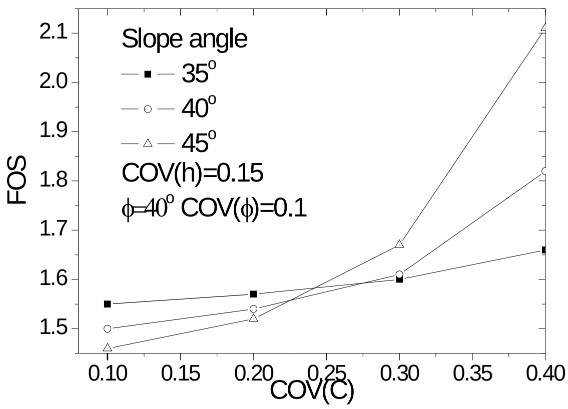

Figure 2b. Target FOS values for slopes where the accuracy of the wetting front depth prediction is uncertain

3 EMBANKMENT STABILITY ANALYSIS

3.1 Overview

The use of helical piles as a remediation measure to stabilise an embankment with a marginal factor of safety was analysed. The helical pile solution was modelled using Plaxis 8.2 software. This software uses the finite element method to analyse the soil/structure behaviour. 15 noded elements were used throughout the modelling process. The analysis assumed that the embankment behaved as a plane strain model, and was symmetrical about the central axis.

3.2 Geometry Model

The base case analyses were performed using the geometry of a typical Irish railway embankment (Xue and Gavin [17]). A 5m high embankment, with a 45° slope was considered, See Figure 3. The top width of the embankment was 10m, the supporting soil layer extended to 10m below original ground surface, and a lateral distance of 35m from the embankment centreline to the end of the modelled section was chosen in order to minimise boundary effects. The boundary conditions were set such that lateral movement was constrained at the horizontal boundaries and both lateral and vertical movement was restrained along the base of the geometry.

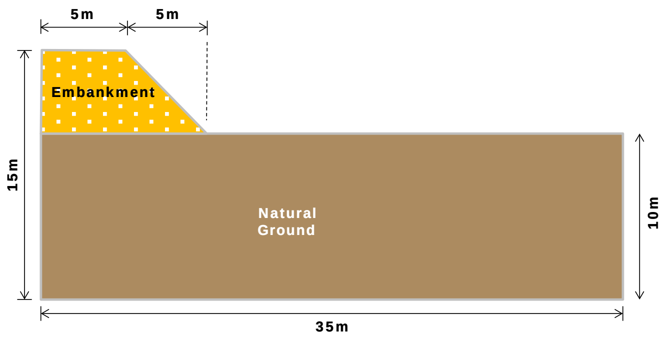

Figure 3. Embankment Geometry.

Two helical piles were installed in the model embankment at a spacing of 2.83m (See Figure 4). The head of the upper anchor was located ≈1.4m from the slope crest. The anchors were installed at an angle of 90 degrees to the slope face. The anchors were fitted with a single 400mm diameter helix, which was modelled as a plate element. The pile shaft was modelled as a node-to-node anchor. The anchor properties were determined by assuming that the anchor shaft was a solid steel bar 44mm in diameter, which had an out of plane offset spacing of 2 metres. A stiffness value, E, for steel of 200GPa was used in modelling the pile shaft.

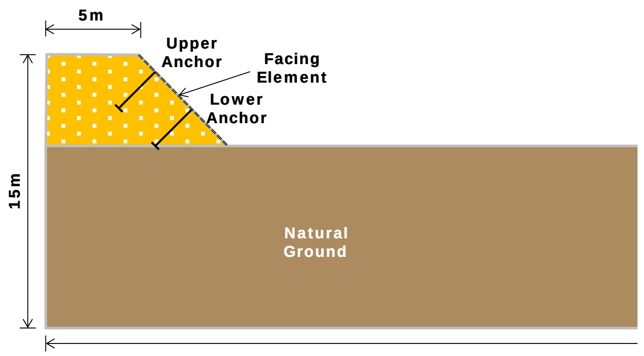

Figure 4. Anchor Geometry.

3.3 *Soil Properties*

The soil was modelled as a drained material, which was governed by the mohr-coulomb soil model. The embankment and foundation soil were assigned standard strength and stiffness properties of glacial till, See Lehane and Simpson [18] and Gavin et al. [19] and also Table 1. A constant volume friction angle, ϕ'_{cv} = 34° and dilation angle, ψ = 6° were considered, resulting in a peak friction angle of ϕ'_p = 40°. The embankment was segregated into two soil layers to represent the embankment core and a wetted front along the surface of the soil slope (See Figure 5). The wetted front was given a lower apparent cohesion than the embankment core to model the effect of reduced suction forces arising from the infiltration of rainfall into the slope face. A maximum apparent cohesion of 8 kPa was considered for the soil outside the wetted zone (i.e. the area unaffected by infiltration). Assuming that $\tan\phi^b$ is equal to $\tan\phi$ (See Eqn.1), this corresponds to a suction value of ≈12 kPa. Brady and Johnson [20] reported measurements of suction from laboratory tests on compacted glacial till samples. In these tests, samples were initially compacted at their natural moisture contents, before being subjected to artificial rainfall events which were continued until a residual suction value was determined. In the limited tests considered, the residual suction tended to a value of between 3.5 and 4.4 kPa. Therefore, a minimum C value of 2.25 was adopted in the FE analyses presented herein.

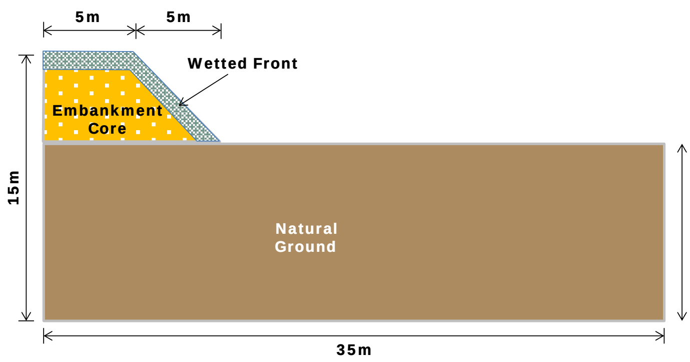

Figure 5. Modelling Wetted Front of Embankment

Table 1: Soil Parameters Assumed in the Analysis

Soil parameters		
Property	Clay mass	Wetted front
Friction angle (degrees)	34	34
Dilation angle (degrees)	6	6
Cohesion (kpa)	8	2.25

3.4 *Modelling Procedures*

Once the geometry was established and the soil properties were determined, the model then proceeded to the next stage in the analysis. This stage involved meshing the geometry into finite elements, connected by adjacent nodes. A typical mesh, which is illustrated in Figure 6 consisted of 959 elements and 7875 nodes. The average element size was 740mm. Local mesh refinement was used around the pile anchor elements to reduce the element size and increase the analysis accuracy. A mesh sensitivity study showed that further mesh refinement provided similar numerical results and was therefore unnecessary. The specified initial conditions included a phreatic water table at original ground level and a coefficient of earth pressure, K_0 value of 0.44 to determine the in-situ lateral stresses. The facing element was modelled as a geotextile.

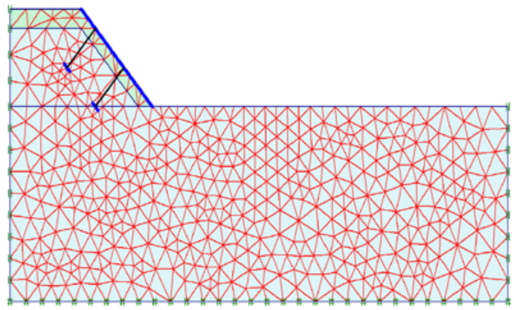

Figure 6. Typical Mesh used in FE Analyses

3.5 *Results – Embankment Stability*

A phi-c reduction analysis was used to determine the factor of safety (FoS) of the original embankment prior to any remediation measures. The factor of safety is defined as the ratio of the true strength to the computed minimum strength required for equilibrium. The safety factor can therefore be determined by comparison of the available mohr coulomb shear strength with the equilibrium shear strength. During the phi-c procedure, the FoS value is first determined using the available soil strength parameters (i.e. the input cohesion and friction angle). An iterative procedure is then performed in which the cohesion and the tangent of the friction angle are reduced in the same proportion. The analysis continues until the reduced soil parameters are just sufficient to maintain equilibrium. The FoS thus determined for the base case analysis was 1.06 and the failure pattern consisted of a shallow 1m deep translational slide constrained within the upper wetted zone, See Figure 7. This displacement pattern is consistent with observed slope failures (Xue and Gavin 2008) for Irish embankments. This failure type often develops after periods of high rainfall, which results in infiltration of water into the slope, and a reduction of suction stresses. This process was modelled implicitly using a reduced apparent cohesion in the wetted zone and suggests that, under high rainfall, slopes of this type have a marginal factor of safety against shallow failures. The development of the failure mechanism is illustrated by the relative shear shadings shown in Figure 8, where the highest values (shown in red) are concentrated near the embankment surface. The relative shear shadings illustrate the ratio of the maximum shear strength with the current effective stress (i.e. the radius of the mohr stress circle) to the maximum possible shear strength obtained by expanding the mohr circle to touch the coulomb failure envelope, with the intermediate principal stress being maintained constant. The relative shear stress therefore illustrates the proximity of the current effective stresses to the failure stress. The relative shear shadings are shown to be around one at the slope face and within the upper wetted zone. However, the relative stresses reduce outside this zone, showing that the failure surface is contained within the wetted zone.

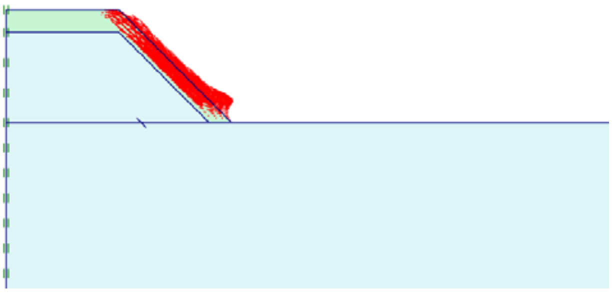

Figure 7. Total Displacement Vectors (scale factor = 5*10-6).

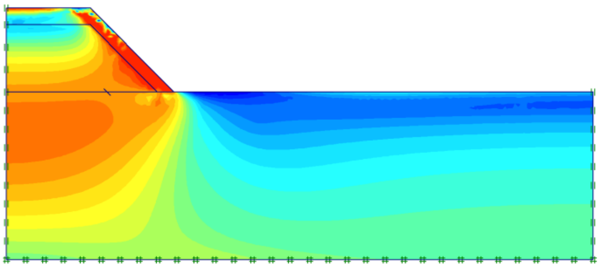

Figure 8. Relative Shear Shadings for Embankment.

3.6 Results – Anchor Performance

The anchors were then installed in the embankment and the phi-c reduction process was repeated to determine the new factor of safety. The FoS value of the embankment after installation of the helical anchors was found to be 1.33. This was a significant improvement on the initial FOS of 1.06. The potential failure pattern is illustrated by the total displacement vectors in Figure 9. The mobilisation of the relative shear stresses shown in Figure 10 offers further insight into the embankment failure mechanism. Comparison of Figure 8, where the maximum shear stresses are mobilised within the wetted zone (failure surface) and Figure 10 illustrate that anchors are successful in transferring loads to a large area of soil at depth. These are seen to approach unity for a large part of the embankment cross section, indicating that most of the embankment soil mass is at the maximum shear stress. This indicates that as slope movements occur, the helical anchors transfer stress into the embankment body in order to mobilise extra resistance. This load transfer occurs at relatively small soil movements. This is particularly obvious when comparing the relative shear stresses in Figure 10 and Figure 8, where much higher stresses are observed in the soil surrounding the helical plates. This comparison shows that load has been transferred from the soil in the upper failure zone, into the anchors, and subsequently into the deeper soil within the embankment core. This load transfer process illustrates that helical piles can prevent slope failures by providing additional resistance against failure. As a further point of interest, the highest displacements and mean shear stresses are located near the toe of the embankment. As a result, the lower anchor is seen to transfer more load to the deeper soil, illustrated by the uniform high relative shear stress contours around the helix of the lower anchor in comparison to the upper anchor in Figure 10. This suggests that the lower anchor is more efficient. This aspect of the slope response is explored further in section 5.4. The anchor performance can be quantified by the improvement ratio, defined as the percentage increase in embankment FOS due to anchor installation. In this instance, the improvement ratio is 26%.

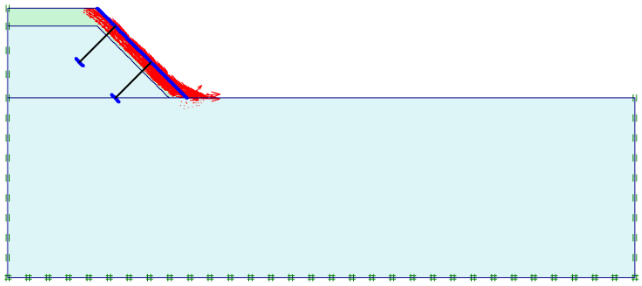

Figure 9. Total Displacement Vectors (scale factor = 5*10-6).

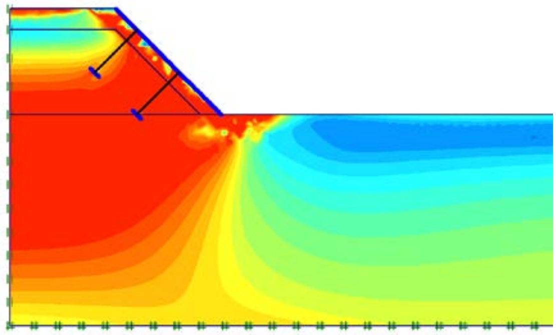

Figure 10. Relative Shear Shadings for Piled Embankment.

3.7 Conclusions

The embankment soil was modelled as having a central core and a 1m deep wetted zone at the slope face. During a prolonged heavy rainfall event, the suction in the wetted zone could approach a residual value, which will cause the apparent cohesion to reduce to ≈ 2.25kPa. As a result, a shallow translational failure was seen to develop. The introduction of helical piles was shown to enhance the stability of the embankment significantly, with the FoS value increasing from 1.06 to 1.33. This resulted in an improvement ratio of 26% and suggests that helical piles are an appropriate means of stabilising embankment slopes.

4 SENSITIVITY ANALYSIS

4.1 Overview

A sensitivity analysis was performed to determine the impact of the soil conditions (apparent suction) on the helical pile performance predicted using the FE analyses.

4.2 Soil Conditions

The soil conditions considered within the original analysis were determined as the most likely soil parameters to exist for an embankment slope formed from compacted glacial till. However, considering the likely variation in soil parameters for different embankments, and in particular the variation in suction likely to occur during rainfall periods, it was decided to complete a number of simulation runs, where the apparent cohesion within the wetting front was varied. All other parameters were the same as those used in the the base case analysis. The apparent cohesion was varied from the residual value of 2.25 to an upper limit of 8kPa, which agreed with the cohesion of the embankment core (essentially modelling the embankment as one uniform soil type). The variation in FoS with the apparent cohesion of the soil in the wetting front is shown in Figure 11, where FoS is seen to increase with increasing cohesion or conversely seen to decrease with increasing rainfall infiltration.

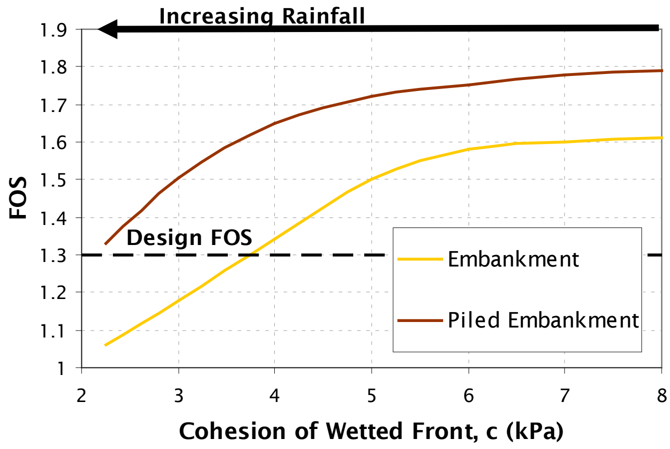

Figure11. Impact of Cohesion on Factor of Safety.

Prior to pile installation, the FoS ranged from 1.06 (C=2.25kPa), to 1.6.(C=8kPa) The range in FoS for embankments with helical piles ranged from 1.33 to 1.8. The corresponding improvement ratios are shown in Figure 12. It is clear that the helical piles were most effective when the apparent cohesion dropped below 5kPa.

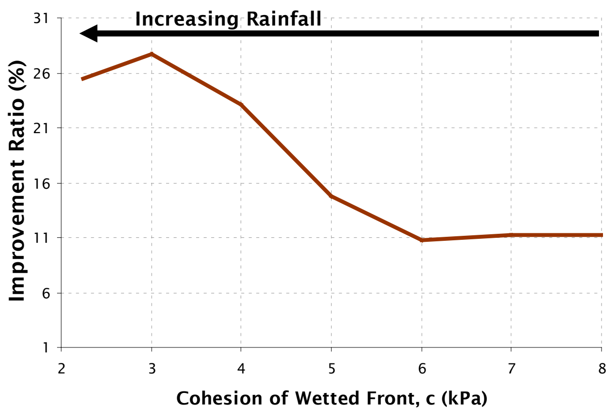

Figure 12. Impact of Cohesion on the Improvement Ratio

It is intriguing to consider the type of failure that develops when no rainfall is modelled (i.e. the entire embankment has an apparent cohesion of 8kPa). The total displacement vectors for this analysis are shown in Figure 13. These reveal that instead of the shallow rainfall induced slide, a deep-seated rotational failure mechanism develops. Even in this scenario, the helical piers provide an improvement ratio greater than 11%. The displacement pattern predicted with the anchors installed is set out in Figure 14.

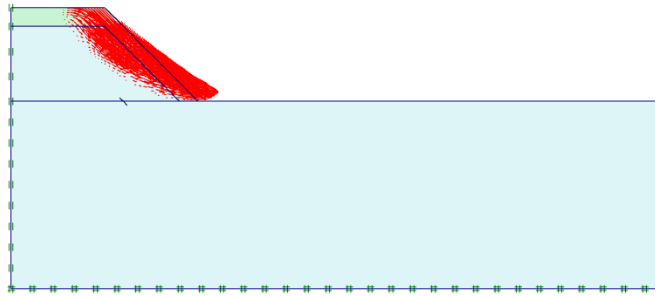

Figure 13. Failure mechanism when C = 8kPa in wetted zone.

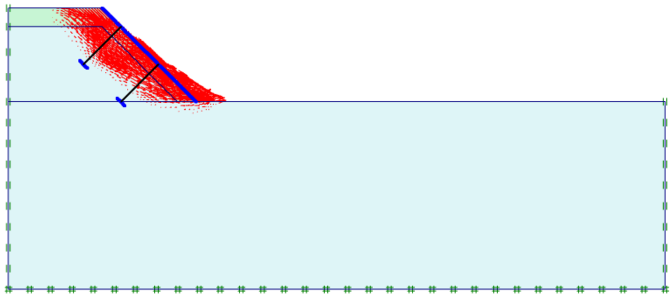

Figure 14. Effect of helical piles on failure mechanism when C = 8kPa in wetted zone.

4.3 Anchor Pull-Out Tests

To confirm the accuracy of the treatment of the helical piles in the FE analyses, a pull-out test was modelled. The following procedure was followed (i) The initial stress conditions in the embankment were first determined, (ii) the helical piles were installed (iii) the pile was pulled 20mm, i.e. 5% of the pile diameter and (iv) the pile was pulled 40mm (10% of the pile diameter). The displacement pattern developed when the pile was pulled 40mm is shown in Figure 15.

The pull-out force estimated from the analyses when the pile head movement was 40mm equaled 182kN. This can be compared to a theoretical estimate of the pull-out capacity, P of a pile, of width B, embedded at a depth H in a fully drained material (Murray and Geddes [21]), where the large displacement values of ϕ was taken to be equal to $\phi_{cv} = 34°$:

$$P = \gamma\, BH\,(1 + H/B\,(\sin\phi + \sin\phi/2)) \quad (3)$$

Eqn 3 yieds a pull-out capacity of 145kN. Given that the theoretical approach ignored the contribution of apparent cohesion to the pile capacity, the FE prediction of the pull-out capacity seems reasonable.

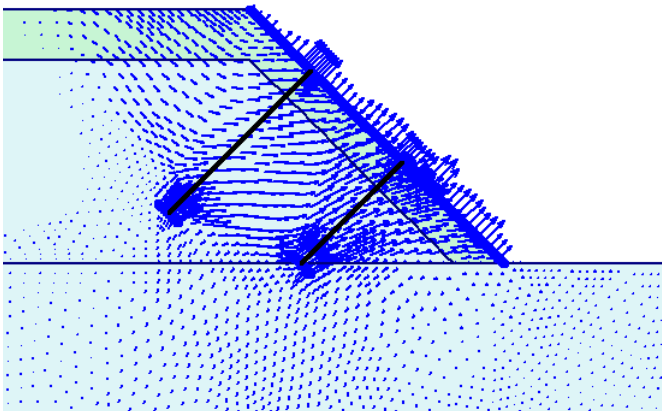

Figure 15: Displacement profiles for pull-out test when settlement = 10% of pile diameter (Scale x 10).

5 DISCUSSION & RECOMMENDATIONS

The use of helical anchors to increase the stability of slopes which are susceptible to rainfall induced landslides was considered. The piles were modelled as wished-in- plcase anchors and therefore instllations effects were not considered. A base case scenario was examined in which a typical 5m high embankment with a 45° slopes was analysed. When subjected to a rainfall event which resulted in the formation of a 1m deep wetting front, the FoS of the slope reduced to 1.06, suggesting imminent failure. The introduction of helical piers resulted in an increase in the FoS value of approximately 25%, and therefore ensured continued serviceability of the slope.

Sensitivity analyses were performed which considered the effects of; apparent cohesion, revealed the following that helical piles provided significant improvement to FoS values of typical 45° slopes when the apparent cohesion reduced below 5kPa. Simulated anchor pull-out tests were consistent with theoretical estimates of the pile capacity and suggest that the FoS against a catastrophic failure of the slope is enhanced by values much higher than the improvement ratios quoted in this paper.

REFERENCES

[1] Fourie, A. B., D. R. Owe and G. E. Blight. The effect of infiltration on the stability of the slopes of a dry ash dump. 1999, Geotechnique, 49(1): 1-13.

[2] Fredlund, D. G., N. R. Morgenstern and R. A. Widger. The shear strength of unsaturated soils. Canadian Geotechnical Journal, 1978, 15(3): 313-321.

[3] Springman, S. M., C. Jommi and P. Teysseire. Instability on moraine slopes induced by loss of suction: a case history. Geotechnique, 2003, 53(1): 3-10.

[4] Zhang, L. L., L. M. Zhang and W. H. Tang. Rainfall-induced slope failure considering variability of soil properties, Geotechnique, 2005, 55(2): 183-188.

[5] Babu, G. L. S. and D. S. N. Murthy. Reliability analysis of unsaturated soil slopes. Journal of Geotechnical and Geoenvironmental Engineering. ASCE, 2005, 131(11): 1423-1428.

[6] Xue, J. and Gavin, K (2007) Simultaneous determination of the critical slip surface and reliability index of earth slopes using a genetic algorithm, ASCE Journal of Geotechnical and Geoenvironmental Engineering, Volume 133, No.7, July 2007, pp 878-886.

[7] Eurocode 7: Geotechnical Design - Part 1, Published by the European Committee for Standardisation, Brussels. 2004.

[8] Xue, J. F. Reliability analysis and the simulation of rainfall infiltration into partly saturated soil Slopes. School of Architecture, Landscape and Civil Engineering. Dublin, University College Dublin, 2007.

[9] Gavin, K and Xue, J.F. A simple approach to analyze infiltration into unsaturated slopes, Computers and Geotechnics, 2008, Volume 35, Issue 2, March 2008, (In Press).

[10] Ng, C. W. W. and Q. Shi. A numerical investigation of the stability of unsaturated soil slopes subjected to transient seepage. Computers and Geotechnics, 1998, 22(1): 1-28.

[11] Benjamin, J.R, and Cornell C.A Probability, statistics, and decision for civil engineers, McGraw-Hill New York, 1970.

[12] Whitman, R. V. Evaluating calculated risk in geotechnical engineering. Journal of Geotechnical Engineering ASCE, 1984, 110(2): 143-188.

[13] Paikowsky, S. G., B. Birgisson, M. Mcvay and T. Nguyen. Load and resistance factor design (LRFD) for deep foundations. Washington, D.C., Transportation Research Board, 2004.

[14] Chowdhury, R. and P. Flentje. "Role of slope reliability analysis in landslide risk management." Bulletin of Engineering Geology and the Environment, 2003, 62: 41-46.

[15] USACE: ETL 1110-2-556, Risk-based analysis in geotechnical engineering for support of planning studies, Appendix A, U.S. Army Corps of Engineers Document, 1999.

[16] Design charts for the stability analysis of unsaturated soil slopes' Kenneth Gavin and Jianfeng Xue, Journal of Geotechnical and Geological Engineering, Vol 28 pp 79-90 (2010). DOI 10.1007/s10706-009-9282-z

[17] Xue, J and Gavin K. Infiltration analysis in unsaturated soil slopes, First European Conference on Unsaturated Soils, pp 823-827, July (2008).

[18] Lehane B.M. and Simpson B. Modelling the behaviour of a glacial till using a 3-D BRICK soil model. Canadian Geotechnical J., 2000, 37 (5), 1078-1088.

[19] Gavin, K, Cadogan, D and Twomey, L. Axial resistance of CFA piles in Dublin boulder clay. Proceedings of ICE, Geotechnical Engineering, Vol. 161, Issue 4, pp. 171-180. August 2008. DOI 10.1680/geng.2008.161.4.171

[20] Brady, C and Johnson, E, (2011) Effect of climate change on slope stability in Ireland, Final Year Project, School of Architecture, Landscape and Civil Engineering, University College Dublin

[21] Murray, E.J. and Geddes, D, Uplift of Anchor Plates in Sand, ASCE Journal of Geotechnical Engineering, Vol 113, No. 3. March 1987

Optimisation of earthworks for road schemes

Kevin Stephens, Alan O'Connor, Eric Farrell
Dept. of Civil, Structural and Environmental Engineering, Trinity College Dublin, Dublin, Ireland.
email: kmstephe@tcd.ie, alan.oconnor@tcd.ie, efarrell@tcd.ie

ABSTRACT: In contrast to most other civil engineering disciplines which deal predominantly with synthetic materials, the natural materials encountered during earthworks for road schemes tend to have highly variable properties. The uncertainty of the ground conditions which would be encountered on each of the feasible routes at route selection stage present considerable financial risks. The key risks for earthworks are the acceptability of the glacial till as a construction material, the depth of any soft deposits and the rippability of any rock encountered. Presented in this paper is the progress in the development of an earthworks risk assessment methodology. The interface between the different materials is accurately identifiable from geological mapping. It is the depth of, and the properties of the materials, particularly the glacial till, which are uncertain. From the findings of a thorough reconnaissance study, mean, standard deviation and correlation lengths for each of the parameters can be estimated and complemented by expert opinion where necessary. A Monte Carlo simulation using a method called random field is used to simulate a large number of 2D geological profiles along the longitudinal profile of an alignment. Discrete values for the thickness of the various deposits as well as strength values at regularly spaced intervals for the glacial till are simulated. Each of the profiles are then assessed for the potential risks and a probability of occurrence calculated for each risk on that particular alignment. This risk assessment will bring about increased awareness of the risks and will bring greater certainty to the overall cost of the earthworks for each of the potential routes. This will allow engineers to make a better informed decision when selecting the preferred route.

KEY WORDS: Alignment Optimisation; Earthworks; Uncertainty; Random field; Reliability Based Design.

1 INTRODUCTION

Roads play a major role in the socio-economic development and activity of a region. They offer a unique and flexible mode of transportation and facilitate the unrivalled door to door service which often proves to be invaluable. However, roads require a massive initial investment. Although the acquisition of land is a considerable cost the bulk of the initial investment can be attributed to construction costs. The major construction costs are earthworks, bridges and pavement. The magnitude of these three cost items is largely predetermined by the selection of the preferred alignment during the route selection stage. Although minor adjustments can be facilitated during the detailed design the opportunity for significant alterations diminishes dramatically as the design progresses.

In order to curtail expenditure it is imperative that these cost items are considered from the initiation of the design process. It is important that the alignments of the feasible route corridors are optimised in terms of construction costs, particularly earthworks, as well as avoidance of constraints. Earthworks can be divided into earthmoving and compaction. In earthmoving, soil is excavated, transported and deposited in a disturbed state some distance from its source. When the excavated soil is of an acceptable quality to be used as a construction material, it is formed according to the design by laying it in layers. Each layer is compacted with the prime intension of decreasing the air voids and consequently increasing its shear strength. Quantitative measurements of geologic material properties, which have differentiated the modern discipline of soil mechanics from the earthworks which have been practiced since antiquity, confirm that the material has highly variable properties. These measurements regularly uncover a great deal of variability in the properties of the material, not only from site to site and stratum to stratum, but even within what initially appear to be homogeneous deposits. Along with the depth of any soft deposits and the rippability of any rock encountered, it is the inherent variability of the blanket of drift material which poses the greatest risk to the earthworks strategy for a particular route. The strength of glacial till excavated, which varies tremendously, will determine whether it can become a valuable construction material or in fact a considerable liability. At route selection stage it is difficult to quantify the risk associated with a route from an earthworks perspective and often preferred routes are selected based largely on 'intangible' considerations and a commitment is made before any intrusive investigations are completed.

The current approach to route selection is largely intuitive and iterative. Corridors are envisaged and alignments are developed manually by experienced engineers, based largely on past experience, intuition and *"rules of thumb"* with the optimisation of the design unproven. There is considerable scope for significant savings by optimising alignments to reduce construction costs such as earthworks activities by utilising computer models to optimise the alignments.

This research has two objectives: to analyse existing alignment optimisation models and to develop an earthworks risk assessment methodology to bring greater certainty to the overall cost of earthworks for each potential route at route selection stage.

2 ALIGNMENT OPTIMISATION

The advancement of optimisation models for road alignment design has gone hand in hand with the advancement of the computer over the past fifty years. As new optimisation techniques, software and hardware have been developed, so too have new alignment optimisation models. An extensive analysis of alignment optimisation models has been conducted and the evolution of the models has been mapped. From early inefficient models which produced basic alignments and considered only basic design criteria and limited objectives, progressively to modern efficient multi-objective models which produce optimal alignments in the conventional form. Full scale experimentation has been carried out with the leading model identified on a circa 40km section of the N3 (Edenburt to Cavan Bypass). The experimentation revealed that an exhaustive search of a study area can be preformed and a range of multi-objective optimal alignments in the conventional form can be produced in a relatively short period of time. The N3 study area is shown in Figure 1 and a range of optimised alignments produced by the model are shown in Figure 2.

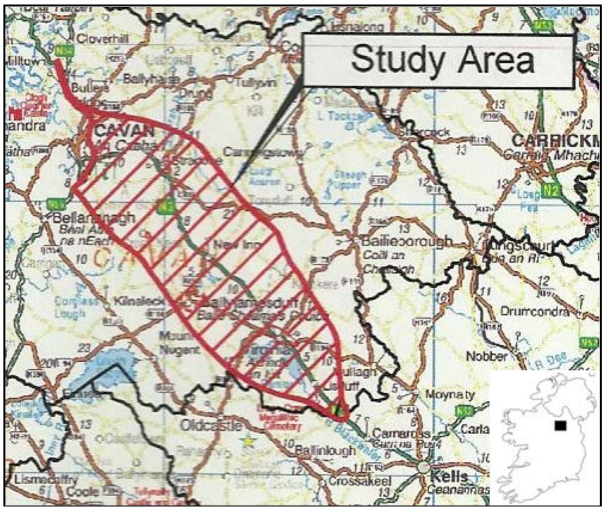

Figure 1. Study area for upgrade on the N3.

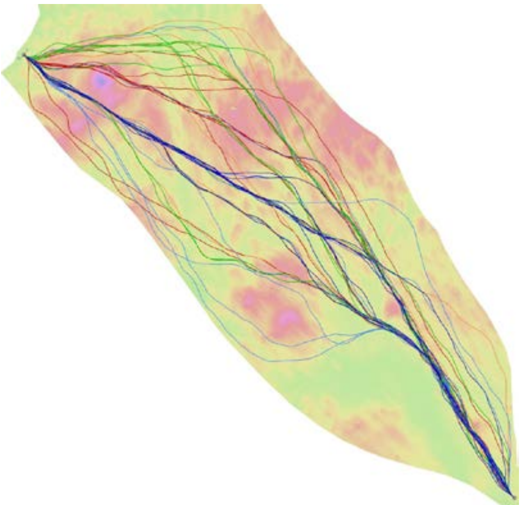

Figure 2. Range of optimised alignments for realignment on the N3.

One facet of the multi-objective optimisation carried out by the model is the optimisation of earthworks. The earthworks optimisation results in horizontal alignments which avoid unfavourable ground conditions where possible and vertical alignments with minimal and balanced quantities of cut and fill which require minimal haulage.
A weakness in the system exists in the manner in which the geological profile is created. Based on the classification of the subsoil material the study area is divided horizontally into regions, and the regions divided vertically into layers. The depth of the layers and percentage usability as a construction material of each layer are each given a single characteristic value. This creates a geologic profile similar to that shown in Figure 3. As a result of this the optimisation does not take account of the spatial variability of the geologic materials and this creates a significant degree of uncertainty.

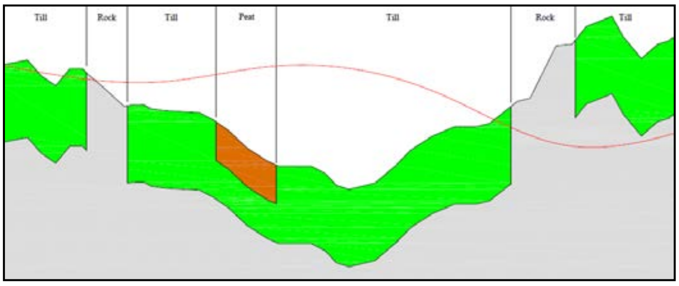

Figure 3. Single characteristic values.

3 RELIABILITY, STATISTICS & RANDOM FIELDS

Phoon (2002) summarises current practice in geotechnical engineering by quoting: “Procedures for selecting nominal soil strengths are not well defined or followed uniformly. Some engineers use the mean value, while others use the most conservative of the measured strengths” Whitman (1984). Phoon then suggests although existing practice has undoubtedly served the profession well for many years, genuine improvements are possible if our practice were to be complemented by reliability-based design (RBD) methodologies. Phoon suggests that: “a fundamental change in the mindset, similar to what has taken place in the structural community since the 1970s is needed for the profession to take the next step”. Fenton and Griffiths (2010) further reinforce this idea: “geotechnical engineers must increasingly be willing to deal with questions relating to the reliability of their designs. Probabilistic approaches will not remove the uncertainty and will not alleviate the need for experience and engineering judgement, but it can provide a way of quantifying uncertainties and handling them consistently”. Given the rapid advancement of personal computers simulation has recently become one of the most popular methods for approximating the reliability of a system. Particularly Monte Carlo Simulation which involves generating a large number of random samplings which are used in repeated execution of an existing deterministic solution process. In many ways Monte Carlo simulations are analogous to real life, much of our knowledge about the safety of structures is based on years of full-scale ‘simulations’.

Variability between soil properties is called spatial variability and has recently been modelled as a random variable (Spry, Kulhawy, & Grigoriu, 1988). Properties of soil are suitably represented by a mean trend and a random residual (Spry et al. 1988). As such, the in-situ soil property at depth $\xi(z)$, can be represented by two additive components as given by Brockwell and Davis (Time Series: Theory and Methods, 1987):

$$\xi(z) = t(z) + w(z) \tag{1}$$

Where $t(z)$ is a smoothly varying trend
$w(z)$ is the fluctuating residual

A mean trend can be found by regression analysis which creates an equation to describe any statistically significant relationships between the predictor and the response variables. The equation for a linear regression is in the form:

$$Y = \hat{\beta}_0 + \sum_{i=1}^{n} \hat{\beta}_i X_i + \varepsilon \tag{2}$$

Where Y is the response
$\hat{\beta}_0$ is the regression intercept
$\hat{\beta}_i$ are the slopes of the regression line with respect to the predictor variables X_i
ε is the error due to chance variation.

Once the data is detrended, the remaining residual, w(z), is generally modelled as a random variable with no trend or in other words a stationary process. Probabilistic modelling of soils as defined by Vanmarcke (Probabilistic Modeling of Soil Profiles, 1977a), involves undertaking a statistical analysis of the residual, w(z). If the residual is represented by a continuous random variable, X, with a probability density function, f(X), then the first two statistical moments of the distribution of a residual are the mean and the variance. The mean is the most important characteristic of a random variable, in that it describes the central tendency. The mean, μ_X, is given by:

$$\mu_X = E[X] = \int_{-\infty}^{\infty} X f_X(X) dx \tag{3}$$

The variance is a measure of the dispersion or the variability of the random variable, it describes whither the distribution is 'wide', 'narrow', or somewhere in between, The variance, ${\sigma_X}^2$, is given by:

$${\sigma_X}^2 = Var[X] = E[(X - \mu_X)^2]$$
$$= \int_{-\infty}^{\infty} (X - \mu_X)^2 f_X(X) dx \tag{4}$$

Using the trend and the statistical moments a random field can be simulated. At its most basic, a random field is a list of random numbers whose indices are mapped onto a space of n dimensions. Values in a random field are usually spatially correlated in one way or another i.e. values with adjacent indices do not differ as much as values that are further apart.

One method for simulating such random fields is Covariance Matrix Decomposition. Given a sequence of points in the random field,

$$X = \{X_1, X_2, \dots, X_n\}^T \tag{5}$$

then the values of X can be simulated using

$$X = \mu + LG \tag{6}$$

Where μ is the mean at each point in the field,
G is a vector of n independent zero mean, unit variance, normally distributed random variables,
L is a lower triangular matrix satisfying $LL^T = C$
C is the matrix of covariances, $Cov[X_i, X_j]$

L is commonly referred to as the square root of C. It is commonly computed using a Cholesky Decomposition. For example Figure 4 shows a random field with a trend and low variance, and Figure 5 shows a random field with the same trend but with increased variance.

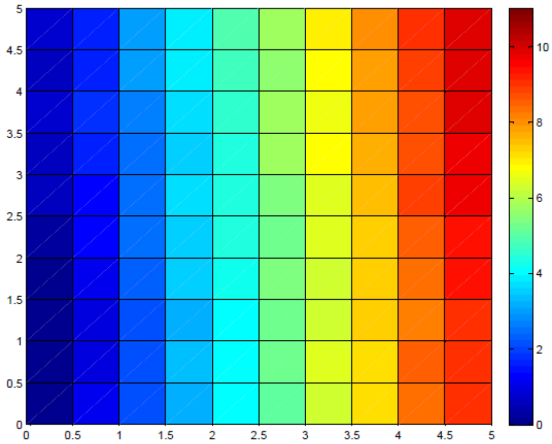

Figure 4. Random field with trend.

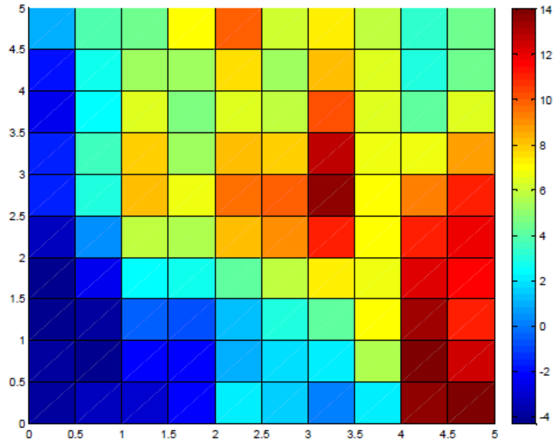

Figure 5. Random field with trend and variance.

4 EARTHWORKS RISK ASSESSMENT

The objective of the risk assessment procedure is to quantify the risk associated with a particular alignment based on the geology of the area through which it passes. A large number of possible geologic profiles will be generated along the profile of the alignment based on known data and statistical representation for the unknown data in a Monte Carlo style simulation. Each profile will then be assessed for the potential risks and so the probability of occurrence for each of the risks for that particular route can be quantified.

For a particular study area a reconnaissance study can indicate statistical parameters and where necessary they can be complimented by expert opinion. For example significant indicators found from the reconnaissance study of the N3 study area include: 1) Records of a very large number of well borings. These can be analysed to give an indication of the mean and the variation in the depth to bedrock. 2) Reports on intrusive investigations for past roads projects in the area. Standard Penetration Tests (SPT) were carried out in many of the boreholes. The results can be analysed to determine a trend and other statistical moments which, with caution, can be used as representative values for the strength of the glacial till in the area. Figure 6 shows a trend of increased strength with depth for the glacial till in the N3 study area.

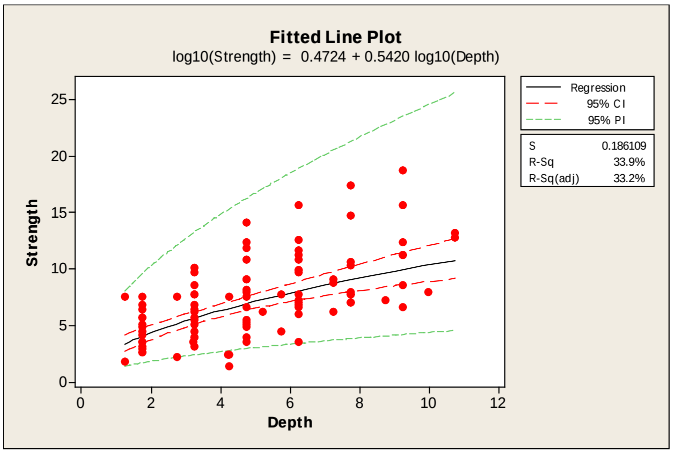

Figure 6. Strength/Depth regression for glacial till.

The interfaces of the geologic material at the surface, which are easily identifiable from geological mapping, can be inserted on a section of an alignment and the corresponding profile of the natural ground profile as shown in Figure 7. The section in Figure 7 is 1 km in length and is taken form one of the alignments generated by the alignment optimisation model used on the N3.

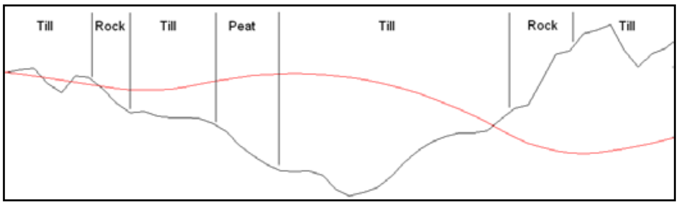

Figure 7. Geologic material interfaces.

Values for the depth to bedrock and the depth of soft deposits can be simulated using a 1-Dimensional random field. The required inputs are 1) mean depth, 2) variation in the depth and 3) correlation length. Figure shows three different simulations of the depths of the deposits based on the same statistical properties over the same 1 km section. Discrete values for the depths can be generated at a defined interval. A 20m interval is used in the examples in Figure 8.

Once the depths of the various layered have been simulated the boundaries of the glacial till are defined. By offsetting the alignment by the depth of the road foundation the formation level can be found. This defines the area of glacial till which will be excavated during the earthworks. As already indicated above, the properties of the glacial till are uncertain. Its strength will determine whether it can become a valuable construction material or in fact a liability. The strength of the material can be simulated using a 2-Dimensional random field as shown in Figure 9. The required inputs are 1) mean strength, 2) variation in the strength and 3) correlation length in the horizontal and vertical directions.

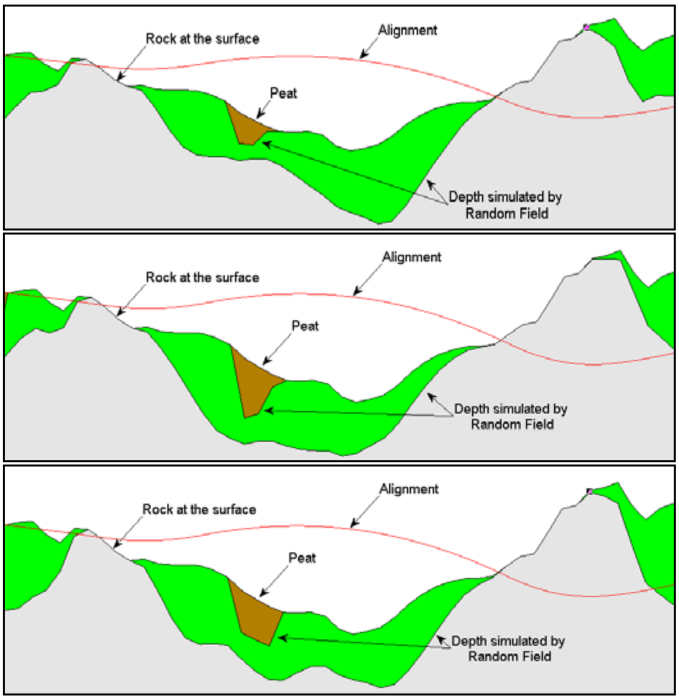

Figure 8. Profiles generated by 2D random field.

In the case of the N3 the mean strength of the material was found to increase with increased depth. In which case, the mean can be represented by the intercept and the slope of the regression line. As shown in Figure 9 the strength of the till increases with depth from low strength which is represented by the dark blue colour to high strength material represented by the red colour. The mesh upon which the field is created comprises of quadrilaterals 5 m horizontally and 1 m vertically. The strength value simulated is equivalent to a California Bearing Ratio % (CBR). Generally a minimum value, which is usually site specific, is selected as the cut off between acceptable and unacceptable as a construction material. If this is applied to the simulation in Figure 9 and a CBR value of 2% is taken as the cut off the grid can easily be divided into acceptable and unacceptable as shown in Figure 10.

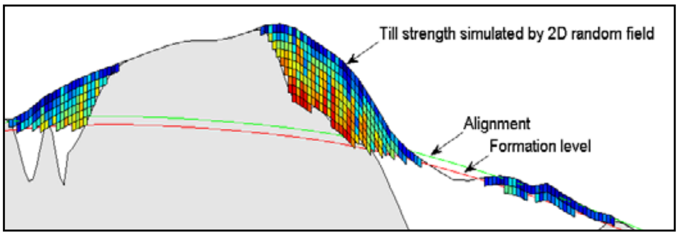

Figure 9. Glacial till strength generated by 2D random field.

Once a simulation of the geologic profile along an alignment has been completed it can be tested for each of the potential risks. When this is repeated a very large number of times a probability of occurrence and be calculated or a ‘probability of failure’ as it is commonly termed in reliability based design. This can be used to estimate the overall risk associated with a particular route from an earthworks perspective. Quantifying the risk in this way will help planners to make a better informed decision when selecting the preferred alignment from the range of optimised alignments produced by an alignment optimisation model.

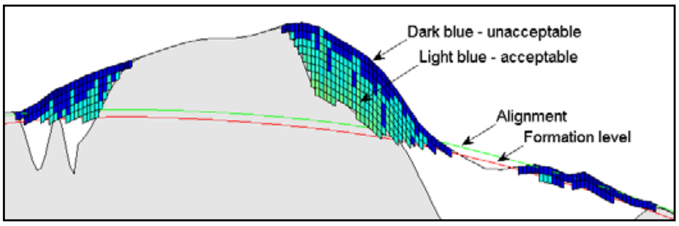

Figure 10. Acceptable and unacceptable material.

5 CONCLUSIONS

In conclusion, the use of alignment optimization models at route selection stage offers a multitude of benefits not least of which is the simultaneous optimisation of the horizontal and vertical alignment form an earthworks perspective. When combined with the alignment optimisation, the risk assessment methodology presented above will highlight the potential risks and bring greater certainty to the cost of earthworks for each of the potential routes at route selection stage. This will allow engineers to make a more informed decision when selecting the preferred route.

ACKNOWLEDGMENTS

This research is funded by the National Roads Authority (NRA) and the authors wish to express sincere thanks not only the financial support but also for the invaluable help and information they have provided.

REFERENCES

[1] K.K. Phoon, & F.H. Kulhawy., Observations on geotechnical reliability-based design development in North America, Foundation Design Codes and Soil Investigation in view of International Harmonization and Performance, 2002.

[2] M.J. Spry, F.H. Kulhawy, & M.D. Grigoriu., Reliability-Based Foundation Design for Transmittion Line Structures: Geotechnical Site Characterization Strategy, Research Report, California: Cornell University USA, 1988.

[3] P.J. Brockwell, & R.A. Davis., Time Series: Theory and Methods, Springer-Verlag, New York, USA, 1987.

[4] R.V. Whitman,. Evaluating calculated risk in Geotechnical Engineering, J. Geotech. and Geoenvir. Engrg., ASCE, 126(7): 583-593.

[5] V.H. Vanmarcke., Probabilistic Modeling of Soil Profiles, Journal of the Geotechnical Engineering Division, (103(GT11)), pp.1277-46, 1977a.

Structural health monitoring of novel concrete arch system

M. Lydon[1], V. Sivakumar[1], S.E. Taylor[1] and D Robinson[1]
[1]School of Planning, Architecture and Civil Engineering, Queen's University Belfast, NI
email: mlydon01@qub.ac.uk, v.sivakumar@qub.ac.uk, s.e.taylor@qub.ac.uk, des.robinson@qub.ac.uk

ABSTRACT: This paper describes structural health monitoring of the FlexiArch™ under moving axle loads to understand the soil-structure interaction in this system. The full system has been developed under a Knowledge Transfer Partnership between Queen's University Belfast (QUB) and Macrete Ltd. but little research has been done to understand the interaction of granular backfill with the arch ring/spandrels and the distribution of pressures through the backfill under a moving axle load. This paper discusses the results of a laboratory model study at QUB. A scaled arch system was loaded with a simulated moving axle and various sensors were used to monitor the arch under the moving load with particular emphasis on the interaction of the arch ring and well-graded backfill. The experiments show the level of backfill has a significant effect on the overall strength of the system.

KEY WORDS: soil-structure interaction, FlexiArch, structural health monitoring, finite element analysis.

1 INTRODUCTION

Bridge construction and maintenance can contribute greatly to the environmental impact of our infrastructure. As increasing life cycle costs caused by high maintenance requirement of bridges with corrodible rebar alternatives must be found. Masonry arches are of particular interest and the FlexiArch system has become a viable option. The FlexiArch is a novel system which offers a more environmentally friendly alternative to RC structures. The system consists of a number of unreinforced pre-cast concrete voussoirs which are connected together with a polymeric grid (Figure 1). To date, there has been limited knowledge on how the arch ring interacts with the backfill material, particularly in relation to the lateral pressures under moving loads. This paper reports on the observations made on a model FlexiArch system tested at QUB under various loading conditions, varying soil stiffness and with different heights of backfill at the crown level. The model was instrumented with a structural health monitoring (SHM) system in order to evaluate and understand the interaction between the FlexiArch and the backfill material. The response of the structure to the applied moving traffic load was monitored and recorded. The SHM has also validated non-linear finite element analysis (NLFEA) of the system particularly in respect to soil-structure interaction.

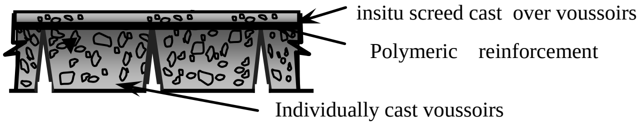

Figure 1. Construction of arch unit using pre-cast individual voussoir concrete blocks.

2 ARCH PROFILE AND MONITORING

2.1 *Arch system detail*

A one sixth scale 5m span by 2m rise arch ring was used for this study. The arch was constructed based on the configuration reported by Taylor [1]. The arch ring was monitored during the backfilling process. To examine the effect of lateral movement on the behaviour of the arch bridge system the abutments were supported horizontally with a spring on each side to represent weaker soil or not fully compacted backfill at the abutments.

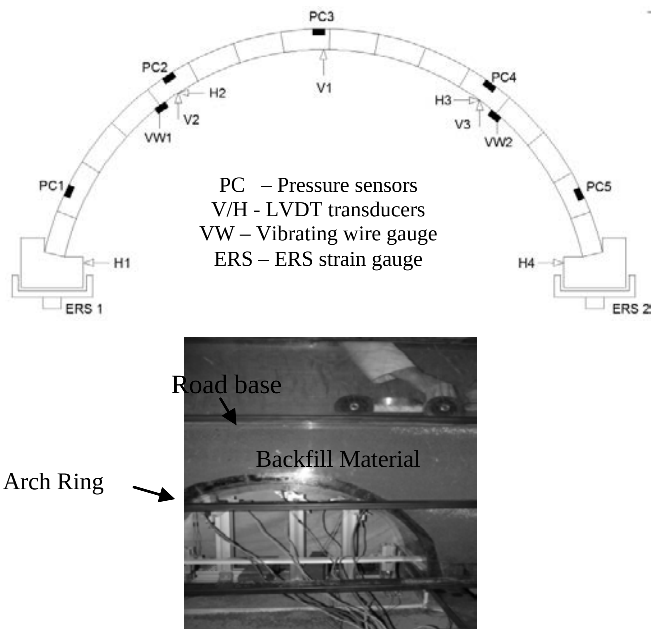

Figure 2. Typical arrangement of instruments and general set up.

2.2 Instrumentation and monitoring

A range of sensors was used to understand the behaviour of the structure, particularly with respect to the arch ring and backfill interaction. A typical arrangement and loading scheme is shown in Figure 2. Pressure cells were installed into five of the voussoirs. Seven LVDT (Linear Variable Differential Transformer) were used to measure the deflection of the arch ring. As the direction of movement is two dimensional, vertical and horizontal LVDT(s) were used to capture the resultant deformation. The opening between the voussoirs was measured using vibrating wire strain gauges (VWG). The arch was supported on rigid steel beams (as shown in Figure 2b) and it was gauged with ERS (Electrical resistance strain) sensors to determine the vertical reactions at the supports,

2.3 Loading Conditions

A major aim of this research was to model real traffic loading and to investigate its effects on the structure and the interaction of the soil and structure. A scaled trolley (representing a vehicle with two axles) was used. A road base was constructed on the backfill, and a flexible track system was built over the road base to enable movement of the model vehicle and to simulate a real road surface. The height of the backfill above the extrados of the crown was varied; equivalent to full scale heights of 0.5m, 0.3m and 0.2m. The lower the level of backfill the less dispersal of load occurs creating a more onerous loading effect on the arch ring. The mass of the vehicle was changed by stacking dead weights on the trolley. The track was marked at intervals of 0.08m along the entire span of the roadway (equivalent to 0.5m intervals on the full scale system). A complete loading cycle involved moving the vehicle from left to right (1.2m travel) and returning to the starting location. The readings were taken when the model vehicle come to halt at the pre-selected locations on the track. A typical test involved three full cycles on the track; including the forward and return travel.

3 STABILITY TEST AND MONITORING

3.1 Test procedure

A previous stability test on a 5m span by 2m rise arch ring, Taylor [2] showed the arch was stable during backfilling. However, due to the use of light weight voussoirs in this investigation, the arch could be less stable and experience greater uplift at the crown during backfilling operations. To measure the stability during backfilling, the deflection of the arch ring was monitored. The backfilling operation was carried out by placing ~50mm deep layers of the well-graded and appropriately scaled backfill material to each side of the arch. The distribution of load equally to either side of the arch ring was aimed at minimising the effects of asymmetric loading. Readings for all of the sensors were taken at each increment height of backfill, and the results are shown in Figure 3.

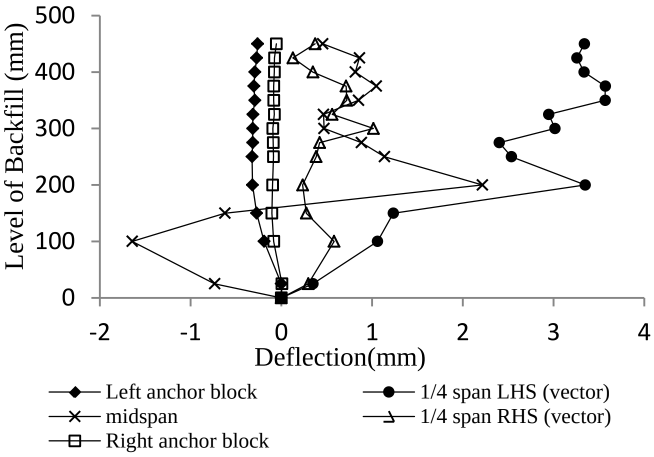

Figure 3. Arch deflections during backfilling operations.

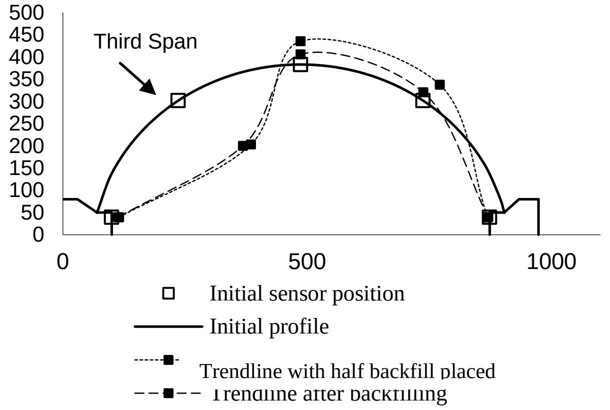

Figure 4. Exaggerated deflections of the arch after backfill.

3.2 Results from the monitoring of backfilling

The readings show a non-symmetric response to the backfilling operation and the results show a greater sway to the left which may have been caused by the first layer of backfill being applied to the right side causing sway in the whole arch ring. The deflection response with increasing backfill heights is shown in Figure 3 and Figure 4 shows the exaggerated (x 50) deflected shape of the arch ring when the backfill level was just above the crown of the arch. The maximum movement in the crown was 1.04mm upwards, this occurred when the granular backfill was at the height of the crown of the arch. This was due to the lateral pressure of granular backfill creating an inwards movement at the sides of the arch and subsequent upwards movement at the crown. Additional backfill over the top of the crown had a beneficial effect on this deflection. The maximum movement at the sides of the arch occurred in the transducers on the LHS at the third span. At the end of the backfill operation, the maximum inwards movement was 3.5mm at the third span. The results of the monitoring showed that the arch was sufficiently stable during backfill operations.

4 MONITORING RESULTS

When the trolley load was at a maximum of 250kg (equivalent to a full scale partial axle load of 300kN for full scale bridge structure) and the backfill at the minimum level of 50mm above the crown extrados, there were no visible signs of hinge formation in the arch ring. The Flexi Arch tends to fail in a hinge mechanism [2]. However, the bearing capacity of the road and backfill was exceeded which prevented any further increase in loading.

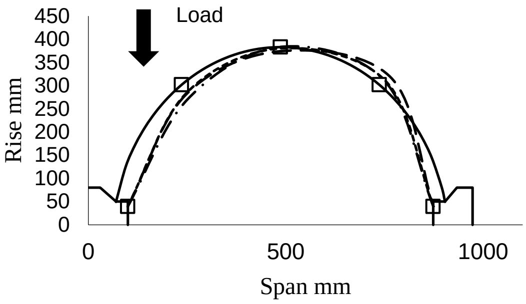

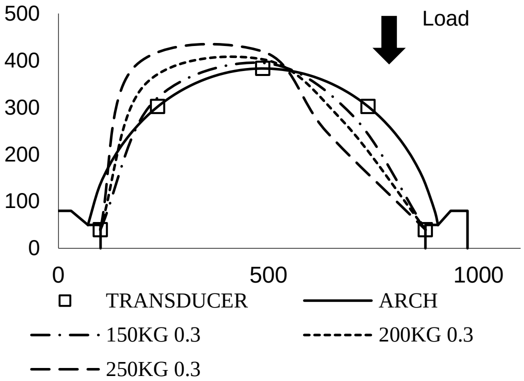

Figure 5. Exaggerated deflections of the arch during loading.

4.1 Deflections

The deflections of the arch ring increased with increasing axle load and the largest deflections occurred when the load was applied over the third span, where a hinge is likely to occur. Figure 5 shows the data for the axle load at the third span and the inward movement of the arch ring below the load and outward movement of the ring on the opposite side. The initial loading for each test was from left side and the results show that this caused permanent deformations in the arch ring. Therefore for all three tests there are greater deflections on the left side (Figure 5).

For the majority of tests the greatest deflection was encountered on the third run. In general when a load of 250kg was applied the deflections increased by about 15% between the first run and the third run. In some cases the recovery of the H2/V2 (fig.2) deflections was as little as 53% which is not within the acceptable limits. The results show that the structure exceeded its elastic limit and permanent deformations occurred.

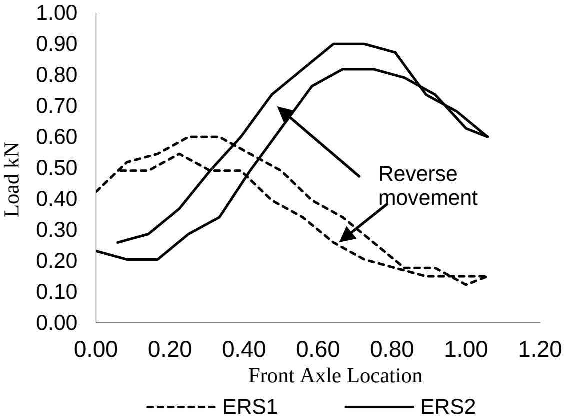

Figure 6. Distribution of Vertical load between ERS strain monitors.

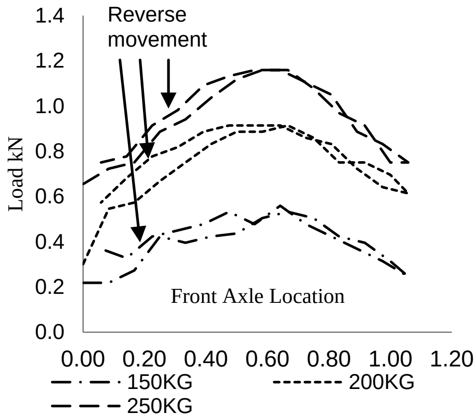

Figure 7. Combined vertical load on ERS strain monitors for varying load.

4.2 Strain results

There was an uneven distribution of vertical load in the support beam as shown by the ERS results in Figure 6; the ERS2 recorded a greater strain, which corresponded with the higher deflections when the load was directly above the right side of the arch ring. This could have been caused by a longitudinal surcharge through the backfill from the axle as it travelled across the pavement. Both ERS show a similar behaviour but Figure 6 shows that ERS2 had higher strain due to higher pressure. The results for varying the load showed that the greatest combined load occurred when the load is at the centre of the arch, corresponding to the location with the least amount of backfill as shown in Figure 7, highlighting that as predicted the vertical load transferred to the beam increased as the level of backfill decreased.

4.3 Pressure Sensor results in the arch ring

Pressure sensors (PC1-5) were installed into five of the voussoirs (as Figure 2). The pressure sensors were installed in order to gain a clearer understanding of the soil/structure interaction. The results from the pressure sensors were not as consistent as the other sensors. In most cases such sensors are subjected to a constant pressure. During the tests a variation in pressure across the surface occurred due to change in the arching thrust between and through the voissoir. The granular backfill acted to disperse the axle load but may have created concentrated loading points on the sensors. The arch was also free to deflect inwards creating a negative drop in pressure at the interface. Ideally, the pressure sensors should have been contained wholly within the backfill or voussoir. Further testing of these sensors in granular materials will give more information on the correct means of application for monitoring of soil/structure interaction. At PC1, under the maximum load and lowest level of backfill above the crown, the pressure was higher under forward movement in comparison to the load travelling in reverse. This indicated that the dispersal of load spread was more concentrated in the direction of travel as shown in Figure 8.

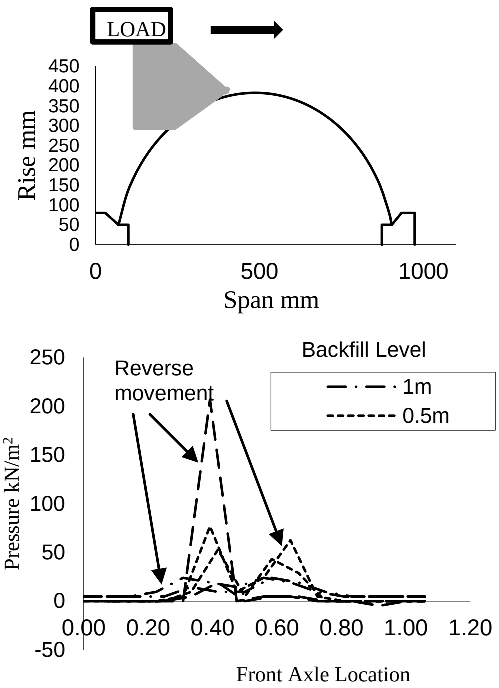

Figure 8. Load spread in forward movement and pressure Cell 3 results varying backfill level with a constant load of 250kg.

The results of PC3 in Figure 8 show that highest pressure occurred with the lowest level of backfill that is 0.3m above the extrados crown. A pressure of 206kN/m^2 was measured when the front axle was over the midspan location under reverse movement; this is close to the bearing capacity of the unconstrained soil. Figure 8 shows the differences in pressure under forward and reverse movement and is consistent with the results for this PC3. The results also showed a significant difference between run 1 and run 2 of the same test, and this may have been due to permanent damage caused to the road base after the first run. This could also explain the difference in pressures under run 1 to run 2. The additional peak in the reverse run occurs when the back axle was close to the midspan. The axle on the track acted as a series of point loads, and movement of the track probably changed the dispersal of loading through the backfill. Another possible explanation for the change in dispersal of load was the differences in pulling and pushing the vehicle. It was much easier to pull and was faster but with more dynamic amplitude compared to pushing.

4.4 Vibrating Wire strain gauge (VWSG) results

VWSG were used to measure joint openings between the voussoirs. The results of the VWSG were consistent with the transducer results. The strain measured by the sensors was converted to a joint opening as all of the tensile strain was due to the joint opening. Similarly to previous results the reverse movement had a more significant effect on the openings, as the axle load increase the joint openings increased as shown in Figure 9.

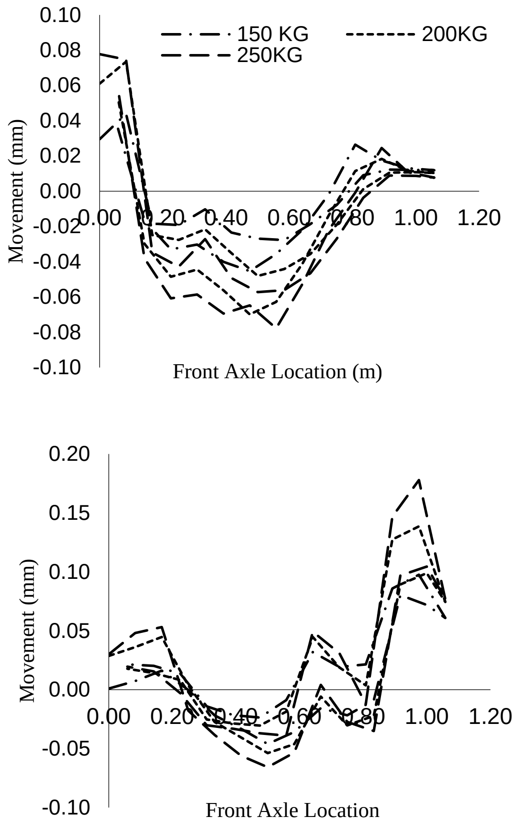

Figure 9. Results for Vibrating wire gauge 1 and 2 for varying load with a constant backfill level of 0.3m.

As the axle load was applied VW1 measured tension but when the load is moved over towards the location of the VW1 the arching thrust caused compression at this position. This is similar to the findings in the deflection results where H2/V2 had a maximum outward movement. Sensor VW2 showed a similar of the pattern to that of VW1 but with slight difference due to the asymmetric dispersal pattern under forwards and reverse movements. Additionally in VW2, there was a shift in tensile strains at the same time as a shift in compression strains at the opposite third span, showing that these were the most likely positions for a hinge to form. The maximum tension strain or joint opening occurred at VWG2 and was almost double that of VWG1; this corresponds with previous findings that the right side of the arch was stiffer therefore allowing less movement in that direction, the greater movement in the left direction allows for greater hinge opening at the location of VWG2. The large peak in compressive stress on VWG2 at 0.6m only occurred when the backfill level was reduced to 0.3m, and there was no peak in tensile strain in VWG1 at higher backfill levels. A much smaller peak in compressive strain in VWG2 did occur at the same location for the 0.5m backfill which also corresponds to a small peak in tensile stress in VWG1. This shows that as there would be hinge opening on one side this would cause compression on the opposite side.

5 NON LINEAR FINITE ELEMENT ANALYSIS (NLFEA)

5.1 Finite Element Model

The finite element model was created using the commercial package ABAQUS and various nonlinear material properties were adapted to model the behaviour of the arch. A Concrete Damaged Plasticity model was adopted for the arch ring. The material for the arch ring is defined as one with high compressive strength and little or no tensile strength. The granular backfill is modelled using a Drucker-Prager plasticity model. The Drucker-Prager material law requires three material parameters the internal angle of friction Ø, cohesion c, and the dilation angle of the backfill material [3]. The material properties were obtained from the backfill used in the laboratory model study. The angle of friction and angle of dilation are taken to be 40^0, Young's Modulus is 50MPa, Poisson's Ratio as 0.2 and the cohesion as 0.015MPa. In reality the backfill which was used was very sandy and therefore would have little or no cohesion. However if a value is not entered the analysis is unstable unless side supports are constructed. The load model is created with a Young's Modulus of $2x10^5$ MPa and a Poisson's Ratio of 0.3. The density of the material varied to represent the different loads used in the laboratory testing.

The numerical modeling program has the capability to analyse using implicit or explicit methods. An explicit analysis was used as it allows dynamic analysis and this does not require equilibrium of the externally applied loads and the internal forces at each load increment to continue. This provides a solution to the convergence problem which can occur in a static implicit analysis. Previous studies have shown that, due to the nonlinearity of the backfill and arch ring, the explicit method is more suitable [4-5]. The boundary conditions are applied to the model [6]. Once the boundary conditions have been applied the load is applied in steps. The load is applied in two steps the first being the gravity loading step and the second step is the applied loading

5.2 Results

The results from the NLFEA give an insight into the behaviour of the material and also model the behaviour of the structure. The model can be used to determine the peak load on the arch and the most critical loading position. The NLFEA is part of ongoing research as the changes in the material properties due to confinement and loading history are not fully established. However the behaviour of the structure under the dynamic loading was analysed and this showed that the location of the initial application of the load had a permanent effect on the structure. Figure 10 shows permanent damage in the soil at the location of the applied load even after the load has moved across the structure and the strain pattern in the NLFEA is similar to that measured by the sensors. The VWSG results showed that when the load was at this location, there was opening in VWG2 and compression in VWG1. Compression in the extrados would cause tension in the intrados. The laboratory model tests show that there was a higher vertical load on the right side of the model. The results in Figure 10 suggest that the results from NLFEA are consistent with this.

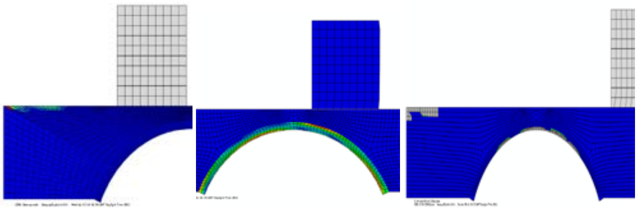

Figure 10. Stresses on backfill material after initial loading, stresses in the arch ring and permanent damage caused to arch ring and backfill by applied load.

6 CONCLUSIONS

The results from the SHM showed the significance of the backfill in contributing considerably to the overall strength and stability of the arch system. The sensors were able to show the effects of a dynamic load and, in particular, the results of longitudinal surcharge causing asymmetric loading on the arch ring. The sensors were also able to validate the NLFEA model. However, the SHM results showed greater deflections on one side of the arch and this was probably due to an overall sway in the system. To examine this further, a parametric study is to be carried out using the NLFEA and varying the geometry to provide asymmetrical response. The NLFEA in this study provided horizontal and vertical reactions at the support locations which showed reasonable agreement with the pressure sensors but further studies are ongoing to investigate the use of pile foundations for the support the structure.

REFERENCES

[1] Taylor S E, Gupta A, Kirkpatrick J, Long A E, Rankin G I B and Hogg I. (2009) Monitoring of Tievenameena Flexiarch Bridge, Proceedings of Advanced Composites in Construction. P342-351. 2009

[2] Taylor S E, Gupta A, Kirkpatrick J, Long A E, Rankin G I B and Hogg I. (2006) Development of a novel flexible concrete arch system, 11th International Conference on Structural Faults and Repairs, Edinburgh, June 2006.

[3] Audenaert, A. Fanning, P. Sobezak, L & Peremans, H. (2008). 2-D analysis of arch bridges using an elasto-plastic material model. Engineering Structures. 30 (3), P845-855.

[4] Robinson, D., Johnston, R. & Taylor, S. (2010). Finite element analysis of skewed FlexiArch.

[5] Zheng, Y. (2010). Non-linear finite element analysis of masonry arch bridges reinforced with FRP. Proceeding of 10th International Arch Bridges Conference .

[6] Fanning P J and Boothby T E, (2001) Three-dimensional modelling and full-scale testing of stone arch bridges, Computers and Structures, v 79, n 29-30, November, 2001, p 2645-2662

Development of instrumented piles to investigate pile ageing

Lisa Kirwan[1], David Igoe[1], Kenneth Gavin[1]
[1] Department of Civil Structural & Environmental Engineering, University College Dublin, Belfield, Ireland
email: lisa.kirwan@ucdconnect.ie, david.igoe@ucd.ie, kenneth.gavin@ucd.ie

ABSTRACT: Foundation costs can account for 35-45% of the total capital cost of offshore wind farm developments. Design methods for offshore foundations are calibrated to predict the short to medium term axial capacity of piles (typically within 10 to 30 days of pile installation). Whilst time dependent changes in pile capacity in clay are expected and can be theoretically understood though consolidation processes, there is significant evidence that the capacity of piles installed in sand also increases with time. The physical mechanisms that govern this process, known as ageing, are poorly understood. This paper describes an experimental programme currently underway at the UCD dense sand test bed at Blessington where 14 full scale piles have been driven into dense siliceous sand. One of the purposes of this experiment is to study how the capacity of these piles changes over time. This is partly achieved by measuring the radial effective stresses acting on the pile shafts and examining how these fluctuate over a period of months. If the mechanisms controlling the change of the radial stresses can be understood, then the increase in axial capacity can be quantified, resulting in smaller and more cost effective foundations. In order to ensure that these measurements are reliable, robust instrumentation and a thorough understanding of the errors associated with them are essential. This paper sets out details as to how the instrumentation was installed, and also the problems that were overcome. In addition to this, the paper outlines the calibration tests conducted on the sensors which show how various factors need to be taken into account in order to be sure of obtaining trustworthy results.

KEY WORDS: Geotechnical instrumentation; Pile foundations; Pile ageing; Offshore wind turbines.

1 INTRODUCTION

In recent years, a drive to increase the proportion of the world's energy supply derived from offshore renewable sources has led to a rapid expansion in the offshore piling industry. Development of offshore wind resources in deep waters brings new challenges for pile designers, as the foundation typically represents 30 - 40% of the development cost for an offshore turbine. The proposed deployment of many thousands of turbines off the UK and Irish over the next two decades is dependent on achieving more efficient designs to reduce the capital expenditure (CAPEX) cost of these projects. Pile ageing is an area that could potentially provide huge improvements in the efficiency of pile design. Field tests reported by Chow[1] and Axelsson [2] suggest that the capacity of piles driven in sand can increase by up to 250% over a time period of one year after driving. If such increases could be properly understood and implemented in pile design, significant reductions in pile length and therefore resultant large cost savings could be made. This paper describes how different types of piles were instrumented for the purpose of measuring the radial stresses acting against these piles both during installation and over a period of time thereafter.

2 BACKGROUND

Chow [1] reported results from tension load tests performed on 324 mm diameter steel pipe piles which were driven into dense sand at Dunkirk, France. When the pile was retested five years after the initial load test, the pile capacity had doubled. This prompted Jardine et al. [3] to instigate a systematic experimental program to investigate the issue of pile ageing at the Dunkirk test site. A total of eight 457mm diameter steel pipe piles were driven 18m into the dense sand at Dunkirk. Load tests were performed on piles at different time intervals after installation. Because previous studies had suggested that ageing might be affected by loading history, tests were performed on *fresh* piles (i.e. ones that had not been previously loaded). The results showed that the piles exhibited an increase in tension capacity of 250% in the 235 days following installation. The increase in capacity was believed to be as a result of increases in radial effective stresses acting on the pile shaft. The mechanism which allowed this increase is the relaxation, as a result of creep, of circumferential arching established around the pile shaft during installation [3]. Research by Axelsson [2], who measured the horizontal stresses on 235mm square precast concrete over time, broadly reinforced these preliminary conclusions.

The piles tested at Dunkirk did not allow for measurement of radial effective stress and these measurements are essential in order to understand the mechanisms controlling pile ageing in sand. Reliable radial stress data is difficult to obtain due to the difficulty in instrumenting piles, the errors associated with the various types of pressure sensors, and indeed the harsh conditions experienced during pile driving which make a robust instrumentation design essential. The design and construction of an instrumented pile to allow the measurements of radial effective stresses on piles installed in dense sand is discussed in this paper.

3 EXPERIMENT DETAILS

An experimental investigation with the aim of understanding the effects of pile ageing is currently being conducted by the Geotechnical Research Group at UCD. The UCD field test site is located in the Redbog Quarry near Blessington, Co. Wicklow. The site is extremely uniform and the ground conditions described by Gavin and Lehane [4] and Igoe et al. [5] comprise of very dense sand to great depth with a Cone Penetration Test (CPT) end resistance q_c in the range of 15 – 30 MPa. A total of seven 285 mm square concrete piles and six 340mm diameter open-ended steel pipe piles were driven to a penetration depth of 7m. The dimensions (See Table 1) of the open ended pile were chosen such that the D/t ratio would resemble that of common offshore open-ended piles (where t is the wall thickness of the pile). One steel pile (S6) and one concrete pile (PC5) were instrumented, with the remaining piles being used for used for un-instrumented static or dynamic load testing. The pile was only recently completed and installed (2012). The results of this experiment are currently under analysis and will be published in due course.

4 INSTRUMENTATION

A summary of the instrumentation used for the steel (S6) and concrete (PC5) piles can be found in Table 1:

Table 1. Details of instrumented piles S6 & PC5.

Pile	**S6**	**PC5**
Material	Steel (open-ended)	Concrete
Pile diameter/width (m)	0.339	0.275
Depth driven to, *L* (m)	7.0	7.0
Wall thickness, *t* (mm)	14	NA
Strain Gauges	10 levels x 2	No
Radial Total Stress Sensors	4 levels x 3	3 levels x 1
Pore Pressure Sensors	None	None
Temperature sensors	5 levels x 2	3 levels x 1

4.1 Steel Pile (S6)

The open-ended steel pile (Pile S6) was instrumented with miniature total stress sensors, strain gauges and temperature sensors. As the pile was due to be installed in Blessington above the water table, and as previous instrumented pile and CPTu tests failed to record any excess pore water pressures, it was deemed unnecessary to measure the pore-water pressure. Mechanical protection for the sensor cables was provided by two channels which we formed from two outer walls of steel (16 mm thick) covered over with a 40 mm wide strip of steel, see Figure 1 (a). After the cables containing the lead wires were in place between the channel walls, the steel cover was stitch welded over the top of the channel walls. The welds were spread to avoid excess heat build up which could damage the cables. The channels were placed diametrically opposite each other and ran the length of the pile, stopping 500mm from the top of the pile to allow the cables to exit. The strain gauges and temperature sensors were housed inside the channels while the miniature total stress sensors were housed outside the channels and offset by 90 degrees to minimize disturbance in the radial stress regime caused by the change in geometry due to the channels. The total stress sensors were placed in pre-drilled slots with the cable exiting through a bevel which was ground into the pile wall and ran into the steel channel. Once the cable was glued in place, the bevel was back filled with a liquid steel epoxy resin to provide mechanical protection during driving, see Figure 1 (b). At the top of the pile, the sensor cables were extended using a heavily shielded multi-core cable and plugs were soldered to the end of this for connection to the datalogger.

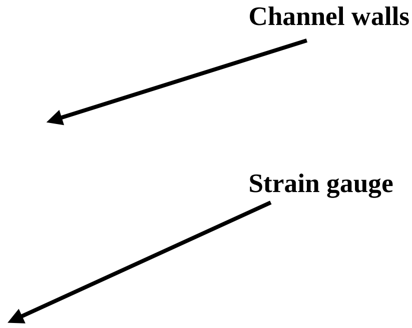

(a) Channel

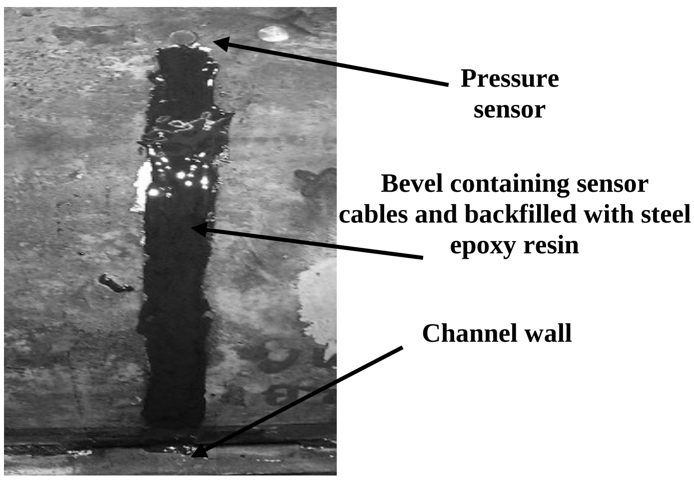

(b) Sensor bevel

Figure 1. Details of instrumentation for steel pile

4.1.1 Total Stress Sensors

The miniature total stress sensors (See Figure 1b) were installed at four levels along the pile shaft, with three sensors at each level. The sensor levels were chosen such that they matched those used in tests performed using model piles at the same test site [5] and were located at 1.5, 5.5, 10.5 and 17.5 diameters from the pile toe. The total stress sensors used for the steel pile were TML PDA-PA miniature pressure sensors. In order to provide redundancy and to measure the total stress accurately at low stresses while maintaining sufficient sensor stiffness to avoid errors due to cell action (discussed later), two 3 MPa capacity sensors and one 500 kPa capacity sensor were used at each level. The sensors were chosen because the small diameter of the sensing face (6.5 mm) minimized distortion of the shaft geometry (and associated errors) caused by the curvature of the tube. The sensors consist of four electrical resistance based strain gauges, the central two in compression and the outer two in tension making a full Wheatstone bridge. These strain gauges are mounted on the back of a stiff diaphragm which forms the sensing face of the pressure cells. When a pressure is applied to the diaphragm, the strain gauges change length, causing a change in resistance in the wires which can be correlated to the amount of pressure acting against the diaphragm of the sensor. There are several errors associated with this type of stress sensor which must be addressed before an accurate measurement of the radial stresses can be achieved:

1. Electrical Resistance Strain gauges (ERS) are susceptible to voltage drops resulting from poor electrical contacts. It is important that all solders/electrical contacts be tested to ensure a good connection prior to deployment in the field. Sufficient mechanical protection should be provided near any connections to prevent these connections from becoming damaged.
2. ERS gauges are susceptible to moisture ingress. It is imperative that all electrical connections from the sensor to the datalogger are fully moisture resistant. Solder sleeves can provide protection from moisture ingress at any solder joints. ERS gauges are susceptible to changes due to temperature. This is particularly important during pile driving when the temperature of the pile can change significantly, depending on the pile material and rate of installation. The temperature should be measured directly at multiple locations along the pile using thermocouples or PRT gauges. The pressure sensors should then be calibrated and temperature compensated.
3. In order to quantify the effect of temperature changes on the zero reading of the pressure sensors, the sensors were placed in a container of water placed over a hot plate. A thermometer in the water was used to measure the temperature as the water and pressure sensor were heated. As the water was heated, the sensor readings were noted along with the corresponding temperature. This experiment yielded a relationship showing the zero shift per degree of temperature change from the initial temperature that the sensor was zeroed in. Thus, by noting the temperature at which the pressure sensors were zeroed at and the temperature at which subsequent readings were taken, a temperature correction can be applied to the sensor output.
4. The sensors can be affected by cell action whereby the deflection of the sensing face of the pressure sensor causes a reduction in stress in the soil at the measurement location. This effect can be minimized by using sensors that are sufficiently stiff. Calibration tests performed in a sand chamber, see Figure 2 have shown that this effect is minimal provided that the sensors are not loaded in excess of 33% of their rated capacity (i.e. the radial stresses should not exceed 1 MPa for a 3 MPa rated sensor).

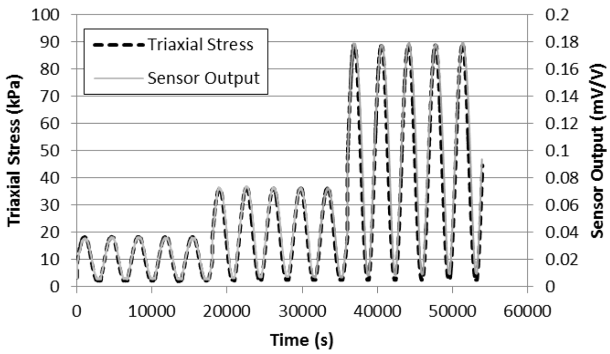

Figure 2. Calibration tests performed on a 500 kPa sensor tested at low stress.

A series of calibration tests were conducted using this type of pressure sensor to investigate the potential errors due to cell action. These tests involved installing a sensor flush into a steel plate. The plate formed the bottom of a cylinder which was filled with sand (from the Blessington site). Figures 3 and 4 illustrate this set-up. Stresses similar to those experienced during pile driving were then applied to the sand at the top of the cylinder using a triaxial apparatus, with the loads measured using the triaxial load cell.

A number of parameters which was felt might influence the sensor response in the lab tests were varied. In particular, the effect of sand state was taken into account by comparing the sensor response in both loosely packed and dense sand. This allowed the effect of compaction of the sand to be analysed. All other things equal, it was shown that the response of the sensor in the loose sand was to register slightly higher loads (about 20% higher), than when the sensor was in dense sand. This could be due to higher friction losses in dense sand mobilised along the side wall – sand sample interface in the calibration chamber which appears to have compensated compaction effects of the sand in the region of the pressure sensor. This effect of interface friction is currently being modelled using finite element analysis to quantify the influence on the calibration of sensors.

The results of the tests showed that the high capacity sensors (3 MPa) had a higher stiffness which reduced the negative effects of cell action. As mentioned above, in addition to these tests, finite element analysis is underway to model how these sensors interact with the soil and how cell action affects their readings. The results of these calibration tests and modelling will be published in due course. As a result of the calibration tests, the linear calibration factor (recommended by the sensor's manufacturer) was used to convert the raw data into pressure readings.

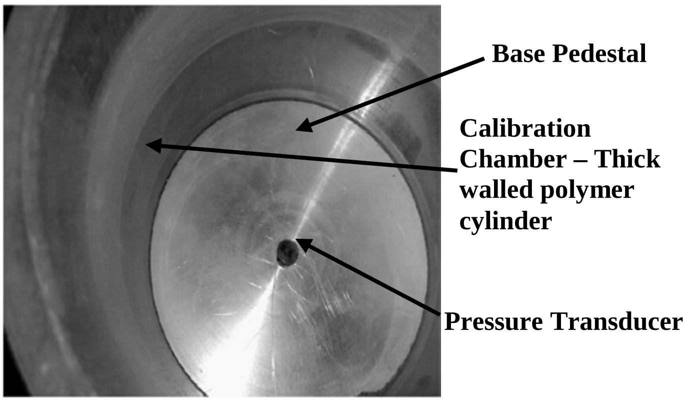

Figure 3. Calibration chamber with specially fabricated base pedestal.

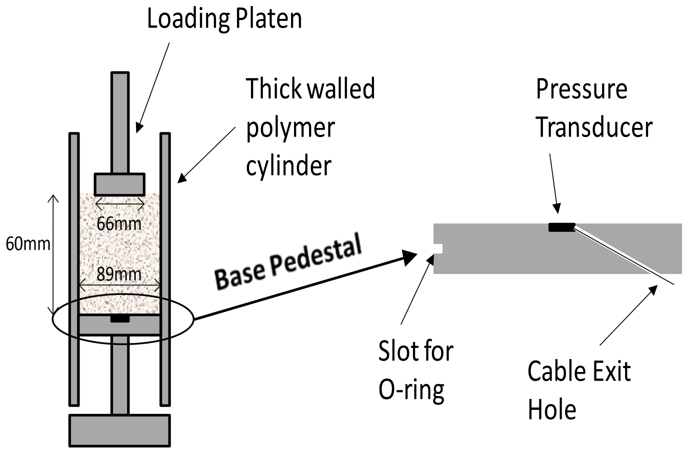

Figure 4. Experimental set-up for miniature pressure sensor calibration tests.

4.1.2 Strain Gauges

The strain gauges used for pile S6 were KFG-5-120-C1-11-L5 strain gauges. These were installed to measure the load breakdown along the pile shaft during static load testing and thus allow an estimation of the shear stress distribution to be made. This data is used to verify the radial effective stress measurements recorded by the miniature pressure sensors. The use of four strain gauges at each level would have been preferable as the bending at each level could have been averaged out more effectively. However, this would have required the use of four channels. The principle aim of the instrumented pile is to measure radial stress fields around driven piles. Since the channels introduce a disruption to the stress field surrounding the pile, it is necessary to place the pressure sensors as far away as possible from the protruding channels. Adding an additional two channels would have halved the distance to the nearest channel that the pressure sensors were placed and caused stress fields which are untypical of circular driven piles.

Figure 5 illustrates one of these strain gauges installed inside a channel. Since these strain gauges are not waterproof, a layer of waterproofing tape was applied over each sensor to protect from damage due to water ingress.

Figure 5. Strain gauges installed inside the channels of pile S6.

4.1.3 Temperature Gauges

The temperature gauges used were CRZ-2005, Platinum RTD temperature sensors. Figure 6 illustrates one of these temperature sensors installed inside one of the channels. These are resistance temperature detectors which work by correlating the resistance of the element with temperature. The advantages of using this type of sensor are that they are highly accurate, stable and provide excellent repeatability.

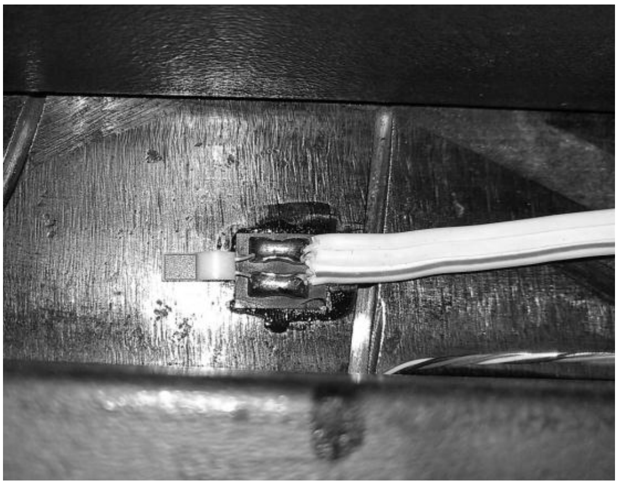

Figure 6. Temperature sensors installed inside the channels of pile S6.

4.2 Concrete pile

The concrete pile was instrumented with pressure sensors only. The square cross section of the pile allowed much larger pressure sensors to be used (as there was no error due the curvature as with the steel pile). The pile was instrumented with three P6-2.1-MS-30-T Soil Instruments vibrating wire pressure cells. The sensors had a diameter of 240mm, came with an inbuilt thermistor and a capacity of 3MPa. The sensors consist of two sheets of steel welded together around their periphery with the gap between the two plates filled with hydraulic oil.

A short piece of tubing connects a vibrating wire transducer to the cell, forming a closed hydraulic system. The cells work by the vibrating wire principle, where a tensioned wire is attached to a diaphragm. There is a relationship between the pressure acting on the diaphragm and the tension of the wire. The resulting resonant frequency (which changes depending on the tension in the wire) is then read and converted into a pressure reading using a calibration factor. The primary advantage of the VW sensor is the output, which is a frequency rather than an electrical resistance or a voltage. This results in a more stable output which is unaffected by voltage drops resultant from poor electrical contacts. Additional benefits include a resistance to moisture ingress and temperature changes, both of which significantly impact on ERS gauges. Signal loss due to excess cable length can also be a significant issue for ERS gauges. However, VW applications are unaffected by changes in cable length due to the nature of the output. One disadvantage of VW sensors is the limited logging frequency (typically only 1 reading per 30s) which makes them unsuitable for dynamic applications but very suitable for long term ageing measurements.

The pressure sensors were installed by making a mould of the sensor and its transducer housing out of polystyrene which was then tied to the reinforcing before the concrete was poured. Heavy duty hoses were also run alongside the reinforcing bars to hold the sensor cables. Once the concrete was poured and set, the moulds were chipped out leaving room for the sensors to be installed flush against the pile wall and a channel running through the pile to hold the cables. The sensors were secured in place by using a special type of epoxy adhesive (Sikadur-31 Rapid epoxy adhesive) and grout and the cables were fed through the hose and out the top of the pile where they could be connected to the datalogger. Figures 7 (a) and (b) illustrate the instrumentation process of pile PC5.

(a) Polystyrene pockets

(b) Pressure sensors.

Figure 7. Instrumentation Process of Piles PC5.

5 CONCLUSIONS

An open-ended steel pile and a square precast concrete pile were instrumented for the purposes of measuring the radial effective stresses acting on the pile shaft, and how they change over time. The method of instrumentation, including a novel way of protecting the sensor cabling, was presented. The potential errors associated with these types of measurements and the methods used to minimize these errors were described. A laboratory calibration of the total stress sensors was performed in a triaxial apparatus to account for any potential errors caused by cell action. The errors due to cell action were seen to be negligible provided the sensors are not loaded in excess of 33% of their rated capacity.

ACKNOWLEDGEMENTS

The first author would like to acknowledge the support of Science Foundation Ireland (Grant No. 10/RFP/GEO2895) and Enterprise Ireland through the Industry Partnership Programme (Grant No. IP/2010/0085) and would also like to thank the following industry partners for their on-going support: Mainstream Renewable Power, Bullivant Taranto and Lloyds Acoustics. The author would like to further thank the following colleagues and technical staff at University College Dublin who provided invaluable help during the instrumentation of the piles and field tests; Dr. Paul Doherty, Mr. Tim Hennessy, Mr. Weichao Lee, Mr. George Cosgrave and Mr. Frank Dillon.

REFERENCES

[1] Chow, F. (1997) ‘Investigations into behaviour of displacement piles for offshore structures’, *Civil Engineering*. London: University of London (Imperial College).

[2] Axelsson, G. (2000) ‘Long term set-up of driven piles in sand’, *Dept. of Civil and Environmental Engineering*. Stockholm: Royal Institute of Technology.

[3] Jardine, R., Standing J., and Chow, F. (2005) ‘Some observations of the effects of time on the capacity of piles driven in sand’, *Geotechnique*, Vol. 55, No. 4, pp 227-244.

[4] Gavin, K.G. and Lehane, B.M. (2007) ‘Base Load-Displacement Response of Piles in Sand’, *Canadian Geotechnical Journal*, Vol. 44 No. 9, September 2007, pp 1053-1063

[5] Igoe, D., Gavin, K. and O'Kelly, B. (2011), ‘The shaft capacity of pipe piles in sand’, *ASCE Journal of Geotechnical and Geoenvironmental Engineering*. Vol 137, No.10, pp 903-912 (DOI 10.1061/(ASCE)GT.1943.5606.0000511)

Characterisation of a polyvinylidene fluoride (PVDF) material for energy harvesting from road infrastructure

Paul Cahill[1], Vikram Pakrashi[1], Alan Mathewson[2], Nathan Jackson[2]
[1]Department of Civil and Environmental Engineering, University College Cork, College Road, Cork, Ireland.
[2]Heterogeneous Systems Integration Group, Microsystems Centre, Tyndall National Institute, University College Cork, Ireland.
Email: p.a.cahill@umail.ucc.ie, v.pakrashi@ucc.ie, alan.mathewson@tyndall.ie, nathan.jackson@tyndall.ie

ABSTRACT: This paper investigates the possibility of energy harvesting from infrastructure systems using an embedded PolyVinyliDene Fluoride (PVDF) piezoelectric material. The authors report the characterisation of the behaviour of a PVDF material. Reasons for the choice of PVDF film are provided and a PVDF film is calibrated against varying control parameters and harvested energy. The control parameters consisted of varying harmonic loading conditions employing a fatigue testing device. Calibration curves for the generation of energy were established. The feasibility of the use of PVDF for energy harvesting from road infrastructure systems was investigated. Practicalities of such harvesting and the endurance of PVDF against environmental and chemical factors were taken into account. The effects of location and orientation of PVDF type solutions for energy harvesting were assessed. Potential applications of PVDF type materials for energy harvesting from infrastructure systems was deemed feasible.

KEY WORDS: Energy Harvesting, Piezoelectric, PVDF, Embedded Sensors, Infrastructure.

1 INTRODUCTION

The recent focus in the search for viable and sustainable energy sources has gained emphasis in recent years and has resulted in the recovery of significant wasted energy from the environment. Recent advances in smart sensors may allow for the possibility of remote structural health monitoring of infrastructural elements through sensors which are independent of external power supplies. The ability of piezoelectric materials to convert mechanical stress into electrical energy has resulted in significant research into its use both for energy harvesting and as a sensor for the purposes of monitoring. However, the potential for energy generating from infrastructural elements using embedded sensors has yet to be investigated thoroughly.

PolyVinyliDene Fluoride (PVDF) is a semi-crystalline high-molecular weight polymer. There exist substantial investigations on the physical properties of PVDF films. Roh et al. [1] conducted a study into the characterisation of the material properties of PVDF films. The elastic constants c_{44}^D and c_{55}^D, the dielectric constraints ε_{11}^T and ε_{22}^T and the piezoelectric constants g_{15} and g_{24}, for uniaxially orientated poled PVDF films were found through ultrasonic measurements using an impedance analyser and a least square data-fitting technique. Lanceros-Mendez et al. [2] investigated the structural change occurring within a PVDF film during a mechanical deformation process. The two most common crystalline phases, the α and β phases, were investigated and comparisons drawn on the differing properties. Significant research has been conducted into the use of PVDF films for use as a sensor. Obara et al [3] investigated the use of PVDF films for use as a stress gauge for fast pressure measurements. A simple and reliable PVDF gauge was constructed and calibrated up to 1GPa against thin-foil manganin stress gauge. Wang et al. [4] investigated the impulse pressure generated by captivation bubble collapse using PVDF sensors. A PVDF piezoelectric array of pressure sensors was developed using laser micro-machining technique which was attached on the solid boundary attacked by the collapse of the bubble. Sahaya Grinspan & Gnanamoorthy [5] studied the impact force caused by oil and water droplets at varying velocity using a PVDF piezoelectric sensor. The voltage output from the PVDF sensor due to the impact of the droplets, coupled with high speed cameras used to determine the parameters of the droplets, was used to quantify the impact force of the droplets. Luo & Hanagud [6] developed removable and reusable PVDF film sensors for the purposes of damage detection. These sensors were applied to structures such as beams and plates and used to detect impact damages. Meng & Yi [7] investigated the use of a PVDF sensor to determine the stress-strain curves of concrete. The sensors were calibrated using a split Hopkinson pressure bar and embedded in cylindrical concrete specimens. These specimens were subjected to axial impacting testing and the stress-strain curves were found through the calibrated PVDF sensor.

The purpose of this paper is to investigate the potential for use of a PVDF sensor as an energy harvesting device from concrete. Based on the aforementioned studies, the use of impact testing for the generation of electrical power was decided upon. The construction of a PVDF energy harvesting device and a finite element model are outlined and the potential power outputs from such a system are discussed in detail.

2 DESIGN AND CALIBRATION OF PVDF SENSOR

2.1 *Design of PVDF Sensor*

The sensor for the purpose of energy harvesting investigated in this study consisted of a PVDF film of thickness 52 µm. PVDF has excellent piezoelectric and physical properties which makes it suitable for the purposes of energy generating from ambient energy in infrastructure elements. It has a very high piezoelectric-strain, is resilient to chemical attack from a wide range of constituents, including those of concrete, and has low moisture absorption. It also possesses a high mechanical strength while retaining high flexibility. These properties make PVDF the preferred option for use as an embedded sensor for the purposes of energy generation when compared to other commercially available piezoelectric materials. The physical properties of the PVDF film are displayed in Table 1. The sensor was created by attaching two electrodes to the PVDF film using conductive tape. The sensor has been configured as a stack generator, operating in the 33-mode, for optimum energy generation.

Table 1. Physical properties of PVDF film.

Properties	Value	Unit
Density, ρ	1780	kg/m^3
Young's Modulus, E	8.3	GPa
Shear Modulus, G	3.5	GPa
Poisson's Ratio, υ	0.18	

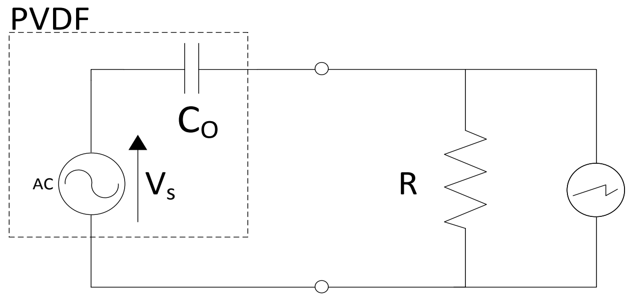

Figure 1. Equivalent circuit of PVDF sensor.

The equivalent circuit of the PVDF sensor when connected to an oscilloscope is shown in Figure 1. The enclosed section labeled PVDF is the electrical equivalent of the internal components of the PVDF sensor. The voltage source marked V_S is the piezoelectric generator itself and is directly proportional to the applied stress, while the capacitance marked C_O is the internal capacitance of the sensor.

2.2 Calibration of PVDF Sensor

Calibration of the energy harvesting sensor involved determining the dynamic piezoelectric constant, which is the ratio of the output charge of the sensor and the force being applied to the sensor, expressed mathematically as

$$k_c = \frac{Q}{F} \tag{1}$$

Where k_c is the dynamic piezoelectric constant and the output charge, Q, is expressed as

$$Q = \frac{\varepsilon_O \varepsilon_r VA}{t} \tag{2}$$

Where ε_r is the relative dielectric constant, ε_o is the dielectric constant of air, V is the output voltage and A and t are the area and thickness of the sensor respectably.

For the purpose of calibration, the sensor was placed within a substrate which consisted of an upper and lower solid layer of identical shape to the sensor. The sensor was then placed flat on a steel base and held in place with double sided tape down to prevent unwanted movement. An upper cover was then attached to complete the sensor system, as illustrated in Figure 2. This configuration was found to be the most desirable of the designs considered, as it best mirrors the stress conditions to which the energy generating sensor will be subjected to once embedded in infrastructural elements.

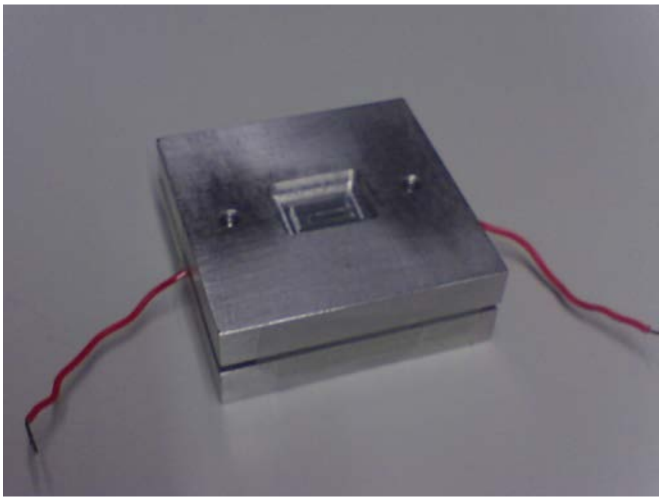

Figure 2. PVDF sensor enclosed in steel casing.

Calibration of the encased sensor was carried out using an INSTRON fatigue testing device. Forces up to 3N were applied to the sensor in the form of a sinusoidal load at a frequency of 5 Hz. The calibration curve for the sensor is shown in Figure 3. The average dynamic piezoelectric constant was found to be 28.29×10^{-12} C/N with a standard deviation of $\pm 4.118 \times 10^{-12}$ C/N, which when compared to the 33×10^{-12} C/N from the manufacture is acceptable.

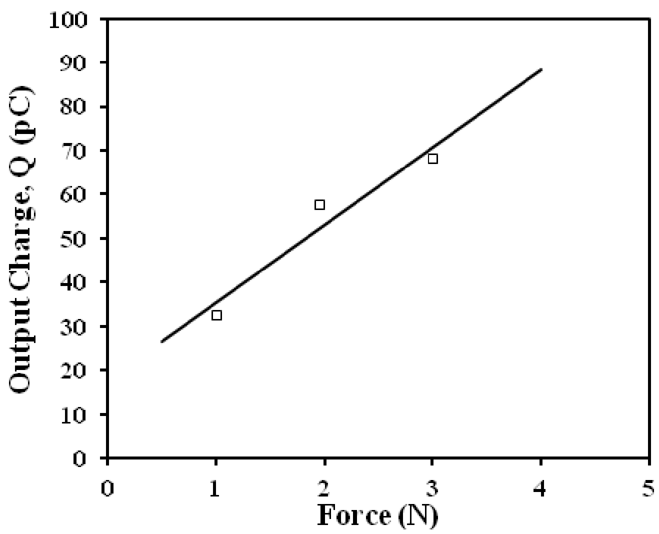

Figure 3. Calibration curve for PVDF sensor.

2.3 Identification of Optimum Sensor Location

Optimum location of the sensor for the purpose of energy harvesting from a concrete testing cube was determined using finite element software. The sensor is pressure actuated and thus the optimum location is the position with the largest pressure variance over the surface of the sensor.

A Three dimensional model of a concrete cube was created using the Strand7 Finite Element Analysis (FEA) Software System [8]. A Model cube of standard testing size, 0.15 x 0.15 x 0.15 m, was created using 8-node hexahedral (Hexa8) element bricks. Each Hexa8 brick was of the size 0.0075 x 0.0075 x 0.0075 m, with a total of 8000 bricks used for the creation of the models. Properties assigned to the brick elements are outlined in Table 2.

The model cube was restrained against translation in the x, y and z direction on its bottom face and gravity was assigned of the order as -9.80665 m/s^2. The load case was applied to the model in the form of sinusoidal wave, over a circular area of radius 0.075 m on the upper face of the model cube. The maximum load applied to the model cube was 1000 N compressive load, at a frequency of 5Hz which will best mirror the frequency of the load applied to the sensor.

Table 2. Properties assigned to model.

Properties	Value	Unit
Compressive Strength, fc	32	MPa
Young's Modulus, E	30.96	GPa
Density, ρ	2400	kg/m^3
Poisson's Ratio, υ	0.2	

The model was solved using firstly a nonlinear static solver, followed by a nonlinear transient dynamic solver. For the transient solver, a total of 50 time steps were solved, equating to the models being solved for every 0.004 seconds. The nonlinear transient dynamic solved model, as illustrated in Figure 4, was analysed to determine the optimum location for the energy generating sensor, with all nodes being examined for the optimum location of varying stress. A cover of 0.015 m was decided upon, with nodes located in the cover zone being excluded for potential locations of the sensor.

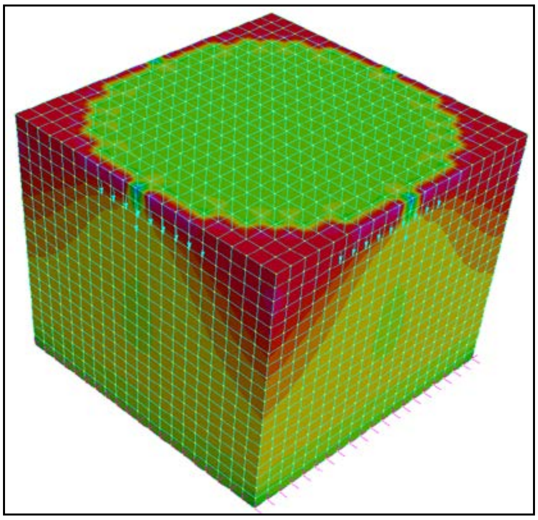

Figure 4. Illustration of solved Finite Element model.

It was found that the maximum stress change of any brick element occurred at the four brick elements located at the centre of the model at a height of 0.12 m from the base. It was determined, however, that the optimum location for the sensor was at a height of 0.1275 meters from the base, placed horizontal with its centre being aligned with the centre of the model cube. The reason for this location being the optimum position is that it provides the maximum stress variance over the surface area of the sensor. The possibility of angling the centre of the sensor through the position of maximum stress change was investigated, but this was found to have a lower stress variance than the horizontal placement at 0.1275 meters.

For optimum stress variance to act on the sensor, the rectangular sensor is placed with either its length or breadth being aligned with the x axis. The reason for this is due to the stress being symmetrical about the centre of the model due to geometric and loading conditions. Figure 5 illustrates a section through the centre of the cube, with the optimum sensor location having been exposed.

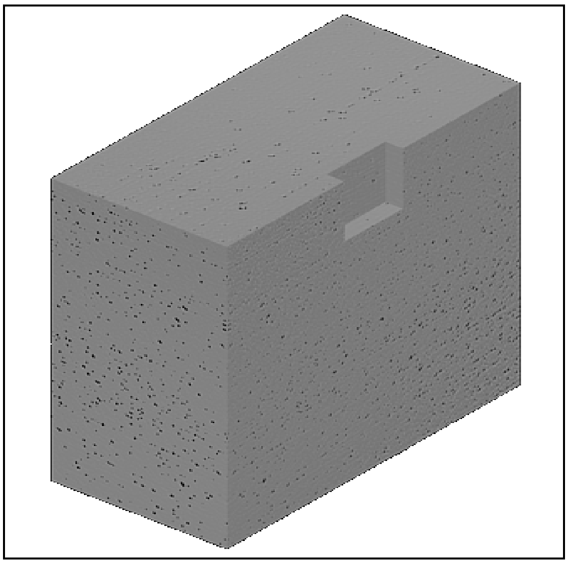

Figure 5. Illustration of section through centre of concrete cube with optimum sensor location.

At the maximum load of 1000 N, the stress change over the area of the sensor embedded in the model was found to be of the order of 0.05654 MPa. The cube was analysed at every 100 N load and the internal stress conditions at the optimum location was determined. The ratio of the force applied to the model cube and the average stress located at the optimum sensor height is illustrated in Figure 6.

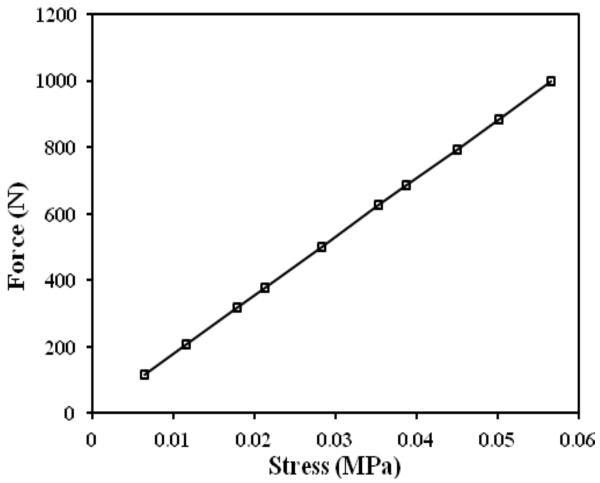

Figure 6. Average stress at optimum sensor location versus force applied to cube.

3 RESULTS

3.1 Potential Voltage and Power Output from Sensor

The voltage output from the sensor for increasing loading was calculated using the calibrated dynamic piezoelectric constant. The voltage output for the maximum force of 20 N was calculated to be of the order of 0.845 V. The linear force-voltage relationship is illustrated in Figure 7.

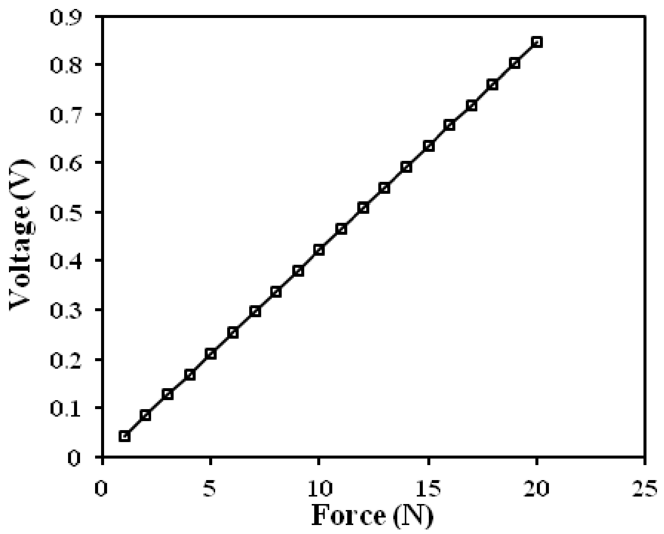

Figure 7. Potential voltage generated from sensor versus applied force.

Figure 8 illustrates the projected power output of the sensor against the stress acting over the area of the sensor. The forces on the sensor area were converted into stress, with the maximum force of 20 N resulting in a stress on the sensor of 0.061 MPa. The resistance of the PVDF based system was found experimentally and was determined to be of the order of 808 kΩ. This was then used to determine the power as a result of the stress acting on the sensor. The maximum stress acting on the sensor provided a power output from the sensor of 893.08 nW and a power density of 0.27249 µW/cm^2.

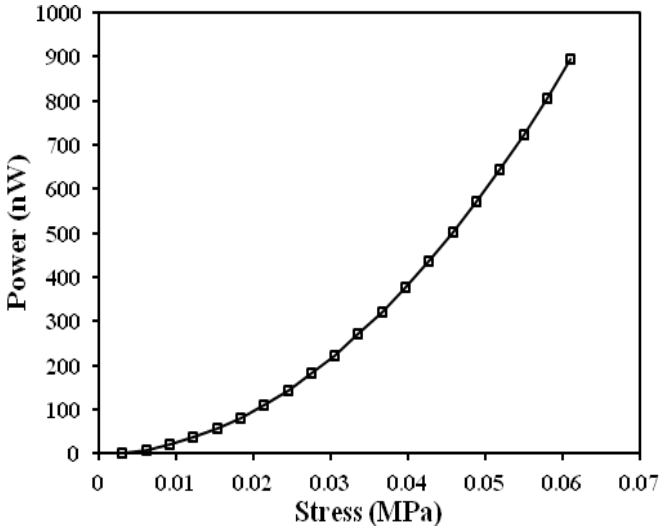

Figure 8. Potential power output versus stress applied to sensor.

3.2 Potential Power Output from Embedded Sensor

The potential power output curve of the sensor was used to determine the potential output of power from the sensor when embedded within the finite element model cube. At the chosen sensor location, the potential power output due to change in stress caused by loading being applied to the model was determined at increments of 100 N loads. At a maximum force of 1000 N being applied to the model, the potential power output from the sensor was determined to be 795.18 nW. Figure 9 illustrates the potential power output from forces being applied to the surface of the model curve.

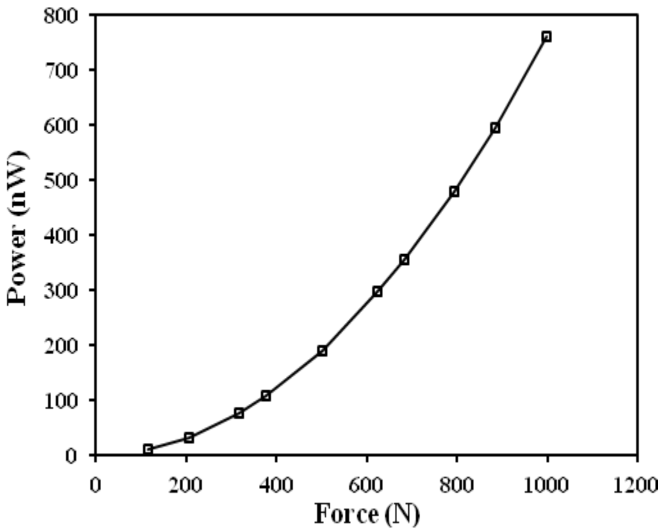

Figure 9. Potential power output from embedded sensor versus force applied to cube.

4 CONCLUSION

The physical properties of PVDF make it the optimum piezoelectric material for use as a power generating sensor. The sensor was calibrated up to a force of 3N and the potential voltage output of the sensor for forces up to a maximum of 20 N was established. The potential power output generated from increasing stress acting on the sensor was found and determined to be 893.08 nW generated from a stress change of 0.061 MPa at a power density of 0.27249 μW/cm^2. A finite element model was created to determine the optimum sensor location for embedment in a concrete cube. It was found the optimum location was located at the centre of the model at a height of 0.1275 meters from the base. The change in stress at the optimum location was found to be 0.05654 MPa when the cube was subjected to a 1000 N force. A potential power output curve from the energy generating sensor due to a loading being applied to the surface of the model was determined. It was found for the maximum loading of 1000 N, the potential power output from the embedded sensor was of the order of 795.18 nW. The feasability of energy generation from infrastructural elements using a PVDF based sensor was deemed feasable.

REFERENCES

[1] Roh Y, Varadan V & Varadan V (2002), 'Characterisation of All the Elastic, Dielectric, and Piezoelectric Constants of Uniaxially Oriented Poled PVDF Films' *IEEE Transactions on Ultrasonics, Ferroelectrics and Frequency Control,* June, 49- 6, 836-847.

[2] Lanceros-Mendez S, Moreira M V, Mano J F, Schmidt V H & Bohannan G (2001) 'Dielectric 'Behaviour in an Oriented β-PVDF Film and Chain Reorientation upon Traverse Mechanical Deformation' *Ferroelectrics*, 273:1, 15-20.

[3] Obara T, Bourne N K, Mebar Y (1995) 'The construction and calibration of an inexpensive PVDF stress gauge for fast pressure measurements' *Measurement Science and Technology*, April, 6 345-348.

[4] Wang Y-C, Huang C-H, Lee Y-C & Tsai H-H (2006) 'Development of a PVDF sensor array for measurement of the impulse pressure generated by cavitation bubble collapse' *Experiments in Fluids*, 41:365-373.

[5] Sahaya Grinspan A & Gnanamoorthy R (2010) 'Impact force of low velocity liquid droplets measured using piezoelectric PVDF film' *Colloids and Surfaces A: Physicochemical and Engineering Aspects'* 356:162-168.

[6] Luo H & Hanagud S (1999) 'PVDF Film Sensor and Its applications in Damage Detection' *Aerospace Engineering*12:1:23.

[7] Meng Y & Yi W (2011) 'Application of a PVDF-based stress gauge in determining dynamic stress-strain curves of concrete under impacting testing' *Smart Materials and Structures* 20:065004.

[8] Strand7 Finite Element Analysis Software © Copyright Strand7 Pty Ltd. Suite 1 Level 5, 65 York Street, Sydney NSW 2000, Australia.

The use of LiDAR in testing asphalt for resistance to permanent deformation

Eanna Fallon[1], Ciaran McNally[1] and Amanda Gibney[1]
[1]UCD School of Civil, Structural and Environmental Engineering, University College Dublin, Newstead, Belfield, Dublin 4, Ireland
email: eanna.fallon@ucdconnect.ie, ciaran.mcnally@ucd.ie & amanda.gibney@ucd.ie

ABSTRACT: LiDAR (Light Detection And Ranging) is a widely used technique in creating three-dimensional (3-D) models. It is typically used to create virtual models of cityscapes, buildings, etc; these applications exploit the LiDAR speed and ability to record a high density 3-D image of a target object. This paper reports on the application of LiDAR scanning to determine asphalt resistance to permanent deformation. Permanent deformation is promoted in asphalt samples by tested using a unique circular wheel tracking device. The specimens are subjected to a moving wheel load under temperature controlled conditions and the development of a rut in the wheel path is monitored. Whereas in other wheeling tracking tests the rut depth is only measured along the wheel path, the LiDAR is used to record the full surface of the specimen. The scan is repeated at pre-determined loading intervals and in this way a series of 3-D images are formed of each specimen as it deforms. These series of images can then be examined to determine the extent and type of deterioration of the asphalt specimens during the test.

KEY WORDS: Asphalt, LiDAR, wheel tracking.

1 INTRODUCTION

LiDAR (light detection and ranging) is a widely used technique in creating 3-D models. LiDAR, which is also known as terrestrial laser scanning, is a non contact method of making physical surface measurements. A laser pulse is emitted onto the surface of interest and through using known information such as the angular components of the laser beam path from a reference position and the time taken for laser pulse to be reflected back, a three-dimensional (3-D) visualisation of the surface can be created. The quality and intensity of the laser pulse that bounces back to the LiDAR unit is dependent on the characteristics of the surface being scanned.[1]

LiDAR is becoming a widely used in surveying applications. This paper reports on the application of LiDAR scanning in laboratory tests to determine asphalt resistance to permanent deformation. The asphalt resistance to permanent deformation is tested by a unique circular wheel tracking device.

2 UCD CIRCULAR WHEEL TRACKING DEVICE

A circular wheel tracking device was developed at University College Dublin (UCD) and has been described previously [2] and [3] been used to study fatigue crack growth in asphalt. The design of this device has since been adapted to incorporate an additional four sample stations at which resistance to permanent deformation can be examined. At these stations asphalt slab specimens of dimensions 305mm x 305mm x 100m are held in place on a solid steel base to limit slab flexure and to promote failure of the specimen through densification and shear flow.

The design of the circular wheel tracking device consists of a circular motor driven table onto which a beam is attached. The beam has a wheel fixture connected at each end, via a hinged joint, which it drives around the track, as shown in Figure 1. The wheel tracker uses solid rubber wheels which have a diameter of 200 mm and are 36 mm wide. The wheel fixtures are loaded through a dead load system by placing steel weights on to each of them, as shown in Figure 2.

Figure 1. Circular wheel tracking device.

Figure 2. Loaded wheel fixture.

The circular wheel tracking device is contained within a temperature controlled chamber that is capable of maintaining a set temperature between 10 ^{o}C and 40 ^{o}C, allowing elevated temperatures to be used to promote accelerated deformation of the asphalt specimens.

3 LIDAR AND THE UCD CIRCULAR WHEEL TRACKER

In adapting the UCD circular wheel tracking device to undertake resistance to deformation testing, it was necessary to select a method to record the deformation of the specimens at various intervals of wheel loadings, with the minimal interference with the specimens. It was also strongly desirable to be able to record additional measurements of the specimen surface rather than just the rut depth as is the case with other wheel tracking tests [4]. LiDAR appeared to have the potential to be ideally suited to this.

The first step in investigating if LiDAR would be suitable was to examine if it could scan an asphalt surface in sufficient detail. It was found that laser pulse that bounces back from the black surface was of a poor intensity and hence scan quality was poor. It was necessary to spray paint the surface of the specimens white to ensure the laser pulse bounced back was of sufficient intensity to overcome this problem.

The LiDAR unit available (Trimble GS200 3-D scanner) is generally used with a tripod in a setup of a similar nature to other surveying equipment. This setup was unsuitable to be used with the circular wheel tracker. It was necessary to manufacture a simple frame to position the scanner unit above the turntable of the wheel tracking device to provide setup that would enable each of the specimen station locations to be scanned in a time efficient manner. This setup is shown below in Figure 3.

Figure 3. LiDAR setup.

3.1 *Trial Experiment*

A trial experiment was conducted to assess the viability of using LiDAR to measure the deformation of asphalt specimens during resistance to deformation tests with the UCD circular wheel tracking device. Four asphalt slab specimens were produced. The top surface of each of the specimens was painted white and the specimens were placed the specimen stations of the track, shown in Figure 4.

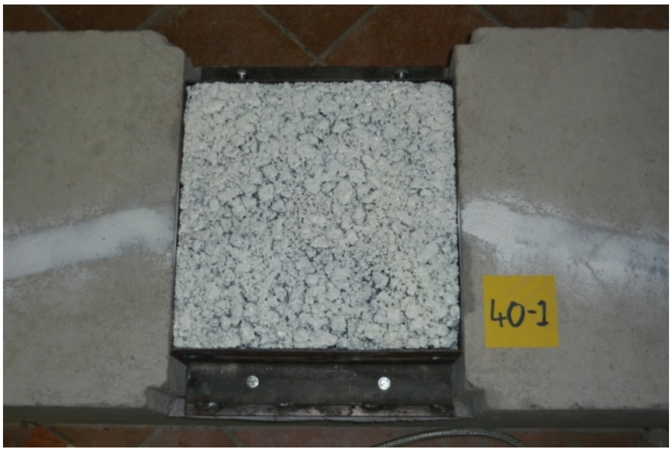

Figure 4 Asphalt slab specimen.

The temperature controlled chamber was then brought to 40^{o}C. A 24 hour period to enable the temperature of all equipment and specimens to stabilise at the test temperature was allocated before proceeding further.

A scan of the surface of each of the specimens with the LiDAR unit was conducted. The scan was setup (i.e. select area and parameters of the scan) and recorded on a laptop connected to the LiDAR unit. Points on the surface of the specimens were recorded on a 1mm x 1mm grid.

Deadweight was added to each of the wheel fixtures resulting in a wheel load of 953 N and a contact stress of 670kPa. The circular wheel tracking device applies 14 wheel passes to each specimen per minute and 10000 wheel passes were applied. Deformation to the specimens could be observed as shown in Figure 5.

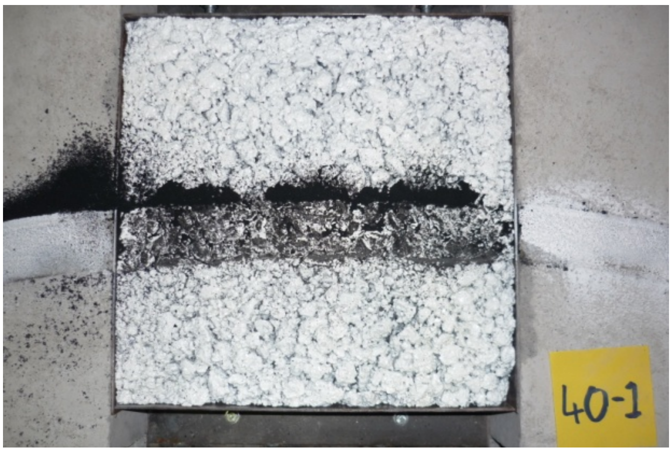

Figure 5. Specimen after 10000 wheel passes.

A LiDAR scan of each of the specimens was again conducted using the same parameters as in the initial scan.

3.2 Processing of LiDAR scan data

The output of each LiDAR scan is a point cloud file in which for each point there is five values attached: X, Y, Z, RGB true colour and return intensity. The point cloud for each LiDAR scan is in turn imported into Trimble RealWorks Survey software where a 3-D visualisation of the point cloud can be viewed. In the process of scanning the surface of the asphalt specimens, some of the adjoining concrete track and surrounds is also scanned. It is possible to isolate only the surface of the asphalt specimen and to export just these data points into text file format containing just the X, Y, Z values for each data point.

The X, Y, Z values are recorded based on the location of the LiDAR scanner unit being the reference or (0,0,0) point. In order to simplify the comparisons of the initial and subsequent scans of the same asphalt specimens, it is necessary to adjust location of the reference point of the scan. The desired coordinate system is such that:

- The bottom left hand corner of the specimen surface is the (0,0,0) point.
- X values represent distance along the bottom side of the specimen surface.
- Y values represent distance along the left side of the specimen surface.
- Z values represent the elevation of the specimen surface.

This is illustrated below in Figure 6.

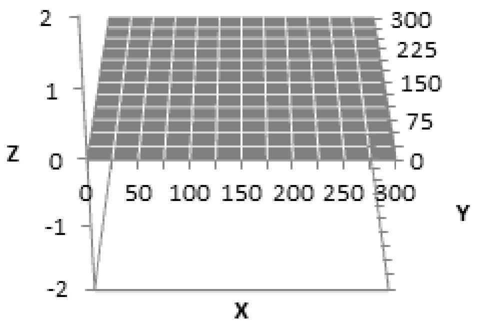

Figure 6. Slab specimen coordinate system.

The necessary translation and rotation about each of the axes necessary to achieve this coordinate system was calculated for each scan.

In the area of each of the specimen slab surfaces, approximately 90,000 data points are recorded. In order to apply the necessary translation and rotation to each of these data points, it was decided to utilise the MATLAB software. A m file was written to conduct this operation.

The next step in the process was to be able to produce a surface plot of the data points. To do this it was necessary to create a regular grid of X and Y data points and to select the appropriate Z value for this point. A regular 2mm x 2mm X Y grid was used. The MATLAB m file was written such that for each point on the regular grid, the full set of data points was searched to find the nearest one. The Z value of this point was taken to be the Z value for the regular grid point. In this way a full set of data points of the surface of the specimen slab to a regular 2mm x 2mm grid is created. A plot of the surface of the specimen to this regular grid can now be created. The surface of one of the specimens from before and after 10000 wheel passes are shown in Figure 7 and Figure 8 respectively.

It has to be acknowledged that this method of selecting the Z value may result in values that are not as accurate as is possible. A more accurate way would be to interpolate the Z value from the three nearest points. But it should be remembered that the objective of this trial experiment is to evaluate the potential of using comparisons of LiDAR scans of the specimen surfaces to measure deformation and that further development and refinement of the method can be conducted if it can be seen from the trial experiment that there is sufficient potential in this method.

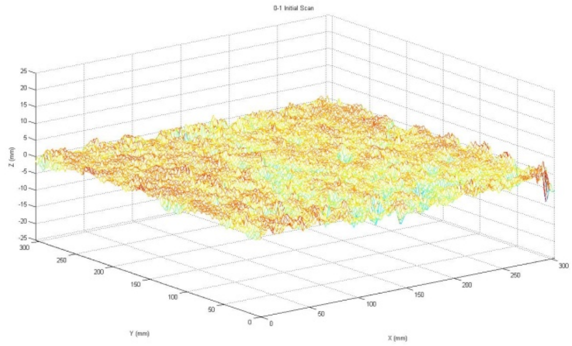

Figure 7. Initial specimen scan.

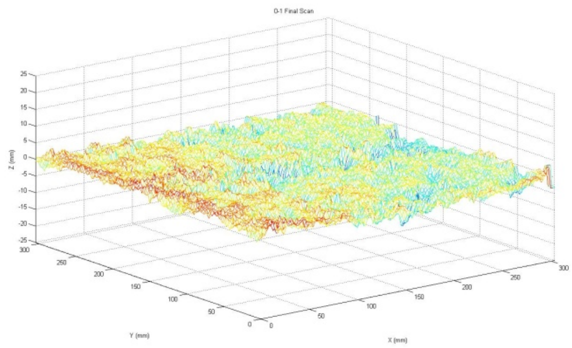

Figure 8. Specimen scan after 10000 wheel loads.

As there now is a set of data points to a regular grid, and by having previously defined the reference point of the coordinate system such that it is the same for each scan of the specimen, it is now possible to directly compare the surfaces created from the LiDAR scans and observe any deformation of the specimen. This can be done by simply calculating the difference in the Z value between each scan at each of the regular grid points for the specimen in question and the deformation can be shown by plotting the resulting surface. This is shown for a specimen in Figure 9. The area of the wheel path or the deformation can be identified in this surface.

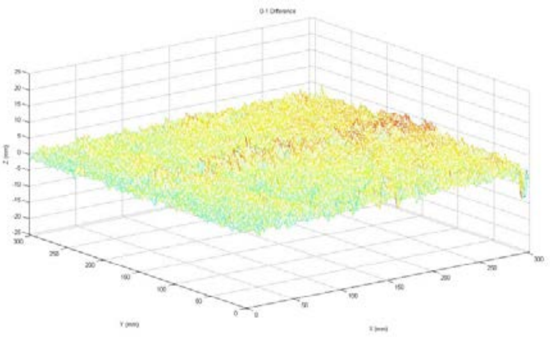

Figure 9. Deformation of specimen.

4 COMPARISON OF LIDAR MEASUREMENTS WITH STANDARD WHEEL TRACK TEST

The standard wheel tracking tests are described in [4], with the testing using the small scale device frequently used in Ireland. This test is conducted on asphalt specimens of dimensions 305mm x 305mm x 50mm, the same surface dimensions as used in specimens for the UCD circular wheel tracking device. In the standard test the rut depth is calculated by using a LDVT to record the vertical movements of the wheel. Measurements are recorded along the centre 100 mm of the wheel path at intervals of at least every 4 mm. The mean of these recording is the final rut depth. This standard test was seen as appropriate to compare the results from the application of LiDAR scanning to.

In order to carry out a comparison between the result of the standard wheel tracking test and that calculated from the use of LiDAR scanning, three hot roll asphalt specimens were selected that the standard wheel tracking test to [4] had be conducted on using the Cooper Technology Wheel Tracker CRT-WTEN1 device. These specimens were prepared and scanned as described previously in section 3. The data from the each scan was then processed, an example of the results of which are shown in Figure 10.

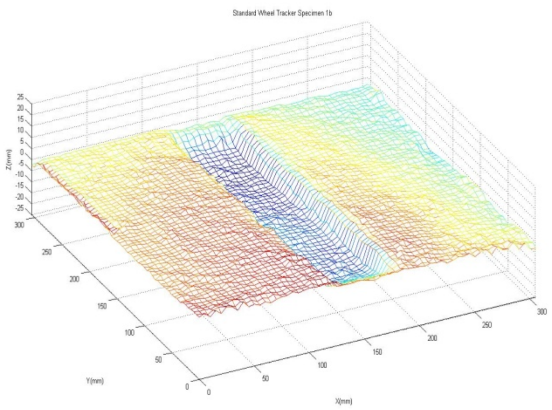

Figure 10 Specimen used in a standard wheel tracker test.

It was then necessary to calculate a rut depth from the LiDAR scans. Three lines of points along the wheel path were selected, one along the centreline and one on a 15mm offset from the centreline on either side of it. From each of these three lines of points the middle 100 mm portion was isolated. The rut depth was calculated as the mean value of the isolated data points. The rut depth was calculated in this manner so as to be as consistent as possible with the method used in the standard wheel tracking test. A comparison of the rut depth calculated from both the standard wheel tracker test and from the LiDAR scanning for each specimen is shown below in Table 1.

Table 1. Rut depths.

Specimen	**Standard Wheel Tracker rut depth (mm)**	**Calculated LiDAR scanning rut depth (mm)**
hrac_1	6.92	7.45
hrac_3	5.23	6.68
hrac_4	5.04	5.47

The rut depths calculated from the LiDAR scanning are larger than those measured by the standard wheel tracker test. It should be noted that in this instance it had not been possible to conduct any LiDAR scans of these specimens prior to the standard wheel tracker test being conducted. Without this initial scan it was not possible to correct for any variation that may have been present in the surface of the specimen, and thus further increase the accuracy of the calculated rut depth. This may account for some of the difference in the between the rut depth values. Some further investigation into this is required to increase the understanding of any measurement errors present in the LiDAR scans.

5 CONCLUSIONS

LiDAR scanning has been used in conducting resistance to deformation testing with the UCD circular wheel tracking device. It has provided possible to observe the areas of deformation using this method. It has been possible to calculate a value for rut depth from LiDAR scans. Further development and refinement of the processing of the LiDAR data is required but it has been demonstrated that there is potential in the novel application of this technique.

There is also potential for the use of LiDAR for applications in the field. It could be an effective technique to assist in pavement evaluation and management due to its ease of use.

ACKNOWLEDGMENTS

The authors would like to acknowledge that the research leading to the results has received funding from the European Community's Seventh Framework Programme (FP7/2008-2013) under grant agreement nº218747.

REFERENCES

[1] Laefer, D. and D. Lennon. Viability assessment of terrestrial LiDAR for retaining wall monitoring. in Proceedings of GeoCongress 2008: Geosustainability and Geohazard Mitigation, GSP 178, ASCE 2008. Orleans, Louisiana: American Society of Civil Engineering (ASCE). p. 247-254

[2] Hartman, A.M., M.D. Gilchrist, and D. Nolan, Wheeltracking Fatigue Simulation of Bituminous Mixtures. Road Materials and Pavement Design, 2001. 2(2): p. 141-160.

[3] Taboković, A., et al., Influence of Recycled Asphalt Pavement on Fatigue Performance of Asphalt Concrete Base Courses. Journal of Materials in Civil Engineering, 2010. 22(6): p. 643-650.

[4] NSAI, IS EN 12697-22:2003 Bituminous mixtures – Test methods for hot mix asphalt – Part 22: Wheel tracking. 2003, NSAI: Dublin.

Surface wave testing of asphalt pavements

Zhangli Wang[1], Ciaran McNally[1], Tianchun Yang[2]
[1] School of Civil, Structural and Environmental Engineering, University College Dublin, Ireland
[2] School of Civil Engineering, Hunan University of Science and Technology, China
Email: Zhangli.wang@ucdconnect.ie, ciaran.mcnally@ucd.ie

ABSTRACT: Multichannel analysis of surface waves (MASW) is a widely used seismic technique to deduce the S-wave velocity (and subsequently small strain stiffness) of near surface materials. In recent years, MASW has been applied in geological survey and geotechnical engineering and received very good results. An alternative testing methodology called MISW (Multiple Impact Surface Waves) has recently been developed for certain applications, but has difficulties in assessing pavements where the layer stiffness decreases with depth; this is the opposite to what is seen in geotechnical engineering where stiffness increases with depth. When one considers the pavement layered medium, the lower layers (e.g. pavement subgrade) are unable to trap the seismic energy, leading to some wave energy being continually radiated from the low-velocity layer in pavement. The pavement system is no long a perfectly trapped system, which means that measured dispersion curve mode for the pavement is no longer a fundamental mode; instead it is transformed into a series of multiple modes with unconnected dispersion curves. The traditional process for interpreting the data will lose the virtual roots that correspond to radiation of low-velocity layer, referred to as leaky mode. This paper investigates a theoretical approach to the problem, whereby an additional layer is added beneath the pavement subgrade. The 3 layer medium will change to 4 layers and the system now becomes trapped. This will remove the virtual roots corresponding to the leaky mode, which will change the dispersion equation and avoid the loss of calculation results. It can directly calculate the final dispersion curves and use vertical flexibility coefficients to determine which modes will be received at a specific frequency. This modified approach will allow the use of surface wave testing to determine pavement structure and properties which are of key interest in assessing pavement properties in service.

KEY WORDS: Surface wave, pavement, geophysics, non-destructive testing

1 INTRODUCTION

In recent years multichannel analysis of surface waves (MASW) has become widely used for geological surveys and geotechnical engineering. An advantage of multichannel recording is that it permits effective identification and isolation of noise; this is achieved through distinctive trace-to-trace coherency in arrival time and amplitude which can be obtained with high speed [1]. However a further advantage is that MASW test results include high modes of dispersion curves which make it possible to use the information for pavement assessment.

Seismic testing of pavements is often uneconomical due to survey expenses and inconvenient field procedure with many components and complicated wiring deployed in a small area. An alternative is a method whereby the multichannel recording can be simulated with only one receiver and single-channel recording device: Multiple Impact Surface Waves [2]. As a seismic non-destructive testing (NDT) technique it can be used to obtain the thickness, Poisson's ratio (υ) and Young's modulus of the different layers in pavement. Previous models which were used for soil and foundation seismic test are all based on the assumption of a slow layer above a fast substrate. However, some researchers studied the case of a fast layer on a slow substrate, and the multilayered half-space with large velocity contrasts and decreasing velocity with depth [3-5]. The results indicated that the discontinuous dispersion curves are caused by the change of dominant modes with frequency. Different mode branches due to mode jumping, connect with low-velocity substrate caused by a different surface displacement distribution with frequency for each mode.

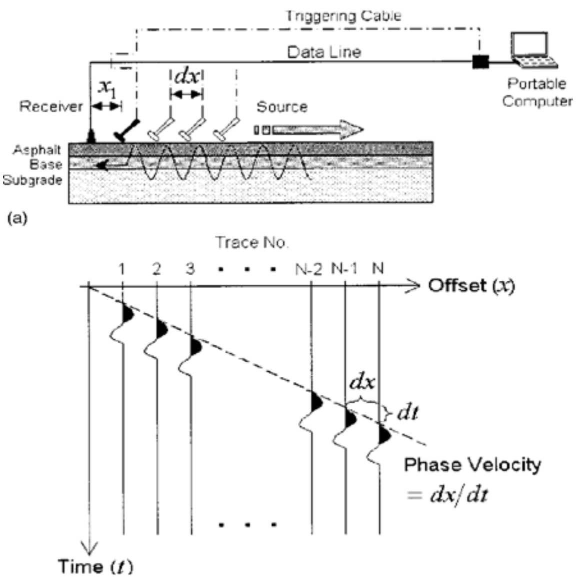

Figure1. The MISW (Multiple Impact Surface Wave) test and surface wave trace combination [2].

Generally speaking, guided waves propagated along a stratified structure generate infinite modes, which can be divided into two kinds in principle:

- surface waves, whose energy concentrates near the free surface;
- trapped waves, whose energy concentrates within an area under the free surface [6].

This means that surface waves cannot be propagated along the free surface in some frequency ranges when there exists low-velocity layers. In pavement engineering low-velocity layers correspond to the lower layers in the road construction. However, the trapped waves can still be excited in this situation and can be received and utilised. This arrangement whereby the velocity of the pavement layers decreases with depth leads to dispersion curve calculations that are more difficult than that associated with traditional Rayleigh wave models. The reason for this is that the model system is no longer bounded due to the weak lower layers, meaning that energy is lost from the system. This paper describes a novel method of overcoming this problem. A theoretical bottom layer is added to the system which has the same properties as the top layer. The effect of this is to modify the calculation model which can then use vertical flexibility coefficients to calculate the largest displacement mode which can be received by detector.

2 VIBRATION THEORY

Consider a semi-infinite medium made of N-parallel, homogeneous, isotropic, elastic solid layers, with a cylindrical coordinate system (r, θ, z) and the z-axis vertically downwards. The j^{th} layer is bounded by z_{j-1} above and z_j below. Its properties parameters contain $V_p(j)$ (P-wave velocity), $V_s(j)$ (S-wave velocity), $\rho_p(j)$ (density), $h(j)$ (thickness). If one then only considers the P-SV wave, the classical propagator matrix method used by Zhang Bixing [7] can be adopted.

There are two wave types propagating in isotropic media: compression (P) and shear (S) waves. The particle motion of the S wave can then be divided into two directions: vertical plane (SV) and horizontal plane (SH). Here only the P-SV wave is considered. The Love wave corresponding to SH wave is not considered in this paper.

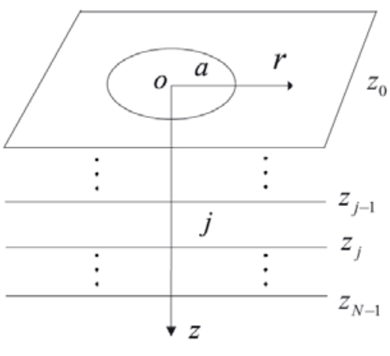

Figure 2. The constitution of a multilayered medium.

Zhang Bixing [7] defines displacement by

$$u \quad = \quad \nabla\varphi + \nabla\times\nabla\times\left(\frac{1}{k}\psi\,\mathrm{e}_z\right) \qquad (1)$$

Here u is the displacement; k is the wave number, φ and ψ are the potential functions, respectively corresponding to P and SV waves. If a symmetric point source is used to excite the Rayleigh waves, the point source must be in the top layer at the same time. Therefore, the angle θ does not appear.

$$u \quad = \quad \mathrm{e}_r\frac{\partial}{k\partial r}(k\varphi + \frac{\partial\psi}{\partial z}) + \mathrm{e}_z(\frac{\partial\varphi}{\partial z} + k\psi) \qquad (2)$$

Introducing three basis vectors:

$$\begin{cases} \mathrm{e}_B = \mathrm{e}_r\dfrac{\partial}{k\partial r} + \mathrm{e}_0\dfrac{\partial}{kr\partial\theta} \\ \mathrm{e}_C = \mathrm{e}_r\dfrac{\partial}{kr\partial\theta} - \mathrm{e}_0\dfrac{\partial}{k\partial r} \\ \mathrm{e}_p = \mathrm{e}_z \end{cases} \qquad (3)$$

The displacement $\boldsymbol{u}_B$, $\boldsymbol{u}_p$ in the direction $\boldsymbol{e}_B$, $\boldsymbol{e}_p$ respectively are:

$$\begin{cases} u_B = k\varphi + \dfrac{\partial\psi}{\partial z} \\ u_p = \dfrac{\partial\varphi}{\partial z} + k\psi \end{cases} \qquad (4)$$

Then, the stresses τ_B, τ_P in the direction $\boldsymbol{e}_B$, $\boldsymbol{e}_p$ are:

$$\begin{cases} \tau_B = 2\mu(k\dfrac{\partial\varphi}{\partial z} + \Omega\psi) \\ \tau_p = 2\mu(\Omega\varphi + k\dfrac{\partial\psi}{\partial z}) \end{cases} \qquad (5)$$

Here $\Omega = k^2 - \frac{\rho\omega^2}{2\mu} = k^2 - \frac{1}{2}k_s{}^2$, define the following vectors of S (motion stress) and ξ (displacement potential):

$$\begin{aligned} S \quad &= \quad (\frac{U_B}{k}, \frac{U_P}{k}, \frac{\tau_P}{\omega^2}, \frac{\tau_B}{\omega^2})^T \\ \xi(z) \quad &= \quad (Ae^{iaz}, Be^{-iaz}, Ce^{ibz}, De^{-ibz})^T \\ &= \quad (\varphi^+, \varphi^-, \psi^+, \psi^-)^T \end{aligned} \qquad (6)$$

Where $S = M\,\xi$ and $\xi(z_j) = \lambda\,\xi(z_{j-1})$

$$\lambda = \mathrm{diag}\,(P, 1/P, Q, 1/Q) \qquad (7)$$

$$M = \begin{bmatrix} 1 & 1 & \gamma_s & -\gamma_s \\ \gamma_p & -\gamma_p & 1 & 1 \\ \rho(\gamma-1) & \rho(\gamma-1) & \rho\gamma\gamma_s & -\rho\gamma\gamma_s \\ \rho\gamma\gamma_p & -\rho\gamma\gamma_p & \rho(\gamma-1) & \rho(\gamma-1) \end{bmatrix}$$

In the matrix above

$P = e^{\gamma_p kh}$; $\quad Q = e^{\gamma_s kh}$; $\quad \gamma = 2(V_S{}^2/c^2)$;

$\gamma_p = -\sqrt{(1-c^2/V_s^2)}$; $\gamma_s = -\sqrt{(1-c^2/V_s^2)}$

$ia = k\gamma_p$; $ib = k\gamma_s$; $c = \omega / k$

An implicit time dependence of the field is $e^{-i\omega t}$

$$\begin{aligned}\varphi &= \varphi^+ + \varphi^- = Ae^{iaz} + Be^{-iaz}\\ \psi &= \psi^+ + \psi^- = Ae^{ibz} + Be^{-ibz}\end{aligned}$$

Here φ and ψ in the frequency-wave number domain are the displacement potentials of P and SV waves. For φ^+ and ψ^+, positive means the wave propagates along the positive z-axis, similarly φ^- and ψ^- denote the wave propagating along the negative z-axis. Therefore, the real parts of γ_p and γ_s should be smaller than or equal to zero.

Depending on the boundary conditions of each interface,

$$\begin{aligned}S_{j+1}(z_{j+1}) &= P(z_{j+1,} z_j) S_j(z_j)\\ &= P(z_{j+1,} z_j) P(z_{j,} z_{j-1}) S_j(z_{j-1})\end{aligned} \tag{8}$$

The propagator matrix $P(z_{j,} z_{j-1}) = M_j \lambda_j M_j^{-1}$,It is easy to use the following vector to simplify the matrix

$$E = (E_1, E_2, E_3, E_4, E_5, E_6)^T \tag{9}$$

Here E is different for each layer and the relationship between $E^{(j-1)}$ and $E^{(j)}$ is:

$$E^{(j-1)} = F^{(j)} E^{(j)} \quad (j = 2, 3, \ldots, N) \tag{10}$$

The matrix F in each layer then be decomposed into

$$F = \frac{1}{4\rho^2 \gamma_P \gamma_S} U\lambda * V \tag{11}$$

In previous study, E, λ* and V can be referenced [7]. Following the previous derivation, we can obtain the dispersion equation of Rayleigh waves is

$$E_6^{(1)} = 0 \tag{12}$$

The point source supposed in the first layer $z = z$, $r = 0$, the components S_1 and S_2 of vector S at free surface are:

$$S_1 = \frac{u_B}{k} = \frac{\Delta_1}{E_6^{(1)}} = \frac{(-T_{11}E_6^{(1)} + T_{31}E_3^{(1)} - T_{41}E_2^{(1)})A_{sn} + (-T_{12}E_6^{(1)} + T_{32}E_3^{(1)} - T_{42}E_2^{(1)})B_{sn}}{E_6^{(1)}}$$

$$S_2 = \frac{u_p}{k} = \frac{\Delta_2}{E_6^{(1)}} = \frac{(-T_{21}E_6^{(1)} + T_{31}E_5^{(1)} - T_{41}E_3^{(1)})A_{sn} + (-T_{22}E_6^{(1)} + T_{32}E_5^{(1)} - T_{42}E_3^{(1)})B_{sn}}{E_6^{(1)}}$$

Here A_{sn}, B_{sn} and the matrix T are the quantities related to the source [7]. The displacement in radial and vertical direction can be written as below in the frequency domain. All the modes of Rayleigh waves propagating in stratified half-space can be calculated by equation (12). Equation (13) includes all the body and Rayleigh waves. The excitation amplitudes of Rayleigh waves can be obtained by residues of the poles which are determined by equation (12) [7].

$$\begin{cases} u_r(r,z;\omega) = \dfrac{1}{k}\dfrac{\partial u_B}{\partial r} = \dfrac{\partial}{\partial r}\displaystyle\int_0^\infty \dfrac{\Delta_1}{E_6^{(1)}} J_0(kr) k dk \\ u_z(r,z;\omega) = u_p = \displaystyle\int_0^\infty \dfrac{\Delta_1}{E_6^{(1)}} J_0(kr) k dk \end{cases} \tag{13}$$

$$u_r(r,\theta,z;\omega) = i\pi\Delta_1 \left[\frac{nH_n^{(1)}(kr)}{kr} - H_{n+1}^{(1)}(kr) \right] k^2 \cos(n\theta) / \frac{\partial E_6^{(1)}}{\partial k}$$

$$u_z(r,\theta,z;\omega) = i\pi\Delta_2 H_n^{(1)}(kr) k^2 \cos(n\theta) / \frac{\partial E_6^{(1)}}{\partial k} \tag{14}$$

Where k is wave number, $H_n^{(1)}(kr)$ is Hankel function of the first kind and n is related to source; when using a symmetric point source n = 0.

Finally, using equation (12) and (14) together, it is possible to calculate dispersion curves and the excitation amplitudes of Rayleigh waves.

3 DISPERSION ANALYSIS

When calculating the dispersion equation (12) for pavement structures, it must be accepted that complex solutions corresponding to the leaky mode will be lost. As such, only the real part of the guided wave need be considered. A result of this limitation is that the dispersion curve will display a cut-off point. To illustrate this, the flexible pavement structure which Ryden used in 2004 [2] is adopted here. Using a three layer structure it is easy to calculate the dispersion curve as below. The dispersion curve has a cut-off frequency at 1.2 Hz and the minimum V_R corresponding to 0Hz is the Rayleigh wave associated with the third layer. (V_R = 93.5 m/s).

Table 1. Typical flexible pavement structure.

Layer	V_s (m/s)	V_p (m/s)	ρ (kg/m^3)	Thickness(m)
1	1400	2914	2000	0.2
2	500	1041	2000	0.6
3	100	208	2000	∞

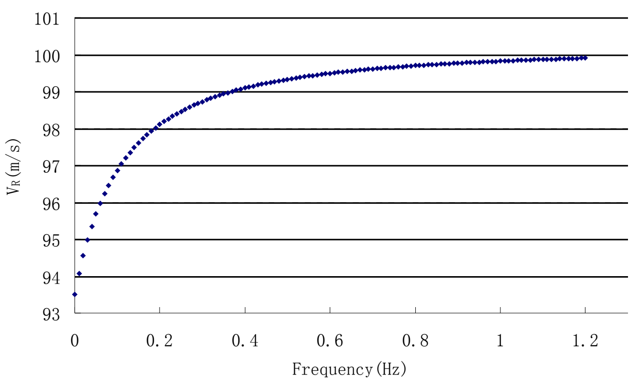

Figure 3. The dispersion curve has a cut-off frequency for pavement structure.

Table 2. Flexible pavement structure with an additional layer.

Layer	V_s (m/s)	V_p (m/s)	ρ (kg/m^3)	Thickness(m)
1	1400	2914	2000	0.2
2	500	1041	2000	0.6
3	100	208	2000	>>0.6
4	1400	2914	2000	∞

This method obviously does not completely reflect Rayleigh wave dispersion characteristics in pavement structure. The reason is the dispersion equation (12), where roots are limited to (0, V_{S3}). If we consider the possibility of complex solutions the calculations become more complicated. Therefore, we instead recommend that an additional theoretical layer is placed below the third layer, and the fourth infinite layer has the same properties as the top layer. At the same time, we define the third layer thickness to be much larger than the second layer (in accordance with real pavement structures). The new pavement structure is described in Table 2.

If the third layer thickness is large enough (much larger than second layer), the impact of the fourth layer can be ignored as the Rayleigh wave phase velocity will be close to that of the lowest layer when the frequency is low, to the higher layer when the frequency is high [8]. Using this method, one can easily obtain the dispersion curve for a 3 layer flexible pavement structure. In order to prove the similarity of both pavement structures, we will use the pavement structure described in Table 2 and compare the result to that previously calculated by Ryden [2], presented in Figure 4-1.

In figure 4-2, the black line represents the Rayleigh wave modes within the entire frequency range from 0 to 2000Hz. This is drawn using the software package *Disperse*, developed by Imperial College and commonly used by geophysicists.

It can be seen that the received modes at specific frequencies in Figure 4 came from the calculation of amplitude in 5 m offset. Here the largest amplitude corresponded to the mode which can be received by detector. For the data presented in Figure 5 an offset of 5 m is also defined and the vertical flexible coefficient [9] is used to calculate displacement, which is related to excitation energy.

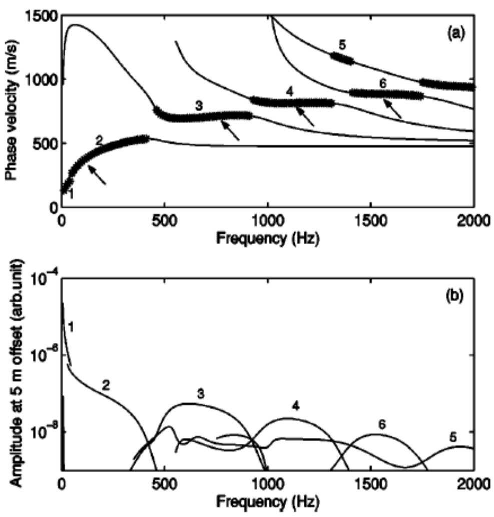

Figure4. Dispersion curve determined by Ryden [2].

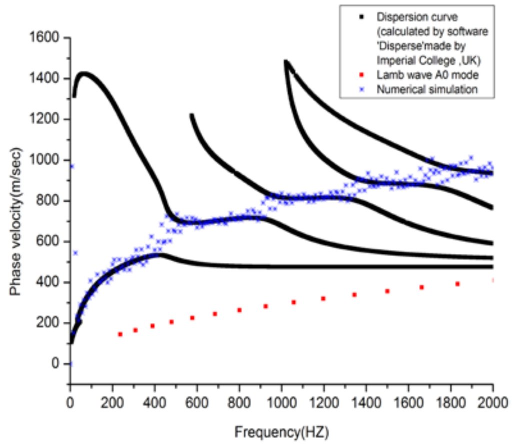

Figure 5. Dispersion curve obtained using the additional layer method.

Here it can be seen that the first two modes are anti-symmetric and look like the Lamb wave A_0 mode. As frequency increases one can see that the third mode is symmetric and there is a clear 'jump' between the second and third mode. The fourth mode also has the same 'jump'. This method can be used to determine the Rayleigh wave mode which can be received automatically by Matlab program.

The similarity between Figures 4 and 5 is quite high, but the additional layer method is more convenient and fast. However, the inversion process is not as easy as it was previously.

4 'JUMP POINT' FREQUENCIES

The purpose of this section is to discuss the relationship between 'jump point' and other parameters such as h (layer thickness), V_p (P-wave velocity), V_s (S-wave velocity), ρ (density). Because previous studies focused on dispersion curves of Rayleigh waves containing low-velocity layer, the discussion tended to focus on the appearance of jump points, rather than the causes for their appearance. The flexible pavement structure in Table 1 will be used as a basis for an explanation.

First, an excitation source is needed; the symmetric point source used earlier will be employed. Next we define a 20% increase for each parameter. As there are layers to the structure, this will lead to nine parameter changes.

Finally, we define an objective function as below:

$$\mathrm{Obj}(P_j) = \sqrt{\frac{\sum_{i}^{N}\left(V^{i}_{new}(p_j) - V^{i}_{orig}\right)^2}{N}} \tag{15}$$

Here, P_j are the parameters of j^{th} layer individual (Figure 2), N is the number of frequency points (can be defined at the beginning of program). V^i_{new} (p_j) is the phase velocity after each individual P_j increasing, and V^i_{orig} is the phase velocity for the reference model in Table 1. Using this approach it will be possible to determine the variation between the two and allow analysis of the sensitivity of each parameter by this function.

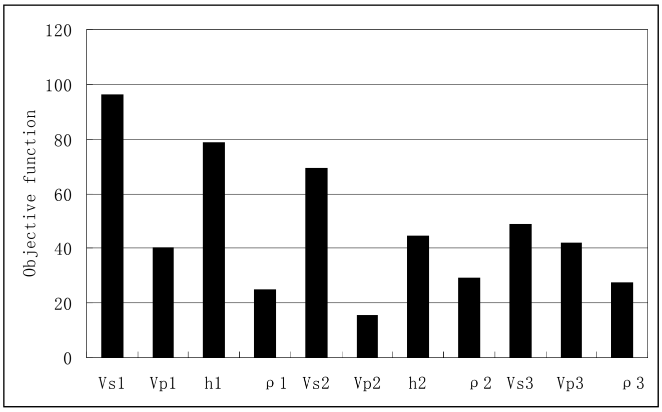

Figure 6. Sensitivity analysis of the reference model in Table1. Bars represent the objective function result.

The results in Figure 6 indicate the parameters that affect the phase velocity most severely. All these parameters must be set as variables for the next inversion program. Here V_{s1}, h_1, V_{s2}, h_2 and V_{s3} are set as variables; h_3 is not considered as the flexible pavement subgrade is an infinite half-space.

To illustrate the process, the data corresponding to a 20% increase in Vs1 is shown in Figure 7. In reality there are far too many modes present to clearly illustrate the process. Instead a trendline corresponding to the peak of each mode is shown.

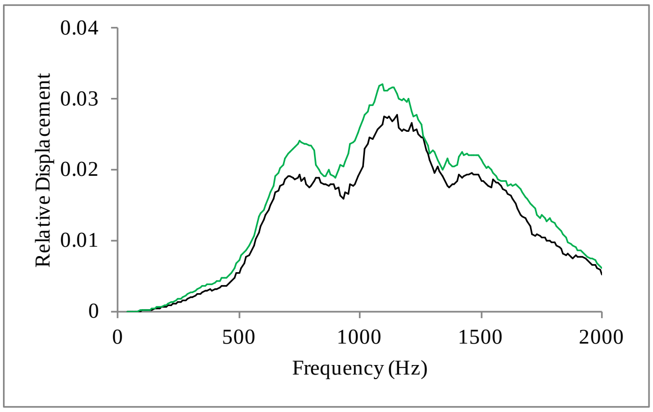

Figure 7. The relative displacement of (i) reference model and (ii) model with 20% increase in V_{s1}.

Here it is clear to see that there has been a higher effect on the displacements, rather than the ‘jump point’ for the phase velocity. For a 20% increase in V_{s1} two ‘jump points’ corresponding to 400Hz and 900Hz (approximately) are observed. There is no significant change compared to the reference model, although there is a significant change in displacement.

Similar analysis can be conducted on other pavement properties to determine the key parameters for analysing pavements using surface waves.

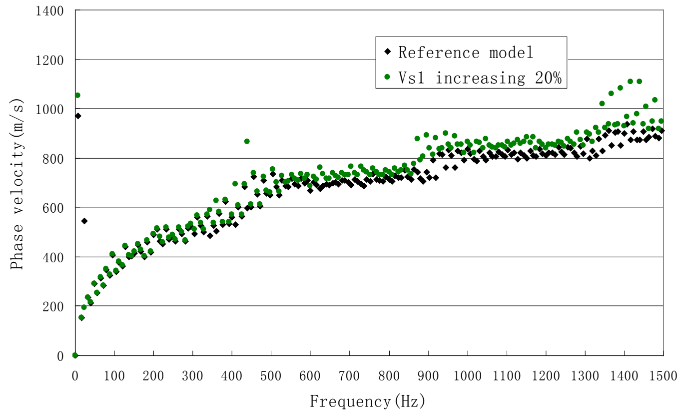

Figure 8. Dispersion curves corresponding to the data in Figure 7.

5 CONCLUSION

This paper investigated a theoretical approach to a challenging problem when assessing pavements. By adding an additional layer beneath the pavement subgrade, we have changed the structure to 4 layers instead of 3. This will remove the virtual roots that correspond to the leaky mode, which will change the dispersion equation and avoid the loss of calculation results. It can directly calculate the final dispersion curves and use vertical flexibility coefficients to determine which modes will be received at a specific frequency. This modified approach will allow the use of surface wave testing to determine pavement structure and properties which are of key interest in assessing pavement properties in service.

At the same time, we search the connection between each parameter to the shape of dispersion curve to determine their influence on pavement response. This will allow a more fundamental understanding of pavement response to surface wave techniques and facilitate inversion and analysis in the future.

ACKNOWLEDGMENTS

This research is part of the TEAM project, a Marie Curie Initial Training Network funded by the European Commission 7th Framework Program (PITN-GA-2009-238648).

REFERENCES

[1] Park, C. B., Miller, R.D. & Xia, J. (1999), ‘Multichannel analysis of surface waves’, *Geophysics*, 64(3): 800-808.

[2] Ryden, N., Park, C.B., Ulriksen, P. & Miller, R.D. (2004), ‘Multimodal approach to seismic pavement testing’, *Journal of Geotechnical and Geoenvironmental Engineering*, ASCE 130(6): 636-645.

[3] Lu, L. & Zhang, B. (2006), ‘Inversion of Rayleigh waves using a genetic algorithm in the presence of a low-velocity layer’ *Acoustical Physics*, 52(6): 701-712.

[4] Lu, L., Wang, C. & Zhang, B. (2007), ‘Inversion of multimode Rayleigh waves in the presence of a low-velocity layer: numerical and laboratory study’, *Geophysical Journal International*, 168(3): 1235-1246.

[5] Ryden, N. & Lowe, M.J.S. (2004), ‘Guided wave propagation in three-layer pavement structures’, *Journal of the Acoustical Society of America*, 116(5): 2902-2913.

[6] Zhang, B. & Lu, L. (2003), ‘Guided waves in a stratified half-space’, *Acoustical Physics*, 49(4): 420-430.

[7] Zhang, B., Yu, M., Lan, C.Q. & Xiong, W. (1996), ‘Elastic wave and excitation mechanism of surface waves in multilayered media’, *Journal of the Acoustical Society of America*, 100(6): 3527-3538.

[8] Barnes, C.L. & Trottier, J.F. (2009), 'Evaluating high-frequency visco-elastic moduli in asphalt concrete', *Research in Nondestructive Evaluation*, 20(2): 116-130.
[9] Hunaidi, O. (1998), 'Evolution-based genetic algorithms for analysis of non-destructive surface wave tests on pavements', *NDT & E International* 31(4): 273-280.

Stabilised soil blocks for use in a European context.

Declan Gavigan[1], Jamie Goggins[1], Bryan McCabe[1]
[1]College of Engineering & Informatics, National University of Ireland, Galway.
email: d.gavigan1@nuigalway.ie, Jamie.Goggins@nuigalway.ie, Bryan.Mccabe@nuigalway.ie

ABSTRACT: Stabilised soil blocks (SSBs) are cost-effective masonry units formed by compressing a suitable mixture of soil, cement and water into a mould. These masonry units have a less negative impact on the environment than alternative masonry technologies, such as clay fired bricks or concrete masonry blocks, as their main component, the soil, is often sourced directly from the site of construction. The most commonly-used stabiliser used in the manufacture of SSBs is Ordinary Portland Cement (OPC), which is their most expensive and energy-intensive ingredient. Replacing OPC with alternative materials is a cost-effective process, and their use in SSBs can benefit the environment, especially where disposal to landfill is the alternative. This paper investigates the feasibility and suitability of SSBs for use in a European context through extensive testing in terms of strength, stiffness, durability and appearance. The ability of the soil in the blocks to resist prevailing rain, wetting and drying cycles, freezing and thawing cycles, and chemical attack are critical if there are to be applicable in a European climate. SSBs containing 5%, 7.5% and 10% cement were tested in terms of compressive strength and modulus of elasticity at 7, 14, 28 and 56 days. The durability of these blocks was evaluated by cyclic freezing/thawing and wetting /drying tests, drip test as well as determining the sorptivity and absorption characteristics of the blocks. This testing regime was also carried out on SSBs containing a combination of cement and alternative materials, namely GGBS and peat fly ash, and their performance as potential alternative stabilisers is compared against those containing OPC only as a stabiliser. The results generated from the strength and durability testing are very promising and compares well to conventional masonry materials.

KEY WORDS: Stabilised Soil Blocks (SSBs), Masonry, Durability, Alternative Binders/Stabilisers, Sustainability, Strength and Testing of Materials.

1 INTRODUCTION

Those who choose to build their own homes often are motivated by the desire to create an environmentally-friendly, energy-efficient, economical and durable dwelling that meets their needs now and in the future. A key to their choice of construction materials and technologies may be that they do not require special skills and machines for their fabrication, which can result in sustainable construction practices. Building materials (predominantly bricks and blocks) account for the main cost of shelter and housing, which amounts to 60% in the case of masonry units [1]. Furthermore, many building materials are transported long distances to site, increasing their embodied energy and carbon. Therefore, there is a need for the exploration of alternative, locally-sourced, cost-effective building materials and methods to meet the present and future demands of the building industry. However, we can turn towards developing countries for inspiration in this regards.

One construction technology used for houses in developing countries that has very low impact on the environment is stabilised soil blocks (SSBs), as seen in Figure 1. SSBs are cost-effective masonry units formed by compressing a suitable mixture of soil, cement and water into a mould. SSBs are used in the construction of both structural and non-structural elements (Figure 2). These blocks can be formed to be interlocking in nature, built dry stacked without the need for mortar joints. Alternatively, mortar jointing can be employed with plain or interlocking blocks. These masonry units are easy to manufacture and require relatively simple construction methods, requiring no specialised equipment, making it particularly suitable for self-builders [2-4].

Figure 1. Interlocking Stabilised Soil Block (SSB).

In terms of sustainability, SSBs are a superior choice of construction which boasts many environmental benefits, including low energy consumption, pollution and CO2 emissions during production, resulting in lower embodied energy, as well as a lessening demand and dependence on non-renewable resources and materials [5-9]. It is reported that SSBs typically require less than 10% of the input energy used to manufacture similar fired clay and concrete masonry units [4]. The manufacture of SSBs on site requires minimal transportation, further adding to their environmentally friendly features. Building with locally sourced materials, such as soil, creates local employment, which is arguably the most sustainable strategy [6]. Soil-based construction creates the potential for good-quality housing to be available to people regardless of the political situation of the country, and retains money in the local economy.

Figure 2. Multi-purpose centre built from interlocking SSBs.

The lower life cycle costs of SSBs, when compared with other masonry materials, are a great incentive for the use of SSBs [9, 10]. This has allowed SSBs to compete strongly with other conventional building materials. Soil, the primary raw material, is in abundance and inexpensive [3]. SSB production maximises the utilisation of locally sourced, readily available materials allowing for direct site to service application, with minimal transport costs incurred [11, 12].

SSBs may posses many architectural benefits in that buildings constructed using SSBs can have appealing, unique aesthetics and an elegant profile (Figure 2). If the soil used in the manufacturing of the SSBs is sourced from the construction site or vicinity, then the natural appearance and colours help buildings integrate into the landscape. Buildings made with earth also offer high thermal and acoustic insulation properties and with soil being non-combustible, it boasts excellent fire resistance properties [3, 9, 10, 12].

Earth as a construction material is not novel in itself. It has a cultural heritage and has been used for the construction of buildings since ancient times all over the world [3, 5, 11]. Although there is ample literature on the application of SSBs in tropical countries, their potential use in a European climate has not been fully investigated. Through this research project, the development of this cost-effective sustainable building technology or product for use in a European context is being proven through extensive testing in terms of durability, strength and appearance. The ability of the soil in the blocks to resist prevailing rain, wetting and drying cycles and freezing and thawing cycles has been determined. Through this project, the development of a comprehensive code of practice on the manufacturing and use of SSBs is envisaged to aid the future development of SSBs.

The strength and durability performance of SSBs is dependent on the following variables:

- Cement content
- Use of alternative stabilisers
- Soil properties, most significantly clay content, particle size distribution and organic content.
- Compaction pressure during manufacturing
- Curing regime
- Moisture content at testing

The effect of these parameters on the strength, durability and stiffness of SSBs is illustrated and discussed in this paper. The only parameter which is not investigated as part of this study is the effect that soil properties such as clay content, organic content and particle size have on the performance of these masonry units. The soil used in the manufacturing of SSBs generally refers to a sandy, loam sub-soil with a particle size distribution ranging from medium gravel to fine sand, which result in better strength and durability performance [5, 7, 9]. A similar study found that the peak compressive strengths corresponded to an optimum clay content in the range of 13–16%, above which strength is significantly reduced [13].

2 TESTING PROGRAMME AND METHODOLOGY

2.1 Materials

In the present study, soil was obtained from an Irish site close to where there are plans to construct a dwelling from SSBs. The material was characterised as per test methods in BS1377-2 [14]. The soil characteristics are shown in Table 1.

CEM I cement was used in the stabilisation of the soil while Ground Granulated Blast Furnace Slag (GGBS) and peat fly ash from Edenderry peat-fired power station were used as alternative stabilisers to cement. The symbols C, G and P used in this study refers to CEM I cement, ground granulated blasfurnace slag (GGBS) and peat fly ash respectively. The stabilisation combinations used are shown in Table 2.

The chemical compositions of the cement, GGBS and peat fly ash used are shown in Table 3. Although there is a minimum limit of 70% of the sum of SiO_2+ Al_2O_3+ Fe_2O_3 for fly ash outlined in BS EN 450-1[15], the current peat ash falls below this limit with a total sum of 48%.

Table 1. Soil characteristics.

Specific gravity	2.60
Organic content (%)	0.66
pH	7.65
Combined clay and silt content (%)	9.70
Plastic limit (%)	21.00
Plasticity index (%)	8.00

Table 2. Stabilisation combinations (% by dry weight of soil).

5C	5% cement
7.5C	7.5% cement
10C	10% cement
5C5G	5% cement and 5% GGBS
7.5C2.5G	7.5% cement and 2.5% GGBS.
5C5P	5% cement and 5% peat fly ash
7.5C2.5P	7.5% cement and 2.5% peat fly ash.

Table 3. Chemical composition of materials used (%).

Oxide	*C*	*G*	*P*
SiO_2	18.75	34.67	36.87
Al_2O_3	4.62	11.37	3.16
Fe_2O_3	3.15	0.60	7.97
CaO	60.68	40.34	36.36
MgO	1.95	8.59	2.34
K_2O	0.48	0.33	0.72
Na_2O	0.10	0.16	0.40
P_2O_5	0.09	0.01	0.63
TiO_2	0.30	0.62	0.23
SO_3	2.97	2.34	4.20
LOI	4.66	0.00	5.67

2.2 *Experimental Procedures*

The stages involved in the manufacturing of SSBs are shown in Table 4. The soil is first dried and sieved through a 6.3mm sieve as lumps of clay soil can prevent even compression, producing weak spots within the blocks and can lead to non-uniform drying of the blocks causing cracking [12, 16].

SSBs were stabilised with CEM I cement at contents of 5%, 7.5% and 10% by dry mass of soil. Furthermore, GGBS and peat fly ash were used to replace 25% and 50% of the 10% cement stabiliser content to assess the effect of alternative stabilisers on block performance. The mixing process was carried out in two stages; soil and stabiliser were first mixed in a dry condition before the gradual addition of water, followed by wet mixing. As the stabiliser content used in SSBs is relatively small, the stabiliser must be mixed thoroughly, otherwise it will not be evenly distributed and the final block quality will be significantly affected [17].

Table 4. Stages involved in SSBs manufacturing.

Mix Preparation	Compaction
Sieving of soil	Filling of mould
Batching	Moulding or compaction of blocks
Mixing of constituents	Block ejection and stacking

Water is necessary to compact the soil and to allow for the hydration of the cement [5]. However, if too much water is present, capillary water occupies the soil pore spaces, reducing the level of achievable compaction and increasing the porosity when the block is dried [9]. It is crucial that the optimum moisture content (OMC) of the soil mix is determined for compaction to maximise the quality of the product, obtaining the maximum dry density since density is related to strength and durability characteristics [7, 9, 10]. In this study, the OMC was determined using the 2.5kg Proctor test according to BS 1377-4:1990 [18] for 0, 5, 7.5 and 10% cement contents. Values of OMC fell in the range 8-10%. Therefore, a water content of 9% was adopted for all subsequent SSB mixes to facilitate direct comparison.

The specimens were prepared in accordance with ASTM D1632 [19] and ASTM D1633 [20]. The mix was compacted in Duriez (120 mm diameter x 250 mm high) cylindrical moulds to a pressure of 10 MPa using a hydraulic controlled ram. The stabilised soil specimens were extruded from the mould immediately and cured until testing. The specimens were tested in terms of wet compressive strength (tested in fully saturated state), dry compressive strength (dried at 105^{o}C in oven until constant mass and tested) and modulus of elasticity at 7, 14, 28 and 56 days. As part of this study, the Young's Modulus was determined from the initial, linear part of the stress-strain plot up to one third of the compressive strength, as outlined in BS 1881-121[21]. The dry tensile strength of the blocks was also determined at 28-days using the indirect tensile splitting test.

The durability of these blocks was evaluated by determining the absorption [22] and sorptivity [23] characteristics of the blocks, drip test, as well as cyclic freezing/thawing [24] and wetting /drying tests [25]. Although there are no definitive standard procedures to determine the absorption and sorptivity characteristics for SSBs, standardised test procedures for concrete were adapted for use with SSBs. The absorption tests were carried out in accordance with ASTM C642-06 [22] to determine the total absorption value of the SSBs. The sorptivity test, carried out in accordance with ASTM C1585-04 [23], involved measuring the increase in mass of the specimen resulting from the absorption of water as a function of time when only one surface of the specimen was exposed to water. Water ingress was dominated by capillary suction during initial contact with water.

Furthermore, a drip test was carried out on SSB specimens containing 0, 5 and 10% cement content. The test entails subjecting a soil specimen to dripping water, before inspecting the specimen for damage induced by the dripping water. The test consists of releasing 100 ml of water in drops at a controlled rate on to the surface of the block, which is inclined at 27^o to the horizontal, as seen in Figure 3.

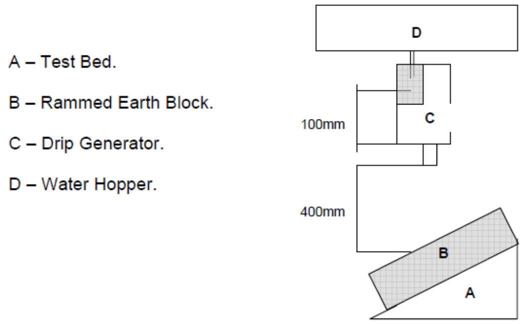

Figure 3. Drip test set-up [5].

3 RESULTS

3.1 *Strength and Stiffness*

The effect of cement content on both the wet and dry compressive strength with age is shown in Figure 4. As expected, the compressive strength increases with increasing cement content and age (Figure 4).

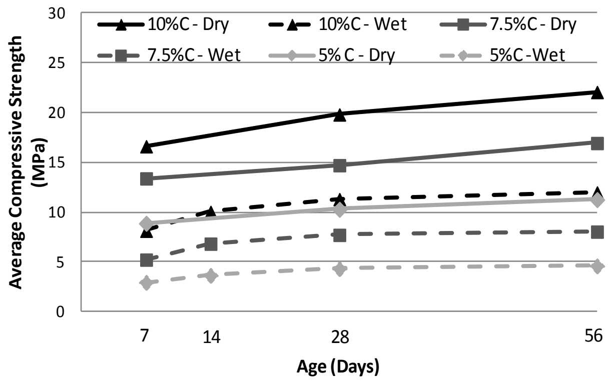

Figure 4. Effect of cement content.

Provided the cement content is a minimum 7.5% by dry weight of soil, the wet strength of the specimens are stronger than the conventional 5 Newton concrete block. Increasing the cement content from 5% to 10%, increase the 28-day dry strength from 10.3 to 19.8 MPa and increases the wet strength from 4.3 to 11.3 MPa. Figure 5 highlights the effect the various stabiliser contents and combinations have on the 28 day dry and wet compressive strength. The moisture content of SSBs specimens at testing has a significant influence on the resultant compressive strength [26]. Without exception, the tensile and compressive strength of wet blocks are consistently lower than the dry strength for identical specimens. Therefore, it is recommended that the wet compressive strength of SSBs be used to predict the compressive strength [12, 27]. Reduction in compressive strength with saturation can be attributed to the development of pore water pressures, decrease in soil cohesion, the softening of binders by water and the liquefaction of unstabilised clay minerals in the block matrix [4, 12, 26].

The ratio of 28-day wet to dry strength ranges from 0.36 for the 5C5P specimens to 0.57 for the 10C specimens. Many authors have proposed that the ratio of wet to dry strength be used as an indicator of durability [28, 29]. In terms of durability assessment, it is reported that a value of 0.33 to 0.50 represents adequate durability characteristics [7, 28].

As seen in Figure 5, the addition of GGBS to SSBs is effective in terms of strength development. The 28-day compressive strength of specimens containing GGBS as a replacement for CEM I are approximately equal if not greater than those containing CEM I only. The rate of strength gain for specimens containing GGBS can be lower than those specimens containing CEM I only at early ages due to reduction in cement hydration reaction rate (Figure 6). However, although the specimens containing 10% cement had the highest 7-day wet strength, the specimens containing GGBS have higher 56-day strengths as seen in Figure 6 (5C5G and 7.5C2.5G).

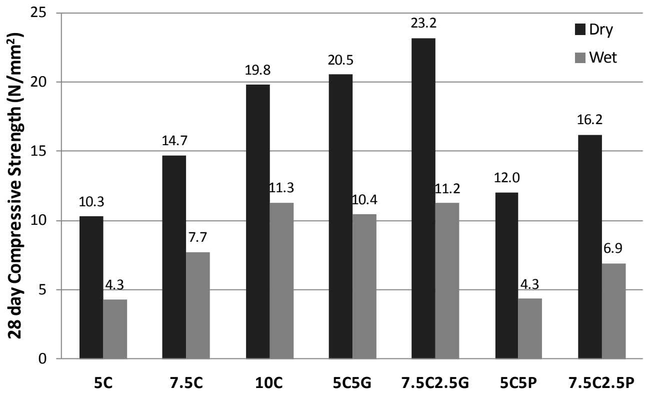

Figure 5. Effect of various alternative binders on 28-day compressive strength.

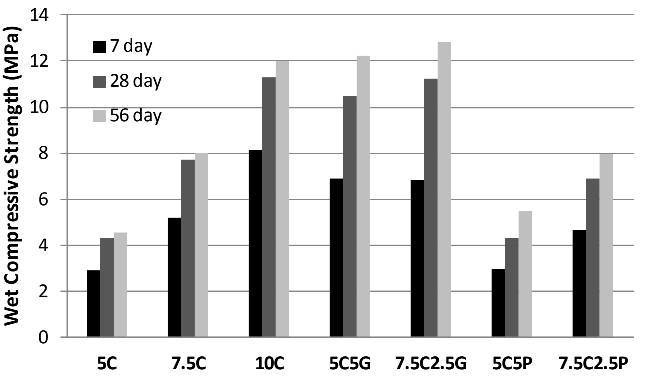

Figure 6. Strength development with age for all stabiliser variations.

This enhancement in strength is due to the fine GGBS particles filling extra voids between the soil particles, packing tightly together producing a dense matrix [30]. On the other hand, the peat ash seems to be inert, contributing very little to strength gain, which may be due to the chemical composition of the peat ash as it does not fully meet requirements set out in BS EN 450-1[15], as the sum of SiO_2+ Al_2O_3+ Fe_2O_3 falls well below the 70% minimum limit at 48%. Furthermore, the coarse nature of the material reduces the reactivity of the ash. Similar to compressive strength, a linear relationship exists between tensile strength and cement content with the tensile strength increasing with increasing cement content. As seen in Figure 7, the tensile strength of the blocks is 9% of its compressive strength for a cement content range of 5 to 10%. The standard deviations of each result are also illustrated. In a similar study, it was found that for cement contents of 6% and 12%, the direct tensile strength of the blocks were in the range of 5% to 6% of the compressive strength [31].

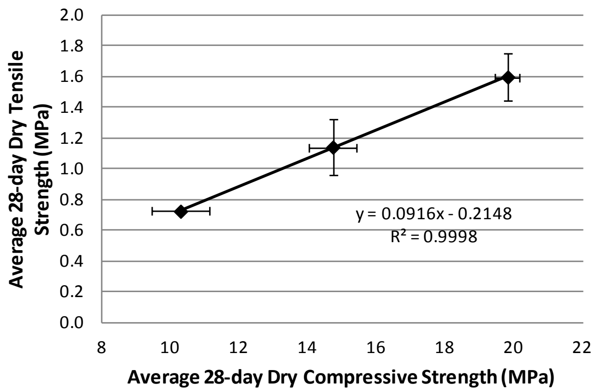

Figure 7. Relationship between 28-day dry tensile and compressive strength.

Increasing the compaction pressure during the manufacturing process increases both the 28-day wet strength and stiffness, until a compaction pressure of approximately 15 MPa is reached, after which increase in compaction effort has little benefit in terms of enhancement of strength and stiffness, as seen in Figure 8. An optimal compaction pressure of 10 MPa is recommended and which was used in the manufacturing of the blocks as part of this project, which represents a practical and economic upper limit of block quality [32].

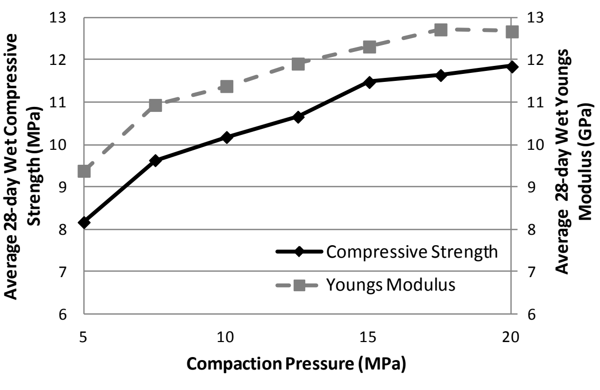

Figure 8. Effect of compaction pressure on 28-day wet compressive strength and 28-day wet Young’s Modulus.

The availability of moisture for curing, to ensure adequate supply for the cement hydration reactions, is essential if the blocks are to achieve their maximum potential strength. As part of this project, SSBs were subject to different curing regimes. It was found that the most efficient curing method for SSBs is fully immersing specimens in a water tank, although curing under polythene and watering twice daily is also adequate and is a more economical option. More information of the effect of various curing regimes can be found in [30].

The Young's modulus for SSBs was found to lie in the range of 4 to 14 GPa. A correlation between Young's modulus (E) and average dry and wet compressive strength (C) for SSBs is shown in Figure 9. Regression analyses give correlations between Young's modulus (E), dry compressive strength (C_{dry}) and wet compressive strength (C_{wet}), as:

$$E = 0.51C_{dry} \quad (1)$$

$$E = 1.13C_{wet} \quad (2)$$

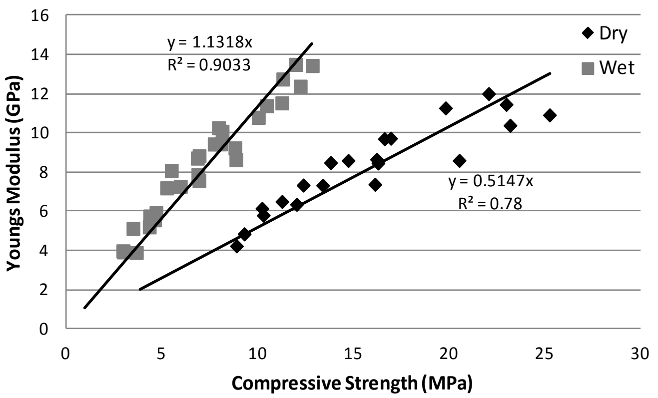

Figure 9. Relationship between the stiffness and compressive strength of SSBs.

3.2 Durability

Preliminary results for durability tests outlined in Section 2 are presented in this section. The 14 and 28 day absorption characteristics of SSB specimens with various stabiliser contents and combinations are shown in Figure 10. It is evident that the addition of GGBS slightly decreases the absorption characteristics in comparison to the specimens containing CEM I cement only, while the peat ash has an opposite effect. This phenomenon may be due to the absorptive nature of the peat ash. The absorption characteristics are approximately constant with age after 14 days.

The results of the sorptivity test, carried out in accordance with ASTM C1585[23], are shown in Table 5. As expected, the sorptivity decreases with increase in cement content. Furthermore, specimens containing GGBS show the lowest sorptivity values and the addition of peat ash increases the sorptivity characteristics, which are similar trends observed in the absorption tests.

The pitting depths due to the drip test are illustrated in Figure 11. It is evident that the performance of unstabilised soil specimens (i.e. 0% cement content) is unsatisfactory and is not a viable option for construction, where blocks may be exposed to weathering. However, adding as little as 5% cement has a significant effect in improving the specimen's resistance to weathering due to dripping water (Figure 11).

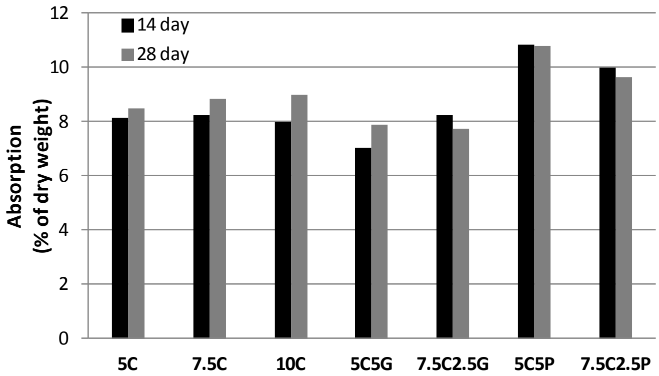

Figure 10. Absorption characteristics of all stabiliser combinations.

Table 5. Sorptivity results for all stabiliser combinations.

Mix	Average Sorptivity (mm/√s)
5C	0.0380
7.5C	0.0130
10C	0.0077
5C5G	0.0081
7.5C2.5G	0.0065
5C5P	0.0344
7.5C2.5P	0.0303

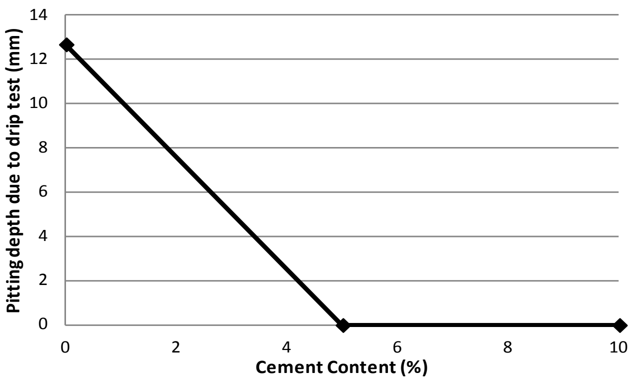

Figure 11. Pitting depth due to drip test for various cement contents.

Findings from additional durability testing, including shrinkage, wetting/drying cyclic tests and freeze/thaw cyclic tests are presented elsewhere [30].

Although these accelerated durability tests are a standardised means of assessing the performance of stabilised soil specimens, they are subject to much controversy. The vast majority of literature written on the subject of durability testing on SSBs is unanimous in the opinion that accelerated durability tests bear little practical correlation with actual long-term field performance. Researchers suggest that they do not give reliable forecasts of the longer term performance of the specimens, as they are too aggressive, over simplified, unrealistic and fail to replicate actual environmental conditions [6, 29, 33]. Therefore, long term durability tests are currently being carried out at NUI Galway, which includes exposing specimens to natural weather conditions and placing blocks in a specially designed rainfall simulator.

4 CONCLUSIONS

Through this extensive experimental testing program, it is expected that the successful development and implementation of stabilised soil blocks (SSBs), incorporating cement and other stabilisers, will be confirmed for a European climate. The results generated from the strength and durability testing are very promising and compares well to conventional masonry materials. Currently, the commercial development of SSBs as a sustainable building product or technology seems to be highly promising. However, it is important that similar studies on the long-term performance and durability of SSBs are undertaken to further promote the commercial development of the product. The implementation of the product can contribute to the development of a more sustainable and 'green' economy. With respect to an energy conscious, environmentally friendly design, the fact that SSBs can meet several functions, including structural integrity and durability, makes it an excellent walling material when compared to other modern masonry construction materials. Further tests are ongoing at NUI Galway as part of this project.

ACKNOWLEDGMENTS

The first author would like to thank the Irish Research Council for Science, Engineering and Technology (IRCSET) who are funding this research project under the Embark Postgraduate Scholarship Scheme. The authors would also like to acknowledge the significant input of the Civil Engineering technical staff at NUI Galway.

REFERENCES

1. Alutu, O.E. and A.E. Oghenejobo, *Strength, durability and cost effectiveness of cement-stabilized laterite hollow blocks.* Quarterly Journal of Engineering Geology and Hydrogeology, 2006. **39**(1): p. 65-72.
2. Khedari, J., P. Watsanasathaporn, and J. Hirunlabh, *Development of fibre-based soil-cement block with low thermal conductivity.* Cement and Concrete Composites, 2005. **27**(1): p. 111-116.
3. Deboucha, S. and R. Hashim, *A review on bricks and stabilized compressed earth blocks.* Scientific Research and Essays, 2011. **6**(3): p. 499-506.
4. Walker, P.J., *Strength, durability and shrinkage characteristics of cement stabilised soil blocks.* Cement and Concrete Composites, 1995. **17**(4): p. 301-310.
5. Browne, G. *Stabilised Interlocking Rammed Earth Blocks: Alternatives to Cement Stabilisation*. in *11th International Conference on Non-Conventional Materials and Technolgies (NOCMAT 2009)*. 2009. Bath, UK.
6. Bui, Q.B., et al., *Durability of rammed earth walls exposed for 20 years to natural weathering.* Building and Environment, 2009. **44**(5): p. 912-919.
7. Jayasinghe, C. and N. Kamaladasa, *Compressive strength characteristics of cement stabilized rammed earth walls.* Construction and Building Materials, 2007. **21**(11): p. 1971-1976.
8. Walker, P. and T. Stace, *Properties of some cement stabilised compressed earth blocks and mortars.* Materials and Structures, 1997. **30**(9): p. 545-551.
9. Hall, M. and Y. Djerbib, *Rammed earth sample production: context, recommendations and consistency.* Construction and Building Materials, 2004. **18**(4): p. 281-286.
10. Bahar, R., M. Benazzoug, and S. Kenai, *Performance of compacted cement-stabilised soil.* Cement and Concrete Composites, 2004. **26**(7): p. 811-820.
11. Venkatarama Reddy, B.V. and A. Gupta, *Strength and Elastic Properties of Stabilized Mud Block Masonry Using Cement-Soil Mortars.* Journal of Maerials in Civil Engineering, 2006. **18**(3): p. 472-476.
12. Walker, P., *Strength and Erosion Characteristics of Earth Blocks and Earth Block Masonry.* Journal of Materials in Civil Engineering, 2004. **16**(5): p. 497.
13. Venkatarama Reddy, B.V., R. Lal, and K.S.N. Rao, *Optimum Soil Grading for the Soil-Cement Blocks.* Journal of Materials in Civil Engineering, 2007. **19**: p. 139-148.
14. British Standards Institution, *BS 1377-2: 1990*, in *Methods of test for Soils for civil engineering purposes — Part 2: Classification Tests*. 1990, BSI: London.
15. British Standards Institution, *BS EN 450-1:2005+ A1:2007*, in *Fly ash for concrete — Part 1: Definition, specifications and conformity criteria*. 2005, BSI: London.
16. Mulenga, M.N., et al., *Cement and lime stabilized soil blocks and their quality evaluation*, in *Research report, Department of Civil and Environment Engineering, UNZA*. 2005.
17. Rigassi, V., *Compressed Earth Blocks: Volume I: Manual of Production*. A Publication of the Deutsches Zentrum für Entwicklungstechnologien - GATE in: Deutsche Gesellschaft für Technische Zusammenarbeit (GTZ) GmbH in coordination with BASIN. 1995, Eschborn, Germany.
18. British Standards Institution, *BS 1377-4: 1990*, in *Methods of test for Soils for civil engineering purposes — Part 4: Compaction-related tests*. 1990, BSI: London.
19. ASTM, *ASTM D1632 – 07*, in *Standard Practice for Making and Curing Soil-Cement Compression and Flexure Test Specimens in the Laboratory*. 2007, ASTM International: Pennsylvania.
20. ASTM, *ASTM D1633 – 00 (Reapproved 2007)*, in *Standard Test Methods for Compressive Strength of Molded Soil-Cement Cylinders*. 2007, ASTM International: Pennsylvania.
21. British Standards Institution, *BS 1881-121: 1983*, in *Testing concrete — Part 121: Method for determination of static modulus of elasticity in compression*. 1983, BSI: London.
22. ASTM, *ASTM C642 – 06*, in *Standard Test Method for Density, Absorption, and Voids in Hardened Concrete*. 2006, ASTM International: Pennsylvania.
23. ASTM, *ASTM C1585 – 04*, in *Standard Test Method for Measurement of Rate of Absorption of Water by Hydraulic- Cement Concretes*. 2004, ASTM International: Pennsylvania.
24. ASTM, *ASTM D560 – 03*, in *Standard Test Methods for Freezing and Thawing Compacted Soil-Cement Mixtures*. 2003, ASTM International: Pennsylvania.
25. ASTM, *ASTM D559 – 03*, in *Standard Test Methods for Wetting and Drying Compacted Soil-Cement Mixtures*. 2003, ASTM International: Pennsylvania.
26. Morel, J.-C., A. Pkla, and P. Walker, *Compressive strength testing of compressed earth blocks.* Construction and Building Materials, 2007. **21**(2): p. 303-309.
27. Pave, R.F., *Strength Evaluation of Dry-Stack Masonry*, in *School of Civil and Environmental Engineering*. 2007, University of Witwatersrand: Johannesburg.
28. Heathcote, K.A., *Durability of earthwall buildings.* Construction and Building Materials, 1995. **9**(3): p. 185-189.
29. Guettala, A., A. Abibsi, and H. Houari, *Durability study of stabilized earth concrete under both laboratory and climatic conditions exposure.* Construction and Building Materials, 2006. **20**(3): p. 119-127.
30. Gavigan, D., J. Goggins, and B. McCabe, *Strength and durability performance of stabilised soil block masonry units*, in *IABSE Conference: Global Thinking in Structural Engineering: Recent Achievement*. 2012: Sharm El-Sheikh.
31. Venkatarama Reddy, B. and A. Gupta, *Characteristics of soil-cement blocks using highly sandy soils.* Materials and Structures, 2005. **38**(6): p. 651-658.
32. Kerali, A.G. and T.H. Thomas, *Simple durability test for cement stabilized blocks.* Building Research & Information, 2004. **32**(2): p. 140-145.
33. Ogunye, F.O. and H. Boussabaine, *Development of a rainfall test rig as an aid in soil block weathering assessment.* Construction and Building Materials, 2002. **16**(3): p. 173-180.

Probabilistic modelling of reinforced concrete bridge deterioration and repair efficiency in marine environments

P.C. Ryan[1], A. O Connor[1], J. Kelly[1]
[1]Department of Civil, Structural and Environmental Engineering, Trinity College Dublin, Dublin, Ireland
email: ryanp7@tcd.ie, oconnoaj@tcd.ie, Kellyj44@tcd.ie

ABSTRACT: This paper investigates the durability of a number of concrete bridge repair options through an experimental programme and subsequent probabilistic deterioration modelling. The results of an extensive laboratory study are presented. The study investigated the durability characteristics of five concrete repair options in marine environments through accelerated chloride-ion ingress testing using salt (fog) spray chambers. The repair options studied were CEM I Ordinary Portland Cement (OPC), OPC with increased cover, OPC with Silane treatment, OPC with Ground Granulated Blastfurnace Slag (GGBS) as a partial cement replacement and OPC with Pulverised Fuel Ash (PFA) as a partial cement replacement. The mix designs and materials utilised in the experimental programme were identical to those used in the innovative repair of a marine bridge on the South East coast of Ireland in 2007. A probability based deterioration model is also presented within the paper with the choice of model parameters discussed in light of the existing literature. The results of the laboratory testing regime serve to inform input variables employed in the probabilistic deterioration model. The output of the probability based deterioration analysis is presented allowing the efficiencies of the repair materials to be considered in a robust probabilistic manner, highlighting the whole life cost implications associated with choice of repair strategy.

KEY WORDS: Concrete Durability, Chloride, Reinforcement Corrosion, Initiation Phase, Probabilistic, Laboratory Testing

1 INTRODUCTION

Chloride induced corrosion in reinforced concrete elements is a major durability issue in transportation infrastructure. It is recognised to be the primary cause of deterioration of reinforced concrete elements in structures which are subject to de-icing salts or are located in marine environments [1-3]. Each year the effects of chloride induced corrosion result in major capital expenditure on maintenance and strengthening of concrete structures around the world [4], significantly contributing to the ever increasing maintenance costs associated with the world's aging bridge infrastructure stock. In the United Kingdom it was estimated in 2001 that the annual cost of bridge maintenance for the National road bridge network was €225 million [5]. Germany's annual expenditure on bridge repairs, strengthening and replacement was reported to be between €300 million and €350 million in 2005 with this figure set to rise to €500 million in subsequent years [6].

The solution to the chloride induced corrosion problem is however far from simple. The process by which chlorides ingress into concrete is highly complex with various physical–chemical interactions among silane solutions, solid phases of concrete and moisture [7]. The complicated nature of the process leads to uncertainty when modelling chloride ion ingress. In addition there is significant uncertainty associated with the variation of environmental conditions from marine structure to marine structure. These modes of uncertainty have lead researchers in more recent times to represent chloride ion ingress and subsequent reinforcement corrosion using probabilistic methods [8-13]. However the probabilistic studies published in the literature, have in general been limited to the study of OPC concrete, and have not explored the effect of utilising alternative concrete types. In a recent publication McNally and Sheils [14] did however utilise probabilistic methods to investigate the effect of adding Ground Granulated Blastfurnace Slag (GGBS) to Cem II cement. This paper investigates the effect of utilising five different repair options, through employing the results of an extensive experimental programme as input parameters in a probabilistic model. This allows the efficiency of the five repair methods in resisting chloride ion ingress to be analysed in a robust probabilistic manner which incorporates uncertainty.

Four of the five repairs investigated herein are identical to those used in the innovative repair of a marine bridge on the South East coast of Ireland in 2007 as discussed in Section 2. The focus of this paper is on the initiation phase of chloride induced reinforcement corrosion. Typically, this phase has a far longer duration than either the crack initiation phase or the crack propagation phase [8]. Consequently the initiation phase of chloride induced reinforcement corrosion has the most significant impact on a marine structure's overall service life. The paper predicts the time to initiation of corrosion for each of the repairs considered in the study through the utilization of a probability based deterioration model. Section 2 of this paper presents the experimental programme carried out as part of the research. Section 3 of the paper presents the probability based deterioration model utilised and discusses the choice of statistical model parameters in light of the existing literature. Section 4 of the paper presents the probabilistic model results and discusses the consequence of the findings in the context of the whole life cost of reinforced concrete marine structures.

2 EXPERIMENTAL PROGRAMME

The basis for the experimental programme was derived from the repair of Ferrycarrig Bridge, a marine bridge on the South East coast of Ireland. The repair of Ferrycarrig Bridge is discussed in detail in [15] however it will be discussed briefly herein for the sake of clarity.

The bridge repairs were conducted in 2007. The work was carried out with a dual purpose, firstly to repair the deteriorated structure, and secondly, to gather information on the efficiency of typical concrete repair options in Irish marine environments. As part of the essential repairs the cover concrete on the bridge's seven crosshead beams was removed to a depth of approximately 50mm beyond the level of the reinforcement. Additional steel reinforcement was put in place to strengthen the crosshead beams. Then one of each of the following concrete repair options was utilized on a crosshead bridge beam facilitating the comparison of the performance of the repair options over time.

- CEM I Ordinary Portland Cement (OPC) concrete
- OPC with silane surface treatment (OPC-S)
- OPC with increased cover
- OPC with corrosion inhibitor
- OPC with 60% ground granulated blastfurnace slag as a partial cement replacement (OPC + GGBS)

The process of chloride-ion ingress and the resultant reinforcement corrosion is slow. It could therefore be 20 years or more before any real conclusions can be drawn on the relative efficiencies of the repair options from Ferrycarrig Bridge. Consequently, an experimental programme was carried out at TCD in order to investigate the repair methods utilized at Ferrycarrig Bridge in the short to medium term through accelerated laboratory testing. This allowed information to be obtained on typical repair options while they are still widely used.

The experimental testing was carried out in the TCD materials laboratory using a salt (fog) spray chamber. The salt (fog) spray chamber subjects test samples to periodic wetting and drying cycles over the exposure duration through the utilization of a venturi spray nozzle system which emits a salt mist or fog that fills the chamber during wet cycles. The fog evenly disperses throughout the chamber significantly reducing the effect of spatial variability over a cruder salt spraying system which emits salt solution in larger droplet form. During the wetting cycles a 5% sodium chloride solution mist fills the chamber and saturates the surface of the samples. The nature of the salt (fog) spray tests means that both wetting and drying is taking place during the testing period. This is an important factor as the majority of laboratory tests published in the literature investigate concrete in a fully submerged state. In the real marine environment corrosion is unlikely to occur in concrete elements which are constantly submerged, as the corrosion reaction is prevented by a lack of oxygen at the reinforcing steel surface. This was illustrated by Hussain in an experimental study where the corrosion rate for submerged reinforced concrete samples was found to be so low that it is of little practical importance [16]. In the tidal, splash and atmospheric zones however, where reinforcement corrosion commonly occurs, the concrete is subject to both wetting and drying. Salt spray tests, as with ponding tests [1, 17] incorporate both wetting and drying cycles.

Three 100mm cube samples were tested in the salt (fog) spray chamber for each of the repair options utilized at Ferrycarrig Bridge. The mix designs and materials used were identical to those used for the crosshead repairs at Ferrycarrig Bridge in 2007. In addition to the Ferrycarrig Bridge repair methods, the use of Pulverized Fuel Ash (PFA) as a partial cement replacement was also investigated as part of the laboratory testing regime due to it's documented advantages in resisting the ingress of chloride ions [18-20]. The list of the concrete repair methods examined in the experimental programme and investigated further via the probabilistic model in the next section are thus as follows;

- CEM 1 Ordinary Portland Cement (OPC)
- OPC with increased cover (70mm)
- OPC with silane surface treatment
- OPC with 60% GGBS as partial replacement
- OPC with 30% PFA as partial replacement

The testing was focused on the initiation phase of corrosion and thus is solely concerned with the ability of the various repair options to resist the ingress of chlorides. Consequently, no reinforcement was utilized in the test samples. The water/binder ratio for the mixes was 0.44 in accordance with the XS3 exposure class in EN206-1:200 [21]. A 10mm coarse aggregate was used for all concrete mixes and the proportion of fine to coarse aggregate was 2.3 : 1. A plasticizer and a super-plasticizer were used in the mix. The samples were cured in a curing tank at 20 ± 2ºC for 28 days in accordance with the relevant standard [22]. Compressive strength tests were carried out on 100mm cubes at 7 and 28 days for each of the mixes. The results of these tests can be seen in Table 1.

Table 1. Compressive strengths of OPC and GGBS mixes at 7 and 28 days.

Repair Type	7 Day Strength (N/mm^2)	28 Day Strength (N/mm^2)
OPC	57.0	68.9
OPC-S	58.1	70.7
OPC + GGBS	46.7	67.0
OPC + PFA	39.9	57.5

After the curing period the samples were painted with epoxy sealant paint on all but one face in order to rule out edge effects during testing. Upon commencement of the exposure period the concrete test samples were subject to periodic wetting and drying cycles comprising of two days of salt fog and five days of drying per week. During the wetting cycles a 5% sodium chloride solution mist filled the chamber saturating the surface of the samples. The samples were exposed to the aggressive accelerated chloride ingress environment for a period of 8 months. This duration was necessary to ensure penetration of chlorides to a sufficient depth to allow for the fitting of full chloride profiles. Once the 8 month testing had been completed dust samples were collected from each sample at 2.0mm depth increments using a profile grinder. The dust samples were analyzed using acid soluble potentiometric titration to calculate the total chloride content at each depth increment in accordance with BS EN 14629:2007 [23]. These values were used to create chloride profiles for each of the samples. As is common place in the literature Fick's second law with Crank's solution was fitted to the chloride profiles in order to obtain the apparent diffusion coefficients, $D_{app,}$ and surface chloride contents, C_s, for the test samples [1, 18, 24]. It is these values of surface chloride content and apparent diffusion coefficient which are used in the probabilistic deterioration model to assess the durability of the repairs through the comparison of probability based time to initiation of corrosion.

3 PROBABILITY BASED DETERIORATION MODEL AND MODEL PARAMETERS

The theoretical background for the probability based deterioration model utilizes Fick's second law of diffusion with Crank's error solution:

$$T_i = \frac{x^2}{4 \times D_{app}} \times \left[erf^{-1}\left(\frac{(C_{cr} - C_s)}{(C_i - C_s)} \right)^{-2} \right] \tag{1}$$

where x is cover depth, D_{app} is the apparent diffusion coefficient, erf is the error function, C_{cr} is the critical chloride content, C_s is the surface chloride content C_i is the initial chloride content in the concrete and T_i, is the time to initiation of corrosion. This formula has been used throughout the literature to provide an estimate of, T_i, the time to the initiation of reinforcement corrosion for concrete structures [9, 11, 12].

It is clear that the parameters in Equation 1 are subject to variation. In order to represent the uncertainty associated with the variables, each variable in Equation 1 was assigned a statistical distribution with a predefined mean and coefficient of variation (CoV). The mean and CoV values used for the model parameters are a combination of experimentally calibrated values and values adopted from the literature as presented in Table 2. Both normal and lognormal distributions were utilized, as suggested in the literature [10, 13, 25, 26]. Each of the parameters utilized are discussed below.

3.1 Probabilistic model parameters

Table 2. Statistical parameters for model variables

Property	Units	Mean	CoV	Dist.	Parameter Origin
OPC C_s	*%	1.77	0.02	N	Exp.
PFA C_s	*%	1.80	0.11	N	Exp.
GGBS	*%	1.70	0.04	N	Exp.
OPC + Silane	*%	1.00	0.02	N	Exp.
OPC Dapp	m^2/s	2.28E-12	0.04	N	Exp.
OPC + PFA D_{app}	m^2/s	1.51E-12	0.08	N	Exp.
OPC + GGBS D_{app}	m^2/s	1.24E-12	0.11	N	Exp.
OPC + Silane D_{app}	m^2/s	1.65E-12	0.07	N	Exp.
C_{cr}	^{a}%	0.100	0.20	LN	[10, 13, 25]
Cover, x	mm	Spec .+ 1.6	σ = 11.1	N	[10, 13, 26]

*Percentage by weight of concrete, N is normal distribution, LN is log normal distribution, Exp. is Experimental Work

For the purpose of this illustrative example a cover of 50mm was adopted for the repair options in accordance with the relevant Eurocodes for a bridge beam in a marine splash zone [21, 27]. The one exception to this was the OPC with increased cover repair option for which a 70mm cover was adopted. Stewart and Suo [10, 13] adopted a cover standard deviation and mean bias in a probabilistic model in 2009 based on data collected from RC beams by Mirza and MacGregor [26]. These mean bias and standard deviation values were utilized herein resulting in a mean cover value of 51.6mm with a standard deviation of 11.1mm. The mean cover value used for the OPC with increased cover option was 71.6mm with a standard deviation of 11.1mm.

There is much debate about the exact value of the critical chloride content C_{cr}. Angst conducted a comprehensive study of experimental testing and site measurements and found that on the basis of the literature it was not possible to select a reliable range of chloride threshold values [28]. Researchers such as Bastidas-Arteaga et al. and So et al. used a mean C_{cr} value of 0.0375% by weight of concrete in probability based deterioration models [11, 12]. Stewart in his earlier papers adopted a similar value[9, 29], however in more recent papers by Stewart a higher value of 0.100% by weight of concrete has been utilized [10, 13, 25]. It is this mean value which is used for the purpose of this analysis. The CoV value adopted for the C_{cr} value in this analysis is 0.2. A value of 0.19 or 0.2 is broadly used across the literature for C_{cr} even when the value of the mean C_{cr} differs [9-13, 25, 29]

The values utilized in the probability based deterioration model for surface chloride content, C_s were obtained from the accelerated chloride ion ingress testing detailed in Section 2. As can be seen from Table 2, the mean C_s values range from 1.80% by weight of concrete for OPC + GGBS to 1.00% by weight of concrete for OPC + Silane. The CoV of the C_s values obtained from the experimental data range from 0.02 to 011. When compared to the literature it can be said that the mean C_s values are high and the CoV values obtained from experimental testing are low. Val and Stewart in 2003 and Bastidas-Arteaga et al. in 2009 used a mean C_s value of 0.306% by weight of concrete and a C_s CoV of 0.70 [12, 30]. These values were obtained from a comprehensive field-based study carried out by McGee [31] which presented data from 1,158 bridges in the Australian state of Tasmania.

Firstly, considering the CoV values, it is logical that the CoV for C_s would be far less for a controlled laboratory experiment than for the real marine environment. The data from 1,158 bridges would vary considerably about a mean due to factors such as variable exposure conditions from site to site, tidal zone data, splash zone data and atmospheric exposure data compiled together, spatial variability on the structure itself, etc. The examination of the repair materials in a controlled experiment allows a fair comparison to be drawn without variation due to environmental conditions and material variation from bridge to bridge effecting the outcome i.e. a comparison can be drawn between the repair options with all other factors being equal. The purpose of estimating T_i for the repair materials in this study is not to predict when exactly corrosion might initiate in a real marine structure. What is important in the analysis is the relative performance of the repair concretes in resisting chloride ingress under the uniform laboratory conditions.

In terms of the mean C_s values, the nature of the accelerated tests results in mean C_s value that will be higher than those experienced in the real marine environment due to the frequent exposure of the samples to the 5% NaCl fog. This however is necessary in order to obtain results over a practical laboratory experimental duration.

The mean D_{app} values obtained from the experimental testing for the OPC repair concrete the repair is 2.28E-12 m^2/s. The OPC D_{app} CoV value obtained is 0.04 as can be seen from Table 2. Morocous et al. utilized data collected from a field study whereby D_{app} was measured at 35 locations along the length of a bridge [32]. The resultant mean D_{app} value was 1.6E-12m^2/s with a CoV of 0.3. So et al. used a mean D_{app} value of 1.032E-12m^2/s with a CoV of 0.1 [11]. Stewart and Rosowsky used a mean D_{app} value of 2E-12m^2/s with a CoV of 0.75 [33]. Thus the mean D_{app} value for OPC obtained from the experimental work is of the same order of magnitude as those used for OPC in probabilistic deterioration models in the literature. Little work has been done investigating the effects of the use of blended cements on probabilistic deterioration models. McNally and Sheils did however use a value of 0.81E-12m^2/s for 50% GGBS replacement and 1.00E-12m^2/s for 70% GGBS in a probabilistic deterioration model [14]. These values were inferred from Rapid Chloride Migration tests in accordance with the work of Tang and Neilson [34], who developed a rapid test for determining chloride diffusivity using a submerged concrete sample and the application of an external electrical potential to accelerate the chloride ingress process. McNally and Sheils used a CoV value of 0.2 for the the GGBS D_{app} value. These values for D_{app} and the D_{app} CoV are of the same order of same magnitude as the values used herein.

4 RESULTS AND DISCUSSION

Figure 1 shows the probability based time to initiation of corrosion, T_i, values represented by probability density functions (PDFs). For clarity, the mean T_i values, along with standard deviations and CoV's, are also presented in Table 3. The PDF plot shows the shape of the Ti probability distribution for each repair method and gives an indication of the best performing repair method. The mean value for all of the distributions shown is slightly to the right of the peak value. The shorter the mean time to initiation of corrosion, the sooner corrosion is likely to occur when the particular repair method is utilized and thus the less durable the repair solution. It is clear from Figure 1 that the OPC repair concrete performs the worst of the options considered with the peak of the PDF at the shortest duration. The OPC + GGBS, OPC + Silane and OPC with 70 mm cover all perform very similarly with the peaks of these distributions all around the 10 year mark. This is confirmed by the values presented in Table 3. The OPC + PFA performance lies somewhere between the OPC and the other three repair options.

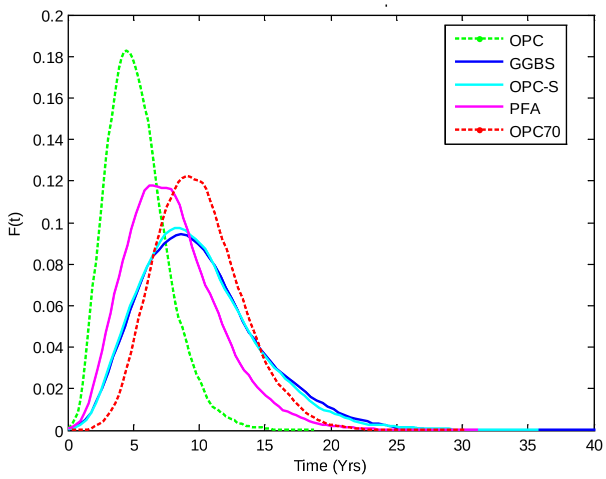

Figure 1 Probability density functions of T_i for each repair.

Table 3. T_i Statistical parameters from Monte Carlo simulation.

Repair	Mean T_i	St Dev. of T_i	CoV of T_i
OPC	5.3	2.3	0.43
PFA	8.0	4.5	0.56
OPC-S	9.9	4.4	0.44
GGBS	10.1	3.5	0.35
OPC-70	10.0	3.2	0.32

The results of the analysis are presented in different form in Figure 2 in a cumulative distribution function plot. This plot presents the cumulative probability of the initiation of reinforcement corrosion with progression of time. The plot does not give information on the variation associated with each repair like Figure 1, however it gives a more easily interpreted picture of the effect of using each of the repair materials at a given time. There is little to separate the three best performing repair options which can be seen in Figure 2 to be OPC + GGBS, OPC + Silane repair and OPC with increased cover. It is interesting to note however that when considering the 0.5 probability of corrosion the OPC with increased cover performs slightly better than the OPC + Silane and OPC + GGBS, however at the 0.9 probability of initiation of corrosion the OPC + GGBS and OPC + Silane repairs outperform the OPC with increased cover. This is due to the fact that the OPC has a higher apparent diffusion coefficient than either of the other two repair options. This means that as time passes the ratio of the rate of chloride front movement to distance between the chloride front and the reinforcement is less for the OPC with increased cover than it is for either of the other two repair options. The OPC + PFA concrete performance again lies somewhere between the OPC concrete and the other three repair options. The cumulative probability of corrosion initiation for the OPC standard repair option is higher at each yearly interval than any of the other repair options.

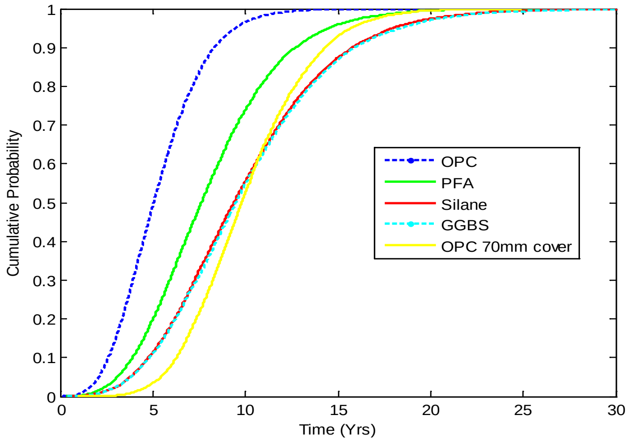

Figure 2 Cumulative probability distribution of T_i for the five repair options.

As expected for such accelerated exposure conditions, the times to initiation of corrosion calculated are relatively short when compared to the real marine environment. As previously stated however it is the relative performance of the repair materials which we are interested in herein. To this end Figure 3 presents each of the mean Ti values obtained from the probabilistic modelling normalized with respect to OPC by dividing by the Ti value obtained for the OPC repair. Figure 3 thus presents the performance of each repair option relative to the performance of the standard OPC repair concrete.

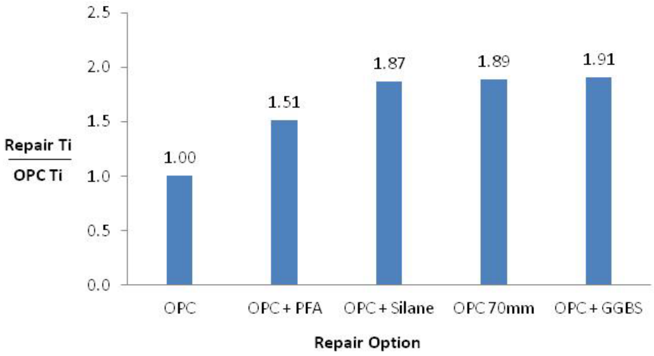

Figure 3. Relative performance of each repair material when compared to OPC.

As can be seen from Figure 3 the calculated mean time to initiation of corrosion for OPC + Silane, OPC with increased cover and OPC + GGBS is approximately 1.9 times greater than the calculated T_i for the standard OPC repair. It is interesting to note that the effect of adding 20mm cover to the OPC concrete is very similar to the effect of applying Silane surface treatment or utilizing 60% GGBS as a partial replacement in the design mix. However, the continued performance of a chemical surface treatment over a long period of time needs further examination. In addition the reduced performance of the OPC with increased cover with progression of time as observed in Figure 2 must be considered. It can however be said that based on the experiments carried out and the probabilistic deterioration model utilized the mean time to initiation of corrosion is almost doubled through the utilization of one of the top three performing repair materials. There is little information on the comparative performance of such alternatives from the real marine environment in the literature however, in 2009 Melchers and Li published details of a comprehensive study of the available literature on corrosion activation and initiation times in concrete structures exposed to severe marine environments [35]. One finding of the study, which was based on real structure data, was that structures constructed with OPC + GGBS had a time to initiation of corrosion between 2 and 3 + times greater than structures constructed of OPC alone. Thus, according to Melchers' and Li's study [35] the relative merit for OPC + GGBS over OPC concrete was found to be between 2 and 3 +. This is of the same order of magnitude as the value of 1.9 found in this study.

5 CONCLUSIONS

The paper presented details of an experimental programme carried out to investigate the durability characteristics of five alternative concrete repair options which were utilized on a real marine bridge in 2007. The results of the experimental programme served as input parameters in a probability based deterioration model facilitating an investigation into the relative efficiencies of the five repair options in marine environments through the examination of the time to initiation of corrosion in a robust probabilistic manner. For the experiments conducted and the probabilistic deterioration model utilized it was found that when compared to the standard OPC repair option, the time to initiation of corrosion was approximately doubled if either OPC + GGBS, OPC + Silane treatment or OPC with cover increased by 20mm were utilized. The use of OPC + PFA was found to have less of an effect. It must be noted however that the OPC + PFA still preformed 50% better than the standard OPC repair. This is a considerable improvement when the whole life cost implications for a structure are considered. The choice of concrete repair thus has considerable implications for the whole life cost of a deteriorated marine structure while the choice of standard repair method adopted by a management authority will have a substantial impact on the maintenance costs of a bridge network as a whole.

ACKNOWLEDGMENTS

The Irish National Roads Authority and the Irish Research Council for Science Engineering and Technology are gratefully acknowledged for the financial support provided in facilitating this research. In addition the authors would like to acknowledge the support of the DURATINET Project.

REFERENCES

[1] McPolin, D., et al., *Obtaining progressive chloride profiles in cementitious materials.* Construction and Building Materials, 2005. **19**(9): p. 666-673.

[2] Yuan, Q., et al., Chloride binding of cement-based materials subjected to external chloride environment - A review. Construction and Building Materials, 2009. **23**(1): p. 1-13.

[3] Bastidas-Arteaga, E., et al., A comprehensive probabilistic model of chloride ingress in unsaturated concrete. Engineering Structures, 2011. **33**(3): p. 720-730.

[4] Guoping, L., H. Fangjian, and W. Yongxian, *Chloride ion penetration in stressed concrete.* Journal of Materials in Civil Engineering, 2011. **23**(Compendex): p. 1145-1153.

[5] BRIME Project, *BRIME D14 Final Report*, 2001, Funded Under European Commission under the Transport RTD Programme of the 4th Framework Programme.

[6] Hearn, G., et al., *Bridge Preservation and Maintenance in Europe and South Africa*, 2005, INternational Technology Exchange Program.
[7] Climent, M.A., et al., A test method for measuring chloride diffusion coefficients through nonsaturated concrete: Part I. The instantaneous plane source diffusion case. Cement and Concrete Research, 2002. **32**(7): p. 1113-1123.
[8] Lu, Z.-H., et al., Probabilistic evaluation of initiation time in RC bridge beams with load-induced cracks exposed to de-icing salts. Cement and Concrete Research, 2011. **41**(3): p. 365-72.
[9] Vu, K.A.T. and M.G. Stewart, Structural reliability of concrete bridges including improved chloride-induced corrosion models. Structural Safety, 2000. **22**(Compendex): p. 313-333.
[10] Stewart, M.G. and Q. Suo, Extent of spatially variable corrosion damage as an indicator of strength and time-dependent reliability of RC beams. Engineering Structures, 2009. **31**(1): p. 198-207.
[11] So, K.K.L., M.M.S. Cheung, and E.X.Q. Zhang, *Life-cycle cost management of concrete bridges.* Bridge Engineering, 2009. **162**(September 2009 BE3): p. 103-117.
[12] Bastidas-Arteaga, E., et al., Probabilistic lifetime assessment of RC structures under coupled corrosion-fatigue deterioration processes. Structural Safety, 2009. **31**(1): p. 84-96.
[13] Suo, Q. and M.G. Stewart, Corrosion cracking prediction updating of deteriorating RC structures using inspection information. Reliability Engineering & System Safety, 2009. **94**(8): p. 1340-1348.
[14] McNally, C. and E. Sheils, Probability-based assessment of the durability characteristics of concretes manufactured using CEM II and GGBS binders. Construction and Building Materials, 2012. **30**(3): p. 22-29.
[15] Ryan, P.C., et al., Repair, Monitoring & Experimental Work Associated with Ferrycarrig Bridge, in Bridge Maintenance, Safety and Management: Proceedings of the Fifth International IABMAS Conference, R. Sause, D. Frangopol, and C. Kusko, Editors. 2010: Philadelphia.
[16] Hussain, R.R., Effect of moisture variation on oxygen consumption rate of corroding steel in chloride contaminated concrete. Cement and Concrete Composites, 2011. **33**(1): p. 154-161.
[17] Saraswathy, V. and H.-W. Song, Evaluation of corrosion resistance of Portland pozzolana cement and fly ash blended cements in pre-cracked reinforced concrete slabs under accelerated testing conditions. Materials Chemistry and Physics, 2007. **104**(2-3): p. 356-361.
[18] Thomas, M.D.A. and J.D. Matthews, *Performance of pfa concrete in a marine environment--10-year results.* Cement and Concrete Composites, 2004. **26**(1): p. 5-20.
[19] Dhir, R.K., W.Z. Zhu, and M.J. McCarthy, *Use of portland pfa cement in combination with superplasticizing admixtures.* Cement and Concrete Research, 1998. **28**(9): p. 1209-1216.
[20] Cheewaket, T., C. Jaturapitakkul, and W. Chalee, *Long term performance of chloride binding capacity in fly ash concrete in a marine environment.* Construction and Building Materials, 2010. **24**(8): p. 1352-1357.
[21] European Standard Institution CEN, BS EN 206-1: 2000, Concrete, Part 1: Specification, Performance, production and conformity., 2000.
[22] British Standards Institution, Method of Normal Curing of Test Specimens BS 1881-111:1983., 1983, HMSO London.
[23] European Standard Institution CEN, BS EN 14629: 2007, Products and systems for the protection and repair of concrete structures - Test methods - Determination of chloride content in hardened concrete., 2007.
[24] Nokken, M., et al., *Time dependent diffusion in concrete--three laboratory studies.* Cement and Concrete Research, 2006. **36**(1): p. 200-207.
[25] Vu, K.A.T. and M.G. Stewart, *Predicting the likelihood and extent of reinforced concrete corrosion-induced cracking.* Journal of Structural Engineering, 2005. **131**(Compendex): p. 1681-1689.
[26] Mirza, S.A. and J.G. MacGregor, *Variations in Dimensions of reinforced concrete members.* 1979. **105**(Compendex): p. 751-766.
[27] European Standard Institution CEN, BS EN 1992-1-1:2004, Design of concrete structures — Part 1-1: General rules and rules for buildings, 2004.
[28] Angst, U., et al., *Critical chloride content in reinforced concrete -- A review.* Cement and Concrete Research, 2009. **39**(12): p. 1122-1138.
[29] Stewart, M.G. and D.V. Rosowsky, *Structural safety and serviceability of concrete bridges subject to corrosion.* Journal of Infrastructure Systems, 1998. **4**(Compendex): p. 146-155.
[30] Val, D.V. and M.G. Stewart, Life-cycle cost analysis of reinforced concrete structures in marine environments. Structural Safety, 2003. **25**(Compendex): p. 343-362.
[31] McGee, R., Modelling of durability performance of Tasmanian bridges, in Applications of statistics and probability in
[32] *civil engineering*, Melchers RE and M. Stewart, Editors. 2000: Rotterdam: Balkema. p. p. 297-306.
[33] Morcous, G., Z. Lounis, and Y. Cho, An integrated system for bridge management using probabilistic and mechanistic deterioration models: Application to bridge decks. KSCE Journal of Civil Engineering, 2010. **14**(Compendex): p. 527-537.
[34] Stewart, M.G. and D.V. Rosowsky, *Time-dependent reliability of deteriorating reinforced concrete bridge decks.* Structural Safety, 1998. **20**(Compendex): p. 91-109.
[35] Tang, L. and L.O. Nilsson, Rapid determination of the chloride diffusivity in concrete by applying an electrical field. ACI Materials Journal, 1993. **89**(1): p. 49-53.
[36] Melchers, R.E. and C.Q. Li, Reinforcement corrosion initiation and activation times in concrete structures exposed to severe marine environments. Cement and Concrete Research, 2009. **39**(Compendex): p. 1068-1076.

Pre-stressed timber using threaded steel rods

E McConnell[1], N Campbell[1], D McPolin[1], S Taylor[1]
[1]Department of Civil Engineering, Queens University Belfast, University Road, Belfast, Northern Ireland
Email emcconnell10@qub.ac.uk, ncampbell23@qub.ac.uk, d.mcpolin@qub.ac.uk, s.e.taylor@qub.ac.uk

ABSTRACT: Timber is a fundamental structural material, but it is not without its limitations and, as such, it has been forced to undergo many transformations to continually keep abreast of the ever-changing demands of the construction world. This research was aimed at continuing the development of timber by enhancing its natural structural properties through the process of pre-stressing. Initial designs based upon first principle calculations were carried out to demonstrate the theoretical advantages provided by pre-stressing. As well as proving that there is benefit in pre-stressing the material, the calculations provided numerical values for the maximum amount of pre-stressing force that can safely be applied to the member to avoid failure. Laboratory investigations of pre-stressing timber with threaded steel bars were conducted with encouraging results. The pre-stressing force was applied using a hollow ram jack and the force was monitored with a load cell. Deflections were measured with LVDT during testing, while a 'locking nut' was used to secure the rod at either end of the timber beam. It was found that there was an increase in load carrying capacity, a more favourable ductile failure mode and a further benefit of less net deflection due to the precamber induced by the pre-stressing prior to load application.

KEY WORDS: Pre-stressed; Glulam; Timber; Steel.

1 INTRODUCTION

Timber, as a natural resource, has been in existence throughout the ages and as a result has been utilised in many various forms within numerous building techniques to create a large variety of structures: from basic shelters to large intricate places of worship and even long-spanning highway bridges.

Timber that has been sourced from sustainable forests is not only considerably less damaging to the environment than other materials, but it also has many advantageous structural properties, such as a high strength to weight ratio as well as relatively comparable strength in both compression and tension. Additionally the act of forestry is regarded as beneficial to the environment as it has the potential to reduce the concentration of atmospheric carbon dioxide by sequestrating carbon. Despite the many advantages possessed by timber over other construction materials it remains underused in the industry. The aesthetic qualities of the material make it a popular choice with designers for facades etc., however;

'timber is not widely used for primary structural elements in Britain and Ireland, even though a substantial volume of renewable native material is available.' [1]

The underuse of timber as a primary structural material may be attributed to the fact that it is a naturally occurring resource and as such contains certain defects. As timber grows it develops an intricate chemical composition with finely balanced structural properties. This means that timber as a structural material has a number of undesirable characteristics, such as the presence of knots and grain defects, susceptibility to the effects of moisture and other time dependent vulnerabilities, such as the occurrence of creep.

The limitations experienced when using timber in construction have been continually addressed in the past with the development of laminated veneer lumber and glulam to reduce the presence of natural defects, and more recently the extensive work that has been completed regarding the reinforcement of the material using both various metals and novel fibre reinforced polymers as an attempt to enhance the timber's strength and stiffness.

Although extensive work reinforcing timber beams has been completed in the past, many researchers have concluded that the addition of the expensive FRP material is akin to the addition of a single timber lamina, making this method ineffective and uneconomical [2-3]. It is therefore arguable that the FRP's utilised in these investigations are not being fully exploited as only a fraction of their structural potential is used. By pre-tensioning the material and therefore using active reinforcement rather than passive a number of advantages may be realised as,

'Prestressing effectively increases flexural strength by introducing an initial compressive stress into the timber fibres that in service are under tension.' [4].

2 RESEARCH OBJECTIVES

This study was initiated by Queen's University Belfast to evaluate the feasibility of strengthening timber beams through the use of a pre-stressed steel rod inserted through the beam's length. Throughout the investigation a combination of unreinforced and pre-stressed GL28 timber beams were tested to determine the structural advantages that the process would create. The investigation required the development of a suitable and safe method of pre-stressing the 8 mm steel bar.

Additionally theoretical examinations of the various stresses occurring within the materials during testing were undertaken and analysed to create a theoretical stress model capable of accurately predicting the behaviour of the system.

3 THEORETICAL INVESTIGATION

As part of the testing program undertaken, the timber was tested using guidance from BS EN 408 [5] so that the material properties could be obtained for use within the theoretical investigations. The results of the various tests can be seen below in Table 1 and were used throughout the theoretical analysis.

Table 1. Mean Mechanical Properties of GL28 Timber.

Test Orientation	Strength (N/mm^2)
Bending Strength	44.3
Compression Strength (Parallel to Grain)	42.8
Compression Strength (Perpendicular to Grain)	3.9
Tension Strength (Parallel to Grain)	26.6
Modulus of Elasticity (Parallel to Grain)	10600
Shear Strength	11.85

Previously extensive work has been conducted by Queen's University with regards to timber stress blocks and how they vary according to a range of factors. Patrick [6] developed stress blocks for singly reinforced glulam beams and it was expected that similar results would be found within this investigation as the pre-stressing would force the failure to occur within the compression zone of the timber, just as the reinforcement would. Figure 1 below shows the stress blocks developed by Patrick [6] which were used within this investigation.

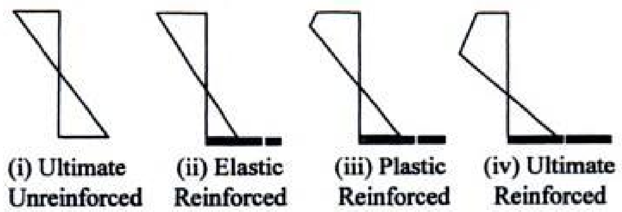

Figure 1. Stress Blocks for Unreinforced and Reinforced Beams, Patrick [6].

3.1 *Elastic Analysis*

The principle of linear elastic stress is a well-understood theory and is common within the concrete industry, where pre-stressing is a frequent occurrence. The theory has been applied to this process and can be split into three distinct sections. By applying a pre-stress force to the bar the stresses are initially going to be equivalent to the applied pre-stressing force divided by the cross sectional area of the timber beam.

Furthermore by placing the steel bar near the soffit of the beam the pre-stressing action is increased as an eccentricity is introduced, which induces favourable bending stresses. This additional stress is equivalent to the pre-stressing force multiplied by the eccentric distance, divided by the elastic modulus, z. This eccentricity causes a tensional force within the top fibres of the beam, whereas compression stresses are introduced to the bottom fibres, as shown in Figure 2.

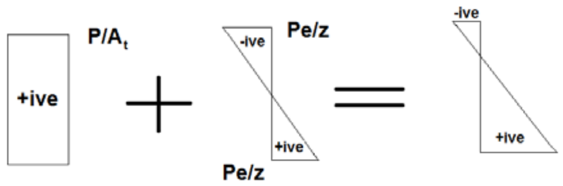

Figure 2. Stress Blocks for Eccentrically Added Pre-stressing.

As shown in Figure 2, above, the process of pre-stressing will introduce beneficial stresses into the beam, which will reduce or eliminate any stresses due to applied loads. Figure 3, below shows that any loading that is applied to the pre-stressed beam will initially have to overcome the stresses created by the pre-stressing process, meaning that the beam should be capable of withstanding a greater load than normally would be tolerated.

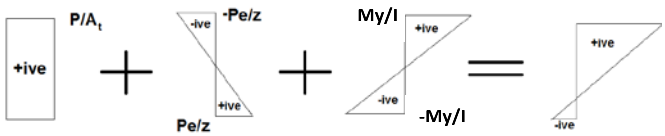

Figure 3. Stresses Induced by Pre-stressing and Load Application.

A spreadsheet was developed as a design tool, based upon the stress blocks discussed above. The initial allowable pre-stressing force was calculated by limiting the stresses to those that would remain within the timber's strength. Additionally using the principle highlighted in Figure 3, it was evident that further loading would be tolerated by the beam and it was therefore possible to calculate a value for this allowable increase.

3.2 *Deflection*

There are a number of theoretical advantages that may be appreciated in terms of the timber's deflection. The deflections experienced by a timber beam should be reduced by pre-stressing in the following ways:

- flexural stiffness will increase resulting in lower deflection under applied loads, due to the increase of the I value,
- the action of pre-stressing will induce a precamber into the beam, which will counteract any initial service deflection,
- it has been previously demonstrated that pre-stressing will cause a reduction in creep [7].

3.3 *Pre-stressing Force*

Before any experimental work was completed it was necessary to ensure the tensile forces acting within the reinforcing bar do not exceed its elastic limit, thus causing it to yield or deform. Although further investigation is required into this area, for the purposes of this investigation, simple calculations were completed to ensure that the bar could withstand the initial applied pre-stressing force.

3.4 *Plastic Analysis*

Information was gathered at the timber's ultimate limit state, which may be used in future research to predict plastic behaviour. As seen previously in Figure 1 the stress block corresponding to the ultimate state of the reinforced beam is of trapezoidal form. Figure 4, below, shows two stress profiles obtained from the experimental testing of the timber beam pre-stressed to 10 kN. The red line representing the stress profile just before failure, while the green line represents the profile just after rupture, when a tensile failure had occurred in the bottom laminate.

The profiles below, derived from vibrating wire gauges fixed at increments along the beams depth, verify the theory that the pre-stressed beam behaves in a similar manner to the singly reinforced beams investigated by Patrick [6].

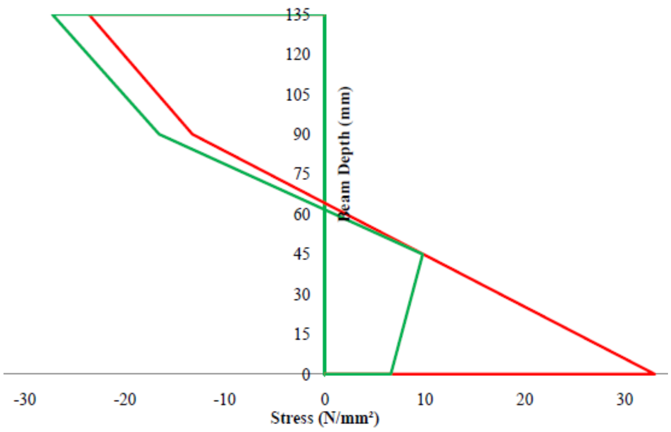

Figure 4. Ultimate Stress Block of Pre-stressed Timber.

4 EXPERIMENTAL TESTING

A large part of this research was developing a feasible pre-stressing method. Once a method had been developed and verified the testing program consisted of the following:

- 2 No. 45x135x2800 mm control beams, tested both elastically and to failure,
- 1 No. 45x135x2800 mm beam, tested elastically with varying pre-stress forces applied, finally tested to failure.

Again, as this was a pioneering investigation within the university it was decided to complete small scale tests, thus keeping the required pre-stressing forces to a minimum.

4.1 *Method of Pre-stressing*

As the method adopted throughout this investigation is an approach similar to post-tensioning, the steel rods were threaded through the beams length and secured at either end rather than being adhesively fixed along the length. This meant that initially the beam had to be split along its length to allow a groove to be routed to accommodate the bar. A 22 mm slip of timber was cut from the beam as this would correspond to a bar being inserted between the bottom two laminates on a large scale sample. As the steel bar used was to be 8 mm in diameter a 5 mm deep semi-circle was cut into each portion of the beam. Once it was evident that the steel bar could be installed comfortably into the void the timber was bonded together using a Rotafix gap filling epoxy and allowed to cure for 7 days.

As the pre-stressing forces used within this investigation were small, the largest being 10 kN, the method of pre-stressing was straightforward and achieved using a hollow core load cell and a spanner. As the steel bar was threaded a nut was placed on the bar and tightened until the load cell indicated the required force was acting through the bar. 20 mm thick steel plates were used at either end of the bar to ensure sufficient load spreading was achieved to avoid any end crushing of the timber. The method can be seen in Figure 5.

Figure 5. Pre-stressing Method and Apparatus.

4.2 *Testing Procedure*

Initially the unreinforced, control beams were tested in accordance with BS EN [5] where they were initially loaded with settlement loads and then finally tested to failure. The settlement load, designed to simulate the beam's previous working load, was determined to be 5 kN as this value would ensure the elastic limit was not reached. Once this process was completed the beams were tested to failure to allow data to be gathered regarding the timber's behaviour in the plastic region.

The beam that was to be pre-stressed was initially stressed by applying a 5 kN tensile load to the bar. The same elastic testing as above was completed and then the pre-stressing force was increased to 6 kN. This process was repeated for pre-stressing loads of 7, 8 and 10 kN, until the beam was tested to failure with the pre-stressing load of 10 kN applied.

The force acting within the pre-stressed bar will increase as the beam is loaded and it was this that determined the maximum applied pre-stressing force that would be used within this investigation. As the steel bars used were of 8 mm diameter they would only support an applied tensile load of approximately 22.0 kN. If the beam had failed due to a rupture of the steel bar, any gathered results would not have been relevant and it was therefore decided to limit the pre-stressing force to 10 kN to ensure that this scenario did not occur.

All the beams used within this investigation were tested using the Dartec Hydraulic Ram using a four point loading system, as shown in Figure 6, to replicate the bending that a uniformly distributed load would cause. To obtain as many results as possible from the limited testing conducted the beam's deflection was monitored using transducers placed at the centre span, while vibrating wire gauges were placed along the beams depth at the mid span to monitor the strains occurring throughout loading.

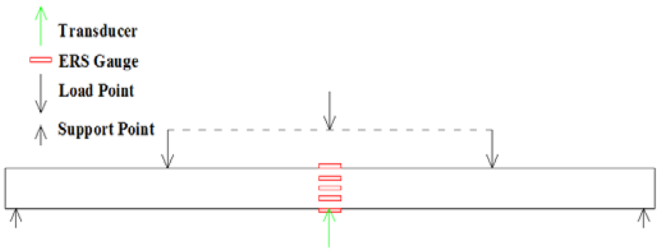

Figure 6. Diagram of Experimental Set-up and Gauge Positions.

5 RESULTS

5.1 Flexural Strength

As expected the unreinforced timber beams that were tested to provide a benchmark for this investigation failed with a tensile rupture occurring within the bottom laminates of the beam. The first beam failed at a load of 12.1 kN with the rupture beginning at a knot in the timber, situated on the soffit of the beam. The increased stress around the defect caused a split in the beam that quickly spread along the member's length, causing failure. The second control beam failed in a similar brittle manner, at 14.2 kN, with a failure occurring and quickly spreading throughout the beam's tensile region.

Comparatively, to the above failure values achieved by the unreinforced control beams, the 10 kN pre-stressed beam achieved a failure load of 17.75 kN, showing a strength increase of approximately 35% on average. Despite the increase in strength, however, the pre-stressed beam still failed in tension, with the failure originating at the location of a knot on the beam's soffit. Conversely, as the failure spread longitudinal cracks became visible on the top of the beam, indicating that some compression failure had occurred, further indicating the benefits of pre-stressing. If a larger diameter bar had been used in the investigation, allowing a greater pre-stressing force to be applied to the system, it is a logical assumption that the failure of the beam may have been forced to occur further into the compression zone of the timber, indicating that further research into this area would be beneficial.

5.2 Stiffness

In contrast to simply reinforced timber beams, one of the previously discussed advantages that it was believed pre-stressing would provide timber members was an increase in stiffness. As the beams stiffness is related to EI, the product of Young's modulus and the second moment of area, it is expected to increase with the inclusion of reinforcement.

Despite this, however, the results gathered from the experimental work were inconclusive, as although a slight increase in stiffness was observed when considered as a percentage the increase may be considered insignificant as the accepted value for the variability of timber is greater.

This indicates that further investigation into this area would be necessary before definite conclusions may be drawn as to whether pre-stressing has a positive effect on a beams stiffness.

5.3 Deflection

The deflection of the two unreinforced beams occurred as expected with the load deflection graphs producing straight lines, as shown in Figure 7. As the load applied is directly proportional to the deflection up until the point of failure this indicates that the beams experience a sudden, brittle failure, as is expected with timber and as was witnessed during the experimental testing.

Again comparatively, the pre-stressed beam experienced a number of benefits from being stressed prior to and following the application of a load. Initially as the pre-stressing force was transferred from the steel bar into the timber the beam flexed upwards, as Figure 3 would indicate, the combination of stresses would cause the beam to arch. This precamber is one of the benefits predicted from the pre-stressing process. By causing the timber to initially flex upwards any load applied would initially have to overcome this 'positive' deflection, before any service deflection is experienced, thus the pre-stressing is effectively reducing the overall deflection experienced by the member.

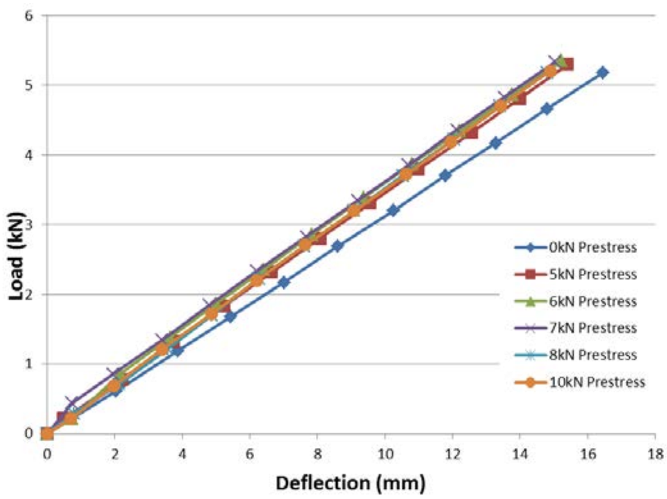

Figure 7. Total Load Deflection Graph for Beam with Varying Pre-stressing Force (Does not Illustrate Effect of Precamber).

Additionally, further analysis of the results indicates that a small degree of ductility within the failure is experienced by the pre-stressed members, indicating further benefits that the pre-stressing process would provide.

5.4 Stress and Strain

As experimental data relating to the strains and therefore the stresses experienced by the pre-stressed beams were gathered, conclusions may be drawn between the theoretical and experimental findings. By considering the results from the theoretical approach, discussed in section 3.1, against the data gathered by the vibrating wire gauges during the testing procedure the below tables may be formulated.

Although the natural variations in timber, combined with the expected small changes in the stress values make it difficult to derive firm conclusions some deductions may be possible.

As shown in both Table 2 and 3 the addition of a pre-stressing force does decrease the stresses experienced by the timber, indicating that the pre-stressing force is being transferred to the timber and positively affecting it by allowing it to resist the applied loading more readily.

Table 2. Experimental and Theoretical Top Fibre Stresses.

Pre-stress Force (kN)	Applied Load (kN)	*Experimental Top Fibre Stress (N/mm^2)	Theoretical Top Fibre Stress (N/mm^2)
0	5.18	12.1	12.4
5	5.30	12.5	12.0
7	5.33	12.0	11.7
10	5.20	12.1	11.2

*Values calculated from experimentally obtained strains, E = 10600 N/mm^2 (from experimental testing)

Table 3. Experimental and Theoretical Bottom Fibre Stresses.

Pre-stress Force (kN)	Applied Load (kN)	Experimental Bottom Fibre Stress (N/mm^2)	Theoretical Bottom Fibre Stress (N/mm^2)
0	5.18	-11.6	-12.4
5	5.30	-10.9	-10.4
7	5.33	-10.4	-9.4
10	5.20	-10.4	-8.2

Despite this, however, more beam testing, encompassing a larger variance of the applied pre-stress force, is necessary before any conclusions may be drawn with regards to both the experimental and theoretical findings. As shown above the theoretical values derived from the stress profiles previously discussed vary in comparison to the experimental data. Interestingly this variation is the most pronounced when considering the bottom fibre stresses, where the steel bar is located.

Again this may have arisen for a number of reasons and further testing is essential before any firm conclusions are made, however these tests have shown that the experimentally obtained stress block, shown in Figure 8, confirms the basic principle and form used by this approach.

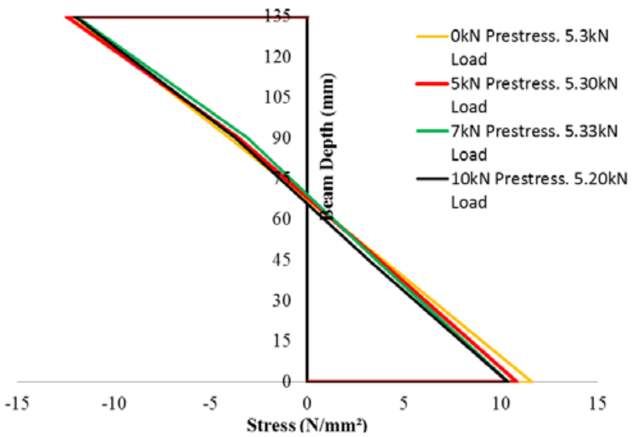

Figure 8. Stresses Experienced by a Beam at a Load of Approximately 5 kN at Varying Pre-stressing Forces.

6 CONCLUSION

Although further research into this subject is necessary before definite conclusions may be drawn there are several positive indications that may be drawn from this investigation. Initially pre-stressed beams were successfully manufactured and tested in the university, opening this area of research to future investigations.

Additionally several positive structural advantages were found when pre-stressing was applied to reinforcement threaded through timber members:

- an applied pre-stressing force of 10 kN reduced net deflections in the elastic region by 36% compared to unreinforced members
- the ultimate capacity of a pre-stressed timber beam was seen to be 35% greater, on average, than unreinforced members
- there are indications that the failure mode of the pre-stressed beams shifted from a brittle mode to a more ductile form, which is more desirable in modern design.

Further to the structural advantages, theoretical research has shown that simple linear elastic theory can be used to suitably predict the stresses that will occur in a pre-stressed beam throughout the elastic region.

The previously discussed benefits of pre-stressing timber are strong indicators that this is a viable method of strengthening and that further research should be completed in this area.

6.1 *Continued Research*

Continued work relating to pre-stressing timber is currently being completed within Queens University Belfast and it is hoped that a feasible method and theoretical approach will successfully be developed in the future.

6.2 *Future Work*

There are areas of research that must be addresses before pre-stressing timber would become industrially viable. When considering this investigation a more conclusive set of results may have been achieved if a stronger pre-stressing material had been available, as this would have allowed a more effective pre-stressing force to be applied prior to loading. The emphasis of the further work, however, should be on the long-term behaviour of pre-stressed timber beams, including monitoring for effects such as creep and loss of pre-stress. Also investigations into the variations between pre-tensioning and post-tensioning should be explored, as the addition of a bonded bar may considerably affect the results. Finally, as previously mentioned further work into the theory of increased stiffness and the correlation between the pre-stressing force and stiffness should be further investigated.

ACKNOWLEDGMENTS

This work was made possible by the help of Queen's University Belfast and the authors would like to thank all the technical members of staff involved in the process.

REFERENCES

[1] Gilfillan, J.R., Gilbert, S.G. & Patrick, G.R.H. 2003, The use of FRP composites in enhancing the structural behaviour of timber beams, *Journal of Reinforced Plastics and Composites*, vol. 22, no. 15, pp. 1373-1388.

[2] Negrao, J. Brunner, M. & Lehmann, M. 2008. Pre-stressing of Timber. Bonding of Timber: Core document of the COST Action E34. Vienna: University of Natural Resources and Applied Life Sciences.
[3] Martin, Z.A. Stith, J.K. & Tingley, D.A. 2000. Commercialisation of FRP reinforced glulam beam technology. Proceedings of the 6th world conference on timber engineering. Whistler Resort, Canada, Date Unknown. UBC Press
[4] Brady, F. & Harte, A. 2008, Prestressed FRP Flexural Strengthening of Softwood Glue-Laminated Timber Beams, 10 th World Conference on Timber Engineering (WCTE), 2 - 5 June 2008.
[5] British Standards Institution, 2010. *BS EN 408:2010 Timber structures. Structural timber and glued laminated timber. Determination of some physical and mechanical properties*: BSI
[6] Patrick, G. 2004, The structural performance of FRP reinforced glued laminated beams made from homegrown Sitka spruce, Thesis. Ph.D. (Faculty of Engineering), Queen's University of Belfast.
[7] Dolan, C.W. Galloway, Z. & Tsunemori, A. 1997. Prestressed Glue-Laminated Timber Beam Pilot Study. *Journal of Compositics for Construction*. Issue 1 Vol 1. pp.10-16.

Iarnród Éireann emergency response procedures to flood events around bridges

Cathal Mangan[1] , Brian Devlin[2]
[1] Iarnród Éireann
[2] CEI Collins Engineers Ltd
email: cathal.mangan@irishrail.ie, bdevlin@collinsengr.com

ABSTRACT: The Iarnród Éireann (IÉ) railway network is approximately 1,919 route kilometres in length, with seven routes radiating from the two main railway terminals in Dublin (Connolly Station and Heuston Station). Physical assets include in excess of 6,000 safety critical infrastructure assets including 1,204 overbridges and 1,926 underbridges in the network, and of the 1,926 underbridges, 780 are viaducts. IÉ is responsible for managing the design, installation, testing, inspection, maintenance and renewal of these physical assets and for the safe provision of these for the operation of rail services. Following the Malahide Viaduct Collapse in August 2009, IÉ has introduced improvements to their bridge management and inspection programme. In particular, ÍE is currently developing a documented risk-based approach for flood and scour risk to railway structures through:

- Monitoring of scour risk at sites through scour depth estimation, debris and hydraulic loading checks, and visual and underwater examination;
- Provision of physical scour/flood protection for structures at high risk;
- Imposing of line closures during periods of high water levels where effective physical protection is not in place.

This paper describes the documented procedures that IÉ has put in place and implemented during flood occurrences around their bridges to ensure the safety of the travelling public. The paper also discusses the field techniques used by CEI Collins Engineers Ltd to check for potential scouring and undermining of the substructure elements at time of major flooding or immediately following such an event. Examples of such activities are outlined for bridges affected during the major flooding in Dublin City and the Wicklow area in October 2011 and flooding that occurred in November 2009 in the western area of the country.

KEY WORDS: Scour; Flooding; Bridge; Hydraulic Action; Infrastructure Asset Management System; Soundings; Underwater Inspection; Acoustic Imaging.

1 INTRODUCTION

IÉ has maintenance responsibility for over 6,000 safety critical infrastructure assets of which 780 are viaducts.

It is the policy of Iarnród Éireann that risks posed by Flooding, Scour, Wave and Tidal Action (collectively referred to as Hydraulic Actions) are managed proactively to control the potential risks to railway infrastructure and operations.

This applies to all structures that may be subjected to hydraulic action for which Iarnród Éireann has responsibility.

Section 2 of this paper describes the documented procedures that IÉ has in place to control the risk from general flooding events which have the potential to cause scour or instability. The inspection techniques used by CEI Collins Engineers Ltd (Collins) to check for potential scouring and undermining of the substructure elements during and immediately following flood events are discussed in section 3, along with examples of such activities undertaken following major flooding events in 2009 and 2011.

2 FLOOD AND SCOUR RISK DOCUMENTED PROCEDURES

2.1 Standards and Processses

A number of standards and processes are in place to proactively manage flood and scour as part of the asset management system. Structures are inspected and managed in accordance with these standards and processes:

a) CCE-TMS-415 – Flood and Scour Management Standards - This standard sets out the management requirements for controlling the risk at flood-and-scour vulnerable locations and the risk from general flooding which has the potential to cause scour or instability.
b) CCE-TMS-360 – Track and Structures Inspection Requirements – This standard sets out the requirements for the inspection of track and structures within the Chief Civil Engineer Department.
c) CCE-STR-STD-2100 – Technical Standard for Structural Inspections – This standard sets out the requirements for structural inspections within the CCE Department and includes the requirement for planned scour inspections.
d) CCE-TMS-361 – Technical Standard for Track Patrolling – This standard sets out the requirements for tack patrolling within the CCE Department.
e) CCE-TEB-2011-6 – This technical bulletin highlights the availability of Six Day weather Forecasts from Met Éireann on Iarnród Éireann’s internal IT system.
f) IÉ Draft Weather Management Protocol – This defines conditions and relevant actions associated with different weather events as well as areas of responsibility.

The following key roles exist within the Chief Civil Engineer Department:

- Technical Manager (TM) – responsible for track and structures safety on the IÉ network and for setting the standards associated with flood management and ensuring they are implemented.
- Senior Track and Structures Engineer (STSE) – 3 of these regionally based across the 3 Divisions of the network and with each responsible for track and structures safety in their areas. They are responsible for ensuring maintenance and renewal to work assets are carried out in line with standards and for identifying and managing risks associated with assets.
- Infrastructure Manager (IM) - 3 of these regionally based across 3 Divisions of the network and with each responsible for the undertaking of maintenance and renewal works to assets in line with standards and for carrying out risk mitigation measures identified by the STSE.

2.2 Identification of flood-and-scour vulnerable locations

A list is maintained of all flood-and-scour vulnerable locations. These consist of locations or individual structures. These structures or locations are identified and recorded in IAMS, the Infrastructure Asset Management System, as flood-and-scour vulnerable locations.

Structures and locations considered for listing as flood-and-scour vulnerable locations are:

a) Bridges and culverts over watercourses where scour has been shown to be an issue in the past or is considered to be likely.
b) Earthworks and structures, including retaining walls adjacent to watercourses or areas subject to flooding, which are considered to be vulnerable to damage from flooding/scour effects.
c) Coastal defences likely to be subject to the effects of flooding events or tidal and wave action.
d) Other structures likely to be subjected to the effects of flooding events or tidal and wave action, e.g. openings in earthworks which may allow the passage of water during a flooding event.
e) Locations where there is a known history of flooding or scour.

The list is reviewed by the STSE, in conjunction with the IM on an annual basis. Following this, any new locations or structures added to the list are reviewed and classified. Any new high risk locations or structures are notified to the TM. All changes are then updated in the Infrastructure Asset Management System.

All structures or locations identified as flood-and-scour vulnerable locations are classified as Low, Medium or High based on the risk due to the relevant hydraulic action.

Appropriate control measures and a cycle for review of the classification are applied as per Table 1 below.

The review is intended to establish if the existing classification is still considered to be an accurate reflection of the on-site situation and is therefore still valid. It should identify any significant changes which have occurred. Where this is the case, the classification should be updated.

A review of the classification is carried out by the STSE in the following instances:

a) When work has been carried out on the structure at a point below the highest recorded flood level or at supports that may reasonably be expected to be exposed to hydraulic action.
b) When work has been carried out on the structure that may affect its susceptibility to scour.
c) When there is evidence of changes to flow characteristics around the structure.
d) When debris has struck, been trapped against or adjacent to the structure.
e) When major works affecting the watercourse have taken place within 400 m of the structure (e.g dredging, construction of new structures in the watercourse).
f) When there is evidence that the watercourse or coastline has changed or been altered and this may affect the susceptibility of the structure to scour/flooding.
g) Following every underwater inspection.
h) As determined necessary by the STSE.

If none of the conditions outlined above apply, then the review cycle shall be as per Table 1.

The hydraulic classification is recorded and maintained in IAMS.

Table 1: Review of Classification of Flood-and-Scour Vulnerable Locations

Hydraulic Classification	**Control Measure**	**Classification Review Cycle (Max intervals)**
Low / Insignificant Risk	No specific mitigations required.	Every 6 years and following every known flood or extreme sea level event in the vicinity or following in the events outlined below.
Medium Risk	Additional control measures may be considered for the management of risk at each medium risk location or structure at the discretion of STSE.	Every 3 years and following every known flood or extreme sea level event in the vicinity or following in the events outlined below.
High Risk	a) The Structure or location shall be recorded on the STSE's Track & Structures Risk Register. b) Additional control measures shall be considered for the management of risk at each high location or structure. c) A review of the structure / location shall be carried out by the STSE to consider the options for protective or remedial works necessary to reduce the hydraulic classification. Works shall be implemented on a practicable and risk-prioritised basis.	Every 1 year and following every known flood or extreme sea level event in the vicinity or following the events outlined below.

2.3 Measures for consideration at high-risk flood-and-scour vulnerable locations

Additional measures for consideration at high-risk locations or as required by the STSE are as follows:

a) Weather alerts and protocols that are relevant to the vulnerable location.
b) Identification of the structures to be checked/monitored within the location if specific conditions occur.
c) The parts of the structure not affected under normal conditions of flow.
d) Defined trigger levels and corresponding actions – e.g. defining the level to which the water may rise before the line must be closed. This may be indicated by installing specific marker plates on vulnerable structures or locations. Signs installed should be located such that they may be read from a position of safety during an extreme weather event.
e) Installation of monitoring equipment to provide early warnings. If remote monitoring systems are installed, define clear lines of responsibility, threshold values and associated actions, limits of the monitoring system.
f) A safe means of access and positioning of suitably competent persons to monitor the situation at the site – this may involve requirements to remain on site or carry out checks on a frequent or ongoing basis.
g) A procedure for closing and re-opening the line to traffic with clear lines of communication and responsibility.
h) Any other actions necessary to manage the safe operations of the railway until conditions have returned to normal and all affected structures and track elements have been checked, e.g. speed or traffic restrictions, monitoring, increased frequency of inspections.

The additional measures above may be employed at the discretion of the STSE in planning the actions required or suitable in certain situations in order mitigate risks resulting from flood or scour. Suitable additional measures are agreed between the STSE and the Infrastructure Manager (IM).

Where additional measures have been arranged or implemented, a review of these measures is undertaken jointly be the STSE and the IM on an annual basis or after any flood or extreme sea level event in the vicinity. This is to ensure that they are still appropriate for the anticipated conditions and to allow any ‘lessons learnt’ from actual events to be incorporated.

2.4 Management of Risk During Flood and Scour Events

Additional measures may be required at structures or locations identified at high risk or as required by the STSE. The requirements of the relevant patrolling, track and structure standards also apply.

2.4.1 Weather Forecasts and Weather Management Protocol

a) Six-day weather forecasts are available for reference on the internal Iarnród Éireann IT systems.
b) Iarnród Éireann also operates a weather management protocol for the management of services and operations during periods of severe weather that may affect rail services and assets. The weather management protocol outlines the actions to be taken and by whom when a Met Éireann weather alert is received.
c) Met Éireann weather alerts are sent to Central Traffic Control (CTC) when threshold values are exceeded or expected to be exceeded. CTC then issue that alert to the appropriate Line Managers for all departments through the CTC text alert system.

2.4.2 Track Access Restrictions

The IM or nominated deputy is responsible for putting in place any restrictions such as emergency or temporary speed restrictions or closing the line as he may determine to be necessary based on conditions identified by Patrol Gangers, Permanent Way staff or other staff as a result of a flood or scour event.

In all cases, track access shall be removed from the affected section of line if any of the following conditions occur or are observed:

a) Flooding to a depth of more than 80 mm above the top of the lowest rail.
b) Water levels approaching the bearing level of a flat soffit bridge structure or the springing level of arch bridges.
c) Any visible or suspected damage has been caused to the structure e.g. impact damage caused by debris or waterborne objects.
d) Significant accumulation of debris (e.g. trees) against a bridge or structure.
e) Water overtopping or penetrating behind wingwalls.
f) Abnormal changes in turbulence at piers or abutments.
g) Any apparent damage to coastal defences (e.g. large gaps appearing in rock armour) or undermining/destabilisation of embankments or retaining walls.
h) When it is likely that water or overtopping waves may have caused damage to the track support system.
i) In any other case as instructed by the STSE or deemed necessary by the IM/RM or his nominated representative.

2.4.3 Reinstating Track Access

If a line has been closed or access restricted due to concerns over flooding or scour, then arrangements are made to carry out an appropriate inspection of the structures likely to be affected prior to reopening the line or returning the line to normal operation (this may include an underwater inspection or other specialist activity). Note that:

a) Scoured areas may refill with weaker material as water flows decrease; in such cases, a visual examination may not be sufficient to identify any undermining of supports.
b) Normal access to the structure to be inspected/examined may be altered or restricted and special arrangements may need to be put in place to cater for this.
c) Consideration should also be given to the prevailing conditions and how these may impact on inspection/examination e.g. daylight, darkness, reduced visibility etc.

Structures should be examined for the following:

a) Signs of loss of material or undermining.
b) Movement (e.g. overturning, sliding or uplift); track or structure misalignment; deformation or changes in geometry; tilting or bulging.
c) Noted or suspected collision damage.

d) Debris in watercourse near structures.
e) Unusual flows (turbulent or high water flows).

Prior to reinstating track access, remedial or mitigation measures are implemented as required, based on the results of the inspection. As part of the process and where considered safe to do so, a light engine may be useful to examine or prove the line prior to the track being reopened.

Monitoring, supplementary inspections or other control measures may be retained in place by the Per way Inspector or IM/RM until conditions and water levels return to normal.

3 EMERGENCY INSPECTION TECHNIQUES

The most common method of inspecting for scour at bridges is to take soundings around the substructure units and the area adjacent to the bridges. Lead lines and sounding poles are commonly used for shallow streams, but electronic depth sounders (sonar), some in conjunction with surveying total stations or Global Positioning Systems (GPS), are also routinely employed. For larger waterways, hydrographic survey systems are also utilised. Hydrographic survey software makes it relatively easy to plot sounding lines, contours and cross sections. Refer to Figure 1 below.

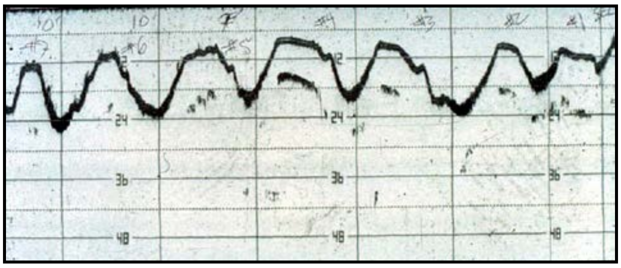

Figure 1. Example of Soundings Plot along Bridge Fascia (vertical lines indicate upstream noses of piers).

Unfortunately, the greatest scour depths at a bridge will occur during periods of extreme flow, when it may not be safe to be on the water in a boat. Also, at that time, the current may be too strong for engineer-divers to undertake an inspection, use a lead line or sounding pole, and turbulence, especially near piers, when clay materials may be suspended in the water column, could preclude the use of electronic depth sounders. As the water level recedes and the current velocities decrease, infilling may occur as equilibrium is re-established. Taking soundings immediately after a flood flow is better than much later, but even then the soundings may not indicate the scour depths that occurred during the flood.

During the major flooding event that occurred in November 2009 in the western part of Ireland, and in particular around the area of Ballinasloe, County Galway, IÉ had concerns about a number of structures which resulted in Track Access Restrictions.

Collins was engaged by IÉ to undertake monitoring of structure UBG 125 which is located over the River Suck in Ballinasloe on the Dublin-Galway Railway line. Refer to Figure 2 below.

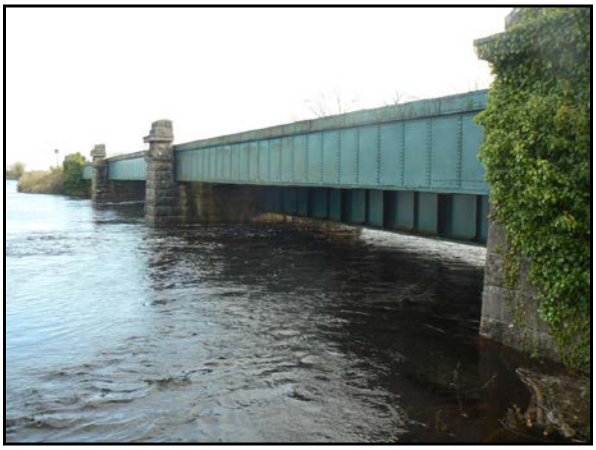

Figure 2. UBG 125.

The very high currents at the time prevented the deployment of engineer-divers to undertake an underwater inspection of the substructures elements to check for potential scouring and undermining.

Consequently, Collins utilised additional equipment to aid in the assessment of the structure and surrounding channel bottom underwater.

One simple technique adopted was the use of an echo-sounder connected to a steel pole. This was lowered from the bridge deck to the water level and channel bottom soundings were taken along the face of each pier and abutment and between the structure units at the upstream and downstream elevations of the bridge. As IÉ had commissioned a regular underwater inspection of the bridge four years previous, the channel bottom level at that time had already been recorded. This allowed Collins' engineer-divers to undertake a direct comparison between the channel bottom elevation recorded during the flooding event with those of 2005. The findings of the comparison confirmed that no major channel bottom movement was occurring. Refer to Figure 3.

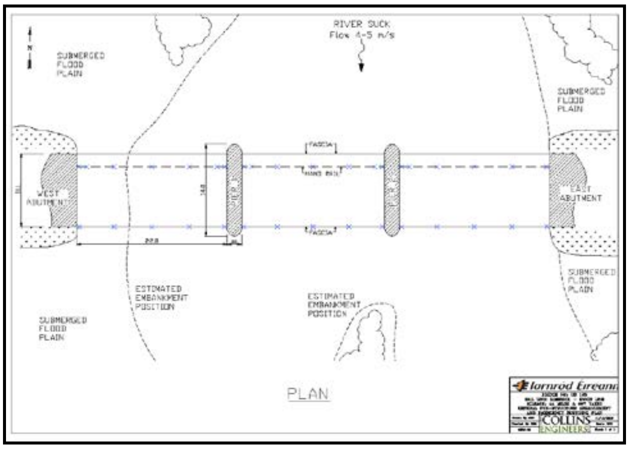

Figure 3. Channel Bottom Sounding Plan.

A secondary tool deployed to the bridge site was a Kongsberg Mesotech MS1000 high resolution scanning sonar device (as Per Figure 4) to allow underwater acoustic imaging of the substructure elements to be undertaken. Collins custom built a support apparatus to properly position and stabilize the sonar unit to optimize accuracy during both imaging and profiling scanning operations.

Figure 4. Kongsberg Mesotech MS 1000 High Resolution Scanning Sonar Device.

Use of the acoustic imaging allowed a high resolution scan to be performed of the underwater portions of the bridge, as well as the channel bottom profile. Refer to Figure 5 below. The scan, undertaken from deck level enabled IÉ to be shown exactly what the structure condition underwater was, regardless of water clarity and this technology assisted in determining the integrity and stability of the bridge during the major flood event.

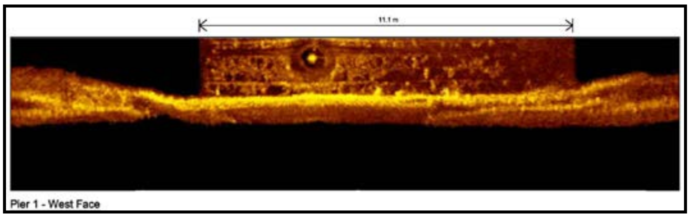

Figure 5. Acoustic Image of Pier 1 at Channel Bottom.

A second major flood event that impacted upon IÉ bridge infrastructure occurred in the Dublin and Wicklow areas in October 2011. Collins was again engaged to mobilize quickly to 11 key structures as a result of unusually high river flows at these locations.

During the emergency inspections, Collins' engineer-divers identified a drop in channel bottom elevation at UBR 63 which spans over the River Dodder in Ballsbridge. Refer to Figure 6 below.

Figure 6. UBR 63.

This immediately highlighted a potential problem at this structure. As the high flows had receded at this point, Collins mobilized a four person engineer-diver team to undertake an underwater inspection of both abutments. With the aid of a measuring staff, the engineer-divers identified undermining to the south abutment.

In accordance with reporting procedures, IÉ were immediately informed and due to the extent of undermining detected, the railway line was closed.

Rehabilitation works to the abutment commenced immediately and the line was reopened two weeks later.

Underwater Inspectors conducted on the remaining 10 structures using engineer-divers, as the waters had quickly receded, identified some minor lowering of the channel bottom at several of the bridges.

4 CONCLUSIONS

It is vitally important that all Bridge Owners put in place Flood and Scour Risk Management Procedures to protect their infrastructure, as much as practically possible, from both progressive deterioration and catastrophic failure, similar in nature to those currently being adhered to by Iarnród Éireann.

REFERENCES

[1] E.Ballance, C. Mangan and F. Cooney, CCE-TMS-415 – *Flood and Scour Management Standards*, Version 1, 2011.

Long Life Bridges

E.J. O'Brien[1], A.J. O'Connor[1], M. Tucker[1]
[1] Roughan & O'Donovan Innovative Solutions, Arena House, Arena Rd, Sandyford, Dublin 18, Ireland.
email: eugene.obrien@rod.ie, alan.oconnor@rod.ie, mark.tucker@rod.ie.

ABSTRACT: Bridges, like many Civil Engineering structures, are designed quite conservatively – the probability of dying due to collapse of a new bridge is about 1 in 10 million. Part of the reason for this conservatism is that adding extra strength to a bridge when it is being built is not expensive. For older bridges however, the situation is quite different. There is a huge difference between the cost of strengthening an existing bridge and not doing so. It is frequently possible to prove that a bridge is perfectly safe despite having deteriorated since it was first built. Sometimes the deterioration is in a non-critical element of the bridge and often the bridge has significant reserve capacity due to conservatism in the initial design process. Long Life Bridges investigates the use of probabilistic techniques in analysing the performance of bridges. This approach reduces the conservatism present in current deterministic methods, particularly in the Dynamic Amplification Factor (DAF) employed in the code. This will allow bridges to be kept in service that would otherwise have been deemed unsafe preventing unnecessary repair or replacement works and resulting in significant savings for the bridge owner.

KEY WORDS: Bridges, probabilistic analysis, dynamics, life cycle evaluation.

1 INTRODUCTION

Transportation infrastructure is a foundation stone for any developed economy. For Europe in particular, the single market depends on an effective transportation system to bring together people and to facilitate trade across the entire euro zone. With a huge stock of ageing bridges present on the European transport network, many of these structures will soon need maintenance/intervention strategies to optimize their remaining service life. Across Europe there are a significant number of bridges that are vital to the economies they serve, and which, if taken out of commission would have a devastating impact on local, national, and international economies. Take for example, the Firth of Forth Bridge in Scotland which connects Edinburgh to Fife (Figure 1).

Figure 1. Forth Road Bridge, Scotland.

This bridge, which opened in 1964, is a vital element of Scotland's transportation infrastructure and is of prime importance for the local and national economies. Due to inadequate maintenance strategies, the bridge, which was designed to be serviceable up to 2084 was found to be undergoing significant deterioration, with the result that by 2017 it was predicted that it would no longer be able to safely carry vehicular loading. As a result a new bridge is currently under design.

Traditionally, this replacement of infrastructure, usually at the end of its design life, has been the adopted strategy. However, advanced analysis techniques, which *Long Life Bridges* aims to exploit, now exist to accurately assess and identify, on an ongoing basis, maintenance and repair strategies that would prevent a recurrence of the Forth Road bridge scenario. Normally, due to conservatism in their initial design, many bridges may have sufficient reserve capacity to remain in service for an extended period of time beyond their initial design life. The goal of the *Long Life Bridges* project is to develop techniques to extend the lives of these bridges. It will allow identification of old bridges that are safe to remain in service and those that need maintenance plans to optimise their remaining life. In times of economic recession this is particularly important, ensuring the maximum return possible from the existing bridge infrastructure as opposed to undertaking expensive new design and build projects. *Long Life Bridges* aims to deliver:

- More road and rail bridges being proven to be in a safe state.
- Higher speeds on our (non-high-speed) railway lines.
- Less demand for non-renewable and carbon intensive resources.
- Less cost associated with achieving these goals.

The project is a collaboration between two Small/Medium Enterprise (SMEs); Roughan and O'Donovan consulting engineers in Ireland (the consortium leaders), and Phimeca in France, and two university partners; The Royal Institute of

Technology, KTH, in Stockholm, Sweden, and Aalborg University in Denmark. The partnership brings together experts in the fields of structural assessment, probabilistic analysis and risk quantification from both academic and industrial backgrounds. Three main research threads are studied in the project: Bridge Dynamics, Life Cycle Evaluation and Fatigue. These topics are discussed in the following sections.

2 BRIDGE LOADING AND DYNAMICS

A bridge is safe if the stresses due to the applied loads are less than its capacity to resist those stresses (load < resistance). Many assessments of bridge safety – with or without dynamics – come back to this basic point and calculate some indicator of the probability that load is less than resistance. It can be argued that both sides of this equation – load and resistance – are equally important. Site-specific measurement of traffic load and quantification of the associated uncertainty [1] has great potential as there are many bridges where the actual load is much less than that for which the bridge was designed. Recent improvements in Weigh-In-Motion (WIM) technology [2] have made this possible, by providing road authorities with large databases of vehicle weights, axle configurations and inter-vehicle gaps. Even with years of WIM data, combinations of vehicles can occur in the lifetime of a bridge that were not recorded. To comprehensively explore the complete design space of loading scenarios, most researchers simulate many more loading scenarios than measurement would allow and apply statistical approaches to the results. The peaks over threshold approach [3], Rice level-crossing technique [4] and extreme value probability distribution fits [5] have been used to extrapolate from simulated results to find characteristic maximum loading effects. The variability in results can be significant – all of these processes are essentially extrapolations from data collected over a relatively small time to a very large return period.

This branch of the *Long Life Bridges* Project deals with bridge dynamics. There is a substantial body of literature on vehicle/bridge dynamic interaction [6, 7, 8] but most of it is deterministic in nature. Even in the derivation of the Eurocode, a probabilistic model was used to represent the uncertainty in static loading and simple Dynamic Amplification Factors (DAFs) were applied to the result. A small number of researchers, including the authors, have been developing probabilistic approaches to the dynamic interaction between traffic and bridges [9, 10]. There is great potential in this as the Eurocode factors range from 20% to 70% (see Figure 2) whereas the true dynamic amplification is generally less than 10%. By finding the true dynamic allowance, bridges can be safely retained in service that would otherwise be replaced or strengthened. Equally, for railway bridges, trains can be allowed to travel at higher speeds than would otherwise be allowed.

The evaluation of bridge dynamics is most often studied using the DAF. This is the ratio of the total load effect to the static load effect for a particular loading scenario, expressed in equation 1. Values of DAF as high as 4 have been recorded by Prat [11].

$$DAF = \frac{LE_{\text{Total}}}{LE_{\text{Static}}} \tag{1}$$

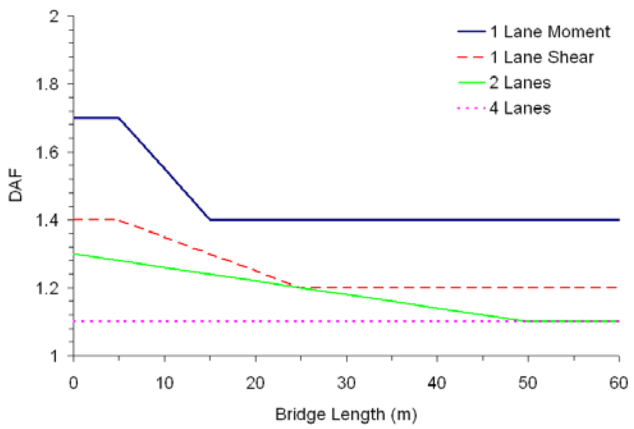

Figure 2. Eurocode DAFs.

However, this method makes the assumption that the maximum total load event also results in the maximum static load event which may or may not be the case. An alternative measure of dynamics, known as the Assessment Dynamic Ratio (ADR), recognizes the reduced probability of both the static and total load effect occurring simultaneously [5]. This measure of dynamics is defined as the ratio of the characteristic total load effect, to the characteristic static load effect, described by equation 2.

$$ADR = \frac{\tilde{LE}_{\text{Total}}}{\tilde{LE}_{\text{Static}}} \tag{1}$$

The characteristic value is the maximum expected load effect for all loading scenarios for the specified return period, typically 1000 years. The ADR method provides a less conservative approach than the more traditional DAF, whilst ensuring an adequate allowance for bridge-vehicle interaction. In *Long Life Bridges* a greater understanding of how to quantify the uncertainty associated with bridge dynamics will be developed. The theory outlined in this section has been applied successfully to road bridges. In the *Long Life Bridges* project it will be extended to assess the dynamic behaviour of railway bridges which have important differences such as absence of road surface roughness, presence of ballast and less variability in vehicle properties and in speeds. A semi-active damping system will also be developed to reduce the risk of dynamic excitation.

3 LIFE CYCLE EVALUATION

Life Cycle Analysis (LCA) has been developed on the basis of statistical decision theory and applications of the general theory to infrastructure systems, especially bridges, which have been described by, for example, Frangopol et al. [12], Ang & De Leon [13] and Ellingwood [14]. All uncertainties, and all costs and benefits in the life cycle are accounted for. The main objective is to minimize the total expected costs by optimising the maintenance actions taken during the design lifetime of the structure. Figure 3a shows the life cycle performance of a structure with no intervention measures, with Figure 3b illustrating the effect of preventative and corrective actions.

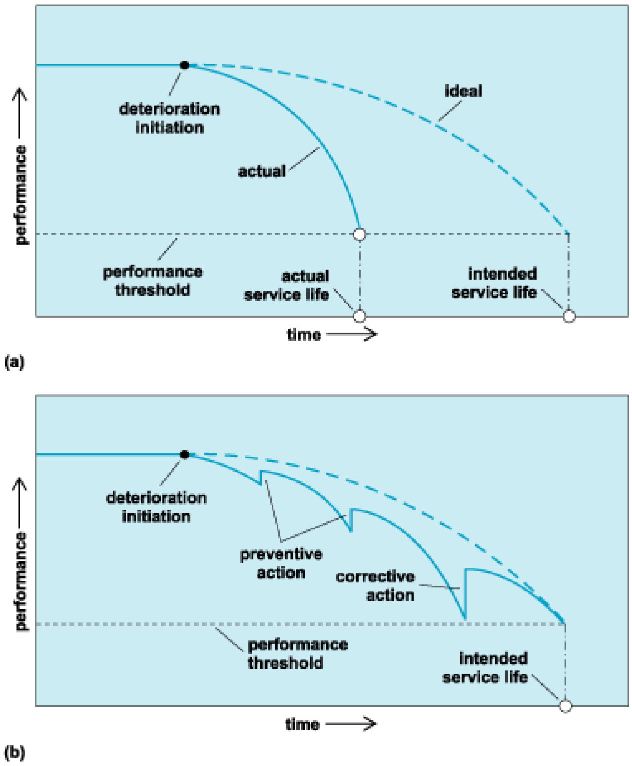

Figure 3. Optimisation of life cycle performance.

Sustainability aspects can be included using the principles in the risk assessment guideline of the Joint Committee on Structural Safety [15]. Probabilistic life cycle evaluations have also been applied for fixed offshore structures by, for example, Sørensen & Faber [16]. The results show that the total life cycle costs related to these structures can be reduced significantly if strategic planning of inspection, maintenance and repair is performed. Reduction of the total life cycle costs will reduce the total project costs but will also reduce the use of limited non-renewable material resources.

As part of *Long Life Bridges*, LCA techniques will be applied to calculate the probability of a bridge failure. Generally, this is a calculation at one specific point in time indicating as to whether or not the bridge in question, in its current condition, is safe to remain in service. More recently, consideration of the complete remaining life of the bridge, allowing for its deterioration through time, is the state of the art approach. *Long Life Bridges* will investigate the use of probabilistic measures in the assessment of bridges and implement them in a case study. Focus will be given to development of a probabilistic framework for the whole life assessment of new cable stay bridges, such as the Boyne Bridge shown in Figure 4, designed by *Long Life Bridges* consortium leader Roughan and O'Donovan.

Figure 4. Boyne Bridge, M1 Dublin – Belfast.

4 FATIGUE EVALUATION

The evaluation of fatigue in civil engineering structures (including bridges) often involves significant uncertainties as investigated by, for example, Sorenson et al. [17]. These uncertainties should be taken into account in the design process by using a probabilistic approach from which the reliability of the structure can be estimated.

Sørensen & Toft [18] divide the uncertainties related to fatigue design into physical, model and statistical uncertainty which can be estimated from tests using classical statistical methods. During the structure's service life, information from monitoring can be used to update the reliability using Bayesian methods as described by Faber et al [19].

This branch of *Long Life Bridges* will develop a probabilistic framework for fatigue design of steel bridges building on the fatigue model described by Paris' Law (Figure 5) which relates the crack growth to the number of stress cycles. The graph is split up into three distinct regions. Region 1 is the threshold zone where below the value of ΔK_{Th} cracks do not propagate, while the linear behaviour in region 2 represents Paris' Law (note the logarithmic scale on both axes), which is expressed as:

$$\frac{da}{dN} = C\left(\Delta K\right)^{m} \tag{2}$$

where a is the crack length, N is the number of cycles, ΔK is the range of the stress intensity factor and C and M are material factors. Finally region 3 represents the zone where failure occurs.

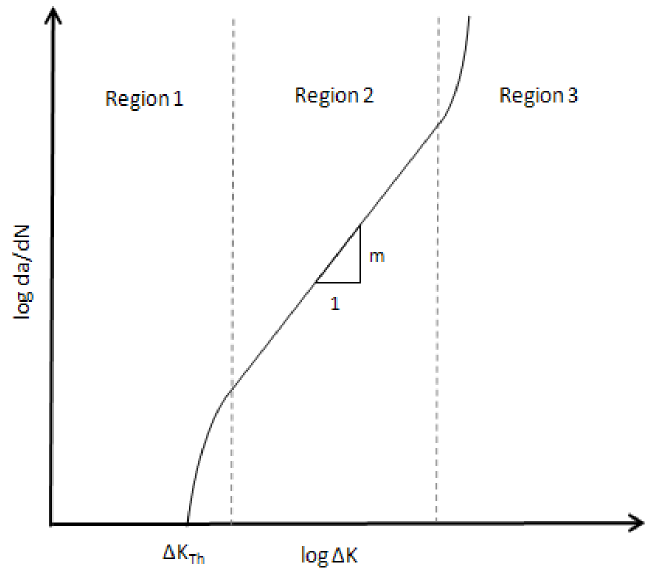

Figure 5. Paris' Law.

Further to the development of a fracture mechanics model, the work will include a probabilistic description of both the fracture parameters and the time-variant loading.

The structural reliability assessment will be incorporated into a maintenance planning approach, whereby measurements of crack length are monitored in time. This will lead to an optimal maintenance planning framework (such as that shown in Figure 3) that combines fracture models and monitoring data.

5 CONSORTIUM OVERVIEW

Long Life Bridges is a Marie Curie Industry Academia Partnerships and Pathways project. The consortium involves four partners; two SMEs, and two leading European Universities, each with particular expertise key to the success of the project.

Roughan and O'Donovan (ROD) consulting engineers are a SME based in Dublin, and are the project coordinators of *Long Life Bridges*. They are recognised as one of the leading civil engineering consultancies in Ireland with particular expertise in bridge structures. They are developing an increasing reputation on a European level, having recently designed the New Wear Bridge in the United Kingdom which will be the tallest bridge in the British Isles when completed (Figure 6). A subsidiary company, Roughan and O'Donovan Innovative Solutions (RODIS) is a partnership with staff of Trinity College Dublin and University College Dublin. The subsidiary focuses on the application of recent research developments in advanced structural design and assessment. Staff have developed software and published extensively on probabilistic approaches to bridge safety assessment, bridge dynamics, bridge traffic loading and Bridge Weigh-In-Motion.

Figure 6. New Wear Bridge, Sunderland, UK.

Phimeca is an SME in France with expertise in uncertainty, particularly in the nuclear industry in the quantification of extremely remote risks. Their expertise will allow development of a probabilistic approach to the analysis and design of fatigue critical details in cable stay bridges.

The two university partners, Aalborg University (AAU) in Denmark and The Royal Institute of Technology (KTH) in Stockholm both conduct world class research in areas key to the success of the Project. AAU perform research in structural reliability and risk analysis with experience in application to industrial sectors such as offshore structures, bridges and wind turbines. This also includes development of reliability and risk based methods for life-cycle assessment and optimal planning of inspection, operation and maintenance of structures. KTH conduct research into the analysis and design of bridges, with particular expertise in dynamic behaviour including the instrumentation and monitoring of several bridges across Sweden.

The project involves the secondment of staff between the partners as shown in Figure 7 to enhance knowledge transfer and exploitation of the results on a European wide basis. The three research objectives of the project, Railway Bridge Dynamics, Life Cycle Evaluation and Fatigue Evaluation are illustrated in the schematic with each arrow representing an exchange of staff between the partners concerned.

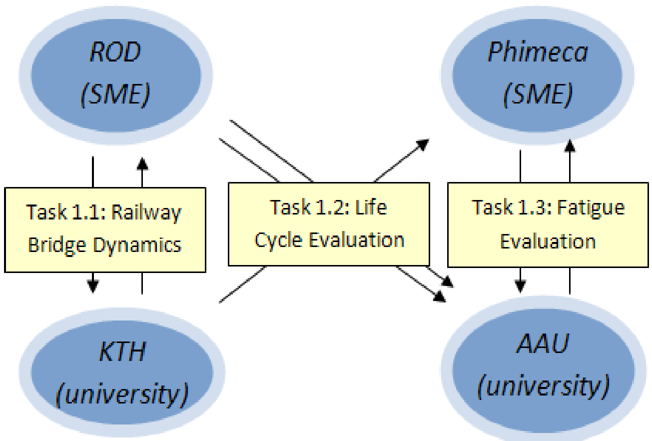

Figure 7. Staff transfer of Long Life Bridges Project.

6 CONCLUSIONS

The goal of *Long Life Bridges* is to extend the lives of the existing bridge stock in Europe. 'Europe 2020, A European Strategy for Smart, Sustainable and Inclusive growth', is the EUs policy which sets out an economic growth strategy for the coming decade. *Long Life Bridges* will make a significant contribution to the goals set out in this plan by:

(i) Integrating sensor information with computer software. This will promote smart growth, thus delivering market-leading assessment tools giving much better information about the safety of bridges. This is a growth market, especially during recession, when infrastructure budgets are under tight constraints.

(ii) Extending the safe working lives of bridges. This improves the sustainability of the transport infrastructure and reduces the demand for new construction involving non renewable resources.

(iii) Promoting bridge monitoring. This will encourage long term sustainable and local employment of semi-skilled workers promoting the 3rd strand of the Europe 2020 strategy of inclusiveness.

The project has three main research areas: (i) Bridge Dynamics, (ii) Life Cycle Assessment, and (iii) Fatigue Evaluation, involving partners from Ireland, France, Denmark and Sweden. The collaboration brings together experts in the fields of structural assessment, probabilistic analysis and risk evaluation.

ACKNOWLEDGMENTS

Long Life Bridges is a Marie Curie 7th Framework Project funded under the Industry and Academia Partnerships and Pathways call. The Project commenced in September 2011 and is continuing for 3 years until August 2014.

REFERENCES

[1] O'Connor, A.J. and Eichinger, E.V. (2007), 'Site-specific traffic load modelling for bridge assessment', *Proceedings of the Institution of Civil Engineers, Bridge Engineering* 160, 185-194.

[2] OBrien, E.J., Znidaric, A. and Ojio, T. (2008), 'Bridge-weigh-in-motion – latest developments and applications worldwide', *Proceedings of the International Conference of Heavy Vehicles - ICWIM5*, Paris, France, 39-56.

[3] Crespo-Minguillon, C. And Casas, J.R. (1997), 'A comprehensive traffic load model for bridge safety checking', *Structural Safety* 19, 339-59. doi:10.1016/S0167-4730(97)00016-7

[4] Cremona, C. (2001), 'Optimal extrapolation of traffic load effects', *Structural Safety*, 23, 31-46. doi:10.1016/S0167-4730(00)00024-2

[5] OBrien, E.J., Rattigan, P., Gonzalez, A., Dowling, J. And Znidaric, A. (2009), 'Characteristic dynamic traffic load effects in bridges', *Engineering Structures*, 31, 1607-1612.

[6] Cantieni, R. (1983), *Dynamic load tests on highway bridges in Switzerland*, Swiss federal laboratories for material testing and research report 211.

[7] Green, M.F. and Cebon, D. (1995), 'Dynamic interaction between heavy vehicles and highway bridges', *Computers & structures*, 62, 253-264.

[8] Kim, C.W., Kawatani, M. and Kwon, Y.R. (2007), 'Impact coefficient of reinforced concrete slab on a steel girder bridge', *Engineering Structures*, 29, 576-590.

[9] Gonzalez, A., Rattigan, P.H., OBrien, E.J. and Caprani, C.C. (2008), 'Determination of bridge lifetime dynamic amplification factor using finite element analysis of critical loading scenarios', *Engineering Structures*, 30, 2330-2337.

[10] OBrien, E.J., Cantero, D., Enright, B. And González, A. (2010), 'Characteristic dynamic increment for extreme traffic loading events on short and medium span highway bridges', *Engineering Structures*, 32, 3287-3835.

[11] Prat, M. (2002), 'Traffic load models for bridge design: recent developments and research', *Progress in Structural Engineering and Materials*, 3, 326-334.

[12] Frangopol, D.M., Kong, J.S. and Gharaibeh, E.S. (2001), 'Reliability-based life-cycle management of highway bridges', *ASCE Journal of Computing in Civil Engineering*, 15, 27-34.

[13] Ang, A.H.-S. and De Leon, D. (2005), 'Modelling and analysis of uncertainties for risk-informed decision in infrastructures engineering', *Structure and Infrastructure Engineering*, 1, 19-31.

[14] Ellingwood, B.R. (2005), Risk-informed condition assessment of civil infrastructure: state of practice and research issues. *Structure and Infrastructure Engineering*, 1, 7-18.

[15] Joint Committee on Structural Safety (JCSS), *Risk Assessment in Engineering - Principles, System Representation & Risk Criteri*, 2008. http://www.jcss.ethz.ch/publications

[16] Sørensen, J.D. and M.H. Faber, (2002), 'Codified Risk Based Inspection Planning', *Journal of Structural Engineering International*, 12 (3), 195-199.

[17] Sorenson, J.D., Tychsen, J., Anderson, J.U. and Brandstrup, R.J. (2006), 'Fatigue analysis of load-carrying fillet welds', *Journal of Offshore Mechanics and Arctic Engineering, ASME*, 128, 65-74.

[18] Sørensen, J.D. and Toft, H.S. (2010), 'Probabilistic design of wind turbines', *Energies*, 3, 241-257.

[19] Faber, M.H., Sørensen, J.D., Tychsen, J. and Straub, D. (2005), 'Field Implementation of RBI for Jacket Structures', *Journal of Offshore Mechanics and Arctic Engineering*, 127, 220−226.

Reducing traffic loading on long-span bridges by means of lane-changing restrictions

C. Carey, C.C. Caprani, B. Enright
Department of Civil & Structural Engineering, Dublin Institute of Technology, Ireland
email: colm.carey@dit.ie, colin.caprani@dit.ie, bernard.enright@dit.ie

ABSTRACT: Congested traffic is the governing form of traffic on long-span bridges and truck platoons dominate the characteristic traffic loading events. Drivers changing lane on the approach to a bridge cause truck platoons to form or elongate, increasing the traffic load on the bridge. A lane-changing restriction zone on the approach to a bridge could help reduce truck platoons and consequently reduce the traffic loading on the bridge. This research examines the positioning and length of the lane-changing restriction zone necessary to reduce the traffic loading on the bridge. Weigh-In-Motion measured traffic is passed through a traffic microsimulation program in which a bottleneck is used to induce congestion. Varying lane-changing restriction zone lengths and positions, relative to the bridge, are introduced on the virtual road. The effect these restrictions have on bridge traffic loading, and travel time, are examined. While the level of disturbance to traffic flow increases with the length of the restriction zone, it is evident that restriction zones may significantly reduce traffic loading. The results of this work can help bridge owners implement simple control measures to prolong the service lives of bridges.

KEY WORDS: Bridge; Loading; Traffic; Long-span; Congestion; Control; Microsimulation.

1 INTRODUCTION

1.1 Background

Long-span bridges are expensive to construct and are only built where there is a clear need. The cost involved in their maintenance is two-fold: firstly, the cost of repairing the bridge and secondly, the cost associated with the restriction of traffic flow during the bridge rehabilitation period. The traffic loading to which such bridges are subject is an important parameter in keeping them operational. Congested traffic is known to be the governing traffic loading scenario for these bridges.

Previous modelling of congested traffic has been based on some simplifying and conservative assumptions. For example, the arrival of successive vehicles has generally been taken to be independent and random [1, 2, 3]. Also, the gap between successive vehicles is often collapsed to a fixed length: for example, a 5 m gap between vehicles was used in the background studies to the Eurocode [1, 4, 5].

Recent work has found that, in congested traffic, trucks tend to travel in groups or platoons [6, 7]. These truck platoons were found to have a significant effect on the traffic loading for long-span bridges. Truck platoons form and elongate in the breakdown from free-flow to congested traffic due to cars changing lane [6]. Therefore, a method of controlling lane changing during this traffic flow transition may lead to a reduction in traffic loading.

1.2 Lane-changing restriction zones

Previous work by the authors introduced the concept of lane-changing restriction zones (LCRZ) to reduce the traffic loading on long-span bridges [8]. In a traffic microsimulation model, traffic was passed across the virtual road with and without the LCRZs and the influence different zone lengths had on bridge traffic loading was calculated. Interestingly, longer zones were found to actually increase loading.

In heavily congested traffic, lane-changing opportunities are infrequent. Since congestion typically travels upstream at approximately 15 km/h [9], a static restriction zone may prove ineffectual once the congested traffic envelops it.

1.3 Overview of research

This work investigates a dynamic lane-changing restriction zone that moves upstream in front of the congested traffic wave. Six months of recorded traffic is used as input to a traffic microsimulation model which can reproduce complex phenomena based on driver interactions. Virtual road features are used to produce congested traffic.

Multiple restriction zone scenarios are examined and the traffic loading is calculated for bridges of different lengths. Flow is monitored at the start and end of a zone, and the lane-changing restriction is considered active when the traffic at the start is free-flowing, and congested at the end. Bridge loading caused by the traffic obtained during the active period of the restriction zone is calculated. In this way, the traffic loading relates to times where the LCRZ is in the optimal position to restrict lane changing, and thus the formation of truck platoons. The influence of the different restriction zones on travel times through the road segment is also investigated.

In practice, the control system would be implemented by a system of flow detectors and variable message signs. When a detector identifies that the traffic flow is congested, an electronic “no lane changing” sign would be activated some distance upstream. If the congestion travels upstream to the next flow detector, the process would be repeated. When the congested traffic dissipates, the signs would be deactivated.

2 BASIS OF WORK

2.1 Traffic data

This work uses WIM data obtained from the A4 (E40) at Wroclaw, Poland. In total, over 22 weeks of traffic, including cars, was recorded from 1 January to 5 June 2008. Two lanes of traffic, in one direction, were recorded. Weekend traffic is not used in this research as traffic compositions are different than that on week days. Figure 1 shows the average hourly traffic flows, percentage of trucks and truck Gross Vehicle Weight (GVW) from the site data. In this work, trucks are defined as any vehicle with a GVW over 3.5 t with all other vehicles defined as cars.

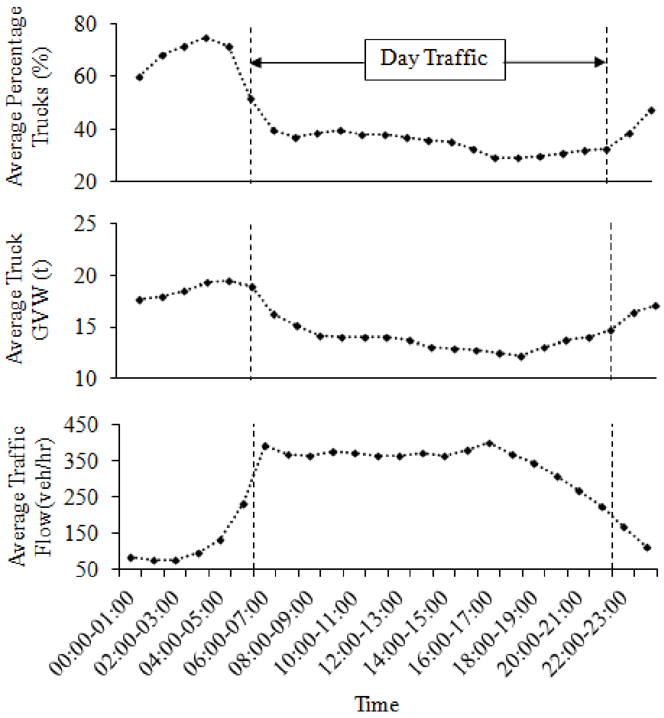

Figure 1. Traffic statistics from Wroclaw WIM data.

Due to the difference between the night and day traffic illustrated in Figure 1, only day traffic is considered in this work. The flow during the day is significantly higher than that of night traffic, and so congestion is more likely to occur during the day.

2.2 Vehicle overhangs

The bridge loading caused by a stream of congested traffic is static in nature, with no dynamic component, since the vehicles crossing the bridge are not travelling fast enough to generate a dynamic load [10, 11]. For a given set of vehicles, larger loading will result from more closely spaced vehicles. In particular, higher loading will result from close front and rear axles of successive vehicles. For this reason, inter-vehicle gaps are an important factor in modelling loading caused by congested traffic. The parameters influencing the gap between adjacent front and rear axles are not only those of driving characteristics, but include the vehicle front and rear overhangs of the vehicle body (i.e. distance from the front and rear of the vehicle to the front and rear axles respectively).

Vehicle overhangs are not typically measured and are not present in the WIM data used in this study. A database of vehicle dimensions was compiled from information supplied by European vehicle manufacturers. Over 1000 vehicles are included in this database. These vehicle dimensions, along with other published data [12], are used to categorize vehicles by axle configuration. Front and rear overhangs are fitted to the WIM data based on each vehicle's axle configuration.

2.3 Microsimulation

Microsimulation is used here to induce congestion in the recorded free-flowing traffic. A computer program, *Simba – Sim*ulation for *B*ridge *A*ssessment [13, 14], based on the Intelligent Driver Model (IDM) developed by Treiber and others [15, 16], is used in this work. The model is based on a continuous function of acceleration and deceleration components which describes the motion of a vehicle in response to its surroundings, given a set of mechanical and driver performance parameters. In particular, the IDM uses the idea that a driver tries to minimize braking decelerations. The acceleration a vehicle undergoes is defined by:

$$\frac{dv(t)}{dt} = a\left[1-\left(\frac{v}{v_0}\right)^{\delta}-\left(\frac{s^*(v,\Delta v)}{s}\right)^2\right] \qquad (1)$$

where: v is the current velocity of the vehicle, v_0 is its desired velocity, δ is the acceleration component, s is the gap between the vehicles, and Δv is the velocity difference (approaching rate) of the vehicle to the lead vehicle. The desired gap, s^*, is calculated using:

$$s^*(v,\Delta v) = s_0 + s_1\sqrt{\frac{v}{v_0}} + Tv + \frac{v\Delta v}{2\sqrt{ab}} \qquad (2)$$

where: s_0 is the minimum jam distance; s_1 is the elastic jam distance; T is the safe time headway; a is the maximum acceleration; and b is the comfortable deceleration.

2.4 Lane changing model (MOBIL)

To allow for lane changing in the microsimulation, the model developed by Kesting et al. [18] is used. This model, MOBIL (Minimizing Overall Braking Induced by Lane changes), is based on two criteria: (1) Incentive criteria – where the driver considering changing lane weighs up the advantages for the proposed change, and (2) Safety criteria – where the lane-changing operation the driver is considering must be safe.

Figure 2 illustrates a possible lane-changing scenario. For car c to change lane, there must be a clear advantage for doing so, outweighing the disadvantages to the surrounding drivers that will be influenced by the manoeuvre. This decision is calculated using:

$$\tilde{a}_c - a_c > p\left[\left(a_n - \tilde{a}_n\right) + \left(a_o - \tilde{a}_o\right)\right] + \Delta a_{th} \qquad (3)$$

where a_c, a_n, a_o are the vehicles c, n, and o current accelerations respectively; and $\tilde{a}_c$, $\tilde{a}_n$, $\tilde{a}_o$ are the vehicles' accelerations after the possible lane change. Δa_{th} is the lane-changing threshold which is added to avoid lane changing with only a marginal advantage, and p is the politeness factor of the driver in car *c*. The politeness factor is generally less than 1, and the greater the factor, the more consideration the driver of car *c* gives to the drivers in vehicles *n* and *o*.

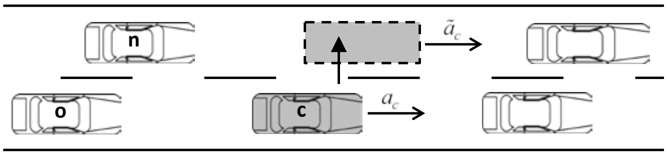

Figure 2. Vehicles involved in lane-changing manoeuvre (adapted from Kesting et al. [18]).

The lane-changing manoeuvre must also adhere to the following safety criterion:

$$\tilde{a}_n \geq b_{safe} \quad (4)$$

The deceleration imposed on the new following vehicle, vehicle *n* in Figure 2, must not be greater than the safety limit deceleration, b_{safe} which in this work is set at -12 m/s^2. Lane-changing restriction model.

The IDM and MOBIL parameters used in this work are taken from Helbing et al. [17] and Kesting et al. [18] respectively, and are given in Table 1.

Table 1. IDM parameter values used in the microsimulation.

Parameter	Car	Truck
Safe time headway, T (s)	1.2	1.7
Maximum Acceleration, a (m/s^2)	0.8	0.4
Comfortable deceleration, b (m/s^2)	1.25	0.8
Minimum jam distance, s_0 (m)	1	1
Elastic jam distance, s_1 (m)	10	10
Desired velocity, v_0 (km/h)	120 (±20)	80 (±20)
Acceleration exponent, δ	4	4
Lane change politeness factor, p	0.25	0.25
Outside lane bias factor, Δa_{bias}	0.3	0.3
Lane change threshold, Δa_{th} (m/s^2)	0.1	0.1

2.5 Road layout

In the microsimulation a 10 km two-lane road with open boundaries is defined. In order for congested flow to occur, flow-restricting road features, i.e. bottlenecks, are added between 9.5 and 10.0 km. The road features consist of a speed limit, which reduces each vehicle's desired speed to 20 km/h, and a gradient, which increases the safe time headway by 0.5 s. Congested traffic builds at the start of the bottleneck and travels upstream. As only day traffic is used (06:00-22:00), congested traffic dissipates each night. Bridges of lengths 100 m, 200 m, 500 m and 1 km are considered in this work and all begin at 8.25 km on the virtual road.

2.6 Lane-changing restriction zones (LCRZs)

Four LCRZ lengths (scenarios) are investigated in this work, shown in Table 2. Scenario 1 has no restriction on lane changing and is used as the benchmark for comparison. A number of simulations are carried out for scenarios 2, 3, and 4, and the starting position of the LCRZ changes in each simulation. A simulated flow detector is placed at a lead-in distance of 250 m from the beginning of the LCRZ, as shown in Figure 3. This lead-in distance is used to prevent anticipatory lane-changing on approach to the LCRZ. In the first simulation, the LCRZ ends at the beginning of the bridge. In the next simulation, the start of the LCRZ is moved upstream so that it begins at the position of the flow detector, plus the length of the LCRZ, in the previous simulation (Figure 3). This process is carried out for scenarios 2, 3, and 4 until the LCRZ reaches 1.5 km from the start of the virtual road. While the lead-in distance used in this work is 250 m, further investigation is needed to determine the influence of this distance on traffic loading.

Table 2. Scenarios considered.

Scenario	Lane-Changing Restriction Zone
1	None
2	1.0 km
3	2.5 km
4	5.0 km

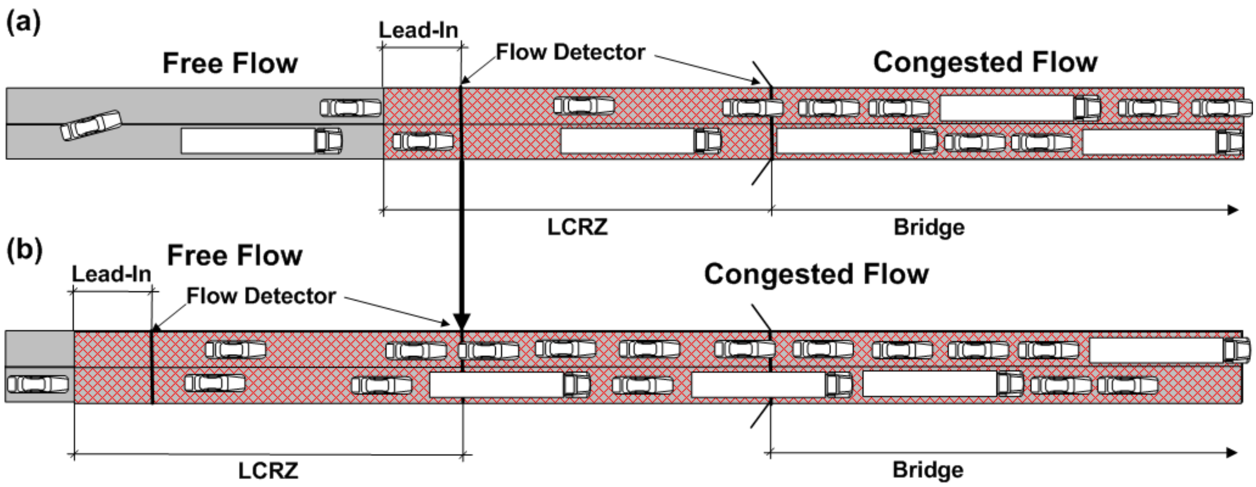

Figure 3. Overview of proposed LCRZ model: (a) LCRZ position when congested flow front is at start of bridge; (b) LCRZ position when congested flow front is at flow detector in (a).

For each simulation, the Wroclaw WIM day traffic, with fitted overhangs, is passed across the virtual road. Congestion builds at the bottleneck and moves upstream during the day, and dissipates during each night. For scenario 1 the traffic is outputted at the beginning of the bridge. For scenarios 2, 3, and 4, in each simulation, only the traffic that passed through the LCRZ when it was active is used. The LCRZ is defined as being active when there is congestion at the downstream end of the restriction zone and free-flowing traffic at the upstream flow detector. A vehicle is taken to be part of congested traffic if its speed is below 28 km/h, and the 60s average flow is below 800 veh/hr [9]. In each scenario, for each possible position of the LCRZ, all the recorded traffic is passed through a complete simulation and output at the upstream detector and at the beginning of the bridge. For each position of the LCRZ, the outputted traffic is then analysed:

1. The traffic that passed through the LCRZ when it was active is captured;
2. If traffic passed through an active LCRZ in multiple simulations, the traffic is captured from the simulation where the zone is furthest downstream;
3. This traffic is passed over bridges of different length and the total traffic load is recorded.

For each day's traffic, this typically produces a total of 5.5 hours of congested traffic. Only vehicles captured in scenarios 2, 3 and 4 were used in the traffic loading for scenario 1. In this way the same vehicles were used for calculating traffic loading for each scenario, with the sequence of the vehicles changing between scenarios.

3 LOADING RESULTS

3.1 Extrapolation

The traffic loading for each scenario is determined as described above. The maximum total load that occurs in a congested traffic day (taken to be two hours of congested traffic) is recorded. The Generalized Extreme Value distribution [19], is used to extrapolate the daily maximum values from each scenario, and is given by:

$$G(z) = \exp\left\{-\left[1-\xi\left(\frac{z-\mu}{\sigma}\right)\right]_+^{1/\xi}\right\} \tag{5}$$

where $[h]_+ = \max(h, 0)$ and μ, σ, ζ are the location, scale and shape parameters respectively.

The results from each scenario are extrapolated to a 1000-year return period (which is the value with approximately 5% probability of exceedance in 50 years) as used in the Eurocode 1 for design [4], and a 75-year return period which may be suitable for bridge assessment. This is carried out for each bridge length investigated. The ratio of total load for scenarios 2-4 to those of scenario 1 (no LCRZ) are used as the basis for comparison.

3.2 Results

Figures 4 and 5 give the extrapolated total load ratios for the 75-year and 1000-year return periods respectively. It can be observed that the LCRZ can significantly reduce the traffic loading, with a maximum reduction of 29%. There is no significant variation between the results for the different LCRZ lengths, maximum 5%. The reductions in loading are quite sensitive to bridge length, with the effectiveness of the LCRZ as a traffic load reduction measure decreasing with increasing bridge length.

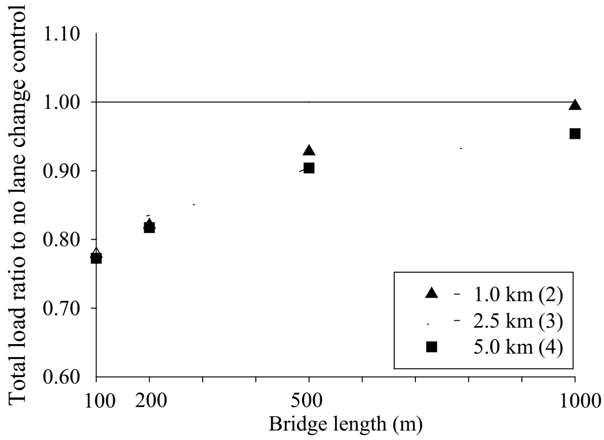

Figure 4. Ratios of 75-year loading for scenarios (2-4), compared to no lane change scenario (1).

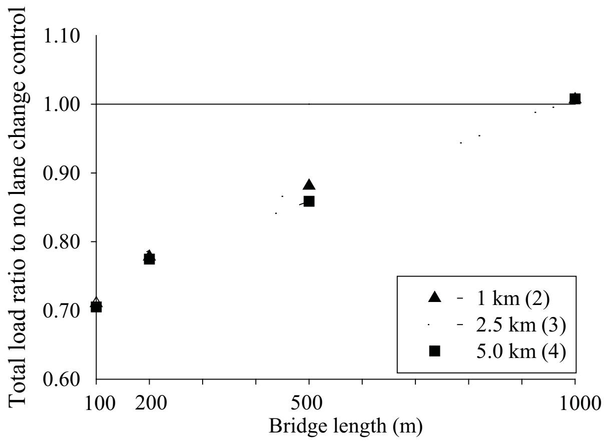

Figure 5. Ratios of 1000-year loading for scenarios (2-4), compared to no lane change scenario (1).

In order to interpret these results, it is necessary to examine the lane-changing behaviour that occurs in the breakdown from free-flowing to congested traffic. In Figure 6, lane change rates (events/km/hr) and traffic densities with respect to road length from scenario 1 (no restriction zone) are shown for two selected days of traffic in the microsimulation. The lane change rates and traffic densities are recorded in 500 m sections along the 10 km road at 30 minute intervals. It can be seen (Figure 6 (b) and (d)) that there are many lane changes in the first 1 km of road, but this is simply a consequence of the microsimulation settling into a steady state, and is not significant here as the traffic in each scenario is not restricted in this region. There is a concentration of lane changing activity during breakdown to congested flow, in the 1 km just ahead of the congested traffic front (indicated by the large increase in traffic density in Figure 6 (a) and (c)). Therefore, the control of lane changing in this region can have a significant effect in reducing traffic loading, and may explain why there is relatively minor variations in the reduction in loading between the different restriction zone lengths.

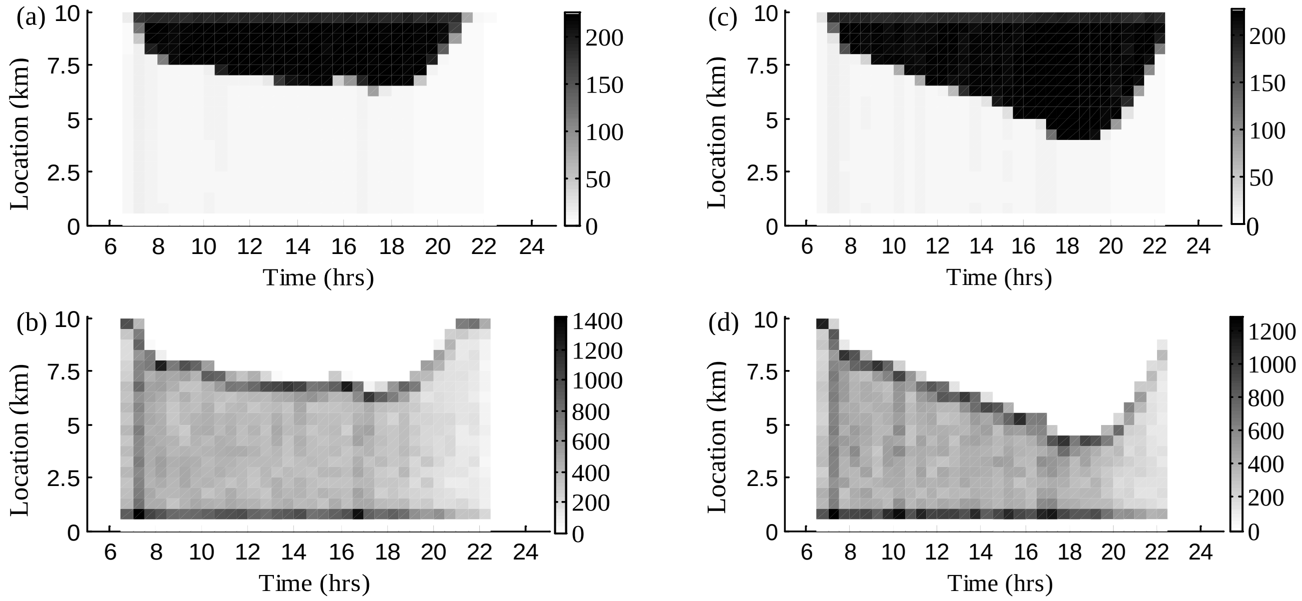

Figure 6. Spatio-temporal distribution of: (a) Day A - density (veh/km); (b) Day A - lane change rate (events/km/hour); (c) Day B - density (veh/km); (d) Day B - lane change rate (events/km/hour), from two sample days of microsimulation.

4 EFFECT OF LANE-CHANGING RESTRICTIONS ON TRAVEL TIME

The aim of the LCRZ is to reduce traffic loading on a given bridge. However, it will also adversely affect the traffic flow. An overly restrictive LCRZ is not desirable due to the economic cost associated with congested traffic. Therefore, the effect of an LCRZ on traffic flow is assessed using the travel time across the road segment. For each simulation, with the LCRZ in the initial position, see Figure 3(a), the time taken for each vehicle to traverse the virtual road is recorded. Figure 7 shows the distributions of the difference in travel times for all scenarios compared with scenario 1. Traffic is congested in all four scenarios.

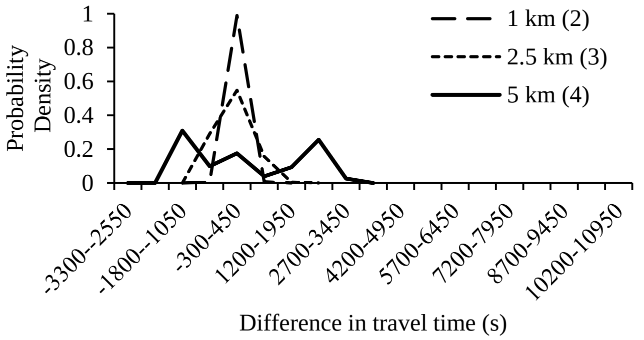

Figure 7. Difference in travel time between scenario 1 (no LCRZ) and scenarios 2, 3, and 4.

It can be seen that as the length of the restriction zone increases, the variation in travel times also increases. For scenario 2 (1 km LCRZ), there is only a slight variation in travel time over the 8.25 km road segment with the majority of travel times varying by between -300 to +450 s. For the other scenarios the variation in travel time increases. The travel time for some vehicles decreases when compared with scenario 1, indicated by the negative travel time differences.

Figure 8 shows the distributions of travel time differences for the two lanes separately, and it can be seen that reductions in travel time occur only in the fast lane (Figure 8(b)). This is because lane-changing restrictions prevent the re-balancing of traffic flows between the two lanes that occurs normally in the breakdown to congestion.

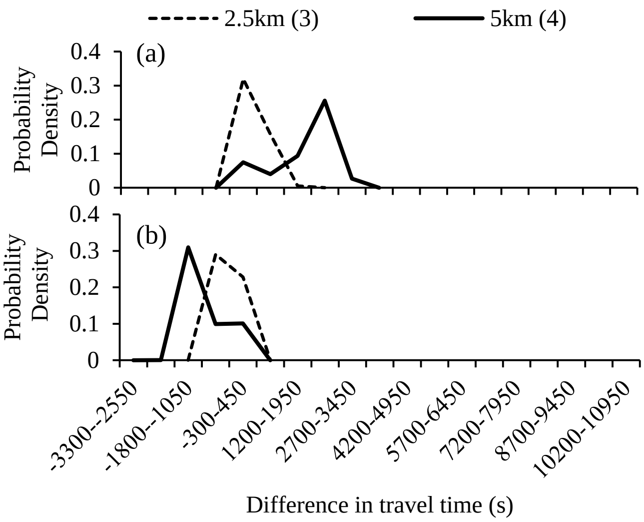

Figure 8 Difference in travel time between scenario 1 (no LCRZ) and scenarios 3, and 4, (a) slow lane, (b) fast lane.

For the data used in this study, the flow rate in the slow lane is typically 25% greater than the fast lane during free-flowing traffic. During congested traffic (in Scenario 1), the opposite is true, with the flow rate in the fast lane exceeding that of the slow lane by an average of 20%. This reversal in flow rate ratios is partly due to the vehicles changing from the slow lane to the fast lane in the breakdown from free flow to congested flow. If a lane-changing restriction zone is present, vehicles are prevented from changing lane, which leads to disturbances in the traffic flow. The increased variation in the travel time differences which is evident in Figures 7 and 8 shows that the disturbance to travel times increases with increasing restriction zone lengths.

5 SUMMARY AND CONCLUSIONS

5.1 Summary

This work presents a method of controlling traffic loading on long-span bridges. This is achieved through the use of a model in which a lane-changing restriction zone moves upstream, remaining just in front of congested traffic. In this manner, the zone always captures traffic as it breaks down from free flow to congested flow. This was found to be an area where there is a high lane change rate and by controlling these lane changes, the traffic loading can be reduced.

A virtual road is used in a traffic microsimulation with restriction zones of different lengths imposed. The zones are positioned in a way that mimics the way a variable messaging system might work, and the resulting impact on bridge loading and travel times is investigated.

The restriction zones are found to significantly reduce the characteristic traffic loading on long-span bridges by up to 29%. Further, it is found that longer restriction zones result in an overall average increase in travel times.

5.2 Conclusions

The lane-changing control method presented in this research proves to be an effective method of reducing traffic loading on long-span bridges. Reductions in traffic loading of up to 29% are found to occur with the introduction of dynamic lane-changing restriction zones. However, these zones affect the travel time, with longer zones causing greater disturbance to travel times. Restriction zones longer than 1 km are found to have little or no additional effect on traffic loading, and therefore should not be used due to the consequences to traffic flow. The effect of the restriction zones on traffic loading were found to be sensitive to bridge length, and for bridge lengths of 1 km the zones had a minimal effect on reducing traffic loading.

The proposed control system is reasonably simple to implement and has the potential of yielding savings for bridge owners, by prolonging the service lives and increasing the maintenance interval for long-span bridges.

ACKNOWLEDGMENTS

The authors would like to acknowledge the Dublin Institute of Technology ABBEST Scholarship Programme for funding this research.

REFERENCES

[1] Flint, A.R. and Jacob, B.A. (1996), 'Extreme traffic loads on road bridges and target values for their effects for code calibration', *Proceedings of IABSE Colloquium*, Delft, The Netherlands, IABSE-AIPC-IVBH, 469-478.

[2] Flint and Neill Partnership for TRRL (1986), 'Interim design standard: long span bridge loading', *Transport and Road Research Laboratory*: Crowthorne (Contractor Report 16).

[3] Crespo-Minguillón, C. and Casas, J.R. (1997), 'A Comprehensive traffic load model for bridge safety checking', *Structural Safety*, 19, 339-359.

[4] Bruls, A., Croce, P., Sanpaolesi, L. and Sedlacek, G. (1996), 'ENV1991 – Part 3: Traffic Loads on Bridges; Calibration of Load Models for Road Bridges', *Proceedings of IABSE Colloquium*, Delft, The Netherlands, IABSE-AIPC-IVBH, 439-453.

[5] EC1.2, *Eurocode 1: Actions on Structures, Part 2: Traffic loads on bridges*, European Standard EN 1991-2: European Committee for Standardisation, Brussels, 2003.

[6] Enright, B., Carey, C., Caprani, C.C. and OBrien, E.J. (2012), 'The Effect of Lane Changing on Long-Span Highway Bridge Traffic Loading, *Proc. 6th Intl. Conf. on Bridge Maintenance, Safety and Management*, IABMAS, Lake Como, Italy.

[7] OBrien, E.J., Hayrapetova, A. and Walsh, C. (2010), 'The use of micro-simulation for congested traffic load modelling of medium- and long-span bridges', *Structure and Infrastructure Engineering*, 269-276.

[8] Caprani, C.C., Enright, B. and Carey, C. (2012), 'Lane changing control to reduce traffic load effect on long-span bridges', *International Conference on Bridge Maintenance*, Safety and Management, IABMAS, Lake Como, Italy.

[9] Kerner, B.S., Rehborn, H., Aleksic, M. and Haug, A. (2004), 'Recognition and tracking of spatial-temporal congested traffic patterns on freeways', *Transportation Research Part C: Emerging Technologies*, 12(5)**,** 369-400.

[10] Buckland, P.G., McBryde, J.P. and Francis, P.D. (1978), 'Traffic loading of long span bridges', *Conference on bridge engineering proceedings*, Transportation Record Research, 146-154.

[11] Buckland, P.G. (1981), 'Recommended design loads for bridges (Committee on loads and forces on bridges of the committee on bridges of the structural division)', *Journal of the Structural Division*, ASCE, 1161–213.

[12] Page J. and Ricketts, N.J. (1997), 'Traffic Data for Highway Bridge Loading Rules', Rep. 251, *Transport Research Laboratory*, Crowthorne, Berks.

[13] Caprani, C.C. and OBrien, E.J. (2008), 'The governing form of traffic for highway bridge loading', *Proceedings of 4th Symposium on Bridge and Infrastructure Research in Ireland*, E. Cannon, R. West, P. Fanning (Eds.), National University of Ireland, Galway, 53-60.

[14] Caprani, C.C. (2010), 'Using Microsimulation to Estimate Highway Bridge Traffic Load', *Proc. 5th Intl. Conf. on Bridge Maintenance, Safety and Management*, IABMAS, Philadelphia, (2010).

[15] Treiber, M., Hennecke, A. and Helbing, D. (2000), 'Microscopic Simulation of Congested Traffic', *Traffic and Granular Flow '99*, D. Helbing, H.J., Herrmann, M. Schreckenberg, D.E. Wolf (Eds.), Springer, Berlin, 365-376.

[16] Treiber, M., Hennecke, A. and Helbing, D. (2000), 'Congested Traffic States in Empirical Observations and Microscopic Simulations', *Physical Review E*, 62(2), 1805-1824.

[17] Helbing, D., Hennecke, A., Shvetsov, V. and Treiber, M. (2002), 'Micro- and macrosimulation of freeway traffic', *Mathematical and Computer Modelling* 35(5/6), 517-547.

[18] Kesting, A. Treiber, M. and Helbing, D. (2007), 'General lane-changing model MOBIL for car-following models', *Transportation Research Record: Journal of the Transportation Research Board*, Volume 1999/2007, 86-94.

[19] Coles, S.G. (2001), *An Introduction to Statistical Modelling of Extreme Values*, London: Springer-Verlag.

Probabilistic analysis of an indeterminate beam subjected to moving loads considering material nonlinearity

C.C. Caprani[1], L.A. McCarthy[1]
[1]Department of Civil & Structural Engineering, Dublin Institute of Technology, Bolton Street, Dublin 1, Ireland
Email: colin.caprani@dit.ie, liam.mccarthy@dit.ie

ABSTRACT: In the probabilistic assessment of existing bridge structures, elastic structural models are typically used. At the ultimate limit state this may not be appropriate. In this work, the response of an indeterminate beam structure subjected to static and moving loads is assessed using a one dimensional nonlinear material finite element model. A deterministic study is used to calculate the load factor required to cause structural collapse for static and moving loads. A probabilistic assessment of the structure is conducted using the first order reliability method for static loads. Importance Sampling is used for moving loads. It is found that in some cases the common assumption used to locate the load does not lead to the true collapse load factor.

KEY WORDS: Bridges; Loading; Reliability analysis; Nonlinear; Finite element; Importance sampling.

1 INTRODUCTION

1.1 Bridge Structural Safety

Bridge maintenance is an ever-growing concern due to reducing financial budgets and increasing traffic volumes. Accurate bridge assessment is now a necessity as it is no longer acceptable to assess a bridge structure using excessive conservatism. According to a recent survey, one major reason for a bridge structure to fail an assessment is “conservative or inappropriate methods of assessment” [1]

Typically, bridge failure is deemed to occur when the load effects found using an elastic structural assessment reach the resistance capacity at single location in the structure [2]. According to the Lower bound Theorem of plastic theory, this ensures safety against structural collapse. However, this ignores the structure’s ability to carry further load by redistribution of bending moments. For efficient assessment, this extra reserve of strength can be accounted for when using sufficiently ductile materials and cross-sections.

1.2 Nonlinear Modelling in Reliability Analysis

Several researchers have used a nonlinear structural model in probabilistic analysis methods. These methods are grouped as follows: 1) Monte Carlo Simulations; 2) the Response Surface Method, and; 3) sensitivity-based analysis [3]. Monte Carlo simulation, including efficient sampling techniques such as Importance Sampling, produce high levels of accuracy but can require extensive simulations, especially when dealing with low probabilities of failure [4]. The response surface method uses a polynomial to approximate an unknown limit sate function, thereby allowing a closed-form probabilistic analysis such as the first order reliability method to be carried out. This method has proved to be successful [5] and [6]. However, it may be inaccurate when dealing with several modes of failure [3]. Sensitivity-based methods have a high level of accuracy [7], but are not easily adapted to practical applications [3]

This study uses the first order reliability method (FORM) to examine static loads considering material nonlinearity. When the problem is extended to a moving load, Importance Sampling combined with a nonlinear finite element model is used to determine the probability of failure. The results are compared to those established using the common assumption that locates the load according to the elastic critical location.

By incorporating a nonlinear structural model into a reliability assessment, an improved estimate of the structure’s true safety level can be determined for a given traffic loading scenario. This is because a better model of material behaviour is accounted for. Consequently, this work can find practical application in safety assessment of existing highway infrastructure due to the considerable potential savings to maintenance budgets that may be realized.

2 STRUCTURAL RELIABILITY

2.1 Introduction

For a basic structural problem with a known limit state function, the probability of failure can be defined as follows:

$$p_f = \int_{g(x)\le 0} \cdots \int f_X(x)\, dx \tag{1}$$

where $g(x)$, is a limit state function of basic random variables x, and $f_X(x)$ is the joint probability density function of those variables.

Failure is often deemed to occur when an applied load effect (S) is greater than the structural resistance (R) giving a limit state function (g) of:

$$g = R - S \tag{2}$$

Equation 1 can be rewritten as:

$$p_f = \int \ldots \int I\left[g(r,s) \le 0\right] f_R(r)\, f_S(s)\; drds \tag{3}$$

Where: $I[\ ]$ is an indicator function which takes on a value of unity if the term in the brackets is true, or zero if the term in the brackets is false; and f_R and f_S are the probability density functions of resistance and load.

Evaluation of the probability integration outlined above can prove difficult when a large number of random variables (the vector X) are involved. Generally this equation cannot be solved in closed form due to the complexity of establishing the joint probability density function. Also, the limit state can often only be evaluated using simulation models such as finite element analysis. For this reason, approximate methods such as the FORM have been developed.

2.2 First Order Reliability Method

FORM simplifies the integration process by transforming variables from their original random space (X-space) into a standard normal space (U-space). This may be done using the Rosenblatt transformation [4] to ensure the contours of the integrand $f_X(x)$ are regular and symmetric:

$$U = \Phi^{-1}\left[F_X(X)\right] = \Phi^{-1}\left[\Phi\left(\frac{X-\mu}{\sigma}\right)\right] = \frac{X-\mu}{\sigma} \tag{4}$$

where Φ is the standard normal cumulative distribution function (cdf), Φ^{-1} is the inverse of the standard normal cdf, $F_X(.)$ is the cdf of variable X, μ is the mean value of X and σ is the standard deviation of X.

Another measure FORM takes to simplify the integration process is to linearize the limit state $g(X) = 0$. A first order Taylor series expansion is performed at the Most Probable Point (MPP); that is, the point on the limit state function which has the largest probability density (denoted U^*). An iterative process is implemented to establish this point and the reliability index, β, can be evaluated as follows [8]:

$$\beta = \frac{g(U^*) - \sum_{i=1}^{n} \frac{\partial g(U^*)}{\partial x_i}\sigma_{x_i} u_i^*}{\sqrt{\sum_{i=1}^{n}\left(\frac{\partial g(U^*)}{\partial x_i}\sigma_{x_i}\right)^2}} \tag{5}$$

The probability of failure and reliability index are related:

$$p_f = \Phi(-\beta) \tag{6}$$

where β, originally defined by Cornell (1969), represents the shortest distance from the origin to the limit state function in standard normal space and Φ is the standard normal cdf.

2.3 Importance Sampling

Monte Carlo simulation can be used to estimate the probability of failure. Samples of the random variables are generated and the limit state function evaluated for each set. The probability of failure is then given by:

$$p_f = \frac{1}{N}\sum_{j=1}^{N} I\left[g(x) \le 0\right] \tag{7}$$

where N is the total number of samples. This approach is inefficient when dealing with low probabilities of failure because a very large sample set is required.

Importance Sampling can produce an accurate estimate of the probability of failure. If sampling occurs around random variables that are more likely to contribute to the probability of failure fewer samples are required. This is achieved by using a biased sampling distribution. This bias is corrected for by weighting the outputs of the simulation. The probability integral may be estimated as follows:

$$p_f = \int \ldots \int I\left[g(x) \le 0\right] \frac{f_X(x)}{h_v(x)} h_v(x)\, dx \tag{8}$$

where $h_v(x)$ is the importance sampling function. It is common to use a normal distribution for h with the mean shifted to the MPP (Melchers, 1999). The above integral may be then estimated using:

$$p_f = \frac{1}{N}\sum_{i=1}^{N}\left(I\left[g(x) \le 0\right]\frac{f_x(x)}{h_v(x)}\right) \tag{9}$$

3 NONLINEAR FINITE ELEMENT MODEL

3.1 Finite element model

One-dimensional Euler-Bernoulli elements are used to model the beams for this work. Using the element stiffness matrices end forces and moments are calculated on each element. To minimize computation but retain accuracy, a non-uniform mesh is used. A fine mesh of 0.2 m is used at critical mid-span locations while a coarse mesh of 1 m is used for the remainder of the structure.

3.2 Material nonlinearity model

The approached used to represent the nonlinear response is that established by Clough et al (1990) as outlined in [9]. The spread of plasticity through the section is traced using force recovery parameters (R). The force recovery parameters are established from the following yield function:

$$\Gamma = \frac{M}{M_p} \tag{10}$$

where M is the moment currently on the cross section, and M_p is the plastic moment capacity of the section. The values of the force recovery parameters can be seen in Figure 1 at different stages of loading. When the structure is subject to loading and is behaving in an elastic manner (Stage 1) the force recovery parameters are equal to one, as no reduction in stiffness has taken place:

$$\Gamma \le \Gamma_y : \; R = 1 \tag{11}$$

The slope of the moment rotation curve for this stage is EI, where E is the modulus of elasticity of the material and I is the second moment of area of the section.

Once the initial yield capacity (Stage 2) has been reached, the force recovery parameters and the stiffness of the structure reduce as follows:

$$\Gamma_y \le \Gamma \le \Gamma_p : \qquad R = 1 - \frac{\Gamma - \Gamma_y}{\Gamma_p - \Gamma_y} \tag{12}$$

When a plastic hinge has fully formed (Stage 3) the force recovery parameter at that location equals the value of strain hardening (q) of the critical material in the section. The slope of the moment rotation curve for this stage is qEI:

$$\Gamma \ge \Gamma_p : \; R = q \tag{13}$$

During an unloading event at any point (Stage 4), the structure is assumed to behave elastically [9]. Hence the unloading force recovery parameter is:

$$\text{Unloading}: \quad R = 1 \tag{14}$$

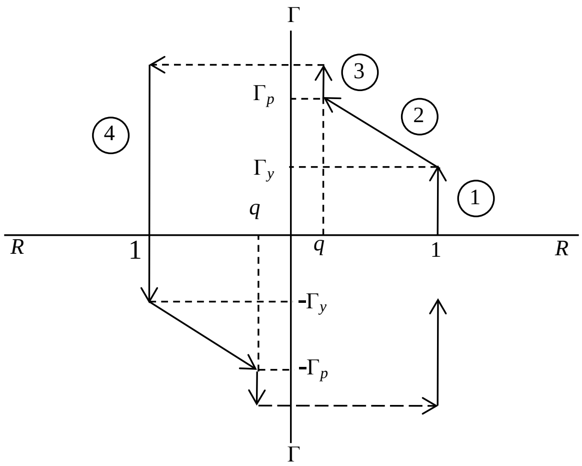

(a) Force recovery parameters under cyclic loading;

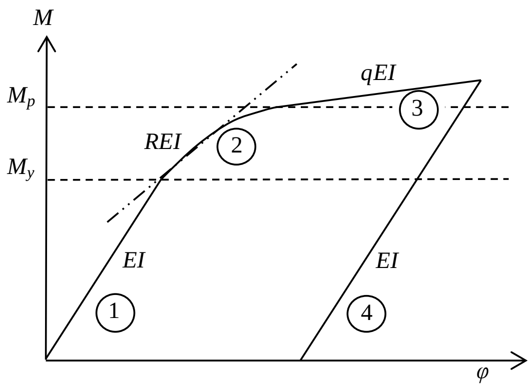

(b) Moment rotation relationship;

Figure 1. Stages in the behaviour of the cross section.

Once the force recovery parameters have been identified at each end of the element, the local stiffness matrix of each element is altered as follows:

$$R_1 \geq R_2 : \left[k_g\right] = R_2\left[k_e\right] + \left(R_1 - R_2\right)\left[k_2\right] \tag{15}$$

$$R_2 \geq R_1 : \left[k_g\right] = R_1\left[k_e\right] + \left(R_2 - R_1\right)\left[k_1\right] \tag{16}$$

in which k_g is element tangent stiffness matrix at the current state of loading. The elastic element stiffness matrix, k_e, is given by:

$$\left[k_e\right] = \frac{EI}{L^3}\begin{bmatrix} 12 & 6L & -12 & 6L \\ 6L & 4L^2 & -6L & 2L^2 \\ -12 & -6L & 12 & -6L \\ 6L & 2L^2 & -6L & 4L^2 \end{bmatrix} \tag{17}$$

The stiffness matrix with an element with a hinge at end 1, k_1, is given by:

$$\left[k_1\right] = \frac{EI}{L^3}\begin{bmatrix} 3 & 0 & -3 & 3L \\ 0 & 0 & 0 & 0 \\ -3 & 0 & 3 & -3L \\ 3L & 0 & -3L & 3L^2 \end{bmatrix} \tag{18}$$

The stiffness matrix with an element with a hinge at end 2, k_2, is given by:

$$\left[k_2\right] = \frac{EI}{L^3}\begin{bmatrix} 3 & 3L & -3 & 0 \\ 3L & 3L^2 & -3L & 0 \\ -3 & -3L & 3 & 0 \\ 0 & 0 & 0 & 0 \end{bmatrix} \tag{19}$$

where EI is the flexural rigidity of the cross section and L is the element length.

3.3 *Incremental Loading/Unloading Approach*

The incremental loading procedure outlined in [10], [11], and [12] is implemented to model the stress history at a cross section. At each increment the equilibrium equation is formulated and solved:

$$\lambda\{F\} = \left[K_g\right]\{u\} \tag{20}$$

where λ is the load factor, F is the external force vector, K_g is the global stiffness matrix, and u is displacement vector. The stiffness is altered after each increment using the force recovery parameters as previously outlined. At the onset of the nonlinearity the equilibrium path drifts away from the actual path. This drift can be minimized by using sufficiently small increments [12].

As extreme loads traverse the structure, plastic hinges may form and so load redistribution along the structure may occur. The incremental procedure is adapted to represent a moving load. This is implemented using a loading-unloading process, illustrated in Figure 2. The load at Position 1 unloads as the load at Position 2 loads. Hence, a residual rotation remains after plastic behaviour ensues in the beam once the load is unloaded. In this manner a true representation of the moving load is accounted for.

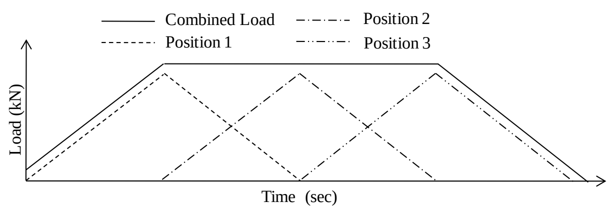

Figure 2. Incremental Loading/Unloading Procedure.

4 DETERMINISTIC ANALYSIS

4.1 *Problem parameters*

A two-span beam of 10 m equal spans is examined. To size the beam initially, the maximum elastic bending moment when subjected to moving 100 kN point load is used. A minimum resistance formula ignoring dead load (Nowak, 2001) is used:

$$R_{MIN} = \left[\alpha_L \left(M_L \right) \right] / \phi \qquad (21)$$

where α_L is live load factor (1.5), ϕ is the resistance factor (0.88) and M_L is the live load on the structure. The section used is a 457×152×74 hot-rolled universal beam. The steel is assumed to have yield strength of 265 N/mm^2 and a modulus of elasticity of 210 kN/mm^2.

Failure is defined to occur when the global stiffness matrix becomes singular in the nonlinear analyses [13]. This corresponds to the formation of a mechanism [14]. For comparison, a moving elastic analysis and a moving nonlinear analysis taking strain hardening into account are also presented in some cases. The strain hardening stiffness is taken to be 1.5% of the elastic stiffness [9]. This prevents the global stiffness matrix turning singular and a collapse mechanism forming. However, significant ductility and rotation of cross sections can occur numerically using this assumption. Whilst these rotations should be checked for real sections, for this work, the allowance of strain hardening identifies the residual moments in the structure and provides a comparison to an elastic analysis of the moving load

4.2 Example moving single point load analysis

A moving single point load of 100 kN is considered. To establish the collapse load factor, that is, the ratio of failure load to the working load of 100 kN, the load is increased after each complete run across the structure, and this is continued until a collapse mechanism forms. An arbitrary speed of 1 m/s is used with a time step of 1 s. It must be noted that vibration of the beam is ignored. The bending moment time-history is shown in Figure 4 at each plastic hinge location.

From Figure 4(b) and 4(c), it can be seen that a collapse mechanism forms when the point load is approximately 4 m from the left hand side. As the load traverses the structure, plastic hinges successively form at 3 m, 4 m, and 10 m. The plastic hinge formed at 3 m is not present at collapse as the load has travelled beyond this point and unloading has taken place. This is identified in Figure 4(a).

4.3 Collapse load factors for a single moving point load

Typically, the collapse load factor for moving load problems is found by first identifying the location of the loads that causes the maximum elastic moments. Then, a nonlinear analysis is carried out with the load(s) located statically at this location [3]. A difficulty arises in choosing what is meant by the critical elastic location. For example, in the two-span continuous beam considered here, the point load locations causing the maximum sagging moment and maximum hogging moment are different. Furthermore, the load factors corresponding to failure of the beam are different for these two different locations. However, the true collapse load factor can be found using the nonlinear moving load approach developed here.

The load factors (λ) corresponding to failure are found for three scenarios: a static nonlinear analysis is carried out with the load located at the critical elastic maximum sagging (1) and hogging (2) positions; and a moving load nonlinear analysis (3) is carried out using the procedures outlined earlier. The results for each of these scenarios are given in Table 1. It is clear from these results that the location identified by the maximum elastic sagging moment is the closest to the true collapse load factor. However, it is significant that the true result (scenario (3)) is not given by either elastic means of locating the load.

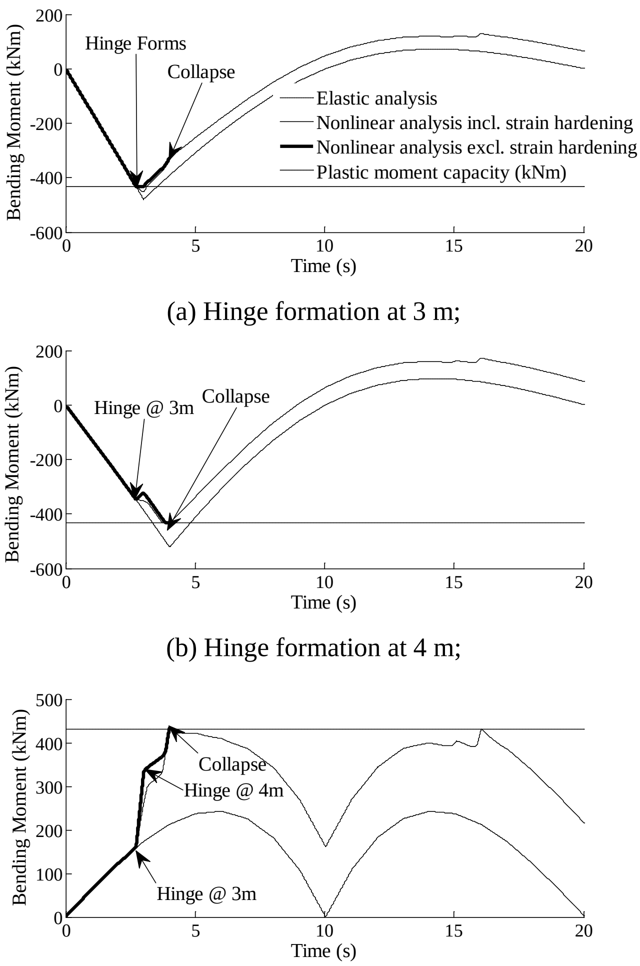

(a) Hinge formation at 3 m;

(b) Hinge formation at 4 m;

(c) Bending moment at 10 m through time;

Figure 4. Time history of bending moment.

Table 1. Failure Load Factors.

Loading scenario*	(1)	(2)	(3)
Position (m)	4.3	5.8	---
λ	2.516	2.796	2.524

* Refer to text for description of scenarios.

4.4 Collapse load factors for two point loads travelling in the same direction

A range of inter-load spacings (ILS) for two same-direction 50 kN point loads are considered. The ILS is expressed as a ratio of the spacing (x) to the length of the beam (L = 20 m). The elastic critical location collapse load factors (sagging position-λ(1) and hogging position-λ(2)) are found for comparison. The results are shown in Figure 5, expressed as a ratio of the true collapse load factor.

Figure 5 shows that for the majority of inter-load spacings the load factor found using sagging is close to the true collapse load factor. The collapse load factors found using hogging are often far higher than the true value, and this could lead to an unsafe assessment.

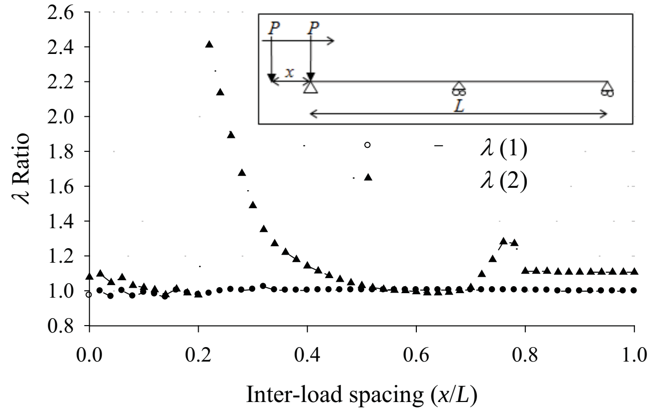

Figure 5. Two point loads moving in the same direction.

4.5 Collapse load factors for two point loads travelling in opposite directions

Two 50 kN point loads travelling in opposite directions are considered for a range of relative starting positions (again termed inter-load spacings). The results are again compared to those found using the elastic critical locations through a ratio of load factors and are shown in Figure 6.

It can be seen from Figure 6 that similar to the uni-directional case, the elastic sagging critical location generally gives load factors close to the true collapse load factor. However, for an ILS of 0.2 the elastic locations give load factors higher than the true load factors and so are unsafe. Further, for an ILS of around 0.8, the elastic hogging location gives unsafe load factors.

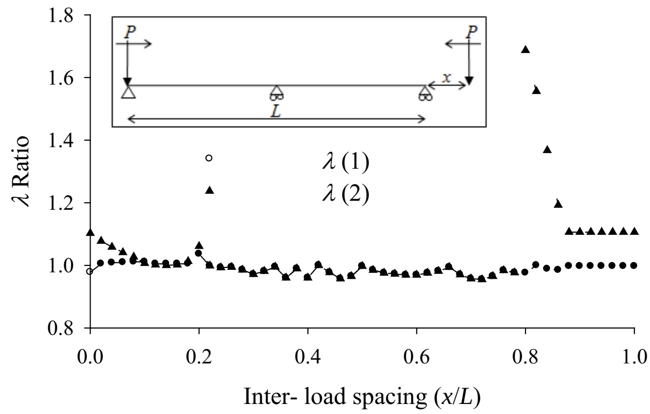

Figure 6. Two point loads moving in opposite directions.

5 PROBABILISTIC ANALYSIS

5.1 Reliability analysis of static loads

Loads located at the critical elastic sagging moment location are examined further using reliability analysis. This is to reflect common practice for bridge reliability analyses [3][15]. The results are compared to the actual failure probabilities obtained using a moving-load nonlinear analysis.

The section plastic moment capacity and the point load are the random variables of the problem and are assumed independent: all other variables are taken to be known. The coefficients of variation (CoV) of the random variables given in Table 2 are taken from [16] and [17].

Table 2. Statistical Properties.

Variable	μ	CoV	Distribution
M_p	431.16 kNm	0.075	Normal
P	100 kN	0.25	Normal

Only flexural failures are considered and other failure mechanisms were ignored. Two limit sates are considered. An elastic limit state is used in which failure occurs when the elastic moment exceeds the plastic moment capacity:

$$g = M_p - \frac{Pab}{4L^3}\left(4L^2 - a(L+a)\right) \tag{21}$$

This in effect assumes an ideal elastic-plastic material.

Ultimate collapse due to the formation of a mechanism brought about by the formation of plastic hinges is also considered. Virtual work for the collapse mechanism (one hinge forming at the position of the point load and the other at the interior support) gives the plastic limit state function:

$$g = M_p(1 + \frac{2a}{b}) - aP \tag{22}$$

5.2 First-order reliability analysis results

The FORM results are given in Table 3 for the two limit state functions of Equations (21) and (22). The functions are plotted in standard normal space (*U*-space) in Figure 6. This allows a visual comparison between reliability indices to be made.It can be seen clearly that a higher reliability index (β) can be achieved when using a less conservative limit state function. This expected result corresponds to a lower probability of failure.

Table 3. FORM Results

	Elastic	Plastic
β	3.69	4.84
p_f	1.121×10^{-4}	6.492×10^{-7}
M_p *(design value)*	337.78 kNm	178.186 kNm
P (design value)	336.93 kNm	196.54 kNm

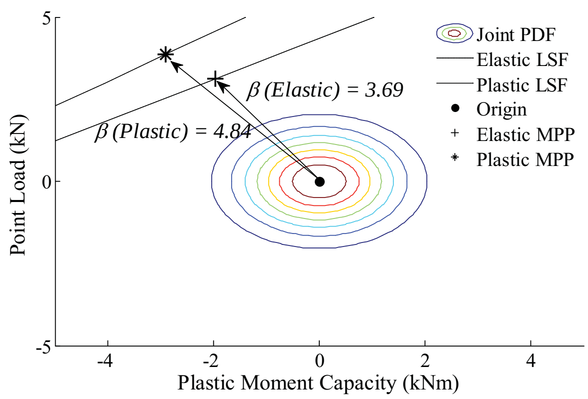

Figure 7. Limit state comparison in standard normal space.

5.3 Importance sampling for reliability analysis of moving load

The common assumption of locating the loads at the elastic critical locations for a reliability analysis is assessed using Importance Sampling and the moving load analysis model. The design point found using the FORM analysis considering a plastic limit state function is used as the MPP for the Importance Sampling (see Section 3). Ten thousand samples are generated around this design point. Each combination of random variables is analysed using a constant speed of 1 m/s and a refined time step of 0.2 s.

A ‘success’ rate of approximately 50 % is found and so the estimate of MPP is reasonable. Figure 9 gives the histogram of point load locations at failure. All failures occur while the load is on the first span. Most occur when the moving load is positioned 3 metres from the left hand support.

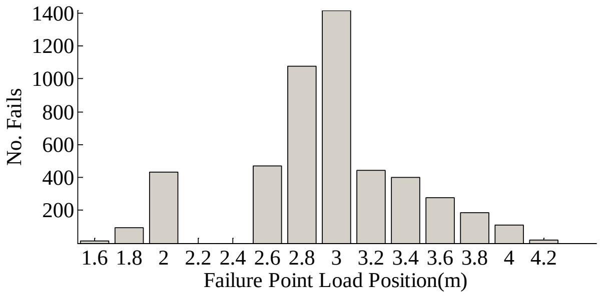

Figure 8. Number of fails at each point load position

A reliability index of 4.84 is found corresponding to a probability of failure of 6.488×10^{-7}. This is only marginally different to the probability of failure found using the plastic static critical load location (Table 3 – $p_f = 6.492\times10^{-7}$). This interesting result means that locating the loads using an elastic analysis may not give the true probability of failure.

6 DISCUSSION & CONCLUSIONS

A moving nonlinear analysis method is proposed in this work. The response of an indeterminate steel beam subjected to moving loads is examined and compared to that when subjected to static loads. Both deterministic and probabilistic analyses are performed.

The deterministic study is used to establish load factors causing collapse for moving loads and critically placed static loads. Static load positions were identified as positions causing maximum sagging and hogging bending moments using an elastic analysis. For this particular structure and the various loading scenarios analysed, it is established that the static load factor found using the position causing maximum sagging moment closely relates to the load factor found using the proposed moving load approach. For the majority of circumstances examined the load factor found using the maximum hogging position over-estimates the strength capacity of the structure.

A probabilistic study is presented examining a single static load, using FORM and Importance Sampling when examining a moving load. An elastic limit state function which is typically implemented in practice is analysed and compared to a plastic limit state function. The plastic limit state function has a less conservative definition of failure and produces a higher reliability index and a lower probability of failure as expected.

The reliability index found when analysing the moving load corresponded exactly to that found using a static analysis. The common assumption of locating the point load at a critical position can be deemed appropriate for this structure subjected to a single point load. However the moving load approach provides a more complete overall assessment of failure.

It can be concluded from this study that taking a less conservative definition of failure, significantly higher reliability indices can be found, more indicative of the true safety of the structure. An accurate representation of a structure’s nonlinear behaviour when subjected to moving loads can be found using the proposed method. Both these findings when applied to practical problems may lead to a more accurate assessment of existing bridge structures and consequently a more informed decision on required rehabilitation measures.

REFERENCES

[1] Parsons & Brinckerhoff, (2003), A review of bridge assessment failures on the motorway and trunk road network. *Final Project Report prepared for the Highways Agency. Parsons Brinckerhoff Ltd.*

[2] Imhof,D. (2004). *Risk Assessment of Existing Bridge Structures*. Ph.D Thesis. King's College, UK.

[3] Wisniewski D.F., Casas J.R. & Ghosn M, (2009). Simplified probabilistic non-linear assessment of existing railway bridges. *Structure and Infrastructure Engineering: Maintenance, Management, Life-Cycle Design and Performance*. 5, 6, 439-453.

[4] Melchers, R.E., *Structural Reliability Analysis and Prediction*. Sussex: John Wiley and Sons, 1999

[5] Soares, R.C., Mohamed, A., Venturing, W.S. & Lemaitre, M., (2001), Reliability analysis of non-linear reinforced concrete frames using the response surface method. *Journal of Reliability Engineering and System Safety*, 75, 1-16.

[6] Neves, R.A., Chateauneuf, A., Venturini, W.S. & Lemaire, M. (2005), Reliability analysis of reinforced concrete grids with nonlinear material behavior, *Journal of Reliability Engineering and System Safety*. 91,735-744.

[7] Torrii, A.J. & Machado, D.A., (2010), Reliability analysis of nonlinear reinforced concrete beams. *Proceedings for Asociacón Argentina de Mecánica Computacional Conference*, Buenos Aires, Argentina.

[8] Choi, S.K., Grandhi, R.V. & Canfield, R.A., *Reliability - based structural design*. London: Springer, 2007.

[9] Li, G.Q. & Li, J.J., *Advanced Analysis and Design of Steel Frames*. Sussex: John Wiley & Sons, 2007.

[10] Ghali, A. Neville, A & Brown, T., *Structural Analysis-A unified classical and matrix approach*. London: Spon Press, 2009.

[11] Becker, A., *An Introductory Guide to Finite Element Analysis*. Suffolk: Professional Engineering Publishing, 2004.

[12] Chen, W., Goto, Y. & Richard Liew, J., *Stability Design of Semi-Rigid Frames*. New York: John Wiley & Son, 1996.

[13] Val, D., Bluger, F. & Yankelevsky D., (1997), Reliability evaluation in nonlinear analysis of reinf*orced concrete structures. Journal of Structural Safety, 19, 2,203-21.*

[14] Ghosn, M & Moses, F., Redundancy in highway bridge superstructures. NCHRP Report. 406, TRB - Transportation Research Board, Washington D.C., 1998.

[15] Biondini, F., Bontempi, F., Frangopol, D., & Melerba, P.,(2004), Reliability of material and geometrically non-linear reinforced and prestressed concrete structures, *Computers and Structures* 82, 1021 - 1031.

[16] Ellingwood, B.R. and Galambos,T.V.,(1982), Probability -based criteria for structural design, *Journal of Structural Safety*,1, 15 - 26

[17] Nowak, A.S. & Park, C.H. (2001), R*eliability analysis of prestressed concrete bridge g*irders: comparison of Eurocode, Spanish Norma IAP and AASHTO. *Journal of Structural Safety* 23,331-344.

Looking after our assets through current best practice inspection, testing, remediation and monitoring

Brian McFarland[1], Paul Callender[1], Enda McKenna[1]
McFarland Associates Ltd, 366, Woodstock Road, Belfast, BT6 9DQ
email: brian.mcfarland@mcfassoc.com, paul.callender@mcfassoc.com, enda.mckenna@mcfassoc.com

ABSTRACT: In an era of austerity ever tightening budgets are expected to stretch further and further. Having suffered cutbacks across all aspects of infrastructure, new build is being superseded by clever and innovative remediation and asset management. The challenge to asset managers is to accurately assess the current condition of their structure in order that its serviceability life can be determined. Only when we know the nature, source, extent and significance of an assets deterioration and condition can we safely model its future safe performance. With the aid of current best practice inspection, testing and monitoring techniques, coupled with an in depth knowledge of structures, we are now able to safely manage assets more effectively and maximise the benefits of any budget expenditure. Where repair work is inevitable, particularly with aged concrete structures, the use of innovative products, such as hybrid anodes, and other techniques has allowed bespoke, cost effective solutions to be designed. Likewise, the embedment of smart sensors has allowed the effectiveness of these repairs and the general condition of the structure to be monitored. In Northern Ireland over the past few years we have adopted this approach with a number of large multi-span concrete bridges and a large dry dock. Each of the structures selected for this paper has had its own unique challenge ranging from access difficulties to complex construction detailing. This paper is intended to provide a review of current best practice remediation asset management as applied to a selection of structures in Northern Ireland.

KEY WORDS: Asset Management; Concrete; Inspection; Testing; Monitoring; Remediation; Anodes

1 BACKGROUND

With our economy hopefully in the recovery phase, following the financial crisis, there is an emphasis on rebalancing from an “over-dependence on the public sector and away from debt-fuelled consumption to growth based on export and investment. Investment in infrastructure is critical to that ambition” [1].

However, the UK was ranked 33rd in last year’s World Economic Forum infrastructure quality index, a position below Germany, France and Spain. Whilst we know that we need to improve, moving up the rankings is becoming an increasingly more difficult task [2].

Our challenge is to maintain and replace an ageing and outdated infrastructure asset base, some of which dates from the 19th Century. This is against a backdrop of increased demand with UK roads, for example, being amongst the most congested in Europe.

In fact, it is estimated that the cost of “maintaining, renewing and expanding the United Kingdom’s transport infrastructure will be around £350 billion over the next two decades” [3].

2 INTRODUCTION

The environment provided by good quality concrete to steel reinforcement is one of high alkalinity due to the presence of the hydroxides of sodium, potassium and calcium produced during the hydration reactions. The bulk of the surrounding concrete acts as a physical barrier to many of the steel’s aggressors. In such an environment, steel is passive and any small breaks in its protective oxide film are soon repaired. If, however, the alkalinity of its surroundings are reduced, such as by neutralisation with atmospheric carbon dioxide and sulphur dioxide or depassivating anions such as chloride are able to reach the steel, then severe corrosion of the reinforcement can occur.

Corrosion of reinforcement within concrete is only one form of metallic corrosion but it is the single largest cause of deterioration of our infrastructure. The two primary sources of such deterioration are Carbonation, which is the loss of concrete alkalinity and Chloride Attack, which is due to the adverse effects that chloride ions have on the reinforcement. The addition of moisture and oxygen to reinforcement, in the presence of carbonation and/or chloride ions, can cause corrosion and the formation of rust. The volume occupied by the rust product is eight times greater than the original steel product and the expansive forces are sufficient to cause concrete cracking, delamination and eventually spalling. Other forms of corrosion may occur such that the reinforcement is pitted locally without generating expansive rust products.

In industrial countries, the total cost of metallic corrosion related deterioration is believed to be of the order of 4% of GNP. This value includes direct costs such as metal wastage, replacement, maintenance and repair as well as the indirect costs associated with shut-downs, disruption and Health & Safety [4].

This paper outlines the refurbishment approaches adopted for repairing five key structures in Northern Ireland. In each instance, the asset was maintained in service and the remediation was tailored to the structure’s individual needs.

3 CATHODIC PROTECTION

Electrochemical treatments for chloride-induced corrosion include cathodic protection and chloride extraction. Chloride extraction is a temporary treatment with the onerous objective of removing the chloride. Cathodic protection is a permanent treatment and may be applied using impressed or galvanic current. Impressed current systems require sustained management by skilled personnel to ensure successful installation and operation. Galvanic systems are not as powerful and may not arrest an active corrosion process. However, they do function in a preventative role, they are very simple to install and they require very little maintenance.

A new treatment to arrest an active corrosion process and maintain steel passivity combines a brief pit-re-alkalisation treatment, impressed off a sacrificial anode system, with galvanic protection subsequently delivered from the same anode system.

The high pH at the steel is restored by the pit-re-alkalisation process and maintained by galvanic protection. This novel combination is referred to as a hybrid electrochemical treatment. The power of an impressed current electrochemical treatment is combined with the low maintenance requirements of galvanic protection. The maintenance of the impressed current treatment is limited to a brief period during installation when steel passivity is restored [5].

4 CASE STUDIES

4.1 Hillhall Road Bridge [6]

Hillhall Road Bridge, Lisburn was constructed in 1963 during the development of the M1 Motorway between Belfast and Dungannon. It is a cast in-situ structure comprising three piers and fours spans over the M1 motorway at Lisburn. An overall general inspection identified significant deterioration on the western pier. Consequently, in-depth testing was carried out to this pier. This testing included:

- Visual inspection;
- Cover to reinforcement depth measurements;
- Concrete carbonation depth measurements;
- Incremental concrete dust sampling and subsequent chloride and cement analysis;
- Half –cell potential measurements;
- Resistivity measurements; and
- Corrosion rate measurements.

The structure had previously been protected by an impressed current cathodic protection system that had subsequently broken down. Behind the surface applied anode, extensive concrete delamination and spalling had occurred.

Following analysis of the test information, it was found that only the east face of the west pier had suffered deterioration but this was not over the entire surface. Pictorially overlaying the various items of test information quickly revealed the **nature, source, extent and significance** of the problem as shown in Figure 1 below.

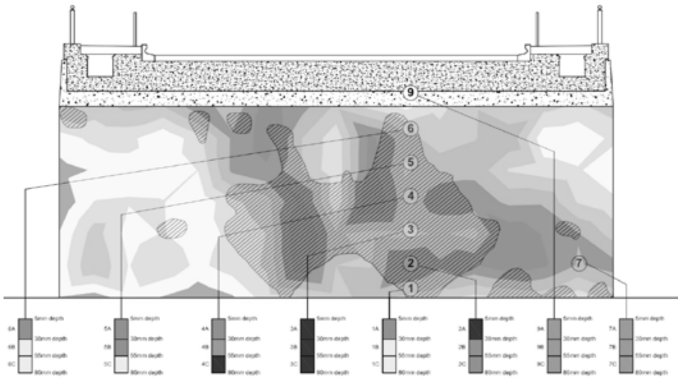

Figure 1. Summary of testing information.

Darker areas highlight centres of corrosion activity on the pier, as indicated through half-cell potential measurements. Hatched areas represent concrete delamination and spalling. Chloride concentrations within these areas were found to be above currently acceptable limits. Resistivity and corrosion rate measurements, combined with localised breakouts, confirmed that there was no significant loss of steel section and consequently negligible reduction in structural capacity.

Through an in-depth understanding of the structure and its condition, concrete repairs were minimised and the need for either propping or lane closures was avoided. Accompanying the minimised removal of delaminated concrete will be the installation and charging of hybrid anodes to mitigate the effects of the residual chloride contamination.

4.2 Queen Elizabeth Bridge, Belfast [7]

Queen Elizabeth Bridge was built in 1966 and is one of eight bridges over the River Lagan. The main bridge comprises a reinforced concrete slab in composite action with eleven steel plate girders of tapering sections to form a three span structure. The central span comprises two cantilevered sections adjacent to each pier and a simply supported suspended span between the ends of the cantilevers.

Inspection and testing was carried out on the top surface and sub-structure during five phases which allowed the structure to remain in service during the works. Access to the underside proved difficult due to its span across the River Lagan. However, a complex, hung scaffold system was developed allowing access to all areas of the soffit. The scaffolding system was additionally clad in a welded, re-cyclicable, plastic membrane to create a controlled enclosure enabling the temperature and humidity to remain constant – important factors for the repainting of the steelwork.

Concrete cracking, delamination and spalling were evident across much of the half- joints. Test results indicated high corrosion rates and chloride ingress at the four half joints – both on the deck surface and the soffit beneath.

Again, through an in-depth understanding of the structure and its condition, concrete repairs were minimised and the need for either propping or additional lane closures was avoided.

A hybrid, sacrificial galvanic anode system was recommended as a long term remedial treatment at areas where the reinforcement was found to be corroding as a result of chloride ingress – notably at the half-joints on both the deck surface and the soffit as well as within the viewing galleries at both abutments. The anodes work by corroding preferentially to the surrounding steel protecting it from further corrosion damage.

Figure 2. Exposed concrete deck at half-joint.

Following the removal of defective concrete, anodes were installed within the surrounding unrepaired but chloride contaminated concrete at typically 500mm centres. Galvanic anodes can either be charged or self-driven, depending on the test results and structural conditions. This enables a rapid installation and as a targeted application, minimises costs. The anodes have an additional benefit in that they can be remotely monitored and their residual life determined. This fact allows us to provide real time assessment of ongoing structural performance and future serviceability.

4.3 Strule Bridge, Omagh [8]

Strule Bridge was constructed in 1966 and spans the Strule River in Omagh. The structure is statically determinate and takes the form of 2no. cantilevered end spans that carry a simply supported 'drop in' span which rests on concrete halving joints. Both the 'drop in' and cantilevered end spans are composed of post tensioned beams supporting an insitu deck slab. The cantilevers side spans also have a partial bottom slab between the end supports and the intermediate piers.

Inspection and testing of the structure was carried out during seven phases allowing the structure to remain in service during the works.

Again, access proved problematic due to the structure's span over the River Strule and its regular flooding posed a physical threat to the scaffold.

Visual inspections and testing revealed areas of reinforcement corrosion and chloride ingress, particularly around the half-joints, abutment walls and, more importantly, to the supporting ends of the post-tensioned beams of the sub-structure.

Figure 3. Post-tensioned beam ends.

Initially it was thought that a "blister" repair would have to be placed around the ends of the post-tensioned beams and a lateral post-tensioning introduced through Macalloy bars. However, with careful removal of infill concrete, the parent concrete was found to be in better condition than was first envisaged and the ends of the strands had suffered only surface corrosion.

Figure 4. Exposed, corroding post-tensioned reinforcement at cantilevered beam.

In this instance, a specially designed sacrificial, 'patch' anode was developed for inclusion in the repairs. The size and capacity of this anode was designed to be such that it would protect the corroding reinforcement and strands but would not pose a risk of hydrogen embrittlement.

4.4 Shillington's Bridge, Portadown [9]

Shillington's Bridge, also known as Northway and the Garvaghy Road Flyover, was officially opened in June 1970. The bridge, situated beside Shillington's yard at Portadown, carries the A3 over the River Bann. The structure is approximately 200m long and comprises a cast in-situ deck slab spanning from two end abutments to a central pier. Cast in-situ circular columns provide interior supports.

Inspection and in-depth testing was carried out on both the deck surface and sub-structure of the bridge. It was found that both abutments as well as the central supporting pier were heavily deteriorated. Bearing pads at both abutments were observed to be deformed as a result of movement of the deck slab.

The abutments were structurally less sensitive than the anchor pier and their repair, whilst extensive, was relatively straightforward. Hydro-demolition was the means of removal of the concrete.

Figure 5. Abutment repairs.

Of greater concern, was the damage to the central, anchor pier particularly at its upper level and directly beneath the bearings. The complex design of the structure, particularly in the vicinity of the anchor pier, meant that if propping had to be utilised it would be prohibitively expensive.

Figure 6. Extensive concrete spalling and exposed corroding reinforcement on the central pier.

The restrictions posed by the extent of deterioration within the anchor pier and its bearing arrangements meant that a type of concrete 'keyhole surgery' was adopted. Our in-depth inspection and testing identified the areas of concrete to be removed and an initial repair methodology was adopted. This proposed the removal of concrete in 1m square patches in phases that controlled any additional load being added to the parent concrete. The difficulty with this approach was where reinforcement had to be either supplemented or replaced, the need to achieve lap lengths, necessitated the extent of breakout to be extended. It was therefore decided that, as a secondary stage, all loose and delaminated concrete would be removed. Loose and delaminated concrete was deemed to be structurally redundant and therefore its removal would not add load to the parent concrete. With this layer of defective concrete removed, a clearer picture was obtained of the underlying reinforcement and the need for its replacement. This allowed for a refinement of the sequence of patch repairs whereby, as an additional stage, defective bars were individually water-jetted out and either supplemented or replaced.

Again, a hybrid anode system was installed to compensate for the existence of chloride contamination both behind the reinforcement and in areas of concrete not needing to be removed.

The hybrid anode is a dual technology anode based on the use of a sacrificial metal in both an impressed current role and a sacrificial anode role. Initially, an impressed current is driven from the anode to the steel using a temporary power supply. In the process, corroding sites on the steel are moved to the surface of the installed anode. This occurs because the treatment generates inhibitive hydroxide ions at the steel and aggressive chloride ions are drawn from the concrete to the installed anode. At the end of the brief impressed current treatment, the anode is connected to the steel to act as a sacrificial anode in a long term corrosion prevention role.

Figure 7. Hybrid anode being installed.

4.5 Belfast Dry Dock [10]

Figure 8. Overview of the Belfast Dry Dock.

The Harland and Wolff Dry Dock (known as the Belfast Dry Dock) was constructed between 1965-68 by Charles

Brand and Sons to a design by Rendel, Palmer and Tritton. It is 1150 feet long by 160 feet wide and, when constructed, was one of the five largest docks in the world. The dock can accommodate ships up to 200,000gt. The dry dock is used for the construction, maintenance and repair of ships, boats and other watercraft.

Inspection and in-depth testing confirmed that the vast majority of the concrete deterioration was within the galleries at the upper levels of the dry dock. In particular, the gallery walls had suffered extensive concrete cracking, delamination and spalling as a result of reinforcement corrosion.

In this instance, the extent of damage to the walls was such that the only option was to remove the concrete through hydro-demolition and replace with a sprayed repair.

A sacrificial hybrid anode system was also utilised to protect the soffit and deck slab of the gallery adjacent to the newly reformed walls. The threat of incipient anodes being set up in these adjacent chloride contaminated members was significant.

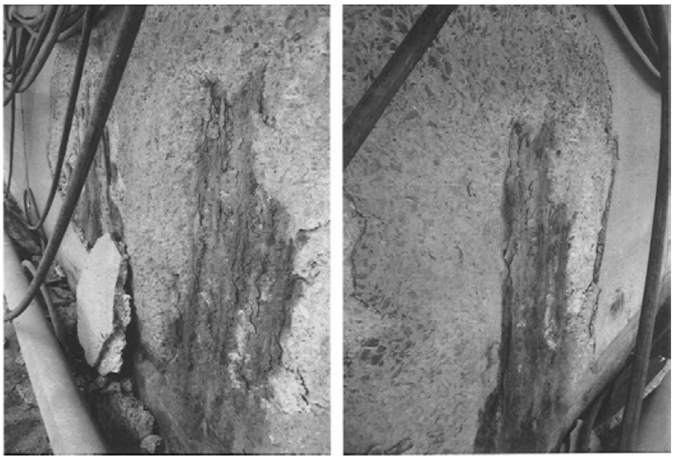

Figure 9. Extensive concrete spalling and exposed corroding reinforcement on walkway galleries

The day to day workings of this valuable asset posed additional complications to the repair works as the client insisted on the continued use of the facility. This resulted in the galleries being flooded on numerous occasions during the repair process. There was also a requirement to monitor and assure the future serviceable condition of the galleries for a period in excess of 25 years.

To meet this requirement, a steel reinforcement monitoring system was installed which utilised a series of embedded reference electrodes, placed at specific locations on the structure, to monitor the potential of the reinforcing steel and any corrosion activity. The system is powered via an attached solar panel and is interrogated remotely. Such a monitoring system can be used in new, old and repaired structures and, over time, can be used to monitor and predict the current and future rates of deterioration. This has significant advantages for the long-term management of assets.

Figure 10. Preparing the steel reinforcement monitoring system for remote access following installation

5 DISCUSSION

With comprehensive inspection and testing, a structure can be placed at an appropriate place in its lifecycle timeframe (see graph 1 below for clarity). With this knowledge and understanding, an informed decision can be made as to when intervention is most cost effective and when to implement optimum solutions to reduce or reverse deterioration, thus extending the life of the asset.

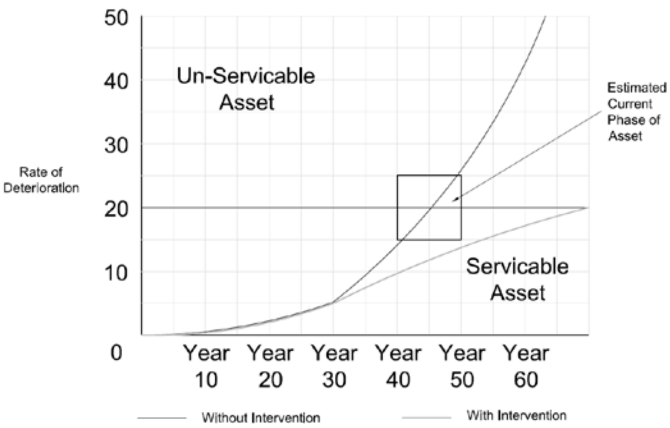

Graph 1. Estimated rate of a structures deterioration over time – without intervention and with intervention

6 CONCLUSION

Prevention is always better than cure and the same can be said for carbonation and chloride ingress. However, if carbonation has reached or passed the level of reinforcement and/or if chlorides have reached the reinforcement in sufficient quantities to cause corrosion, there are better ways of dealing with the problem than traditional breaking out of concrete.

Traditional breaking out of concrete with breakers is both noisy and disruptive and is often responsible for causing micro-cracking within the parent concrete. It can involve the removal of perfectly sound concrete because it is carbonated or chloride contaminated and can also introduce new planes of weakness. It is worth remembering that the vast majority of concrete repairs we undertake are superficial and non-structural and should therefore be kept as small as possible.

The wide variety of electrochemical techniques available offer a great ability to undertake non-destructive repair. It can be described as fighting 'fire with fire' with the benefit of providing future corrosion protection and therefore preventing incipient anode formation. The most difficult problem for specifiers, however, is deciding which technique is most appropriate having, of course, identified what is wrong with the structure in the first instance.

With recent developments in monitoring, instead of repairing structures that are already starting to fail we are now able to pro-actively manage our assets and make better commercial decisions at an earlier stage in the deterioration process.

REFERENCES

[1] Lord Sassoon, (July 2011), 'Speech by the Commercial Secretary to the Treasury, Lord Sassoon, at Innovations in Financing Europe Infrastructure'.

[2] HM Treasury and Infrastructure UK, (2011), 'National Infrastructure Plan 2011', *HMSO*.

[3] Mills, J., Shilson, S., Woodley, Q., Woodwark, A. (2011), *Keeping Britain Moving: The United Kingdom's transport infrastructure needs,* McKinsey & Company.

[4] McFarland, B. (2012), 'Carbonation, Chlorides & Electrochemical Concrete Repair'.

[5] Davison N., Roberts, A.C., and Glass, G. K., 'Hybrid corrosion protection of chloride-contaminated concrete**'**, *Proceedings of the Institution of Civil Engineers, Construction Materials*, 161 (4) (2008) 163-172.

[6] McFarland, B., Callender, P., McKenna, E., (2011), '11507_Hillhall Road Bridge Inspection and Testing' *Company Report.*

[7] McFarland, B. , Callender, P., McKenna, E., (2011), '11679_Queen Elizabeth Bridge Inspection and Testing' *Company Report*.

[8] McFarland, B. , Callender, P., McKenna, E., (2011), '11643_Strule Bridge Inspection and Testing' *Company Report*.

[9] McFarland, B. , Callender, P., McKenna, E., (2011), '11578_Shillington's Bridge Inspection and Testing' *Company Report.*

[10] McFarland, B. , Callender, P., McKenna, E., (2011), '11540_Belfast Dry Dock' *Company Report*.

The influence of fibrous grass silage extract on the shrinkage properties of cementitious mortars

C. King[1, 2], M. Richardson[2], J. McEniry[1], P. O'Kiely[1]
[1]Animal & Grassland Research and Innovation Centre, Teagasc, Grange, Dunsany, Co. Meath, Ireland
[2]School of Civil, Structural and Environmental Engineering, University College Dublin, Belfield, Dublin 4, Ireland.
email: colman.king@teagasc.ie

ABSTRACT: Shrinkage of cementitious systems, such as unreinforced floor screeds, can occur at the early curing stage causing problems such as cracking and crazing. One method of minimizing the effect of shrinkage is the addition of fibres to the mix. Typical materials for fibre manufacture include polypropylene. Grass fibres have long been used to enhance the tensile strength of mud bricks and it is postulated that products from plant biomass may provide sustainable solutions to enhancing the tensile strength of cementitious mortars during the first critical hours. It is during this period when restrained shrinkage of the weak material may lead to cracking. Grass represents Ireland's largest biomass resource for renewable energy, chemicals and materials. In a 'green biorefinery' plant biomass is separated into press-cake and press-juice fractions. The press-cake fraction can be used in a range of fibrous applications. This paper reports the findings of an optimisation study of fibre characteristics and the effect of three levels of fibrous grass silage press-cake inclusion on the shrinkage properties of mortar specimens. Following an optimisation study of grass type, harvest date, nitrogen treatment and fractionation the material used in the shrinkage experiments was selected. Three replicate plots of perennial ryegrass were harvested while in the primary growth and were then preserved as silage for 100 days. These three replicate silages were then subjected to hydrothermal conditioning (three washing steps with water and detergent at 60˚C), pressed at 4.5 MPa and oven dried (40˚C for 48 h) in order to produce a fibrous-rich press-cake fraction. The three replicate plots of press-cake were then mixed and added to mortar specimens at 0, 0.1 and 0.2 % fibre inclusion rates to investigate the effects on restrained and long-term drying shrinkage. Comparative studies with grass-fibre reinforced modelling clay and with polypropylene-reinforced mortars were also conducted. It was found that the grass-fibre press-cake was very effective in restraining shrinkage in modelling clay thus demonstrating its potential use as an engineering material. Surprisingly, higher overall free shrinkage occurred in specimens containing fibres – both press-cake and polypropylene – at early ages (all inclusion rates). Despite higher overall drying shrinkage the press-cake fibres were as effective as polypropylene fibres in respect of mitigating the risk of cracking due to early-age restrained shrinkage in mortars. This demonstrates that the material is worthy of further research in this context.

KEY WORDS: Shrinkage; mortar; grass fibre, cementitious materials.

1 INTRODUCTION

Early-age shrinkage of cementitious-based building products is an inevitable consequence of the inclusion in the mix proportions of water contents above the level required solely for full hydration. Workability requirements typically demand inclusion of excess water, over and above that which can be chemically bound during hydration. This free water is released from the hardened concrete or mortar at a rate which is dependent on ambient atmospheric conditions. Some degree of drying shrinkage is therefore inevitable. The resultant shrinkage rarely occurs in unrestrained conditions. Internal or external restraints inhibit free shrinkage and this generates tensile stresses in the element. Stresses may also arise through early thermal effects as the material cools from peak temperature caused by hydration reactions. These internal stresses, whether from drying shrinkage or thermal effects are released through crack formation if the tensile strain capacity is exceeded [1].

Addition of small quantities of fibrous material can enhance the tensile strain capacity of concrete or mortar, especially in the critical early stages of setting and hardening [2]. Crack formation may then be either eliminated or at least minimised in respect of the number of cracks or the individual crack widths. Fibre inclusion, to minimise shrinkage of elements used in building construction, dates back to biblical times and the use of straw in mud brick elements is referred to in the Book of Exodus [3].

Commonly used fibres in concrete and mortars include steel and polypropylene. A search for less energy-intensive fibres, in the context of sustainable development, has refocused interest in natural materials. Straw is a good example of such a material in that it may be classified as a waste product after the extraction of valuable nutritional material from the crop. In the same way, grass (or more specifically, fibrous material derived from grass) may provide a multi-use material with benefits for sustainable construction.

The pre-eminent use of grass in the European beef and dairy production industries [4] has recently diminished to some extent due to economic factors and alternative uses of this abundant resource are being explored [5]. Its use as a renewable energy source, through a 'green biorefinery' is of particular interest. The fibre fraction which would result from such a 'green biorefinery' would be one of the largest material streams and environmental considerations demand that a viable role be found for it. Deployment in conditions where it assists replacement of existing energy-intensive products is of particular interest.

The building industry provides many opportunities for the use of more sustainable materials than those employed at present. Examples of press-cake usage could include use in stabilised soil blocks to partially replace the extensive use of concrete block in domestic housing or other low-rise buildings. Recent interest has been reported in this form of construction for greater use in the developed world by Goggins [6]. Equally it is postulated that it might provide a material source for use as fibre reinforcement in cementitious-based construction products as a replacement for steel or polypropylene fibres. Sarigaphuti et al. [7] have reported promising results with cellulose fibres derived from coniferous and deciduous trees. Since grass fibre press-cake is rich in hemicelluloses, cellulose, and lignin [8] it is thus worthy of further study in the context of crack control.

Modelling of shrinkage in cementitious systems owes much to the seminal work of Bazant, such as that published in 1988 [9]. Many authors have built on this work and significant influences of fibres on shrinkage have been determined through research by, for example, Zhang and Li [10]. The following have been identified as significant parameters:

- effective length of fibres parallel to the direction of shrinkage strain
- fibre spacing
- fibre aspect ratio
- and fibre content.

Additionally the bond characteristics of the fibre-matrix interface is significant in the case of minimisation of crack risk in restrained shrinkage, as reported, for example, by Grzybowski and Shah [11]. Many of these parameters are independent of the material type. Thus as long as the induced stress in the fibres does not exceed its tensile strain capacity, any fibrous material with fibres of sufficient length is worthy of consideration.

Given that grass fibre press-cake can be produced in a way that optimises the cellulosic building blocks it was decided to investigate the cellulosic nature of grass fibre rich press-cake; its tensile strength properties; and its role in shrinkage-induced crack control in cementitious based composite materials.

2 MATERIALS AND METHODS

2.1 Selection of grassland species

The selection of grassland species for use in the shrinkage trials was based on experimental work [12] which determined the yield and chemical composition of a range of common grassland species. These were grown under two rates of inorganic nitrogen fertiliser input (0 kg N ha^{-1} and 125 kg N ha^{-1}) and harvested fortnightly at five different harvest dates in the primary growth season, from May to July. The grasses studied were perennial ryegrass (*Lolium perenne* L. var. Gandalf); Italian ryegrass (*Lolium multiflorum* Lam. var. Prospect); tall fescue (*Festuca arundinacea* Schreb. var. Fuego); cocksfoot (*Dactylis glomerata* L. var. Pizza); and timothy (*Phleum pratense* L. var. Erecta).

The performance of the grass species in respect of fibre production is indicated in Table 1. This table shows, of particular relevance to this paper, the concentrations of neutral detergent fibre (NDF, i.e. total fibre), acid detergent fibre (ADF, i.e. cellulose and lignin) and acid detergent lignin (ADL, i.e. lignin) that were produced.

Table 1. Average dry matter (DM) yield, neutral detergent fibre (NDF), acid detergent fibre (ADF) and acid detergent lignin (ADL) concentration and dry matter digestibility (DMD) of five grass species.

Grass species	**DM yield (t DM ha^{-1})**	**NDF (g kg^{-1} DM)**	**ADF (g kg^{-1} DM)**	**ADL (g kg^{-1} DM)**	**DMD (g kg^{-1})**
PRG	8.40	556	318	20	713
IRG	8.07	518	303	20	698
Tall fescue	7.92	574	331	24	574
Cocksfoot	6.54	587	330	27	587
Timothy	8.13	608	347	29	608

PRG Perennial ryegrass
IRG Italian ryegrass

Despite there being little difference in the dry matter yield between the ryegrasses, tall fescue and timothy, it may be seen that timothy (*Phleum pratense* L. var. Erecta) performed best in terms of both high yields of dry matter and chemical fibre concentration. Cocksfoot performed worst in terms of dry matter yield.

Ensiling is a method of preserving plant material in the absence of oxygen so as to provide a supply of the crop outside the growing season. If grass were to be used as an industrial fibrous material this method of preservation would be necessary. The most suitable grass for ensiling, and therefore bioenergy, was Italian ryegrass. However it is necessary to consider selection of a species that also has high dry matter digestibility making it suitable for bioenergy potential. Perennial ryegrass is the predominant grass species sown in Ireland, primarily because its high dry matter digestibility makes it suitable for use in animal production. It therefore had a number of potential advantages.

In the context of this study, the optimal time of harvest is that which yields highest dry matter and chemical fibre concentration. A study was therefore conducted of the fibre composition of the five grass species [12]. The herbages were chemically analysed for neutral detergent fibre concentrations.

The performance of the grass species in respect of fibre production by harvest date (i.e. maturity) may be ascertained from the results presented in Table 2.

Table 2. Average dry matter (DM) yield, neutral detergent fibre concentration (NDF) and dry matter digestibility (DMD) by harvest dates (fortnightly from H1 – H5, respectively) in the primary growth.

Harvest date	**DM yield (t DM ha^{-1})**	**NDF (g kg^{-1} DM)**	**DMD (g kg^{-1})**
H1	4.86	483	794
H2	6.40	532	745
H3	8.60	593	687
H4	10.27	617	642
H5	8.93	618	611

In general it was found that fibre concentrations increased with advancing plant maturity in all species. Given that high yields of dry matter and chemical fibre concentration were higher for grass harvested at a later date, it was decided to use a later harvested grass due to the greater proportion of stems than leaves at this harvest date.

Further study concentrated on two grass species: timothy and perennial ryegrass, due to the findings in respect of high yields of dry matter/chemical fibre concentration and predominance/high dry matter digestibility respectively. The tensile strength of these two species was studied [13].

The performance of the leaf and stem in respect of tensile strength by grass species may be ascertained from the results presented in Table 3.

Table 3. Average tensile strength of the leaf and stem sections of perennial ryegrass and timothy at two harvest dates (H2 = 25 May and H4 = 22 June) in the primary growth [13].

Harvest date	Grass species	Plant part	Tensile strength (Nmm^{-2})
H2	PRG	Leaf	19.8
H2	Timothy	Leaf	20.4
H4	PRG	Leaf	16.4
H4	Timothy	Leaf	22.1
H2	PRG	Stem	36.8
H2	Timothy	Stem	49.1
H4	PRG	Stem	42.6
H4	Timothy	Stem	61.2

PRG Perennial ryegrass

It was found that the average tensile strength of stems was higher than leaves and that the average strength was approximately 25% higher for later harvest date (circa 50 N mm^{-2}). This further supported use of the later harvest date for optimising fibrous concentration. It was confirmed that the tensile strength of perennial ryegrass stems was higher than that of leaves.

Individual fibre cells in perennial ryegrass range from 0.94 – 1.44 mm in length and 0.010 – 0.018 mm in width [14]. However, in the current study the grass was not processed to isolate individual fibres but instead was chopped to a nominal length by a precision chop harvester.

Fractionation of grass into a press-cake and press-juice is also an important processing step in isolating a fibre rich product for industrial purposes. This was achieved by hydrothermal conditioning (three washing steps with water and detergent at 60˚C), pressing at 4.5 MPa and oven drying at 40˚C for 48 hours in order to produce a fibrous rich press-cake fraction [15].

Taking account of significant optimisation factors, perennial ryegrass harvested at later age (*Lolium perenne* L. var. Gandalf) was chosen in the current study to determine its effect on the shrinkage properties while acting as reinforcement in both a homogenous media (minimising variables in the experiment) and a very rich mortar (to study the potential value for further research on its application in the building construction industry).

2.2 Materials and sample preparation

In the current study, two contrasting media were used as a means of investigating the reinforcing effect of fibre-rich press-cake. Standard terracotta pottery clay was chosen because of its uniform composition. This provided a means of studying the performance of the press-cake in a situation where variables in the experiment were eliminated as far as possible to highlight the influence of variables related to the fibre. The mortar mix deliberately contained a high content of cement and a low content of sand, to encourage the maximum effect of shrinkage in mortar.

Triplicate field plots of perennial ryegrass were grown. It had been determined [12] that the effect of nitrogen fertiliser on neutral detergent fibre (NDF) concentration and dry matter digestibility (DMD) was not significant. The grass was treated with a fertiliser nitrogen application of 125 kg N ha^{-1} and harvested using a Haldrup forage plot harvester (J. Haldrup, Løgstor, Denmark) on the 22 June 2010. These plots of perennial ryegrass were then precision-chopped (19 mm nominal chop length) and representative samples of each plot were ensiled in laboratory pipe silos at 15°C. After 100 days ensilage, representative silage samples (n = 3) were subjected to hydrothermal conditioning (3 water + detergent: 1 silage at 60ºC for 30 minutes, with mixing) prior to mechanical pressing (hydraulic press) at 4.5 MPa to isolate the fibre-rich press-cake fraction. The press-cake fractions were oven-dried at 48°C for 48 hour prior to being thoroughly mixed together (Figure 1). This press-cake and wheaten straw (sourced from Teagasc, Grange) were included at rates of 0 (i.e. control) and 3.0 % (by weight) to standard terracotta pottery clay (dried, crushed and sieved to 2 mm) with a water content of 17.5 % (by weight) to determine the cracking behaviour of restrained shrinkage specimens.

Figure 1. Press-cake derived from perennial ryegrass

For both early restrained and long term drying shrinkage tests, the press-cake described above was also included with mortar at rates of 0.0 (i.e. control), 0.1 and 0.2 % (volume fraction). A cement: sand: water mix with a ratio of 1:1:0.5 was made for both tests using CEM II / A-LL Limestone Cement, 2 mm sieved sand and tap water. To ensure uniformity of water addition the press-cake was added to the mortar in a saturated state by being soaked in tap water for 24 h and then drained of excess water using a sieve. The quantity of water absorbed by the press-cake due to soaking was deducted from the figure of total water added to the mortar mixes, for both press-cake inclusion rates. Regarding mix procedure, all of the required sand and half the cement were first added to the pan mixer. The press-cake, water and the rest of the cement was added gradually to the running mixer. The mortar mix was then placed into pre-oiled ring moulds (Figure 2) and prism moulds (25 x 25 x 305 mm). The specimens were compacted through 25 drops on a standard flow table top for standard testing of mortars.

Figure 2. Restrained shrinkage mould (External PVC cylinder mould: diameter = 150 mm, height = 50 mm; Internal PVC core: 70 x 70 x 70 mm). The illustration shows cracks forming at pre-determined high stress points, following exposure to drying conditions.

2.3 Test methodology: Drying shrinkage of reinforced mortar

Free shrinkage was determined by comparator readings on specimens exposed to drying conditions. The prism moulds containing the above mortar mixes (with the addition of a monofilament polypropylene fibre mortar mix; 0.1 % volume fraction) were placed in a controlled environment (25°C and 30% relative humidity). After 24 hours the samples were removed from moulds. Using a comparator (Mitutoyo, ID-C112GE, Kawasaki, Japan) the percentage strain was determined (by change in sample length) at 1, 3, 7, 28 and 56 days. The total number of samples for this test was 32 (8 replicates per treatment).

2.4 Test methodology: early restrained shrinkage of reinforced clay and mortar

Restrained shrinkage was determined by monitoring the time to first crack and the steady state crack width of specimens exposed to drying conditions.

For restrained shrinkage of clay, ring moulds with 8 replicates of clay reinforced with either press-cake or straw at 0 and 3.0 % (by weight) were placed in a controlled environment (32°C, 30 % relative humidity and fan providing a constant air flow around samples) for a duration of 24 h. These conditions (i.e. high temperature, low humidity and high wind velocity) were chosen to encourage the effects of shrinkage on the samples. The total number of samples made for the restrained shrinkage of clay was 24 (8 replicates per treatment). A USB camera with a fixed focal lens was used to capture images of the samples at 0.07 frames per second. The camera software package (UEye, IDS) was used to process the recorded images. Time to first crack and crack width were recorded after 24 h. To determine restrained shrinkage of mortar, ring moulds with 8 replicates of press-cake (0.0, 0.1 and 0.2 % volume fraction) were subjected to the same conditions as above. The total number of samples for the restrained shrinkage of mortar was 24 (8 replicates per treatment).

3 RESULTS AND DISCUSSION

3.1 Free drying shrinkage of mortar specimens

The results from the drying shrinkage tests indicated that the addition of fibres (both press-cake and polypropylene) increased the total shrinkage strain (Figure 3). As expected the rate of shrinkage strain was greatest for all treatments up to Day 7, at which stage most of the free water had been released from the samples. The finding that early-age free shrinkage rates were found to be higher with the inclusion of press-cake fibres agrees with the findings of Toledo Filho [16], who reported that the addition of fibres increases the matrix porosity thus leading to an increase in the drying shrinkage of the cement composites.

Over the period of the test (56 days) the total shrinkage of the plain mortar and polypropylene-reinforced specimens was similar. This most probably reflects the fact that the total free water was the same but the rate of release was initially higher in the fibre-reinforced specimens. The total shrinkage strain in the specimens reinforced with press-cake fibres was higher at 56 days than the control specimen. This would reflect the release of the water contained in the fibres at time of mixing. The rate of shrinkage was initially higher but was similar to the other specimens after Day 3 and throughout the remaining duration of the experiment. This may indicate that the fibres can form a useful reservoir of moisture over the critical early period. Although this would not have a beneficial influence on overall free shrinkage strains, it may be of benefit in the case of restrained shrinkage. This is discussed further in Section 3.2.

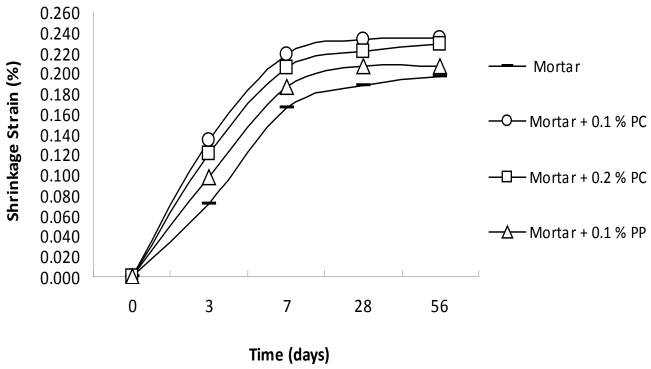

Figure 3. Drying shrinkage of mortar reinforced with different fibre types (PC = press-cake; PP = polypropylene fibre): Shrinkage strain.

3.2 Restrained shrinkage of reinforced clay and mortar

The effect of the moisture reservoir created by inclusion of saturated press-cake is clearly demonstrated in the case of the clay specimens. The difference between the time to first crack and the resulting crack width is clearly evident in the results presented in Figure 4 and Figure 5. These values represent the average of eight values. A similar trend is observable in the case of mortar, however the overall differences in the control specimens are apparent, with considerably less shrinkage of the mortar compared to clay.

On average, clay reinforced with press-cake delayed cracking by over 5 hours compared to the control. The unreinforced clay cracked on average after 2.8 hours and the average crack width was 5 mm. The specimens reinforced with straw performed considerably better. The time to first crack was 7.5 hours and the average crack width was less than 1 mm. The performance of the press-cake reinforced clay was even more impressive (8.2 hours and less than 0.5 mm respectively).

Regarding the mortar specimens it was found that inclusion of press-cake fibres could eliminate cracking completely in the harsh test environment. On average, the inclusion rate of 0.1 % press-cake caused cracking in mortar to be delayed by 18 minutes in comparison to the plain mortar samples which cracked on average after 180 minutes (Figure 4). This result also agrees with Toledo Filho et al. [16] who reported that crack development was delayed with the addition of coconut and sisal fibres to mortar composites. The average crack width of the mortar specimens reinforced with 0.1 % press-cake was half that of the control specimens. Furthermore, cracking was prevented completely in the 24 hour period of test by increasing the volume fraction of press-cake in the mortar to 0.2 %. The delay in time to first crack and the narrower crack widths associated with the reinforced samples, attributed to the press-cake increasing the tensile strength of the matrix and transferring stress across the cracks, agrees with the findings of Cyr et al. [17].

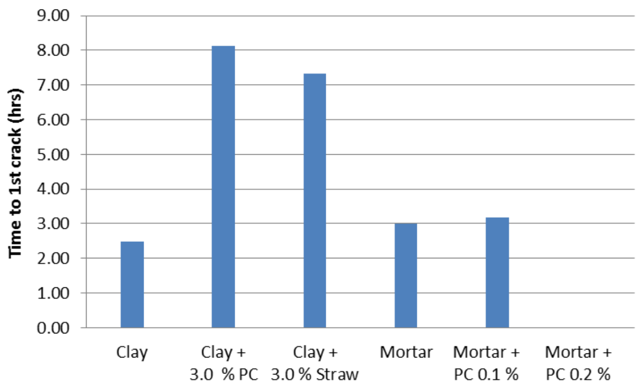

Figure 4. Restrained shrinkage properties of clay and mortar reinforced with different fibre types (PC = press-cake): Time to 1st crack (Mortar + PC 0.2 % did not crack).

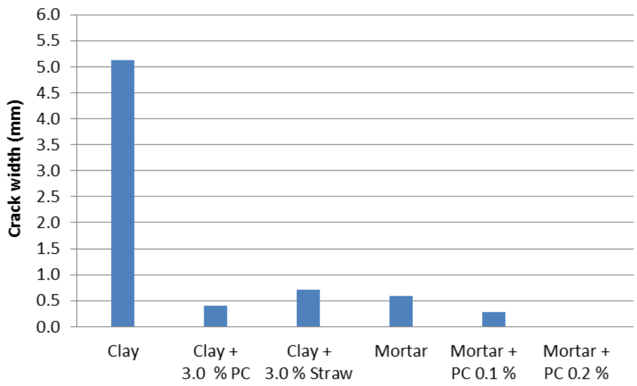

Figure 5. Restrained shrinkage properties of clay and mortar reinforced with different fibre types (PC = press-cake): Crack width (Mortar + PC 0.2 % did not crack).

4 CONCLUSIONS

Grass is in abundant supply in Europe and the volume being produced may exceed that required for its traditional role as a feedstock in animal production. Alternative use in biorefineries is being researched, as is the use of the fibrous fraction which remains once the valuable juice stream has been extracted.

This study found that the optimal grass species for further research in this context in Ireland were perennial ryegrass and timothy. This was based on their characteristics in respect of fibre concentration.

The characteristic of the fibres of greatest interest was the tensile strength. It was found that fibres from perennial ryegrass and timothy stem sections had higher tensile strengths (approximately 50 N mm^{-2}) compared to the leaf sections (approximately 20 N mm^{-2}). This indicates that optimal material is produced by delaying harvest date to maximise the stem fraction. Timothy had slightly better tensile strength but the relative abundance of perennial ryegrass in the Irish context cannot be discounted in considering market factors.

The tensile strength of fibre-rich press cake derived from perennial ryegrass was demonstrated to be sufficient to cope with the induced stresses during restrained shrinkage trials with high water content modelling clay. Onset of cracking was delayed from approximately 2 hours to 8 hours by inclusion of press-cake fibres at 3% by weight. Crack widths were reduced from approximately 5 mm to a value less than 0.5 mm.

The effectiveness of this technology in cementitious systems also yielded very promising results. Inclusion of press-cake at rates of 0.2% (by volume) eliminated crack formation completely, which had been observed after 3 hours in the unreinforced mortar specimens. This occurred despite the fact that early-age free shrinkage rates were found to increase with press-cake fibre inclusion. Of greatest encouragement was the finding that the press-cake fibre reinforcement was as effective as polypropylene fibres in minimising the risk of cracking due to restrained shrinkage. This demonstrates a potentially greater role for this waste material in sustainable building construction. Further research is merited to examine its application at an industrial scale.

ACKNOWLEDGMENTS

Funding for this research was provided under the National Development Plan, through the Research Stimulus Fund (#RSF 07 557), administered by the Department of Agriculture, Food & the Marine, Ireland.

REFERENCES

[1] Harrison, T.A., *Early-age thermal crack control in concrete*, CIRIA Report No.91, London, 1992.

[2] Swamy, R.N., *New reinforced concretes*, Surrey University Press, UK, 1984.

[3] King James Bible (5:7-5:19), Exodus, http:www.kingjamesbibleonline.org/Exodus-5-7/

[4] J.M. Wilkinson, *Silage*, Chalcombe Publications, Marlow, UK, 2005

[5] Kromus, S., Wachter B., Koschuh, W., Mandl, M., Krotscheck, C. and Narodoslawsky M. (2004), 'The green biorefinery Austria – development of an integrated system for green biomass utilization', *Chemical and Biochemical Engineering Quarterly*, 18, 1, 7-12.

[6] Goggins, J. (2010), 'Stabilised Soil Blocks – A cost-effective sustainable construction technology', *Proceedings of a Joint Symposium on Bridge and Concrete Infrastructure Research in Ireland*, Cork, 439-447.

[7] Sarigaphuti, M., Shah, S.P. and Vinson, K.D. (1993), 'Shrinkage cracking and durability characteristics of cellulose fiber reinforced concrete', *ACI Materials Journal*, 90, 4, 309-318.

[8] Kromus, S., Kamm, B., Kamm, M., Fowler, P. and Narodoslawsky M. (2006), 'The green biorefinery concept – fundamentals and potential', in Kamm, B., Gruber PR, Kamm, M., Eds., Biorefineries – industrial processes and products, Wiley, Germany, 253-285.

[9] Z.P. Bazant Ed., *Mathematical modelling of creep and shrinkage of concrete*, Wiley, Chicester and New York, 1988.

[10] Zhang J. and Li, V.C. (2001), Influences of fibers on drying shrinkage of fibre-reinforced cementitious composite', *Journal of Engineering Mechanics*, January, pp.37-44.

[11] Grzybowski, M. and Shah, S.P. (1989), 'Model to predict cracking in fibre reinforced concrete due to restrained shrinkage', *Magazine of Concrete Research*, 41, 148, 125-135.

[12] King, C., McEniry, J., Richardson M. and O'Kiely, P. (2012), 'Yield and chemical composition of five common grassland species in response to nitrogen fertiliser application and phenological growth stage' Acta *Agriculturae Scandinavica, Section B - Soil & Plant Science*, 62, 1-15.

[13] King, C., McEniry, J., O'Kiely and Richardson M. (2012) 'The tensile strength of two grass species at two contrasting growth stages and their subsequent reinforcement properties in clay blocks' *Grassland Science in Europe*, 17

[14] King, C., McEniry, J., Richardson, M., Wilson, G. and O'Kiely, P. (2011) 'Characterisation of the fibre anatomy of two grasses sampled at various stages of maturity', *Proceedings of the British Grassland Society 10th Research Conference*, 20 & 21 September, Belfast, Northern Ireland, 81-82.

[15] King, C., McEniry, J., O'Kiely and Richardson M. (2012) 'The effects of hydrothermal conditioning, detergent and mechanical pressing on the isolation of the fibre-rich press-cake fraction from a range of grass silages' *Biomass and Bioenergy*, 42, 179-188.

[16] Toledo Filho, R.D., Khosrow, G., Sanjuan, M.A., George, L.E. (2005). 'Free, restrained and drying shrinkage of cement mortar composites reinforced with vegetable fibres'. Cement Concrete Composites, 27, 537-546.

[17] Cyr M.F., Ouyang C., Shah S.P. (2003) 'Design of hybrid-fiber reinforcement for shrinkage cracking by crack width prediction'. In: Brant AM, Li VC, Marshell LH, editors. Brittle matrix composites 7. England, Woodhead Publishing Ltd. p. 242-252.

Impact of water retainers in the strength, drying and setting of lime hemp concrete

Rosanne Walker[1], Sara Pavia[1]
[1]Department of Civil, Structural and Environmental Engineering, Trinity College, Dublin 2, Ireland
email: walkerro@tcd.ie, pavias@tcd.ie

ABSTRACT: Lime hemp concrete is a sustainable, carbon negative building material that can be used in certain applications lowering the environmental impact of construction. Hemp absorbs large quantities of mixing water (325% of its own weight at 24hours), and this may not leave sufficient moisture in the binder for hydration or carbonation to take place adversely affecting curing and strength development. This paper investigates the effect of using water retainers to ensure that sufficient water is available for proper curing. Hemp concrete including a lime: pozzolan (either GGBS or metakaolin) binder and three water retainers (methyl cellulose and two commercial water retainers one of which is methyl cellulose based) were investigated. This paper studies the impact of the water retainers on strength, drying, setting and microstructure. It was found that the three water retainers delayed setting and drying. The commercial binders did not significantly affect strength however the methyl cellulose improved the compressive strength of both lime:pozzolan pastes and hemp concrete at later ages (100 days). The increase in compressive strength is partially attributed to an enhanced binder water retention that improves hydration. This assumption is based on the increase in the amount of pozzolanic cements, evidenced with SEM at the hemp interface, in the composite with methyl cellulose.

KEY WORDS: lime hemp biocomposite; pozzolan; water retainer; methyl cellulose; setting; drying; compressive strength.

1 INTRODUCTION

Lime hemp biocomposites are sustainable, carbon negative materials that can replace high embodied energy materials in certain applications, lowering the environmental impact of construction. They are non-load bearing materials with good thermal and insulation properties which are usually site-cast, projected or prefabricated as blocks or slabs. They have been used in France since the 1990s and are gaining popularity in Europe, for example in Ireland there are now over 20 buildings constructed using lime hemp biocomposites and a further 100 that have been thermally upgraded [1].

Lime hemp composites contain a lime based binder and hemp shiv which is the woody interior of the hemp stalk. Cement is usually incorporated to produce an early hydraulic set and improve early age properties such as setting and strength. This paper is part of a wider research programme which aims at formulating a binder where cement is replaced by pozzolan, resulting in a biocomposite with a lower environmental impact. Pozzolans are materials with an amorphous siliceous or siliceous and aluminous content that react with portlandite ($Ca(OH)_2$) in the presence of water to form cementitious hydration products (calcium silicate hydrates and calcium silicate aluminate hydrates) thereby accelerating hardening of calcium limes by imparting a hydraulic set.

The purpose of this paper is to investigate the behaviour of water retainers in the lime-pozzolan hempcrete. Water retainers improve the binder ability to hold water, and were developed for use when rapid dehydration occurs either by absorption of a substrate or evaporation due to drying [2]. They are often used when the mortar is mixed with high suction brick. The mortar water retention becomes more important as the suction rate of the brick increases [3 referring to 4]. Similarly, in hemp concrete, the water retention capacity of the binder is very important due to the high suction rate of the hemp.

The hemp aggregate (shiv) is a complex woody tissue from the xylem layer of the hemp stem whose main function is conducting water therefore, as an aggregate, it absorbs large amounts of water. The lime binder counteracts this high suction ability: Lime binders typically possess a high water retention, values ranging from 94.2 to 99.5% have been consistently measured in 3:1 mortars made with hydrated and natural hydraulic limes [5], [6].

In the biocomposite, water is needed for pozzolanic reactions to take place in the lime:pozzolan binder. Water is chemically bound to hydration products calcium silica hydrate (CSH) and calcium silica alumina hydrate (CSAH) and, if water is not present, these hydration products cannot form. Nozahic and Colinart state that following mixing, the high absorption of the hemp shiv induces a competition between the hemp and binder for water [7] [8].

This study uses water retainers in an attempt to ensure that sufficient water remains in the binder to be used for carbonation and hydration. This is particularly important in lime:pozzolan binders, where water is required both initially and at later ages, due to the fact that pozzolanic reaction starts early, but it is slower than cement hydration and continues for long time periods.

Insufficient water in the binder also delays carbonation (as $Ca(OH)_2$ and CO_2 must be in solution to react) however, carbonation typically occurs over months and years and does not significantly contribute to early age properties.

The effect of the water retainers is investigated by studying the microstructure of the biocomposite as well as properties including drying, setting and strength. Setting and drying are important parameters as lime concrete requires a large amount of mixing water that leads to long setting and drying times, which are not acceptable at industrial scale [9]. Hemp concrete is a non load-bearing material therefore, compressive strength is not a critical consideration, however, compressive strength gives an indication of the integrity of the composite including degree of carbonation/hydration and cohesion at the binder/hemp interface.

2 MATERIALS AND METHODS

2.1 Materials

A hydrated commercial lime (CL90s) complying with EN 459-1 was used. Two pozzolans: Metakaolin and GGBS, were identified as having potential for use in the lime hemp biocomposite on account of their fast setting times and high reactivity [10,11]. The pozzolans' chemical composition, rate of amorphousness and surface area are included in Table 1. The chemical composition was assessed by XRF using a Quant'X EDX Spectrometer and UniQuant analysis package. The rate of amorphousness was indicated by X-Ray diffraction (XRD), using a Phillips PW1720 XRD with a PW1050/80 goniometer and a PW3313/20 Cu k-alpha anode tube at 40kV and 20mA. The specific surface area was measured using a Quantachrome Nova 4200e and the BET method, a model isotherm based on adsorption of gas on a surface.

Three water retainers were investigated; modified hydroxypropyl methyl cellulose (MC) and two commercial water retainers referred to in this paper as A (which is methyl cellulose based) and B, whose composition is unknown due to commercial considerations. Industrial hemp shiv was supplied by La Chanvrière De L'aube in central France.

Table 1. Chemical and mineral composition, rate of amorphouseness and surface area of pozzolans.

Pozzolan	GGBS	Metakaolin
SiO_2	34.14	51.37
Al_2O_3	13.85	45.26
CaO	39.27	-
Fe_2O_3	0.41	0.52
SO_3	2.43	-
MgO	8.63	0.55
Mineralogical composition	no crystalline fraction	quartz, tohdite, aluminium oxide, wollastonite and paragonite
Rate of amorphousness	Totally	Mostly
Surface area m^2/g	2.65	18.3

2.2 Preparation of samples

Due to the nature of the material, both pastes and composites needed to be investigated. For example, it is not possible to determine the setting time of the biocomposite using the Vicat test as the organic aggregate impedes needle penetration and absorbs water; hastening the drying of the paste and giving inaccurate results. Therefore, setting time was measured in pastes in which the hemp shiv was replaced by hemp water. This hemp water was prepared by soaking the hemp shiv for 45 minutes so that it releases its water soluble constituents including pectins.

2.3 Preparation of pastes

The composition of the pastes is set out in Table 2. Pastes made with water were included as control samples. The water content was fixed for all pastes to equally compare the effect of the water retainer.

Table 2. Paste composition

Sample	Pozzolan	Lime	WR	Water
MW	40g M	160g	-	W 172g
MH	40g M	160g	-	HW 172g
MH + MC	40g M	160g	4g MC	HW 172g
MH + WR (A)	40g M	160g	4g WR (A)	HW 172g
MH + WR (B)	40g M	160g	4g WR (B)	HW 172g
GW	60g G	140g	-	W 172g
GH	60g G	140g	-	HW 172g
GH + MC	60g G	140g	4g MC	HW 172g
GH + WR (A)	60g G	140g	4g WR (A)	HW 172g
GH + WR (B)	60g G	140g	4g WR (B)	HW 172g

M- metakaolin; G- GGBS; W- water; H- hemp water; MC-methyl cellulose; A,B- water retainers A and B.

Mixing was in accordance with EN 459-2 [12] except for the addition of the pozzolan (added after 1 minute). The samples were demoulded after 1 day and stored in a curing room at 20°C±3°C and relative humidity 65%±10%.

2.4 Preparation of hemp concrete

Biocomposites were made with 20% metakaolin/80% lime and 30%GGBS/70% lime; 2% water retainer (by weight of binder) was added. These pozzolan contents were considered the most suitable on the basis of reactivity, setting behaviour in the presence of hemp and environmental impact [10,11]. The binder:hemp:water ratio was fixed at 2:1:3.1 for all samples.

The binder and three quarters of the water were mixed into a paste for 1 minute and the hemp and remaining water then added. The samples were mixed in total for 5.5 minutes. After mixing, the samples were transferred into 100mm cube moulds in a single layer and lightly tamped. The samples were transferred to a curing room at temperature 20°C±3°C and relative humidity 65%±10%. The samples had a dry density of c.430kg/m^3.

2.5 Water absorption of the hemp aggregate

Hemp particles were suspended in a porous bag in a beaker of water. Overtime, the hemp absorbed water reducing the water content in the beaker. The quantity of water absorbed by the hemp was determined by weighing the beaker at regular intervals. A control sample monitored weight loss due to evaporation and absorption of the bag.

2.6 Setting time of paste

The effect of the water retainers on setting time was determined by comparing the Vicat test [EN 459-2] results of lime:pozzolan pastes with and without the water retainers.

The Vicat test determines the rate of stiffening of the paste/mortar by dropping a needle from a fixed height and measuring its penetration. Stiffness is related to drying and flocculation, the formation of hydrates and the rate of carbonation. The initial and final setting times (at 35mm and

0.5mm respectively) were recorded as standard references to provide comparative data between samples. During setting, the effect of the water retainer on drying was measured by weighing the pastes at regular intervals.

2.7 *Drying*

The rate of drying of the hemp concrete was monitored by weighing the biocomposite at regular intervals over 100 days. Overtime there was a net weight loss due to water loss. However, carbonation causes a small weight gain as the calcium carbonate is heavier than portlandite. This has been disregarded as carbonation weight gain is very low at early ages and should be similar in all samples.

2.8 *Compressive strength of pastes and biocomposite*

The unconfined compressive test of half 40*40*160 prisms was measured with a Zwick loading machine according to EN 459-2 with a loading rate of 400N/s. No standards currently apply to lime-hemp concrete and EN 459-2 was used. Typically, the composite does not break but continuously deforms, therefore, the ultimate strength was set as the stress at which the stress/strain curve departs from a linear relationship (Figure 3).

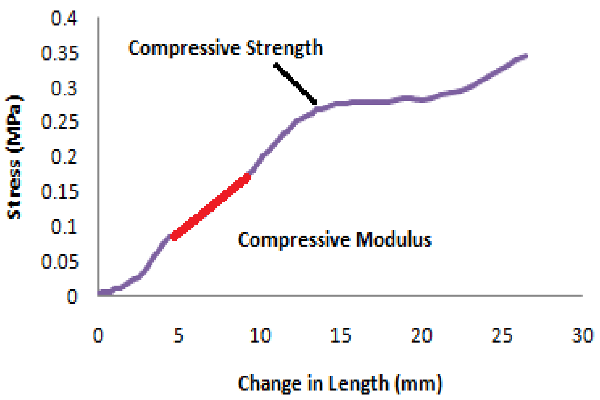

Figure 3. Representative stress/strain curve of a specimen of hemp concrete illustrating the ultimate compressive strength and compressive modulus.

2.9 *Compressive modulus*

The deformation of the biocomposite when load is applied is plastic [13]. The compressive modulus measures the stiffness of the material and is calculated as the slope of the linear part of the stress vs strain curve (between 5mm and 10mm deformation) (Figure 3). It was calculated by dividing the stress (force (F) / area (a)) by the strain (the distance travelled by the loading point (ΔL) and the original height of the sample (h)) according to equation 1 below:

$$E = \frac{F / a}{\Delta L / h} \qquad (1)$$

2.10 *Microstructure of the hemp concrete*

The effect of the water retainer on the microstructure of the binder, and the formation of pozzolanic reaction products were investigated using a Tescan MIRA Field Emission Scanning Electron Microscope. The samples were freshly fractured and covered with a gold coating in an 'Emscope SC500' plasma coating unit. The effect of the water retainer methyl cellulose was investigated in the bulk mortar and at the hemp interface at 100days. Only the methyl cellulose was considered as the two commercial water retainers did not appear to impart a beneficial effect to the biocomposite.

3 RESULTS AND DISCUSSION

3.1 *Water absorption of hemp*

Hemp shiv absorbs large amounts of water due to its highly porous structure [7]. Mixing water is primarily absorbed by capillary action through the tracheids of the shiv which are typically oriented along the long side of the hemp particle (Figure 4).

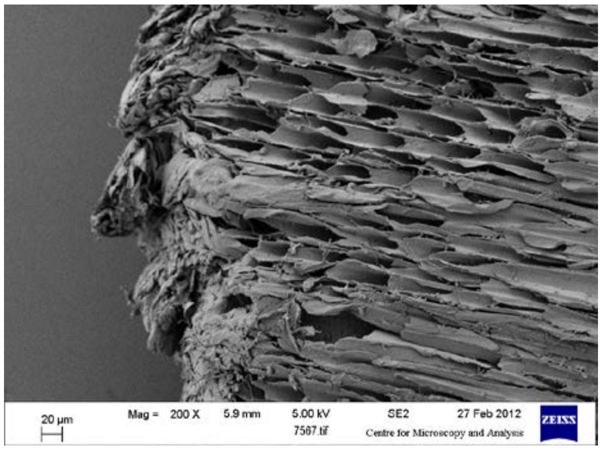

Figure 4. SEM image of the end of a hemp aggregate showing the open tracheids that absorb the mixing water.

The hemp was found to absorb approx 225% and 325% of its own weight, at 5 minutes and 24 hours respectively, as shown in figure 5. This is lower than the absorption measured by Nozahic [7] who observed a 300% percent increase at 5 minutes. The typical hemp:water ratio in hemp concrete is approximately 1:3 (by weight- in this research is 1:3.1). As the hemp absorbs 325% of its own weight at 24hours, at these proportions, the hemp has the potential to absorb all the mixing water. Therefore, the water retention capacity of the binder is of great importance. Brick masonry also has the potential to absorb large amounts of water from the mortar. Brocken [14] states that the water extraction rate from the mortar by brick is primarily determined by the sorption of the brick, but the amount of water that remains in the mortar after reaching equilibrium strongly depends on the mortar type (its water retention capacity).

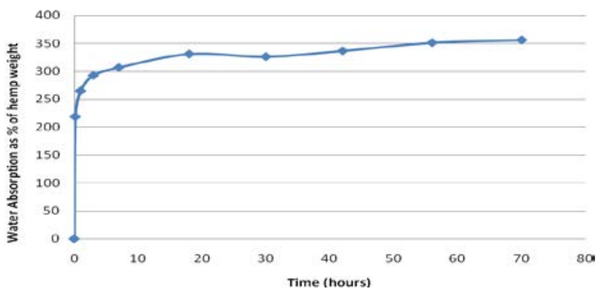

Figure 5. Water absorption of hemp aggregate.

3.2 Setting time

It has been demonstrated that the soluble constituents of hemp delay setting of lime:pozzolan pastes, and that the delay is greater in the lime:GGBS than in the lime:metakaolin pastes [15]. This is evidenced in the results (Figures 6 and 7), where the pastes made with hemp water (GH, MH) are delayed when compared to those made with water (GW, MW). In addition, it is well established that water retainers delay setting time [2]. This is also observed in the results in Figures 6 and 7, where all three water retainers delay setting. Commercial water retainers A and B cause a similar delay while MC delays setting the furthest.

Setting is due to drying, flocculation and the formation of hydration products (in this particular hemp concrete as a result of pozzolanic reaction). The water retainers certainly slow drying: this is demonstrated by the reduced weight loss of the pastes with water retainers in table 3.

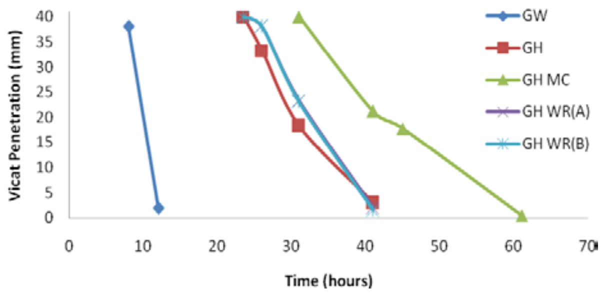

Figure 6. Effect of water retainers on the setting of lime: pozzolan (GGBS) pastes. GH WR(A) is concealed behind GHWR(B). G-GGBS; W-water; H-hemp water; MC-methylcellulose; WR(A),WR(B)-commercial water retainers A and B.

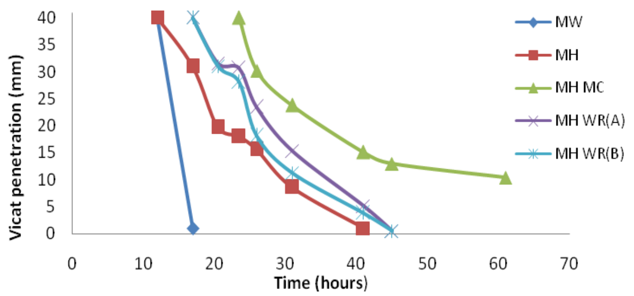

Figure 7. Effect of water retainers on the setting of lime: pozzolan (metakaolin) pastes.

Table 3. Weight loss of samples (between 0 and 60 hours) due to drying during setting

Sample	Weight Loss	Sample	Weight Loss
MW	2.8	GW	2.4
MH	2.9	GH	2.4
MH + MC	2.5	GH + MC	2.1
MH + (A)	2.7	GH +WR (A)	2.3
MH +(B)	2.4	GH +WR (B)	2.3

*M- metakaolin; W- water; H- hemp water; MC-methyl cellulose; (A) (B)-commercial water retainers A and B.

3.3 Drying of the hemp concrete

Drying refers to the removal of the free water so that the composite is in equilibrium with the ambient humidity. The open connected porosity of the biocomposite allows the internal transfer of fluid and facilitates the release of water during drying [13]. In the initial drying phase, liquid water will move by capillary forces to the surface and, later, due to sorption of water vapour [16]. In hemp concrete, the rate of drying drops as the moisture content of the sample decreases. According to the results, the GGBS hemp concrete dries faster than the metakaolin concrete, and the water retainers slow drying for both. The methylcellulose and commercial water retainer B delay drying to a greater extent than A (Figure 8 and 9). The drying delay caused by the water retainer has a negative impact on the concrete as long drying times are a major drawback in construction.

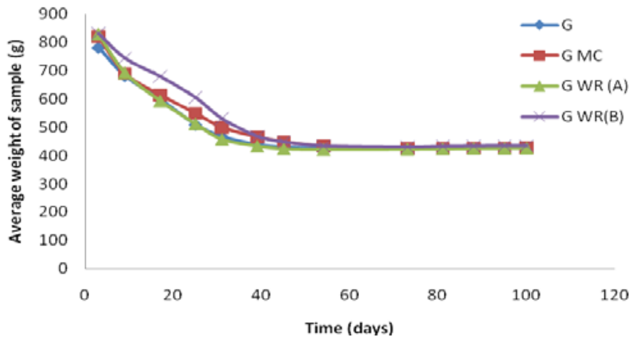

Figure 8. Effect of water retainers on the drying of the lime:pozzolan (GGBS) hemp concrete

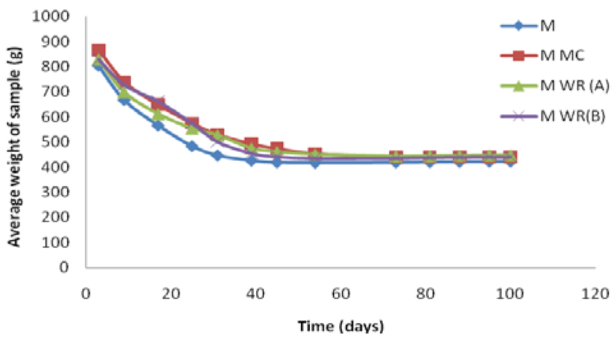

Figure 9. Effect of water retainers on the drying of the lime:pozzolan (metakaolin) hemp concrete

3.4 Compressive strength of pastes and hemp concrete

The trend in the compressive strength results is similar in both the pastes and the composites: methyl cellulose significantly increases compressive strength at 100 days (MMC and GMC in Figures 10 and 11), while the commercial water retainers A and B tend to slightly reduce it, but do not have a consistent significant effect (90% confidence) on compressive strength (MWR(A) (B) and GWR(A) (B) in Figures 10 and 11).

The methyl cellulose increases the strength of both the paste and the hemp concrete, this suggests that the compressive strength enhancement of the concrete is not solely due to the water retainer improving the water retention capacity of the binder in the presence of hemp.

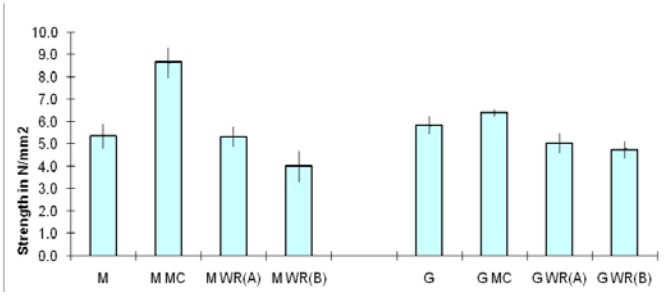

Figure 10. Compressive strength of lime:pozzolan pastes at 100days. (The error bars are ± standard deviation).

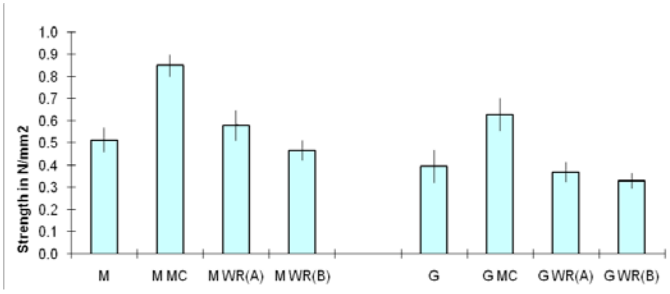

Figure 11. Compressive strength of hemp concrete at 100days.

Previous authors have reported contradictory results on the effect of different cellulose based water retainers and dosages on the compressive strength of cement mortars. The results above agree with Mischa [17] who observed increased compressive strength in portland cement mortar at 91 days for carboxymethyl-cellulose water retainer contents up to 1%. In contrast, Paiva [2] observed a reduction of the 28 day strength in a cellulose methyl–hydroxypropyl cement based render; and, similarly, Fu and Chung [18] also found a decrease in compressive strength with increasing methylcellulose content blaming this effect on the disruption of the continuity of cement phases by the presence of the methylcellulose.

3.5 Compressive Modulus

As it can be seen from Figure 12, the samples made with methyl cellulose are stiffer than those without water retainer or with commercial retainers A and B. This agrees with the strength results evidencing that methyl cellulose enhances compressive strength at 100days. The results also agree with Fu and Chung [18], who, investigating PC mortars, found an increase in the compressive modulus with increasing methylcellulose content.

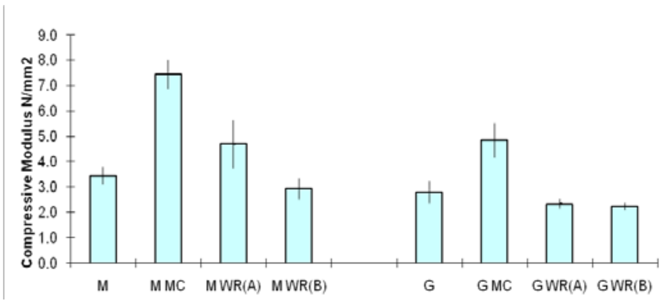

Figure 12. Compressive modulus of hemp concrete at 100 days.

3.6 *Microstructure of hemp concrete*

No significant difference was found in the paste microstructure in specimens made with and without methyl cellulose. However, differences were noted at the hemp interface. This agrees with Arizzi [19] who observed that a cellulose water retainer did not produce any mineralogical and morphological change in mortar pastes.

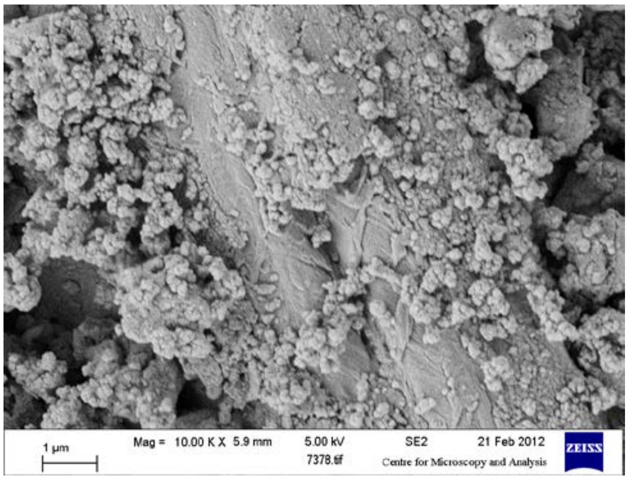

Figure 12. Hemp particle covered with calcium carbonate in a lime:pozzolan (GGBS) hemp concrete at 100 days.

As expected, the surface of the hemp particles was largely covered with small scalenohedral calcite crystals, typically smaller than 1 μm (Figure 12) [15]. These showed cracked/corroded surfaces similar to those observed by Cizer et al. [20]. Differences were noted at the hemp interface: While hydration products did not appear at the interface in the concrete without methyl cellulose (Figure 12), a few clusters of needle-shaped hydration products were evident in those containing methyl cellulose (Figures 13). This may be due to the methyl cellulose retaining water in the binder facilitating the pozzolanic reaction.

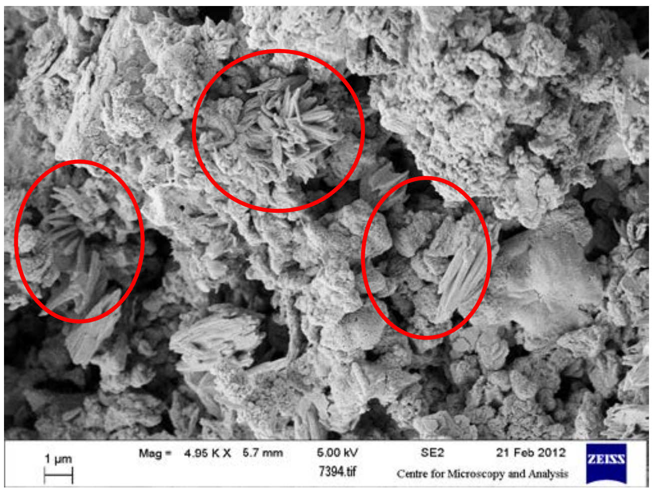

Figure 13. Hemp particle covered with calcium carbonate and clusters of hydraulic needle-like phases, in a lime:pozzolan (GGBS) hemp concrete, with methyl cellulose (at 100days).

4 CONCLUSION

All water retainers delay setting and drying of hemp concrete, however, the methyl cellulose significantly improves compressive strength at 100 days.

The methyl cellulose delays setting the furthest and (together with commercial water retainer A) also delays drying the furthest, however, it significantly improves compressive strength at 100 days. The cause of this increase has not been fully identified, however, it can be attributed to the improvement of water retention by the methyl cellulose leading to enhanced hydration (more hydrates are present at the hemp interface in the concrete including methyl cellulose).

The results also evidenced that the GGBS hemp concrete dries faster than the metakaolin concrete. In addition, it was evidenced that, at the typical hemp:water ratio of hemp concrete, the hemp aggregate has the potential to fully absorb the mixing water compromising hydration. Therefore, it is of vital importance to use a binder with high water retention.

The different behaviour of the commercial water retainers when compared to the methyl cellulose may be partly due to their lower dosage. Water retainer behaviour is strongly dosage dependent and the commercial products were diluted (in liquid form) and consequently their concentration was lower.

ACKNOWLEDGEMENTS

The authors wish to thank the Environmental Protection Agency for funding this research. The authors also thank the Traditional Lime Company, Clogrennane Lime and Ecocem for providing materials and also Dr Heath Bagshaw, Mr. Neal Leddy and Mr. Colin Reid (Centre for Microscopy and Analysis) and Dr. Robbie Goodhue (Geology Department) for their help with the SEM and XRD respectively.

REFERENCES

[1] Pronchetti, R. (2010), *Lime Hemp Workshop*, Mullingar, Co. Westmeath, Ireland.
[2] Paiva, H., Esteves, L. P., Cachim, P. B. and Ferreira, V. M. (2009), ‘Rheology and hardened properties of single-coat render mortars with different types of water retaining agents’, *Construction and Building Materials*, 23, 1141-1146.
[3] Tate, M. (2005), ‘The most important property of cement- lime motar in masonry construction is’, *Proceeding of International Building Lime Symposium*, Florida.
[4] Palmer, L. A. and Parsons, D. A. (1934), ‘A study of the properties of mortars and bricks and their relation to bond’, *National Bureau of Standards Journal of Research.*
[5] Pavía, S. and Hanley, R. (2010), ‘Flexural bond strength of natural hydraulic lime mortar and clay brick’, *Materials and Structures*, 43, 913-922.
[6] Costigan, A. (2012), ‘Improvement of properties of lime mortar masonry’, PhD Thesis, Trinity College, Ireland.
[7] Nozahic, V., Amziane, S., Torrent, G., Saïdi, K. and De Baynast, H. (2012), ‘Design of green concrete made of plant-derived aggregates and a pumice–lime binder’, *Cement and Concrete Biocomposites*, 34, 231-241
[8] Colinart, T., Glouannec, P. and Chauvelon, P. (2012), ‘Influence of the setting process and the formulation on the drying of hemp concrete’, *Construction and Building Materials*, 30, 372-380
[9] Elfordy, S., Lucas, F., Tancret, F., Scudeller, Y. and Goudet, L. (2008), ‘Mechanical and thermal properties of lime and hemp concrete (“hempcrete”) manufactured by a projection process’, *Construction and Building Materials*, 22, 2116-2123.
[10] Walker, R., Pavía, S. (2010), ‘Behaviour and Properties of Lime-Pozzolan Pastes’. Proceeding of 8th International Masonry Conference, Dresden, ed. by W. Jäger, B. Haseltine, A. Fried, 353-362.
[11] Walker R, Pavía S. (2011) ‘Physical properties and reactivity of pozzolans, and their influence on the properties of lime–pozzolan pastes’, *Journal of Materials and Structures*, 44, 1139–1150.
[12] EN 459-2 Building lime, part 2: Test Methods. (2010), *European Committee for Standardisation CEN*, Brussels.
[13] Evrard, A. (2003), ‘Hemp Concrete- A synthesis of physical properties’, *Construire en Chanvre*.
[14] Brocken, HJP. and Larbi JA., (1999), ‘Composition of mortar as a function of distance to the brick-mortar interface: a study on the formation of cured mortar structure in masonry using NMR, PFM and XRD’, *HERON*, 44, 257-270
[15] Walker, R., and Pavía, S. (2012), ‘Influence of hemp’s soluble components on pozzolanic reactions and on the properties of the hemp biocomposite’ –in press.
[16] Holcroft, N. and Rhydwen, R., (2011), ‘Effects of evaporative cooling of drying hemp-lime walls on heating load’, *Proceeding of Science Symposium*, Centre for Alternative Technology, Wales.
[17] Mishra, P. C., Singh, V. K., Narang, K. K. and Singh, N. K. (2003), ‘Effect of carboxymethyl-cellulose on the properties of cement’, *Materials Science and Engineering*, 357, 13-19.
[18] Fu, X., and Chung, D.D.L. (1996), ‘Effect of methylcellulose admixture on the mechanical properties of cement’ *Cement and Concrete Research*, 26, 4, 535-538.
[19] Arizzi, A. and Cultrone, G. (2012), ‘Aerial lime-based mortars blended with a pozzolanic additive and different admixtures: A mineralogical, textural and physical-mechanical study’, *Construction and Building Materials*, 31, 135-143.
[20] Cizer, O., Van Balen, K., Elsen, J. and Van Gemert, D. (2008), ‘Crystal Morphology of precipitated calcite crystals from accelerated carbonation of lime binders’, *Proceedings of 2nd International Conference on Accelerated Carbonation for Environmental and Materials Engineering*, Italy, 149-158.

Influence of loading rate and specimen geometry on lime mortar strength

R. Patterson [1], S. Pavía[1]
[1]Department of Civil Engineering, Trinity College Dublin.
email: pavias@tcd.ie, pattersonr@tcd.ie

ABSTRACT: Compressive and flexural strength are important properties because they relate to the quality and durability of a material, and its suitability for a particular design or application. In addition, compressive strength is a principal parameter used to classify and compare materials and establish their requirements in building standards. Therefore, it is important to establish the parameters that affect these properties so that results are comparable. It is known that specimen size and shape, water content, curing conditions, aging and compaction determine the strength of mortars and concrete. This paper sets out the influence of loading rates, increasing from 5 to 900 Newton per second, and specimen geometry (cubes and half prisms) on the compressive and flexural strengths of hydraulic lime mortars. The limes used are NHL5, NHL2 and FL2 which develop strength as a result of hydration and carbonation. The paper concludes that compressive and flexural strength are a function of the loading rate, increasing significantly as the loading rate increases; and that the possible reason for this is that, at high strain rates, micro-cracks do not have sufficient time to search for paths of minimum energy but are forced to propagate along the shortest paths with higher resistance, and this increases the peak load at which the material fails thus increasing its strength. In addition, the results indicate that the shape and size of the specimens also impact strength (half prisms being on average 37% stronger than cubes). The ratio of length to height which determines how strains build up in the specimen is probably one of the main shape parameters that affect the strength measured.

KEY WORDS: Compressive strength; Flexural strength; Loading rate; Hydraulic lime mortar; Specimen shape.

1 INTRODUCTION

Compressive and flexural strength relate to the quality and durability of a material, and its suitability for a particular design or application. They are good indicators of long-term durability as, generally, stronger materials will have longer lives. When the stress carried by a material cannot be sustained, major strains result largely produced by displacement upon fracture surfaces or pore collapse mechanisms. On loading, Portland cement (PC) composites sustain major strains, undergoing elastic deformation with a marked brittle behaviour. In contrast, lime mortars and concrete sustain lower strains while they undergo a plastic-elastic deformation resulting in a marked plastic behaviour [1].

Compressive strength measures the resistance to an increasing crushing load and it is used as a principal parameter to classify materials and establish their requirements in building standards. For example, building limes are classified according to their compressive strength in EN459-1 [2], which also sets the standard strength requirements for hydraulic limes.

Flexural strength dictates the strength in bending; being therefore essential for building designers (it impacts the maximum lateral stress that a wall may take). In addition, flexural strength is important because it indicates strength in tension, for example, that induced by expansion due to freeze-thaw or salt crystallization. It also indicates how much movement the material will allow within the structure, thus adequate values can eliminate the need for expansion joints.

The strength of a composite is largely dependent on the hydraulic strength of its binder. The binders in this study are hydraulic limes (NHL5, NHL2 and FL2) which develop strength as a result of hydration and carbonation. At early ages, the excess water is lost and shrinkage occurs and almost simultaneously, carbonation begins. Carbonation is a slow process that leads to hardening as portlandite- $Ca(OH)_2$ transforms into calcite- $CaCO_3$ by the absorption of CO_2 from the atmosphere. The amount of hydraulic set depends on the hydraulic strength of the lime: in an eminently hydraulic lime such us NHL5, hydraulic set is significant and carbonation has a smaller impact on hardening and strength development, while in feebly hydraulic limes such us FL2 and NHL 2, carbonation is more significant and hydraulic set less relevant. The curing environment (temperature and humidity) impacts the speed of carbonation and hydration that lead to hardening, consequently affecting strength development and ultimate strength. Higher temperatures usually increase the rate of carbonation and hydration thus speeding strength development while low temperatures can impede hardening and strength development. Strength increases with age, due to the progress, over time, of the reactions responsible for hardening.

This paper investigates the effect of loading rates (increasing from 5 to 900 Newton per second) and specimen geometry (cubes and half prisms) on mortar strength and mechanical behaviour. The loading rates were selected to include those above, below and within standard rates; and the specimen shapes are those featured in standards and material testing recommendations.

Several factors (other than curing conditions, age and binder hydraulicity) influence strength including: binder/aggregate ratio, aggregate characteristics, porosity and density. Strength is also determined by workmanship, for example an excess of mixing water undermines strength. Particle size distribution is amongst the most important aggregate attributes that influence strength. It is well known that an adequate grain size distribution including a wide range of particle sizes triggers a physical filler effect whereby the smaller aggregate fills spaces between larger particles, and this enhances packing, increasing density and lowering porosity, thus leading to greater strength and durability. Previous studies have concluded that good grading enhances strength and bulk density simultaneously lowering porosity, water absorption and capillary suction [3-8]; and that an aggregate with small average particle size enhances strength [9-10]. It is also widely accepted that angular aggregate improves mechanical strength and bulk density lowering porosity, water absorption and capillary suction [3,4,8,11-15].

Porosity and density also impact strength. They depend on the properties of the raw materials and their compaction. Strength usually rises with furthering compaction, as this enhances density and lowers porosity. However, rising porosity by increasing the amount of binder has led to strength enhancement in hydrated lime (CL-calcium lime) and NHL5 mortars [3,9].The binder/aggregate ratio also affects strength, NHL5 and CL mortars increase compressive and flexural strength with increasing binder content [3,9]. Proportioning mortars by mass or by volume impacts strength because it affects binder/aggregate ratio: significantly more binder is used when prescribing proportions by volume because the aggregate is denser than the binder, therefore, when prescribing mortars by volume, the lower the density of the binder the higher the binder amount prescribed [16].

Previous authors have found relationships between specimen shape and strength in PC mortar and concrete: cubes are stronger than cylinders. A factor of 1.2 is used to convert cylinder to cube strength for normal-strength concrete. However, this factor becomes smaller as the concrete strength increases so that for high-strength concrete, the influence of specimen shape is much less significant [17]-citing Gonnerman 1925, Gyengo 1938 and Murdock and Kesler 1957. The influence of shape on strength also drops as the specimen size increases [17,18]: strength is an inverse function of the specimen size for both cubic and prismatic samples whereas for the larger cylinders the effect of size on strength is almost negligible.

Finally, loading rates also affect the ultimate strength and mechanical behaviour of materials. The compressive strength of PC concrete increases significantly as the strain rate increases [19, 20]; the fracture energy and peak load increase as a function of the loading rate [21] and [22]. The reason is not yet clear as the mechanisms involved in fracturing due to loading rate and/or duration are not fully known however, experimental evidence indicates that, high loading rates impact on the two stages at which fracture occurs. In the first stage, high strain rates delay the growth micro-cracks [20, 23]. In the second stage, micro-cracks propagate simultaneously, and micro-voids and micro-cracks nucleate and grow to induce discrete cracks. At this stage, at high loading rates, micro-cracking does not have sufficient time to search for paths of minimum energy or minimum resistance, thus micro cracks are forced to propagate along the shortest path with higher resistance and this increases the material strength – its fracture energy and peak load.

2 MATERIALS AND METHODS

2.1 *Mixing, curing and compaction*

Natural Hydraulic Lime (NHL) of strength 2 and 5 and a Formulated Lime (FL) of strength 2 complying with EN459-1 [24] were used. The aggregate was 5 mm sand sourced in Wexford. A standard ratio of 3:1 (sand: lime) was used; and the amount of water was fixed to produce flows as prescribed by EN459-2 [1] and Hanley and Pavía [16]. Mixing, moulding and compaction were carried out according to EN196-1[25]. Cubes ($50mm^3$) and prisms were moulded. The prisms comply with the flexural strength specimens specified in EN196-1 with dimensions 40x40x160 mm. The mortars were placed in the moulds in two layers immediately after mixing. The fist layer was compacted with sixty jolts of a metal rod, and the second layer added and compacted. The specimens were then covered with damp hessian fabric to prevent initial shrinkage and cured for 28days according to EN 459-2 [2].

2.2 *Compressive strength*

The load per unit area under which the specimen fails was measured in accordance with EN 196-1 [25]. Several tests were performed at different loading rates: 10, 100, 500 and 900N/s. A uniformly distributed load was applied at each loading rate until failure occurred, and the maximum force applied to the cube (*fc*) noted. Testing was carried out on the 28-35th day. The mean of six (half prisms) and three (cubes) for each loading rate was recorded and the compressive strength calculated using Equation 1 below.

$$Rc = fc/A \tag{1}$$

Where;

Rc compressive strength, N/mm^2
fc maximum load applied at failure, Newton (N)
A cross sectional area, mm^2

2.3 *Flexural strength*

The flexural strength was tested using the centre point loading method, according to EN 196-1 [25], at four different loading rates: 5, 10, 50 (standard loading rate) and 100N/s. The prisms were placed in the centre of the rig and loaded uniformly until failure. The mean of three readings for each loading rate was recorded and the strength calculated using equation 2.

$$R_f = 3PL / 2d^3 \tag{2}$$

Where;

R_f flexural strength, N/mm^2
P maximum load applied to the prism at failure, N
L span of supports, 100mm
d side of the cross section of the prism, 40mm.

2.4 *Initial flow*

The water demand to produce flow diameters as prescribed by EN459-2[1] and Hanley and Pavía [16] was measured according to EN 459-2. A truncated cone was placed in the centre of the flow table and filled with mortar. After 10 seconds, the mould was lifted and the mortar spread by jolting the plate, mechanically, 15 times at one jolt per second. The resulting diameter was measured in two perpendicular directions and the mean value recorded.

Figure 1. Flexural strength measured with the centre point loading method.

3 RESULTS AND DISCUSSION

3.1 *Compressive strength*

The compressive strength of cubes and half prisms of NHL 2 mortar at increasing loading rates appear in Figure 2. The strength of the cubes steadily increases from 1.91 to 2.30 N/mm^2 with increasing loading rates, while the half prisms show a general upward trend with the exception of the samples tested at 100 N/s. This can be due to anomalies in mixing and compaction. The half prisms are, on average, approximately 35% stronger than the cubes. The compressive strength of NHL5 mortars complies with the standard requirement of EN 459-2 [2] as this prescribes the strength of 5 N/mm^2, at 28 days, tested on half prisms at a loading rate of 400N/s. The compressive strength of the NHL5 mortars at increasing loading rates appears in Figure 3. As for the NHL2 mortar, the strength of the half prisms steadily increases from 5.76 to 6.16 N/mm^2 with increasing loading rates, with the exception of the samples tested at 500 N/s. The cube strength does not show a consistent trend. The half prisms are on average approximately 47% stronger than the cubes. The compressive strength of the FL2 mortar (Figure 4) shows a similar trend: the strength of both prisms and cubes is higher at higher loads (500 and 900 N/s), and the half prisms are stronger than the cubes (30% on average). The percentage variation in compressive strength between the lowest and the highest loading rate (10 and 900N/s) is included in Table 1. These results evidence an increase in the compressive strength of lime mortars as the loading rate increases agreeing with previous research on PC composites [19,20,21,22]. The NHL5 inconsistency can be due to an error in mixing and compaction. Deviations due to the nature of the material (natural source) may have contributed to this anomaly. In all mortars, the half prisms are significantly stronger than the cubes (37% stronger on average). This disagrees with former results on PC composites stating that strength is an inverse function of the specimen size [17,18] (according to this, the bigger half prisms should be weaker). However, while their volumes are comparable (cubes are 50mm3 while half prisms measure on average 40x40x80mm), the ratio of length to height is different (1:1 for cubes *vs* 2:1 for the half prisms). The length to height ratio determines how strains build up in the specimen, these will build up in a more uniform manner for the cubes as a result of the 1:1 ratio, and this can contribute to an early failure.

Table 1. Variation in compressive strength between the lowest and the highest loading rate (10 and 900 N/s).

Mortar	Cubes	half-prisms
NHL 2	+17 %	+6%
NHL 5	-15%	+7%
FL 2	+10%	+8 %

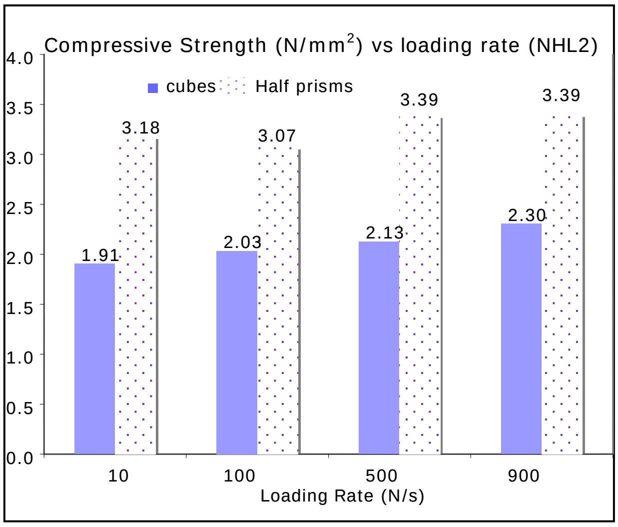

Figure 2. Compressive strength of NHL2 mortar at increasing loading rate.

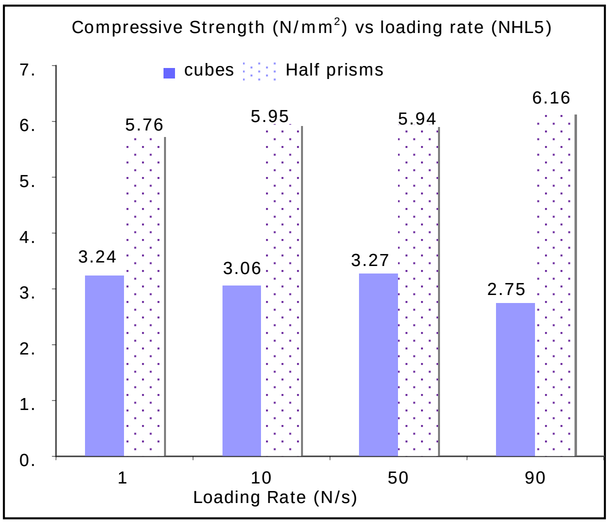

Figure 3. Compressive strength of NHL5 mortar at increasing loading rate.

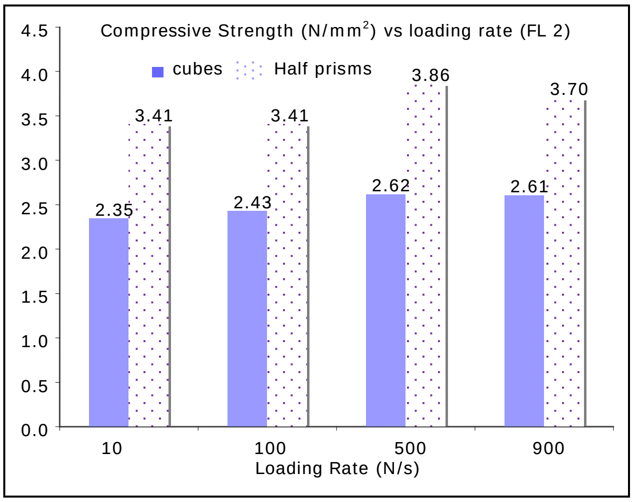

Figure 4. Compressive strength of FL 2 mortar at increasing loading rate.

3.2 *Flexural strength*

The flexural strength of the NHL2, NHL5 and FL2 mortars is included in figures 5, 6 and 7 respectively. As in the compressive strength results, there is a general upward trend in flexural strength as the loading rate increases with the exception of the NHL5 mortars. This inconsistency was expected, as the same specimens were used for both tests (as specified by EN196-1, the prisms were first tested in flexion and the remains then crushed under compression- Figure 1). As aforementioned, this anomaly is probably due to an error in mixing and compaction and common deviations inherent to the nature of the material. The percentage change in flexural strength between the lowest and the highest loading rate (5 N/s and 100N/s) is included in Table 2.

Table 2. Flexural strength variation between the lowest and the highest loading rate (5 and 100 N/s).

Mortar	% change
NHL 2	+20%
NHL 5	-13%
FL 2	+6%

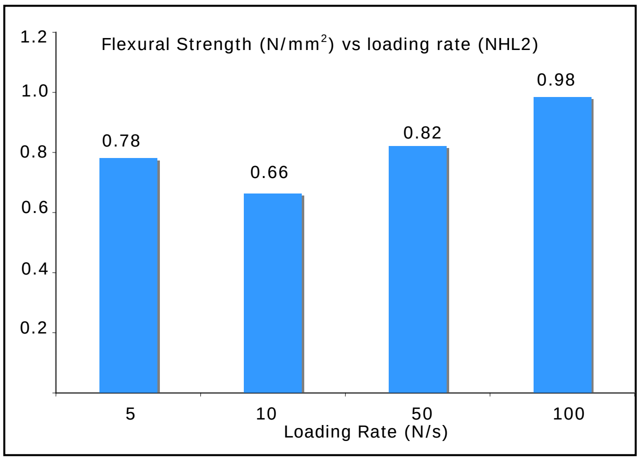

Figure 5. Flexural strength of NHL2 mortar at increasing loading rate.

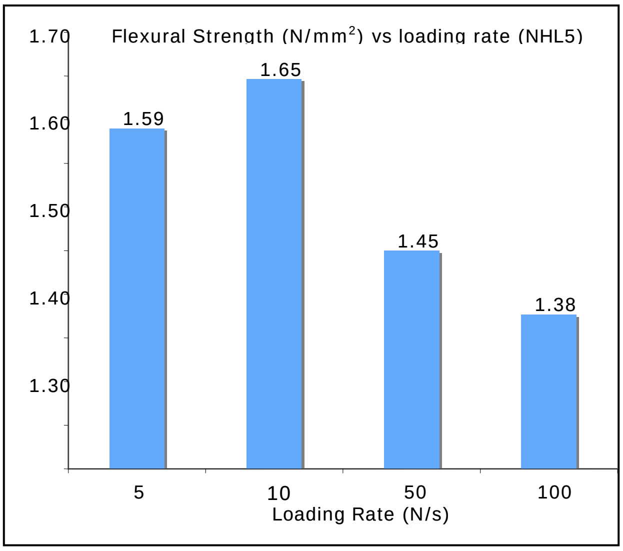

Figure 6. Flexural strength of NHL5 mortar at increasing loading rate.

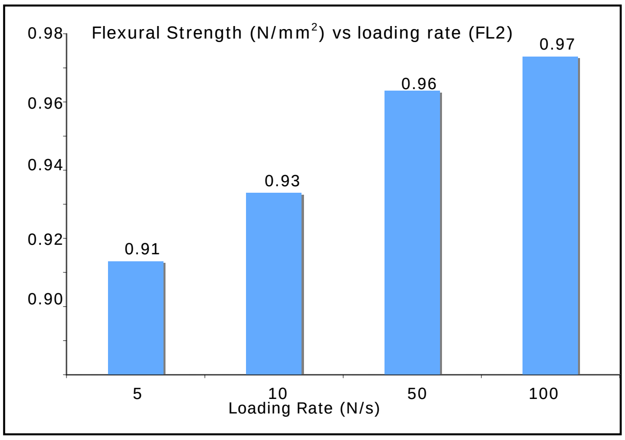

Figure 7. Flexural strength of FL2 mortar at increasing loading rate.

4 CONCLUSION

In view of the results, it can be concluded that the compressive and flexural strength of lime mortars are a function of the loading rate, increasing as the loading rate increases. Based on former experimental evidence, the possible reason for this is that, at high strain rates, microcracks do not have sufficient time to search for paths of minimum energy (minimum resistance) but are forced to propagate along the shortest paths with higher resistance, and this increases the peak load at which the material fails thus increasing its strength.

In addition, the results indicate that the geometry (shape and size) of the specimen also impacts strength (the half prisms were on average 37% stronger than the cubes). The ratio of length to height which determines how strains build up in the specimen is probably one of the main shape parameters that affect the strength measured.

ACKNOWLEDGMENTS

The authors thank The Traditional Lime Company and Clogrennanne, Ireland and St Astier/CESA, France, for donating materials. The testing was undertaken in the

Department of Civil Engineering, Trinity College Dublin. The authors thank Mr Kevin Ryan, Mr Sean Downey, Mr. Dave McAuley and Chief Technician Mr. Chris O'Donovan, for facilitating our laboratory work and their assistance with testing.

REFERENCES

[1] Costigan, A. and Pavía, S. (2012) 'Influence of the mechanical properties of lime mortar on the strength of brick masonry'. J Valek Ed. Historic Mortars: Characterisation, Assessment and Repair. RILEM publications, s.a.r.l. Paris, 349-359

[2] EN 459-2:2001 Building lime. Part 2. Test methods. CEN.

[3] Lanas, J. and Alvarez-Galindo, JI. (2003) 'Masonry repair lime based mortars: factors affecting the mechanical behaviour', *Cement and Concrete Research* 33(11), 1867–1876

[4] Cowper AD (1927) Lime and Lime Mortars. Department of Scientific and Industrial Research. Building Research Special Report No. 9. His Majesty's Stationery Office. Reprinted Shaftesbury, Donhead 1998

[5] St Astier/CESA (2001) http://www.stastier.com/

[6] Pavía, S. and Bolton, J. (2002) Stone, brick and mortar: historical use, decay and conservation of building materials in Ireland, Wordwell, Bray

[7] Allen, G., Allen, J., Elton, N., Farey, M., Holmes, S., Livesey, P., Radonjicet, M. (2003) Hydraulic lime mortar for stone, brick and block masonry, Donhead, Shaftesbury

[8] Pavía ,S. and Toomey, B. (2008) 'Influence of the aggregate quality on the physical properties of natural feebly-hydraulic lime mortar', *Materials and Structures* 41:559–569. DOI 10.1617/s11527-007-9267-4

[9] Lanas, J., Perez Bernal, JL., Bello, MA., Alvarez Galindo, JI. (2004) 'Mechanical properties of naturally hydraulic lime based mortars', *Cement and Concrete Research* 34, 2191–2201

[10] Stefanidou, M., Papayiannai, I. (2005) 'The role of aggregate on the structure and properties of lime mortars', *Cement and Concrete Composites* 27

[11] Martin, R. (1976) Palladius Traite´ D'Agriculture. Livre I. Societe´ D'Edition 'Les Belles Letres'

[12] Eichholz, Pliny the Elder (1962) Natural History. William Heinemann Ltd., Harvard University Press, London, 1962, 2nd edition 1971

[13] Hicky Morgan, M. (1914) Vitruvius: the ten books on architecture. Cambridge: Harvard University Press

[14] Plommer, F. (1973) Vitruvius and later Roman building manuals. Cambridge University Press, London

[15] Holmes, S. and Wingate, M. (1997) Building with lime: a practical introduction. ITDG, London

[16] Hanley, R. and Pavía, S. (2008) 'A study of the workability of natural hydraulic lime mortars and its influence on strength', *Materials and Structures*, 41 (2), 373 – 381

[17] Seong-Tae Yia, Eun-Ik Yangb, Joong-Cheol Choic (2006) 'Effect of specimen sizes, specimen shapes, and placement directions on compressive strength of concrete', *Nuclear Engineering and Design,* Volume 236, 2 , 115–127

[18] del Viso J.R., Carmona J.R., Ruiz G. (2008) 'Shape and size effects on the compressive strength of high-strength concrete', *Cement and Concrete Research* 38, 3, 386-395

[19] Filiatrault, A. and Holleran, M. (2001)'Stress-strain behavior of reinforcing steel and concrete under seismic strain rates and low temperatures', *Materials and Structures* Vol. 34, 235-239

[20] Rosa, A.L., Yu, R.C., Ruiz, G., Saucedo, L., Sousa, J.L.A.O. (2012) 'A loading rate dependent cohesive model for concrete fracture' *Engineering Fracture Mechanics*, Volume 82, 195-208

[21] Ruiz, G., Zhang, XX., Yu, RC., Rorras, R., Poveda, E., del Viso JR. 'Effect of loading rate on fracture energy of high-strength concrete'. Strain doi:10.1111/j.1475-1305.2010.00719.x. 2010. Strain. An Int. J. for Exp. Mechanics, Vol. 47, p. 518

[22] Ruiz, G., Yu, RC., Rosa, AL. (2008) 'A viscous cohesive model to analyze rate-dependent fracture in concrete'. *In: 8th world congress on computational mechanics (WCCM8), Venice, Italy*. Int. Center for Numerical Methods in Engineering Pub., Barcelona, Spain.

[23] Reinhardt, H.W., Weerheijm, J. (1991) 'Tensile fracture of concrete at high loading rates taking into account of inertia and crack velocity effects' *International Journal of Fracuret,* 51, 31–42

[24] EN 459-1:2001. Building Lime – Part 1: Definitions, Specifications and Conformity Criteria.

[25] EN 196-1:2005. Methods of Testing cement. Determination of Strength.

Orthotropic deck fatigue: renovation of 8 bridges in the Netherlands

Pat Moore[1], Edo Vonk [2], Gerland Nagtegaal[3]
[1,2]Arup, Beta Building, Naritaweg 118, 1043 CA Amsterdam, the Netherlands
[3]Rijkswaterstaat, Dienst Infrastructuur, Griffioenlaan 2, 3526 LA Utrecht, the Netherlands
email: pat.moore@arup.com, edo.vonk@arup.com, gerland.nagtegaal@rws.nl

ABSTRACT: A large ongoing project involves the renovation of 8 large steel (landmark) bridges in the Netherlands which are suffering early fatigue in the orthotropic decks. The Rijkswaterstaat (RWS) is the agent of the Netherlands Government responsible for the management of bridges, roads and waterways. RWS have appointed a Managing Contractor(MC) (Royal Haskoning, Arup and Greisch) to deliver the project.
The objectives are:

- To assess the structures static capacity and their fatigue performance.
- To improve the fatigue performance of the structures (using high strength concrete overlay) and extend their working life
- To strengthen the main structures for current loading
- To minimise traffic disruption through the project, and
- To develop strengthening methods that are applicable to long span, heavily trafficked structures

One key output will be the development of a mutually beneficial working methodology that can be applied on many future bridges whilst minimising traffic hindrance. This will include not only strengthening techniques but also potentially innovative operating relationships between Client, Designers and Contractors. This paper presents some aspects of the current state of the work, which is currently over 3 years into a 6 year project. It gives an overview of the technical, contractual and practical methodologies adopted, and provides some specific information with regard to the bridge at Ewijk.

KEY WORDS: Orthotropic, Fatigue, Investigation, Assessment, Strengthening, Restoration, Cable stay, Steel, Bridges, High Strength Concrete, Fibre Reinforced Concrete, Eurocodes, System Engineering, 3D Finite Element Fatigue Analysis, NDT, Insitu Stress Measurement, Traffic.

1 INTRODUCTION

In the Netherlands, a large-scale renovation project is in progress to renovate 8 large steel bridges. A number of key highway structures are part of this renovation project. The common feature for all the bridges is the fatigue issues in the steel orthotropic deck plate. The renovations involve both local and global strengthening. This paper presents an overview of this project, and describes some of the assessment and strengthening aspects. One bridge is described in more detail to give some insight to the resulting renovation works.

The Dutch national authority responsible for the road and inland water transport system, Rijkswaterstaat (RWS), discovered the fatigue problem about 17 years ago. During this time, RWS have worked to prioritize and manage the most urgent items, and in parallel, work to develop long term solutions.

The 8 bridges which form the basis of this paper were built between 1969 and 1985 during a period of rapid infrastructure development. They are 8 of the largest and most strategically important landmark bridges in the country.

All bridges have orthotropic steel decks, and evidence of through-plate cracking is found below the asphalt surfacing in the wheeltracks in the slow traffic lanes (truck lanes). In addition, cracking is present in steel plates and welds at other locations, such as at the transverse girders and at troughs. Prior to renovation, these structures are managed using a comprehensive system of inspection and testing, with a continuous programme of temporary repair works.

The approach and implementation of a long term solution for this issue is presented, which is achieved using a high strength concrete overlay.

2 PROJECT DESCRIPTION

Since the 1990's there has been a concerted effort by RWS to determine the cause of the fatigue problems in many of the large steel bridges, and to verify this by calculation. Prior to renovation, suitable methods to inspect and repair damage have been determined and are implemented to ensure the safety of the bridges under consideration. As a parallel process, there is a focus to determine appropriate solutions which extend the remaining life of the existing bridges.

The solution which has been determined by RWS is the application of an overlay of high strength concrete (HSC) to the top of the steel deck plate. In order to monitor and confirm this method, the overlay has been applied initially to two bridges. At these bridges, the existing asphalt wearing course has been removed and the HSC overlay applied. Calculations and measurements at these bridges prove this method to be effective.

After this stage, 14 bridges have been selected for renovation. These bridges form the RWS project known as

"Renovatie Stalen Bruggen". The location of the bridges is spread throughout the country, as shown in Figure 1 below.

Figure 1 Location of bridges part of the Steel Bridge Renovation project

Rijkswaterstaat has appointed a so called "Managing Contractor" (MC) to deliver the project. The role of the Managing Contractor (MC) is performed by a partnership of three engineering companies, Arup, Royal Haskoning and Greisch.

The MC is responsible for many activities, including:

- assessing the existing bridges;
- undertaking inspections at these bridges;
- the design of strengthening measures for fatigue and static strength
- procurement of the construction works
- supervision of the construction management
- project management and third party liaison.

The contract between Rijkswaterstaat and the MC is designed to promote the goals from both parties. The common goal for RWS and the MC is to achieve an economic solution to the problems at the bridges and to minimize the traffic disruption during execution. Other project goals are related to safety and customer satisfaction.

In addition, Rijkswaterstaat has appointed TNO/TUDelft as advisors. They undertake reviews of the design and assessments by the MC. In addition they play an important role in advising on matters outside the normal codified design rules, for example crack growth calculations to prove fatigue life. TNO/TUDelft also provides a basis for knowledge sharing with regard to existing steel bridges within the Netherlands.

To deliver the construction activities, RWS and the MC are currently procuring the works for 8 of the bridges under a framework agreement with three Dutch contractors; Heijmans, Koninklijke Volker Wessel Stevin and a joint venture Strukton Betonbouw – Ballast Nedam. The intention of the framework contact is to promote knowledge generation and sharing across the 8 bridges.

3 DESIGN LOADS AND LOAD FACTORS

As part of work undertaken by RWS to investigate the causes of the early onset of fatigue damage, research was undertaken on static traffic loading, fatigue traffic loading and fatigue classification.

The traffic loading research undertook traffic measurements (axle loads and truck loads) at many locations in the Netherlands [1]. Statistical extrapolation was used to determine the design value of axle and truck loads. For lane loads, Monte Carlo simulation and analytical simulation was used for different spans and number of lanes. In addition, dynamic effects, statistical uncertainties, environmental variations, model uncertainties and trends were incorporated to form the basis for comparisons with the codified loads.

The general conclusion of the research undertaken was that for static loads the Eurocode 1991-2 traffic loads are marginally conservative when compared to the traffic on the Dutch network.

The Eurocode EN 1991-2 traffic load models were used as the basis for the characteristic static loads for the existing bridges in this project, with the following modifications:

- Instead of using the notional number of lanes, the actual number of lanes on the bridge with a loaded width of 3m each are taken into account. (Reduction compared to Eurocode loading depends on bridge layout.)
- The reference period of the loads are reduced from 100 years to the predicted remaining time of usage of the bridge. In the case of this project, the remaining design life is taken as 30 years. (Reduction about 8 % compared to Eurocode loading).
- The trend, taken into account in the Dutch Eurocode verification for a period of 100 years, is reduced to the predicted remaining time of usage of the bridge. (The reduction depends on the influence line length, and can varying from 0 to 10 %.)
- Consideration is given to emergency and maintenance design situations, but with a reduced reference period.

The Dutch National standard, NEN8700 [2] provides guidance on existing structures. It permits that for existing structures the safety level may be less than for newly built structures. New bridges, constructed in or over highways and main waterways are designated as Consequence Class 3 (CC3) resulting in a reliability index, ß = 4.3. For existing bridges a rejection level design load factors are adopted based on ß = 3.3. The bridge is then assessed using design load factors applicable to a reliability index, $\beta = 3.3$. If a bridge or a part of a bridge does not meet the design capacity criterion, then strengthening measures are required. When strengthening of an element is undertaken, then renovation level design load factors are adopted. For the strengthening of existing bridges, the design load factors are based on a reliability index of ß = 3.6.

In the case of fatigue loading, similar research and investigations have been undertaken [3]. For the existing bridges on this project, a project specific fatigue load model (FM5) has been generated. This load model is based on actual traffic data from the past and a prediction of traffic characteristics for the future [4].

4 DESCRIPTION OF DESIGN & ANALYSIS

At each of the 8 bridges, the both static and fatigue analyses are undertaken.

Typically the first step is to undertake an assessment of the existing bridge to determine the design capacity with regard to static and fatigue strength. During this phase, extensive inspections are undertaken to identify the condition of the existing structure to determine if there is any damage or evidence of distress in the structure.

Where the structure, or parts of the structure, does not meet the assessment capacity criterion, then measures to strengthen or relieve the structure are investigated, for both local and global issues.

Following selection of the preferred renovation measures, detailed analysis is undertaken to complete the design and produce the construction documentation.

For the static analysis the design loads are applied in accordance with the approach identified in Section 3.

With regard to fatigue analysis, the project specific fatigue load model is used in both the global fatigue assessments, which consider the main structural elements, and also the local fatigue assessment of the orthotropic deck.

5 STEEL DECK FATIGUE

The primary fatigue problem that initiated the work on the bridges is fatigue cracks evident in the deck plate, as shown in Figure 2.

However, there are other locations of fatigue crack initiators within the orthotropic steel decks. These other locations include deck trough splices, deck plate weld, trough terminations, and at main girder to cross-girder connections.

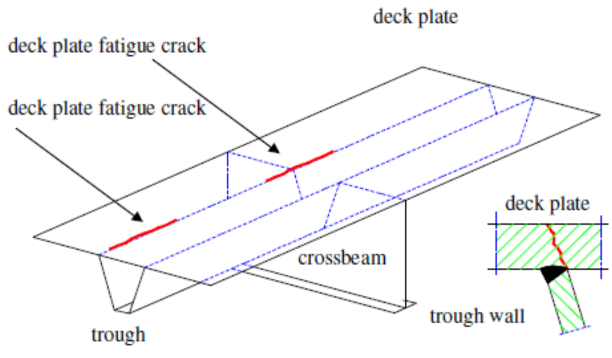

Figure 2. Deck plate fatigue cracks.

5.1 *HSC as a renovation solution*

The HSC overlay is seen as a system that can be applied to large bridge structures in an economic fashion, and in a way which can minimise traffic hindrance.

The HSC overlay is capable of reducing the local stresses in the deck plate by a combination of improved dispersal of localised wheel loading, and by the composite action of the concrete with the steel structure. The analysis considers both cracked and un-cracked HSC properties in the design.

5.2 *Local Fatigue Analysis*

The design stresses are determined using a local detailed 3-dimensional finite element (FE) model. The extent of the local model is determined based on the effects to be investigated and the configuration of the global structure. An example is shown for one of the 8 bridges (Brug bij Ewijk) in Figure 3 below.

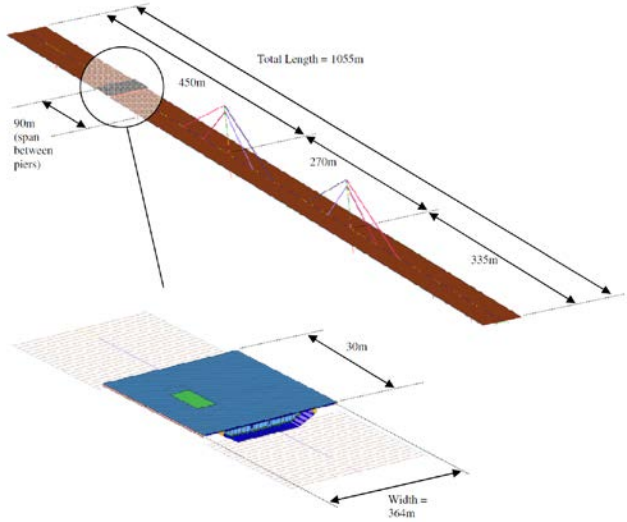

Figure 3. Local analysis model.

For each bridge, the model includes the deck plate, troughs, main girders, cross beams, existing asphalt for the existing condition or new concrete overlay in the renovated condition. The steel members are modelled using shell elements. The asphalt and concrete overlay, including epoxy bonding layer, are modelled using 3D solid elements.

The mesh density is sufficiently fine to allow adequate prediction of stress concentrations. Hence the mesh size, locally, needed to be approximately the size of the deck plate thickness. A close-up of the model is given in Figure 4.

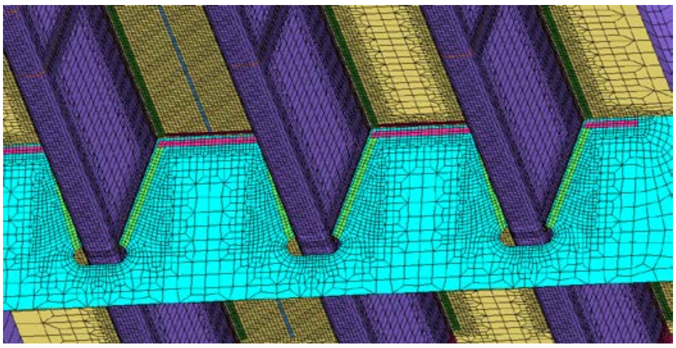

Figure 4. Close up of local analysis model.

Using the fatigue load model and the output from FE analysis, the fatigue damage calculation is undertaken. Correlation has been demonstrated between the fatigue design calculations and the observed cracks in the steel plates. The calculation also shows that if the cracks in the deck plate are repaired and concrete overlay applied to the deck, then the results indicate that the deck plate would be adequate for an additional 30 years of service.

In other locations showing design fatigue damage, which is not solved by the HSC overlay, a system of repairs is implemented. This is applicable at locations such as such as trough splices, trough to cross girder connection locations.

6 WAAL BRIDGE AT EWIJK

The Waal Bridge at Ewijk (Brug bij Ewijk) is one of the 8 bridges within the scope of the MC project. The Waal Bridge at Ewijk is located on the A50, near the city of Nijmegen, in the west of the Netherlands. It spans the River Waal and the flood plains of the Waal. The bridge has 10 spans, and the total bridge length is 1055 meters.

Figure 5. Photograph of Brug bij Ewijk

The bridge has 4 no. approach spans to the south, a southern span for the cable stayed bridge, the main span of the cable stayed bridge, the northern span of the cable stayed bridge and finally 3 northern approach spans. The main span is 270m long. The total width of the bridge deck is 37m. The superstructure consists of a steel trapezoidal box girder, approximately 26m wide, with cantilevers on both sides. The box girder has a structural depth of approximately 3.5 m, with diaphragms spaced at 5m centres. An elevation and typical cross section of the bridge is given Figure 6.

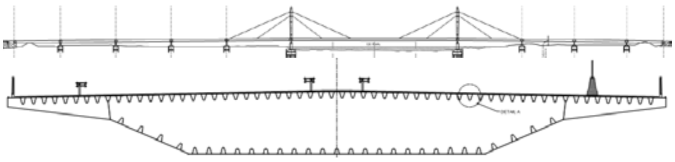

Figure 6. Elevation and cross section of Brug bij Ewijk.

The plates which form the girder and the deck plate are stiffened with trapezoid troughs. The troughs are placed at 600 mm centres typically. The troughs are typically 350 mm deep with 6 mm thick side walls. The deck plate thickness is generally 10 mm but locally at supports and at the cable connection locations, it is thickened to 14 and 18 mm. The web plates are typically 12mm. The bottom flange plates have a varying thickness of 10, 14, 18, 20 or 25 mm depending on location.

Over the river spans, the box is supported by a single plane of cable stays. At each pylon, there are two sets of cables, a lower and an upper cable stay. The cables consist of fixed length locked coil cables. The cables are continuous over the saddles in the pylons, and connected to the deck via an anchor block at each end of the cable stays.

The main features of the renovation works at Ewijk are summarized below:

- Deck plate repairs & strengthening – HSC application
- Steelwork strengthening
- Cable Stay replacement
- Jacking for clearance
- Bearing replacement
- Expansion joint replacement

6.1 Deck repairs & strengthening

Steel repairs are determined using both inspection and design calculations.

Fatigue damage is calculated at several locations. The inspections confirm the calculated damage locations.

- Cracks in the deck plate (above trough webs, above cross beams, at deck plate joints).
- Cracks in welds of trough splices and trough terminations.

6.1.1 Deck Plate

The adopted strengthening solution for the deck plate is the application of a high strength concrete overlay to the steel plate. At Brug bij Ewijk, the HSC overlay has a minimum thickness of 75mm, with a combination of steel fibres and normal reinforcement bars. The steel fibre density is 75kg/m^3. The reinforcement is typically one layer of B12 bars at 75mm centres in each orthogonal direction.

The concrete compressive strength is C90/105. The connection between the HSC and the steel deck plate is achieved using an epoxy bonding layer. The HSC is not directly bonded to the epoxy, rather the HSC is poured onto particles of bauxite set into cured epoxy. The concrete overlay is subsequently overlaid with asphalt. A typical cross section is shown in Figure 7 below.

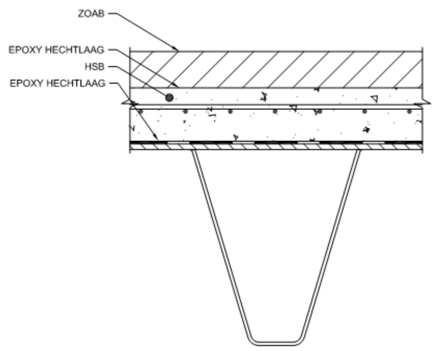

Figure 7. Typical cross section at HSC overlay.

The full shear stiffness of the epoxy cannot be claimed. To simulate this, a reduced Young's modulus of 5GPa has been used for the elements representing the interface. The sensitivity of the results to this assumption was checked by re-running a key load case with this stiffness both halved and doubled.

Before placing the HSC overlay, the fatigue cracks in the steel deck plate are repaired. An established inspection methodology has been developed to measure crack depths in the deck plate using Time of Flight Diffraction techniques (TOFD). This technique can detect cracks of a depth greater than 3mm, and the detected cracks are repaired using established repair techniques. Where significant cracks occur, for example through-and-through cracks with a length greater than 800mm, then a local part of the deck plate is replaced with a new and thicker inserted plate.

The HSC overlay extends the remaining design life of the existing steel deck plate to at least 30 years.

6.1.2 Weld between trough and deck plate

The weld between the trough and the deck plate is one of the most important welds of the orthotropic deck plate, but often the weakest link (refer to Figure 2). The weld initiates fatigue cracks in the steel deck plate and also fatigue cracks occur in the weld itself. Before placing the HSC overlay, the fatigue cracks in the weld are repaired. However the HSC overlay does not fully solve the predicted damage in the weld. Hence a combined approach of fracture mechanics, close visual inspections, and weld replacement with a higher category of weld is currently used to address this issue.

6.1.3 Trough Splice and Trough Termination repairs

The detailing of the existing trough splices and trough terminations is poor with regard to fatigue performance, resulting in a low fatigue classification. The HSC overlay does not resolve the high fatigue damage predicted at these locations. Hence, the approach which has been adopted is to replace the splice and terminations with improved details.

6.2 Steelwork strengthening

The overlay increases the dead load on the structure by approximately 50%. The global static analysis indicated that strengthening to the existing steel deck was required, when the bridge is assessed in the renovated situation.
Consequently, the existing steel box girder requires strengthening to achieve the required design resistance.

The static shear capacity of the box girder is insufficient and the girder top and bottom flanges are overstressed near the support locations. The renovation design introduces bracing elements between the top and bottom flanges and the diaphragms in the middle of the box girder. This provides a new shear path and activates more existing steel in the flanges to increase bending capacity.

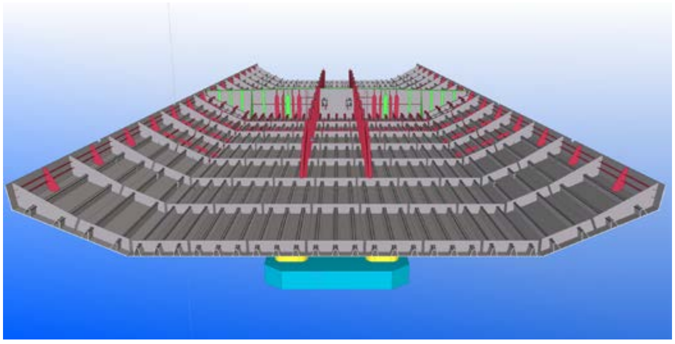

Figure 8. Box girder steelwork strengthening (deck plate and diaphragms not shown).

The strengthening at the top and bottom flanges is achieved by providing additional steel elements (T-sections) to the existing troughs. At the bearing and jacking points, the stiffener capacity is increased by the introduction of additional stiffeners and steel elements. The new bracing (centre) and additional steelwork to the bottom flanges is shown in red in Figure 8.

6.3 Cable Stay Replacement

The replacement of the existing locked coil cables is necessary due to the increased loads imposed as part of the renovation works, and also due to concerns over the residual design life of the existing cables. Some wire fractures have occurred in the existing cables, and it has been decided to replace all the cables with new cables as part of the renovation project.

There are two sets of cable stays at each pylon. The upper (longer) cable stays consist of two sets of 5 locked-coil cables, and the lower (shorter) cable stays consist of two sets of 3 locked-coil cables. The locked coil cable diameter is 101mm, with a minimum breaking force of 903tonnes per cable. Each cable is continuous over the saddle in the pylon, and connected to the deck at an anchor block arrangement. The replacement design is a like-for-like replacement of the existing cables with new equivalent diameter locked coil cables.

The existing cables were tensioned by jacking of the cable saddles located in the pylons and it was not envisaged during the original design that the locked coil cables would require replacement. The replacement of the cables is undertaken by first removing one of the lower cables at one of the pylons. This is achieved by first un-jacking the saddle in the pylon to remove the cables, installing the new cables, and then re-jacking the saddle to install the required pre-load in the cables. This procedure is repeated at the 3 remaining sets of cables. No temporary supports are envisaged, and the existing box girder is assessed for each stage. During these operations, traffic is not present on the deck, and the existing asphalt is removed. The works occur prior to application of the HSC overlay.

During and post-renovation there is an increased load in the cables compared to the existing loads. As a result, the anchor blocks which attach the cables to the deck require strengthening to accommodate the increase loads and suitably distribute the loads to the main box girder structure. At the cable saddles within the pylon, the assessment as shown that the existing saddles are suitable without the need for strengthening.

6.4 Jacking for Clearance

Increased clearance requirements for navigation traffic require the bridge to be lifted by 1.25m at the midspan. The bridge is jacked on the nine pier supports, so that the revised vertical alignment is achieved gradually over the length of the bridge, and the required clearance is provided.

6.5 Bearing and expansion joint replacement

Replacement of the existing bearings and expansion joints are undertaken as part of the renovation works.

7 CONCLUSION

The issues associated with fatigue and static strength of a number of large structures in the Netherlands is an ongoing concern for RWS. The MC project, addresses the issues at 8 landmark crossings. The work to date has successfully demonstrated the effectiveness of the adopted concrete overlay solution for the deck plate fatigue problems. The design solution is under continuous development, and other solutions or variations are being progressed. These include the use of precast concrete elements and fibre-only reinforced concrete. In addition, the use of steel plate overlay has been used.

Many of the structures, such as the Brug bij Ewijk are subject to additional renovation works, such as global strengthening, cable replacement and jacking for clearance. The construction works at Brug bij Ewijk are expected to commence in 2012, and the experiences from this project will be captured to ensure the knowledge and lessons learned will be implemented on the remaining bridges within the MC project, and within the industry in general.

ACKNOWLEDGEMENTS

The authors wish to acknowledge the support and vision of the client, RWS, and for their permission to publish this paper.

REFERENCES

[1] Traffic measurements (axle loads and truck loads) on several locations in the Netherlands TNO report 98-CON-R1813

[2] NEN 8700:2011 Beoordeling van de constructieve veiligheid van een bestaand bouwwerk bij verbouw en afkeuren - Grondslagen (Assessment of existing structures in case of renovation and rejection – Basic Rules).

[3] Summary of research activities in trying to make a Dutch code fatigue load model TNO overview-report 2007-D-R0366/B.

[4] Gration, D., van Dooren, F., Nagtegaal, G., Ashurst, D., Kunst, P., den Blanken, S. (2008) 'Orthotropic Deck Fatigue: Renovation Of 8 Bridges In The Netherlands'. *Structural Faults & Repairs, 12th International Congress and Exhibition*

[5] NEN-EN 1993-1-9:2006 - Eurocode 3: Design of steel structures – Part 1-9: General – Fatigue strength

Procedures for calibration of Eurocode traffic Load Model 1 for national conditions

E.J. O'Brien[1], A.J. O'Connor[1], M. Tucker[1]
[1]Roughan & O'Donovan Innovative Solutions, Arena House, Arena Rd, Sandyford, Dublin 18, Ireland.
email: eugene.obrien@rod.ie, alan.oconnor@rod.ie, mark.tucker@rod.ie

ABSTRACT: Since April 2010 Eurocode Load Model 1 (LM1) is the prescribed traffic load model to be employed in the design of highway bridges in the European Union (EU). Uniquely, the code permits member states to calibrate the load model, through the application of 'α-factors' to allow for national or regional conditions. Some countries with high volumes of very heavy traffic may find that they require α–factors in excess of unity whilst other less heavily trafficked road networks may require much lesser values. The importance of accurate calibration of the α-factors is clear from a safety and economic point of view. This paper describes procedures for calibration of α-factors using Weigh in Motion (WIM) data. WIM data allows classification of the traffic loads in individual countries, enabling the specific Gross Vehicle Weights (GVWs), axle loads and frequencies of heavy trucks to be taken into account. Simulations calibrated using this data, for a wide range of structural forms (i.e., influence lines, spans and numbers of lanes) and scenario types (i.e., free flowing, congested and mixed traffic conditions); allow comparison of the load effects generated by the site-specific traffic to those obtained when employing LM1. Statistical Extreme Value Distributions (EVDs) are fitted to simulated results to determine characteristic load effect values using the same methodology as was employed in the calibration of LM1 itself. Appropriate α adjustment factors are then determined to cater for variation in predicted characteristic extreme load effects on a network by network basis. Where α<1.0, the prescribed approach delivers significant savings by preventing unnecessary overdesign of bridges. On the other hand, for cases where α>1.0 it allows bridge designers to design bridges with adequate levels of safety.

KEY WORDS: Eurocode; LM1; Weigh in Motion; WIM; Characteristic Loading; Bridge Loading.

1 INTRODUCTION

Over the last number of decades road traffic in Europe, and in particular freight transport, has increased significantly, approximately in line with economic growth (Figure 1).

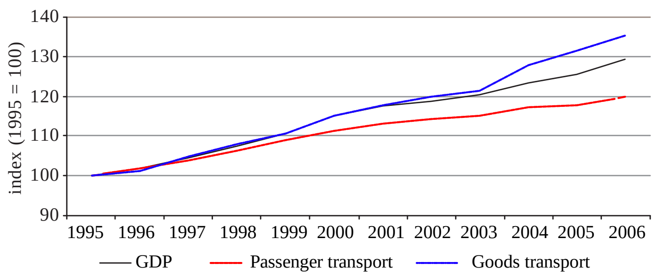

Figure 1: Evolution of transport demand and GDP in the EU-25 for period 1995-2006 [1].

Eurocode 1: Actions on Structures, Part 2 – Traffic Loads on Bridges, is the current design standard employed across the EU. Load Model 1 (LM1) is applied for the design of new bridges with spans of up to 200m. It consists of a tandem axle load, $\alpha_{Qi}Q_{ik}$, and a Uniformly Distributed Load (UDL), $\alpha_{qi}q_{ik}$, where α_{Qi} and α_{qi} are the load adjustment factors for lane number i. The tandem axle load is placed at the most adverse location on the influence line under consideration to determine the worst load effect on the bridge. The remaining area of the road (the section outside the defined traffic lanes) is also subjected to a UDL, denoted $\alpha_{qr}q_{rk}$. It allows member states to calibrate the code to their own national traffic conditions. When correctly employed it facilitates a cost effective bridge design that allows for variations between countries in the frequency of heavy vehicles. This is achieved through calibration of the adjustment factors for the specific country under consideration.

The model takes account of traffic scenarios ranging from free-flowing to congested conditions with a high percentage of heavy trucks. The magnitude of the tandem axle loads and UDLs depend on the lane number and are specified in the code, reproduced in Table 1 and Figure 2.

Table 1. Eurocode LM1 [2]

Location	Tandem system Axle loads Q_{ik} (kN)	UDL system q_{ik} (kN/m^2)
Lane Number 1	300	9
Lane Number 2	200	2.5
Lane Number 3	100	2.5
Other Lanes	0	2.5
Remaining Area	0	2.5

As can be observed, as the number of lanes on the bridge increases, the tandem axle load and the UDL in the new lane is reduced. For bridges with more than 3 lanes no tandem axle load is considered.

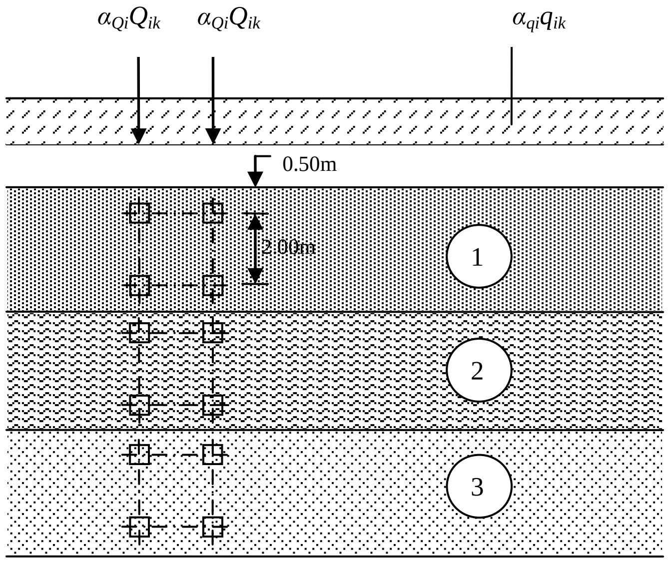

Lane Nr. 1: Q_{1k} = 300kN, q_{1k} = 9kN/m^2
Lane Nr. 2: Q_{2k} = 200kN, q_{2k} = 2,5kN/m^2
Lane Nr. 3: Q_{3k} = 100kN, q_{3k} = 2,5kN/m^2
*for w_l = 3,00m

Figure 2: Eurocode LM1 for 3 lanes [2]

This paper outlines methods for analysing real traffic data acquired by Weigh-In-Motion (WIM) systems to allow calibration of the Eurocode LM1 α-factors. WIM data allows the individual loads in countries to be classified, enabling the specific Gross Vehicle Weights (GVWs), axle loads and frequencies of heavy trucks to be taken into account. Simulations are calibrated using this real life data, considering a wide range of bridge lengths and influence lines. Statistical Extreme Value Distributions (EVDs) are fitted to simulated results to determine the characteristic load effects. Appropriate α-factors are then determined to cater for the variation in predicted characteristic extreme load effect on a network-by-network basis. As this approach is specifically tailored to the real-life loading, identification of lightly travelled roads can result in significant savings in bridge design. Similarly for heavily trafficked roads, it identifies the need to employ high α-factors, ensuring a safe design.

2 WEIGH IN MOTION DATA

Weigh in Motion technology is the process of acquiring the real loads on bridges through the use of sensors inbuilt into the road. This allows the load effects on bridges to be determined on a network by network basis. WIM systems allow identification of the Gross Vehicle Weights (GVW), axle loads and axle spacings for each truck as well as the inter-vehicle gap data. It enables the frequency of abnormally loaded vehicles, such as that shown in Figure 3, to be identified. Statistical models can be developed using the data obtained from WIM sensors, such as the GVW histogram shown in Figure 4. The bimodal nature is a result of empty and fully laden trucks.

Figure 3: Abnormal vehicle

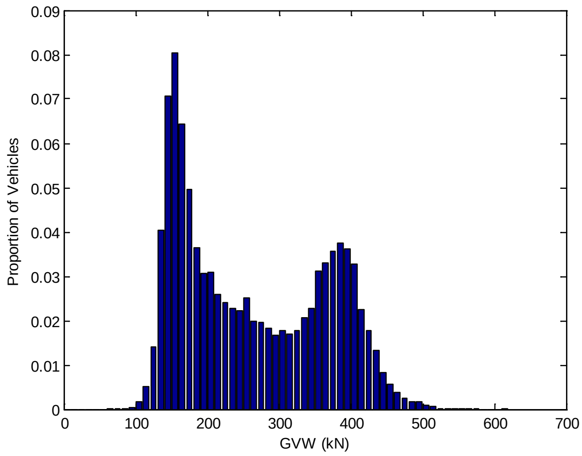

Figure 4: GVW histogram, 5 axle trucks

The authors favour the fitting of a 'semi-parametric' distribution to the histogram of measured GVSs. This has been proposed by OBrien et al. [3]. It involves:

- using bootstrapping to directly simulate from the histogram where there is sufficient data to justify this and
- fitting the tail of a Normal distribution to the data for extremely heavy vehicles, as shown in figure 5.

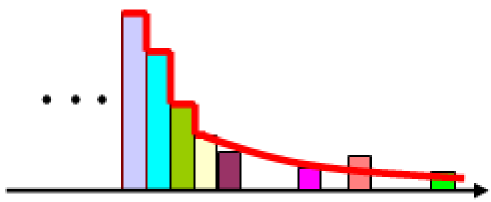

Figure 5: Semi-parametric fitting

This approach provides for significantly improved accuracy in the tail of the histogram allowing for the frequency of very heavy trucks to be accounted for in the analysis. The spacing between trucks is also an important consideration. The fitting of statistical distributions to gap data acquired by WIM sensors has been used to account for this [4].

The critical load cases for short span bridges are governed by individual axle and axle group loads. For shorter bridges free-flow conditions are generally more critically than congestion [5]. Allowance for dynamics is incorporated when free-flowing conditions are dominant using the Dynamic Amplification Factors (DAFs) of the Eurocode, reproduced in Figure 6.

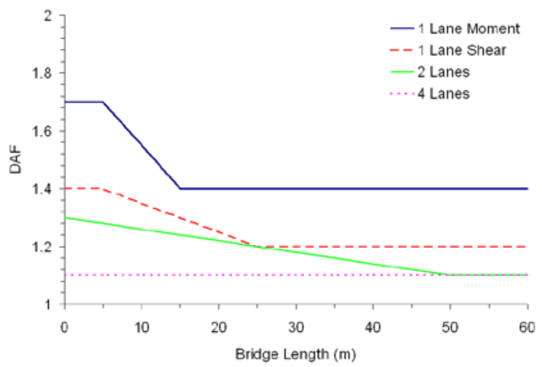

Figure 6: Eurocode DAFs

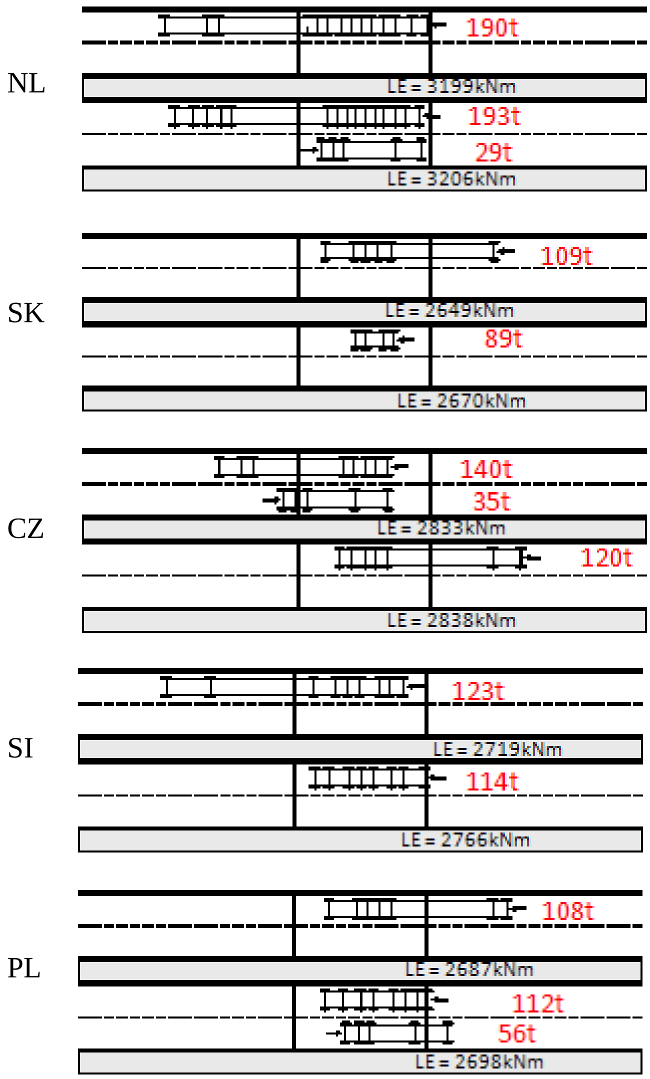

Figure 7: 1 in 1000 year loading scenarios for mid span moment in a simply supported 15m span (NL = Netherlands, SK = Slovakia, CZ = Czech Republic, SI Slovenia, PL = Poland).

Monte Carlo simulations [6] of traffic streams are generated using the acquired WIM data allowing determination of the load effects (shear forces, bending moments etc.) for the bridge under consideration. Characteristic 1 in 1000 year loading events are then determined by extrapolation or by simulating thousands of years of traffic. Enright and O'Brien [7] found typical characteristic maximum loading scenarios based on WIM data from five European countries shown in Figure 7.

The critical load case is sometimes an extreme vehicle on its own and sometimes an extreme vehicle meeting a more typical 5 or 6 axle truck. For example, the second critical loading scenario shown for the Dutch data is a 193 tonne 15 axle vehicle meeting a 29 tonne 5 axle semi-trailer.

3 CHARACTERISTIC LOAD DETERMINATION USING EXTREME VALUE DISTRIBUTIONS

For identification of characteristic load effects using the acquired WIM data, statistical extrapolations can be performed to the required return period (usually 1000 years). A standard Cumulative Distribution Function (CDF) plots the probability of non-exceedance against the load effect (moment or shear force) as shown in Figure 8.

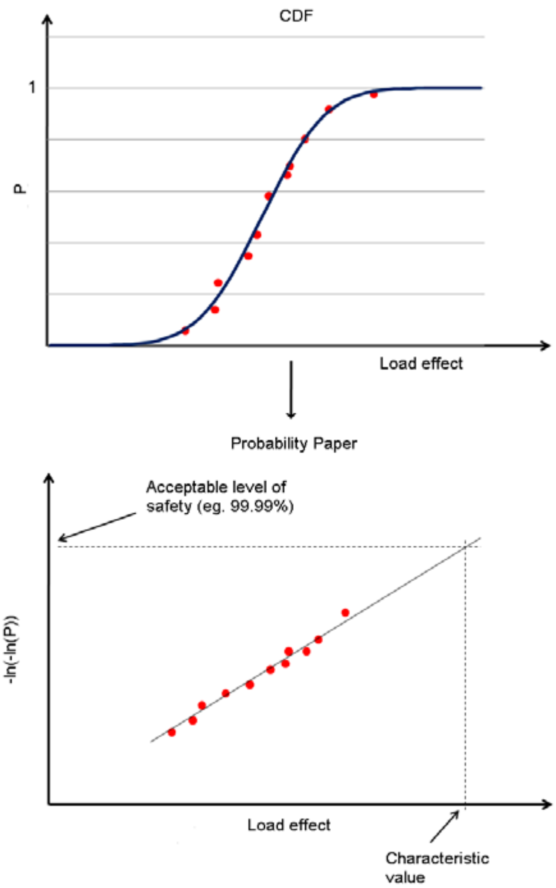

Figure 8: Gumbel probability paper plot

Each point represents a maximum-per-day or maximum-per-month load effect. The CDF has been replotted in the lower graph of Figure 8 to a Gumbel probability scale. The characteristic maximum load effect can then be found by extrapolating this trend to the predetermined acceptable level of safety. An alternative method can be employed whereby thousands of years of traffic can be simulated using Monte Carlo simulation and the 1000 year maximum found by interpolation. This approach is computationally intensive; however, it has the advantage that typical extreme loading scenarios can be identified.

The straight line in Figure 8 indicates that the data corresponds to a Gumbel Distribution. More usually bridge load effect data fits a Weibull distribution, which appears as a concave plot on Gumbel probability paper. A Weibull distribution is given by:

$$y = F(x,\lambda,\beta,\delta) = \exp\left[-\left(\frac{\lambda - x}{\delta}\right)^{\beta}\right] \tag{1}$$

where x = variable in question (i.e. the load effect), λ = threshold parameter, β = shape parameter and δ = scale parameter.

The probability of exceedance of the 1000 year load is given by

$$F(x) = 1 - \frac{1}{R.P} \tag{2}$$

where R.P = Return Period. Rearranging equation 1 and substituting for $F(x)$ allows calculation of the characteristic (i.e., 1000 year) load effect:

$$x = \lambda - \delta\left(-\ln\left(F(x)\right)\right)^{\frac{1}{\beta}} \tag{3}$$

Castillo recommends extrapolation after fitting to the final $2\sqrt{n}$ points, where n = number of points in the dataset [6]. However, it is not clear why this term is chosen and other authors have used others, such as the top 30%.

4 LOAD SHARING IN MULTIPLE LANE BRIDGES

Monte Carlo simulation is used to generate streams of single lane traffic, with the characteristics of the traffic flow (i.e. GVW, axle weight, axle spacing etc.) representative of the WIM measurements. For two lane roads with opposing traffic flow, i.e. a national primary/secondary route, the traffic in the two lanes can be assumed to be statistically independent. This allows simplification of the calculations as the effects of the two streams can be combined and the total load effect calculated for any point on the bridge. The results are sensitive to the transverse stiffness of the bridge: for example, the bending moment in the outer beam of a flexible bridge is less influenced by the traffic in the remote lane than is the case for a stiff bridge. Lane factors are applied to account for this, calculated so as to cover the range of expected transverse stiffness values. A lane factor of unity is applied to the lane making the greatest contribution to the load effect, i.e. the lane directly under the traffic flow. The factor applied for the other bridge lanes reflect their relative contribution to the load effect and ranges from as low as 0.05 for shear force in flexible bridge to 1.0 for bending moments in stiff bridges.

For two lane roads with same direction traffic (i.e. a motorway/dual carriageway), the loading scenario is more complicated. In the slow traffic lane, the frequency and weights of the heavy trucks are greater. The result is affected by a number of correlations. The weight of a lead vehicle is correlated with the weight of a following vehicle. This can be explained by, for example, heavy crane ballast vehicles travelling in convoy with cranes, sometimes without escort vehicles, shown in Figure 9.

Figure 9: Correlated vehicle event (courtesy Rijkswaterstaat)

The correlation is slight – of the order of 2% – but has a significant influence on the results. The weight of a lead vehicle in the slow lane is also correlated with the weight of an adjacent vehicle in the fast lane. This can be explained by overtaking events – the overtaking vehicle tends to be lighter than the vehicle it overtakes. Gaps are a difficult issue – it is possible to generate gaps consistent with measurements in each lane but this results in inter-lane gaps that are not consistent with measurements. This effect also has a significant influence on the results.

All of the issues with same-direction multi-lane simulations can be addressed using 'scenario modelling', as described by Enright and OBrien [7]. Traffic 'scenarios' – weights, within-lane and inter-lane gaps – are selected at random from the WIM database (Figure 10). The gaps and weights are then 'perturbed' using Kernel Density estimators to give a better coverage of all possible scenarios.

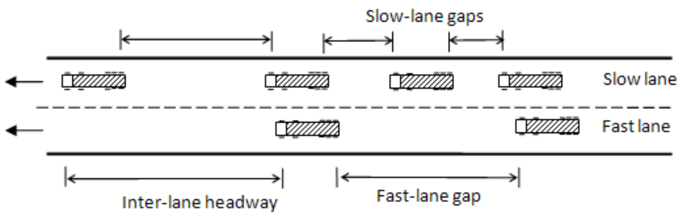

Figure 10. Typical traffic scenario [7]

5 CALIBRATION OF EUROCODE ALPHA FACTORS

The techniques outlined previously can be used to determine suitable adjustment factors (i.e. α factors) for Eurocode LM1. EC1 was originally developed considering a series of spans and influence lines, shown in Table 2. For each influence line, the characteristic load effects are found and compared to the corresponding load effect as calculated from the UDL and tandem axle load of LM1.

Enright and OBrien [7] calculated α factors for a range of load effects using WIM data from five European countries: the Netherlands (647,000 trucks), Slovakia (748,000 trucks), Czech Republic (730,000 trucks), Slovenia (148,000 trucks) and Poland (430,000 trucks). The number of trucks over 70 tonnes ranged from 892 in the Netherlands to 3 in Slovenia and the number over 100 tonnes ranged from 238 to 1.

Table 2: Influence lines used in EC1 calibration

Influence Line Number	Representation	Description of the Influence Line
LE0	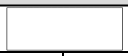	Total load.
LE1, LE2	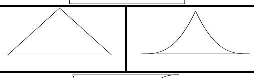	Maximum bending moment of a simply supported and double fixed[1] span, respectively.
LE3	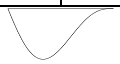	Maximum bending moment at the support of the former double fixed beam[1].
LE4, LE5	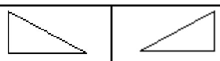	Shear force at the ends of simply supported bridge (assuming traffic flowing left to right)
LE6[2], LE7	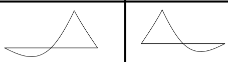	Minimum and maximum bending moment at mid-span of the first of two spans of a two span continuous beam.
LE8	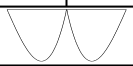	Continuous support moment of the former two span beam.
LE9	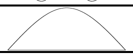	Continuous support reaction of the former two span beam.

[1]with an inertia strongly varying between mid span and the ends
[2]the second span only in loaded

Three load effects were considered from Table 2:

- LE1: Mid-span moment
- LE4: Shear force at support
- LE8: Central support hogging moment in 2-span continuous bridge

For bi-directional 2-lane bridges, the α-factors were calculated for four bridge lengths: 15 m, 25 m, 35 m and 45 m. The results for the four spans are shown in Figure 11. It is observed that for the Dutch traffic, LM1 is non-conservative for the recorded traffic by up to as much as 45% for low lane factors. End shear is a problem for all five countries considered, with α-factors greater than 1.0 required.

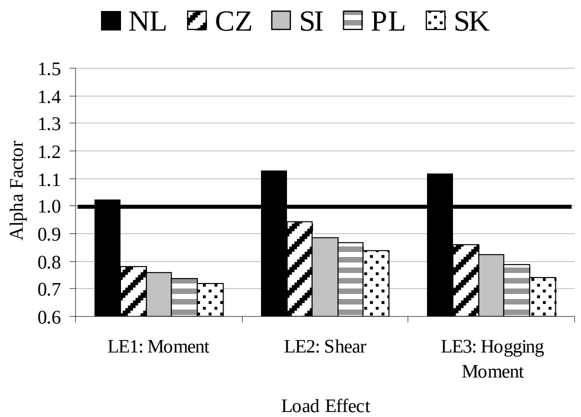

(a) High lane factors

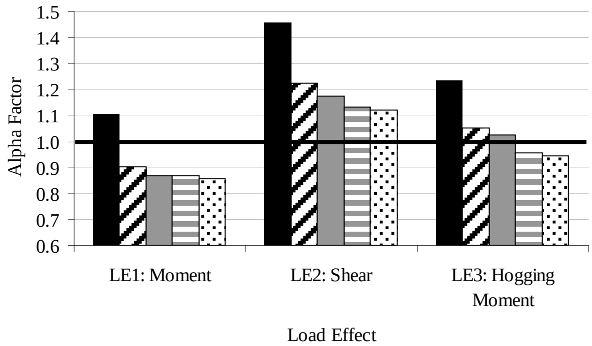

(b) Low lane factors

Figure 11: Maximum α-factor of four spans, bi-directional traffic [7]

It should be noted that both permit and non-permit trucks were included in the WIM database so the Dutch bridges would be expected to be governed by the abnormal load model as opposed to LM1.

The inconsistency between stiff and flexible bridges (high and low lane factors respectively) suggests that the relative loading in the lanes of the load model are incorrect: the slow lane loading of 9 kN/m^2 should be increased to reduce the α–factors in the flexible bridges relative to the stiff bridges. Figure 12 shows the α–factors for a same direction 2 lane bridge. While the results are generally similar, differences of up to 10% exist in some cases.

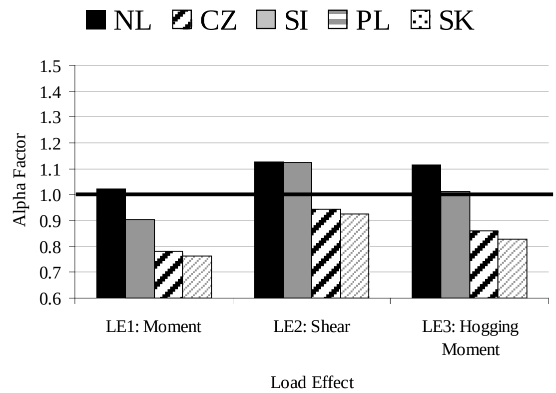

(a) High lane factors

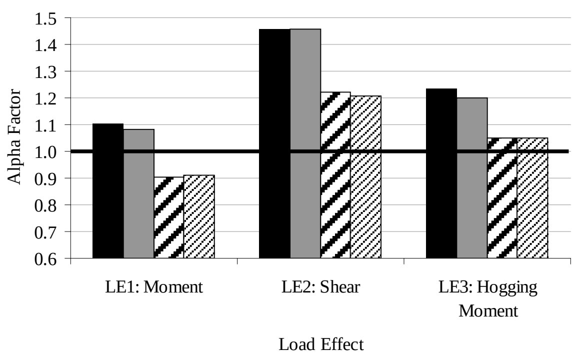

(b) Low lane factors

Figure 12: Maximum α-factor of four spans, same-direction traffic [7]

The α-factors for Ireland and the United Kingdom are listed in Table 3. As can be seen, the uniform loading of 9 kN/m^2 is significantly reduced in the most heavily loaded lane and other lane loadings of 2.5 kN/m^2 are more than doubled. This is contrary to the findings for the five continental European countries considered. If traffic in the British Isles is similar to that elsewhere in Europe, this will result in some bridges being over-designed while others are under-designed.

Table 3: Ireland/United Kingdom α-factors

Location	α_Q for tandem axle loads	α_q for UDL loading
Lane 1	1.0	0.61
Lane 2	1.0	2.2
Lane 3	1.0	2.2
Other Lanes	-	2.2
Remaining Area	-	2.2

6 CONCLUSIONS

This paper outlines techniques for the determination of load adjustment factors for Eurocode LM1 for a specific network, or on a case by case basis. Methods for calculating the characteristic load effects from the WIM data by extrapolation on probability paper are presented, and the alternative of simulating thousands of years of traffic and interpolating. These characteristic maximum load effects are compared to those obtained using Eurocode LM1 to determine appropriate α-factors. It was shown that for a range of load effects and spans, Eurocode LM1 is conservative for four out of five countries except for shear force. It is non-conservative for almost all cases at the Dutch site which is very heavily trafficked.

Furthermore, there is an inconsistency between the factors for stiff and flexible bridges. This could be corrected by using α-factors in excess of unity to the slow lane loading of 9 kN/m^2.

REFERENCES

[1] Eurostat (2009), *Panorama of Transport,* Office for Official Publications of the European Communities, Luxembourg.

[2] EN 1991-2:2003: Eurocode 1: Actions on structures – Part 2: Traffic Loads on Bridges.

[3] OBrien, E.J., Cantero, D., Enright, B., González, A., (2010), 'Characteristic dynamic increment for extreme traffic loading events on short and medium span highway bridges', *Engineering Structures*, 32, 3287-3835.

[4] OBrien, E.J. and Caprani, C.C., (2005), 'Headway Modelling for Traffic Load Assessment of Short to Medium Span Bridges', *The Structural Engineer*, 83(16): 33-36.

[5] Flint, A.R. and Jacob, B., (1996), 'Extreme Traffic Loads on Road Bridges and Target Values of their Effect for Eurocode Calibration', *Proceedings of IABSE Colloquium, Delft, The Netherlands: IABSE – AIPC-IVBH*, 469-78.

[6] E. Castillo, 1988. *Extreme Value Theory in Engineering.* Academic Press, Boston, USA, 1988

[7] Enright, B. and OBrien E.J., 2011, 'Bridge Friendliness Index from Weigh-in-Motion Data'. *Transport Research Board Annual Meeting, Washington.*

Spatially variable assessment of lifetime maximum load effect distribution in bridges

D. Hajializadeh[1], E.J. OBrien[1,2], E. Sheils[2], B. Enright[3]
[1]Department of Civil, Structural and Environmental Engineering, University College Dublin, Dublin, Ireland
[2]Roughan & O'Donovan Consulting Engineers, Ireland
[3]Dublin Institute of Technology, Bolton St., Dublin 1, Ireland
email: donya.hajializadeh@ucd.ie, eugene.obrien@ucd.ie, emma.sheils@ucd.ie, bernard.enright@dit.ie

ABSTRACT: Bridge structures are key components of highway infrastructure and their safety is clearly of great importance. Safety assessment of highway bridges requires accurate prediction of the extreme load effects, taking account of spatial variability through the bridge width and length. This concept of spatial variability is also known as random field analysis. Reliability-based bridge assessment permits the inclusion of uncertainty in all parameters and models associated with the deterioration process. Random field analysis takes account of the probability that two points near each other on a bridge will have correlated properties. This method incorporates spatial variability which results in a more accurate reliability assessment.
This paper presents an integrated model for spatial reliability analysis of reinforced concrete bridges that considers both the bridge capacity and traffic load. A sophisticated simulation model of two-directional traffic is used to determine accurate annual maximum distributions of load effect. To generate the bridge loading scenarios, an extensive Weigh-in-Motion (WIM) database, from five European countries, is used. For this, statistical distributions for vehicle weights, inter-vehicle gaps and other characteristics are derived from the measurements, and are used as the basis for a Monte Carlo simulation of traffic . Results are presented for bidirectional traffic, with one lane in each direction, with a total flow of approximately 2000 trucks per day.

KEY WORDS: Random field, spatial variability, traffic, load, bridge, probabilistic, safety, assessment.

1 INTRODUCTION

The response of reinforced concrete (RC) bridge structures depends on many uncertain factors such as traffic load, environmental condition, material properties (concrete strength, concrete density), concrete cover and geometric dimensions. The response is considered satisfactory when the desired limit state (such as load carrying capacity) is fulfilled with an acceptable degree of certainty.

Probabilistic assessment of limit state violations at any stage during a structure's lifetime is often done using reliability analysis. The reliability assessment of a bridge is a complex problem requiring the modelling of aleatory and epistemic uncertainties existing in both load and response to the load. These uncertainties fluctuate within the length, width and depth of the structure and the response of the bridge is accordingly affected by these fluctuations. Random field analysis is a means of mathematical representation of the spatial variability which takes account of the correlation between any two individual elements.

Random field analysis offers significant advantages such as rational assessment of bridge deck safety that can produce a whole design space instead of just a one point result. It accounts for the contribution of spatial variability of load and resistance to the overall reliability of the bridge structure.

Methods of evaluating the spatial capacity of bridges has received a great deal of attention (Karimi et al., 2005, Kenshal, 2009, Li et al., 2004, Vu, 2003). However, the uncertainty associated with the load model has not been considered extensively with the exception of Kenshal (2009) who provides an insight on methods used to generate the load effects from site specific traffic data obtained using Weigh in Motion (WIM).

WIM is the process of measuring the weights of trucks travelling at full highway speed. The WIM traffic records in this study are used to calibrate a comprehensive model of traffic loading. In conventional approaches statistical distributions such as those from the Extreme Value (EV) family are fit to measured or simulated block-maximum load effects. One day is widely used as a block size in EV distributions such as the Weibull or Type 2. A Monte Carlo (MC) simulation approach is used here to develop a very efficient algorithm simulating different bridge loading scenarios, allowing many lifetimes – thousands of years of traffic – to be simulated. The resulting lifetime maximum distribution can be expected to be considerably more accurate than that calculated using the conventional approach.

This paper presents a method of probabilistic assessment of safety which considers an entire 2-dimensional bridge deck, including an allowance for the spatial variability of load effect. The bridge deck is divided into rectangular segments with properties assumed to be statistically independent. Once load effect and resistance distributions are found for each individual area, the theorem of total probability is used to determine the probability of failure. The failure criteria used in this paper is defined as that of load effect exceeding resistance.

2 RANDOM FIELD ANALYSIS

Structural safety assessment depends on a number of structural properties and operating conditions. Furthermore, these properties and conditions exhibit random variation across the surface of a structure. There can be variation due to the quality of concrete properties, concrete cover, inconsistency in traffic load, environmental condition, workmanship, etc. (Kenshal, 2009, Vu, 2003). Traditionally, these random variables are modelled deterministically with a single characteristic value which is unable to account for their variations (Vu, 2003). Homogeneous random variables, with associated probability density functions, is another conventional approach to modelling. This takes account of the inherent variability of properties (Melchers, 1999). Hence, spatial variability of variables across the length and width of a structure is simply ignored (Kenshal, 2009, Vanmarcke & Grigoriu, 1983, Vu, 2003, Vu & Stewart, 2005). Neglecting such sources of uncertainty has a significant impact on the evaluated safety (Kenshal, 2009). Thus, it is important to include the spatial variability of parameters in a safety assessment.

Random field analysis takes account of the probability that any pair of points corresponding to any locations within the structure will have correlated properties. This is achieved by discretising the corresponding random fields into a set of spatially correlated random variables. Several methods have been proposed for the discretisation of random fields into random variables. The midpoint method, which represents the random field by the value at the centroid, is widely used in the literature. This method is relatively easy to implement, provides numerically stable results and is applicable to Gaussian and non-Gaussian random fields.

The statistical correlation between any pair of elements can be modelled through the use of a mathematical function, termed the autocorrelation function. This function is based on the correlation characteristic of the corresponding random field. The autocorrelation function represents the correlation coefficient between two elements separated by the interval ξ. Different models may be used to define the spatial correlation between two elements within the given structure. The exponential autocorrelation function has been used widely to represent the spatial variability of material properties and loading in other fields of engineering (Hisada & Nakagiri, 1985, Kersner et al., 1998, Liu & Der Kiureghian, 1989, Mahadevan & Haldar, 1991, Yamazaki, 1988). For a 2-dimensional random field, it is defined as:

$$\rho(\xi) = exp\left(-\left(\frac{|\xi_x|^2}{d_x^2}\right) - \left(\frac{|\xi_y|^2}{d_y^2}\right)\right) \tag{1}$$

where d_x and d_y are the correlation lengths for a 2-dimensional random field in the x and y directions respectively. The distances between the centroid of elements i and j are $\xi_X = x_i - x_j$ and $\xi_X = x_i - x_j$ in the x and y directions respectively.

It should be noted that some parameters, such as steel strength, have low spatial variability due to quite strict quality control whereas adopting certain quality control measurement for other parameters does not have significant influence, e.g., concrete strength and cover. As a result, it is not necessary to consider all parameters as spatially random. Sensitivity analysis can be used to determine how the uncertainty in the probability of failure can be influenced by the spatial variability of different parameters.

This general method of random field analysis has been adopted by various authors. Vu & Stewart (2005) divide the structural element into N statistically independent areas (i.e., with no correlation between these areas). Each independent area is considered as a random field (see Figure 1). The optimal size of the discretised elements needs to be specified for random filed analysis. This size of element should not be too large to avoid underestimation of spatial variability (Vu, 2003). On the other hand, numerical problems associated with the decomposition of a large covariance matrix will result from choosing very small elements.

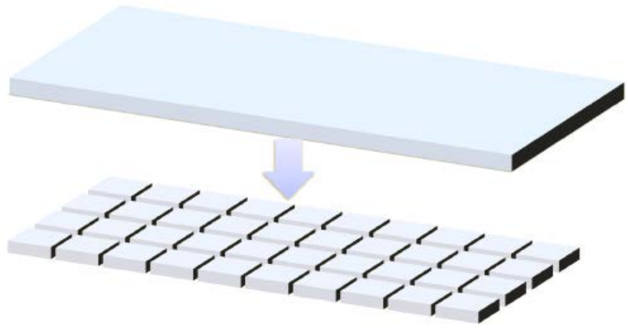

Figure 1. Independent areas and correlated elements.

For this study, the authors adopt an approach similar to that of Vu & Stewart (2005), combining the spatial variability of resistance with spatial variability of loading across a bridge deck. The main focus of this paper is the spatial variability of the load model and to highlight the significant influence of this variability on the result.

3 SAFETY ASSESSMENT

Structural reliability consists of the following steps. The relevant limit state is first identified and the structure broken into N independent elements. The load and resistance model is developed for each element and the autocorrelation function specified. For each element, the probability density functions for the load effect and resistance of each element are defined. Quantify the probability of failure for each element. Finally, the theorem of total probability is used to find the marginal probability of failure of whole deck.

An example will be used to illustrate the approach. It consists of a simply supported reinforced concrete solid bridge deck of length 40 m and width 8m.

3.1 Traffic load model

Non-permit traffic load, sometimes termed ‘normal’ is distinguished from special vehicles which require permits to carry weights above the usual legal limits (Minervino et al., 2004, EC1, 2003). As permit vehicles are a critical factor in bridge loading (Moses, 2001, Sivakumar, 2007), the model developed for this study includes all vehicles, whether permit or non-permit, that likely to cross a bridge at full highway speed in its lifetime.

Monte Carlo simulation is used to generate bridge traffic loading scenarios for a number of years. Statistical distributions for vehicle properties such as weights and inter-vehicle gaps are taken from Weigh-in-Motion (WIM) measurements.

This study focuses on short to medium span bridges, where the combination of static load effect and dynamic amplification governs over congestion (Flint & Jacob, 1996). WIM data was collected for 290 weekdays over a 19 month period in 2005/2006 from the two slow lanes of the 4 lane D1(E50) highway near Levoča in Slovakia. A small percentage of vehicles – 13 327 out of a total of 761 665 – were removed in a series of data quality assurance checks. Of the remaining 748 338 vehicle, 349 606 were traveling in one direction and 398 732 in the other. The average daily flows were 1031 truck per day in one direction and 1168 in the other. The maximum number of axles in a vehicle observed at this site was 11.

There were 78 vehicles having gross vehicle weight (GVW) exceeding 70 t, 8 vehicles in excess of 100 t and a maximum observed GVW of 117.1 t. In the Monte Carlo (MC) simulation, the GVW and number of axles for each truck are generated using the 'semi-parametric' approach (OBrien et al., 2010). This involves the use of an empirical bivariate distribution (i.e., bootstrapping) for GVW and number of axles up to a specified GVW threshold, chosen here as 64 t. Above this threshold, a parametric fit is used, not only to smooth the trend but also to generate vehicles with weights and numbers of axles greater than those observed. A truncated Normal distribution is used for this purpose.

The MC simulation generates streams of traffic in each direction with GVW, axle spacing and inter vehicle spacing consistent with the measured site data. Bending moment is calculated at all elements in the bridge for each increment in time during each truck(s) crossing event. Two extreme loading scenarios are illustrated in Figure 2. The first includes a very large individual vehicle, in this case 162 t on 12 axles. The second involves a large vehicle meeting a common vehicle type, in this case, 152 t on 11 axles meets a 31 t vehicle on 5 axles.

Figure 2. Typical extreme loading scenarios.

Two hundred years of traffic is simulated and the load effects calculated for each element of bridge deck. The Weibull extreme value distribution is found to fit well to the data. The load effect distributions for three elements are shown in Figure 3a and 3b. The elements are labelled as $A_{i,j}$, counting from element $A_{1,1}$ in the South West corner (front left in Figure 3a). The elements considered are $A_{5,1}$, $A_{7,1}$ and $A_{5,2}$, corresponding to coordinates (x,y) = (5,1), (7,1) and (5,2) respectively.

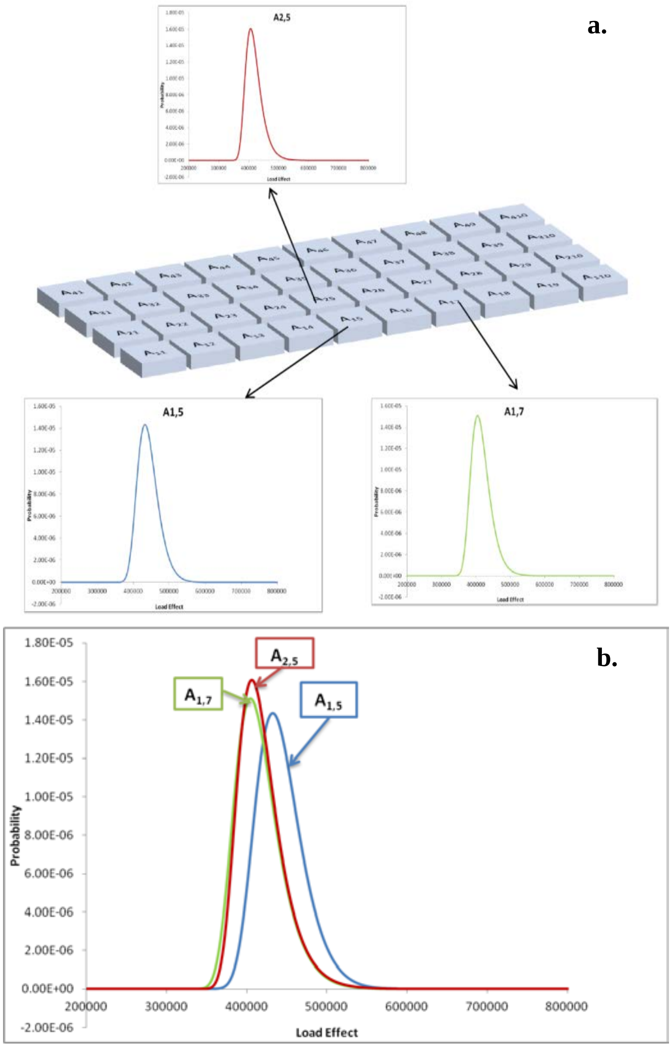

Figure 3. Maximum-in-life load effect distributions.

3.2 *Resistance model*

Design or assessment codes can be used to derive models for the capacity of members to resist load effects such as bending moment or shear force. For the purposes of this paper, a lognormal distribution is assumed for moment resistance with a mean of 6.95×10^5 and a standard deviation of 5.92×10^8 for all individual elements.

4 RESULTS AND DISCUSSION

When the limit state function is not time-dependent, it can be defined as

$$z = G(R, S) = R - S \tag{2}$$

where z is limit state margin, G is limit state function, R is random variable representing the capacity and S is the random variable representing the corresponding load effect. The limit state histograms for three elements (discussed before), $A_{1,5}$, $A_{1,7}$, $A_{2,5}$ are illustrated in Figure 4.

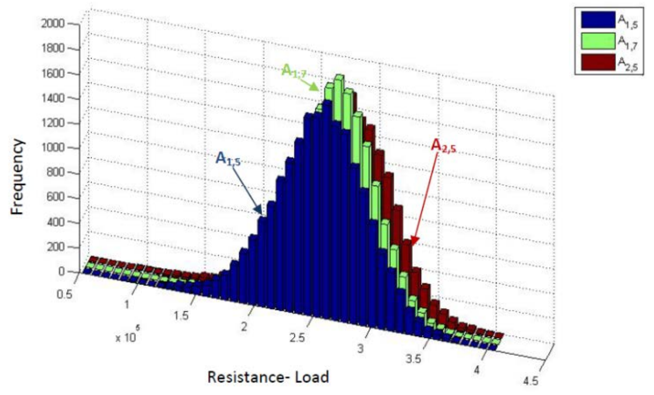

Figure 4. Limit state histogram.

The probability of limit state violation is used here as a proxy for the probability of failure:

$$P_f = P(G(x) \leq 0) = \int \dots \int_{G(x)\leq 0} f_x dx \qquad (2)$$

Using the defined resistance and load models, the probability of failure is calculated for each element. The results are presented in Table 1.

Table 1. Probability of Failure

		A(:,j)			
	i/j	1	2	3	4
A(i,:)	1	7.77×10^{-16}	7.77×10^{-16}	7.77×10^{-16}	7.77×10^{-16}
	2	7.77×10^{-16}	7.77×10^{-16}	7.77×10^{-16}	7.77×10^{-16}
	3	7.77×10^{-16}	6.42×10^{-13}	2.66×10^{-15}	1.55×10^{-11}
	4	3.65×10^{-09}	1.35×10^{-07}	3.92×10^{-08}	6.00×10^{-08}
	5	9.83×10^{-09}	8.04×10^{-07}	2.13×10^{-06}	1.06×10^{-06}
	6	1.80×10^{-07}	1.91×10^{-06}	9.89×10^{-06}	2.52×10^{-06}
	7	2.36×10^{-08}	1.18×10^{-06}	2.59×10^{-06}	2.73×10^{-07}
	8	7.77×10^{-16}	1.72×10^{-09}	4.68×10^{-11}	5.48×10^{-10}
	9	7.77×10^{-16}	1.11×10^{-15}	1.33×10^{-15}	7.77×10^{-16}
	10	7.77×10^{-16}	7.77×10^{-16}	7.77×10^{-16}	7.77×10^{-16}

Using the equation $\beta = -\phi^{-1}(P_f)$ the corresponding reliability index for each element is calculated for all elements. The results are illustrated in Figure 5.

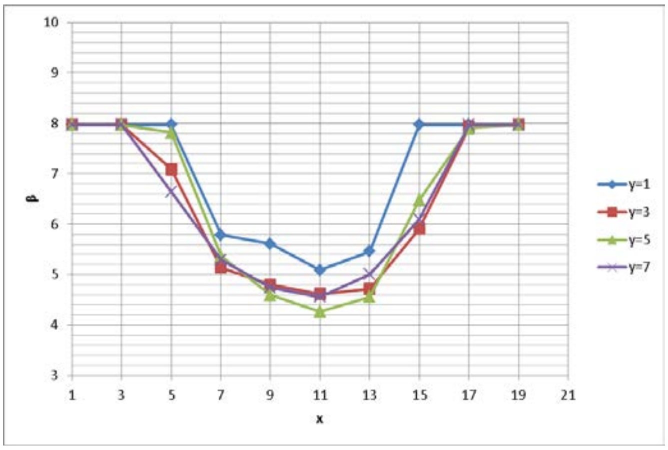

Figure 5. Reliability index at midpoint of each element.

As resistance was assumed to have the same distribution throughout the bridge length, the lowest reliability index corresponds to mid-span, where the load effect of bending moment is greatest. Reliability index variation across the width arises from a difference in the intensity of traffic within the two directions (349 606 vehicles in one direction as opposed to 398 732 in the other). There is also an edge effect due to greater bending moment at the edges transversely.

The theorem of total probability is used to calculate the failure probability of the entire structure based on the calculated probability of failure for each element.

$$Total\ Probability\ of\ Failure = 1 - \prod_{a=1}^{N}(1 - P_{fa}) \qquad (4)$$
$$= 2.281 \times 10^{-05}$$

Where N is total number of elements and P_{fa} is probability of failure of element a with renumbering elements from 1 to N.

The spatial approach to the calculation of failure probability gives 2.281×10^{-5} which is about 2.3 times greater than the conventional approach where each element of the bridge is considered in isolation. This indicates that the conventional approach may be highly conservative.

5 CONCLUSION

A framework is presented for the reliability assessment of a 2-dimensional solid slab bridge deck. The bridge is divided into independent elements and the probability of failure and reliability index calculated for each element. Probability density functions are assumed for resistance and are calculated using Monte Carlo simulation for load effect. Random field analysis is proposed as a method of modelling the spatially variable resistance.

For the example considered, the conventional approach of reliability evaluation, considering individual elements in isolation, is inaccurate on the conservative side.

ACKNOWLEDGEMENT

The TEAM project is a Marie Curie Initial Training Network and is funded by the European Commission 7th Framework Programme (PITN-GA-209-238648).

REFERENCES

[1] Choi, S. K., Grandhi, R. V. & Canfield, R. A. Reliability-based structural design. Reliability-based Structural Design, by S.-K. Choi, RV Grandhi, and RA Canfield. Berlin: Springer, 2006.

[2] Flint, A. & Jacob, B. Extreme traffic loads on road bridges and target values of their effects for code calibration. IABSE REPORTS, 1996: 469-478.

[3] Hisada, T. & Nakagiri, S. Role of the stochastic finite element methods in structural safey and reliability. Proceedings 4th Intenational Conference Structural Safety and Reliability, ICOSSAR 85, Kobe, Japan, 1985.

[4] Karimi, A., Ramachandran, K., Buenfeld, N. & Crowder, M. Probabilistic analysis of reinforcement corrosion with spatial variability. Ptoceedings of ICOSSAR '05-Ninth International Conference on Structural Safety and Reliability, Millpress, Rotherdam, 2005: 679-686.

[5] Kenshal, O. Influence of spatial variability on whole life management of reinforced concrete bridges. Ph.D Thesis, Trinity College Dublin, 2009

[6] Kersner, Z., Novák, D., Teply, B. & Rusina, R. Modeling of deterioration of concrete structures by stochastic finite element method. Proceedings 7th Intenational Conference Structural Safety and Reliability, ICOSSAR 97, Rotterdam, Balkema, 1998.

[7] Li, Y., Vrouwenvelder, T., Wijnants, G. & Walraven, J. Spatial variability of concrete deterioration and repair strategies. Structural concrete, 2004, 5(3): 121-129.

[8] Liu, P. L. & Der Kiureghian, A. Finite element reliability methods for geometrically nonlinear stochastic structures. Report No. UCD/SEMM-89/05. California, University of California at Berkelly. 1989.

[9] Mahadevan, S. & Haldar, A. Practical random field discretization in stochastic finite element analysis. Structural safety, 1991, 9(4): 283-304.

[10] Melchers, R. E. Structural reliability: Analysis and prediction John Wiley & Sons New York, 1999

[11] Minervino, C., Sivakumar, B., Moses, F., Mertz, D. & Edberg, W. New AASHTO guide manual for load and resistance factor rating of highway bridges. Journal of Bridge Engineering, 2004, 9(1): 43-54.

[12] Moses, F. Calibration of load factors for LRFD bridge evaluation, Report No. NCHRP 454. Transportation Research Board, United States, Federal Highway Administration, 2001

[13] OBrien, E. J., Caprani, C. & O'Connell, A. J. Bridge assessment loading: A comparison of west and central/east europe. Bridge Structures-Assessment, Design & Construction, 2006, 2(1): 25-33.

[14] OBrien, E. J., Enright, B. & Getachew, A. Importance of the tail in truck weight modeling for bridge assessment. Journal of Bridge Engineering, 2010, 15: 210.

[15] Sivakumar, B. Legal truck loads and AASHTO legal loads for posting. Report No,.NCHRP 575, Transportation Research Board , United States, Federal Highway Administration, 2007

[16] Standardization, E. C. f. Eurocode 1: Actions on structures Part 2: Traffic loads on bridges. 2003.

[17] Vanmarcke, E. & Grigoriu, M. Stochastic finite element analysis of simple beams. Journal of engineering mechanics, 1983, 109(5): 1203-1214.

[18] Vu, K. Corrosion induced cracking and spatial time dependent reliability analysis of reinforced concrete structures. NSW, Australia: The University of Newcastle. PhD Thesis, 2003.

[19] Vu, K. A. T. & Stewart, M. G. Predicting the likelihood and extent of reinforced concrete corrosion-induced cracking. Journal of Structural Engineering, 2005, 131: 1681.

[20] Yamazaki, F. Neumann expansion for stochastic finite element analysis. Journal of engineering mechanics, 1988, 114: 1335.

The effect of clusters within crowds of pedestrians on the vertical response of a flexible footbridge

J. Keogh[1], C.C. Caprani[1], P. Archbold[2], P. Fanning[3]
[1]Department of Civil and Structural Engineering, Dublin Institute of Technology, Bolton St., Dublin, Ireland
[2]Structurs and Materials Research Group (STRAIT), Athlone Institute of Technology, Dublin Road, Athlone, Ireland
[3]School of Civil, Structural & Environmental Engineering, University College Dublin, Belfield, Dublin 4, Ireland
email: joe.keogh1@dit.ie, colin.caprani@dit.ie, parchbold@ait.ie, paul.fanning@ucd.ie

ABSTRACT: The issue of excessive vibrations of footbridges due to the passage of pedestrians has been well documented in the past decade. Despite this there still remains great uncertainty as to how to predict the acceleration response of a footbridge due to crowd loading. This paper investigates the vibration response of a flexible footbridge subjected to crowd loading. Using a statistical model which caters for the variability of pedestrians, the vibration response of the footbridge is obtained. In this work, the effect of social groups or clusters of pedestrians in a crowd is investigated. Herein a cluster is defined as two or more pedestrians walking together with the same velocity. The predictions of this model are compared to a model which uses only lone pedestrians walking within a crowd. None of the current design codes or guidelines considers the possibility of pedestrians walking together. The size of the clusters is found in literature to follow a Poisson distribution. In this paper variations of the probability of clusters appearing in the crowd are assessed. It is found that the response of a crowd with clusters present is similar to the predictions of the UK National Annex to Eurocode 1.

KEY WORDS: Bridge, Vibration, Pedestrian, Vertical, Pacing frequency, Cluster

1 INTRODUCTION

1.1 Background

Modern developments in the design of structures and progress in structural materials have led to longer and lighter footbridges. Increasingly, these typically low-frequency structures are experiencing serviceability problems.

Due to the dynamic nature of pedestrian loading, vibrations of the bridge deck can be expected if the bridge natural frequency is within, or close to, the typical pacing frequency range (1.5Hz to 2.5 Hz). Such vibrations are often magnified by the presence of a crowd of pedestrians crossing the structure. If these vibrations are large enough they can lead to discomfort for the pedestrians, resulting in failure of the serviceability limit state. Bridges that have experienced vibrations of this nature have been well documented in the last decade, including high profile bridges such as; the Millennium Bridge, London [1], the Pont du Solferion, Paris [2], and the T-Bridge, Japan [3].

1.2 Approach of this work

In this work the vertical vibrations induced by crowds on a flexible footbridge are examined. Typically, bridge vibrations produced from a crowd of pedestrians are estimated by using an enhancement factor applied to the effect caused by a single pedestrian. However, the models for the determination of the single pedestrian response are commonly deterministic and do not consider the sensitivity of bridge vibrations to slight changes in pacing frequency. The model presented here uses statistical distributions to model the variability of pedestrians in a crowd.

In a development of the model presented by Caprani et al [4] this model assesses the effect on the footbridge response of social groups or clusters of pedestrians walking within a crowd. For this work, a cluster is defined as a social group of two or more pedestrians who intentionally walk together. In order of the cluster to remain intact, each pedestrian within the cluster must have the same velocity.

The proposed cluster model of this work differs from the model presented by Caprani et al [4] which modelled a crowd as a collection of lone pedestrians. In this form of crowd the individual velocities are determined as the product of a random pacing frequency and step length, both chosen from predetermined statistical distributions. It was reported by Ebrahimpour et al [5] that pedestrians consciously make changes in their pacing frequency to synchronize their movements with those around them. This indicates that pedestrians tend to walk in phase while walking in a crowd. As a result, varying levels of synchronization were investigated by Caprani et al [4]. In the model presented here, no synchronization is forced between the pedestrians in order to assess the effect of clusters only.

2 CURRENT DESIGN CODES AND GUIDELINES

Many of the current design guidelines [6-10] for the prediction of crowd loading are based on different assumptions. As a result, their prediction of the response due to a typical crowd loading scenario on a low frequency footbridge was found to vary by as much as a factor of four [11].

Eurocode 5 [6] is a recent design code for the design of timber structures and includes recommendations for vibrations. The response model defined is not material-dependent and so can be used for the prediction of vibrations for a footbridge constructed from any material. To predict the response, a_1, of a footbridge with a natural frequency in the range 1.5 to 2.5 Hz resulting from single pedestrian loading, Eurocode 5 [6] uses the formula:

$$a_1 = \frac{200}{M\zeta} \quad (1)$$

Where M is the bridge mass and ζ is the damping ratio of the bridge. The pedestrian is assumed to be walking at the same natural frequency as the bridge and so no other parameters are required for the calculation. As a result, use of Equation (1) means that the single pedestrian response is found to be constant for any footbridge with a natural frequency within the given range. This approach neglects the sensitivity of vibrations of the deck to the pedestrian pacing frequency found by several authors including Keogh et al [12] and Pedersen and Frier [13], for example.

For the prediction of crowd loading, Eurocode 5 [6] multiplies the single pedestrian response by an enhancement factor to determine the response for N pedestrians, a_N (m/s^2):

$$a_N = 0.23 a_1 N k \quad (2)$$

where k is a reduction factor which reduces from 1 above and below the natural frequency range which is sensitive to vertical vibrations (1.5 Hz to 2.5 Hz).

ISO 10137 [7] uses a Fourier series with 5 harmonics to represent the force due to a single pedestrian given as:

$$F_1(t) = W\left[1 + \sum_{i=1}^{n} \alpha_i \sin\left(2\pi i f_p + \varphi_i\right)\right] \quad (3)$$

where W is the pedestrian weight, i is the harmonic number, $\alpha_1 = 0.37(f_p\text{-}1)$, $\alpha_2 = 0.1$, $\alpha_3 = \alpha_4 = \alpha_5 = 0.06$ and ϕ_i is the phase angle for the specific harmonic, and f_p is the pacing frequency. Inclusion of the pacing frequency in the equation means that this code considers changes in the force with variations in the pacing frequency. The guideline does not give guidance on what pacing frequency to use nor does it specify if the force is static or moving. It was assumed by Pavic [11] that the pacing frequency is chosen to match the bridge frequency and that the pulsating force given by Equation (3) is moving across the bridge. To obtain the total effective pedestrian load due to a crowd of N uncoordinated pedestrians, the dynamic load defined by Equation (3) is multiplied by $\sqrt{N}$. Although this is reported by Pavic [11] to be an improved method of prediction, work by Ingolfsson et al [14] found that the response due to crowd loading is overestimated using this approach.

The method applied in both the SETRA guideline [8] and the UK National Annex to Eurocode 1 [9] are similar in that both represent the mass of the pedestrians as a uniformly distributed load on the bridge which has the effect of reducing the natural frequency. The load applied by the crowd is defined as a load per unit area of the bridge deck. HIVOSS [10] uses a frequency domain response spectrum approach when calculating the response of footbridge to streams of pedestrians.

3 SOCIAL CLUSTERS IN CROWDS

3.1 Overview

The existence of clusters of pedestrians (two or more) walking in a crowd is typical of a real life situation. Moussaid et al [15] highlighted that there a high probability that small groups or clusters of pedestrians will be present in crowds. Despite this, none of the current guidelines mentioned in Section 2 make reference to this possibility. Moussaid et al [15] state that simulation of crowds with all the pedestrians walking individually, with their individual desired speed, is not representative of real life. If pedestrians intentionally walk in small social groups they will be travelling at the same velocity as the others in the group. Crowds of pedestrians were observed using video recordings, walking along a popular commercial walkway on two different days; population A (P_A) was observed at lunch time on a week day whilst population B (P_B) was observed on a Saturday afternoon [15]. It was found that a higher percentage of P_B walked in clusters of two or more pedestrians when compared to P_B. The higher percentage for P_B was expected due to a higher tendency for people to walk with friends on a Saturday [15]. It was also found that pedestrians in P_A also walked faster than those in P_B.

3.2 Cluster Size Distribution

Moussaid et al [15] find that a Poisson distribution, with a mean value (λ) of 0.83, could be used to represent the cluster sizes within the crowd of P_A, as shown in Figure 1. This shows that 33.2% (1 – 0.668) of the pedestrians walking on this day, during the video recording, were in a cluster.

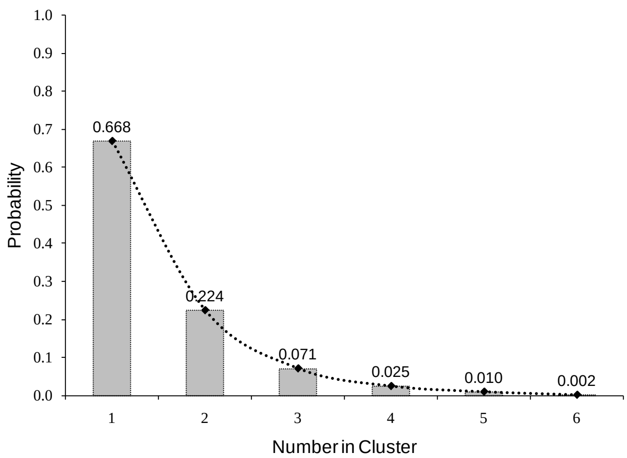

Figure 1. Cluster Size Distribution (after Moussaid et al [15]).

4 PEDESTRIAN AND BRIDGE MODELLING

4.1 Pedestrian parameters and model

In this work, pedestrians are considered to be non-homogeneous and so their individual parameters follow statistical distributions. The pedestrians in the model are considered to be healthy adults for the purpose of assigning pedestrian properties. The pedestrian mass is represented by a lognormal distribution with a mean of 73.9 kg and a coefficient of variation of 21.2% [16]. The pedestrian step length is taken to be normally distributed with a mean of 0.66 m and given a coefficient of variation of 10% [17]. The pacing frequency is taken to be normally distributed with a calculated mean of 1.96 Hz and a standard deviation of 0.209 Hz following a literature survey [5, 18-21]. The pedestrian velocity is calculated as the product of the pacing frequency and the step length, the mean velocity is found to be 1.29 m/s with a standard deviation of 0.19 m/s.

Brownjohn et al [22] reported on a phenomenon, termed intra-subject variability, that a pedestrian can never repeat exactly the same step twice. Despite this it is commonly assumed that the force applied by both feet of a pedestrian is of the same magnitude and periodic [23, 24]. Since there is constant contact between the pedestrian and the walking surface during walking, the ground reaction force (GRF) produced from consecutive footfalls (left and right) overlap in time (see Figure 2).

The total force applied to the structure is the sum of the forces applied at any point in time. This total GRF can be represented by a Fourier series (Equation (3)). The number of harmonics used in the representation varies in the literature [22]. However Fanning et al [25] found that using just the first harmonic did not significantly influence the accuracy of the results. As a result for this work just the first harmonic of Equation (3) is used. Therefore the walking force is given by the following sine wave approximation:

$$F(t) = W\left[1 + \alpha \sin\left(2\pi f_p\right)\right] \tag{4}$$

where W is the pedestrian weight, f_p is the pacing frequency (Hz) and the Fourier coefficient, α, is given by [25]:

$$\alpha = 0.25 f_p - 0.1 \tag{5}$$

and is shown in Figure 2.

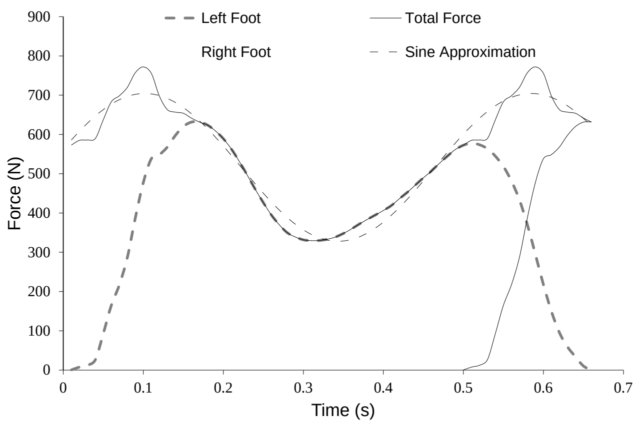

Figure 2. Typical shape of the ground reaction force due to a single pedestrian.

4.2 Bridge parameters

The bridge considering in this work is the 50 m long simply-supported beam with a mass of 500 kg/m, a width of 2 m and a natural frequency of 1.96 Hz. A modulus of elasticity of 200×10^{11} N/m^2 is used.

The damping ratio of the bridge is taken to be 0.5% with Rayleigh damping assumed thereafter [26]. This damping level is similar to a number of studies reported on low frequency structures (circa. 2 Hz) in the literature [8, 27-29].

The effect of humans on a structure's damping ratio is neglected in this paper. This is consistent with other researchers in the field, including the SETRA Guideline [8] and Pavic [11], who in his keynote address at the conference Footbridge 2011, used a bridge with a frequency of 2.16 Hz and a constant damping ratio of 0.6% in predicting the response for a non-stationary crowd (density of 0.5 p/m^2).

It should be noted that some authors indicate that the presence of pedestrians on a structure has a significant effect the damping ratio. Ellis and Ji [30] reported that this effect is dependent on whether the pedestrians are stationary or non-stationary. They report that standing or sitting people affect the damping of a structure but that people walking do not, and so should be represented as a load only. On the other hand, Zivanovic et al [31, 32] and Brownjohn et al [22] report that walking pedestrians can also increase the damping ratio of a bridge in the vertical direction. Zivanovic et al [31] in laboratory tests found an increase in damping for both standing and walking pedestrians (crowd density = 0.46 p/m^2), though the increase found for walking pedestrians was significantly lower than that for standing pedestrians. Zivanovic et al [32] and Brownjohn et al [22] also found an increase in damping due to walking pedestrians on as-built bridges; the Podgorica Bridge in Montenegro and a long span footbridge at Singapore Changi airport, respectively. However, further tests by Zivanovic et al [32] on the Reykjavik City footbridge in Iceland did not show an increase in damping.

4.3 Finite element model

The work presented here is based on a moving force model, similar to that used in the design standard BS 5400 [24]. It is acknowledged that this may be conservative as it does not consider the possible interaction between the pedestrian and the moving surface as the moving force is independent of the bridge movement [23].

A finite element model is used to establish the vibration response resulting from the passage of pedestrians across the bridge. The bridge is modelled with 10 Euler-Bernoulli beam elements, with lumped mass assumed. A sensitivity analysis was carried out and showed that 10 element was sufficiently accurate for comparison of the bridge vibrations. Transient solutions are obtained using the Newmark-β integration method. A one-dimensional model is used, and so torsional and lateral effects are ignored.

The vibration response of interest is taken as the mid-span acceleration and is assessed using a 5-second root-mean-square (RMS) moving average from the acceleration history of each simulation. To establish a characteristic response, 1000 simulations are carried out using randomly generated pedestrian parameters. The characteristic response is then defined as the response with a 5% probability of exceedance [8, 12, 22].

5 SIMULATIONS AND RESULTS

5.1 Cluster model results

In this model, no synchronization is considered between the pedestrians. Instead, those pedestrians deemed to be walking in a cluster were given the same velocity and thus they stayed together while crossing the bridge. This velocity is randomly chosen for each cluster from the statistical distribution given in Section 4. The pacing frequency for each pedestrian is also chosen from the statistical distribution and thus the step length is determined as velocity divided by the pacing frequency.

Figure 3 shows pedestrian location against time plot for ten pedestrians crossing the 50 m footbridge, following a single simulation. The time at which each pedestrian enters and leaves the bridge during the simulation is shown. Only 10 pedestrians are simulated in this instance to allow clarity in this figure. It can be seen that some of the pedestrians remain walking on their own (solid line) while others are walking in clusters (dotted lines). It is evident that the single pedestrians have different velocities as the time taken to cross the bridge varies; on the other hand, those deemed to be in a cluster have the same velocity and so remain together while crossing.

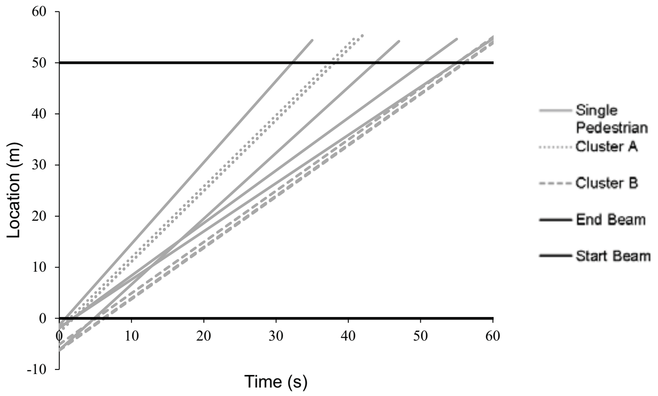

Figure 3. Analysis of pedestrian's (single and clustered) velocity whilst on the bridge

For all simulations, the bridge was subjected to a crowd of pedestrians with an average density of 0.5 p/m2 (persons per square metre). This is a typical crowd loading condition for unrestricted walking [11]. To investigate the effect of the size of a cluster on the bridge vibrations, simulations were carried out with a constant number of pedestrians in each cluster from one pedestrian (lone pedestrian crowd model [4]) up to five pedestrian in each cluster. No synchronization is forced between the pedestrian but each cluster has its own velocity. The results of this are shown in Figure 4. It can be seen that there is a gradual increase in the response despite a constant mean crowd density of 0.5 p/m^2.

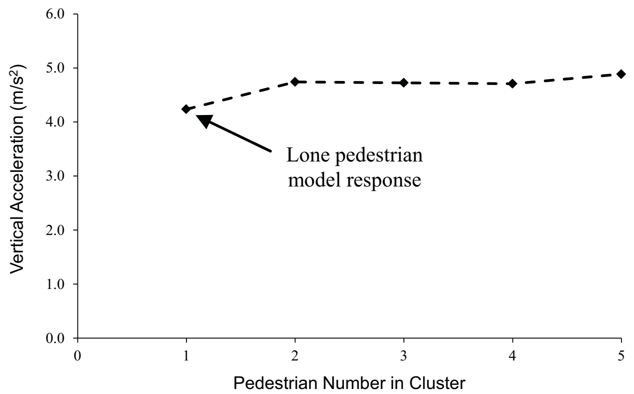

Figure 4. Increase in acceleration with the increase in the number of pedestrians in the clusters

To investigate a distribution of the probability of clusters being present in the crowd, different mean cluster sizes are considered within the range from 0.5 to 1.5, this resulted in simulations ranging from 60% clusters (λ = 0.5) to 23% clusters (λ = 1.5). Figure 5 shows that as the probability of a cluster appearing in the crowd increases, the acceleration response increases gradually. The result of the lone pedestrian crowd model is also shown, where the probability of a cluster is zero.

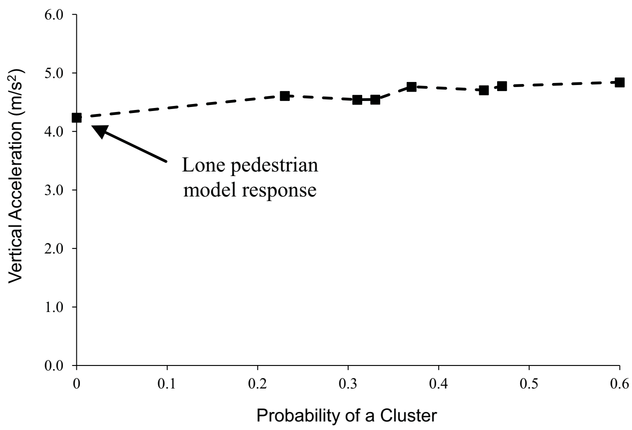

Figure 5. Increase in acceleration with the increase in cluster probability

5.2 *Comparison with design codes and guidelines*

The approach investigated here is compared to the predictions of some design guidelines [6, 8-10] and a lone pedestrian crowd model [4]. To allow direct comparison with published results, the bridge considered by Pavic [11] is analysed. The bridge is 38.85 m long, 2.5 m wide, has a mass of 1456 kg/m and has a natural frequency of 2.16 Hz. In the model presented here, similar to the SETRA Guideline [8] and the UK national Annex to Eurocode 1 [9], the mass of the crowd is taken to act as a uniformly distributed load on the bridge. This has the effect of reducing the unloaded natural frequency, f_n, to a loaded natural frequency, $f_n' = 2.10$ Hz :

$$f_n' = \frac{\pi}{2l^2}\sqrt{\frac{EI}{M + M_P}} \tag{6}$$

where l is the bridge length, EI is the flexural stiffness, M is the bridge mass per metre length, and M_P is the mass of the crowd per metre length.

The predicted characteristic response from the cluster model is shown compared to several design codes in Figure 6. It can be seen that the prediction is almost identical to that of the UK National Annex to Eurocode 1 [9]. It should be noted from this figure, as identified by Pavic [11], there is a large difference between the predictions of the design codes considered [6, 8-10]. The prediction by Eurocode 5 [6] is four times larger than the predictions of the UK National Annex to Eurocode 1 [9] for this particular crowd loading condition. UK National Annex to Eurocode 1 [9] is reported by Pavic [11] to give the most realistic response when compared to as built testing of bridges.

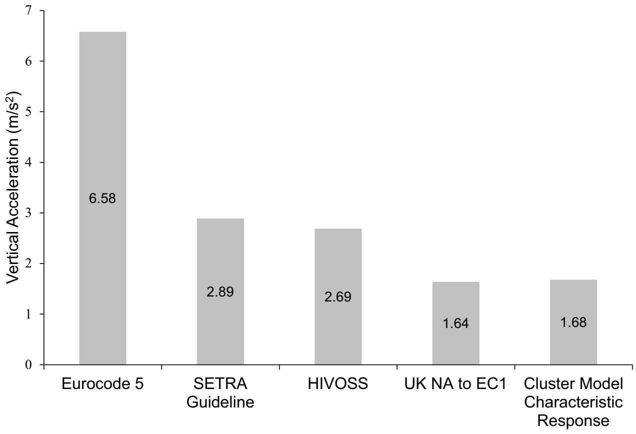

Figure 6. Comparison of the Cluster model characteristic response with those from current design codes and guidelines for the bridge used by Pavic [11].

Figure 7 shows the comparison of the prediction of the cluster model presented here to those of the lone crowd model [4] which allows for varying levels of synchronization. The lone pedestrian crowd model [4] is developed for pedestrians walking individually but allows for varying levels of synchronization within the crowd. Synchronization is enforced by assigning the pedestrians deemed to be synchronized the same pacing frequency and phase angle [24]. The pacing frequency assigned is randomly selected according to its distribution (mean 1.96 Hz and standard deviation of 0.209 Hz) while the phase angle of the pedestrians vertical harmonic force is taken to be uniformly random in the interval 0 to 2π. It is shown (Figure 7) that this lone pedestrian crowd model matches well with the predictions of the cluster model and UK NA to Eurocode 1 [9] at a synchronization of approximately 13%. This is similar to the findings of Grundmann et al [33] who reported that a synchronization level of 13.5% was typical in crowd loading.

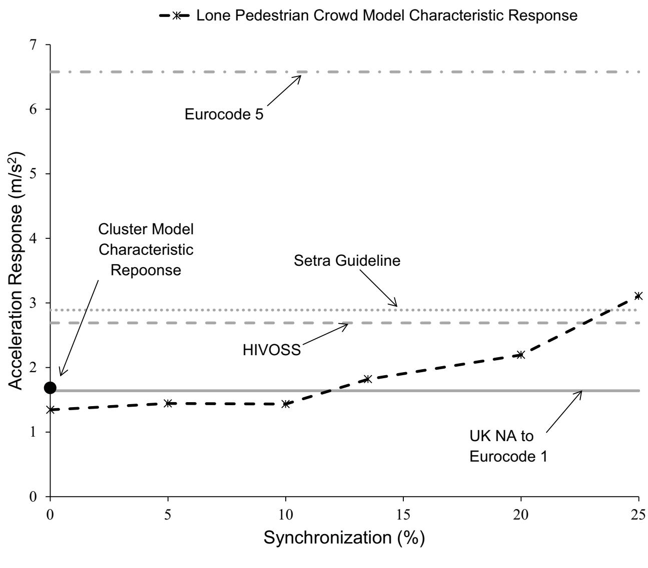

Figure 7. Comparison of the cluster model characteristic response with current design codes and guidelines and simulated response with varying levels of synchronization using the lone crowd model for the bridge used by Pavic [11].

6 SUMMARY AND CONCLUSIONS

In this work a model is presented for the prediction of footbridge vibrations resulting from clustered crowd loading. The clustered crowd used in this model allows for the possibility of clusters or social groups of pedestrians (two or more) being present within the crowd, as well as lone pedestrians. A Poisson distribution of cluster size taken from the literature is used. The model is compared to design codes and a published lone pedestrian crowd model.

It is shown that the clustered crowd model gives a good match with the predictions of the UK National Annex to Eurocode 1 [9]. The results also compare well with the predictions of a published lone pedestrian model in which synchronization is forced to cater for pedestrians walking instep.

The conclusion from this work is that it is possible to predict the response of a footbridge resulting from crowd loading by modelling the crowd as containing clusters of pedestrian, within which the pedestrians are walking at the same velocity. This is more typical of a real life situation.

ACKNOWLEDGMENTS

The authors would like to acknowledge the Dublin Institute of Technology ABBEST Scholarship Programme for supporting this research.

REFERENCES

[1] Dallard, P., Fitzpatrick, T., Flint, A., Low, A., Ridsdill Smith, R.M., Willford, M. and Roche, M. (2001), 'London Millennium Footbridge: pedestrian-induced lateral vibration', ASCE Journal of Bridge Engineering, 6(6), 412-417.

[2] Danbon F. and Grillaud, G. (2005), 'Dynamic behaviour of a steel footbridge. Characterization and modelling of the dynamic loading induced by a moving crowd on the Solferino Footbridge in Paris', Proceedings Footbridge 2005.

[3] Fujino, Y., Pacheco, B.M., Nakamura, S. and Warnitchai, P. (1993), 'Synchronization of human walking observed during lateral vibration of a congested pedestrian bridge', Earthquake Engineering and Structural Dynamics, 22(9), 741-758.

[4] Caprani, C.C., Keogh, J., Archbold, P. and Fanning, P. (2012), 'Enhancement Factors for the Vertical Response of Footbridges Subjected to Stochastic Crowd Loading', Computers and Structures, In Print.

[5] Ebrahimpour, A., Hamam, A., Sack, R.L. and Patten, W.N. (1996), 'Measuring and Modeling Dynamic Loads Imposed by Moving Crowds', ASCE Journal of Structural Engineering, 122(12), 1468 – 1474.

[6] EN1995-2 (2004) 'Eurocode 5: Design of timber structures – Part 2: Bridges', EN 1995-2:2004, European Committee of Standardization, Brussels.

[7] ISO (2007) 'Bases for Design of Structures – Serviceability of Buildings and Walkways against Vibrations', ISO 10137:2007, International Organization for Standardization.

[8] SETRA (2006), 'Footbridges, Assessment of Vibration Behaviour of Footbridges Under Pedestrian Loading, Technical Guide', Service d'Etudes Technique des Routes et Autoroutes, Paris.

[9] BSI (2008) 'UK National Annex to Eurocode 1: Actions on Structures – Part 2: Traffic Loads on Bridges', NA to BS EN 1991-2-2003, British Standards Institution, London, UK.

[10] HIVOSS (2008) 'Design of Footbridges Guideline: Human Induced Vibrations of Steel Structures', RFS2-CT-2007-00033. Available at: http://www.stb.rwth-aachen.de/projekte/2007/HIVOSS/docs/Footbridge_Guidelines_EN03.pdf

[11] Pavic, A. (2011), 'Vertical Crowd Dynamic Action on Footbridges: Review of Design Guidelines and Their Application', Proceedings of the 4th International Conference Footbridge 2011, Wroclaw, 6-8 July.

[12] Keogh, J., Archbold, P., Caprani, C. and Fanning, P. (2010), 'Estimating the characteristic vertical response of a flexible footbridge due to crowd loading', Proceedings of the BCRI conference, Cork, Ireland.

[13] Pedersen, L. and Frier, C. (2010) 'Sensitivity of footbridge vibrations to stochastic walking parameters' Journal of Sound and Vibrations, 329, 2683 – 2701.

[14] Ingolfsson, E., Georgakis, C., Jonsson, J. and Ricciardelli, F. (2007), 'Vertical footbridge vibrations: Towards an improved and codifiable response evaluation', Proceedings of 3rd International Conference on Structural Engineering, Mechanics and Computation, Cape Town, South Africa.

[15] Moussaid, M., Perozo, N., Garnier, S., Helbing, D. and Theraulaz, G. (2010), 'The walking behaviour of Pedestrian social groups and its impact on crowd dynamics', *Plos ONE*, 5(4), 1-7.

[16] Portier, K., Tolson, J.K., and Roberts, S.M. (2007), 'Body weight distributions for risk assessment', Risk Analysis, 27(1), 11-26.

[17] Barela, A.M.F. and Duarte, M. (2008), 'Biomechanical characteristics of elderly individuals Walking on land and on water', Journal of Electromyography and Kinesiology, 18(3), 446-454.

[18] Matsumoto, Y., Nishioka, T., Shiojiri, H. and Matsuzaki, K. (1978), 'Dynamic design of footbridges', IABSE Proceedings, 2, Paper P-17/78, Zurich.

[19] Grundmann, H and Schneider, M. (1990), 'Stochastic Representation of Footbridge Vibrations Taking into Account Feedback Effects', in W.B. Krätzig et al. (Eds.), Proceeding of the European Conference on Structural Dynamics, Eurodyn '90, Bochum, Balkema, Rotterdam.

[20] Pachi, A. and Ji, T. (2005), 'Frequency and velocity of people walking', The Structural Engineer, 83(3), 36–40.

[21] Kramer, H. and Kebe, H.W. (1980), 'Man-Induced Structural Vibrations', Der Bauingenieur, 54(5), 195 – 199.

[22] Brownjohn, J. M. W., Fok, P., Roche, M. and Omenzetter, P. (2004), 'Long span steel pedestrian bridge at Singapore Changi airport – Part 2: Crowd loading tests and vibration mitigation measures', The Structural Engineer, 82 (16), 28-34.

[23] Zivanovic, S., Pavic, A. and Reynolds, P. (2005a), 'Vibration serviceability of footbridges under human-induced excitation: A literature review', Journal of Sound and Vibration, 279(1-2), 1-74.

[24] Bachmann, H. and Ammann, W. (1987), 'Vibrations in Structures-Induced By Man and Machines', IABSE, Structural Engineering Document 3, Zurich.

[25] Fanning, P., Archbold, P. and Pavic, A. (2005), 'A Novel interactive Pedestrian load model for Flexible Footbridges', Proceeding of the 2005 Society for Experimental Mechanics Annual Conference on Experimental and Applied Mechanics, Portland, Oregon, June 7-9.

[26] Chopra, A. (2007), Dynamics of Structures – Theory and Applications to Earthquake Engineering', 3rd Edn. Pearson, Prentice Hall, New Jersey.

[27] Heinemeyer, C., Butz, C., Keil, A., Schlaich, M., Goldack, A., Trometer, S., Lukic, M., Chabrolin, B., Lemaire A., Martin, P. O., Cunha, A. and Caetano, E. (2009), 'Design of Lightweight Footbridges for Human Induced Vibrations', JRC Scientific and Technical Reports, Eds: Sedlacek, G., Heinemeyer, C., Butz, C. and Geradin, M. European Commission

[28] Caetano, E., Cunha, A., Magalhaes, F. and Moutinho, C. (2010), 'Studies for Controlling Human-Induced Vibration of the Pedro e Ines Footbridge, Portugal. Part 1: Assessment of Dynamic Behaviour', Engineering Structures, 32, 1069-1081.

[29] Fanning, P.J., Healy, P. and Pavic, A. (2010), 'Pedestrian Bridge Vibration Serviceability: A case study in Testing and Simulation', Advances in Structural Engineering, 13(5), 861-873.

[30] Ellis, B. R., and Ji, T. (1997) 'Human-Structure Interaction in Vertical Vibrations' Proceedings of the Institution of Civil Engineers, Structures and Buildings, 122, 1-9.

[31] Zivanovic, S., Diaz, I. M. and Pavic, A. (2009), 'Influence of walking and standing crowds on structural dynamic performance', Proceedings of IMAC XXVII, Orlando, Florida, USA, February 9-12.

[32] Zivanovic, S., Pavic, A. and Ingolfsson, E. T. (2010), 'Modelling spatially unrestricted pedestrian traffic on footbridges', ASCE Journal of Structural Engineering, 136(10), 1296-1308.

[33] Grundmann, H and Schneider, M. (1990), 'Stochastic Representation of Footbridge Vibrations Taking into Account Feedback Effects', in W.B. Krätzig et al. (Eds.), Proceeding of the European Conference on Structural Dynamics, Eurodyn '90, Bochum, Balkema, Rotterdam.

The response of a footbridge to pedestrians carrying additional mass

D. O'Sullivan, C.C. Caprani, & J. Keogh
Department of Civil Engineering & Structural Engineering, Dublin Institute of Technology, Ireland
email: darragh.osullivan@ocsc.co.uk, colin.caprani@dit.ie, joe.keogh1@dit.ie

ABSTRACT: Footbridges with low natural frequency are susceptible to excessive vibration serviceability problems if the pedestrian pacing frequency matches the bridge natural frequency. Much research has been done into describing the response of a footbridge to single pedestrian loading. However, many pedestrians carry additional mass such as shopping bags and backpacks, and this has generally not been accounted for in previous research. This work examines this problem using an experimental bridge excited with many single pedestrian events, both with and without additional mass. The vertical acceleration response is measured and compared to moving force, moving mass, and moving spring-mass-damper models. The influence of the additional mass on the results is assessed. It is shown that current theoretical models do not provide an accurate description of the walking forces applied by a pedestrian traversing an excessively vibrating structure. When a pedestrian carries additional mass the response of the footbridge increases however the theoretical models overestimate this increase.

KEY WORDS: Pedestrian; Bridge; Vibration; Mass; Modal; Finite element; Experiment.

1 INTRODUCTION

1.1 Background

With improved design techniques, modern footbridges have become increasingly slender and often have a low vertical natural frequency. Pedestrian pacing occurs at a frequency of about 2 Hz and if this is similar to the footbridge natural frequency, vibration problems can result. The mass of the pedestrian is also an important component of the excitation imparted to the bridge. Further, many pedestrians also carry additional mass, especially in a city environment (such as commuters or shoppers, for example).

In the assessment of footbridge vibrations, the mass used in pedestrian excitation models is commonly understood to be the body mass of the pedestrian. Additional carried mass has not been generally included in the literature [1]. It has been noted [2] that a pedestrian carrying a loaded backpack will adjust their gait to reduce the energy cost of walking and make it more comfortable. The response of a lively footbridge to a pedestrian carrying mass is examined in this paper.

1.2 Approach of this work

This work examines the influence of additional mass on footbridge excitation using physical testing and numerical models. A timber footbridge with low natural frequency is constructed and experimental modal analysis is carried out to determine its dynamic properties. A range of pedestrian loading scenarios are measured. The midspan acceleration response under different pedestrians, both with and without mass, is measured.

The numerical models typically employed to estimate pedestrian excitation are a moving force, moving mass, and a moving spring mass damper model. These models are calibrated to the test conditions and used to predict the measured responses.

1.3 Bridge structure test specimen

A timber footbridge deck is used for the physical testing, as shown in Figure 1. It is designed to have a vertical fundamental natural frequency within a range which is sensitive to pedestrian-induced vibrations. The bridge is simply-supported, 8 m long, and 0.7 m wide. It has a mass of 14.14 kg/m and a flexural stiffness of 422 kNm^2. Transverse bridging pieces are used at 1 m centres to ensure load sharing across the cross-section. The plywood skin is glued to the joists and bridge pieces to ensure full composite action.

(a) experimental set up;

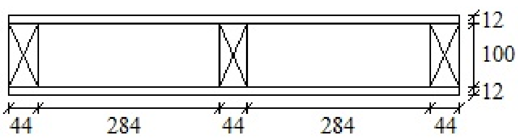

(b) cross-section through bridge deck;

Figure 1. Laboratory testing arrangement.

2 EXPERIMENTAL MODAL ANALYSIS

2.1 Overview of testing

An experimental modal analysis (EMA) is performed on the bridge structure to determine its natural frequencies and their associated damping ratios and mode shapes. The EMA involves simultaneously measuring an input force, $f(t)$, and the resulting output response, $x(t)$. The input force is applied using an instrumented impact hammer. This excitation method is chosen in order to overcome the effects of mass loading which is a critical consideration in the testing of lightweight structures [3].

This paper examines the mid-span response of the model footbridge. As a result, the odd-numbered modes of vibration are of most interest. However, an accelerometer is mounted at quarter span to identify the second mode of vibration also. The impact application and the response measurement are located centrally in the cross-section so that torsional modes are not excited insofar as is possible.

The bridge structure was impacted at three locations along the span; the mid-span and the two quarter-spans (Figure 2) and the resulting acceleration response measured. This results in a time-domain description of the behaviour of the structure. However the frequency-domain behaviour provides a more convenient description from which modal parameters may be extracted. Data is transformed between the time and frequency domain using the Fast Fourier Transform (FFT).

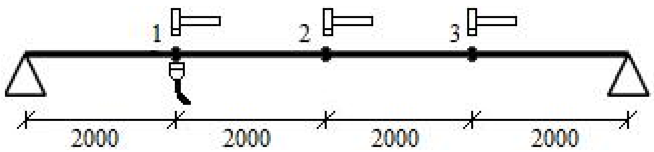

Figure 2. Location of accelerometers and impacts.

A sample period of 25 seconds is measured to allow the vibrations to decay. However, as the structure is very lightly damped, the transient response does not always decay to zero within the sampling period. To minimise the effects of leakage in the transformed data a window (or weighting function) is applied to the measured data. For impact excitation a force window is applied to the input force and an exponential window to the output response [4], [5].

2.2 Estimation of Frequency Response Function

The transducers used to measure the input and output inevitably contain unwanted noise and so averaging is required to minimize its effect on the measurements. The power spectrum of the recorded signal is used for averaging. The Frequency Response Functions (FRFs), $H(\omega)$, for impact testing have been estimated in terms of the cross- and auto-power spectra by Dossing [4] and Ramsey [6] using:

$$H(\omega) = \frac{G_{FX}(\omega)}{G_{XX}(\omega)} \tag{1}$$

where $G_{FX}(\omega)$ is the cross spectral density between the input $f(t)$ and the output $x(t)$, and is given by:

$$G_{FX}(\omega) = F(\omega)X^*(\omega) \tag{2}$$

$G_{XX}(\omega)$ is the auto power spectral density of the output $x(t)$:

$$G_{XX}(\omega) = X(\omega)X^*(\omega) \tag{3}$$

In the above, $F(\omega)$ is the Fourier spectrum of the input $f(t)$, $X(\omega)$ is the Fourier spectrum of the output, and a superscript asterisk denotes the complex conjugate. Equation (1) then yields a complex-valued function of frequency from which the magnitude and phase of the response is calculated [5].

The coherence, $\gamma^2(\omega)$, is a measure of the noise in the system and is defined as [4]:

$$\gamma^2(\omega) = \frac{|G_{FX}(\omega)|^2}{G_{FF}(\omega).G_{XX}(\omega)} \tag{4}$$

where $0 \le \gamma^2(\omega) \le 1$ and $G_{FF}(\omega)$ is the auto power spectral density of the input $f(t)$ and is given by:

$$G_{FF}(\omega) = F(\omega)F^*(\omega) \tag{5}$$

Ramsey [6] described the coherence in a system as a measure of the '*causality*', that is the proportion of the measured response that is caused totally by the measured input. A coherence of 1 implies that there is no noise in the measurements (and so they are 'perfect') whereas a coherence of 0 implies the measurement is pure noise. Of course, in practice perfect measurements are not possible and so coherence will typically be under unity. According to Dossing [4] the coherence will be less than 1 if the location and direction in which the impact is applied is '*scattered*', meaning that if the impact is not in the same location and direction each time some variations in results may be expected. The coherence is also expected to be less than 1 where there is an anti-resonance (i.e. where the signal-to-noise is ratio is poor) or the impact point is close to a node point for a particular mode of vibration.

2.3 FRF of unloaded bridge

Using the procedure described, the estimates for the FRF and coherence for each excitation point are determined. The averaged results are shown in Figure 3. Resonant points can be identified by a peak in the FRF magnitude or a value of +/-90° for the phase. The coherence for each point is low at the lower frequencies for each of the excitation points since the accelerometers have difficulty in recording low frequency signals. The response of the bridge to low frequency excitation is very small. Therefore the signal recorded by the accelerometers at low frequencies is small in comparison to the noise and so a low coherence value is expected. The magnitude of the response at location 2 (mid-span) (shown in Figure 3(d)) is small in comparison to the other three peaks. This is because point 2 is a node point for the second mode. Each of the excitation points is a node point for the fourth mode and so its response is not distinguishable.

The recorded resonant peaks are widely spaced and so locally the FRF is dominated by a single mode. Therefore each peak in the FRF plot can be approximately analysed as the frequency response of a single-degree-of-freedom system. Hence, the modal parameters for the structure are extracted from the FRF magnitude plot of Figure 3(a) and shown in Table 1. Further, the mode shapes can be found from the FRF magnitude and phase plots and are shown in Figure 4.

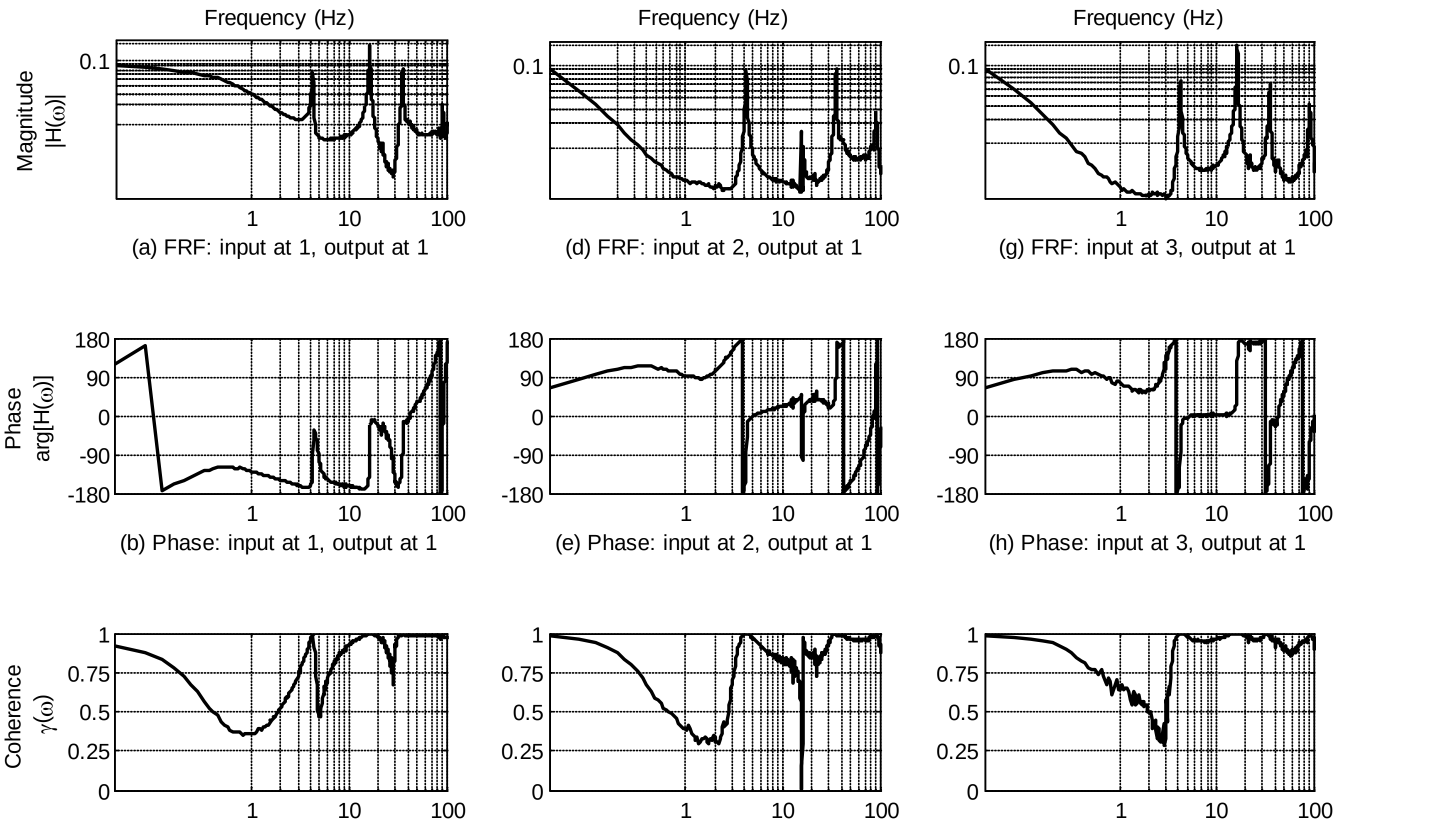

(a) FRF: input at 1, output at 1 (d) FRF: input at 2, output at 1 (g) FRF: input at 3, output at 1

(b) Phase: input at 1, output at 1 (e) Phase: input at 2, output at 1 (h) Phase: input at 3, output at 1

(c) Coherence: input at 1, output at 1 (f) Coherence: input at 2, output at 1 (i) Coherence: input at 3, output at 1

Figure 3. Results of experimental modal analysis (refer to Figure 2 for location numbering).

Table 1. Dynamic properties of the test structure.

Mode	Natural Frequency (Hz)	Magnitude $\|H(\omega)\|$	Phase $\angle[H(\omega)]$	Damping Ratio
1	4.24	0.0647	-90°	0.0133
2	16.32	0.17260	-90°	0.0092
3	35.64	0.07208	-90°	0.0105
4	n/a	n/a	n/a	n/a
5	91.6	0.01971	-90°	0.0128

The number of mode shapes that can be measured is a function of the number of excitation points on the bridge when a roving output test is used in EMA. In this test set up three impact points were specified and so three mode shapes are determined from the FRF plots. The magnitude of the mode shape is determined from the magnitude of the FRF and the direction from the phase.

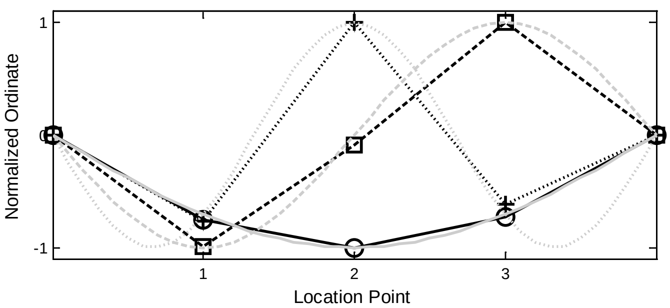

Figure 4. Normalised mode shapes:
Measured – Mode 1 (–o–); Mode 2 (--□--); Mode 3(···+···);
Theoretical – Mode 1 (——); Mode 2 (- - -); Mode 3(·······).

2.4 *Experimental modal analysis with added mass*

Due to the low mass of the bridge, the ratio of pedestrian mass to the mass of the test structure is quite large (e.g. 0.71 for an 80 kg pedestrian). Therefore the presence of the pedestrian on the bridge will affect the modal parameters and so further investigations are carried out on these variations. In particular, the variation of the modal parameters as the pedestrian traverses the bridge is of interest. However, this form of EMA is beyond the scope of the present research.

The modal parameters of the structure are determined for two mass scenarios: (a) an 80 kg pedestrian; and (b) an 80 kg inert mass. Both masses are located at mid-span. The driving-point FRF for point 1 (quarter-span) with mass at mid-span is found for both scenarios and the results shown in Figure 5.

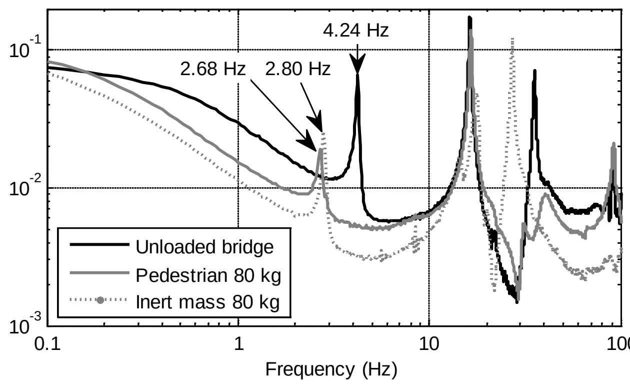

Figure 5. Frequency response functions at point 2 for pedestrian and inert 80 kg masses at mid-span.

By comparison with the unloaded bridge, it can be seen from Figure 5 that the natural frequencies are reduced by the presence of the additional mass as might be expected. Interestingly, there is an additional mode (possibly torsional) with natural frequency at 14.56 Hz for the inert mass.

Using the single-mode approximation described previously, the damping is assessed for each scenario and the results given in Table 2 (along with those for the unloaded bridge from Table 1 for reference). A slight increase in damping is noted for the inert mass. However, under the pedestrian loading, a significant increase in damping of the first mode is evident. This agrees with the findings of Ellis and Ji [7] who suggested the use of a spring-mass-damper model in theoretical analyses to represent human-structure interaction.

Table 2. Damping ratios for bridge loaded with pedestrian and inert 80 kg masses at mid-span.

Mode	Unloaded bridge	Pedestrian mass 80 kg	Inert mass 80 kg
1	0.0133	0.0320	0.0162
2	0.0092	0.0112	0.0301
3	0.0105	*	0.0097
4	n/a	n/a	n/a
5	0.0128	0.0194	**

* Very heavily damped

** No frequency response function peak

3 THEORETICAL MODELLING

3.1 Pedestrian vertical load model

A typical vertical pedestrian force is shown in Figure 6. It is represented by the first harmonic of its Fourier series [8], [9], shown in Figure 6, and given as follows:

$$P(t) = m_P g\left[1 + r\sin\left(2\pi f_p t\right)\right] \tag{6}$$

In which, m_P is the pedestrian mass, g is the acceleration due to gravity, f_p is the pacing frequency, and r is the dimensionless dynamic force component from Fanning et al [10], given by:

$$r = 0.25 f_p - 0.1 \tag{7}$$

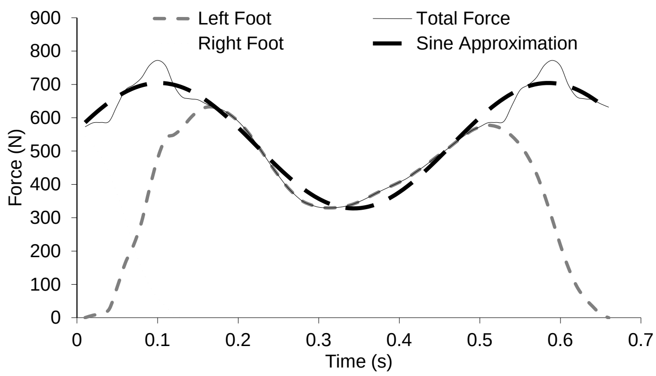

Figure 6. Typical vertical ground reaction force and approximated model force.

3.2 Pedestrian-bridge systems models

The pedestrian-bridge system models used are shown in Figure 7. They increase in complexity from the moving force model to the rarely-used spring-mass-damper (SMD) model. The moving force model has been commonly used in analysing the pedestrian loading on footbridges [1]. The moving mass model has been used by a few authors, whilst the SMD model is rarely used [11].

The moving force model (Figure 7(a)) does not account for any shift in modal properties due to the presence of the pedestrian, as are internal effects due to the pedestrian mass. These deficiencies are overcome with the moving mass model (Figure 7 (b)) which potentially accounts for both changes in modal properties and inertia of the pedestrian mass. However, the moving mass model assumes equal deflection of the centre of mass of the pedestrian and the bridge surface. This is evidently not correct, as is evident from human location studies [12]. The SMD model of Figure 7(c) accounts for the difference in deflection between the bridge surface and the pedestrian centre of mass by linking the two through a Kelvin-Voight material model representing the human body.

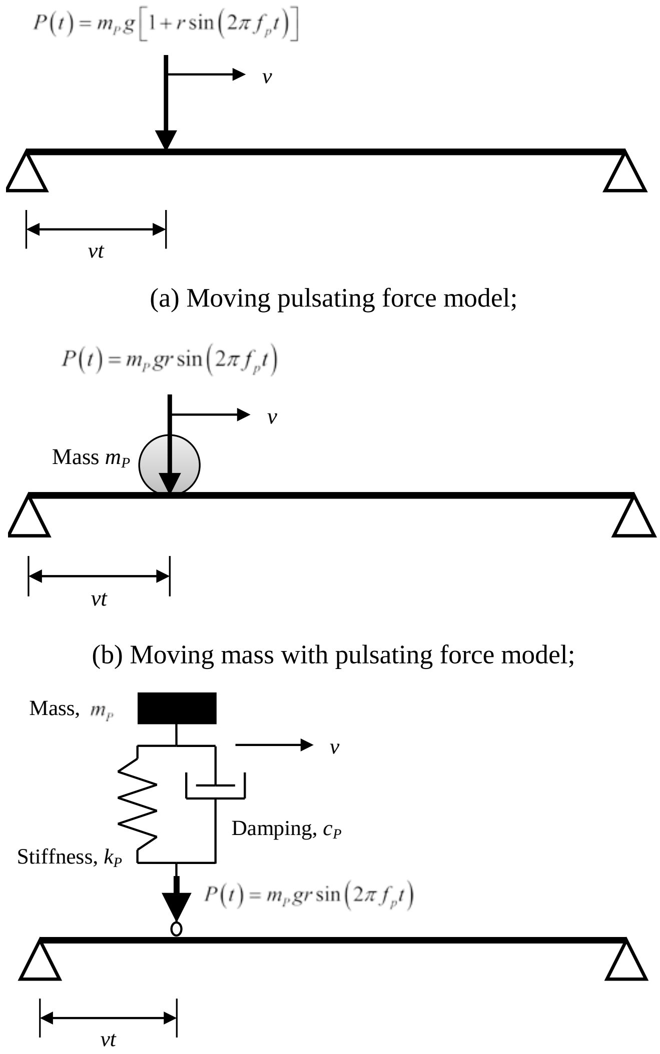

(c) Moving spring-mass-damper with pulsating force model;

Figure 7. Pedestrian-bridge system models.

3.3 Modal superposition models

Modal superposition can be used to solve for the bridge response for each of the three models of Figure 7. However the modal superposition method cannot account for any changes in modal properties due to the presence of the pedestrian on the bridge. This may be important when the ratio of pedestrian to bridge mass is significant.

The solution for each of the N modes is found through summation of the equivalent generalized coordinates, q, single-degree-of-freedom model solutions. In this work 10 modes have been used to establish the response. For the moving force (MF) model these are given by [13]:

$$\ddot{q}_j + 2\xi_j\omega_j\dot{q}_j + \omega_j^2 q_j = \frac{m_P g}{M_j}\left[1 + r\sin\left(2\pi f_p t\right)\right]\phi_j\left(vt\right) \quad (8)$$

In which M_j, ξ_j, and ω_j are the modal mass, damping ratio; and circular natural frequency for mode j respectively. The pedestrian position at time t is vt assuming constant velocity v and the mode shape is described by $\phi_j\left(x\right)$. The equation of motion for mode j under the moving mass (MM) model is:

$$\ddot{q}_j + \left\{\frac{m_P}{M_j}\sum_{j=1}^{N}\ddot{q}_j\phi_j^2\left(vt\right)\right\} + 2\xi_j\omega_j\dot{q}_j + \omega_j^2 q_j = \frac{m_P g}{M_j}\left[1 + r\sin\left(2\pi f_p t\right)\right]\phi_j\left(vt\right) \quad (9)$$

Finally, the equation of motion for the mode j of the bridge under the SMD model is [13]:

$$\ddot{q}_j + 2\xi_j\omega_j\dot{q}_j + \omega_j^2 q_j + \frac{m_p}{M_j}\ddot{y}\phi_j\left(vt\right) = \frac{m_P g}{M_j}\left[1 + r\sin\left(2\pi f_p t\right)\right]\phi_j\left(vt\right) \quad (10)$$

where y is the coordinate describing the motion of the centre of pedestrian mass which has its own equation of motion:

$$m_P\ddot{y} + c_P\dot{y} + k_P y - c_P\dot{q}_j\phi_j\left(vt\right) - k_P q_j\phi_j\left(vt\right) = 0 \qquad j = 1,....,N \quad (11)$$

For the simply supported beam used in this work the modal mass is $mL/2$ where m is the mass per metre of the beam of length L. The mode shape is given by $\phi_j\left(x\right) = \sin j\pi x/L$.

3.4 *Finite element models*

Finite element models are developed for each of the three pedestrian loading models based on the work of Filho [14], Lin and Trethewey [15], and Majumder and Manohar [16]. For each of these models, the beam is discretized into 10 1-dimensional Euler-Bernoulli beam elements and solved using the Newmark β method assuming consistent mass and Rayleigh proportional damping.

The finite element models have the advantage that changes in modal properties are accounted for as the pedestrian traverses the bridge. However, the discretization of the bridge means that the solution is approximate. However, just as the modal superposition is truncated, it is not expected that much error will results from the use of 10 elements.

4 PEDESTRIAN-INDUCED VIBRATION RESULTS

4.1 *Sample result*

A typical measurement is shown in Figure 68 along with its calibrated finite element (FE) spring-mass damper model. The response of the bridge is described by a 1 second root-mean-square (RMS) mid-span vertical acceleration. The measured RMS accelerations differ most from the FE SMD model results as the pedestrian reaches mid-span and the response is at its greatest. The sharp peaks in the measured response are due to the heel strike phase of the pedestrian's walking force. This is highest when the pedestrian walks 'downhill', towards mid-span, since the heel has further to travel, prior to making contact with the bridge deck, than it does on a level walking surface. Thus, these heel strike peaks are highest before the pedestrian reaches mid-span and are smaller thereafter.

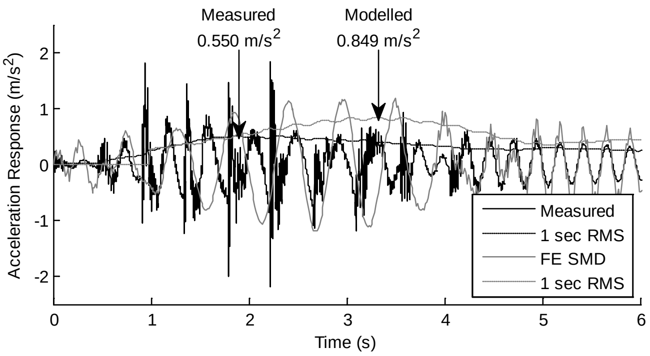

Figure 8. Acceleration response of the bridge to a 64 kg pedestrian with 1.8 Hz pacing frequency.

4.2 *Test descriptions*

A series of walking tests were conducted and the vertical acceleration response of the footbridge at mid-span was measured. Two male pedestrians traversed the footbridge at a controlled pacing frequency regulated using a metronome. The first pedestrian, Ped_1, with mass 80 kg traversed the bridge with pacing frequencies ranging from 1.8-2.2 Hz in increments of 0.1 Hz, while Ped_2 with mass 64 kg, traversed the bridge with pacing frequencies of 1.8 Hz and 2.0 Hz. A mass of 16 kg was added to Ped_2 to bring his total mass to 80 kg and the tests repeated.

The numerical models previously described are calibrated using the EMA results. The phase of the pedestrian walking force is estimated based on the free-vibration response (e.g. Figure 68). For the SMD models, the spring stiffness and damping is first estimated using population means (see [13]) but then calibrated to give the best-match results.

4.3 *Experimental and theoretical results*

The complete set of experimental and numerical model results is given in Table 3. The measured results are an average of 2 runs for Ped_1 and 3 runs for Ped_2.

The theoretical accelerations for the 64 kg pedestrian carrying an additional 16 kg are different to that of the 80 kg pedestrian because the test subjects each walked with a different velocity to maintain the required pacing frequency.

Table 3. Measured and numerical 1-second RMS mid-span vertical acceleration responses (m/s^2).

Pedestrian	f_p (Hz)	Measured	FE MF	FE MM	FE SMD	MA MF	MA MM	MA SMD
80 kg	1.8	0.492	0.813	1.209	0.837	0.811	0.815	0.823
	1.9	0.622	0.963	1.567	0.901	0.963	0.965	0.875
	2.0	0.695	1.151	2.192	0.953	1.150	1.153	0.937
	2.1	0.739	1.417	3.292	1.078	1.416	1.421	1.070
	2.2	0.733	1.694	5.300	1.269	1.688	1.702	1.237
64 kg	1.8	0.550	0.650	0.871	0.849	0.649	0.652	0.828
	2.0	0.587	0.917	1.399	1.000	0.918	0.919	0.987
64 + 16 kg	1.8	0.579	0.803	1.182	0.841	0.801	0.805	0.825
	2.0	0.634	1.147	2.142	0.956	1.148	1.149	0.936

From Table 3 it can be seen that each of the theoretical models overestimates the measured acceleration response of the footbridge. Interestingly the least fidelity model, the moving force model, yields the closest match to the measured responses. Further, the theoretical models are more accurate in predicting the response for Ped_2 than for Ped_1. The measured accelerations for Ped_2 carrying additional mass is much lower than the theoretical predictions.

The unknown stiffness and damping parameters of the SMD models are calibrated to give the best match to the measured data. Typically a low value of stiffness gives the best match. As a result, in most cases the SMD model is closest to the measured accelerations.

5 SUMMARY AND CONCLUSIONS

5.1 Summary

The effect of additional mass carried by pedestrians is assessed. Experimental modal analysis is used to determine the properties of the bridge unloaded, loaded with an 80 kg pedestrian, and loaded with an 80 kg inert mass. The masses are found to have a considerable effect on the dynamic properties of the structure. In particular, under the pedestrian, the first-mode damping is found to increase significantly. Acceleration responses are measured for a range of pedestrian loading scenarios, including the carrying of additional mass. It is found that the pedestrian carrying additional mass does not have the same response as a pedestrian of same total mass.

The measured results are compared to predictions from a range of numerical models and are found to be consistently lower than the theoretical predictions. The moving force model is found to give reasonable match to the measurements.

5.2 Conclusions

During the execution of the tests, both pedestrian test subjects remarked on the difficulty in maintaining a controlled pacing frequency on such a lively structure. The ‘unpredictability’ of the response forced them to alter their gait in order to maintain a controlled pacing frequency while traversing the bridge. The theoretical models do not account for such adaption of stride and this is certainly a source of error. However, the deflection of the test structure is unrealistic for a publicly accessible bridge. It is envisaged that a pedestrian would either slow down, or stop completely if vibrations of such an excessive response occurred thus reducing the vibration of the structure.

ACKNOWLEDGMENTS

The authors would like to thank David Thompson and Ronan Hogan of DIT Bolton St. Structures Laboratory and Tom O’ Sullivan for their assistance with this research.

REFERENCES

[1] Zivanovic, S., Pavic, A. and Reynolds, P. (2005a), ‘Vibration serviceability of footbridges under human-induced excitation: A literature review’, *Journal of Sound and Vibration*, 279(1-2), 1-74.

[2] Ren, L., Jones, R.K. and Howard, D. (2004), ‘Dynamic analysis of load carriage biomechanics during level walking’, *Journal of Biomechanics*, 38, 853-863.

[3] Avitabile, P. (2009), ‘Modal Space – In Our Own Little World’, Collected articles, available from: http://macl.caeds.eng.uml.edu/umlspace/mspace.html

[4] Dossing, O. (1988), ‘Structural testing- Part I, Mechanical Mobility Measurements’, Bruel and Kjaer, Naerum, Denmark

[5] Inman, D.J. (2001), *Engineering Vibration*, 2nd Edn., Prentice-Hall

[6] Ramsey, K. A. (1975), ‘Effective Measurements for Structural Dynamics Testing, Part I’, Sound and Vibration, Vo.. 9, No. 11, 24-35.

[7] Ellis, B. and Ji, T. (1997), ‘Human-structure interaction in vertical vibrations’, *Structures & Buildings*, ICE, Vol. 122, 1-9.

[8] Rainer, J., Pernica, G. and Allen, D. (1988), ‘Dynamic loading and response of footbridges’, *Canadian Journal of Civil Engineering*, 15(1), 66-71.

[9] Bachmann, H. and Ammann, W. (1987), *Vibrations in Structures-Induced By Man and Machines*, IABSE, Structural Engineering Document 3, Zurich.

[10] Fanning, P., Archbold, P., Pavic, A and Reynolds, P. (2003), ‘Transient response simulation of a composite footbridge to crossing pedestrians’, *Recent Developments in Bridge Engineering*, K. Mahmoud, Ed., Swets & Zeitlinger Publishers, Lisse, The Netherlands. ISBN 90 5809 606 8.

[11] Archbold, P. (2008), ‘Evaluation of novel interactive load models of crowd loading on footbridges’, *Proceedings of 4th Symposium on Bridge and Infrastructure Research in Ireland*, National University of Ireland, Galway, 35-44.

[12] Racic, V., Pavic, A., Brownjohn, J.M.W. (2009), ‘Experimental identification and analytical modelling of human walking forces: Literature review’, *Journal of Sound and Vibration*, 326(1-2), 1-49.

[13] Caprani, C.C., Keogh, J, Archbold, P. & Fanning, P. (2011) ‘Characteristic vertical response of a footbridge due to crowd loading’, *Proceedings of the 8th International Conference on Structural Dynamics*, Eurodyn 2011, Leuven, Belgium, July 4th – 6th, 2011.

[14] Filho, F.V. (1978), ‘Finite element analysis of structures under moving loads’, *Shock and Vibration Digest*, 10(8), 27-35.

[15] Lin, Y.H. and Trethewey, M.W. (1990), ‘Finite element analysis of elastic beams subjected to moving dynamic loads’, *Journal of Sound and Vibration*, 136(2), 323-342.

[16] Majumder, L. and Manohar, C.S. (2003), ‘A time-domain approach for damage detection in beam structures using vibration data with a moving oscillator as an excitation source’, *Journal of Sound and Vibration*, 268, 699–716.

The influence of spatial parameters on pedestrian lateral loading

B. Mullarney[1] & P. Archbold[1]
[1] STRAIT, Structures & Materials Research Group, Athlone Institute of Technology
Dublin Road, Athlone, Co. Westmeath
email: bmullarney@research.ait.ie, parchbold@ait.ie

ABSTRACT: Dynamic loading from pedestrians walking on flexible structures such as footbridges is the subject of much research at present. The interest is stimulated by several notable instances of uncomfortable perceptible vibrations on prominent footbridges in the recent past. Some of this research has revealed that the phenomenon is not entirely due to modern construction techniques with examples of pedestrian-induced vibrations from as early as the 1600s being reported. Such pedestrian-induced vibrations can occur in vertical and lateral directions with the latter being the focus of this paper. Recently published international design guidelines direct the designer to estimate the response of the footbridge due to crossing pedestrians, and then to measure this against prescribed limits set out either directly or indirectly by the guidelines. Some of these guidelines provide force functions to simulate pedestrian loading, while others are less prescriptive. The load functions that are provided tend to be deterministic in nature and have been shown to be deficient in accurately modelling actual pedestrian loading. Consequently, research is currently being conducted into the exact nature of pedestrian loading and the parameters which influence it. Previous research by the authors has examined the impact of walking velocity and pacing frequency on both vertical and lateral loading. This paper presents the results of recent walking trials, conducted along an 11m walkway to investigate the influence of spatial parameters on pedestrian lateral loading.

KEY WORDS: Pedestrian loading, spatial parameters, lateral, force plate, walking trials

1 INTRODUCTION

Vibrations induced on footbridges due to human loading have increasingly become the focus of considerable research in the structural engineering domain in the past decade. The vibrations induced occur due to two main reasons. Firstly, modern footbridges are elegant and slender, hence quite flexible and lightweight. Secondly, information and data on the direct nature of the producers of such vibrations – the pedestrians – is somewhat lacking; particularly in the lateral direction. Currently, designers can monitor actual vibrations post-construction and perform remedial action if required. This approach drove the final cost of The London Millennium Bridge up by 30% [1] (construction cost was €48 million, quoted as a 2010 equivalent by [2]). More desirably, at design stage, there are two approaches to avoiding excessive bridge vibrations; namely the frequency avoidance approach and the vibration limit approach. The former of these approaches is rather restrictive and conservative [3-5]. For these reasons the later approach is the one most often favoured by the design codes; however, it suffers as there is a dearth of knowledge on the nature of pedestrian loading and interaction between pedestrian and moving bridge. Attempts have been made to address this through direct measurement of the forces applied from individual footfall force traces in laboratories, employing techniques and equipment traditionally belonging to the biomechanics domain. These individual footfall force traces are commonly referred to as ground reaction forces (GRFs).

The following paper, therefore, focuses on the energy source which can give rise to lateral vibrations on footbridges – i.e., pedestrian loading. Reported are the three forces that occur due to pedestrian walking, with particular emphasis been placed on the lateral (medial-lateral) directed force. The paper then presents a review on the parameters most associated with this loading direction, hence providing the structural engineer with a detailed background on this load and what influences it most. The main part of this paper then investigates the influence foot landing position and step width has on medial-lateral pedestrian loading via an experimental investigation. These two parameters are 'pin pointed' as they are deemed the least investigated in terms of reported literature, yet are thought to influence medial-lateral loading significantly.

1.1 Ground reaction forces

Walking imparts forces, GRFs, in three orthogonal planes; namely, a vertical (inferior) in the coronal (frontal) plane, a lateral (medial-lateral) in the transverse (horizontal or axial) plane, and a anterior/posterior (longitudinal) in the mid-sagittal plane. Such forces are generally measured using force plates or sensor mats [6]. Instrumented treadmills have also been used for this purpose, however the loads and walking parameters observed on treadmill devices cannot be used to describe normal walking; as the participant will be forced to walk at a 'forced' speed [7, 8]. Bachmann & Ammann [9] report that the vertical force is of greatest magnitude, followed by the longitudinal and then the medial-lateral (M-L) forces; Figure 1. In terms of pedestrian loading on footbridges, the longitudinal forces are not considered to be of consequence as the structure will almost certainly be rather stiff in this principal direction of walking. The M-L force pattern is of concern when analysing relatively flexible structures, even though it is of smaller magnitude than the loading applied in either of the other planes. Moreover there appears to be a dearth of reliable published data on the magnitude and nature of this particular loading regime. Zivanovic et al. [10] carried out a comprehensive review of existing data on pedestrian loading and report only two references ([9, 11]), which provide values for the magnitude of M-L loading in terms of the individual weight of the pedestrian. Further, these two reports vary considerably in their estimation of these values, with the dynamic load factor (the maximum M-L load expressed as a percentage of the static weight) ranging from 3.9% to 10%. Other authors offer values of approximately 4% to 5% as the ratio of peak M-L force to static weight ([12]; [13] cited in [14]). Kirtley et al. [14] also cite [15] who claim that the magnitude of the M-L force increases with step width. A sequential combination of these individual footfall traces will produce the relevant continuous M-L load pattern exerted by pedestrians walking. The exact nature of this continuous M-L load function will be influenced by both gait parameters and anthropometric data for the pedestrians involved. The primary anthropometric data of concern is the static weight of the person, while the gait parameters which have been asserted to influence the M-L load function are described below.

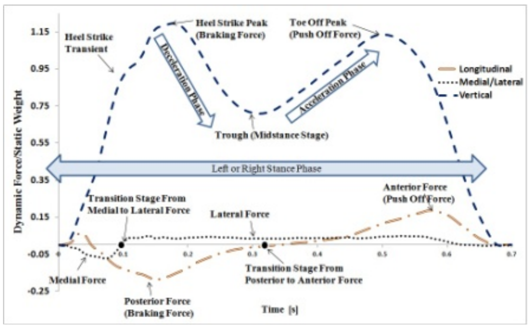

Figure 1. Ground reaction forces traces in three orthogonal planes.

1.2 Foot landing position

Foot landing position (FLP) is perhaps more commonly referred to as angle of gait, although it has also been termed foot placement angle (FPA) (Kernozek & Ricard, [16]) or angular deviation of the foot ([17] cited by [16]). The term generally refers to the angle made between the centreline of the foot and the forward direction of walking, but exact definitions of the foot reference line can vary between authors [18]. Simpson and Jiang [19] defined this reference line as "a line drawn from the midpoint of the posterior aspect of the calcaneus to the head of the second metatarsal", a definition which will be used here. The same authors also reported tests, which revealed that FLP influenced the force applied by the pedestrian. They categorised their test participants into categories of "toe-in", "neutral" and "toe-out" depending on their FLP during straight line walking and they claim that toe-out participants exerted significantly greater M-L forces than those in the toe-in category. Values for FLP are reported in degrees, with positive representing toe-out and negative representing toe-in. Reported values for FLP range between $+14.3^0$ (toe-out) and -3.8^0 (toe-in) [19]. This parameter presents the most variability of all of the spatial gait parameters in healthy test subjects. Indeed, [20] citing [21, 22] suggests FLP can be influenced by factors such as walking speed, walking substrate, friction on walkway, hip motion, *tibial* and *malleolar* torsion and, adduction or abduction of the foot. Menz et al. [23], as example, report mean FLPs for two trials each on the left and right foot respectively as 6.73^0, 7.32^0, 5.01^0 and 5.02^0 with accompanying standard deviations of 4.96^0, 5.36^0, 5.77^0 and 5.92^0. Nonetheless, Kirtley [14] suggests a neutral FLP of $+15^0$, i.e.; slightly abducted or "toe-out" when measured from the plane of walking, while [20] measured a mean value of approximately 9^0. Chung et al. [24] report a mean neutral value of 13.4^0 and claim that toe-out participants exerted significantly greater M-L forces than either toe-in or neutral participants in walking trials.

1.3 Step width

Step width, w_s, is defined as the distance between the centre lines of the two feet, perpendicular to the plane of walking. Reported values of step width have proven to be quite variable, with standard deviations up to 30%. Further, there is less reported data on this particular spatial parameter than others such as step length. Archbold & Mullarney [25] report a review of current literature, citing references which yield values between 0.09m and 0.19m for adults, with no apparent link between subject height and step width. Interestingly, values reported by [26, 27] that Korean adults exhibit greater step widths than others reported. Donelen et al. [28] and Bauby & Kuo [29] both linked step width to step length reporting that the step width was approximately equal to 12% and 13%, respectively, of the step length. However, this relationship has not been found by others. Kirtley et al. [14] reported that step width can vary with age and so recommended normalizing the value by dividing it by the pelvic width. They also stated that step width increases with disequilibrium (lack of balance). As previously stated, [15] have contended that the magnitude of the M-L load is proportional to step width.

1.4 Pacing frequency

Pacing frequency, f_s, is the most relevant of the temporal gait parameters in terms of pedestrian loading, particularly where resonant effects on structures are to be considered. It is defined as the inverse of the time taken from the initial contact of the left foot with the ground to the initial contact of the right foot immediately thereafter and corresponds to the rate of application of vertical forces. In biomechanical terms, this parameter is often measured as cadence, which is the number of steps per minute rather than the number per second. Reported values of normal pacing frequencies indicate that the average pacing rate is between 1.8Hz and 2.2Hz. Keogh et al. [30] reviewed 7 references and derived an average pacing frequency of 1.96Hz, with a standard deviation of 0.21Hz. Archbold & Mullarney [25] present the results based on a survey of a further 20 sources of information and report a mean value of 1.92Hz.

2 MEDIAL-LATERAL LOAD SIMULATION

As previously mentioned, there is relatively little published information on direct simulation of M-L loads from walking humans. A number of approaches have been employed however, the most common being the Single Harmonic Sine Function approach.

2.1 Single harmonic sine function (SHSF)

The majority of guidelines and codes define the M-L load pattern as a sinusoidal varying function with a single harmonic, which is a function of the pacing frequency. According to one guideline [31], for instance, there is no hint in the literature that onerous vibration of footbridges due to the second harmonic of pedestrian forces in the M-L direction having occurred. The SHSF approach assumes that the function is perfectly periodic and that the load contributions from alternate footfalls are equal. It also assumes that the use of a single harmonic of the frequency of load application is sufficient to capture the nature and magnitude of the load. It is convenient to note some of the characteristics of such a function at this point. Firstly, the fundamental frequency of application of M-L walking loads is half the pacing frequency as it is related to successive contact of either the left or right foot with the walking surface. Secondly, the magnitude of the force is assumed to be directly related to the static weight of the pedestrian. The magnitude is thus expressed as a proportion of this static weight through use of a dynamic load factor (DLF). The function can thus be represented as follows:

$$F_{(t)} = L_f . G . sin(\pi . f_s . t) \tag{1}$$

where $F_{(t)}$ is the continuous M-L load function, L_f is the dynamic load factor associated with the function, G is the static weight of the pedestrian, f_s is the pacing frequency and t is time. The magnitude of L_f has been reported as ranging from 0.03 [32] to 0.1 [11]. Archbold [33] asserted that the value of L_f may also be influenced by individual temporal & spatial parameters such as FLP and not just the static weight of the person. This was used to explain the significant differences in M-L response caused on a lightweight, flexible footbridge by two people of similar weight and height, walking at the same pacing frequency. Erlicher et al. [34] meanwhile demonstrated an increase in the recorded values for M-L force as the pacing velocity increased. The dynamic load factor appears to have increased from approximately 4% while walking at 3.75km/hr up to approximately 6% while walking at 6.0km/hr. Ingolfsson et al. [35] calculated a RMS value of the M-L load and equated this to 4.1% of the static weight. While Archbold & Mullarney [6] have shown that higher order harmonics may be significant in terms of the overall load function, only the fundamental harmonic will be considered here for simplification.

3 EXPERIMENTAL PROGRAMME

The experimental programme reported herein consists of walking trials involving 14 female and 25 male healthy adult participants. The participants conducted the walking trials in the laboratory on a specially constructed rigid walkway as described in the following section.

3.1 Participants

Participants were recruited from staff and students at AIT, Ireland. All were aged between 20 and 55 years. The ethnical composition of the participant sample was predominantly Caucasian with a small proportion being of African and Chinese background. Persons were excluded from participation if they had a history of previous injury with ongoing symptoms, or significant previous injury that would hamper their gait. All participants gave written consent according to the ethical procedures approved by AIT and its Research Ethics Committee.

3.2 Anthropometric data

The following parameters were recorded for each test participant prior to the walking trials being carried out: age; height (with and without footwear); weight. A summary of the recorded values is presented in Table 1.

Table 1. Age and anthropometric data for each gender group.

	Male		Female	
Parameter	Mean	SD	Mean	SD
Age (Year)	32.1	18.2	27.0	3.5
Height (m)(with footwear)	1.81	0.06	1.65	0.06
Weight (kg)	81.31	11.68	62.25	8.61

3.3 Equipment

A rigid walkway was specially constructed to carry out the walking trials. The walkway is 0.9m wide x 11.0m long and is constructed from three 50mm thick laminated fibreboard panels framed with timber battens and cross members at 600mm centres, which were bolted together longitudinally and placed directly on the laboratory floor. A 500mm x 500mm AMTI AccuGait balance platform (force plate) was mounted at the mid-point of the walkway to record the ground reaction forces: the top surface of the force plate was made level with the top surface of the walkway. In the vertical direction, Fz, the force plate has a natural frequency of 150Hz and a loading capacity of 1334N and the force plate was calibrated prior to the walking trials through measurement of static forces. Three Monitran MTN1800 accelerometers, with a sensitivity of 1.020 V/g@80Hz, were mounted to the underside of the walkway at approximately one-third span, mid-span, and two-third span; respectively.

Data were recorded from the accelerometers through a virtual instrument (VI) developed in National Instruments (NI) LabView 8.5. These data were used to determine the time interval between consecutive footsteps. Grid paper measuring 3.5m x 0.6m and containing a 20mm x 20mm grid size was placed over the middle section of the walkway to assist in recording the spatial parameters such as step length, step width and FLP from the trials. A schematic layout of the test set-up is shown in Figure 2.

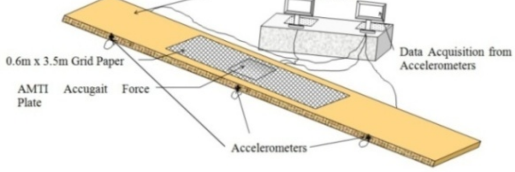

Figure 2. Schematic representation of walkway and set up.

3.4 Experimental procedure

The participants were asked to wear their regular clothing and comfortable, flat-soled shoes for the walking trials. Prior to the recorded traversing of the walkway, each participant completed a number of 'dummy' runs to ensure they felt comfortable with the process. For these dummy trials and the actual walking trials, the test subjects were requested to walk in a straight line along the length of the walkway at their normal speed and gait, while looking straight ahead – this was aided through using visual targets on the facing walls. Immediately prior to each trial the participant coated the soles of their shoes with blue chalk dust, which aided the recording of the footfall positions and thus measurement of the spatial gait parameters. This procedure has been successfully used by other authors [20], [36],and [37]. In addition [20] citing [21, 38-41] and by conclusion of their own experimental work suggests the footprint method of assessing gait parameters easy, reliable, valid, inexpensive and clinically feasible. Each test subject completed a minimum of two recorded trials at their normal speed and gait. A quarter of the participants then carried out additional trials; i.e., they walked with an exaggerated toe-out, toe-in, and/or natural (close to zero degrees) FLP. The type of FLP the participants used depended on their normal style, e.g., if the participant had a relatively straight FLP he/she then carried out a minimum of two toe-out and toe-in FLP trial sets. The spatial and temporal gait parameters recorded for each trial were step length, step width, FLP, and pacing frequency. Step length is measured as the distance from the heel strike of one foot to the next heel strike of the opposite foot and is measured in the direction of walking. Step width is measured as the distance between the centrelines of consecutive heel strikes and is measured normal to the direction of walking as shown in Figure 3. This figure also shows the measurement of the FLP, which is defined as the angle made by a line drawn from the centre of the heel, through the head of the second *metatarsal* and a line drawn parallel to the direction of walking.

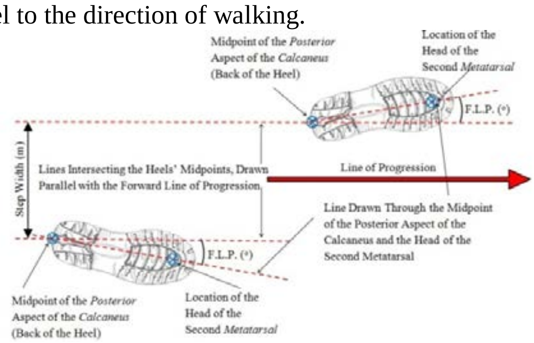

Figure 3. Measurement of spatial parameters.

The spatial and temporal gait parameters recorded for each trial were step length, step width, FLP, and pacing frequency. Pacing velocity was determined from the product of pacing frequency and step length. Also, the ground reaction forces (GRFs) in all three orthogonal directions were measured for the instance of a footfall striking the force plate. These GRF traces also enabled the determination of the single foot stance support phase.

4 RESULTS & DISCUSSION

4.1 Temporal & spatial parameters

Table 2 presents a summary of the mean and standard deviations (SDs) results for both the temporal & spatial gait parameters recorded during the normal walking trials. Also recorded in Table 2 are the Mean and SD M-L DLF results. The overall mean pacing frequency for the trials was 1.90Hz; males had a mean of 1.85Hz and females 2.00Hz. The females meanwhile had a shorter step length than their male counterparts; 0.72m versus 0.78m respectively. Interestingly the pacing velocity for both gender sets were the same, 1.46m/s; these three sets of results are in close agreement with results published previously by the authors [6] in a different trial set and by [42]. Moreover, the hypothesis suggested by [14] (citing data from [43]) that females will have on average a quicker pacing frequency due to their shorter on average limb length is a plausible reason for these results. Figure 4 endeavours to illustrate this more clearly. Step width for the entire group was 0.07m; 0.08m for males and 0.07m for females. It must be remarked however that the SDs were quite high, for instance; the overall group value was 57%. Foot land position, although normally distributed overall (Figure 5), shows a large difference between genders, i.e.; females had an average of 3.16^0 versus 6.92^0 for males. An important aspect of Figure 5 is that only a few 'outliers' have results in the negative range, which suggests most people it seems do not walk with a toe-in FLP.

Table 2. Gait parameters recorded during normal walking.

		Medial-Lateral DLF	Step length (m)	Step width (m)	FLP (^{0})	Pacing freq. (Hz)	Pacing vel. (m/s)
Male	Mean	0.085	0.78	0.08	6.92	1.85	1.46
	SD	0.026	0.06	0.03	4.46	1.17	0.14
Female	Mean	0.059	0.72	0.07	3.16	2.00	1.46
	SD	0.025	0.07	0.04	5.49	0.20	0.20
Overall	Mean	0.076	0.76	0.07	5.45	1.90	1.46
	SD	0.028	0.07	0.04	5.22	0.19	0.16

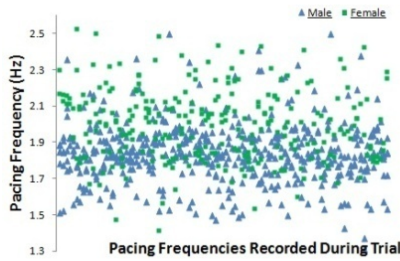

Figure 4. Comparison of male and female pacing frequencies recorded during normal walking.

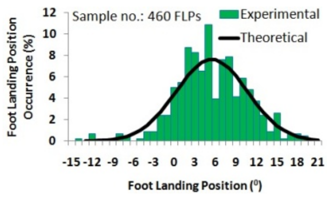

Figure 5. Distribution graph for foot land positions recorded during normal walking.

4.1 Gait & anthropometric relationships

Previously the authors [44] have identified a number of useful relationships regarding gait parameters and anthropometric data; Eq. 2:

$$f_s = \sqrt{\frac{v_s}{0.23h}} \tag{2}$$

Where f_s, v_s, and h are representative of pacing frequency, pacing velocity, and height; respectively. For the equation to hold true the following relationship needs to be realised:

$$l_s = 0.23h.f_s \tag{3}$$

Where l_s is reprehensive of step length. Equation 2 is based on Eq. 3 and the fact that pacing velocity is the product of step length and pacing frequency. The trials carried out as part of this paper proved consistent with Eq. 3, with respect to normal walking. A coefficient of 0.44 was also found between height and step length for normal walking, which is also consistent with previous trials [44]. As noted earlier some authors [28, 29] have suggested that step width is approximately 12% to 13% of step length for normal walking. In the case of these trials, however, the approximation is 10% for normal walking with a rather low co-relationship.

4.2 Medio-lateral load & gait relationship

The M-L DLF or L_f was obtained by dividing the maximum M-L dynamic force by the subject's static weight for each trial run. The maximum dynamic force is the maximum force form a continuous walking trace, i.e., once the left and right foot overlap have been summated; Figure 6. This approach assumes the force form each footstep is the same. The overall average M-L DLF is shown in Table 2 to be 0.073, which is close to a previous value, 0.066, provided by the authors [6].

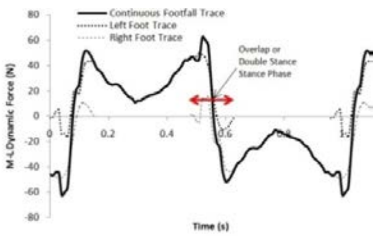

Figure 6. Continuous Footfall Trace.

Potential relationships between gait parameters, anthropometric data, and the M-L DLFs were explored. By inspection the most closely related parameter associated with the M-L DLF for positive FLP was step length, as presented in Figure 7. In terms of toe-in FLP (i.e., negative FLP) this apparent relationship ceased. However, a separate relationship seemed to exist for this category with step width instead of step length (Figure 8). Acknowledged at this stage through assessment of Figure 5 (Distribution of FLPs) is that the majority of people will walk with a FLP of between -2^0 and $+11^0$, as the female and male means are $3^0 \pm 5^0$ and $7^0 \pm 4^0$; respectively. For this reason both Figure's 7 & 8, are somewhat unproductive; hence a more progressive method may be to cover the more average range, i.e., -2^0 to $+11^0$ FLPs. Through inspection step length seems to have the closest relationship to the M-L DLF for this particular FLP range (i.e., -2^0 to $+11^0$) – Figure 9.

Hence, Eq. 1 form earlier can be rewritten as:

$$F_{(t)} = (0.16l_s - 0.04)G.sin(\pi.f_s.t) \tag{4}$$

This provides a rather useful relationship as step length, is easily quantifiable once height and/or pacing frequency are known (see Section 4.1).

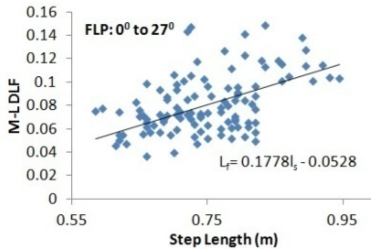

Figure 7. Step length, M-L DLF, and FLP relationship.

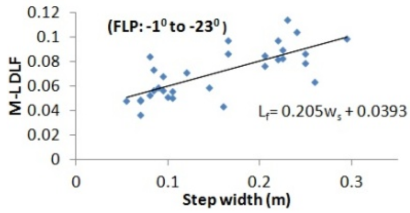

Figure 8. Step width, M-L DLF, and FLP relationship.

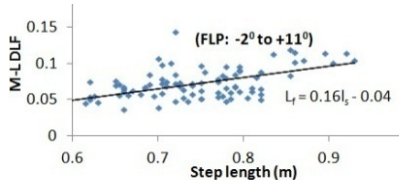

Figure 9. Step length and M-L DLF relationship for the 'more average' range of FLPs.

5 CONCLUSIONS

This paper reports on data form over 140 walking trials by a healthy adult test population involving 25 males and 14 females. Trials involved walking at a 'self selected' gait style and speed, and then walking with exaggerated FLPs (toe-in, toe-out, and relatively straight) along an 11m fixed walkway. The mean FLP, step width, step length, pacing frequency, and pacing velocity for normal or 'self selected' walking was 5.45^0, 0.07m, 0.76m, 1.9Hz, and 1.46m/s; respectively. Mean values for the M-L dynamic load were 7.6%, 8.9%, and 8.5% of the static weight of the subject for the overall, female, and male groups; respectively. Various gait parameters and anthropometric data relationships were explored and proved consistent with previous findings such as [44].

A relationship seemed to exist with toe-in FLP, step width, and the M-L DLFs, while another existed with toe-out FLP, step length, and the M-L DLFs. The later was narrowed down to include the more average FLP range of walking found during these trials, i.e., -2^0 to $+11^0$. This relationship may provide the structural engineer with an easily quantifiable way in which to determine the M-L DLF. This is because step length is easily calculated once height and/or pacing frequency are known; which was again highlighted in this paper. An interesting aspect of this paper is that step length proved to be closely related to the M-L force; yet published literature rarely if ever makes reference to this. For this reason it may be worth investigating this parameter's relationship with the M-L DLF more closely.

REFERENCES

[1] V. Racic, and J. M. W. Brownjohn, “Stochastic model of near-periodic vertical loads due to humans walking,” *Advanced Engineering Informatics*, vol. 25, no. 2, pp. 259-275, 2011.

[2] B. Duguid, "Benchmarking cost and value of landmark footbridges." Proceedings of the 4th International Footbridge Conference: Footbridge 2011-Attractive Structures at Reasonable Costs, 6-8 July, Dolnoslaskie Wydawnictwo Edukacyjne, Wroclaw, Poland, 2011.

[3] R. L. Pimentel, A. Pavic, and P. Waldron, “Evaluation of design requirements for footbridges excited by vertical forces from walking,” *Canadian Journal of Civil Engineering,* vol. 28, no. 5, pp. 769-777, 2001.

[4] R. L. Pimentel, “Vibrational Performance of Pedestrian Bridges Due to Human Induced Loads, PhD Thesis,” Department of Civil & Structural Engineering, University of Sheffield, England, UK, 1997.

[5] M.-H. Huang, “Dynamic Characteristics of Slender Suspension Footbridges, PhD Thesis,” School of Urban Development, Faculty of Built Environmental and Engineering, Queensland University of Technology, Queensland, Australia, 2006.

[6] P. Archbold, and B. Mullarney, “Lateral loads applied by pedestrians at normal walking velocities,” *Bridge Structures-Assessment, Design & Construction,* vol. 7, no. 2, pp. 75-86, 2011.

[7] M. Kasperski, and C. Sahnaci, "Serviceability of pedestrian structures." Proceedings of the International Modal Analysis Conference (IMAC XXC), Orlando, USA, 2007.

[8] C. Sahnaci, and M. Kasperski, "Simulation of random pedestrian flow." Proceedings of the 8th International Conference on Structural Dynamics, EURODYN 2011, Lauven, Belguim, 2011, pp. 1040-1047.

[9] H. Bachmann, and W. J. Ammann, *Vibrations in structures : induced by man and machines*, Zu\0308rich: International Association for Bridge and Structural Engineering, 1987.

[10] S. Zivanovic, A. Pavic, and P. Reynolds, “Vibration serviceability of footbridges under human-induced excitation: a literature review,” *Journal of Sound and Vibration,* vol. 279, no. 1-2, pp. 1-74, 2005.

[11] H. Bachmann, A. J. Pretlove, and H. Rainer, *Dynamic forces from rhythmical human body motions, in: VibrationProblems in Structures: Practical Guidelines, Birkha¨user, Basel, Appendix G.*, 1995.

[12] S. C. Wearing, S. R. Urry, and J. E. Smeathers, “The effect of visual targeting on ground reaction force and temporospatial parameters of gait,” *Clinical Biomechanics,* vol. 15, no. 8, pp. 583-591, 2000.

[13] G. Giakas, and V. Baltzopoulos, “Time and frequency domain analysis of ground reaction forces during walking: an investigation of variability and symmetry,” *Gait & Posture,* vol. 5, no. 3, pp. 189-197, 1997.

[14] C. Kirtley, *Clinical gait analysis : theory and practice*, Edinburgh: Elsevier Churchill Livingstone, 2006.

[15] S. Carlsöö, A. G. Dahlöf, and J. Holm, “Kinetic analysis of the gait in patients with hemiparesis and in patients with intermittent claudication,” *Scandinavian Journal Of Rehabilitation Medicine,* vol. 6, no. 4, pp. 166-179, 1974.

[16] T. W. Kernozek, and M. D. Ricard, “Foot placement angle and arch type: effect on rearfoot motion. ,” *Arch Phys Med Rehabil,* vol. 71, no. 12, pp. 795-800, 1990.

[17] P. R. Cavanagh, “The biomechanics of lower extremity action in distance running,” *Foot & Ankle,* vol. 7, no. 4, pp. 197-217, 1987.

[18] M. J. Whittle, *Gait analysis: an introduction.*, 2nd ed., Oxford: Butterworth and Heinemann, 2002.

[19] K. J. Simpson, and P. Jiang, “Foot landing position during gait influences ground reaction forces,” *Clinical Biomechanics,* vol. 14, no. 6, pp. 396-402, 1999.

[20] J. Taranto, M. J. Taranto, A. Bryant *et al.*, “Angle of gait: a comparative reliability study using footprints and the EMED-SF®,” *The Foot,* vol. 15, no. 1, pp. 7-13, 2005.

[21] B. H. Clarkson, “Absorbent paper method for recording foot placement during gait: suggestion from the field,” *Physical Therapy: Journal of The American Physical Therapy Association,* vol. 63, no. 3, pp. 345-346, 1983.

[22] Holden J, Cavanagh P, Williams K *et al.*, *Foot angles during walking and running. In: Winter D, Norman R, Wells R, Hayes K, Patla A, editors. Biomechanics IX-A, 0 ed. Champaign: Human Kinetics Publishers. p. 451–6.*, 1985.

[23] H. B. Menz, M. D. Latt, A. Tiedemann *et al.*, “Reliability of the GAITRite® walkway system for the quantification of temporo-spatial parameters of gait in young and older people,” *Gait & Posture,* vol. 20, no. 1, pp. 20-25, 2004.

[24] C.-T. Chung, C.-C. Yang, C.-H. Chiu *et al.*, “Toe-out landing position increases medial ground reaction force during walking in young individuals,” *Taiwan Journal of Physical Medicine and Rehabilitation,* vol. 38, no. 2, pp. 65-73, 2010.

[25] P. Archbold, and B. Mullarney, "A review of gait parameters pertinent to pedestrian loading." The 5th Joint Symposium Proceedings of Bridge & Infrastructure Research in Ireland, and Concrete Research in Ireland, 2-3 September, Cork, Ireland, 2010, pp. 25-34.

[26] S. H. Cho, J. M. Park, and O. Y. Kwon, “Gender differences in three dimensional gait analysis data from 98 healthy Korean adults,” *Clinical Biomechanics,* vol. 19, no. 2, pp. 145-152, 2004.

[27] T. Ryu, H. Soon Choi, H. Choi *et al.*, “A comparison of gait characteristics between Korean and Western people for establishing Korean gait reference data,” *International Journal of Industrial Ergonomics,* vol. 36, no. 12, pp. 1023-1030, 2006.

[28] M. J. Donelen, R. Kram, and K. A. D., “Mechanical and metabolic determinants of preferred step width in human walking,” in Proceedings of the Royal Society of London: Series B, UK, 2001, pp. 1985-1992.

[29] C. E. Bauby, and A. D. Kuo, “Active control of lateral balance in human walking,” *Journal Of Biomechanics,* vol. 33, no. 11, pp. 1433-1440, 2000.

[30] J. Keogh, P. Archbold, C. Caprani *et al.*, "Estimating the effect of pacing frequency on the vertical response of a flexible footbridge." The 5th Joint Symposium Proceedings of Bridge & Infrastructure Research in Ireland, and Concrete Research in Ireland, Cork, Ireland, 2010, pp. 35-42.

[31] Hivoss, "Design of Footbridges Guideline. Human Induced Vibrations of Steel Structures RFS2-CT-2007-00033," 2008.

[32] A. Pavic, P. Reynolds, P. Cooper *et al.*, "*Dynamic Testing and Analysis of Aberfeldy Footbridge, University of Sheffield, Department of Civil & Structural Engineering, Mappin Building, Sheffield S1 3JD, UK*," 2000.

[33] P. Archbold, “Novel Ineractive Load Models for Pedestrian Footbridges, PhD Thesis,” School of Architecture, Landscape & Civil Engineering, University College Dublin, Dublin, 2004.

[34] S. Erlicher, A. Trovato, and P. Argoul, “Modeling the lateral pedestrian force on a rigid floor by a self-sustained oscillator,” *Mechanical Systems and Signal Processing,* vol. 24, no. 5, pp. 1579-1604, 2010.

[35] E. T. Ingólfsson, C. T. Georgakis, F. Ricciardelli *et al.*, “Experimental identification of pedestrian-induced lateral forces on footbridges,” *Journal of Sound and Vibration,* vol. 330, no. 6, pp. 1265-1284, 2011.

[36] A. L. McDonough, M. Batovia, S. Kwon *et al.*, “The validity and reliability of the GAITrite system's measurement: a prelimainary evaluation,” *Archives of Physical Medicine & Rehabilitation,* vol. 82, no. 3, pp. 419-425, 2001.

[37] M. J. Wilkinson, and H. B. Menz, “Measurement of gait parameters form footprints: a reliability study.,” *The Foot,* vol. 7, no. 1, pp. 19-23, 1997.

[38] C. N. Burnett, and E. W. Johnson, “Development of gait in childhood: Part II,” *Developmental Medicine & Child Neurology,* vol. 13, no. 2, pp. 207-215, 1971.

[39] P. K. Levangie, J. Brouwer, S. H. McKeen *et al.*, “The effects of the standard rolling walker and two posterior rolling walkers on gait variables of normal children,” *Physical & Occupational Therapy in Pediatrics,* vol. 9, no. 4, pp. 19-31, 1990.

[40] P. Freychat, A. Belli, J. P. Carret *et al.*, “Relationship between rearfoot and forefoot orientation and ground reaction forces during running,” *Medicine & Science in Sports & Exercise,* vol. 28, no. 2, pp. 225, 1996.

[41] M. Shores, “Footprint analysis in gait documentation: an instructional format,” *Physical Therapy: Journal of The American Physical Therapy Association,* vol. 60, no. 9, pp. 1163-1167, 1980.

[42] T. Oberg, and A. Karsznia, “Basic gait parameters: Reference data for normal subjects, 10-79 years of age,” *Journal of Rehabilitation Research & Development,* vol. 30, no. 2, pp. 210, 1993.

[43] D. H. Sutherland, K. R. Kaufman, M. P. Wyatt *et al.*, “Effects of botulinum toxin on gait of patients with cerebral palsy: Preliminary results,” *Gait & Posture,* vol. 2, no. 1, pp. 52-52, 1994.

[44] P. Archbold, and B. Mullarney, "The influence of selecteced gait parameters on vertical pedestrian loading." Proceedings of the 4th International Footbridge Conference: Footbridge 2011-Attractive Structures at Reasonable Costs, 6-8 July, Dolnoslaskie Wydawnictwo Edukacyjne, Wroclaw, Poland, 2011, pp. 759-768.

The potential for the elimination of expansion joints from existing road bridges in Ireland: a case study

Conor Keena[1], Kieran Ruane[1, 2], John J. Murphy[1]
[1]Department of Civil, Structural & Environmental Engineering, Cork Institute of Technology, Rossa Avenue, Bishopstown, Cork, Ireland
[2]RPS Group, Innishmore, Ballincollig, Co. Cork, Ireland
email: conor.keena@mycit.ie, kieran.ruane@rpsgroup.com, john.justinmurphy@cit.ie

ABSTRACT: All new road bridges of length less than 60m and of skew less than 30° are designed to be fully integral to the requirements of NRA BD57. Most road bridges constructed before the first introduction of this document have been constructed using expansion joints and bridge bearings, which give rise to maintenance issues. These issues include the repair and replacement of bridge bearings, which can be expensive work. This paper focuses on a road bridge constructed before the NRA requirement was introduced, that is a bridge constructed using expansion joints and bridge bearings. A suitable existing structure was selected and an analysis was carried out to determine whether it is feasible to eliminate the expansion joints and make the bridge integral, thus eliminating the maintenance costs associated with expansion joints. A structural analysis of the bridge, using LUSAS finite element software, before and after the elimination of the expansion joints is included in the paper. The main focus of the analysis is on the movements of the structure due to thermal fluctuations and their effect on the structure.

KEY WORDS: Highway bridges; Expansion joints; Joint elimination; Bridge retrofit.

1. INTRODUCTION

Road bridges built in Ireland before 2001 were mostly constructed using expansion joints and bridge bearings to allow for thermal movement of the bridge deck. In 2001, the NRA introduced a new advice note, BD57 [1], stating that road bridges of less than 60m length and of skew less than 30° should be designed and built as integral bridges, thus eliminating the expansion joints and bridge bearings. This has a significant effect on the whole life costing of the bridge. The repair and maintenance of the expansion joints and bridge bearings can incur a large cost, as well as disrupting traffic while repairs are taking place.

This paper is a step towards showing that the expansion joints and bridge bearings on some existing road bridges can be eliminated, thus making them integral and cheaper to maintain. This paper focuses on one bridge in particular. Analysis of the bridge was carried out using LUSAS finite element analysis software.

The analysis was carried out with aims to establish that:

- The bridge structure is strong enough to deal with the thermal movements of the bridge deck;
- The soil properties are such that, when subjected to the cyclical thermal loading from the bridge structure, the soil does not deform significantly, which could cause damage to the structure itself, or the adjoining road.

Retrofitting bridges to make them integral has been done in other countries, but little or no work has been done in Ireland. Tsiatas & Boardman [2] produced a report on the elimination of expansion joints from steel bridges in the United States. Similar work has been carried out in other countries, but the published reports may be of little relevance to Ireland due to the difference in range of temperatures between the environments.

2. SCOPE & OBJECTIVE

To assess whether or not a simply supported bridge can be made integral, it was decided that the most practical approach was to take a case study and assess the feasibility of the works on that structure.

The bridge that was analysed for this report is Bridge D3 located on the N8, near the Dunkettle Roundabout in Cork, as shown in Figure 1.

Figure 1. Location of Bridge D3 [3].

The bridge, shown in Figure 2, spans 15.63m and is 32.9m wide. The deck was constructed using precast prestressed bridge beams, supported by in-situ abutments. The foundations are reinforced concrete direct bearing foundations resting on dense sand and gravel. There is no skew and no curvature, but the deck is on a gradient, falling from north to south. There is a 20mm expansion gap at each end of the deck to allow for thermal expansion and contraction, and the deck is supported on elastomeric bridge bearings. According to BD57, this bridge, had it been built after 2001, would have been designed as an integral bridge.

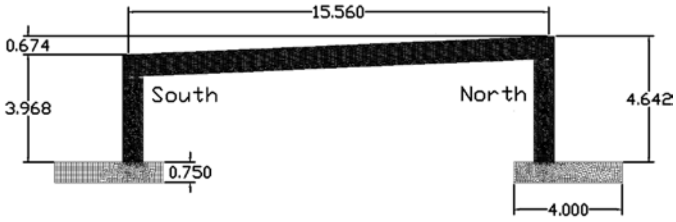

Figure 2. Dimensions of the bridge (dimensions in metres).

Finite element analysis was carried out on the structure, with three different connection types between the abutment and the deck, to examine the structural implications of making the bridge integral.

3. LUSAS FINITE ELEMENT ANALYSIS

3.1. Introduction

Three separate analyses of the bridge have been carried out to assess the stresses occurring in the bridge under its current conditions, and under integral and semi-integral conditions.

- The first step was to analyse the bridge as it is to determine what forces and bending moments currently occur in the deck and the abutments, i.e., a model that includes the bridge bearings and an expansion gap.
- The second analysis was to model the bridge as a fully integral structure, and to determine the forces and bending moments in the structure.
- The third step was to carry out an analysis of the bridge as a semi-integral structure. Details of this type of structure are shown in Figure 4 and Figure 5. This type of detail may be necessary to make the works economically viable, as making the structure fully integral may be too costly. The analyses in this paper were carried out using the geometry shown in Figure 4 with other details to be considered in future work.

3.2. Analysis of existing bridge

The analysis of the bridge as it currently stands was carried out with reference to design drawings [4] and information from a recent bridge inspection [5]. The structure was modelled as a 2D surface model, as shown in Figure 2 and in Figure 3. This was considered appropriate in the absence of a skew on the bridge.

The supports on the model are springs under the foundation of the bridge and behind the abutment walls. These springs represent the soil and were modelled using Winkler springs [6]. The stiffness in the springs was calculated assuming that the soil was a dense sand and gravel, with a Young's modulus of elasticity of 350N/mm^2 and a Poisson's ratio of 0.3. These values are representative of a typical structural backfill [7].

The elastomeric bridge bearings were modelled using a material with a Young's modulus of 2000N/mm^2, a shear modulus of 0.9N/mm^2, and a Poisson's ratio of 0.49. These values are typical for elastomeric bridge bearings [8].

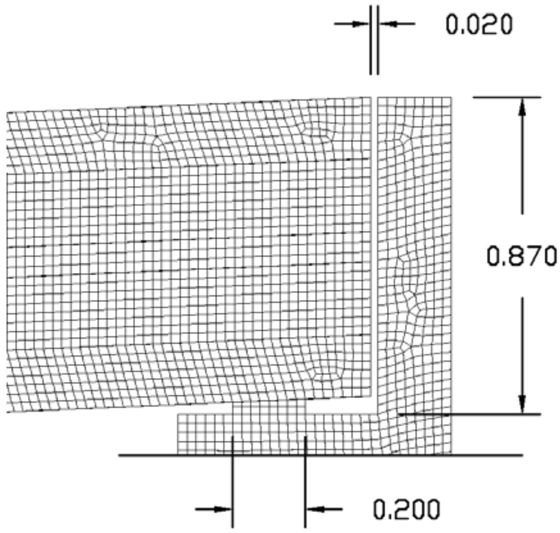

Figure 3. North end of the bridge deck with expansion gap and bridge bearing (dimensions in metres).

3.3. Analysis of bridge as a fully integral structure

The bridge was then modelled as a fully monolithic structure. The soil and backfill properties were modelled in the same manner as in the analysis of the existing structure. Results are presented in Part 4 of this paper.

3.4. Analysis of bridge as a semi-integral structure

A number of drawings were prepared to illustrate what details may be used in making the bridge integral. Figure 4 shows the detail that has been used in the analysis for this paper, and Figure 5 shows an alternative detail that will be used in future analysis. Further details will be developed as the research continues.

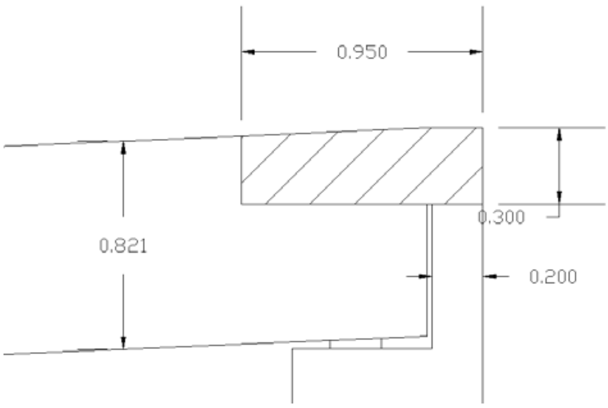

Figure 4. Detail of proposed works to be carried out on the bridge (dimensions in metres).

The detail in Figure 4 shows part of the bridge deck and the top of the abutment removed, the removed parts being represented by the hatched area. If these works were to take place, the bridge deck would be jacked up and the elastomeric bridge bearing would be removed and replaced by a concrete plinth. The bridge deck would then be allowed to settle on the plinth. Reinforcing bars would be dowelled into the existing structure to a suitable anchorage depth. The deck and abutment would be joined by a reinforced concrete detail in the hatched area. The design of this detail would allow for moments induced by creep effects in the prestressed beam.

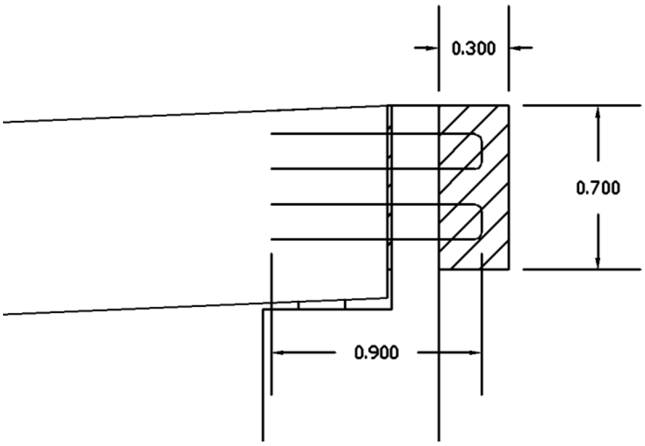

Figure 5. Alternative detail of proposed works to be carried out on the bridge (dimensions in metres).

An alternative detail involves casting a reinforced concrete block onto the back of the abutment. This would be done by removing the bridge bearings as in the first method. The soil behind the abutment wall would then be excavated. Reinforcing bars would be dowelled through the abutment and into the deck of the bridge. The end of the steel would then be cased in concrete as shown in Figure 5.

3.5. Loadcases

The loadcases included in the analyses are as follows:

Loadcase 1:

- Thermal contraction;
- Load Model 1 – Lane load;
- Self-weight of structure.

Loadcase 2:

- Thermal expansion;
- Load Model 1 – Lane load;
- Self-weight of structure.

Load Model 1 in IS EN 1991-2 [8] comprises a uniformly distributed load (UDL) and a tandem axle load. It is proposed to use the UDL component to represent nominal traffic loading for the purposes of comparing the three models. The UDL component is given as 9kN/m^2 for Lane 1 and 2.5kN/m^2 for all subsequent lanes and the remaining area. Table NA.1 in the Irish National Annex for IS EN 1991-2 gives the lane factors (α_{Q1}) to be applied to the UDL. These are given as 0.61 for Lane 1 and 2.2 for all subsequent lanes and the remaining area. Hence a UDL of 5.5 kN/m^2 for each lane is proposed.

There are general rules for combining load effects. For the characteristic combination, a factor of 1.0 is applied to the leading variable load (generally traffic load) and a factor φ_0 (= 0.6) is applied to variable loads such as thermal loads [9].

Loading due to temperature change is applied to the bridge deck according to IS EN 1991-1-5 [10]. The temperature changes are distributed through the deck as shown in Figure 6. The maximum change in temperature ΔT_1 was taken as 13°C for heating, and -7.7°C for cooling.

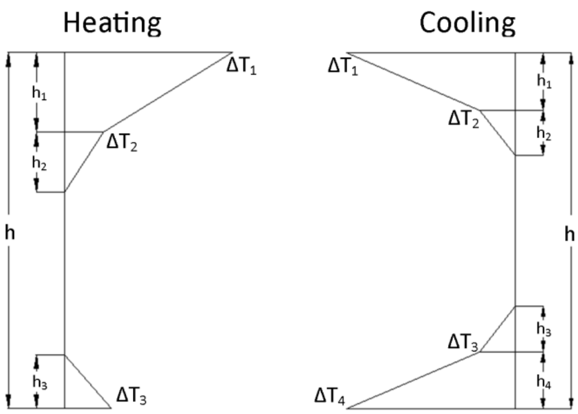

Figure 6. Temperature change gradients for heating and cooling of the bridge deck.

3.6. Model attributes

The 2D surface models created were meshed using a quadratic plane stress mesh. Quadrilateral elements were used with a quadratic order of interpolation. The mesh was refined to an element length of 25mm, and results converged satisfactorily. The model was assigned a surface thickness of 33m, which is the width of the bridge. The concrete in the bridge was assigned a short term C40 concrete material property, selected from the material library in LUSAS.

4. LUSAS RESULTS

A slice can be taken along any part of the structure. The normal stresses along that slice can be graphed. Bending moments and axial forces in the element can be determined using these graphs.

The graphs displayed in Figures 8 to 19 show the normal stresses through key locations of the bridge structure for both Loadcase 1 and Loadcase 2. The locations of the slices taken through the bridge are displayed in Figure 7. The graphs show the superimposed stress distributions for the semi-integral, fully integral and jointed bridge models.

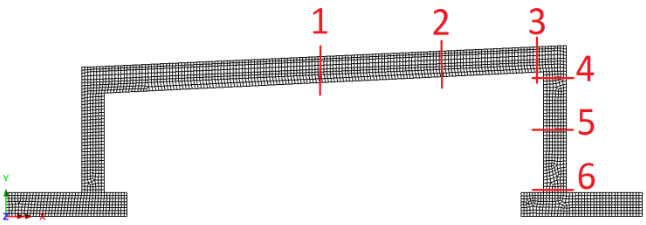

Figure 7. Locations of the slices taken through the structure.

4.1. Loadcase 1: Thermal contraction, LM1 & self-weight

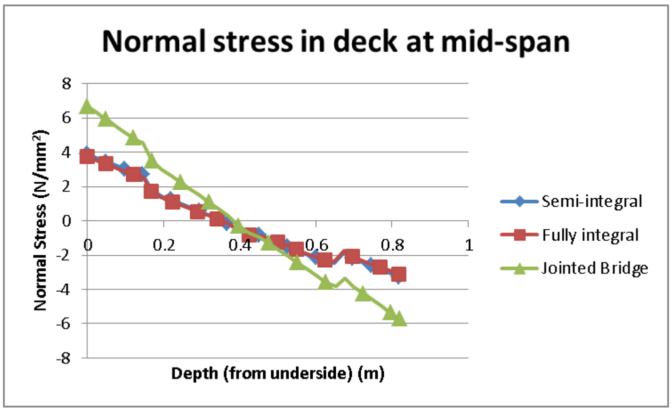

Figure 8. Normal stress in deck at mid-span (Loadcase 1).

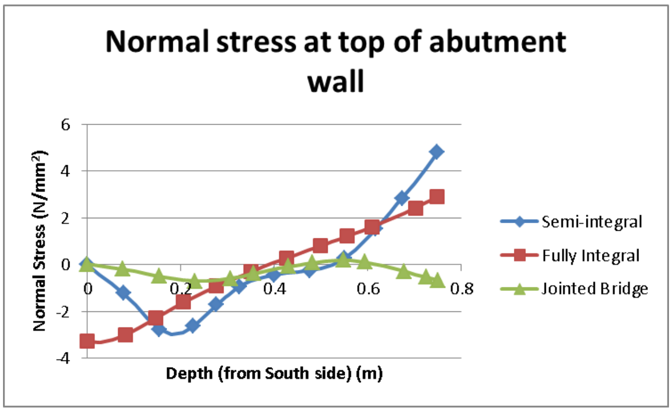

Figure 9. Normal stress at top of the abutment wall (Loadcase 1).

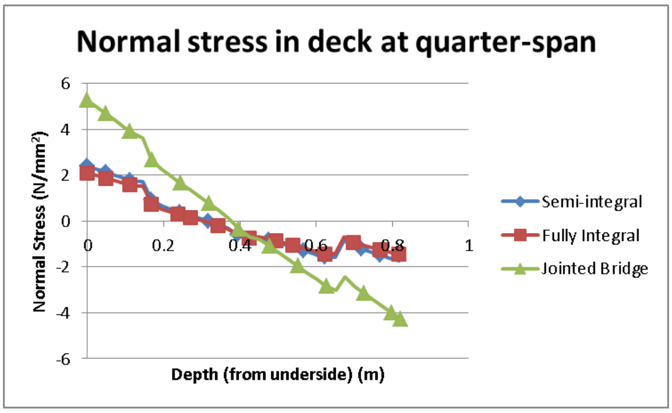

Figure 10. Normal stress in deck at quarter-span (Loadcase 1).

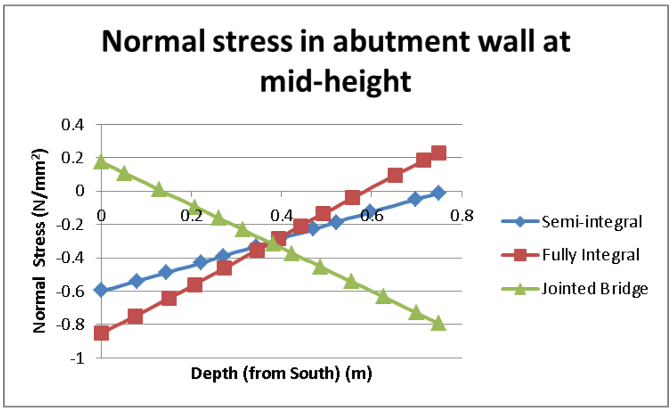

Figure 11. Normal stress in abutment wall at mid-height (Loadcase 1).

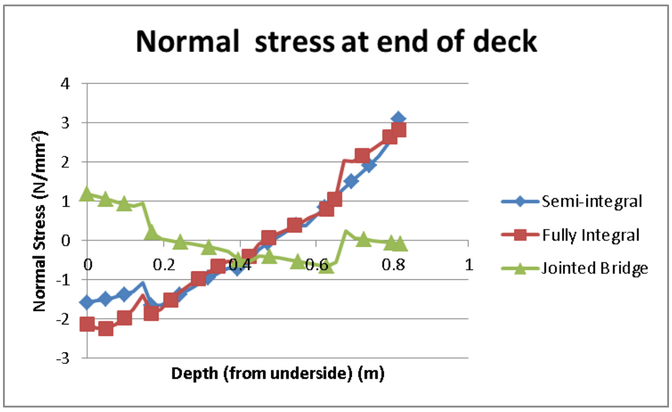

Figure 12. Normal stress at end of the deck (Loadcase 1).

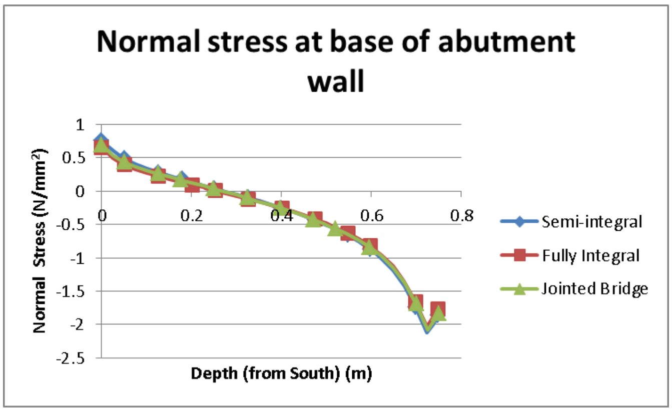

Figure 13. Normal stress at base of the abutment wall (Loadcase 1).

4.2. Loadcase 2: Thermal expansion, LM1 & self-weight

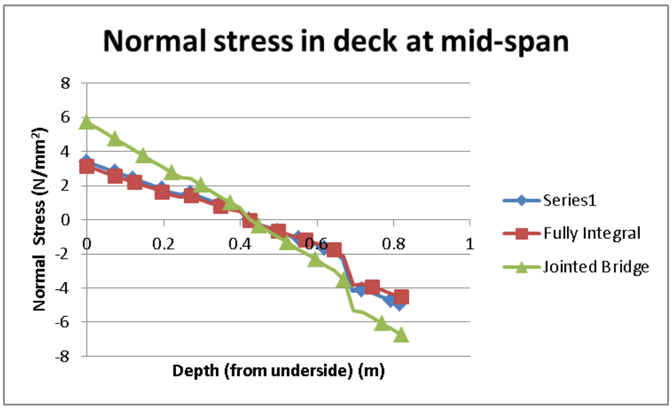

Figure 14. Normal stress in deck at mid-span (Loadcase 2).

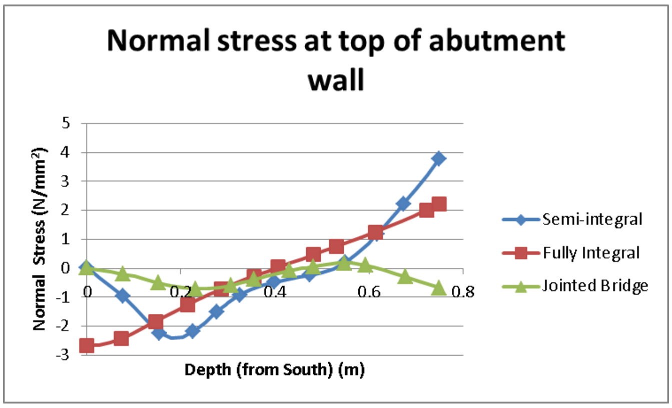

Figure 15. Normal stress at top of the abutment wall (Loadcase 2).

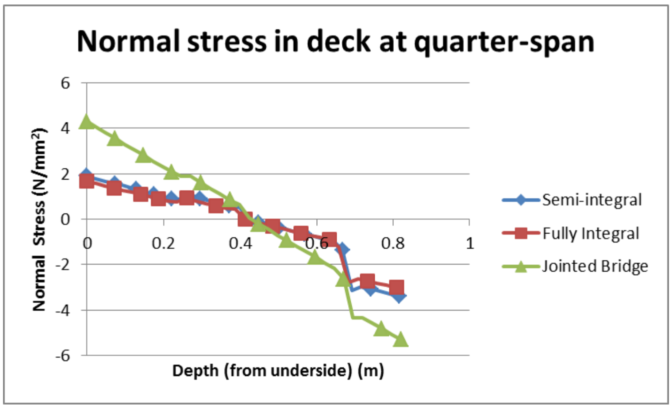

Figure 16. Normal stress in deck at quarter-span (Loadcase 2).

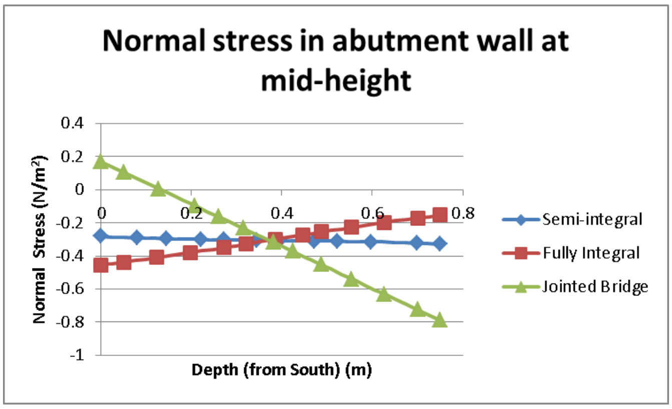

Figure 17. Normal stress in abutment wall at mid-height (Loadcase 2).

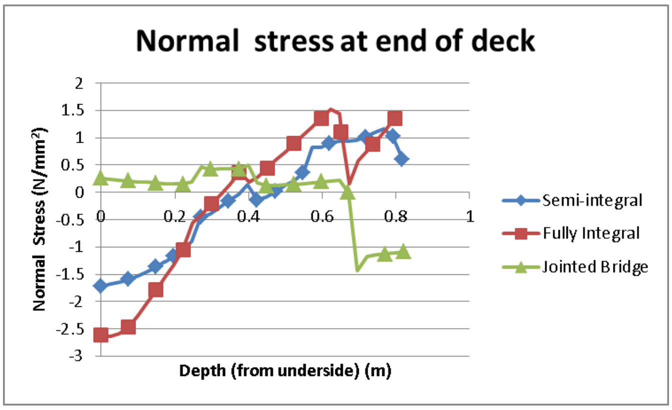

Figure 18. Normal stress at end of the deck (Loadcase 2).

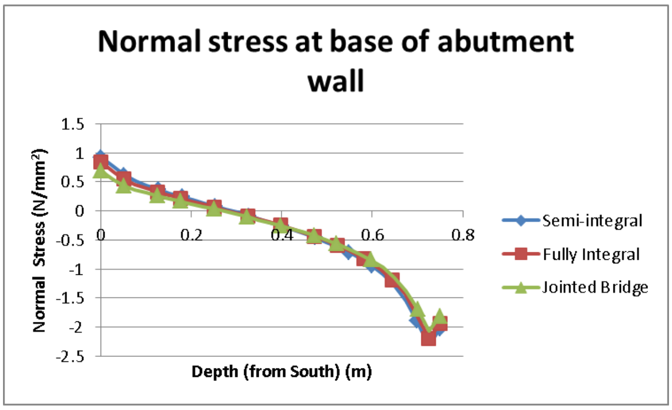

Figure 19. Normal stress at base of the abutment wall (Loadcase 2).

5. CONCLUSIONS

For the purpose of analysis of the results, the graphs were grouped together by location of the slice on the bridge.

5.1. Deck: half-span and quarter-span

It is clear from the graphs that the stresses in the deck at mid-span and at quarter-span were reduced when the bridge is made integral, for both loadcases included in this paper.

5.2. Deck / Abutment junction

When the bridge is made integral, the stresses at the end of the bridge deck and at the top of the abutment wall are increased due to the restraint of the deck. This indicates that a detailed design will need to be carried out at these locations. Additional reinforcement may be required to ensure that the stresses in the integral bridge can be adequately resisted.

5.3. Abutment wall: Mid-height

For both loadcases the stresses in the abutment wall change significantly when the bridge is made integral. As a jointed structure, the highest compressive stresses occur on the soil side of the abutment wall, and the lowest compressive stresses are on the road side. For the integral structure, this situation is reversed, with the highest compressive stresses occurring on the road side of the wall. Tensile stresses develop on the soil side of the wall in Loadcase 1. After the bridge is made integral, tensile stresses at mid-height in the wall do not exceed $0.3N/mm^2$, and compressive stresses do not exceed $1N/mm^2$. These stresses are quite low and are unlikely to be critical in the overall design.

5.4. Abutment wall: Base

There is very little change in the stresses at the base of the abutment wall for both loadcases when the bridge is made integral.

6. FURTHER WORK

The results presented in this paper were focused only on the stresses in the deck and in the abutment wall. To fully determine whether it is possible to safely make current road bridges integral, the structure will need to be analysed in more detail. This further study will include a more detailed analysis of the forces and bending moments occurring in the joints between the deck and the abutments. The soil will also need to be modelled to determine how the integral structure will interact with the soil. The effects of creep may also have a significant effect on the behaviour of the structure and will be incorporated into future analysis.

Further loadcases will also have to be considered, such as abnormal vehicle loading, prestressing effects, braking loads and impact loads.

Other future work will include taking on more case studies, including skewed bridges and bridges with longer spans.

A cost analysis will be carried out to assess whether or not making existing jointed bridges integral is economically viable.

ACKNOWLEDGMENTS

The authors would like to extend their thanks to Mr David Hodge for the help and advice that he has given and continues to give for this research.

REFERENCES

[1] National Roads Authority, *NRA BD 57/10 Design for Durability*, National Roads Authority, Dublin, Ireland, 2010.

[2] G. Tsiatas and W. G. Boardman, *Expansion Joint Elimination for Steel Highway Bridges*, University of Rhode Island, Kingston, USA, 2002.

[3] Google, “Google Maps,” Google, 2012. [Online]. Available: http://maps.google.com. [Accessed 24 January 2012].

[4] Cork County Council, *Glanmire Bypass - N8. Bridge D3*, Cork County Council, Cork, Ireland, 1986.

[5] Eirspan, *Inspection Report C1-N08-006.00 Dunkettle Road*, National Roads Authority, Dublin, Ireland, 2002.

[6] E. Hambly, *Bridge Deck Behaviour*, London: Taylor & Francis, 1990.

[7] T. Zhu, 'Some Useful Numbers on the Engineering Properties of Materials', *Geophysics At Stanford University*, unknown. [Online]. Available: http://www.stanford.edu/~tyzhu/ Documents/Some%20Useful%20Numbers.pdf. [Accessed 6th March 2012].

[8] Freyssinet, *Elastomeric Bearings*, Freyssinet, Telford, UK, 2008.

[9] National Standards Authority of Ireland, *IS EN 1991-2. Eurocode 1: Actions on structures - Part 2: Traffic loads on bridges*, NSAI, Dublin, Ireland, 2003.

[10] National Standards Authority of Ireland, *IS EN 1990. Eurocode - Basis of structural design*, NSAI, Dublin, Ireland, 2002.

[11] National Standards Authority of Ireland, *IS EN 1991-1-5. Eurocode 1: Actions on structures - Part 1-5: General actions - Thermal actions*, NSAI, Dublin, Ireland, 2003.

A finite element study of precast prestressed concrete circular tanks subject to elevated temperatures

M.J. Minehane[1], B.D. O'Rourke[2]
[1]RPS Group Ltd., Innishmore, Ballincollig, Cork, Ireland
[2]Department of Civil, Structural and Environmental Engineering, Cork Institute of Technology, Rossa Avenue, Bishopstown, Cork, Ireland
email: michael.minehane@rpsgroup.com, brian.orourke@cit.ie

ABSTRACT: The present study investigated the influence of heated water storage, upward to 95 C, on precast prestressed concrete circular tanks. Modern design standards for concrete liquid-retaining structures require that thermal effects be considered for the serviceability limit state and the ultimate limit state when deemed significant. Most recognized standards, however, do not provide guidance for the analysis of such effects. Research in the area of thermal stresses is limited and almost exclusively concerned with ambient thermal conditions, with a maximum temperature gradient of 30 C in any instance. A finite element study incorporating thermo-mechanical coupling investigated the magnitude of stresses associated with thermal storage. A linear eigenvalue analysis examined the ultimate limit state of buckling for restrained tank walls due to the thermally induced combined axial compression and bending. Consequent design implications were established and recommendations made for accommodating thermal loading.

KEY WORDS: Buckling; Elevated temperature; Finite element analysis; Prestressed concrete; Reservoirs; Thermal storage.

1 INTRODUCTION

The significance of thermal effects on concrete reservoir walls for ambient conditions is long established. An early study by Priestley [1] determined that temperature gradients of 30 C through the wall thickness can exist in warm climates when the effects of solar radiation are considered. Priestley [1] demonstrated that the resulting tensile stresses were large enough to overcome the residual compression and cracking would inevitably occur. Ghali and Elliott [2] developed closed form solutions for the thermal analysis of elastic tank walls of varying base restraint and free at the top. Through numerical examples it was shown that a gradient of 30 C through the wall thickness was sufficient to cause cracking. This supported Priestley's [1] proposal that the design should be based upon a serviceability criterion of limiting crack widths rather than a limiting tensile stress. Although modern design standards require that thermal effects are considered for the serviceability limit state, few provide guidance for the analysis of such effects. Pioneering design codes with regard to this are NZS 3106 [3] and AS 3735 [4] which provide design tables, originally derived by Priestley [1], to calculate hoop forces and vertical moments for tank walls free at the top and either free-sliding, pinned or fixed at the base.

The studies reviewed were exclusively applicable to tank walls free at the top retaining water at ambient temperature. As thermal storage tanks require a roof, the associated radial restraint at the top of the wall alters the internal force distribution. Moreover, the magnitude of the internal forces resulting from the thermal expansion of the tank walls will be shown to be excessive from a design perspective, unless provision is made for radial displacement during service.

1.1 *Research significance*

This paper investigates the feasibility and implications of thermal storage/heated liquid storage using cylindrical concrete reservoirs, for which there is currently a paucity of information. The research has practical applications in thermal storage for district heating and related schemes. Although particular reference is made throughout to precast prestressed concrete storage tanks, the research is also applicable to partially prestressed and reinforced concrete reservoirs.

2 INFLUENCE OF ELEVATED TEMPERATURES ON MATERIAL PROPERTIES

2.1 *Mechanical properties*

EN 1992-1-2 [5], EN 1992-3 [6] and FIB Bulletin 55: Model Code 2010 [7] each define the reductions in the mechanical properties of both the concrete and steel reinforcement for elevated temperatures. For the temperature range under consideration for the current study, the associated strength reductions are insignificant. It is reasonable to suggest that any minor reduction in the strength and stiffness of concrete may be discounted when the effect of long term thermal exposure is considered. Mears [8] tested concrete specimens subjected to a constant temperature of 65 °C for 5000 days and observed that the long term exposure had, in fact, the effect of increasing the compressive strength and modulus of elasticity of concrete. The same trend was also recorded by Komendant *et al.* [9] who tested concrete at 71 °C for 270 days and Nasser and Lohtia [10] who tested concrete at 121 °C for 200 days.

It would appear, however, that this trend is only valid for temperatures below 150 °C, as long-term exposure to temperatures in excess of this resulted in a reduction in the mechanical properties of concrete [10, 11].

2.2 *Creep*

Creep of concrete increases at higher temperatures. Extensive research has been carried out on the influence of temperature on concrete creep for structures used in nuclear containment.

It would appear from the literature that the use of a thermal scaling factor, or creep coefficient multiplier, is appropriate in accounting for temperature effects on creep. Figure 1 presents a comparison of creep coefficient multipliers from guidance provided by CEB 208 [12] and FIB Bulletin 55: Model Code 2010 [7] in addition to experimental studies carried out by Brown [13], Gross [14] and Nasser and Neville [15]. For a temperature of 95 °C, the creep coefficient multipliers range from approximately 1.95 to 2.45.

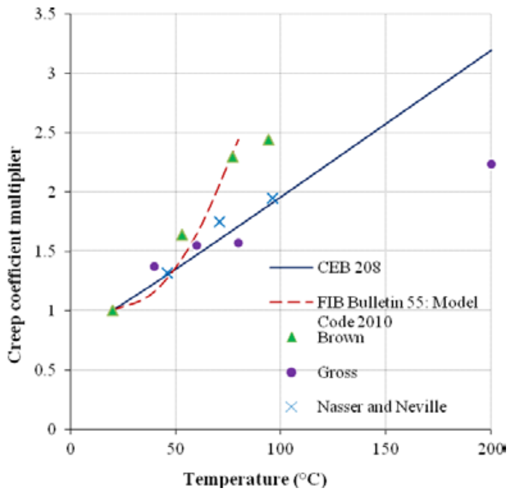

Figure 1. Creep coefficient multipliers with increasing temperature.

An accurate evaluation of creep at elevated temperatures is difficult to attain, as creep is sensitive to the evaporable water in the mix. Consequently, an accurate value of the moisture content is desirable if a precise assessment is to be made. The moisture content, particularly at elevated temperatures, is sensitive to the member thickness. The majority of the experimental results were developed for the walls of nuclear containment structures, which are generally members of wall thicknesses in the range of 1000-1500 mm. Since the walls of precast prestressed storage tanks are much thinner, typically 150-250 mm, the walls would lose much more moisture comparably, which would suggest a lower value of a creep coefficient multiplier may be more appropriate. The experimental results are generally based upon uniaxial tests. As prestressed concrete circular tanks are subject to a multiaxial state of stress, a further reduction in the predicted creep strain would be appropriate, in line with the findings of Hannant [16] and McDonald [17].

2.3 *Bond strength*

Numerous experimental studies conclusively reveal that the bond strength decreases with increasing temperature. This is primarily attributed to the differing coefficients of thermal expansion for steel and concrete. Figure 2 compares test results from studies by Harada *et al.* [18], Kagami *et al*. [19], Haddad et al [20], Chang and Tsai [21], Bazant and Kaplan [22] and Huang [23]. A wide scatter in the residual bond strength ratios (ratio of bond strength of heated specimen to that of a specimen at ambient temperature) is observed. This is primarily due to the many variables involved including concrete mix, compressive strength, exposure duration, method of cooling and bar size.

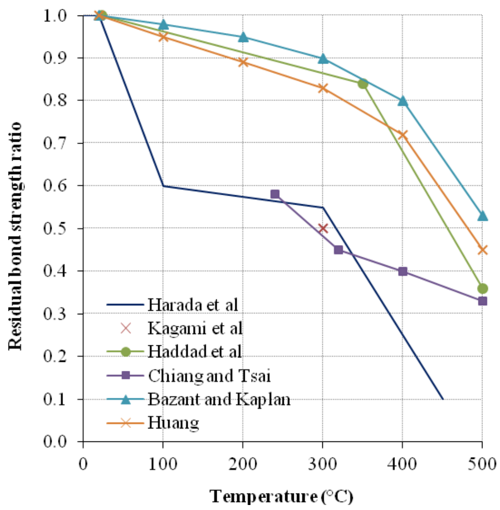

Figure 2. Residual bond strength ratios with increasing temperature.

2.4 *Stress relaxation*

Owing to different coefficients of thermal expansion, steel expands relative to concrete with increasing temperature. Consequently, for pretensioned members, this will effectively increase the loss of prestress due to stress relaxation. FIB Bulletin 55: Model Code 2010 [7] quantifies the increase in loss due to stress relaxation with increasing temperature for a duration of 30 years (Figure 3). The significance of high temperatures on the stress relaxation is evident as a value of approximately 2.5% at ambient increases to approximately 15.0% at a temperature of 100 °C.

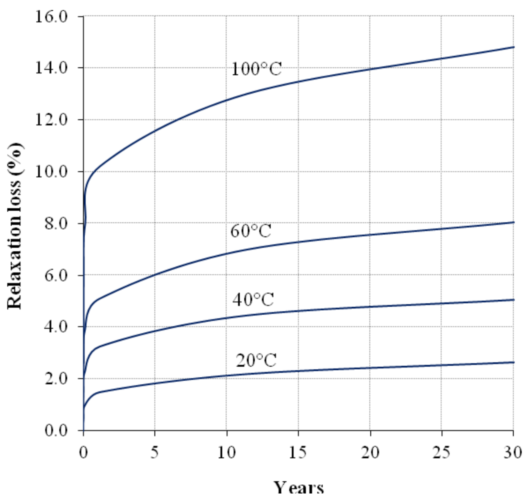

Figure 3. Increase in stress relaxation with increasing temperature, after FIB Bulletin 55: Model Code 2010 [10]

3 FINITE ELEMENT ANALYSIS

Finite element (FE) analysis was carried out to establish the elastic thermal response using LUSAS v14.5 finite element software. The cylindrical structure was idealised using two-dimensional axisymmetric models comprising quadrilateral solid field and continuum elements. The axisymmetric elements comprise four nodes with two degrees of freedom at each node. The thermo-mechanical transient analysis incorporated a semi-coupled procedure and was time-stepped according to pre-defined intervals. A semi-coupled analysis involves running the thermal and structural analyses separately and is conducted when the thermal solution is not considerably affected by changes in geometry. The thermal analysis, which runs first, is governed by the quasi-harmonic transient heat conduction equation. The resulting temperature distribution for a given time step is subsequently fed to the structural analysis for the calculation of displacements and consequent stresses and strains. A maximum element size of 0.3 m was established following a mesh convergence study. The material properties used throughout the finite element study are given in Table 1.

Table 1. Material properties used in finite element study.

Material property	Value
Modulus of elasticity, GPa	33.0
Poisson's ratio	0.2
Coefficient of thermal expansion, /K	10×10^{-6}
Thermal conductivity, W/mK	1.5
Specific heat, J/kgK	900
Convective heat transfer coefficient, W/ m^2K	8.33

3.1 *Verification of modelling procedure*

The modelling procedure was verified with existing ambient temperature results in the literature from Priestley [1] (FE solution), Ghali and Elliott [2] (closed form solution) and Vitharana and Priestley [24] (frame analogy). In each case, the numerical examples considered a tank wall pinned at the base, free at the top and subject to a 30 C ambient temperature gradient. As is evident from Figure 4, good agreement for hoop forces and vertical bending moments was observed in each instance.

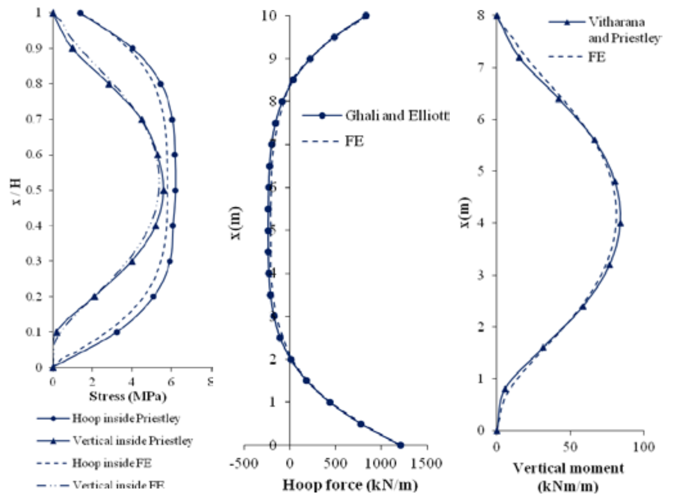

Figure 4. Verification of modelling procedure with Priestley, Ghali and Elliott, and Vitharana and Priestley.

3.2 *Idealisation and boundary conditions*

As precast concrete tanks retaining heated liquids require a roof, the wall ends were restrained from radial displacement but free to rotate. The top of the wall was also free to displace vertically since the strain due to thermal expansion far exceeds that imposed by the self-weight of typical roof construction comprising precast flooring on a grid of columns. Figure 5 shows the mesh discretisation for the axisymmetric models and displays a deformed contour of hoop forces obtained from the structural analysis. The thermal boundary conditions are set up such that there is little temperature difference experienced across the concrete section. In practice, with the provision of adequate external insulation, the concrete section is effectively heated through with the temperature difference predominantly experienced across the insulation layers.

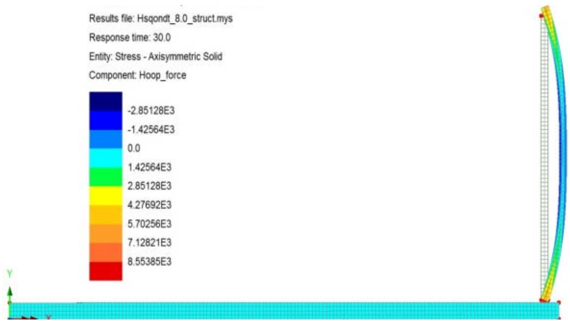

Figure 5. Finite element model showing a deformed contour of hoop stresses (MPa).

4 DESIGN IMPLICATIONS

4.1 *Limiting compressive stress*

For a tank restrained radially at its ends, the hoop force induced by thermal storage is compressive over the entire height of wall and is significant in magnitude. It is necessary to check the resulting compressive stress against limits provided in design standards and guidance. Table 2 presents compressive stress limits from standards and guidance including EN 1992-1-1 [25], BS 8007 [26], PCI [27] and NZS 3106 [3]. The limits are expressed in terms of the concrete cylinder strength, f_{ck}. The limit stipulated by BS 8007 is given in terms of the cube strength, f_{cu}, but an approximate conversion is made here. Although compressive stresses exceeding those given in Table 2 may not lead to failure, non-linearity associated with creep at higher stress-strength ratios would need to be accounted for.

Table 2. Limiting compressive stress at service.

Design standard/guidance	Limiting compressive stress at service
EN 1992-1-1	$0.45\ f_{ck}$
BS 8007	$\approx 0.41\ f_{ck}\ (0.33\ f_{cu})$
PCI	$0.45\ f_{ck}$
NZS 3106	$0.40\ f_{ck}$

Figure 6 gives hoop compressive stresses for various average temperatures for a tank with dimensions D = 30.4 m; H = 7.0 m; t = 0.2 m. A concrete cylinder strength of 40 MPa and a modulus of elasticity of 33 GPa is assumed. These section dimensions and material properties are used for each numerical example presented in this study. As thermal storage tanks commonly incorporate external insulation, the resulting temperature distribution involves predominantly a constant temperature across the concrete section with a small temperature differential. As such, for simplicity, the small differential that may be present is ignored here. Figure 6 shows that an average temperature of approximately 50 C across the concrete section produces localized hoop compressive stresses at the wall ends that exceed each of the limits given in Table 2.

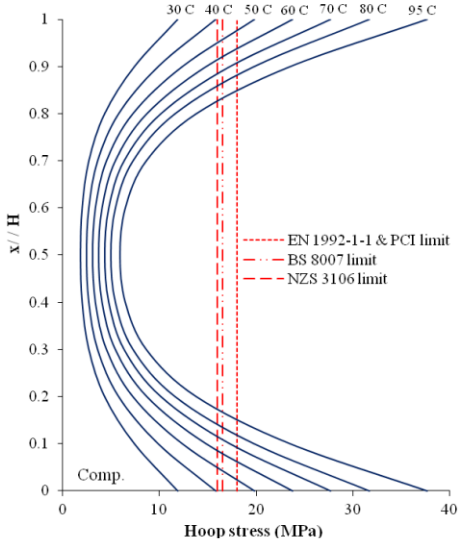

Figure 6. Compressive hoop stresses with increasing temperature.

4.2 *Circumferential post-tensioning*

As the thermally induced hoop forces over the wall height are compressive, the circumferential post-tensioning requirements remain unchanged. The hoop tension arising from hydrostatic loading when the liquid is not heated is the critical loading condition that the circumferential post-tensioning is designed to cater for. Figure 7 includes the tensile force distribution resulting from hydrostatic loading derived using beam-on-elastic foundation analogy.

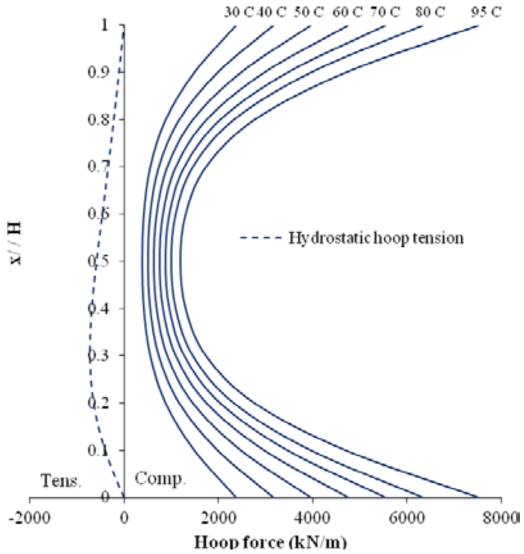

Figure 7. Compressive hoop forces with increasing temperature.

4.3 *Vertical prestressing*

The vertical bending moment distribution arising from hydrostatic and thermally induced loading is given in Figure 8. In order to establish an approximate upper limit on the vertical moments, a cracking moment was calculated from the following equation:

$$M_{cr} = \left(f_t + f_{\max} \right) \left(\frac{I}{t/2} \right) \tag{1}$$

I is the second moment of area, t is the wall thickness, f_t is the concrete tensile strength and f_{max} is the concentric pre-compression stress required to eliminate tensile stresses whilst also satisfying maximum compressive stress limits at the extreme fiber.

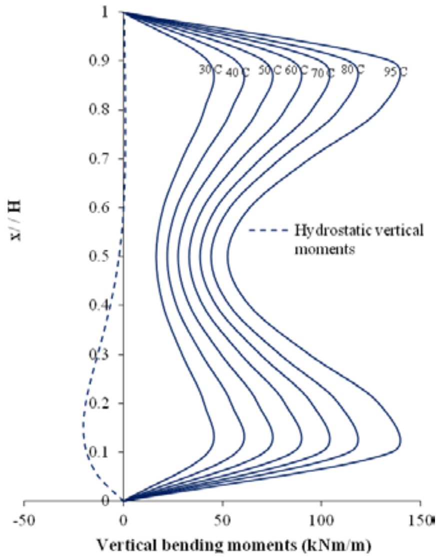

Figure 8. Vertical bending moments with increasing temperature.

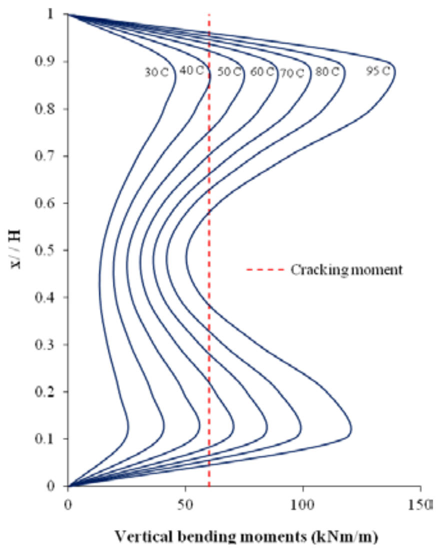

Figure 9. Total vertical moments with increasing temperature.

Figure 9 applies the cracking moment to the previously derived vertical bending moments. The moments represent total moments, that is, the hydrostatic moments subtracted from the thermally induced moments, since the two loadings are coexistent. It is apparent that an average temperature across the concrete section of approximately 40 to 50 C produces vertical moments that exceed the cracking moment.

This temperature limit is approximately consistent with that for the compressive stress requirement.

5 BUCKLING ANALYSIS

It has been established that thermal loading subjects restrained tank walls to significant combined axial compression and bending. Since precast prestressed concrete tanks are essentially shell structures, buckling stability should to be addressed. For relatively stiff structures, linear eigenvalue buckling analysis is a technique that can be applied to approximate the maximum load that can be sustained prior to structural instability or collapse. The underlying assumptions of a linear eigenvalue buckling analysis are that the linear stiffness matrix remains unchanged prior to buckling and the stress stiffness matrix is a multiple of its initial value. Accordingly, provided the pre-buckling displacements from applied loading have an insignificant influence on the structural response, the technique can be used effectively to predict the load at which a structure becomes unstable.

LUSAS v14.5 finite element software was used to carry out the linear eigenvalue buckling analysis. The three-dimensional models comprised thick shell elements. The thermally induced compressive hoop forces and vertical bending moments, derived from the axisymmetric modelling, were simulated using a combination of internal stress-strain loading and externally applied radial pressure loading. The applied loading includes a partial safety factor of 1.55 for persistent thermal actions in accordance with EN 1990 [28] and EN 1991-1-5 [29]. For most structures, it is prudent to include an initial geometric imperfection, as the buckling load is often sensitive to any deviation from the true geometry. Bradshaw [30] made efforts to measure concrete cylindrical shells in the field and concluded that imperfections were observed to be as large as the shell thickness. Therefore, for the current study, an initial geometric imperfection of order of magnitude of the shell thickness was adopted and was represented as out-of-roundness/non-circularity (elliptical).

The mode of buckling obtained from the finite element analysis is given in Figure 10, with the same mode observed for all tank sizes. The buckled shape displays the characteristic sinusoidal buckle waves of a pin-ended tank subject to axial compression.

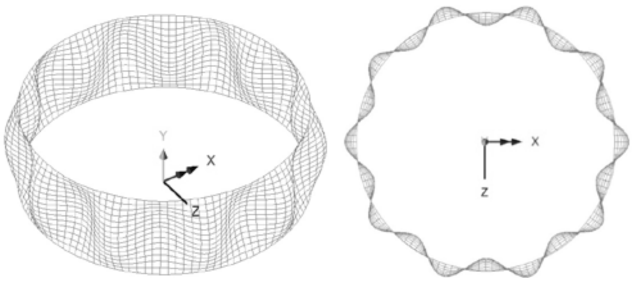

Figure 10. Buckled shape of cylindrical shell restrained at its ends and subject to combined axial compression and bending.

Figure 11 presents the eigenvalues extracted from the finite element study for various constant temperatures across the wall thickness and H^2/Dt ratios. The eigenvalues, λ, are ratios of the buckling load to the applied load. An eigenvalue equal to or less than unity indicates that structural instability or buckling has occurred. The lowest eigenvalue extracted from the buckling analysis was 2.52. Thus, the ULS of buckling was not reached for the temperature range considered.

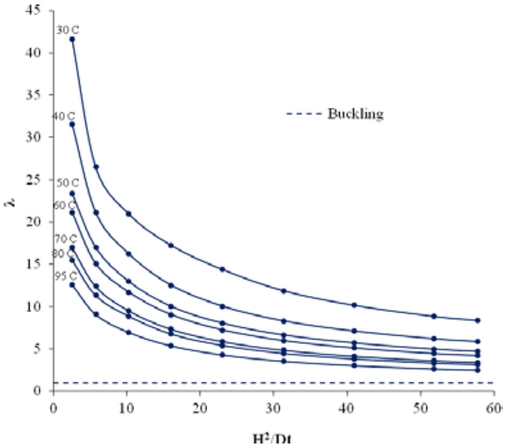

Figure 11. Eigenvalues from finite element linear buckling analysis.

6 FREE-SLIDING CONDITION

Theoretically, for the free-sliding condition, a constant temperature across the concrete section does not induce any additional stresses. For a gradient experienced across the wall thickness, however, associated hoop and vertical bending stresses develop. Figure 12 is an example for a free-sliding wall subject to a temperature distribution resulting from the storage of heated liquids. The inside and outside temperatures are taken as 95 C and 80 C respectively. This arrangement is slightly conservative as the presence of sufficient external insulation would generally result in a temperature difference between the inside and outside faces less than 10 C.

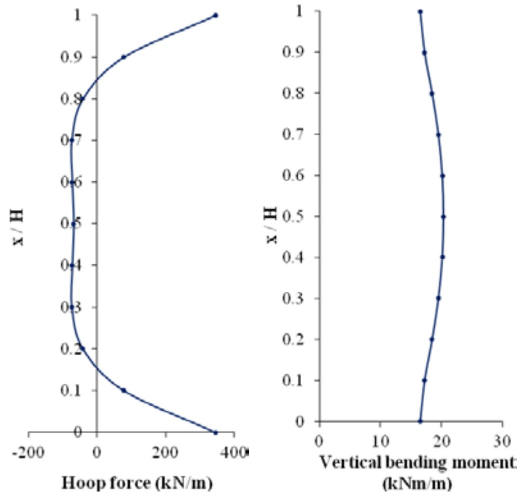

Figure 12. Internal forces resulting from thermal storage for a fee-sliding base.

Comparing the results observed in Figure 12 with those in Figures 7 and 8 it is evident that the magnitude and significance of the internal forces are far less for a free-sliding wall. A noteworthy observation is the hoop tension developed over the majority of the wall height which, although not excessive in magnitude, would need to be summed to the hydrostatic hoop tension when calculating circumferential post-tensioning requirements.

7 CONCLUSIONS AND RECOMMENDATIONS

For the most part, the temperature under consideration for the present study does not have a significant adverse effect on the material properties. The most important factors that require consideration are creep of the concrete, bond strength and stress relaxation for pretensioned and non-pretensioned reinforcement. Where material properties form inputs for analysis and design, any associated reduction should be accounted for, particularly if unfavorable.

For a tank wall restrained radially at its ends, the internal forces resulting from the storage of heated liquids have been shown to be significant. As such, an average temperature exceeding approximately 50 C across the concrete section appears to be prohibitive based upon compressive stress limits and vertical prestressing constraints. Consequently, it is recommended internal insulation be provided to prevent temperatures from exceeding this.

A linear eigenvalue buckling analysis has revealed that the ultimate limit state of buckling for a wall with restrained ends was not reached for the temperature range considered. A minimum eigenvalue of 2.52 was observed.

Where provisions are made for radial displacements at the wall ends during service, the 95 C maximum temperature does not induce excessive stresses. Complications may arise, however, surrounding possible leakage at the joints. Accordingly, it is recommended that a heavy-duty polymer liner be included, thereby eliminating concerns regarding liquid-tightness.

NOTATION

D	= diameter
$E_{c,eff}$	= age-adjusted concrete modulus of elasticity
E_{cm}	= secant concrete modulus of elasticity
f_{ck}	= concrete compressive cylinder strength
f_{cu}	= concrete compressive cube strength
f_{max}	= maximum concentric pre-compression stress
f_t	= concrete tensile strength
H	= wall height
I	= second moment of area
M_{cr}	= cracking moment
R	= radius
T	= wall thickness
x	= height from base of wall
λ	= eigenvalue
$\varphi(\infty, t_0)$	= final creep coefficient

ACKNOWLEDGEMENTS

The research reported in this paper was conducted as part of the taught MEng (Structural Engineering) programme at Cork Institute of Technology.

REFERENCES

[1] Priestley, M. J. (1976), 'Ambient Thermal Stresses in Circular Prestressed Concrete Tanks', *ACI Journal*; 73(10), pp. 553-560.

[2] Ghali, E., and Elliott, E. (1992), 'Serviceability of Circular Prestressed Concrete Tanks', *ACI Structural Journal*; 89(3), pp. 345-355.

[3] NZS 3106, *Code of Practice for Concrete Structures for Retaining Liquid*, Standards Association of New Zealand, 1986, 77 pp.

[4] AS 3735, *Concrete Structures for Retaining Liquids*, Standards Australia, 1991, 40pp.

[5] EN 1992-1-2, *General rules – Structural fire design*, Brussels, Belgium, 2004.

[6] EN 1992-3, *Design of concrete structures, Part 3: Liquid retaining and containment structures*, Brussels, Belgium, 2006.

[7] Fédération Internationale du Béton (FIB*), FIB Bulletin 55 Model Code 2010: Volume 1 First Complete Draft*, Lausanne, Switzerland, 2010, 317 pp.

[8] Mears, A. P. (1972), 'Long Term Tests on the Effect of Moderate Heating on the Compressive Strength and Dynamic Modulus of Elasticity of Concrete', *American Concrete Institute*, SP-34, Volume 1, pp. 355-375.

[9] Komendant, J., Nicolayeff, V., Polivka, M., and Pirtz, D. (1978), 'Effect of Temperature, Stress Level, and Age at Loading on Creep of Sealed Concrete', Douglas McHenry International Symposium on Concrete and Concrete Structures, *American Concrete Institute*; SP-55, pp. 55-81.

[10] Nasser, K. W., and Lohtia, R. P. (1971), 'Mass Concrete Properties at High Temperatures', *Journal of the American Concrete Institute*, SP-26, pp. 180-186.

[11] Carette, G. G., and Malhotra, V. M. (1985), 'Performance of Dolostone and Limestone Concretes at Sustained High Temperatures', *Temperature Effects on Concrete, ASTM STP 858*, T. R. Naik, Ed., American Society for Testing and Materials, Philadelphia, pp. 38-67.

[12] Comité Euro-International du Béton (CEB), *Fire design of concrete structures: in accordance with CEB/FIP model code 90*, Vol. 21 of Bulletin D'Information, Lausanne, Switzerland, 1991, 120 pp.

[13] Brown, R. D. (1968), 'Properties of Concrete in Reactor Vessels', Conference on Prestressed Concrete Pressure Vessels, Westminster; Paper 13, pp. 131-151.

[14] Gross, H. (1975), 'High-temperature creep of concrete', *Nuclear Engineering and Design*, 32(1), pp. 129-147.

[15] Nasser, K. W., and Neville, A. M. (1965), 'Creep of Concrete at Elevated Temperatures', *Journal of the American Concrete Institute*; December, pp. 1567-1579.

[16] Hannant, D. J. (1968), 'Strain Behaviour of Concrete Up to 95°C under Compressive Stresses', *Conference on Prestressed Concrete Pressure Vessels*, Westminster, pp. 177-192.

[17] McDonald, J. E. (1978), 'Creep of Concrete under Various Temperature, Moisture and Loading Conditions', Douglas McHenry International Symposium on Concrete and Concrete Structures, *American Concrete Institute*; SP-55, pp. 31-53.

[18] Harada, T., Takeda, J., Yamane, S., and Furumura, F. (1972), 'Elasticity and Thermal Properties of Concrete Subjected to Elevated Temperatures', *American Concrete Institute*; SP-34, Volume 1, pp. 377-406.

[19] Kagami, H., Okuno, T., and Yamane, S. (1975), 'Properties of Concrete Exposed to Sustained Elevated Temperatures', 3rd International Conference on Structural Mechanics in Reactor Technology; Paper H1/5, London, pp. 1-10.

[20] Haddad, R. J., Al-Saleh, R. J., and Al-Akhras, N. M. (2008), 'Effect of elevated temperature on bond between steel reinforcement and fibre reinforced concrete', *Fire Safety Journal*, Vol. 43, pp. 334-343.

[21] Chiang, C., and Tsai, C. (2003), 'Time-temperature analysis of bond strength of a rebar after fire exposure', *Cement and Concrete Research*, Vol. 33, pp. 1651-1654.

[22] Bazant, Z. P., and Kaplan, M. F. (1996), 'Concrete at high temperature: material properties and mathematical models', Longman Group Limited, England, 1996.

[23] Huang, Z. (2010), 'Modelling the bond between concrete and reinforcing steel in a fire', *Engineering Structures*, Vol. 32, pp. 3660-3669.

[24] Vitharana, N. D., and Priestley, M. J. (1999), 'Significance of Temperature-Induced Loadings on Concrete Cylindrical Reservoir Walls', *ACI Structural Journal*; 96(5), pp. 737-749.

[25] EN 1992-1-1, *Design of concrete structures, Part 1: General rules and rules for buildings*, Brussels, Belgium, 2004.

[26] BS 8007, *Code of practice for design of concrete structures for retaining aqueous liquids*, BSI, London, 1987.

[27] PCI Committee on Precast Prestressed Concrete Storage Tanks. (1987), 'Recommended Practice for Precast Prestressed Concrete Storage Tanks', *Journal of the Prestressed Concrete Institute*; 32(4), pp. 80-125.

[28] EN 1990, *Basis of structural design*, Brussels, Belgium, 2005.

[29] EN 1991-1-5, *Actions on structures – Part 1-5: General actions – Thermal actions*, Brussels, Belgium, 2008.

[30] Bradshaw, R. R. (1963), 'Some Aspects of Concrete Shell Buckling', *ACI Structural Journal*; 60(3), pp. 313-328.

Assessing the performance of structural elements within the Engineering Building at NUI Galway

David Byrne[1], Jamie Goggins[1], Eamonn Cannon[1]
[1]College of Engineering and Informatics, National University of Ireland Galway.
email: david.byrne@nuigalway.ie, jamie.goggins@nuigalway.ie, eamonn.cannon@nuigalway.ie

ABSTRACT: The Engineering building at NUI Galway was officially opened on the 15th July 2011 and it represents a milestone in the construction of engineering educational facilities by incorporating the use of various sensors to create an interactive learning environment for engineering students. A number of these sensors were placed in several major structural elements within the building during construction; namely a novel void form flat slab (the first of its kind to be used in Ireland), a prestressed concrete double tee beam, a prestressed concrete box beam and a structural steel truss. In all over 260 sensors were installed within the various structural elements within the building. The sensors are monitoring the strain and temperature profiles of the structural elements and these are also being complemented by sensors within the Building Management System which are monitoring surrounding environmental conditions such as ambient temperature and relative humidity. The continual monitoring of the sensors has allowed a detailed history of the behaviour of the structural elements to be generated. It has been possible to identify the response of the elements in relation to a number of interesting structural topics. Those of primary interest include the response of the elements to loading events during construction, the time varying behaviour of the concrete elements arising from creep and shrinkage effects, the thermal response of the concrete elements and other topical issues such as the redistribution of forces due to restraint conditions.

KEY WORDS: Structural engineering education; Concrete structures; Instrumentation; Vibrating wire gauges; Void-form flat slabs; Creep; Shrinkage; Thermal mass.

1 INTRODUCTION

At 14,250m^2 the new Engineering building (NEB) (Fig.1) at the National University of Ireland, Galway (NUIG) is the largest engineering school in the country. The building unites all five engineering disciplines within the university into a state of the art academic facility. It provides facilities for over 1300 students, both undergraduate and postgraduate, and includes space for classrooms, laboratories, workshops, computer suites, lecture halls and research facilities. The civil engineering department alone has been provided with high-tech laboratories in specialised areas such as soil mechanics, fluids and hydraulics, timber, structures (heavy and light), concrete and environmental engineering.

The opening of the NEB itself represents a milestone in the construction of engineering educational facilities. It offers a new approach to teaching by incorporating the use of a variety of sensors to create an interactive teaching tool for engineering students. The overall aim is to create a building that is a 'living laboratory' for students. The vision is for a building whereby students can analyse and understand the defining characteristics of a building at first hand and on a personal level. The initiative stemmed from a series of reports [1-2] highlighting the need to provide engineering students with a deeper understanding of the general concepts required in the engineering field. As such data measuring strains, temperatures and movements due to loading of the building, along with its energy demands and performance are all being monitored. These will be used to illustrate structural engineering and building performance concepts in undergraduate teaching but also in the development of full-scale research in these areas. This paper gives an overview of the instrumentation process involved in the NEB, an outline of the concepts to be used in developing the building as a teaching tool for students and also an overview of results from a structural engineering perspective found to date.

Figure 1. The new Engineering building at NUIG.

2 INSTRUMENTATION PROCESS

Previous papers [3-4] have outlined the objectives and benefits of the instrumentation process implemented within the NEB and as such this paper will only give a brief overview of the process involved. The intention when instrumenting the NEB was to monitor as many structural aspects as possible. Structural topics which were highlighted for investigation included the response of the structural elements to dead and live loading; the behaviour of concrete elements in relation to time dependent effects (TDE) such as creep, shrinkage and temperature; possible effects caused by the restraint of support conditions; the load-sharing capacity of elements; the benefit of using concrete to reduce the energy demands of the building by utilising its thermal mass and finally the reduction of embodied energy by using ground granulated blastfurnace slag (GGBS) as a cement replacement. In total four structural elements were instrumented within the building. These included:

- 40-tonne prestressed concrete beam, precast by Banagher Concrete.
- prestressed double-tee unit, precast by Banagher Concrete.
- Cobiax void form flat slab system, manufactured by Oran precast.
- Structural steel truss, manufactured by Duggan Steel.

The prestressed beams were installed with vibrating wire (VW) gauges (Fig.2), the void form flat slab (VFFS) were installed with VW gauges and electrical resistance (ER) gauges, while the structural steel truss was instrumented with just ER gauges. The VW gauges are being used to monitor strain and temperature within the concrete elements, while the ER gauges are being used for monitoring strains on the steel elements. In total over 260 gauges were installed within the different structural elements. Results outlined in this paper will focus on the behaviour of the VFFS system to date.

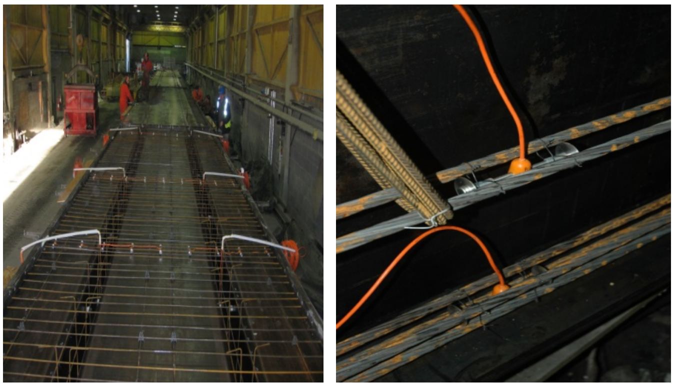

Figure 2. Installation of vibrating wire gauges in the prestressed concrete double tee unit.

2.1 *Void form flat slab*

Void form flat slab systems are an innovative and novel form of flat slab system. They consist of high density polyethylene void-formers, positioned in the middle of a concrete cross section to reduce its overall self weight. Unlike hollow core slabs they manage to maintain full flexural strength, allowing two-way or bi-axial load transfer. The reduction of self-weight, up to 35%, allows for savings in overall materials, reduces overall costs and also permits longer spans allowing for more complex geometry. VFFS's are typically constructed using two methods; traditional in-situ concrete or in combination with pre-cast elements. Those used in the NEB comprised of semi-precast elements (Fig.3).

The slab system instrumented within the NEB consisted of a 7.5x12.65m bay located on the third floor of the building. The slab was constructed using a 65mm thick precast biscuit in combination with a 385mm thick in-situ element; thus giving an overall slab thickness of 450mm. A total of 164 gauges (100 ER gauges and 64 VW gauges) were installed over fifteen sections in the slab. ER gauges were installed on reinforcement bars both in the precast and in-situ elements at five of the sections. The gauges were positioned in the same vertical plane; the idea being to monitor the load transfer between the bars in the in-situ and precast elements. Additional VW gauges were installed in the in-situ element at each of the 15 sections to monitor strains in both the long and short spans. The VW gauges were placed in the top, middle and bottom of the in-situ element so as to give a strain profile across the section. Details of a typical cross-section can be seen in Figure 3.

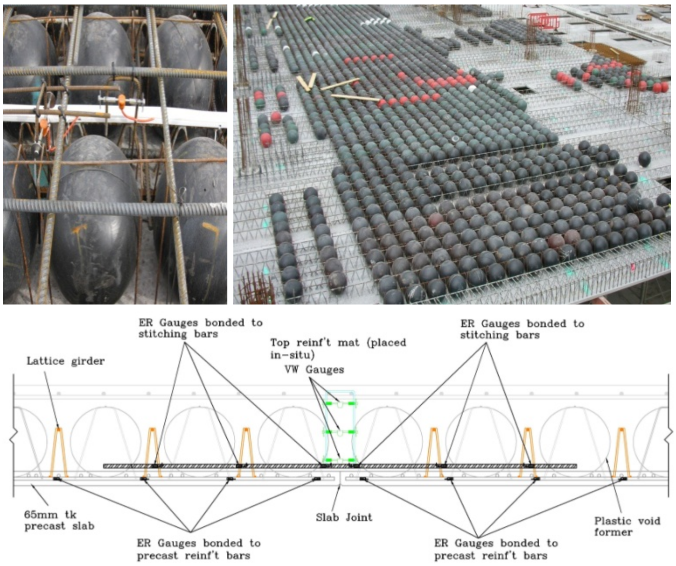

Figure 3. Void form flat slab unit in the NEB (top left), with vibrating wire gauges installed (top right) and a typical cross-section showing layout of gauges (bottom).

3 DEVELOPING THE NEB INTO AN INTERACTIVE TEACHING TOOL

To harness the data from instrumentation of the building a series of methods and procedures are being developed that will help create an interactive environment for the student. At present a 3D Building Information Model (BIM) (Fig. 4) is under construction. The model will show the overall building layout and highlight the location of the various sensors and gauges throughout the building. Users will be able to 'walk through' the model, clicking on relative sensors, bringing up the relevant time history of the sensor showing all the recently collected data. In addition students will be able to access real time data from the building by connecting into data ports located throughout the building. This will allow students to develop their data acquisition and analysis skills. Furthermore, it is envisaged to use the medium of the internet to develop and enhance the Building Management System (BMS) within the structure. At present students can access data recorded from the BMS in a centralised computer located in one of the labs which stores all of the buildings operational data. However by integrating control networks and developing internet protocols users will be able to remotely access the BMS via the internet. This could facilitate the dissemination of data from sensors to a wider audience and not just for students and academic staff on campus.

Figure 4. The 3D BIM model which will be used to provide an interactive environment for students.

One such model is already operational with data from the BMS weather station accessible via the NUIG website and through an Android Smartphone application.

There are also future plans for the creation of interactive structural laboratories for students. Some laboratory experiments require substantial equipment in both size and power. With the implementation of further load cells, gauges and sensors throughout the building it will be possible to develop various models to replicate experiments, which in normal laboratory conditions would be hard to achieve. Recently one of the expansion joints within the building was instrumented to monitor the movement within the building over an extended period of time. Another example utilises a lightweight steel stairs within the building, which has been specifically designed by Arup, structural engineers for the NEB, to be susceptible to footfall-induced vibrations. It will act as a teaching tool, demonstrating the phenomenon of footfall vibrations to engineering students. The vibrations will be monitored through the use of accelerometers and the experiments validated through the use of relevant analytical and numerical models. The measured response of the accelerations obtained using accelerometers will then be made available for the students online. Another possibility for an interactive laboratory is through the instrumentation of the overhead crane in the structures laboratory. This will make it possible to demonstrate to students the theory and concept behind influence lines. The development of these virtual laboratories will also act to complement the evolution of local laboratory exercises. Through virtual laboratories the student will become more engaged; they will play an active role where they can actively manipulate a scenario and analyse the consequences.

A number of the building's constructional elements have consciously been left exposed (Fig.5) to form visual learning tools. Recesses were created to show the reinforcement arrangements in a VFFS, wall and foundation element. The recesses were covered with glass panels and are now visible while walking through the building.

Figure 5. Some of the visual teaching tools in use in the NEB[4].

The final stage in the creation of an interactive environment is through the creation of various teaching and learning tools. One such visualisation tool has already been created and demonstrates the theory and design behind prestressed concrete [5]. These tools will incorporate data obtained from instrumentation and will be similar in principle to other well known teaching tools (such as CALCrete and West Point Bridge Designer). These engineering education software tools will help bring to life engineering concepts that are quite often lost in a normal classroom. Construction drawings are also to be made available to students along with detailed video and photographic records of the construction sequence. These have been compiled into a timeline to help illustrate to students the evolution of a building; from its initial groundworks to the final fitting of equipment and services.

4 RESULTS TO DATE

There has been a wealth of data collected from the NEB to date and this will prove invaluable for research and teaching in a number of engineering disciplines. Stresses and strains within the slab system have been monitored in relation to daily temperature cycles, loading and TDE. Analysis has also been carried out to assess deflections and the thermal properties of the slab system. The following gives an outline of just some of the results found to date in relation to the VFFS system with analysis also ongoing for the other instrumented elements.

4.1 Stresses and strains

The stresses and strains experienced within the slab system to date have been established through interpretation and analysis of site data. The strains have been classified as either stress-dependent or stress independent in line with guidelines issued by FIB [6]. Stress dependent strains are those created as a result of creep and elastic strain, while stress independent strains are those arising from thermal and shrinkage strains. For practical purposes material properties (i.e. compressive strength, tensile strength, modulus of elasticity etc.) were derived in accordance with both BS EN 1992-1-1[7] and ACI 209[8]. At present there is a comprehensive material testing programme ongoing to establish the characteristic properties of the concrete mixes used in the NEB. This will be compared with values obtained from the codes and relevant adjustments made to the calculated stresses and strains in the future. The stresses to date were calculated by multiplying the stress-dependent strain by the elastic modulus as defined in accordance with both BS EN 1992-1-1[7] and ACI 209[8].

The overall stress and strain pattern in the slab followed a typical profile for a flat slab. Peak strains occurred at positions of maximum hogging close to the columns, while maximum sagging moments were found in the centre of the slab. It was noted that the elastic strains due to loading were found to be lower than expected. The highest forces experienced corresponded with the pouring of the overhead slab, which was supported by formwork resting on the instrumented slab. Figure 6 shows a comparison between bending moments experienced in-situ and those from a finite element analysis. They both correspond to bending moments experienced in the longitudinal direction for the central portion of the slab following depropping of the slab on site.

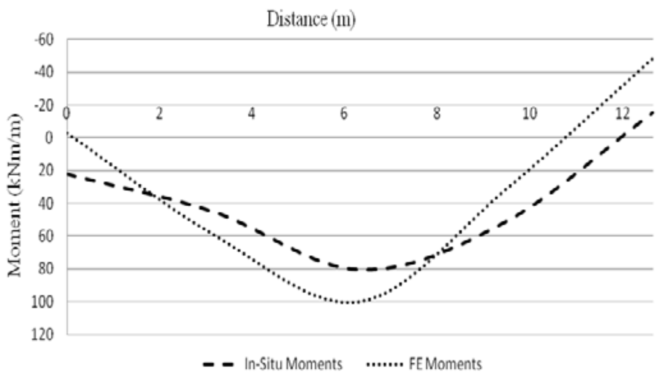

Figure 6. Graph showing comparison between in-situ and finite element moments experienced within the VFFS system.

It is clear to see a close correlation between the results with regard to the maximum sagging moment. Furthermore strains in the vibrating wires close to the columns were high enough to suggest that cracking occurred.

Another interesting realisation was that during the early stages of curing the slab experienced considerably large thermal stresses and strains as it underwent temperature variation due to daily diurnal cycles. Results showed a downwards curling effect occurring at night as the top contracted relative to the bottom and in contrast an upward curling effect during the day with the top expanding relative to the bottom. In some cases these strains exceeded those experienced from subsequent loading events. It was found that the maximum tensile strains experienced across the slab as a result of temperature fluctuation were quite close to the theoretical tensile capacity of the slab and in some cases were slightly exceeded (Fig. 7). This highlights the possibility that cracking may have occurred during the early stages of the slabs life.

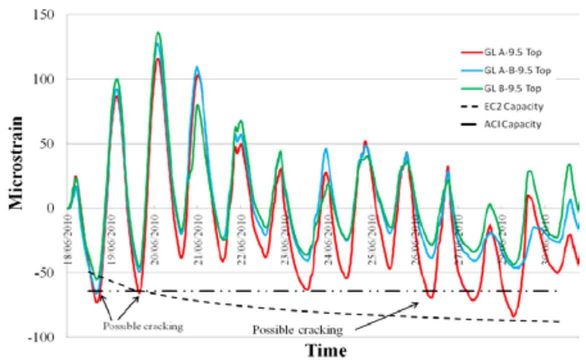

Figure 7. Graph showing strains experienced within the VFFS during initial days of curing and evidence of possible cracking.

4.2 Deflection

The deflections of two-way slab systems, in particular flat slabs, are quite difficult to estimate accurately. The thickness of a slab is often governed by restrictions due to long term deflections under service loads. Deflections are often influenced by varying material properties, location of reinforcement and variability in loading especially during construction. The reduction in stiffness due to the presence of the void formers in VFFS systems means deflection takes on even greater importance. By analysing data from the slab system in the NEB it has been possible to model the deflections experienced. The deflection can be found by finding the strain in the extreme compression fibre by interpolating measured data from the VW gauges. From its location in the section it is possible to calculate the curvature at the given point. By carrying out a series of iterations for the gauges across the slab bay it has been possible to identify the deflection of the slab. Predicted deflections and curvature of the slab were also analysed using the rigorous method outlined by The Concrete Centre's *Technical Report 58* [9]. This method was deemed most suitable as it takes account of loading sequence during construction, reinforcement arrangement, concrete properties and time dependent effects such as creep and shrinkage. To date the deflections lie within those outlined in the code. It must be noted that TDE are having a significant effect on increasing deflection and it will be interesting to monitor the long term deflection in this regard. There are limitations when using the rigorous method, particularly with regard to estimating the tensile strength of the concrete (used in calculating the cracking moment), the elastic modulus and accurately estimating construction loading. Records of construction loading were taken for all the structural elements instrumented in the NEB and when the material testing (as outlined in Section 4.1) is completed it should be possible to get a stronger correlation between predicted and in-situ models. Thus, an accurate numerical model can be created to predict deflections in VFFS.

4.3 Thermal properties

It has also been possible to establish some of the thermal properties of the concrete slab using the temperatures and strains from the embedded vibrating wire gauges. By plotting the total strain versus temperature and calculating its average slope it has been possible to determine the coefficient of thermal expansion of the concrete. The average value across the slab was found to be 8.58 microstrain/°C, which is slightly larger than those quoted in literature[10] for typical limestone concretes. The coefficient of thermal expansion is an important parameter to consider, as strains can be experienced due to the difference between the coefficient for the VW gauges and the corresponding coefficient for the surrounding concrete. These need to be subtracted from the total strains to ensure consistency in the results.

Furthermore, it has been possible to establish the response of the slab in relation to thermal mass. The utilisation of thermal mass is becoming more prevalent as buildings move towards a more holistic design approach. From results (for example Fig.8) it is clear to see a temperature lag between peak ambient temperatures and those experienced within the concrete slab. Measured data has shown that peak temperatures in the slab (top) occur typically five hours after peak ambient temperatures, while temperatures within the middle of the concrete do not peak for a further hour and a half. There was similar correspondence with regard to low temperatures. The difference between ambient temperatures and those within the concrete is also striking and was particularly evident during the early phases of construction when the slab was exposed to direct sunlight. The average ambient temperature change between night and day ranged between 10 to 15°C.

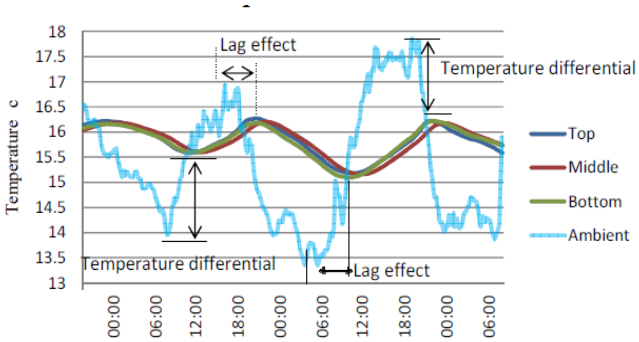

Figure 8. Graph illustrating the response of the VFFS unit with regard to thermal mass.

The fluctuation was much less within the slab with temperatures varying an average of 3°C in the top and middle of the slab and 4°C in the bottom of the slab. This small fluctuation, in comparison to the ambient temperature, is a clear reflection of the ability of the concrete slab to absorb and store heat and its ability to regulate its own temperature.

4.4 Time Dependent Effects (TDE)

Of particular interest are the TDE experienced within the slab system. TDE have long been established as one of the main causes of non-structural cracking in concrete elements and are thus an important consideration in any concrete analysis. Data from the sensors within the slab have been used to establish the short term serviceability behaviour of the flat slab system. The gauges have made it possible to determine how the slab responds to TDE by examining the internal stresses and deformations of the slab to give an improved understanding of its in-situ structural behaviour. The predicted strains outlined in various literature [11-13] and design codes [7-8] were calculated and then compared with the measured strain distributions that occurred within the slab system.

To date it has been possible to establish a clear correlation between creep prediction models and those experienced in-situ. Results show that the in-situ results relate strongly to the models outlined by BS EN 1992-1-1[7] and ACI 209[8]. However, these models do not account for restraints within the slab system such as reinforcement. When comparisons were made taking account of the restraint caused by reinforcement by using transformed section properties and the age adjusted effective modulus it was found that the in-situ creep was greater than expected (Fig 9).

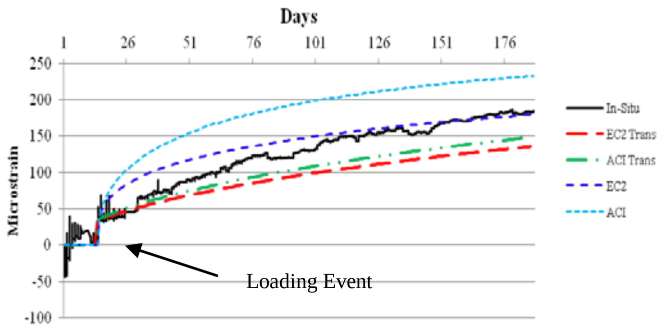

Figure 9. Graph showing comparison between in-situ creep strain and predictive time-dependent models.

At present creep strain is over twice the elastic strain. Long term analysis of creep in the NEB should be able to categorically define whether creep in VFFS's is greater than typical solid slab sections. It was also noted that the creep detected in the areas around columns was significantly reduced; however, this is more than likely due to the dense reinforcement provided in these locations.

Strains caused by in-situ shrinkage have also been determined. Plots (Fig. 10) have shown a decrease in concrete total strain over time even when the temperature cycles are the same. This is evidence of the drying shrinkage effect and the phenomenon was quite clear during the initial days of curing prior to loading of the slab. The drying shrinkage strain was obtained by using the coefficient of thermal expansion of concrete to establish thermal strain and subtracting this from the total concrete strain. It was found that shrinkage strains within the slab were tensile towards the surface primarily due to the fact that these are exposed to a greater rate of drying. It was also found that tensile strains were greater in areas of the slab where a greater percentage of reinforcement was provided (i.e. close to columns), evidence that the presence of reinforcement acts as a restraint to shrinkage.

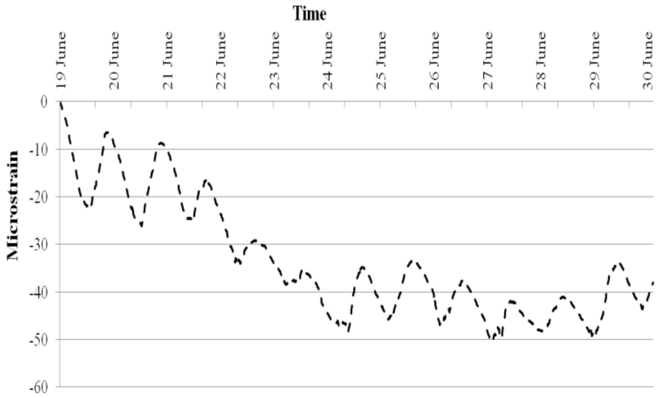

Figure 10. Graph showing the development of in-situ drying shrinkage strain.

5 CONCLUSION

This paper has showed that the data from the instrumentation of the NEB is being successfully used to measure the structural response of a VFFS system. The results to date have helped to give a clear insight into the real time-varying behaviour of the structural elements within the NEB. The gauges, both VW and ER gauges, have performed effectively and the strain readings are highly consistent. They have supplied constructive data in relation to the performance of the VFFS system and all of the instrumented elements within the NEB. Time dependent effects such as creep and shrinkage have been successfully measured along with establishing other properties such as the coefficient of thermal expansion. Important issues such as the deflection of the slab system, distribution of moments and load sharing characteristics have also been successfully monitored.

The data generated has already led to a number of projects being undertaken by final year undergraduate students, allowing these students to achieve a deeper understanding of structural behaviour and the data will undoubtedly form the basis of many postgraduate projects. For example the authors are currently using the data to analyse the behaviour of shear and load transfer in VFFS systems. The research strategy combines numerical simulation using finite element models, data obtained from the field measurements and a comprehensive laboratory testing programme. Essentially the finite element models of the instrumented slab system will be validated by comparison and continual updating of data obtained from measurements on site and from results from laboratory tests. From the in-situ data it will be possible to determine the response of the slab system with regard to TDE such as creep, shrinkage and temperature and the effect these have on load transfer and deformation.

Other future projects include optimising the BMS to minimise the energy usage in the building by utilising the thermal mass of the in-situ concrete together with passive ventilation strategies. Results outlined in Section 4.3 already demonstrate how it has been possible to establish the thermal behaviour of the slab system via the instrumentation process. The idea is to identify the optimal decrement delay and decrement factors to reduce heat gains within the building during the summer but also heat losses during the winter. Comparisons will be made between Computational Fluid Dynamic (CFD) models of the building and the in-situ data. The project itself will help improve the energy efficiency of the NEB but will also act as a demonstrator building to develop the energy management strategy that can be employed in other buildings.

In summary the data will be central in creating interactive teaching tools and facilitating the advancement of engineering education within the NEB. Students will be able to gain an excellent grounding in structural engineering through the development of these new teaching methods. The building represents a new approach to the teaching of engineering students; one which will be central to the continuous development of excellent engineering practice.

ACKNOWLEDGMENTS

A great debt of gratitude is owed to all members of the project team involved in the design and construction of the NEB who have facilitated our work throughout the project. A special mention is owed to the technical staff at NUI Galway for their assistance during the instrumentation process. The first author is extremely grateful for the ongoing support of Arup Consulting Engineers and the Irish Research Council for Science, Engineering and Technology (IRCSET) through the Enterprise Partnership Scheme.

REFERENCES

[1] Royal Academy of Engineering, "Educating engineers for the 21st century," Royal Academy of Engineering, London, 2007.

[2] L. H. Jamieson and J. R. Lohmann, "Creating a culture for scholarly and systematic innovation in engineering education," American Society for Engineering Education, Washington D.C., 2009.

[3] E. Cannon and J. Goggins, "The New Engineering Building at NUI Galway as a Teaching Tool for Structural Engineering," Joint symposium proceedings of BCRI 2010, Cork, Ireland, 2010, pp. 609-617.

[4] J. Goggins, D. Byrne and E.Cannon, "The creation of a ‘living laboratory’ for structural engineering at the National University of Ireland, Galway " *The Structural Engineer*, 2012. vol. 90,(4), pp. 12-19.

[5] E. Cannon, A. McDonagh and J. Burke, "Use of 3D Modelling and Animation in the Teaching of Concrete Structural Design," presented at the Bridge & Infrastructure, Concrete Research in Ireland (BCRI), University College Cork, 2010, pp. 83.91.

[6] Federation International de Béton, *Structural Concrete: Textbook on the behaviour, design and performance* vol. 1, 1999.

[7] British Standards Institution, "BS EN 1992-1-1, Eurocode 2: Design of concrete structures. General rules for buildings," ed, 1992.

[8] American Concrete Institute, "Prediction of creep, shrinkage and temperature effects in concrete structures," in *ACI 209R-92*, ed. Detroit, 1992.

[9] The Concrete Society, "Technical Report No.58: Deflection in concrete slabs and beams," The Concrete Society, 2005.

[10] A. M. Neville, *Properties of Concrete*, Fourth Edition ed.: Longman 1995.

[11] A. M. Neville*, et al.*, *Creep of plain and structural concrete*. New York: Construction Press, 1983.

[12] A. Ghali*, et al.*, *Concrete Structures - Stresses and Deformations*, 3rd Edition ed. New York: Spon Press, 2002.

[13] R. I. Gilbert, *Time Effects in Concrete Structures*. Amsterdam: Elsevier Science, 1988.

Determining the locations of high stresses on a floating concrete structure to aid in the structural health monitoring of wave energy converters

William Finnegan[1], Jamie Goggins[2]
[1]Ryan Institute for Environmental, Marine and Energy Research, National University of Ireland, Galway, Ireland
[2]College of Engineering and Informatics, National University of Ireland, Galway, Ireland
E-mail: w.finnegan1@nuigalway.ie, jamie.goggins@nuigalway.ie

ABSTRACT: A vital aspect of ensuring the cost effectiveness of wave energy converters (WECs) is being able to monitor their performance remotely through structural health monitoring, as these devices are deployed in very harsh environments in terms of both accessibility and potential damage to the devices. Thus, the development of computational methods to continuously assess and monitor these devices through the use of measuring equipment, which are strategically placed on the device, is necessary. In order to achieve this, analysis of the floating axisymmetric concrete structure has been undertaken using a boundary element method. The analysis is carried out over one wave period from crest to crest and over a range of ocean wave frequencies. The locations of these sensors are determined by examining the variance in pressure, or stress, over the submerged surface of a floating structure. The locations of high stresses, or strains, on a given WEC can be taken as key points for the placement of sensors in order to provide efficient structural health monitoring of the structure. In this paper, the methodology for carrying out the analysis and a case study of a floating vertically axisymmetric concrete structure is presented.

KEY WORDS: Boundary element method; Hydrodynamic forces; Offshore structures; Structural health monitoring; Wave energy converters.

1 INTRODUCTION

Ocean wave energy is the latest natural resource to be exploited as a renewable source of energy, while also coinciding with the aim of reducing our reliance on non-renewable energy sources. The concept of harnessing ocean wave energy is by no means a new idea. However, the topic only gained international interest in the 1970's with the publication of Stephen Salter's groundbreaking paper on his Wave Energy Duck[1]. Since then thousands of patents have issued for wave energy converters (WECs), incorporating a variety of methods. However, as of yet, no 'winning' WEC design has being established.

One of the main reasons why this technology is taking time to mature is that there are a number of challenges associated with offshore wave energy that are not present for the other renewable energy sources. These challenges are as follows:

- The loadings on WECs vary greatly and storms can generate loads of up to 100 times greater than the average wave loading.
- Wave energy is most dense in deep waters, which are located far offshore.
- The period of a wave varies over a number of time-steps, e.g. wave-to-wave and season to season.

Therefore, a main aspect in the design of WECs is their survivability and the efficient structural health monitoring of these WECs, once they have been deployed into this harsh environment.

The structural health monitoring of buildings has been undertaken for decades for both economic and social reasons, including health and safety issues. In 2003, Chang et al[2] published a comprehensive review of the damage detection methods in the structural health monitoring of all types of civil infrastructure. In 2004, Guo at al[3] explore the use of improved generic algorithms of structural health monitoring to determine the optimum positioning of sensors and the resulting algorithms are then compared to traditional methods. In 2007, Goggins et al[4] used wavelet analysis to develop a structural health monitoring algorithm to investigate the seismic response of braced frames. In 2007, Brownjohn[5] details the motivations and reasons for the recent increased interest in the structural health monitoring of civil infrastructure and discusses the possible future advances in the area.

Structural health monitoring techniques have also been developed for offshore structures, although not specifically for wave energy converts. For example, in 2003, Nichols[6] experimentally examined the use of low order structural health monitoring techniques on two simple models of an articulated offshore structure undergoing ambient excitation. In 2010, Murawski[7] examined measurement and calculation error estimation and damage detection of offshore structures using traditional fibre optics techniques for damaged and undamaged models.

In order to explore the pressure distribution on a WEC, a numerical hydrodynamic analysis using a boundary element method of the structure can be performed. In recent years, many numerical approaches have been explored and developed in order to explore the wave-structure interaction using a numerical wave tank. For example, in 2000, Contento[8] used a 2-D numerical wave tank, which was based on the BEM technique, to simulate the nonlinear motions of arbitrary shaped bodies in order to develop improved seakeeping techniques. In 2006, Sun and Faltinsen[9] developed a 2-D numerical tank using the boundary element method in order to simulate the impact of a horizontal cylinder on the free surface. In 2007, Ning and

Teng[10] used a three-dimensional higher order boundary element model to simulate a fully nonlinear irregular wave tank. In 2008, Ning et al[11] expanded this study to infinite water depth for nonlinear regular and focused waves. On the other hand, in 2011, Yan and Lui[12] developed a 3-D numerical wave tank using a high-order boundary element method in order to simulate nonlinear wave-wave and wave-body interactions. In 2012, Finnegan and Goggins[13] developed a methodology for generating linear deep water waves and performing wave-structure interaction using finite volume method software to solve the Reynolds' averaged Navier-Stokes equations.

In this paper, the hydrodynamic boundary element method software, ANSYS AQWA[14], is used to determine locations of high stresses, or strains, by examining the variance in pressure, or stress, over the submerged surface of a floating structure. This analysis is carried out over one wave period from crest to crest and over a range of ocean wave frequencies. Particular interest is taken when the structure becomes resonant, as this is when the maximum stresses will occur. Finally, a case study of a floating vertically axisymmetric concrete structure is undertaken and optimum orientation for the placement of sensors is discussed.

2 METHODOLOGY

2.1 Hydrodynamic analysis

The total pressure distribution on a floating structure is defined by Bernoulli's equation[15]:

$$p = -\rho \frac{\partial \Phi}{\partial t} - \rho g z \tag{1}$$

where, p is pressure, ρ is the density of water, g is gravity, Φ is the velocity potential, t is time and z is the downwards distance from the SWL. The first term in Equation (1) refers to the hydrodynamic pressure distribution of the incident wave and the second term in Equation (1) refers to the hydrostatic pressure on the body in still water. Therefore, when performing the hydrodynamic analysis on a floating or fixed structure only the first term is of interest. The velocity potential, Φ, is discretised as follows:

$$\Phi = \Phi_I + \Phi_D + \Phi_R \tag{2}$$

where the incident wave velocity potential is $\Phi_I = Re[\phi_I e^{-i\omega t}]$, the diffraction velocity potential is $\Phi_D = Re[\phi_D e^{-i\omega t}]$, and the radiation potential is $\Phi_R = Re[-\sum_{k=1}^{6} i\omega u_k \phi_R e^{-i\omega t}]$. $i = \sqrt{-1}$, ω is the angular frequency, t is time, u_k is the k-component of the dynamic response of the structure and k = 1,2,3,4,5,6, corresponding to surge, sway, heave, roll, pitch and yaw. The calculation is then divided into two problems: the scattering problem, where the structure is held in a fixed position in the presence of an incident wave, to obtain the diffraction velocity potential and the radiation problem, where the structure is forced to oscillate, to obtain the radiation velocity potential.

In this paper, the numerical method used to perform the hydrodynamic analysis is based on a non-linear approximation, Stokes' 2nd order expansion[16]. Therefore the boundary conditions that need to be satisfied, in the boundary value problem, are: Laplace's equation, the kinematic free surface condition, the dynamic free surface condition, the deep water condition and the structural boundary condition, respectively[17]:

$$\nabla^2 \Phi = 0 \tag{3}$$

$$\frac{\partial \eta}{\partial t} + \frac{\partial \Phi}{\partial x}\frac{\partial \eta}{\partial x} + \frac{\partial \Phi}{\partial y}\frac{\partial \eta}{\partial y} = \frac{\partial \Phi}{\partial z},\ on\ z = \eta(x, y, t) \tag{4}$$

$$\frac{\partial \Phi}{\partial t} + \frac{1}{2}|\nabla \Phi|^2 + g\eta = 0, on\ z = \eta(x, y, t) \tag{5}$$

$$|\nabla \Phi| \to 0,\ as\ z \to \infty \tag{6}$$

$$\frac{\partial \phi}{\partial n} = \begin{cases} 0 & for\ scattering\ problem \\ n_j & for\ radiation\ problem \end{cases} \tag{7}$$

where, η is the vertical elevation of a point on the free surface, n_j is the unit normal in the j-direction, j = 1,2,3,4,5,6, corresponding to surge, sway, heave, roll, pitch and yaw and *(x, y, z)* is the Cartesian coordinate system. The j-component of the excitation force, in the frequency domain, $\hat{F}_{ext,j}$, is calculated from the scattering problem as follows:

$$\hat{F}_{ext,j} = i\rho\omega \int_{S_B} (\phi_I + \phi_D) n_j\, dS \tag{8}$$

where S_B is the wetted surface of the floating structure. The j-component of the radiation force, in the frequency domain, $\hat{F}_{R,j}$, is calculated from the radiation problem and, in turn, the hydrodynamic coefficients, the added mass and radiation damping, are determined as follows:

$$\hat{F}_{R,j} = \rho\omega^2 u_k \int_{S_B} \phi_R n_j\, dS = \omega^2 u_k a_{m,jk} + i\omega u_k \upsilon_{jk} \tag{9}$$

where a_m is the added mass and υ is the radiation damping. The dynamic response of the body can then be calculated using the response amplitude operator (RAO), which is given as:

$$\frac{u_k}{A} = \frac{\hat{F}_{ext,j}/A}{-\omega^2(m + a_{m,jk}) + i\omega\upsilon_{jk} + \tau_{jk}} \tag{10}$$

where A is the amplitude of the incident wave, m is the mass of the structure and τ is the hydrostatic stiffness of the structure.

In order to determine the various velocity potentials and calculate the hydrodynamic coefficients and forces, the boundary element method software, ANSYS AQWA[14], is used. The Green's function equation, the method for which is detailed by Garrison[18], is utilised in order to satisfy the boundary conditions in determining the velocity potentials.

2.2 Structural health monitoring

The hydrodynamic analysis is used to determine the locations of maximum pressure, p_{max}, or maximum stress, and these locations are used as critical locations for the positioning of sensors for the structural health monitoring of the structure. Examples of the type of sensors which can be used to monitor the pressure distribution, or change in force at a point on the structure, are force sensing resistors. These are a polymer thick film device which exhibit a decrease in resistance with an increase in force applied to the active surface. These can also be water proofed so would be ideal for use on a WEC.

The other variable that must be taken into account when optimising the locations of sensors is the wave energy spectrum for the sea, or ocean location, where the WEC is being designed for, as this will define the most probable frequencies that the WEC will be exposed to. Where no wave energy spectrum is available for the design sea, a theoretical spectrum, known as the modified Pierson-Moskowitz Spectrum[19], $S_{PM}(f)$, may be determined using the significant wave height, H_s, and the average period, T_{av}, which is given as:

$$S_{PM}(f) = \frac{A_S}{(2\pi)^4 f^5} \exp\left(\frac{-B_S}{(2\pi)^4 f^4}\right) \qquad (11)$$

where, f is frequency and the coefficients $A_S = \frac{173 H_S^2}{T_{av}^4}$ and $B_S = \frac{691}{T_{av}^4}$.

The maximum pressure, or stress, occurs when the structure is oscillating at resonance and occurs at the still water level at this frequency. Therefore, it is necessary to have one or a number of sensors at the still water level depending on the direction of the incoming wave. The locations of the other sensors are defined by a combination of the factors, which are the locations of maximum pressure and the wave energy spectrum of the design sea.

3 CASE STUDY

In this section, a basic floating concrete wave energy convertor is used to demonstrate the methodology of analysis for structural health monitoring presented in Section 2. The structure has a radius, *a*, of 8 metres with a total draft, *b*, of 20m below the still water level, with the bottom 8m being a hemisphere. The results of the hydrodynamic analysis of the case study are shown graphically in Figures 1 to 3, which details the added mass and radiation damping coefficients, the normalised heave and surge excitation forces and the normalised dynamic response with phase angle, respectively. The wave excitation forces are normalised as follows:

$$\frac{\hat{F}_{ext,j}}{\pi \rho g A a^2} \qquad (12)$$

The normalised maximum pressures and the distances below the still water level at which they occur are detailed in Figure 4 for the WEC under consideration. The maximum pressure is normalised using the following expression:

$$\frac{p_{max}}{\rho g A} \qquad (13)$$

The boundary element method is used to analyse the pressure distribution over the wetted surface of the structure. A wave frequency range, *f*, of *0.02* to *0.25 Hz* is used in the analysis with the water depth set to *1000m* in order to simulate deep water conditions. A range of wave directions are specified with no forward speed and the connection details connecting the structure to the sea floor is specified as the default, catenary data. The structure is a floating structure which is allowed to oscillate in all directions of motion. The centre of gravity of the structure is set equal to its centre of buoyancy and the moments of inertia for the structure are defined via its radii of gyration and coincide with this stipulation.

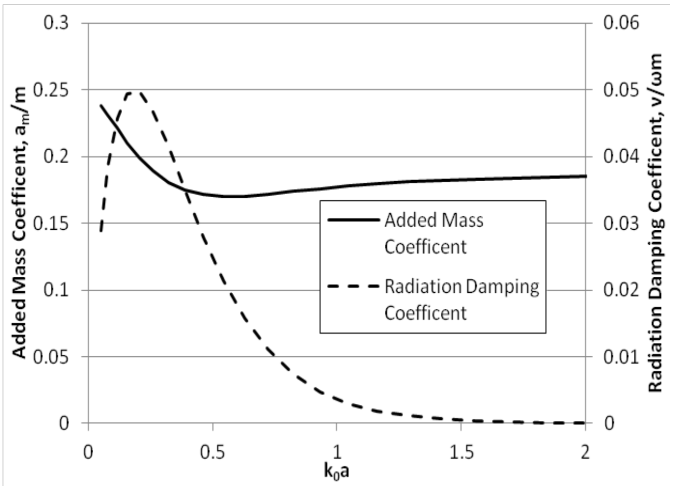

Figure 1. The normalised hydrodynamic coefficients for the case study.

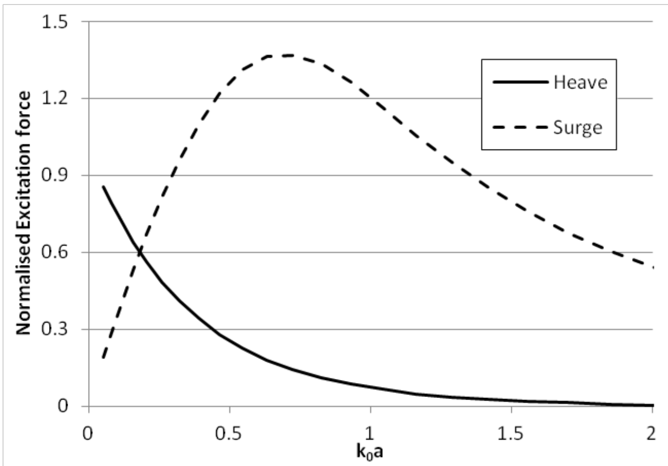

Figure 2. The normalised wave excitation forces, in the heave and surge motion, for the case study.

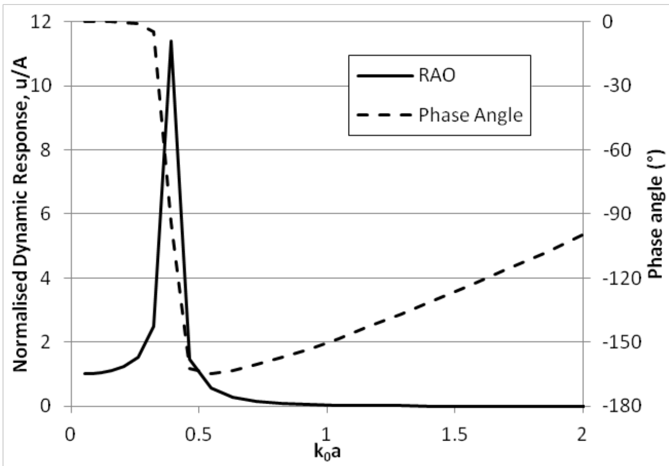

Figure 3. The normalised dynamic response, and its phase angle, for the case study.

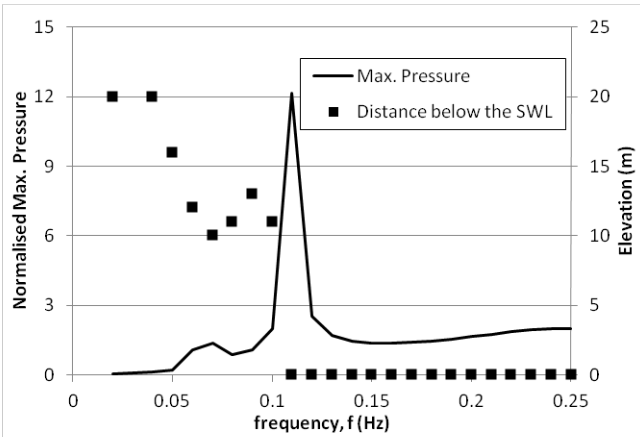

Figure 4. The normalised maximum pressure and depth below the still water level against wave frequency.

The hydrodynamic pressure distribution on the structure is shown in Figure 5 for the case where the structure is oscillating at resonance. A number of elevations are displayed in Figure 5 and this illustrates the importance of the wave direction on the location of maximum pressure. The analysis is performed with an incident wave of amplitude, *A*, of *1m* and the units displayed are Newton's per square metre (N/m^2). Furthermore, Figure 6 details hydrodynamic pressure distribution on the structure for incident waves of different frequencies, above and below the natural frequency. Again, an incident wave of amplitude, *A*, of *1m* is used and the units displayed are Newton's per square metre (N/m^2).

4 DISCUSSIONS AND CONCLUSIONS

As can be seen for Figure 4, the maximum pressure occurs when the structure is oscillating at resonance, when the natural frequency, f_n, of the structure matches the frequency of the incident wave, f,. This occurs at a natural frequency, f_n, of *0.11Hz* for the case study presented in this paper. Furthermore, the hydrodynamic pressure distribution on the structure, when it is oscillating at resonance, is illustrated in Figure 5. Therefore, it is necessary to place sensors at the location where this maximum pressure occurs, which is at the still water level when the wave frequency is the same as or greater than the natural frequency of the device. In the design of WECs, mechanical tuning is used to control or adjust the natural frequency of the converter. One of the design considerations is the avoidance of slamming and this is achieved by restricting the maximum dynamic response of the WEC by detuning away from resonance. However, high pressures will still occur close to resonance, which also can be seen in Figure 4.

It is also noted in Figure 4 that the distance below the still water level where the maximum stress occurs is greatest when the maximum pressure is lowest. In other words, the greater the maximum pressure the closer to the still water level it occurs when the frequency of the waves is less than the natural frequency of the device (i.e. $f < fn$). When the frequency of the waves is equal to or greater than the natural frequency of the device (i.e. $f \geq fn$), the maximum pressure occurs at the still water level. The hydrodynamic pressure

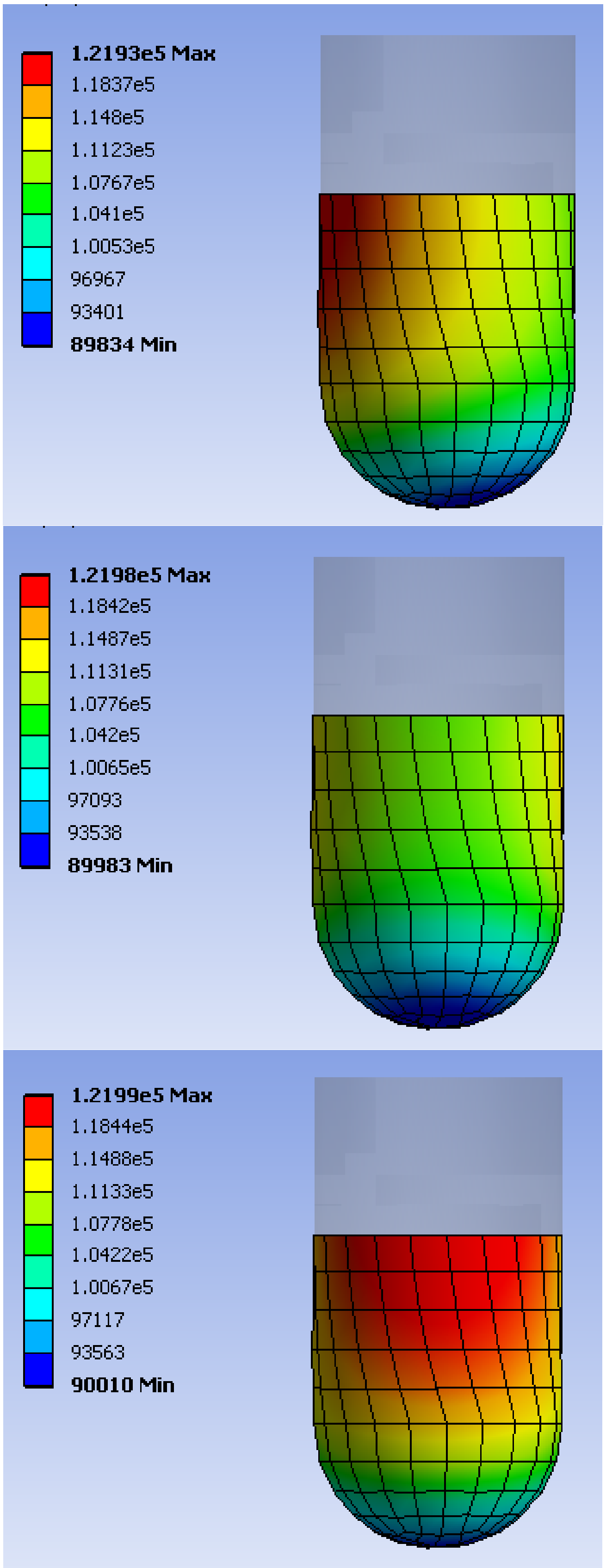

Figure 5. Hydrodynamic pressure distribution on the structure when it is oscillating at resonance with an incident wave coming from left to right. Top: Front elevation. Middle: Right end elevation. Bottom: Left end elevation (Units in N/m^2).

distribution on the structure shown in Figure 6 illustrates this observation for a number of key incident wave frequencies. For a wave of amplitude 15*m*, a maximum pressure of 1.83 N/mm^2 will occur on the structure and this is much lower than the compression strength of the concrete, typically 30 N/mm^2. Therefore, for this case, it is necessary to have a set of primary sensors in place on the structure at the still water level, as when maximum pressure, or stress, is high it occurs at this location. Furthermore, it is necessary to have a set of secondary sensors located 10 to 13*m* below the still water level. Since the maximum pressure below this point is so low compared to that at higher frequencies, this orientation of sensors is sufficient.

ACKNOWLEDGMENTS

The first author would like to acknowledge the financial support from the National University of Ireland under the College of Engineering & Informatics Postgraduate Fellowship.

REFERENCES

[1] Salter S.H., 1974. Wave power. *Nature*. 249(5459): p. 720-724.
[2] Chang P.C., Flatau A., Liu S.C., 2003. Review Paper: Health Monitoring of Civil Infrastructure. *Structural Health Monitoring*. 2(3): p. 257-267.
[3] Guo H.Y., Zhang L., Zhang L.L., Zhou J.X., 2004. Optimal placement of sensors for structural health monitoring using improved genetic algorithms. *Smart Materials and Structures*. 13(3): p. 528.
[4] Goggins J., Broderick B.M., Basu B., Elghazouli A.Y., 2007. Investigation of the seismic response of braced frames using wavelet analysis. *Structural Control and Health Monitoring*. 14(4): p. 627-648.
[5] Brownjohn J.M.W., 2007. Structural health monitoring of civil infrastructure. *Philosophical Transactions of the Royal Society A: Mathematical, Physical and Engineering Sciences*. 365(1851): p. 589-622.
[6] Nichols J.M., 2003. Structural health monitoring of offshore structures using ambient excitation. *Applied Ocean Research*. 25(3): p. 101-114.
[7] Murawski L., Opoka S., Ostachowitz W., *Measurement and calculation errors estimation and damage detection possility analysis for SHM of offshore structure*, in *5th European Conference on Structural Health Monitoring, 2010*. 2010.
[8] Contento G., 2000. Numerical wave tank computations of nonlinear motions of two-dimensional arbitrarily shaped free floating bodies. *Ocean Engineering*. 27(5): p. 531-556.
[9] Sun H., Faltinsen O.M., 2006. Water impact of horizontal circular cylinders and cylindrical shells. *Applied Ocean Research*. 28(5): p. 299-311.Ning D.Z., Teng B., 2007. Numerical simulation of fully nonlinear irregular wave tank in three dimension. *International Journal for Numerical Methods in Fluids*. 53: p. 1847-1862.
[10] Ning D.Z., Teng B., Eatock Taylor R., Zang J., 2008. Numerical simulation of non-linear regular and focused waves in an infinite water-depth. *Ocean Engineering*. 35(8-9): p. 887-899.
[11] Yan H., Liu Y., 2011. An efficient high-order boundary element method for nonlinear wave-wave and wave-body interactions. *Journal of Computational Physics*. 230(2): p. 402-424.
[12] Finnegan W., Goggins J., 2012. Numerical simulation of linear water waves and wave-structure interaction. *Ocean Engineering*. 43(0): p. 23-31.
[13] ANSYS-Inc., *ANSYS AQWA, Release 13*. 2010.
[14] McCormick M.E., 1973. *Ocean Engineering Wave Mechanics*. New York: John Wiley & Sons Inc.
[15] Coastal Engineering Research Center, 1977. *Shore protection manual / U.S. Army Coastal Engineering Research Center*. Fort Belvoir, Va. Washington: Supt. of Docs., U.S. Govt. Print. Off.
[16] Linton C.M., McIver P., 2001. *Handbook of Mathematical Techniques for Wave/Structure Interactions*. Boca Raton, FL: Chapman & Hall/CRC.
[17] Garrison C.J., *Hydrodynamic loading of large offshore structures: three-dimensional source distribution methods citation*, in *Numerical methods in offshore engineering*. 1978, Wiley.
[18] Perez T., 2005. *Ship Motion Control: Course Keeping and Roll stabilisation using Rudder and Fins*. London: Springer-Verlag London Limited.

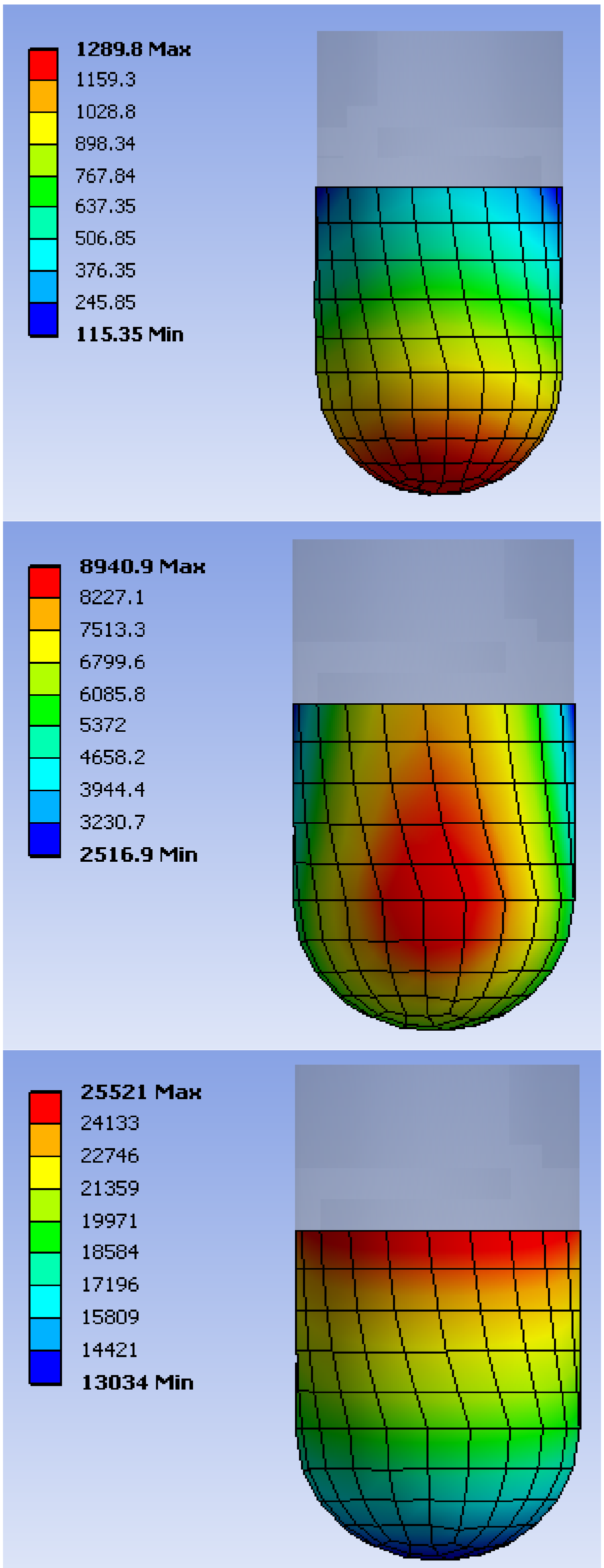

Figure 6. The maximum stress and the locations at which it occurs for incident waves of different frequencies. Top: f = 0.04Hz. Middle: f = 0.08Hz. Bottom: f = 0.12Hz. (Units in N/m^2).

Development of a novel self-centering concentrically braced frame system for deployment in seismically active regions

Gerard O'Reilly[1], Jamie Goggins[1], Stephen Mahin[2]
[1] Civil Engineering, College of Engineering and Informatics, National University of Ireland, Galway, Ireland.
[2] Department of Civil and Environmental Engineering, University of California, Berkeley, California, USA.
email: gerard.oreilly@nuigalway.ie, jamie.goggins@nuigalway.ie, mahin@berkeley.edu

ABSTRACT: Conventional concentrically braced frames (CBFs) undergo many cycles of inelastic deformation during seismic excitation. This inelastic deformation leads to the possibility that after a significant seismic event, the structure will remain in an out of plumb position, even if the system has performed exactly as required by current design codes. This paper presents an improved braced framing system that eliminates such residual deformations of the structure by using a post-tensioning arrangement that will ensure the structure self-centres following an earthquake. This is achieved by combining the bilinear elastic response of the post-tensioning frame with the inelastic behaviour of the tubular steel bracing members to give a system that both dissipates hysteretic energy and ensures self-centering behaviour. The mechanics of the system are first presented along with some simple expressions of the frames behaviour, followed by the development of a numerical model that captures the behaviour of such a system. The results from the numerical model indicate that this self-centering concentrically braced frame (SC-CBF) is capable of undergoing many cycles of inelastic deformation whilst ensuring recentering behaviour. Using this numerical modelling, further analysis can be performed for larger structures using this novel self-centering technology.

KEY WORDS: Braced steel frames; Earthquake engineering; Numerical modelling; Seismic loading; Self-centering.

1 INTRODUCTION

During the design basis earthquake (DBE), most seismic resisting systems are expected to undergo many cycles of inelastic deformation to dissipate energy during a seismic event. For concentrically braced frame (CBF) systems, the dissipating mechanism is the diagonal bracing members, which often consist of steel tubular bracings. These tubular bracings are expected to exhibit inelastic behaviour through tensile yielding and global inelastic buckling. This means that under the DBE, the structure is expected to significantly yield, which can result in large residual deformations throughout the structure. Following an earthquake, these residual deformations can be extremely problematic considering the difficulties associated with attempting to straighten a building that has experienced permanent lateral inter-storey displacements (or drifts) of, for example, 2.5%, which is within codified limits. Furthermore, residual drifts can also reduce the performance of some structural systems during earthquakes.

McCormick et al. [1] conducted a study on residual drifts in structures following earthquakes and concluded that residual drifts greater than 0.5% are perceivable by occupants. It was concluded that in Japan, it was generally cheaper to rebuild the structure rather than attempting to repair if residual drifts present in the structure exceeded this amount. This demonstrates that residual deformations require consideration during the design process. Attempts have been made by Erochko et al [2] to estimate the residual drifts in a structure following the DBE and how to incorporate these into the initial design process. An alternative approach has been to develop systems that inherently re-center following seismic events. These systems have been called self-centering systems and have been present in seismic design since the construction of the bridge over the South Rangitikei bridge in New Zealand in 1981.

Major development in self-centering systems was completed during the early 1990's through the PRESSS initiative, where self-centering concrete frame and wall systems were developed by use of unbonded post-tensioning (PT) to combine the dissipative behaviour of the concrete system with the elastic restoring force of the PT arrangement to give the 'flag-shaped' hysteresis loop (Figure 1.). This concept has been extensively developed for concrete [3, 4], steel [5, 6, 7, 8] and timber systems [9] for use in seismic zones. The focus of this paper is to introduce a new self-centering concentrically braced frame (CBF) that exhibits self-centering behaviour through a PT arrangement and dissipates hysteretic energy through inelastic yielding and buckling of the tubular bracing members. The general arrangement and behaviour is first described followed by the development of a numerical model to demonstrate the behaviour under cyclic loading and how self-centering behaviour is always achieved under numerous cycles of inelastic deformation.

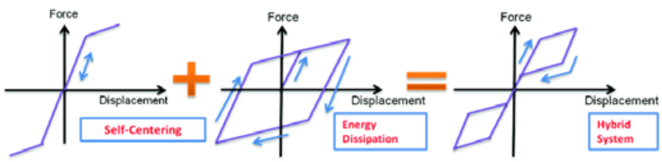

Figure 1. Flag Shaped Hysteresis Loop.

2 SELF-CENTERING SYSTEMS

2.1 *Introduction*

Numerous self-centering systems have been developed in earthquake engineering since the inception of the PRESSS program to apply the PT technology to systems to give self-centering behaviour. One of the principle ways to achieve this self-centering is through gaps opening during loading in areas such as wall-floor interface [10], or in the beam-column interface [6, 7, 8, 9], where the gap opening is forced closed by the post-tensioned cables that act across the connection to give self centering, while the structure deformation causing this gap opening also causes the inelastic behaviour of the dissipative system. For steel systems, the most common method of post-tensioning has been to post-tension the beam column connection, where different systems differ by the means to which they dissipate energy, as the PT arrangement must remain elastic to achieve self-centering. Many of these systems [6, 7, 20] are adaptations of the traditional moment resisting frame system, while [8] uses shear plate wall system to dissipate energy.

2.2 Self-Centering Concentrically Braced Frame (SC-CBF)

This paper presents a new system for CBF similar to the aforementioned self-centering systems that combine the rocking beam-column connection with a dissipative mechanism, where for this SC-CBF system, the diagonal bracings are the dissipating elements. Figure 2 shows the general arrangement of the system, which consists of a 2 bay CBF that has an additional PT element added to the beams and is anchored at the columns to re-center the system. The hysteretic behaviour of this SC-CBF is shown in Figure where it can be seen that the combined hysteresis of both the braces and the PT elements gives the flag-shaped hysteresis described earlier.

The self-centering behaviour of the SC-CBF primarily depends on the compressive resistance of the brace, where if more slender braces are used, the brace buckles quite early and the level of PT required to ensure that the force at point 5 in Figure is greater than zero is less than that what would be required if a more stocky brace was used and the compressive resistance was higher. Another key feature of the SC-CBF is the connection detail of the gusset plates, where traditionally gusset plates are connected using either welds or bolts to both beam and column.

By connecting the gusset plates to both beam and column in the SC-CBF, this would result in a restraint on the rocking behaviour of the beam column connection, which is paramount to the self centering behaviour of SC-CBF. To avoid this, a longer bay width may be used to result in the use of gusset plates connected only to the beam and not the column. Ongoing experimental testing and numerical modelling at NUI Galway [11] for the behaviour and design of these beam only gusset plate connections is being conducted, so the design and detailing of these gusset plates is not discussed here.

Another feature of using wider bay braced frames is that the effective length of the brace increases, therefore increasing its slenderness and decreasing its compressive buckling load, which has already been deemed to be advantageous in SC-CBFs as the level of PT required is reduced with increased slenderness.

3 SC-CBF HYSTERETIC PROPERTIES

This section describes the construction of the hysteretic response of the SC-CBF shown in Figure 3, by examining the response of the individual contributions. First the force-deformation relationship for the braces is examined, followed by the initial frame response before decompression of the rocking connection and the post-decompression stiffness of the system.

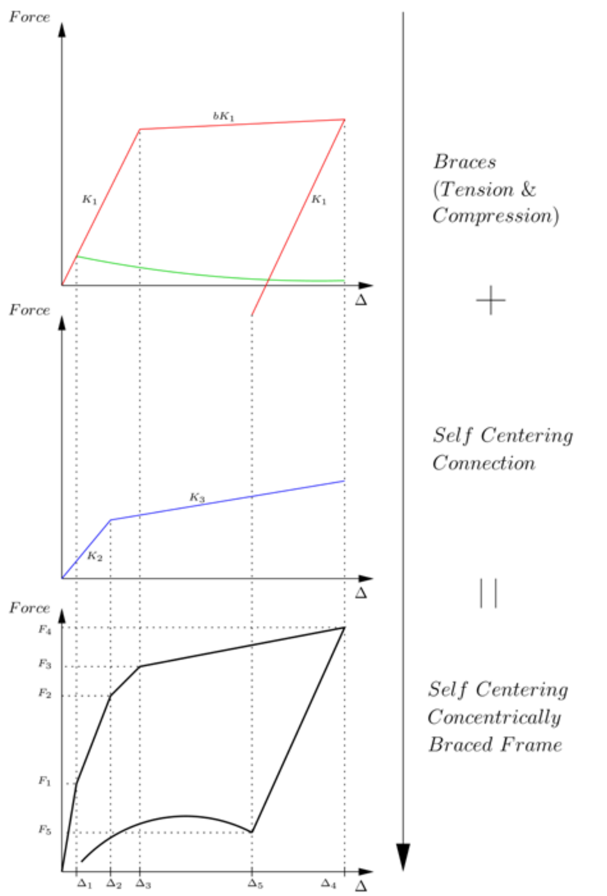

Figure 3. Combined hysteretic response of the SC-CBF.

3.1 Brace Response

For a frame similar to that in Figure 2, but with no PT arrangement and only simple connections, the quantities K_1 and Δ_1 can be determined. The initial lateral stiffness K_1 can be derived to be the following:

$$K_1 = \frac{A_{br}EB^2}{L^3} \tag{1}$$

where A_{br} is the area of the tension brace, E is the Young's Modulus, B is the bay width and L is the length of the brace member. The corresponding displacement Δ_3 at which the braces yield in the frame is given by:

$$\Delta_3 = \frac{f_y L^2}{BE} \tag{2}$$

where f_y is the yield strength of the steel tubular member. The contribution of the compression brace to the response of the frame is a function of the brace slenderness. In addition to this, during seismic loading, the braces will have undergone many cycles of tensile yielding and inelastic buckling. The

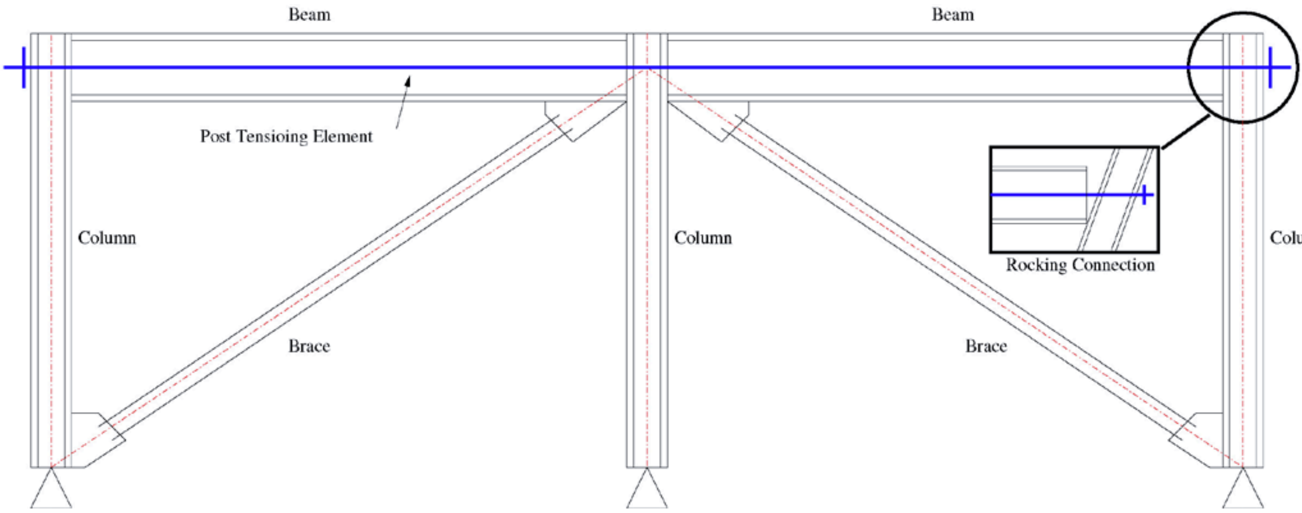

Figure 2. General arrangement of SC-CBF.

buckling load may be determined using the Euler buckling formula, but during inelastic buckling cycles the actual resistance is significantly less. The contribution of the buckled brace has been experimentally investigated by many [12, 13, 14, 15] with equations developed that are a functions of both displacement ductility and brace slenderness. For example, Wijesundara [14] suggested that 25% of the buckling load of the brace be considered in the response of the frame, while Goggins [12] suggested 33% of the brace buckling capacity be included up until a non-dimensional slenderness ($\overline{\lambda}$) of 2.4, with no contribution being added for higher slenderness values. This is an important factor in the design of SC-CBFs where it is necessary to ensure that the inelastic buckling capacity is less than restoring force being provided by the post-tensioned connection.

3.2 *Rocking frame response*

Prior to decompression, the SC-CBF without any bracing members will behave as a moment frame, so the initial stiffness K_2 can be determined using the principle of virtual work. For the frame in Figure 2, this can be determined as:

$$K_2 = \left[\frac{H^3}{8EI_C} + \frac{H^2 B}{24EI_B}\right]^{-1} \tag{3}$$

where H is the height of the frame and I_C and I_B are the second moment of area of the column and beams respectively. The corresponding displacement at which the response of the frame changes to post decompression stiffness depends on the level of PT applied to the frame and the depth of the beam. The compressing moment given by an initial PT force P_{T0} on a beam with height b_h is given by:

$$M_c = P_{T0}\frac{b_h}{2} \tag{4}$$

Assuming that the four connections will develop similar moments simultaneously at decompression, then:

$$4M_c = K_2\Delta_2 H \tag{5}$$

which can then be rearranged to give and expression for the roof displacement at which decompression occurs:

$$\Delta_2 = \frac{2P_{T0}b_h}{K_2 H} \tag{6}$$

Following decompression, the stiffness of the frame depends on the forces generated in the PT elements as the gap opening at the rocking at the connection results in an increase in the PT force P_T. Christopoulos [21] derived an expression for the increase in PT forces due to the gap opening and expansion of the frame. Using this derivation, the increase in PT force as function of relative rotation at the connection θ can be expressed as

$$P_T = P_{T0} + 2K_{PT}\left(1-\frac{1}{\Omega}\right)b_h\theta \tag{7}$$

where Ω is given by:

$$\Omega = 1 + \frac{K_b}{(K_c + 2K_{PT})} \tag{8}$$

and K_B, K_C and K_{PT} are the stiffness's of the beam, column and PT elements, respectively. This can then be arranged to give an expression for the post decompression stiffness K_3 as follows:

$$K_3 = 4K_{PT}\left(1-\frac{1}{\Omega}\right)\frac{b_h^2}{H^2} \tag{9}$$

4 NUMERICAL MODELLING OF SC-CBF

A numerical model for the SC-CBF has been developed that captures the behaviour of both the rocking frame and the braced frame. The model is developed using OpenSees [16], which is an object oriented open source framework. Numerous publications are available [14, 17, 18] on how to accurately capture the behaviour of tubular bracing members subjected to cyclic loading. These models have been calibrated against numerous experimental test results for validation and are used herein as the modelling parameters for the bracing members in the SC-CBF.

The rocking frame is a relatively new concept in steel systems and has been in use for various steel self-centering systems [6, 7, 8]. The modelling of this has been discussed by Christopoulos and Filiatrault [19], where they developed a model consisting of a bilinear elastic rotational spring to represent the rocking behaviour of the connection. A more realistic approach that has been used by many researchers [6, 7, 8] is to use a series of contact springs and rigid links to represent the rocking of the beam against the column during cyclic loading. Figure 4 shows the basic arrangement, where the rigid links are used to represent the face of the column and also the face of the end of the beam. Using as series of contact springs, the rocking of the connection can be modelled. Further details on this connection model that accounts for beam depth can be found in [20]. Figure 5 shows the complete model used for the SC-CBF, where the bracing members are connected to the beams, as for beam-only gusset plate connections. This modelling procedure has been verified against existing experimental data by [6, 7], where the post-tensioned rocking connection was tested under cyclic loading. Using the modelling procedure discussed here for the rocking connection, these experimental results were closely replicated numerically using OpenSees, therefore validating this approach to modelling the rocking connection, and hence is used for the modelling of the SC-CBF.

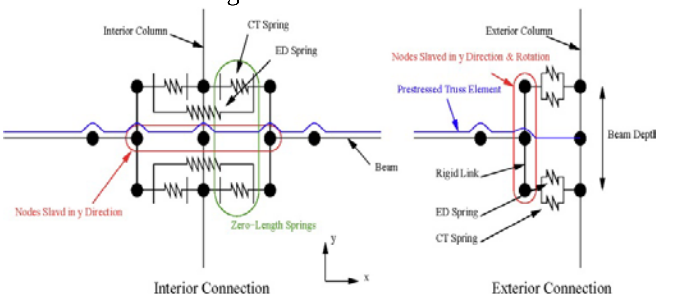

Figure 4. PT connection accounting for beam depth (Adapted from [19]).

5 CYCLIC LOADING

Using the numerical model previously discussed, a simple single-storey frame is examined to observe the behaviour of the SC-CBF under cyclic loading. An example SC-CBF similar to Figure 2 using *HE320A* members for the columns, *IPE600* members for the beams, *100x100x8-SHS*-S275 braces and two no. 30*mm* diameter cables with a initial PT force of 500*kN* is analysed by cycling it through a series of cycles corresponding to 0.5, 1, 2, 3 and 4% interstorey drift. The results of this simulation are shown in Figure 6, where it can be seen that the flag-shaped hysteresis is achieved through the combination of the PT and the brace response. It is evident that the relatively low contribution of the brace in compression is advantageous in terms of achieving the flag-shaped loop. This bracing used here corresponds to a non-dimensional slenderness ($\bar{\lambda}$) of 1.92, assuming an effective length factor of 0.9, which is a more slender brace than what would typically be used in CBFs. Also shown in Figure 6 is a plot of the expressions developed in Equations (1) to (9), where it can be seen that these expressions produces hysteretic loops that closely matches those of the numerical simulation using Opensees.

6 CONCLUSIONS

A new arrangement for CBFs has been introduced where PT elements were used to provide a bilinear elastic restoring force to the system during cyclic inelastic loading of the braced frame. It has been shown how the response of the single storey SC-CBF is that of a flag shaped hysteresis loop. Thus, during seismic loading, the occurrence of residual interstorey drifts due to inelastic behaviour of the bracing members will be prevented. A numerical model of the SC-CBF was developed where this flag shaped hysteresis was observed using modeling procedures that have been extensively examined for traditional CBFs, and also experimental data to validate the use of the rocking connection model. From these results, this new SC-CBF system can be further developed into a new seismic resisting system with superior overall performance of traditional CBFs.

ACKNOWLEDGMENTS

The first author acknowledges the funding provided by the Irish Research Council for Science Engineering and Technology (IRCSET).

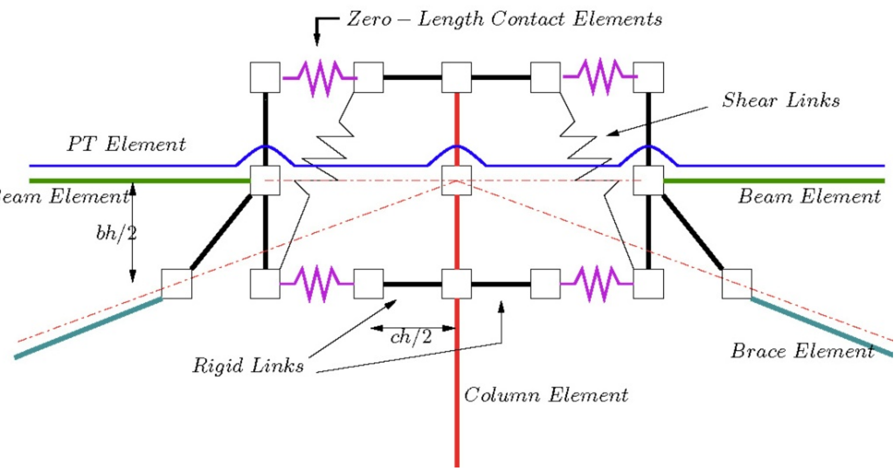

Figure 5. SC-CBF model arrangement.

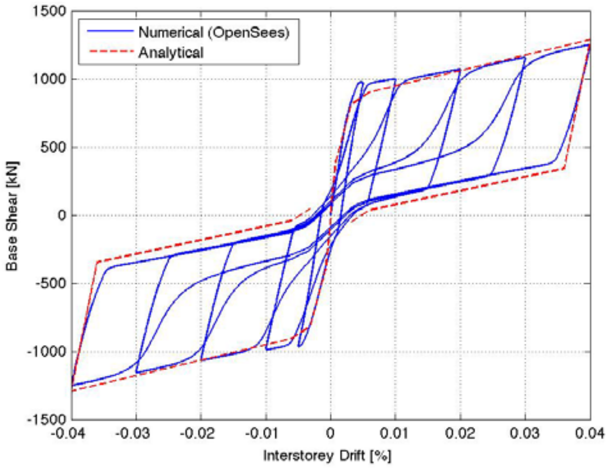

Figure 6. Force-deformation of 1-Storey SC-CBF.

REFERENCES

[1] J. McCormick, H. Aburano, M. Ikenaga, and M. Nakashima. *Permissible residual deformation levels for building structures considering both safety and human elements*. In Proceedings of the 14th World Conference on Earthquake Engineering, Beijing, China, 2008.

[2] J. Erochko, C. Christopoulos, R. Tremblay, and H. Choi. Residual drift response of SMRFs and BRB frames in steel buildings designed according to ASCE 7-05. *Journal of Structural Engineering*, 137(5):589-599, 2011.

[3] Golden Bay Cement. *PRESSS technology seminar gets enthusiastic support in New Zealand.*, 27/05/2011 2011.http://www.goldenbay.co.nz.

[4] R. S. Henry. *Self-Centering Precast Concrete Walls for Buildings in Regions with Low to High Seismicity*. PhD thesis. University of Auckland, New Zealand. 2011.

[5] J.M. Ricles, R. Sause, M.M. Garlock, and C. Zhao. Post-tensioned seismic-resistant connections for steel frames. *Journal of Structural Engineering*, 27(2):113-121, 2001.

[6] M.M. Garlock. *Design, Analysis, and Experimental Behaviour of Seismic Resistant Post-Tensioned Steel Moment Resisting Frames*. PhD thesis, Lehigh University, Lehigh, PA, USA, 2002.

[7] C. Christopoulos, A. Filiatrault, Chia-Ming Uang, and B. Folz. Post-tensioned energy dissipating connections for moment-resisting steel frames. *Journal of Structural Engineering*, 128(9):1111-1120, 2002.

[8] P.M. Clayton, J.W. Berman, T. Winkley, and L.N. Lowes. *Development of a self-centering steel plate shear wall*. In Proceedings of the 8th International Conference on Urban Earthquake Engineering, Tokyo Institute of Technology, Tokyo, Japan., March 7th - 8th 2011.

[9] M. Newcombe. *Seismic Design of Multistorey Post-Tensioned Timber Buildings*. Master's Thesis. European Centre for Training and Research in Earthquake Engineering (EUCENTRE), Pavia, Italy. 2007.

[10] D. Roke, R. Sause, J.M. Ricles, C.Y. Seo, and K.S. Lee. *Self-centering seismic-resistant steel concentrically-braced frames*. In Proceedings of 8th US National Conference on Earthquake Engineering, San Francisco, USA., 2006.

[11] J. English. *Seismic Design of Gusset Plate Connections for Braced Frames*. PhD thesis, National University of Ireland, Galway,Ireland, (Under Preparation).

[12] J.M. Goggins, B.M. Broderick, A.Y. Elghazouli, and A.S. Lucas. Experimental cyclic response of cold-formed hollow steel bracing members. *Engineering Structures*, 27(7): 977-989, 2005.

[13] A.M. Remennikov and W.R. Walpole. A note on compression strength reduction factor for a buckled strut in seismic-resisting braced system. *Engineering Structures*, 20(8): 779-782, 1998.

[14] K.K. Wijesundara. *Design of Concentrically Braced Steel Frames with RHS Shape Braces*. PhD thesis, European Centre for Training and Research in Earthquake Engineering (EUCENTRE), Pavia, Italy, 2009.

[15] R. Tremblay. *Inelastic seismic response of steel bracing members. Journal of Constructional Steel Research*, 58(5-8):665-701, 2002.

[16] F. McKenna, G. Fenves, F. Filippou, and S. Mazzoni. *Open system for earthquake engineering simulation (OpenSees).* http://opensees.berkeley.edu/wiki/index.php/Main_Page, 2000.

[17] S. Salawdeh. *Seismic Design of Concentrically Braced Steel Frames*. PhD thesis, National University of Ireland, Galway, Ireland, 2012.

[18] P. Uriz and S.A. Mahin. *Towards earthquake resistant design of concentrically braced steel structures*. Technical Report 2008/08, Pacifc Earthquake Engineering Research Center, 2008.

[19] C. Christopoulos, A. Filiatrault. *Principles of Passive Supplemental Damping and Seismic Isolation*. 1st Ed. IUSS Press, Pavia, Italy. 2006.

[20] H.J. Kim and C. Christopoulos. Numerical models and ductile ultimate deformation response of post-tensioned self-centering moment connections. *Earthquake Engineering & Structural Dynamics*, 38(1):1-21, 2009.

[21] C. Christopoulos. *Self-Centering Post-Tensioned Energy Dissipating (PTED) Steel Frames for Seismic Regions*. PhD Thesis. University of California, San Diego, California, USA. 2002.

Experimental and finite element study of the loading response of steel trimmer brackets incorporated within hollow core floor slabs

D.F. Hodge[1], B.D. O'Rourke[1], J.J. Murphy[1] & J.R. Harrington[2]
[1]Department of Civil, Structural & Environmental Engineering,
[2]School of Building & Civil Engineering,
Cork Institute of Technology, Bishopstown, Cork, Ireland.
email: david.hodge@cit.ie, brian.orourke@cit.ie

ABSTRACT: Precast concrete flooring currently accounts for more than 50% of the floor and roof systems in modern commercial and domestic buildings, with a large proportion of these being constructed using pre-stressed hollow core slabs. Within these floors substantial openings may be required for stairs, services, skylights, etc. These can be formed using steel trimmer brackets, which support a shorter slab, thereby providing an opening. To date there is a lack of published guidance on the analysis and design of these brackets. This paper describes an experimental and finite element study of these brackets.
The aim of this study was to ascertain the load that causes bracket failure, and to compare this to the loads applied to a bracket within a HC floor system. The finite element program LUSAS (Version 14.5.2) was used to create three dimensional volumetric finite element models to replicate the structural response of the trimmer brackets. The trimmer brackets were modelled using a non-linear steel material model, which can accurately model the yielding and strain hardening of the steel. The brackets were modelled both individually and as part of a complete three dimensional floor system. Experimental testing was undertaken on trimmer brackets for a 150mm x 1200mm floor slab, with the results being used as a means of verification of the finite element models.

KEY WORDS: Trimmer brackets; Hollow core floors; Finite element analysis; Precast concrete; LUSAS.

1 INTRODUCTION

Precast concrete flooring currently accounts for more than 50% of the floor and roof systems in modern commercial and domestic buildings worldwide, with a large proportion of these being constructed using pre-stressed hollow core (HC) slabs [1]. Precast concrete HC floors contain a number of individual HC slabs, which are placed alongside each other and joined with a concrete / mortar joint to create a floor diaphragm. Within these floors large openings may need to be created to facilitate stairs, services, skylights etc. These openings may be formed using steel trimmer brackets, which support a shorter slab, thereby providing an opening. Figure 1 shows an example of an opening being created for a stairs using two trimmer brackets.

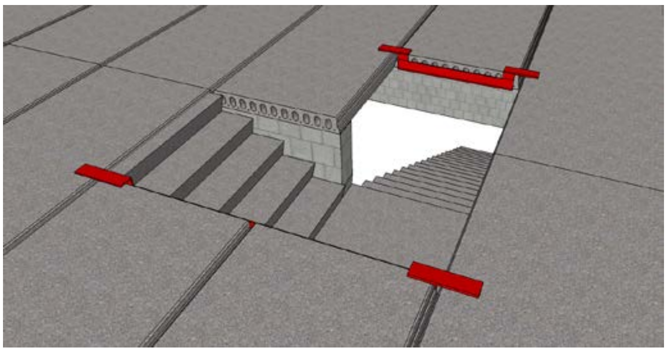

Figure 1. Trimmer brackets to create a stairs opening.

The brackets are generally fabricated by the precast concrete manufacturer from steel equal angle sections and plates. The openings are formed while the slabs are being placed. Brackets are fabricated for different widths and depths of slab and can be fabricated to support either one or two slabs as shown in Figure 1.

Currently there is a lack of published guidance on the design and analysis of these brackets. They are mentioned in design documents such as the Precast / Prestressed Concrete Institute (PCI) manual for the design of HC slabs [2] and other research [3], but little design guidance is provided.

Heretofore, finite element (FE) modelling of HC floor systems has been undertaken by modelling the HC slabs as surfaces using shell or plate elements and modelling the joints as lines. Research by Stanton states that "To model every void explicitly would make the analysis too cumbersome" [4]. Whilst this was true in the past, developments in computing power and FE packages now make it possible to model and analyse full three dimensional (3D) volumetric precast concrete HC floor systems with exact material and geometric properties.

This paper describes the use of the FE software LUSAS (Version 14.5-2) to create three dimensional solid volume models to replicate the structural response of trimmer brackets incorporated within hollow core floor systems. Previous research has shown that three dimensional FE solid modelling of HC floor systems without openings can be accurately modelled using LUSAS [5, 6]. The FE models of the brackets are based on a non-linear steel material model.

Experimental testing has been undertaken in the Heavy Structures Laboratory at Cork Institute of Technology. Two trimmer brackets for a 1200mm wide by 150mm deep HC slab were fabricated and tested to failure. The first test involved a bracket subjected to a point load at midspan while the second test involved the bracket loaded with a HC slab.

The results from these tests have been used to calibrate the FE analysis.

The aim of this research is to establish the magnitude of load that causes bracket failure and to compare this with the load typically applied to the bracket during service. It is suggested by a Finnish trimmer bracket manufacturer that the load (W) typically applied to the bracket is 50% of the self-weight of the slab and a part of the variable action as described in Equation 1 [7];

$$W = \gamma_G \left(g_{HC} \frac{L_o}{2} \right) + \gamma_Q \left(0.866 L^2 q \right) \qquad (1)$$

where: q is the applied load in kN/m^2, L is the width of the slab in m, L_o is the length of the slab in m, g_{HC} is the self-weight of the slab in kN/m and γ_G, γ_Q are partial safety factors for permanent and variable actions respectively.

Previous research has shown that when a slab is loaded with a linear loading such as a wall loading, the vertical reactions at the slab supports may increase by 50% of the self-weight of the slab and 50% of the wall load [8].

2 FINITE ELEMENT ANALYSIS

FE analysis is a method of simulating the structural responses of complex objects such as trimmer brackets and HC slabs to applied loads such as forces, temperature, pressure, etc.

The object is divided into a mesh of simpler shapes called finite elements. These finite elements are tied together at their shared nodes and are amenable to automatic numerical analysis. Solution is by means of simultaneous analysis of all finite elements within the object with due consideration to their location within the mesh.

Geometric and material non-linear behaviour can be modelled using an iterative solution control, which applies the loads incrementally and iterates to a solution.

The modelling has been undertaken for three different cases: Model TB#1 for a point load at midspan, Model TB#2 for a slab loaded along the span of the bracket, both corresponding to the experimental testing programme, and finally Model TB#3 incorporating a bracket within a complete five slab hollow core floor.

2.1 Model Geometry

All the models have been created as 3D solid volumes. A cross section of a HC slab geometry was first drawn in AutoCad and then imported into the LUSAS pre-processing graphical user interface (GUI), where it was swept out to form a 3D solid volume. The geometry of the trimmer brackets and bearing pads was created using the LUSAS pre-processing GUI.

Figure 2 shows FE model TB#1, which simulates the first experimental test undertaken on a trimmer bracket with a point load applied at centre span. The trimmer bracket is spanning onto concrete bearing pads that represent the adjoining slabs. An 80mm x 80mm patch load is applied to the centre of the span.

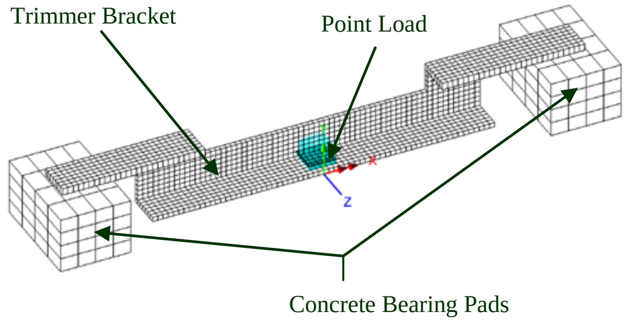

Figure 2. LUSAS Model TB#1.

Figure 3 shows FE model TB#2, which simulates the second experimental test undertaken, a trimmer bracket supporting a 150mm deep x 1200mm wide x 1.5m long HC slab. The trimmer bracket is again spanning onto concrete bearing pads representing the adjoining slabs. A patch load is applied to the centre of the slab.

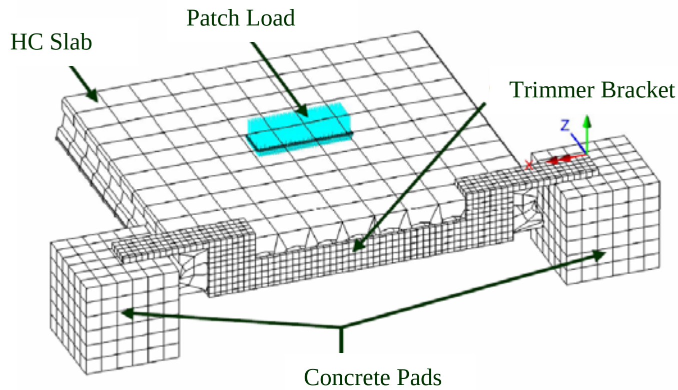

Figure 3. LUSAS Model TB#2.

Figure 4 shows FE model TB#3, which simulates a trimmer bracket incorporated into a five slab 150mm x 1200mm HC floor arrangement with span 4m. The trimmer bracket is supporting the central slab that is of 3m length thereby providing a 1.2m x 1.0m opening.

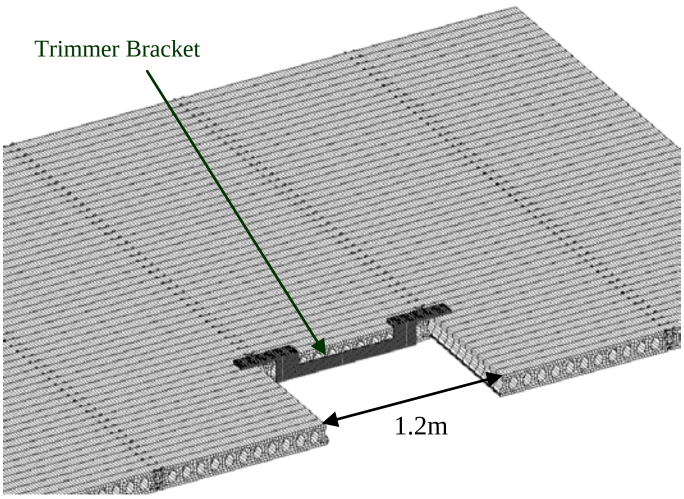

Figure 4. LUSAS Model TB#3

2.2 *Material Model*

A Von Mises non-linear steel material model was assigned to the bracket. The strain hardening properties have been obtained from previous research undertaken on steel equal angles [9]. Young's modulus of the steel was assumed to be 200kN/mm^2 with 300N/mm^2 being assigned as the yield stress. A linear concrete material model was assigned to both the HC slabs and the bearing pads with an assumed Young's modulus of 30kN/mm^2.

2.3 *Mesh Refinement*

Mesh refinement studies were undertaken on each of the models to identify an optimal mesh density that would produce accurate results without being unduly penalising in computational processing time. Due to the non-linear analysis and the 3D properties of the models, computational time can be extremely penalising if the number of elements is excessive. Hexahedral eight node, 3D, solid volume elements (HXM8) were assigned to all objects within the models.

2.4 *Boundary Conditions*

In models TB#1 and TB#2 the boundary conditions at the bottom of the bearing pads were pinned. The contact surfaces between the trimmer bracket and the bearing pads were modelled using slidelines. In model TB#3 the HC slabs were pinned at their ends with the contact between the HC slabs and the trimmer bracket being modelled using slidelines. Slidelines are an effective means of modelling contact and do not require knowledge of the exact location of contact [10].

3 LABORATORY TESTING

Two tests to failure have been undertaken on trimmer brackets for a 150mm x 1200mm HC slab. The first test reproduced model TB#1 and the second test reproduced model TB#2. Testing of a 200mm deep x 1200mm wide bracket within a full scale HC floor is currently being undertaken.

The brackets were fabricated to a clear depth dimension of 160mm to allow for a 10mm tolerance in the depth of the slab. Figure 5 shows the dimensions of the two trimmer brackets that have been tested.

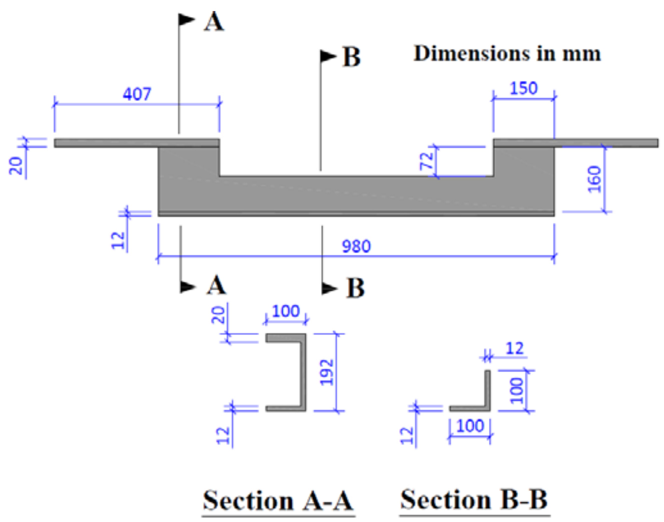

Figure 5. Dimensions of trimmer bracket.

The bracket fabrication follows the detail from the PCI manual for the design of HC slabs [2]. The brackets were fabricated partly from 100mm x 100mm x 12mm mild steel equal angle sections onto which sections consisting of 20mm and 12mm thick plates were welded.

3.1 *Test TB#1*

The test setup and measurement systems for Test TB#1 are described in full in previously published work [11].

3.2 *Test TB#2*

Figure 6 shows the setup for test TB#2, which is a HC slab, 150mm x 1200mm x 1.2m long, spanning onto a trimmer bracket that is bearing onto concrete pads; the bearing is 147mm x 100mm. The load was applied onto the centre of the slab by means of a 20 tonne hydraulic jack through a load cell.

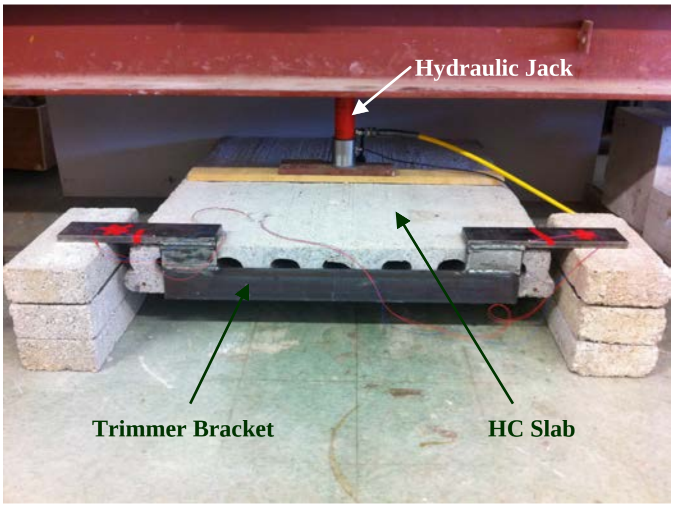

Figure 6. Test setup for TB#2.

The test data were collected using an electronic data logger recording at ten scans per second. The measurement apparatus included a load cell, strain gauges and displacement transducers. Additional displacement transducers were placed at the supports to record bedding in of the supports.

4 RESULTS COMPARISON FOR TB#1 & TB#2

The tests resulted in two different failure modes. In test TB#1 the bracket was subjected to a point load at the centre and it failed at the centre of the equal angle section, while in test TB#2 the bracket was loaded as shown in Figure 6 and the failure occurred in the 20mm plates at the top of the section.

4.1 *TB#1 Point load test*

Figure 7 shows the failure mode of the trimmer bracket when tested with a point load at midspan along with the locations of strain gauges 1 and 2. As seen the failure mode is the same in the test specimen and the FE model (Figure 8) with the bracket failing at the centre of the equal angle section.

At a maximum load of 50kN the strain contours (ε_x) in the FE model show a concentration of compressive strain with a maximum compressive strain of 19,141 microstrains at the top of the section with a concentration of tensile strain occurring at the bottom.

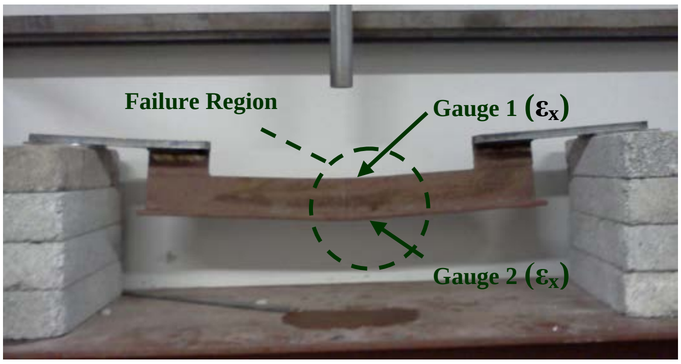

Figure 7. TB#1 test.

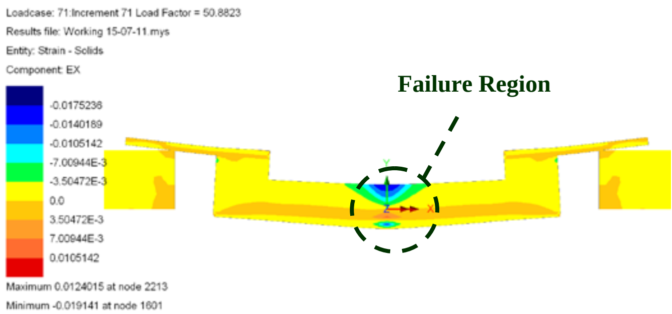

Figure 8. FE Model axial strain contours.

Figure 9 shows the graphical comparison, of load versus strain between the laboratory test and the FE analysis for strain gauge 1. Figure 10 shows the graphical comparison, of load versus strain between the laboratory test and the FE analysis for strain gauge 2.

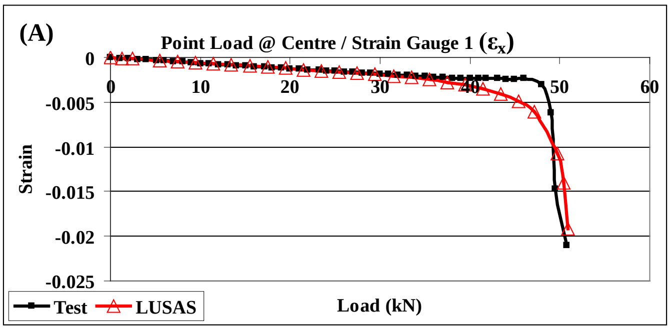

Figure 9. Load Vs. strain (gauge 1 TB#1).

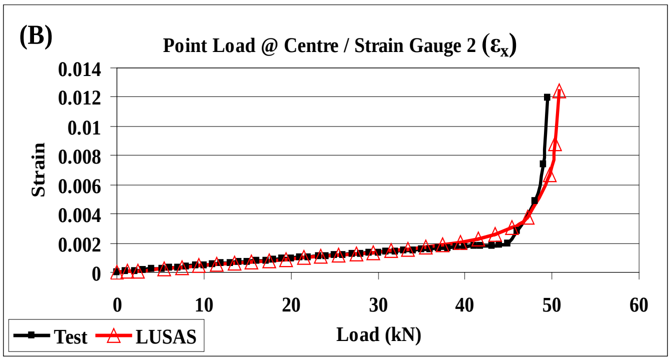

Figure 10. Load Vs. strain (gauge 2 TB#1).

On comparison of the results for strain and displacement for TB#1 a strong correlation between the test data and the FE data was found. While some localised yielding occurred in the top plates, the bracket failed at midspan, experiencing the largest strain in both the test an FE analysis data.

From the test data and the FE analysis, the safe load capacity of the bracket when subjected to a point load was estimated as approximately 45kN. The maximum load applied was 50kN.

4.2 TB#2 Slab test

Figure 11 shows the trimmer bracket for TB#2 after failure along with the location of strain gauge 5 and displacement transducer B. Figure 12 shows the FE model, outlining the failure regions. The failure mode of both the test and the FE analysis was the same with the top plates yielding.

During the test, at a load of 50kN, the HC slab split longitudinally through the centre as shown in Figure 11. As a result of this, the graphs in Figure 13 and Figure 14 show a sudden drop in load from 50kN to 40kN. As the FE analysis results conducted prior to the test had indicated that at this stage the bracket had already experienced considerable yielding, and had essentially failed, it was decided to continue the test without unloading.

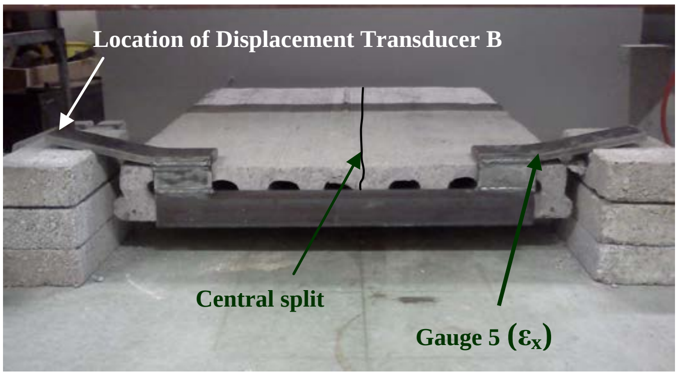

Figure 11. TB#2 test.

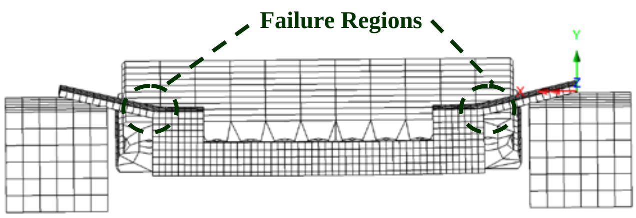

Figure 12. FE model failure mode.

Figure 13 shows the graphical comparison, of load versus displacement, between the laboratory test and the FE analysis for the displacement at transducer B. The test displacement results have been adjusted to take into consideration the bedding in that occurred at the supports. Figure 14 shows the graphical comparison, of load versus strain for strain gauge 5. Both graphs show a strong correlation between the test and the FE analysis with the safe load capacity of the trimmer bracket again being approximately 45kN. The maximum load applied to the bracket was 63kN.

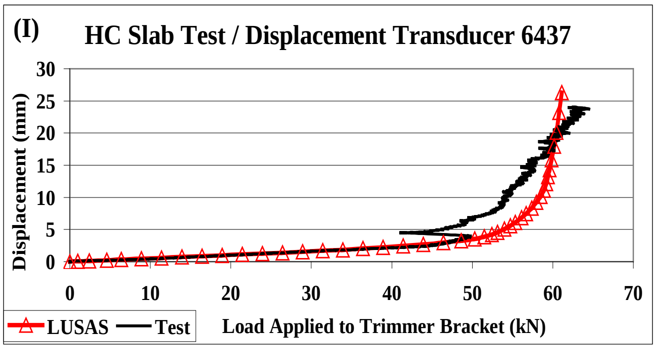

Figure 13. Load Vs. displacement (transducer B TB#2).

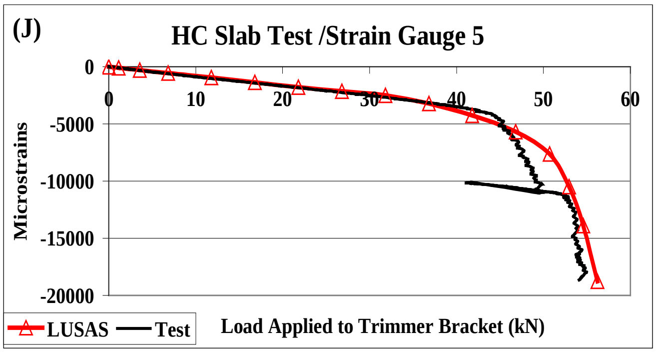

Figure 14. Load Vs. strain (gauge 5 TB#2).

5 LUSAS MODEL TB#3

A trimmer bracket incorporated within a five slab 150mm deep x 1200mm wide x 4m span floor has been modelled as shown in Figure 15. The slabs and the joints were modelled as described in previously published papers [5, 6]. The model was first analysed with all the joints in place. The load applied to the model was a uniformly distributed load (UDL) of 5kN/m^2, which was applied to the central slab that is supported by a trimmer bracket.

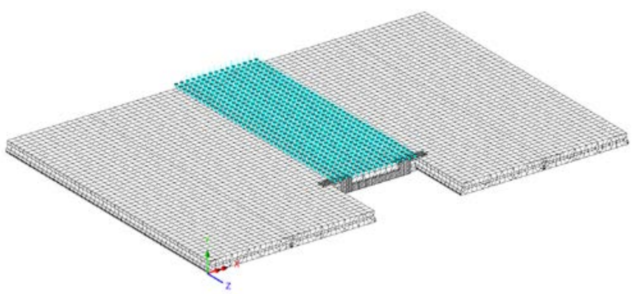

Figure 15. Floor with UDL on centre slab

The trimmer bracket was assigned the same attributes as the previous models. Figure 16 shows the axial stress contours for the bracket under this load case. The maximum stress in the bracket is a compressive stress of 4.15N/mm^2.

In order to evaluate the response of the trimmer bracket to the loadings from Equation 1, the joints between the HC slabs in the model were deleted, and an equilateral triangular UDL of 5kN/m^2 was applied to the model as shown in Figure 17. The maximum stress in the bracket due to the triangular UDL is 49.24N/mm^2 as shown in Figure 18. This is considerably larger than the 4.15N/mm^2 obtained from the previous analysis.

This implies that Equation 1 may be conservative with a greater proportion of the load being distributed to the adjoining slabs, with the bracket only being required to support the self-weight of the HC slab and any construction loading that may be applied.

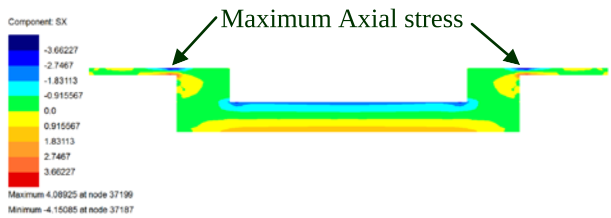

Figure 16. FE model TB#3 axial stress contours.

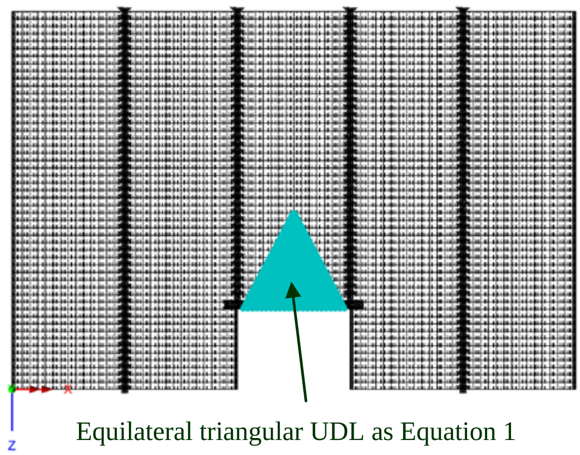

Figure 17. Loading as Equation 1.

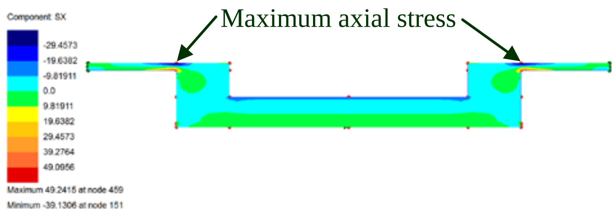

Figure 18. FE axial stress contours from Equation 1.

6 BRACKET LOAD CAPACITY

The trimmer brackets are typically loaded with 50% of the self-weight of the slab and a portion of the variable actions. While the FE analysis suggests that Equation 1 may be conservative, it can still be used to calculate the total load that will be applied to the bracket.

The tested brackets were for a slab 150mm deep x 1200mm wide x 11 core with a self-weight of approximately 3kN/m (308kg/m).

Typical spans and imposed loads for these slabs range from 7m with an imposed load of 1kN/m^2, to 4m with an imposed load of 6.67kN/m^2.

From Equation 1, W_{7m}=16.05kN and W_{4m}=20.58kN. These loads are well within the 45kN load capacity of the trimmer brackets, obtained from the laboratory testing and FE analysis.

7 FURTHER WORK

Full scale testing of a HC floor spanning 8m and containing five 200mm deep x 1200mm wide pre-stressed slabs is currently being undertaken at Cork Institute of Technology. Within this floor, it is planned to place a trimmer bracket at various locations to further validate the results presented in this paper.

A FE parametric study is currently being undertaken on trimmer brackets supporting a single slab incorporated in various HC floor depths and spans. The openings are being placed at various positions throughout the models.

Brackets supporting two slabs (Figure 19) are also being investigated. Preliminary FE analysis has suggested that the failure mode of these brackets may be more comparable to those of test TB#1 with the failure of the bracket occurring in the centre of the bracket. Results also suggest that these brackets carry a greater proportion of the variable actions than a bracket supporting a single slab.

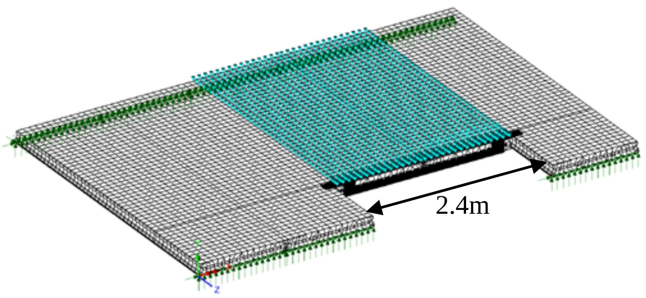

Figure 19. Trimmer bracket supporting two slabs.

Linear loads such as wall loadings are to be investigated as their load path may be that of an arch and the structural response may not be fully distributed to the adjoining slabs with the trimmer bracket being subjected to a higher load than predicted.

8 CONCLUSIONS

A non-linear FE analysis of the structural response of steel trimmer brackets can be undertaken to predict the structural response of the brackets. The trimmer bracket as fabricated and modelled in this paper (150mm deep x 1200mm long) is suitable, in the authors' opinion, for its intended use with the load capacity being approximately twice the estimated largest applied load.

Equation 1 has been shown to be conservative, but should still be used to represent the loads that a trimmer bracket will be subject to during service conditions due to self-weight and variable actions.

In situations where linear loads such as walls are being applied to the trimmer bracket supported slab, separate calculations should be undertaken to ensure that the load capacity of the bracket is adequate.

This study has identified the need for further testing and FE analysis of trimmer brackets incorporated within HC floors. As part of this research, design guidance will be prepared for the design of trimmer brackets incorporated within HC floors.

ACKNOWLEDGMENTS

The authors would like to thank the staff of the Civil, Structural & Environmental Engineering Department at Cork Institute of Technology for their assistance, particularly Mr James Morgan for his ongoing help and advice during the testing phase of this research.

The authors would also like to acknowledge support from DUCON Concrete Ltd. (Kanturk, Co. Cork) for providing technical advice and product for testing (hollow core slabs and trimmer brackets).

REFERENCES

[1] Elliott, K.S., *Precast concrete structures*. 2002, Oxford: Butterworth-Heinemann.

[2] Buettner, D.R. and R.J. Becker, *PCI manual for the design of hollow core slabs*. 1998, Precast/Prestressed Concrete Institute: Chicago.

[3] Hoogenboom, P., *Analysis of hollow-core slab floors.* Heron, 2005. 50(3): p. 173.

[4] Stanton, J.F., *Response of Hollow-Core Slab Floors to Concentrated Loads.* PCI Journal, 1992. 37(4): pp. 98-113.

[5] Hodge, D.F., B.D. O'Rourke, and J.J. Murphy, *Finite Element Modelling of Transverse Load Sharing Between Hollow Core Floor Slabs*, in *Bridge, Concrete and Infrastructure Research in Ireland*. 2010, ISBN No. 978-0-9542973-3-6: Cork. pp. 61-72.

[6] Hodge, D.F., B.D. O'Rourke, J.J. Murphy, and J.R. Harrington, *Three-Dimensional Solid Finite Element Modelling and Analysis of Precast Hollow Core Floors*, in *The Thirteenth International Conference on Civil, Structural and Environmental Engineering Computing*, B.H.V. Topping and Y. Tsompanakis, Editors. 2011, Civil-Comp Press: Crete.

[7] Peikko *PETRA Support for Hollow Core Slabs for Floor Openings*. 28. http://81.167.44.246/pdf_eng/PETRA_EN-3-2010.pdf [Accessed 01 Febuary 2012]

[8] Moss, R.M., *Load testing of hollow plank concrete floors.* The Structural Engineer, 1995. 73(10): pp. 161-168.

[9] Sun, J. and J.W. Butterworth, *Behaviour of steel single angle compression members axially loaded through one leg*, in *Australian Structural Engineering Conference*. 1998: Auckland. pp. 859-866.

[10] LUSAS, *Theory Manual* LUSAS, London. 2011

[11] Hodge, D.F., B.D. O'Rourke, J.J. Murphy, and J.R. Harrington. *Finite Element Analysis of Trimmer Brackets incorporated within Hollow Core Floors*, in *Forum Bauinformatik.* 2011: Cork. http://zuse.ucc.ie/forumbau2011/papers/11.pdf [Accessed 26 June 2012]

Generating dynamic time history responses for concrete wind turbine towers

Aidan Quilligan[1], Alan O'Connor[1]
[1]Department of Civil, Structural and Environmental Engineering, Trinity College, Dublin 2, Ireland
email: quilliga@tcd.ie, alan.oconnor@tcd.ie

ABSTRACT: Recent advances in wind turbine technology are pushing the boundaries of the current structural configurations of wind turbine towers. With hub heights now stretching to almost 150 m, rotor diameters of 130 m and power outputs approaching 7.5 MW, it has become evident that alternative tower solutions are necessary to help advance these systems. Towers of approximately 90 m and taller are now constructed from a variety of precast or slip-formed prestressed concrete as well as hybrid (prestressed concrete and steel) solutions. This paper addresses the dynamic analysis of such prestressed concrete structures. A Lagrangian approach is employed in the derivation of the system equations of motion to facilitate the accurate coupling of the various rigid (nacelle) and flexible (blades, rotor shaft, tower) components of a wind turbine system, allowing for the generation of dynamic time history responses to the specified loading regime. The external loading of the system is developed through stochastically modelled wind loads and the application of earthquake ground motion acceleration time histories. The resulting displacement and acceleration time history responses may be utilised for detailed analysis of displacements and stresses induced by the prescribed loading. This is a valuable tool for the analysis, design and optimisation of prestressed concrete wind turbine towers.

KEY WORDS: Concrete wind turbine towers; Lagrangian; Modal analysis; Flapwise vibration; Stochastic loading.

1 INTRODUCTION

The growth of the global wind energy sector is undisputable with 215GW of installed capacity as of June 2011 (over 100 times the installed capacity of 1990) [1], and the expectation of providing for almost 3% of the global electricity demand by the end of 2011. As the industry strives to innovate by reducing the unit price of wind generated electricity, eliminating destructive carbon emissions and providing a reliable, cheap alternative to fossil fuel based generation, there is an ever-increasing requirement for research in this domain.

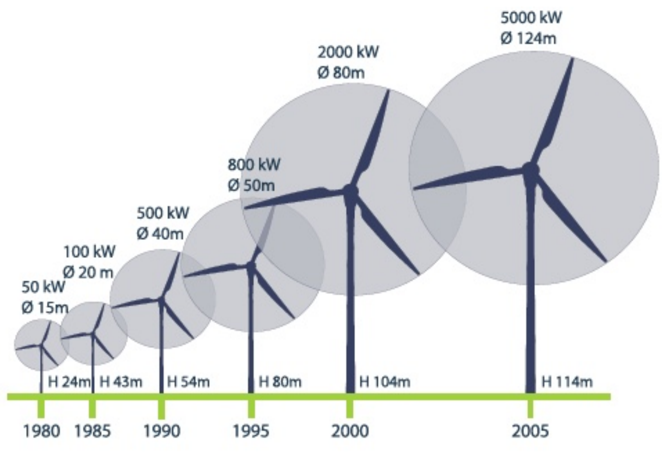

Figure 1. Growth in wind turbine size.

A considerable aspect of this growth can be seen in the ever increasing size of the wind turbine units and consequently the support structures such as the tower. Figure 1 outlines this trend up until 2005. Current models are rated up to 7.5MW with hub heights of up to 150m. Due to the wind shear effect, taller hub-heights result in greater and more stable wind inflow speeds. Coupled with the fact that larger turbine units will generate greater amounts of electricity, this means that wind turbine sizes will tend to increase for the foreseeable future.

As these hub heights increase, and the size of the wind turbine units they support continue to get larger, there becomes a necessity to reconsider the tower design and possibly utilise more advanced materials in an effort to balance flexibility of the components, along with ease of construction and transportation. For the case of the industry standard steel towers, Hau [2] highlights the serious manufacturing difficulties with steel sections for tower heights beyond 90m. An additional constraint is that the transportation of the lower tower sections by road is no longer feasible in many cases. In Ireland, for example, road traffic regulations specify that the maximum overall height of a vehicle may not exceed 4.65m [3], which is unavoidable for tower heights of 90m and above.

The shortcomings of steel towers for large scale modern wind turbines has led to the emergence of a number of alternative designs. Prestressed concrete appears to play a primary role in each of these options. Techniques such as precasting and cast-in-situ construction of prestressed concrete towers eliminates the issue of transporting large diameter sections along public roads. Some designs incorporate a hybrid solution of both prestressed concrete and steel while others opt for a complete concrete configuration. Authors such as Murtagh et al. [4], Bazeos et al. [5], Chen et al. [6] and Negm and Maalawi [7] have each considered the tower in their investigations of wind turbine design and

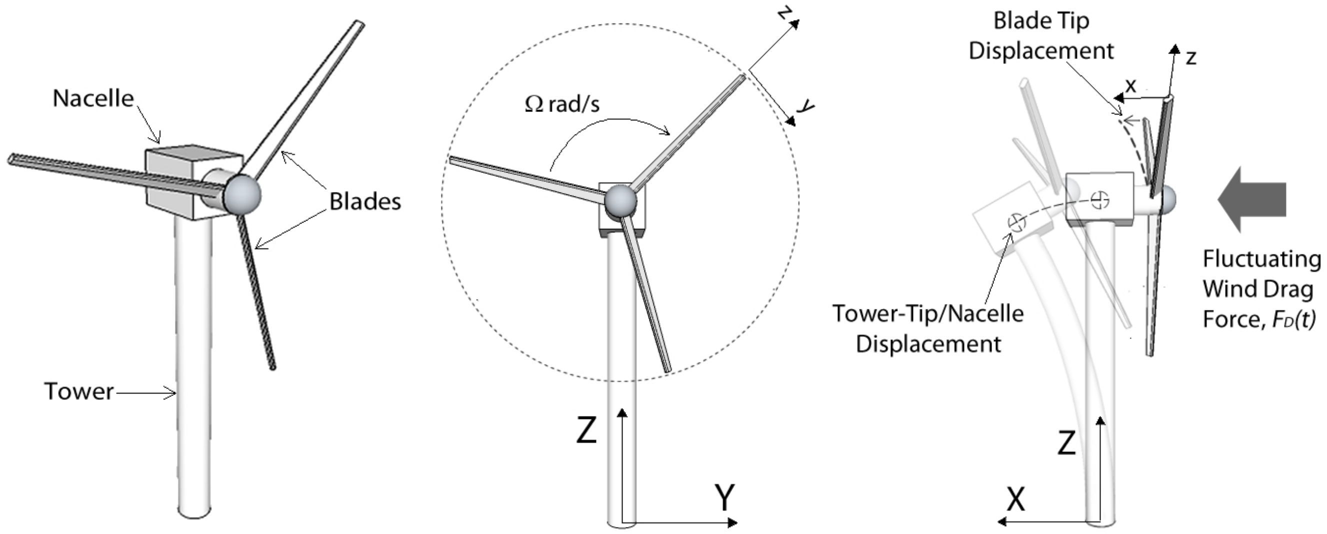

Figure 2. Wind turbine model configuration.

performance. Investigations of towers beyond the height of 90m are not available, however. Moreover, the concept of prestressed concrete towers is relatively new in the commercial wind turbine industry with few examples of studies of the dynamic performance of these towers in the literature [8-9].

This paper proposes a two dimensional wind turbine model which incorporates coupling between the blades and tower. The model is applied to a series of concrete towers, ranging in height from 88m to 120m. The Kaimal spectrum [10] is employed to generate stochastic wind loading on both the blades and tower. Both out-of-plane (flapwise) and in-plane (edgewise) blade loading is considered. The model also allows the incorporation of earthquake loading which is becoming more important in the design of wind turbines. This is emphasised with the growth in wind turbine installations in countries such as China and the USA, who now account for 44% of the global installed capacity [1], and have regions which are particularly susceptible to seismic activity.

The structural model allows a series of realistic displacement, velocity and acceleration time histories to be compiled which may be used for further analysis and comparisons of the structures. These can be calculated for any point along the tower or blades which permits a detailed examination of the component behaviours.

2 STRUCTURAL MODEL

The purpose of this model is to represent the dynamic response of the numerous flexible and rigid bodies which interact through the rotation of the rotor and the vibration of the whole system. The most vital aspect in the structural modelling is the precise incorporation of the coupling between the various components. This is commonly achieved by formulating the equations of motion through an energy method, such as the Lagrangian method. This method facilitates the accurate representation of all coupling within the system by directly minimising the total energy functions of the dynamic system. The complexity of the model may subsequently be altered based upon the requirements of the analysis being carried out. As this paper primarily considers tower vibration response, a functional blade model is employed which incorporates flapwise and edgewise bending but not blade torsion, which is an important aspect when blade design is being considered.

2.1 Lagrangian Model

Quilligan *et al.* [11] proposed a detailed flapwise (blade) and longitudinal (tower) vibration model of a wind turbine system which was assembled through the Lagrangian formulation. In the current investigation this model is extended to incorporate two dimensional motion (flapwise-longitudinal and edgewise-lateral). Hansen [12] outlines a similar Lagrangian formulated model which focuses on the blade and nacelle vibrations in a study of stall-induced vibrations of wind turbines. Arrigan *et al.* [13] provides a similar model in an investigation of the vibration control of wind turbine blades. In an effort to accurately capture the dynamics of the wind turbine system modal analysis is employed for the flexible blade and tower components. The formulation also takes account of nacelle tilt, roll and yaw as well as rotor shaft rotation as described in Figure 2. Lagrange's equations of motion, as defined in Clough & Penzien [14], may be expressed as follows:

$$\frac{d}{dt}\left(\frac{d(KE)}{d\dot{q}_i}\right)-\frac{d(KE)}{dq_i}+\frac{d(PE)}{dq_i}=Q_i \qquad (1)$$

where KE is the kinetic energy of the system, PE is the potential energy of the system, q_i is the displacement, $\dot{q}_i$ is the velocity and Q_i is the generalised loading corresponding to degree of freedom i.

As illustrated in Figure 2 the model includes two coordinate frames of reference, a local co-rotating system for each blade (x, y, z) and a global ground-fixed system for the combined elements which includes the tower and nacelle (X, Y, Z). At the root of each blade exists the origin of the local blade system. Wind inflow is solely considered in the global X-direction as significantly less inflow occurs in the other directions [15]. Flapwise blade vibration and longitudinal tower vibration occur in the local 'x' and global 'X' directions respectively while edgewise blade vibration and lateral tower vibration correspond to the 'y' and 'Y' axes respectively.

A modal approximation of the motion of the tower and blades, as illustrated in Equation 2, is established by considering the motion to be a summation of the products of a series of predefined modeshapes, $\phi_i(z)$, and their corresponding temporal modal displacements, $q_i(t)$, for an arbitrary number of modes i.

$$u(z,t) = \sum_{i=1}^{I} \phi_i(z) \times q_i(t) \tag{2}$$

By representing the blade and tower motion in this manner and utilising the formulation outlined by Hansen [12] the total potential and kinetic energy for input into Equation 1 may be represented as in Equations 3 - 5 respectively. The accuracy of this form of model has previously been verified against experimental results in [12] and other analytical results in [13].

$$\begin{aligned} PE_{Total} &= \frac{1}{2}\int_0^H \left[EI_{tx}(u''_{tx})^2 + EI_{ty}(u''_{ty})^2\right] dZ \\ &+ \frac{1}{2}G_x\theta_{tx}^2 + \frac{1}{2}G_y\theta_{ty}^2 + \frac{1}{2}G_z\theta_{tz}^2 \\ &- g_{xy}\theta_{ty}u_{nx}(t) + g_{xy}\theta_{tx}u_{ny}(t) + \frac{1}{2}G_s\theta_{ts}^2 \\ &+ \frac{1}{2}\sum_{k=1}^{3}\left\{\int_0^R \left[EI_{bx}(u''_{x,k})^2 + EI_{by}(u''_{y,k})^2\right] dz\right\} + V_C \end{aligned} \tag{3}$$

In Equation 3, EI_{tx} and EI_{ty} represent the tower stiffness as a function of Z, u''_{tx} and u''_{ty} are the second spatial derivatives with respect to Z of the tower position, G_x, G_y and G_z are the roll, tilt and yaw stiffnesses of the nacelle support, g_{xy} is the coupling stiffness of the nacelle support, G_s is the torsional stiffness of the drive-train, EI_{bx} and EI_{by} signify the blade stiffness as a function of z, while $u''_{x,k}$ and $u''_{y,k}$ are the second spatial derivatives with respect to z of the blade position. V_C represents the additional stiffness induced in a blade due to its rotation about the hub, also known as centrifugal stiffening. This may be devised as follows:

$$V_C = \frac{1}{2}\Omega^2 \sum_{k=1}^{3} \left\{ \begin{aligned} &\int_0^R \left[(u'_{x,k})^2 + (u'_{y,k})^2\right] dz \\ &+ \int_z^R m(\xi)\, d\xi\, dz \end{aligned} \right\} \tag{4}$$

where Ω is the blade rotational frequency in (rad/s), R is the total length of the blade and $m(\xi)$ is the mass per unit length of the blade (kg/m).

$$\begin{aligned} KE_{Total} &= \frac{1}{2}\int_0^H m_t(Z)\left[\dot{u}_{tx}^2(Z,t) + \dot{u}_{ty}^2(Z,t)\right] dZ \\ &+ \frac{1}{2}I_x\dot{\theta}_{tx}^2 + \frac{1}{2}I_y\dot{\theta}_{ty}^2 + \frac{1}{2}I_z\dot{\theta}_{tz}^2 + \frac{1}{2}I_s\dot{\theta}_{sx}^2 \\ &+ \frac{1}{2}M_{nac}\left[\dot{u}_{nx}^2(t) + \dot{u}_{ny}^2(t)\right] \\ &+ \frac{1}{2}\sum_{k=1}^{3}\left\{\int_0^R m_{b,k}(z) \times \left|\dot{p}_{cg,k}\right|^2 dz\right\} \end{aligned} \tag{5}$$

In Equation 5, $m_t(Z)$ is the tower mass as a function of its height, $\dot{u}_{tx}(Z,t)$ and $\dot{u}_{ty}(Z,t)$ are the first temporal derivatives of the position of the centre of gravity axis of the tower with respect to the ground fixed frame in both the X and Y directions, I_x, I_y, I_z and I_s are the mass moments of inertia of the nacelle about the X, Y and Z axes and the rotor shaft and drivetrain about its local axis. M_{nac} is the total mass of the nacelle and hub components excluding the blades, while $\dot{u}_{nx}(t)$ and $\dot{u}_{ny}(t)$ are the X and Y positions of the centre of the nacelle with respect to the ground fixed frame. $m_{b,k}(z)$ is the mass of blade k as a function of its length along the centre of gravity axis and $\dot{p}_{cg,k}$ is the position vector from the ground fixed frame of an arbitrary point along the centre of gravity axis of the blade k. Once the potential and kinetic energy of the system has been formulated it is now necessary to assess the generalised loading component.

2.2 Wind Loading

As the wind passes through a wind turbine rotor it generates both a lift force and drag force on the blades. This equates to the edgewise and flapwise directions respectively. The magnitude of these forces can be represented as:

$$P_D(x,t) = \frac{1}{2}\rho c U^2 \left\{C_L \cos\phi_0 + C_D \sin\phi_0\right\} \tag{6}$$

$$P_L(x,t) = \frac{1}{2}\rho c U^2 \left\{C_L \sin\phi_0 - C_D \cos\phi_0\right\} \tag{7}$$

where ρ is the air density, $U = \sqrt{v^2 + z^2\Omega^2}$ is the relative inflow velocity of the air, which is a function of z, $\phi_0 = \tan^{-1}(v/z\Omega)$ is the relative inflow angle, while C_L and C_D are the respective lift and drag coefficients of the blade which are a function of the angle of attack and c is the blade chord length. For a non-uniform blade these coefficients vary as a function of z also. According to Clough & Penzien [14], the generalised modal loading associated with an arbitrary mode n may subsequently be formulated as:

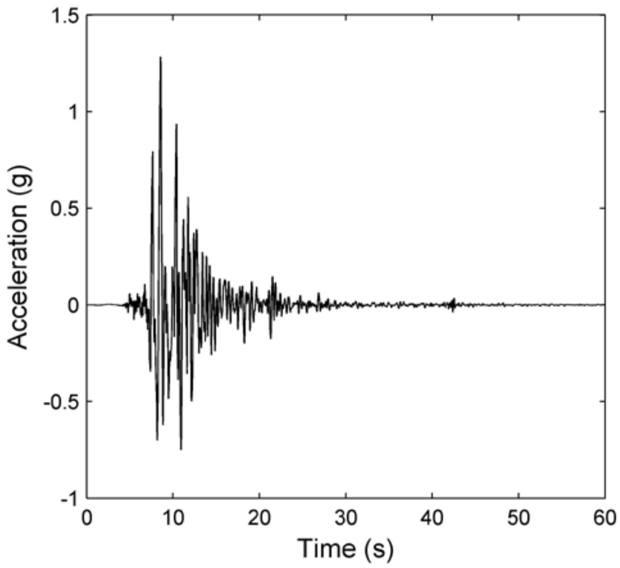

Figure 3. Sample earthquake ground motion time history.

$$P_n(t) = \int_0^R \phi_n(z)\, p(z,t)\, dz \tag{8}$$

where $\phi_n(z)$ is the n^{th} modeshape of the blade. The wind inflow, $v = \bar{v} + v'(t)$ is modelled as a stochastic wind model with a fluctuating component $v'(t)$, as well as a mean component, $\bar{v}$, which includes the effects of wind shear. The fluctuating, or turbulent, wind velocity time histories, $v'(t)$, are generated using the Discrete Fourier Transform (DFT) method, as detailed by Murtagh *et al.* [16] which utilises the Kaimal spectrum.

2.3 Earthquake Loading

A sample acceleration ground motion time history is provided in Figure 3. The earthquake loading is introduced to the system by the following equation:

$$P_{n,eff} = -\ddot{u}_g(t)\left[\int_0^H m_t(Z)\phi_n(Z)dz + M_{top}\phi_{n,top}\right] \tag{9}$$

where $\ddot{u}_g(t)$ is the recorded or generated earthquake ground motion acceleration, M_{top} is the total mass of the components supported by the tower (blades, nacelle, hub, etc.) and $\phi_{n,top}$ is the value of the corresponding modeshape $\phi_n(Z)$ at the top of the tower. Once computed for each mode the generalized earthquake loading may be added to the wind loading specified in Section 2.2.

Both 'x' and 'y' components of the ground motion acceleration time histories are provided. The loading applied to the wind turbine structure, therefore, acts in two dimensions. In all cases of seismic loading the rated wind speed of the turbine, 11.4 m/s, is utilised as the mean hub-height wind speed throughout the entire simulation.

Table 1. Basic properties of 5MW wind turbine [17].

Property	**Value**
Rating	5 MW
Rotor Diameter	126 m
Hub Diameter	3 m
Cut-in Wind Speed	3 m/s
Rated Wind Speed	11.4 m/s
Cut-out Wind Speed	25 m/s
Cut-in Rotor Speed	6.9 rpm
Rated Rotor Speed	12.1 rpm
Nacelle Mass	240,000 kg
Rotor Mass	110,000 kg
Blade Material	Glass-fibre
Blade Length	61.5 m
Blade Mass	17,740 kg
Blade CM (From Blade Root)	20.475 m
Blade Damping Ratio (All Modes)	0.48%

Table 2. Basic properties of 88 m prestressed concrete tower.

Property	**Value**
Height	87.6 m
Base Diameter	8.2 m
Top Diameter	4.8 m
Concrete Thickness	0.25 m
Modulus of Elasticity	26 GPa
Concrete Density	2,450 kg/m^3
Total Mass	1,053,500 kg
Location of CM (Above Base)	37.95 m
Tower Damping Ratio (All Modes)	1%

3 MODEL IMPLEMENTATION

For the purposes of this investigation a standard wind turbine, the NREL baseline 5MW turbine, is chosen for implementation in the analysis. The properties of the nacelle and rotor components are outlined in Table 1. Further detailed descriptions of the parameters may be found in reference [17]. While the tower specified for this specific turbine is an 88 m steel tubular tower, in this instance an equivalent 88 m prestressed concrete tower will be employed. Due to the recent emergence of prestressed concrete and hybrid tower solutions as an alternative to the industry standard steel towers, there exists a significant lack of information in the literature pertaining to the specified structural properties of such towers. Therefore, the properties of the 88 m tower, detailed in Table 2, are based on some basic properties acquired for a tower of this size.

An important aspect of the analysis of the towers described above is to take appropriate consideration of the influence of the prestressing forces applied. The effect of prestress force on the dynamic performance of prestressed concrete elements is a topic which has been widely debated. The work of Hamed & Frostig [18], however, states that, "it has been mathematically rigorously proven that the magnitude of the prestressed force does not affect the natural frequencies of bonded or unbonded prestressed beams". Consequently, it is considered appropriate to discount the prestress force from the

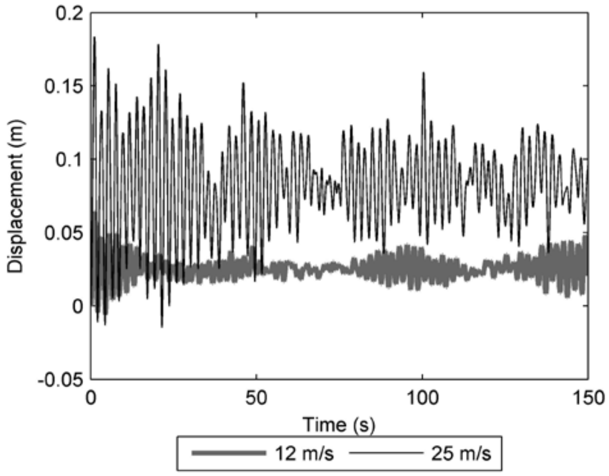

Figure 4. Longitudinal nacelle displacements for wind loading.

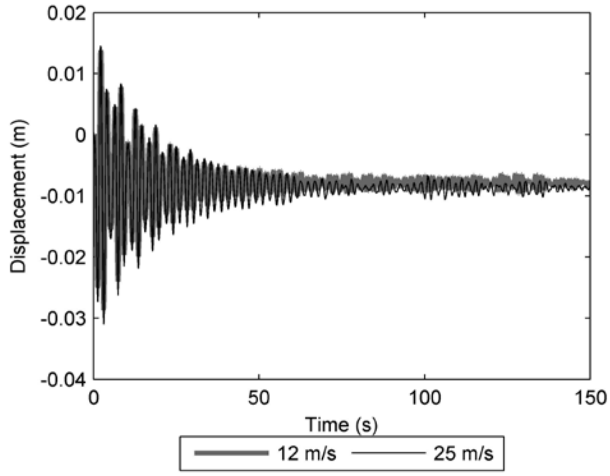

Figure 5. Lateral nacelle displacements for wind loading.

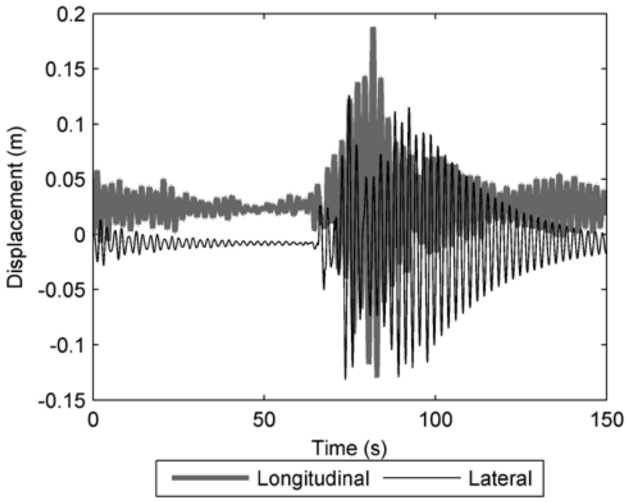

Figure 6. Nacelle displacement for 0.1g PGA earthquake.

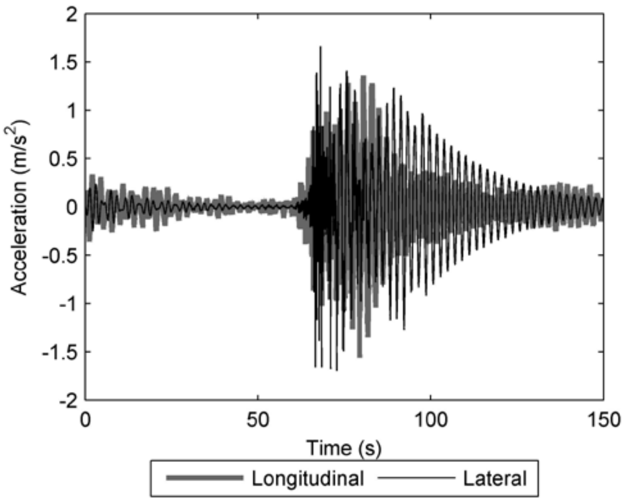

Figure 7. Nacelle acceleration for 0.1g PGA earthquake.

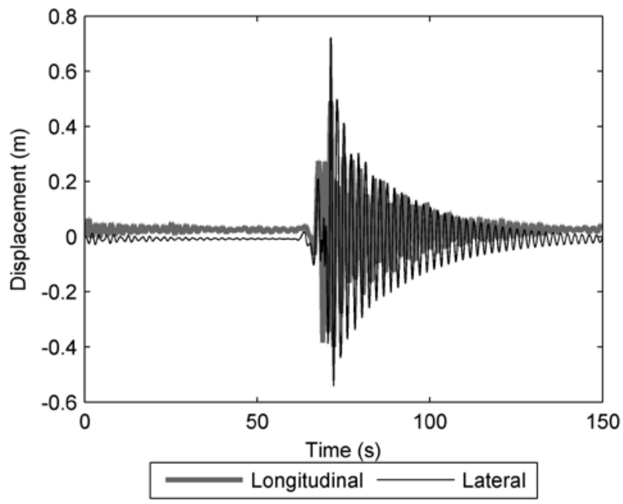

Figure 8. Nacelle displacement for 1.0g PGA earthquake.

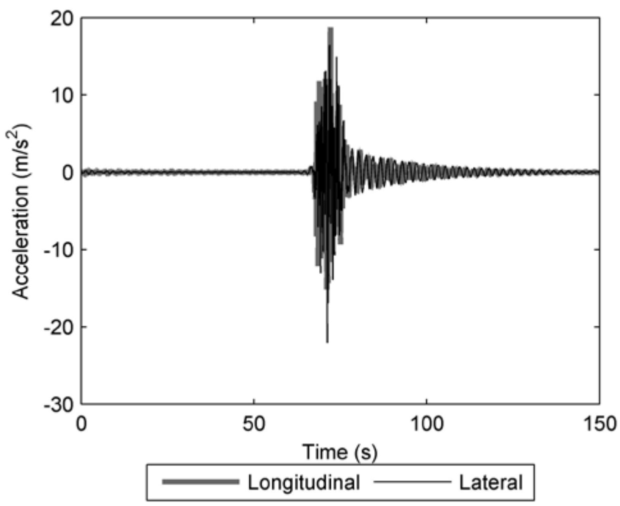

Figure 5. Nacelle Acceleration for 1.0g PGA earthquake.

tower model and employ linear elastic beam theory in the analysis.

For the purposes of this analysis a variation of simulations will be carried out to illustrate the capabilities of the model. These include simulations of:

- Longitudinal nacelle displacement for the rated wind speed, 11.4 m/s, and the cut-out wind speed, 25 m/s.
- Lateral nacelle displacement for the same wind inflow conditions
- Lateral and longitudinal nacelle displacement and acceleration for a relatively small scale earthquake with a peak ground acceleration (PGA) of 0.1g, where 'g' signifies the acceleration due to gravity. A mean hub-height wind speed of 11.4 m/s is also applied to the turbine throughout the simulation.
- Lateral and longitudinal nacelle displacement and acceleration for a large scale earthquake with a peak ground acceleration (PGA) of 1.0g. Again, the rated turbine wind speed is applied to the turbine.

Figures 4-9 present the results of the analysis. Figure 4 illustrates the displacement response at the nacelle for the two mean hub-height wind speeds of 11.4 m/s and 25 m/s. It is evident that the longitudinal displacements are increased considerably with the increase in wind speed. Once a steady state has been reached the lower wind speed induces displacements in the range of 30-50 mm while the cut-out wind speed increases this to approximately 150 mm. For the case of lateral displacements, Figure 5, the increase is not quite as significant. Both displacements are in the range of 10-15 mm once the steady state is reached. The cut-out wind speed shows an increase in displacements of only 2-5 mm.

Figure 6 demonstrates the induced displacements from the earthquake with 0.1g PGA. In the steady state the nacelle exhibits noticeably less lateral displacement. Once the seismic excitation begins at approximately 65 seconds into the simulation a considerable increase in displacement is evident. Lateral displacements achieve maximum amplitude of 120 mm while longitudinal accelerations reach 190 mm. The corresponding accelerations are presented in Figure 7. A similar pattern is noticeable with smaller magnitude lateral accelerations than longitudinal accelerations prior to the onset of seismic loading. At the commencement of the seismic loading at approximately 65 seconds, maximum lateral and longitudinal accelerations of 1.5-1.8 m/s^2 are induced with the longitudinal accelerations returning to steady state levels at a considerably faster rate than the lateral accelerations.

Figures 8 and 9 illustrate a comparable pattern for the larger earthquake event. The magnitudes of the displacements and accelerations are considerably higher, however, with maximum lateral and longitudinal displacements of 700 mm and 350 mm respectively. Lateral and longitudinal accelerations achieve levels of 21 m/s^2 and 19 m/s^2. These levels of accelerations would undoubtedly cause damage to sensitive components housed in the nacelle.

4 CONCLUSION

This paper set out to address the need for a greater understanding of the dynamics of prestressed concrete wind turbine towers, as this type of tower configuration is one possible structural solution which allows wind turbines to reach higher into the atmosphere to achieve greater and more stable wind speeds. The Lagrangian approach is employed to formulate the dynamic equations of motion in a two dimensional numerical model which takes account of both flapwise and edgewise blade vibrations, lateral and longitudinal tower vibrations, rotor shaft torsion, as well as nacelle roll, tilt and yaw motion. The loading configuration of the model allows for a combination of stochastically modelled wind loading and seismic loading generated from ground motion acceleration time histories. The resulting time history responses allow for detailed analysis of the displacements and stresses induced by the prescribed loading.

ACKNOWLEDGMENTS

Research funding by Banagher Precast Concrete Ltd and IRCSET (Irish Research Council For Science, Engineering & Technology) under the IRCSET Enterprise Partnership Scheme is gratefully acknowledged.

REFERENCES

[1] Half-year Report 2011. The World Wind Energy Association; 2011.

[2] Hau E. Wind Turbines: Fundamentals, Technologies, Applications, Economics. 2 ed: Springer, Berlin; 2006.

[3] Irish Road Traffic (Construction and use of Vehicles) (Amendment) Regulations. Office of the Attorney General; 2008.

[4] Murtagh PJ, Basu B, Broderick BM. Along-wind response of a wind turbine tower with blade coupling subjected to rotationally sampled wind loading. Engineering Structures. 2005;27:1209-19.

[5] Bazeos N, Hatzigeorgiou GD, Hondros ID, Karamaneas H, Karabalis DL, Beskos DE. Static, seismic and stability analyses of a prototype wind turbine steel tower. Engineering Structures. 2002;24:1015-25.

[6] Chen X-b, Li J, Chen J-y. Wind-induced response analysis of a wind turbine tower including the blade-tower coupling effect. Journal of Zhejiang University - Science A. 2009;10:1573-80.

[7] Negm HM, Maalawi KY. Structural design optimization of wind turbine towers. Computers & Structures. 2000;74:649-66.

[8] Paredes JA, Barbat AH, Oller S. A compression–tension concrete damage model, applied to a wind turbine reinforced concrete tower. Engineering Structures. 2011;33:3559-69.

[9] Harte R, Van Zijl GPAG. Structural stability of concrete wind turbines and solar chimney towers exposed to dynamic wind action. Journal of Wind Engineering and Industrial Aerodynamics. 2007;95:1079-96.

[10] Kaimal JC, Wyngaard JC, Izumi Y, Coté OR. Spectral Characteristics of Surface Layer Turbulence. Quarterly Journal of the Royal Meteorological Society. 1972;98:563-89.

[11] Quilligan A, O'Connor A, Pakrashi V. Fragility Analysis of Steel and Concrete Wind Turbine Towers. Engineering Structures. 2012;36:270-82.

[12] Hansen MH. Improved Modal Dynamics of Wind Turbines to Avoid Stall-induced Vibrations. Wind Energy. 2003;6:179-95.

[13] Arrigan J, Pakrashi V, Basu B, Nagarajaiah S. Control of flapwise vibrations in wind turbine blades using semi-active tuned mass dampers. Structural Control and Health Monitoring. 2011;18:840-51.

[14] Clough RW, Penzien J. Dynamics of Structures. Singapore: McGraw-Hill; 1993.

[15] Wind Turbines-Part 1: Design Requirements. British Standards Institution; 2005.

[16] Murtagh PJ, Basu B, Broderick BM. Wind force time-history generation by discrete Fourier transform (DFT). In: Rahnejat H, Rothberg S, editors. Multi-body Dynamics - Monitoring and Simulation Techniques - lll: John Wiley & Sons; 2004. p. 147-54.

[17] Jonkman J, Butterfield S, Musial W, Scott G. Definition of a 5-MW Reference Wind Turbine for Offshore System Development. Golden, Colorado: National Renewable Energy Laboratory; 2009.

[18] Hamed E, Frostig Y. Natural frequencies of bonded and unbonded prestressed beams-prestress force effects. Journal of Sound and Vibration. 2006;295:28-39.

Response of a simply supported beam with a strain rate dependent elasticity modulus when subjected to a moving load

Hussein Aied[1], Arturo González[1]
[1]School of Civil, Structural and Environmental Engineering, University College Dublin, Belfield, Dublin 4, Ireland
email: hussein.aied@ucdconnect.ie, arturo.gonzalez@ucd.ie

ABSTRACT: The response of a simply supported Finite Element (FE) beam model is simulated under single moving load at different velocities. The beam is discretized into small elements and strain and displacement measurements are obtained at each time step. Contrary to previous work based on a constant modulus of elasticity, here the strain measurements use a time-variant (dynamic) modulus of elasticity. A time-variant modulus influences the bridge response, being more significant at highest velocities.

KEYWORDS: Modulus of Elasticity; Strain rate; Dynamic response; Beam; Concrete.

1 INTRODUCTION

In general a constant modulus of elasticity is used to calculate the load effect caused by moving loads for simply supported bridges. Existing researchers [1, 2] have shown that the moving loads cause the changed modulus that subsequently affects stress-strain relationship and concrete strength properties. Dynamic loads commonly impact all the properties of the concrete structure but most noticeably its tensile and compressive strengths. For a nonlinear elastic material such as concrete, the stiffness (mainly secant modulus) exhibits high sensitivity at high loading rates [3]. This enhancement in stiffness is caused by reduction in micro-cracking at high strain rate. Most of the literatures confirm that the modulus of elasticity increases with increasing strain rate. Previously, dynamic load tests for concrete are undertaken by using an impact hammer on a concrete specimen with a specified strain rate [4, 5]. Strain rates applied are generally high and in the range of 10^{-3} to 10^{-1} s^{-1}, which correspond to values slightly higher than that of an earthquake. However, strain rates due to a moving load are much lower than ones derived from the impact hammer.

Furthermore, Soroushian and Obaseki [6] and Fu, et al. [7] proved that impact loading has small influence on the stiffness of reinforced concrete and negligible effect on modulus of steel [8]. The CEB Information Bulletin No. 187 has been recently used [9, 10] to conduct dynamic analysis on concrete and reinforced concrete specimens. Results showed significant increase in the tensile strength, and ultimate tensile stress and strain. Strain rates used were in the range of 1 s^{-1} and 50 s^{-1}, which are considered for soft and hard impact. For concrete, the modulus of elasticity increased moderately at high strain rates, in comparison compressive strength changes for the same material were more noticeable.

A relationship between strain, strain rate and modulus of elasticity is provided by CEB-FIP Model Code [11] given by:

$$E_d / E_c = (\dot{\varepsilon}/\dot{\varepsilon}_0)^{0.026} \quad (1)$$

where E_d (time-variant modulus) and E_c (constant modulus) are respectively the modulus of elasticity due to impact and static load, $\dot{\varepsilon}$ and $\dot{\varepsilon}_0$ are the strain due to impact and static loads, respectively, and 0.026 is a constant that relates the strain rate to the time-variant modulus. The strain rate limit, $\dot{\varepsilon}_0$ is a constant and can be taken as 3×10^{-6} s^{-1} in tension region. In compression, the value of $\dot{\varepsilon}_0$ is different and given by 30×10^{-6} s^{-1}. Bischoff and Perry [3] provide different limits of constant strain rate that range from 10^{-6} to 6×10^{-5} s^{-1} for static load and 2×10^{-5} s^{-1} to 6×10^{-5} s^{-1} for quasi-static load.

To date, practically and theoretically little or no consideration is given to the problem of moving load across a Finite Element (FE) discretized beam and how it impacts the modulus of elasticity. Therefore this investigation is carried out to clarify the impact on a simply supported bridge. The point force moving across the beam model represent this case and calculation of strain with respect to time results in obtaining an appropriate value for time-dependant modulus of elasticity. The mathematical model employed in the simulations is described in next section. Then the level of the strain is investigated to calculate the time-variant modulus and strain rate. Finally, the impact of the use of a strain-rate dependent modulus on the bridge response is evaluated by comparing to the traditional practice based on the use of a constant modulus.

2 MATHEMATICAL MODEL EMPLOYED IN SIMULATIONS

The model involved a simple FE beam (having the length L) nodal load (P) moving at a velocity v (m/s) is adopted to investigate an effect of changing strain (Figure 1).

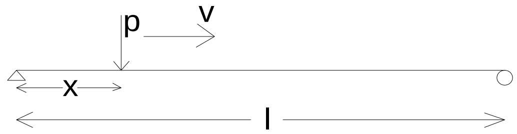

Figure 1. Moving load model.

The beam is modelled with 100 finite elements with 2 degrees of freedom at each node. Stiffness and mass matrices are defined for each element and then assembled into the global stiffness and mass matrices. Complex damping is usually ignored because it has negligible influence on the overall results of strain and displacement [12]. Moreover, the time of impact on the structure due to the load is relatively short. As such a linear damping model is adopted in this case. The global damping matrix is expressed as a linear combination of stiffness and mass matrices in the form of the following equation [12]:

$$[C_g] = a_0[M_g] + a_1[K_g] \tag{2}$$

where C_g is the damping matrix, M_g is the mass matrix, and K_g is the stiffness matrix. a_0 and a_1 are respectively the Rayleigh coefficients of first and second modes of the bridge. These coefficients are adjusted as to provide a damping ratio of 3% for typical small to medium sized bridges [13].

In this investigation, the beam is 10 m long with a cross-sectional area by 10.4 m^2, which is made of concrete having a constant modulus of 35×10^9 N/m^2 and a density of 2400 kg/m^3. The single point load P of 100 kN is applied at nodes. Therefore, a first natural frequency of the beam is 11.25 Hz.

Time step defined in the calculations is 0.001 s. The total time that the load is applied on the nodes was determined based on loading velocity, and the equation of motion of the FE beam model is solved to find the displacements at each node. At each time step, the strain is obtained from the displacements using shape functions and the time-variant modulus is subsequently calculated for each element based on the CEB-FIP equation [Equation (1)]. The modulus of elasticity is calculated for each fiber within a cross-section (as each fiber has a different strain rate), and then an equivalent modulus of elasticity determined for each cross-section. These equivalent modulus of elasticity are then used to populate the global stiffness matrix before equations of motion are solved in the time step that followed. A more detailed description of the model can be found in Aied and González [14].

3 LEVELS OF STRAIN IN A MOVING LOAD PROBLEM

The increase in strain rate depends on the mechanical properties of the structure, as well as the magnitude and velocity of the load. In Figure 2, the rate of change in strain is plotted in the main vertical axis together with the strain-rate dependent modulus in the secondary vertical axis for each time-step. The load is 100 kN travelling at 25 m/s (Figure 2a) and 5 m/s (Figure 2b). These velocities present typical values of vehicles crossing a bridge at fast and slow speeds. The properties of the beam are as stated above. In Figure 2a, strain rate exceeds the specified static limit for most of the run except at 0.1 s where the strain rate is 0.0, and for the first 0.2 s the strain rate is positive and vice versa for the last 0.2 s. Maximum difference between constant and time variant modulus is 8%, which occurs at a strain rate of 7×10^{-5} s^{-1}. In Figure 2b, the strain rate exceeds the static limit but the increase is much less than that in Figure 2a. A maximum difference of 4% corresponding to a strain rate of 1.35×10^{-5} s^{-1} is obtained. Also, the strain rate reaches almost a constant value after 1 s (Figure 2b).

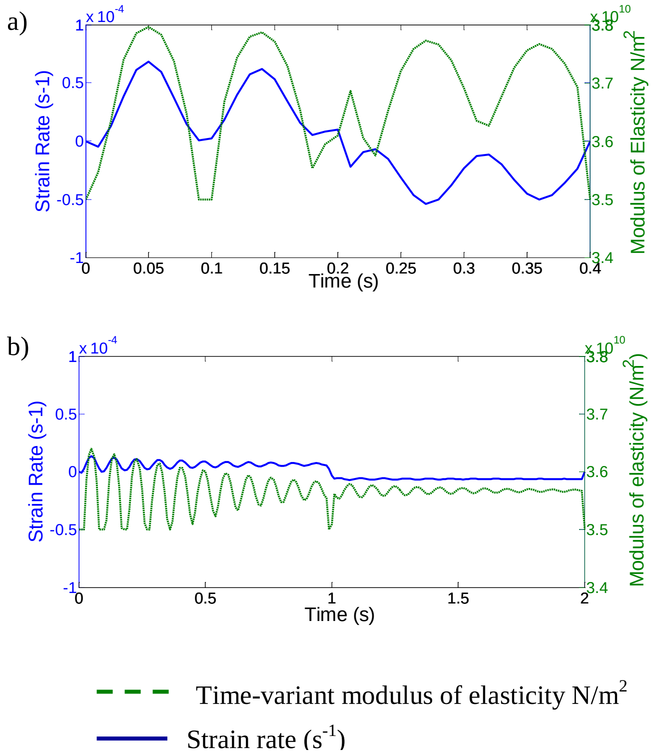

Figure 2. Time-variant modulus with strain rate versus time at mid-span; at velocity (a) 25 m/s, (b) 5 m/s.

Throughout work of Aied and González [14] on investigating effect of the velocity on the strain rate, the results showed the maximum time-variant modulus of elasticity increase rapidly when the velocity changes from 5 m/s to 25 m/s (Figure 4). However, gradual increase was found for a velocity in range of 25 m/s to 60 m/s. For example, the maximum time-variant modulus of elasticity were 4% (3.65×10^{10} N/m^2 vs. 3.5×10^{10} N/m^2) , 8% and 10.2% corresponding to 5 m/s, 25 m/s and 60 m/s when compared to the constant modulus of elasticity. Thus, the strain rate at 25m/s was of interest.

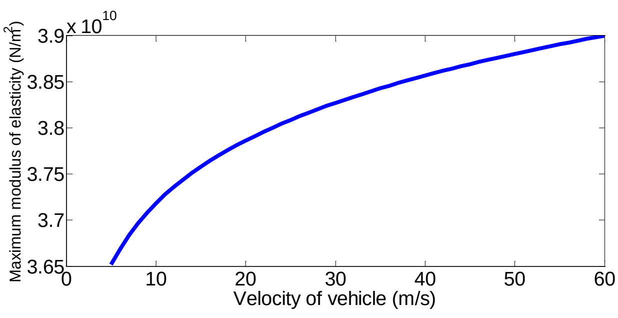

Figure 3. Change in time-variant modulus with velocity at mid-span section (adapted from Aied and González [14]).

The relationship between strain rate and ratio of time-variant to constant modulus of elasticity is illustrated by Figure 4 using the formulation of CEB-FIP (equation 1). This presents how the strain rate is related to the time-variant modulus. The ratio of modulus rapidly increases between strain rate of 3×10^{-6} (close to 0) and 0.5×10^{-4} with 8% increase, and after that the ratio gradually increases. Figure 4

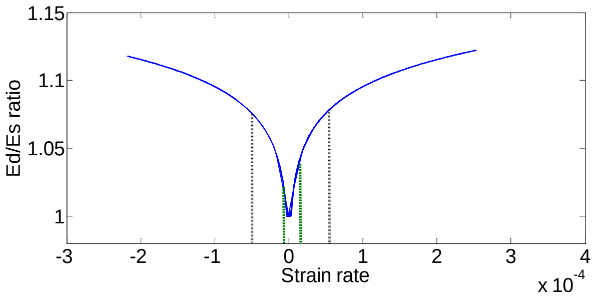

Figure 4. Ratio of time-variant modulus to constant modulus versus strain rate; maximum strain rate at 25 m/s (dotted line) and 5 m/s (dashed line).

shows the intersection points of strain rates at 25 m/s (5.5×10^{-5} s^{-1} and -5×10^{-5} s^{-1}) and 5 m/s (1.5×10^{-5} s^{-1} and -0.5×10^{-5} s^{-1}), showing how faster velocity produces higher strain rates modulus ratio.

Strains at beam sections other than mid-span shown in Figures 3 and 4, are subject to strain rates associated to different values of modulus of elasticity. Generally the strain rate gets smaller the closer to the support. A time-variant modulus of elasticity that depends on strain rate is used to calculate the strain and displacement at each time step. Beam properties and sections under investigation are varied in order to investigate the impact of a varying modulus on different scenarios.

3.1 Strain and displacement at mid-span section

Strain rate and time-variant modulus are calculated at every single discretized beam cross-section for every simulation. Figure 5 compares strain at the mid-span section when using a constant modulus (based on ‘static’ or low strain rates) or a time-variant modulus at a velocity of 25m/s and load of 100kN. As the time-variant modulus of elasticity is greater than the constant one, strain based on the time-variant modulus of elasticity is somewhat smaller than ones based on the constant modulus of elasticity (Figure 5). For this particular case, when the load is near or on the mid-span point the strain based on the time-variant modulus is the same as the ones of constant modulus because at mid-span the strain rate reaches 0.0 and the time-variant modulus is the same as the constant modulus of elasticity (Figure 2a). However, strain derived from time-variant modulus is 3% higher than one based on the constant modulus near the mid-span. Additionally, the largest divergence between the strain from the time-variant modulus and one from the constant modulus occurs at the peaks of excitation response (8%).

Similarly, displacements calculated from the time-variant modulus are also smaller than ones derived from the constant modulus (Figure 6). Maximum variation between displacements using a time-variant modulus and displacement using constant modulus are at 0.16 s (9%). When the load is on the reference point (mid-span) both displacements are close although displacement using a time-variant modulus is slightly higher.

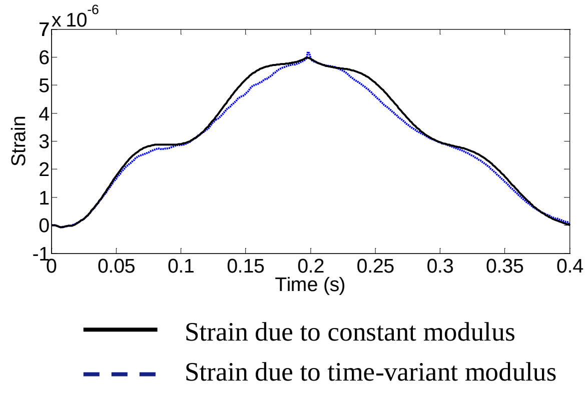

Figure 5. Strain based on a time-variant modulus and strain based on a constant modulus versus time at mid-span of the beam.

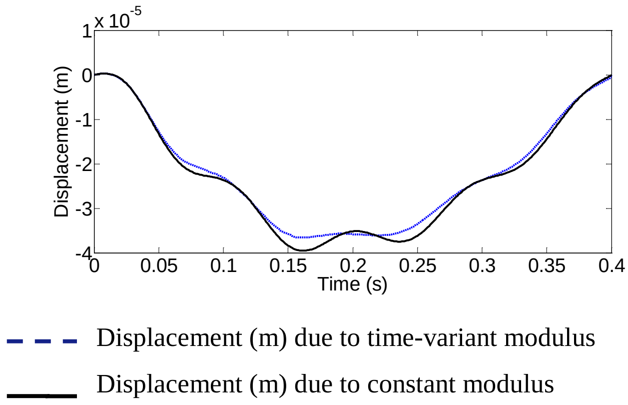

Figure 6. Displacement at mid-span when using a time-variant modulus or a constant modulus.

3.2 Strain at different locations

As the load crosses the beam, strain and strain rate varies throughout the structure. Figure 7 presents the strain at the lower fibre of quarter span cross- section and Figure 8 presents the strain at different cross-sections on the beam. All sections provide a similar output and differences between using a constant or a time-variant modulus are small. On the quarter span calculations, the strain using time-variant modulus is sometimes higher than strain using constant modulus and at other points the strain using time-variant modulus is higher (at times 0.12 s and 0.22 s). A maximum difference of 3% is obtained close to maximum strain using a constant modulus. When the load is exactly on quarter span strain using constant modulus is similar or close to the strain using time-variant modulus. A detailed study of the effect of load magnitude and velocity on modulus of elasticity for different cross-sections along the beam can be found in Aied and González [14].

Strain calculations for a number of nodal points along the beam are plotted against time using a time-variant modulus (Figure 9). Behaviour of the strain is such to produce a sharp ascending and descending slope when the load is close to the reference node. These peaks are caused by a time-variant modulus similar to the constant modulus when the load is near the reference point (mid-span).

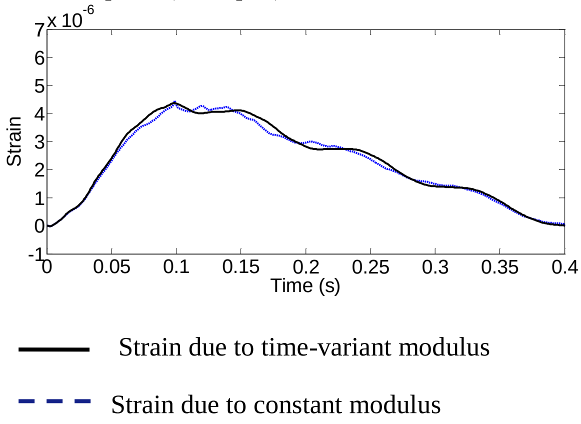

Figure 7. Strain based on constant and time-variant modulus of elasticity.

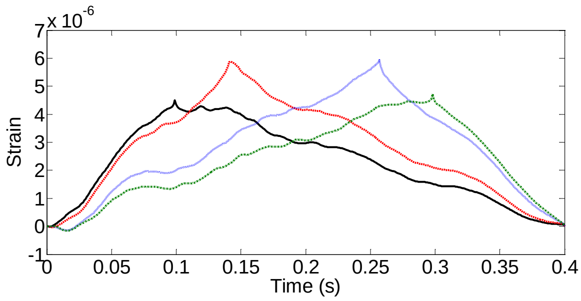

Figure 8: Strain based on time-variant modulus of elasticity; ¼ span (solid line), 35th element (dashed line), 65th element (dotted line), ¾ span (dashed and dotted line).

The strain is taken at the lowest fibre of the cross-section where tension is highest (i.e., 0.325 m from centroid). Previous findings show that the modulus of elasticity in compression is more affected by high strain rates than in tension [3, 15]. Therefore, in the compression region the modulus of elasticity has more influence. This indicates that, although the strain in the compression region is lower than in tension, greater rate of increase in the modulus of elasticity is likely to occur due to high strain rates.

3.3 Strain at varying velocity

To investigating influence of moving velocity on time-variant modulus of elasticity, various speeds involving 5m/s, 10 m/s, 15 m/2 and 20 m/s (with interval speed of 5 m/s for range from 5 m/s to 25 m/s) were used at mid-span cross-section. The results are shown in Figure 9. At the slowest velocity of 5m/s the strain based on time-variant modulus is smaller than strain based on the constant modulus but at the maximum point the strains are similar. A maximum difference of 3.7% is found at 5 m/s but when the load is on the reference node the strains are similar. At faster velocities of 10 m/s and 15 m/s a similar pattern in the strain measurements is observed but at 15m/s the strain based on the time-variant modulus is 5.6% lower than the strain based on the constant modulus which is at 0.35 s just after the load crosses the mid-span point. The fastest velocity of 20 m/s produces 7.6% maximum change in the strain using the time-variant modulus. It can be concluded that a proportional relationship exists between the maximum difference of the strains and the loading velocity. In addition, it can be seen that, slow velocities (5 m/s and 10 m/s) higher peak responses occur for strains using time-variant modulus but as the velocity increases (15 m/s and 20 m/s) the contrary starts to take place.

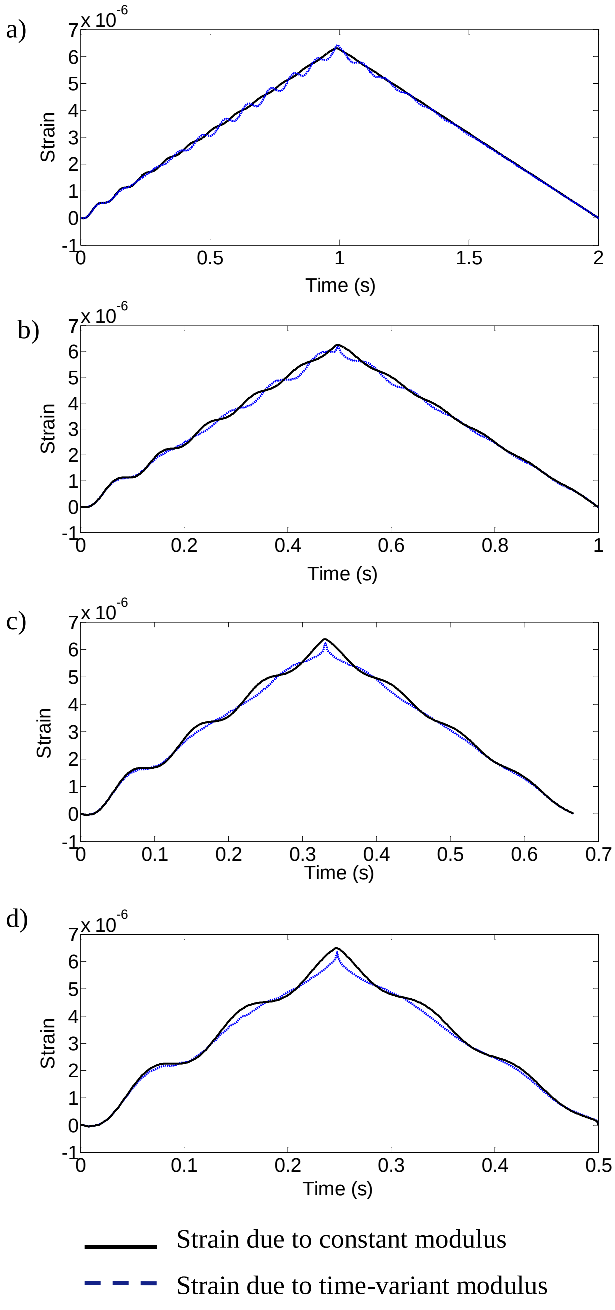

Figure 9. Strain based on constant modulus or time-variant modulus at (a) 5m/s, (b) 10m/s, (c) 15m/s, and (d) 20m/s.

The impact of velocity on the displacement response is equivalent to that obtained for strain. When using a constant modulus, there are no constricting factors that limit the increase in displacement due to higher dynamic effects. However, faster loads cause the time-variant modulus to reach higher values, therefore displacement is reduced following the stiffer response of the structure.

3.4 *Strain for different beam lengths*

Earlier, a 10m long bridge has been used for analysing the dynamic response of a beam. Two different beam spans of 20m and 30m are simulated with cross-sectional depths of 1m and 1.5m respectively (Figure 11). The two spans have a constant modulus of elasticity of 35×10^9 N/m^2 and a density of 2400 kg/m^3. Frequencies of 2.8 Hz and 4.3 Hz for 20m and 30m long span bridges respectively resulted from the adopted beam properties. The number of discretized elements is 100 and the time step of simulation is 0.001 s for both beam spans with a load of 100 kN travelling at 25 m/s. Simulated measurements are obtained at the mid-span point of the beam.

Results of strain for 20m long span (Figure 11a) give very small variations between the two strain calculations and at the peak (mid-span) the strain is almost the same with maximum difference occurring close to the mid-span (at 0.39 s and 0.42 s). Longer beam span of 30m strain difference is even smaller with most visible difference near the mid-span. Therefore, the longer the span length of a beam the lower the impact of time-variant modulus for midpoint of the beam is observed.

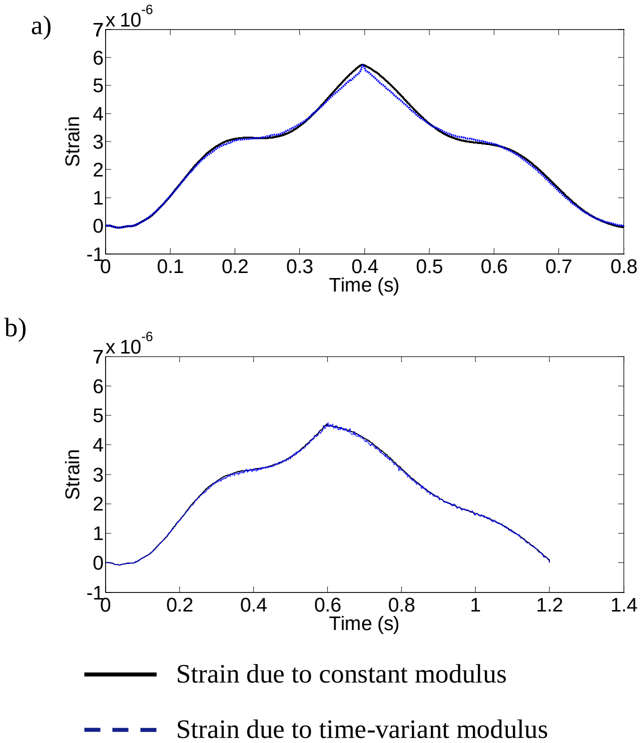

Figure 11. Strain based on constant or time-variant modulus for (a) 20 m span and (b) 30 m span beam.

4 IMPACT OF DYNAMIC AMPLIFICATION

Dynamics on the bridge are primarily affected by vehicle velocity, matching bridge and vehicle natural frequency, and roughness of approach road and the bridge surfaces [16]. The bridge responses are typically characterized in the codes through the use of static response and a dynamic amplification factor (DAF) [calculated by a ratio of maximum total response (static + dynamic) over maximum static response] [13]. A number of authors [17-19] have found that as the velocity of the vehicle increases the DAF alternates from high to low in a pattern characterized by a series of peaks and troughs that increase with speed. The pattern depends on the frequency of the bridge and a pseudo-frequency that depends on the load velocity and bridge length.

In Figure 11, the DAF using constant and time-variant modulus is plotted for a range of load velocities for a bridge length of 10m at mid-span. Significant difference between the DAF from the time-variant modulus and ones from the constant modulus is noticed at a loading velocity of 25 m/s. At low velocities, it is noticeable how the DAF based on a time-variant modulus is generally below one. This is a result of the structure responding in a stiffer manner under loads at speed than under a static load. Therefore, these loads at low speed are not able to generate sufficient large dynamics and strains as to produce DAFs above one. When using a time-variant modulus, it is necessary to reach speeds above 45 m/s to enter a region where DAFs are consistently above one.

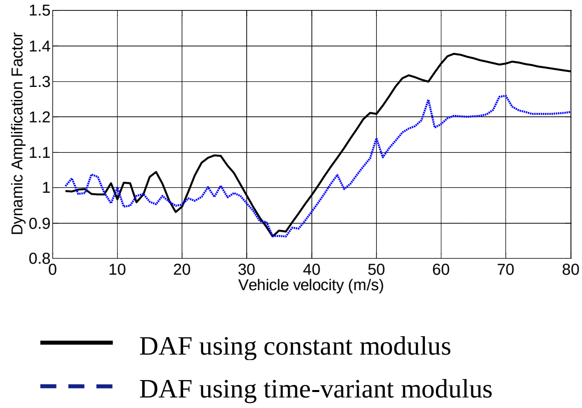

Figure 10. DAF versus velocity.

DAF is affected to a large extent by the variation in the modulus. However, these results are based on Equation (1) which might be exaggerated for a true bridge. A more accurate picture of how DAF can be affected by strain rate for a particular bridge can be experimentally obtained by measuring the response of the bridge to a number of vehicles travelling with different loading and velocity conditions.

5 SUMMARY AND CONCLUSIONS

The response of a one dimensional FE beam to a point force is simulated to calculate the change in strain and displacement due to a time-variant modulus. For this purpose, the relationship between strain rate and time-variant modulus provided by CEB-FIP Model Code is used in the analysis. The velocity of the vehicle has a high impact on the dynamic response given that as the force travels faster, the modulus rises and restricts the increase in the response. Responses at high velocities lead to lower maximum strain and displacement peaks using a time-variant modulus than using a constant modulus of elasticity. These differences between using a constant or time-variant modulus are clearly observed when investigating DAF. If the assumption of time-variant modulus is adopted, very high speeds are necessary to identify DAF values of 1.1, i.e., 50 m/s. However, if a constant modulus is employed, a DAF of 1.1 can be reached at 25 m/s. These results are based on the application of the CEB-FIP equation and a simplistic point load model on a one-dimensional beam. Therefore, a site-specific equation will need to be calibrated (i.e., using a traffic population in the case of a bridge) to draw conclusions for other scenarios.

ACKNOWLEDGMENTS

The authors would like to thank Patrick McGetrick and Jason Dowling for their help and expertise in the numerical modelling of the beam.

REFERENCES

[1] S. Kolias and R. Williams, "Relationships between the static and the dynamic moduli of elasticity in cement stabilised materials," *Materials and Structures,* vol. 13, pp. 99-107, 1980.

[2] I. E. Shkolnik, "Influence of high strain rates on stress–strain relationship, strength and elastic modulus of concrete," *Cement and Concrete Composites,* vol. 30, pp. 1000-1012, 2008.

[3] P. Bischoff and S. Perry, "Compressive behaviour of concrete at high strain rates," *Materials and Structures,* vol. 24, pp. 425-450, 1991.

[4] A. Filiatrault and M. Holleran, "Stress-strain behavior of reinforcing steel and concrete under seismic strain rates and low temperatures," *Materials and Structures,* vol. 34, pp. 235-239, 2001.

[5] D. Yan and G. Lin, "Dynamic properties of concrete in direct tension," *Cement and concrete research,* vol. 36, pp. 1371-1378, 2006.

[6] P. Soroushian and K. Obaseki, "Strain rate-dependent interaction diagrams for reinforced concrete sections," *ACI Journal Proceedings,* vol. 83, 1986.

[7] H. C. Fu, M. A. Erki, and M. Seckin, "Review of Effects of Loading Rate on Reinforced Concrete," *Journal of Structural Engineering,* vol. 117, pp. 3660-3679, 1991.

[8] M. Wakabayashi, T. Nakamura, S. Iway, and Y. Hayashi, "Effects of strain rate on the behavior of structural members," *Proc. 8th World Conference on Earthquake Engineering,* vol. 4, pp. 491-498, 1994.

[9] D. Asprone, R. Frascadore, M. Di Ludovico, A. Prota, and G. Manfredi, "Influence of strain rate on the seismic response of RC structures," *Engineering Structures,* vol. 35, pp. 29-36, 2012.

[10] D. Asprone, E. Cadoni, and A. Prota, "Experimental analysis on tensile dynamic behavior of existing concrete under high strain rates," *ACI Structural Journal,* vol. 106, pp. 106-113, 2009.

[11] Rowe R. E. and W. R., Eds., *CEB-FIP Model Code 1990* (No. 203. lausanne switzerland: Comite Euro-International du Beton, 1991, p.^pp. Pages.

[12] Y. B. Yang, J. Yau, and Y. Wu, *Vehicle-bridge interaction dynamics: with applications to high-speed railways*: World Scientific Pub Co Inc, 2004.

[13] S. P. Brady, E. J. O'Brien, and A. ZnidariC, "Effect of Vehicle Velocity on the Dynamic Amplification of a Vehicle Crossing a Simply Supported Bridge," *Journal of Bridge Engineering,* vol. 11, pp. 241-249, 2006.

[14] H. Aied and A. González, "Structural Analysis of bridges with time-variant modulus of elasticity under moving loads," presented at the The 6th International Conference on Bridge Maintenance, Safety and Management, (IABMAS 2012), Lake Magiore, Italy, 2012.

[15] D. Grote, S. Park, and M. Zhou, "Dynamic behavior of concrete at high strain rates and pressures: I. experimental characterization," *International Journal of Impact Engineering,* vol. 25, pp. 869-886, 2001.

[16] M. F. Green, D. Cebon, and D. J. Cole, "Effects of vehicle suspension design on dynamics of highway bridges," *Journal of Structural Engineering,* vol. 121, p. 272, 1995.

[17] A. González, E. J. Obrien, D. Cantero, Y. Li, J. Dowling, and A. Žnidarič, "Critical speed for the dynamics of truck events on bridges with a smooth road surface," *Journal of Sound and Vibration,* vol. 329, pp. 2127-2146, 2010.

[18] A. Greco and A. Santini, "Dynamic response of a flexural non-classically damped continuous beam under moving loadings," *Computers & Structures,* vol. 80, pp. 1945-1953, 2002.

[19] S. P. Brady, "*The influence of vehicle velocity on dynamic amplification in highway bridges*," PhD, University College Dublin, Dublin, 2004.

Applying static capacity approaches to pile driveability analysis for dense sands

Tiernan Byrne[1], Paul Doherty[1], Ken Gavin[1]
[1]Department of Civil, Structural & Environmental Engineering, University College Dublin, Belfield, Dublin 4, Ireland.
Email: Tiernan.Byrne@ucdconnect.ie, Paul.Doherty@ucd.ie, Kenneth.Gavin@ucd.ie

ABSTRACT: Considerable research in recent years has resulted in a greater understanding of the pile-soil interaction under axial loading, and has led to the development of improved methods when predicting the capacity of displacement piles in sand. The formulation of the Imperial College (ICP) and the University of Western Australia (UWA) approaches has allowed for greater accuracy and more certainty in assessing the medium term capacity of piles in sand. ICP and UWA were developed predominantly for open-ended pipe piles with recommendations for use with closed-ended piles. In order to evaluate the applicability and feasibility of adopting these approaches for driveability purposes, certain modifications must be considered to account for the relatively low displacements mobilised during driving, and among other factors, the absence of pile strength gain with ageing. The dense sand found at the University College Dublin (UCD) Blessington test site is used for analysis in this paper, where five 7.5m long, 340mm outer diameter (O.D), 14mm wall thickness (W.T) steel pipe piles were driven in addition to seven 7.5m, 275mm square precast concrete piles, respectively. The ICP and UWA are examined along with existing driveability approaches by incorporating static resistance to driving (SRD) models and dynamic damping parameters into a one dimensional wave equation analysis programme (GRLWEAP). Piling records are used to test the accuracy of the models by comparing the measured and predicted blow counts.

KEY WORDS: Pile Driveability, Dense Sand, Axial Static Capacity, ICP, UWA.

1 INTRODUCTION

Pile driveability is an integral component of modern pile design and is an influential factor in the selection of an appropriate driving system. Accurately predicting the pile response to driving is becoming increasingly important, with the use of large 3 to 6m diameter steel monopiles becoming commonplace in offshore applications. Pile driveability assesses the ability for a pile to be safely and economically driven, and ultimately reach a desired penetration or capacity within a reasonable number of blows without overstressing the pile material. Factors which influence driveability include the makeup of the hammer driving system, pile dimensions and soil resistance.

Methods to estimate the soil resistance to driving that are commonly used include procedures proposed by Toolan & Fox [1], Stevens et al. [2] and more recently, Alm & Hamre [3]. Many of these empirical design approaches were developed for the offshore oil and gas industry for open ended steel pipe piles when the majority of piles installed had a diameter of less than 2m, similar to the 340mm O.D steel pipe piles driven at the Blessington site. A close correlation would be expected for these piles but uncertainty exists as to how accurate a prediction will be produced for the 275mm square precast concrete piles. This paper aims to evaluate the accuracy of existing driveability approaches for both open and closed-ended piles installed in dense sand and to investigate the feasibility of applying more recent static capacity models, namely ICP [4] and UWA [5] to pile driveability. Piles driven in the dense sand found at the UCD Blessington test site are used to assess the driveability models in the paper.

2 UCD BLESSINGTON TEST SITE

The test site is located in a quarry near Blessington, Co. Wicklow, Ireland. A number of researchers have investigated the geological history of the site [6] and have described in detail the glacial movements which formed the underlying sand deposits. Dense to very dense horizontally bedded, heavily over-consolidated sand layers originating from a glacial lake with particle grading ranging from silty sand to coarse sand are the dominant site conditions.

The Blessington site has been developed by UCD's Geotechnical Research Group (GRC) to facilitate extensive research into foundation behaviour. Site characteristics and properties have been documented by past workings at the site and conditions are summarised as having residual (soil-steel) interface friction angles varying between 33º-38º, unit weights of between 19.0-20.0kN/m^3 and relative densities near 100%.

Multiple Cone Penetration Tests (CPT) were conducted at the site which confirmed the dense ground conditions with cone point resistance values (q_c) increasing from 10MPa at the ground surface to 25MPa at depth of 10m (see Figure 1).

3 PILE DRIVING

A Junttan HHK-4A accelerated hydraulic impact hammer was used to drive five 7.5m, 340mm O.D, 14mm W.T steel pipe piles and seven 7.5m, 275mm square precast concrete piles to penetrations of 7m. The pipe piles were driven directly with the hammer assembly impacting on the steel annulus, while the driving system for the concrete piles included 75mm Beech wood pile cushions. Selected piles were instrumented with strain gauges and accelerometers.

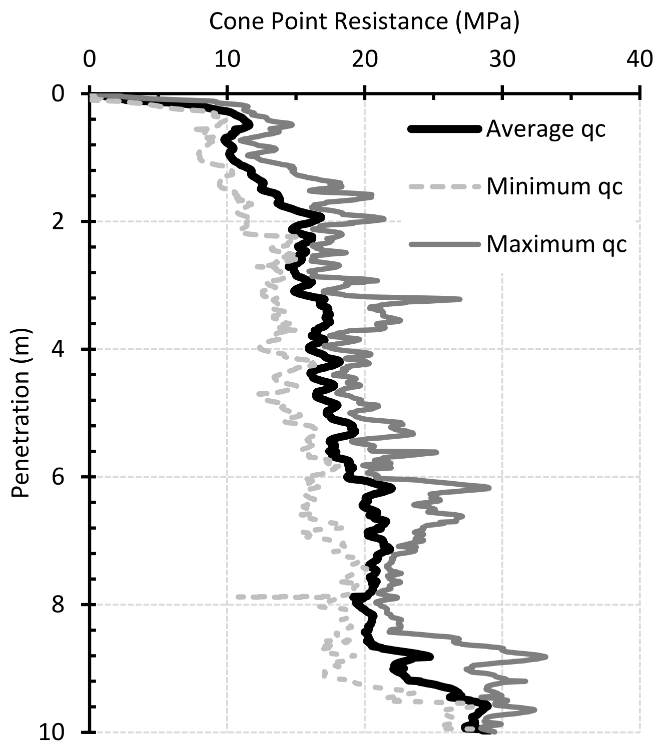

Figure 1. Blessington CPT Profile.

With a ram weight of 4,000kg, and a maximum stroke height of 1.2m, the max rated energy of the hammer is 47kNm. The operating efficiency is 95% and is capable of up to 100 blows per minute. Stroke heights for the steel pipe piles were kept constant at 0.3m, corresponding to a hammer energy of 11.77kNm, whereas the stroke heights for the concrete piles were varied from 0.2-0.5m (7.85-19.62kNm), adjusted when necessary to prevent excessive blow counts which can affect the structural integrity of the pile. It was evident that the blow counts for both the concrete and steel pile increased with increasing pile penetration, with the recorded blow counts for the steel pile generally half of those for the concrete pile. Average, maximum, and minimum recorded blow counts from both the steel and concrete piles are presented in Figures 3-6. The high degree of scatter for the concrete piles can be somewhat attributed to the varying stroke heights. The piles were installed by Bullivant Tarranto and the instrumented piles monitored by Lloyd Acoustics. Selected blow counts at different depth increments were analysed using CAPWAP, with results and analysis presented by Doherty et al. [7].

4 PILE DRIVEABILITY METHODS

The total resistance of a pile to driving includes the initial static resistance to driving (SRD), increases in pile capacity due to viscous rate effects, and dynamic increases in capacity due to inertia. A number of driveability SRD approaches have been presented over the years and are still commonly used in pile design today. Pile driveability was mainly concerned with the offshore sector and the initial models developed in the late 1970's and early 1980's were designed for pipe piles with diameters of less than 2m, typical of those used in the offshore oil and gas industry at the time.

Although not specifically intended for closed-ended square piles frequently used onshore, the principles on which they were based remain relevant and are therefore considered appropriate. Closed-ended piles will be considered in the fully plugged condition for the purposes of this study (e.g. the soil beneath the pile tip displaces with advancing pile penetration, leaving the inner cylindrical core of an open-ended pipe completely free of soil). An adjustment is necessary to account for the square nature of the concrete piles as most of the procedures refer to circular piles. It is common practice to calculate an equivalent diameter (D_{equiv}) based on the pile area (A), i.e. $D_{equiv} = \sqrt{4A/\pi}$. The earlier models also do not directly take into account the phenomenon of "friction fatigue", which is now widely accepted as having a significant influence on pile driveability. Recent SRD models include such effects and are calibrated using piles of larger diameters and modern, higher efficiency hydraulic hammers. Three driveability approaches were selected for the purposes of this paper and a brief summary of each is described below. The performance of each model will be assessed against the recorded blow counts from the concrete and steel pipe piles driven at the Blessington test site. The suitability of the described methods with closed ended piles will also be investigated.

4.1 *Toolan & Fox (1977)*

The intention of the paper [1] was to assist engineers in the planning of offshore jacket platforms supported on driven piles and it proposes recommendations for pile driveability. The SRD model calculates both the shaft and toe resistance separately. The unit toe resistance, for sands and clays alike, is evaluated from a weighted average of the cone point resistance (q_c) over a number of pile diameters above and below the pile tip. The unit skin friction in sands is calculated as a fraction of the recorded cone resistance, (1/300 for dense sand) and is limited to 120kPa. For a fully coring pile, the unit toe resistance is applied to the pile annulus and skin friction to the internal and external shaft equally. A plugged or closed-ended pile has skin friction acting on the external shaft area only and toe resistance applied to the gross toe area.

4.2 *Stevens et al. (1982)*

Guidelines are provided for estimating pile driveability in clay, sand and rock [2]. For granular materials, both unit toe and skin resistances are calculated using the standard static capacity procedures outlined in the 1982 API RP 2A code [8]. The model defines lower and upper bound static resistances for plugged and coring conditions. For the coring lower bound case, internal skin friction is assumed to be half that of the external, with the upper bound prediction adopting equal internal and external skin friction. The recommendations suggest that the lower bound plugged case provides the best agreement with recorded blow counts for dense sands, even if the pile does not completely plug.

4.3 *Alm & Hamre (2001)*

The Alm and Hamre approach was first introduced in 1998, with an updated version presented in 2001. The update sought to address issues with variability and uncertainty in selection of soil parameters and modelling changes in radial stress during driving. A direct correlation for both unit base (qb) and shaft (τf) resistance with the cone penetration test, CPT (q_c)

was introduced as a result. This model incorporated friction fatigue directly in its formulation and was calibrated using a database of piles of lengths of up to 70 m and diameters up to 2.7 m. The approach specifies a best prediction and upper bound profile with details provided in Alm & Hamre [3].

4.4 Advanced CPT Models

Considerable advances have been made in assessing the capacity of piles under static loading in recent years. Improved understanding in particular of the pile-soil interface response from effective stress measurements on instrumented piles have led to the development of the ICP and UWA models for predicting the capacity of piles to static loading. Whilst these methods were not developed as an SRD model for driving, given modifications they should be considered relevant and applicable.

Previous driveability approaches were based on static analyses and it is proposed to apply the ICP and UWA to predict driveability. It is intended to apply them as one would for a static analysis, using the procedures specified in Lehane et al. [5] and Jardine et al. [4] respectively. Overy and Sayer [9] describe a case-study where the ICP approach was successfully implemented to investigate drill-drive operations for an offshore platform in the North Sea. They report that the method gave a reasonable estimate of the measured soil resistance. Schneider and Harmon [10] used a modified version of the UWA method to perform driveability analyses on piles from three sites with acceptable results.

5 STATIC RESISTANCE TO DRIVING AND WAVE EQUATION ANALYSIS

In pile driveability analyses, a wave equation programme can be used to analyse the enthru (energy transferred to pile) from each hammer impact. In this paper, GRLWEAP Offshore 2010 [11] was used to perform the analyses. During driving, a pile experiences both static and dynamic resistances. The dynamic forces are represented by damping factors in GRLWEAP which account for inertial and viscous rate effects. The static resistance to driving (SRD) is usually estimated using static capacity approaches for both the end resistance and shaft friction. The SRD value is highly dependent on the soil type and its mode of installation (i.e. whether the pile is coring or plugged). Soil plug measurements were recorded for the steel tubular pipe pile during driving and are presented in Figure 2. It is clearly evident that it partially plugged with an incremental filling ratio (IFR) varying from 100% at the ground surface to give a final filling ratio (FFR) of approximately 50% at final penetration, where IFR is defined as the incremental change in soil plug length over pile penetration ($IFR = \Delta h_{plug}/\Delta h_{pile}$).

Only the UWA approach considers partial plugging explicitly in the calculation of unit toe/skin resistances, and interpretation between the plugged and unplugged conditions will be required in assessing driveability for the other methods. For instances where soil plug readings were not taken, the UWA model proposes and estimation of the mean IFR (IFR_{MEAN}) based on the internal pile diameter (D_i), where;

$$IFR_{MEAN} \approx min\left[1, \left({}^{D_i(m)}/_{1.5m}\right)^{0.2}\right] \qquad (1)$$

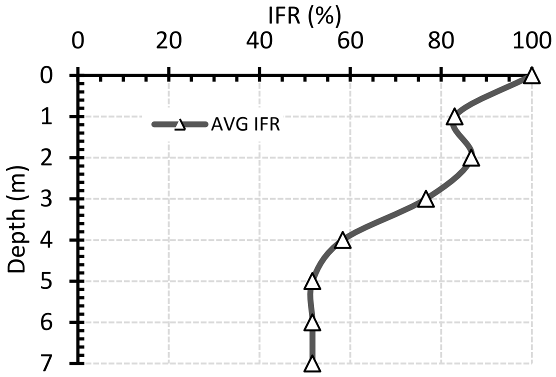

Figure 2. Average IFR's for Steel Pipe Piles.

For the steel pipe pile of 0.312m internal diameter, IFR_{MEAN} is approximated as 73% which correlates well to the averaged value recorded of 70%.

Models used to evaluate SRD were discussed in Section 4. It is usual for an SRD model to be accompanied by a set of damping factors and quake values. Quake is defined as the displacement required to achieve yield. The parameters used in this paper were either from the original reference or from GRLWEAP recommendations in the absence of specified values.

GRLWEAP has a comprehensive catalogue of hammer types with a database of their properties, hammer mass etc. allowing the hammer performance/efficiency to be modelled correctly in order to realistically simulate the driving process.

Soil profiles calculated from the models were incremented to give approximately 100 elements for input into GRLWEAP. Issues arose with methods which incorporated friction fatigue, as the distribution of shaft friction varies with pile tip penetration. Schneider and Harmon [10] found that the shape of the shaft friction distribution had little effect on the resultant bearing graph, and they suggested that the change in shaft capacity between two successive increments could be used to calculate the pseudo average shaft friction ($\Delta\tau_{f,avg}$):

$$\Delta\tau_{f,avg} = \frac{\sum Q_{S,L} - \sum Q_{S,L-1}}{\pi D.\Delta L} \qquad (2)$$

Where:

$\sum Q_{S,L}$ = cumulative shaft resistance at tip depth,
$\sum Q_{S,L-1}$ = cumulative shaft resistance previous depth inc,
ΔL = depth increment, and
D = pile diameter.

6 ANALYSIS & DISCUSSION

6.1 Driveability Models

The driveability predictions provided by the Toolan and Fox (T&F), Stevens et al. (Stevens) and Alm & Hamre (A&H) methods are compared to the measured response at Blessington in Figures 3 & 4 for the steel pipe and precast concrete piles, respectively. The predictions for the steel pile, in general, fall within a relatively narrow range and are predominantly bounded by the upper and lower blow counts with the exception of the Stevens et al. coring case. By contrast, the predictions for the precast concrete pile are scattered (ranging by a factor of 4) and typically under estimate the blow counts, falling below the minimum values

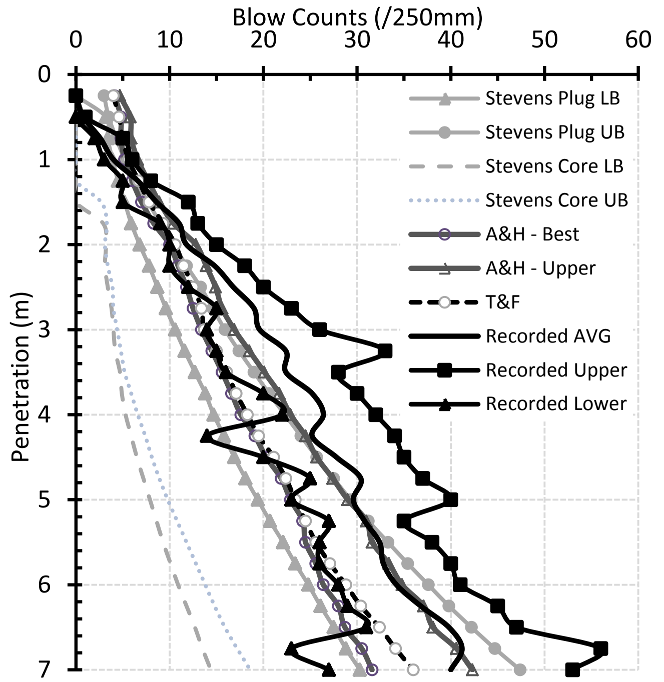

Figure 3. Steel Pipe Pile Driveability Predictions.

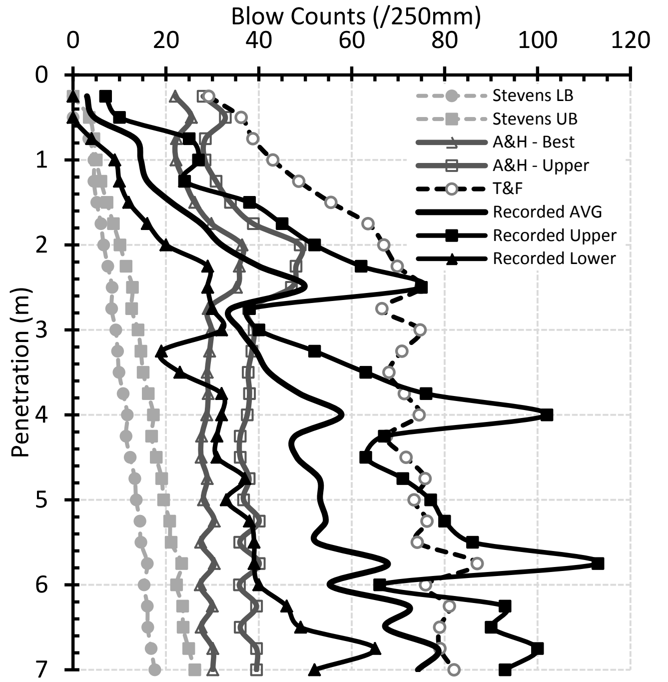

Figure 4. Precast Concrete Driveability Predictions.

recorded. In general, the concrete pile blow counts are roughly double that for the steel pile. Specific comments on the individual methods can be put forward as follows:

6.1.1 Toolan & Fox

The method produces reasonable predictions for both piles, albeit a slight under-prediction for the steel and over-prediction for the concrete based on the average recorded blow counts, with both essentially contained within the min-max range. The model's strong relationship with in-situ CPT cone resistance may lead to uncertainty in piles of increasing diameter for both closed and open-ended conditions.

6.1.2 Stevens et al.

The model generates four profiles of the predicted response for pipe piles, and two for closed-ended piles. The predictions varied significantly based on the assumption of plugging/coring and whether the upper bound (UB) or conservative lower bound (LB) properties were assumed. In practice, the use of the lower bound plugged condition is recommended for use in dense sand. This is shown to provide a reasonable fit to the measured resistance for the steel pipe pile, with the upper bound profile giving an almost exact prediction. However, for the concrete pile, even the upper bound condition severely under-predicts the blow counts.

6.1.3 Alm and Hamre

The Alm & Hamre method provides a good best estimate and sensible upper bound prediction for the steel pile but results in blow counts which initially over-predict and eventually under-predict for the concrete pile.

The inclusion of a mechanism to account for the effect of friction fatigue gives Alm & Hamre a distinct advantage over the previous two methods discussed. The general under-prediction of the closed-ended concrete pile suggests a stiffer base response than estimated which is reasonable given that the soil under the pile tip will most likely undergo densification or compaction to some degree during driving. Uncertainty exists as to how the methods would perform for closed-ended piles of larger toe area and the extent of the under-prediction.

No method estimated a reasonable upper-bound profile which is essential for a driveability analysis.

6.2 SRD from Static Resistance Models

In an effort to improve pile driveability models, the ICP and UWA approaches which include the effects of friction fatigue and soil plugging were applied. In the first instance, the approaches were applied as per the recommendations of their respective guidelines and as intended for a static capacity analysis to obtain an upper-bound resistance.

Predictions obtained by implementing the ICP and UWA procedures in their "raw" form are presented in Figures 5-6&8 (as ICP, UWA & UWA FFR) With UWA, the IFR_{MEAN} (Equation 1) was utilised in the calculations whereas UWA FFR refers to when the actual recorded IFRs were used.

Initially examining the steel piles (Figures 5-6), it is clear that UWA and UWA FFR grossly over-estimate the blow counts, as indeed does the ICP Plugged case. Only the ICP Coring prediction provides an accurate prediction, even though ICP guidelines suggest that the pile is likely to plug. It is clear that modification of the approaches is necessary to account for factors which include:

- Pile ageing;
- The mechanism of base failure;
- Uncertainties over the contribution of internal shaft friction; and
- Relatively low displacements experienced during a hammer blow.

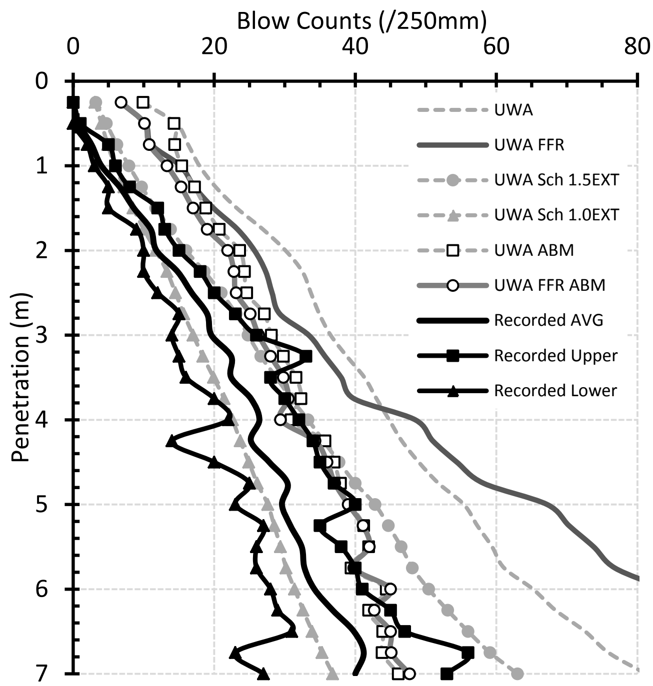

Figure 5. Steel Pile - UWA Static Predictions & Modifications.

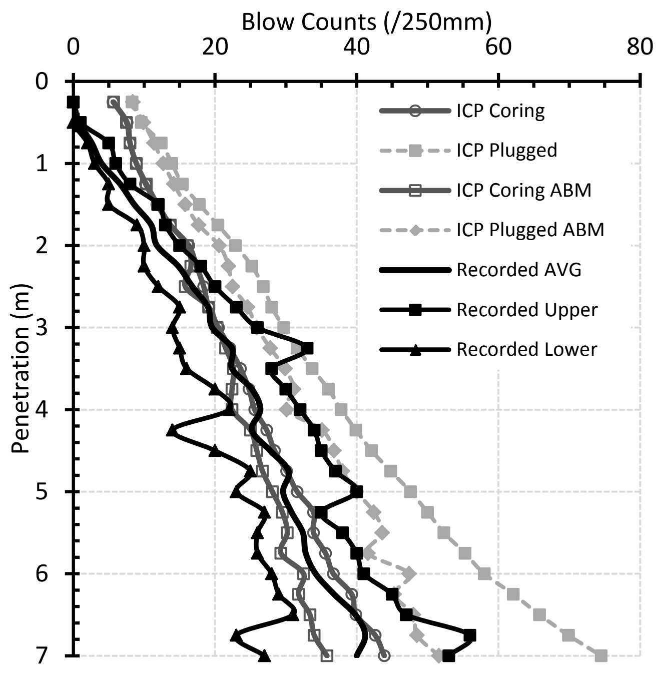

Figure 6. Steel Pile - ICP Static Predictions & Modifications.

Chow et al. [12] and others have demonstrated that the shaft capacity of piles in sand increases with time. Both the ICP and UWA approaches are estimates of the capacity 9 to 10 days after installation. The resistance may therefore be overestimated leading to a slight overestimation of the blow counts. The extent of this increase is difficult to quantify and is dependent on the in-situ state of the sand and the installation procedure, amongst other features.

With respect to base failure mechanisms, the ICP method has a procedure to predict whether plugged or unplugged failure occurs. For the steel pipe pile, a plugged failure was indicated which merits a scaled percentage of the full CPT resistance applied over the pile gross area. For a coring scenario, the full CPT resistance is applied over the annular base area and the plug resistance (internal shaft friction) is not considered explicitly. In the UWA method, the plug is assumed not to fail during static loading and a modified unit base resistance (which accounts for the effective area ratio) acts over the gross area of the pile. This accounts for the reduced base stiffness developed during coring installation of the pile. While this may produce an accurate static capacity, it does not model or represent the interaction between the pile and soil plug during driving.

Schneider and Harmon suggest adaptations of the UWA approach for estimating base resistance. They advise that a value of 0.35qc is assumed to act on the pile annulus, whilst the soil plug develops internal friction which is equal to 50% of the external friction. Adopting these assumptions in Figure 5 (UWA Sch 1.5 EXT) provided a good upper bound fit. Ignoring the contribution of internal friction (UWA Sch 1.0 EXT) resulted in an appropriate lower bound prediction.

The base capacity estimated by both the ICP and UWA are based on pile tip displacements (w_b) of up to 10% of the pile diameter, (i.e. $w_b/D = 0.1$). This settlement is far in excess of the penetration per blow experienced by the pile during installation by driving. A reduction factor must be applied to the mobilised resistance based on the expected set per blow.

A simple 3 stage base resistance-settlement model, proposed by Gavin and Lehane [13] was employed to calculate the base resistance mobilised during each hammer blow. The model, shown in Figure 7, consists of the pile tip displacement (w_b), normalised by the pile diameter (D) plotted against the base resistance (q_b). The residual base stresses (q_{bres}) associated with pile driving can be ignored for fully coring piles. The resistance has linear displacement until a yield strain (w_{by}/D) is reached, (assumed to occur at 1.5%) followed by a non-linear stage, of parabolic form to a strain of 10%, (i.e. $q_{b0.1}$). The linear stage ($w_b/D < w_{by}/D$) is controlled by the small strain stiffness (E0) and can be described by:

$$q_b = [k(w_b/D)] + q_{bres} \tag{3}$$

Where:

k = $(4/\pi)E0/(1-\nu^2)$, and
ν = Poisson's Ratio.

The parabolic portion ($w_{by}/D < w_b/D < 0.1$) is given as:

$$q_b = \left[k(w_{by}/D)^{1-n}\,(w_b/D)^n\right] + q_{bres} \tag{4}$$

The unit base resistances computed from the UWA and ICP methods were adjusted to a reduced value using this model and input into GRLWEAP for analysis, retaining the original unit shaft values. The results obtained are also shown in Figure 5 and 6 (as ABM). The model provides better predictions of the steel pile resistance for both UWA and ICP plugged methods and are similar to the upper bound recorded blow counts. Based on these results, applying ICP and UWA approaches with the base mobilisation modification may be utilised to estimate an upper-bound blow count prediction which was inadequately described by the driveability models.

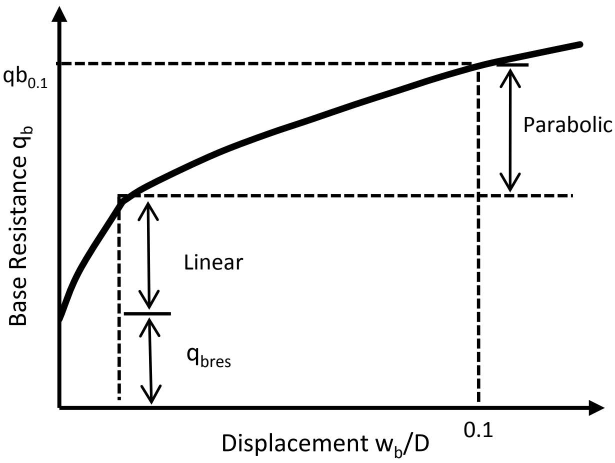

Figure 7. Base resistance-settlement (Gavin & Lehane [13]).

The adjusted base resistances show little difference for the recorded IFR values and the IFR_{MEAN} estimation for the UWA model. The IFR_{MEAN} estimation proposed by the UWA is adequate, and accurate IFR values are non-essential.

Investigating the predictions for the precast concrete piles in Figure 8, UWA and ICP in their raw form are shown to provide fair predictions of the recorded blow counts, marginally over-estimating, but a significant improvement over traditional driveability approaches illustrated in Figure 4. Similar base mobilisation operations (ABM) were conducted in an effort to increase the accuracy but resulted in predictions below the recorded value, largely due to the significant influence of the residual base stresses (q_{bres} - assumed equal to zero) which are considerable when closed-ended piles are driven. Schneider and Harmon's approach (UWA Sch) was also applied and produced reasonable results. It is unclear whether the UWA and ICP methods, applied as for a static capacity analysis, can offer an improvement over the existing driveability approaches for closed-ended piles, or if it was coincidence in this case.

Overall, the results are encouraging and could possibly be developed to form a new driveability method, although further sites need to be investigated. Addressing the limitations of the current model is part of on-going research and seeks to include the impact of successive hammer impacts and base residual stresses on the analyses.

7 CONCLUSIONS

1. Current approaches to predict driveability provide reasonable best estimates for open-ended pipe piles in dense sands but poorly predict square closed-ended piles.
2. Recent static capacity approaches (UWA & ICP) can be applied successfully to pile driveability and produce similar, and in certain instances better results than traditional models.
3. Modifications to static models are necessary for open-ended piles but appear non-essential for closed-ended piles.
4. Considerable uncertainty exists when applying static capacity models for predictions of closed-ended piles where adjustments for influences affecting driving appear unnecessary.

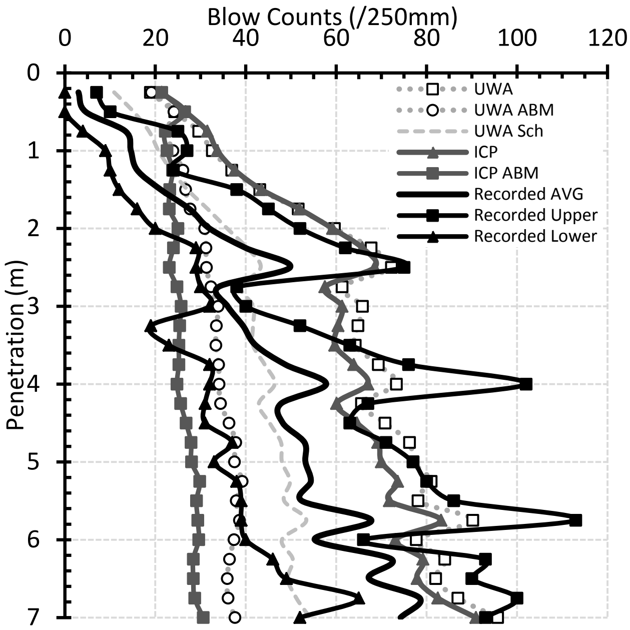

Figure 8. Concrete Pile - UWA and ICP Predictions & Modifications.

ACKNOWLEDGEMENTS

The lead author is grateful for EU FP7 funding. The authors wish to thank Roadstone Ltd for use of the quarry, an In-Situ Site Investigations Ltd for performing the CPT tests.

REFERENCES

[1] Toolan, F.E., and Fox, D.A. (1977) Geotechnical planning of piled foundations for offshore plat-forms. Proc. Institution of Civil Engineers, Lon-don, Part 1, 62,

[2] Stevens, R.S., Wiltsie, E.A. and Turton, T.H. (1982) Evaluating pile driveability for hard clay, very dense sand and rock. Proc. Offshore Technology Conference, OTC, Houston, OTC paper no.4205.

[3] Alm, T. & Hamre, L. (2001). Soil model for pile driveability predictions based on CPT interpretation. Proc. 15th International Conference on Soil Mechanics and Geotechnical Engineering, 2, Istanbul, Turkey, 1297–1302.

[4] Jardine, R. Chow, F. Overy, R. & Standing, J. (2005). ICP design methods for driven piles in sands and clays. London: Thomas Telford.

[5] Lehane, B.M., Schneider, J.A. & Xu, X. (2005). The UWA-05 method for prediction of axial capacity of driven piles in sand. Proc. International Symposium on Frontiers in Offshore Geomechanics, Perth Australia, 683–690.

[6] Syge, F.M, 1977 West Wicklow, In South-East Ireland International Union of quaternary research field guide, Vol.56

[7] Doherty, P. Gavin, K. Igoe, D. (2012). Dynamic Analysis of Pile Driving in Dense Sand. BCRI 2012.

[8] American Petroleum Institute (1981). Recommended Practice for Planning, Designing and Constructing Offshore Platforms. API RP2A, 12th edition.

[9] Overy, R. & Sayer, P. (2007). The use of ICP Design Methods as a Predictor of Conductor Drill-Drive Installation. Proc. 6th Int. Offshore Site Investigation and Geotechnics Conference, London, UK. 333–340

[10] Schneider, J.A. & Harmon, I.A. (2010). Analyzing Drivability of Open Ended Piles in Very Dense Sands. Journal of the Deep Foundation Institute, 4(1): 32–44.

[11] Pile Dynamics, Inc. (2010). GRLWEAP Offshore: Wave Equation Analysis of Pile Driving. 4535 Renaissance Parkway, Cleveland, Ohio, 44128

[12] Chow, F.C., Jardine, R. J., Brucy, F. & Nauroy, J. F. (1997). Time related increases in the shaft capacities of driven piles in sand. Geotechnique, 47(2): 353–361.

[13] Gavin, K.G & Lehane, B.M. (2007). Base load-displacement response of piles in sand. Canadian Geotechnical Journal, 44(9): 1053–1063.

Experimental investigation of novel foundation solutions for offshore wind turbines

G. Murphy[1], D. Cadogan[2], P. Doherty[1], K. Gavin[1]
[1] Geotechnical Research Group, Dept. of Civil Engineering, University College Dublin, Ireland
[2]Dept. of Civil, Structural and Environmental Engineering, Cork Institute of Technology, Cork, Ireland
email: gerry.murphy@ucdconnect.ie

ABSTRACT: This paper presents an experimental investigation into the behaviour of the experimental innovative "winged-monopile" foundation concept through a series of in-situ tests. Instrumented model piles, fitted with wings of varying geometries, were tested in the field under lateral loading conditions. The behaviour of the novel wings is compared to that of a standard reference pile which was installed at the same site. The load-displacement performance of the pile and the recorded bending moment profile along the pile shaft were examined to assess the potential benefits of adding wings to monopile foundations.

KEY WORDS: Piling, Foundations, Offshore Wind Turbines, Renewable Energy, Lateral Loading

1 INTRODUCTION

Irish government policy calls for the development of 4.5 GW of offshore wind power by 2030 [1]. Current cost models estimate the total development cost of offshore wind energy at €2 million/MW, which values the potential Irish market at approximately €9 billion. Assuming conservatively that the cost of foundation systems at these wind farms is 30% of the project cost, this values the potential Irish market for offshore foundations at €2.7 billion to 2030. In the UK, the British Government has previously committed to offshore wind developments of 32 GW by 2020, and has recently released additional sites on the Scottish and Northern Irish coasts. Based on the same cost model, the 32 GW capacity developments represent a total investment cost of €64 billion with a market for foundation systems of about €20 billion by 2020. Considering that the cost of the foundations constitutes approximately 30% of the capital expenditure, any improvement in regard to the efficiency of the substructure could significantly improve the economic feasibility of exploiting offshore wind energy. Currently, over 75% of installed offshore turbines have been supported on large diameter steel tubes known as monopiles. The monopile foundation solution is favoured in relatively shallow water depths where the environmental loading conditions are not classed as severe. Future Irish wind farm developments are expected to be located in increasingly deeper waters and will employ larger capacity turbines, thus increasing the loads beyond the capabilities of the traditional monopile concept. Therefore, more efficient foundation solutions will be needed to support turbines in water depths between 25 metres and 60 metres. One such solution is the "winged-monopile" concept. This innovative substructure adopts an additional plate element to mobilise extra resistance in the near surface soils and improve foundation efficiency. Given the relatively high cost of the sub-structure for offshore wind turbines within the overall project budget, any such improvement in efficiency could be highly beneficial to the Irish wind energy industry and the broader European market.

This paper focuses on a preliminary series of lateral load tests conducted at the Cork Institute of Technology's (CIT) geotechnical test site in Garryhesta, County Cork. The tests were conducted on three monopiles of identical dimensions, with two of the piles fitted with experimental wing sections and one without wings, to act as a reference pile.

2 LATERALLY LOADED MONOPILES

Monopiles for the offshore wind industry are subjected to strong static and cyclic lateral loading due to the wind and wave forces. Currently the API-2A WSD [2] document is the design guide used for the construction of monopiles for offshore wind turbines. The API guide uses the "P-y curve" method which models the soil-pile interaction due to lateral loading as a series of uncoupled springs in accordance with the Winkler beam theory. However, this design method is based on empirical results from limited field tests conducted on relatively flexible piles with high length to diameter (L/D) ratios and diameters of less than 1.2m. The monopiles currently used in the offshore wind industry typically have diameters of 4 m to 7 m and L/D ratios of approximately 6. Therefore, recent research has raised concerns over the validity of this design method.

3 WINGED-MONOPILE CONCEPT

The use of an enlarged pile cross-sectional area near the pile head is used in order to improve the strength and stiffness of the foundation system. One proposed method of achieving this is the addition of wings near the ground surface. This concept was first proposed in the US by Rocker [3], however little research was conducted on the concept at that time as stiff monopile foundations on this scale were not required.

In recent years, the requirements of the offshore wind industry have led to the investigation of the winged pile concept as a method of improving the efficiency of foundation structures for offshore wind turbines. Preliminary laboratory tests on statically loaded wing-piles have shown that the wings can reduce pile head displacements by up to 65% [4], while laboratory-based cyclic tests have also found displacement reductions of up to 50% [5]. Centrifuge tests on small-scale statically and cyclically loaded piles have also been conducted and have found that the addition of wings can reduce displacements by up to 50% and increase the foundation bearing capacity by 40% [6]. The additional bearing capacity generated by the wings has the potential to allow monopile foundations to be deployed in deeper waters or allow the designer to reduce the pile dimensions resulting in reduced steel and fabrication costs. In recent finite element modelling (FEM) analysis conducted by Peng et al. [7] and Clarke et al. [8], it was found that savings on steel costs between 26% and 32% can be achieved by comparing the performance of winged and plain piles of varying dimensions.

4 SITE INVESTIGATION

The model pile tests were conducted in the Roadstone Wood sand pit in Garryhesta, which is located approximately three kilometres west of Ballincollig in Co. Cork. The site has a large supply of dense fine-grained silty sands and gravels. Prior to pile testing, a series of laboratory and field tests were conducted to determine the in-situ soil properties on site. The results of a series of cone penetrometer (CPT) tests yielded a relatively consistent CPT profile, with the tip resistance, q_c, ranging from 8 to 10 MPa, as shown in Figure 1.

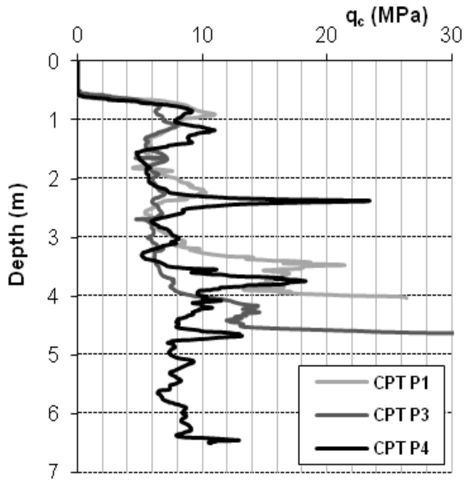

Figure 1. Garryhesta CPT data.

The shear wave velocity (V_s) of the soil was measured using Multi-Channel Analysis of Surface Waves (MASW) equipment, with the data as presented in Figure 2. The relative density of the sand deposit was calculated to be approximately 70% using the CPT correlation proposed by Lunne and Christoffersen (1983):

$$D_r = 1/2.9 *1 \ln [(qc*0.6) / [60 (\sigma'_{vo})0.7] \quad (1)$$

The peak angle of shear friction (φ') was calculated to be 40° using Equation 2 [9]:

$$\varphi' = 17.6 + 11.0 \log [(qt/\sigma_{atm}) / (\sigma'_{vo}/\sigma_{atm})\text{^}0.5] \quad (1)$$

The constant volume friction angle (φ_{cv}) was measured as 32° in shear box texts conducted in the CIT laboratory. The natural water content of the samples was found to be approximately 12%. Soil classification tests were also conducted and the soil was deemed to be "very silty SAND SM" with 15% fines and a uniformity coefficient of 2.5, suggesting that the soil is well graded.

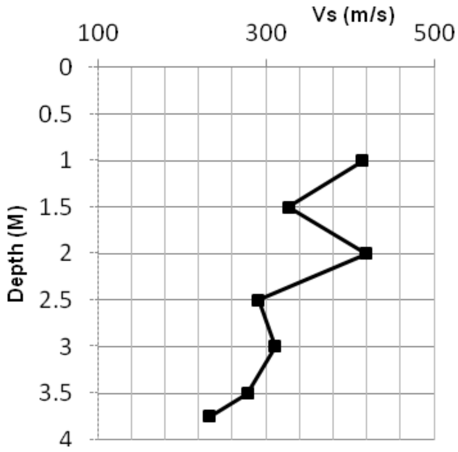

Figure 2. Garryhesta MASW data.

5 TEST PILE DEVELOPMENT

The tests piles were designed and constructed in the CIT Heavy Structures Laboratory. Three open ended piles of the same dimensions were fabricated, two of which had steel plates welded to the shaft near ground level. The pile without wings could then be used as a reference in order to judge any increase in lateral bearing capacity.

Table 1. Test pile dimensions.

Monopile Model:	**Plain**	**Wing 1**	**Wing 2**
Length (mm)	2000	2000	2000
Diameter (mm)	244.5	244.5	244.5
Wall Thickness (mm)	8	8	8
Wing Width (mm)	-	185	185
Wing Length (mm)	-	280	560
Wing Thickness (mm)	-	8	8

The two winged piles were fitted with wings of varying geometries in order to gain a further understanding of how to design the wing dimensions to maximise efficiency. The experimental wings are only fitted to the pile perpendicular to the loading plain as the piles will only be loaded in one direction in this test series. This configuration also allows for the attachment of stain gauges along the tension and compression faces of the pile shaft. The wing dimensions were designed according to Duhrkop et al [6]. The dimensions of the test piles are presented in Table 1. Strain gauges were attached to the test piles at eight levels along the compression and tension faces of the piles, as shown in Figure 3. The strain gauges enabled the bending moments to be calculated along the pile shaft, in order to determine how the wings affect the distribution of lateral loading in the piles. The locations of the strain gauges were covered with a protective bracket to prevent them from being damaged during the pile driving process. The test piles were calibrated in the laboratory to determine the bending stiffness of the piles. This pile stiffness was then used to calculate the bending moments in the pile shaft using the strain readings.

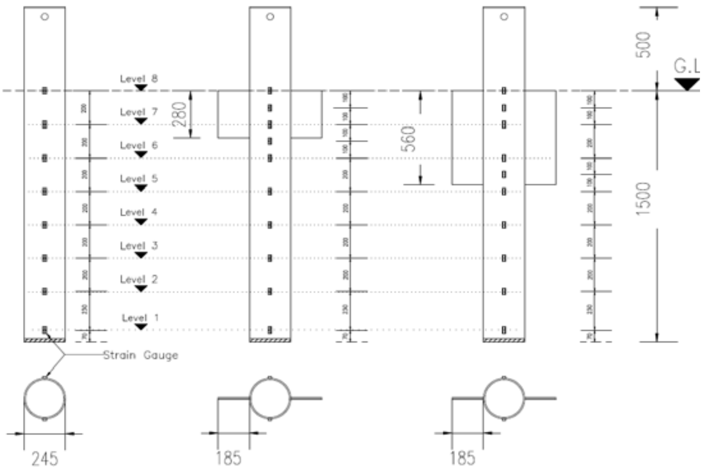

Figure 3. Test pile configuration.

6 TEST SETUP

The model piles were installed at the test site, using a heavy tracked excavator to push them into the ground and the guide frame shown in Figure 4 to maintain verticality. The piles were laterally-loaded using a 25-tonne hydraulic jack and employing a 30-tonne excavator for reaction.

Figure 4. Pile driving.

The test piles were loaded in a series of predetermined stages in order to record the pile behaviour at various lateral load levels. Each load stage lasted a minimum of ten minutes to allow for the affect of soil creep and compaction. During each load stage, the additional load was applied and then maintained by constantly applying additional pressure using the jack, as the applied load can reduce because of pile deflection and soil creep. The applied load was constantly monitored using the digital display unit attached to the load cell. The test piles were incrementally loaded until they reached a displacement of approximately 40 mm at the pile head. The configuration of the experimental apparatus used in the tests is presented in Figure 5. The strain along the pile shaft was measured using the strain gauges, whilst the displacement of the pile head was measured at two levels using linear displacement transducers, which allowed the pile rotation to be calculated. The applied load was monitored using the load cell, with all test data monitored and recorded using a *Vishay System 7000* data logger system.

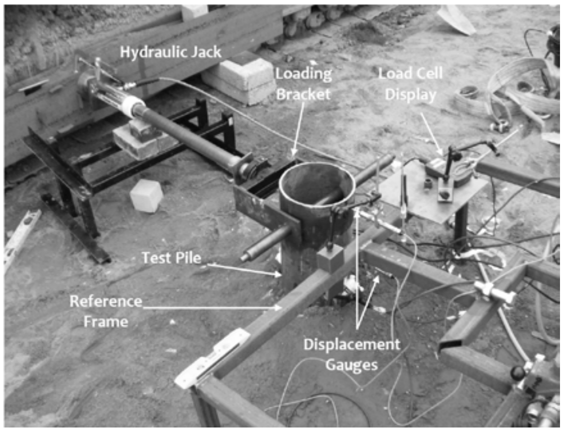

Figure 5. Pile testing apparatus.

7 TEST RESULTS

The primary aim of the in-situ test series was to determine if adding wings to the monopile near the ground surface can reduce the lateral displacement of the pile under static loading.

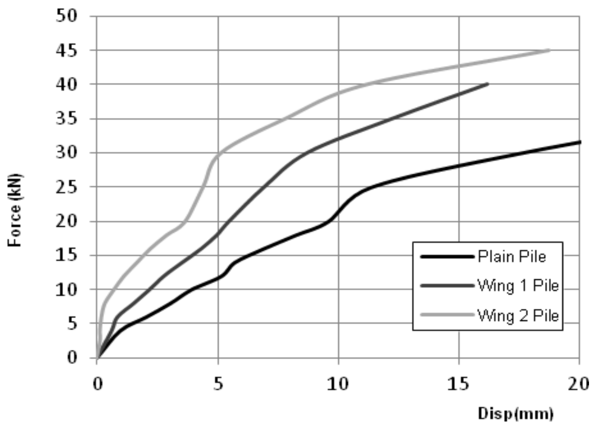

Figure 6. Applied lateral load versus displacement.

In order to compare the performance of each pile, the lateral displacement at the pile head for each pile was plotted against the applied load, which is presented in Figure 6. It can be seen that the piles fitted with wings developed higher lateral load resistance when achieving the same displacement as the regular monopile. It can be observed the pile fitted with larger wings (Wing 2) had a higher resistance to lateral loading than the Wing 1 pile, in addition to a higher initial stiffness. On average, Wing 1 developed 45% less displacement than the plain pile at any given load stage. The results for the Wing 2 pile show that displacement is reduced by up to 70% at a given lateral load.

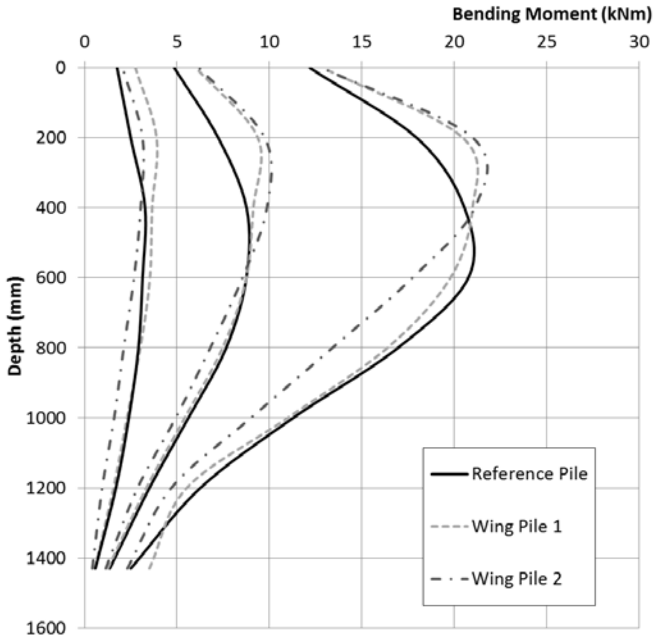

Figure 7(a). Bending moment along pile shaft (6kN,16kN, 35kN).

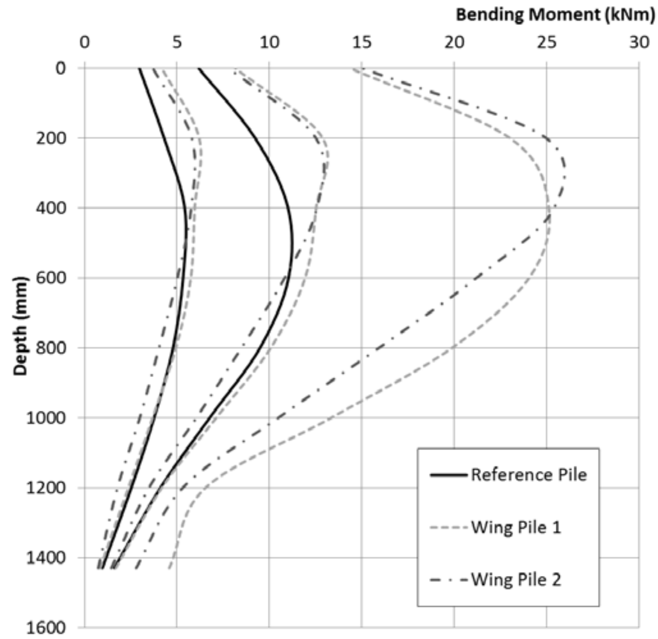

Figure 7(b). Bending moment along pile shaft (10kN, 20kN, 40kN).

The bending moment was calculated along the pile shaft using the recorded strain readings and the bending stiffness of the pile. The bending moment profile can be used to calculate the P-y curves along the pile shaft and determine the soil-pile interaction response. The bending moment in the pile was also compared at various lateral load levels. A comparison of the test results for a range of applied lateral load values is presented in Figures 7(a) and 7(b). These graphs illustrate that the larger bending moments were measured in the piles fitted with wings.

8 ANALYSIS OF RESULTS

The results of the horizontal displacement analysis show that the addition of wings significantly increased the horizontal resistance of the monopiles. It was found that, for the two wing arrangements, the displacement of the pile can be reduced by up to 45% and 70% with increases in steel weight of 14% and 28%, respectively. The displacement reductions are in line with previous research [5][4][10][11] , however the performance of the wings is highly dependent on both the sand density and stiffness and further testing is required to determine how these wings perform in different sand densities [11]. It can also be observed in Figure 6 that the winged-piles initial stiffness response is far greater than that of the plain monopile.

The bending moment profile of each test pile was recorded at each individual loading stage. These moment profiles can be used to form the differential equations in order to calculate the P-y curve of each test pile, by fitting a fifth order polynomial curve to the moment profile. By examining the bending moment profiles in each pile for the same applied load stages, it can be observed that the largest bending moments were recorded in the two piles fitted with wings. However, the differences in maximum moment are relatively small and are of little significance. It can be observed in Figures 7(a) and 7(b) that the shape of the bending moment profile for the winged piles is altered considerably from that of the reference pile. For the plain monopile, the maximum moment was developed at approximately 500 mm below ground level. However, in the case of the winged monopiles, the maximum moment was found at approximately 200 mm. The greater bending moments found near the ground surface suggest that the wings provide additional fixity to the pile near ground level.

The maximum bending moments recorded in the pile shaft did not reduce as suggested by Songlin [11]. Therefore, it may not be feasible to reduce the pile wall thickness. Finite element modelling conducted by Peng et al. [7], has suggested that the additional stiffness provided by the wings has allowed them to develop model winged piles with reduced length, wall thickness and diameters that have similar lateral stiffness as a larger traditional monopile. Therefore, further research is required to determine the true potential of this novel foundation concept. Repeat testing of the model piles has been proposed and is currently being conducted in the very dense sand deposit found at the UCD test site in Blessington in County Wicklow.

9 SUMMARY AND CONCLUSIONS

A series of lateral load tests was conducted on three model monopile foundations at the CIT geotechnical test site in Garryhesta in County Cork. The preliminary analysis of the test results has primarily concentrated on the geotechnical aspects of the pile performance. However, the recorded strain data along the pile shaft can allow further investigation of the structural effects resulting from the addition of wings to a monopile foundation.

The lateral load test series proved the potential of the addition of wings to the pile shaft near ground surface level as a method of improving the lateral resistance of a monopile foundation. Displacement reductions of up to 70% were achieved for an 28% weight increase.

The bending moments recorded along the tension and compression faces of the pile suggest that the addition of wings to the pile shaft increased the fixity of the pile near ground level.

10 FUTURE RESEARCH

The winged-monopile concept is still in the development stage and requires significant additional research before it can be adopted for the offshore wind industry. A P-y curve analysis is currently being conducted on the test data presented in this paper to determine how the distribution of soil reaction is affected by the addition of the wings. The model piles are also to be installed and further tested under static and cyclic loading conditions at the UCD GRG test site in Blessington, Co. Wicklow to gain further understanding of the wing performance in various soil conditions.

ACKNOWLEDGMENTS

The author wishes to thank the staff of CIT's Dept. of Civil, Structural and Environmental Engineering, especially Mr. Jim Morgan for all his assistance and hard work, Mr. Tim O'Mahony of Roadstone Wood Ltd for access to the test site and plant, and to all the members of the GRG for their assistance and advice.

REFERENCES

[1] S. E. A. of I. SEAI, “Offshore Renewable Energy Development Plan (OREDP),” 2010.

[2] API, API RP2A: Recommended Practice for Planning, Designing and Constructing Fixed Offshore Platforms - Working Stress Design, 22nd edn., no. October. Washington DC: API, 2007.

[3] K. Rocker, Naval Civil Engineering Laboratory, and U. D. of the Navy, Handbook for Marine Geotechnical Engineering. Naval Civil Engineering Laboratory, 1985.

[4] J. Grabe and J. Dührkop, “Laterally loaded piles with bulge,” International Conference on Offshore Mechanics and Arctic Engineering, 2007.

[5] J. R. Peng, B. G. Clarke, and M. Rouainia, “Increasing the Resistance of Piles Subject to Cyclic Lateral Loading,” Journal of Geotechnical and Geoenvironmental Engineering ASCE, no. October, pp. 977-982, 2011.

[6] J. Dührkop, J. Grabe, B. Bienen, D. J. White, and M. F. Randolph, “Centrifuge experiments on laterally loaded piles with wings,” Physical Modelling in Geotechnics – Springman, Laue & Seward (eds) © 2010 Taylor & Francis Group, London, ISBN 978-0-415-59288-8, pp. 919-924, 2010.

[7] J. R. Peng, M. Rouainia, and B. G. Clarke, “Finite element analysis of laterally loaded fin piles,” Computers & Structures, vol. Vol. 88, no. No. 21–22, pp. 1239-1247, Nov. 2010.

[8] B. G. Clarke, J. Irvine, P. Allan, and J. R. Peng, “FinPile: Improving the lateral stability of monopile foundations,” in Proceedings of the 6th international conference: Confronting New Challenges and Sharing Knowledge, 11 -13 September 2007, London, UK, 2007.

[9] P. W. Mayne, “In-Situ Test Calibrations for Evaluating Soil Parameters,” Overview Paper on In-Situ Testing - Singapore Workshop, Nov. 29- Dec. 01,2006, 2007.

[10] J. Dührkop and J. Grabe, “Design of Laterally Loaded Pile with Bulge,” in Proceedings of OMAE 2009 OMAE 2009 28th International Conference on Ocean, Offshore and Arctic Engineering May 31-June 6, 2009, Honolulu, USA, 2009.

[11] W. Songlin, “Horizontal resistance behaviour of pile with wings in sand,” in Key Laboratory of Geotechnical Mechanics and Engineering of the Ministry of Water and Resources, Changjiang River Scientific Research Institute, Wuhan, Hubei 430010, China, 2007, pp. 253-259.

Dry soil mixing trials and scale column testing with an Irish organic silt

Martin J. Timoney[1], Bryan A. McCabe[1], Michael Faherty[1] & Cathal Mac an tSearraigh[1]
[1]College of Engineering and Informatics, National University of Ireland, Galway, Ireland.
martin.timoney@nuigalway.ie, bryan.mccabe@nuigalway.ie

ABSTRACT: Deep dry soil mixing (DDSM) is a method of ground improvement used in soft soils to create stabilised soil columns through the addition of dry cementitious and pozzolanic binder materials to a soil. The binders react with the soils natural water content to initiate the hydration reactions which leads to increased strength and deformation properties. The stabilisation of organic soils is more difficult than the stabilisation of inorganic soils, as the humic acids present create insoluble products which hinder the strengthening reactions thus requiring site specific binder trials to help estimate achievable strengths. Two common methods used for testing stabilised columns are the push in resistance test (PIRT) and the pull out resistance test (PORT), where the force required by a winged penetrometer to penetrate through the column is related to the strength of the stabilised soil column. This paper presents some laboratory work to date carried out on the creation and testing of scale stabilised soil columns in an organic *sleech* from Belfast, which aims to gain a better understanding of the test methods and the relationship between the penetration force and the strength of the column. Data from a series of binder trials carried out on the *sleech* using cement, ground granulated blast furnace slag (GGBS) and lime binders is presented and show a 50:50 cement-GGBS binder provides the most beneficial strength gain. Data is presented from some initial tests investigating the current relationship between the penetration force and the column strength, determined from samples taken throughout the column. Investigation of the data to date has shown the tests are producing similar factors to those used in practice.

KEY WORDS: dry soil mixing, organic soils, laboratory testing

1 INTRODUCTION

Dry soil mixing (DSM) is a ground improvement method typically used to improve the geotechnical characteristics of very soft soils and in particular organic silts or clays and peats. Improvements to the soil may include increased strength, improved settlement properties and the confinement and/or remediation of contaminated soils. The process is carried out *in situ* and no spoil is produced.

DSM uses compressed air (rather than water used in wet soil mixing) to inject a dry cementitious or pozzolanic binders, such as lime, cement, ground granulated blast furnace slag (GGBS) or pulverised fly ash, into a soft soil. The binder is hydrated by the pore water in the soil leading to improved geotechnical characteristics for the soil. Two main methods of DSM exist; Deep Dry Soil Mixing (DDSM) the focus of this paper and Mass Stabilisation.

1.1 Deep Dry Soil Mixing

The Deep Dry Soil Mixing (DDSM) method is used to create stabilised columns of diameters from 0.5*m* to 1.0*m* and to depths typically up to 30*m* using equipment similar to that shown in Figure 1. The mixing process is carried out as follows:

1. The mixing tool is rotated into the soil to the design depth, breaking up the soil structure, as shown in Figure 2.
2. Once the tool reaches its design depth, it is lifted out while continuing to rotate as the binder is injected and mixed with the soil by the rotating tool.
3. A temporary surcharge, up to 1.0*m* in depth may be placed on the stabilised area to aid compaction and removal of any air entrained in the soil during mixing. This surcharge can also act as a working platform from which further

Figure 1. DDSM Rig courtesy of Keller Group.

columns can be constructed.

4. After curing, construction may begin on the columns.

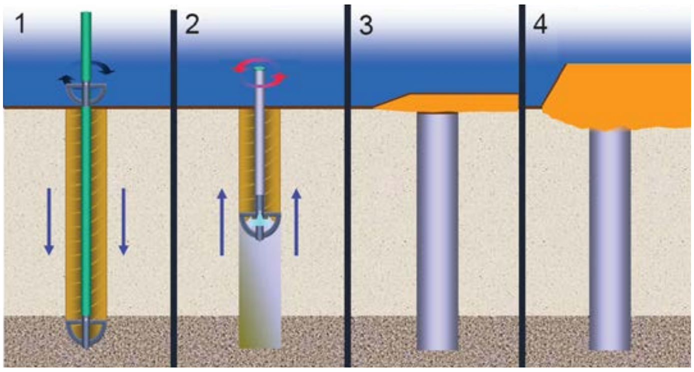

Figure 2. Deep Dry Soil Mixing process (courtesy of Keller Group).

Columns may be formed as single units or can be overlapped to create rows or interlocking grids.

1.2 Mass stabilisation

Unlike DDSM, during mass stabilisation the entire soil profile is stabilised to depths typically up to 5m deep. Mixing is carried out using a mixing tool mounted on the arm of a tracked excavator and occurs in all directions as opposed to the solely vertical mixing seen in DDSM. This method is typically used to stabilise large areas of very soft highly organic soils and is used in peat soils in particular.

1.3 Stabilisation of Organic Soils

Unlike the stabilisation of inorganic soils, the stabilisation of organic soils is more difficult, requiring higher binder contents. Inorganic soils typically require less than 100kg/m^3 to achieve good strengths while highly organic soils such as peats require contents up to and over 300kg/m^3[1]. Humic acids present in the soil react with the calcium hydroxide from the binder to produce insoluble products. These products coat the soil particles and prevent bonds being formed between adjacent soil particles.

Tremblay et al. [2] conducted a series of tests in which organic contents were artificially induced on a clay and a silt using a number of organic compounds, and concluded that a pH of the pore solution in the stabilised mix lower than 9 prevented the development of strengthening products. This is supports the proposal by Axelsson et al. [3] that a minimum binder content is required to neutralise the acids present in the soil before strengthening reactions will occur.

2 SOIL CLASSIFICATION

2.1 Site Location and Description

The organic silt used in the binder trials and scale column tests was sourced from a site adjacent to the Kinnegar Wastewater Treatment Plant approximately 8*km* north-east of Belfast City.

The site has previously been used for pile tests and extensive geotechnical data is available for the site. The profile consists of approximately 1*m* of topsoil mixed with a gravel fill, overlying a thin layer of sand. Beneath this a soft, dark grey organic silt of high plasticity known as *sleech* extends to an average depth of 8.5*m* as shown in Figure 3 [4]. The water table exists at 2*m* below ground level. A number of oyster shells and other shell types were found in the *sleech* during the tests, along with small decayed wood and root remnants.

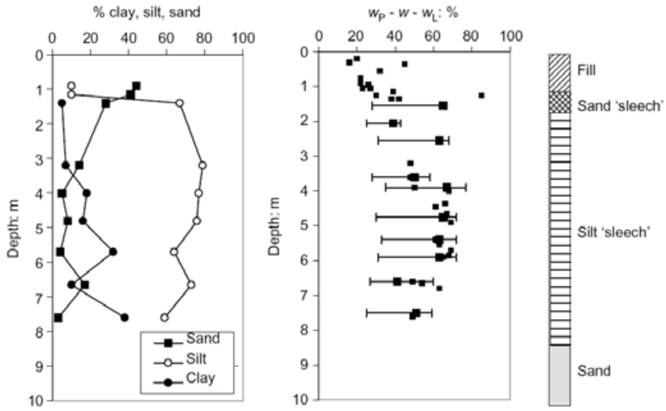

Figure 3. Kinnegar Site Profile [4].

2.2 Soil Classification

5m^3 of *sleech* was sampled from a depth of 4*m*+ below ground level and transported to NUI Galway where soil classification tests were carried out. Table 1 provides a summary of the properties of the *sleech* determined in accordance with BS1377-2:1990 [5]. Moisture contents of between 60% and 63% were obtained and compare well to those found by McCabe & Lehane [6]. Samples dried at a lower temperature of 70°*C* were seen to give similar values.
The organic content was found to be 5.2% using the loss on ignition method by burning samples of the *sleech* at 440°*C*. These values are lower than the 11.5% found by McCabe & Lehane [6] in their classification tests.

The density of the sleech was found to be 1,620kg/m3 with a specific gravity of 2.73 determined using the gas jar method. The liquid limit of 75% and plastic limit of 27.5% indicate a very high plasticity soil, while a pH value of 7.94 indicates the soil is slightly alkaline.

Table 1. Kinnegar Sleech Classification.

Sampling Depth	4-5*m*
Moisture Content	61%
Organic Content	5.2%
Bulk Density, ρ	1,620kg/m^3
Specific Gravity	2.73
Liquid Limit	75%
Plastic Limit	27.5%
pH	7.94

Swedish fall cone tests carried out on undisturbed samples cut from excavated blocks of the *sleech* indicate an undrained strength of 15*kPa* and a remoulded strength of 4.5*kPa*.

3 BINDER TRIALS AND RESULTS

3.1 Binder Trials

The *sleech* was stabilised with ordinary Portland cement, ground granulated blast furnace slag (GGBS) and lime at binder contents of 50, 100 and 150*kg/m³*. Compound cement-GGBS and cement-lime binders were trialled at 50:50 proportions.

Samples were mixed in accordance with the methods set out for column stabilisation trials in EuroSoilStab [7]. The raw sleech was first homogenised in a thirty litre mixer for five minutes with any stones or shells removed and a sample taken to determine the moisture content of the raw sleech. The binder was added in stages and mixed for five minutes or until a visually homogenous mixture was achieved with no pockets of binder remaining; a sample was taken to determine the moisture content after mixing. The mixture was compacted into 65mm dia. by 320mm PVC split moulds in 30 to 40mm layers applying thirty compacting tamps and a stress of 100kPa for six seconds. The samples were then sealed in plastic, the total mass recorded and stored at 20°C until the desired test times of 7, 28 and 91 days.

3.2 Unconfined Compression Strength Tests

Unconfined compression strength (UCS) tests were carried out in accordance with BS1377-7:1990 [8] at a compression rate of 1*mm* per minute on two samples from each binder mix. The UCS is typically used to assess the strength of stabilised soil mixes and is defined as twice the undrained shear strength, c_u.

3.2.1 Strength with Binder Content

Figure 4 shows the increase in UCS at 28 days after mixing (UCS_{28}) with increasing binder content. Strength improvements were seen in all cases and cement-GGBS and cement binders show the best strength improvements particularly at contents of 150*kg/m³*. Cement and cement-lime binders show a linear increase in strength with binder content. The low strengths achieved with lime and GGBS binders alone result from the lack hydrates present in the mixture.

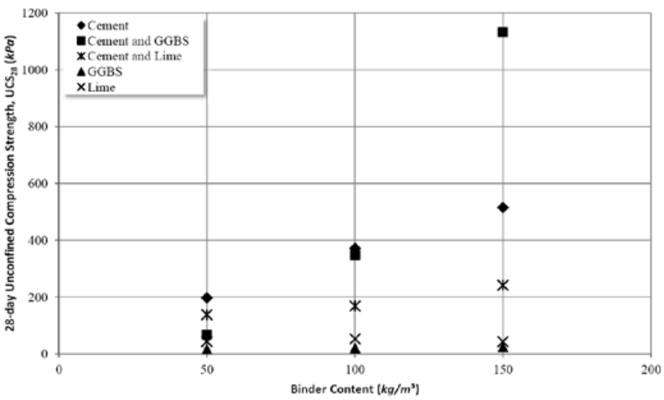

Figure 4. Unconfined Compression Strength at 28 days with Binder Content.

3.2.2 Strength with WTBR

Timoney *et al.*, [1] defines the water to binder ratio (WTBR), η to be the mass of water per unit volume (m_w) divided by the mass of binder per unit volume (m_b). The value of η, calculable from Equation 1, allows data from different stabilisation projects to be compared, taking into account the density of the soil (ρ), its moisture content (w_i) and amount of binder added during stabilisation (m_b).

$$\eta = \frac{m_w}{m_b} = \frac{\rho}{m_b\left(1+\frac{1}{w_i}\right)} \tag{1}$$

Figure 5 plots the strengths achieved at the three η values used in the trials. It can be seen that as the WTBR reduces an increased strength is obtained. Best results were seen to occur at a η of 4.1. Timoney *et al*, [1] in a compilation of European and Japanese stabilisation data in peat observes similar trends and highest strengths in the range η = 4±1.

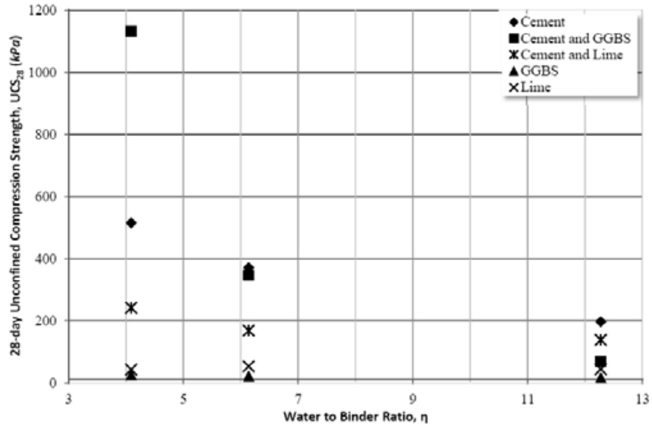

Figure 5. Unconfined Compression Strength at 28 days with Water to Binder Ratio.

3.2.3 Strength with Time

Figure 6 plots the increase in strength with time for a number of binders and binder contents. At the higher binder contents the initial increase in strength in the first seven days is high. Cement binders alone follow a steady increase in strength from seven days onwards while cement-GGBS binders show very high increases in strength in the long term; 150*kg/m³* of cement-GGBS reaches a strength of over 1.8*MPa* after 91 days. In contrast, lime at 150*kg/m³* shows poor trend, similar to that for 50*kg/m³* of cement.

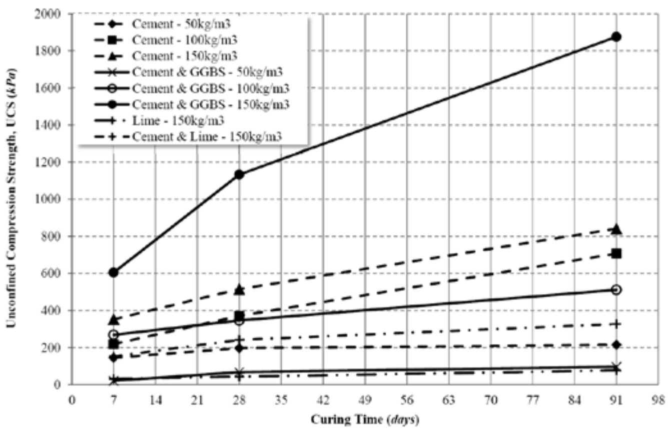

Figure 6. Unconfined Compression Strength with Time.

3.3 Stiffness

The 28 day stiffness, determined from the slope of the stress-strain plot at fifty percent of the failure stress, can be seen to increase with binder content in Figure 7. The highest stiffness was observed with cement and cement-GGBS and sudden failure of the sample was noted on testing.

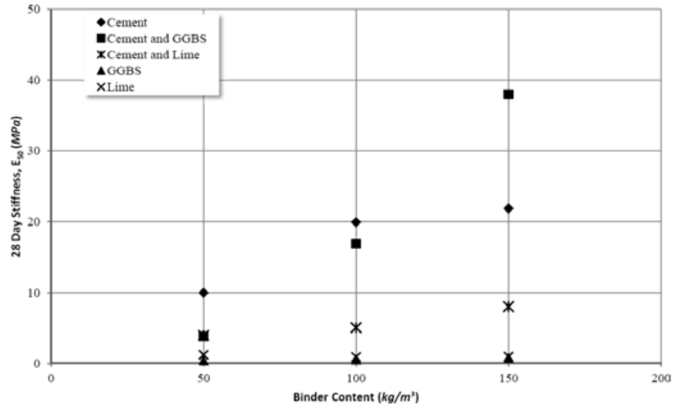

Figure 7. Stiffness (E50) with Binder Content.

Using the undrained shear strength, cu the stiffness of a soil may be approximated using a factor applied to cu. For cement this factor was found to be 115, 76 and 70 at 7, 28 and 91 days respectively. For cement-GGBS binders lower values of 90, 62 and 42 were observed at the respective durations.

4 STABILISED COLUMN PENETRATION TESTING

Strengths achieved in the laboratory may not reflect those achieved in the field for a number of reasons: variations in the soil profile, changes in the moisture content between laboratory sampling and field testing and lower *in situ* curing temperatures. Some authors have noted the ratio between laboratory and field strengths to be between 2 and 5 [9], while Braaten [10] notes that higher strengths were observed in the field and Topolnicki [11] notes a ratio of between 0.5 and 1 for wet soil mixing. As such, verification of the field strengths is required.

4.1 Cone Penetration Testing (CPT)

CPT is a very popular form of site investigation but when used for testing stabilised soil columns it has a number of drawbacks: (i) the CPT cone tends to deviate off vertical after a few metres, particularly in strong columns, (ii) the CPT cone may travel along a weakest route in the column, for example along the route the Kelly bar took during mixing, (iii) CPT only provides a resistance at one location on a column cross section and (iv) there is a lack of calibration data for CPT in stabilised soil columns. For these reasons CPT is not commonly used for this application.

4.2 Push In Resistance Test (PIRT)

During this test a winged penetrometer, similar to that shown in Figure 8, is pushed down through the centre of the column at a rate of 20*mm/sec*. Unlike the CPT, this method provides the average strength across the width of the column, but in very hard columns the penetrometer can deviate off vertical and out of the column.

Figure 8. 400mm PIRT Penetrometer.

4.3 Pull Out Resistance Test (PORT)

The PORT is very similar to the PIRT but the penetrometer is extracted from the column by pulling it up through the column using a 12*mm* wire rope. Unlike the PIRT, deviation out of the column is not an issue but very high strengths may snap the wire rope. The penetrometer is installed up to 1*m* beyond the base of the column either during the initial downward pass of the mixing tool or by pushing it in soon after construction. To prevent the wire rope binding with the column the penetrometer is raised 100-200*mm* within 3 days of creation of the column.

Figure 9. 600mm PORT Penetrometer.

4.4 Current Strength Relationship

Currently the relationship set out in Equation 2 is used to determine the undrained shear strength, c_u of a stabilised column using the penetrating force, P, the frontal area of the penetrometer, A and a bearing factor, N:

$$\textit{Shear Strength},\ c_U = \frac{1}{N} \times \frac{P}{A} \qquad (2)$$

Typically N has been taken to be 10 [7, 12] although higher values of 11 and 15 are sometimes used [13]. Currently work is under way at NUI Galway to investigate the factors influencing the value of N though a series of 1:4 scale column tests using fabricated stainless steel scale penetrometers. Some of the preliminary test results are discussed.

4.5 PIRT on a 350mm Long Column

To investigate the force acting on the penetrometer a 200*mm* dia. 350*mm* high column was created in two lifts using cement at a binder content of 200kg/m^3. The stabilised soil was compacted in the form pipe using 65*mm* dia. tamping bar in 40-50*mm* layers and each layer roughened before adding more stabilise soil. The column was allowed to cure for three days before a PIRT was carried out using a 1:4 scale penetrometer at a rate of 1*mm* per second. During the test, the penetrating force, P and the penetrometer displacement were recorded with time. After the test 50*mm* dia. by 100*mm* high cylindrical samples were taken from the column for UCS testing. Mix samples taken and stored in moulds were tested at this time too.

Figure 11 shows a plot of the penetration force with depth. As the conical head of the penetrometer enters the column the force required to push it can be seen to increase to a near constant 0.75*kN*. As the wings of the penetrometer enter the column the force increases again, as expected, reaching a value of 2.13*kN* and then peaking at 2.5*kN*.

Figure 10. Exposed Penetrometer in the Mini Column.

Table 2. Mini Column PIRT Strengths and N Values.

UCS	Location	P	N
kPa	*mm*	*kN*	-
305.4	50	2.239	14.8
366.8	50	2.239	12.3
297.8	50	2.239	15.2
235.9	195	2.495	21.4
325.2	195	2.495	15.5

The UCS values obtained from the samples taken from the column and the respective forces at the relevant depths allow for the N factor to be calculated using Equation 2, and can be seen in Table 2. An initial assessment of the results shows the factors to be in relative good agreement with the factors currently used; higher factors are seen where the strengths are low although this may be as a result of sample preparation issues encountered due to their brittle nature and size.

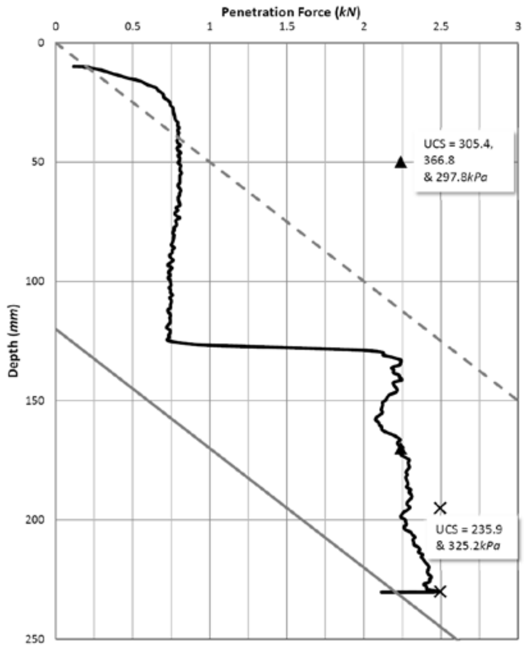

Figure 11. Penetration Force with Depth.

4.6 750mm PORT Column

Multiple tests were carried out to define a procedure to produce a suitable stabilised column for PORT in 750*mm* dia. basins. A number of the tests failed in construction and testing due to the 200*mm* dia. column binding with the column mould, the column breaking during construction and the PORT penetrometer lifting the column during the pull out test. The use of two semi-circular pipes to form the column, a layer of raw *sleech* between the penetrometer and column base and a loading on the column were found to solve these problems.

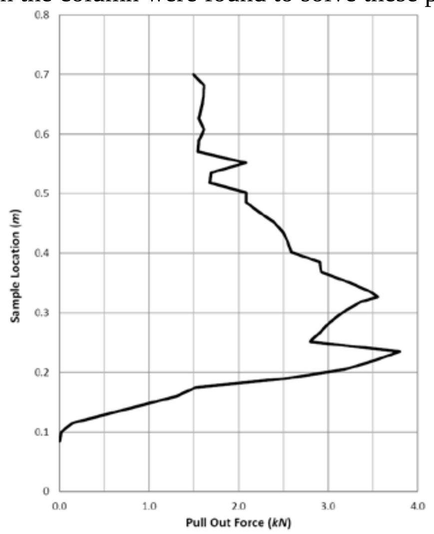

Figure 12. Pull Out Force with Depth.

Figure 12 shows the results from a successful PORT carried out on a 200*mm* column in a 750*mm* dia. basin surrounded by raw *sleech*. It can be seen that the force increases initially to a peak of 3.8*kN* and then drops off reaching a near constant of between 1.5 and 1.7*kN* at a height of 500*mm*, with a peak occurring due to a pause in the test. The initial high force is thought to be due to mobilisation of the penetrometer with a portion of the force being relative to friction between the wire rope and the column.

Strengths determined from column samples and the pull out force show some of the N factors to be comparable to current practices; cracking of the column during testing, sampling disturbances and preparation are thought give rise to lower strengths and thus the higher N factors observed.

Table 3. 750mm PORT Strengths and N Values.

UCS *kPa*	Location *mm*	P_{Act} *kN*	N_{Act} -
272.3	0.729	1.61	13.1
193.6	0.729	1.61	18.4
315.4	0.573	1.55	10.9
263.9	0.414	2.55	21.4
247.8	0.414	2.55	22.8

On comparing the column sample UCS values and the mould sample UCS values it was seen that lower strengths were obtained in the column than the moulds. This is thought to be due to poorer curing with in the scale column basin and the lower temperature created due to the surrounding raw *sleech*, and is supported by higher moisture contents seen in the column indicating fewer hydration reactions.

5 CONCLUSIONS

Dry soil mixing is a method of improving the strength and stiffness characteristics of soft soils and is widely used in Europe to improve organic soils. The stabilisation of organic soils is more difficult than that of inorganic soils as humic acids present in the soil hinder the strengthening reactions. To estimate the strengths achieved in a DSM project binder trials must be carried out to ensure adequate strengths are achieved to meet the design requirements, which then must be followed up by field verification of the actual stabilised soil.

From a series of binder trials on the sampled sleech, strengths are shown to increase with the addition of cementitious and pozzolanic binders to the soil. Cement-GGBS binders are shown to provide the highest UCS values up to 1,132kPa at 28 days and 1,876kPa at 91 days at binder contents up to 150kg/m3. The significant increase in strength in the long term with cement-GGBS binders is clearly visible. Cement alone as a binder, provides a lesser but none the less good strength improvement overall. Cement-lime binders were shown to produce lower strengths again and very low strengths were observed with 100% lime and 100% GGBS binders due to the low level of hydrates to initiate hydration reactions.

Preliminary push in resistance tests and pull out resistance tests carried out on 200mm dia. stabilised columns using scale penetrometers have yielded forces similar to that predicted in the design of the penetrometers and the N factors calculated relate well to those used in current practice. The methods for constructing the columns have been refined to ensure well compacted, uniform columns are created. Analysis of the strengths achieved in the columns compared to that of the mix samples have shown poorer strengths to occur in the scale columns with in the test basins due to poorer curing. Further work is underway to test longer columns and investigate the contribution of each part of the penetrometer and curing time to the N factor.

ACKNOWLEDGEMENTS

The principal author acknowledges the financial support provided by the Irish Research Council for Science, Engineering and Technology under the EMBARK Initiative, the technical help provided by Dr Alan Bell of Keller Group and the funding provided by Keller Group to carry out the testing programme.

REFERENCES

1. Timoney, M.J., B.A. McCabe, and A.L. Bell, *Experiences of Dry Soil Mixing in Highly Organic Soils.* Ground Improvement, 2012. **165**(1): p. 3-14.
2. Tremblay, H., et al., *Influence of the nature of organic compounds on fine soil stabilization with cement.* Canadian Geotechnical Journal, 2002. **39**: p. 535-546.
3. Axelsson, K., S.-E. Johansson, and R. Andersson, *Report 3: Stabilization of Organic Soils by Cement and Puzzolanic Reactions - Feasibility Study*, S.D.S.R. Centre, Editor. 2002, Swedish Deep Stabilization Research Centre c/o Swedish Geotechnical Institute: Linkoping. p. 44.
4. Lehane, B.M., *Vertically loaded shallow foundation on soft clayey silt.* Geotechnical Engineering, 2003. **156**(1): p. 17-26.
5. BSI, *BS 1377-2:1990 Methods of test for soils for civil engineering purposes*, in *Part 2: Classification tests*. 1996, British Standards Institution.
6. McCabe, B.A. and B.M. Lehane, *Behaviour of Axially Loaded Pile Groups Driven in Clayey Silt.* Journal of Geotechnical and Geoenvironmental Engineering, ASCE, 2006. **132**(3): p. 401-410.
7. EuroSoilStab, *Development of design and construction methods to stabilise soft organic soils*, in *Design Guide: Soft Soil Stabilisation*. 2001, BRE & IHS.
8. BSI, *BS 1377-7:1990 Methods of test for soils for civil engineering purposes*, in *Part 7: Shear strength tests (total stress)*. 1994, British Standards Institution.
9. Hayashi, H. and J. Nishikawa, *Mixing efficiency of dry jet mixing methods applied to peaty ground*, in *Dry Mix Methods for Deep Soil Stabilization*, H. Bredenberg, G. Holm, and B.B. Broms, Editors. 1999: Stockholm, Sweden. p. 333-338.
10. Braaten, A., R. Aaboe, and F. Oset, *Development of insitu control methods for lime/cement columns*, in *Dry Mix Methods for Deep Soil Stabilization*, H. Bredenberg, G. Holm, and B.B. Broms, Editors. 1999: Stockholm, Sweden. p. 295-301.
11. Moseley, M.P. and K. Kirsch, *Ground Improvement, Second Edition*. 2004, London: Spon Press.
12. Carlsten, P., *Lime and Lime Cement Columns: Guide for Design, Construction and Control*. 1996, Swedish Geotechnical Society. p. 111.
13. Porbaha, A., *State of the art in quality assessment deep mixing technology.* Ground Improvement, 2002. **6**(3): p. 95-120.

Active confinement in concrete members

Claire O'Shea[1], Dervilla Niall[2] & Niall Holmes[2]
[1]Track Engineering, Tube Lines, Stratford Market Depot, Burford Road, London E15 2SP
[2]Department of Civil and Structural Engineering, Dublin Institute of Technology, Bolton Street, Dublin 1, Ireland
email: claire.oshea@tubelines.com, dervilla.niall@dit.ie, niall.holmes@dit.ie

ABSTRACT: One strategy for the rehabilitation of deficient reinforced concrete structures is to target the improvement of specific critical areas of concrete columns that exhibit poor ductility and strength. A rehabilitation and repair technique using external steel bands to confine the concrete was investigated for concrete short columns through experimental and numerical analysis. The bands restrain the concrete in the directions perpendicular to the applied stress and hence delay the formation of microcracks. The main scope of the study is based on establishing the benefits and uses of "Active" confinement. As a result, the external steel bands were prestressed. Ten unreinforced concrete cylindrical specimens were cast in order to establish the effect the confinement had on the stress-strain behaviour of concrete as a material. A number of parameters were investigated such as, passive application of bands, varying spacing and volumetric ratio and the level of initial "Active" confining forces provided. Through extensive literature research an established confinement model was chosen and theoretical stress-strain curves prepared. From experimental results, it was clear that with increasing confinement a significant increase in strength and ductility was achieved. The level of prestress did not appear to have any effect on the overall strength enhancements. However, this was as a result of using a low tensile strength material and high volumetric ratios. The theoretical stress-strain model was able to capture the behaviour of confined concrete with only a small percentage error recorded.

KEY WORDS: Confinement, concrete, prestress, steel bands.

1 INTRODUCTION

Significant advances in the understanding of structural behaviour and the geologic science of earthquakes have occurred over the past 40 years. Design codes before the 1970's relied mainly on the provision of strength to resist seismic loads without giving consideration to proper detailing to enhance ductility and energy dissipation at potential locations of plastic hinges [1]. The lack of strict design criteria in older reinforced concrete structures has made them particularly susceptible to failure under seismic loading conditions. A common column detailing deficiency found in older reinforced concrete structures is that of widely spaced transverse ties giving poor confinement and support to longitudinal reinforcement.

Confinement is required to delay the strength degradation of concrete under ultimate load conditions and allow a ductile response of the column. Failure of a primary member, and particularly a column, can be catastrophic and can lead to partial or complete structural collapse. As a result, many older buildings in seismic regions require rehabilitation. In addition to the potential for seismic activity, there are also many functional reasons that may require rehabilitation such as change in use of occupancy or a planned structural addition which requires strengthening of the existing building.

As a result of the benefits confinement provides to concrete columns, many of the aspects that are beneficial for seismic rehabilitation are also beneficial for static strengthening. Providing confinement to columns through externally applied transverse reinforcement configurations such as jackets, collars, straps or wraps has been identified by researchers as a suitable rehabilitation method for under designed concrete columns. The factors affecting rehabilitation of old columns such as material and labour costs as well as the disruption of the use and operation of the structure have led researchers to develop more efficient and more economically viable methods of obtaining similar if not better enhancements in existing structures.

A particularly innovative avenue of research is that of confinement methods which engage the use of active confining forces. Where passive confinement methods rely on the dilating concrete material due to load application to initiate the generation of confining pressures, active confinement methods apply an initial confining pressure through prestressing of confinement materials resulting in confinement being effective prior to loading. It is this area of research which the study aims to conduct further investigation.

2 BEHAVIOUR OF CONCRETE UNDER COMPRESSION

Among the early studies that investigated the behaviour of concrete under stress is the study by Richard [2] which investigated the failure of concrete under compressive stress in uniaxial, biaxial and triaxial directions. The internal action of the material as it broke down under compressive stress was studied and the influence of lateral stress upon the ability of concrete to resist longitudinal stresses was also documented. This research is the basis from which all further work in this area is improved upon.

Concrete as a material contains a large number of microcracks, especially at interfaces between coarser aggregates and mortar even before any load has been applied.

It is this property that determines the mechanical behaviour of concrete. The increase in these microcracks during loading contributes to the nonlinear behaviour of concrete at low stress levels and causes volume expansion near failure. Many of these microcracks are caused by segregation, shrinkage or thermal expansion in the mortar. Other microcracks may be developed during loading as a result of differences in stiffness between aggregates and mortar [3].

3 CONCRETE IN UNIAXIAL COMPRESSION– UNCONFINED

The behaviour of concrete under uniaxial compression is well documented [3] and is best explained using stress-strain curves. A typical stress-strain curve for plain concrete under uniaxial compression is shown in Figure 1.

The first region of the curve exhibits a nearly linear-elastic response. This is present up until approximately 30% of its maximum unconfined compressive strength (f'_{co}). At stresses beyond this point the curve displays a gradual increase in curvature up to approximately 0.75 f'_{co} to 0.90 f'_{co} at which point the curvature increases sharply and reaches the peak point f'_{co}. Beyond this peak, the stress-strain curve has a descending branch until crushing failure occurs at an ultimate strain (ε_{cu}).

In Figure 1(b) corresponding volumetric strain (ε_v) is plotted against stress. The volumetric strain ε_v (dilation) is defined as the volume change per unit volume.

It can be seen that the initial change in volume is relatively linear up to approximately 0.75 f'_{co} to 0.90 f'_{co}. The ratio of lateral to axial strain increases continuously, highlighting the increasingly expansive tendency of the damaged material.

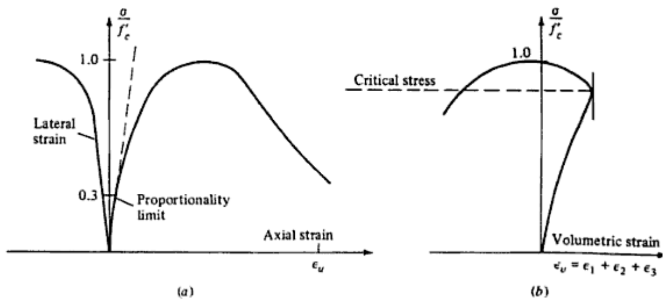

Figure 1. Typical plot of axial compressive stress vs. axial, lateral and volumetric strain [3].

Due to the increasing rate of lateral expansion, the initial volumetric contraction of the material is counteracted and it can be seen from the graph the direction of the volume change is reversed resulting in a volumetric expansion near or at f'_{co}. The stress at which the volumetric strain ε_v is a minimum is called the critical stress [4].

4 CONCRETE IN TRIAXIAL COMPRESSION – CONFINED

Richart et al [3,4] were one of the first researchers to conduct a series of tests on concrete under triaxial compression i.e. where load is applied to concrete specimens in three principle directions. As discussed previously, the response of concrete to mechanical load is characterized by continuous damage of its microstructure, a process which is clearly noticeable by cracking and volumetric expansion of the material specimen.

Partial restraint against this expansive tendency provided by confining mechanisms (such as applying pressure in three principle directions) generally results in a state of triaxial stress, the magnitude of which depends on the damage properties of concrete. Therefore, with increasing lateral confinement (application of smaller compressive stresses) the concrete material experienced enhanced strength and ductility.

The delay in the loss of stiffness and strength is evident in the stress-strain curve. Past the peak point, the response of unconfined or lightly confined concrete is characterized by the strength degradation with increasing deformation. The strength degradation is caused by the formation of microcracks in the material structure. These result in debonding of the material particles, an action that effectively reduces cohesion and decreases the material resistance. With increasing deformation, inter particle cohesion continues to decrease until it is entirely eliminated.

In the case of uniaxially loaded concrete, the frictional action cannot be mobilised, as there are no applied lateral forces present to keep the debonded material together after cohesion vanishes. The strength generated from frictional action, referred to as residual strength, becomes apparent when concrete is confined laterally and is in a state of triaxial stress. Frictional strength increases with increasing confining stress. At some critical level of triaxial stress, the residual strength may eventually equal the peak stress of the material. Beyond this transition point, concrete experiences no strength degradation but exhibits a ductile response that resembles plastic flow [5].

5 EFFECT OF SPACING ON CONFINING REINFORCEMENT

It is well documented that the effectiveness of confinement increases as spacing decreases. Sheikh et al [6] tested twenty seven concrete columns, reinforced with longitudinal steel and internal spiral links, under axial compression. As the hoop spacing of the spiral link reduced, confinement effectiveness increased resulting in greater peak stresses being achieved. The reduced spacing improves the distribution of confining pressures over the column height increasing the area of effectively confined concrete. Maximum confining pressures are found at the points where lateral reinforcement, ie, links are located with confining pressures being a minimum at the midpoint between links. Larger link spacing results in greater areas of unconfined concrete which may spall away during loading.

Iyengar et al [7] also tested for confinement effectiveness and found that if the spacing of the steel links is greater than the least lateral dimension of the column, no strength or ductility enhancements are achieved.

6 EXPERIMENTAL WORK

The experiments described in this section are small scale cylindrical specimens tested axially. A detailed analysis of the band clamp was carried out in order to assess its capacity to apply confining pressure through pre-stressing. Details concerning the properties of materials used, test specimen layout, instrumentation and data acquisition equipment and testing procedures are subsequently discussed. The experimental programme described examines the effectiveness of the confinement mechanism and also highlights the influence of important parameters.

6.1 Selection of confinement mechanism

As mentioned previously, the main focus of this research is the effect of active confinement on the stress-strain relationship of concrete. Many innovative methods are being developed to simplify the application of pre-stress in retro-fitting techniques. One detailed earlier is the use of shape memory alloys. As these alloys are quite expensive a more economical alternative was employed. A number of different clamps and metal strips were explored.

When considering a retrofit method, ease of application is a key factor. To apply bands and pre-stress through bolts or threaded couplings, the band must be in half pieces so as that they can be placed around existing columns. Whilst this is a more realistic approach which could be used in practice, it was also noted that the confining force would be at a maximum in the middle of the band as it is compressed against the face of the column and a minimum where bolts are located. Whilst this effect could be studied and accounted for, it was believed that a better solution which could better demonstrate the desired effect could be found.

For the tests, the super hose clamp (W1) by Mikalor was chosen (Figure 2). It consisted of a mild steel band with a grade 8.8 bolt for applying torque. In practice, as a retrofit method, this band would not suffice for large columns as the large opening required to place the band around the column would cause large bending stresses in the band possibly causing local yielding. However, it was decided that this band could demonstrate the desired "active" confinement effect by imposing the required lateral pressure in a uniform manner. The band also provided a simple method of applying the prestress force.

Figure 2. Chosen band clamp.

6.2 Concrete

Twelve cylindrical concrete specimens were cast for the experimental testing. As only three cylinder moulds were available in the college, formwork had to be made in order to permit casting of all cylinders in one batch to eliminate the variation in concrete strength with numerous batches. The concrete mix details are shown in Table 1.

Cylinders were cast in three levels, each level being compacted with the vibrator. Unlike cube samples which already have plane surfaces, the open end surface of the cylinders have to be prepared so as the end is perfectly level with only small tolerances allowed. Therefore the top of the sample was prepared with a stiff mortar cap so that the end planes of the cylinder and the steel loading plates are perfectly parallel. The mortar was a 3:1 sand to cement mix and having a water/cement ratio less than that of the concrete. The mortar was compacted and left with a slightly convex surface above the mould. A glass capping plate was then pressed against the mould with a rotary motion until it made complete contact with the rim of the mould. The author notes that 32,5N cement was used however EN206-1 requires 42'5N cement to be used for structural concrete.

Table 1 Concrete mix details

Characteristic strength	30N/mm2
Cement content	436kg/m3 (OPC, 32.5N)
w/c ratio	0.47
Water content	205kg/m3
Fine aggregate	827kg/m3
Course Aggregate	932kg/m3

6.2.1 Series 1 – Unconfined

Series one consisted of four cylindrical specimens. All specimens were unconfined, that is to say contained no confining mechanism. All four were placed in the compressive testing machine to obtain the unconfined cylinder strength of the concrete material. One cylinder contained a longitudinal and a lateral strain gauge in order to obtain an unconfined specimen stress-strain curve as shown in Figure 3.

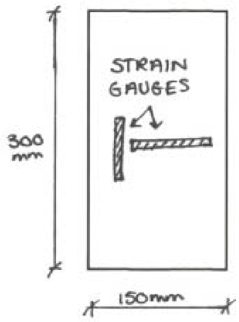

Figure 3. Series 1 - Specimen layout.

6.2.2 Series 2 – Passive

Series two consisted on one cylindrical specimen. This specimen contained four bands at equal spacing (56mm). A 10mm gap was left top and bottom of the cylinder to ensure the bands were not directly loaded. The cylinder was wrapped in tape along the regions where bands were to be applied and grease applied to bands and concrete to reduce frictional effects. Bands were finger tightened only. The group was to demonstrate "passive" confinement as the initial force generated through finger tightening was minimal. A longitudinal and a lateral strain gauge were placed in the centre of the specimen between bands in order to obtain a passive specimen stress-strain curve (Figure 4).

6.2.3 Series 3 – Constant prestress, varying spacing

Series three consisted of three cylindrical specimens. This series was to determine the effect of spacing and corresponding changes volumetric ratio (ratio of lateral reinforcement to concrete) on peak compressive stress of confined concrete. Three spacing arrangements were designed consisting of two, three and four bands. An initial prestress of 2.66MPa with a lateral strain of 0.007×10^{-6} was applied to each band. Strain gauges were affixed in the locations shown in Figures 5 and 6.

6.2.4 Series 4 – constant spacing, varying prestress

Series four consisted of three cylindrical specimens. This series was to determine the effect the level of initial "active" confining pressure had on the peak compressive stress of confined concrete. All specimens contained the same number of bands at equal spacing. The initial levels of prestress applied were 1.34MPa, 2.66MPa and 3.93MPa and arranged as shown in Figures 7 and 8.

6.2.5 Specimen testing

Axial compressive tests were conducted using the cube crushing machine in the concrete laboratory. The load was increased based on a displacement-controlled strategy until strength decay was recorded, which indicates failure of the specimens. Typically a decrease in strength of 2% indicates failure and the compressive machine terminates loading. This percentage was adjusted to approximately 7-10% strength decay. The axial load was increased with an average load rate of 0.3MPa/s. The ASTM standard loading rate for strength of cylindrical specimens is within the range 0.14-0.34MPa/s. Therefore the selected loading rate falls within the ASTM standard. The strain gauges on all specimens were connected to the relevant ports and strain data recorded on the computer.

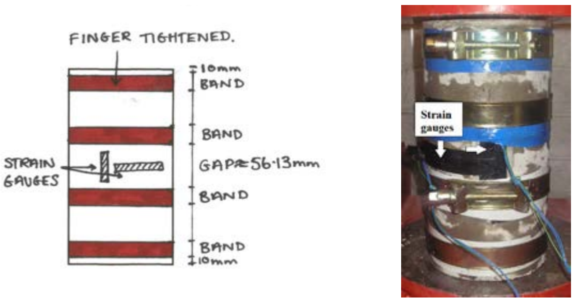

Figure 4. Series 2 - Test specimen.

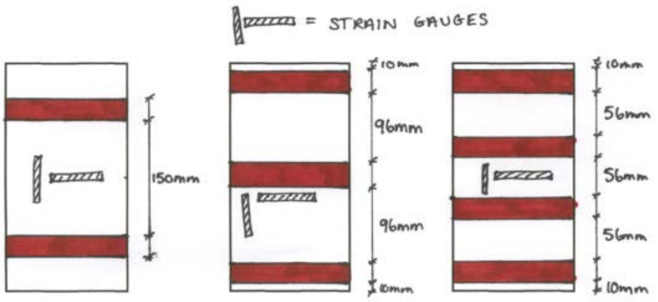

Figure 5. Series 3 - Specimen layout.

Figure 6. Series 3 - Test specimens.

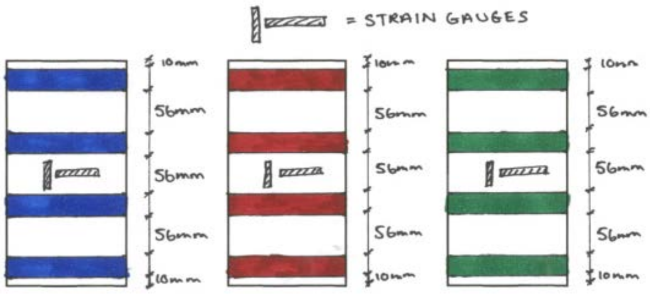

Figure 7 Series 4 - Specimen layout.

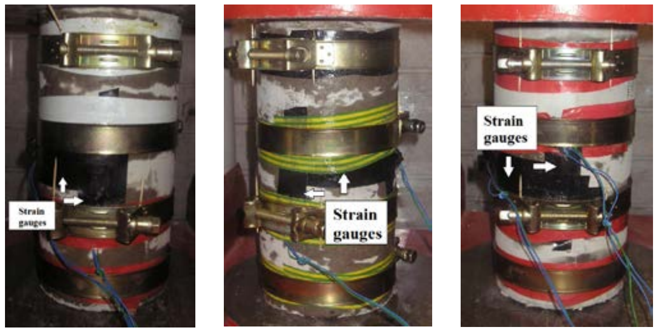

Figure 8. Series 4 - Test specimens.

7 EXPERIMENTAL RESULTS

7.1 Series 1 – Unconfined

Series one consisted of four unconfined specimens, one of which was fitted with strain gauges in order to obtain an experimental stress-strain curve. The average of the four tests is taken as the unconfined compressive strength of the concrete (f'_{co} = 14.18N/mm^2).

The stress-strain graph obtained, shown in Figure 9, indicated that the gauges broke before the peak compressive stress was reached. This is most likely as a result of the cracking of the outer surface of the cylinders under the location of the gauges. As a result of this an incomplete stress-strain curve was obtained. In order to obtain the peak axial strain, the following formula proposed by Legeron and Paultre (2003) was used, $\varepsilon_{co} = 0.0005(f'_{co})$.

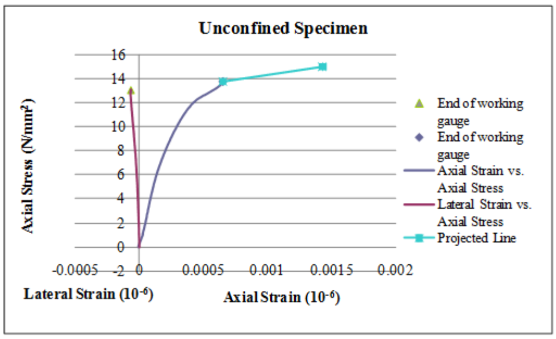

Figure 9. Unconfined specimen stress-strain.

7.2 Series 2 - Passive

This series consisted of one specimen which contained four bands that were finger tightened. Similar to that of the unconfined specimens, an incomplete stress strain graph was obtained due to the rupture of the longitudinal gauge as shown below in Figure 10. A peak compressive stress of 14.03N/mm^2 was obtained. It was noted before testing of this specimen was carried out that due to finger tightening only, the band did not fully conform to the shape of the cylinder and there were areas of misfit around the circumference of the band. This misfit allowed the concrete to behave as if it were unconfined with the bands only containing cracked concrete instead of delaying the onset of crack formation, hence only an unconfined compressive strength was reached.

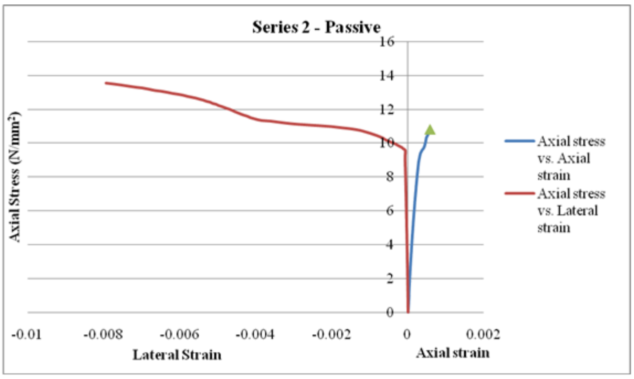

Figure 10 Passive specimen stress-strain

Although the gauge broke due to crack formation under the location of the gauge, the passive specimen resisted strength degradation unlike its unconfined counterpart. With the bands containing the damaged concrete a gradual decrease in compressive strength was observed with increased loading. The mode of failure changed from that of the unconfined concrete. Whilst cracks formed normal to the vertical axis in between bands, it was the crushing of the concrete in the perpendicular direction to the axis of loading which was more prominent.

7.3 Series 3 – Constant prestress, varying spacing

This series consisted of three cylinders with varying spacing of bands. It is clear from the results (Figure 11) that as the spacing decreases, the peak stress increases. This is as a result of the increased volumetric ratio of steel to concrete. The peak strain increases with increasing spacing with the exception of the 96mm spacing specimen. This is considered to be experimental error from the gauge and it is unsure whether the gauge broke prior to reaching the peak point.

The lateral gauge on the 96mm spacing specimen broke relatively early during the testing procedure possibly due to faulty application. It is clear to see from Figure 12 that the point of unstable crack propagation (corresponding to critical stress of concrete) is delayed further and further as spacing decreases.

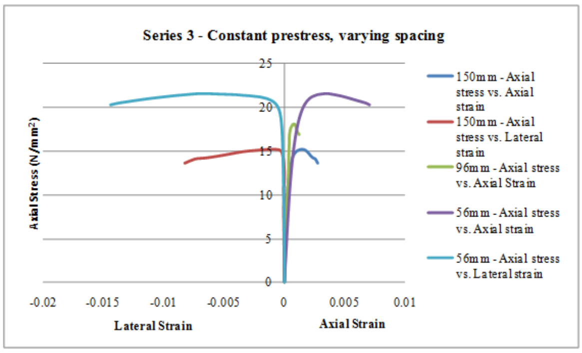

Figure 11. Constant prestress, varying spacing stress-strain.

Again, it can be seen that the mode is failure is primarily the crushing of concrete in regions between bands. It is also noted that the specimen containing spacing of 150mm did not exhibit a great increase in strength as a result of the confinement. This is as a result of the spacing being the same as the lateral dimension of the cylinder As a result diagonal cracks can also be seen in between bands in this specimen.

7.4 Series 4 – Constant spacing, varying prestress

This series consisted of three cylinders with varying levels of initial "active" confining pressure applied to the bands. It is clear from the results (Figure 12) that the varying level of initial active confining pressure applied had no significant effect on the peak compressive stress reached in each specimen. There is however a marked difference between the peak strains recorded for specimens corresponding to level 1 (1.34MPa) and level 3 (3.93MPa). Whilst they obtained similar peak stresses, the specimen corresponding to level 3 did so at a smaller peak strain.

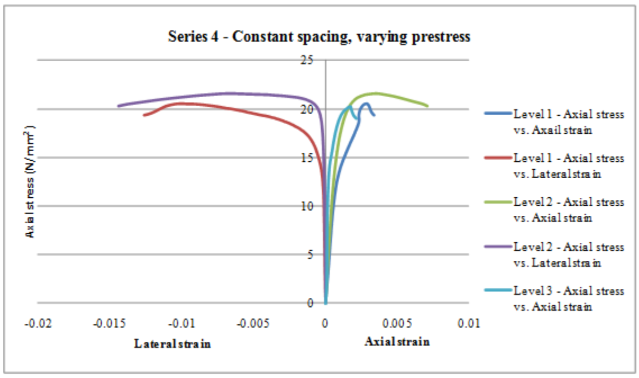

Figure 12 Constant spacing, varying prestress stress-strain

The stress-strain graph corresponding to level 1 indicates that some level of deterioration in stiffness began at approximately 12N/mm2. Whilst the specimen reached its peak compressive stress, the strain readings indicate that it did so with considerably more internal damage. The lateral gauge corresponding to Level 3 broke during the initial loading.

8 CONCLUSIONS

A summary of the general conclusions are presented below.

1. In the case of passive confinement, an increase in ductility can be achieved through the application of steel straps. At high levels of confinement, the passive force generated is usually near or at yield stress of the straps. However, when confinement effectiveness is approaching zero the lateral reinforcement only reaches a portion of the yield stress available and it is this value which must be used in calculating the peak compressive stress.
2. Active confinement is of benefit where confinement effectiveness is low and the yield capacity of the strap is not reached before failure of the concrete.
3. Active confinement also affects the stress-strain relationship of concrete. As the active lateral force is exerted on the column before any axial load is applied the concrete is in compression laterally. Therefore the presence of this initial compressive force delays the onset of dilation of concrete and passive forces are generated once this initial lateral compressive force is overcome. This results in a significant increase in compressive stiffness (or apparent elastic modulus) in the early stages of loading demonstrated by a stiffer pre-peak slope of the stress strain curve.
4. Where active confinement is used, yielding of lateral reinforcement occurs with damage of the concrete (onset of unstable crack propagation), unlike passive confinement where the concrete damages first and the confining material yields during the descending slope of the stress-strain curve containing the yielded concrete.
5. The presence of prestress in lateral confinement, whilst increases peak compressive stress through optimal utilisation of the confining strap, results in speeding up post-peak degradation indicating loss of ductility and a lower ultimate strain.

REFERENCES

[1] Hussain, M.A., Driver, R.G. “Experimental investigation of external confinement of reinforced concrete columns by HSS collars.” 2005, *ACI Structural Journal*, Vol. 102, No. 2, pp. 242-251

[2] Richart, F.E.; Brandtzaeg, A.; and Brown, R.L., “A study of the Failure of the Concrete under Combined Compressive Stresses,” University of Illinois Engineering Experiment Station, Bulletin No. 185, Urbana, IL, Nov.1928.

[3] Chen, W.F., “Plasticity in Reinforced Concrete.” McGraw Hill, New York, 1982.

[4] Richart, F.E.; Brandtzaeg, A.; and Brown, R.L., “The Failure of Plain and Spirally Reinforced Concrete in Compression,” University of Illinois Engineering Experiment Station, Bulletin No.190, Urbana, IL, Nov.1929.

[5] Imran, I., Pantazopoulou, S.J., “Plasticity Model for Concrete under Triaxial Compression”, *Journal of Engineering Mechanics*, Vol.127, No.3, March 2001, pp 281-289

[6] Sheikh, S.A.; and Toklucu, M.T., “Reinforced Concrete Columns Confined by Circular Spirals and Hoops”, *ACI Structural Journal*, Vol.90, No.5, Sept.- Oct 1993, pp.542-553.

[7] Iyengar, K.T.S.R., Desayi, P. and Reddy, K.N. “Stress-strain characteristics of concrete confined in steel binders.” 1970, *Mag Concr Res*, Vol. 22, No. 72, pp. 173-184

[8] Legeron, F., Paultre, P. “Uniaxial confinement model for normal and high strength concrete columns.” 2003, *ASCE J Struct Eng*, Vol. 129, No.241-252.

Nonlinear finite element analysis of FRP reinforced concrete structures

G. Tharmarajah[1] & P. Archbold[1]
[1,1]STRAIT, Structures & Materials Research Group, School of Engineering
Athlone Institute of Technology, Dublin Road, Co.Westmeath.
Email: tgobithas@ait.ie, parchbold@ait.ie

ABSTRACT: Fibre Reinforced Polymer (FRP) reinforcement is a non-corrosive alternative to steel and is gaining popularity for use in reinforced concrete structures exposed to corrosive environments. A major difference between the two reinforcing materials is their behaviour at failure. Steel tends to undergo ductile elongation, while FRP is a brittle material, which ruptures suddenly. Accordingly, while steel reinforced concrete members are generally designed to fail through yielding of the steel, FRP reinforced structures are designed to fail through compressive failure of the concrete. This crushing of the concrete represents plastic deformation. Accurate modelling of the failure of FRP reinforced concrete structures has proven challenging to researchers in the field. However, improvements in the development of material models, among other advances, mean improved accuracy from nonlinear finite element models is now achievable. This paper discusses the challenges of modelling reinforced concrete structures for concrete crushing failure. Results are presented from nonlinear finite element models of FRP reinforced concrete slabs, which were tested to failure and compared to the experimentally derived values.

KEY WORDS: NLFEA, BFRP, Concrete, DIANA, ANSYS.

1 INTRODUCTION

Nonlinear finite element analysis is increasingly used in civil engineering applications for structural investigations. The interest in using finite element analysis to solve complex structural problems can be traced back to 1941 when Alexander Hrennikoff first introduced a solution method to solve a plane elasticity problem using a finite element approach [1]. Since then the finite element approach has been widely used by engineers, physicist and mathematicians. Understanding of the behaviour of concrete and reinforcement materials and development of advanced material models to simulate this behaviour has given nonlinear finite element analysis the capability to expand to a wide range of applications.

Fibre Reinforced Polymer (FRP) is a generic title for a corrosion resistant composite reinforcement produced using various fibres and resin. The type of fibre used determines the name of the material, which is normally referred to by the appropriate abbreviation. Popular fibres used and the composite abbreviations are thus Glass (GFRP), Carbon (CFRP), Aramid (AFRP) and Basalt (BFRP). Along with its corrosion resistant attributes, FRP reinforcement materials demonstrate high tensile strength and light weight compared to traditional steel reinforcement. Moreover, where corrosion resistant reinforcement is required, FRP materials offer advantages over traditional alternatives such as stainless steel, primarily from an economic perspective.

One of the challenges associated with the use of FRP reinforcement is the lack of design guidance available to designers. The most prominent international code of practice in this area is produced by the American Concrete Institute [2]. Of particular concern is the fundamental difference between FRP and steel reinforcement at ultimate failure. Whereas steel tends to yield, leading to a gradual collapse, FRP composites are brittle, with a lower modulus of elasticity, leading to a sudden rupture without prior warning.

In order to address this failure mode associated with brittle reinforcement, ACI 440 recommends the use of over reinforced concrete sections, thereby forcing the structural member to fail through concrete crushing rather than FRP rupture. This is considered a marginally preferable failure scenario [2].

FRP materials fail by rupture at their peak stress and it may not be preferable in concrete structures as the failure could be catastrophic. Therefore, concrete structures reinforced with FRP bars are often designed to fail by concrete crushing failure, which is a typical failure of in-plane restrained slabs. Restrained slabs such as deck slabs in beam and slab bridges show concrete crushing failure due to compressive membrane action ([3], [4]and [5], etc.). Hence, it is important to understand the behaviour of the nonlinear finite element analysis (NLFEA) models where structures fail by concrete crushing. In such cases, the behavior of the concrete material model becomes of critical importance.

The authors are currently investigating the potential for use of FRP as an alternative to steel reinforcement in precast concrete products where the issue of durability of reinforcement is critical factor in terms of the product design and limitations. The steel and BFRP reinforced representative concrete sections tested with other unreinforced sections in a series of load tests are discussed here. The first author was also previously involved in the testing of in-plane restrained slab sections again reinforced with BFRP bars [6].

This paper presents the results of the experimental load tests on the concrete samples and compares the measured responses to those predicted from nonlinear FE models. The simply supported slabs were analysed using commercially available Ansys V11.0 [7] while the restrained slabs were analysed using both Ansys and DIANA 9.2 [8] for the service and ultimate behaviour of the test slabs.

2 EXPERIMENTAL INVESTIGATION

The concrete slab sections tested by the authors were subjected to four-point loading with simple supports as shown in Figure 1 (a) & (b). The slab response to loading was measured in terms of mid-span deflection up until the point of failure. The serviceability performance of the slab sections in terms of crack generation before failure was monitored visually. Prior to load testing the slabs were all painted with white emulsion paint to emphasis any crack development that may occur. Figure 2 shows a slab being tested with cracks highlighted.

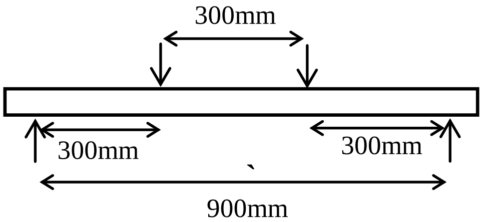

Figure 1(a). Test setup of simply supported slabs.

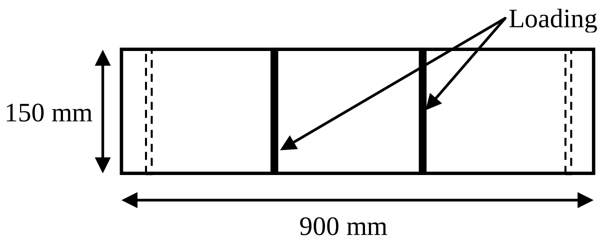

Figure 1(b). Plan view of the test panel and loading point.

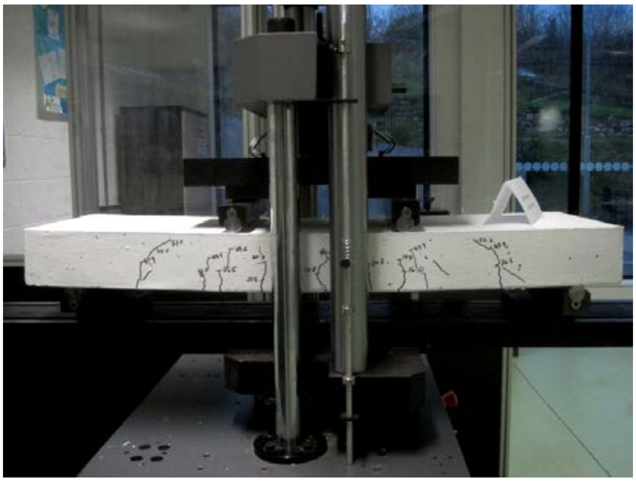

Figure 2. Simply supported slab being tested.

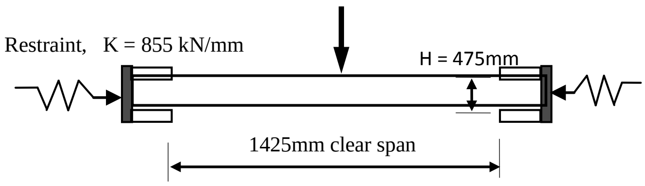

Figure 3. Test setup of restrained slabs (Reproduced from Tharmarajah et al., 2010).

The restrained slabs were subjected to single point loading and also were subjected to horizontal restraint as shown in Figure 3. The steel reinforced simply supported slab was used as the reference sample. The details of the test slabs are given in Table 1.

Table 1. Details of test panels used for investigation.

Test Slabs*	Rebar percentage	Effective Depth (mm)
BFRP 0.6%_12_125 T&B*	0.60%	119
BFRP 0.6%_16_300 T&B*	0.60%	117
BFRP_60/SS†	0.67%	60
STEEL_60/SS†	0.67%	60

** Dimensions: 1765mm (length) x 475mm (width) x 150mm (depth). 0.6% - amount of reinforcement, 12- bar diameter, 125-the spacing between bars and T&B – Top and bottom two layers of reinforcement*
† Dimensions: 900mm (length) x 350mm (width) x 100mm (depth). BFRP/Steel denotes the type of bar and SS- simply supported. 60-effective depth

3 NONLINEAR ANALYSIS

The simply supported slabs and in-plane restrained slabs were modelled with ANSYS. The restrained slabs analysed with ANSYS are also compared with the DIANA analysis results [9]. Both Ansys and DIANA are commercially available NLFEA tools which are widely used in nonlinear analysis of reinforced concrete structures.

3.1 Material model and numerical discretisation

3.1.1 Material Properties and Model

The compressive and tensile properties of the concrete were obtained from compressive tests and tensile tests respectively carried out on concrete samples taken during the test slab production. Details of these concrete material properties are given in Table 2. Similarly, material properties for steel and BFRP were obtained from tensile strength tests carried out on BFRP and steel bars (Table 3).

Table 2. Concrete properties of the test slabs.

Test Slabs*	Con. comp. strength $f_{ck,cube}$ N/mm^2	Tensile strength of conc. f_t N/mm^2
BFRP 0.6%_12_125 T&B*	69.3	3.77
BFRP 0.6%_16_300 T&B	66.1	3.13
BFRP_60/SS†	57.1	3.55
STEEL_60/SS	57.1	3.55

Table 3. Properties of the reinforcement.

Reinforcement	Tensile strength N/mm^2	Modulus of elasticity N/mm^2
BFRP*	920	54000
STEEL	460	210000

** The data used was obtained from the tests carried out by Tharmarajah et al. [6]*

3.1.2 *Concrete and Reinforcement*

The linear properties of concrete are the modulus of elasticity and Poisson's ratio. The modulus of elasticity was established from the compressive strength of the concrete. The compressive strength of the concrete was observed from testing of 100mm x 100mm x 100mm cubes. Young's modulus of elasticity can be calculated from the cube compressive stress $f_{ck,cube}$ using the equation 1 [10], where the crushing stress under compression was used to derive the modulus of elasticity. Poisson's ratio of 0.2 was considered throughout the analysis as it was an average typical value for concrete.

$$E_c = 4.73\ (f_{ck,cube})\text{^}0.5\ \text{kN/mm}^2 \quad (1)$$

The plasticity of concrete in compression is crucial for structures where the failure is dominated by the failure of concrete. Unlike steel reinforced structures, where the failure occurs due to the yielding of steel, FRP reinforced structures are designed to fail by the concrete failure. In such cases, the post peak softening behaviour of the concrete is critical. The post peak stress strain behaviour of the concrete for both tension and compression needs careful investigation as it is difficult to establish [11]. Therefore, the strain hardening and softening of concrete was modelled using Thorenfeldt compression behaviour [12]. Thorenfeldt compression behaviour is capable of handling post peak stress of concrete in compression. Typical uniaxial stress strain behaviour of thorenfeldt model is shown in Figure 4. Unlike ideal plasticity models which are often used in steel reinforced structures, the thorenfeldt model is capable of predicting failure due to concrete crushing.

Steel and BFRP were modelled with Von Mises plasticity model with ideal plasticity. Although BFRP bars are brittle in nature, the ideal plasticity was considered as the slabs failed by concrete crushing. Since the stress on bars stays within linear region due to concrete rupture, it is appropriate to use ideal plasticity.

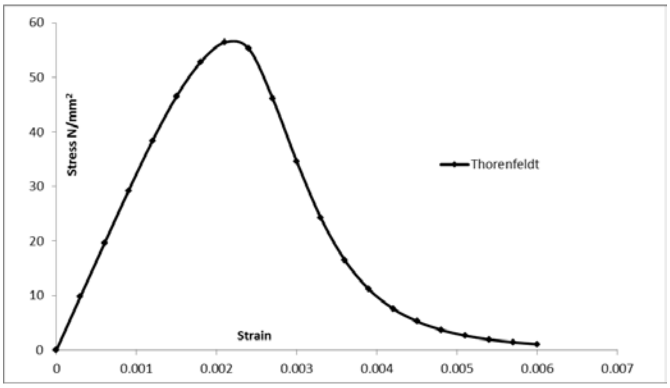

Figure 4. Uniaxial stress strain behaviour of thorenfeldt compression model.

3.2 *Numerical discretisation*

The restrained slabs had a single mid span loading and simply supported slabs were tested with four point bending. Since both are symmetric, half of the slab was considered for modeling. A three dimensional volume model used for the ANSYS analysis (Figure 5) and a two dimensional plane stress model was considered for DIANA analysis.

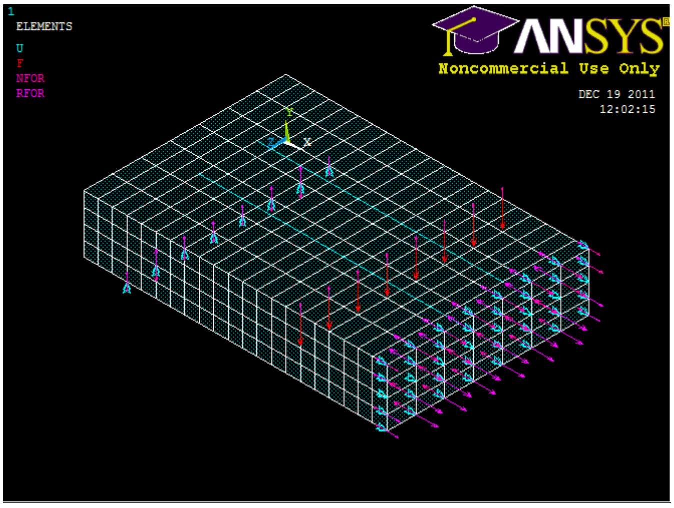

Figure 5. ANSYS model used for simply supported slabs.

Numerical discretization of the model can influence the results of the slab analysis. The size of the finite element mesh can lead to either over estimated or under estimated failure load of a slab [13]. Small mesh size leads to a reduced failure load as energy dissipation decreases and higher mesh size increases the failure load due to decreased crack progression [13].

While taking in to account the influence of the mesh size and aspect ratio, a 25mm element size was chosen with an aspect ratio of 2. A previous study by Duchaine and Champliaud [14] showed that, the error between the prediction and actual failure load could increase with an increase in aspect ratio. Therefore, to minimize the error, it was decided to use an aspect ratio 2 to reduce the error to as low as 1%. Duchaine and Champliaud did find that the error between nonlinear predictions and actual failure load was 12% for an aspect ratio of 20:1 and 1% for an aspect ratio 6:1.

4 RESULTS AND DISCUSSIONS

4.1 *Results*

A comparison for the in-plane restrained slabs analysed with DIANA and Ansys and the behaviour of simply supported slabs analysed with Ansys are discussed. Load versus deflection and the ultimate failure load are shown of both types of structures.

4.1.1 *Ultimate behaviour*

Table 4 presents the measured and predicted failure loads for the respective simply supported and restrained slabs. Restrained slabs were analysed using both DIANA and ANSYS where only ANSYS analysis was carried out on simply supported slabs. The nonlinear models were capable in predicting the ultimate failure load of the tests panels with a good accuracy. The comparison between the failure loads predicted by nonlinear analysis and experimental investigation is shown in Figure 6 for restrained slabs and in Figure 7 for simply supported slabs.

Table 4. Comparison of test results with NLFEA predictions.

Test Slabs	Observed ultimate failure load kN	ANSYS Prediction kN	DIANA Prediction kN
BFRP 0.6%_12_125 T&B	300.4	305.1	303.3
BFRP 0.6%_16_300 T&B	295.1	308.2	299.8
BFRP_60/SS	56.3	54.4	N/A
STEEL_60/SS	45.9	44.0	N/A

The deviation on failure loads predicted by DIANA and Ansys models were within 1% to 5% of the actual failure load of both simply supported and restrained test slabs.

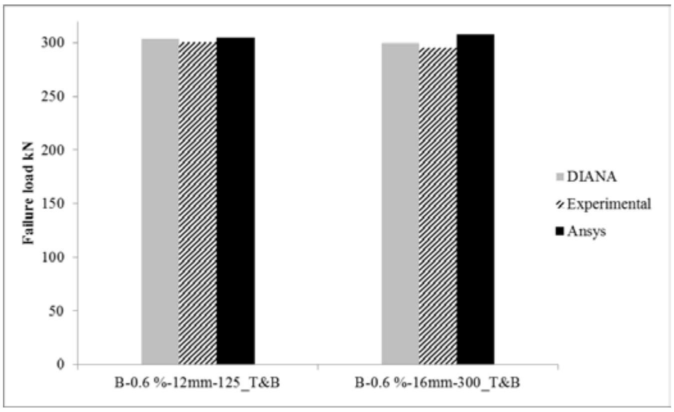

Figure 6. Comparison of ultimate failure load of the restrained slabs with DIANA and Ansys model predictions.

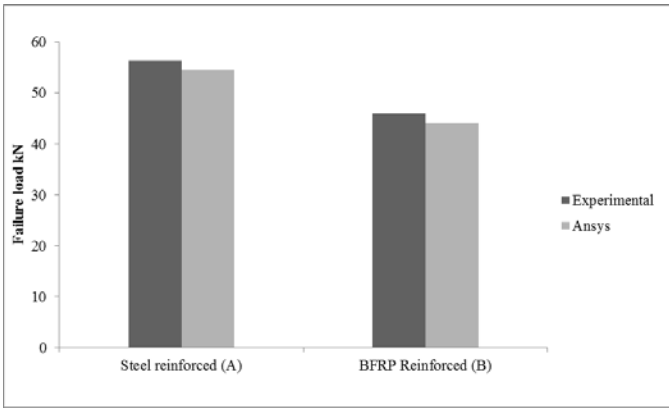

Figure 7. Comparison of ultimate failure load simply supported slabs with Ansys model predictions.

4.1.2 Service behaviour

While the ultimate load behaviour of the slabs was accurately predicted by the nonlinear FE models, the load-deflection response prediction was not as successful. Previous investigations on FRP reinforced restrained slabs and nonlinear finite element analysis (NLFEA) of such slabs using DIANA and later analysis on ANSYS showed that the nonlinear models predict a stiffer response than that observed during the experimental investigation [9]. This phenomenon was again observed on the simply supported slabs reinforced with both steel and BFRP bars. Figure 8 and Figure 9 show the load versus deflection behaviour of restrained slabs and simply supported slabs for both experimental and nonlinear evaluation.

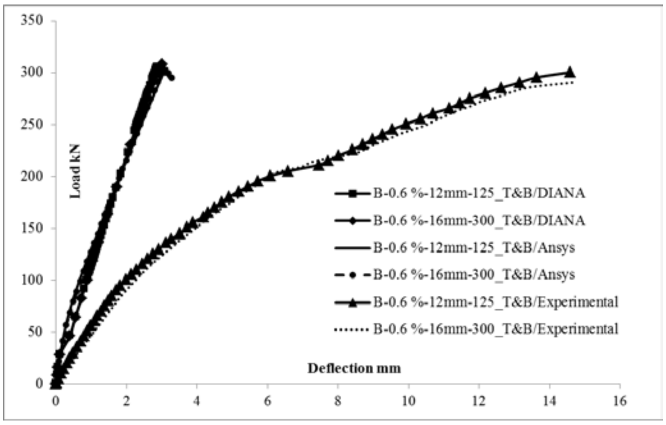

Figure 8. Load versus deflection behaviour of restrained slabs are compared with DIANA and ANSYS model results.

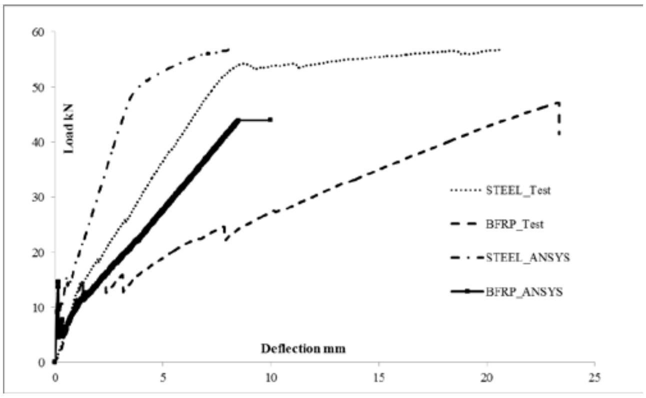

Figure 9. Load versus deflection behaviour of simply supported slabs are compared with Ansys results.

In order to investigate this discrepancy between the predicted and recorded response, a comparison was carried out between the experimental results and nonlinear predictions against theoretical predictions (Equation 2 and Equation 3) within linear load levels (which is prior to the first crack formation). This shows that the nonlinear predictions give better agreement with the theoretical predictions than actual test results and both theoretical and nonlinear responses are much stiffer than experimental results (Figure 10). Deflection of four point bending was calculated using equation 2 while the deflection for single mid-point loaded restrained slabs was estimated using equation 3.

$$\delta = \frac{FL^3}{192EI} \tag{2}$$

$$\delta = \frac{Fa^2(3L-4a)}{6EI} \tag{3}$$

Where, δ – deflection, F-Load applied, a-distance between support and the load, L-Length, E- Modulus of elasticity and I- Second moment of area

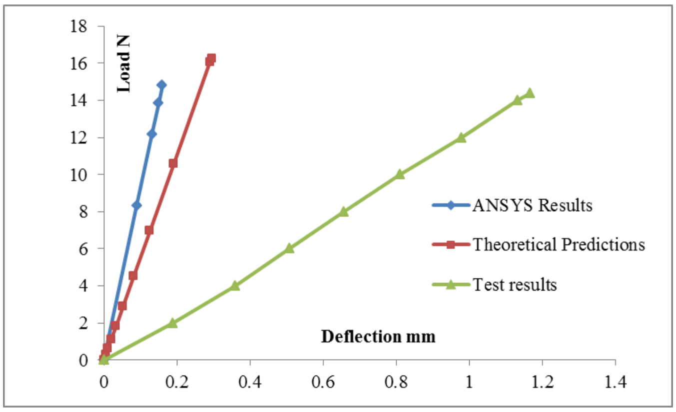

Figure 10. Ansys, theoretical and test results comparison of simply supported steel reinforced panel.

Although the NLFEA models showed a stiffer response in predicting the load versus deflection behaviour, they did display good accuracy in predicting the crack load and crack pattern for the relevant test slabs.

4.2 Discussions

Despite the stiff response of the nonlinear results in predicting load versus deflection behavior, the NLFEA models are capable of predicting the ultimate failure load of different types of reinforced concrete panels with good accuracy. Higher deflection noticed on experimental investigation leads to a question on what causes the variation between nonlinear predictions and experimental results. Since this issue has been noticed in various other occasions and in different research studies, the future research study will investigate the factors which cause the fluctuation in load versus deflection predictions.

The restrained slabs and the slabs reinforced with BFRP bars are designed to fail by concrete crushing. Thus, ideal plasticity of the concrete cannot be used in such situations as ideal plastic conditions could cause misleading conclusions. Therefore, it is important to incorporate appropriate softening behaviour of the concrete in the post peak stress level. The current study considered a Thorenfeldt compression model to study the failure behaviour of FRP reinforced sections.

The results show that for both restrained and simply supported slabs, the failure load predictions using nonlinear models demonstrate a good correlation to the experimental investigation.

Although the test slabs showed good agreement in terms of failure load, the load versus deflection behaviour of the test panels obtained from nonlinear models showed a stiffer response compared to experimental investigation. A similar behaviour was noticed by several other researchers in different occasions.

A 1800mm length, 240mm depth and 150mm width beam tested by Hibino et al. [15] was modelled using DIANA FEA and the load versus deflection behaviour observed showed a good agreement with the test results of the beam. The same beam modelled by Parvanova et al [16] using ANSYS also gave a good agreement with test results. However, in another research publication, Al-Azzawi et al [17] compared Ansys results of 450mm (long) x 150mm (width) x 150mm (depth) beams and 600mm (long) x 200mm (width) x 50mm (depth) beams. The Ansys analysis carried out on both deep and shallow beams demonstrated that the deep beams with 150mm depth had a good agreement with the nonlinear results while the shallow 50mm deep beam showed relatively stiffer response to about 6 times of the actual stiffness of the test slab.

A research by Dirar and Morley [18] also observed that the DIANA FEA nonlinear models show a stiffer response in the linear stage. However a good agreement was noticed at the post cracking stage. Therefore, it could be noticed from the authors' nonlinear FE results and the results discussed by the other researchers on their nonlinear FE analysis, that the NLFEA models show variation in predicting the behaviour of the test model. In some occasions the models showed a good correlation with the test results and sometimes they did not.

5 CONCLUSIONS

The following conclusions can be made from the studies.

1. Nonlinear FE models are capable of predicting the actual strength of the test panels regardless of physical and material characteristics of the test model.
2. Nonlinear investigation on experimentally tested model lead to an observation, that, in some situations the models predict stiffer response than experimental results.
3. The stiffer response found in nonlinear models for some slabs could be due to material properties used and requires further investigation.
4. Further research investigates beams with various depth and widths to study the difference between experimental and numerical results.

6 FUTURE RESEARCH

The future work will investigate the factors that cause the stiffer response of the nonlinear model in the linear and nonlinear region. Experimental investigations are expected to be carried out on beams with various depths and widths to evaluate the stiff response noticed on reinforced simply supported slabs for both nonlinear and theoretical evaluations.

The future research also expects to investigate the relationship between the compressive stiffness and the flexural stiffness of concrete in experimental, numerical and theoretical investigations.

ACKNOWLEDGMENTS

The authors would like to gratefully acknowledge the support of Killeshal Precast Concrete and Enterprise Ireland for funding the project and Magmatech, U.K. for supplying the BFRP bars and technical staff at the Athlone Institute of Technology for their support in laboratory testings.

REFERENCES

[1] Oden, T. J. (1990)., ―Historic comments of finite elements‖, In S. G. Nash, A history of scientific computing, New York: ACM, pp. 152-166

[2] ACI. (2006). ―ACI 440.1R-06 Guide for the Design and Construction of Concrete Reinforced with FRP Bars‖, American Concrete Institute, Michigan, USA

[3] Park, R. (1964)., ―Ultimate strength of rectangular concrete slabs under short-term uniform loading with edge restrained against lateral movement‖, Paper 6705, ICE Proceedings, Vol.28.
[4] Rankin, G., and Long, A. (1998). ―Arching action strength enhancement in laterally restrained slab strips‖, Proc.Institute of Civil Engineers Structures and Buildings, Vol.122, 461-467.
[5] Taylor, S.E., Rankin G.I.B. and Cleland D.J. (2001), ―Arching action in high strength concrete slabs‖, ICE Proceedings—Structures and Buildings, No. 146, Issue 4, Nov 2001, pp. 353-262
[6] Tharmarajah, G, Taylor, S.E, Robinson, D., and Cleland, D.J. (2010), Composite Reinforcement for bridge deck slabs, Bridge and Infrastructure Research in Ireland; Concrete Research in Ireland 2010, Cork, Republic of Ireland.
[7] ANSYS, ANSYS User's Manual Revision 11.0, ANSYS, Inc., Canonsburg, Pennsylvania, 2010.
[8] DIANA. (2007)., ―User' s Manual‖, TNO DIANA bv. Delft
[9] Tharmarajah, G. (2011), "Compressive Membrane Action in Fibre Reinforced Polymer (FRP) Reinforced Concrete Slabs", PhD Thesis, Queen's University Belfast
[10] Hognestad, E. (1952)., ―Fundamental concepts in ultimate load design of reinforced concrete members‖, ACI Proceedings, Vol.48, No.10, June 1952, pp.809-832.
[11] Ren, X., Yang, W., and Zhou, Y. (2008)., Behaviour of high-performance concrete under uniaxial and biaxial loading‖, ACI Materials Journal, 105(6) , 548-557.
[12] Thorenfeldt, E., Tomaszewicz, A., and Jensen, J. J. (1987), "Mechanical properties of high-strength concrete and applications in design". In Proc. Symp. Utilization of High-Strength Concrete (Stavanger, Norway) (Trondheim, 1987), Tapir.
[13] Shayanfer, M., Kheyroddin, A., and Mirza, M. (1997). "Element size effects in nonlinear analysis of reinforced concrete members", Computers & Structures, 339-352.
[14] Duchaine, F., and Champliaud, H. (2007). "Structured mesh generation by kriging with local refinement with a new elliptic scheme‖", Engineering with Computers, Vol.23 (1), November, pp.61-69.
[15] Hibino, K., Kojima,T. and Takagi,N., (2002), "FEM study on the shear behavior of RC beam by the use of discrete model", Proceedings of Third DIANA World Conference, Tokyo, Japan (Publication: Taylor and Francis).
[16] Parvanova, S.L, Kazakov, K.S., Kerelezova1, I.G., Gospodinov, G.K., and Nielsen, M.P., (2005), "Modelling the nonlinear behaviour of R/C beams with moderate shear span and without stirrups using Ansys", Proc. of International Conference, VSU, Sofia, Bulgaria.
[17] Al-Azzawi, A.A., Ali, A.S., and Risan, H.K., (2011) "Behaviour of ultra high performance concrete structures", ARPN Journal of Engineering and Applied Sciences, Vol. 6, No. 5, May.
[18] Dirar,S.M.O.H., and Morley, C.T., (2005) "Nonlinear finite element analysis of reinforced concrete deep beams", Proceedings of VIII International Conference on Computational Plasticity, Complas VIII, Barcelona.

An investigation into shear reinforcement in reinforced concrete corbels

M.J. Minehane[1], B.D. O'Rourke[2]
[1]RPS Group Ltd., Innishmore, Ballincollig, Cork, Ireland
[2]Department of Civil, Structural and Environmental Engineering, Cork Institute of Technology, Rossa Avenue, Bishopstown, Cork, Ireland
email: michael.minehane@rpsgroup.com, brian.orourke@cit.ie

ABSTRACT: The current study examines numerous discrepancies between design standards and guidance regarding the provision and orientation of shear reinforcement in reinforced concrete corbels. Much of the research to date is concerned with shear strength predictions and the proposal of analytical models based on shear-friction or strut-and-tie modelling. It is widely acknowledged that secondary/shear reinforcement enhances the shear strength and ductility of corbelled joints, whilst also serving to prevent sudden failure. Information regarding the effectiveness of differing detailing arrangements, however, is limited and often contradictory. This experimental and finite element study investigates the inconsistencies, whereby horizontal, vertical and inclined shear links are examined under monotonic loading of asymmetrical joints. It is shown that the traditional approach with the provision of horizontal shear reinforcement in accordance with ACI 318-11 and BS 8110 performs most efficiently. It is also determined that the use of vertical links in accordance with EN 1992-1-1 results in a premature failure.

KEY WORDS: Corbel; Finite element analysis; Shear strength; Stirrup; Strut-and-tie model.

1 INTRODUCTION

Corbels are short cantilever projections with a shear span-to-depth ratio less than unity. Corbelled joints are widely used in practice to support concentrated loads from a variety of precast members. Owing to their geometry and since they are controlled by shear, corbels exhibit non-linear, non-flexural and highly complex strain distributions. Strut-and-tie modelling, which is based upon the lower bound theorem of plasticity, has emerged as a practical and intuitive tool for the analysis of such disturbed regions (D-regions). Pioneers of this form of truss analogy include Hagberg [1] and Schlaich *et al.* [2, 3].

Code requirements for the design of reinforced concrete corbels are primarily based on experimental results. Influential early tests by Kriz and Raths [4] and Mattock *et al.* [5], in addition to photoelastic modelling by Franz and Niedenhoff [6], Mehmel and Becker [7] and Mehmel and Freitag [8], established typical failure modes, derived elastic stress distributions and proposed shear strength predictions based either on empirical results or shear-friction theory. ACI 318-95 [9] subsequently included the shear-friction method, originally developed by Mast [10], for corbel design. Studies by Yong and Balaguru [11], Hwang *et al.* [12] and Ali and White [13] revealed that the shear-friction approach underestimated the corbel shear capacity when compared to test results. Recent design codes permit the use of a simplified strut-and-tie model for shear strength calculation. Standards that have adopted such an approach include ACI 318-11 [14], BS 8110 [15], CEB-FIP MC 90 [16] and EN 1992-1-1 [17].

1.1 Typical failure modes

The typical modes of failure observed from the aforementioned experimental results are outlined in Figure 1.

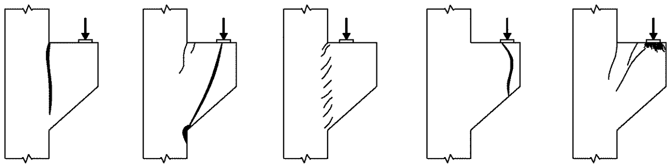

Figure 1. Typical corbel failure mechanisms.

Corbels have been shown to exhibit several failure mechanisms dependant on factors such as the shear span-to-depth ratio, loading conditions, reinforcement ratio, anchorage and bearing. A flexural tension failure arises from yielding of the main tensile reinforcement at the top of the corbel, resulting in wide cracks forming at the column-corbel interface. Diagonal splitting results from crushing of the concrete strut, usually beginning at the root of the corbel. Constrained, or sliding shear, occurs predominantly for low shear span-to-depth ratios and is characterised by a series of steep inclined cracks at the corbel-column interface. The position of the load itself serves to prevent or constrain the cracks from extending horizontally. This type of failure mechanism is best described through shear-friction theory, whereby a combination of aggregate interlock and dowel action are mobilised. Anchorage splitting occurs as a result of inadequate anchorage of reinforcement at the front of the corbel or in situations where the bearing plate is positioned too near the front edge of the corbel. Anchorage is typically achieved with a welded transverse bar or with the use of a looped anchorage. Bearing failure is characterised by localised crushing due to inadequate bearing area provisions or in situations where the bearing plate is too flexible. From these, flexural tension is the only ductile mode of failure. Although ductility is always more preferable, a brittle failure is permitted in the standards provided a compressive stress limit is satisfied.

Indeed, the behaviour of corbels is heavily dependent on adequate detailing. The experimental studies in the literature show the failure load to vary considerably for differing detailing arrangements. It is broadly accepted, and has been frequently reported experimentally, that secondary reinforcement improves the corbel load capacity, improves ductility and reduces the likelihood of premature failure. As such, the current study examines varying arrangements of corbel secondary reinforcement, particularly where discrepancies exist between modern design standards and guidance.

2 EXPERIMENTAL PROGRAMME

2.1 Test specimens

Physical testing comprised four corbel specimens with varying shear reinforcement provisions (See Figure 2). Specimen 1 was detailed with horizontal shear reinforcement comprising half of the main tensile reinforcement, in accordance with both ACI 318-11 [14] and BS 8110 [15]. The reinforcement is positioned in the upper two-thirds of the effective depth of the corbel. This arrangement is considered the traditional approach to the provision of corbel secondary reinforcement and originates from test results by Mattock *et al*. [5] who examined corbel behaviour with varying arrangements of horizontal secondary reinforcement. The arrangement is also consistent with the recommendations made by Kriz and Raths [4]. A recent finite element study by Rezaei *et al*. [18] investigated horizontal secondary reinforcement and concluded that placing the stirrups near the primary tension reinforcement increases the load capacity

Specimen 2 was also detailed with horizontal links, but they are spread more evenly throughout the effective depth as per the recommendations provided in a joint publication by the Institution of Structural Engineers and The Concrete Society [19].

Specimen 3 investigated the use of inclined links. Theoretically, inclined links should increase a joints resistance to cracking as they are orientated to take a proportion of the shear load. EN 1992-1-1 [17] highlights this and recommends their use where serviceability is a concern. Mehmel and Freitag [8] suggested that an optimised combination of horizontal and inclined reinforcement may result in a reduced overall steel demand. Contrary to this, a study carried out by Franz and Niedenhoff [6] concluded that inclined links were inefficient in comparison to horizontal links.

Specimen 4 is detailed in accordance with EN 1992-1-1 [17] which outlines that if the shear span-to-depth ratio exceeds 0.5, the shear reinforcement is to comprise half the main tensile reinforcement and to be placed vertically within the shear span. This arrangement is consistent with that of a cantilever beam with a shear span-to-depth ratio exceeding unity where flexural shear predominates. Its application to corbels, however, is not common and it does not appear to be supported by experimental results in the literature.

Nominal reinforcement is provided elsewhere. The column links are increased locally by 50% above the corbel in accordance with the recommendations of Franz and Niedenhoff [6] for columns with low axial forces.

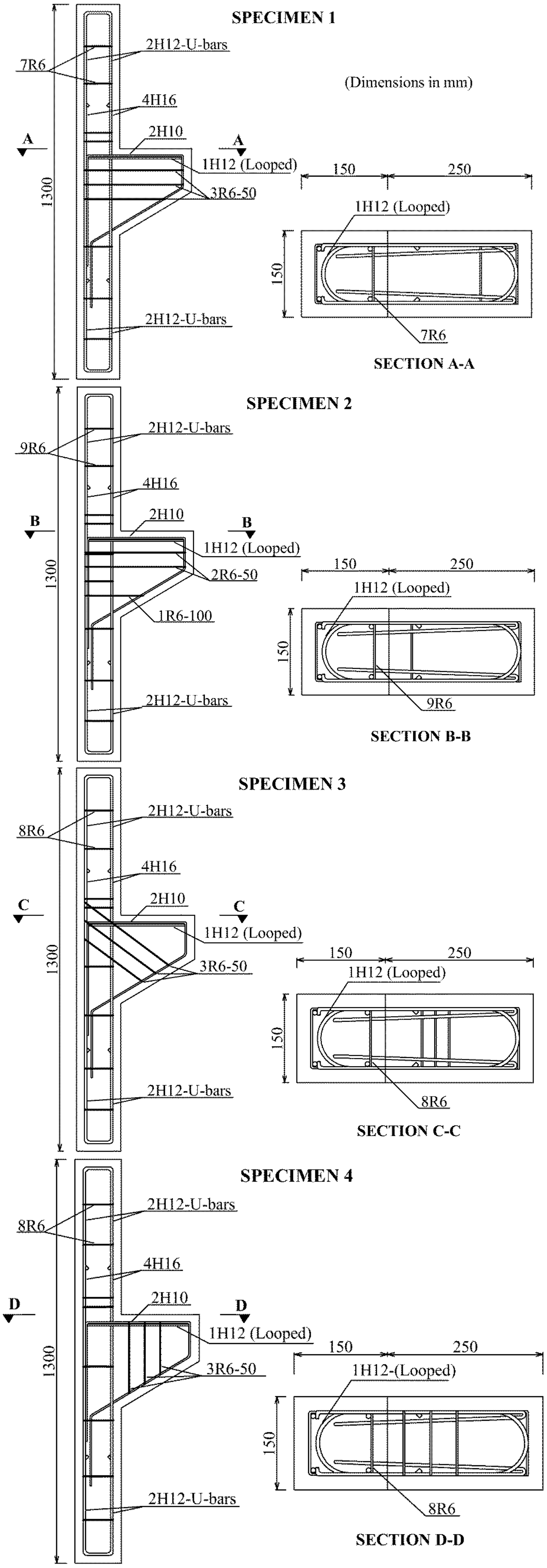

Figure 2. Specimen details.

(a) (b)

Figure 3. Reinforcement for specimen 1 (a) and specimen 3 (b).

2.2 Test procedure

Each specimen was loaded to failure by means of a hydraulic jack positioned 170 mm from the column face. The coexistent horizontal force, which may arise due to creep, shrinkage and thermal effects experienced by the supported member, has been ignored as it cannot exist in a test scenario. Concrete strength remained constant throughout. Two strain gauges were attached to the main tensile looped reinforcement of each specimen. Vertical displacements were measured at the front of the corbel and horizontal displacements were measured along the column. The test setup is shown in Figure 4.

Figure 4. Testing setup.

3 FINITE ELEMENT ANALYSIS

Finite element (FE) analysis has been used to analyse corbels with reported success. Studies by Mordini [20], Ridha [21], Rezaei *et al.* [22], Syroka *et al.* [23] and Razzak and Ali [24] show good correlation with experimental results. Indeed, with current computing capabilities and advanced constitutive concrete models, it has often been proposed that finite element analysis is a feasible and accurate alternative to physical testing.

Each test specimen was modelled and analysed using LUSAS v14.5 finite element software. 2D and 3D non-linear models were developed with the loading applied incrementally. It was found that the rigors associated with 3D models could be avoided in the case of corbels as the results were very close to those of the 2D models. This finding is consistent with that of Mordini [20] and may be attributed to the largely two-dimensional behaviour of corbels.

The concrete was represented by a non-linear plastic-damage-contact model with a capability to predict cracking, crushing, aggregate interlock and strain softening. Concrete strengths were inputted from cube test results for each specimen. The reinforcement was represented by embedded bar elements sandwiched between continuum elements with a perfect bond assumed. Initial yield and strain hardening parameters were determined from tensile tests carried out on the reinforcement. A maximum element size of 25 mm was chosen following a mesh convergence study. The finite element models are shown in Figure 5.

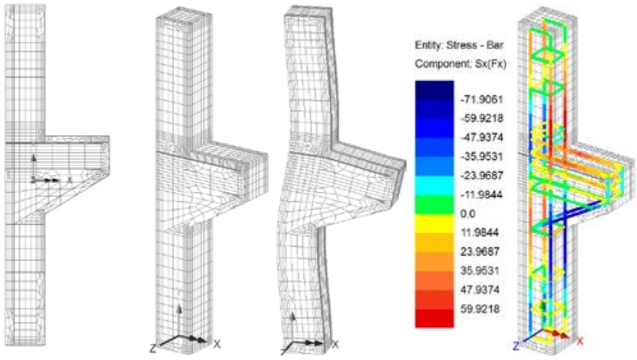

(a) (b) (c) (d)

Figure 5. Mesh discretisation for 2D model (a), 3D model (b), deformed mesh (c) and reinforcement stress contour (d).

4 RESULTS

4.1 Primary observations

Table 1 outlines results and failure criterion from the experimental and finite element study.

Table 1. Experimental and finite element results.

Specimen	1	2	3	4
Design code/ guidance	ACI 318-02 & BS 8110	IStructE & The Concrete Society	-	EN 1992-1-1
Cube strength, MPa	41.7	39.5	43.1	44.2
First crack load, kN	34 (41)	37 (31)	57 (52)	32 (26)
Failure load, kN	147 (153)	135 (141)	126 (124)	121 (118)
Failure mode	Strut crushing	Strut crushing and splitting	Strut crushing	Strut crushing

(FE results in parentheses)

The dominant failure mechanism was crushing of the concrete strut occurring at the root of the corbel (Figure 6(a)). This was consistent for all experimental specimens and finite element results. The first crack was always a flexural crack occurring at the top of the corbel, along the column joint, which propagated into the column with increasing load. As failure approached, a diagonal crack started at the root of the corbel and extended to the bearing plate. Crushing of the concrete strut followed, and in the case of specimen 2, resulted in splitting of the strut along the diagonal crack (Figure 6 (b)).

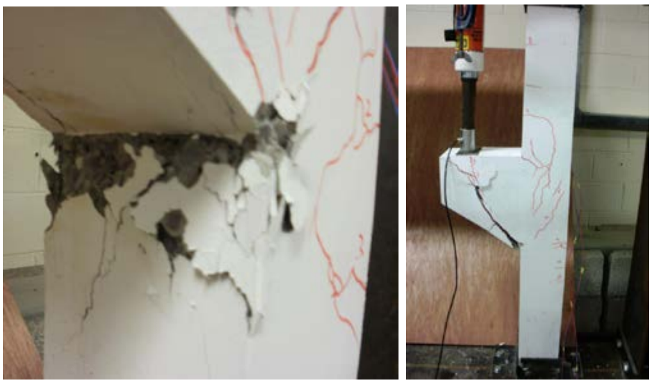

(a) (b)

Figure 6. Crushing of concrete strut for specimen 1 (a) and splitting of strut for specimen 2 (b).

The measured vertical displacements at the front of the corbel for each test specimen are compared with the non-linear FE modelling in Figure 7. Good agreement is observed in each instance.

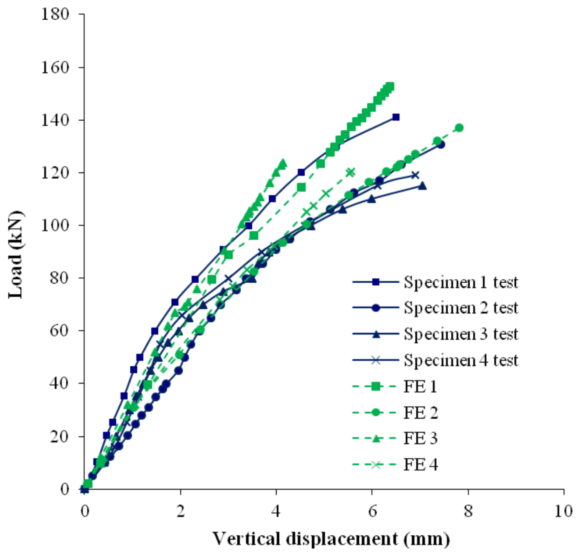

Figure 7. Comparison of measured vertical displacements with non-linear FE results.

Finite element modelling can be used effectively to verify the accuracy of strut-and-tie models by using principal stress trajectories to model the load path. The simplified strut-and-tie model used in corbel design shows good correlation with the principal stress trajectories obtained from the FE analysis shown in Figure 8. In addition, the location and extent of cracking and crushing at failure obtained from the FE analysis, given in Figure 9, show good agreement with that observed through testing (Figure 6). Flexural cracking along the column and crushing of the strut at the root of the corbel are consistent with that observed experimentally.

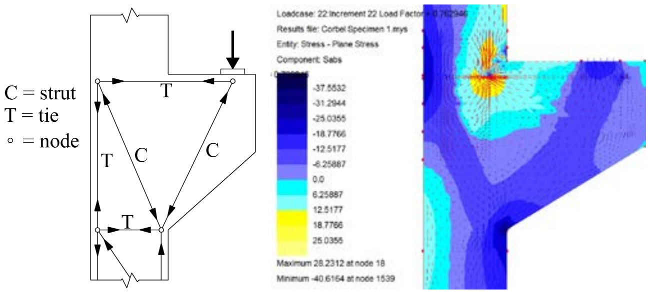

(a) (b)

Figure 8. Simplified strut-and-tie model (a) and principal stress contour from FE analysis (b).

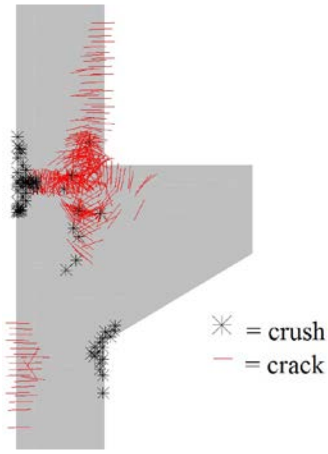

Figure 9. Predicted cracking and crushing for specimen 1 at failure from FE analysis.

4.2 *Strut capacity*

The capacity of the inclined strut, F_c, may be calculated as follows:

$$F_c = \frac{V_{Ed}}{Sin\beta} \tag{1}$$

V_{Ed} is the applied vertical force and β is the angle the inclined strut makes with the horizontal. Table 2 gives strut compressive stress limits recommended in EN 1992-1-1 [17], BS 8110 [15], FIB Bulletin 56: Model Code 2010 [25] and Schlaich and Schäfer [2].

Table 2. Strut compressive stress limits.

Design code/ guidance	Limiting compressive stress	Additional expressions
EN 1992-1-1	$0.85v'f_{cd}$	$v' = 1 - \frac{f_{ck}}{250}$; $f_{cd} = \frac{\alpha_{cc} f_{ck}}{\gamma_m}$
BS 8110	$0.67f_{cu}/\gamma_m$	-
FIB Bulletin 56	$0.75\left(\frac{30}{f_{ck}}\right)^{\frac{1}{3}} f_{cd}$	$f_{cd} = \frac{\alpha_{cc} f_{ck}}{\gamma_m}$
Schlaich and Schäfer	$0.8f_{cd}$	$f_{cd} = \frac{\alpha_{cc} f_{ck}}{\gamma_m}$

f_{ck} = concrete compressive cylinder strength
f_{cu} = concrete compressive cube strength
α_{cc} = 0.85
γ_m = 1.5 (partial safety factor for concrete)

Table 3 compares the strut capacities observed in the current study with those predicted analytically using the compressive stress limits given in Table 2.

Table 3. Experimental and analytical strut capacities.

	Strut capacity, kN			
	Specimen 1	Specimen 2	Specimen 3	Specimen 4
Experimental	186.5	171.3	159.9	153.6
Non-linear FE	194.2	178.9	157.4	149.7
EN 1992-1-1	144.0	137.7	148.2	151.0
BS 8110	192.8	182.6	199.2	204.3
FIB Bulletin 56	141.7	136.6	144.8	146.9
Schlaich and Schäfer	156.5	148.3	161.8	165.6

Strut angle, β = 52° for calculation of analytical strut capacities
$f_{ck} = 0.8 f_{cu}$ for the purpose of comparison

4.3 *Reinforcement stresses*

The stresses in the main tensile reinforcement in the top of the corbel measured experimentally are given in Figure 10. The results indicate the degree to which the sections are over-reinforced as only half the design yield stress is reached. This may be attributed to the high percentage of main tensile reinforcement positioned at the top of the corbel resulting from lapping the main tensile looped reinforcement with the compression bars.

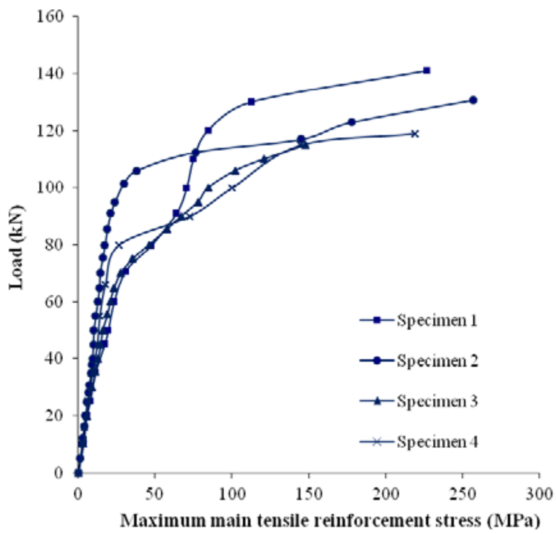

Figure 10. Maximum measured main tensile reinforcement stress.

Figure 11 presents a comparison of maximum shear reinforcement stresses for each specimen obtained from the finite element study. Surprisingly, the vertical shear reinforcement for specimen 4 was found to be in compression throughout the loading history, which may provide an indication as to why this specimen failed at the lowest applied load. The shear reinforcement for all other specimens appeared to behave in a similar fashion. The stress was relatively low until a load corresponding with significant crack development was reached, thereby increasing the stress in the reinforcement until failure occurred.

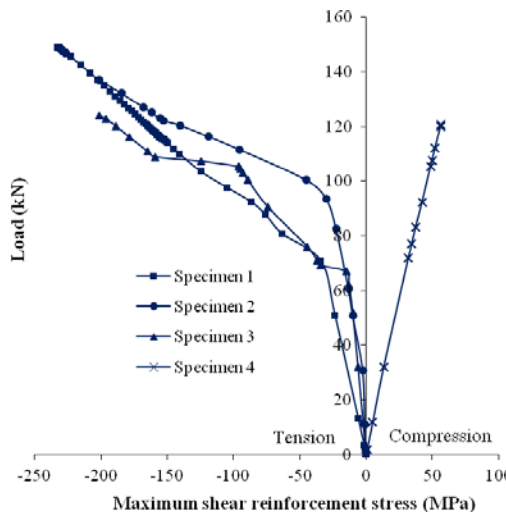

Figure 11. Maximum shear reinforcement stress from non-linear finite element models.

5 DISCUSSION

The results of the experimental and FE investigation show that horizontal shear reinforcement positioned in the upper two-thirds of the effective depth performed most efficiently. It was verified that for specimen 3, inclined links served to increase the sections resistance to cracking. The arrangement did not, however, provide a significant increase in the load capacity when compared to the specimens containing horizontal links. Testing by Franz and Niedenhoff [6] would support this finding. On testing double corbels, Franz and Niedenhoff [6] reported that corbels reinforced with horizontal links carried a 23% greater load than those reinforced with inclined links. Similar results were observed in the current study with a 16.7% and 23.4% greater load resistance obtained from the experimental and FE studies respectively. Park and Paulay [26] proposed that the inefficiency is a result of considerable dowel forces acting on the inclined links. This arises due to the corbel rotating about the compression root, with the resulting displacements at the top of the corbel being approximately horizontal. This is undesirable as, for a bar in tension, the tensile strength is reduced when also subject to dowel action.

Vertical links performed poorly in both the experimental and FE studies. It was found through finite element modelling that the links were in compression throughout. As such, the vertical secondary reinforcement serves only as additional compression reinforcement. On studying the many corbel failure mechanisms observed in the literature, Park and Paulay [26] concluded that vertical links, intended for shear resistance, would be ineffective in all situations. Kriz and Raths [4] tested 195 corbel specimens and concluded that horizontal links should be used rather than vertical links due to the steep inclination of the diagonal cracks. It has also been recognised in the literature that horizontal links serve to restrain the compression bars at the front of the corbel from buckling. Vertical links, as such, would not provide for the required restraint. ACI 318-11 [14] stipulate that horizontal links are necessary in order to prevent a premature diagonal tension failure.

It would appear that the EN 1992-1-1 [17] recommendations regarding vertical links originates from the study by Mattock *et al.* [5] and subsequent ACI code revisions suggested by MacGregor and Hawkins [27]. The design approach given in the suggested revisions, which is based upon shear-friction theory, indicate that the efficiency of horizontal shear reinforcement decreases when the shear span-to-depth ratio exceeds 0.5, while the efficiency of vertical reinforcement increases beyond this limit. Accordingly, it was recommended that horizontal reinforcement be used with caution for shear span-to-depth ratios greater than 0.5.

Considering the shear-friction approach where a constrained/sliding shear failure is likely, vertical links do not contribute additional reinforcement across the critical section at the column-corbel interface. Therefore, it does not contribute to increasing the resistance due to dowel action. Considering the strut-and-tie approach, reinforcement will behave most efficiently if it is located approximately parallel to tension stress trajectories. For corbels, the tension stress trajectories are horizontal (Figure 8). Thus, the provision of vertical links would be ineffective in this regard.

6 CONCLUSIONS

The experimental and finite element results revealed that the ultimate load resistance of reinforced concrete corbels is significantly affected by the orientation of secondary/shear reinforcement. Differences in failure loads up to 21.5% and 29.7% were obtained from the experimental and finite element study respectively. The observed failure mechanism was crushing of the concrete strut, occurring at the root of the corbel, and was consistent for all specimens. The non-linear finite element study shows excellent correlation with the experimental results.

The use of looped bar anchorages resulted in an over-reinforced section, and consequently, a brittle failure developed. In pursuit of a ductile failure with yielding of the main tensile reinforcement, the use of a welded transverse bar anchorage would result in a more balanced section.

Detailing of horizontal links, positioned in the upper two-thirds of the effective depth, in accordance with ACI 318-11 [14] and BS 8110 [15] is recommended as it behaved most efficiently. Inclined links did not perform as efficiently as horizontal links but did provide an enhanced resistance to cracking.

Although EN 1992-1-1 [17] provides comprehensive guidance on strut-and-tie modelling, detailing of vertical links in accordance with this code is not recommended as failure occurred at the lowest applied load. It was established from the finite element study that the links were in compression and, as such, only served as additional compression reinforcement within the shear span.

REFERENCES

[1] Hagberg, T. (1983), ‘Design of Concrete Brackets: On the Application of the Truss Analogy’, *ACI Journal*, American Concrete Institute, Vol. 80, No. 1, pp. 3-12.

[2] Schlaich, J., and Schäfer, K., (1991), ‘Design and detailing of structural concrete using strut-and-tie models’, *The Structural Engineer*, Institution of Structural Engineers, Vol. 75, No. 4, pp. 53-57.

[3] Schlaich, J., Schäfer, K., and Jennewein, M., (1987), ‘Toward a consistent design of structural concrete’, *PCI Journal*, Precast Prestressed Concrete Institute, Vol. 32, No. 3, pp. 74-150.

[4] Kriz, L., and Raths, C. (1965), ‘Connections in Precast Concrete Structures-Strength of Corbels’, *PCI Journal*, Precast Prestressed Concrete Institute, Vol. 10, No. 1, pp. 16-61.

[5] Mattock, A.H., Chen, K.C., and Swoongswang, K., (1976), ‘The Behaviour of Reinforced Concrete Corbels’, *PCI Journal*, Precast Prestressed Concrete Institute, Vol. 21, No. 3, pp. 18-42.

[6] Franz, G., and Niedenhoff, H., (1963), *The Reinforcement of Brackets and Short Deep Beams*, Cement and Concrete Association, Library Translation No. 114, London.

[7] Mehmel, A., and Becker, G. (1965), ‘Schubbemessung des Kutzen Kragarmes’, *Der Bauingenieur*, Vol. 40, No. 6, pp. 224-231.

[8] Mehmel, A., and Freitag, W. (1967), ‘Tragfähigkeitsversuche an Stahlbetonkollsolen’, *Der Bauingenieur*, Vol. 42, No. 10, pp. 362-369.

[9] ACI Committee 318, (1995), Building Code Requirements for Structural Concrete (ACI 318-95) and Commentary (ACI 318R-95), American Concrete Institute, Farmington Hills, Michigan, USA.

[10] Mast, R. F. (1968), ‘Auxiliary Reinforcement in Concrete Connections’, *Proceedings of the American Society of Civil Engineers*, Vol. 94, No. ST6, pp. 1485-1501.

[11] Yong, Y.K., and Balaguru, P., (1994), ‘Behaviour of reinforced high-strength-concrete corbels’, *Journal of Structural Engineering*, ASCE, Vol. 120, No. 4, pp. 1182-1201.

[12] Hwang, S.J., Lu, W.Y., and Lee, H.J., (2000), ‘Shear strength prediction for reinforced concrete corbels, *ACI Structural Journal*, American Concrete Institute, Vol. 97, No. 4, pp. 543-552.

[13] Ali, M.A. and White, R.N., (2001), ‘Consideration of compression stress bulging and strut degradation in truss modeling of ductile and brittle corbels’, *Engineering Structures*, Elsevier Press, Vol. 23, pp. 240–249.

[14] ACI Committee 318, (2011), Building Code Requirements for Structural Concrete (ACI 318-11) and Commentary (ACI 318R-11), American Concrete Institute, Farmington Hills, Michigan, USA.

[15] BS 8110 (1997), Structural Use of Concrete, Part 2, Code of Practice for Design and Construction, London, British Standards Institution.

[16] CEB-FIP, (1990), Comité Euro-International du Béton, *CEB-FIP Model Code 1990*, Thomas Telford, Lausanne, Switzerland.

[17] EN 1992-1-1 (2004), Eurocode 2: Design of concrete structures – Part 1-1: General rules and rules for buildings, CEN, Brussels, Belgium.

[18] Rezaei, M., Osman, S. A., and Shanmugam, N. E. (2012), ‘Secondary Reinforcement in Concrete Corbel’, *Applied Mechanics and Materials*, Vol. 147, pp. 24-27.

[19] Institution of Structural Engineers and The Concrete Society, (2006), *Standard Method of Detailing Structural Concrete: A manual for best practice, 3rd ed.*, IStructE, London.

[20] Mordini, A., (2006), *Three-Dimensional Numerical Modelling of Reinforced Concrete Behaviour*, PhD Thesis, University of Parma, 228pp.

[21] Ridha, M.S., (2008), ‘Nonlinear Finite Element Analysis of High Strength Fiber Reinforced Concrete Corbels’, *Eng. & Tech.*, Vol. 28, No. 1, pp. 1-15.

[22] Rezaei, M., Osman, S.A., and Shanmugam, N.E., (2010), ‘Finite Element Analysis of Reinforced Concrete Corbels’, *Proc. 3rd International Conference on Engineering Mechanics, Structures, Engineering Geology*, WSEAS Press, pp. 448-452.

[23] Syroka, E., Bobiński, J., and Tejchman, J., (2011), ‘FE analysis of reinforced concrete corbels with enhanced continuum models’, *Finite Elements in Analysis and Design*, Elsevier Press, Vol. 47, pp. 1066-1078.

[24] Razzak, A. A., and Ali, M. A. (2011), ‘Influence of cracked concrete models on the nonlinear analysis of High Strength Steel Fibre Reinforced Concrete corbels’, *Composite Structures*, Elsevier Press, Vol. 93, pp. 2277-2287.

[25] Fédération Internationale du Béton (FIB), *FIB Bulletin 56 Model Code 2010: Volume 2 First Complete Draft*, Lausanne, Switzerland, 2010, 311 pp.

[26] Park, R., and Paulay, T., *Reinforced Concrete Structures*, John Wiley & Sons Inc., 1975, pp 614.

[27] MacGregor, J. G., and Hawkins, N. M. (1977), ‘Suggested Revisions to ACI Building Code Clauses Dealing with Shear Friction and Shear in Deep Beams and Corbels’, *ACI Journal*, American Concrete Institute, November 1977, pp. 537-545.

Generation of a building typology for risk assessment due to urban tunnelling

Julie A. Clarke[1], Debra F. Laefer[1]
[1]School of Civil, Structural and Environmental Engineering, University College Dublin, Belfield, Dublin 4, Ireland.
email: julie.clarke.1@ucdconnect.ie, debra.laefer@ucd.ie

ABSTRACT: Major underground infrastructure projects are often located beneath dense urban environments in an effort to relieve congested areas. The effects of urban tunnelling works can impinge on hundreds, if not thousands of structures, many of which are historically significant. Tunnel-induced ground movements can result in significant building damage and, therefore, require an accurate risk assessment of the existing built heritage and the selection of appropriate preventative measures. Damage prediction techniques extend from traditional empirical and analytical methods to modern computational modelling techniques. A common requirement for many damage assessment methodologies is the development of a building typology. Such typologies can provide critical information where measured drawings, particularly of structural elements (e.g. floor and wall thickness), are not otherwise available. This study begins to establish a building typology for a historic area of Dublin's city centre for which an underground railway system has been planned.

KEY WORDS: Tunnelling; Building Damage; Risk Assessment; Building Typology.

1 INTRODUCTION

A rapid railway system, Metro North, has been granted planning permission in Dublin, Ireland [1]. The initial 5.5km is routed beneath a portion of Dublin's city centre, which currently holds nomination for UNESCO World Heritage Status (Figure 1) [2].

Figure 1. Study area.

This paper examines the study area outlined in Figure 1 with a view to categorically determining the nature of the built environment to assist in damage prediction from tunnel subsidence. This region contains a high number of historic buildings, with the majority of this region forming an Architectural Conservation Area [3]. Since damage prediction techniques often focus on individual buildings, the development of a building typology is commonly employed as part of risk assessments for large projects of this nature. This can provide engineers with a basis upon which to make design assumptions where individual building information is unavailable. Such an effort is initiated in this paper; the importance of which is significant as measured drawings are not available for the majority of the structures and those that are available more often focus on architectural elements than items of structural concern.

2 BACKGROUND

2.1 *Damage Prediction Methods*

Risk assessments for structures subject to adjacent tunnelling works employ a variety of methodologies. Procedures range from empirical methods based on observed limits to modern numerical methods, which can fully account for the soil-structure interaction. However, what is common to all methodologies is the need for building information.

Traditionally, prediction methods for buildings subject to tunnelling works, were estimated based on empirical methods relating to ground settlements and according to a greenfield scenario, whereby the presence of the building is neglected. Peck [4] idealised the resulting settlement trough at ground level according to a Gaussian distribution. This profile was later extended to the case of twin tunnels by New and O'Reilly [5]. Damage limits were subsequently employed, such those proposed by Skempton and MacDonald [6] and Rankin [7] which were based on building dimensions and tunnel layout.

The concept of critical tensile strain, whereby the onset of visible cracking for a building was associated with a value of tensile strain, was introduced by Polshin and Tokar [8] thereby incorporating building material properties into the discussion. Burland and Wroth [9] employed this concept in their analytical methodology where the building was idealised as a deep, elastic, simply-supported beam and the critical tensile strain calculated. This concept was later extended by Boscardin and Cording [10] to account for the effects of horizontal strain.

With the recent advancements in computing technology, numerical modelling of the problem has become increasingly popular. Whilst both empirical and analytical methods tend to examine the ground and the building independently, the use of computer modelling enables the soil-structure interaction to be addressed. A study by Potts and Addenbrooke [11] revealed a reduction in greenfield settlements due to building stiffness through the use of two-dimensional (2D) finite element modelling of the soil and adjacent building.

2.2 Dublin's Built Environment

A variety of literature is available relating to Dublin's built heritage, but that related to the vernacular structures that comprise the bulk of Dublin’s architectural fabric is highly limited. For example, in Casey’s [12] seminal work on Georgian Dublin, the greater portion of this text describes public buildings, including religious buildings, monuments and sculpture. Only limited sections are included on traditional domestic architecture, and that which is included relates mainly to the larger castles and townhouses.

The more common terraced house consisting of brickwork of Georgian Dublin, is described in limited detail [12] as being built in large numbers from the 1720s onwards. Houses of the C18th generally consisted of three of four storeys over a basement. For some structures Casey provides details of individual street buildings including construction dates, building materials, and façade detailing, but little else.

There are a few other resources. Publications by the Dublin Civic Trust [13,14] relating to specific street addresses provide further building information including: year of construction; number of storeys; building material; façade ornamentation; repair details; and interior details. Furthermore, databases such as Historic Ireland's Building Environment and Road Network Inventory Access (HIBERNIA) [15] provide a means for gathering large amounts of data relating to Ireland's built environment. While there does exist a National Inventory of Architectural Heritage (NIAH) [16] devoted to identifying and recording the architectural heritage of Ireland from 1700 until present, this has yet to be conducted for the region of Dublin.

Although these sources provide a framework for the creation of a building typology, most lack relevant structural information. Dublin City Council's website contains measured drawings for buildings for which planning permission had recently been sought [17]. However, these documents are limited to requests which were sought since 2005 and are inconsistent in both their quality and the level of detail provided.

3 SCOPE AND METHODOLOGY

Thus, to date the resources have not been readily available to generate building typology. This study attempted to overcome this through an extensive field investigation. Within the proposed study area, 449 individual buildings were identified within Figure 1. Data collection involved a combination of fieldwork, image collection, and archival investigation. Physical building attributes were primarily sought.

Measured drawings of some type were available for 27.6% of the dataset. These mainly provided building heights, widths, lengths and number of basement levels. Where measured drawings were not available, estimates were made based upon fieldwork. This involved the creation of an image collection, whereby the front façade of each building was photographed. Not only did this provide a means for visually analysing each of the buildings in the study area, it also acted as a historical record.

A range of building attributes were sought in order to generate the building typology. Since the purpose of the typology in this instance is for risk assessment due to adjacent construction works, physical building properties were primarily sought. Specifically, risk assessments in the case of ground movements tend to examine structural building properties relating to material behaviour, building dimensions, and percentage of openings. Architectural properties were also examined, which included year of construction, architectural details, window shapes and architectural classification. Furthermore, specifically relating to the proposed project, building location and respective orientation in relation to the tunnel were sought.

4 RESULTS

This section will present a classification of the 449 buildings examined according to the main physical and architectural findings. Items relevant to general building typologies are introduced first, while more project specific items are presented subsequently.

4.1 Year of Construction

Dates of construction were sought since this information can often serve as an indicator of building composition and its attendant structural system. The year of construction was obtained for 42% of the buildings. The majority (37% or 70 buildings) are shown to have been built in the first half of the C20th (Figure 2). Significant proportions were built in the latter half of the C18th (17%) as well as the latter half of the C19th (23%).

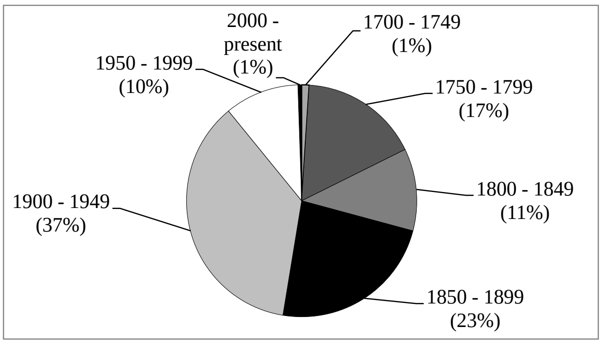

Figure 2. Year of construction.

4.2 Building Material

Eight main exterior building finishes were identified (Figure 3). Figure 4 shows their distribution within the study area. Overall, 91% of the study area consists of masonry. A further 4% consist of a rendered façade. However, judging by the configuration of these buildings, it would seem reasonable to assume that these buildings also consist of masonry. Brickwork was the predominant building material of Dublin architecture throughout the C18th [12] and the majority (67%) of buildings in the study area are exclusively of brickwork.

Heavier cut ashlar and stone appears to dominate more prominent buildings, often ecclesiastical or public in nature.

Figure 3. Sample images of exterior building finishes.

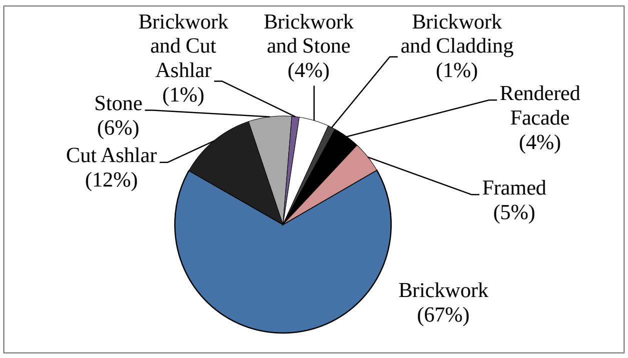

Figure 4. Exterior building finishes.

4.3 *Number of Building Storeys*

Four-storey structures predominated, typifying 62% of the buildings (Figure 5). These mainly consisted of terraced masonry buildings which, in the past, formed the bulk of Dublin's domestic architecture. Nowadays however, the majority of these buildings are commercial spaces, with shop fronts at the ground level.

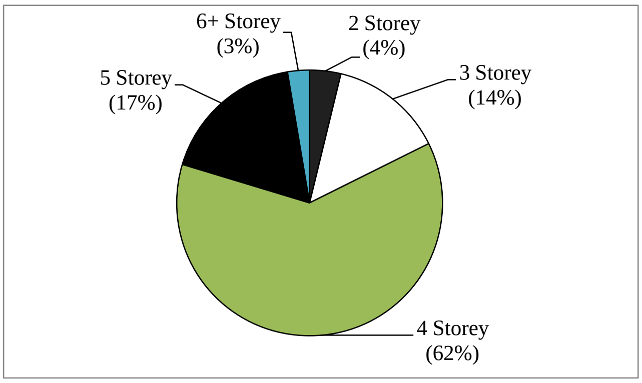

Figure 5. Number of storeys.

4.4 *Building Dimensions*

Figure 6 illustrates the distribution of building dimensions for the full study set. The typical building is 11-15m in height, less than 5m wide, and 6-10m long. Thus, slender buildings with relatively small footprints predominate the study area.

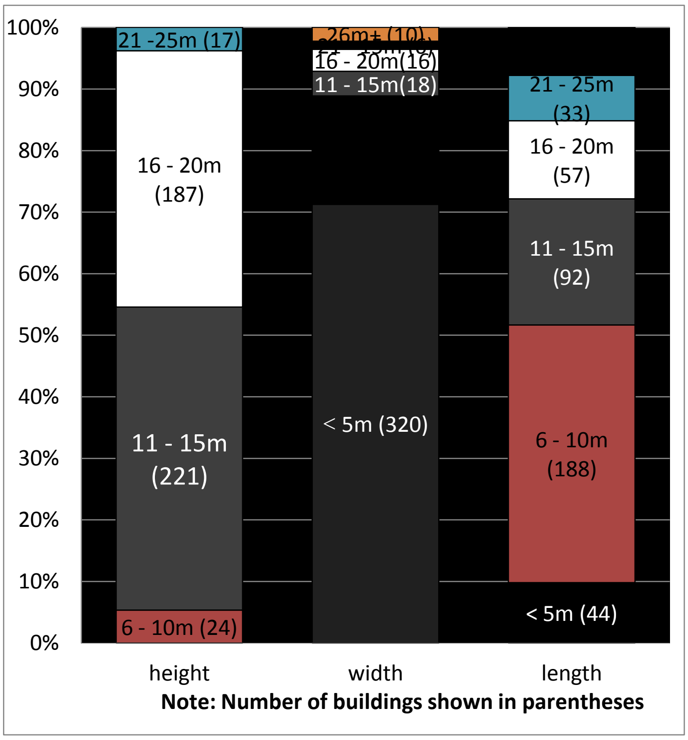

Figure 6. Building dimensions

4.5 *Floor and Wall Thickness*

Floor thickness information was available for 11.4% of the buildings and wall thickness for 10.2% of them. The predominant floor thickness varied between 300 and 349mm, while the most prevalent wall thickness exceeded 400mm (Figure 7).

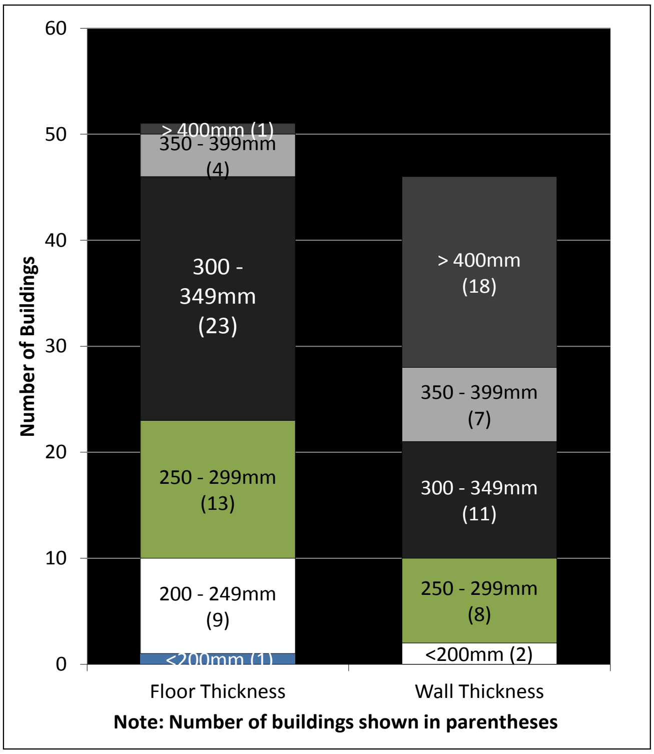

Figure 7. Floor and wall thicknesses.

4.6 Opening Ratio

Many studies have examined the influence of openings in walls since this may control the overall building stiffness. Opening Ratio (OR) may be defined as the ratio of the total area of openings (including windows and doors) to the total possible wall area of solid wall (see Equation 1).

$$OR = \frac{Area_{openings}}{Area_{wall}} \tag{1}$$

Figure 8 reveals the distribution for the full study area where opening ratios of 0.3 (26% or 115 buildings) and 0.4 (22% or 100 buildings) predominate for the front façades; notably most of the buildings have at least one party wall and are generally inaccessible from the back.

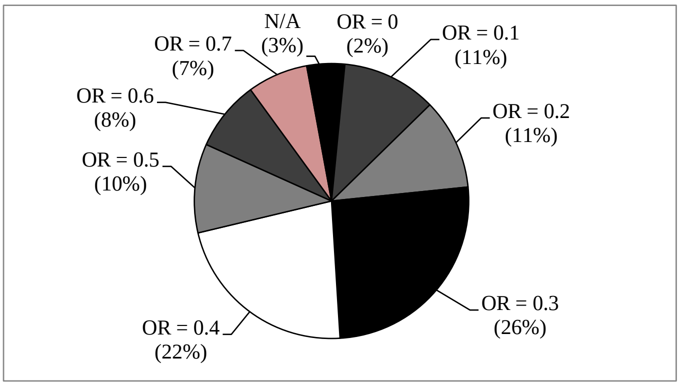

Figure 8. Opening ratio.

4.7 Basement Levels

Information regarding basement levels was available for 77 buildings, just 17% of the study area. Of these, 81.8% had a single basement level, 10.4% had a double basement, and the remaining 7.8% had no basement.

4.8 Foundation Type

Foundation type was identified for just 17 buildings (only 3.8% of the study area). Of these 67% had raft foundations, 25% strip foundations, and the remaining 8% piled foundations. The identification of foundation type is important, particularly with regard to building response to ground movement, as is the case for tunnelling works. In general, buildings founded on deep foundations are more likely to undergo deformation since the bearing level of the foundation elements is closer to the tunnel's crown. However, the extent of deformation depends on the building's location with respect to the tunnel [18].

4.9 Architectural Detailing

Significant ornamentation was identified for 22% of the buildings (Figure 9a). Minor ornamentation was noted for 12% (Figure 9b), and the remaining 66% possessed no ornamentation (Figure 9c).

a) Significant b) Minor c) None

Figure 9. Example images: architectural detailing.

Specific building details were also noted which were found to be characteristic of the local architecture. A parapet, defined as 'a low wall…placed to protect the spot where there is a sudden drop'[19] was identified at roof level for 29% of the study area (131 buildings). A fan window located above the front doorway, as illustrated in Figure 10, was identified for 10% of the study area (46 buildings). The remainder consisted solely of a rectangular doorway.

Figure 10. Fan window.

4.10 Window Shape

The typical windows for most of the buildings (81% or 364 buildings) were rectangular (Figure 11a). Another 11% (50 buildings) contained arch-shaped openings (Figure 11b) and just 1% (2 buildings) included wedge-shaped openings (Figure 11c). For the remaining 7% (33 buildings), window shape was not relevant for the following reasons: the building façade contained no window openings; the building consisted of window decorative structures where opening shape is difficult to determine (Figure 12); or the building consisted of a framed structure.

a) Rectangular b) Arch c) Wedge

Figure 11. Window shape.

Figure 12. Window decorative structure.

4.11 Architectural Significance

Dublin City Council (DCC) classifies 43% of the study area (193 buildings) as protected structures [20] The study area is also classified by DCC according to land usage [3] Four distinct zones were designated: 1) residential with mixed use; 2) commercial, retail, business use; 3) educational, institutional, community, civic use; 4) car parks. The distribution of buildings in the study area is illustrated in Figure 13, where the vast majority of buildings (90%) are now commercial.

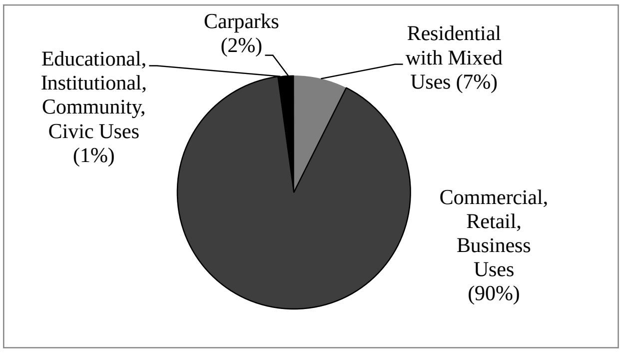

Figure 13. Land usage.

4.12 Building Orientation and Respective Location

Building orientation and location do not generally form part of traditional building typologies. However, since this purpose of this building typology is for risk assessment for tunnelling works, consideration of a building's orientation and location relative to the tunnel is relevant.

Buildings that have their front façade lying approximately parallel to the tunnel axis (Figure 14, location A) account for 52% of the study area (233 buildings). The remaining 48% of the study area (216 buildings) lie with their front façade perpendicular to the tunnel axis (Figure 14, location B). The latter orientation is generally considered more vulnerable, as will be described below.

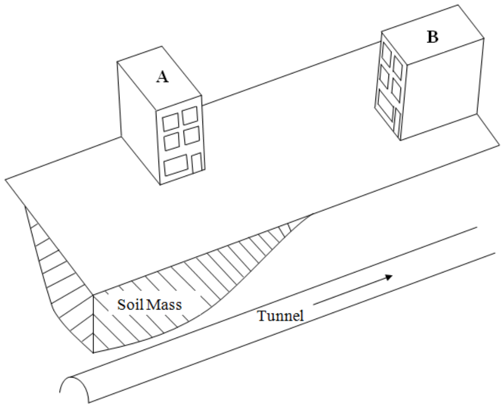

Figure 14. Building orientation.

Tunnel-induced ground movements result in a variety of modes of building movement. In general, buildings subject to the hogging mode are more susceptible to damage.[21] Particularly for masonry structures, this is the case due to their low tensile capacity. The proposed project examined as part of this study is for twin tunnels. Since narrow structures are primarily of interest as part of this study, four main building locations were examined, as illustrated in Figure 15.

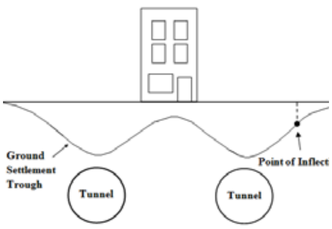

a) Building located between tunnels

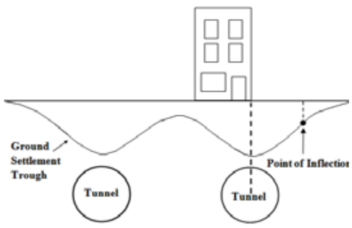

b) Building located between tunnels with tunnel axis at edge of building - *sagging mode*

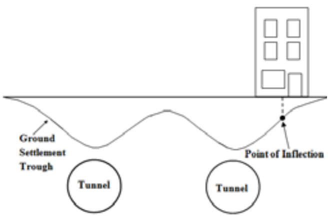

c) Inflection point at centre of building

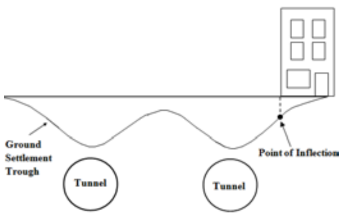

d) Inflection point at edge of building - *hogging mode*

Figure 15. Building Location within Settlement Trough.

For the buildings located greater than 30m away from the nearest tunnel (54.8% of study area), settlement effects are assumed to be negligible since the generated settlement trough at ground level generally does not exceed a 30m distance from the tunnel axis, as derived from the Environmental Impact Statement.[22] For the remaining 45.2% of the study area, the distribution of locations is illustrated in Figure 16.

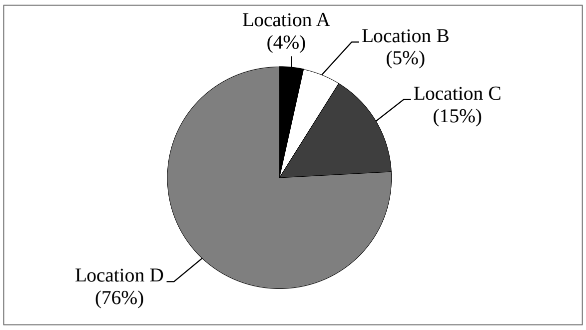

Figure 16. Building Location.

The majority of these buildings (154 buildings) are shown to be positioned in the hogging mode (location D). A significant number is also shown to be positioned in location C (31 buildings). These building locations are arguably the most vulnerable, particularly for masonry structures whose material properties cannot withstand tensile forces. For those positioned in either location C or D, 59% (109 buildings) are placed in orientation A (see Figure 14) while 41% (76 buildings) are situated in the more vulnerable orientation B.

From the above results, it would appear that the most common building for the study area is a four storey brickwork structure between 11 - 15m in height, roughly 5m in width, and between 6 and 10m in length. It most likely consists of a single basement level, rectangular window openings with an opening ratio of 0.3 - 0.4, and no architectural detailing.

5 CONCLUSIONS

This study has generated a building typology for a prestigious area of Dublin's City Centre for which the first portion of an underground railway system has been planned. The majority of structures are terraced masonry dating from Dublin's Georgian period (1720-1840), as well as buildings from later in the C19th.

Four-storey slender structures predominate, many with a single basement level. Architectural detailing is shown to be limited to the minority of the buildings, even though almost half are protected structures. In the past, the majority of these buildings formed the bulk of Dublin's domestic architecture. However, today 90% have commercial usage.

Specifically relating to the proposed tunnelled project for this region, almost equal proportions are situated parallel and perpendicular to the direction of the tunnel's axis. Furthermore, over half the study area is situated beyond the influence of the resulting settlement trough. Meanwhile, for those within this region the hogging mode of building deformation is shown to predominate.

This study provides a solid basis for risk assessment of a large number of buildings to be subjected to major infrastructure works. This process forms an important part of urban projects of this nature, as it contributes to the prevention of damage being caused to national heritage, as well as ensuring costs due to damage payouts are minimized.

ACKNOWLEDGMENTS

The authors would like to acknowledge the funding received from the Irish Research Council for Science, Engineering and Technology (IRCSET). The original data set was collected as part of Science Foundation Ireland Grant 05/PICA/I830 GUILD: Generating Urban Infrastructure from LiDAR Data.

REFERENCES

[1] Transport 21, (2011), <http://www.transport21.ie/Projects/Metro_-_Luas/Metro_North.html> (Accessed14th March 2012).

[2] UNESCO, (2010), *The Historic City of Dublin.* <http://whc.unesco.org/en/tentativelists/5523/> (Accessed 14th March 2012).

[3] Railway Procurement Agency, (2008),<http://www.dublinmetronorth.i> (Accessed 7th February 2009).

[4] Peck, P. B. (1969), 'Deep excavations and tunnelling in soft ground', *Proceedings of 7th International Conference on Soil Mechanics and Foundation Engineering,* Mexico City, 225 - 290.

[5] New, B. M. and O'Reilly, M. P. (1991), 'Tunnelling induced ground movements; predicting their magnitude and effects', *Proceedings of the Institution of Civil Engineers,* Geotechnical Engineering, v. 118, no. 1, 25 - 46.

[6] Skempton, A. W. and MacDonald, D. H. (1956), 'The allowable settlements of buildings', *ICE Proceedings, Engineering Divisions (05432-2767),* 5(6), 727.

[7] Rankin, W. J. (1988), 'Ground movements resulting from urban tunnelling: predictions and effects', *Geological Society, London, Engineering Geology Special Publications,* v.5, 79 - 92.

[8] Polshin, D. E. and Tokar, R. A. (1957), 'Maximum allowable non-uniform settlement of structures', *Fourth International Conference on Soil Mechanics and Foundation Engineering,* 402 - 405.

[9] Burland, J. B. and Wroth, C. P. (1975), 'Settlement of buildings and associated damage', *Proceedings of Conference on Settlement of Structures,* Cambridge, 611 - 654.

[10] Boscardin, M. D. and Cording, E. J. (1989), 'Building response to excavation induced settlement', *Journal of Geotechnical Engineering, ASCE,* v. 115, no. 1, 1 - 21.

[11] Potts, D. M. and Addenbrooke, T. I. (1997), 'A structure's influence on tunnelling-induced ground movements', *Proceedings of the Institution of Civil Engineers, Geotechnical Engineering,* v. 125, no. 2, 109 - 125.

[12] Casey, C. (2005). *The Buildings of Ireland: Dublin.* Yale University Press, New Haven CT.

[13] Craig, J. (1999). *South William Street: a study of the past, a vision for the future.* Dublin: The Dublin Civic Trust.

[14] Usher, R. (2008). *Dawson Street, Molesworth Street & Kildare Street.* Dublin: The Dublin Civic Trust.

[15] Historic Ireland's Built Environment and Road Network Inventories Access (HIBERNIA). (2008), <http://www.ucd.ie/hibernia/> (accessed November 2010).

[16] National Inventory of Architectural Heritage (NIAH). (2008), <http://www.buildingsofireland.ie> (accessed March 1, 2012).

[17] Dublin City Council, (2012). <http://www.dublincity.ie/planning/planningsearch/pages/planningsearch.aspx> (accessed June 2008).

[18] Leca, E. and New, B. (2007), 'Settlements induced by tunneling in soft ground', *Tunnelling and Underground Space Technology*, 22 (2007) 119 - 149.

[19] Fleming, J., Honour, H. and Pevsner N. (1972). *The Penguin Dictionary of Architecture.* Harmondsworth: Penguin, 1972.

[20] Dublin City Council, (2010), < http://www.dublincity.ie/Planning/HeritageConservation/Conservation/ProtectedStructures> (Assessed January 2011).

[21] Houlsby, G. T., Burd. H. J., and Augarde, C. E. (1999) 'Analysis of tunnel-induced settlement damage to surface structures', *Proceedings of the 12th European Conference on Soil Mechanics and Geotechnical Engineering,* Amsterdam, 7-10th June, Balkema: Rotterdam, Vol. 1, 147 -152.

[22] Dublin Metro North, (2008). *Environmental Impact Statement.* Railway Procurement Agency, v.2 Book 7.

Design of ground anchors to Eurocode – possible future changes

E R Farrell[1]
[1]AGL Consulting and Department of Civil, Structural and Environmental Engineering, Trinity College, Dublin, Ireland
email: eric.farrell @agl.ie

ABSTRACT: Section 8 of EN1997-1:2004, which covers the geotechnical design of anchors, is currently being revised to cover deficiencies in the current document. Evolution Group 1 of SC7, which has been tasked with this revision, has reviewed current design practice and is drafting revisions which will make anchor design more transparent and more consistent with the limit state design philosophy of Eurocode. This paper discusses some of the likely changes that may be introduced in such a draft and identifies areas which should be researched in order to enable Ireland to select testing methods and correlation and partial factors appropriate to Ireland.

KEY WORDS: anchor, Eurocode.

1 INTRODUCTION

The development of a procedure for the limit state design of anchors within the Eurocode system is proving to be more difficult than envisaged. These difficulties arise from a combination of philosophical and practical issues relating to the limit state design and to the way that the design of anchors has developed in the different countries over the years. This paper includes some topics and issues raised in the very healthy debate in the Evolution Group 1 (EG1) of TC250/SC7 which has been tasked with developing this section of Eurocode (EC7). The members of this group are listed in the acknowledgements and whilst the views expressed in the paper are solely those of the author, the experience and knowledge of the members was a valuable source of information.

This paper will discuss the design of grouted anchors for embedded walls only. The construction of these anchors is covered by the execution standard EN 1537 'Execution of special geotechnical work – Ground anchors' [1]. Tests are important in the design and verification of the construction of anchors and the testing standard for anchors is currently being prepared by TC 341. A draft of this standard, which is designated ISO/DIS 22477-5:2004 [2] is currently available. There is a debate as to whether passive/non-prestressed anchors have to be subjected to acceptance tests (see section 4 for a description of acceptance tests), which will be of relevance to geotechnical engineers in Ireland, however this will not be discussed in this paper.

The terminology used in this paper is that currently adopted in the drafts within EG1, however these may change in the final documentation. For example, there is a question as to whether the force F_{Serv} (which is defined later in the paper) will be accepted when the drafts go beyond this group stage.

The design of anchors is covered in Section 8 of IS EN1997-1:2004[3] and EG1 is tasked with revising the current Section. Revisions will be required to allow the current practices of different countries to be adapted to any changes. Reference will be made to the way some countries handle particular issues.

2 DEFINITION OF AN GROUND ANCHOR

The definition of a ground anchor used in this paper is a 'Structural element consisting of an anchor head, a tendon with a free length and a bonded length designed to transmit a tensile force to a load resisting formation of soil or rock'. Terms such as anchorage or anchor system are not used. The bonded length will be the term used for the length of tendon over which the resistance is developed.

The significant features that distinguish an anchor from tension piles are the tendon free length and the fact that the ground/rock resistance is achieved remote from the anchor head. The tendon free length means it can be a) prestressed to minimise deformations in the structure and b) also that it can easily be load tested using a jack thus avoiding the need for expensive reaction frames and kentledge/reaction anchors. These tests can assess not only the load carrying capacity of the anchor but also that the bonded length is correctly located by comparing the measured extension under load with that calculated using the designed free length.

Other important features which have to be considered in the design of anchors are the relatively high loads taken by an anchor, the strain energy stored in a stressed and prestressed anchor and the creep experienced by an anchor under the relatively localised high loads that can be imposed in the ground around the bonded length.

3 MEASURING THE ULS ($R_{ULS,m}$) AND SLS ($R_{SLS,\ m}$) RESISTANCE OF AN ANCHOR

Two types of anchor resistance (capacity) are referred to in this paper (The values measured in an anchor tests are designated $R_{ULS.m}$ and $R_{SLS,m.}$):-

R_{ULS} = ultimate resistance of an anchor

R_{SLS} = serviceability resistance of an anchor.

The interpretation of anchor capacity from load tests is based on the relationship between load and creep rate rather than the load displacement relationship which is used for piles. The creep rate is determined from the displacement/time measurements where the load is maintained or from the loss of load/time measurements where the displacement of the anchor head is held constant.

Three test methods are recognised in the current draft of ISO/DIS 22477-5[2] and are referred to as Methods 1 to 3. An indication of the measurements to be made in anchor tests and the type of loading can be got from those required for Investigation tests, which can be taken to failure, and which are summarised on Table 1.

Table 1 Summary of anchor test methods 1 to 3 for investigation tests.

	Method 1	Method 2	Method 3
Type of loading	Cycle loading	Cycle loading	In steps
Rest periods	Maintained loads	Maintained deflection	Maintained load
Measurements	Tendon head displacement vs applied load at end of each cycle	Load-loss vs time at the highest load of each cycle	Anchor head displacement vs anchor load at the beginning and end of each load step.,
	Tendon head displacement vs time	k_1 versus anchor load	Anchor head displacement vs time for each load step.
	α_1 versus anchor load		α_s versus anchor load or bond load, if possible.
	Displacement vs load for all cycles		
$R_{SLS,m}$	Not defined	P_c (based on k_1 vs load)	Pc (from α_s vs load, end of pseudo linear portion)
$R_{ULS,m}$	Currently α_1=2mm	When curve of k_1 vs load is asymptote	When plot of α_s vs load, is asymptote or α_s =5mm

Note:-

$\alpha_1 = (s_B - sa)/\mathrm{Lg}(t_B/ta)$ from linear part of α_1 vs log time plot;

k_1=expressed as percentage of applied load;

$\alpha_3 = (s_2 - s_1)/\mathrm{Lg}(t_2/t1)$ based on last two time readings.

A variety of methods of interpreting anchor tests are used in European countries. For example, Test Method 1 is used in Germany where $R_{ULS,m}$ is taken as the load corresponding to α_1=2mm (where $\alpha_1$is a creep rate - see Note above), however $R_{SLS,m}$ is not separately identified. Test Method 3 is used in France and $R_{ULS,m}$ is interpreted from a plot of α_3 (also a creep rate- see Note above) when the curve of creep rate versus load becomes asymptotic to the load axis or when α_3 is 5mm.

SLS resistance ($R_{SLS,m}$) is taken in France as the 'Critical Creep Load, P_c, interpreted from the 'knee' in the creep/load plot (see Figure 1).

The UK (BS8081) is less definitive but has two criteria to be satisfied which could be interpreted to represent ultimate and serviceability resistances.

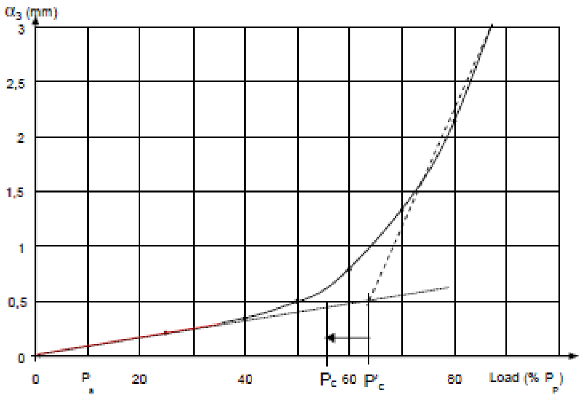

Figure 1. Determination of critical creep load Pc (from draft of ISO/DIS 22477-5).

4 TYPES OF ANCHOR TESTS

Three types of tests are generally recognised in Europe and are covered in EC7, namely Investigation tests, Suitability tests and Acceptance tests. Investigations test are carried out on sacrificial anchors and can be tested to failure whereas suitability tests are on working anchors and are taken to a 'Proof load', the value of which is selected to ensure that the anchor has the required R_{ULS} and R_{SLS}. The role of Acceptance tests is currently under discussion as they are used in some countries to ensure that a working anchor has the required R_{ULS} and R_{SLS}, however the Proof Load of Acceptance test in some countries is set to confirm R_{SLS}, with some margin of safety, and relies on a database/experience and the results of investigation tests, to give confidence that this indicates that the anchor has the required R_{ULS}.

$R_{ULS,m}$ can be determined from investigations tests or from suitability tests that fail at the Proof load as is expressed in Eq 1 for $R_{ULS,m}$:

$$R_{ULS,m} = \mathrm{Min}\ \{R_m\ (\alpha_{1,ULS} \text{ or } k_{l\ ULS} \text{ or } \alpha_{3,ULS}) \text{ and } P_P\} \quad (1)$$

Currently a $R_{SLS,m}$ is not defined using Test method 1,the method used in Germany, which as stated previously, does not distinguish between $R_{ULS,m}$ and $R_{SLS,m}$. However the creep rate, α_1 , may be a convenient method of redefining some of the current practices of some countries.

5 DETERMINING THE ULS AND SLS DESIGN RESISTANCE OF AN ANCHOR

The design anchor resistance can be determined as for piles in EC7 from the measured resistances using correlation and partial factors. For example, for ULS design ($R_{SLS;d}$ can be obtained in a similar fashion):

$$R_{ULS;k} = R_{ULS;m} / \xi_{ULS} \quad (2)$$

and

$$R_{ULS;d} = R_{ULS;k} / \gamma_{a;ULS} \quad (3)$$

Where ξ_{ULS} is a correlation factor related to the number and type of test and $\gamma_{a;ULS}$ is a partial factor. The correlation factor would generally be unity if all anchors are subjected to tests which indicate the required resistance.

6 DETERMINING DESIGN ANCHOR FORCE

6.1 Introduction

EC7 requires that a structure be designed to prevent the exceedance of ULS and SLS limit states. Similarly the anchor itself must be designed to have the required margin of safety in ULS and SLS.

The design of anchors to EC7 has to consider three special design situations:-

- the actual force in the anchor under normal working conditions can exceed that required to prevent a SLS limit state in that structure (or in supporting structures).
- There is a need to ensure that the margin of safety of the anchor against ULS and SLS is satisfactory as well as the requirement for the structure and supporting structure.
- The anchor force required to prevent a SLS in the structure or supported structure may be the controlling force.

6.2 Ultimate limit state design of an anchor

Two forces are relevant in anchor design, namely:-

- $F_{ULS,d}$ = design value of the axial force sufficient to prevent the exceedance of a ULS in the structure.
- $F_{Serv,k}$ = cautious estimate of the maximum force that is expected within the design life of the structure including effect of lock off load, and sufficient to prevent a SLS in the supported structure.

The inequality to be satisfied by the anchor is:-

$$R_{ULS;d} \geq F_{ULS,a;d} \tag{4}$$

where

$$F_{ULS,a;d} = \text{Max}\{\, F_{ULS,d} \,;\, F_{Serv,d} \,\} \tag{5}$$

and

$$F_{Serv,d} = \gamma_{serv}\, F_{Serv,k} \tag{6}$$

where γ_{serv} is a partial factor to be given in the National Annex of each country.

The anchor force required to prevent a SLS in the structure or supported structure is given the symbol F_{SLS} in this paper. $F_{Serv,k}$ can be equal to or greater than F_{SLS}, but cannot be less.

An example of how these forces may typically be derived in a simple design situation is given for a quay wall as shown on Figure 2.

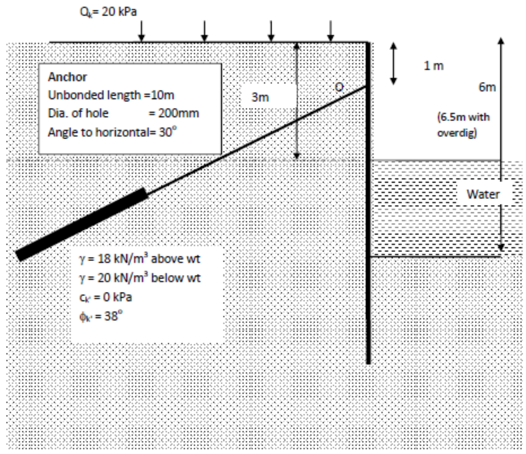

Figure 2. Design Example of Quay Wall.

6.2.1 Determination of anchor load to prevent ULS of structure ($F_{ULS,d}$)

The anchor force required to prevent an ULS in the structure can be determined by selecting one of the design approaches of EC7 and applying the required partial factors on actions and ground properties/resistances to a calculation model in the normal fashion. Taking the Quay Wall example shown in Figure 2 and an anchor spacing of 3m, and using the simple limit equilibrium analysis (LEM) of the free anchor support method, the anchor force to prevent overturning of the quay wall ($F_{ULS,d}$) is 270kN/anchor using Design Approach 1. As there is no particular requirement on serviceability there is no value for $F_{SLS,d}$.

The structure has the required ULS margin of safety with that anchor load, however such an analysis does not consider the margin of safety on the anchor itself against, in this case, pull-out, nor does it consider if the anchor could have excessive creep under the forces that it will experience during construction and its design life. In this simple case the effect of prestress has also been ignored. In some design situations, the force required to prevent a SLS in the structure or supporting structure (F_{SLS}) has also to be considered and this may be the controlling force in determining $F_{Serv,k}$.

$F_{ULS,d}$ for anchor design in Germany is not taken directly as the ULS force determined from an analysis of the overall structure. For the simple case of the Quay wall example shown of Figure 2, a simple beam analysis would be carried out using active pressure determined from characteristic values with the reactions at the anchor and at the centroid of the passive resistance (personnel communication). This analysis is carried out for permanent actions and variable actions to give $F_{G,k}$ and $F_{Q,k}$. The design anchor force, $F_{ULS,d}$, is then:-

$$F_{ULS,d} = 1.35\, F_{G,k} + 1.5\, F_{Q,k} \tag{6}$$

6.2.2 Determination of anchor ‘service’ load ($F_{Serv,d}$)

The introduction of the concept of an anchor ‘service’ force is a relatively radical measure and has yet to get approval from EC7. It is required because the anchor creep under ‘working’ or ‘service’ conditions can be the controlling criterion in anchor design in those countries which have defined a $R_{ULS,m}$

and a $R_{SLS,m}$. This has been taken further in some countries in that the Proof Load for Serviceability and Acceptance tests is related to this 'working' or 'service' force. The derivation of this force, possibly, requires further research and standardisation. For prestressed anchors, the use of a relationship between the lock-off force and the estimated 'service' load possibly means that the latter is close to the estimated value.

The force $F_{Serv,k}$ is defined as a cautious estimate of the maximum force that is expected within the design life of the structure including the effect of lock off load, and which is sufficient to prevent a SLS in the supported structure. This force can be determined from a soil/structure interaction analysis, such as finite elements, which also allows prestress to be included and the effect of the construction sequence to be modelled. Such analyses are carried out using characteristic values of actions and soil properties/resistance and without the overdig allowance. Where the maximum force in the anchor is that required to prevent a SLS in the structure (F_{SLS}) or supported structures, then $F_{Serv,k} = F_{SLS}$.

For the simple design situation of the Quay Wall given in Figure 2, the value of $F_{Serv,k}$ is frequently estimated by carrying out a simple LEM analysis using characteristic values of actions and soil parameters/resistances, using the length of the sheet pile wall required for equilibrium with these forces, i.e with a sheet pile shorter than that required for ULS. For the Quay Wall example, this would give $F_{Serv,k}$ = 158 kN/anchor. The design value of this force for ULS design is obtained from Eq. 6.

The value of γ_{serv} would be set in the National Annexes but would typically be 1.35, thus $F_{Serv,d}$ for Example 1 would be 1.35x158 = 213.3kN/anchor.

Note that different values of $F_{Serv,k}$ are obtained if a finite element method is carried out. However the value obtained would depend on the soil model and sequence of loading adopted.

6.2.3 ULS design of an anchor

The anchor would be required to resist the greater of $F_{ULS,d}$ and $F_{Serv,d}$ which could be designated as $F_{ULS,a;d}$. Thus the inequality given in Eq. 8 has to be satisfied.

$$R_{ULS;d} \geq F_{ULS,a;d} \tag{8}$$

For the Quay Wall example, $R_{ULS;d}$ must be equal to or greater than 270 kN/anchor as $F_{ULS,d} > F_{Serv,d}$.

6.3 Serviceability limit state design of an anchor

Currently not all countries carry out a separate SLS analysis of an anchor. France, as stated previously, defines a critical creep load, P_c, that is used in SLS design of an anchor. This is to be distinguished from SLS of the supporting structure.

Where the anchor is required to satisfy a SLS, for example, when it is to be suitably less than the creep load Pc, then

$$R_{SLS;d} \geq F_{Serv,k} \tag{9}$$

Thus in the Quay Wall example, $R_{SLS;d} \geq 158$ kN/anchor. Note that there will be an appropriate margin of safety between the measured and design value of R_{SLS} as shown in Eq. 10 and 11:-

$$R_{SLS;k} = R_{SLS;m} / \xi_{SLS} \tag{10}$$

and

$$R_{SLS;d} = R_{SLS;k} / \gamma_{a;SLS} \tag{11}$$

6.4 Lock-off load

Lock off load (P_o) has an influence on $F_{Serv,k}$. It is generally set about 80% of $F_{Serv,k}$ in some countries, although the current practice in the UK is equivalent to 110% of the 'working load'. There is a requirement in steel code (1991-1-1:2004) for the lock off load of such anchors to satisfy equation 12, where R_{tk} is the $R_{t,d}$ is the design tensile resistance of the anchor's tendon free lengths (The recommended values for k_7 is 0,75 and for k_8 is 0,85).

$$P_0 \leq \min. \{k_7 \cdot R_{tk} \,;\, k_8 \cdot R_{t0,1k}\} \tag{12}$$

7 TESTING OF ANCHORS AND PROOF LOADS

Testing of anchors is an integral part of their design. This paper deals only with prestressed anchors and it is generally accepted that all prestressed anchors should be subjected to Acceptance tests.

Tests on anchors are normally designed to give the following information:-

- The capacity of an anchor ($R_{SLS,m}$ and $R_{ULS,m}$ or $R_{SLS,m}$ only)
- Proof that the anchor is fixed/bonded at a certain depth

There are three load tests, as mentioned previously, Investigation tests, Suitability tests and Acceptance tests. Investigation tests would normally be designed to determine $R_{ULS,m}$ at failure of the grout/ground interface and may therefore have a greater strand/bar capacity than a working anchor. Suitability and Acceptance tests are carried out on working anchors.

The requirement for the Proof load for Investigation and Suitability tests is that:

$$P_P \geq \xi_{ULS}\, \gamma_{a;ULS}\, F_{ULS,a;d} \tag{13}$$

This relationship comes from the requirements of Eqs 2, 3 and 9. Where all anchors are tested, which is a requirement for all prestressed anchors, the correlation factor ξ_{ULS} would be unity. The partial factor, $\gamma_{a;ULS}$, currently proposed in different countries is between 1.1 and 1.3, thus the proof load for Investigation and Suitability tests for Example 1 would be 297kN or 351 kN. This level of proof load is sufficient to ascertain whether or not the anchor satisfies the criteria for $R_{ULS,d}$ and $R_{SLS,d}$.

There is less agreement in Europe on the level to which Acceptance tests should be taken. Some countries relate the Proof load for acceptance tests to $F_{ULS,a;d}$ whereas other relate this load to $F_{Serv,k}$. For example in Germany the level of Proof load for acceptance tests is similar to that for Suitability tests, i.e 1.1 $F_{ULS,a;d}$, however with some of the time intervals relaxed in Acceptance tests. France takes a different approach in requiring a lower Proof load for Acceptance tests of 1.25x $F_{Serv,k}$ for permanent anchors (1.15 for temporary anchors), however requiring this to satisfy SLS creep criteria. Confidence that R_{ULS} is satisfactory is achieved by a combination of their database/experience from results at this level of Proof load, and from the results of investigation tests to determine R_{ULS} and the critical creep load (R_{SLS}), which are mandatory in France. The low value of the Proof Load for Acceptance tests in France is based on this knowledge of the critical creep load and of R_{ULS}.

8 STRUCTURAL DESIGN OF ANCHOR

The structural capacity of an anchor will generally be expected to satisfy:-

$$R_{t,d} \geq \gamma_{p,anc} P_P \tag{14}$$

When not subjected to proof tests $R_{t,d}$ shall be the greater than $F_{ULS;a;d}$. Prestressed steel tendons are designed in accordance with EN1992-1-1.

9 DISCUSSION/CONCLUSIONS

This paper gives some indication of the possible future revisions of Section 8, Anchors, which will be incorporated into EN1997-1. These revisions will offer an opportunity to rationalise the design of anchors in this country. The current practice, while functional, does not clearly show the areas of uncertainty and the margins of safety. For example, anchor design in Ireland is currently based on BS8081 which applies Factors of Safety to the anchor 'working' load (T_w) without clearly stating how this load is determined or without any reference to the load that may be required to prevent an ULS of the structure. Furthermore, the magnitude of the Proof Load is based on T_w, again without reference to the load required to prevent an ULS in the supported structure.

EC7 will give a logical framework for the design of anchors that considers the ULS and SLS of the structure, the supported structure and also of the anchors themselves. It is important that the anchor testing method selected is suitable to our ground conditions and experience and also that the correlation and partial factors are appropriate. To this end, research into anchor behaviour in Irish soils, and into design examples of typical situations encountered would be welcomed. Comparative tests of the behaviour of the ground using three anchor testing methods would be useful in assisting in the selection of the criterion of measured anchor resistance, both $R_{ULS,m}$ and $R_{SLS,m}$, as would a database of anchor tests in Irish soils. A risk assessment of different anchored structures using anchor test results would be a significant contribution to this area.

ACKNOWLEDGMENTS

The author would like to acknowledge the information exchanged in EG1 which members are Klaus Dietz, Yves Legendre, Caesar Merrifield, Ole Møller, Pierre Schmitt, Arne Schram Simonsen, Brian Simpson.

REFERENCES

[1] prEN1537:2011, 'Execution of special geotechnical work – Ground anchors'.
[2] ISO/DIS 22477-5:2004, Tentative Final Draft of ISO TC 182/SC1 'Geotechnical investigation and testing – Testing of geotechnical structures Part 5: Testing of Anchorages'.
[3] EN 1997-1:2004, 'Eurocode 7:Geotechnical design – Pt 1 – General Rules'.

LIST OF SYMBOLS

$F_{ULS,d}$ = design value of the axial force sufficient to prevent the exceedance of a ULS in the structure.

$F_{ULS,a;d}$ = Max{ $F_{ULS,d}$; $F_{Serv,d}$ }

$F_{Serv,k}$ = cautious estimate of the maximum force that is expected within the design life of the structure including effect of lock off load, and sufficient to prevent a SLS in the supported structure.

$F_{Serv,d}$ = design value of $F_{Serv,k}$

$F_{G,k}$ = characteristic value of permanent actions

$F_{Q,k}$ = characteristic value of variable actions

R_{ULS} = ultimate resistance of an anchor

R_{SLS} = serviceability resistance of an anchor.

$R_{ULS,k}$ = characteristic value of the ultimate resistance of an anchor

$R_{SLS,k}$. = design value of the serviceability resistance of an anchor

$R_{ULS,d}$ = design value of the ultimate resistance of an anchor

$R_{SLS,d}$. = characteristic value of the serviceability resistance of an anchor

$R_{ULS,m}$ = measured ultimate resistance of an anchor

$R_{SLS,m}$. = measured serviceability resistance of an anchor

$R_{t,d}$= structural capacity of anchor

α_1 = $(s_B\text{-}sa)/\mathrm{Lg}(t_B/ta)$ from linear part of α_1 vs log time plot

k_1=expressed as percentage of applied load

α_3 = $(s_2\text{-}s_1)/\mathrm{Lg}(t_2/t_1)$ based on last two time readings.

P_P = Proof Load

P_C = Critical Creep Load

P_o = Lock off Load

Tw = anchor 'working' load

ξ_{ULS} , ξ_{SLS} correlation factors

$\gamma_{a;ULS}$, $\gamma_{a;SLS}$ γ_{serv}, $\gamma_{p,anc}$ partial factors,

Soil properties at the UCD geotechnical research site at Blessington

Paul Doherty[1], Lisa Kirwan[1], Kenneth Gavin[1], David Igoe[1], Shane Tyrrell[2] , Darren Ward [3], Brendan O'Kelly[4]
[1]School of Civil, Structural and Environmental Engineering, University College Dublin, Belfield, Dublin, Ireland
[2]Department of Geology, University College Dublin, Belfield, Dublin, Ireland
[3] In-situ Site Investigations, Penetration House, UK
[4] Department of Civil, Structural and Environmental Engineering , Trinity College Dublin
email: paul.doherty@ucd.ie

ABSTRACT: Over the past ten years, the Geotechnical Research Group (GRG) at University College Dublin have developed a research site at Blessington, County Wicklow, for the purpose of testing foundation systems. This paper presents the results of field and laboratory tests conducted to obtain the geotechnical parameters of Blessington sand. The in-situ tests included cone penetration and dilatometer tests. Sonic coring was performed in three boreholes at the site and complete recovery was obtained in boreholes up to 14 m deep. Additional disturbed samples were taken from trial pits which were up to 6 m deep. The classification tests performed on samples compared favourably with those inferred from correlations with in-situ test data. The strength, stiffness and mineralogy were also determined by a suite of laboratory tests including SEM imagery, triaxial tests and ring shear testing. The accuracy of conventional correlations in predicting the laboratory measured parameters is discussed.

KEY WORDS: Soil testing, soil classification, mineralogy

1 INTRODUCTION

Over the past ten years, the geotechnical research group (GRG) at University College Dublin have developed a field testing facility at Blessington, County Wicklow (see [1]). This test site was developed to accommodate a series of research projects, which investigated aspects of foundation behaviour including axial pile behaviour, lateral pile resistance, cyclic loading response, eccentric loading and pile ageing. This test site was chosen because of the consistent nature of the sand deposits and the similarity of the strength and stiffness properties of the sand to those encountered in offshore seabed deposits in the North Sea.

This paper compiles data from site characterisation testing that has been undertaken to-date and combines this to develop a holistic interpretation of the test site properties.

2 TEST SITE LOCATION

The Blessington test site is located in the Redbog Roadstone quarry approximately 25km south-west of Dublin, see Figure 1. The site access is approximately 800m to the north-west of Blessington village, comprises of an area of approximately 30m x 30m, and consists of uniform dense sand from ground surface to considerable depth.

Over the years in which experimental work has been performed on the test site, excavation has proceeded in adjacent areas, and the test area now occupies an elevated position (See Figure 2). These excavations and recently completed sonic coring provided an opportunity to sample the sand from much greater depths than had been possible previously.

3 SITE GEOLOGY

3.1 Geological History

The geological history of the area has been investigated by a number of researchers (eg. [2]), who describe the complex glacial movements that formed the underlying sand deposits. The sediments of the Blessington sand and gravel pits represent the deposits of a lacustrine delta complex (where sediment carried by a river is deposited as the water slows down as it flows into a lake), with the envisaged glacial lake impounded by the Midlandian ice sheet to the west and by the Wicklow Mountains to the east. The sediments, locally underlain by slates and shale of Silurian age, have a maximum thickness of 60 m, but the exact age of these deposits is uncertain. Divided into two phases of deposition, the earlier stage (part of which forms the site area investigated in this study) is linked to the retreat of the ice sheet; hence was likely bracketed between 20–24 kiloannum (ka) (the maximum extent of the sheet) and a later ice re-advance dated at 17 (ka) [3].

Figure 1. Blessington test site location.

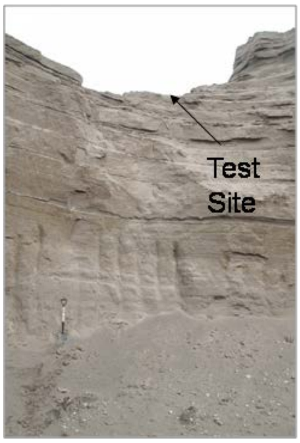

Figure 2. Excavations at Blessington test site (after [4]).

The complex is comprised of a frequently contorted sequence of dominantly gravelly to coarse- to medium-grained sand beds and facies associated with a typical Gilbert-type delta (a specific type of delta characterised by predominantly coarse sediments). However, the site investigation is specifically focused on a relatively well-sorted, fine- to medium-grained sand facies. The sediments at the test site correspond to the Light Brown Unit, described by Philcox [5], and form the uppermost part of a significant local fluvial channel system. Comprising horizontal, interlaminated (5–15 cm scale), rippled cross-laminated sands and silts, these sediments represent the deposits of a low energy fluvial current.

A later, but limited, ice re-advance (associated with the 17 ka event) was likely to have covered the study area, the final retreat of which resulted in the deposition of a minimum of 7 m overburden depth above the test area. The section was potentially buried under significantly more than the observed 7m – and this additional sedimentation may have been removed by erosion during the Holocene (last 12 ka). Unquantified post-glacial isostatic rebound during this period means that it is difficult to constrain the thickness of any sediment removed, but there is certainly sufficient potential overburden (ice and/or sediment) to account for a degree of over-consolidation at the test site.

3.2 Petrographic Analysis

Thin sections were prepared from samples at four depths (1.75m, 4.5m, 7.7m and 11.9m) within the studied section and optical petrography was used to assess both mineralogy and grain morphology. The sand fraction is dominated by highly angular fragments of quartz (Figure 3).

The sand is also comprised of a significant calcite component, both as fragments of spar and as fine-grained micritic mud (presumably derived from nearby limestone bedrock). Subordinate minerals present include feldspar and minor muscovite mica – consistent with derivation from a granitic source. A matrix of clay mineral pervades the interstices and coats the framework grains (Figure 3a). The topmost sample at 1.75m includes the highest clay content, with deeper samples appearing to have less clay. However, this apparent correlation between clay content and depth is unlikely to be consistent throughout the whole section. Rather, the clay content is likely to vary on a smaller scale than the sampling interval, reflecting the inherently laminated nature of the section and transitions between medium and fine-grained sediments. Framework grains appear fractured to varying degrees. This is especially apparent in the quartz fraction (Figure 3c). The degree of fracturing also appears to vary at the different sampling levels (Figure 3b, c).

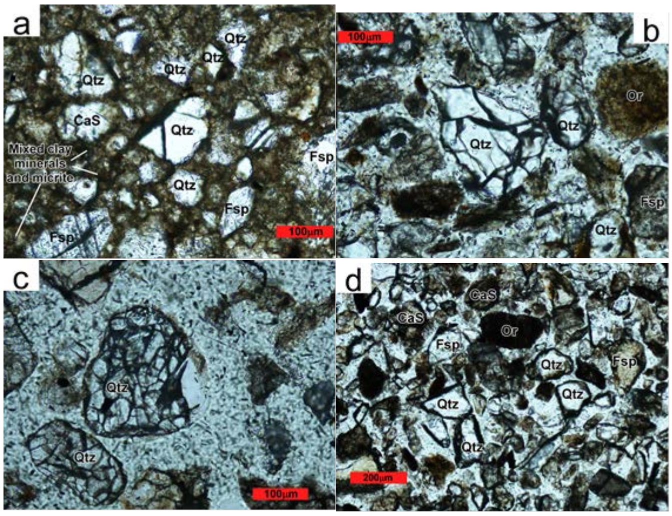

Figure 3. Photomicrographs, in plane polarized light, of samples from a) 1.75m; b) 4.5m; c) 7.7m and d) 11.9m.. Qtz = quartz, fsp = feldspar, CaS = calcite spar, Or = organic material.

3.3 Microstructure from SEM Imagery

A scanning electron microscope was used to investigate the micro-structure of the particles. To gather high resolution images, samples were prepared using carbon tab mounting studs and the thin sections described previously in Section 3.2.. The observed samples showed a mixture of larger particles surrounded by smaller particles, with the proportion of fine particles varying with depth. The variation in particle size within a given sample is illustrated in Figure 4.

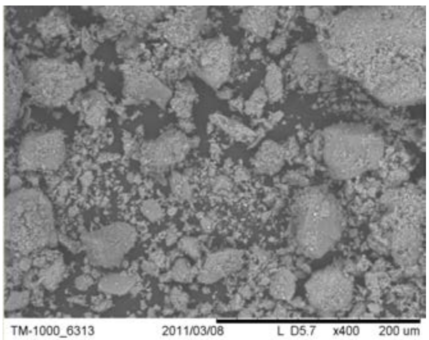

Figure 4. Sand particle matrix.

The large particles appear to be highly fractured, making them very coarse. However, the edges of the particles are still sharp rather than rounded. This means that the particles have a low sphericity but a high level of roughness.The angularity of the particles is very high. These features are illustrated in Figures 5, 6 and 7.

At smaller scales, the particles tended to appear similar to larger particles suggesting that they are particles of rock flour that had broken away from larger (parent) particles. However, some samples contained plate-like particles of clay minerals, which were shown to be kaolonitie (see Figure 8). For the most part, the sand grains were consistent with clean quartz sand as observed by the conchoidal fracture patterns (see Figure 9). This mineralogy was confirmed using X-ray diffraction analysis (XRD), which showed that the majority of particles were composed of pure silica and could be identified as quartz material.

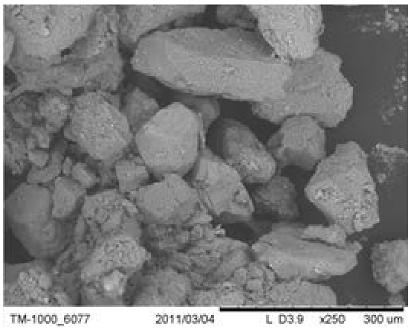

Figure 5.Sand shows high angularity but low sphericity.

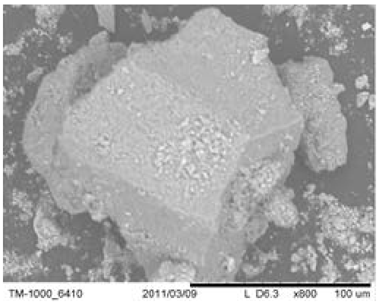

Figure 6. Individual sand grain.

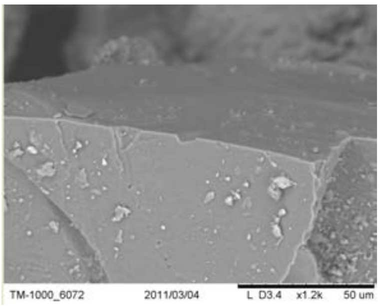

Figure 7. Clean edges on sand grain.

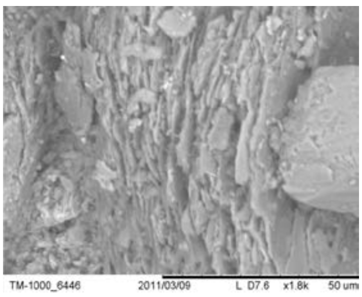

Figure 8. Clay minerals observed within fines fraction.

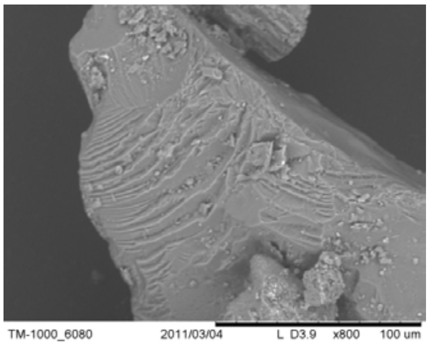

Figure 9. Conchoidal fracture pattern.

Highly angular and fractured particles were observed at all depths. The only difference in depth-dependent variation is the quantity of fines in the sample. This was apparent from macroscale observations from the site, where depositional lenses are present as shown in Figure 2. This observation was also visible in the petrographic and SEM imagery. Particle size analysis was undertaken by dry sieving as shown in Figure 10, where the percentage fines is shown to vary from 4% to 13%. The variation in fines content can be attributed to the mechanism by which the deposit formed – i.e. a glacial delta complex. During periods of high flow rates, fewer fines were deposited to the lake bed, and vice versa.

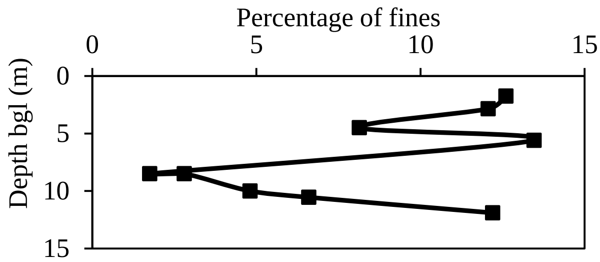

Figure 10. Fines content.

SEM imagery and XRD analysis suggest that the fines are either calcium (limestone rock flour) based or composed of pure silica (quartz), although some clay-like profiles were observed. This also agrees with the petrographic analysis of the mineralogy of the samples. The variation in clay content was also apparent in the samples taken from sonic coring, which showed large variations in cohesion. Notably, the sample taken at 1.75m depth retained excellent cohesion indicating a high level of clay and silt as shown by Figure 11.

Figure 11. Sample from 1.75m depth. Diameter of sample roughly 100mm.

4 IN-SITU TESTING

4.1 CPT Tests

Fifteen Cone Penetration Test (CPT) soundings were performed at the site by InSitu Ground Investigation Ltd. The CPT soundings were taken in a grid pattern at regular intervals across the test site to depths of between 10m and 14m. The CPT cone end resistance traces, q_c (see Figure 12), show q_c values that increased from 10MPa at the ground surface to 25MPa at 10m depth. Such large q_c values suggest a very dense deposit. The sleeve friction values from the cone, f_s, also increased with depth and the resulting friction ratio, F_r, was typically between 1% and 3%. The CPT values allowed the Blessington deposits to be classified using the Robertson [6] classification chart as a clean to silty dense sand. This agrees with the visual observations from the SEM analysis which showed mostly clean sand with smaller silty size particles.

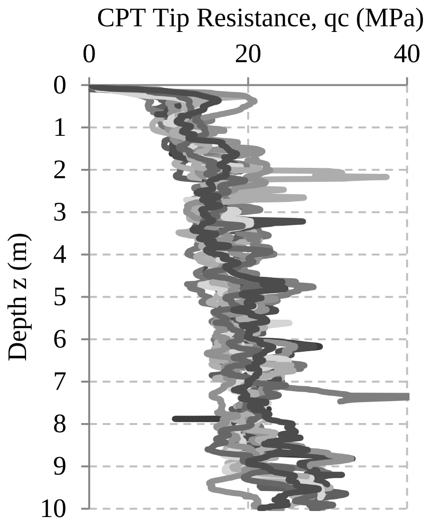

Figure 12. CPT tip resistance.Dilatometers.

Dilatometer tests performed at the site involved pushing a blade cell into the underlying sand and pausing every 250mm in order to undertake lateral expansion of the cell face (comprised of a flexible membrane) to a displacement of 1.1mm. The pressures required to initiate the expansion (the lift-off pressure p_0) and also to generate the final strain level (the limit pressure, P_L) were recorded, see Figure 13.

The dilatometer soundings terminated at 6m depth as the force required to advance the spade below this depth exceeded the 20t reaction force available from the CPT truck. The lift-off pressure, P_0, increased with depth from 500kPa at shallow soundings to greater than 1000kPa at 6m depth. The limit pressure showed similar increases with depth from 2MPa at 0.5m depth to 4MPa at 6m depth.

The high lateral pressures required to expand the cell at such shallow depths is indicative of high lateral earth pressures resulting from past over-consolidation. This observation ties into the geological history of the area which suggests that past layers of soil above the current ground level were removed by erosion in the past 12ka, leaving behind an over-consolidated soil mass.

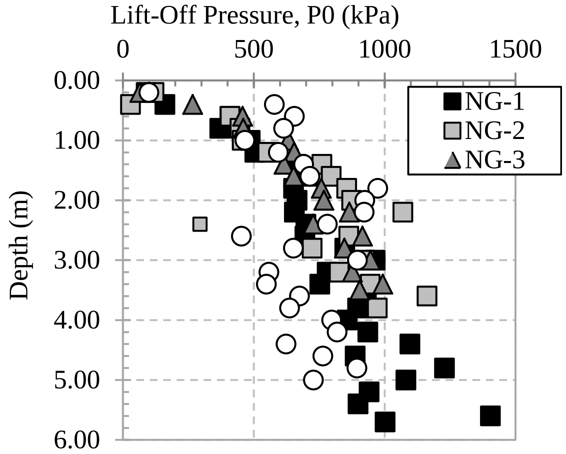

Figure 13(a). Dilatometer lift-off pressure.

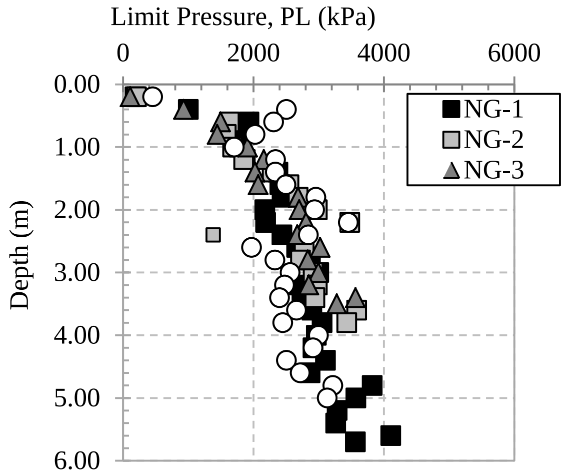

Figure 13(b). Dilatometer limit pressure.

5 OVERCONSOLIDATION

5.1 Oedometer Testing

The sonic coring procedure resulted in relatively intact cores which allowed laboratory testing to be undertaken on trimmed samples. Oedometer tests were performed on samples retrieved from depths of between 1.75m and 14m. A typical loading and unloading response is shown in Figure 14, where the void ratio is seen to decrease from an initial value of 0.17 to a final value of 0.06 under an applied vertical stress of approximately 4MPa.

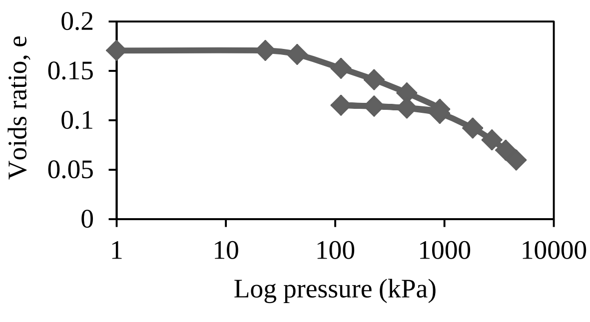

Figure 14. 1-D compression behaviour.

Using the Cassagrande method, the pre-consolidation stress was estimated to range between 600 and 1000 kPa. The resulting overconsolidation ratios (OCR) are plotted in Figure 15 as a function of depth, where a decrease from OCR = 15 at 1m depth to approximately 5 at 5m depth is observed, after which a relatively constant OCR is observed. It should be noted that there is a level of subjectivity in using the Cassagrande method to determine the pre-consolidation pressure as readings must be taken from a log scale and points selected through judgement rather than an exact algorithm.

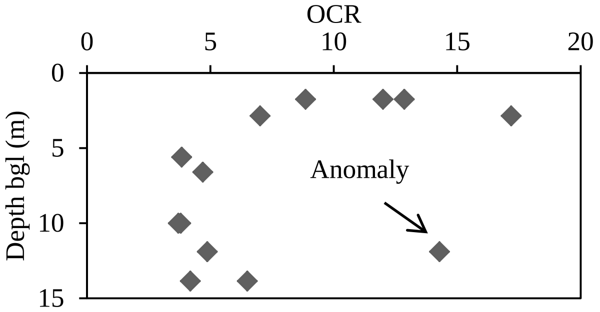

Figure15. OCR determined from Oedometer Tests.

5.2 OCR Correlations

Because of issues such as sampling disturbance, specimen preparation and apparatus compliance at low strain levels, there is a high degree of uncertainty associated with the laboratory-determined OCR profile.

Correlations between OCR and in-situ test data determined from calibration tests on clean un-cemented un-aged quartz sands have been proposed by a number of researchers [7] [8] [9], etc. Mayne [9] proposed the following equation to determine OCR for cohesionless soils:

$$OCR = \left[\frac{1.33 q_t^{0.22}}{K_{oNC} \left(\sigma'_{vo} \right)^{0.31}} \right]^{\frac{1}{(\alpha - 0.27)}} \quad (1)$$

where q_t = cone tip resistance (MPa) and σ_{v0}' is the effective overburden pressure (kPa). The parameter α can be taken as $\alpha = (1 - K_{oNC}) \approx \sin\phi'$ for a first approximation [9]. Comparison of the CPT-determined OCR profile with the oedometer test results in Figure 16 show excellent agreement.

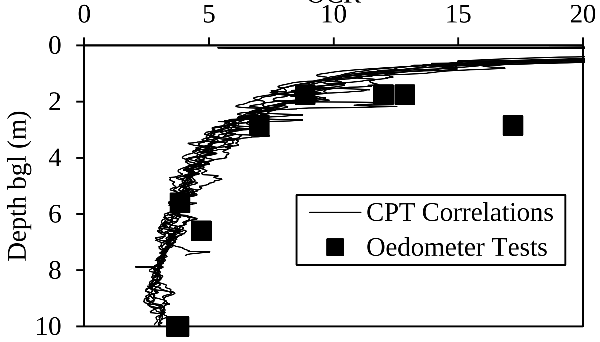

Figure 16. Comparison of OCR from CPT and oedometer data.

While correlations to predict the stress history of a deposit using dilatometer measurements are not as well established as CPT-based empirical relationships, Marchetti et al [10] have proposed a correlation from dilatometer measurements made in a study of a test embankment constructed in Venice (described in [11]). The structure was comprised of a cylindrical vertical-walled 40m diameter embankment that was kept in place for four years before being removed. The embankment loading and subsequent un-loading history were thus known, allowing a relationship between the stress history and dilatometer lift-off pressure, P_0 , porewater pressure, u_0 and vertical effective stress, σ'_{vo} to be established for the site:

$$OCR = 1.6454 \ln(K_D) - 0.3693 \quad (2a)$$

$$\text{where : } K_D = (P_o - u_o) / \sigma'_{vo} \quad (2b)$$

The OCR profiles for the Blessington test site determined from the dilatometer correlation above are shown in Figure 17, where it is seen that OCR decreases slightly from 5 at the ground surface to 3.5 at 5m depth.

At shallow depths, the dilatometer-determined OCR values were significantly lower than those suggested by the oedometer test data and CPT correlations.

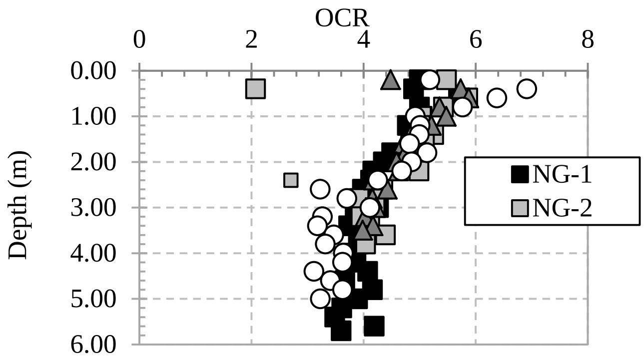

Figure 17. OCR determined from dilatometers.

6 FRICTION ANGLE

6.1 Friction Angle from Lab and Field Testing

Tolooiyan and Gavin [12] report the results of triaxial compression tests on samples of Blessington sand reconstituted at the in-situ relative density (≈ 100%). These revealed that the sand has a constant volume friction angle, ϕ'_{cv} of 37° and a peak friction angle, ϕ'_p which decreased from 54° to 42° for stress levels corresponding to depths ranging from 1 m to 5 m below the ground surface.

The residual friction angle measured in ring shear tests performed in the Bromhead apparatus at the appropriate effective stress level and stress history are shown in Figure 18. The soil-on-soil residual friction angle (analogous to a critical state friction angle) ranged between 39° and 31°, with an average value of 36°. This is in keeping with estimates for ϕ'_{cv} based on the soil grading and mineralogy after Stroud [13], for a uniform highly-angular silica sand. It also agrees very well with the constant volume friction angle measured by Tolooiyan and Gavin [12].

The sand-steel residual friction angle determined in the ring shear tests using a rough steel interface produced similar values to the soil-soil tests, suggesting minimal influence of the rough interface.

Interface ring shear tests using a smooth steel interface similar to those used to construct model piles tested at the site (see [14]) mobilised residual friction angles of 30°. This high residual friction angle can be explained by the angular edges of the sand particles as observed by the SEM.

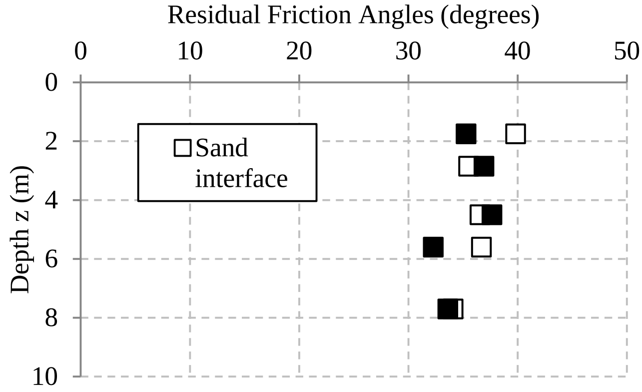

Figure 18. Residual stress friction angle.

The peak friction angle ϕ'_p can be estimated from correlations with the CPT q_c values, e.g. Robertson and Campanella [15] or more recently, Kulhawy and Mayne [16]:

$$\phi' = 17.6 + \log((q_c - \sigma_{v0}) / \sigma'_{v0}) \qquad (3)$$

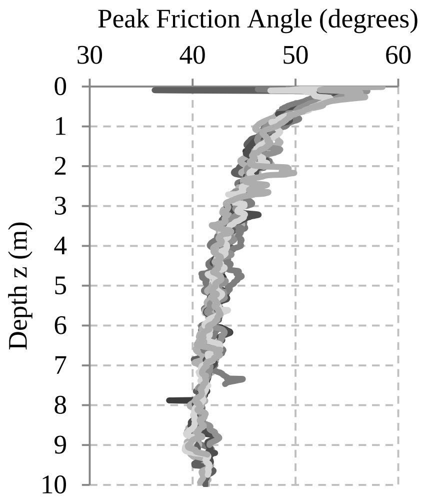

Figure 19. Peak friction angles determined from CPT resistance.

The friction angles determined from the CPT correlations (Figure 19) ranged from 55° at very shallow depths (and corresponding low effective stresses) to approximately 40° at 10 m depth is broadly in keeping with values reported from the triaxial tests performed by Tolooiyan and Gavin [12].

7 CONCLUSIONS

This paper presents site investigation results determined from laboratory and in-situ testing at a geotechnical research site at Blessington. The following should be noted:

1. The in-situ sand is very dense and heavily over-consolidated, with high mean stress levels, which were confirmed by both in-situ and laboratory tests.
2. Peak friction angles were observed to decrease with depth from over 50° at ground surface to 40° at 10m depth. The constant volume friction angle was 36°. In interface shear tests using rough steel interfaces (comparable for example to mild steel piles), the mobilised friction angle was comparable to the soil-soil constant-volume friction angle.
3. Field testing (and in particular the CPT test) was shown to provide excellent correlations with laboratory estimates of the stress and strength characteristics of the deposit.

ACKNOWLEDGMENTS

The authors wish to express their gratitude to Mainstream Renewable Power, the Irish Research Council for Science and Technology (IRCSET), Science Foundation Ireland (through grant number 10-RFP-GEO2895) and Enterprise Ireland for co-financing these field tests. In addition, the authors wish to thank Irish Geotechnical Services (IGSL) and Boart Longyear for performing the sonic coring and Martin Carney at TCD for assisting with the ring shear tests.

REFERENCES

[1] Igoe D. (2010) *Offshore Foundations: A comparison of full-displacement and partial displacement piles in sand,* PhD Thesis, University College Dublin

[2] Syge, F.M, (1977) *West Wicklow*, In South-East Ireland International Union of quaternary research field guide, Vol.56

[3] Coxon, P., 1993. Irish Pleistocene biostratigraphy. *Irish Journal of Earth Sciences*, 12,83-105.

[4] Doherty P. and Gavin K. (2010) "Statistical use of CPT data and implications for pile design" *Proc. Of the 2nd International Conference on Cone Penetration Testing*

[5] Philcox, M.E., 2000. The glacio-lacustrine delta complexat Blessington, Co. Wicklow and related outflow features. In: *Guidebook of the 20th Regional Meeting of the International Association of Sedimentologists*, Graham. J.R and Ryan,A. (eds). Trinity College Dublin. 129-152.

[6] Robertson (1990) Soil Classification using the CPT *Canadian Geotechnical Journal*

[7] Mayne, P.W. (1995). CPT determination of OCR and Ko in clean quartz sands. Proceedings, *Symposium on Cone Penetration Testing*, Vol. 2, Swedish Geotechnical Society, 215-220.

[8] Lunne, T., Robertson, P.K., & Powell, J.J.M. (1997). *Cone Penetration Testing in Geotechnical Practice*, Blackie Academic & Professional, Chapman and Hall, London, 312 p.

[9] Mayne, P.W. (2001). Stress-strain-strength-flow parameters from enhanced in-situ tests. *Proceedings, Intl. Conf. on In-Situ Measurement of Soil Properties & Case Histories*, Bali, Indonesia, 27-48.

[10] Marchetti et al (2012) "Overconsolidation and stiffness of Venice lagoon sands from SDMT and CPTU" *ASCE Jnl GGE*, in press.

[11] Marchetti, S. , P. Monaco, M. Calabrese & G. Totani (2006) Comparison of moduli determined by DMT and back figured from local strain measurements under a 40 m diameter circular test load in the Venice area. Proc. From the *second international flat dilatometer conference*

[12] Tolooiyan, A. and Gavin, K.; (2011) 'Modelling the Cone Penetration Test in sand using Cavity Expansion and Arbitrary Lagrangian Eulerian Finite Element Methods'. *Computers and Geotechnics*, 38 (4):482-490

[13] Stroud M. A (1974) The standard penetration test in insensitive clays and soft rocks. *Proc. Of the European Conference on Penetration Testing.* Vol 2(2) Stockholm 367-375

[14] Gavin, K.G, Igoe, D.I and O'Kelly, B. The effect of soil state on the shaft capacity of piles in sand, *paper submitted to ASCE Journal of Geotechnical and Geoenvironmental Engineering*

[15] Robertson, P.K., and Campanella, R.G., 1983. Interpretation of cone penetration tests – Part I (sand). *Canadian Geotechnical Journal*, 20(4): 718-733.

[16] Kulhawy, F.H., and Mayne, P.H., 1990. *Manual on estimating soil properties for foundation design*, Report EL-6800 Electric Power Research Institute, EPRI, August 1990.

Dynamic analysis of pile driving in dense sand

Paul Doherty[1], Kenneth Gavin[1], David Igoe[1]
[1]Department of Civil Engineering, University College Dublin, Ireland
email: paul.doherty@ucd.ie, kenneth.gavin@ucd.ie, david.igoe@icd.ie

ABSTRACT: A major series of pile tests were recently performed at the University College Dublin (UCD) dense sand research site to investigate aspects of pile behaviour for offshore renewable energy projects. One major uncertainty in the sector is whether pile driveability models developed from static load tests can be used to estimate pile resistance during installation. The accuracy of pile driveability models has major implications on the size and the cost of the equipment required when performing offshore installations. This paper describes the installation resistance developed by 275mm square concrete piles, which were driven to a penetration depth of 7m in very dense sand. One of the piles was instrumented with strain gauges and accelerometers for dynamic monitoring throughout the installation process. Signal matching analyses were used to determine the load distribution along the pile shaft at various penetration depths in order to investigate the development of pile resistance. The analysis suggested that friction fatigue effects experienced during driving were much more significant than those predicted using standard design equations. These tests also suggested that there was a significant ageing effect on the pile capacity, with the end of drive resistance being considerably lower than both the predicted medium-term capacities and the one-day restrike capacities.

KEY WORDS: driven piles, sand, pile dynamics

1 INTRODUCTION

Piles are used to support a vast array of engineered structures which include; offshore platforms, high-rise buildings, heavily loaded commercial developments, bridges, wind turbines, etc. In the case of all of these structures, piles are used to transfer the loads from the superstructure into competent bearing strata. To ensure a robust pile design, a complete lifetime assessment needs to be undertaken to consider the pile performance from the initial installation process right through to long-term loading and in-service conditions. The key factor in ensuring a suitable design is accurately quantifying the stresses surrounding the pile, and how these stresses change as the pile is installed and subsequently loaded. This paper analyzes the installation records of piles installed at a dense sand research site, and uses dynamic measurements to quantify the effective stresses acting on the pile shaft and base. These measurements are then compared to typical design methods so as to qualitatively assess the accuracy and reliability of these procedures.

2 COMMON DESIGN PROCEDURES

2.1 Shaft Capacity

Traditional design methods for estimating the shaft capacity of driven piles are based on the earth pressure approach which uses an empirical factor β to relate the local unit shaft friction, τ_f, to the vertical effective stress, σ'_{v0},:

$$\tau_f = \beta\ \sigma'_{v0} \tag{1}$$

Recent research to improve our understanding of the mechanisms controlling pile shaft friction were driven by the offshore industry, and cited the poor reliability of traditional design approaches in database studies [1,2,3]. Research campaigns were initiated in several research centres around the world to address this problem, most notably at Imperial College London. Tests performed in sand by Lehane [4] and Chow [2] using the closed-ended Imperial College Pile (ICP), which allowed continuous measurement of radial effective stress, shear stress, and unit end-bearing resistance (q_b) profiles during installation and load testing. The result of this is a significant insight into the mechanisms governing the mobilization of radial effective stress on closed-ended piles. Lehane [4] and others have shown that the local radial effective stress at failure, σ'_{rf}, which controls τ_f can be described using the Coulomb failure criterion:

$$\tau_f = \sigma'_{rf}.\tan \delta_f \tag{2}$$

where δ_f is the interface friction angle at failure. These tests showed that σ'_{rf} was primarily dependent on the radial effective stress after pile installation and equalization, σ'_{rc}, but an increase in stress was also demonstrated due to dilation during loading, $\Delta\sigma'_{rd}$, such that:

$$\sigma'_{rf} = \sigma'_{rc} + \Delta\sigma'_{rd} \tag{3}$$

A key finding of the Imperial College research was the phenomenon known as friction fatigue, whereby the equalized radial effective stress, σ'_{rc} (the primary component controlling the shaft friction), reduced with relative distance from the pile tip. Friction fatigue was thought to be caused by two main factors, namely; a high stress zone near the pile tip, and the increased number of load cycles experienced by the soil further up the shaft. Jardine et al. [5] proposed a direct correlation between σ'_{rc} and the CPT cone resistance, q_c, which is known as the IC–05 method. The effects of friction fatigue are considered through a geometric term, h/R (where h is the distance from the pile toe to the point under consideration, and R is the pile radius):

$$\sigma'_{rc}=0.029.q_c\,.[\max(h/R,8)]^{(-0.38)}\,(\sigma'_{v0}/P_{ref})^{\,0.13} \qquad (4)$$

where p_{ref} =100 kPa. To account for the lower degree of soil displacement which occurs during the installation of an open-ended pile, an effective radius R^* parameter is substituted into Eq. (4) which results in a stronger friction fatigue effect (i.e. a quicker reduction in radial stresses away from the pile tip).

$$R^*=\sqrt{(R^2\text{-}Ri^2\ )} \qquad (5)$$

An alternative expression for σ'_{rc} that is known as the UWA–05 method was suggested by Lehane et al. [3]:

$$\sigma'_{rc} = 0.03.q_c.[\max(\ h/D\ ,\ 2)]^{(-0.5)}.A_{r,eff}^{\ 0.3} \qquad (6)$$

where D is the outer pile diameter and $A_{r,eff}$ is the ratio of soil volume displaced to gross pile volume ($A_{r,eff}$ = 1 for closed-ended piles and reduces to approximately 0.1 – 0.2 for fully coring open-ended piles). The UWA-05 method has the ability to account for partial plugging during installation, using the $A_{r,eff}$ parameter. This is not possible using the ICP-05 R^* approach.

2.2 Base Capacity

Traditional design approaches for estimating the unit base resistance, q_b, of driven piles take the form:

$$q_b = N_q\ .\ \sigma'_{v0} \qquad (7)$$

where N_q is a bearing capacity factor that is usually related to the soil friction angle or relative density. These approaches have been shown to have poor predictive reliability in database studies [6]. The similarities between a CPT cone and a pile make the CPT an ideal tool when estimating the pile base resistance. In the IC-05 methodology, it was suggested that for closed-ended piles, the base resistance decreased (relative to the CPT q_c) as pile diameter increased and suggested an equation in the form:

$$q_b\ /\ q_c = 1 - 0.5\ \text{Log}\ (D\ /\ D_{CPT}) \qquad (8)$$

where D_{CPT} is the CPT cone diameter (typically 36 mm). For an unplugged open-ended pile it was suggested that $q_b = q_c$ but only acted over the annular area of the base. The effect of pile diameter on base resistance suggested by Eqn. 8 has been questioned by some workers. Lehane et al. [3] suggested that by averaging the CPT q_c value over 1.5 diameters above and below the pile base, no diameter effect on base resistance is evident. Consequently the UWA-05 method for closed-ended piles suggests:

$$q_b\ /\ q_{cav} = 0.6 \qquad (9)$$

Noting that the base resistance for open-ended piles was strongly dependent on the degree of soil displacement or plugging (as captured by the $A_{r,eff}$) which occurred during installation, Lehane et al. (2005) suggested that whilst the end bearing developed underneath the pile wall (annular area of the pile) would be expected to be equal to that developed by a closed ended pile (q_{ann} = 0.6 q_{cav}), the resistance developed below the pile plug would be lower. The plug resistance is assumed to vary from 0.15 – 0.6 q_{cav} depending on the degree of plugging during installation

In database studies both the ICP-05 and UWA-05 have shown significantly improved capacity prediction reliability over traditional methods [3,7] and have been included in the commentary of the American Petroleum Institute offshore pile design guidelines [8]. The guidelines suggest that these recent CPT based methods are in theory the preferred method over traditional approaches. However, it is suggested that more experience is required with these new methods before any one method is suggested for routine design.

3 BLESSINGTON TEST SITE

The piling described in this paper was conducted at a dense sand research site in Blessington, a small village located 25 km to the southwest of Dublin, Ireland. The test area is a dedicated research site within an active quarry, where the underlying deposits of uniform sand have been confirmed by extensive excavations. The dense sand at this site was formed by combined glacial and fluvio-glacial action that has impacted on the engineering properties of the deposit. The inter-bedded sand layers have a particle grading from silty sand to coarser sand depending on the lake level at the time of deposition. The sand is heavily over-consolidated from a combination of post depositional glacial processes and more recent excavations at the quarry. The result of this is a maximum pre-consolidation pressure of 1000kPa at ground surface. The sand is classed as fine,with D_{50} ranging from 0.1-0.15 mm. The moisture content measured in a series of boreholes has a range of 10±2%.

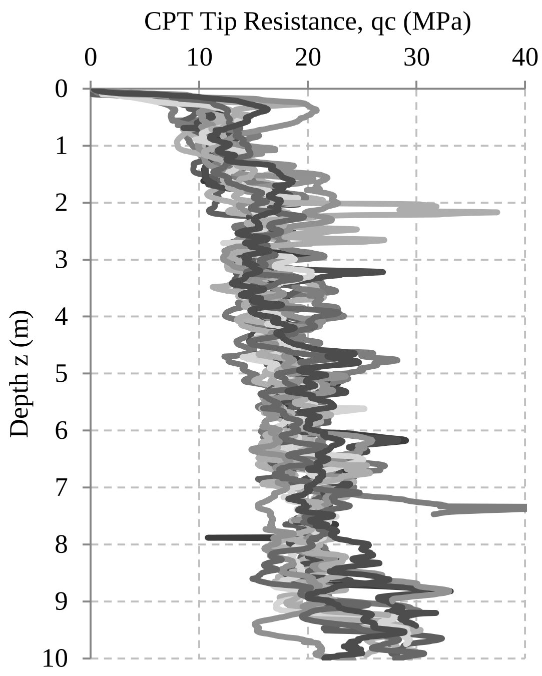

Figure 1. Cone Penetration Tests at the Blessington Site.

The cone end resistance developed during Cone penetration tests (CPT) conducted at the site are shown in Figure 1. The tip resistance value, q_c, is seen to increase from approximately 10MPa at ground surface to 25 MPa at 10 m depth. The relative density of the deposit was determined to be close to 100%. Ring shear tests were also conducted on samples of Blessington sand (Doherty et al. 2012) revealed interface friction angles which remained constant with depth. The average constant volume interface friction angle measured using a rough steel interface ranged from 33 to 38 degrees. Similar values were obtained for soil on soil shearing. These values are consistent with those expected for clean angular sand.

4 PILE DRIVING

The Blessington test site is used as a research site for field testing prototype foundations and for developing improved design procedures to quantify soil-structure interaction. As part of this project, a total of five concrete square precast piles (PC1 to PC5) with a concrete compressive strength in excess of 50 MPa were driven 7 m into dense sand. The piles were driven with a Junttan HHK4A hydraulic impact hammer mounted on a Junttan PM16 compact crawler rig, (see Figure 2). The piling rig details and hammer properties are listed in Tables 1 and 2 respectively. A beech cushion was used to reduce the peak impact stresses during driving and to protect the concrete from structural damage.

Figure 2: Pile Driving at Blessington.

Table 1. Piling Rig Properties.

Pile Driving Rig	PM16
Recommended Hammer Weight	3000-4000kg
Maximum Pile Length	16m
Leader Type	Fixed
Engine Power	179kW

Table 2. Hammer Properties.

Hammer Model	Junntan HHK 4A
Max Energy	47kNm
Max Drop Height	1.2m
Blows/minute	40-100
Raw weight	4000kg
Power Output	71kW
Operating Pressure	141 bar

The piles were driven using drop heights ranging from 200 mm to 500 mm. The theoretical energy imparted to the piles ranged from 17% to 42% of the maximum hammer energy. The hammer drop heights were increased as the piles were installed to deeper bearing strata and the soil resistance increased. This was evident by the steadily increasing blow-counts with depth illustrated in Figure 3. The maximum blow-count exceeded 100blows/250 mm as the piles approached the target embedment depth of 7m. A value of 100blows/250 mm represents an upper limit to the desirable blow-count, with higher blow-counts usually associated with structural damage of the concrete piles. In this instance, one of the concrete piles (PC3) exhibited structural damage at the pile head, and premature refusal at a depth of 6 m, whereas the remaining piles were installed without issues. The steadily increasing blow-counts suggests an increasing total resistance with depth. However, it is impossible to derive the resistance distribution over the pile from blow-counts in isolation. The dynamic tests conducted on these piles offer more insight into the load distribution along the pile.

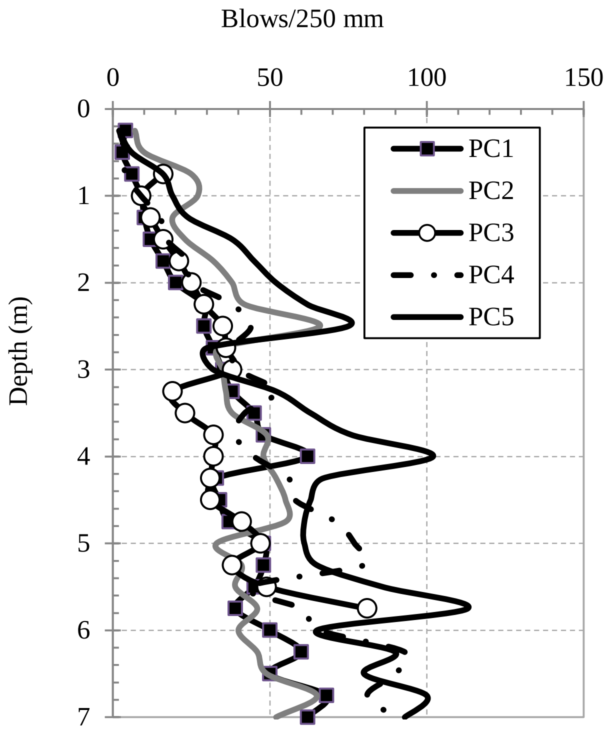

Figure 3. Blow-Counts for Concrete Piles

The cumulative blow counts required to install the piles is shown in Figure 4. Despite the relatively consistent ground conditions revealed by Figure 1, the piles required a relatively wide range (between 1000 to 1700) of blow counts to achieve the final penetration depth.

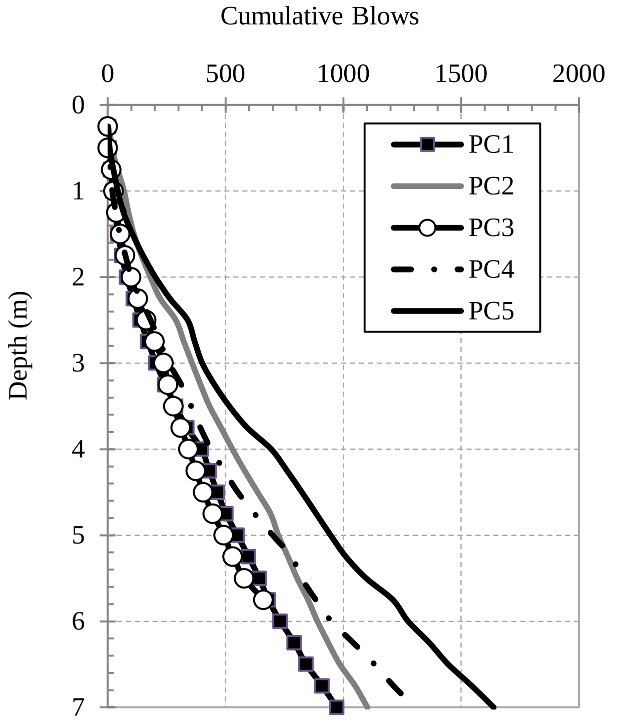

Figure 4. Cumulative blow-counts for Concrete Piles.

5 DYNAMIC TESTING

Dynamic pile testing was used to provide insight into the distribution of load on the instrumented pile. The accelerations and strains imparted into the pile are measured using gauges mounted on the pile head. The gauges record the strain and acceleration signals for every hammer impact during pile installation. This allows the total energy to be determined. The force required to advance the pile into the ground can be calculated and the total static pile resistance can be estimated by assuming a set value for the dynamic soil resistance, inertia and damping. Furthermore, by analysing the entire wave form of the strain and accelerometer signals, and by using signal matching procedures (eg. CAPWAP), it is possible to determine the distribution of resistance between the pile shaft and base. It is also possible to determine the load distribution along the pile shaft. In this study, CAPWAP analysis was performed at 3 m, 5 m, and 7 m tip embedment to determine the load distribution at various embedment depths.

6 ANALYSIS OF RESULTS & DISCUSSION

6.1 Base Resistance

The base resistance determined at three penetration depths (3 m, 5 m and 7 m below ground level) was seen to range from 857 to 1050 kN in CAPWAP analysis. The inferred base resistance was divided by the solid cross section of the piles to determine the unit end-bearing beneath the piles shown in Figure 5.

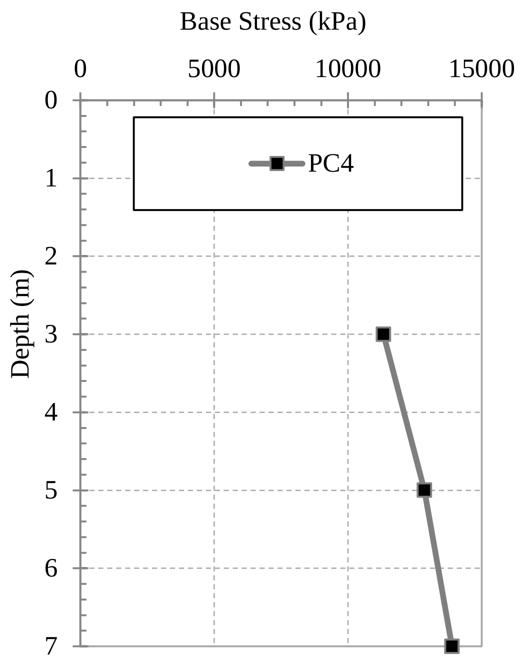

Figure 5. Unit base stresses determined from CAPWAP analysis.

The mobilised base stress is seen to increase consistently with depth. The base stress was normalised by the CPT tip resistance, averaged over a zone 1.5 diameters above and below the pile base in Figure 6. The data indicates a consistent trend with depth and an average q_b/q_c ratio between 0.6 and 0.7 which is in close agreement with predictions using the UWA-05 method (See Equation 9).

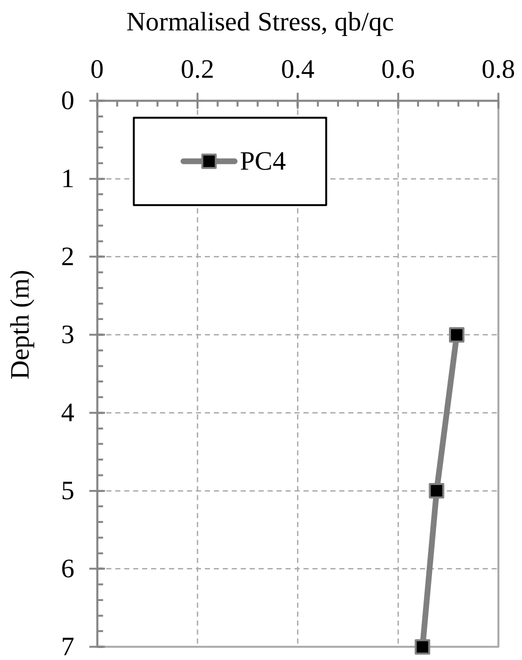

Figure 6: Normalised unit base stress.

6.2 Shaft resistance during installation

The shaft shear stresses estimated from the CAPWAP analysis is shown in Figure 7. It is worth noting that these profiles were derived from the signal matching analysis and therefore do not represent unique values but rather a best estimate of the shaft shear stresses. The shear stresses were derived for three separate pile penetrations, namely; 3 m, 5 m and 7 m. The following trends are noteworthy:

1. The maximum shear stress developed near the tip of the pile was seen to increase with depth, from 95 kPa when the pile tip was at 3 m, to 185 kPa when the pile reached 7 m.
2. A striking feature of the results is the effect of friction fatigue (the reduction of shear resistance at a given depth in the ground as the pile tip is driven further into the ground or cyclic loading is applied). For example, at 3 m below ground level the max shear stress reduced from 95 kPa when the pile tip was at 3 m, to 30 kPa (pile tip at 5 m) and finally to 1-2 kPa when the pile tip reached its final level.
3. For the deeper pile penetration levels (5 m to 7 m), there was no shaft resistance mobilised along the upper portion of the pile shaft (between 2 and 3 m below ground level).

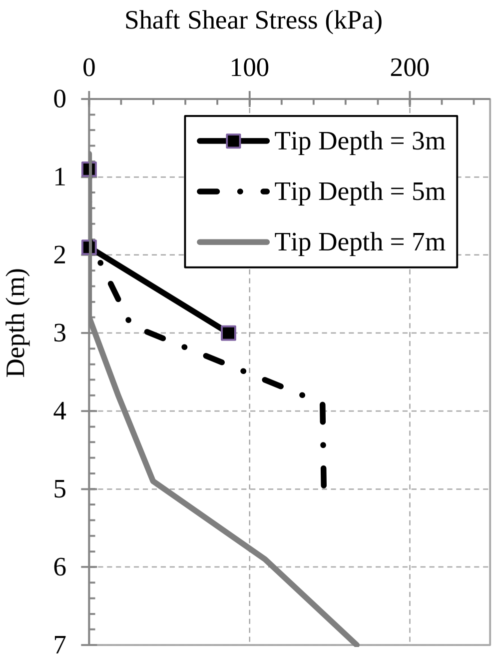

Figure 7: Shaft shear stress for concrete pile.

6.3 *Time Effects*

Re-drive tests were performed both 1 day and 10 days after pile installation (See Figure 8). These revealed that the pile shaft resistance increased substantially over time, particularly in the initial 24 hours after driving.

This observation is in keeping with observations from static tension load tests performed on 340 mm diameter, 7 m long steel open-ended piles installed at this test site. These static load tests revealed that the shaft resistance of the piles increased by ≈300% in the period between two days and 219 days after pile installation, with the majority of the capacity gains occurring in the days after pile installation.

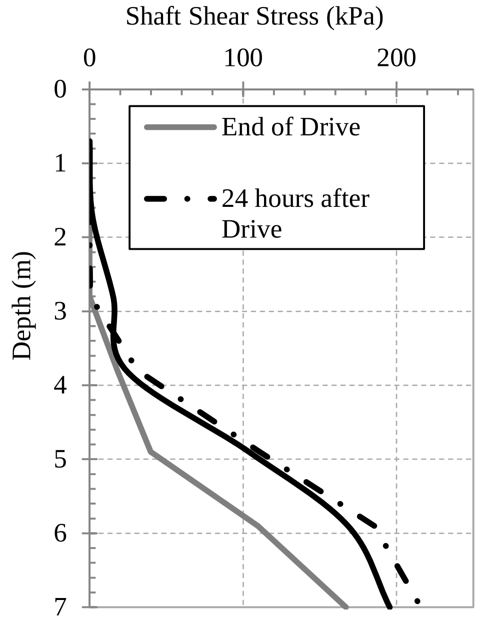

Figure 8: Re-drive test results.

6.4 *Accuracy of shaft capacity predictions*

Using the shear stress distribution inferred from the CAPWAP analyses and the measured interface friction angles, the radial effective stresses at failure, $\sigma`_{rf}$ can be estimated using Equation 2. These values are normalised by the CPT tip resistance and shown as a function of the distance from the pile tip, *h*, normalised by the pile radius, *R*, in Figure 9. The normalised stresses exhibit a steady reduction with h/R in a manner similar to the trends predicted by the UWA-05 and IC-05 design approaches. At low *h*/*R* values (i.e. near the pile base) the magnitudes of the stresses are similar to those predicted. However, as the *h*/*R* values increase, the design methods significantly over-estimate the normalised radial stress.

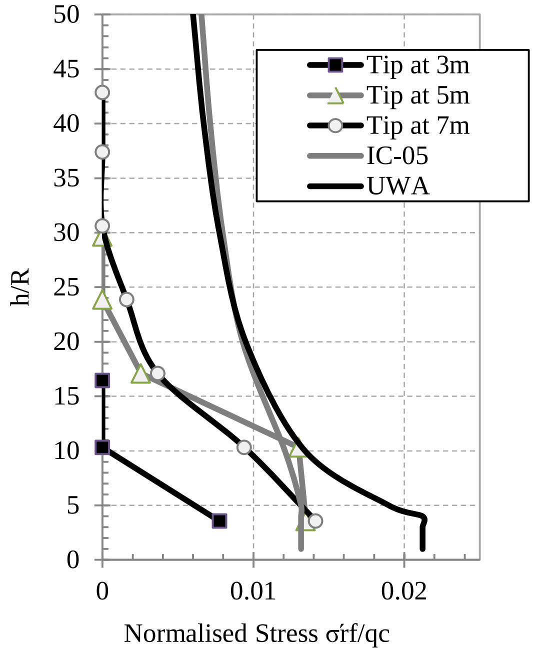

Figure 9: Normalised radial stresses for concrete pile.

7. CONCLUSIONS

A series of piles were driven at the UCD test site at Blessington. One of the piles was monitored dynamically during driving in order to determine the shaft and base shear stresses with depth. The main observations were:

1. The unit base resistance mobilised during installation was approximately 60% of the q_c resistance average over 1.5 pile diameters above and below the pile tip.
2. The maximum shaft stress which was mobilised near the toe of the pile increased with depth.
3. Friction fatigue effects were larger than those suggested using popular design methods such as IC-05 and UWA-05.
4. The measured stresses were considerably lower than the design values remote from the pile tip. This could be partly explained by near-surface effects and also partly attributable to time effects.
5. Restrike tests indicate a significant increase in shaft resistance.

ACKNOWLEDGEMENTS

The authors wish to express their gratitude to Lloyds Acoustics, Bullivant Tarranto, Science Foundation Ireland, and Enterprise Ireland for co-financing these field tests. The first author is grateful for funding received from Mainstream Renewable Power and IRCSET.

REFERENCES

[1] F. E. Toolan, and M. R. Horsnell (1992). The evolution of offshore pile design codes and future development. *Proceedings, Conference on offshore site investigation and foundation behaviour,* London, Society for Underwater Technology.

[2] Chow, F. C. (1997). *Investigations into the behaviour of displacement piles for offshore foundations*. Imperial College of Science, Technology and Medicine. London, University of London. PhD.

[3] Lehane, B. M., J. A. Schneider, et al. (2005). The UWA-05 method for prediction of axial capacity of driven piles in sand. *International Symposium on Frontiers in Offshore Geotechnics*, University of Western Australia, Perth, Taylor and Francis, London.

[4] Lehane, B. M. (1992). *Experimental Investigations of pile behaviour using instrumented field piles*. London, Imperial College PhD.

[5] Jardine, R. J., F. C. Chow, et al. (2005). *ICP design methods for driven piles in sands and clays*. London, Imperial College London: 105.

[6] Xu, X. (2007). *Investigation of the end bearing performance of displacement piles in sand*. The school of civil and resource engineering. Perth, the University of Western Australia. Phd: 403.

[7] Gavin, K. G, Igoe D., Doherty P (2011) 'Piles for offshore wind turbines: A state of the art review'. *Proceedings of ICE Journal, Geotechnical Engineering*, Volume 164, Issue 4, pp 245-256

[8] API (2007). *Recommended Practice for Planning, Designing and Constructing Fixed Offshore Platforms-Working Stress Design,* API RP2A, 22nd Edition, American Petroleum Institute, Washington, D.C.

The assessment of embodied energy and carbon of residential buildings in Ireland

Alan Armstrong [1,2], Jamie Goggins [1, 2]
[1] College of Engineering and Informatics, National University of Ireland, Galway, University Rd, Galway, Ireland
[2] Ryan Institute for Environmental, Marine and Energy Research, National University of Ireland, Galway
email: a.armstrong1@nuigalway.ie, jamie.goggins@nuigalway.ie

ABSTRACT: This paper presents a study on the embodied energy (EE) and embodied carbon (EC) of masonry residential buildings in Ireland, calculated using process based analysis in conjunction with data from the ICE V2.0 materials database [1]. This paper identifies sectors within the Irish construction industry which contribute to its carbon footprint effect, highlighting the need to tackle greenhouse gas (GHG) emissions at source through the examination of case studies. Sustainable development and the sustainability credentials of construction materials are gaining increasing importance as the environmental impact of the construction industry becomes apparent [2]. With Ireland committed to the Kyoto Protocol Agreement, it is imperative that GHG emissions associated with building materials, and indeed the entire construction industry, are minimised. Carbon footprint analysis is the first step in this regard. Furthermore, if Ireland is to establish itself as a green economy, energy efficient construction must be the way forward. Process based 'cradle-to-gate' analysis was carried out on different types of residential buildings in Ireland. EE and EC results were derived for each sub-section of construction and a carbon footprint figure allocated. Hotspot construction phases and environmentally friendly building materials, in terms of EE and EC, could be easily identified. A comparison between embodied energy and operation energy is also carried out, highlighting the significant contribution of embodied energy in the life cycle (LC) energy of residential buildings in Ireland. The contribution is proportionately higher for buildings with better Building Energy Ratings (BER).

KEY WORDS: Concrete Materials.

1 INTRODUCTION

The building industry is the greatest consumer of energy in the world, being responsible for 40% of all energy used in society [3] and responsible for 50% of global greenhouse gases emissions [4]. In 2005, the Irish construction sector was responsible for the emission of 13.81 mtCO_{2e} [5]. As a result, reducing the environmental impact and GHG emissions associated with the building industry has become essential. With Ireland committed to the Kyoto Protocol Agreement by limiting GHG emissions to 113% of 1990 levels over the period 2008-2012 and to 84% of 2005 levels by 2020, it is imperative that emissions associated with building materials, and indeed the entire construction industry, are minimised. Therefore, the sustainable development and sustainability credentials of construction materials are gaining increasing importance as the environmental impact of the construction industry becomes apparent [2].

This research aims to investigate the true carbon footprint of Irish residential masonry buildings through the life cycle assessment (LCA) of their building materials. Environmental LCA studies of buildings encompass the whole life cycle attributes; for example, energy used, pollutants and waste of installed building materials and subsequent operational usage. Energy consumption and carbon dioxide equivalent (CO_{2e}) emissions are used as metric indicators. 'Carbon dioxide equivalent', CO_{2e}, is calculated using the 100 year global warming potential (GWP) of GHG emissions according to the Kyoto Protocol and the United Nations Framework Convention on Climate Change (UNFCCC) [6], as given in Figure 1: carbon dioxide (CO_2), methane (CH_4), nitrous oxide (N_20), hydroflourocarbons (HFCs), perflourocarbons (PFCs) and sulphur hexafluoride (SF_6).

Embodied energy (EE) is the total energy consumed from direct and indirect processes associated with a product or service over its life cycle, ideally with boundaries from extraction of raw materials (cradle) to the end of the product's lifetime (including manufacturing transport, operation, and so on). System boundaries specify the confines of the processes included [7]. Embodied carbon (EC) is the sum of fuel and process related carbon emissions [7]. CO_{2e} is used as a quantifying metric indicator for EC in this study.

This paper will highlight the importance of considering the EE and EC in the construction of residential buildings through both international and national case studies. It will also show that EE and EC hotspot construction phases and environmentally friendly building materials, in terms of EE and EC, can be easily identified.

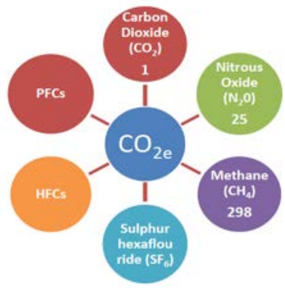

Figure 1. GWP for GHG.

2 LIFE CYCLE ASSESSMENT AND PREVIOUS INTERNATIONAL STUDIES

Currently, a lot of emphasis is placed in the construction industry and research on abating operational energy (OE) usage and resulting operational carbon (OC) emissions. It is natural for the OE and OC to be concentrated on first, as it is directly related to expenditure and costs for many energy consumers. However, serious consideration should also be given to EE and EC. Furthermore, international studies quantifying the EE and EC for residential buildings throughout the world have shown the significant contribution of EE and EC to the overall energy consumption and carbon emissions through LCA [8-11]. The Irish government has started to more closely consider this area by publishing important documentation such as the national strategy on Green Public Procurement (GPP) in 2011 [12].

This is why the entire construction system needs to be comprehensively studied. Intuitively, as OE use in homes reduces and homes become 'zero' carbon, the EE and EC in a building becomes a higher proportion of the overall energy and carbon consumption and, thus, even more significant over a complete LC. Sartori and Hestnes [13] conducted a literature survey on conventional and low-energy buildings' LC energy use across 60 case studies over 9 countries and showed that design of low-energy buildings included both a net benefit in total LC energy demand and increase in initial EE. For example, in order to achieve lower levels of OE consumption and carbon emissions, greater amounts of insulation and materials must be included at the construction stage, increasing initial EE and EC.

Material emissions and energy flows are quantified and evaluated according to LCA system boundaries. Boundaries contain the quantity of inputs and outputs associated with a product or service (building) over its LC. The ICE database v2.0 [1] selected a common boundary condition of 'cradle-to-gate' when compiling the database of building materials. This research uses the same boundary condition. Other system boundaries exist namely; 'cradle-to-site', 'cradle-to-grave' and 'cradle-to-cradle'.

Previous LCA studies carried out have shown that EE can contribute as high as 45% of the total energy consumed over a residential buildings LC [8]. International studies position the contribution of EE to overall energy consumption in the range of 26 to 45%, as summarised in Table 1[8-11]. Table 1 demonstrates the proportional breakdown of energy attributed to both OE and EE, the LCA methodology used and subsequent system boundary in some of the aforementioned international studies.

Variations exist in the international studies from a LC system boundary, lifespan, building type, structure type, location and material database perspective. Thus, widespread comparison is difficult. Assuming a linear relationship between a buildings lifespan and its OE contribution and neglecting to account for reoccurring energy and system boundary differences, an average EE contribution of 38% is calculated for the studies in interpolating for a lifespan of 60 years. Subsequently, OE holds a calculated value of 62% of the total energy usage based on the linear assumption. Focussing only on concrete built dwellings, EE and OE contributions of 35% and 65% were estimated.

Table 2 summarises the board range of LCA figures in terms of EE and EC per square metre calculated for residential properties of various structural types by international researchers [4, 8-11, 14-20]. The quantity of studies has increased in recent years due to growing popularity and significance of LCA, EE and EC. Seven from the selected studies have been conducted in the preceding four years demonstrating the gradual growth popularity. Consequently, EE and EC has filtered into governmental policy with the publishing of important documentation such as the national strategy on Green Public Procurement (GPP) for Ireland [12]. It signifies the importance EE and EC now hold at national level in Ireland.

A discrepancy is present between EE and EC values calculated for semi-detached homes in the UK [15-17] in Table 2. A difference of 3,975MJ/m^2 exists between Scottish and other UK values despite close geographic locations [15, 16]. LC system boundary differences exist, but the maximum logical extent causing an error would be transportation. Other explanations can be attributed to different building material databases and UK building regulations not applying to the Scottish system [21]. Even by accounting transportation and other differences, the gap in resulting figures is significant (3,862MJ/m^2). Thus, as the EE value presented in the Scottish study [15] seems to be well out of line with other studies, it was not further considered in this research in comparative studies.

Due to the small number of completed studies, large samples of homes were not attainable. The Irish semi-detached homes selected [11] calculated a slightly lower EC than studied UK figures [16, 17, 22]. The Irish study may have accounted for more energy efficient production methodologies of certain building materials or the minor differences in building regulations may cause the gap in calculations. Thermal insulation properties (U-value) requirements for walls in Part L of both Building Regulations differ slightly; however large similarities exists in both sets of regulations [21, 23].

A study of a Swedish apartment block [8] gave higher EE values than those in Western Europe studies [11, 15-17] by

Table 1. International residential building studies with OE and EE proportions.

Source	Building Type	Construction Type	Location	Year of Construction	Area (m^2)	Lifespan (years)	Life Cycle Boundary	Method	Percentage of OE (%)	Percentage of EE (%)
[8]	Apartment	Concrete	Sweden	2000	120	50	Cradle-to-grave	Process	55	45
[9]	BIAC Standard House	Light Timber	New Zealand	2004	94	100	Cradle-to-grave	Process	74	26
		Concrete							71	29
		Super-insulated Timber							57	43
[10]	Terraced House	Concrete	Spain	2009	222	50	Cradle-to-gate	Process	69	31
[11]	Semi-detached	Concrete	Ireland	2010	105	60	Cradle-to-gate	Process	64	36
	Apartment				75				69	31

between 433 and 733MJ/m^2 or 6 to 10%. An explanation may be due to extra thermal efficient materials requirements in Scandinavian countries to counteract climatic conditions. Similarly calculations for an Italian apartment block [14] also differ from Swedish or UK based figures [8, 16]. Building material databases are not consistent and may cause discrepancies. The Italian residential area was also built specifically to reduce its construction carbon footprint and needs consideration when interpreting results.

Adobe homes built in India [19] and Indonesia [18] are significantly less harmful to the environment than homes built in the UK or Europe according to the results obtained. The studied passive house in India [19] has 58% less EE intensity than an average analysed detached UK home [16]. Similarly, a clay single storey home in Indonesia [18] has 90% less EE intensity than an average UK bungalow [16]. Research carried out in New Zealand on a standard single storey template home found timber framed homes to be 7% less energy intensive than equivalent concrete sized homes [9]. A super-insulated timber frame home was calculated to hold greater EE/m^2 values than a concrete home and, hence, promoting construction of concrete homes in New Zealand from an EE and EC perspective. A significant difference exists in calculated EE/m^2 values between European and New Zealand figures.

UK and Irish based residential values should, in theory, relate to this research results due to geographical, legislative and climatic circumstances. Couple this with the use of the ICE database from the University of Bath [1] as a lifecycle inventory for the Irish case study buildings presented in this paper, results should be comparable. There are a very limited number of case studies buildings in Ireland whose EE and EC have been accurately estimated. The following section will present a small number of case studies to highlight the importance of further studies.

3 LCA OF IRISH MASONARY RESIDENTIAL BUILDINGS

The current Building Energy Rating (BER) system [24] of allocating alphabetical grades to residential properties based on annual OE and OC efficiency has been in operation in Ireland since the introduction of the Energy Performance Buildings Directive (EPBD) [25] in accordance with EU Directive 2002/91/EC.

The BER system is an asset rating certification system and not LCA methodology. It has limitations in relation to estimation of OE and OC. For example it assumes constant

Table 2. EE and EC intensities for International case study buildings.

Source	Building Type	Construction Type	Location	Year of Construction	Area (m^2)	Lifespan (years)	Life Cycle Boundary	Method	EE (MJ/m^2)	EC ($kgCO_{2e}/m^2$)
[8]	Apartment	Concrete	Sweden	2000	120	50	Cradle-to-grave	Process	7,033	--
[14]	Apartment Block (3-storey) – Prior to EPBD	Concrete	Northern Italy	2001	1,050	50	Cradle-to-grave	Process	4,007	-
	Apartment Block (3-storey) – Current EPBD Standards								4,158	-
	Apartment Block (3-storey) – Local Construction Methods								4,428	-
[9]	BIAC Standard Single Storey House	Light Timber	New Zealand	2004	94	100	Cradle-to-grave	Process	4,425	-
		Concrete							4,764	-
		Super-insulated Timber							5,041	-
[15]	Semi-detached	Concrete	Scotland	2005	140	-	Cradle-to-gate	Process	1,624	-
[16]	Apartment (3-storey)	Concrete	UK	2006	50	60	Cradle-to-site	Process	6,600	480
	Apartment (4-storey)				50				6,300	460
	Terraced				68				4,900	370
	Semi-detached				73				5,600	425
	Bungalow				76				8,200	620
	Detached				125				5,500	410
[17]	Semi-detached	Lightweight Timber	Southern UK	2008	65	100	Cradle-to-site	Process	-	493
		Mediumweight Concrete							-	512
		Medium-heavyweight Concrete							-	539
		Heavyweight Concrete							-	567
[11]	Semi-detached	Concrete	Ireland	2008	105	60	Cradle-to-gate	Process	-	369
	Apartment				75				-	299
[18]	Singe-landed house	Clay & Bricks	Indonesia	2008	55	40	Cradle-to-grave	Process	837	-
		Concrete							818	-
[19]	Passive House	Adobe	New Delhi, India	2009	94	50	-	Process	2,299	1,000
[10]	Terraced House	Concrete	Spain	2009	222	50	Cradle-to-gate	Process	2,757	-
[22]	Semi-detached	-	UK	2010	100	-	-	Process	-	550
[4]	Residential Area	Concrete	Finland	2011	70,000	25	Cradle-to-grave	Hybrid	-	3,200

occupancy and internal temperature. On the other hand, it only considers energy use and GHG emissions for space heating, water heating, ventilation, lighting and associated pumps and fans calculated on the basis of a national standard family with a standard pattern of occupancy [24].

Current BER [24] procedures incorrectly discount embodied or indirect features. Utilising a comprehensive LCA tool will help towards reducing emissions associated with residential buildings across Ireland. One key action published in the GPP [12] asked to explore the feasibility of developing a national methodology for LC analysis and LC costing for construction projects. This ensures LCA will hold an important role in the future of the Irish construction industry and, thus, practical application to Irish residential buildings is relevant.

More accurate methods including obtained operational data from dwellings will be considered in future work. Nevertheless, for the purpose of this study OE and OC usage was assumed from obtained BER. As OE and OC of buildings decreases in the future, the EE and EC of building materials and 'thoughtful' construction will become a predominant feature to stakeholders [20].

To properly conduct analysis a structured LCA format is required [26]. Common practice consists of four phases: goal and scope definition, life cycle inventory (LCI), impact assessment and interpretation of results [27].

3.1 Phase 1: Goal and scope of LCA

Buildings are allocated a carbon footprint based on the initial installed building materials, replacements required during its lifespan and building operational efficiency. Other aspects are ignored due to their minimal impact on the final result as demonstrated by previous studies [20, 28]. Initial building EE and EC values are calculated based on installed building materials properties and their corresponding ICE database EE and EC intensities [1].

Reoccurring EE and EC analysis is also calculated for each property based on assumptions of replacement and repair over the lifespan of the building. Agrément, National Standards Association of Ireland (NSAI), and manufacturers' technical installation documents were referred to for material's lifespan [29]. OE values are based on the BER of the building, as estimated from [24]

The lifespan of the buildings is assumed to be 60 years in Ireland [11]. Once analysis is completed a comparison between EE and OE of the buildings is carried out, highlighting the significant contribution of EE to the LC energy of residential buildings in Ireland. .

3.2 Phase 2: Life cycle inventory (LCI)

The life cycle inventory (LCI) involves the collection of data and calculations to quantify material and energy inputs and outputs of the system according to its boundaries [27]. Data collection was completed through available bills of quantities (BOQ) for each case study building. EE and EC intensities from the ICE v2.0 database were utilised [1]. Calculation methodologies are outlined in Section 4.

3.3 Phase 3 and 4: Impact Assessment and Interpretation of Results

The impact assessment evaluates the significance of potential environmental impacts based on the LCI [27]. EC (in $kgCO_{2e}$) values are calculated for each building displayed in Section 5. Results, interpretation and conclusions from the LCA are discussed in more detail in Sections 6 and 7.

4 METHOD OF ASSESSMENT

LCA methodologies are grouped into two forms – process based (PB) analysis and input-output (I-O) based analysis. Hybrid based methodologies also exists, incorporating the best attributes of both by reducing errors and improving accuracy of results [2, 30-33]. The majority of investigated research on buildings has been PB and for practicability, PB analysis is also carried out on the buildings in this research. A LCA boundary of 'cradle-to-gate' is used in this research.

Specific Agrément NSAI installation documents [29] were utilised appropriately to retrieve information if required. A consistent data selection approach was taken throughout and where no data available, a 'best fit' approach was used. Reoccurring EE and EC figures were also calculated. OE and OC values were extracted from obtained BER.

5 RESULTS

Results of the LCA carried out on the case study buildings are shown below in Figure 2 and Figure 3 demonstrating that OE and OC contribute highest to the studied buildings total energy use over a lifespan and showing a breakdown of LC energy and carbon for each building. The comparison of operational and embodied properties proves the significance EE and EC hold in the LC of a building. Table 3 gives details of each case study building and total calculation values.

OE and OC are calculated based on a 60 year lifespan using the BER obtained for each property. From the examined buildings, OE and OC contribution varies from 73 to 84% and 66 to 77% of total LC energy use and GHG emissions, respectively. These values are slightly higher than the international studies presented in Section 2, which positioned OE contribution between 55 and 74% of total energy consumption [8-11].

Conversely, initial EE and EC values calculated range from 13 to 22% and 19 to 30%, respectively. Previous research found EE to account for between 29 and 45% with an average value of 35% [8-11]. Some of the aforementioned studies may have accounted reoccurring values as total EE and EC. Reoccurring EE and EC represent the smallest proportion of LC use in the Irish residential case study buildings, averaging between 3 and 5% of total consumption for both. Reoccurring energy can be as high as 12% of total energy consumption [34]. Thus, for the Irish case study residential buildings, the total EE and EC contributions are between 16 and 27% and 23 and 34%, respectively.

As future buildings reach 'zero carbon' standard, the proportion of OE and OC will drop substantially. EE and EC will begin to dominant energy and carbon consumption of buildings.

An assumption that OE or OC contribute less to total energy or carbon consumption as the BER improves is provisionally satisfied. The B2 rated bungalows are operationally more energy efficient than a B3 2-storey house or C1 rated apartment. OE and OC contribute less in the bungalows than in the apartment block or 2-storey house. The difference between the apartment block and detached house is more complex. The 2-storey detached house analysed slightly deviates from the assumption. Further examination finds that a large house area and various property features significantly increase initial EE.

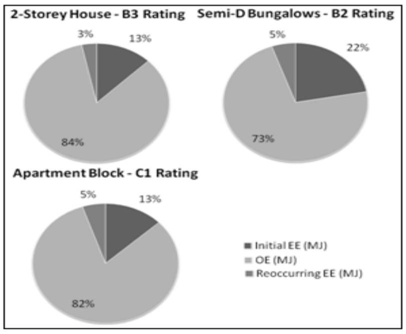

Figure 2. Breakdown of life cycle carbon in case study.

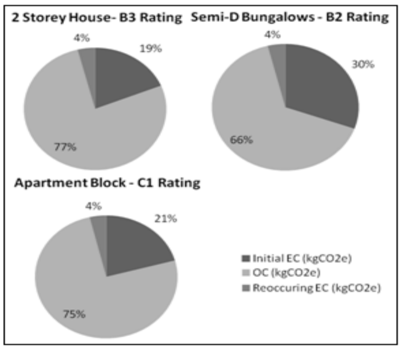

Figure 3. Breakdown of life cycle energy in case study.

The studied apartment block contained a tiered unorthodox structural design. Features did not represent common apartment blocks. If a conventional design was in place, results may reduce initial EE of materials and satisfy initial study assumptions.

Figure 4 demonstrates initial EE and EC values calculated for each dwelling per m^2 of floor plan. Each value is reached by summing EE and EC values for each construction phase (substructure, superstructure, roof, finishes). External works were not considered to allow for comparison and consistency.

The semi-detached bungalows hold the highest EE and EC values per m^2 of floor area. Bungalows have shown to contain the largest EE and EC per m^2 of floor from previous research [16]. The proportion of EE and EC required for the roof to that of the house for single storey dwellings often leads to higher overall EE and EC per m^2 compared to multi-storey buildings constructed of similar materials, see for example Table 4. Hammond and Jones [16] found similar values for EE and EC per m^2 of floor plan. Both studies utilize the same LCI.

6 DISCUSSION

Table 4 shows the majority of buildings' initial EE and EC are contained in the substructure and superstructure. On average, 66% EE and 75% EC is held in both. The total contribution of installed concrete, steel, insulation and aggregate building materials is responsible for between 55-68% EE and 70-75% EC respectively. Environmentally friendly products, from an EE and EC perspective, and their sustainable LC credentials are highlighted. Early material selection at design phase of construction can greatly reduce carbon output of a building over its lifespan.

It is a significant EE and EC construction phase hotspot observation which is important in reducing the overall carbon footprint of a building into the future. Previous studies prove that in order to reduce overall energy use in buildings, great importance needs to be focused on not only reducing OE but also paying attention to building material choice [35].

Consideration for the sustainable LC credentials of building materials installed in the substructure and superstructure will have a major influence on a buildings LC environmental impact. Manufacturers of building materials may be forced to implement more environmentally favourable methods of production.

Table 3. LCA - Energy and carbon breakdown in case study.

Building Type	Year of Construction	Area (m^2)	Total LC Energy Use (MJ)	Total LC Carbon Use ($kgCO_{2e}$)
Semi-D Bungalows	2004	180	5,356,755	329,177
2-storey House	2006	405	13,523,006	818,596
Apartment Block	2006	370	14,644,999	882,024

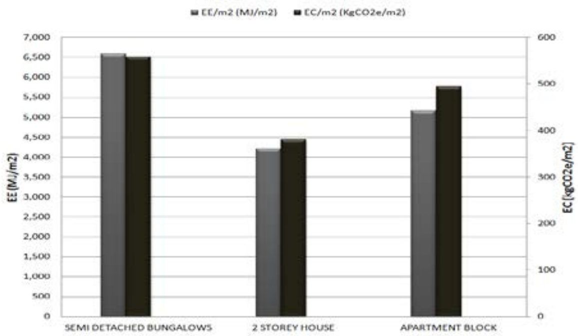

Figure 4. Initial EE & EC per m^2 of floor plan distribution in case studies.

7 CONCLUSION

The results presented in this study demonstrate the breakdown in LC energy and carbon in some residential masonry buildings in Ireland. With the construction industry as the greatest consumer of global energy [3], associated GHG emissions caused by the sector need to be correctly reduced or mitigated where possible. Full carbon footprint analysis of residential buildings is one method of addressing the problem. With Ireland wishing to promote 'green' energy efficient construction, examination of residential case study buildings was imperative. The LCA approach has been vindicated through the publication of the GPP document [12]. Current BER procedures fail to account for embodied features of a building, focusing solely on the operational properties.

A comparison between embodied and operational energy and carbon highlighted the contribution of EE and EC in the LC of some Irish residential buildings. This contribution is proportionately higher for buildings with better BERs.

OE and OC contribution varies from 73-84% and 66-77% of total LC energy and carbon use respectively. Total EE and EC calculated values range from 16-27% and 23-34% respectively, inclusive of reoccurring values. Future 'zero carbon' homes will increase the embodied contribution from a LC perspective and so, EE and EC of building materials will gain more intense observation and scrutiny. Hotspot construction phases, in terms of EE and EC, were pinpointed as areas to focus GHG emission mitigation strategies. Substructure and superstructure initial EE and EC contribution to total embodied consumption were calculated at 66% and 75% respectively.

Table 4. Initial EE and EC Construction Phase Analysis.

EE (%)	Substructure	Superstructure	Roof	Finishes
Apartment Block	31%	38%	15%	17%
Semi-detached Bungalows	27%	33%	27%	13%
2-Storey House	32%	37%	19%	12%
Average	*30%*	*36%*	*20%*	*14%*
EC (%)	**Substructure**	**Superstructure**	**Roof**	**Finishes**
Apartment Block	40%	36%	12%	13%
Semi Detached Bungalows	40%	31%	20%	10%
2-Storey House	41%	37%	13%	8%
Average	*40%*	*35%*	*15%*	*10%*

ACKNOWLEDGMENTS
The first author would like to acknowledge the financial support of the Irish Research Council for Science Engineering and Technology (IRCSET) to this research.

REFERENCES

[1] Hammond G. and Jones C. Inventory of Carbon and Energy (ICE) v2.0. 2011 20th September 2011]; Available from: <http://people.bath.ac.uk/cj219/ >.
[2] Goggins J., Keane T., and K. A., The assessment of embodied energy in typical reinforced concrete building structures in Ireland. Energy and Buildings, 2010. 42(5): p. 735-744.
[3] Berge Bjorn, The ecology of building materials, Architectural Press, Editor. 2000: Oxford, UK.
[4] Heinonen, J., A. Säynäjoki, and S. Junnila, A Longitudinal Study on the Carbon Emissions of a New Residential Development. Sustainability, 2011. 3(8): p. 1170-1189.
[5] Acquaye A. A. and D.A. P., Input -output analysis of Irish construction sector greenhouse gas emissions. Building and Environment, 2009. 45(3): p. 784-793.
[6] UNFCCC, Kyoto Protocol to the United Nations Framework Convention on Climate Change, http://unfccc.int/resource/docs/convkp/kpeng.pdf, Editor. 1998.
[7] Hammond, P.G. and C. Jones, A BSRIA guide Embodied Carbon The Inventory of Carbon and Energy (ICE), F. Lowrie and P. Tse, Editors. 2010, BSRIA.
[8] Thormark, C., A low energy building in a life cycle—its embodied energy, energy need for operation and recycling potential. Building and Environment, 2002. 37(4): p. 429-435.
[9] Mithraratne, N. and B. Vale, Life cycle analysis model for New Zealand houses. Building and Environment, 2004. 39(4): p. 483-492.
[10] Bribián, I.Z., A.A. Usón, and S. Scarpellini, Life cycle assessment in buildings: State-of-the-art and simplified LCA methodology as a complement for building certification. Building and Environment, 2009. 44(12): p. 2510-2520.
[11] O'Loughlin, N., Embodied CO2 of housing construction in Ireland, in Architecture Ireland 247. 2010. p. 70-71.
[12] Department of Environment Community and Local Government, National Action Plan on Green Public Procurement (GPP), Department of Environment Community and Local Government, Editor. 2011: Dublin, Ireland.
[13] Sartori, I. and A.G. Hestnes, Energy use in the life cycle of conventional and low-energy buildings: A review article. Energy and Buildings, 2007. 39(3): p. 249-257.
[14] Aste, N., R.S. Adhikari, and M. Buzzetti, Beyond the EPBD: The low energy residential settlement Borgo Solare. Applied Energy, 2009. 87(2): p. 629-642.
[15] Asif, M., T. Muneer, and R. Kelley, Life cycle assessment: A case study of a dwelling home in Scotland. Building and Environment, 2007. 42(3): p. 1391–1394.
[16] Hammond, G.P. and C.I. Jones, Embodied Carbon: The Concealed Impact of Residential Construction in Global Warming: Engineering Solutions, A.M. Ibrahim Dincer, Arif Hebasli, T. Hikmet Karakoc, Editor. 2010, Springer: New York. p. 367-384.
[17] Hacker, J.N., et al., Embodied and operational carbon dioxide emissions from housing: A case study on the effects of thermal mass and climate change. Energy and Buildings, 2008. 40(3): p. 375-384.
[18] Utama, A. and S.H. Gheewala, Life cycle energy of single landed houses in Indonesia. Energy and Buildings, 2008. 40(10): p. 1911-1916.
[19] Chel, A. and G.N. Tiwari, Thermal performance and embodied energy analysis of a passive house – Case study of vault roof mud-house in India. Applied Energy, 2009. 86(10): p. 1956-1969.
[20] Smith, B.P., Whole-life carbon footprinting, in The Structural Engineer. 2008. p. 15-16.
[21] Department for Communities and Local Government UK, Building Regulations - Energy efficiency requirements for new dwellings, Department for Communities and Local Government, Editor. 2007: Department for Communities and Local Government, Eland House, Bressenden Place, London, SW1E 5DU.
[22] Jones, C., Embodied Carbon: A Look Forward, in Sustain Insight Article: Volume I. 2011, Sustain Ltd.
[23] Department of Environment Community and Local Government, Building Regulations 2011 - Technical Guidance Document L - Conservation of Fuel and Energy - Dwellings, Department of Environment Community and Local Government, Editor. 2011: Dublin, Ireland.
[24] Sustainable Energy Authority of Ireland. Building Energy Rating (BER). 2010; Available from: <http://www.seai.ie/Your_Building/BER/>.
[25] European Commission, Directive 2002/91/EC of the European Parliament and of the Council of 16 December 2002 on the energy performance of buildings. Energy Performance Buildings Directive, E. Union, Editor. 2003: Official Journal of the European Communities.
[26] ISO, ISO 14040 - Environmental Management—Life Cycle Assessment—Principles and Framework. 1997: International Organization for Standardization.
[27] T. Ramesh, Ravi Prakash, and K.K. Shukla, Life cycle energy analysis of buildings: An overview. Energy and Buildings, 2010. 42(10).
[28] Chen, T.Y., J. Burnett, and C.K. Chau, Analysis of embodied energy use in the residential building of Hong Kong. Energy, 2001. 26(4): p. 323-340.
[29] 2National Standards Association of Ireland (NSAI). Agrément Certificates. 2011; Available from: <http://www.nsai.ie/Our-Services/Certification/Agement-Certification/Search-Agrements-Certificates.aspx>.
[30] Treloar, G.J., A Comprehensive Embodied Energy Analysis Framework, in Faculty of Science and Technology. 1998, Deakin University: Geelong, Australia.
[31] McCaffrey, M.F., An I-O hybrid methodology for environmental LCA of embodied energy and carbon in Irish products and services - A study of reinforced concrete, in College of Engineering and Informatics. 2011, National University of Ireland, Galway (NUIG): Galway, Ireland.
[32] Crawford, R.H., Validation of the Use of Input-Output Data for Embodied Energy Analysis of the Australian Construction Industry. Journal of Construction Research, 2005. 6(1): p. 71-90.
[33] Bullard, C.W., P.S. Penner, and D.A. Pilati, Net Energy Analysis - Handbook for Combining Process and Input-Output Analysis. Resources and Energy, 1978. 1(3): p. 267-313.
[34] Shukla, A., G.N. Tiwari, and M.S. Sodh, Embodied energy analysis of adobe house. Renewable Energy, 2009. 34(3): p. 755-761.
[35] Thormark, C., The effect of material choice on the total energy need and recycling potential of a building. Building and Environment, 2006. 41(8): p. 1019-1026.

Rotation capacity and plastic redistribution of forces in reinforced concrete beams

Niklas Bagge[1], Alan O'Connor[2], Claus Pedersen[3],
[1,3]Department of Bridges, Rambøll Danmark A/S, Hannemanns Allé, Copenhagen, Denmark
[2]Department of Civil, Structural and Environmental Engineering, Trinity College Dublin, Museum Building, Ireland
email: [1]nklb@ramboll.dk, [2]alan.oconnor@tcd.ie, [3]clp@ramboll.dk

ABSTRACT: According to standards for concrete structures, such as Eurocode 2, it is allowable to make use of plastic redistribution of sectional forces in continuous beams at the ultimate limit state for the design and assessment of existing structures. Plastic analysis, where applicable, can result in an increased load carrying capacity. It can therefore be beneficial for owners/managers of structures in reducing maintenance costs through avoidance of unnecessary repair and/or optimisation of the repairs which are shown to be necessary. An essential factor to determine the degree of plastic redistribution of sectional forces is the rotation capacity of critical regions, also expressed in terms of the structural ductility, which depends on material, structural and loading factors. In this regard, this paper presents a study of deformable strut-and-tie model for the analysis of plastic rotation capacity. The model takes into account parameters of importance, such as nonlinear behaviour of reinforcing steel and concrete, shear forces and shear reinforcement. Fundamental to the proposed model is the truss analogy, describing the flow of internal forces and subsequently the deformation of the structure.

KEY WORDS: Nonlinear analysis; Plastic rotation capacity, Reinforced concrete beams.

1 INTRODUCTION

Due to ageing bridge stocks, higher load rating requirements and limited budgets, it is necessary for bridge owners/managers to optimize maintenance actions and thereby reduce costs. One way to accomplish cost savings, is via avoidance of unnecessary repair and/or optimisation of the repairs which are shown to be necessary, through the use of more sophisticated techniques in assessment of existing bridges. In this regard for assessment at the flexural limit state it can prove beneficial, where applicable, to use plastic analysis.

According to Eurocode 2 [1] it is allowable to make use of analysis based on the theory of linear elasticity with limited moment redistribution for continuous reinforced concrete beams at the ultimate limit state without an explicit check of the rotation capacity. The maximum allowed moment redistribution is 20 % or 30 % depending on the ductility of the reinforcing steel. Provided sufficient rotation capacity exists it is also allowable to make use of plastic analysis and non-linear analysis at the ultimate limit state.

The available moment redistribution of reinforced concrete structures is influenced by several factors, with the available rotation capacity of critical regions identified as the most important factor. Further, the rotation capacity depends on factors related to material, structure and loading. The main factors for linear elements in bending are the concrete compressive strength, the reinforcing steel strength and ductility, the level of interaction between reinforcing steel and concrete, the size and shape of the cross section, the tensile and compressive reinforcement ratio, the shear reinforcement ratio, detailing of the reinforcement bars, the slenderness ratio and moreover the static system and associated load characteristics [2].

To ensure sufficient rotation capacity for desired moment redistribution, a numbers of models with various levels of complexity have been developed. Generally the more complex models are based on the definition of moment-curvature or moment-rotation relationship, whilst simpler models are based on graphs for the rotation capacity [2]. For instance Eurocode 2 and Model Code 2010 [1, 3] propose a graphical model for estimating available rotation capacity as a function of the ratio of concrete compression height and effective height, ductility of reinforcement steel, concrete strength and shear slenderness.

2 ANALYSIS OF ROTATION CAPACITY

2.1 General description

A fundamental condition in analysis of the available degree of moment redistribution for statically indeterminate reinforced concrete beams is sufficient ductility. It implies higher or equal plastic rotation capacity in the critical region in comparison to the required rotation capacity for a given redistribution [1]. Based on this consideration it is necessary to combine structural analysis for determination of the distribution of sectional forces and required plastic rotation, with analysis of the rotation capacity.

In this paper the analysis of the plastic rotation capacity of critical discontinuities of a structural member are based upon the deformable strut-and-tie model (DST model). The model originates from the general strut-and-tie model developed by Schlaich and Schäfer [4]. The general strut-and-tie model is further developed by Michalka [5] and refined by do Carmo [6] in order to determine the nonlinear rotation behaviour of plastic regions. Fundamental to the model is the truss analogy, describing the flow of internal forces and subsequently the deformation of the structure. The DST model is composed of struts with parallel stress fields of uniaxial compression, ties with parallel stress of uniaxial tension and nodes in highly bi- or triaxially stressed zones [3].

Generally the strut-and-tie methodology for plastic analysis of discontinuous regions, such as plastic hinges, consists of the following stages:

- define an idealized truss model (orientation of struts and ties),
- determine strut-and-tie forces from equilibrium,
- determine and check the strut-and-tie cross sections,
- check the geometry of nodes,
- refine the model if necessary [3].

In relation to the general strut-and-tie model, the DST methodology is extended with an additional step. The extension consists of determination of the deformation of struts and ties considering the internal forces, cross sections and compatibility conditions, respectively.

Plastic hinges idealized by a truss model consist of compressive, tensile and shear zones. The structure shown in Figure 1 is a typical form of plastic hinge region at the intermediate support of a continuous beam. The idealized truss model in Figure 1 illustrates a compressive zone of concrete and reinforcement bars in the bottom (struts), a tensile zone of reinforcement surrounded by concrete in the top (ties) and a shear zone of concrete between the inclined cracks (inclined struts).

2.2 Compressive behavior of concrete

In order to model the concrete compression behavior in a realistic manner a non-linear constitutive law is considered. The adopted stress-strain relationship is defined by Equation (1) according to Eurocode 2 [1]:

$$\frac{\sigma_c}{f_{cm}} = \frac{k\eta - \eta^2}{1 + (k-2)\eta} \quad (1)$$

where $f_{cm} = f_{ck} + 8\ MPa$, $k = 1.1E_{cm}\varepsilon_{c1}/f_{cm}$, $\eta = \varepsilon_c/\varepsilon_{c1}$, $E_{cm} = 22(f_{cm}/10)^{0.3}$, $\varepsilon_{c1} = 0.71f_{cm}^{0.31}$, $\varepsilon_{cu1} = 3.5$ ‰ for $f_{ck} < 50\ MPa$, $\varepsilon_{cu1} = 2.8+24[(98-f_{cm})/100]^4$ for $f_{ck} \geq 50\ MPa$ and f_{cm} is the cylinder compressive strength. Equation (1) is valid for $0 < |\varepsilon_c| < |\varepsilon_{cu1}|$.

In situations with closed transversal reinforcement in regions where rotation capacity is analysed, the compressive concrete is considered as confined. The confinement, and thereby the additional lateral stresses, leads to increased compressive strength and ductility for the concrete, whilst the other mechanical characteristics are practically unaffected [7]. A practical way to take into account this variation in concrete strength and ultimate strain is through a modification of the constitutive law according to Eurocode 2 [1] and *fib* recommendations [8]. Figure 2 illustrates the stress-strain relationships for confined and unconfined concrete, based upon these constitutive laws. For strains higher than the strain corresponding to the compressive strength, the stress-strain relationship is considered as linear for confined concrete. Eurocode 2 [1] proposes a linear approximation of the increased compressive concrete strength due to confinement according to Equation (2) and Equation (3), the strain corresponding to the maximum concrete stress according to Equation (4) and the ultimate concrete strain according to Equation (5):

$$f_{cm,c} = f_{cm}\left(1.000 + 5.0\frac{\sigma_2}{f_{cm}}\right) \quad if\ \frac{\sigma_2}{f_{cm}} \leq 0.05 f_{cm} \quad (2)$$

$$f_{cm,c} = f_{cm}\left(1.125 + 2.5\frac{\sigma_2}{f_{cm}}\right) \quad if\ \frac{\sigma_2}{f_{cm}} > 0.05 f_{cm} \quad (3)$$

$$\varepsilon_{c1,c} = \varepsilon_{c1}\left(\frac{f_{cm,c}}{f_{cm}}\right)^2 \quad (4)$$

$$\varepsilon_{cu1,c} = \varepsilon_{cu1} + 0.2\frac{\sigma_2}{f_{cm}} \quad (5)$$

where f_{cm} is the unconfined strength, $f_{cm,c}$ is the confined

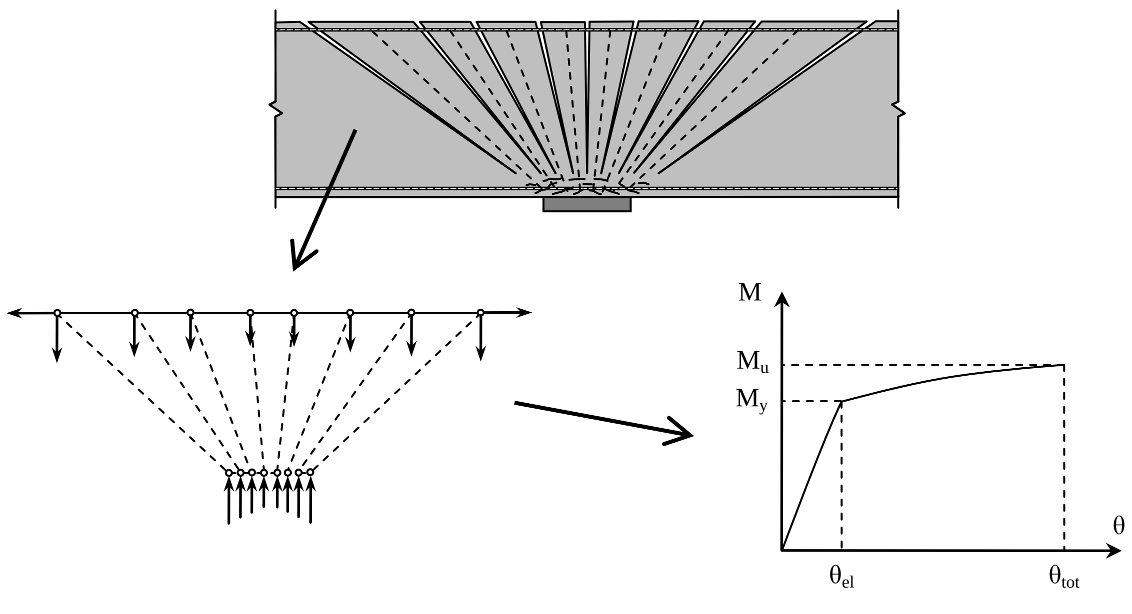

Figure 1. Plastic region and corresponding truss model for DST analysis and its moment-rotation relationship.

strength, σ_2 is the effective lateral confining stress, ε_{c1} is the strain corresponding to f_{cm}; $\varepsilon_{c1,c}$ is the strain corresponding to $f_{cm,c}$, ε_{cu1} is the ultimate strain for unconfined concrete and $\varepsilon_{cu1,c}$ is the ultimate strain for confined concrete.

The proposed model for concrete confinement is defined for elements under axial loads with uniform stress distribution. However, the model is also applicable for beams with varying stress distribution and less effective confinement. In such situations Model Code 1990 advocates a "solid" border in the neutral axis, thereby limiting lateral expansion [7].

2.3 *Tensile behavior of reinforcement*

In the tensile ties which represent reinforcing steel embedded within the concrete, tensile forces is transmitted from the steel bars to the concrete between cracks by bond forces. The impact of the surrounding concrete, leads to increased stiffness for the tensile tie when compared with unembedded reinforcing steel. Neglecting this so-called "tension stiffening effect" underestimates the stiffness of the structural member, and thereby overestimates the rotation capacity [7].

The Model Code 1990 [7] proposes a modification of the constitutive law for tensile reinforcing steel to take the tension stiffening effect into account. In order to consider varying steel strain along the structural member for cracked concrete, mean values of steel strains are used. The deformable behavior of embedded steel is given by Equation (6) to Equation (9) and is represented in Figure 3:

1. Uncracked stage, $0 < \sigma_s \leq \sigma_{sr1}$:

$$\varepsilon_{s,m} = \varepsilon_{s1} \tag{6}$$

2. Crack formation stage, $\sigma_{sr1} < \sigma_s \leq \sigma_{srn}$:

$$\varepsilon_{s,m} = \varepsilon_{s2} - \frac{\beta_t\left(\sigma_s - \sigma_{sr1}\right) + \left(\sigma_{srn} - \sigma_s\right)}{\sigma_{srn} - \sigma_{sr1}}\left(\varepsilon_{s2} - \varepsilon_{sr1}\right) \tag{7}$$

3. Stabilized cracking stage, $\sigma_{srn} < \sigma_s \leq f_{yk}$:

$$\varepsilon_{s,m} = \varepsilon_{s1} - \beta_t\left(\varepsilon_{sr2} - \varepsilon_{sr1}\right) \tag{8}$$

4. Yielding stage, $f_{yk} < \sigma_s \leq f_{tk}$:

$$\varepsilon_{s,m} = \varepsilon_{sy} - \beta_t\left(\varepsilon_{sr2} - \varepsilon_{sr1}\right) + \delta\left(1 - \frac{\sigma_{sr1}}{f_{yk}}\right)\left(\varepsilon_{s2} - \varepsilon_{sy}\right) \tag{9}$$

where $\varepsilon_{s,m}$ is the mean steel strain, ε_{s1} is the strain of reinforcement of uncracked concrete, ε_{s2} is the strain of reinforcement in the crack, ε_{sr1} is the steel strain at the point zero slip under cracking forces reaching f_{ctm}, ε_{sr2} is the strain of reinforcement at the crack under cracking forces reaching f_{ctm}, f_{ctm} is the mean value of concrete tensile strength, β_t is the integration factor for the steel along the transmission length ($\beta_t = 0.40$ for short term loading and $\beta_t = 0.25$ for long term loading in pure tension), ε_{sy} is the strain at yield stress, ε_{su} is the strain for unembedded reinforcement reaching f_{tk}, ε_{smu} is the mean strain reaching f_{tk}, σ_s is the steel stress, σ_{sr1} is the steel stress in the crack, σ_{srn} is the steel stress in the crack when stabilized crack has formed (last crack), f_{yk} is the characteristic yield strength of reinforcement, f_{tk} is the characteristic tensile strength of reinforcement and δ is the coefficient to take into account the ratio f_{tk}/f_{yk} and the yield stress f_{yk}.

2.4 *Rotation capacity*

The procedure to determine the plastic rotation capacity according to the DST model considers the sectional behavior, regarding equilibrium of internal forces, compatibility and constitutive laws, respectively. The adopted compatibility law is based upon the Bernoulli-Euler's hypothesis, whereby plane sections remain plain and perpendicular to the neutral axis during bending. Further, the rotation of the defined strut-and-tie model for a certain load effect (moment and shear force) is calculated according to Equation (10):

$$\theta = \frac{\left|\delta_{tension}\right| + \left|\delta_{compr}\right|}{z} \tag{10}$$

where θ is the rotation for the current load effect, $\delta_{tension}$ is the elongation of tension ties, δ_{compr} is the contraction of the concrete struts and z is the inner lever arm. In Equation (10) the contraction of the inclined compressions struts is neglected.

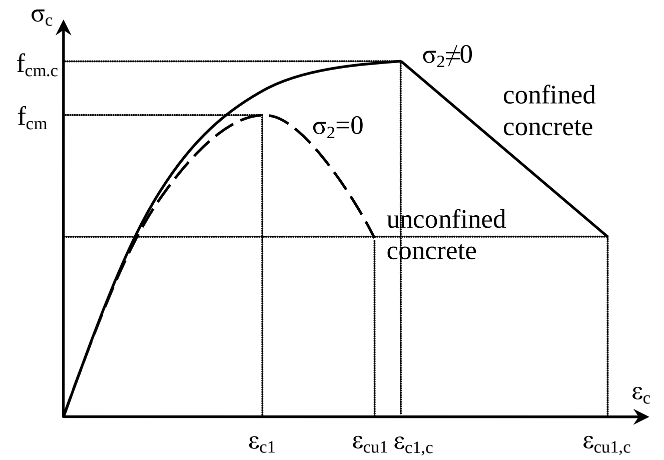

Figure 2. Stress-strain relationship for confined and unconfined concrete in compression.

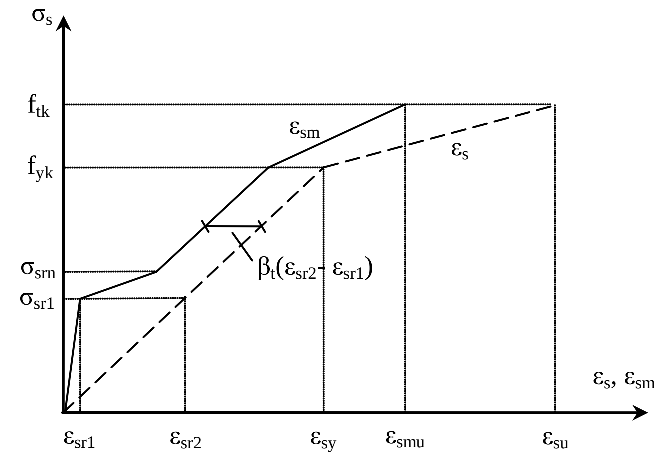

Figure 3. Stress strain for embedded and unembedded reinforcement steel.

The plastic rotation capacity is defined according to Equation (11), as illustrated in Figure 1:

$$\theta_{pl} = \theta_{tot} - \theta_{el} \tag{11}$$

where θ_{pl} is the plastic rotation capacity, θ_{tot} is the total rotation at ultimate load and θ_{el} is the rotation at yield stress of reinforcing steel.

The choice of the angle between the horizontal axis and the inclined struts, representing the shear region, is of importance in analysis concerning the influence of shear forces on plastic rotation capacity [9]. In the original model, according to the classical truss analogy by Mörsch [10], compression struts with an angle of inclination of 45° were proposed. Due to the impact of longitudinal reinforcement and interlocking in the cracks on the inclination of the struts, a balanced truss model was proposed in Eurocode 2 [1], limiting the inclination of shear struts to between 22° and 45°. Analysis presented in this paper is based on recommendation by do Carmo [6], considering average inclination of cracks equal to 35°, 50°, 60°, 70° and 90° in relation to the horizontal axis.

In addition to the inclination of the compression struts, the width of the discontinuous region, i.e. the plastic length, is of importance. The most adequate width of plastic hinge seems to equal the effective depth, but in beams with low tensile reinforcement ratios and low ductile steel the assumption could overestimate the plastic rotation capacity [9].

3 SENSITIVITY STUDY

According the presented DST model, a sensitivity study of the plastic rotation capacity is performed for discontinuities in the reinforced concrete beams. The basic parameters for the study are (except where stated otherwise): cross section 400×200 mm^2, concrete cover 25 mm, concrete strength C50/60, steel yield strength 500 MPa, steel modulus of elasticity 200 MPa, steel ductility class C ($f_{tk} / f_{yk} = 1.15$, $\varepsilon_{uk} = 7.5$), compression reinforcement 2Φ6 mm, shear reinforcement Φ8s100 mm and shear slenderness $\lambda = 3$ ($\lambda \approx M/(V \cdot d)$).

The sensitivity study is presented considering the relationship between the ratio of compression height x, effective cross section height d and the plastic rotation capacity θ_{pl}.

Consequently, the sensitivity analysis considers two types of failure: (i) rupture of reinforcing steel for low amounts of tensile reinforcement and (ii) concrete crushing failure for higher amount of tensile reinforcement. When failure occurs simultaneously in the concrete and the reinforcing steel, a peak value (maximum) of the plastic rotation capacity is expected.

3.1 *Concrete strength*

Three values of concrete strength are investigated: C30/37, C50/60 and C90/105. In Figure 4 the reduction in plastic rotation capacity for increased concrete strength for the same value of *x/d*, considering concrete crushing failure, is observed. The difference is explained by the diverging ultimate strain for the concrete classes C30/37 and C50/60 in comparison to concrete class C90/105, and the relationship between height of the compression zone and concrete strength. For concrete class C90/105 the unconfined ultimate strain is 2.8‰, in comparison to 3.5 ‰ for the concrete classes C30/37 and C50/60. The lower ultimate strain leads to a shift of the peak to the left and thereby a more brittle behavior, i.e. lower plastic rotation capacity. Comparing concrete class C30/37 and C50/60 with equal ultimate strain, the difference indicated in Figure 4 is due the higher concrete strength for the same amount of tensile reinforcement with decreased *x/d* ratio.

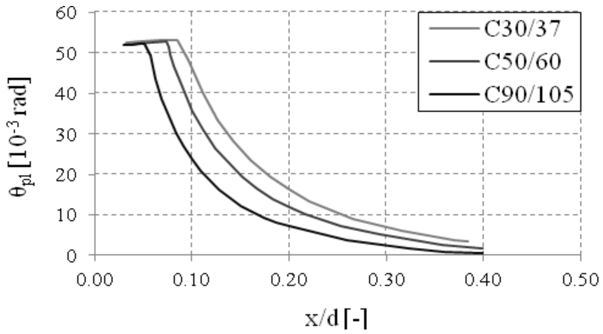

Figure 4. Relationship between *x/d* and θ_{pl} depending on concrete compression strength.

3.2 *Reinforcing steel ductility*

In Eurocode 2 three steel ductility classes are defined based on the ultimate strain and the steel hardening ratio. Table 1 gives the steel ductility parameters adopted in the sensitivity study, based on the lower limit for each class.

Table 1. Reinforcing steel ductility classes.

Class	A	B	C
f_{tk}/f_{yk}	1.05	1.08	1.15
ε_{su}	2.5 %	5.0 %	7.5 %

Figure 5 illustrates the importance of the steel ductility for the structural behavior when failure occurs by rupture of reinforcing steel. The influence of steel ductility is negligible for sections failed by concrete crushing. Figure 5 demonstrates the increase in plastic rotation capacity as the steel ductility increases. The increased ultimate strain results in a shift of the peak to the left with increased plastic rotation capacity, due to higher maximum curvature values. Further, the higher hardening ratio results in an extension in the width of the plastic hinge. Thereby the plastic rotation capacity increases, whilst the peak location remain almost the same [2, 11].

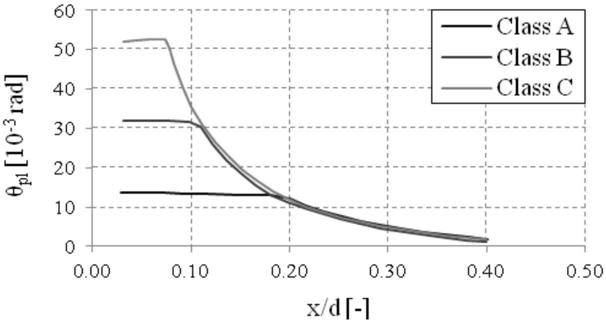

Figure 5. Relationship between *x/d* and θ_{pl} depending on ductility class for longitudinal reinforcement.

3.3 Shear force

The results of the sensitivity study concerning the influence of shear force presented in Figure 6 indicates a negative impact on the structural ductility, i.e. the higher shear force (lower $M/(V{\cdot}d)$ ratio) the lower the plastic rotation capacity. Significantly, this tendency is inconsistent with earlier research [2, 12], where the favorable effect of shear forces on plastic rotation capacity has previously been expected to result from a shift of tensile forces due to the inclination of compression struts thereby enlarging the width of the plastic hinge. In the proposed DST model presented in Section 2, the shift of forces in the tension ties is considered, however due to the adoption of a constant width of the plastic hinge the beneficial effect is neglected. Eurocode 2 [1] implies a corresponding tendency. Similarly, experimental results by do Carmo [13] have suggested an unfavorable influence of shear forces on the plastic rotation capacity.

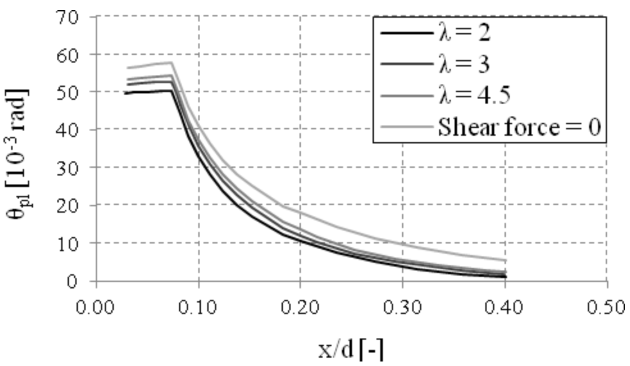

Figure 6. Relationship between *x/d* and θ_{pl} depending on shear slenderness λ.

3.4 Concrete confinement

For analysis of concrete confinement according to the model presented in Section 2, the reinforcement arrangement and concrete characteristics are identified as the inputs to the model. This parameter study focuses on the influence of the arrangement of the transverse and the longitudinal compressive reinforcement.

3.4.1 Shear reinforcement ratio

Figure 7 shows a significant dependence between the amount of transverse reinforcement and the plastic rotation capacity. Because confining of the concrete increases the ultimate strain, the peak is shifted to the right in comparison to the case with unconfined concrete. A higher degree of confinement therefore results in increased plastic rotation capacity. Simultaneously, the concrete confinement gives a slight increased concrete compressive strength, causing a reduction in the depth of neutral axis for the same amount of tensile reinforcement. As shear reinforcement only has an influence on the concrete characteristics, the plastic rotation capacity is only affected when the failure is due to concrete crushing. In Figure 7 Φ is the diameter of the reinforcing bar and s is the distance between the centers of the stirrups.

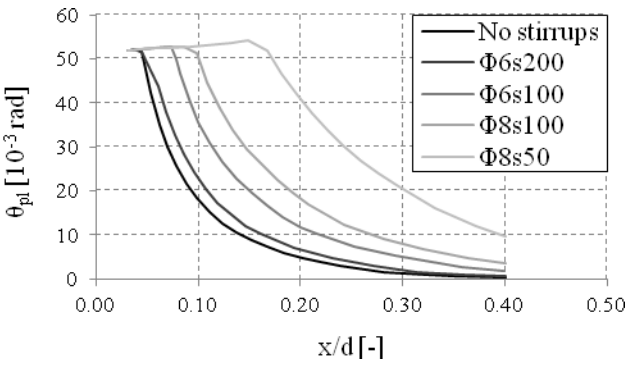

Figure 7. Relationship between *x/d* and θ_{pl} depending on amount of transverse reinforcement.

3.4.2 Longitudinal reinforcement ratio

Considering Figure 8, it is apparent that the influence of compressive longitudinal reinforcement is negligible in terms of the plastic rotation capacity for the investigated beam setup. In Figure 8 Φ is the diameter of the reinforcing bar.

For analysis of sections at the intermediate supports of continuous beams the concrete confinement is expected to be more efficient in comparison to the considered concrete confinement, due to the contribution of the support plate to lateral stresses.

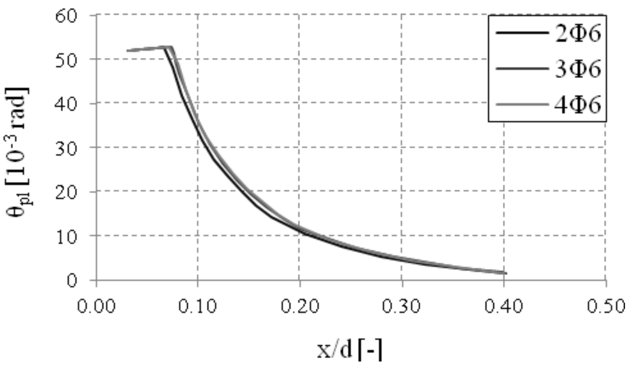

Figure 8. Relationship between *x/d* and θ_{pl} depending on amount of longitudinal reinforcement in compression.

3.5 Plastic width

The applied DST model implies a constant width of the plastic hinge. It is observed in Figure 9 that the obtained plastic rotation capacity is strongly dependent on the adopted width of the plastic hinge.

In application of the DST model, Lopes [9] proposes a constant plastic hinge width equal to the effective height of the cross section, based on experimentally studies by several researchers. This approximation seems to be sufficiently accurate for practical proposes. The simplified model proposed for calculation of the plastic rotation capacity for continuous beams and one way spanning slabs according to Eurocode 2 [1], implies a width of the plastic region equal to 1.2 times the cross section height.

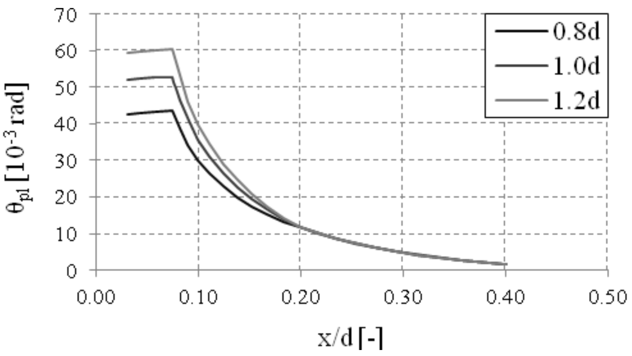

Figure 9. Relationship between *x/d* and θ_{pl} depending on adopted width of plastic hinge.

4 CONCLUSION

This paper presents the deformable strut-and-tie (DST) model for analysis of rotation capacity and level of plastic redistribution of forces in reinforced concrete beams. A sensitivity study is performed to identify the relative influence of modeled parameters. As the DST model is a physical model based on equilibrium of internal forces, it has inherent advantages for understanding the behavior of critical regions of concrete members. However it does require assumptions concerning crack-pattern and plastic hinge width.

The influence of concrete class, steel ductility class, shear force, amount of transverse and longitudinal reinforcement and width of plastic hinge, were investigated. The study demonstrates the importance of adequate models for reinforcing steel and concrete, and their interaction in the member. Steel ductility seems to be a significant parameter in the analysis of the deformable behavior. Moreover the concrete strength and ductility, including the effect of confinement, are essential to consider.

Analysis of the impact of shear forces on the plastic rotation capacity shows some degree of ambiguity. The presented DST model indicates a unfavorable influence of shear forces in accordance to Eurocode 2, but other researchers argue for a favorable influence of shear forces. Thus, a generalization is not advisable.

ACKNOWLEDGEMENTS

The authors would like to gratefully acknowledge the financial assistance provided by the TEAM project, a Marie Curie Initial Network founded by European Commission 7th Framework Program (PITN-GA-2009-238648).

5 REFERENCES

[1] European Committee for Standardization (CEN), *Eurocode 2: Design of concrete structures – Part 1-1: General rules and rules for buildings*, CEN, Brussels, Belgium, 2004.
[2] Comité Euro-International du Béton (CEB), *Ductility of Reinforced Concrete Structures*, Bulletin 242, CEB, Lausanne, Switzerland, 1998.
[3] International Federation for Structural Concrete (fib), *Model Code 2010 – First complete draft*, Bulletin 55-56, fib, Lausanne, Switzerland, 2010.
[4] Schlaich J., Schäfer K. (1984), Konstruieren im Stahlbetonbau (Design and detailing of structural concrete), *Betonkalender 1984*, Part 2, W. Ernst & Sohn, 787-1005
[5] Michalka C. (1986), *Zur Rotationfähigkeit von Plastischen Gelenken in Stahlbetonträgern* (Rotation capacity of plastic hinges in reinforced concrete beams), PhD Thesis, University of Stuttgart, Germany.
[6] do Carmo R. (2004), *Rotação Plástica e Redistribuição de Esforços em Vigas de Betão de Alta Resistência*, PhD Thesis, University of Coimbra, Portugal.
[7] Comité Euro-International du Béton (CEB), CEB-FIP Model Code 1990, Thomas Telford Services Ltd, London, U.K., 1993.
[8] International Federation for Structural Concrete (fib), *Structural Concrete*, Bulletin 51-54, Second Edition, fib, Lausanne, Switzerland, 2009.
[9] Lopes S. and do Carmo R. (2006), Deformable strut and tie model for the calculation of plastic rotation capacity, *Computers and Structures 84*, Elsevier, 2174-2183.
[10] E. Mörsch, *Concrete-Steel Construction (Der Eisenbetonbau)*, The Engineering News Publishing Company, New York, U.S., 1909.
[11] Bigaj A. (1999), Structural dependence of rotation capacity of plastic hinge in RC beams and slabs, PhD Thesis, Delft University, Netherlands.
[12] Shakir A. (2005), *Moment redistribution in reinforced concrete structures*, PhD Thesis, University of Alberta, Canada.
[13] do Carmo R., Lopes S. (2005), Influence of shear force and transverse reinforcement ratio on plastic rotation capacity, *Structural Concrete*, Volume 6, Issue 3, Thomas Telford and fib, July, 1464-4177.

Load capacity of small scale plate girders

Niall Holmes[1]
[1]Department of Civil and Structural Engineering, Dublin Institute of Technology, Bolton Street, Dublin 1, Ireland
Email: niall.holmes@dit.ie

ABSTRACT: This paper presents results from an experimental programme using small scale steel bridge plate girder sections subject to patch and concentrated loading. The sections, 1000mm long x 280mm deep, had varying flange and web thicknesses as well as varying stiffener spacing. The failure loads were compared with predicted capacities derived from large-scale tests and demonstrate that the small scale experimental sections were capable of producing similar responses in terms of behaviour and load capacity in bridge situations. The findings from this study demonstrate the possibility that small scale sections could be used to predict similar responses in large scale tests. The results also highlight the influence of varying member properties on the load capacity and post-buckling behaviour of steel plate girders.

KEY WORDS: Plate girders; patch loading; concentrated loads; buckling.

1 INTRODUCTION

A plate girder, in its simplest form, consists of two flange plates welded on to a web plate to form an I-section, as shown in Figure 1. The top and bottom flanges primarily resist the axial tensile and compressive forces that arise from the bending action due to applied loads. The web plate resists the shear force applied to the beam while the fillet welds, that connect the various members, ensure the transfer of longitudinal shear from the flanges. The vertical stiffeners can increase the load carrying capacity of the section and are required at load points. Stiffeners are also required at supports (known as end posts) to prevent local failure of the web in bearing and buckling.

Where the capacity of other forms of construction is exceeded, plate girders are capable of transmitting higher loads over longer spans. For economic design, they achieve this by employing tension field action, where the stresses in the web panel are redistributed, thus increasing the load capacity in excess of the elastic buckling load. For the tension field to develop the web panel must first undergo buckling and the section evolves from elastic to a post-buckling behaviour, which eventually results in collapse. As loading increases, the combination of shear and bending may initiate yielding, buckling or a combination of both, which depends on the depth of the section (d), the thicknesses of the web (t_w) and flange (t_f), and the stiffener spacing (b).

Plate girders optimise the use of steel, so over the length of the section there is a saving in the self-weight. Also, by altering the thicknesses of the flange and web plates and the stiffener spacing, the load carrying capacity can be increased. Therefore, it is possible to design a plate girder section with a high strength/weight ratio.

This paper will review empirical and theoretical expressions developed to calculate the capacity of plate girders undergoing patch and concentrated loads and compare these with the experimental results from a series of tests using small scale sections. Previous work in this area [1-3] has shown the potential of small scale sections to mimic large-scale beams accurately.

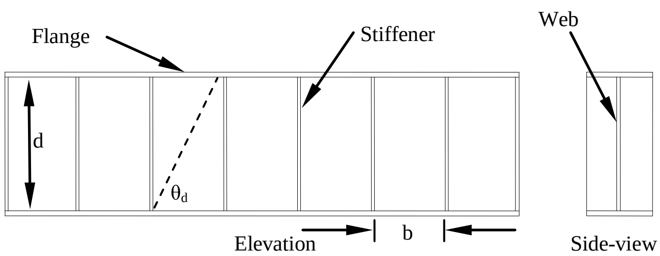

Figure 1. Typical plate girder section.

2 THEORETICAL REVIEW

When a web panel is subjected to a uniform stress (τ), prior to buckling, principal tensile stresses will act at an inclination of 45^0 and 135^0 to the bottom flange, as shown in Figure 2. Upon further loading, this state of stress will continue until τ equals the critical shear stress, τ_{cr} at which point the panel will buckle. Equation 1 is an expression developed [4] to determine τ_{cr} by assuming that the boundary conditions

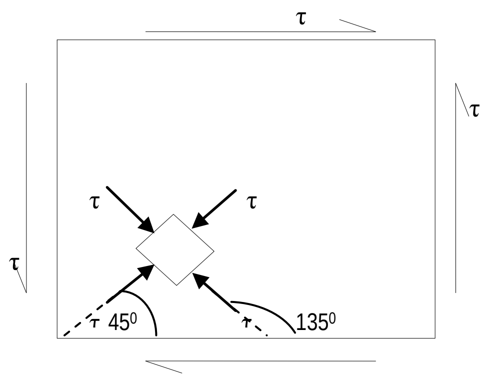

Figure 2. Elastic behaviour.

between the web, flanges and stiffeners are simply supported, where k is a buckling co-efficient depending on the aspect ratio (Equations 2 and 3), E is Young's Modulus and υ is Poisson's ratio.

$$\tau_{cr} = k\frac{\pi^2 E}{12\left(1-\upsilon^2\right)}\left(\frac{t}{d}\right)^2 \tag{1}$$

$$k = 5.35\left(\frac{d}{b}\right)^2 + 4 \qquad \frac{b}{d} \le 1 \tag{2}$$

$$k = 5.35 + 4\left(\frac{d}{b}\right)^2 \qquad \frac{b}{d} > 1 \tag{3}$$

Once the critical stress is reached, the web begins to buckle and loses its capacity to sustain a further increase in compressive stress. Any additional load has to be supported by a tensile membrane stress field (σ_t) that develops at an angle θ. Here the section will behave as a Pratt truss with the vertical stiffeners and the tension field acting as struts and chords respectively. In this state, the flanges bend inwards as they are of finite rigidity.

As the loading increases, the tensile membrane stress exerts a greater pull on the flanges. Eventually, the combination of the tensile membrane stress and the initial buckling stress will cause the web panel to buckle and yield. This stress condition is denoted as σ_{yw}. The membrane stress that causes the web to yield is denoted as σ_t^y. Failure finally occurs when four plastic hinges (XWZY) form in the flanges, as shown in Figure 3.

The three phases (elastic, post-buckling and flange contribution) that contribute to the failure of the section is given in Equation 4 [5] as the ultimate shear capacity where Mp* is a non-dimensional flange strength parameter ($=\frac{Mp}{dt2\sigma_{yw}}$), θ is the angle of inclination for σ_t^y, the tensile membrane stress, σ_{yw} is the yield stress of the web and τ_{yw} is the shear stress of the web.

$$Vs = \tau_{cr} d t_w + \sigma_y^t t_w Sin^2\theta\left(dCot\theta - b\right) + 4 d t_f Sin\theta\sqrt{\sigma_{yw} M_p^* \sigma_y^t} \tag{4}$$

Elastic Post-buckling Flange contribution

It should be noted that these equations assume that the boundary condition between the web and flange is simply supported which leads to a simplification of the calculations. It has been suggested that the actual boundary condition is closer to a fixed one for the practical design of plate girders [6]. This implies that current design specifications who utilize the simply supported condition may present a conservative design for the web panels where the portion of buckling strength from the web may be much greater than the post-buckling capacity.

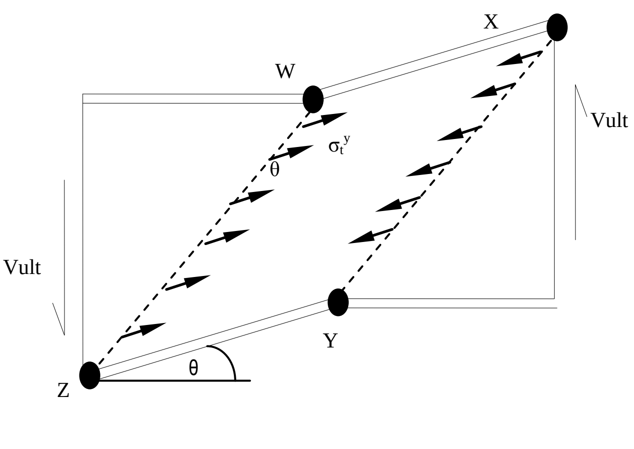

Figure 3. Failure mechanism of a web panel subjected to shear.

3 PATCH LOADING

Patch or localised edge loading is a frequent occurrence on plate girder beams. This type of loading is important to consider as local over-stressing of the beam may lead to structural failure. Concentrated loads can be accommodated by inserting web stiffeners at the point of application but the location of patch loads are more difficult to predict and deal with simply. A useful method to protect against localised loading failure is to limit the magnitude of the applied load (P_u) to a proportion of the contact area (c_p) where $P_u = c_p \times p_y$. However, while this method may be adequate for stocky webs, it does not correlate well with actual failure loads [7]. The ultimate effect of a patch load is the creation of plastic hinges forming in the top flange and yield lines in the web panel, known as web crippling.

Following a series of full-scale tests on slender plate girders subjected to patch loads [8], Equation 5 was developed to calculate the ultimate load where P_u is the ultimate or collapse load (tonnes) and t_w is the web thickness. This equation assumes that the capacity of a member subject to patch loads is only dependent on the square of the web thickness with no other property contributions.

$$Pu = 0.85 t_w^{\ 2} \tag{5}$$

It has been concluded [9] that the poor correlation between Equation 5 and actual collapse loads from experimental testing is due to the post-buckling strength reserve derived from the interaction between the web and flange plates. For this, Equations 6 and 7 were proposed [9,10,11] which are dependent on the mechanism of collapse, either by web yielding or bending respectively where M_f represents the plastic moment of resistance of the flange and σ_w is the stress in the web. The collapse load taken for design purposes is the lesser of the two equations.

$$Pu = 2\sqrt{4M_f \sigma_w t_w} + \sigma_w t_w c_p \tag{6}$$

$$Pu = 0.5 t_w^{\ 2}\sqrt{\left(E\sigma_w \frac{t_f}{t_w}\right)}\left[1 + \frac{3c_p}{d}\left(\frac{t_w}{t_f}\right)^{1.5}\right] \tag{7}$$

4 TESTING PROGRAMME

The experimental programme consisted of constructing 10 mild steel plate girder beams with varying web thicknesses (t_w = 2, 4 (for patch loads only), 5.85 and 8mm), flange thicknesses (t_f = 2, 5.85 and 8mm) and stiffener spacing (b = 450, 267 (for patch loading only) 225 and 100mm). The experimental dimensions and loading regime for each section are shown in Table 1. Each beam was 1000mm long, 280mm deep with a flange breadth of 65mm. Two loading types were employed, namely patch (a localised load over a 200mm portion of the top flange) and concentrated (at mid-span) where a stiffener was placed located under the applied load. The load positions are shown on Figures 4-7.

Table 1. Geometry and loading conditions for each beam

Beam ID	Web thickness (t_w mm)	Flange thickness (t_f, mm)	Stiffener spacing (b, mm)	Loading condition
P1	2	5.85	267	Patch
P2	4	5.85	267	Patch
P3	5.85	5.85	267	Patch
P4	8	5.85	267	Patch
C1	2	5.85	450	Concentrated
C2	8	5.85	450	Concentrated
C3	2	2	450	Concentrated
C4	2	8	450	Concentrated
C5	2	5.85	100	Concentrated
C6	2	5.85	225	Concentrated

The mild steel had yield strength of 275N/mm^2. The weld that connected the web and flange plates and the web and stiffener plates was a 3mm fillet weld. Before testing, a grid was drawn on the web plate of each beam to view the buckling of the plate both during and after the test. The loads on the beams were applied using a Dennison load apparatus with simple supports at each end. The patch load was applied using a 200mm long x 20mm thick plate. This was placed on the top flange in order to spread the concentrated point load from the point of application over a 200mm length of the flange.

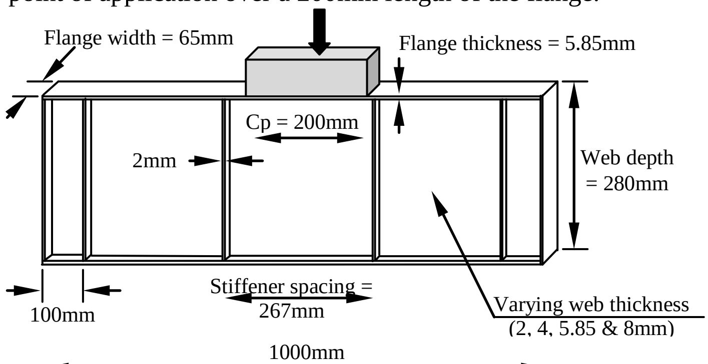

Figure 4. Dimensions for Beams P1-4

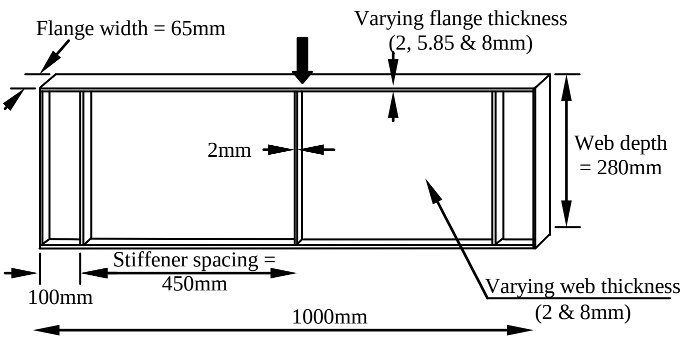

Figure 5. Dimensions for Beams C1-4.

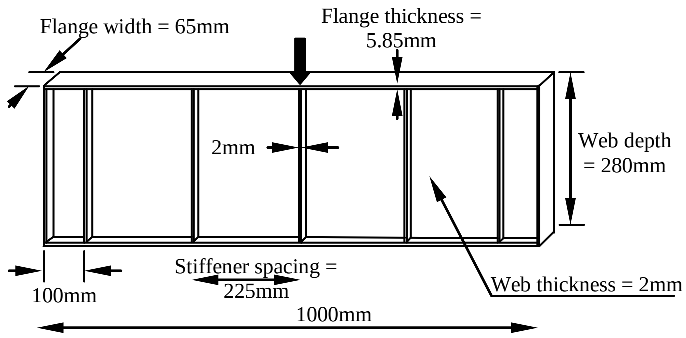

Figure 6. Dimensions for Beams C6.

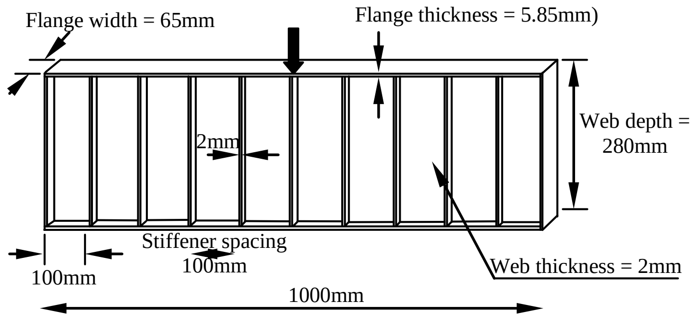

Figure 7. Dimensions for Beam C5.

Load location

5 EXPERIMENTAL RESULTS

5.1 Patch loading results

Figure 8 presents the failure loads for Beams P1-4 with varying web thickness (2, 4, 5.85 and 8mm) subject to patch loads over a distance (c_p) of 200mm. The results show an approximately linear increase in load capacity with increasing web thickness.

This trend of increasing experimental load capacity with web thickness appears to give good agreements with predicted load capacities using Equations 5-7 for web thicknesses up to 4mm. However, beyond this point the relationship is not as accurate, especially using Equation 7. The mode of failure for the thinner web thicknesses (2 and 4mm) was due to web yielding, as demonstrated by the significant yield lines that formed in the web panels (see Figure 9). For the thicker web panels (5.85 and 8mm), the method of failure was by web bending, as yield lines did not form but failure did occur by plastic hinges forming in the flange plates (Figure 10). The poor correlation for the thicker web panels is an unexpected result particularly as the method of failure, for which Equation 7 was developed for, was observed.

Equations 5-7 assume that the other elements of the girder only give a minor contribution to the load capacity. This assumption appears to be valid here for small-scale plate girders up to 4mm web thickness. When using Equation 7, an over-capacity is obtained that could have serious implications as typical web thicknesses for deep plate girder beams (~2500mm) are between 20 and 30mm. For concentrated loads, as will be shown in section 5.1, the other elements of the girder do influence the load capacity.

5.2 Concentrated loading results

5.2.1 Varying flange thickness

Figure 11 presents the failure loads for beams C3 & C4 with a 2mm thick web with 2mm (C3) and 8mm (C4) thick flanges. As can be seen, an increase in failure loads exists with increasing flange thickness. For beam C3 (t_f = 2mm), the results appear to compare reasonably well with Equations 8 and 9, which are simplified expressions derived [5] from Equation 4 where V_{yw} is the shear force required to produce yielding of the web panel and is given as $\tau_{yw} d t_w$.

$$Vs = V_{yw}\left[\frac{\tau_{cr}}{\tau_{yw}} + \sqrt{3}Sin^2\theta\left(Cot\theta - \frac{b}{d}\right)\frac{\sigma_t^y}{\sigma_{yw}}\right] \tag{8}$$

$$\frac{\sigma_t^y}{\sigma_{yw}} = \sqrt{\left(1-\left(\frac{\tau_{cr}}{\tau_{yw}}\right)^2\left(1-\frac{3}{4}Sin^2\theta\right)\right)} - \frac{\sqrt{3}}{2}\frac{\tau_{cr}}{\tau_{yw}}Sin2\theta \tag{9}$$

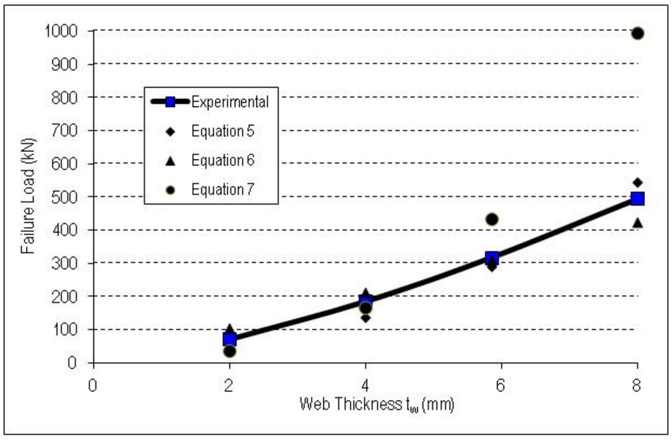

Figure 8. Experimental and predicted loads for beams P1-4

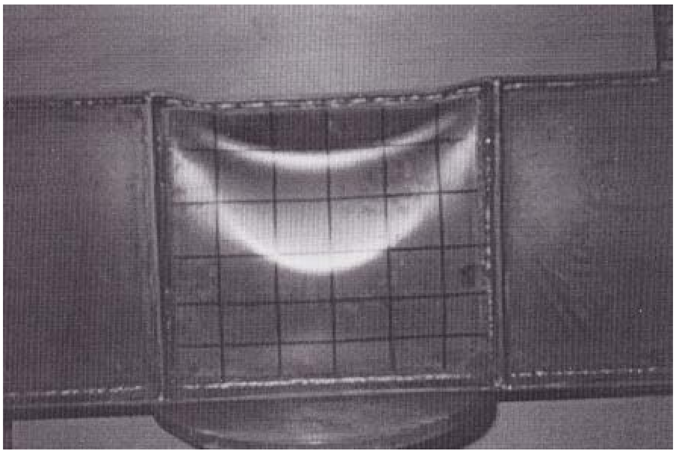

Figure 9. Yield lines formed in the web panels of Beam P1.

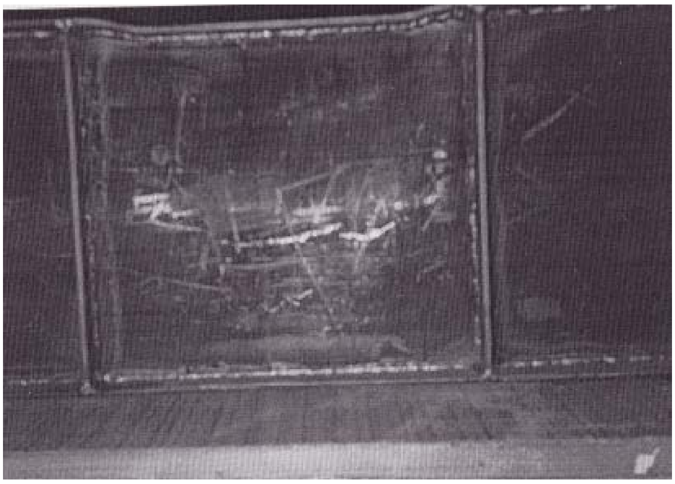

Figure 10. Bending of web panels in Beam P3.

The differences between predicted and experimental results (approximately 6%) may be due to the assumption that they do not consider any contribution to the load capacity from the flanges.

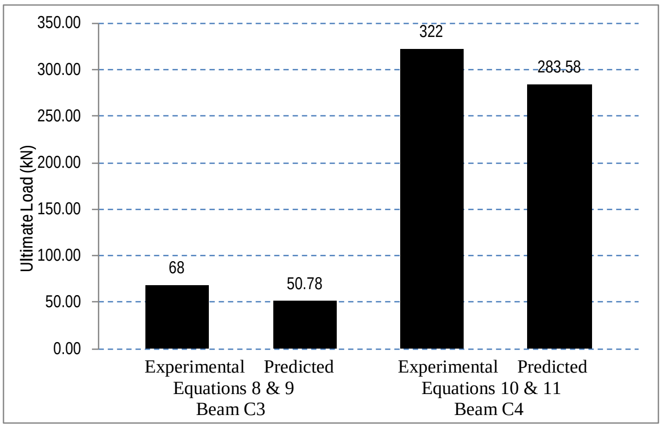

Figure 11. Comparison between experimental and predicted failure loads for beams C3 & C4.

For thicker flanges, it has been proposed [5] that, for full-scale tests, the distance between the plastic hinges on the flange, denoted as c, becomes equal to the stiffener spacing b and a tension field will develop at an inclination of 45^0. By substituting the value for c into b and taking θ as 45^0, Equation 10 has been proposed to calculate the limiting value of flange strength ($Mp^*_{\lim}$) at which point a picture frame mechanism will occur. Equation 10 can be simplified into Equation 11 which determines the ultimate shear capacity for thicker flanges.

$$M^*_{p\lim} = \frac{1}{8}\left(\frac{b}{d}\right)^2\left[\sqrt{\left(1-\frac{1}{4}\left(\frac{\tau_{cr}}{\tau_{yw}}\right)^2\right)} - \frac{\sqrt{3}}{2}\left(\frac{\tau_{cr}}{\tau_{yw}}\right)\right] \tag{10}$$

$$Vs = V_{yw}\left[\frac{1}{4}\frac{\tau_{cr}}{\tau_{yw}} + \frac{\sqrt{3}}{2}\sqrt{\left(1-\frac{1}{4}\left(\frac{\tau_{cr}}{\tau_{yw}}\right)^2\right)} + 4\sqrt{3}\left(\frac{d}{b}\right)M^*_p\right] \tag{11}$$

As shown in Figure 11, Equations 10 and 11 do give a reasonable comparison with the experimental results here.

5.2.2 Influence of thick webs

For thicker webs, like Beams C2 and C6 (t_w = 5.85 and 8mm respectively), Equation 12 was proposed as it is assumed that the web panel may yield before it buckles so no tension field will develop and failure will occur by a picture frame mechanism [5].

$$Vs = V_{yw}\left[1 + 4\sqrt{3}\left(\frac{d}{b}\right)M_p^*\right] \tag{12}$$

As shown in Figure 12, the failure loads for C2 and C6 were 365kN and 113.25kN respectively. Using Equation 12, the calculated failure loads for C2 is 343.1kN which gives a good approximation. A similar result can be seen for the experimental and predicted load capacities in beam C6 where again a reasonable comparison can be observed.

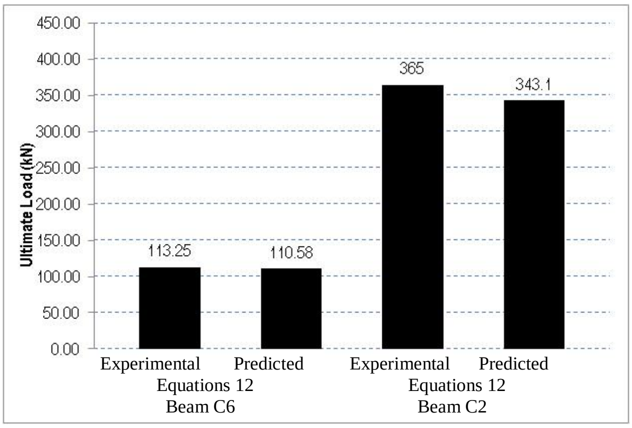

Figure 12. Comparison between experimental and predicted failure loads for beams C2 & C6.

5.2.3 Influence of stiffener spacing

This section investigates the influence of stiffener spacing, *b*, on the ultimate load capacity from centrally applied point loads (Figures 5-7). Vertical stiffeners primarily increase the buckling resistance of the web panel and are an important factor to be considered as it can influence the load capacity significantly. Figure 13 presents the failure loads for Beams C1, C5 and C6 with stiffener spacing of 450, 100 and 225mm respectively. As shown, with increasing stiffener spacing, the experimental load capacity drops significantly from 236kN to 113kN for 100 and 450mm respectively.

However, Beam C5 was tested with no vertical stiffener above the support which resulted in the bottom flanges failing prematurely through bending (Figure 14) and the test had to be stopped. The difference, therefore, between the predicted and measured failure load may be explained by this experimental set-up error. If the stiffener spacing is too small, the stiffener itself may buckle vertically.

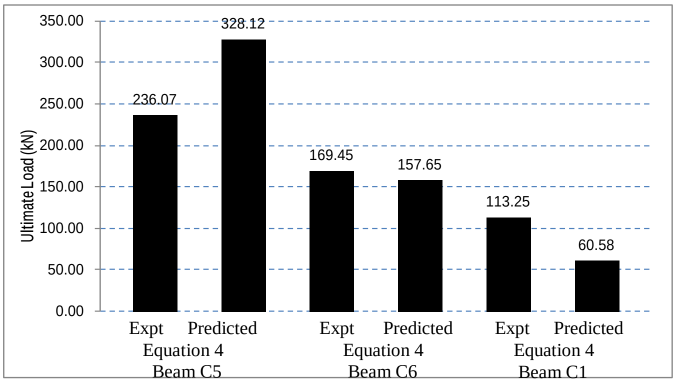

Figure 13. Comparison between experimental and predicted failure loads for beams C1, C5-6.

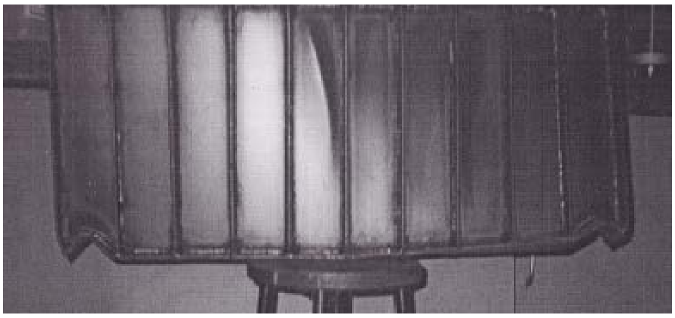

Figure 14. Bending of the bottom flange above the supports with to no vertical stiffener in place (Beam C5).

6 CONCLUSIONS

The paper presents an experimental programme to assess if small scale steel bridge plate girder beams could be used to mimic the behaviour of large scale beams. A review of previously developed empirical and theoretical equations using full-scale tests to calculate the failure load is presented. For this, a number of small scale sections, each 1000mm long, were subject to a series of patch and concentrated (point) loads at mid-span.

The findings from the patch loading tests have shown that an approximate linear increase in load capacity with increasing web thickness exists with yielding of the web panel the main failure mechanism for thinner webs. Comparisons between the experimental and predicted loads have shown that the relationship between the square of the web thickness and the failure load appears to be valid. For thicker webs, the method of failure was web bending but a poor correlation exists between the experimental and predicted loads despite the assumed method of failure occurring. Despite this, it is concluded that these sections gave reasonable comparisons between the experimental and predicted failure loads and of the behaviour under loading.

The main findings from the concentrated loads at mid-span were that, for relatively thick web plates, the webs yielded before they buckled and expressions developed for thick webs are valid for scale sections also. For thick flange plates, the assumption that the distance between plastic hinges becoming equal to the stiffener spacing also appears to be valid as a picture frame failure mechanism did occur. The variation in stiffener spacing shows that the closer the stiffeners are, higher failure can be expected. Also, the experimental tests demonstrated that as a tension field cannot develop in the web, the load causes the vertical stiffener to buckle as the load is not spread into the web. Again, the experimental and predicted loads of these small sections, as well as their behaviour, all point to a correlation with large scale plate girder beams.

It is postulated that these small scale sections can offer a reasonably accurate prediction of the failure load and behaviour of larger, full-scale members and has the potential of saving the need for large scale testing. However, further testing and numerical modelling would be needed to make any definitive recommendations.

7 ACKNOWLEDGEMENTS

The author wishes to thank the technicians in the Civil Engineering department at Trinity College Dublin.

8 REFERENCES

[1] Basker, K and Shanmugam, N.E (2003) Steel-concrete composite plate girders subject to combined shear and bending, *Journal of Constructional Steel Research*, 59: 531–557.

[2] Shanmugam N.E and Baskar K (2002) Behavior of steel–concrete composite plate girder. *Proceedings, SSRC, Annual Stability Conference*: 425–440.

[3] Baskar K, Shanmugam N.E and Thevendran V (2002) Finite element analysis of steel-concrete composite plate girder, *Journal of Structural Engineering*, 128(9): 1–11.

[4] Timoshenko, S.P and Gere, J.M (1961) *Theory of Elastic Stability*, 2nd Edition, McGraw-Hill.

[5] Porter, D.M, Rockey, K.C and Evans, H.R (1975) The collapse behavior of plate girders loaded in shear, *The Structural Engineer*, 8(53): 313-325.

[6] Lee, S.C and Yoo, C.H (1998) Strength of plate girder web panels under pure shear, *Journal of Structural Engineering*, ASCE, 124(2): 184-194.

[7] Roberts, T.M (1983) *Patch loading on plate girders*, Plated structures, Stability and Strength, Ed. R. Narayanan, Applied Sciences Publishers: 77-102.

[8] Grandholm, C.A (1960) *Tests on girders with extremely thin web plates*, Report 202, CTH, Goteborg.

[9] Roberts, T.M (1981), Slender plate girders subjected to edge loading, *Proceedings of the Institute of Civil Engineers*, 2(71): 805-819.

[10] Roberts, T.M and Rockey, K.C (1977) A method for predicting the collapse load of a plate girder when subjected to patch loading in the plane of the web, *University College Cardiff, Department of Civil and Structural Engineering Report*.

[11] Rockey, K.C (1971) An ultimate load method for the design of plate girders, *Proceedings IABSE Colloquium on the design of plate and box girders for ultimate strength*: 253-258.

Sustainable Maintenance and Analysis of Rail Transport Infrastructure (SMART rail)

K. Gavin[1], A.J. O'Connor[2], E.J. O'Brien[1,2], M. Tucker[2]
[1]School of Architecture, Landscape and Civil Engineering, University College Dublin, Belfield, Dublin 4, Ireland.
[2]Roughan & O'Donovan Innovative Solutions, Arena House, Arena Rd, Sandyford, Dublin 18, Ireland.
email: kenneth.gavin@ucd.ie, alan.oconnor@rod.ie, eugene.obrien@rod.ie, mark.tucker@rod.ie

ABSTRACT: Safe and efficient transport infrastructure is a fundamental requirement to facilitate and encourage the movement of goods throughout the European Union. Currently there are in the region of 215,000km of railway lines in the EU. Many of these were not built to conform to modern design standards and suffer from poor maintenance strategies. The SMART Rail project brings together experts in the field of rail transport infrastructure from across Europe to develop state of the art inspection, monitoring and assessment techniques. This will allow rail operators to manage ageing infrastructure in a cost effective and environmentally friendly manner. RODIS will develop models to greatly improve the ability of the track owners to predict the future condition of their infrastructure. A probability based framework will be developed for optimised whole life management of the infrastructural elements. This will encompass not just bridges but all aspects of rail infrastructure such as track susceptibility to settlement and the stability of slopes and embankments. Sensor information will be incorporated into the structural safety models allowing real time analysis to be performed. This will enable the rate of deterioration of the infrastructure elements to be determined and allow implementation of an optimised and cost effective intervention strategy before any significant damage occurs.

KEY WORDS: Sustainable transport, railways, Structural Health Monitoring (SHM).

1 INTRODUCTION

In its mid-term review of the White Paper on Transport [1] the European Commission proposed concentrating on co-modality, the optimal use of all modes of transport combined or otherwise. Whilst good progress was noted in the area of creating a true internal European market in the aviation and road transport sectors, rail transport had not performed as well. There has been some progress – the TransEuropean Transport Network (TEN-T) program, the deployment of the European Rail Traffic Management System (ERTMS), and technical specifications for the application of Telematics Applications to Freight (TAF), were identified as being positive steps towards achieving the policy of creating an efficient European freight network. *The key obstacle to the development of the rail network was identified as the quality and reliability of the infrastructure.*

Several European countries have highly advanced rail networks where the primary areas of concern in relation to infrastructure performance are related to achieving ever higher network speeds. In new member states such as Slovenia, accession states including Croatia and even in some Western European countries with relatively well developed economies, historic lack of investment in rail infrastructure had led to the situation that some elements of the network are in very poor condition. In these countries, parts of the rail infrastructure would be deemed to have reached the end of its useful life when analysed using conventional assessment methods. When incidents occur such as structural failures or derailments, it is common practice in certain regions to simply close the line. Because of the lack of viable alternative modes of transport, such drastic action cannot be adopted in most countries.

Efforts to improve transport safety within the EU have led to significant reductions in fatalities in the last 20 years. Road fatalities in the EU-27 decreased from approximately 76,000 per year in 1990 to around 39,000 in 2008. When compared with road transport, rail is a historically safe mode of transport. Although the number of journeys by road is significantly higher, in this time period there were over 82,000 million kilometres of train journeys undertaken in the EU as a result of which only 1,814 fatalities occurred. Evans [2] provided detailed consideration of the statistics related to rail accidents and noted that the majority of fatalities were caused by collisions, derailment and accidents at level crossings. Again, sustained efforts at improving safety have resulted in the number of fatalities per billion train kilometres reducing from an average of 4 in 1980, to 1.5 in 2009. Climate change effects are increasing the burden on ageing transport networks with the incidence of infrastructure failure increasing. On the 12th of April 2010 a landslide initiated by heavy rainfall, caused the derailment of a train at Merano, in Italy (see Figure 1). Nine people died in the accident and 28 were injured. Similar recent incidents occurred in Guilin, China, on the 23rd of May 2010 where a landslide on the track caused a crash which resulted in 19 fatalities, and near Wellington, New Zealand, on 30th September 2010, a landslide caused a passenger train to derail and hit an oncoming service.

The construction of the trans-European transport network (TEN-T), which aims to provide interconnection and inter-operability of national transport networks within the EU, is seen as vital for the economic competitiveness of the Union and is central to the objectives of achieving balanced and sustainable development. The Cork-Dublin-Belfast rail line in Ireland is one of the 30 TEN-T projects. The Irish railways were amongst the first constructed in Europe, and the 180m span Malahide viaduct which carries the Dublin-Belfast line just North of Dublin is one of the oldest railway viaducts in the world.

Figure 1. Rainfall induced slope failure at Merano, Italy.

In early August 2009 a sailor noticed unusual currents developing around one of the piers of the viaduct and reported this to the network operator. A visual inspection was performed on August 18th and no unusual distress to the structure was noted. On August 21st the pier collapsed as a local passenger train crossed the viaduct and the Belfast-Dublin express service approached. The collapse, which was caused by scour of the foundations (which was not visible to the inspector) caused the line to be closed for seven months and a repair bill in the region of €4 million. The scour problem which caused the failure was accelerated by high flows in the estuary caused by recent flooding.

Figure 2. Collapse of Malahide viaduct.

The SMART Rail concept is to provide a whole life cycle tool which will allow infrastructure operators to optimise the existing, ageing European rail network and ensure it remains operable into the future in the context of increased traffic volume and loading, with particular consideration for increased freight capacity. The techniques must consider the effects of changing climate on infrastructure, for example; incidents of flooding causing accelerated scour of bridge foundations, high intensity rainfall events causing slope failures and freeze-thaw action causing damage to bridge and tunnel structures.

The SMART Rail consortium brings together experts in the fields of infrastructure assessment in the road and rail industries, national infrastructure operators and specialist SME's to achieve these critical aims.

In order to achieve the SMART Rail concept, the following critical and interdependent elements will be developed:

1. A sensor network embedded in key elements of rail infrastructure. These will collect real-time in-situ measurements of key parameters which will be transmitted via an advanced IT network to provide critical input data.
2. State of the art Structural Health Monitoring (SHM) procedures which will provide up to the minute assessments of the safety of the infrastructure elements.
3. A suite of low-cost remediation measures that are region-specific, provide minimal disruption and are environmentally friendly will be investigated. These will be capable of providing short-term remedial solutions for critical sections of the network identified by the SHM models.
4. The sensor networks and SHM techniques will be implemented at demonstration sites (in Slovenia, Hungary and Ireland). After assessments of current safety have been undertaken environmentally friendly forms of remediation will be undertaken and the effect in terms of SHM will be quantified.

2 PROJECT STRUCTURE

There are four main research Work Packages (WPs) in the SMART Rail project, which are highlighted in Figure 3.

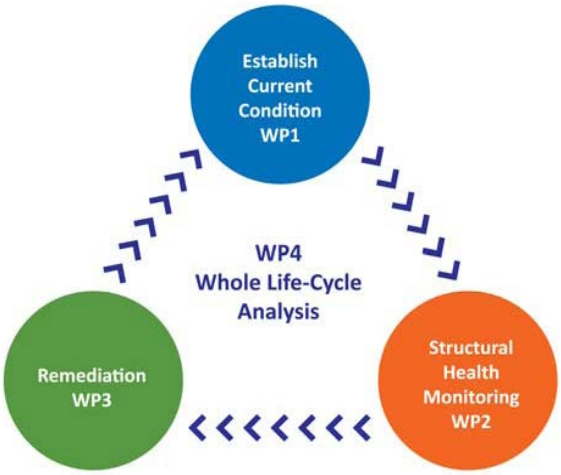

Figure 3. Smartrail Work Packages.

WP 1 examines development of integrated monitoring systems utilising embedded sensor technology to bring about a change in the traditional visually based inspection techniques. WP 2, which is being led by the authors, focuses on the development of models to greatly improve the ability of track owners to predict the future condition of infrastructural elements and to develop efficient maintenance programmes for infrastructure that requires renewal or replacement. WP 3 specifically examines sustainable technologies for the effective rehabilitation and strengthening of older existing rail infrastructure, while WP 4 considers Whole Life Cycle Analysis to assess railway infrastructure rehabilitation techniques both economically and environmentally. This paper subsequently focuses on WP2, highlighting the methodology to be investigated and employed.

3 ASSESSMENT AND MODELLING/STRUCTURAL HEALTH MONITORING

3.1 State of the Art

The current methods of track inspection for the railway networks considered within this project consist largely of visual inspection techniques. The benefits of such an approach are obvious in that trained inspectors and engineers develop intimate knowledge of the visual condition of existing infrastructure and in some cases (e.g. where drainage channels have become blocked) can organise fast remedial works. A further advantage is that it is cost effective as the inspectors are typically employees of the network operator. However, several disadvantages of visual inspections also exist that need to be addressed when new assessments methods are developed:

- safety – visual inspections involve staff walking on usually live railway lines,
- continuity – when experienced staff retire, their knowledge is lost. This was identified as a key factor in the public enquiry of the Malahide Viaduct failure in Ireland (Figure 2), which found that the engineer who performed the critical visual inspection did not in fact have vital information on how the structure maintained stability, and most importantly
- a visual inspection of a slope, tunnel or bridge will not reveal whether some deep-seated mechanism such as a weak soil layer, reinforcement corrosion in concrete or scour beneath a foundation in a river is likely to result in imminent catastrophic failure. For these reasons it is vital that reliable means of providing real-time information on critical sections of infrastructure are deployed.

Assessment of the civil engineering infrastructure of railway networks such as bridges, tunnels and slopes is traditionally performed by defining a model which includes the problem geometry, material properties and loading conditions. Partial safety factors are applied to the loads and material properties (i.e. loads are increased and resistance is decreased) and a snap-shot estimate of the safety of the structure in its current state is obtained. The advantage of the traditional approach is that it is easy and convenient to use. However, the disadvantage of using these techniques for the assessment of existing infrastructure is that, because of adopting unduly conservative safety factors, the capacity and ultimately the remaining safe life of the structure can be underestimated, leading to unnecessary and potentially costly repair works.

In bridge structures, Structural Health Monitoring (SHM) for assessing the performance of a new structure during construction [3] or in its as-built state [4] and the assessment of performance of any rehabilitation [5] or the evolution of safety of a degrading structure [6] are available. The sensor data are analysed to develop SHM markers. The markers typically seek to detect varied events, sudden events and the evolution of the performance of the structure with time. Typically, they include identification of events in the form of some kind of an outlier and the characterisation and calibration of a certain time-span in the form of a defined domain of values. Wavelet based analyses are gaining significant popularity in this regard in the scientific literature [7]. In terms of approach, statistical techniques [8, 9, 10] have also been shown to have great promise. There is some limited existing work based on experiments of full scale bridges. A number of them consider wavelet based techniques [11, 12], while the use of various monitoring devices have also been investigated. Data dependent numerical and statistical algorithms have been observed to be very successful [13, 14] in identifying events. These experiments are extremely important since they not only provide a high degree of confidence regarding the use of a method but also delineate the practical limitations and problems associated with such detection.

To date sensor information has mostly been employed in addressing specific problems in bridge monitoring, maint-enance and management. The direct translation of such data is, as yet, not available for a general condition rating. Some research projects have started to link bridge ratings with sensor data [15]. In principle, such a correlation or a ranking has been seen to be of great importance although work carried out in this regard has been limited to visual inspections [16, 17]. It is concluded that the development of algorithms to link continuously observed sensor data with the rating of a bridge would be of significant benefit in monitoring the safety of a structure. The condition rating derived in this process would be significantly more robust than those currently available for non-instrumented bridges due to the reduction in both epistemic and aleatory uncertainties.

3.2 Probability Based Framework

A probability based framework such as that shown in Figure 4 will be developed for the optimized whole life management of railway infrastructural elements/networks. It will encompass, not just rail structures, such as bridges, but all aspects of rail infrastructure such as track susceptibility to settlement and the stability of slopes that may result in landslides onto the track.

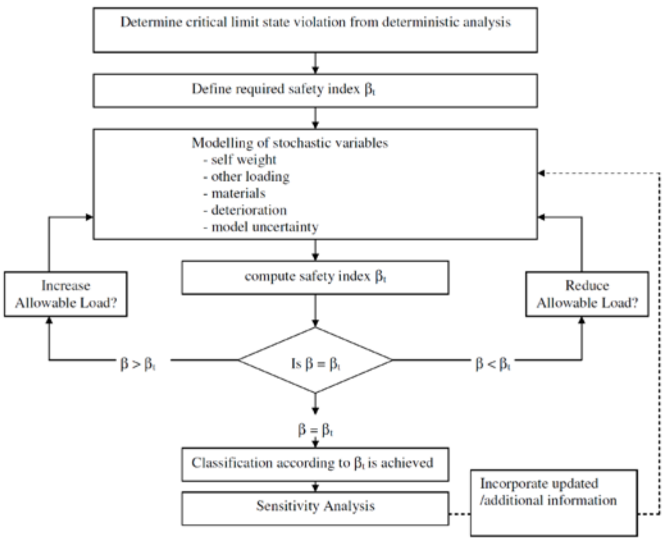

Figure 4. Probability based framework.

This cyclic process will involve determination of a safety index, β_t, at the current time t, allowing real time monitoring of the safety of the system. This continuous 'safety loop' will allow the model to be updated in real time, using a technique such as Bayesian updating, so any deterioration in the safety index will be detected at an early stage. A key element of this approach is the incorporation of data acquired from in-situ sensors into the structural model allowing a more robust determination of the safety of the infrastructure.

Figure 5. Incorporation of sensor data into computer model.

This enables scheduling of preventative action before significant damage occurs to the infrastructure element being monitored, allowing optimization of the rehabilitation efforts to ensure the service life of the infrastructure is maximized in a cost effective manner (Figure 6).

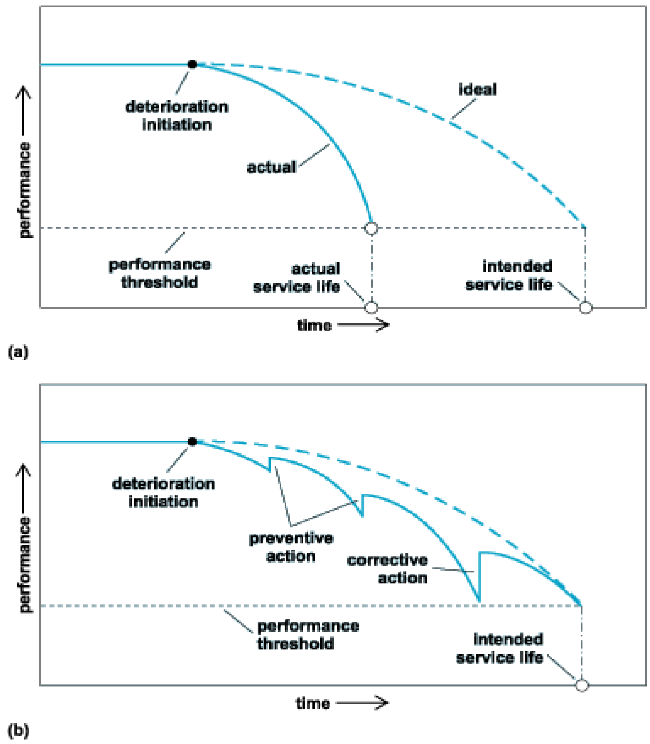

Figure 6. Optimization of service life of infrastructure.

Incorporation of sensor data will not only allow real time updating of the structural model but will also enable deterioration under the surface to be detected that would be missed by conventional visual inspection techniques (e.g. such as that seen in the Malahide Viaduct collapse – Figure 2).

3.3 Slope Stability

Reliability theory and probabilistic approaches are traditionally focused on structural applications such as bridges, however, the frequency and importance of infra-structural elements such as slopes and embankments and the resulting disruption that would occur as a result of failure of these elements, makes them a central consideration in the SMART Rail project. Figure 7 shows the failure of a slope near Castlebar, Co. Mayo.

Figure 7. Slope failure near Castlebar, Co. Mayo.

For slope stability, both below and above the track, models will be developed of rain infiltration, taking account of expected changes in climate and the resulting reliability of slopes. There will be a particular focus on 'legacy rail track' which are much steeper than those built for modern infra-structure networks. Input will be taken from a so-called 'smart slope' with sensors measuring stress, water content and slope deformation. Data from on-site weather stations will also be incorporated. Other inspection techniques such as Ground Penetrating Radar (GPR), used to obtain geophysical measurements, will be investigated for use in the reliability models.

For all the analysis techniques and models developed, direct links will be established with existing approaches allowing probabilistic techniques to be incorporated without completely overhauling current methods. A simplified approach to infrastructure assessment will also be developed, bench-marked against the advanced probabilistic techniques described above. This will ensure the new assessment methods will be adopted widespread across the railway industry down to a local level.

4 CONCLUSIONS

This paper outlines the Marie Curie FP7 SMART Rail research project. The goal of the project is to provide a framework for infrastructure operators to ensure the safe, reliable and efficient operation of ageing European railway networks. This will be achieved through a holistic approach developing whole life cycle cost models which will consider input from state of the art inspection, assessment and remediation techniques. WP 2, being led by the authors, focuses on developing degradation models for real time monitoring of the health of rail infrastructure elements. This will include not just structures, such as bridges, but also the stability of geotechnical elements such as embankments and slopes. The outputs from the project will result in enhanced safety, reliability and capacity of the rail infrastructure network and will address European policy in the areas of transport safety, security, and inter-modality.

ACKNOWLEDGMENTS

SMART Rail is a Marie Curie 7th Framework Project funded under the 'Collaborative Project: Small or medium-scale focused research project' call. The Project commenced in September 2011 and is continuing for 3 years until August 2014.

REFERENCES

[1] EU, *A sustainable future for transport: towards an integrated, technology-led and user friendly system*, 2009 (www.tracea-programme.eu)

[2] Evans, A.W. (2010), 'Fatal train accidents on Europe's railways; 1980-2009, working paper, Centre for Transport Studies, Imperial College London.

[3] Bueno A., Torres B., Barrera D., Calderon P. and Sales P. (2010) 'Monitoring of a Steel Incrementally Launched Bridge Construction with Strain and Temperature FBG Sensors'. *Proceedings of SPIE, Optical Sensing and Detection.*

[4] Idriss R.L. and Liang Z. (2007), 'Monitoring of an Interstate Highway Bridge from Construction Thru Service with a Built- In Fiber Optic Sensor System', *Proceedings of SPIE, Sensors and Smart Structures Technologies for Civil, Mechanical and Aerospace Systems.*

[5] Fujino Y. (2002) 'Vibration Control and Monitoring of Long Span Bridges – Recent Research, Developments and Practice in Japan', *Journal of Constructional Steel Research*, 58(1); 71-97.

[6] Kim J.T., Park J.H. and Lee B.J. (2007), 'Vibration Based Damage Monitoring in Model Plate Girder Bridges under Uncertain Temperature Conditions', *Engineering Structures* 7, 1354-65.

[7] Taha M.M.R, Noureldin A, Lucero J.L. and Baca T.J. (2006), 'Wavelet Transform for Structural Health Monitoring: A Compendium of Use and Features', *Structural Health Monitoring*, 53, 267-95.

[8] Sohn H., Farrar C.R., Hunter N.F. and Worden K. (2001), 'Structural Health Monitoring using Statistical Pattern Recognition Techniques', *ASME Journal of Dynamic Systems, Measurement and Control*, 123(4); 706-11.

[9] Omenzetter P., Brownjohn J.M.W., and Moyo P. (2004), 'Identification of Unusual Events in Multi-Channel Bridge Monitoring Data', *Mechanical Systems and Signal Processing*, 18, 409-30.

[10] Pakrashi V., Basu B. and O'Connor A. (2009), 'A Statistical Measure for Wavelet Based Singularity Detection', *ASME Journal of Vibration and Acoustics*. 131(4), 23-26.

[11] Moyo P. and Brownjohn J.M.W. (2002), 'Detection of Anomalous Structural Behaviours using Wavelet Analysis', *Mechanical Systems and Signal Processing*, 16(2-3), 429-45.

[12] Brownjohn J.M.W., Moyo P., Omenzetter P. and Chakraborty S. (2005), 'Lessons from Monitoring the Performance of Highway Bridges', *Structural Control and Health Monitoring*, 12, 227-44.

[13] Sohn H., Czarnecki J.A. and Farrar C.R. (2000), 'Structural Health Monitoring using Statistical Process Control', *ASCE Journal of Structural Engineering*, 126(11), 1356-63.

[14] Sohn H. and Farrar C.R. (2001), ' Damage Diagnosis using Time Series Analysis of Vibration Signals', *Smart Materials and Structures*, 10, 446-51.

[15] Ramniceanu, A. (2004), *Correlation of Corrosion Measurements and Bridge Conditions with NBIS Deck Rating*, MSc Thesis,Virginia Polytechnic Institute and State University.

[16] Estes, A.C. and Frangopol, D.M. (2003) 'Updating bridge reliability based on bridge management systems visual inspection results', *Journal of Bridge Engineering (ASCE)*, 8(6), 374–382.

[17] Akgul, F. and Frangopol, D.M . (2003). 'Rating and reliability of existing bridges in a network', *Journal of Bridge Engineering (ASCE)*, 8(6), 383–393.

Authors Index

DIT
Dublin Institute of Technology
Institiúid Teicneolaíochta Átha Cliath

TRINITY
COLLEGE
DUBLIN

supported by sfi Science Foundation Ireland

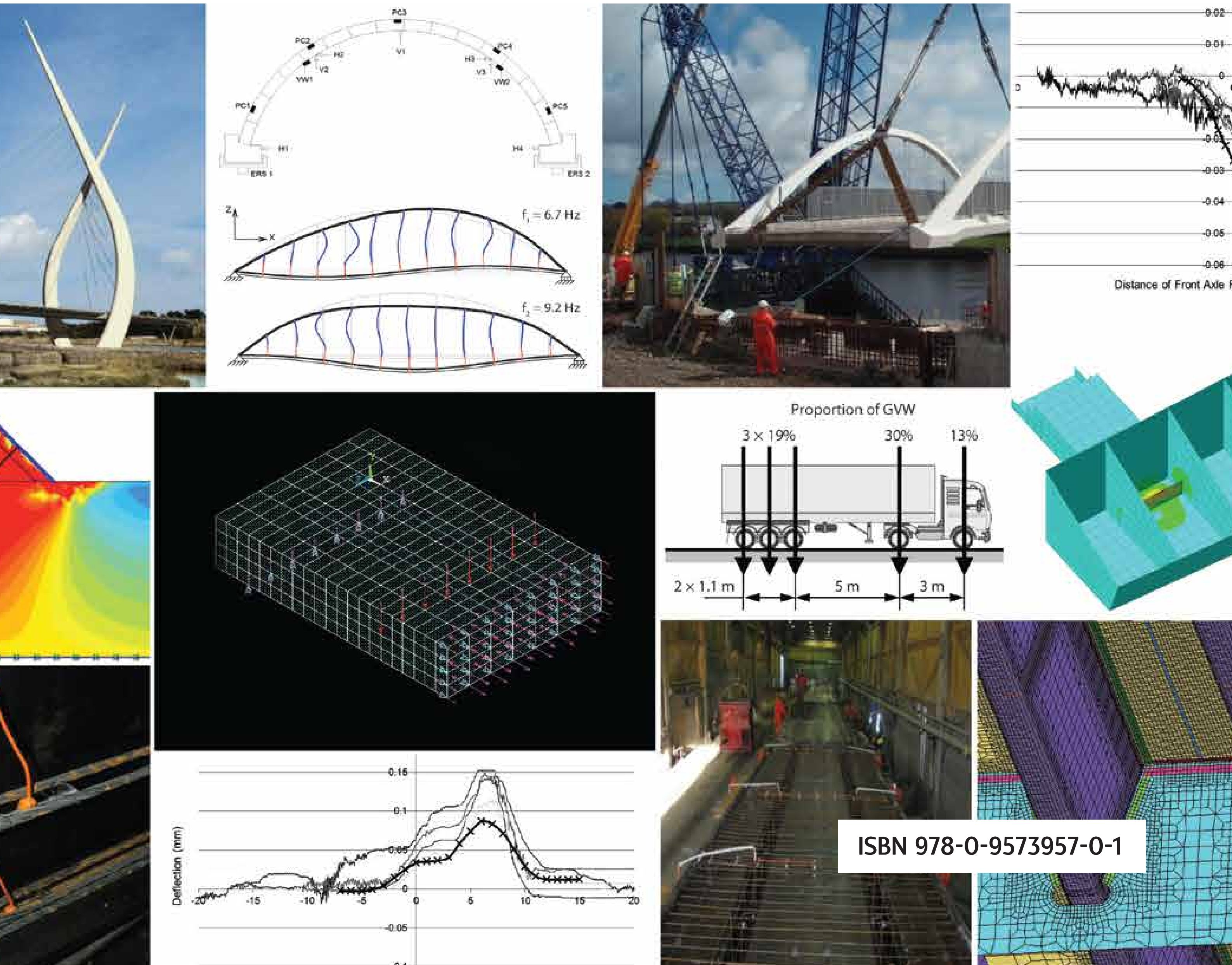

ISBN 978-0-9573957-0-1